Design and Application of High Resolution and Multiobject Spectrographs:

Dynamical Studies of Open Clusters

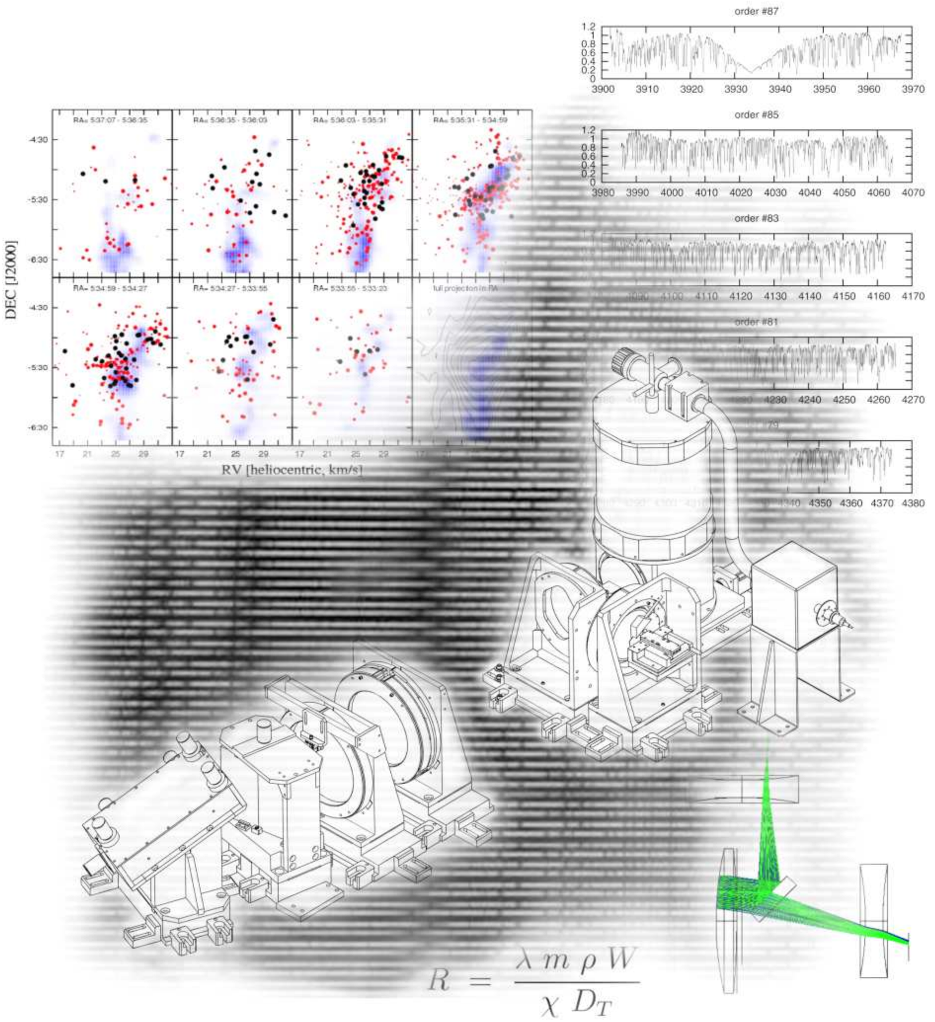
order #87
order #85
order #83
order #81
DEC [J2000]
RV [heliocentric, km/s]
full projection in RA
$R = \frac{\lambda\, m\, \rho\, W}{\chi\, D_T}$

A PhD Thesis

By Gábor Fűrész

Advisors: Andrew Szentgyorgyi and Dave Latham

University of Szeged, Hungary
2008

Minden tanítómnak, akik elvezettek ideáig,
elsősorban annak a kettőnek, akik a legtöbbet adták:
szüleimnek

To all of my teachers who led me here,
especially the two who gave me the most:
my parents

Abstract

My intention writing this thesis was not just to summarize and document what I have learned and accomplished since graduation. I was rather aiming to provide the reader with a comprehensive description on the theory and practice of modern astronomical spectrographs design, and to present some application examples of such instrument.

The word “comprehensive” in this context does not mean I tried to cover every single detail of the design process, but I was hoping to give all the theoretical background necessary to follow and justify the steps of the design and construction of a specific spectrograph I built in collaboration with the CfA OIR instrumental group. A significant fraction of this thesis (Part I) is therefore all about instrumentation. Chapter 1 might seem going too far back to the basics, but, again, I wanted to aid the reader with almost all theoretical background information. At the same time this introductory chapter is a little bit biased towards a specific type of spectrographs: a high resolution, high throughput, single object fiber-fed echelle – the subject of chapter 2. Through the example of TRES (the Tillinghast Reflector Echelle Spectrograph) I show how the theory applies to design and construction. TRES was just commissioned not so long ago, and so I barely had the chance to characterize the instrument, to carry out some scientific observations. Nevertheless I am able to close that chapter with the discussion of some initial results.

However, since the making of TRES took more than four years, the tool for the science examples discussed is an other instrument: Hectochelle. The alignment and characterization of this multi-object, fiber fed echelle was one of my first tasks as a graduate student, therefore I felt to spare a chapter (3) on this work. Especially since high precision radial velocity measurements carried out with multi-object instruments is not straightforward. A lot depends on instrumental stability and calibration system design. Discussing these instrument-specific details leads to some general conclusions, which are not well documented in the literature. Therefore I attempt to summarize these in chapter 4, and this concludes the Instrumentation part.

Part II is a short transition from instrument building to science applications, describing the specific data reduction (chapter 5) and analysis (6) tools used in Part III. The main emphasis is on describing how a grid of synthetic spectra is used to determine the most accurate radial velocities and derive astrophysical parameters for the stellar targets.

In Part III science applications of Hectochelle are presented: utilizing the multi-object capability for collecting hundreds of stellar spectra in open clusters in order to unveil kinematical structure. Because most stars are formed in clusters the processes responsible for cluster formation are important to include in any consideration of the mechanisms of star formation. Observations of very young clusters can provide clues to the initial conditions of cluster formation if the cluster has not dynamically relaxed. With this goal I have studied two of these very young systems, NGC 2264 (chapter 8) and the Orion Nebula Cluster (chapter 9). The outcome of these projects were the first direct evidence of kinematical substructure, likely left over from the primordial hierarchy. A third study is about a more evolved and relaxed cluster, M38 (NGC 1912). Despite of its age there is some dynamical “heat” in that system, likely caused by an other nearby cluster, NGC 1907. In chapter 10 I show some interesting findings regarding the kinematics of this cluster pair.

To conclude, in chapter 11, I list some ongoing instrumental and science projects I am involved in, which are clear continuation of those topics discussed in detail throughout this thesis.

Összefoglaló

Előszó

Jelen értekezsében a diplomám megszerzése utáni munkám, valamint az annak során elért eredményeim összefoglalását kívántam adni. Tevékenységem két fő fonálon futott, egymással párhuzamosan, és egymással szoros összeköttetésben: nagyfelbontású spektrográfok tervezése és építése mellett azok tudományos alkalmazásaival foglalkoztam. Mint azt alább is hagnsúlyozni próbálom, a műszerfejlesztés és tudományos kutatás egymást serkentő, szimbiotikus egységet alkot. Éppen ezért mindkét elemet fontosnak éreztem megtartani dolgozatomban is, annak ellenére, hogy a terjedelmi korlátok túllépése ennek elkerülhetetlen következménye volt. Ezért a Bírálók és Véleményezők, valamint a dolgozatot Olvasók szíves elnézését kérem — bár őszintén rémelem, hogy indokaim legalább érthetőek, ha el nem is fogadhatóak. Ez utóbbi esetben tisztelettel kérném, tekintsék az első 126 oldalt egy hosszúra sikeredett előszónak, mely nem képezi részét a hivatalos dolgozatnak. A fennmaradó (egységét kismértékben elveszítő) rész – a szabályzatnak megfelelően az egész oldalas ábrák és a Kiegészítés fejezet leszámításával – alig néhány lappal haladja meg az előírt 120 oldalas maximális terjedelmet. Az értekezés logikai felépítése talán csak az egész dolgozat áttekintésekor indokolható: a spektrográfok készítésének elméleti és gyakorlati bemutatása (1, 2) során szerzett tapasztalat biztos alapot ad arra, hogy egy adott műszer (3) használata során a legkörültekintőbben megtervezett és kivitelezett mérések készülhessenek, melyek mindennemű szisztematikus hibától (4) mentesek. Ezen megbizonyosodásnak, valamint a tudományos megfigyelések elvégzésének is eszköze az adatok megfelelő kiértékelése (5, 6). A kinyert információkat pedig az adott problémakör tágabb kontextusába helyezve (7) eljuthatunk azok megfelelő értelmezéséhez s az új tudományos eredményekhez (8, 9, 10), melyek előre vetítitk a kutatás további irányát (11). Az alábbi rövid, magyar nyelvű összefoglalás azonban egy ettől kissé eltérő felépítést tükröz, s a dolgozat "hivatalos" részének kíván egy összefoglaló keretet adni.

Bevezetés

Mivel a legtöbb csillag halmazokban születik (Lada & Lada 2003), ezért a csillagkeletkezési folyamatok tanulmányozásásban alapvető fontosságú a halmazkeletkezés körülményeinek vizsgálata. Annak megértése pedig, hogy saját Napunk miként keletkezett, kulcsfontosságú a Föld és a Naprendszer születésének felderítésében. Napjainkban immár több, mint 200 Naprendszeren kívüli (exo-)bolygót ismerünk, ami egyértelműen mutatja, hogy a bolygókeletkezés egy általános folyamat. Ennek megértésehez, az idegen világok tanulmányozásához az első lépés azonban a csillagkeletkezés titkainak feltérképezése.

Ma a halmazok a csillagkeletkezési folyamatok laboratóriumaként szolgálnak a modern (különösen az infravörös és multi-objektum) megfigyelési eszközök számára, aminek köszönhetően halmaz- és csillagfejlődési ismereteink igen részletessé váltak. Az infravörös eszközök érzékenységének növekedése (mind a földfelszíni, mind az űrbeli megfigyelések esetében, l. Spitzer űrtávcső) lehetővé tette újabb fiatal csillagcsoportok felfedezését és azok minden eddiginél részletesebb tanulmányozását – annak ellenére, hogy ezen társulások gyakran sűrű por- és gázfelhőkbe ágyazódva rejtőzködnek a csillagászok szeme elől. Amennyiben sikerül ezekben a legfiatalabb halmaz-embriókban valamiféle szerkezetet felfedezni, az segítséget adhat annak megértésében, miként is alakulnak ki a csillagok ezen bölcsői, milyen folyamatok és körülmények vezetnek csillagok és bolygórendszerek kialakulásához.

Nagy, több parszek (pc) kietrjedésű csillagkeletkezési régiók esetében megfigyeltek kisebb sűrűsödéseket és elkülönülő struktúrákat (pl. az NGC 2264 fiatal nyílthalmaz, lásd Lada, Young & Greene 1993, valamint Teixeira 2006), amik a képződő halmazok építőkövei lehetnek. A közelmúlt Chandra űrtávcsővel végzett röntgen megfigyelései is alátámasztják a finomszerkezet jelenlétét keletkező csillaghalmazok esetén, ami pl. az Orion Köd Halmaz (ONC - Orion Nebula Cluster) esetében abban mutatkozik meg, hogy a centrális tartomány csillagai erősen aszimmetrikus eloszlást mutatnak (Feigelson et al., 2005). Rövid hullámhosszú obszervációk más fiatal, beágyazott csillagbölcsők esetében is feltárták a csillagok határozottan struktúrált sűrűségelolszlást (l. Broos et al. (2007) értekezése az M17 szerkezetéről).

Célkitűzés

A diplomamunkám témája egy közepes felbontású és alacsony költségvetésű spektrográf tervezése, megépítése és alkalmazási lehetőségeinek bemutatása volt, az egyetemi gyakorlati oktatás céljait segítendő. A Harvard-Smithsonian Asztrofizikai Központjának (Center for Astrophysics, CfA) doktori ösztöndíját elnyerve lehetőségem volt a csillagászati műszerépítésnek e terén, valamint a nagyfelbontású spektroszkópiai megfigyelések irányában továbblépni: egy modern echelle színképelemző megépítésén és egy több-objektum spektrográf (Hectoechelle) életre keltésésn keresztül. Nagy segítséget és ösztönző erőt jelentett a napi kapcsolat és együttműködés lehetősége olyan munkacsoportokkal és kutatókkal, akik a nagy pontosságú radiális sebességmérés (RS) terén (Dave Latham, Guillermo Torres, és társaik), valamint a csillagkeletkezés/Spitzer infravörös űrtávcsöves megfigyelések terén (Lori Allen, Charles Lada, Tom Megeath, és társaik) nagy tapasztalattal és nemzetközi szaktekintéllyel rendelkeznek.

Míg a radiális sebességmérésre és nagyfelbontású spektrumok elemzésére specializálódott kutatók az egyedi ill. kettőscsillagok, valamint manapság a bolygórendszerek fizikai tulajdonságait vizsgálják, addíg a csillagkeletkezést megérteni próbálók a rádió- és infraförös hullámhosszakon térképezik fel az optikai tartományban sokszor láthatalan módon, sűrű gázfelhők mélyén játszódó folyamatokat. A két, látszólag elkülönülő területnek azonban van egy keresztmetszete, melyre a Hectochelle műszer képességeinek megismerése során találtam rá. Ez pedig egy eddig hiányzó mozaikdarab a csillag- és halmazkeletkezésről alkotott képünkhöz, mely nagyszámú fiatal csillagot tartalmazó régiók kinematikai vizsgálata során illeszthető a képbe.

Annak ellenére, hogy számos példa ismert halmazokon belüli sűrűsödésekre a halmaztagok *kétdimenziós eloszlását* tekintve, a születőfélben lévő protocsillagok *térbeli vagy dinamikai eloszlása* (ahol a harmadik dimenziót a sebesség, mint a távolságnál sokkal könnyebben mérhető mennyiség) ezideáig relatíve érintetlen terület maradt. Holott nagyfelbontású multi-objektum spektrográfok már évek óta a kutatók rendelkezésére állnak, ezen műszerek teljes kapacitásának kihasználása csak a közelmúltban kezdődött meg e téren. Ennek részben az lehet az oka, hogy a nagyon fiatal halmazok – melyek még nagy valószínűséggel hordozzák magukban a kezdeti csillagközi anyag struktúrális jegyeit – mélyen por- és gázfelhőbe ágyazva rejtőzködnek. Emiatt az optikai tartományban igen nehezen figyelhetőek meg, s csak igen kevés közeli csillagkeletkezési zóna vizsgálható hatékonyan, hiszen a nagyfelbontású infravörös multi-objektum spektroszkópia még nem áll rendelkezésre.

A csillagkeletkezési régiók vizsgálatában a lenyűgöző m s^{-1}–os mérési pontosságnál fontosabb a statisztikailag jelentős mennyiségű adat gyűjtése. Ezt viszont konzisztens módon a legújabb nagyfelbontású több-objektum spektrográfok is csak akkor tudnak szolgáltatni, ha a mérések szisztematikus hibája elmarad a halmazdinamika esetében keresett nem is olyan nagy, pár km s^{-1} nagyságú jeltől. A lehető legnagyobb belső pontosság és -konzisztencia, a megfelelő kalibrációk, és a szisztematikus hibák kiszűrése tehát ezen műszerek esetében is alapvető, hiszen csak így juthatunk el értékelhető adatokhoz és helyes következtetésekhez. Egy műszer kifejlesztése és beható tesztelése pedig a legjobb módszer az ehhez szükséges tudás megszerzésére.

Jobban leszűkítve a doktori dolgozat tudományos célkitűzését egy konkrét halmazkeletkezési elmélet ellenőrzését vettem tervbe: a Burkert & Hartmann (2004) által leírt modell kinemtikára vonatkozó előrejelzéseinek nyomát kerestem fiatal nyílthalmazok esetében. Az elmélet szerint egyszerű izotermális, véges csillagközi gázlemezek gravitációs összehúzódásának eredményeként a kezdeti feltételektől függően olyan változatos struktúrák jönnek létre, melyek nagyban hasonlítanak különböző csillagkeletkezési régiók molekuláris hidrogénfelhőiben megfigyelt mintázatokra. Burkert & Hartmann (2004) numerikus szimulációkon keresztül megmutatta, hogy a csillagközi anyagban lévő áramlatok/ütközések nyomán keletkező kétdimenziós gázsűrűsödések gravitációs kollapszusa egy fonalszerű, elnyúlt alakzat képződéséhez vezet, melynek végpontjai tartalmazzák a kezdeti össztömeg jelentős részét. A kiszámított modellparaméterek szerint nem csak a tömeg, de a kinetikus energia nagy része is ezekben a végpontokban található, mely abnormálisan megnövekedett sebesség-diszperzióként figyelhető meg az összehúzódó felhő többi részeihez viszonyítva. A Hectochelle műszerhez való hozzáférésem lehetővé tette, hogy elsőként keressem és találjam meg ennek a “felforrósodott” dinamikának a jelét kialakulófélben lévő nyílthalmazok csillagainak háromdimenziós eloszlásában, s ezzel igazoljam a modell előrejelzéseit.

Alkalmazott műszerek és módszerek

A többszáz nagyfelbontású spektrum összegyűjtéséhez, mely lehetővé tette a radiális sebességtér és az egyedi csillagok fizikai paramétereinek feltérképezsését, a Hectochelle (Szentgyorgyi et al., 1998) nagyfelbontású több-objektum spektrográfot és az az MMT (Monolithic Mirror Telescope – Egybeöntött Tükrű Teleszkóp) távcsövet használtam. Ennek a műszernek a részletes bemutatása a 3. fejezetben található. Az MMT Obszervatórium a Smithsonian Intézet (Smithsonian Institution) és az Arizónai Egyetem (University of Arizona) közös intézménye. A távcső egy 6.5 méter tükörátmérőjű alt-azimutális szerelésű Cassegrain rendszerű műszer, mely a Mt. Hopkins csúcson található, a Santa Rita hegység (Coronado National Forest, Arizona, USA) második legmagasabb csúcsán, mintegy 55 kilométerre délre Tucson (Arizona, USA) várostól. Az MMT a Smithsonian Intézet Fred Lawrence Whipple Obszervatóriumának (FLWO) területén működik.

A Hectoechelle fejlesztésésnek utolsó fázisában, valamint képességeinek felmérésében és legelső megfigyelésekben kulcsszerepet vállalva a multi-objektum spektrográfok sajátosságait elsőkézből tapasztaltam meg. Ennek során nyílvánvalóvá vált, hogy a mérési adatok kiértékelése igen nagy körültekintést igényel a műszer bonyolultságát tekintve, valamint azt, hogy a szisztemetikus hibáknak mennyiféle forrása lehet. A nagypontosságú, több-objektum spektrográfokkal végzett, radiális-sebességeket felmérő programok technikai kihívásairól meglehetősen szűkös a szakirodalom. Ezért a tudományos mérések egyfajta megfontolt előkészítéseként is felfogható, a mérési pontosságra irányuló vizsgálataimat a 4. fejezetben foglaltam össze. A levont általános érvényességű tapasztalatok későbbi megfigyelések és műszerfejlesztési programok számára fontosak lehetnek. Ezért a 4. fejezetben leírtakat egyben tudományos eredményem egyikének is tekintem.

A csillag- és kalibrációs színképeket (utóbbi ThAr spektrállámpát használ forrásként) $R \simeq 34\,000$-es felbontással készítettem fenti műszert különböző spektrális rendekben használva, melyek a Hα, Mg (5150–5300 Å) és Li (6708 Å) vonalakat tartalmazzák. A színképek kiértékelése és a nyers adatok kalibrálására kifejlesztettem egy autonóm szoftver folyamatot, mely Linux shell keretprogram egyéb, standard képfeldolgozási- és adatbázis kezelő rutinok meghívását koordinálja (5. fejezet). A teljesen automatikus kiértékelést egy műszer-specifikus kalibrációs adatbázis kiépítése tette lehetővé. A keretprogram a Linux/UNIX bash környezetben fut, és többnyire IRAF (Image Reduction and Analysis Facility – képkiértékelő- és feldolgozó szoftver-csomag) programokat, valamint STARBASE[1] adatbázis-kezelő parancsokat hív meg. Ez az adatkiértékelési folyamat később a CfA Távcső Adatközpontjának (Telescope Data Center) hivatalos Hectochelle adatfeldolgozó folyamatává is vált.

A radiális sebességeket és a csillagok asztrofizikai paramétereit a keresztkorrelációs módszer segítségével állapítottam meg, mely részleteit a 6. fejezet diszkutálja. Az analízis során, melyet a CfA által kifejlesztett `rvsao.xcsao` IRAF programot használva végeztem, minden megfigyelt színképet egy többszáz szintetikus spektrumot tartalmazó könyvtárral vetettem össze, keresvén az obszervált színképet legjobban megközelítő párt. Ez a több mintán alapuló összehasonlítás tapasztalataim szerint nagyban növeli a radiális sebesség meghatározásának ponstosságát. A számított spektrumok a Kurucz (1992) csillagatmoszféra modelleken alapulnak, és John Morse (egyelőre publikálatlan), Munari et al. (2005) valamint Coelho et al. (2005) munkájának eredményei.

---

[1] http://cfa-www.harvard.edu/~john/starbase/starbase.html

A radiális sebességmérés műszereinek és módszereinek bemutatásáról azok alkalmazására történő átvezetést a 7. fejezet adja, melyben a fiatal nyílt csillaghalmazoknak és az ezzel összefonódó csillagkeletkezésnek adom egy rövid elméleti hátterét. Ez a fejezet áttekinti a molekuláris felhők tulajdonságait, majd az ebben a közegben meginduló csillagkeletkezés lehetséges prekurzorait, a csillagfejlődés kezdeti szakaszának főbb fázisait. Ezek fényében a célkitűzés konkrét megfogalmazása zárja e fejezetet.

Elért eredmények

Mint fentebb említettem, hozzájárulásomat a Hectochelle nagyfelbontású több-objektum spektrográf üzembe helyezéséhez (az optika végleges beállítása, hatékony kalibrációs rendszer kifejlesztése, valamint az adatredukciós folyamat automatizálása révén, amely lépések elengedhetelnek voltak a műszer sikeres alkalmazásában) fontos eredménynek tekintem. Ezen munkám során olyan általános érvényű, a hasonló műszereket érintő következtetéseket vontam le azok karaketrizálását illetve a belső pontosságukat illetően, melyek eddig teljesen hiányoztak a szakirodalomból. Megmutattam, hogy a szub-optimális hullámhossz kalibrációs rendszer és nem körültekintő optikai elrendezés szisztematikus hibák megjelenéséhez vezet. Ezek pontos felmérése után lehetőség van a korrekcióra, és az utólagos módosítás nagymértékben javítja a nagyvolumenű radiális sebességmérést kitűző programok eredményeinek belső pontosságát.

A 8. fejezetben egy fiatal nyílthalmaz, az NGC 2264 vizsgálatának eredményeit tárgyalom. E társulás esetében még kimutatható a halmaz finomszerkezete nem csak a két-, de a háromdimenziós eloszlásban (égi koordináták mellett a sebességtérben) is. Szignifikáns RS mintázatot találtam ebben a csillagkeletkezési régióban, mely a korábbi megfigyelésekből ismert hierarchikus szerkezettel rendelkezik. Megmutattam, hogy ez a halmazt létrehozó gázfelhő eredeti szerkezetéből visszamaradt mintázat, mivel a dinamikai relaxációs folyamatoknak nem volt lehetőségük a halmaz korára való tekintettel ezen nyomokat teljesen eltörölni. Eredményeim jó összhangban vannak az infravörös többletet mutató források eloszlását feltáró vizsgálatok következtetéseivel, melyek szintén azt mutatják, hogy a legfiatalabb (még anyagkoronggal rendelkező) csillagok előfordulási valószínűsége az eredeti keletkezési helyek mentén magasabb. Mérési eredményeim alapján állítható, hogy a csillagok látóirányú mozgása nagymértékű összhangot mutat a halmazban még mindíg jelen lévő gáz sűrűbb elemeinek kinematikájával. Ezt a ^{13}CO molekula rádiómegfigyelései és az optikailg detektálható csillagok sebességértékeinek összevetése egyértelműen alátámasztja. Ezért azt a következtetést vonhatjuk le, hogy a halmazkeletkezés során a molekulkáris felhőben kialakult szerkezet a született csillagok eloszlás-mintázatában egyértelműen tetten érhető. Ezen kezdeti mintázat kialakulása a Burkert & Hartmann (2004) féle modell szerint várható jelenség: numerikus szimulációk azt mutatták, hogy a kiterjedt gázfelhők gravitációs kollapszusának természetes következménye a kezdeti apró inhomogenitások felerősödése és egy közelítőleg filamentáris szerkezet kialakulása, mely gyakran megfigyelt eloszlás csillagkeletkezési régiók esetében.

A 9. fejezet az Orion Köd Halmazban és annak közvetlen környezetében kivitelezett radiális sebesség felmérést írja le. Ennek eredményeként azt találtam, hogy a régió gáz- és csillag komponensei igen szoros tér- és sebesség-eloszlásbeli összhangot mutatnak. Vagyis igen fiatal a formáció, kora alig egy áthaladási időegység, különben a gravitációs kölcsönhatásoknak sokkal jobban ki kellett volna simítani a megfigyelt finomszerkezetet és jobban elkülöníteni a két komponenst. Ez a más korábbi módszerektől független kormeghatározás $\sim$1 milló évet eredményez, ami a halmaz fizikai méretén és az általam mért 3.1 km s^{-1} nagyságú sebességdiszperzión alapul. A megfigyelési eredményeket a Hartmann & Burkert (2007) féle elméleti modellel összevetve a következő képet rajzoltam fel az Orion Köd Halmazról és környezetéről:

nagy skálán a gáz és a csillagok erős sebesség-gradienst mutatnak az elnyúlt, filamentáris szerkezet mentén észak–déli irányban, ami rotációnak vagy ellentétes irányú mozgásból fakadó nyírásnak az eredménye. A felvett pozíció-sebesség térképek gravitációs gyorsulást mutatnak, mely a halmaz központja felé irányul. A Trapéziumtól északra található gáz- és csillagsűrűsödés kissé az előtérben helyezkedik el és a központ felé esik. A déli régió valószínűleg szintén a centrális tartomány felé mozog, de ennek jelei kevésbé egyértelműek az északi karhoz hasonlítva.

A megfigyelések alapján plauzibilis az a feltevés, miszerint a csillagkeletkezési folyamatok visszacsatolási energiája a déli régió gáztartalmának "kifújását" eredményezte. Ez a gyorsuló sűrűségfront egy kisebb csillag-pupoláció keletkezését indította meg, mely a ma megfigyelhető, enyhe kékeltolódást mutató előtércsillagokat alkotja. E mellett az indukált csillagkeletkezésre utaló más jeleitket is találtam a halmazban, egy pozicióban jól körülhatárolható kisebb csillagcsoport formájában. A sebesség-térben ezen csillagok a környező objektumokkal ellentétben jelentős kékeltolódást és egyértelmű csoportosulást mutatnak a gázhoz viszonyítva. A halmaz ezen területén több ismert Herbig-Haro objektum található, melyek elnyúlt alakzatai az OKH központi vidéke, a Trapézium felé mutatnak. Ez összhangban áll azzal a következtetéssel, hogy a centrális vidéken jelenleg is legaktívabban folyó csillagkeletkezés er?s anyagkiáramlást eredményez, mely kifújás további csillagkeletkezést indukál a külsőbb területeken.

A 10. fejezetben megfigyelési bizonyítékát adom annak, hogy idősebb nyílthalmazok közötti gravitációs kölcsönhatás szétszórhatja a halmaztagokat, amely folyamat a Naphoz hasonló egyedülálló csillagok egyik lehetséges eredete. A legtöbb csillag halmazokban keletkezik, azonban a gravitációsan kötött, idős halmazok száma feltűnően alacsony a fiatal, csillagkeletkezési folyamatokat mutató bölcsőkéhez képest. Vagyis a gázba ágyazott társulások tagjai nagy valószínűséggel szélednek szét alig néhány millió éves időskálán. Az idősebb kort megért, kötötté vált halmazok is felbomolhatnak ár-apály erők hatásásra, amiket a hatalmas molekuláris felhők közelében vagy a galaktikus korong sűrűbb síkján történő el-, illetve áthaladás kelt. Az NGC 1907 és 1912 (M38) halmazok alkotta páros esetében viszont nagy valószínűség szerint a két halmaz gravitációs közjátéka szórja szét a csillagokat. Erre a két társulást összekötő ár-apály híd és a szemközti oldalakon mutatkozó "uszály" enged következtetni. Ezen kinemtikai elemek kimutatásával a Tejútrendszerben ismert második kölcsönható kettős rendszert sikerült kimutatni.

Egyik legfontosabb (fenti módon átalakított logikai szerkezetbe ugyan nem illő) eredményemnek tartom, hogy megterveztem és megépítettem egy nagyfelbontású, teljes vizuális tartományt lefedő, korszerű echelle spektrográfot (TRES – Tillinghast Reflector Echelle Spectrograph), a CfA Optikai és Infravörös tagozatának (Optical and Infrared Division) műszerépítő csoportjával együttműködve. A spektrográf 2007 során került átadásra a FLWO 1.5 méteres Tillinghast távcsövének műszereként. A "hivatalos" dolgozat elejének tekintendő 2.10 alfejezet adja az első tesztek és mérési eredmények leírását. Ezek azt mutatják, hogy a spektrográf az $\sim$5 $m\ s^{-1}$ sebességmérési pontosság elérésére képes a szimultán ThAr kalibrációs technikával, s a teljes rendszer fényhasznosítása (távcsövet és légkört is beleértve) meghaladja a 10%-ot. A TRES műszer folyamatosan veszi át az immáron 25 éves CfA Digitális Sebességmérő (Digital Speedometer, Latham et al 1992) szerepét, és hamarosan kulcsszerepet tölt be a CfA exobolygó kereső programjában, valamint a NASA Kepler missziójának[2] földfelszíni támogatásában.

Egy spektrográf építése meglehetősen műszertechnikai aspektusa a csillagászatnak, ezért talán joggal nevezhető inkább mérnöki tudománynak mintsem csillagászati kutatásnak. Ugyanakkor egy műszer használata az egyetlen út, mely során annak minden tulajdonsága és korlátja kiismerhető, ami pedig elengedhetetlen az adott műszer tökéletesítéséhez, a tudományos igények kielégítéséshez. (Ezt támasztja alá a 3. és 4. fejezet is.) Ezért a műszerfejlesztés az asztrofizikai kutatás alapvető eleme, s mint ilyen természetes és szerves része a csillagászat művelésének. Ez indokolja az "előszó" részletes, áttekintő leírásátt a modern echelle spektrográfok körültekintő tervezéséről és építéséről (1. fejezet), valamint a TRES konkrét példájának bemutatását (2. fejezet).

Jővőbeli tervek

A dolgozat zárásaként a bemutatott műszerfejlesztő és kutatási tevékenységek folytatását vázolom fel a 11. fejezetben, melyek kiterjednek további nyílthalmazok vizsgálatára valamint a már tanulmányozott objektumok további analízisére. A Hectochelle es TRES műszerek várhatóan fontos szerepet játszanak majd a Kepler-éra exobolygó kutatásában, azonban ez a tudományos munka mellett a műszerek továbbfejlesztését is igényli. A csillagkeletkezési régiók tanulmányozása pedig sokat kamatoztathat egy közeli-infravörös multiobjektum spektrográf használatából, mint pl. a MMIRS (MMT and Magellan Near-Infrared Spectrograph), melynek fejlesztésében jelenleg aktívan részt vállalok.

---

[2] http://kepler.nasa.gov/

Acknowledgment

It is impossible to complete work on this scale on one's own. I have many people I am indebted to and I would like to express my gratitude to the following:

Andrew Szentgyorgyi, my doctoral advisor at CfA, who helped and supported me from the very first second we met; not only as a predoctoral fellow, but also in personal life. The list would be very-very long, from material needs to hospital visits, a way beyond an official teacher–student relationship. And he has always been there for my family as well, while I was traveling or observing.

Dave Latham, my advisor at CfA, who has always believed in me and supported me (no matter what). I would be honored if my work reminded him of his early years.

Lee Hartmann, who pushed me with the science cases, pointed me in the right direction, and made sure I kept forging ahead.

József Vinkó and **Károly Szatmáry**, my home institution advisors, without whose help I would not be here. I am thankful to them both for their advocacy support during the university years in Hungary and since then.

My appreciation extends to many others, who I tried to all list below in (sort of) alphabetical order:

Alcock, Charles current, and former CfA director **Saphiro, Irwin**, for continuously supporting the TRES project throughout the years of design, development and construction.

Allen, Lori, for advising on ONC and helping to handle IRAC data, and for supporting the extension of the ONC study.

Alegria, Grace, for managing all those TRES related issues in Arizona, including last minute purchase orders and many, many other things.

Amato, Steve, for making the TRES CCD and exposure meter to work.

Bennett, Kevin, for producing, modifying and assembling all sorts of TRES parts, often A.S.A.P. and last minute, day or night.

Berlind, Perry, **Calkins, Mike** and **Esquerdo, Gil**, the FWLO observers for helping in a lot more than just getting TRES going during the nights of commissioning. They are the ones producing the data, making useful suggestion to increase productivity, and who will run the TRES instrument in the future. Not to mention all those long nights of observing with Hectochelle, including sometimes many daytime hours of troubleshooting to get the fiber positioner going.

Bergner, Henry, for the FE analysis of the TRES front end structure.

Bucchave, Lars, for taking the journey with me into the land of Hectochelle data reduction extremes.

Burke, Mike, for laying down the basics of electrical design, specifying the electrical components.

Caldwell, Nelson, who gave me guidelines and even physical help in Hectochelle alignment. I am much obliged for the supportive observation scheduling, and advising on multi-object spectroscopic data reduction.

Chavarria, Luis, for all those very useful discussions on the young clusters, technical details on data reduction, and for being a *friend* through thick and thin.

Collette, Florine, for assembling those endless TRES cables and electrical connectors.

Conroy, Maureen, for her very extensive software support, even at crazy hours. This was essential to make Hectochelle work and getting my (and all those other) observations done. And for all those relaxing conversation at the office.

Curley, Dylan, for his help in motion control and other software issues, and for giving a support as a *friend* beyond the office doors.

Demski-Hamelin, Sue, for taking such a great care of all my administrative (and even personal) matters. Thanks to her amazing abilities all the travel arrangements, purchases, stipends, support letters, visa issues, etc. – all were arranged in time, and such support has been essential to complete my work.

Ellis, Tim, for all of those long hours of modeling and drafting the TRES parts and assemblies, realizing the conceptual designs as machine drawings ready to turn metal.

Epps, Harland, for optimizing the TRES lens system as good as it got, and for his extensive help during the optical design and manufacturing phase.

Fabricant, Dan, who as my division director was always supporting me with his trust, and for giving very helpful and useful critics on instrument design and regarding science related questions as well.

Falco, Emilio, for his support of TRES at FLWO in many aspects, from giving a hand to lift the instrument to change observing schedules per request for the benefits of commissioning or executing engineering/development on TRES.

Fata, Bob, who introduced me to athermal optical mount design and gave expedient comments which significantly improved the design of TRES. He also performed the FE analysis for the TRES lenses, and played a key role in realizing Hectochelle.

Feldman, Leslie, for taking care of and keeping hidden from me all those financial issues regarding project funding, my stipend and predoctoral fellowship.

Fernandez, Jose, for his help in the commissioning of TRES and in conducting the benchmark observations: doing my job for me during the time I just could not be in two places at once.

Gauron, Tom, for advising on TRES electrical design, motion control and temperature monitoring system.

Geary, John, for designing and building the TRES CCD cameras.

Groner, Ted, for writing the upper level codes for TRES, and integrating it into the 60 inch telescope control system at FLWO; for debugging and fixing all sorts of software and hardware problems, and for the essential and very extensive testing.

Hutchins, Bob, for giving (more than) a hand during TRES installation at FLWO.

Knowles, Larry, for the flexible and helpful support on the machine shop side.

Korzennik, Sylvain, for his valuable advices on instrument design and data reduction, and for sharing his AFOE experience which turned to be very beneficial for TRES.

Major, Csaba, for his contribution to thermal analysis and the top notch help in the lab assembly/alignment of the spectrograph bench.

McLeod, Brian, who helped both physically and mentally, by giving a hand in optical assembly as well as advising on optical design.

Megeath, Tom, sharing his IRAC observations of ONC before publication and thus providing me with an unique target list and valuable additional information about the young stars of the

Orion nursery.

Meibom, Soren, for helping to push Hectochelle to the limit, and for listening and standing next to me as a *friend* in all sort of situations: he was the one I could (and did) call even at 2 in the morning...

Mink, Doug, for his enormous effort put into Hectochelle and TRES data reduction, including customization and development of IRAF tasks to suit the needs of these instruments.

Norton, Tim, for keeping the schedule on the instrumentation projects by coordinating the work of all these people listed here, and for getting me paid – even, if needed, by finding some extra this and that.

Pál, András, who was willing to sacrifice his hours/days of rest to develop and test TRES data reduction tools.

Peters, Wayne, who has been and will be taking care of TRES mechanical and CCD related issues while we are not there in Arizona.

Roll, John, for his everlasting support in the preparation and flawless execution of Hectochelle observations; for teaching me how to use various software tools and making the TRES guider to work.

Teixeira, Paula, for providing NGC 2264 IRAC data, and for useful discussions on that cluster and regarding some non-work related matters.

Tokarz, Susan, for sharing her deep insight and experience in multi-spectral data reduction.

Ordway, Mark, who as the project engineer for TRES kept in his hands and managed all the design related matters, and often beyond that – who therefore created much more than just different parts and assemblies of the TRES instrument.

Winston, Eliane, for those useful discussions on the open clusters, and for just cheering me up in the office (a priceless support in getting through those days...)

Zajac, Joe, who helped and still has been supporting me in all sorts of lab activities, lens bonding and assembly, fiber polishing, conceptual designs, etc. – the best collaborator anyone can wish for, and even more, a true friend when it comes to put something together (let it be "internal") even far beyond those lab doors...

I am also obligated to the **MMT staff and telescope operators**, for their support in the scientific observations and Hectochelle operations. I wish to express my gratitude to all **those who designed, built and has been maintaining the Hectochelle and the MMT f/5 systems**, to provide the scientific community with such a marvelous instrument. I appreciate the advocacy support of the **CfA Time Allocating Committee**, for accepting my observing proposals and for securing so many telescope nights to conduct my thesis projects.

And, last but not least, my undying gratitude to ***my family, Noémi, Gitta and Gergő****, the stars shining closets to me. Their never fading love and absolute support was essential in accomplishing all of this.*

Contents

I Instrumentation: Design and Construction of Spectrographs 1

1 Design Theory 3
- 1.1 History of Astronomical Spectrographs . . . 3
- 1.2 Overview of a Modern Spectrograph . . . 5
- 1.3 Dispersive Elements . . . 6
  - 1.3.1 Prisms . . . 7
    - Angular Dispersion . . . 7
    - Spectral Resolution . . . 8
  - 1.3.2 Gratings . . . 8
    - Grating Equation . . . 8
    - Angular and Linear Dispersion . . . 9
    - Resolution . . . 9
    - Free Spectral Range . . . 10
    - Gratings vs. Prisms . . . 10
  - 1.3.3 Other Dispersing Techniques . . . 11
    - Prisms and Grating Pairs: Grisms . . . 11
    - Volume Phase Holographic Gratings and “vrisms” . . . 11
- 1.4 Grating Efficiency and Spectral Purity . . . 11
  - 1.4.1 Diffraction Efficiency . . . 11
  - 1.4.2 Blazing . . . 13
  - 1.4.3 Absolute Efficiency . . . 15
  - 1.4.4 Finding the optimal grating configuration . . . 15
  - 1.4.5 Echelle Gratings: Cross Dispersing and Spectral Format . . . 16
    - Echelle Gratings . . . 17
    - Order Separating Filters . . . 17
    - Spectral Format . . . 17
    - Effects of altering/choosing dispersers . . . 18
- 1.5 Resolution of Astronomical Spectrographs . . . 19
  - 1.5.1 Resolution in Astronomical Terms . . . 19
  - 1.5.2 Slits or Fibers: Does it matter? . . . 20
    - Illumination of Slits vs. Fibers: Scrambling . . . 23
    - Multiplexing . . . 24
    - Effect of line tilt . . . 26
    - Effective Resolution of Fiber Fed Instruments . . . 27

1.5.3 Merit of a Spectrograph . . . 30
1.6 Calibration of High Res. Spectrographs . . . 30
1.6.1 Absorption lines: Iodine cells . . . 31
1.6.2 Emission Features: Simultaneous ThAr . . . 32
1.6.3 Calibration of Multiobject Spectrographs . . . 33

2 Making of TRES 39

2.1 Design Considerations . . . 39
2.1.1 Scientific Goals . . . 39
2.1.2 Estimated RV Performance at the Photon Noise Limit . . . 41
2.1.3 Determination of Basic Design and Parameters . . . 44
2.1.4 Echelogram calculations . . . 46
2.1.5 Efficiency Predictions . . . 50
2.2 Optical Design . . . 53
2.2.1 Initial Design . . . 53
2.2.2 Optimization . . . 54
Single Pass . . . 54
Double Pass . . . 55
Considerations on the Cross Disperser . . . 58
Image Quality Maps and Further Optimization . . . 58
2.2.3 The Preconstruction Design . . . 59
2.2.4 Incorporating Melt Sheet Data . . . 61
2.2.5 Construction Design — Test Plate Fitting . . . 62
2.2.6 Thermal Analysis . . . 64
2.2.7 Ghost Analysis . . . 66
2.2.8 Tolerance Analysis and Lens Specification . . . 68
Fabrication Tolerances . . . 70
Mounting/Alignment Tolerances . . . 73
Final Re-optimization — The As-Built Model . . . 74
2.2.9 Exposure Meter . . . 74
2.3 Front End Optical Design . . . 75
2.3.1 Focal Reducer . . . 75
2.3.2 Guider . . . 76
2.3.3 Calibration Optics . . . 78
2.4 Spectrograph Bench Mechanical Design . . . 81
2.4.1 Athermal Lens Mounts . . . 81
Supporting Single Elements . . . 87
Mounting the Triplet . . . 89
2.4.2 Supporting the Dispersive Elements . . . 90
Grating . . . 90
Cross-disperser . . . 91
2.4.3 Fiber Selector and Shutter . . . 92
2.4.4 Camera Design . . . 94
2.5 Front End Mechanical Design . . . 96
2.5.1 Mounting Frame . . . 96

Basic Layout 96
Finite Element Analysis 97
2.5.2 Tip-Tilt System 98
2.5.3 Focal Reducer 99
2.5.4 Fiber Feed 100
2.5.5 Calibration Unit 101
Integrating Sphere 101
Periscope assembly 101
Secondary Light Path 103
2.5.6 Iodine Stage 103
2.5.7 Guider 105
2.6 Electrical Design 105
2.6.1 Top Level 106
2.6.2 Motion Control 106
2.6.3 Illumination Control 109
2.6.4 Thermal Control 109
2.6.5 Environment 109
2.7 CCD Cameras 113
2.7.1 Scientific Camera 113
2.7.2 Exposure Meter 113
2.7.3 Guider Camera 114
2.8 Software Development 114
2.8.1 Low Level Codes 114
2.8.2 Top Level and Data Acquisition Interface 115
2.9 Construction 116
2.9.1 Bonding Lenses in Bezels 116
2.9.2 Coupling the Multiplet Lenses 117
2.9.3 Mirror and Auxiliary Lens Mounts 120
2.9.4 Fiber Run 120
2.9.5 Optical Alignment and Lab Testing 122
2.10 Performance and First Results 127
2.10.1 Image Quality and Resolution 127
2.10.2 Measured Efficiency 129
2.10.3 Calibration 130
2.10.4 Stability 133
2.10.5 Guiding 136
2.10.6 Data Reduction 138
2.10.7 Application Examples 140
First Publication with TRES 140
Performance Test: υ And 141
HADS 142
Faint Stars 144

3 **Hectochelle** **147**
- 3.1 Instrument Description . . . 147
  - 3.1.1 The f/5 MMT . . . 147
  - 3.1.2 Fiber Positioner and Fiber Run . . . 148
  - 3.1.3 The Hectochelle Optical Bench . . . 149
- 3.2 Alignment and Performance . . . 150
  - 3.2.1 Optical Alignment — of Mosaic Gratings . . . 150
  - 3.2.2 Image Quality . . . 154
  - 3.2.3 Instrument Stability . . . 154
    - Thermal Effects . . . 154
    - Environmental Effects . . . 154
    - Shear of Mosaic CCDs . . . 154
  - 3.2.4 Benchmarks . . . 156

4 **Accuracy of MOS RV Data** **159**
- 4.1 Wavelength Calibration of MOS . . . 159
  - 4.1.1 Indirect vs. Direct Illumination . . . 159
  - 4.1.2 Variations on a MOS Calibration System . . . 160
  - 4.1.3 Sub-optimal Calibration: Effects on RV Performance . . . 162
  - 4.1.4 Effects on Sky Subtraction, Throughput Correction . . . 164
- 4.2 Fiber-to-Fiber Calibration . . . 165
  - 4.2.1 Hectochelle . . . 165
  - 4.2.2 Hydra . . . 166
  - 4.2.3 FLAMES / Giraffe . . . 166
- 4.3 Solutions/Methods/Problems . . . 167
  - 4.3.1 Solar Calibration . . . 167
  - 4.3.2 Master Wavelength Solution, ThAr Tracking . . . 167
  - 4.3.3 Zero Point Calibration . . . 171
  - 4.3.4 Matching Template . . . 171
  - 4.3.5 Bottom Line: RV Precision Limit . . . 172
- 4.4 Towards Ideal MOS RV Data . . . 175

II **Data Reduction Techniques** **179**

5 **Data Reduction** **181**
- 5.1 Basic Image Processing . . . 181
- 5.2 Extraction of Spectra . . . 183
- 5.3 Wavelength Calibration . . . 183
- 5.4 Throughput Correction and Sky Subtraction . . . 185

6 **Obtaining Radial Velocities** **187**
- 6.1 Multi-template Method . . . 189
  - 6.1.1 Synthetic Libraries . . . 191

III Scientific Application: Dynamical Studies of Open Clusters 193

7 Star-forming regions 195
7.1 Molecular Clouds . . . 195
7.1.1 Properties . . . 195
7.1.2 Evolution . . . 196
7.1.3 Cloud Cores . . . 196
7.2 Birth of a Star . . . 197
7.2.1 Formation of Young Stellar Objects . . . 197
7.2.2 Evolution towards the Main Sequence . . . 198
7.3 Open Clusters . . . 201
7.3.1 Formation . . . 201
7.3.2 Morphology and Properties of Young Clusters . . . 202
7.3.3 Evolution . . . 204
7.4 The Aim of this Thesis . . . 206

8 The Cone Nebula 211
8.1 Observations . . . 212
8.1.1 Target Selection . . . 212
8.1.2 Spectroscopic Observations . . . 212
8.1.3 Radio Observations . . . 214
8.1.4 Data Reduction . . . 215
8.2 Results . . . 215
8.2.1 Distribution of Radial Velocities . . . 215
8.2.2 T Tauri stars . . . 218
8.2.3 Binaries . . . 221
8.2.4 Velocity Correlations between Stellar and Gaseous Component . . . 222
8.3 Discussion . . . 224
8.3.1 A Cluster in Formation . . . 224
8.3.2 Distributional Differences Between IR Excess and Non-excess stars . . . 226
8.4 Summary . . . 227

9 The Orion Nebula Cluster 229
9.1 Observations . . . 230
9.1.1 Target Selection . . . 230
9.1.2 Spectroscopic Observations . . . 230
9.1.3 Radio Observations . . . 233
9.2 Data Reduction . . . 234
9.3 Results . . . 234
9.3.1 Velocity Distribution and Correlations Between Stellar and Gaseous Component . . . 234
9.3.2 Hα Emission profiles . . . 240
9.3.3 Spectroscopic vs. Photometric Disc/Accretion Indicators . . . 242
9.3.4 Binary Stars . . . 243
9.3.5 High Radial Velocity Stars . . . 245

9.4 Discussion . . . 246
    9.4.1 Cluster in Formation . . . 246
    9.4.2 Subgroups and stellar energy input . . . 248
    9.4.3 Other Populations? . . . 248
    9.4.4 Comparison with Other Observations and Models . . . 253
9.5 Summary . . . 254

10 NGC 1907 & 1912 **257**
10.1 Observations . . . 258
    10.1.1 Photometry . . . 258
    10.1.2 Spectroscopic Observations . . . 259
10.2 Data Reduction . . . 259
10.3 Results . . . 263
    10.3.1 Distribution of early-type stars . . . 263
    10.3.2 Velocity Distribution . . . 263
10.4 Discussion and Summary . . . 267

11 Continuation **273**
11.1 Instrumentation . . . 273
    11.1.1 Atmospheric Dispersion Corrector for TRES . . . 273
    11.1.2 Laser Comb for Hectochelle and TRES . . . 276
    11.1.3 Near-Infrared Spectroscopy – MMIRS . . . 277
11.2 Open Clusters . . . 279
    11.2.1 ONC Follow Up — Mg and Li Lines . . . 279
    11.2.2 NGC 2244 – The Rosette Nebula . . . 279
11.3 Future TRES applications . . . 283
    11.3.1 Exoplanet Candidate Follow Ups . . . 283
    11.3.2 RV Survey of M Dwarfs . . . 284

12 Appendix **297**

List of Figures

1.1 Fraunhofer's drawing of absorption lines in the solar spectra, from 1814 4
1.2 Layout of a modern astronomical spectrograph 5
1.3 Full-double pass arrangement 6
1.4 Schematic diagram of a dispersing prism 7
1.5 Schematic diagram of a diffraction grating 9
1.6 The intensity of light from a diffraction grating 12
1.7 Profile of a blazed grating 13
1.8 The intensity of light from a blazed diffraction grating, at blaze wavelength . . . 14
1.9 The intensity of light from a blazed diffraction grating, out of blaze wavelength . 14
1.10 Efficiency and free spectral range for different grating configurations 16
1.11 Spectral format of a cross-dispersed echelle spectrograph 17
1.12 Focal ratio degradation in fibers 21
1.13 Fiber transmission plot for different fibers 22
1.14 Effect of guiding error on line profile 23
1.15 Slit and spectra arrangement in a multi-slit system 25
1.16 Line tilt in a spectrograph 26
1.17 Calculating the effective width of a fiber 28
1.18 Tilt of spectral features in a fiber fed spectrograph 28
1.19 The effect of spectrograph optics PSF on measured resolution 29
1.20 The iodine technique 31
1.21 The simultaneous ThAr technique 32
1.22 Scattered vs. direct illumination of a MOS spectrograph 34

2.1 Quality factor of stellar spectra, versus spectral range 42
2.2 Quality factor versus spectral resolution 43
2.3 Design candidate: #BSL7Y_R2_r50 47
2.4 Design candidate: #BSL7Y_R4_r80 48
2.5 Design candidate: #BSL7Y_R3_r50 49
2.6 Estimated spectrograph efficiency 50
2.7 Estimated throughput from above the atmosphere down to spectrograph entrance 51
2.8 Efficiency of a fiber feed as a function of seeing 52
2.9 Estimated overall spectrograph efficiency, including atmosphere 52
2.10 Layout of TRES initial collimator/camera 53
2.11 Spot diagram of TRES initial collimator/camera 55
2.12 System evaluation plot for single-pass, on axis 55
2.13 Complex evaluation plots for single-pass, multiple field positions 56
2.14 Intermediate result of optimization in full-double-pass 57
2.15 Multi-configuration spot diagrams of a buildable design 57

2.16 Image quality maps comparing RMS spot diameter 58
2.17 Optical layout of the preconstruction design 59
2.18 Multi-configuration spot diagrams of the preconstruction design at different temperatures 60
2.19 Serious ghost image problem of the preconstruction design 60
2.20 Multi-configuration spot diagrams of the construction design 62
2.21 Spot-size maps for thermal analysis on the construction design 64
2.22 Spot-shape maps for thermal analysis on the construction design 65
2.23 Ghost image analysis of the construction design 66
2.24 Secondary ghost images of the construction design 67
2.25 Graphical tolerance analysis report — sample 69
2.26 Optical layout of the exposure meter 75
2.27 Optical layout of the Tillinghast reflector at f/6 77
2.28 Spot diagrams of the Tillinghast reflector at f/6 78
2.29 Optical layout of the TRES guider 79
2.30 Spot diagrams of the TRES guider 79
2.31 Optical layout of the TRES calibration system 80
2.32 Layout of the TRES bench 81
2.33 Cross section of a continuous RTV bonded lens mount 82
2.34 CTE correction vs. shape factor for RTV560–Al bonding 82
2.35 Stress, load and displacement curves for L2 lens mount 85
2.36 Finite element model and surface deformation map of lens L5 86
2.37 Stress, load and displacement curves for L4 lens mount 86
2.38 Isometric and cross-sectional view of a singlet mount 87
2.39 Baffles of L1 and L2 88
2.40 Cross sectional view of the bonded triplet 89
2.41 Isometric and cross-sectional view of the triplet mount 89
2.42 View of the grating support 90
2.43 Isometric views of the grating mount 91
2.44 Cross sectional view of the prism support 92
2.45 Isometric views of the prism mount 92
2.46 Location of the fiber holder/selector and the fiber arrangement 93
2.47 Open view of the fiber holder 94
2.48 The TRES CCD camera assembly 95
2.49 Open view of the CCD camera head 95
2.50 The TRES front end structure 96
2.51 Isometric view of fully assembled TRES front end 97
2.52 Finite element model of the TRES front end structure 97
2.53 The tip-tilt unit 98
2.54 The f/6 focal reducer 99
2.55 The kinematic fiber mount of the TRES front end 100
2.56 Cross section of the fiber mount and slit mirror 101
2.57 The calibration system 102
2.58 The periscope assembly 102
2.59 Selection between calibration and object light 103
2.60 Three positions of the iodine cell 104
2.61 The iodine cell drive mechanism 104

2.62 The guider assembly 105
2.63 Electrical block diagram of TRES 107
2.64 Location and connection of the TRES components 108
2.65 Thermal insulation of the optical bench 110
2.66 Location of temperature sensors 110
2.67 Temperature variations of the uncontrolled environment 111
2.68 Configuration of room heater components 112
2.69 Surface defect of the science detector 113
2.70 The TRES focal plane – as seen from the grating 114
2.71 Screenshot of the TRES guider 115
2.72 Edge details of some TRES lenses 116
2.73 Lens bonding technique 117
2.74 Absorption of Nyogel OCK-451 couplant used in TRES multiplet lenses 118
2.75 Bidirectional transmittance distribution function of Nyogel OCK-451 couplant . 119
2.76 Lens coupling technique 120
2.77 Thermal break design 121
2.78 Bonding the fibers at the spectrograph end 122
2.79 The mounted fibers of the telescope end 123
2.80 Sample evaluation map used for optical alignment 124
2.81 The TRES optical bench arriving to FLWO 127
2.82 Image sample of ThAr lines at the corners of the detector format 128
2.83 Image samples showing order separation 128
2.84 Resolution of the three TRES fibers 129
2.85 Comparison of measured and calculated throughput of TRES 130
2.86 Wavelength solution residuals 130
2.87 Instrumental shifts measured in object and calibration fibers 131
2.88 Temperature changes during an observing run 133
2.89 Instrumental radial velocity changes during an observing run 134
2.90 Performance of the final temperature stabilization system 135
2.91 Image samples of the guider CCD 136
2.92 Guider errors translated into instrumental RV shifts 137
2.93 Synthetic ThAr spectrum used in data reduction evaluation 138
2.94 Testing the RV measuring methods 139
2.95 The first published measurements with TRES 140
2.96 RV curve for υ And 141
2.97 FFT spectrum of the residual RV values 142
2.98 Phased RV curve for the high amplitude δ Scuti star BE Lyn 143
2.99 Spectral samples from different pulsational phases of BE Lyn 143
2.100 Sample spectrum of a $V = 12.3$ star 144

3.1 The MMT/Hecto positioner focal surface 148
3.2 The Hectochelle optical bench 149
3.3 Steps of iterative mosaic grating alignment — I. 151
3.4 Steps of iterative mosaic grating alignment — II. 152
3.5 A sample Hectochelle calibration frame 153
3.6 Instrumental shifts found in Hectochelle 155
3.7 Effect of telescope/building rotation 155

3.8 Shear of the mosaic CCD array 156

4.1 Direct illumination calibration system for Hectochelle 161
4.2 RV errors as a result of a small change in the direct calibration 162
4.3 RV offsets between apertures as a function of wavelength range 163
4.4 Variation of line profiles between apertures 164
4.5 Fiber-to-fiber RV offsets for the Hectochelle spectrograph 165
4.6 Fiber-to-fiber RV offsets for the Hydra spectrograph 166
4.7 Fiber-to-fiber RV offsets for the GIRAFFE spectrograph 167
4.8 Tracking a master wavelength solution of Hectochelle by ThAr - I 168
4.9 Tracking a master wavelength solution of Hectochelle by ThAr - II 169
4.10 Aperutre and wavelength dependent instrumental shifts of Hectochelle - I 170
4.11 Aperutre and wavelength dependent instrumental shifts of Hectochelle 170
4.12 Aperture dependent instrumental shifts for Giraffe 173
4.13 Predicted and measured line tilts for Hectochelle 174
4.14 Measured line tilts for Giraffe 175
4.15 Calibration system design for a NIR MOS 176

5.1 Wavelength solution accuracy for the 240 Hectochelle apertures 184

6.1 Cross-correlation mask samples 188
6.2 Sample multi-template fitting evaluation plot 189

7.1 Evolution of the ISM within a dense cluster, due to stellar winds 196
7.2 The IR classification scheme 199
7.3 Optical and deep JHK infrared images of the embedded Trapezium cluster . . . 202
7.4 Examples for different cluster structures 203
7.5 The Orion OB1 and Taurus T associations 205
7.6 Simulations of an irregular shaped two-dimensional finite, self-gravitating gaseous sheet. 207
7.7 Location of the studied clusters in relation to the the Milky Way - optical 208
7.8 Location of the studied clusters in relation to the the Milky Way - infrared . . . 209

8.1 Targets in the field of NGC 2264 superimposed on a DSS POSS1 image 213
8.2 Radial velocity distribution of stars in NGC 2264 216
8.3 Examples of $H\alpha$ profiles for stars with detected emission in the NGC 2264 sample 218
8.4 Examples of changing Hα profiles in NGC 2264 219
8.5 IRAC color-color diagram of targets in the NGC 2264 field 220
8.6 Binary stars in NGC 2264 221
8.7 A north-south velocity gradient observed in NGC 2264 222
8.8 Velocity chanel map of stars and gas in NGC 2264 223
8.9 Velocity–spatial plot of CTTS and WTTS stars 224
8.10 Simulation of gaseous sheet collapsing to a filament 226
8.11 Velocity–spatial plot of NGC 2264 stars with and without infrared excess 227

9.1 Map of infrared excess sources within the OMC A cloud 231
9.2 Positions of the ONC targets overplotted a IRAC 8 μm mosaic image of the Orion Nebula 232

9.3 The velocity structure of the Orion A Molecular Cloud 233
9.4 Histogram of measured heliocentric radial velocities in the ONC 235
9.5 Velocity channel maps of the ONC region 237
9.6 Channel maps of the ONC region, in right ascension 238
9.7 Channel maps of the ONC region, in declination 239
9.8 Examples of $H\alpha$ profiles for stars with detected emission in the ONC sample . . 241
9.9 IRAC color-color diagram of stars in ONC with measured RV 242
9.10 Binary stars of the ONC region displayed on a spatial–velocity plot 244
9.11 Observations of ONC compared to the model simulations of cluster formation . . 247
9.12 A newly identified, (kinematically) off-cloud subgroup of stars in the close vicinity of the Trapezium 249
9.13 Velocity–spatial plot of ONC stars with and without infrared excess 250
9.14 Comparing the distribution of excess/non-excess stars for the 2MASS ONC selection 251
9.15 Spatial distribution of stars foreground to ONC 252

10.1 Our survey region in NGC 1907 and NGC 1912 258
10.2 Color–magnitude and color–temperature plots for NGC 1912 260
10.3 Color–magnitude and color–temperature plots for NGC 1907 260
10.4 Maps of average stellar color, location of spectroscopic targets and RV members. 264
10.5 Radial velocity histograms for the NGC 1912, inter-cluster, NGC 1907 and for the entire survey region 265
10.6 Proper motion of stars in NGC 1907 and NGC 1912 268
10.7 Radio continuum (6 cm) image of the cluster region, overlayed on a DSS stellar field 269
10.8 Dust emission on the IRAS 100μm images of the cluster region 270

11.1 On-axis spot diagram of TRES for different zenith distances 273
11.2 Light loss due to atmospheric dispersion 274
11.3 On-axis spot diagram of TRES for different zenith distances, with ADC 274
11.4 Matrix spot diagram of TRES for different zenith distances, with ADC 275
11.5 Comparison of ThAr line density in two TRES orders 276
11.6 Comparison of a ThAr and a comb laser reference 277
11.7 Main components of the MMT and Magellan Infrared Spectrograph (MMIRS) . 278
11.8 Class I and II sources in the NGC 2244 region 280
11.9 Location of observed targets in the NGC 2244 region 282
11.10 A sample spectra from the NGC 2244 observations 282
11.11 Phased RV curve of exoplanet TrES-3 284

12.1 Sample TRES spectra of υ And 299
12.2 $H\alpha$ profiles for stars with detected emission in the NGC 2264 sample 332
12.3 $H\alpha$ profiles for stars with detected emission in the ONC sample 387

List of Tables

2.1 Extinction coefficients at FLWO 52
2.2 TRES initial camera/collimator design 54
2.3 Multi-configuration setup 56
2.4 Melt data for Ohara glasses used in TRES camera 61
2.5 Parameters of the construction model #112505AH 63
2.6 Multi-configuration setup of the construction design 63
2.7 Sensitivity of TRES lenses to fabrication errors 70
2.8 Sensitivity of TRES lenses to mounting errors 71
2.9 Fabrication tolerances on lens radii and as-built comparison 72
2.10 Fabrication tolerances on lens wedge and as-built comparison 72
2.11 Annulus flatness tolerances 73
2.12 Tillinghast reflector prescription at f/6 77
2.13 Properties of RTV560 83
2.14 Properties of the TRES RTV bonded lens mounts 85
2.15 Properties of the Nyogel OCK-451 curing gel 118
2.16 Resolution of TRES 128

8.1 Summary of spectroscopic observations of NGC 2264 214
8.2 Members of NGC 2264 — *sample* 217

9.1 Summary of spectroscopic observations in the ONC region 231
9.2 Members of ONC — *sample* 236

10.1 Summary of spectroscopic observations 259
10.2 Clean list — *sample* 262
10.3 Number of cluster members within sub-regions 266

11.1 ADC design for TRES 275
11.2 Summary of further spectroscopic observations in the ONC region 280
11.3 Summary of spectroscopic observations in the NGC 2244 region 282

12.1 TRES glass catalogs for T=13, 18 and 23 °C 298
12.2 Members of NGC 2264 — *full table* 309
12.3 NGC 2264 non-members — *full table* 320
12.4 Members of ONC — *full table* 358
12.5 ONC non-members — *full table* 384
12.6 Clean list — *full table* 426
12.7 Binary star candidates — *full table* 440

Acronyms used in the text:

AR — Anti Reflection (coating)
AU — Astronomical Unit
BFD — Back Focal Distance
CA — Clear Aperture
CfA — Center for Astrophysics
CG — Center of Gravity
CTE — Coefficient of Thermal Expansion
CCF — Cross Correlation Function
CTTS — Classical T Tauri Star
ESO — European Southern Observatory
FE — Finite Element (analysis)
FIR — Far Infra Red
FLWO — Fred Lawrence Whipple Observatory
FOV — Field Of View
FWHM — Full Width at Half Maximum
GTO — Granted Access Time
IRAF — Image Reduction and Analysis Facility
ISM — Inter-Stellar Medium
MC — Molecular Cloud
MMT — Multiple Mirror Telescope
MMTO — Multiple Mirror Telescope Observatory
MOS — Multi Object Spectrograph
MS — Main Sequence
NIR — Near InfraRed
OD —- Outer Diameter
OMC — Orion Molecular Cloud
ONC — Orion Nebula Cluster
PI — Physik Instrumente
PMS — Pre Main Sequence
PSF — Point Spread Function
PTV — Peak To Valley
RMS — Root Mean Square
RTV — Room Temperature Vulcanizing rubber
RV — Radial Velocity
SED — Spectral Energy Distribution
S/N — Signal to Noise (ratio)
TIR — Total Indicated Runout
TRES — Tillinghast Reflector Echelle Spectrograph
TTS — T Tauri Star
UV — Ultra Violet
WTTS — Weak-lined T Tauri Star
YSO — Young Stellar Object

Part I

Instrumentation: Design and Construction of Spectrographs

Chapter 1

Spectrographs – Introduction to Design Theory

The development of spectroscopy in astronomy is really the history of astrophysics. This is a massive history, which I vastly and boldly trim here by briefly mentioning only some of the early highlights (1.1), hoping it will serve as an enjoyable prelude to a more detailed overview of modern astronomical spectrographs. The basic terms and equations of spectrograph design are discussed in Section 1.2, to aid readers not familiar with these instruments. Through Section 1.3 to 1.6 I shortly discuss some of the more specific aspects of astronomical spectrograph design.

1.1 A Brief History of Astronomical Spectrographs

The beginning is marked by the experiments of Isaac Newton, who explored the spectrum of sunlight in 1666. He also observed the spectrum of Venus, collecting the planetary light with a lens, placing a prism just before the focus, and seeing the image ”drawn out into a long and splendid line”, as described in a letter to Henry Oldenburg in 1672. This early instrument was not capable of resolving spectral lines, which were first observed almost 100 years later by Thomas Melvill of Scotland, in 1752. By burning alcohol and introducing salt and other chemicals Melvill noted abrupt brightening of yellow and other colors in the continuous spectrum.

By the turn of the century the spectrum was extended beyond visible colors. William Herschel, in 1800, used a prism and a thermometer to learn that the rays providing the maximum heating effect were beyond the visible red rays. In 1801, J. W. Ritter found that rays beyond the violet caused the greatest blackening of silver chloride, and so ultraviolet light was discovered after infrared rays.

A year later, in 1802, William Wollaston used a slit in front of a prism, and so was able to discover seven dark lines within the solar spectrum. The importance of these lines was not realized by Wollaston or his readers. These lines, known today as “Fraunhofer lines”, named after an optician who created the first detailed catalog listing 350 of these dark spectral features in 1814 (Fig. 1.1). Jospeh Fraunhofer has an eminent position in this history. He was the first to find that there are countless lines in the spectra of bright stars (such as Sirius, Capella, Castor, Pollux, Procyon,Betelgeuse), only some of which were found in sunlight.

Attempts to decompose the spectrum were made in 1823 by John Herschel, who described the

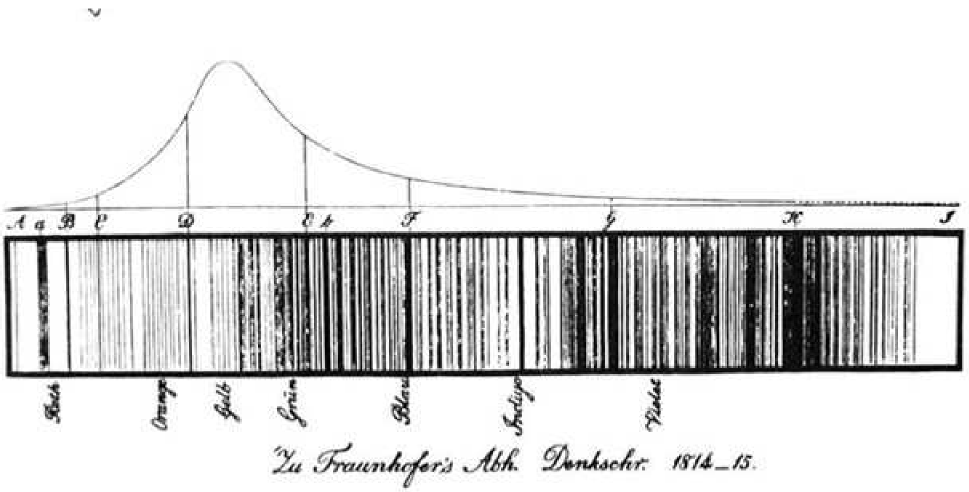

Figure 1.1: ***Fraunhofer's drawing of absorption lines in the solar spectra, from 1814***

use of spectral lines to detect small amounts of chemicals. However, the bright lines of sodium were found in all laboratory spectra, due to impure samples, and this prevented the recognition that each element has a unique spectrum. It was William Swan who realized circa 1856 that samples of an unprecedented purity were needed for spectral analysis.

Leon Foucault made a pivotal observation in 1849 whileurning a carbon arc. He noted the orange emission lines it produced at the location of the D lines in sunlight and the orange absorption lines seen in the continuous spectrum of the glowing arc tips. In 1855, David Alter of Pittsburgh published a paper on the spectra of gases, speculating on the colors of the aurora and on whether the elements in meteors could be found by examining their spectra.

Bunsen & Kirchhoff published their theory in 1860 and 1861 (only one year before Angstrom published a similar study) that the composition of a star could be learned by the study of its light. By observing more than 4000 stars down to 8th magnitude between 1862 and 1868, Angelo Secchi laid down the grounds of spectral classification. Secchi established 5 classes by temperature; discovering carbon stars, finding broadened hydrogen lines in Sirius and deducing that they were wider due to pressure. In 1867, he published a spectral catalog of 209 stars, and included a note on the possibility of measuring radial velocity using the displacement of lines, which was then attempted by William Huggins in 1868. He published a study of Sirius, comparing the hydrogen beta line with that from a discharge tube placed ahead of the objective. The emission line from the tube was slightly offset from the absorption line of the star, by 1.09 Angstroms, and after correcting for the earth's rotation around the sun, he concluded that Sirius was receding by 29 miles per second (although an accurate value is 5 miles per second)

In 1872, Draper produced the first photograph of a stellar spectra (Vega) to reveal the absorption lines, thereby converting spectroscopes to spectrographs and therefore increasing the accuracy of **radial velocity (RV) measurements**. This is the scope, along with instrument design, of this thesis.

1.2 Overview of a Modern Astronomical Spectrograph

The basic layout of a modern astronomical spectrograph is shown in Fig. 1.2. The light collected by the *telescope* of D_T diameter and f_T focal length, enters the spectrograph through the *slit*. The *collimator* of D_a diameter and f_a focal length makes the light parallel before it hits the dispersive element, which is described by the characteristic size W. While the angle of incidence α was the same for all wavelengths, the angle β in the dispersed beam is a function of wavelength, and so the *camera* must have large enough diameter D_2 to collect all the dispersed rays and focus them to the *detector* at a distance of f_2 behind the camera.

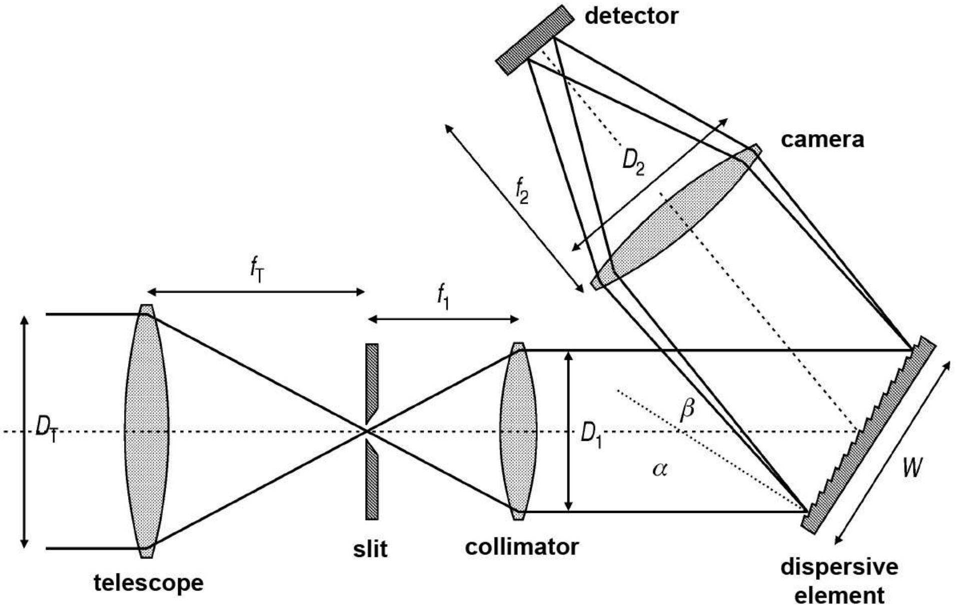

Figure 1.2: ***Layout of a modern astronomical spectrograph***

There are several variations of the above basic layout of optical elements, out of which only a very few is within the interest of later discussions.

As of the dispersive element there are three main categories: dispersive, diffractive or hybrid designs, latter meaning application of a prism and a grating together. Section 1.3 describes the main characteristics of these dispersive elements.

Regarding the optical arrangement the most important is the *Littrow–design*, in which the angles α and β kept equal, or as close as possible (*semi–Littrow*). Using special (blazed, see **??**) gratings and keeping the angle of incidence (α) and diffraction (β) on the same side of the surface normal (unlike on Fig. 1.2), one can construct a very compact instrument and keep the optics at minimum diameter. If the slit and the detector can be placed very close to each other, either physically, or just in optical means by using fold mirrors, the collimator optics can be re-used as a camera lens as well. This is called a *full-double-pass* design (Fig. 1.3), and although being simple and cost efficient by re-utilizing optics, considerations regarding the resolution of the spectrograph (see Section 1.5) might not favor this layout.

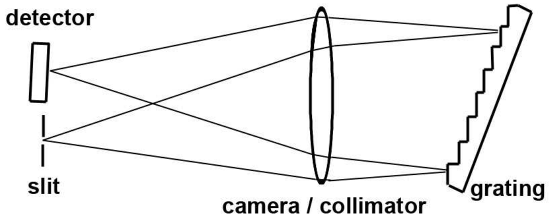

Figure 1.3: ***Full-double pass arrangement***

Modern spectrographs are often not coupled directly to the telescope as shown in Fig. 1.2, but fibers deliver the collected photons from the focal plane to the spectroscopic instrument. Pros and cons of these design variants are briefly discussed in Section 1.5.2.

The slit, from one hand, separates the light of interest from other sources. Considering the point-like images of stars at the focal plane of a telescope the slit has a very small size. The spectrograph, while essentially re-imaging the slit onto the detector at every wavelength, stretches the slit image in one direction only. Today's large, two dimensional detector arrays make it possible to deploy multiple slits, and increase the scientific efficiency of astronomical spectrographs by simultaneously recording spectra of dozens or hundreds of objects. *Multiobject spectroscopy* is briefly overviewed in Section 1.5.2, because the research examples of Part III were carried out by using such an instrument.

From the other hand, the size of the slit influences the level of spectral details the instrument can resolve. But in astronomical applications the resolving power is also driven by the size of the telescope, not just simply by the size of the grating. As this is a very important design issue, and since Part II is all about design and construction of a high resolution spectrograph, it felt important to spare a section (1.5) on the resolving power.

A calibration system must be part of an instrument design and construction, so Section 1.6 discusses the methods and possible implementations of spectral calibration.

1.3 Dispersive Elements

The dawn of astronomical spectroscopy was dominated by prism based instruments, as in the XIX. century the manufacturing of good quality gratings was not possible. Although Lord Rayleigh pointed out early on that diffraction gratings would be better suited to achieve high resolving power, polishing the flat optical surfaces of prisms was a more common technique than ruling fine parallel apertures on a glass or metal substrate. Thanks to the perfection of "ruling engines" by the pioneering work of Henry A. Rowland, J.A. Anderson, than later G. Harrison and G.W. Stroke (introducing the interferometry controlled ruling engines in the 1950's), today's spectrographs use gratings as a (main) disperser.

1.3.1 Prisms

A schematic of a dispersive prism is shown in Fig. 1.4, used at minimum deviation when β is a minimum and rays inside the prism are parallel to the base. Note, that at minimum deviation the dispersed beam has the same diameter as the incoming one, therefore there is no *anamorphic magnification* or $r = 1$:

$$r = \frac{D2}{D1}. \tag{1.1}$$

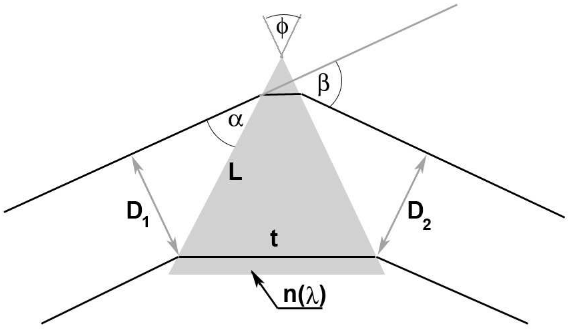

Figure 1.4: ***Schematic diagram of a dispersing prism***

Angular Dispersion

Applying Fermat's principle to the configuration shown in Fig. 1.4:

$$tn = 2L\ cos\ \alpha, \tag{1.2}$$

where t is the base length of the prism and ϕ is the *apex angle*. Since $\beta = \pi - \phi - 2\alpha$, the angular dispersion A of a prism is expressed as:

$$A = \frac{d\beta}{d\lambda} = \frac{t}{D_1}\frac{dn}{d\lambda}, \tag{1.3}$$

where D_1 and D_2 are the diameter of entering/exiting beams, and $dn/d\lambda$ is the rate of change of refraction index with wavelength. This is highly non-linear for almost all suitable optical material, resulting a large variation in dispersion with wavelength. According to the Conrady formula:

$$n(\lambda) = k_1 + \frac{k_2}{\lambda^2}, \tag{1.4}$$

which results a $1/\lambda^3$ dependence of the angular dispersion, as can be seen by substituting Eq. (1.4) into Eq. (1.3):

$$A = -2\frac{t}{D_1}\frac{k_2}{\lambda^3}. \tag{1.5}$$

Spectral Resolution

The resolution of a spectrograph is given by:

$$R = \frac{\lambda}{\delta\lambda}, \tag{1.6}$$

and its maximum is limited by the case when either the slit (s/f_1) or the image of the slit (s') is comparable to the diffraction limit of the collimator or camera optics, e.g. $s/f_1 \approx \lambda/D_1$ or $s'/f_2 \approx \lambda/D_2$. By conservation of the Etendue $s' = s(F_2/F_1)$, where F_1 and F_2 are the focal ratio ($F = f/D$) of the collimator and camera, respectively. As at minimal deviation $D_1 = D_2$ this conservation formula becomes $s/f_1 = s'/f_2$, and so the maximum resolution can be expressed as:

$$R^* = \frac{\lambda}{\delta\lambda} \;=\; \lambda\frac{d\beta}{d\lambda}\frac{1}{d\beta} \;=\; \lambda\frac{d\beta}{d\lambda}\frac{f_1}{s} \;\approx\; \lambda\frac{d\beta}{d\lambda}\frac{D_1}{\lambda} \;=\; D_1\frac{d\beta}{d\lambda}, \tag{1.7}$$

and using Eq. (1.3) it becomes:

$$R^* = t\frac{dn}{d\lambda}. \tag{1.8}$$

It is apparent from Eq. (1.8) that for a prism made of a given glass the theoretical resolution is limited by the size (t) of the prism. As an example, for a UBK7 prism $A = 0.066\ \mu\text{m}^{-1}$ at $\lambda = 500$ nm, and so for a 60° apex angle prism a base length of $t = 150$ mm is needed to reach $R^* = 10,000$. This would correspond to a beam diameter of ≈ 100 mm (and so the camera/collimator diameter has to be at least 100 mm).

1.3.2 Gratings

Grating Equation

A schematic of a transmission and reflection diffractive grating is shown in Fig. 1.5. A surface with a normal N has an array of transmissive or reflective apertures (grooves) with a spacing of σ. These grooves cause the light incident at an angle α to be diffracted through an angle β. A given wavelength λ will interfere constructively only if the following applies:

$$m\lambda \;=\; \Delta s_1 + \Delta s_2 \;=\; \sigma n_1\ sin\ \alpha \;+\; \sigma n_2\ sin\ \beta, \tag{1.9}$$

where $m = 1, 2, ...N$ is the spectral order. By introducing the ruling density $\rho = 1/\sigma$ and assuming $n_1 = n_2$ (which is the case for reflection gratings), the *grating equation* can be re-written as:

$$m\lambda\rho \;=\; sin\ \alpha \;+\; sin\ \beta. \tag{1.10}$$

Note, it is also possible to illuminate the grating at an angle γ with respect to the facet normal (out of the $x-y$ plane of Fig. 1.5), in which case Eq. (1.10) becomes:

$$m\lambda\rho \;=\; (sin\ \alpha \;+\; sin\ \beta)\ cos\gamma. \tag{1.11}$$

In the general discussion below we do not carry this additional $cos\gamma$ term, however we refer to it later (§1.5.2) when it becomes important while discussing realistic optical arrangements and

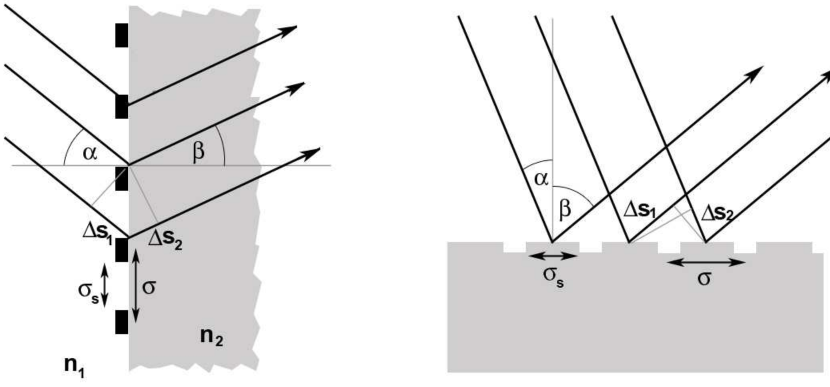

Figure 1.5: ***Schematic diagram of a diffraction grating***

slit tilt.

Angular and Linear Dispersion

The angular dispersion of a grating comes from differentiating Eq. (1.10) with respect to λ for a given α, which gives:

$$\frac{d\beta}{d\lambda} = \frac{m\rho}{cos\ \beta}, \tag{1.12}$$

or

$$\frac{d\beta}{d\lambda} = \frac{sin\alpha\ +\ sin\beta}{\lambda\ cos\ \beta}, \tag{1.13}$$

and for the linear dispersion:

$$\frac{d\lambda}{dx} = \frac{d\lambda}{d\beta}\frac{d\beta}{dx} = \frac{m\rho f_2}{cos\ \beta}, \tag{1.14}$$

where, referring to Fig. 1.2, f_2 is the focal length of the camera and x is the distance measured on the surface of the detector in the dispersion direction.

Resolution

To calculate spectral resolution, defined as the width of the distribution of light projected on the detector, we can write:

$$\delta\lambda = \frac{d\lambda}{dx}s' = \frac{cos\ \beta}{m\rho f_2}s', \tag{1.15}$$

and applying the conservation of the Etendue again, and therefore substituting $s' = (F_2/F_1)s = (D_1\ f_2\ s)/(D_2\ f_1)$ and Eq. (1.15) into Eq. (1.6) we get:

$$R \;=\; \frac{\lambda}{\delta\lambda} \;=\; \lambda\frac{m\rho f_2}{cos\beta\ s'} \;=\; \lambda\ m\ \rho\ \frac{f_2 f_1 D_2}{f_2 D_1 cos\beta\ s}. \tag{1.16}$$

Re-calling the diffraction limit of collimator/camera optics ($s/f_1 \approx \lambda/D_1$ or $s'/f_2 \approx \lambda/D_2$), which was mentioned before to set the upper limit for the resolution, and also applying the $W = D_2/cos\beta$ relation we arrive to:

$$R^* \;=\; m\ \rho\ W. \tag{1.17}$$

This formula gives the maximum theoretical resolution of a diffraction grating, which apparently scales linearly with W, the physical size of the grating. This equation can be directly compared to Eq. (1.8), by relating W to t and $m\rho$ to $dn/d\lambda$. Such comparison reveals the advantage of gratings: assuming the same size ($W = t$) the maximum resolution of a grating can be manipulated and increased by choosing a high spectral order or high ruling density, so the $m\rho$ product is a large multiplying factor compared to the generally low value of $dn/d\lambda$ of optical glasses. In terms of numbers we found the maximal resolution of a 150 mm base length UBK7 prism to be 10000. We also find that this can be achieved with a similar sized grating used at the first order with a ruling density of only 67 lines/mm, or by a 5 mm grating of the same ruling density but used at $m = 40$.

Free Spectral Range

Decreasing the size (and therefore the cost) of a spectrograph by operating a grating at high spectral orders, comes at a price. The grating equation (1.10) could be satisfied for the same α illumination and β diffraction angles by different wavelengths:

$$m\ \lambda_m\ \rho \;=\; sin\ \alpha \;+\; sin\ \beta \;=\; (m+1)\ \lambda_{m+1}\ \rho, \tag{1.18}$$

and so λ_m and λ_{m+1} would be indistinguishable at the detector. Re-arranging the left and right side of above equation, the *free spectral range* (FSR) can be expressed as:

$$\Delta\lambda_{FSR} \;=\; \lambda_m - \lambda_{m+1} \;=\; \frac{\lambda_{m+1}}{m}, \tag{1.19}$$

which gives the extent of a wavelength domain exhibiting a single and unique λ for a given diffraction angle (or for a given location on the detector).

Gratings vs. Prisms

As it was shown, there are advantages and disadvantages of both prisms and gratings. In general, as a summary, we can say the following:

1. assuming the same characteristic size gratings provide higher resolution, although prisms are easier to manufacture and can be made in larger sizes

2. prisms have a highly changing, non-linear $dn/d\lambda$, which leads to a large variation in dispersion and therefore to changing spectral resolution with wavelength

3. the grating directs light to different spectral orders with varying efficiency (see 1.4.2), but prisms are highly transmissive at all wavelengths
4. gratings produce several spectral orders and for large m the issue of spectral purity comes up, while prisms generate only a single spectrum

Therefore, to construct a high resolution spectrograph one should consider a design based on a grating used at high spectral orders. The efficiency can be increased for the desired m values by the use of *blazed gratings* (see §1.4.2), and operating it at high ($m > 30$) orders. To overcome the issue of spectral purity there are some common methods, as described in §1.4.5.

1.3.3 Other Dispersing Techniques

For the completeness some other possible dispersing techniques have to be mentioned, as optical designers have the possibility to choose these options:

Prisms and Grating Pairs: Grisms

A grism consists of a prism with a grating optically interfaced to one side. The prism deflects the zero-order light to one side so that the first order light can propagate directly along the optical axis of the collimator. This allows the camera to be placed on the same optical axis, and therefore to meet the Littrow condition with no anamorphic magnification. Such configuration is useful and mostly applied in high throughput *imaging spectrographs*, where the grism can be replaced by a filter (or just simply removed from the light path) and therefore the spectrograph can be used as a re-imaging optical system (a camera obtaining images of the telescope focal plane with a magnification ratio of f_1/f_2).

Volume Phase Holographic Gratings and “vrisms”

In a VPH grating, the interference condition is provided not by structuring the surface into facets, but by a periodic variation in the refractive index (n) within the body of the material (made from dichromated gelatin or DCG, which is sandwiched in between optical glass). The geometry can be varied so that the lines of constant n (the “fringes”) are perpendicular, parallel, or at some arbitrary angle to the surface. The advantage of such grating is that the peak efficiency can be very high (e.g. 90% compared to 60–70% of blazed gratings), although this high efficiency extends over a smaller spectral range. This restricts the use of VPH gratings in applications requiring a large simultaneous wavelength range.

VPH gratings can be also combined with prisms, and so form a “vrism“, in order to avoid the bent optical arrangement.

1.4 Grating Efficiency and Spectral Purity

1.4.1 Diffraction Efficiency

The intensity of light from a diffraction grating (e.g. Jenkins and White, 1976) is given by:

$$I = IF(\delta')\ BF(\delta), \tag{1.20}$$

where the first term is the interference between rulings, the second term describes the diffraction of light from a single ruling. The first term of Eq. 1.20, the interference pattern can be expressed as:

$$IF(\delta') = \left(\frac{sin\ N\delta'}{Nsin\delta'}\right)^2, \tag{1.21}$$

where δ' is the phase difference between the adjacent rulings and N is the number of rulings lighted up by the incident beam on the grating. The second term of Eq. 1.20 is the blaze function, a diffractive envelope of a single ruling:

$$BF(\delta) = \left(\frac{sin\delta}{\delta}\right)^2, \tag{1.22}$$

where δ is the phase difference between the center and edge of a ruling.

These phase differences are given by:

$$\delta' = \frac{\pi\sigma}{\lambda}(sin\ \alpha\ +\ sin\ \beta),\ \ and \tag{1.23}$$

$$\delta = \frac{\pi\sigma_s}{\lambda}(sin\ \alpha\ +\ sin\ \beta). \tag{1.24}$$

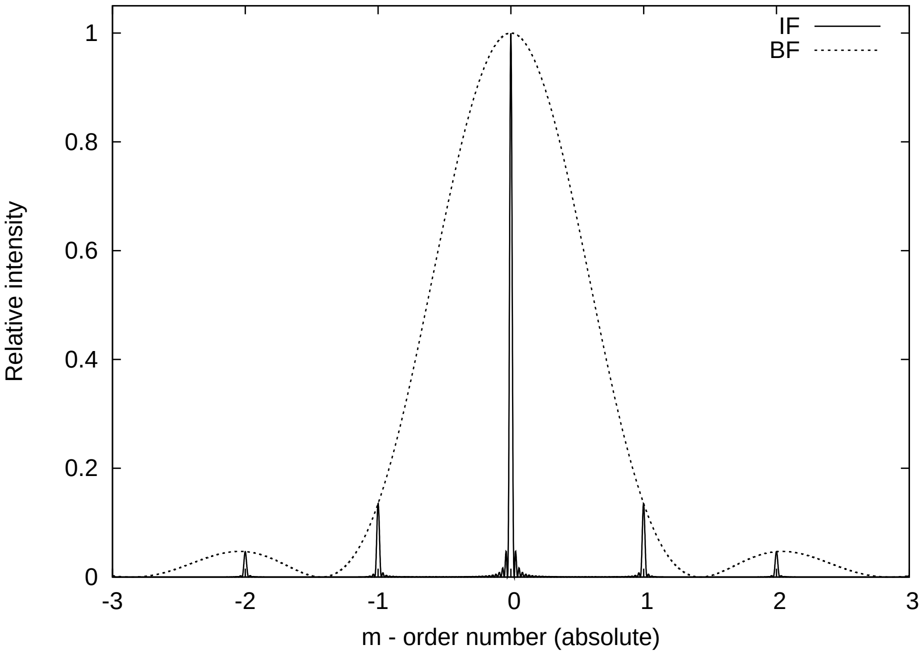

Figure 1.6: ***The intensity of light from a diffraction grating*** *peaks at zero order without shifting the BF blaze function.*

This BF blaze function modulates the interference pattern (see Fig. 1.6). Unfortunately the peak of the diffraction envelope occurs at zero diffraction order ($m = 0$) whereas we would like it to peak at some useful orders, like $m = 60$.

1.4.2 Blazing

The method for maximizing diffraction efficiency at a desired spectral order, which is essentially the shifting of the diffraction envelope of Eq. (1.20) and Fig. 1.6, is termed *blazing*. It can be easily achieved by orienting the grating facets so that the diffraction angle is very nearly the same as the angle of specular reflection, as it can bee seen on Fig. 1.7. For such a blazed grating, the phase difference between adjacent grooves (Eq. (1.24)) becomes:

$$\delta \;=\; \frac{\pi\sigma'_s}{\lambda}\left(sin\;(\alpha-\theta_B)\;+\;sin\;(\beta-\theta_B)\right), \tag{1.25}$$

where $\sigma`_s$ is the effective size of the a clear facet (see Fig. 1.7). This, in case of $\alpha > \beta$ can be expressed as:

$$\sigma`_s \;=\; \frac{\sigma cos\alpha}{cos\theta}, \tag{1.26}$$

which is clearly smaller than the clear facet $\sigma_s = \sigma cos\theta_B$, due to the shadowing effect of neighboring grooves. Unless the Littrow–condition ($\alpha = \beta; \theta_B = 0$) applies, this obstruction decreases efficiency with increasing Littrow–angle (θ). Using the grating with the $\alpha < \beta$ condition, however, also lowers the efficiency. Inthis case not part of incident beam is obscured, but part of the diffracted beam is. Detailed calculations of Bottema (1981) show that in this case the blaze function will be multiplied by $cos\beta/cos\alpha$, and the peak values of interference maxima are also smaller. Therefore the integrated intensity would be lower compared to the former case of ($\alpha > \beta$).

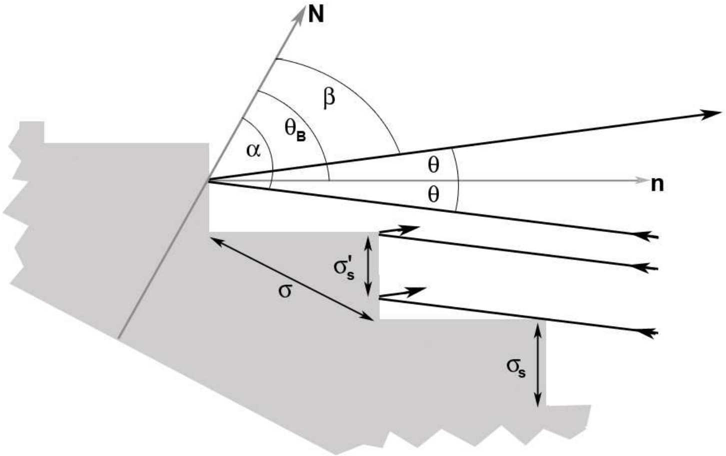

Figure 1.7: ***Profile of a blazed grating***

As a result of blazing Fig. 1.6 would transform to Fig. 1.8, which shows the normalized intensity of a wavelength diffracted by a grating blazed at $\theta_B = 63^{\circ}\!.5$ with a ruling density of 50 line mm^{-1} ($\sigma = 0.02$). The Littrow angle is $0^{\circ}\!.5$ by illuminating the grating at $\alpha = 64^{\circ}\!.0 (> \beta)$. The wavelength ($\lambda = 5966\ \mathring{A}$) has been chosen so that it coincides with the maximum of the blaze function which occurs in order $m = 60$. (The scaling of intensity was changed from linear to logarithmic, in order to emphasize that some of the light is reflected to different orders, although at a modest $< 1\%$ level relative to the main peak.)

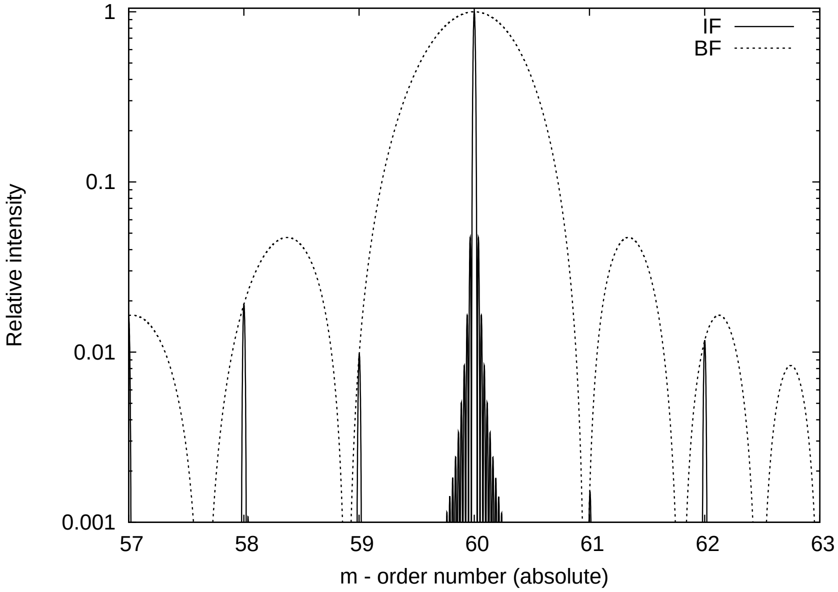

Figure 1.8: ***The intensity of light from a blazed diffraction grating*** *peaks at the selected spectral order (note the logarithmic scale on intensity) – shown for the wavelength corresponding to the blaze angle*

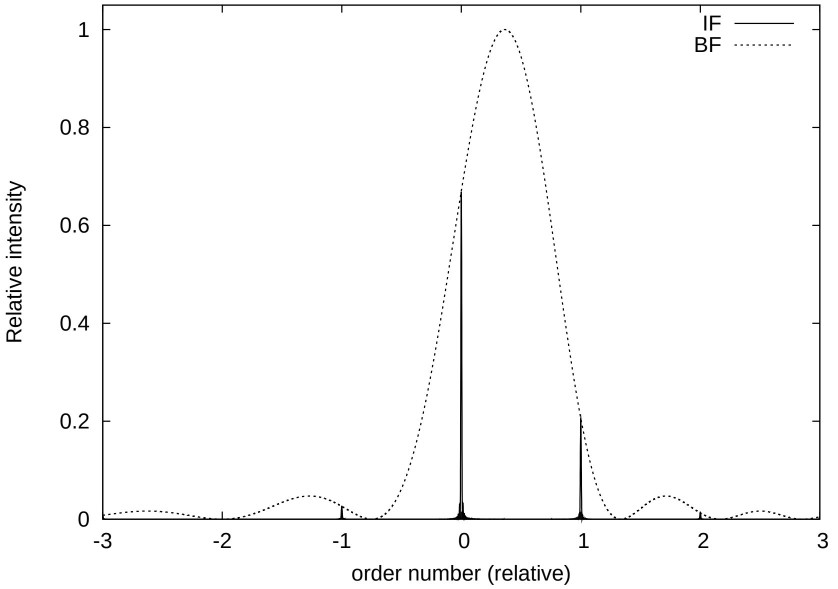

Figure 1.9: ***The intensity of light from a blazed diffraction grating****, out of blaze wavelength*

However, for wavelengths that are not at the center of a blaze function, a significant fraction of their energy would be diffracted to other orders. See Fig. 1.9 displaying the same $m = 60$ blaze function as Fig. 1.8, but with an interference pattern for $\lambda = 5930\ \mathring{A}$. As it can be seen for this wavelength the order +1 ($m = 61$) would contain a significant amount of light.

1.4.3 Absolute Efficiency

In order to calculate the efficiency of a blazed grating as a function of wavelength, it is necessary to determine the distribution of light of a given wavelength across all possible orders, and compute these $absolute efficiency$ values for all wavelengths. Schroder & Hillard (1980) proposes to simply sum the intensities across all possible orders within $\theta_B - 90° \ < \ \beta \ < \ 90°$, and then derive the fraction that is within the order of interest (see Fig. 1.9 as an example). Therefore the absolute diffraction efficiency for order m would be given by:

$$E_{abs} \ = \ \frac{I_{\Delta m=0}}{I_{\Delta m=0} \ + \ \Sigma_{\Delta m\neq 0} I_{\Delta m\neq 0}}, \tag{1.27}$$

where Δm and I are the relative order number and intensity, respectively. (Bottema (1981) commented that above definition of efficiency is not quite correct, but calculated efficiencies for $\theta > 3\,\deg$ and less than 100 grooves per mm, in most cases of interest, would be still in agreement with measured values.)

Detailed calculations and measurements of Schroder & Hillard (1980) show that in order to maximize absolute efficiency one should consider the $\alpha \ > \ \beta$ illumination of a grating, with the possible minimal Littrow angle. A $\theta = 10°$ deviation from Littrow would result a $\sim 40\%$ efficiency loss for a 31.6 grooves per mm grating at $m = 86$, with an additional 5% if $\alpha \ < \ \beta$.

1.4.4 Finding the optimal grating configuration

Another way to realize a buildable configuration instead of $\alpha \neq \beta$, is to consider a quasi-Littrow (QL) mode by deviating the incident and diffracted beams in a plane perpendicular to dispersion. We have mentioned that such a γ tilt would render the grating equation into the form of (1.11). In this case the angular dispersion becomes (as can bee seen by differentiating Eq. (1.10) wit respect to λ for a given α):

$$\frac{d\beta}{d\lambda} \ = \ \frac{m\rho}{cos\ \beta_{QL} \ \ cos\ \gamma}, \tag{1.28}$$

where the average diffraction angle (β_{QL}) is larger than for the $\alpha > \beta$ illumination case, as for that $\beta = \theta_B - \theta$ while now $\beta_{QL} = \theta_B$. The $1/cos\gamma$ term further increases the angular dispersion. As a result the angular extent of a spectral order, the product of angular dispersion (1.28) and $d\lambda$ free spectral range (1.19), becomes:

$$d\beta \ = \ \frac{\lambda\ \rho}{cos\beta_{QL}\ cos\gamma}, \tag{1.29}$$

so the angular extent of a single order increases. This means, since the blaze function does not change shape, that the amount of light going into unwanted orders slightly increases. According to the calculations of Schroder & Hillard (1980) this scales the absolute efficiency with $cos\gamma$, and so even for $\gamma = 10°$ the losses are negligible (at a few percent level) compared to the significant reduction at $\theta = 10°$ (see above).

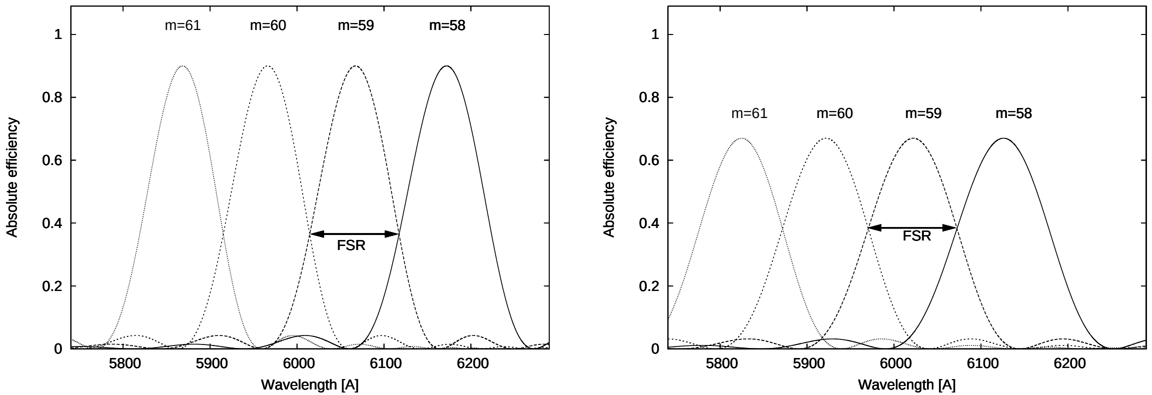

(a) $\theta = 0°$; $\gamma = 7°$ (b) $\theta = 7°$; $\gamma = 0°$

Figure 1.10: ***Efficiency and free spectral range for different grating configurations***

However, the efficiency change within a given spectral order is more pronounced for a QL configuration. This can be clearly seen if blaze functions of consecutive orders are plotted. On Fig. 1.10(a) a QL case is represented ($\gamma = 7°$; $\theta = 0°$) by blaze functions plotted for central wavelengths of order $m = 58, 59, 60$ and 61. Fig. 1.10(b) is the same plot but for a $\alpha > \beta$ illumination case ($\gamma = 0°$; $\theta = 7°$). The peaks on both graphs are scaled to represent absolute efficiencies, according to the results of Schroder & Hillard (1980). Although the efficiency variation across an order (within the free spectral range) is ~ 2.5 for QL mode, comparing it to ~ 1.7 for a Littrow angle of 7°, the averaged efficiency of a given order is not that much higher (~ 0.70 vs. ~ 0.55). Still, the QL mode is more efficient.

In a conclusion we can state that for maximizing efficiency a blazed grating should be mounted in QL mode with $\alpha = \beta$ and $0 \neq \gamma < 10°$, or with the smallest possible Littrow angle in the $\alpha > \beta$ illumination configuration. It has to be noted, though, that the quasi-Littrow mode results in a change in the linear extent of free spectral range (see discussion above and in the next section 1.4.5), causing larger variation of intensities across a spectral order. It also has impact on the resolution through the introduction of line tilt (see §1.5.2).

1.4.5 Echelle Gratings: Cross Dispersing and Spectral Format

Fig. 1.10 also gives a representation of free spectral range, defined in Eq. (1.19). Although the FSR is really the extent of a wavelength domain exhibiting a single and unique λ for a given diffraction angle, the same wavelength is presented in other orders but at other diffraction angles and with different intensities. (Note, that even though the FSR has the same extent in wavelength for the two cases of Fig. 1.10, the linear extent is larger in QL mode due the larger angular dispersion, as shown in see (1.29).)

Therefore a given point of the detector (=a given diffraction angle) corresponds to multiple wavelengths of different orders. To avoid this confusion there are two common methods:

- interference filters can be used to eliminate wavelengths outside of the FSR of given order,

- or cross dispersion can be applied.

The former solution has the drawback of losing significant fraction of the spectrum, especially at high spectral orders. And as we have seen, to minimize the size of the instrument while maximizing resolution, a large m value is desirable.

Echelle Gratings

Gratings specially blazed to operate at high spectral order are called *echelle gratings*. The blaze angle is large and often the tangent of θ_B is used to specify an echelle: R2 refers to a blaze angle of $63^\circ\!.43$, and R4 means $\theta_B = 75^\circ\!.96$.

Such gratings are usually ruled at low densities ($\rho < 300$ lines per mm), and therefore the groove profile and edges are very clean, the facets are high quality optical surfaces. This results in a very low level of scattered light and practically no ghosts in the final optical instrument.

Order Separating Filters

For an R2, 50 grooves per mm grating used in Littrow at $m = 60$ the FSR is only 100 Å, which is only a small fraction of the visible spectrum ($\sim 3800 - 7500\ \mathring{A}$). For some applications this still can be the desired solution, like in multi-object spectroscopy, when the 2 dimensional detector is filled with spectra of several objects, each extending over a small, but identical spectral range.

Spectral Format

Using an element with low dispersing power with its dispersion axis perpendicular to the dispersion of an echelle grating, it is possible to arrange many spectral orders into a 2-dimensional format (called the "*echelogram*") which can be simultaneously imaged by a single camera. Such cross-dispersed pattern is shown schematically in Fig. 1.11.

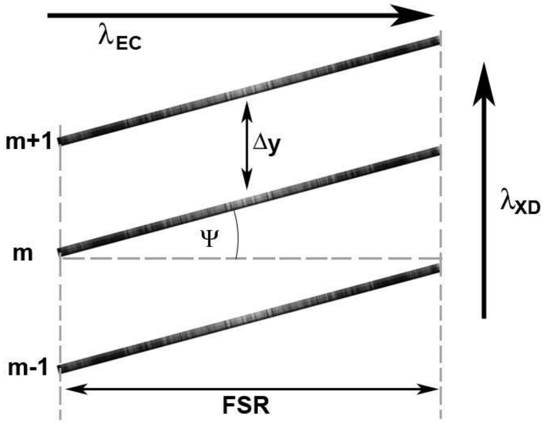

Figure 1.11: ***Spectral format of a cross-dispersed echelle spectrograph***

If the spectrograph camera has a focal length of f_2 (see Fig. 1.2), then the Δy separation between orders would be:

$$\Delta y \;=\; f_2 \, \frac{d\beta}{d\lambda_{XD}} \, \Delta\lambda_{FSR}, \tag{1.30}$$

where $d\beta/d\lambda_{XD}$ is the angular dispersion of the cross-disperser.

The tilt Ψ between orders (see Fig. 1.11) is given by:

$$\Psi \;=\; \frac{d\beta/d\lambda_{XD}}{d\beta/d\lambda_{EC}}, \tag{1.31}$$

where $d\beta/d\lambda_{EC}$ is the angular dispersion of the echelle grating.

As it can be seen from Eq. (1.5) and (1.13) the angular dispersion changes with wavelength. Nomatter whether prisms or gratings are used as cross-disperser the inter-order spacing will vary. Similarly, the Ψ order tilt will be also non-uniform, resulting differently curved orders.

Effects of altering/choosing dispersers

Recalling Eq. (1.29) it is apparent that the angular (and for given camera focus f_2, the linear) extent of an order is proportional to the ρ ruling density of an echelle.

The FSR also depends on rho, as can be seen by expressing $1/m$ from the grating equation 1.10 and substituting it into Eq. 1.19. For the case $\alpha = \beta = \theta_B$ (Littrow mode), in terms of the λ_B blaze wavelength we get:

$$\Delta\lambda_{FSR} \;=\; \frac{\lambda_B^2 \, \rho}{2 sin\theta_B}. \tag{1.32}$$

Linking above equation to Eq. (1.30) it is apparent that the order separation is also a function of ruling density. As a result, the size of the echelogram is scaling with ruling density: higher ρ requires an increase in the detector size, in both directions.

In contrast, changing the blaze angle has little effect on the spectral format. From Eq. (1.30) and (1.32) we can express the order separation as:

$$\Delta y \;=\; const. \times \frac{1}{sin\theta_B}, \tag{1.33}$$

and so the difference between and R2 and R4 gratings, in terms of inter-order spacing, is only $\sim 9\%$.

As it was shown prisms provide generally low dispersion, just as it is preferred for cross dispersing. Prisms also produce a single spectrum, and the high transparency of optical glasses barely change with wavelength, resulting in very high and uniform efficiency. This makes prisms an ideal choice for cross dispersing. In such cases the order separation can be determined by expressing the $d\beta/d\lambda_{XD}$ term of Eq. (1.30) using Eq. (1.5) for λ_B, and also applying Eq. 1.32:

$$\Delta y \;=\; const. \times \frac{1}{\lambda_B}. \tag{1.34}$$

In case a grating is used as a cross disperser one has to worry about secondary spectra, so a very low order operation is preferred which then usually implies a higher ruling density. Similarly as above, but expressing the angular dispersion of the cross-disperser by Eq. 1.12 we get:

$$\Delta y \; = \; const. \times \lambda_B^2. \tag{1.35}$$

Comparing Eq. (1.34) and (1.35) another advantage of prisms can be seen. While gratings cause the order separation to increase rapidly with wavelength, prisms produce a more slowly changing, decreasing inter-order spacing with increasing wavelength. This, together with the above mentioned benefits, makes prisms a particularly attractive choice as a cross disperser.

1.5 On the Resolution and Merit of Astronomical Spectrographs

1.5.1 Resolution in Astronomical Terms

If a spectrograph is directly coupled to a telescope (as it is shown in Fig. 1.2) the following applies:

$$\frac{f_T}{D_T} \; = \; \frac{f_1}{D_1}, \tag{1.36}$$

where f_1 is the focal length of the collimator, D_T and D_1 are the diameter of the telescope and collimator, respectively. Now substitute this into the expression of spectral resolution we derived for grating spectrographs in Eq. (1.16), and also apply the $W = D_2/cos\beta$ relation:

$$R \; = \; \frac{\lambda}{\delta\lambda} \; = \; \lambda \; m \; \rho \; \frac{f_1 D_2}{D_1 cos\beta \; s} \; = \; \frac{\lambda \; m \; \rho \; W \; f_T}{D_T \; s}. \tag{1.37}$$

For astronomical applications the s slit width is rather meaningless, as it can not be compared to the apparent size of astronomical objects. The angle χ subtended by the slit on the sky is more relevant:

$$\chi \; = \; \frac{s}{f_T}, \tag{1.38}$$

where f_T is the focal length of the telescope (see Fig. 1.2). Substituting this into Eq. (1.37) we get the spectral resolution in “astronomical terms”:

$$R \; = \; \frac{\lambda \; m \; \rho \; W}{\chi \; D_T}. \tag{1.39}$$

This formula illuminates important connections between spectrograph parameters (R, ρ, m, W) and design constraints (λ, χ, D_T). It can be written out several ways. One would be: to reach the same resolution at a given wavelength, by using the same angular slit width and a similar grating at the same spectral order, a larger telescope requires a larger grating and therefore a bigger spectrograph. In other words a given spectrograph design scales linearly with the telescope diameter.

The angular slit width χ is listed as a design constraint because for stellar spectroscopy, to fully utilize the light gathering capability of the telescope, all the collected light should be transmitted by the slit. And in presence of the atmosphere, depending on the atmospheric conditions of the observing site, this is roughly a $0.7'' - 1.5''$ *lower* limit, on average. As a result, the resolution of a given telescope and spectrograph can be increased by useing slits narrower than the average *seeing*, but then light is lost and the telescope diameter is virtually decreased. [1]

It was pointed out earlier that resolution can be increased by operating a blazed grating at high orders, but there is a limit for a given W size echelle grating, too. Assuming Littrow mode, the $\lambda m\rho$ term of Eq. (1.39) can be expressed from the grating equation, and so for the λ_B blaze wavelength we get:

$$R = \frac{2\ sin\theta_B\ W}{\chi\ D_T}, \tag{1.40}$$

and it can be seen that assuming the same characteristic size of the grating (W) an R4 echelle ($sin\theta_B = 0.97$) offers some resolution boost over an R2 grating ($sin\theta_B = 0.89$), but not that much. The real advantage is the smaller beam diameter necessary to reach the same (even 9% higher) resolution, as for the same W length a properly illuminated (no overfill, and so no light loss) R2 grating needs a beam diameter $D_1 = W * cos\ 63\overset{\circ}{.}4 = 0.45W$, while an R4 grating can be lit by a smaller, $D_1 = W * cos\ 76\overset{\circ}{.}0 = 0.24W$ diameter beam.

If the D_1 beam diameter is fixed instead of W, Eq. (1.40) can be rewritten as:

$$R = \frac{2\ sin\theta_B\ D_1}{\chi\ D_T\ cos\theta_B} = \frac{2\ tan\theta_B\ D_1}{\chi\ D_T}, \tag{1.41}$$

since in Littrow mode $\alpha = \beta = \theta_B$ and so the following applies: $W = D_1/cos\alpha = D_1/cos\theta_B$. As ($\tan\ \theta_B$) is the R-number, Eq. (1.41) clearly shows that an R4 grating has twice the resolution of an R2 grating, if the beam diameters are the same. However, as we saw above, the R4 grating would be ~ 2 as long.

(As a reminder: it was shown in (1.4.5) that the ρ ruling density scales the spectral format while the θ_B blaze angle has almost no effect on that. Now, we have just demonstrated that θ_B rather scales the resolution.)

1.5.2 Slits or Fibers: Does it matter?

Instead of directly feeding starlight into a spectrograph, as shown in Fig. 1.2, a fiber can be placed at the focal plane of the telescope and the light can be delivered to a remotely placed instrument. In terms of the resolution Eq. (1.39) does not change since the fiber has the same d diameter at both ends, which plays the same role as s in Eq. (1.38):

$$\chi = \frac{d}{f_T}. \tag{1.42}$$

Resolution can not be increased by tapering the fiber without penalty (decreasing its diameter along its length), as the following applies due to the invariance in the optical flux (Gross, 2005):

---

[1] There are techniques to overcome the seeing limited case, by utilizing image slicers (see Thatte et al. (1997), Content (1997), Dubbeldam (2000) for example) or integrated field units (like in Bacon et al. (2001), Allington-Smith et al. (2002), for example) or by compensating the atmospheric disturbance via adaptive optics. These are not within the scope of this thesis, and so are not discussed in detail.

$$\frac{F_{in}}{F_{out}} = \frac{d_{in}}{d_{out}}, \tag{1.43}$$

and so a given F_{in} focal ratio feeding d_{in} diameter fiber results a smaller focal ratio F_{out} for the exiting beam if the d_{out} exit diameter is smaller. Therefore, if the collimator focal ratio F_1 was matched to the telescope focal ratio F_T, light will be lost, just like decreasing the slit width in case of a directly feed spectrograph.

Actually such light loss always exists with fiber fed instruments, even in case $d_{in} = d_{out}$, due to *focal ratio degradation* (FRD, see Angel at al. 1977, Ramsey 1988):

$$\rho = \frac{F_{in}}{F_{out}} \tag{1.44}$$

where the ρ FRD parameter is always greater or equal to 1 (see Fig. 1.12). The value of ρ depends on the fiber properties (core diameter, material, manufacturing process, etc.) and more importantly on F_{in}. For more details see Ramsey (1988). In general we can say that the smaller the input focal ratio is, the closer F_{out} matches that, and feeding a fiber with $F_{in} \leq 6$ usually results in $\rho \leq 1.1$. For fiber fed instruments, therefore, Eq. (1.36) has to be re-written as follows:

$$\frac{f_T}{D_T} = \rho\,\frac{f_1}{D_1}. \tag{1.45}$$

In principle one can preserve all the light by increasing the collimator diameter to compensate for ρ, although it increases the size of the grating and diameter of all optics with no attendant increase in resolution. The f_1 focal length of the collimator also can be decreased, but according to Eq. (1.16) this results in a smaller resolution.

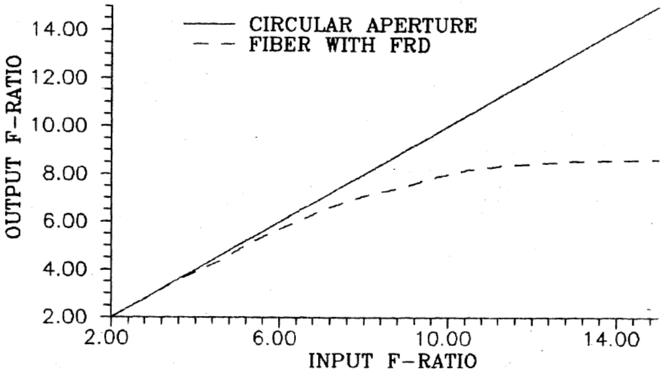

Figure 1.12: ***Focal ratio degradation in fibers****, after Ramsey (1988)*

Another, more "conventional" form of light loss also arises with the use of fibers: material absorption and scattering which have a spectral dependence. (This is also called mode independent loss, unlike FRD, as this is not a function of F_{in} or in other words the distribution of modes propagating in the fiber.) Material absorption in the visible and near infrared is dominated by OH bands at ∼ 7200 Å and ∼ 9500 Å. Scattering is mostly due to density fluctuations in fused silica core fibers, which leads to Rayleigh scattering and sets the lower limit of transmission (see references in Ramsey 1988). While the wide absorption band of "wet" fibers can be sufficiently eliminated by decreasing the OH content of fiber materials, wavelengths shorter than 5000 Å still suffer from significant attenuation (see Fig. 1.13) over length of $\sim 30-50m$ typically needed for realistic applications. However, there is a continuous development to increase the UV and short wavelength transmission (see Haynes et al 2004 as an example).

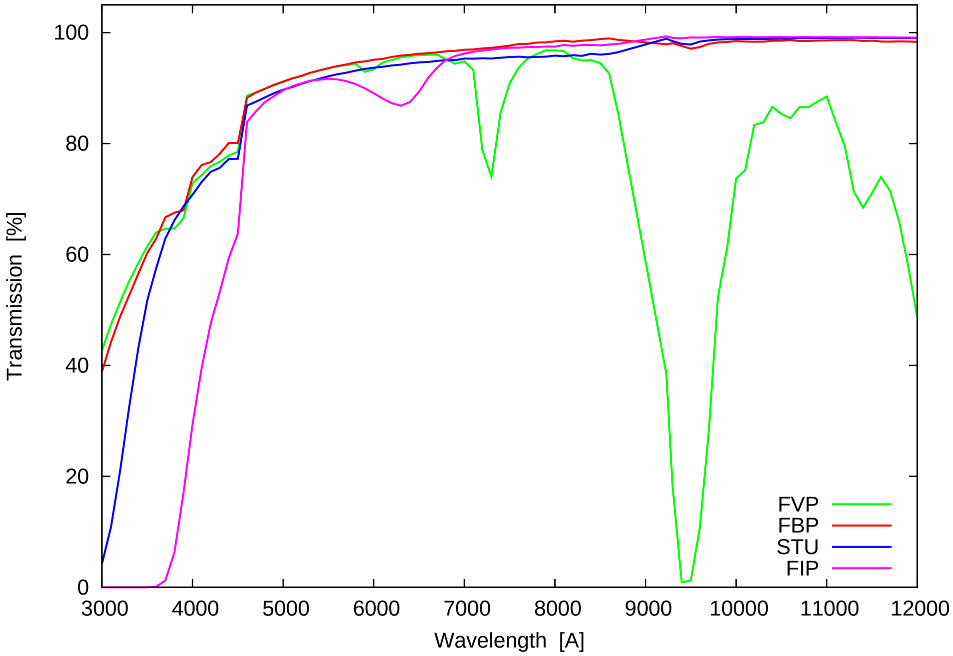

Figure 1.13: ***Fiber transmission plot for different fibers***, *based on data from Polymicro. Transmission of a "wet" (FVP, green) and a low OH content (FBP, red) fiber is shown together with a now obsolete STU (blue) (used in Hectospec/Hectochelle) and an other type called FIP (magenta). Data is shown for 25 m lengths of each. (Plot shows internal transmission only, end reflection and FRD losses not included.)*

The spectral response of a fiber in a real astronomical application, however, still can be very different compared to laboratory measurements. This is caused by the wavelength dependent refraction of the atmosphere, or atmospheric dispersion, which vertically (perpendicular to the horizon) separates the wavelengths of light passing through the atmosphere. At a zenith angle of 45° there is a $\sim 2''$ angular separation between $\lambda = 4000$ Å and $\lambda = 8000$ Å(with most of the difference in the blue), and the situation towards the horizon gets even worse (with no separation at the zenith). A fiber sized for good seeing conditions ($\leq 1''$) therefore would see a wavelength dependent decrease in throughput for objects observed at different zenith angles. Slit spectrographs are less sensitive to this problem if the slit can be oriented in such way (at the parallactic angle) that it is parallel to the atmospheric dispersion. In order to make fiber fed instruments immune to this problem the telescope has to be equipped with a *atmospheric dispersion corrector* or ADC (Wynne & Worswick, 1986). This is a pair of rotating zero deviation prisms, with their dispersion axes set to opposite at zenith and parallel close to the horizon in such a way that the net dispersion nulls out the atmospheric effect. (See Section 11.1.1 for details on a particular design.)

Although some loss or design penalty due to FRD and fiber throughput is unavoidable in astronomical applications, the fiber coupling between telescope and instrument has benefits which can justify such compromises, and so these tiny light guides are widely used in astronomy (Parry, 1998).

Fibers have proved to be essential in achieving high precision velocity measurements by removing the instruments from the back of the telescope and placing the spectrograph in isolated, gravity invariant, controlled environments. This was first done by Hubbard et al. (1979) using an existing spectrograph and by Ramsey et al. (1981) using a spectrograph especially designed for fibers. One of the most recent examples is the HARPS instruments (Pepe et al., 2000), routinely delivering $< 1\ ms^{-1}$ accuracy (Rupprecht et al., 2004). This amazing performance is just partially a result of the extremely stable spectrograph environment (vacuum enclosed instrument to avoid pressure changes, temperature stability at 0.001 K on a daily time scale, see Rupprecht et al. 2004), but the uniform slit (fiber) illumination is also very important.

Illumination of Slits vs. Fibers: Scrambling

Motion of the image delivered by the telescope with respect to the slit (Fig. 1.14.a) causes both a loss of throughput and error in the barycenter of the spectral lines recorded on the detector, unless the object uniformly fills the slit (which, in case of the Airy disk of stellar images, implies a very narrow slit and therefore low throughput). This can cause errors in measurement of radial velocities, at a several 100 m s^{-1} level.

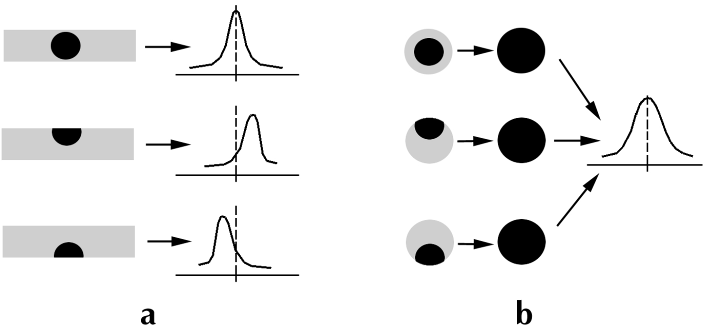

Figure 1.14: ***Effect of guiding error on line profile*** *in case of slit (a) and in case of a fiber (b). The effective scrambling of fibers significantly decreases the change in the line profile.*

Fiber systems are less sensitive to this problem (Fig. 1.14.b) because fibers scramble the input image structure (Heacox 1986 nad 1987). This means that regardless of the distribution of light on the input face of the fiber (variations due to guiding errors, seeing variations, focus drifts, etc.), the output face will appear more uniform. There are two dimensions of scrambling, azimuthal and radial. Azimuthal scrambling means that the intensity in the output beam is symmetric about the axis of the fiber. Radial scrambling describes the constancy of the output beam as the input image is moved from the center to the edge of the fiber. While the former is almost perfect even with a short ($> 0.1\ m$) fiber, radial scrambling is substantial but incomplete, and can result in radial velocity errors at the 10 m s^{-1} level (Hunter & Ramsey, 1992).

A method to increase the efficiency of scrambling via a “double scrambler” was described by Brown et al. (1991). This is basically a re-imaging optics, inserted in a break of the fiber. Its purpose is to invert the positional or "near-field" and angular or "far-field" dependence of rays crossing the junction between the two fiber halves.

The far-field is the cross-sectional distribution of light in the fiber output beam, or in other words, the intensity pattern projected onto a screen placed in the path of the diverging output beam of a fiber. Time-varying illumination will result in changes in the zonal illumination of collimator and camera optics. Therefore aberrations presented in the image will change, resulting in time dependent modification of line profiles, and so result RV shifts. (The far-field pattern corresponds to the telescope pupil, behind the focus. Changes in collimation due to flexures induced by changing gravity and seeing variations are expected to have effect on this pupil image, and therefore on the far-field pattern.)

The near-field pattern is the brightness distribution across the output face of the fiber, which is less sensitive to the angular distribution of rays carried within the fiber. However, changes in the far-field also affect the near-field pattern, as well as the error sources affecting slit illumination (mentioned above). Since the spectrograph images the output end of the fiber directly to the detector, such variations introduce small changes in pixel illumination and lead to RV variations. (As the far-field corresponds to the pupil illumination, the telescope image would be an analogy for the near-field.)

Although double-scramblers are effective in reducing RV errors, there is a drawback: lowering throughput as reflection and alignment errors result in (significant) light loss. Especially for the early designs the total throughput of a double scrambler was very low, around 20% (Hunter & Ramsey, 1992). For HARPS, as a most recent example, the scrambler efficiency is better, but still around 70% (Kohler et al., 2001).

Multiplexing

Fibers, other than very high stability, also offer a convenient way of object multiplexing (Hill et al., 1980), and therefore increase the merit of a spectrograph in terms of scientific output (see more on the definition of *merit* in 1.5.3).

Multi-slit systems in which the field is mapped onto the detector via a mask. This admits only the light of pre-selected objects so that a spectrum is produced at the location of each slitlet. (Some examples of this type are the GMOS (Hook et al., 2003) and Binospec (Fabricant et al., 1998) instruments.) The slit mask has to be custom made for every target field, or for more flexibility re-configurable slit arrays (e.g. the FORS slitlets (Appenzeller et al., 1998) or the MOSFIRE instrument slit system being built for Keck) can be used (which implies some limitations on the total number and arrangement of slitlets). As the distribution of targets maps into the distribution of spectra on the detector (see Fig. 1.15), the spectrum of one object can overlap that of another, or one spectral order can interfere with another. This leads to a restriction in the maximum surface density of targets which may be observed simultaneously. To avoid this problem a careful mask design is necessary to determine an optimal layout and slit orientation. The requirement of a vertical slit is inconvenient for MOS, as a manufactured plate provides the parallactic angle for all slitlets only at one time of the night. In this situtation an ADC is desired.

Sky subtraction is straight-forward with multislit instruments, as the slitlets can be made long enough to sample the sky spectrum immediately adjacent to the object. Or, the slitlets can be kept very small in length and *nod and shuffle* sky sampling can be used (Glazebrook &

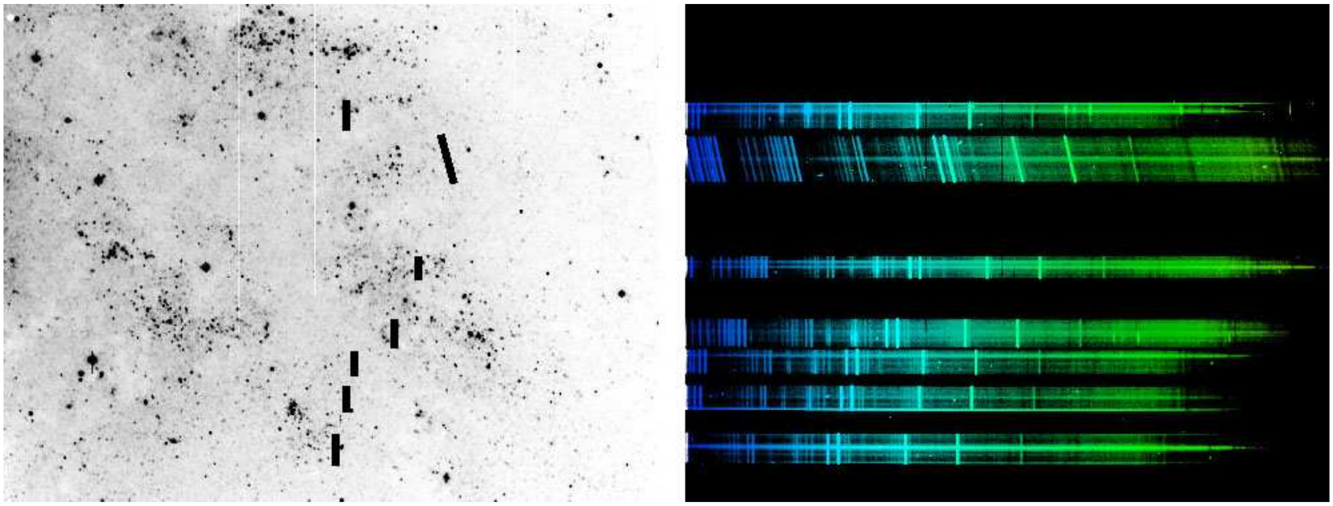

Figure 1.15: ***Slit and spectra arrangement in a multi-slit system.***

Bland-Hawthorn, 2001 and references therein), further increasing the multiplex gain. As intrinsic variation of the sky background, especially over the $0.7-2\ \mu$m range dominated by OH emission of the atmosphere, can happen on a time scale minutes (Ramsay et al., 1992), sky subtraction is critical for faint objects. Multislit sytems provide generally higher throughput than fiber fed instruments, thanks to the direct coupling to the telescope. Therefore they are often preferred for observing faint objects at low–medium resolution.

It is also an advantage that the slit mask and disperser can be removed (or the grating replaced by a mirror) from the light path and direct imaging of the target field can be done. This is not possible with multifiber systems, although coherent fiber bundles can be used to acquire reference stars.

Multi-fiber spectrographs (e.g. HYDRA (Barden et al., 1993) as an early realization, Pasquini et al. (2001), or Hectospec & Hectochelle (Fabricant et al. 2005, Szentgyorgyi et al. 1998); for a comprehensive list see Parry 1997) have several advantages, and of course some drawbacks, over multislit systems. One of the main advantages is that the fibers can be placed anywhere on the focal plane since the distribution of the fiber ends at the spectrograph is independent of target positions. Fibers can be arranged in a line to form a pseudo-slit so that each spectrum can be recorded without any overlapping. Thereby optimally filling the detector format. (Note, that a long pseudo-slit is subject to slit tilt as described in 1.5.2.) It has to be mentioned, though, that fiber systems also have some constraints on target density as the distant of closest approach by fibers is limited by the positioning system and/or the physical size of the fiber mount. The positioning can be done manually or by means of robots. The former requires a so-called *plug plate* machined in advance of observation, which is very similar to slit masks in several ways. Robotic operation enables faster and on-the-fly configuration changes/corrections, but to make such system efficient and fail-free (breaking fibers) means a serious engineering and maintenance task.

As mentioned before, fibers can be very long and so (at the expense of losing some light) the spectrographs can be mounted in a gravitationally-invariant, thermal controlled room off the telescope. Since multi-object capability usually increases the overall size of an instrument, this means removing a significant weight from the telescope mount. But stability is essential for high precision spectroscopy, and so echelle multi-object systems often use fibers even when the sky subtraction is somewhat problematic (the background contamination has to be estimated form sky spectra obtained from different parts of the field, recorded through different fibers). The use of an ADC, just like for single fibers, is unavoidable to minimize spectrophotometric errors.

Infrared MOS systems so far were all multi-slit designs, as warm fibers would pollute the detector by their thermal radiation. Cooling the fibers significantly increases the fragility and results handling and re-configuration problems, along with other issues regarding FRD and transmission. Although recent developments (see Parry (2006), Lee et al. (2001), and references therein) might open up a new era of cryogenic fibers and high resolution infrared echelles.

Effect of line tilt

Although the quasi-Littrow mode of grating illumination offers advantages in terms of efficiency, the non-zero γ angle has the effect of tilting the the slit (or pseudo-slit) image with respect to the dispersion direction. Due to the finite height of the slit there is a change in the angle of incidence with respect to the facet normal, from one end to the other of the slit. As seen in Fig. 1.16 if the change in γ is $\delta\gamma$, then there is a corresponding change in the angle of diffraction, $\delta\beta$, which results in a line tilt τ given by:

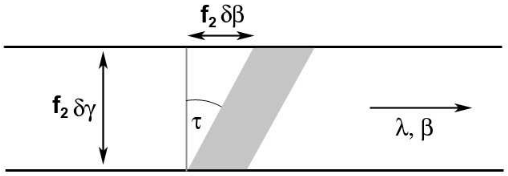

Figure 1.16: ***Line tilt in a spectrograph***

$$tan\ \tau \ = \ \frac{\delta\beta}{\delta\gamma} \ = \ \frac{d\beta}{d\gamma}, \tag{1.46}$$

where $\delta\beta/\delta\gamma$ is not necessarily constant and hence the tilt angle can vary across the slit image height. This curvature would be noticeable only for very long slit heights, and so the long pseudo slit formed by the fibers of a MOS entrance will be heavily effected by this. As a result a given spectral feature of each aperture would appear on the image not along a straight line, like the slit itself, but rather along a curved trace. It follows that:

$$\frac{d\beta}{d\gamma} \ = \ \frac{d\beta}{d\lambda}\frac{d\lambda}{d\gamma}, \tag{1.47}$$

where $d\beta/d\lambda$ is the echelle angular dispersion given by Eq. (1.12), but now with the additional term taking into account the $\gamma \neq 0$ condition:

$$\frac{d\beta}{d\lambda} \ = \ \frac{m\rho}{cos\ \beta\ cos\ \gamma}. \tag{1.48}$$

Expressing $d\lambda/d\gamma$ by differentiating the (1.11) grating equation with respect to γ we get:

$$\frac{d\lambda}{d\gamma} \;=\; -\frac{1}{m\ \rho}(sin\alpha \;+\; sin\beta)\ sin\gamma, \tag{1.49}$$

and therefore substituting these two into Eq. (1.47):

$$tan\ \tau \;=\; \frac{(sin\alpha \;+\; sin\beta)}{cos\beta}\ \frac{sin\gamma}{cos\gamma} \;=\; \lambda\ \frac{d\beta}{d\lambda}\ tan\gamma, \tag{1.50}$$

which can be rewritten for the blaze wavelength λ_B in a simpler form:

$$tan\ \tau \;=\; 2\ tan\theta_B\ tan\gamma. \tag{1.51}$$

From Eq. (1.51) it can be seen that high R-number gratings are more susceptible to line tilt. Eq. (1.50) also reveals that line tilt is a function of wavelength and γ. This means that line tilt is changing across a given spectral order and different in each spectral order. It also has to be pointed out that if cross dispersion is applied before the echelle, the wavelength dependence would be even more pronounced.

For a fiber fed MOS the picture is even more complex. Small misalignments in the pseudo slit (tilts of fiber axes respect to each other) result changes in γ and therefore different line-tilt behavior for each aperture. The light of different fibers also illuminates different zones (sub-apertures) of the collimator/camera optics, and so aberrations and misalignments contribute to the image at very different levels. In other words, a fiber fed MOS is better described as bundle of several independent small spectrographs, forming the spectra on the same detector. This makes the internal comparison of MOS spectra very difficult (see §4.1 and chapter 4).

The slit tilt has an impact on resolution. In most (if not all) data reduction procedures the intensity distribution across the aperture (e.g. perpendicular to dispersion) is evaluated to determine the intensity at that given point of the extracted spectrum. This evaluation (mostly a simple sum or integration of a Gaussian fit) happens along CCD columns or rows (whichever is oriented perpendicular to dispersion). If the spectral lines are tilted respect to the pixel grid then the extracted profile of a spectral feature (called the line spread function, or LSF) is broader than the real instrumental PSF would imply. Imagine vertically collapsing the slit image of Fig. 1.16 and compare the LSF created this way to a case of optimal extraction, when intensities are summed along an axis tilted by τ respect to vertical, along the real spine of the slit.

In direct feed instruments the slit can be counter-rotated (and even shaped as an arc) to compensate for above effects. However, as it has been demonstrated by Schroder & Hillard (1980), restoring resolution by slit rotation results in decreased efficiency in such way that the resolution-throughput product remains the same.

Effective Resolution of Fiber Fed Instruments

The effective resolving power R' of a circular fiber of diameter d is different compared to a rectangular slit of d width and height. Dividing the face of the fiber into many sub-slits ($\Delta h \ll d$, see Fig. 1.17) which have widths w_i equal to the chord parallel to dispersion, it is easy to see that all of these sub-slits but one have smaller than d width. This suggests that the effective slit width is smaller than d. To calculate this the intensity contribution of each sub-slit (proportional to its

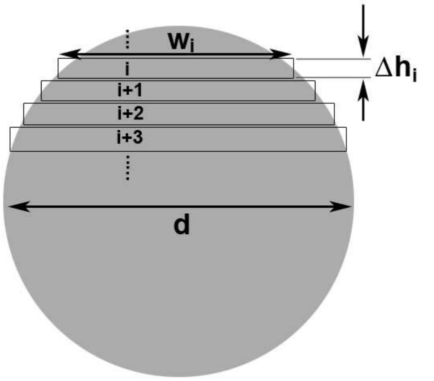

Figure 1.17: ***Calculating the effective width of a fiber***

area) has to be determined and used as a weight when averaging the w_i slit widths. In case the full face of the fiber is serving as the slit (i.e. the fiber is not re-imaged to a slit to gain resolution) the the flux weighted slit width $\bar{w}$ is expressed as:

$$\bar{w} = \frac{8}{3\pi}\, d, \tag{1.52}$$

after Vaughnn (1994). Therefore the effective resolution of a fiber fed instrument becomes larger:

$$R' = \frac{d}{\bar{w}}\, R = \frac{3\pi}{8}\, R = \frac{R}{0.849}. \tag{1.53}$$

If anamorphism is presented (see Eq. 1.1), the circular fiber end would render into an ellipse of axes w (measured along dispersion) and h (perpendicular to dispersion), even without line tilt. In case of favorable illumination ($\alpha > \beta$, as discussed in 1.4.2) the diameter of the dispersed beam (D_2) is larger than the collimated beam (D_1) and the following applies:

$$1 < r = \frac{D_2}{D_1} = \frac{h}{w}, \tag{1.54}$$

or in other words h is the major, w is the minor axis of the fiber image which is “compressed” in the dispersion direction by a factor of r, and so it would increase resolution by the same amount.

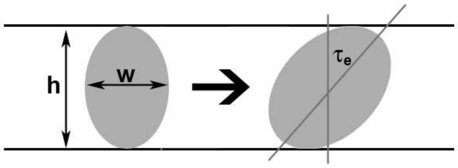

Figure 1.18: ***Tilt of spectral features in a fiber fed spectrograph***

However, the line tilt described above also applies for fiber fed instruments, as one edge of the fiber sees the grating at a slightly different angle compared to the other edge. This ellipse would be sheared along dispersion as a result of τ line tilt (see Fig. 1.18), and render into an other ellipse with a major axis tilted at an even higher τ_e angle as given by (Barnes, 2004):

$$tan\ \tau_e \ = \ tan\left(\frac{h}{w}\ tan\ \tau\right) \ = \ tan\ (r\ tan\ \tau). \tag{1.55}$$

The R' effective resolution in presence of line tilt an anamorphism would become:

$$R''(\tau) \ = \ \frac{R\ r}{0.849}\ \frac{1}{\sqrt{1\ +\ r^2\ \tau^2}} \tag{1.56}$$

assuming small τ tilt angles.

Measured vs. Calculated Resolution The conventional way of determining resolution is to measure the FWHM of a monochromatic light source (single laser line or an un-blended emission line of a calibration lamp). This method makes the assumption that the profile of such single line after extraction to one dimension (the LSF) can be approximated by a Gaussian. However, this is only true for fiber diameters d comparable to the PSF of the spectrograph optics. Otherwise, in the case of nearly perfect optics, when the PSF is significantly smaller than d, the top-hat like illumination function of the fiber will remain dominant on the image. This results in a similar top-hat like intensity distribution within the imaged spectral features. If this is fitted by a Gaussian during the measurement of resolution, the resulting FWHM is smaller than the d' real width of the fiber image.

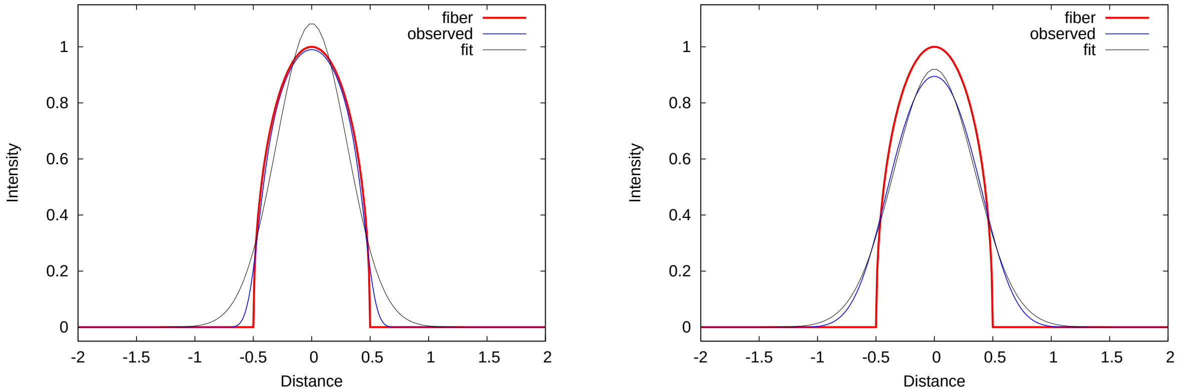

(a) *fwhm* of PSF is 10% of fiber width (b) *fwhm* of PSF is 30% of fiber width

Figure 1.19: ***The effect of spectrograph optics PSF on measured resolution:*** *if the PSF is small compared to the fiber diameter (left), the observed profile (blue) is very close to the original intensity distribution (red), and a Gaussian fit (black) results an unrealistically small FWHM of 0.4. If the optics provides spot sizes comparable to the fiber (right), the observed profile is close to Gaussian (FWHM=0.5).*

Therefore the measured and estimated resolution values (calculated as above) can be different by as much as $\approx R/0.682$, in case of perfect optics (Barnes, 2004), no anamorphism and same focal length for camera and collimator.

Note, that the image of the fiber will be de-magnified by the ratio of camera and collimator focal lengths, as well as the image would be squeezed by the anamorphic factor: $d' = d * 1/r * f_2/f_1$. Therefore in most realistic cases d' is comparable to the PSF of the camera.

1.5.3 Merit of a Spectrograph

The following might seem to be a bit short to be distinguished as a subsection, but it is important enough to get more attention.

A common merit function used for comparing spectrographs is the slit–resolving power product:

$$R\chi = \frac{2\ sin\theta_B\ W}{D_T}. \tag{1.57}$$

However for astronomical applications a more complex form, including instrument throughput T, would be needed. Still, the $R\chi T$ value (Jacquinot, 1954) is not appropriate enough, as pointed out by Vaughnn (1994), since the detector characteristic and sampling (signal-to-noise ratio per spectral resolution element) is not included.

While some merit function like the one described above surely can be constructed to compare instruments, one can argue that a real measure the amount of good quality data and *science produced*. From this point of view the multi-object instruments have some clear advantage, and old spectrographs with data sets a few decade long can not be just ignored.

Resolution Boosting Techniques also have to be mentioned here, as this can increase the RV precision of older or smaller spectrographs, and so increase their merit in comparison of modern instruments. A dispersed fixed delay interferometer (DFDI, or also mentioned in the literature as externally dispersed interferometer or EDI) consists of a Michelson interferometer followed by a medium resolution spectrograph. When using this technique sinusoidal interference fringes are formed in the slit direction at the position of stellar absorption lines. A shift in dispersion direction of the underlying spectra (due to Doppler shifts) results as a phase shift of the sinusoidal fringe pattern. As changes in the fringe (Moire) pattern are larger than the displacement of spectral lines, the spectrograph is more sensitive to RV changes. See Erksine & Ge (2000) and Ge at al. (2002) for details of this technique

1.6 On the Calibration of High Resolution Spectrographs

Spectroscopic observations have to be tied somehow to a wavelength reference, the pixel coordinates on the detector have to be mapped into a wavelength scale. To define such a wavelength solution (and so to fix a zero point of RV measurements) a spectra with well calibrated features has to be recorded. This is usually an emission spectra for which wavelengths of spectral lines are precisely determined (e.g. by Fourier-transform spectrographs). Telluric lines of the atmosphere or absorption lines of a gas cell can be also used, and as discussed later it might have advantages over the arc spectra. But, independently of the source, such spectrum must be recorded through the same slit or fiber providing the scientific observations.

Once such zero point is determined, however, it has to be repeatedly monitored to detect instrumental shifts in between, or *during* exposures. The observed spectral line profile (usually) is given by the instrument but not by the intrinsic stellar profile. Therefore the PSF of the instrument must be stable enough not to introduce systematics in the computation of the position of spectral lines. Intermittent calibration exposures, e.g. before and after a scientific target was observed, are essential for direct mounted spectrographs with no active flexure control, as the gravitational (and thermal) load of the instrument is changing over the time of the exposure as the telescope is tracking. In order to avoid this and have a invariant PSF the instrument must be very stable, or not even a continuous calibration can assure the highest possible, photon limited accuracy. (Active flexure control is basically a continuous calibration–correction servo loop, but it still comes with some level of unavoidable and unreconstructable smearing of the PSF.)

As was also discussed in 1.5.2 this implies the use of fibers for high precision RV work. Even so, to ensure the maximal possible accuracy, the calibration information is best recorded simultaneously with the object spectra to provide confirmation of stability during the exposure. This can be done either using the same fiber (iodine cell technique) or through a dedicated calibration fiber (ThAr technique).

Future instruments might be able to take advantage of laser frequency combs. This possible new technique for precise calibration was described by Murphy et al. (2007b), using femtosecond-pulsed mode locked lasers controlled by a stable oscillator (e.g. atomic clock). Simulations have shown that the photon limited calibration precision would be $\sim$ 1 cm s^{-1}, if the comb can be extended over 4000 Å range. (See also §11.1.2.)

1.6.1 Absorption lines: Iodine cells

Passing the starlight through an absorbing medium before entry into the spectrograph superimposes reference absorption lines that experience the *same instrumental shifts and distortions* as the stellar spectrum. The simplest realization of this approach is the use of telluric lines (Griffin & Griffin, 1973), but the wavelength range is limited to the spectral regions with suitable atmospheric features. To cover a desired wavelength range it is necessary to build a cell and fill it with an absorbing medium which provides sharp and stable fiducials over a large spectral window.

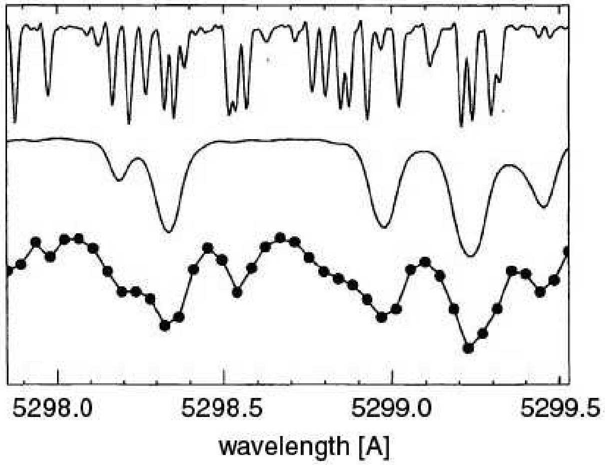

Figure 1.20: ***The iodine technique:*** *the pure I$_2$ spectrum as recorded at very high resolution is shown on the top, while the observed clean stellar spectrum (significantly lower resolution) is in the middle. On the bottom the observed stellar + iodine spectrum is displayed as dots and the calculated composite spectrum as a solid line.*

The first attempts (Campbell & Walker, 1979) used HF, which has several limitations (corrosive, requires large cell, etc.). Marcy & Butler (1992) proposed the use of gaseous iodine (Fig. 1.20), and it has become the most popular choice since then because of its several advantages over other mediums: small cell length; wavelength coverage of 5000 Å to 6300 Å with at least two features per Å; chemically stable and only slightly corrosive; requires almost no maintenance; existing spectrographs can be retro-fitted with an I_2 cell; the cell is sealed and so is very stable over several years. Most importantly the stellar and calibration light passes through the exact same light path along the entire instrument (including the slit/fiber). Marcy & Butler (1992) already proved 6 m s^{-1} precision over short time scales, and 25 m s^{-1} over a year. Current instruments deliver 1-2 m s^{-1} precision using this technique (Bonanno et al., 2008).

However, as always, there are some drawbacks. One obvious is the limited spectral window, which is significantly smaller than the coverage of echelle spectrographs (by a factor os 5). The other issue is throughput, as the cell introduces extra glass/air surfaces and the gas itself also absorbs some of the light resulting an overall light loss of a factor of ~ 2. To decompose the observed spectrum (see Fig. 1.20) the PSF has to be modeled very accurately, using several (up to 10 or so) components to describe it, and allow these to change smoothly over a single echelle order. Therefore the data reduction is a computationally very intensive process.

1.6.2 Emission Features: Simultaneous ThAr

The most commonly used calibration source is the thorium?argon hollow-cathode emission-line lamp. Thorium provides numerous spectral features over the entire visible and near-infrared domains and its mono-isotopic nature and absence of hyperfine structure leads to narrow, highly symmetric line profiles. Calibration lamps are at relatively low cost, but their lifetime is relatively short (depending on the current the lamp is run at) and two lamps, even from the same manufacturer, never provide the exact same spectra. Thorium lines differ widely in intensity and spacing, and positions of single lines determined by the widely used KPNO McMath-Pierce Fourier Transform Spectrometer atlas (Palmer & Engleman, 1983) are only accurate to $16-82$ m s^{-1}. To overcome such limitations Lovis & Pepe (2007) constructed a new ThAr line list based on HARPS calibration data, reaching a weighted RMS dispersion of 10 m s^{-1}, and even $1-2$ m s^{-1} position accuracy for bright individual lines. This enables HARPS to achieve a wavelength solution with a precision of 0.25 m s^{-1}. Still, most of the Th lines are blended at $R \leq 150\,000$ so high resolution or very careful selection of spectral lines (Murphy et al., 2007a) is needed for optimal calibration.

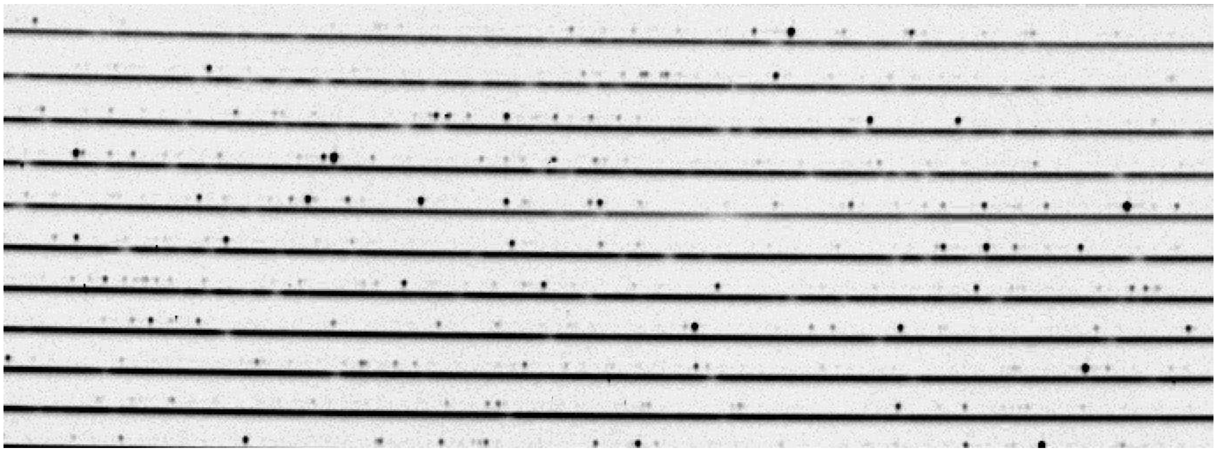

Figure 1.21: ***The simultaneous ThAr technique:*** *the ThAr lines form a secondary spectrum, interleaved between the stellar echelle orders. (A portion of an actual TRES spectrum, inverted.)*

The argon lines are real problem sources as their position can vary at a 100 m s^{-1} level and their relative intensity is much higher compared to Th lines. Intensity levels can be balanced between Th and Ar by increasing the lamp current (Kerber et al., 2007), but this significantly shortens the life of the lamp. Argon lines seem to be more sensitive to pressure changes (due to aging of the lamp or temperature changes) While these bright Ar lines certainly have to be removed from the wavelength solution or drift tracking, they can not be removed from the image. And since a simultaneous calibration echelle spectrum is is interleaved with the object orders, there might be a cross-talk between the two. To maintain appropriate signal-to-noise ratio in the weaker Th lines, the Ar lines, especially beyond 7000 Å , become easily saturated thereby diluting the object spectra. This can be balanced by filters, damping the intensity of calibration light beyond this point, but this would affect Th line of the same region. Or, this part of the spectra can be simply ignored, as the radial velocity information content (Bouchy et al., 2001) is very low.

As the calibration light passes through a different fiber great care has to be taken to make this secondary light path as similar to the target light path as possible. Calibration light must be fed into the fiber at the same focal ratio as the telescope feeds the target fiber. Environmental effects (bending, temperature, etc.) also should be identical for both fibers. The collimator & camera optics must be illuminated almost identically, which implies the two fibers have to be mounted very close to each other (however interleaving the two spectrum also puts some constrain on fiber placement in favor of the former requirement).

1.6.3 Calibration of Multiobject Spectrographs

The calibration of multi-object spectrographs is very different, as not two but rather a few hundred slitlets/fibers have to be illuminated the same way. While this might be maintained at the telescope end, it is unavoidable that each fiber sees different zones of the spectrograph optics. Therefore aberrations affect each spectrum in a different way, resulting individual line profiles at a given wavelength for each aperture. For applications requiring high RV precision, which means looking for shifts on the 0.01 pixel scale, this is a very serious problem. As apertures behave so differently to environmental/illumination changes, line profile changes in a given aperture can not be 100% predicted by variations measured in an other one. Imagine two beams, one crossing a tiny bit to the left of the optical axis of the camera(corresponding to a fiber close to the center of the pseudo-slit), one far at the left edge (a fiber at the edge of the pseudo slit). A slight shift of the beams to the right could transfer the former beam just to the right of the optical axis, and pull the other one closer to the center. As zonal aberrations are significantly smaller at the optical axis, former beam would see almost no change. Image quality of latter beam, though, can be heavily changed. Therefore simultaneous calibration taken through fibers close to the edge of the format likely show different instrumental errors than the rest of the apertures, as it has been reported by Loeillet et al. (2008).

As it was mentioned before due to incomplete radial scrambling of fibers (see 1.5.2) changes in the far field (variations in the pupil illumination of the telescope) can result RV variations. For multi fiber instrument each fiber has a slightly different illumination to start with, as over the wide field of view the fibers placed the PSF of the telescope can change, and time dependency of this illumination is also unique at a given location on the focal plane. Since multi-object scramblers would be so complex systems to align, and so expensive in terms of light loss, that these variations are not corrected for (at least) in recent instruments.

Speaking of the illumination at the telescope end, multi fiber systems face an other challenge: illuminate all fibers exactly the same way with calibration sources and make it to match the way starlight illuminates the focal plane. An obvious choice would be to deploy a diffusing screen in front of the telescope, like the commonly used flat-fielding screens for CCD imaging, and let calibration light travel through the telescope (although even this would provide a somewhat different pattern unless baffling of the telescope is designed accordingly). A serious flaw of this approach is the intensity level it can provide for the very faint ThAr lamps. Experiments at the MMT with Hectochelle showed that 16 arc lamps illuminating such a screen in front of the 6.5 m aperture provided only a dozen usable spectral lines for 30 min exposure time (see 4.1). This is unacceptable for night time calibration, and also the number of lines is not sufficient to establish a good wavelength solution (see Fig. 1.22).

Direct illumination of the fibers, by-passing the optical path through the telescope but simulating the input focal ratio by some small optics, is used by almost all single object fiber spectrographs. It is a highly efficient method but not feasible for multi-object systems with a big field of view, as such small pre-optics and lamps can not be deployed for all fibers at a given configuration. (Or, it might be possible to incorporate a calibration unit into the fiber positioning mechanism, and while a fiber is being placed it could be calibrated.) Replacing the small individual calibration units by a bigger one illuminating all fibers at once is very problematic, as a bright, evenly illuminated surface and/or optics at least as big as the focal plane are required. Such system would be significant in size and might interfere with other telescope components (field flattener, ADC), as it has to be mounted in front of the focal plane. Some telescopes were already built with this issue in mind, and a facility calibration unit is offered to satisfy all sorts of instruments, as a part of the telescope (like the Gemini Facility Calibration unit (Ramsay-Howat et al., 2000) for the Gemini Telescope).

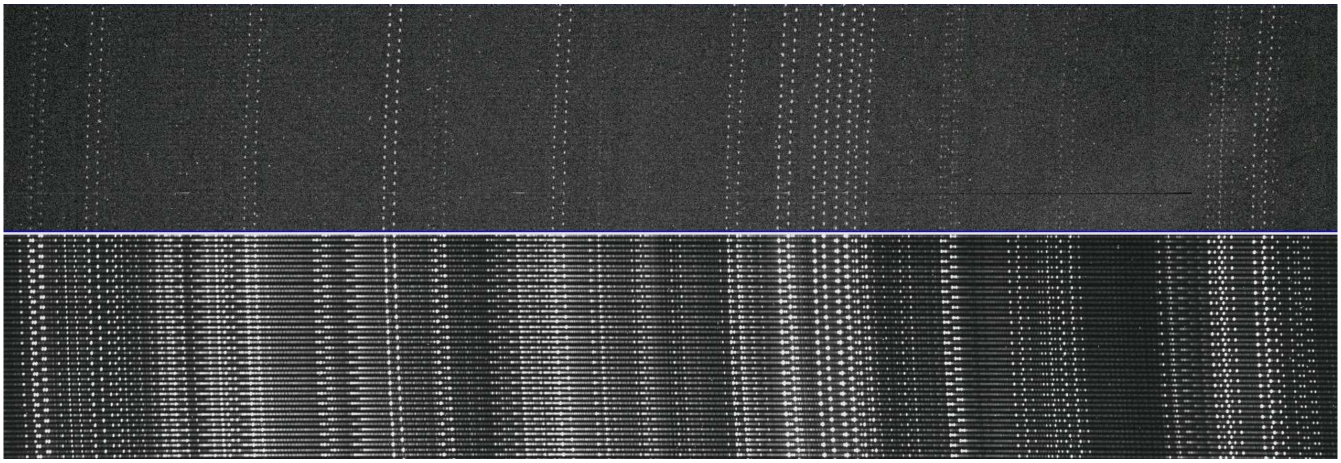

Figure 1.22: ***Scattered vs. direct illumination of a MOS spectrograph****, a comparison of actual Hectochelle frames. Exposure times (900 second) and number of lamps used are the same, but the peak intensities for the same lines on the direct illumination (bottom) image are ∼200 times higher.*

The importance of calibration and maintaining, or at least measuring, the stability can not be emphasized enough, especially for high precision RV applications. The aim of above section was to illuminate this, and lay the grounds for a detailed discussion of an implemented MOS solution described in section 4.1. I feel that discussion on the calibration of high-resolution MOS is an important parts of present work, since literature is very limited on this topic. Also, I was hoping to highlight that an instrument design is not complete without covering the calibration system.

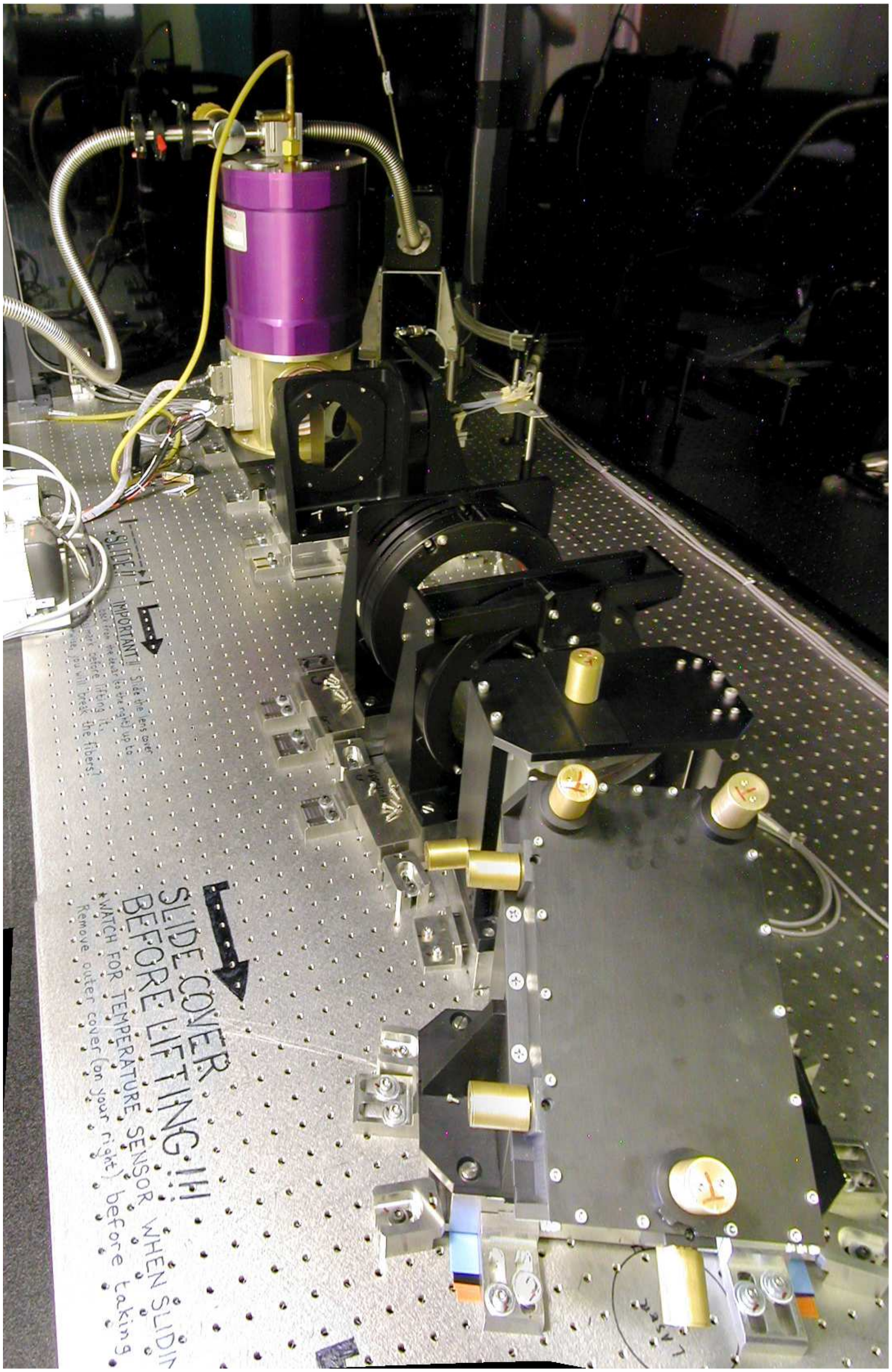
SLIDE!!
IMPORTANT!!
will break the fibers!
SLIDE COVER BEFORE LIFTING!!!
*WATCH FOR TEMPERATURE SENSOR WHEN SLIDIN
Remove outer cover (on your right) before taking
LASER

The TRES optical bench *– as assembled before first light at FLWO*

Chapter 2

TRES – A High Resolution, Fiber Fed Echelle Spectrograph

In this chapter I describe my work on the design and construction of the *Tillinghast Reflector Echelle Spectrograph* (TRES), which instrument was originally proposed in 2002, got funded in 2003 and was delivered to the Fred Lawrence Whipple Observatory (FLWO) in the summer of 2007. First, I overview the science drivers and constraints leading to the initial design (§2.1), followed by a detailed description of the optical (§2.2, §2.3), mechanical (§2.4, §2.5) and electrical design (§2.6, §2.7). Integration, assembly and lab testing is covered in section §2.9, while the real performance and first results are unveiled in §2.10. As a near-future continuation of presented instrumental work, a design of an ADC is outlined in §11.1.1.

2.1 Design Considerations

2.1.1 Scientific Goals

The Tillinghast reflector is a 1.5 meter diameter f/10 Cassegrain telescope, with an spherical primary and a elliptical secondary. Although a 2-element corrector has been implemented, the image quality is acceptable only over a small (few arcmin) angular field of view. Therefore spectroscopy has always been the ideal operational mode of this telescope, which, for example, conducted the widely known CfA Redshift Survey (Huchra et al., 1983) during the moonless nights of 1977-1994 using the reticon based Z-Machine (Latham, 1982). For bright time the telescope has been equipped with the CfA Digital Speedometer (Latham, 1992), a single-order, reticon based echelle spectrograph. This instrument, capable of reaching 0.5 km s^{-1} RV precision using modern data reduction techniques, is still in use after 30 years of service (however running out of spare parts).

In 1994 the Z-Machine was replaced with FAST (Fabricant et al., 1998), a high-throughput, moderate dispersion instrument. The improved efficiency of FAST resulted a 3-fold increase in the scientific output, which pointed out the likely benefits of a modern, high dispersion spectrograph.

Although the FLWO hosted such an instrument between 1993 and 2004, the Advanced Fiber Optic Echelle (AFOE, Brown et al., 1994) did not result such a boost as FAST. While AFOE was a carefully designed, fully cross-dispersed, fiber fed echelle (proved to deliver data with few m s^{-1} precision), its low throughput did not allow the observation of faint targets. (AFOE was re-located to Mt. Wilson in 2004 and got de-commissioned in 2007).

Exoplanet research is undeniably one of the hottest topic in astronomy. As the also FLWO based HATNet transit-survey (Bakos et al., 2002) took off in 2003, local follow-up of planetary candidates become very high priority. The queue observing at the 1.5 m telescope and the CfA Speedometer provided a very unique, quick response spectroscopic confirmation of low mass stellar companions, and the 0.5 km s^{-1} precision was sufficient enough to exclude the numerous stellar impostors. But the ongoing reconnaissance observations were pressing the Speedometer, which up to date acquired $\sim$ 4500 spectra of several hundred candidates. Such workload could have been handled better (e.g. faster) with a fully cross-dispersed echelle providing wider wavelength coverage (therefore better cross-correlation due to the increased number of lines) with $5 - 10$ times better throughput (mostly due to upgrading the intensified reticon to a CCD detector). If RV precision of a few 10 m s^{-1} at $V = 12$ can be reached by a new instrument, a significantly higher fraction of orbits could be determined without the need of larger telescopes.

The involvement of CfA in the Kepler mission (http://kepler.nasa.gov/) implied further increase in the volume of transit candidates which require initial spectroscopic follow-up, starting in February 2009 (according to the current launch schedule). The bulk of that work was proposed to be done by the replacement of the CfA Speedometer. In the meantime the foundation of the Harvard Origins of Life Initiative proposed to build a copy of the HARPS instrument (and got funded), to serve as a dedicated instrument for final confirmation of Kepler planets. Even though this HARPS-NEF (HARPS New Earth Finder) instrument on the 4.5m William Herschel Telescope will have dozens of guaranted nights for Kepler follow-up, the candidates still have to be pre-filtered to make the operation of HARPS-NEF really effective. These reasons put TRES into a very important position in the field of exoplanet research.

Star formation studies at the CfA could also gain from a new echelle providing < 0.5 km s^{-1} accuracy down to $V = 14$ magnitude. A wide wavelength coverage would open up new windows to simultaneous studies of emission and absorption lines, and allow scientists to attack a broad range of star formation issues:

- Determine membership of star forming regions and young associations from RV criteria. Typical clusters and young associations have velocity dispersion of $\sim$ 2 km s^{-1}, so TRES would be extremely efficient at rejecting foreground and background objects.
- Find and characterize spectroscopic binaries, to explore fragmentation in star formation.
- Identify young stars with Hα emission in nebulous regions, where high resolution can separate the broad accretion component from the nebular emission.
- Accurately measure the continuum veiling, the emission from the accretion shock on the star.
- Accurately measure Li I equivalent widths, because depletion of Li can be used as a secondary, but independent age indicator, which is important identifying somewhat older stars with dust debris disks in nearby associations for follow up with SIRTF, SMA, ALMA, etc.
- Study of mass ejection processes in a variety of spectral lines like Hα, Na I & [O I]

For the $V = 11 - 14$ magnitude region this above would mean 350 young and 600 older stars, approximately, within the reach of TRES.

Stellar astrophysics offers a broad range of problems to attack by a high efficiency echelle. In recent years we have witnessed an explosion of photometric time-series data, collected to find a small number of rare sources (like transiting extrasolar planets, gravitational microlenses). These data contain many other variable sources worth to investigate. For example, Devor et al. (2007) has found hundreds of eclipsing binary systems in the TrES (Trans-atlantic Exoplanet Survey) data base, and determined physical properties for the components. To further follow up some of the most interesting candidates surfacing in those data bases an echelle spectrograph reaching $V = 14$ would be an ideal choice, on a telescope not heavily oversubscribed to allow multiple epoch measurements to constrain orbital solutions.

The pulsation of high-amplitude delta Scuti (HADS) variables are associated with huge atmospheric motions (RV amplitudes up to 50-60 km/s). Because of the very short pulsation periods (0.05–0.15 days) measuring HADS radial velocity curves has been quite difficult. The optimal time resolution requires about one measurement every three minutes to avoid phase smearing, which is a hard limitation for getting high spectral resolution observations with high S/N (Wilson et al., 1998). A high throughput echelle covering the entire visible band would allow to trace motions of layers at different optical depths, by measuring velocities of lines of different excitation potential, and so detect shock waves. This can be used to constrain mean dynamical properties of the pulsating atmosphere. Physical parameters and evolutionary status of the observed stars also can be determined, and possible secondary components could be detected.

Cepheid variable stars, because of their role as distance indicators, are popular targets in observational astrophysics. Binarity of such pulsators raises serious issues regarding the calibration of their distance. The mode of pulsation and/or the presence of a possible companion can be inferred from the ratio of the photometric and radial velocity amplitudes (Szabados, 2000). In spite of their general importance, however, there are quite a few Cepheids worthy of immediate observation best suited by an echelle spectrograph on a 1-2m class telescope.

2.1.2 Estimated RV Performance at the Photon Noise Limit

From the scientific considerations above the following expectations could be drawn:

TRES should cover the full visible passband reaching into the NIR to include the Ca triplet. Its throughput has to be high enough to reach $V = 14$ targets with high/moderate resolution within a reasonable ~ 1 hour of exposure time providing a RV precision of ~ 0.25 km s^{-1}or better. This would be suitable for follow up of faint binary systems, but likely the more demanding criteria are the ones set by exoplanet follow-up. As the "sweet spot" for Kepler candidates is going to be $V \approx 12$, and there are going to be candidates even fainter than that, to efficiently filter out stellar blends even on the fainter side the highest possible trhoughput is necessary. A minimum of $20-30$ m s^{-1} precision within ≤ 0.5 hour of exposure time at this magnitude level ($V = 12$) could provide orbits for most of the systems. This implies high resolution, fiber feed and well controlled spectrograph environment. The stability of TRES must be below the above limit to ensure that observations are *photon limited*, not by the systematics of the instrument or calibration.

Bouchy et al. (2001) describes a method of estimating photon limited radial velocity uncertainties of spectrographs. First of all they point out the importance of the *information content* of stellar spectra, as the limiting RV precision heavily depends on the number and sharpness of absorption features and therefore on stellar parameters. The best suited targets for PRV range from F2V to K7V, with solar metallicities, as earlier types have fewer lines and those are usually broadened by high rotational velocity. Bouchy et al. (2001) introduces a *numerical quality factor* (Q) to measure the RV information content, and it is graphically re-presented here form Fig. 1. of their paper.

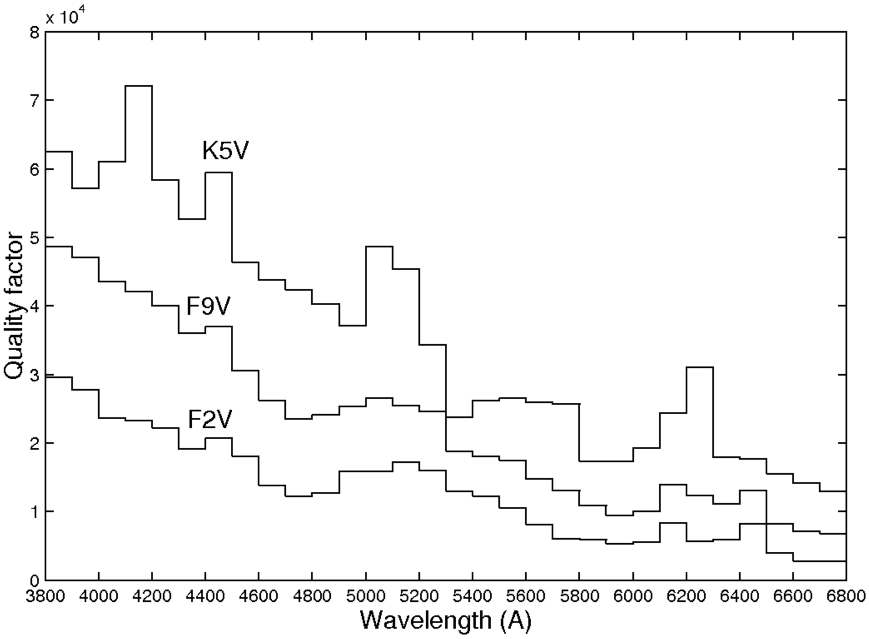

Figure 2.1: ***Quality factor of stellar spectra, versus spectral range***, *from Bouchy et al. (2001), for three late type stars with solar metallicities and no rotation.*

As it can be see on Fig. 2.1 the blue end of the visible band contains more RV information (more, sharper lines), and beyond 7000 Å there are essentially very few significant lines usable for RV determination. As some of the science planned for TRES requires the Ca triplet, being a more general instrument rather than one optimized for PRV, the bandpass of TRES was not solely determined by Q (unlike for HARPS). However this plot predicts that the red orders TRES would be not much of a use for RV work, as those are also heavily effected by telluric absorption bands of OH (and the Ca IR lines are too wide). Although there is some potential at the red end, working between telluric lines, as M dwars (and cool stars in general) have higher intensity at longer wavelengths (see §11.3.2).

An averaged Q value is ~ 35 000 for a K5V and ~ 14 500 for a F2V star exhibiting no rotational broadening (as plotted in Fig. 2.1). The Q value significantly drops if $v\ sin\ i$ increases form 0 to 6 km s^{-1} due to line broadening, and beyond that blending takes over and Q is still decreasing but at a slower rate. Taking 6 km s^{-1} as a (likely) example of real observation, the previously mentioned Q factors shrink to ~ 12 000 and ~ 7 000, respectively.

The resolution of a spectrograph is also influencing the quality factor, as $R \simeq 200\ 000$ is required to fully resolve all spectral lines of a K5V star. Obviously smaller resolution is less of a drawback observing faster rotating stars of the same spectral type, as it is shown in Fig 2.2 (re-producing Fig. 3 of Bouchy et al. 2001).

This graph suggests that $R = 50\ 000$ is probably a lower practical limit for spectrograph resolution, as below that spectral lines are still not resolved even for targets with relatively fast rotations of 10 km s^{-1}. At the same time $R = 100\ 000$ is an upper practical limit, as higher

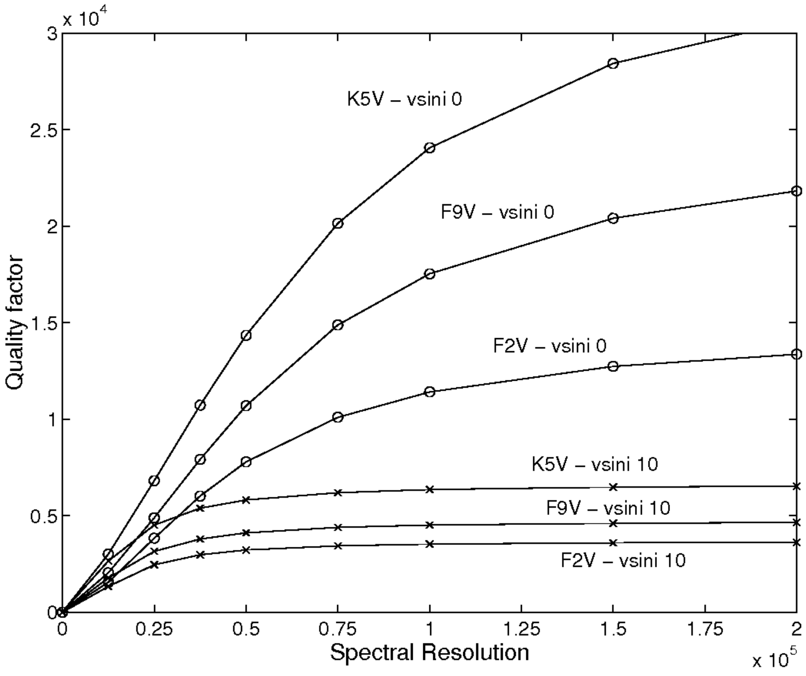

Figure 2.2: ***Quality factor versus spectral resolution***, *from Bouchy et al. (2001), for three late type stars with solar metallicities and rotational velocities of $v\ sin\ i = 0$ and $v\ sin\ i = 10$ km s^{-1}.*

resolution only makes difference in a very few cases. Again, as TRES is meant to be a more general instrument, a compromising 70 000 could be a goal in terms of resolution.

According to Bouchy et al. (2001) the radial velocity precision of a spectrograph is given by the following expression:

$$\delta V_{rms} = \frac{c}{Q\sqrt{N_{e^-}}}, \tag{2.1}$$

where c is the speed of light and N_{e^-} is the total number of photoelectrons. Assume a somewhat pessimistic scenario of an F2V target star exhibiting a $v\ sin\ i = 6$ km s^{-1} rotation, and so a Q factor of 7 000. Also assume $R = 70\ 000$, in which case the spectral resolution would not really have an impact on this Q value. Therefore to reach $\delta V_{rms} = 25$ m s^{-1} one would need $N_{e^-} \approx 2.9 \times 10^6$ photoelectrons over the 3800 – 6800 Å spectral window.

The total number of photoelectrons, from the other hand, also can be expressed for a star with a flux of F_* (given in photons cm^{-2} s^{-1}, outside the Earth's atmosphere) as:

$$N_{e^-} = \frac{F_*\ S_{tel}\ e_{tot}\ t_{exp}}{2.512^{mv}}, \tag{2.2}$$

where S_{tel} is the light collecting area of the telescope in cm^2, e_{tot} is the total instrument efficiency (including atmosphere, telescope, spectrograph and detector), t_{exp} is the exposure time in seconds and mv is the visual magnitude of the star. For a $V = 12$, F2V target F_* is estimated to be $\approx 2.7 \times 10^6$ after Allen (1973), integrated over the same 3000 Å wide bandpass. Therefore the $e_{tot}\ t_{exp}$ product can be calculated based on Eq. (2.2), using above estimated values and assuming a 0.4m central obscuration for the 1.5m Tillinghast reflector.

As a result we get $e_{tot}\ t_{exp} = 4.3$, and assuming a reasonable 5% average efficiency it means that a $t_{exp} \simeq 90$ sec exposure time is necessary to reach 25 m s^{-1} for a $V = 12$, F2V spectral type star observed with a $R \approx 70\ 000$ echelle spectrograph and using all spectral orders over the $3800 - 6800$ Å region. To push the precision down to $\delta V_{rms} = 10$ m s^{-1} the exposure time has to be increased to 600 s, which is still reasonable.

Note, that for 1 m s^{-1} precision either t_{exp} has to be increased by 100 times, or a $V = 7$ star is needed. But below 10 m s^{-1} precision a double scrambler is essential, as $0\farcs5$ guiding offset/centering error (moving the photometric barycenter off the center fiber) can result in a RV shift on the order of 3–5 m s^{-1} , according to Casse & Vieira (1997) and Kohler et al. (2001). But as discussed before the scrambler means a serious hit on the efficiency, and some science programs need TRES to go faint at high resolution. Also, as the primary goal is not confirmation but pre-selection of planet candidates (and probably follow-up of higher amplitude detections), which does not require the level of 1 m s^{-1}precision. The constraints on spectrograph environment would be also very demanding under the 10 m s^{-1} level, as pressure changes of 0.1 mBar or instrument temperature change of 0.1 K can result RV shifts of 10 m s^{-1}.

2.1.3 Determination of Basic Design and Parameters

Seeing conditions at the FLWO are often far from excellent, resulting an average seeing disk of $1\farcs5$. The 1.5m Tillinghast reflector has an f/10 focal ratio resulting a 110 μm diameter stellar image for average seeing. But such slow focal ratio is not preferred for feeding a fiber since due to FRD (see 1.5.2) an f/10 cone at fiber exit would contain only 70% of the input light. Reducing the input focal ratio to f/4 would render the light loss almost negligible, but it would also require a 44 μm fiber to cover the seeing disk. Fiber polishing experiences at the CfA concluded that under 50 μm it is really hard to get a nicely polished, flat fiber face, as properly holding and handling such a small and fragile fiber becomes problematic. Also, at f/4 feed a relatively fast collimator would be necessary.

Choosing f/6 input would refer to a 65 μm fiber diameter, and likely better polishing properties especially if manufacturer can provide a thick cladding and buffer. The FRD losses still would be under 10%, and so an f/6 collimator can be used.

To maximize the throughput of TRES even when the atmospheric conditions are bad, two other fiber diameters and a fiber exchanger were proposed. A 100 and 140 μm core diameter fibers were chosen for the initial design, providing $2\farcs3$ and $3\farcs2$ angular coverage. (The total number of tree (Spanish: *tres*) fibers gives the TRES (Tillinghast Reflector Echelle Spectrograph) acronym an additional meaning.)

The next step is to find a grating which would fulfill the resolution requirement. Choosing an R2 echelle and substituting the 1.5m telescope diameter and $1\farcs5$ angular slit size into Eq. (1.40) the minimal size of the grating to provide $R \geq 50\ 000$ is $W_{min} = 305$ mm. However, this is a little different if the effective resolving power of a fiber is considered, and so according to Eq. see (1.56) and assuming no anamorphic magnification and no fiber tilt we get $W_{min} = 258$ mm and hence a beam size of 115 mm if the grating is properly illuminated with no light loss. To reach the more optimal $R = 70\ 000$ a grating length of 360 mm and a beam diameter of 160 mm is required.

Choosing an R4 grating and fiber feed, for $R = 50\ 000$ a beam diameter of 58 mm and a grating length of 240 mm is necessary, while to reach the 70 000 effective resolution these dimension become 81 mm and 336 mm, respectively.

At this point commercially available gratings should be compared to above requirements. Considering the product line of Richardson Grating Laboratory it is apparent that their largest echelle substrate length of 400 mm would be adequate to reach $R = 70\ 000$, as the next common size to provide several ruling density options is $\sim$ 250 mm. (There is only one 300 mm grating with a fairly low $\rho = 23.2$.) The use of these smaller gratings would mean significant light loss because of overfilling, if the higher resolution limit is considered. The different ruling density options would allow to tweak the spectral format, to better match the detector size and sampling, and so the 400 mm and 250 mm product lines are compelling to avoid the expensive custom ruling (to select a non-catalog ρ for a 300 mm blank) or custom substrate (which would require custom duplication of an existing master grating onto the chosen substrate). However, the cost of a 400 mm characteristic size grating is significantly higher, so budget considerations suggest to accept the $R = 50\ 000$ lower limit (however a slight overfill of a 250 mm grating can provide some resolution boost). An other conclusion regarding standard substrate dimensions that R2 is more preferred over R4, as stock items of latter gratings has to be applied either with overfill or in a mosaic assembly (common aspect ratio is 1:2, 3:4; the use of 2 such gratings would approximate the nominal 1:4 ratio of R4).

As efficiency is the key for TRES a prism cross disperser is preferred. A glass with high near-UV transmission is required as the optical path within the prism can be significant at the base. Therefore the Ohara I-line glasses seem to be a good choice. Also, rejecting a scrambler would help to reach high throughput, and it would not compromise the science planned with TRES. The simultaneous ThAr calibration method also offers advantages regarding efficiency, however the relative low cost and simple implementation of an I_2 cell allows to have both and offer the gas cell as an option.

Regarding the optical arrangement a full-double-pass quasi-Littrow mode with a $\gamma < 5\,\mathrm{deg}$ and $\alpha = \beta$ could provide very high efficiency, with an all-refractive camera/collimator optics. If the tilted grating is facing down, which orientation prevents dust building up on its surface, the collimated and dispersed beams are separated horizontally with above angular constraints. Such layout would result a convenient way for mounting the fiber feed and detector directly on the faceplate of an optical bench. (The separation of these two does not even have to be very small, as we saw that even $\gamma = 10\,\mathrm{deg}$ to be very forgiving in terms of grating efficiency losses.)

The above sketched compact layout is compelling also since the biggest optical bench the dedicated spectrograph room at the FLWO can only accommodate is 1m×2m. Assuming a 115 mm beam diameter and f/6 optics the characteristic length of the collimator/camera is $\sim$ 700 mm, and the cross-disperser and echelle grating would fit within an other $\sim$ 400 mm. Therefore the spectrograph would cover a $\sim$1.2m×0.3m footprint, well within the maximal benchtop dimensions.

Regarding the detector the CfA has plenty of experience with the EEV 42-90 back illuminated, deep depletion CCD sensors (used in Hectochelle (Szentgyorgyi et al., 1998), Hectospec (Fabricant et al., 2005) and Megacam (McLeod et al., 1998) instruments). It is an obvious choice to use the same camera module already proved to be very successful, and so spare the development of a new detector. The 1:1 magnification ratio of the full-double-pass design would sample the 65 μm fiber diameter with 4.8 pixels (13.5 μm pixel size), and while the oversampling is even worse for the larger fibers on-chip binning of the image could help.

(Note: the EDI technique was very young at the time TRES was proposed, and although encouraging results were published since than(Ge et al., 2006), some main characteristic of EDI spectroscopy does not comply with the scientific goals of TRES. To make the sinusoidal fringe pattern visible the spectrum has to be stretched in cross-dispersion direction. This results to a lower S/N ratio and requires larger inter-order separation for an echelle. Also, to re-construct the fringe-free stellar spectra the fringe pattern have to be shifted and multiple observations combined. This is a serious hit on time-resolved observations. For these reasons TRES was rather considered to be a conventional echelle spectrograph.)

2.1.4 Echelogram calculations

Other than the ruling density of grating, prism material and apex angle, all the other design parameters became pretty much constrained in the previous section. The issue driving the determination of final parameters is to fit the echelogram on the 4608×2048 pixel CCD (13.5μm pixel size, or 62.2mm×27.6mm) with order separations large enough to accommodated two interleaving spectra (one for the object, one for simultaneous ThAr). As the largest fiber is 150μm, for clean extraction a minimum of 350–400μm or 26-29 pixel separation is necessary. Therefore the ruling density has to be high enough to provide adequate spacing between spectral orders (see Eq. (1.32) and (1.30) in the previous chapter), while the upper limit on ρ is set by optimal coverage of the CCD in the dispersion direction.

Of course the inter-order distance can be changed by adjusting the angular dispersion of the prism. But according to Eq. (1.3) for a given D_1 beam diameter to increase the order separation a larger baselength is needed, and so (as D_1 is fixed) it means a larger apex angle. Assuming a $n = 1.5$ refraction index incidence angles up to 40° (corresponding to apex angles up to 50°) are acceptable, as reflection does increase more than 0.5% (total of $< 2\%$ loss in full double pass). However, larger apex angles result larger thickness of the prism, and so internal transmission can be an issue.

The common I-line glass BSL7Y (UV transmissive version of BK7) has 3.2% internal loss over a 200 mm thickness (in case of 100 mm midplane thickness of the prism, in double pass) beyond the Ca H & K lines at 3700 Å. There is only one other preferred I-line glass, the S-FSL5Y, which provides better internal UV transmission, 1.6% for the same 200 mm length. But due to its lower $dn/d\lambda$ dispersion ($n_F - n_C = 0.00693$ vs. $n_F - n_C = 0.00803$ for BSL7Y) the angular dispersion of an S-FSL5Y prism is also smaller according to Eq. (1.3), for the same apex angle and beam diameter. Therefore the reflection losses are more severe with such a prism, while maintaining a given order separation with the same grating.

Several possible design candidates were calculated based on the above, using a C code which reads variable inputs similar to the one below:

θ_B – blaze angle [degree]	63.50
ρ – ruling density [line/mm]	52.60
ϕ – apex angle [degree]	37.00
D_1 – beam diameter [mm]	127.00

The fixed parameters were:

CCD pixel count along dispersion	4608
CCD pixel count across dispersion	2048
CCD pixel size [micron]	13.5
Collimator/camera focal ratio	6.0
Telescope diameter [mm]	1500.0
Angular slit size [arcsec]	1.5
Prism material [described by disp. formula]	BSL7Y
Shortest wavelength [Ångstrom]	3800.0
Longest wavelength [Ångstrom]	9000.0

Some of the most important calculated parameters:

W – optimal grating length [mm]
R – effective fiber resolution
f_1 – collimator/camera focal length [mm]
Δy_{min} – minimal order separation [pixel]
FSR_{min} – minimal free spectral range [pixel]
FSR_{max} – maximal free spectral range [pixel]

Some of the most imposing echelograms are presented in Fig. 2.3–2.5, with the input and calculated parameters given in the caption. These models are based on actual gratings of the Richardson Grating Lab.

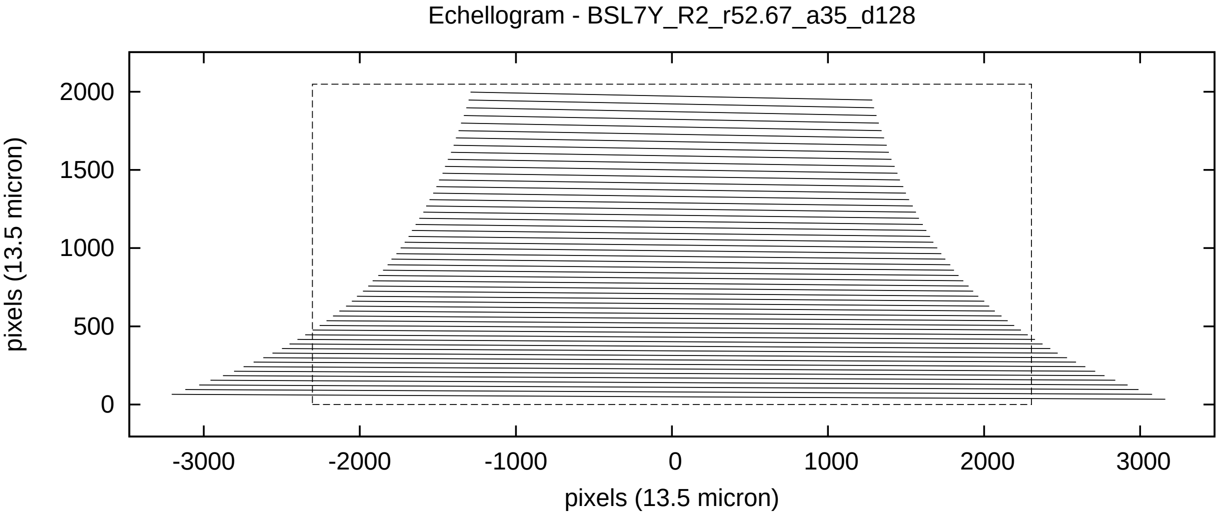

Figure 2.3: ***Design candidate: #BSL7Y_R2_r50***

$\theta_B =$ 63.50
$\rho =$ 52.67
$\phi =$ 35.00
$D_1 =$ 128.00

W = 287.0
R = 55 400
$f_1 =$ 768.0
$\Delta y_{min} =$ 28.9
FSR_{min} / FSR_{max} = 2570 / 6190

The first model, BSL7Y_R2_r50, uses a R2 grating with dimensions of 128mm×254mm and $\rho = 52.67$ line mm^{-1}. The beam diameter is chosen to provide a 10% resolution boost over the $R = 50\ 000$ lower limit. Although the grating is slightly overfilled this way the efficiency only drops 4% due to this. However, this light is not a complete waste as it can be used to feed an exposure meter (see 2.2.9). The minimal order separation requirement is met with an acceptable 35 deg apex angle (which corresponds to a modest 27°.2 angle of incidence at minimal deviation for $\lambda = 5200$ Å.) Even though some portions of the red orders fall off the CCD format, the echelogram fills the detector pretty well. The focal length of the collimator/camera is under 800 mm, and the size of the optics is a reasonable $150 - -170$ mm, as the dispersed beam passing the optical train second time would be wider than the collimated beam illuminating the grating at the first pass.

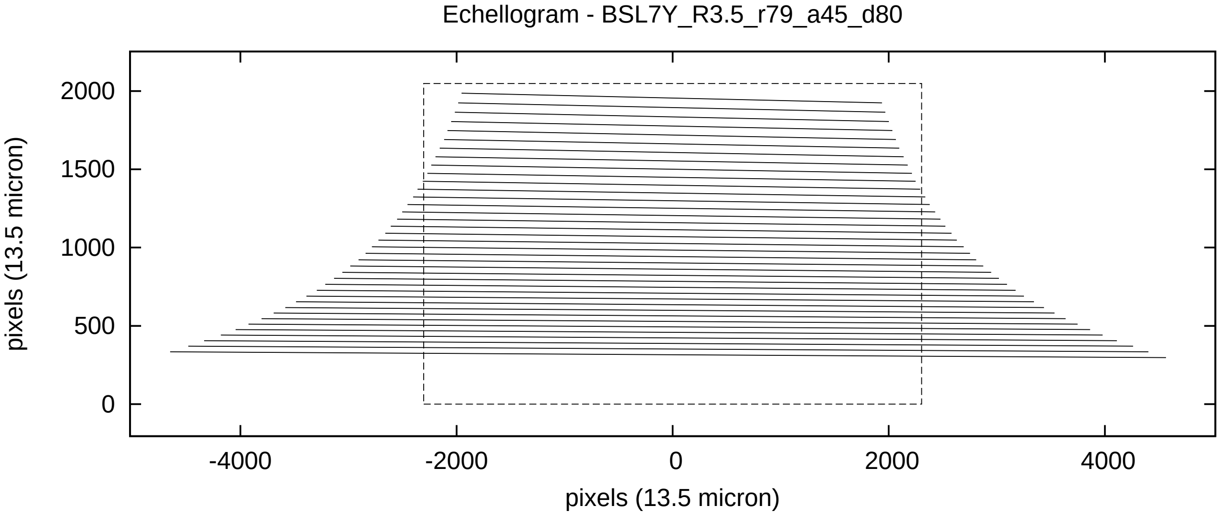

Figure 2.4: ***Design candidate: #BSL7Y_R4_r80***

$\theta_B = 74.0$
$\rho = 79.0$
$\phi = 45.0$
$D_1 = 80.0$
$W = 290.2$
$R = 60\ 200$
$f_1 = 480.0$
$\Delta y_{min} = 35.0$
$FSR_{min} / FSR_{max} = 3890 / 9250$

The second candidate, BSL7Y_R3_r80, is based on a higher R-number grating. Actually this is a R3.5 echelle with the same 128mm×254mm effective area as the previous design, but with a denser ruling of $\rho = 79.0$ line mm^{-1}. Again, the grating is slightly overfilled in the dispersion direction (while not fully utilized in cross dispersion), but just like before this can be justified. The resolution requirement would be still met with an even smaller beam, which in one hand would also decrease the grating overfill but on the other it would further shrink the echelogram. While fewer orders would run out of the CCD in this case, and the generous inter-order spacing would become more optimal, a significant detector area would be unused. Still, as the collimated beam is only $70 - 80$ mm, the instrument is very compact and the optics can be under $\sim 110 - 120$ mm in diameter. The only disadvantage is the apex angle, which results a steep 35°.6 angle of incidence (but still acceptable, see above) and a relatively thick prism (but smaller in overall dimensions, due to the significantly smaller beam size.)

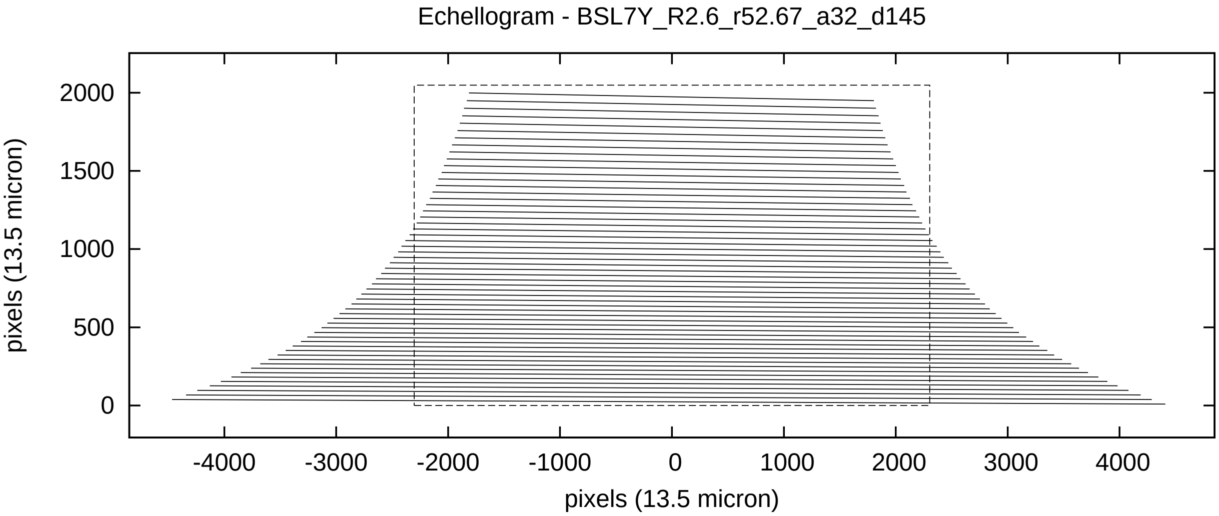

Figure 2.5: ***Design candidate: #BSL7Y_R3_r50***

$\theta_B =$	69.00	W =	404.6
$\rho =$	52.67	R =	81 600
$\phi =$	32.0	$f_1 =$	870.0
$D_1 =$	145.0	$\Delta y_{min} =$	28.1
		FSR_{min} / $FSR_{max} =$	3610 / 8630

To reach a more optimal $R = 70\ 000$ a larger beam diameter or larger R-number grating is required. The BSL7Y_R3_r50 is a feasible design utilizing a 204mm×408mm, R2.6 grating with ruling density of $\rho = 52.67$ line mm^{-1}. As all optical elements are larger due to the 145 mm collimated beam this design is more expensive, but it provides $R \approx 82\ 000$ with a very good detector coverage and proper order spacing. The prism has a very small apex angle, which is favorable, and the collimator/camera focal length is still way within the acceptable limits. Compared to model BSL7Y_R2_r50 the increase is only $\sim 15\%$ in the diameter of optics (except the grating which is almost twice as big) while the resolution advantage is nearly 50%. All other properties are very similar, so this is a very compelling model if fits the budget.

If an R3 grating would be available with the same properties as in above model (204mm×408mm, $\rho = 52.67$ line mm^{-1}), the beam diameter could be pushed down to 128 mm while preserving the resolution and providing the same grating fill, same order separation and very similar detector coverage with a 36° prism. Although this might be an ideal design (and in terms of cost and construction, other than the grating, exactly the same as the BSL7Y_R2_r50 candidate), the custom ruling would drive up the price of the grating significantly.

After carefully reviewing cost/performance ratios of above models in the light of scientific goals, at the end the BSL7Y_R2_r50 design was considered as the baseline for TRES (with a minor modification of lowering the upper wavelength limit to 8700 Å and slightly increasing the apex angle to 37° to provide a bit larger order separation).

2.1.5 Efficiency Predictions

In Section 2.1.2 we have assumed 5% average efficiency to reach 25 m s^{-1} for a $V = 12$ in $t_{exp} \simeq 90$ sec exposure time, for a F2V type star ($v\ sin\ i = 6$ km s^{-1}) observed over the 3800 – 6800 Å wavelength region at $R \approx 70\ 000$. Although the above TRES baseline design has a resolution of 55 000 only, these estimates would still hold since $R \approx c/v\ sin\ i$. To validate the efficiency assumption the total (atmosphere + telescope + fiber + spectrograph) throughput has to be calculated.

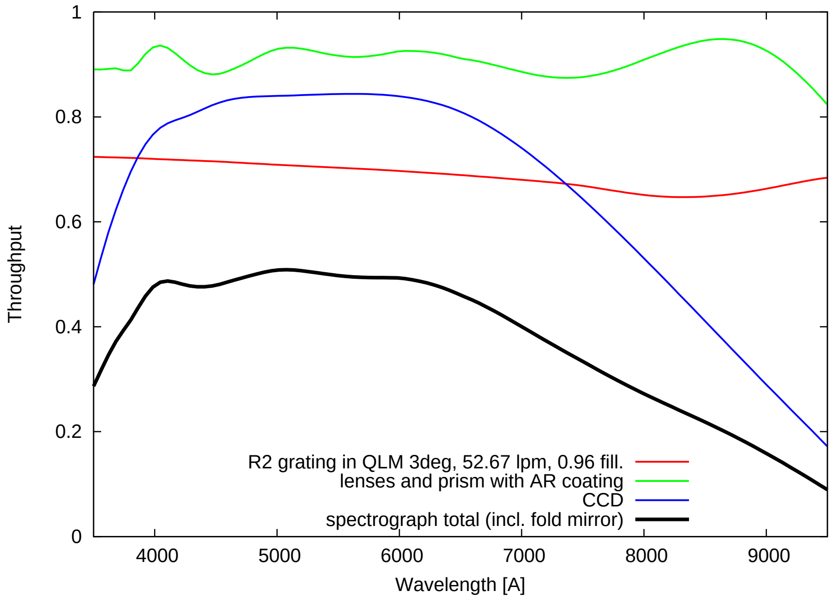

Figure 2.6: ***Estimated spectrograph efficiency***, *without the fiber link.*

On Fig. 2.6 the estimated spectrograph efficiency is shown, based on optical components of a plausible realization of the baseline TRES design. The grating efficiency (red curve) was calculated as described in 1.4.3, assuming a bare aluminum coating, quasi Littrow mounting with $\gamma = 3degr$ off-plane illumination, $\theta_B = 63\overset{\circ}{.}5$ blaze angle, 52.67 line per mm groove density, and a 128 mm beam which overfills the grating by 4%.

All the refractive optical elements, including the cross disperser, are represented by one curve (green) assuming a plausible 5 element / 3 groups collimator/camera design. For all air-glass surfaces (6 × 2 for the lenses and 2 × 2 for the prism) a Spectrum Thin Films BBAR-350-970 anti-reflection coating was applied, which introduces the small short scale variations. The central thickness of the prism is ~ 47 mm according to the TRES baseline design geometry, so internal transmission data of BSL7Y for a ~ 100 mm is used, due to double pass. For each lens element BSL7Y glass with 15 mm thickness was assumed.

The EEV CCD 42-90 quantum efficiency curve is shown in blue, while the total spectrograph efficiency is the black curve. This latter includes one fold mirror (bare aluminum) for the more convenient placement of the fiber feed.

Fig. 2.7 shows the efficiency of the “light delivery train”. For the fiber link (red) a Polymicro FBP type fiber is used and along with the internal losses for 15 m length the end reflection (4%) and FRD losses are also included.

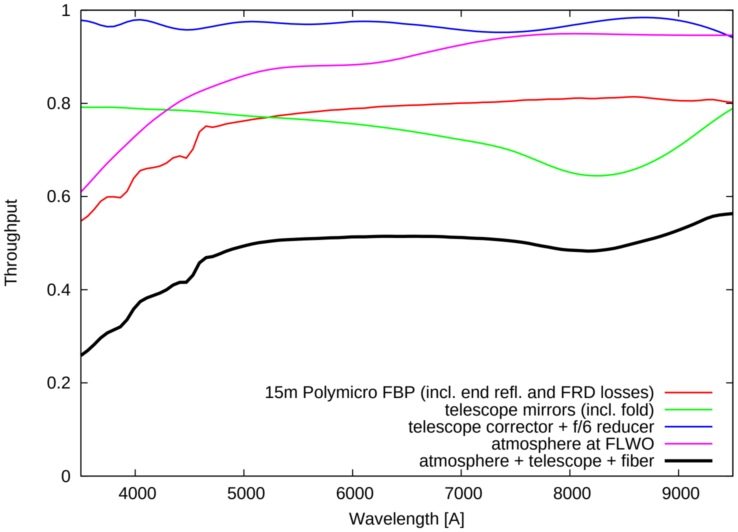

Figure 2.7: ***Estimated throughput from above the atmosphere down to spectrograph entrance***

The telescope mirrors are represented by the green curve, assuming bare aluminum coating on 3 surfaces (including a possible fold mirror for convenient mounting of guider / fiber feed elements). The Tillinghast reflector has a 2 element (fused silica), air-spaced, AR coated field corrector, and the TRES design requires an other refractive element for focal reduction. The blue curve includes the existing corrector and a theoretical, 25 mm thick BSL7Y cemented doublet, with all 6 surfaces AR coated (same BBAR-350-970 coating as above).

The atmospheric transparency at FLWO was estimated based on photometric observations taken at the 1.2m telescope, located just $\sim$ 30m away from the Tillinghast reflector. Extinction coefficients for Johnson-Cousins and Sloan systems (and for a custom filter) were provided by Malcolm Hicken, Dave Latham and Sumin Tang. Data from several dozen nights over several month time span were averaged (see Table 2.1). The transparency values were calculated according to:

$$T(\lambda) = e^{-\frac{\kappa}{1.086}}, \tag{2.3}$$

and the individual values were fitted with a cubic spline (magenta curve on Fig. 2.7).

To estimate the overall efficiency (including atmosphere) the final products of Fig. 2.6 and 2.7 have to be combined, and the seeing has to be accounted for. Assuming a Gaussian PSF a fiber diameter comparable to the seeing disk means a significant light loss, as it can be seen on Fig. 2.8. Only an aperture twice as big as the FWHM stellar profile (x=2.0 on figure) delivers $> 94\%$ into the fiber. That is the reason why the TRES baseline design offers three different fiber diameters, to maximize efficiency even among bad seeing conditions (on the expense of loosing spectral resolution, of course). Therefore the total instrument efficiency, including atmosphere, is plotted in Fig. 2.9, for three proposed fiber diameters of (65, 100 and 140 microns) and assuming $FWHM = 1\farcs5$ seeing with a Gaussian PSF.

Based on Fig. 2.9 TRES would provide $\sim 8\%$ average efficiency over the $3800 - 6800$ Å wavelength range, and so this validates the exposure time & RV performance predictions.

Table 2.1. Extinction coefficients at FLWO

Filter	Central Wavelength [Å]	κ
U	3640	0.473
B	4420	0.235
g	4750	0.190
D51	5200	0.150
V	5400	0.142
r	6220	0.130
R	6700	0.102
i	7630	0.060
I	8500	0.058
z	9050	0.060

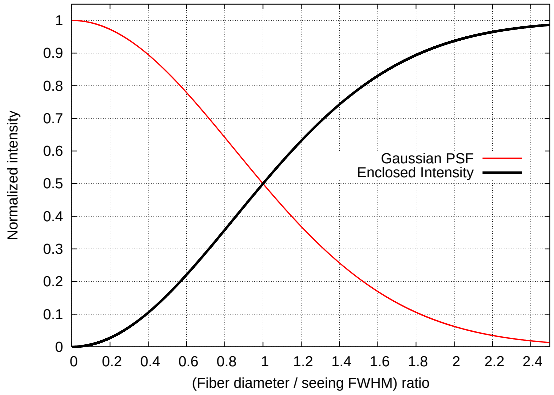

Figure 2.8: ***Efficiency of a fiber feed****, plotted against the ratio of fiber diameter and seeing FWHM, assuming a Gaussian PSF (red curve, normalized to 1). If the angular fiber diameter equals the seeing disk, only 50% of the light enters the fiber.*

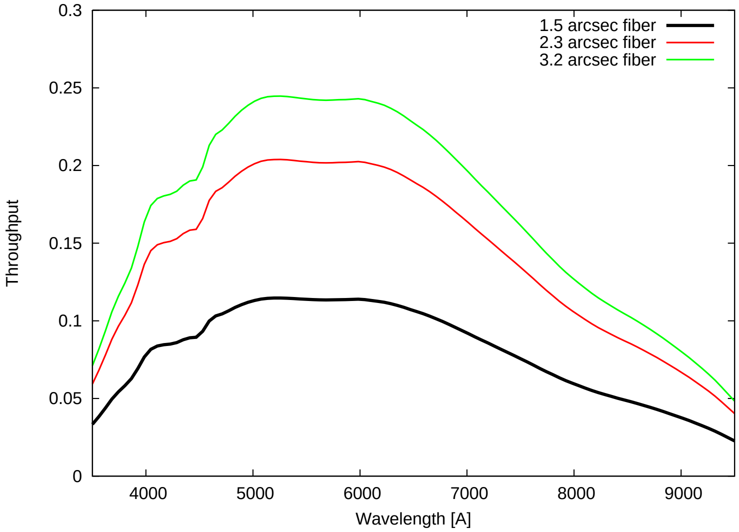

Figure 2.9: ***Estimated overall spectrograph efficiency, including atmosphere*** *for the proposed three different fiber diameters and assuming* $1''.5$ *seeing.*

2.2 Spectrograph Optical Design and Feasibility Analysis

The next step of constructing TRES was to design the refractive collimator/camera optical system. In this section I describe this procedure, by sketching a basic design and follow its evolution. Rather than discussing some intermediate systems I would like to illuminate some optimization constraints and thoughts, and especially the evaluation methods, as these are the key aspects of the optimization process. For image quality evaluation I have developed a graphical tool which I use to describe the final design. After this the feasibility of the design is discussed in terms of ghost-, thermal-, and tolerance analysis.[1]

2.2.1 Initial Design

Looking for similar optical designs in the literature the Sandiford 2.1-m Cassegrain echelle spectrograph (McCarthy et al., 1993) seemed to be a good starting point. The collimator/camera is a all-spherical 5 lens design, with a triplet as a front element and a doublet corrector almost halfway towards the focal plane (see Fig. 2.10). A 6th element was added because of practical reasons, to serve as a dewar window, however it was also allowed to change shape and act as a field flattener/corrector. The initial prescription is given in Table 2.2.

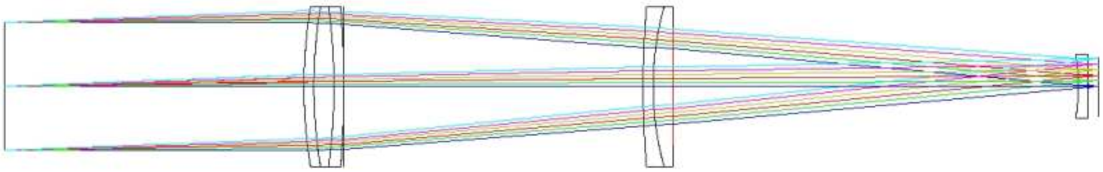

Figure 2.10: ***Layout of TRES initial collimator/camera***, *showing a 128 mm entrance pupil 300 mm away from the front element. Rays are shown for different field locations, up to 30 mm.*

The initial values for radii and thicknesses were set to create plausible lens shapes and reach a focal length close to the desired 762 mm (actual value was 781.5 mm). The lens thicknesses and spacings (except the dewar window to CCD distance and the thickness of window), as well as curvatures (all but for surface 9) were set to be variables and a simple optimization was run in ZEMAX to form realistic images. The merit function was set up for minimal RMS spot radius over the $4000 - 8500$ Å range at 6 field locations (from on axis to 30 mm off axis field positions), and lens data variables were constrained to preserve the main characteristic of the initial design. The spot diagrams of this optimized system are shown on Fig. 2.11. The polychromatic RMS spot radii are listed on the bottom of the figure, and although for all field locations it is smaller than one pixel the blue wavelengths suffer from significant coma.

---

[1] For the optical design described in this section the commercially available ray tracing code ZEMAX was used, together with the OARSA code of Harland Epps, who was a consultant during the design process. For performance evaluation ZPL scripts (ZEMAX programming language) were written.

Table 2.2. TRES initial camera/collimator design

Surface	Radius [mm]		Thickness [mm]		Glass	diameter [mm]
	ini.	opt.	ini.	opt.		
stop	—	300	—	—	—	128
2	500	355.42	10.0	10.0	BAK2	160
3	500	229.50	20.0	29.9	CAF2	160
4	-600	-426.79	10.0	20.0	SK15	160
5	-1000	-1289.36	0	—	—	—
triplet to doublet	—	—	300.0	349.9	—	—
7	1000	681.29	10.0	8.3	SK20	160
8	300	187.78	20.0	255.0	FK5	160
9	inf.	—	0	—	—	—
doublet to window	—	—	406.0	387.6	—	—
11	-200	-135.22	10.0	—	F_SILICA	65
12	-700	-262.42	0	—	—	—
window to CCD	—	—	10.0	—	—	—

Note. — Initial values were approximations to set the desired shape of lenses and get close to the required focal length of 762 mm. The second column of radii and thicknesses are result of a simple optimization to reach minimal RMS spot radius while preserving the basic properties of the initial system. Only parameters with a second value listed were allowed to vary during optimization. All surfaces are spherical.

2.2.2 Optimization

Single Pass

The optimization of the camera/lens system first was done in single pass, as shown in Fig. 2.10. At this point designs were evaluated based on a spotsize–wavelength graph, drawn for on axis (see Fig. 2.11) and for one off-axis position. An other good reason to use such a plot instead of polychromatic spot diagrams is that the lens system used in the spectrograph will form monochromatic images, although with all different field locations for each wavelength.

One advantage of optimizing the system this way that ray tracing is kept at minimum level and axial symmetry can be assumed, therefore computation is fast and a waste number of optical systems can be explored. The prime goal at this stage was to explore different glass types, try to improve the blue performance and make the RMS spot diameter more uniform across the specified spectral domain.

The disadvantage is that aberrations can become very severe after a second pass. Evaluating at one or two field locations can be misleading, too, as a very small wavelength range of a spectral order (essentially a single wavelength from the ray tracing / image quality evaluation point of view) will be spread over up to 75 mm in length (see the echelogram of Fig. 2.3). Therefore several plots like Fig. 2.12 has to be compared simultaneously to evaluate a design (see Fig. 2.13).

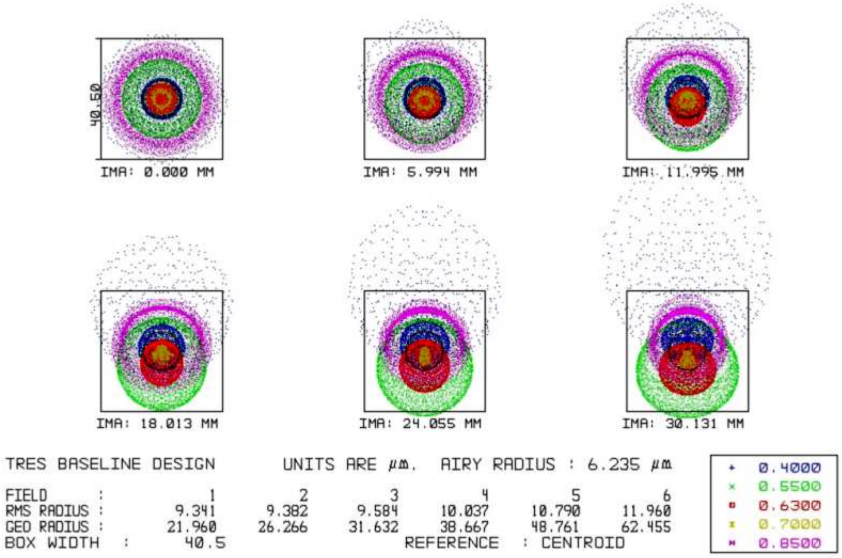
40.50
IMA: 0.000 MM
IMA: 5.994 MM
IMA: 11.995 MM
IMA: 18.013 MM
IMA: 24.055 MM
IMA: 30.131 MM
TRES BASELINE DESIGN
UNITS ARE µm. AIRY RADIUS : 6.235 µm
FIELD : 1 2 3 4 5 6
RMS RADIUS : 9.341 9.382 9.584 10.037 10.790 11.960
GEO RADIUS : 21.960 26.266 31.632 38.667 48.761 62.455
BOX WIDTH : 40.5
REFERENCE : CENTROID
0.4000
0.5500
0.6300
0.7000
0.8500

Figure 2.11: ***Spot diagram of TRES initial collimator/camera***, *for 6 field locations as noted. Reference box size is* 3×3 *pixel* $(40.5 \times 40.5 \mu m)$.

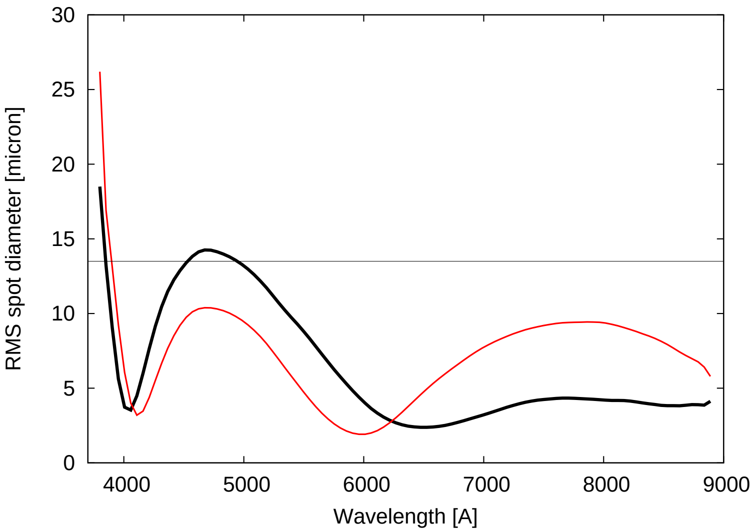

Figure 2.12: ***System evaluation plot for single-pass***, *on axis image formation, for two optical models. The thin horizontal line represents the size of one CCD pixel.*

Double Pass

The next step towards a more realistic performance analysis to set up a double-pass system, by simply placing a mirror at some distance from the front (triplet) element. The polychromatic illumination now has a point-like source placed on the focal plane, on axis, and an almost parallel beam exits the lens system after first pass, then enters it again after bouncing back from the mirror. Images are formed on / near the light source.

The mirror was placed ∼ 400 mm from the triplet, as the grating likely would be that far in the real configuration. As ZEMAX did not allow optimization by setting up a single lens system

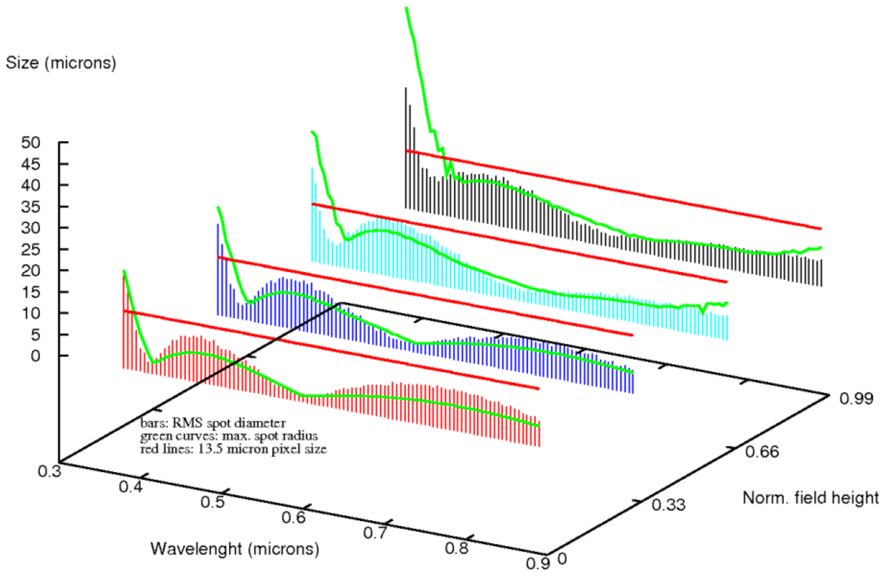

Figure 2.13: ***Complex evaluation plots for single-pass****, for multiple field positions (0, 10, 19 and 29 mm from axis). The bars represent RMS spot diameter, while the green curves show the geometrical spot radius (with the centroid as reference). The red line is a 1 pixel limit.*

Table 2.3. Multi-configuration setup

	Configuration					
	1	2	3	4	5	6
Order	87	77	67	57	47	38
Wavelength 1 [Å]	3889	4391	5041	5917	7162	8836
Wavelength 2 [Å]	3911	4419	5078	5969	7239	8954
Wavelength 3 [Å]	3933	4447	5115	6021	7316	9072

and use a “real” mirror (non-sequential mode)[2], the actual model contained a copy of the lenses in reverse order. (The variable design parameters were tied together, of course, so both copies of the lenses changed simultaneously during the optimization.) The ZEMAX calculations were still fast this way, however assuming axial symmetry for the final system (quasi-Littrow mode with $\gamma \approx 3°$) is not realistic

Therefore the input source was moved off axis so the images also formed off-axis by the same amount, but in opposite directions. Later a full double pass model was created including the prism and grating. This way optimization could take advantage of ignoring lateral color (transverse chromatic aberration), as each wavelength has its own image forming location on the focal plane. (Note that in such a case plots like Fig. 2.12 are not sufficient any more. Also, the shape and intensity distribution within a spot is important, so a more complex evaluation chart is necessary (see below). Optimization was forced to minimize RMS spot radius at 12 locations of the echelogram: 3 wavelengths (start, end and middle of FSR) in 6 different spectral orders. To achieve this a multi-configuration model was set up, with one configuration for each order (see Table 2.3).

---

[2] The latest version of ZEMAX, as of 2008 spring, does allow optimization of such “physical” systems, however the tools are still limited and sequential optimization is still preferred.

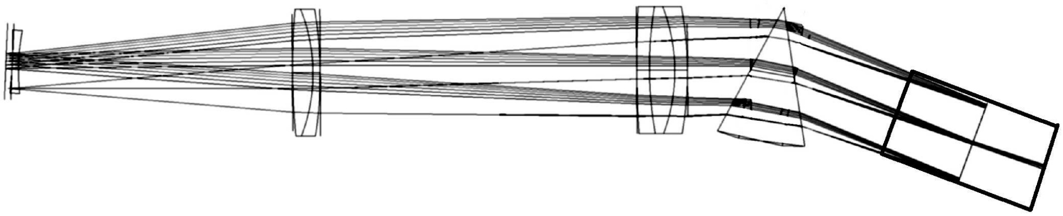

Figure 2.14: ***Intermediate result of optimization in full-double-pass***. *The cross section of the prism can be recognized at the right. The echelle grating is facing down and it is placed at the far right.*

As a result of iterative optimization the system layout became like it is shown on Fig. 2.14, still similar to the initial setup. The lens diameters are 200 mm except for the corrector which has a diameter of 100 mm. This corrector serves as a dewar window, so it is only in the second pass. Also note that the axis of the corrector is coincident with the midpoint of the echelogram, and so off-axis compared to the rest of the system. To compensate for such asymmetry between the input and dispersed beams the focal plane (together with the field corrector) is slightly tilted. The input source (fiber end) obviously would interfere with the dewar (see Fig. 2.14), so in a realistic system there would be a fold mirror in the input beam. (This was not part of the optical model since such a flat mirror has no effect on optical performance.)

The overall performance is already good as it can be seen on Fig. 2.15. For all but the very blue wavelengths the geometrical spot diameters are within a 3 × 3 pixel box (compare it with Fig. 2.11).

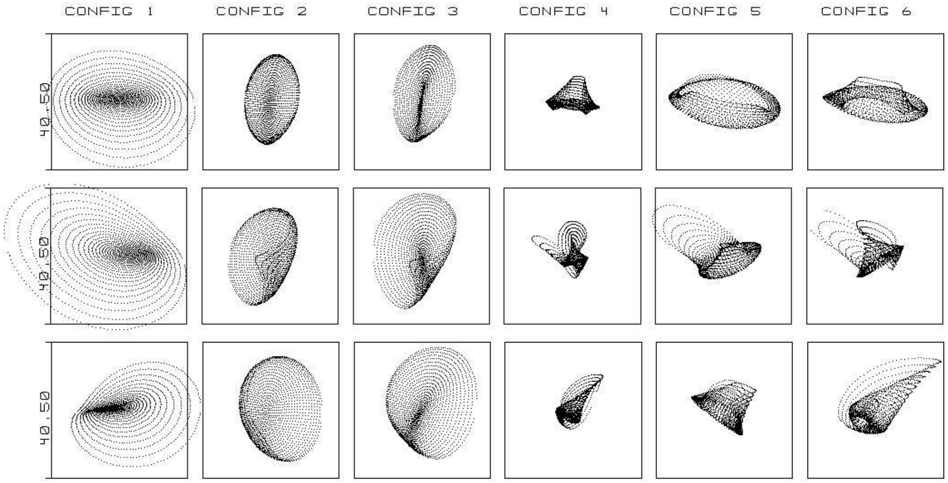

Figure 2.15: ***Multi-configuration spot diagrams of a buildable design***. *The spots are plotted as wavelengths and configuration numbers are listed in Table 2.3, respectively. Boxes represent 3 × 3 pixels, or 40.5 × 40.5 μm.*

Considerations on the Cross Disperser

Regarding the cross disperser a possibility of a fused silica prism was investigated, to further improve the near-UV response of TRES. At 3800 Å the BSL7Y glass has an internal transmittance of 0.998 for 10 mm thickness, while fused silica has a value of 0.9995. For the $\sim$ 70 mm central thickness of a prism in double pass this means 97.2% and 99.3% transmittance, respectively. (The use of the central thickness is a good approximation of the total absorbance of the prism.) However, BSL7Y is cheaper than fused silica, and latter would also require a bit larger apex angle and so steeper angle of incidence at the prism. Also, the 2% different rapidly disappears above 4000 Å. Therefore the fused silica option was rejected.

Inhomogeneity of the prism material, and therefore variation of the refraction index can lead to wavefront errors. Ohara lists $\Delta n = \pm 0.5 \times 10^{-6}$ for standard BSL7Y blanks less than 160 mm in diameter. Assuming a worst case (the $t \approx 150$ mm wide base of the prism has $\Delta n = +1.0 \times 10^{-6}$ compared to the tip of the prism the optical path difference can be as large as $OPD = 2\ \Delta n\ t =$ 0.3 μm, in double pass. Based on the 128 mm beam diameter it corresponds to a $0\farcs5$ tilt in the wavefront, or a $\sim$ 2 μm offset on the focal plane (in case of 762 mm focal length of the camera optics). This is just a fraction of one pixel and also small compared to the RMS spot diameters, so standard grade BSL7Y glass is adequate as a prism material.

Image Quality Maps and Further Optimization

Although multi-configuration spot diagrams (such as Fig. 2.15) are useful tools, an even more informative image quality map was developed to compare subsequent results. The idea was to visualize optical performance over the entire echelogram, not just at specified locations. The result was a set of image quality maps where the intensity values represented the spot diameter, spot symmetry or encircled energy and the coordinates showed the position on the CCD. See Fig. 2.16 as an example, comparing performance of four possible models in terms of RMS spot diameter.

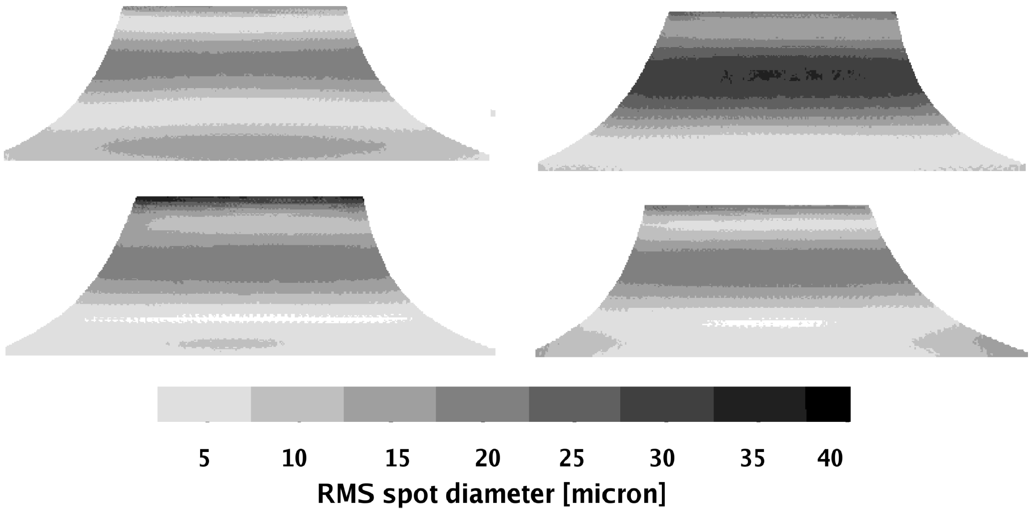

Figure 2.16: ***Image quality maps comparing RMS spot diameter*** *over the entire echelogram area, for four different optical models.*

During the further evolution of the design several changes were made. The overall symmetry of the optical system was restored by bringing the dewar window on axis with the other lenses. Therefore the echelogram forms off axis respect to the field flattener, but the input beam was also considered to pass this element (or, realistically, a copy of the same lens moved to the side by the mean of a flat fold mirror). It is important which way (respect to the prism) to offset the input beam, as the red orders are wider and so those should stay closer to the optical axis.

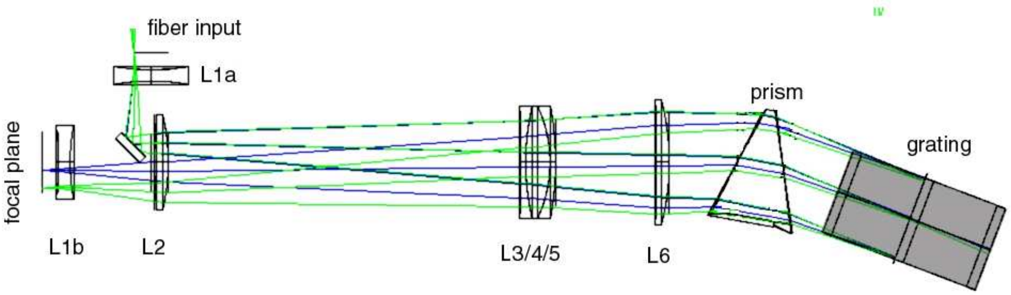

Figure 2.17: ***Optical layout of the preconstruction design*** *Lenses are labeled from 1 to 6, with the L1 element "doubled" for practical reasons.*

To improve image quality in the blue an other CaF_2 element was added, between the triplet and the prism. Since TRES was aiming to have high efficiency below 4000 Åand in double-pass the total thickness of glass was significant, OHARA I-line glasses were introduced for the lens elements. The materials became S-LAL7 / CaF_2 / BSM51Y for the triplet and BSM51Y / FPL51Y for the doublet. Geometrical spot radii at all wavelengths went below 2 pixel limit, but now the lens system was rather complex. At this point the design was optimized by Dan Fabricant and Harland Epps. As a result the doublet became a singlet (S-FSL5Y), the front element (closest to the prism) changed from CaF_2 to S-FPL51Y and the dewar window went from fused silica to BAL15Y. Therefore this so-called #072304AW *preconstruction design* consisted of 6 lenses in 4 groups (one triplet and 3 singlets), with all lenses in double pass. For practical reasons, as mentioned before, the dewar window/field flattener was duplicated and the copy in front of the fiber was moved off axis by a fold mirror (see Fig. 2.17).

2.2.3 The Preconstruction Design

Preliminary thermal-, tolerance- and ghost analysis was performed on the preconstruction model in order to evaluate its feasibility. (Detailed description of such analysis is given below for the construction model.) A lens mounting criteria (see Sec. 2.4.1) was to have lens edge thicknesses larger than 5 mm, which was met by all elements. Manufacturing and alignment errors were found reasonable, although the relative positions of the triplet members and the absolute properties of the CaF_2 element seemed critical.

Image quality was good not just at the $T = 18$ °C design temperature, but 5 °C below/above of it as well, as it can be seen on Fig. 2.18. Although the spots become elongated at different than design temperatures, their size is still small compared even to the smallest fiber of 65 μm in diameter. Convolving the temperature distorted PSFs with such circular fiber face the elongations become unnoticeable, as it was found by geometrical image analysis.

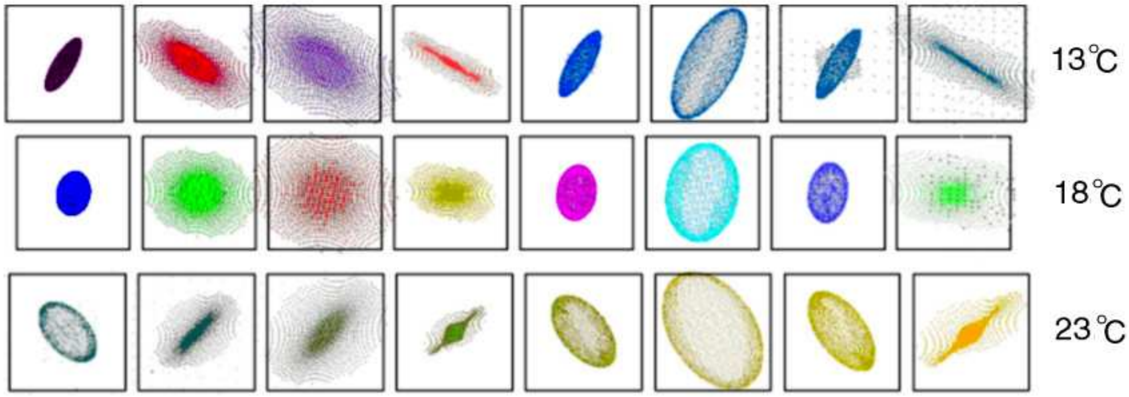

Figure 2.18: ***Multi-configuration spot diagrams of the preconstruction design****, for* $T = 18\ ^\circ C$ *(middle row). The different configurations (from left to right) represent different wavelengths (spectral orders), like on Fig. 2.15, but only for the central wavelength of a given order. The top and bottom row is the same as the middle one, but for different temperatures as noted. The boxes represent* 2×2 *pixels, or* $27 \times 27 \mu m$*.*

One ghost image was very severe, as it is shown on Fig. 2.19. Light from the front surface of L5 could be reflected back and focused just in front of the detector, therefore the ghost image is a well concentrated spot. In spite the reflected light would be only at the ∼ 1% level due to AR coating on L5, the ghost image is relatively bright, and exhibits a strong color. Softening of this ghost seemed feasible by slightly modifying the preconstruction design, but that step was preserved for the final re-optimization when the melt sheet data and so the actual refraction indices of glass substrates become available.

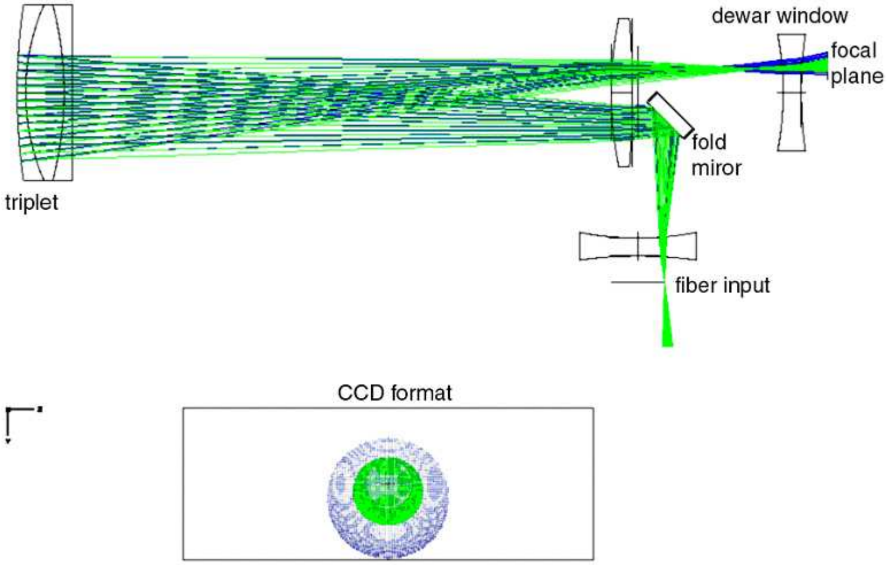

Figure 2.19: ***Serious ghost image problem of the preconstruction design.*** *The blue and green rays represent 9000 and 4000 Å, respectively. The lower diagram displays the detector area and the ghost image as it would appear on the images.*

Table 2.4. Melt data for Ohara glasses used in TRES camera

	Line	Wavelength [Å]	Glass Type **S-LAL7**	**FPL51Y**	**BSM51Y**	**FSL5Y**	**BAL15Y**
	t	10 139.8	1.639024	1.490297	1.592186	1.479252	1.546176
	S	8 521.1	1.642201	1.492011	1.595065	1.481484	1.548853
	r	7 065.2	1.646299	1.494256	1.598749	1.484201	1.552324
	C	6 562.7	1.648237	1.495319	1.600485	1.485445	1.553965
	d	5 875.6	**1.651631**	**1.497188**	**1.603522**	**1.487589**	**1.556850**
	e	5 460.7	1.654287	1.498650	1.605891	1.489242	1.559112
	F	4 861.3	1.659376	1.501441	1.610429	1.492372	1.563449
	g	4 358.4	1.665418	1.504738	1.615808	1.496038	1.568616
	h	4 046.6	1.670431	1.507453	1.620261	1.499049	1.572909
	i	3 650.2	1.678967	1.512036	1.627840	1.504123	1.580250
ν_d			**58.50**	**81.21**	**60.69**	**70.39**	**58.71**
Temperature [°C]			25.3	25.1	25.4	25.0	25.1
Humidity [%]			53.0	50.0	50.0	50.0	50.0
Pressure [hPa]			1013.3	1013.3	1013.3	1013.3	1013.3

All in all, the preconstruction design passed feasibility tests and promised very good image quality. Glass blanks were ordered with some volume contingency (2.5 mm buffer around the maximum dimensions in all directions) in order to allow slight modifications of the final re-optimization step, and also to accommodated fabrication requirements. For the substrates the following were specified:

- striae grade A, per MIL-G-174B (no visible striae)
- bubble Code 1 (total cross section of bubbles is less than 0.1 mm^2 in 100 cm^3, less than 10 bubbles in 100 cm^3)
- fine anneal, maximum birefringence of 10 nm/cm
- each item to come from a single melt
- dimensional tolerances of ±0.2 mm
- standard n_d and ν_d tolerances
- standard I-line homogeneity of given size, except for S-LAL7 (special class A2, $\pm 2.0 \times 10^{-6}$)

2.2.4 Incorporating Melt Sheet Data

The melt data was provided by Ohara Corp. for the purchased S-LAL7, FPL51Y, BSM51Y, FSL5Y and BAL15Y blanks, as refractive indices measured to 6 decimal places at 10 wavelengths (see Table 2.4). This data was used to fit a Schott dispersion formula, and the company provided (standard data sheet) thermal derivatives were used to create a ZEMAX glass catalog at the design temperature of 18 °C(see Table 12.1 in the Appendix, for the derived Schott coefficients).

The CaF$_2$ blank was purchased directly by the company selected for fabrication of the lenses (Coastal Optical Services Inc., Coastal hereafter), and they were not able to provide exact refraction index data on the Nikon manufactured blank. Therefore an investigation was made by Harland Epps to figure out how well published CaF$_2$ refraction index measurements represent the synthetic materials currently produced by different vendors.

The main concern was a wavelength-dependent difference of refraction indices between the classical values of Malitson (1963) and a more recent data by Daimon and Masumura (2002). Also, for an other CfA instrumental project Ohara Corp. measured indices for a Canon Inc. produced CaF_2 sample, and those were consistently lower than Daimon and Masumura (2002) values by some 0.000014, although they were in agreement with data published by Canon itself.

This latter offset might be accounted to the fact weather or not the CaF_2 samples has been specially processed for 157 nm photo-lithography. The deviation from the Malitson (1963) data could be the result that Malitson measured a synthetic and a natural sample and published the averaged values, which is probably not appropriate for modern high-purity synthetic CaF_2.

After all there was no evidence found that any of the measured indices of modern CaF_2 synthetic-crystals differ from any of the others in a wavelength-dependent manner. (This might caused induced axial color in a TRES construction design if the wrong model was chosen to represent the purchased Nikon CaF_2.) Systematic offset differences seen in recent publications could have little or no practical effect on TRES as they would only tend to introduce a small wavelength-independent focus shift. Therefore a Schott dispersion formula was fitted on Ohara measurements of a Canon sample, and that model was used in the ZEMAX glass catalog of TRES.

2.2.5 Construction Design — Test Plate Fitting

After choosing Coastal Inc. as manufacturer for the lenses all radii were forced to meet existing Coastal test plates. During this test plate fitting an effort was made to soften the known ghost of the preconstruction design (See Fig. 2.19), and also to avoid formation of other retro-reflected images. As a result all but one (L3 back) radii was successfully fitted, and the construction design became as it is described in Table 2.5. (For the triplet a 0.1 mm gap was assumed between elements, which was filled with a Dow Corning Q2-3067 couplant. A dispersion formula was provided for this by Harland Epps. (See Table 12.1 in the Appendix, for the Schott coefficients.)

The layout remained nearly the same as shown on Fig. 2.17, and image quality was almost identical to the one delivered by the preconstruction design, too. See Table 2.6 and Fig 2.20 for multi-configuration spot diagrams, and compare it to the middle row of Fig. 2.18 or to Fig. 2.15.

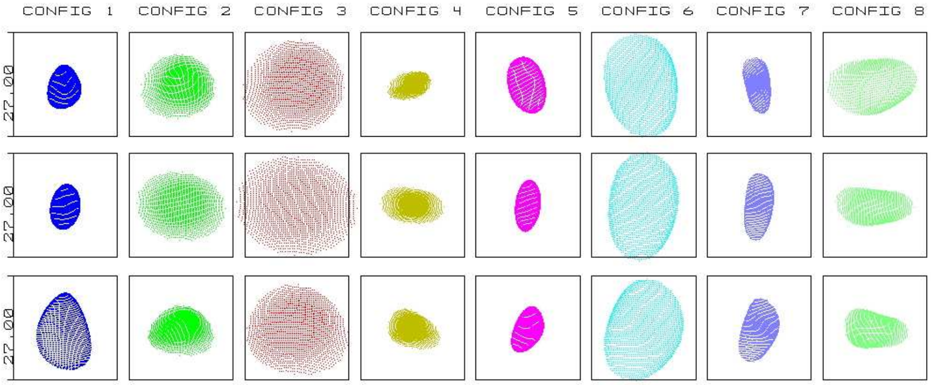

Figure 2.20: ***Multi-configuration spot diagrams of the construction design***. *The spots are plotted as wavelengths and configuration numbers are listed in Table 2.6, respectively. Boxes represent* 2×2 *pixels, or* 27×27 μm.

Table 2.5. Parameters of the construction model #112505AH

Surface	Radius [mm]	Thickness [mm]	Glass type	Diameter [mm]
fiber/detector	—	–	—	
	—	24.93	—	
L1a back	-357.49	17.00	I-BAL15Y	110
L1a front	287.81	—	—	110
L1 to L2	—	125.00	—	
L2 back	842.45	20.00	S-FSL5Y	140
L2 front	-309.84	—	—	140
L2 to L3/4/5	—	520.80	—	
L3 back	-1698.07	8.00	BSM51Y	166
L3 front	362.07	—	—	166
L3 / L4 gap	—	0.10	couplant	166
L4 back	362.07	36.00	CaF_2	166
L4 front	-194.33	—	—	166
L4 / L5 gap	—	0.10	couplant	166
L5 back	-194.33	8.00	S-LAL7	166
L5 front	458.91	—	—	166
L3/4/5 to L6	—	148.30	—	
L6 back	-5714.31	20.00	S-FPL51Y	185
L6 front	-361.28	—	—	185
L6 to prism	—	100.00	—	
prism mid-plane	—	70.00	BSL7Y	
prism to grating	—	200.00	—	

Note. — Single pass listing, starting with fiber input/focal plane followed by lenses L1 through L6. The "Y' in the glass name means Ohara I-line product. Lens radii (except L3 back) are fitted to match Coastal Optical Services Inc. test plates at a construction temperature of $T = 23$ °C. Refraction index of model glasses are based on actual melt sheet data, except for CaF_2 for which Canon Inc. data is used. All dimension are listed for $T = 18$ °Cdesign temperature.

Table 2.6. Multi-configuration setup of the construction design

	Configuration							
	1	2	3	4	5	6		
Order	39	44	49	59	67	79	84	89
Wavelength 1 [Å]	8613	7646	6874	5719	5041	4280	4026	3802
Wavelength 2 [Å]	8725	7734	6944	5768	5078	4307	4051	3823
Wavelength 3 [Å]	8837	7821	7015	5816	5115	4335	4075	3845

2.2.6 Thermal Analysis

The TRES design temperature was $T = 18$ °C. During the final thermal analysis the lens radii and thicknesses were calculated for $T = 13$ and 23 °C, according to the glass CTE values. Refraction indices were also transformed to the given temperature, by re-fitting the Schott dispersion formulas. For this the refraction index melt data were transformed by the thermal derivatives provided in the standard glass data sheets. Results were saved as separate glass catalogs for given temperature (see Table 12.1 in the Appendix, for the derived Schott coefficients). Distances between lens elements were calculated based on the CTE of 400 Series ferromagnetic stainless steel (Newport RS4000 table standard working surface). For the three test temperatures individual ZEMAX models were set up, with the dimensions and glass catalogs corresponding for given temperature.

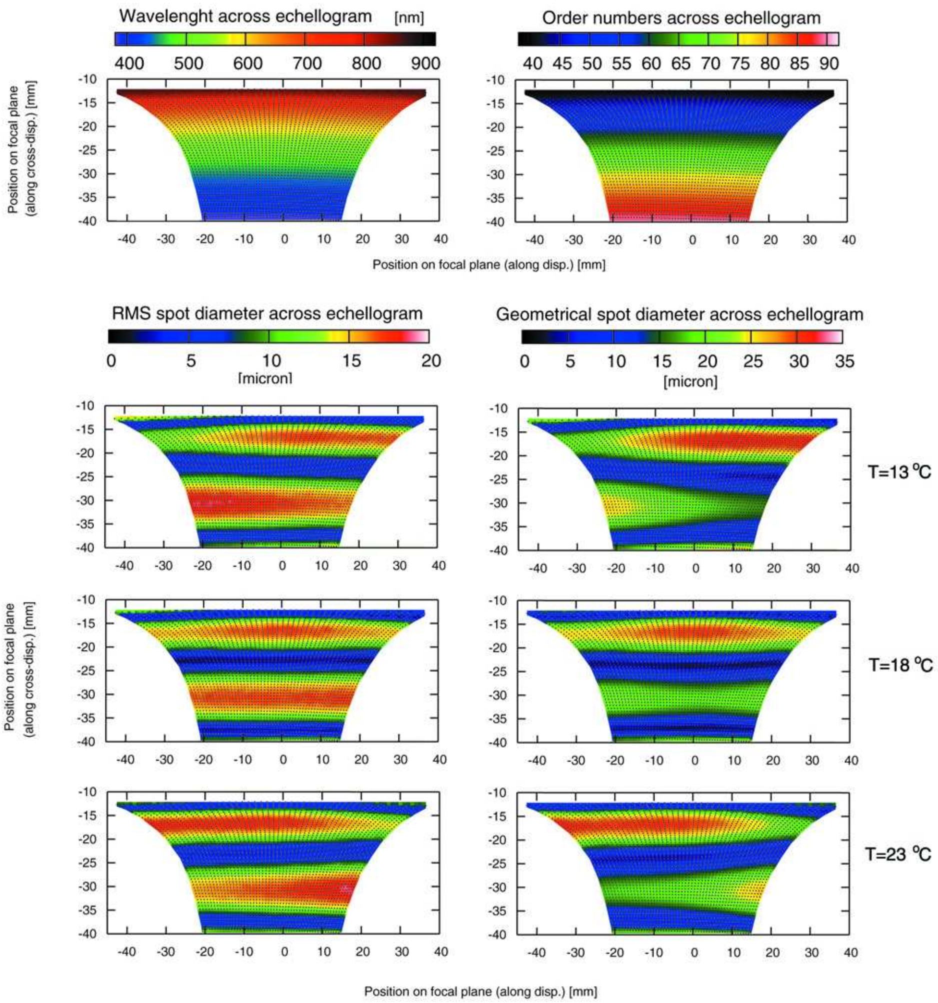

Figure 2.21: ***Spot-size maps for thermal analysis on the construction design***, *displaying RMS spot diameter (left) and geometrical spot diameter (right) over the entire echelogram for* $T = 13, 18$ *and 23 °C, from top to bottom, respectively. The small black dots represent the locations of actual calculations, while the color-coded maps are interpolated using these values. The two very top maps gives the approximate wavelength and order number for a given location.*

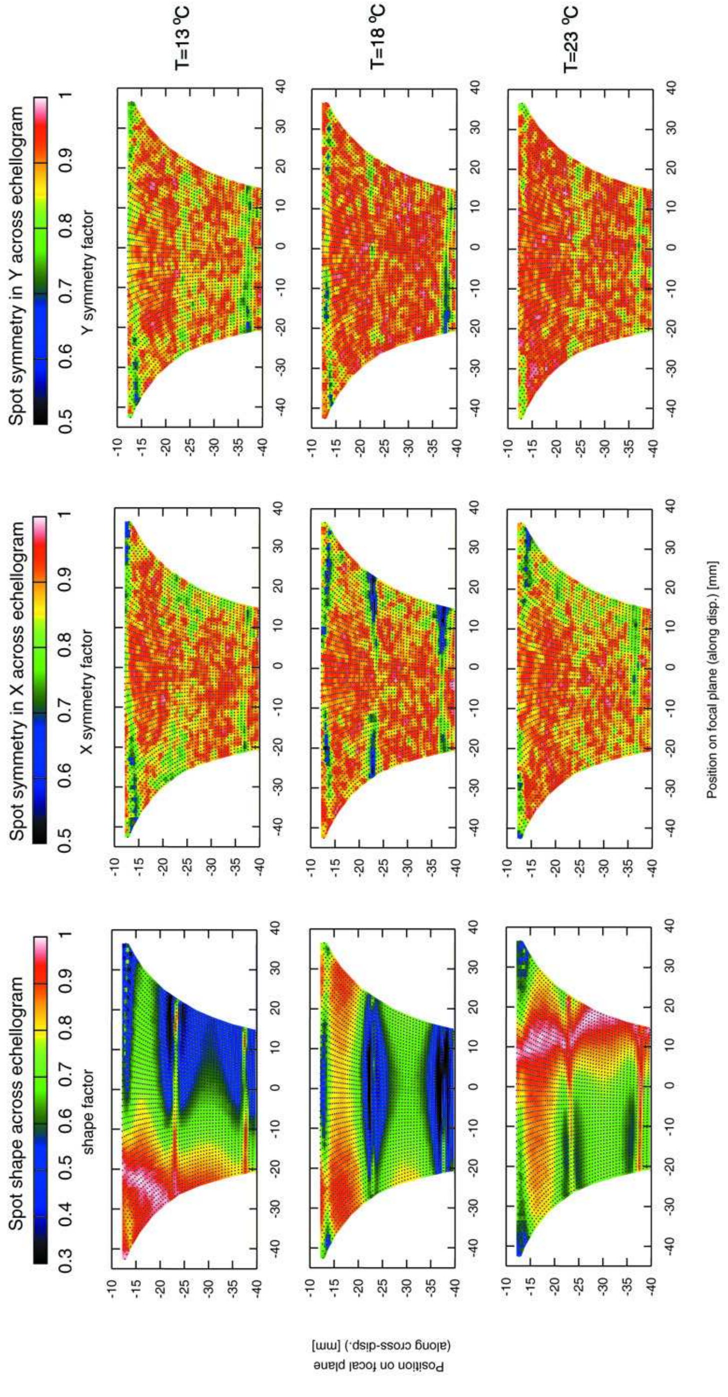

Figure 2.22: ***Spot-shape maps for thermal analysis on the construction design****, displaying shape factor (left), x symmetry (along dispersion, middle) and y symmetry (along cross dispersion, right), over the entire echelogram for $T = 13, 18$ and $23\ ^{\circ}C$, from top to bottom, respectively. The small black dots represent the locations of actual calculations, while the color-coded maps are interpolated using these values. See text on definition of shape and symmetry factors.*

Image quality evaluation was performed by comparing RMS and geometrical spot diameter maps, similar to the ones of Fig. 2.16. As thermal effects tend to influence spot shape more radically than the RMS size, two-dimensional maps showing spot shape and symmetry were also calculated. The former displays the ratio of two sides of a rectangular box enclosing the entire geometrical spot. Values of near 1 mean near circular footprints, as always the longer side is divided by the length of the shorter one. Symmetry is defined in both x (dispersion) and y (cross dispersion), by comparing what percentile of rays do fall on either side of the chief ray. A symmetry factor of 1 means the chief ray coincides with the centroid, while values significantly less than 1 imply the presence of coma.

2.2.7 Ghost Analysis

Ghost image formation is a serious issue with full double pass systems, as any convex lens surface acts as a mirror on the bright input beam. In contrast, for single pass systems the light subject to reflection towards the detector is already reflected from a glass/air interface or from the detector surface, therefore its intensity is very low to start with. On Fig. 2.23 first order ghost images of the construction design are shown. (First order means ghost formed by single reflection of the input beam.)

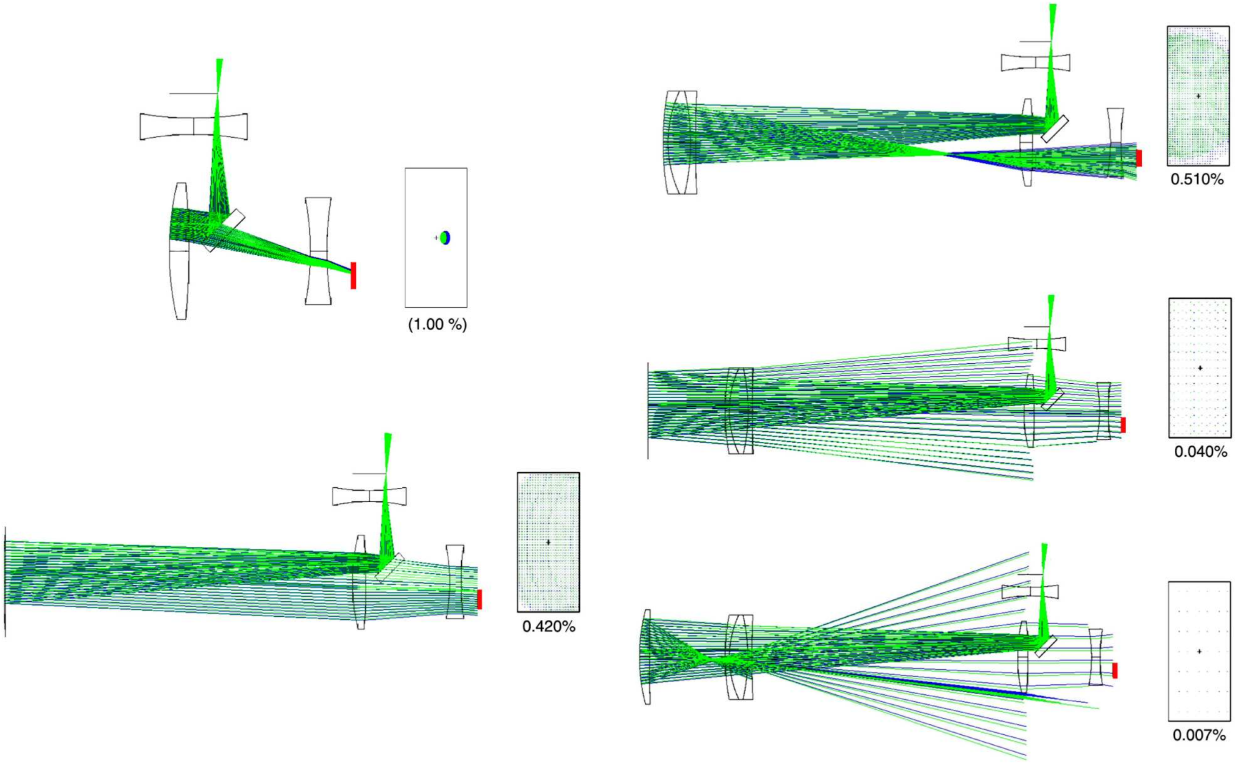

Figure 2.23: ***Ghost image analysis of the construction design***, *displaying ghosts of the input beam, for 9000 Å (blue) and 4000 Å (green), respectively. The CCD area is highlighted in red on the ray tracing diagrams, while the image seen by the detector is shown on the right of each figure. Under these boxes the percentile of the total input light contained by the ghost is given, assuming 1.00% reflectivity on the air/glass surfaces.*

The radius of curvature of L2 front surface is almost exactly twice of its distance from the focal plane. This would result a very sharp and bright ghost image (see upper left figure) but fortunately the fold mirror acts as a baffle. Actually, the location and size of fold mirror was determined to make this protective baffling effective.

The back of L3 forms a relatively bright ghost (lower left panel of Fig. 2.23), but it evenly fills the CCD. The already known image from L5 front is sufficiently softened in this construction design (upper right), and just like the former one evenly fills the CCD. (The front surface of L4 is not considered as a source because the index matching couplant.)

Regarding L6 both surfaces generate a ghost, but these are very defocused and so low intensity ones, evenly filling the detector (lower right figures).

Some portion of focused light (e.g. sharp images of bright spectral lines) is reflected back from the detector surface and becomes subject to retro-reflection and thus ghost image formation (see Fig. 2.24). The front surface of L1b (see Fig. 2.17) is less reflective than the silicon surface of the detector, but it also sees almost focused light and acts on it as a focusing mirror. This concentrated light is subject to ghost image formation by the front surface of L2, too. Fortunately such *secondary ghosts* are not an issue with TRES, as due to the non-zero γ opening angle the spectrum falls at an angle on the CCD and so reflected light moves away from the optics. It only can hit L2, and although the front surface surface of L2 focuses this light but these images form way off the detector (and for the L1b generated one the fold mirror acts as a baffle, again).

Other possible ghost images of the dispersed beam formed by two reflections on air/glass surfaces are very weak (less than 0.01% of the total input light), and all are very spread at the focal plane. Furthermore similarly to the above these form way off the detector.

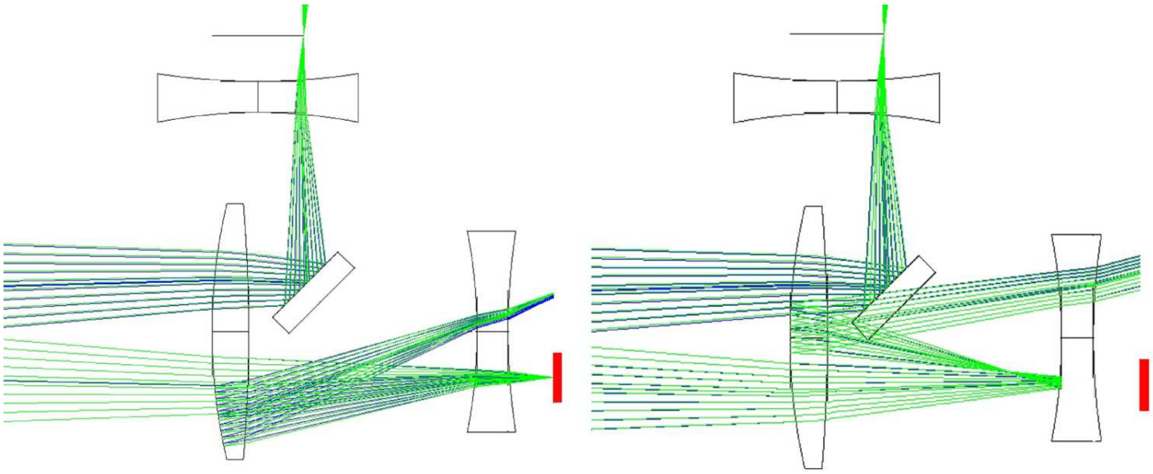

Figure 2.24: ***Secondary ghost images of the construction design****, displaying ghosts of the dispersed beam reflected back from the detector (left) and dewar window (right) and refocused by L2. The CCD area is highlighted in red.*

2.2.8 Tolerance Analysis and Lens Specification

The tolerancing was performed in full double pass, examining image quality change at 6 wavelengths (central wavelengths of spectral orders: 8725 Å in order 39; 6944 Å in order 49; 5767 Å in order 59; 4932 Å in order 69; 4307 Å in order 79; and 3823 Å in order 89). For each optical element effects of all possible error sources were evaluated separately, one by one. For each individual error a nominal magnitude was determined, as a practically achievable smallest value. Then 1, 2, 4, 6, 10, 15, 20, 30, 40 and 50 times the nominal departure/tilt/decenter was applied, and image quality was evaluated after re focusing. (The L1b to L2 distance was allowed to change to act as a compensator.) The wide range of error magnitudes were explored in order to identify non-linear effects.

Results were graphically represented as RMS and geometrical spot size change versus the magnitude of the error (see a sample on Fig. 2.25), for the six wavelength mentioned above. For easier evaluation the spot size values were shown in microns and in percentiles as well, and an overall graph was given representing the average of the six wavelengths, too. The x axis was scaled by the nominal error magnitude, for which the unit value was printed on the plots.

As the ZEMAX model file was rather complex, including several coordinate breaks and multi-configuration setup, custom ZPL scripts were developed to generate these plots. From each graph an acceptable value of the given error was determined, usually the one causing 5% increase of RMS spot diameter on the overall plots. These data are listed as manufacturing (error on radius of curvature and thickness, wedge) and mounting (tilt, decenter, piston) errors in Table 2.7 and Table 2.8, respectively.

Sensitivity to Fabrication Errors Since wedge is measured as indicated runout of a surface, these values were determined as linear TIR (total indicated runout) dimensions. A wedged lens has different effect on image quality depending on its orientation, as the TRES lens system is not symmetrical due to the nonzero γ opening angle. However, the singlet elements can be rotated for best performance. Therefore even though wedge was evaluated in both X (dispersion) and Y (cross dispersion) direction, only an averaged value is listed. Similarly, change in lens radius and thickness were evaluated in a +/- sense, but just an averaged value is listed.

Sensitivity to Mounting/Alignment Errors are rather different in X and Y directions, so these are listed for both. Distance change between optical elements are listed for + and - directions, too. In case of a triplet decenter and tilt are coupled, as the mounting would rely on co-axial centering and keeping constant gap thickness between the cemented surfaces (see Sec. 2.4.1). Therefore only one value is listed as decenter. The sensitivity of L1a to L2 distance might seem to induce very high alignment tolerance, as there is a fold mirror in between the lenses and therefore measuring distance down to 0.1 mm is not straightforward. However, if back-focal distance is allowed to change, this tolerance can be as large as 1 mm. Also, by trial-an-error during the alignment this distance can be fine tuned. The fiber to L1a is easy to set accurately, as those are likely to share a mechanical mount.

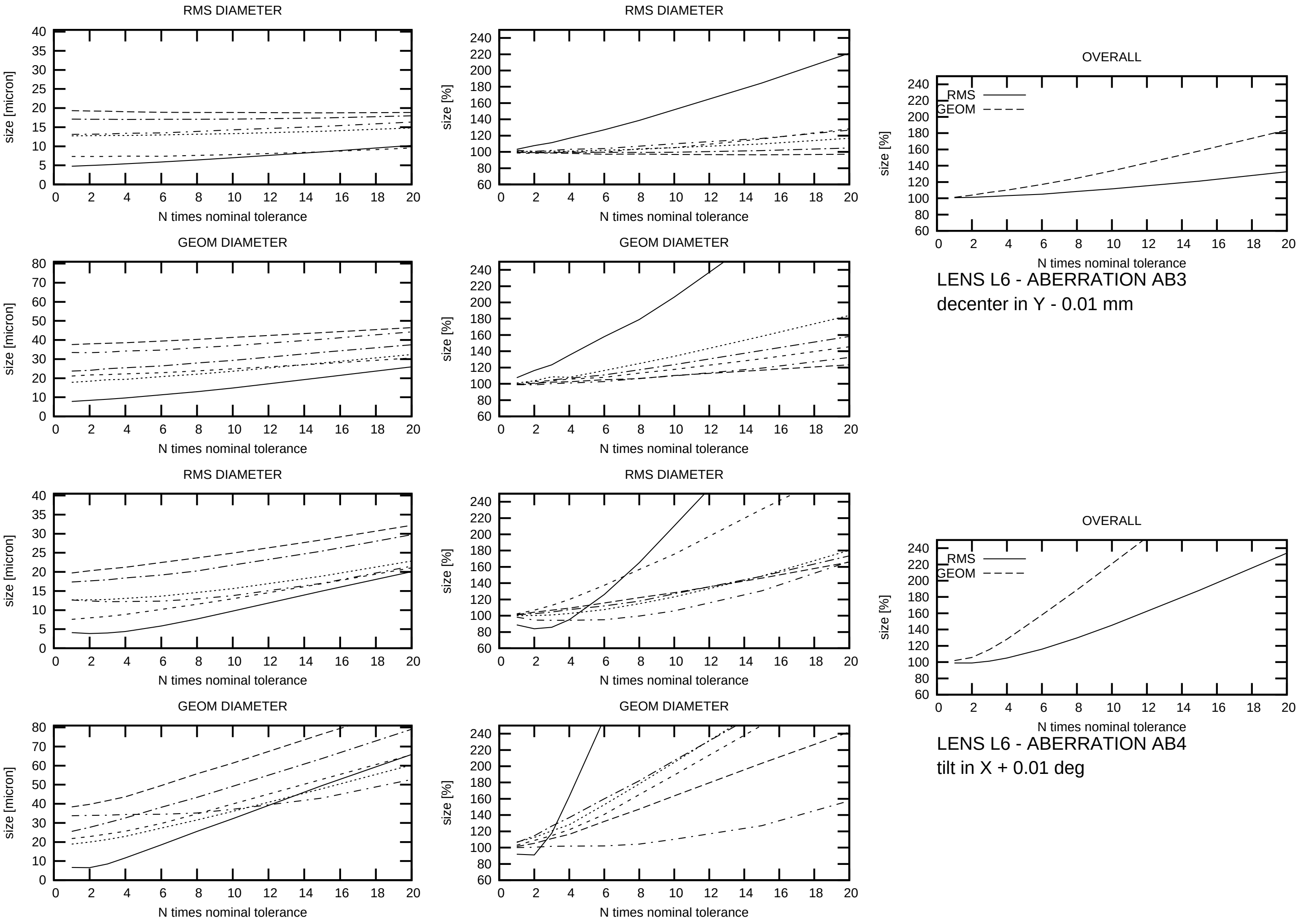

Figure 2.25: ***Sample graphical tolerance analysis report***, *for two possible mounting errors of L6. See text for details.*

Table 2.7. Sensitivity of TRES lenses to fabrication errors

Error source	Magnitude [mm]	Effect [%]	Weight
L1a thickness	0.20	< 5	4
L1a back radius	20.00	< 5	2
L1a front radius	10.00	< 5	3
L1a wedge	0.50	< 5	2
L1b thickness	1.50	< 5	1
L1b back radius	20.00	< 2	1
L1b front radius	20.00	< 2	1
L1b wedge	0.50	< 5	3
L2 thickness	0.10	< 5	5
L2 back radius	8.00	< 5	4
L2 front radius	1.00	< 5	4
L2 wedge	0.10	< 5	3
L3 thickness	0.30	< 5	3
L3 back radius	20.00	< 5	3
L3 front radius	0.10	< 5	5
L3 wedge	0.05	< 5	5
L4 thickness	0.20	< 5	4
L4 back radius	0.20	< 5	5
L4 front radius	0.05	< 5	5
L4 wedge	0.10	< 5	4
L5 thickness	0.10	< 10	6
L5 back radius	0.05	< 5	5
L5 front radius	0.30	< 5	5
L5 wedge	0.04	< 10	5
L6 thickness	0.20	< 5	4
L6 back radius	20.00	< 5	3
L6 front radius	0.10	< 5	4
L6 wedge	0.05	< 5	4

Note. — The **Effect** means average increase on RMS spot radius, in percentile: < 5 means less than 5%. For the smallest (~ 5 μm) spots the effect still can be as large as 50%, so those might become 8 μ or so, but the ~ 30 μm spots do not grow by more than 3-4 microns, for RMS spot diameter. (Geometrical spot size might grow by a little larger amount, but the FWHM of the PSF is more related to RMS than geometrical spot diameter.) **Weight** shows how sensitive the system for the given unity error: 1 is very insensitive, 6 is very sensitive.

Fabrication Tolerances

Axial thickness (AT) errors: these errors are left as loose as possible, since constraining this dimension too much restricts the fabricators abilities to correct figure errors and cosmetics. Parks (1980) suggests that $0.05 - 0.10$ mm are "loose" tolerances. Therefore an AT tolerance of ±0.100 mm was specified for all lenses, which is a reasonable requirement from both an optical and mechanical perspective.

This criteria was met for all lenses except L6, which did go under the nominal thickness by 0.15 mm. Although it is still acceptable (sensitivity analysis suggests 0.20 mm), but obviously Coastal had trouble with this lens/material. It has a short radius with high tolerance on the front surface, so test plate fitting is preferred to match the specification. Coastal did admit that test plate scratched this lens, and re-working the surface resulted the final thickness. The FPL51-Y is known to be a very abrasive glass (its abrasion factor is 5 times higher than BSL7Y), so such fabrication difficulties were expected.

Radius errors: Karow (1993) says "straightforward" spherometry can be performed to 2 μm precision and linear accuracies of 0.5 micron are obtainable with standard ring or ball spherometers, however, a less demanding tolerance is 0.1% of the radius. Such fractional tolerance, as well as the allowed linear radius change is listed in Table 2.9, with values derived from Table 2.7. The radius tolerance is also given as surface sag change, as this is the value can be directly measured by a

Table 2.8. Sensitivity of TRES lenses to mounting errors

Error source	Magnitude X/+	Effect [%]	Magnitude Y/-	Effect [%]	Note
fiber tilt	1.0	< 5	0.5	< 5	3
fiber decenter	1.0	< 2	1.0	< 2	1
fiber–L1 distance	0.2	< 5	0.3	< 5	3
L1a tilt	0.2	< 5	0.4	< 5	4
L1a decenter	1.0	< 5	0.5	< 5	2
L1a–L2 distance	0.1	< 5	0.2	< 5	3/4
L1b tilt	0.2	< 5	0.5	< 5	4
L1b decenter	2.0	< 5	1.0	< 5	1/4
L1b–CCD distance	2.0	< 5	2.0	< 5	1
L2 tilt	0.1	< 5	0.1	< 5	4
L2 decenter	0.5	< 5	0.5	< 5	4
L2–L345 distance	0.4	< 5	0.8	< 5	4/3
L345 tilt	0.1	< 5	0.1	< 5	4
L345 decenter	0.05	< 5	0.05	< 5	5
L345–L6 distance	0.5	< 5	0.5	< 5	2
L3 decenter	0.05	< 10	0.05	< 10	6
L4 decenter	0.03	< 15	0.03	< 15	6
L5 decenter	0.05	< 10	0.05	< 10	5
L6 tilt	0.02	< 5	0.02	< 5	6
L6 decenter	0.1	< 5	0.1	< 5	4

Note. — **Magnitude** is expressed in *degree* for tilt and in *mm* for decenter and piston. Tilt and decenter referenced to the axis X or Y, while distance change can be + or -. The **Effect** means average increase of RMS spot radius, in percentile: < 5 means less than 5%. For the smallest ($\sim 5\ \mu$m) spots the effect still can be as large as 50%, so those might become 8 μ or so, but the $\sim 30\ \mu$m spots do not grow by more than 3-4 microns, for RMS spot diameter. (Geometrical spot size might grow by a little larger amount, but the FWHM of the PSF is more related to RMS than geometrical spot diameter.) **Weight** shows how sensitive the system for the given unity error: 1 is very insensitive, 6 is very sensitive. If two numbers are given first corresponds to the X/+ error, the other for the Y/- one.

spherometer. Bold values are critical ones, for those test plate fitting is necessary, but according to Parks (1980) that method easily delivers the required precision.

The listed demanded tolerances, when applied simultaneously, have a negligible effect on the PSF in the encircled energy sense. According to Table 2.7 each contributes to < 5% increase of the RMS spot diameter, and applying a $\sqrt{\Sigma(err^2)}$ expression to estimate the net simultaneous effect we found it is less than 19% or 3 μm, assuming a reasonable average RMS spot diameter of 15 μm (see Fig. 2.21). This is already negligible compared to the smallest fiber size of 65 μm, but from the as-built numbers of Table 2.9 it can be seen that the expected image degradation of the real system is even smaller than the above estimate.

Total indicated runout (TIR): TIR is a measure of wedge or decenter. Since every lens is registered to an axial flat (annulus), it is most straightforward to specify annulus to R1/R2, and R1 to R2 TIR. (The flat reference surfaces were necessary because of the chosen mounting

Table 2.9. Fabrication tolerances on lens radii and as-built comparison

Surface	R [mm]	ΔR [mm]	$\Delta R/R$	ΔS [mm]	R^* [mm]	ΔR^*
L1a/L1b back	-357.50	2.0	0.006	0.024	356.29/356.81	1.21/0.69
L1a/L1b front	287.82	1.0	0.003	0.019	287.87/288.00	0.05/0.18
L2 back	842.49	4.0	0.005	0.014	842.59	0.10
L2 front	-309.85	1.0	0.003	0.027	310.63	0.78
L3 back	-1698.13	20.0	0.012	0.024	1693.88	4.25
L3 front	**362.08**	**0.4**	0.001	0.011	361.95	0.13
L4 back	**362.08**	**0.4**	0.001	0.011	361.98	0.10
L4 front	**-194.35**	**0.2**	0.001	0.021	194.38	0.03
L5 back	**-194.35**	**0.2**	0.001	0.021	194.36	0.01
L5 front	**458.93**	**0.5**	0.001	0.008	458.63	0.30
L6 back	-5714.70	30.0	0.005	0.004	5710.90	3.70
L6 front	**-361.30**	**0.4**	0.001	0.014	361.88	0.58

Note. — The R radius of curvature is given for $T = 23$ °C, close to the temperature of as-built measurements. $\Delta R/R$ is the dimensionless fractional error, which has a practical lower limit of 0.001 for measurements with a spherometer. ΔS is the sag difference corresponding to the given change in radius, with a practical limit of 0.002 mm. R^* and ΔR^* are as-built values. The critical dimensions are highlighted.

Table 2.10. Fabrication tolerances on lens wedge and as-built comparison

Lens	R1/R2 TIR [mm]	CA [mm]	δ [deg]	$R1/R2$ TIR^* [mm]	R1/A TIR [mm]	$R1/A$ TIR^* [mm]
L1a/L1b	0.500	107.0	0.268	0.003/0.003	(0.010)	0.003/0.003
L2	0.100	137.0	0.042	0.020	(0.010)	0.010
L3	0.050	162.0	0.018	0.003	0.013	0.001
L4	0.100	156.0	0.037	0.003	0.023	0.003
L5	0.040	162.0	0.014	0.013	0.023	0.003
L6	0.050	182.0	0.016	0.011	(0.015)	0.011

Note. — R1/R2 TIR is the allowed total indicated runout for front to back radii; CA is the clear aperture, the TIR measurement should be done just outside of this; δ is the allowed wedge expressed in degrees; $R1/R2$ TIR^* is the as-built value; R1/A TIR is the allowed total indicated runout for one optical surface (R1 or R2) and axial registration flat (annulus); R1/A TIR is the as-built value.

technique, see Sec. 2.4.1.) Requested tolerances and measured values of TIR are listed in Table 2.10.

The Radius-Annulus TIR is determined by a decenter tolerance. Allowable decenter is only critical for the triplet elements, as those are cemented together. Other lenses can be adjusted by their individual mounts. For the triplet elements these tolerances seem to be quite tight, as derived from the $0.03 - 0.05$ mm allowed decenters. But specifying to the the steeper surface helps to achieve greatest sensitivity, and the high curvatures of triplet elements do help to ease these tolerances.

Table 2.11. Annulus flatness tolerances

Lens	δ [deg]	PTV [mm]
L1a/L1b	(0.10)	(0.100)
L2	(0.10)	(0.130)
L3	0.10	0.150
L4	0.10	0.150
L5	0.10	0.150
L6	(0.05)	(0.085)

Annulus flatness: flatness of the axial reference effects tilt. Again, this is relevant only for the triplet elements, as mentioned above. For the values listed in Table 2.11 high and low points are assumed to be 180° apart.

Edge roundness: roundness irregularity can introduce decenter into the mounting of the lenses. As lens diameters are not that different, all lens edges shall deviate from a circle by less than ±0.020 mm PTV. Again, it is critical for the triplet elements, but helps in alignment of the singlets as well.

Edge to annulus perpendicularity: this tolerance also effects lens centration in its bezel. The edge of each optic shall be not taper from the top to the bottom of the edge by more than ±0.010 mm. The edge shall be concentric with the optical axis of the less to ±0.010 mm.

Outer diameter(OD): since we do not want to lose edge thickness or axial flat area, a tolerance of ±0.100 mm applies within the design diameter. This can be easily corrected for during the lens mounting (see Sec. 2.4.1).

Cosmetics (Scratch/Dig): we were requesting a 40-20 scratch-dig cosmetic quality for all lenses. Even in worst case it should cause less than 1% scattering through the entire optical train of lenses, in double pass (Parks, 1980). This scattering is principally due to the dig specification, which cannot be substantially reduced. (The dig specification excludes bubbles, those are included in the substrate, see before).

This criteria was met by all but one lens, L6 was only 60-20 due to the high abrasion factor of FPL51-Y (see above).

Mounting/Alignment Tolerances

General Requirements With the exception of the triplet (L3, L4 and L5) the mounting of the lenses is essentially arbitrary as long as the mechanical requirements for each mounting are met, since we can always shim the mounts meet our requirements. However, it vastly simplifies alignment is mechanical references are present on the mounts. For this reason, we planned to register lenses in their mounts with the following accuracies:

- Centration: ±0.0254 mm
- Tilt: $\pm 0\overset{\circ}{.}050$
- Piston: ±0.100 mm

Mount Stiffness Since TRES is a bench mounted spectrograph, stiffness requirements are somewhat more relaxed than for a Cassegrain mounted instrument, however a lowest frequency greater than 50 Hz has been applied successfully to the Hectochelle spectrograph and should be applied here.

Athermal Mounting The spectrograph room would be controlled to ±0.1 °Cat 18 °C, however the mounts should be athermalized for an operational range of −10 °C — +35 °Cand a survival range of −25 °C — +50 °C(in case heating is permanently lost at FLWO for long time in winter, and also to withstand shipping inside of truck to the warm Arizona, even in summer time.)

Triplet Mounting The co-alignment of the elements of the triplet is critical to the performance of TRES. Furthermore, the mounting must make it possible to cement the optics with some optical couplant to minimize reflection losses. We also note that proper allowance must be made for the disparate coefficients of expansion (CTEs) of the three glasses that constitute the triplet. The gap that is filled with couplant is to be 0.100 mm thick.

Final Re-optimization — The As-Built Model

Based on the as-built lens properties the optical model once more was updated and re-optimized, by allowing primarily the L2 to L1b distance to compensate for errors. Since the lenses were fabricated very close to the specified nominal values, the as-built model was almost identical to the construction one.

2.2.9 Exposure Meter

As the 254 × 128 mm R2 grating is slightly overfilled by the 128 mm beam, by some 4%, this light can be used to feed an exposure meter and thus get real time S/N ratio estimates and quickly recognize guiding errors or other changes decreasing throughput.

Fig. 2.26 shows the location of a flat fold mirror in front of L6, which can be used to reflect back towards the focal plane that portion of the input beam which would miss the grating otherwise. This exposure meter beam forms a sharp image on the focal plane, since it is reflected back from the collimated section of the input beam. Therefore the exposure meter detector can be small and share the dewar/cold plate of the science camera. This secondary CCD can be located conveniently next to the science detector, as its position can be easily set almost anywhere by tilting the pick-off mirror. The only constrain is the fold mirror of the input beam, but as it is shown on Fig. 2.26 the exposure meter beam can pass just above this fold.

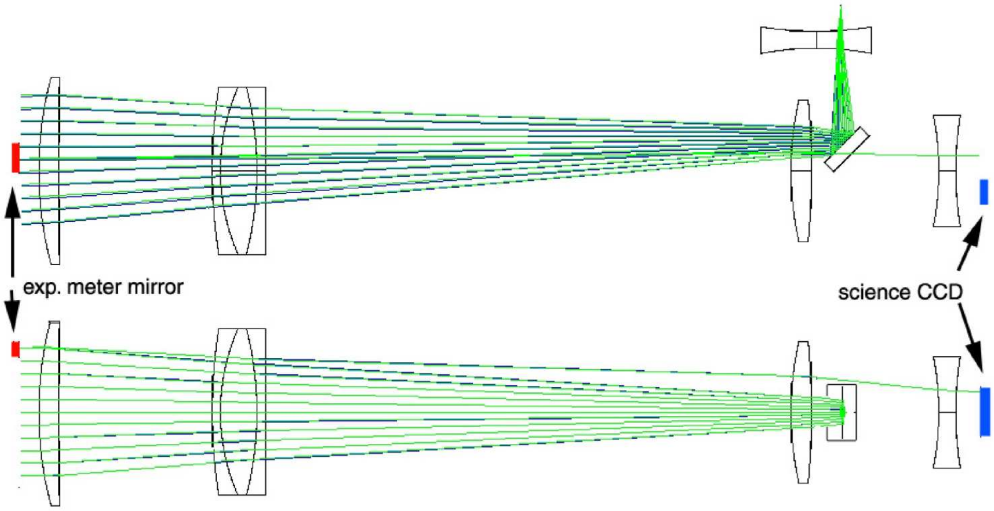

Figure 2.26: ***Optical layout of the exposure meter***. *Red and blue rectangles represent the location of the pick-off fold mirror and science CCD, respectively. The exposure meter beam just passes above the fold mirror of the input beam, and forms an image off the side of the science detector.*

2.3 Front End Optical Design

The so-called *front end* is responsible for feeding the fiber with star or calibration light, and provide guiding during exposures. In order to decrease FRD losses it must include a focal reducer, which has to be designed for the very specific optics of the Tillinghast reflector. Other main optical element is a possibly 1:1 re-imager of the focal plane for guiding. To fulfill this we found a commercially available macro photo lens to be a more cost effective option than designing and manufacturing custom optics. Some auxiliary optics are also needed to manage calibration light, for which off-the-shelf catalog lenses are adequate since there is no demand for high image quality.

As discussed earlier a iodine cell is not a cost driver, so it was considered to be an option for the TRES instrument. Although the I_2 cell can be part of either the spectrograph or the front end, due to the demand of thermal stability any heat source should be avoided on the optical bench (the iodine cell must be heated to ~ 50 °Cto evaporate all of the iodine). Therefore the cell was meant to be mounted in the front end.

2.3.1 Focal Reducer

The design considerations for the focal reducer were the following:

- f/6 focus have geometrical spot diameters smaller than 65 μm (the smallest fiber), over a central $1'$radius (2.6 mm), to provide enough room to mount all three (65, 100 and 140 μm) science and sky/calibration fibers
- have at least $4' \times 4'$ FOV for guiding (and for target identification, see below), with acceptable image quality (less than 80 μm or $2''$RMS spot radius at corners)
- possibly fold the optical path to keep CG point closer to mounting surface, to minimize deflections due to gravity change. This fold mirror can also provide fine guiding via a tip-tilt system, as the old telescope mount has backlash problems

- accommodated a min. 10 cm long I_2 cell in the light path
- have enough room between slit viewing mirror and focal reducer to provide clean view of focal plane for guiding
- the available max. BFD at f/10 is $\sim$ 500 mm, so all above likely has to fit within $\sim$ 400 mm (as f/6 reduction will shorten BFD)
- the entire front end assembly should fit within the largest available bolt pattern of the Tillinghast reflector instrument mounting plate ()

The old telescope mount has known backlash and pointing errors. Latter sometimes (for larger than $\sim$ 90 deg angular movements) results up to $4' - 5'$ offset from target location. Therefore the guider field has to be wide enough to make object/field identification possible and not too time consuming. To overcome the backlash problem a tip-tilt system was also used by the AFOE spectrograph (Nisenson et al., 1999), and it resulted an increased throughput by allowing precise guiding at a 2 Hz correction rate.

We did not plan to use a pellicle beam splitter in front of the focal plane to spare some percent of light on guiding, to maximize throughput. Also, the large fibers could cover the entire seeing disk and so not allow guiding on the annulus of the stellar image outside of the fiber area, but rather require a guide star. Therefore it was a requirement to have the entire guide field unobstructed during data acquisition. This implied that the simultaneous calibration fiber can not be located in close vicinity of the the science fiber, as projecting ThAr light into would come with at least partial obscuration. At the same time for faint objects observer might prefer a sky sampling fiber, which is better be relatively close to the object, especially in case of partially embedded objects of star forming regions (one of the main targets of TRES).

Therefore for each fiber diameter the design incorporates three fibers (a total of 9): a science and sky fiber, close together on the focal plane, and a calibration fiber out of the guider FOV. The reason this calibration fiber was still fed at the front end is twofold. One is to to have the same length and environmental effects (temperature, bending) on these fiber. The other one is to share the same calibration source with the sky/science fibers.

The initial design was based on a all-spherical bonded doublet, and was optimized in ZEMAX for radii, thickness and glass type, with the model including two flat fused silica windows to represent the iodine cell. The result of optimization, together with the optical description of the Tillinghast reflector is given in Table 2.12. The f/6 design was analyzed for temperature effects, ghost images, manufacturing and mounting errors, similarly as the TRES lens system. The table lists the construction values for the focal reducer, with test plate fitted radii (assuming Coastal Inc. as manufacturer).

Figure 2.27 shows the optical layout of the entire Tillinghast telescope, with a zoomed-in view for the front end optics. See Figure 2.28 for the image quality, which is very good over the central $2'$ FOV, with RMS spot radius of 12 μm (approximately FWHM of $0\farcs5$).

2.3.2 Guider

For the guider optics it seemed to be a cheaper and simpler solution to use an off-the-shelf photographic lens designed for 1:1 re-imaging. Such macro lenses are available for a wide range of focal lengths up to f/2.8 focal ratio, for a fraction of the cost a custom optics would imply (optical design and manufacturing, mechanical design of bonding fixtures and lens mounts, etc.). An other

Table 2.12. Tillinghast reflector prescription at f/6

Surface	Radius [mm]	Thickness [mm]	Glass type	Diameter [mm]	Conic constant
primary	-7625.33	—	mirror	1524.07	-0.009092
	—	-2834.35	—		—
secondary	-2634.74		mirror	401.32	6.764913
	—	2834.35	—		—
field corrector lens 1	155.32	11.46	fused silica	120.0	0
field corrector lemns 1	225.17	—	—	120.0	0
air gap	—	15.08	—	—	—
field corrector lens 2	-410.97	8.19	fused silica	120.0	0
field corrector lens 2	Inf.	—	—	120.0	0
to mounting plane	—	541.23	—	—	—
	—	69.85	—	—	—
tip-tilt mirror	Inf.	—	mirror	—-	—
	—	-87.71	—-	—-	—
iodine cell 1st window	Inf.	-7.62	fused silica	60.00	—
iodine cell 1st window	Inf.	—	—	60.00	—
	—	-116.46	—-	—-	—
iodine cell 2nd window	Inf.	-7.62	fused silica	60.00	—
iodine cell 1nd window	Inf.	—	—	60.00	—
	—	-10.00	—-	—-	—
focal reducer lens A	-110.31	-12.70	BSM51Y	42.0	0
focal reducer lens A	-28.73	—	—	42.0	0
focal reducer lens B	-28.73	-16.12	FPL51Y	42.0	0
focal reducer lens B	111.58	—	—	42.0	0
	—	-59.25	—	—	—

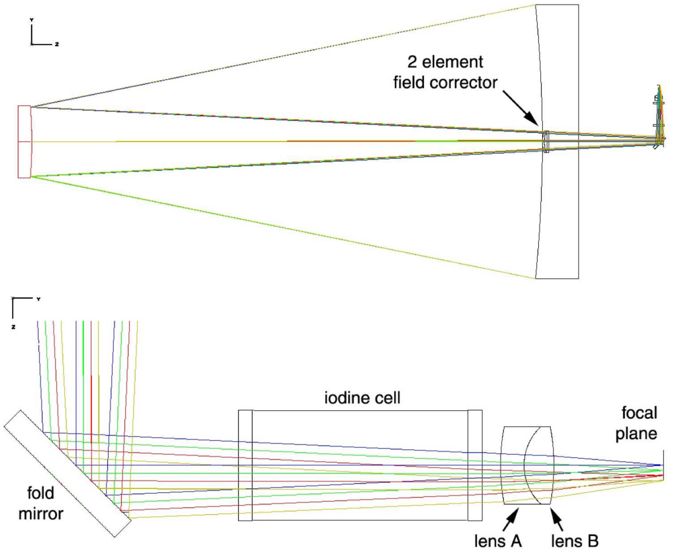

Figure 2.27: ***Optical layout of the Tillinghast reflector at f/6****. The upper plot shows the entire telescope, the location of the field corrector and the front end optics. The lower detailed view shows the TRES front end elements only.*

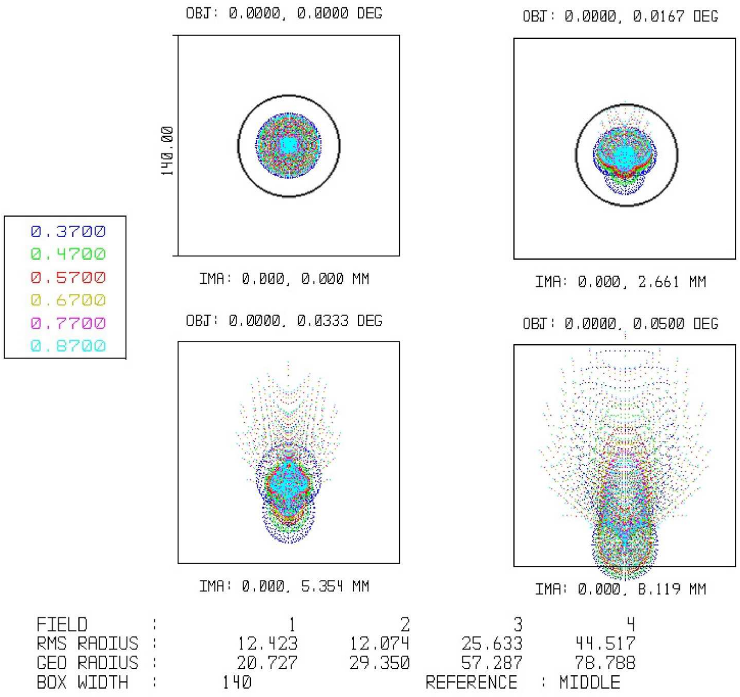

```
FIELD       :          1         2          3          4
RMS RADIUS  :     12.423    12.074     25.633     44.517
GEO RADIUS  :     20.727    29.350     57.287     78.788
BOX WIDTH   :    140                REFERENCE  : MIDDLE
```

Figure 2.28: ***Polychromatic spot diagrams of the Tillinghast reflector at f/6***. *The upper plots represent on axis (left) and 1′ off axis field locations, with a circle corresponding to the size of the smallest fiber (65 μm). Lower plots are for 2′ and 3′ fields, the box is 140 μm for all spots.*

advantage is the internal focusing mechanism of photographic lenses, which although has top be driven by an external stepper in the manual mode but still spares the focus stage of the guider assembly.[3]

The only drawback is the lack of appropriate optical model of such commercial item. These are not published by manufacturer, however some systems can be found in patent data bases. Our choice, the Canon EF 2.8/105 macro lens, was fortunately listed in the US patent data base.

The optical description had some (likely intentional) mistakes, which were relatively easy to correct in ZEMAX by optimizing the system.

The resulting optical layout and guider plane spot diagrams are shown in Fig. 2.29 and 2.30. Although at the corner of a $4' \times 4'$ FOV the expected FWHM would be $\approx 3'$, and dominated by the guider optics, the centroid can be determined at the $< 0.1\ FWHM$ level so guiding should have accuracy of $\sim 0\overset{''}{.}3$ or better.

2.3.3 Calibration Optics

To calibrate the six fibers of the focal plane (science and sky fibers, three diameters for each) a linear stage is required which blocks the stellar light form the telescope and projects the calibration light down the fibers. Preferably the same stage should be used to deliver ThAr light for the

---

[3] The electronic actuation of the focus is beyond possibility, as the communication protocol of different lens makers is proprietary. Reverse engineering is too expensive and apparently even big third party lens manufacturers can not do it right for the lenses of leading camera manufacturers.

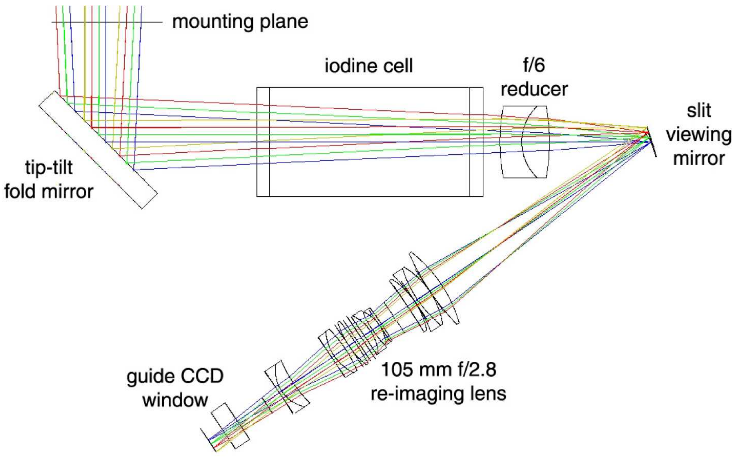

Figure 2.29: ***Optical layout of the TRES guider***. *Rays are shown for on axis, $1'$, $2'$ and $3'$ off-axis image formation.*

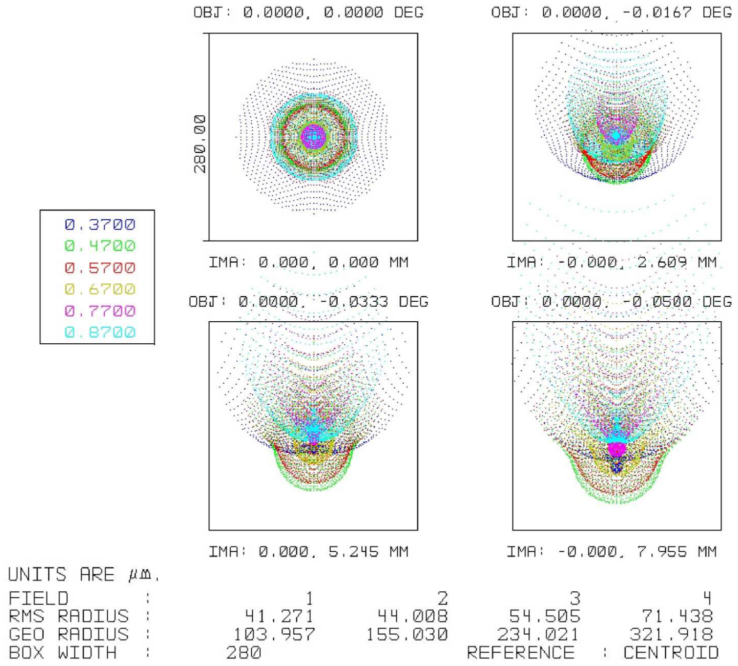

```
UNITS ARE µm.
FIELD       :         1          2          3          4
RMS RADIUS  :    41.271     44.008     54.505     71.438
GEO RADIUS  :   103.957    155.030    234.021    321.918
BOX WIDTH   :       280              REFERENCE  : CENTROID
```

Figure 2.30: ***Polychromatic spot diagrams of the TRES guider***, *for on axis, $1'$, $2'$ and $3'$ off-axis image formation in case of 1:1 re-imaging. The box is 280 μm.*

calibration fibers, as well. Also, the iodine cell has to be illuminated with a tungsten lamp (flat field exposure) in order to record a pure I_2 spectrum, mandatory for the iodine data reduction, so such stage should precede the iodine cell. As it can be seen on Fig. 2.29 the I_2 cell occupies almost all the space between the tip-tilt mirror and the focal reducer. Therefore this moving element has to be narrow, but at the same time "wide" enough to produce a beam in front of the iodine which has the same diameter as the telescope beam.

The science and sky fibers could be calibrated separately by using a narrow beam and essentially re-imaging a small aperture in front of the calibration source. However this puts high requirements on the accuracy of the calibration stage. Those six fibers are also likely to be mounted not in a single row, as image quality of the the telescope (see Fig. 2.28 is satisfactory only over a small FOV. (Mounting all fibers along a straight line within $2' = 5$ mm is not that straightforward.) Therefore to illuminate one fiber at a time with a well-localized spot a 2-axis stage might be necessary.

It is also important to reproduce the telescope beam as close as possible. The axis of the f/6 telescope beam is only perpendicular to the focal plane on axis, at different field locations it slightly decreases. For multi-object instruments it is very important, and even though TRES observes one object at a time the different fibers are at different locations.

As a result of combining all above the TRES calibration system design became as follows:

An integrating sphere holds the ThAr and tungsten lamps, so for lamp selection no stage but simple on/off action is required. The exit aperture of the sphere is projected onto the focal plane and calibration fiber set by virtually moving this aperture at the location of the secondary. This assures that the angle of incidence at every field location is the same as for stellar light. (Although the calibration beam is somewhat slower than f/6.) In one configuration a periscope blocks the telescope beam and routes the light from the sphere towards the iodine cell and focal reducer. The virtual image seen by the focal plane corresponds to have a light source at the secondary and it illuminates the entire field of the guider at once. If the periscope is moved the telescope beam becomes unobstructed and the calibration light travels along a secondary light path, including an other set of projection optics to mimic the secondary-location for the calibration fibers. The iodine cell is also mounted on a linear stage so it can be removed from the telescope beam as well. See Fig. 2.31 for an optical layout.

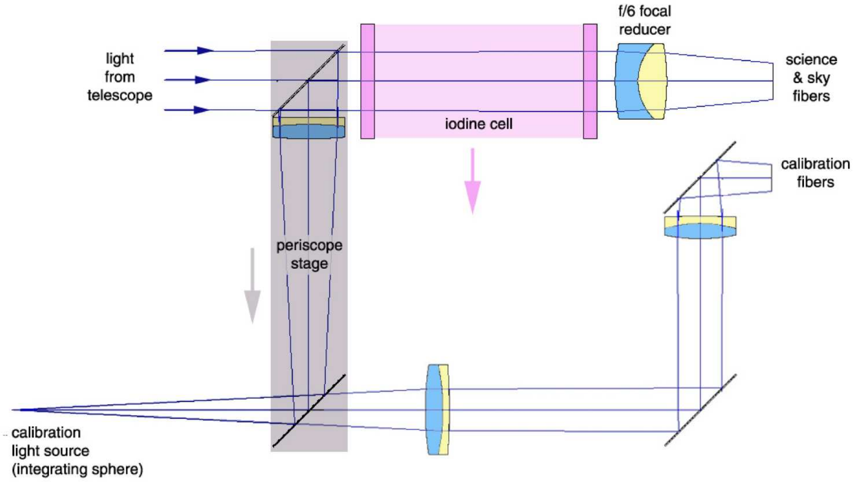

Figure 2.31: ***Optical layout of the TRES calibration system***, *displaying the light-paths of the science/sky and calibration fibers at the same time. The selection between the two can be done by moving the periscope stage (as indicated by the gray arrow). The iodine cell can be removed from the light-path as well (purple arrow).*

The *science and sky path* uses two mirrors and one achromat. The lens was selected from the Edmund Optics catalog. (NT45-354, 50 mm diameter, focal length of 350 mm) The *calibration path* uses one fold mirror and two Edmund achromats. (NT45-180: $D = 50$ mm, focal length 250 mm; NT32-923: $D = 40$ mm, focal length of 160 mm.)

2.4 Spectrograph Bench Mechanical Design

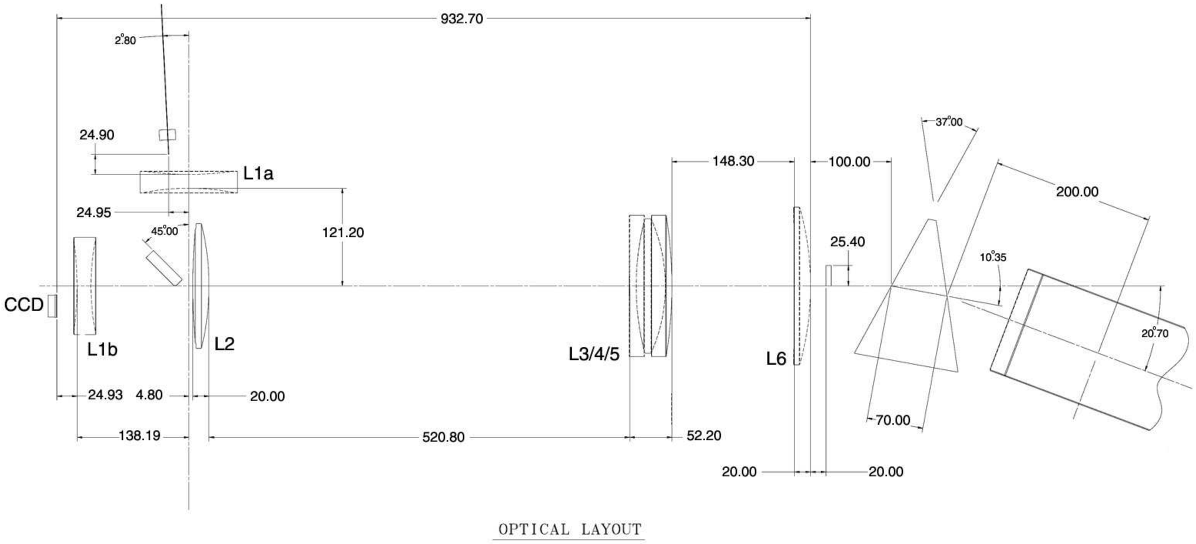

Figure 2.32: ***Layout of the TRES bench**, displaying the main optical elements and dimensions (lengths in mm, angles in degrees)*

The location of optical elements on the TRES bench, with relative distances and angles displayed, is shown on Fig. 2.32. This drawing served as a base for the mechanical design. As the bench is not moving and most of the elements are relatively far away from each other the optical mounts can be relatively simple and robust. However, those must provide athermalized support. It is also preferred to have some sort of kinematic mounting, so the spectrograph can be conveniently aligned in the assembly lab (located in Cambridge, MA, USA) and then re-assembled at the observing location (FLWO, AZ, USA) without the need of further alignment. First the design of such mounts is given, followed by the description of the two moving stages: the fiber selector and the camera focus.

2.4.1 Athermal Lens Mounts

A metallic bezel provides simple and safe handling/mounting of sensitive lenses. Coupling such bezel and optical glass requires careful design and analysis in order to prevent stress building up in the glass. Stress, as a result of thermal or mechanical loads at the glass/mount interface, can result in deformation of the lens and thus degradation of image quality (or in an extreme case it even can destroy the lens). For TRES the requirement was to withstand a 45 °C temperature change in the assembled state without compromising image quality, and survive 75 °C change during shipping. As the bench was going to experience steady gravitational field the mechanical load requirement was a moderate, uni-directional 1 g in operation and to survive 3 g in shipping.

Continuous bonding of lenses in metal rings by room temperature vulcanizing rubber (RTV) were successfully applied for other CfA instruments in the past. If the metal bezel is chosen to have a CTE larger than the glass, and if the thickness of the RTV bond is chosen properly, such mount can be designed to eliminate thermally induced stress (caused by the differential expansion

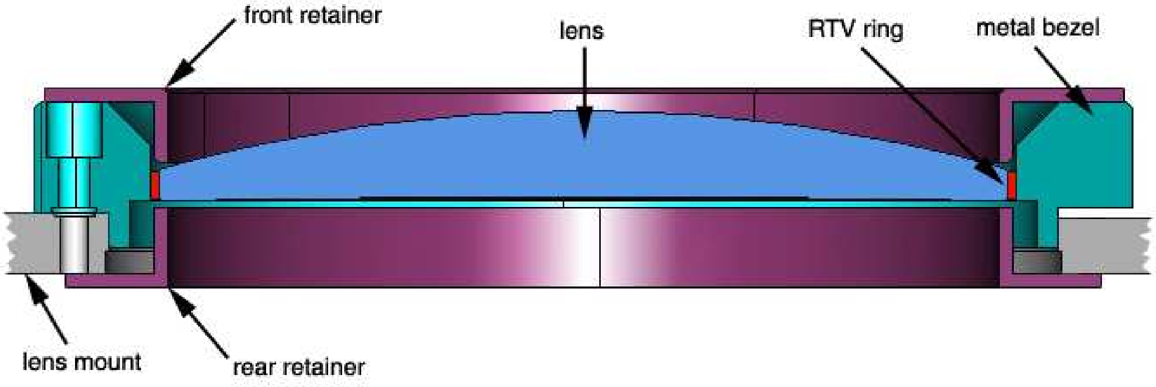

Figure 2.33: ***Cross section of a continuous RTV bonded lens mount.*** *The lens is bonded to a bezel (green), while the bezel is supported by the lens mount (gray). The retainers (purple) are attached to the bezel and do not touch the glass. Their role is only safety, to prevent the lens falling out of the mount in case the RTV bonding fails.*

of the metal and glass). This is possible because RTV has a CTE much higher than typical metals and glasses so that a thin layer of RTV can compensate the thermally varying gap between the lens and the bezel. This is an appealing approach but its success relies on the precise knowledge of the material CTEs.

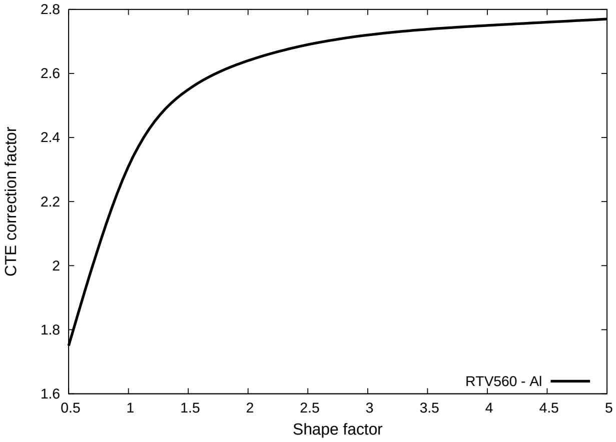

Figure 2.34: ***CTE correction vs. shape factor for RTV560–Al bonding***, *after Fata et al (2004)*

It is very important to note that a restrained elastomer behaves differently compared to an unrestrained sample. For example the α_0 unrestrained CTE of an RTV can be almost three times smaller than the CTE of very thin bonding layers. Dependence of material properties is best described by the the *shape factor*, S, which is defined as:

$$S = \frac{loaded\ \ area}{force\ \ free\ \ area}. \tag{2.4}$$

Fata et al (2004) provides an extensive study of the GE Silicon manufactured RTV560, including its CTE properties, based on both experimental results and finite element (FE) analysis.

Table 2.13. Properties of RTV560

α_0 [10^{-6} / °C]	hardness	E_0 [kPa]	E_∞ [kPa]	G [kPa]	k
200	55	3 171.6	792.9	1 061 792.6	0.64

The CTE correction factor vs. shape factor for an Al–RT560 bonding is represented here on Fig. 2.34[4]. If a continuous bond has a B width and t thickness the shape factor is $S = B / 2t$. From Fig. 2.34 it is apparent that for bond thicknesses $B - 0.25B$ the CTE of RTV is rapidly changing, while for relatively thin bonding layers the CTE correction factor does not vary significantly.

The E_c *compression modulus* of the bonding layer is also depending on the shape factor. According to Lindley (1970) for a continuous ring it is given by:

$$E_c = E_0 \frac{4}{3} \left(1 + kS_i^2\right), \tag{2.5}$$

where E_0 is the unrestrained elastic modulus, k is an empirical stiffness correction factor and S is the shape factor.[5] Table 2.13 summarizes such basic properties of RTV560, including the G shear modulus, according to Fata et al (2004).

For a lens of r radius a temperature change would force the t thickness of the bonding layer to change by the following amount:

$$\delta t = \delta_{lens} + \delta_{RTV} - \delta_{bezel}, \tag{2.6}$$

in which the individual terms are the dimensional changes of the components due to ΔT temperature change:

$$\delta_{lens} = \alpha_{lens} \, \Delta T \; r, \tag{2.7}$$

$$\delta_{RTV} = K_S \; \alpha_{RTV} \; \Delta T \; t, \tag{2.8}$$

$$\delta_{bezel} = \alpha_{bezel} \; \Delta T \; (r + t), \tag{2.9}$$

where K_S is the shape-factor (S) dependent CTE correction value of RTV.

As the compression modulus is the ratio of stress (force per area) to strain (ratio of change):

$$E = \frac{\sigma}{\varepsilon} = \frac{F/A_0}{\delta t/t}, \tag{2.10}$$

the stress seen by the lens at the RTV bond interface is given by:

$$\sigma = \frac{\delta t}{t} \, E_c, \tag{2.11}$$

---

[4] Note, that this curve is slightly different if the RTV is bonded to other materials (e.g. invar), but as the TRES design considered to use Al bezels only this relation is displayed.

[5] Equation (2.5) should be corrected for high shape factors, when the ratio of E_c to the bulk modulus (E_∞) exceeds 10%. As suggested by Lindley (1970) in such case the right side of Eq. (2.5) has to be divided by $(1 + E_c/E_\infty)$.

where E_c is the shape-factor dependent compression modulus of RTV. The load, force per unit bond length, is expressed as:

$$F = \sigma B. \tag{2.12}$$

The RTV bond has to be analyzed in terms of stiffness as well. For TRES the *axial mode* (up-down on Fig. 2.33) is less relevant, as the mounted lenses will experience a gravity vector with a pure radial component (sideways on Fig. 2.33). However, for the triplet and for shipping the axial modes must be examined. The radial displacement of a lens due to its weight can be corrected for singlets (by shimming the mounts), but for the triplet elements it must meet the results of the sensitivity analysis summarized in Table 2.8.

The K_a axial *spring rate* of the RTV bond will consist of a shear term only, while the K_r radial spring rate also contains a compression term:

$$K_a = 2r\pi \; B \, \frac{G}{t}, \tag{2.13}$$

$$K_r = 2r\pi \; B \, \frac{E_c}{2t} + 2r\pi \; B \, \frac{G}{2t}, \tag{2.14}$$

where G is the shear modulus. The axial and radial natural frequencies (F_a and F_r) are given by the well known expression of the resonant frequency of a harmonic oscillator (for units of Hz):

$$F_a = \frac{1}{2\pi}\sqrt{\frac{K_a}{m}}, \tag{2.15}$$

$$F_r = \frac{1}{2\pi}\sqrt{\frac{K_r}{m}}, \tag{2.16}$$

where m is the mass of the lens. The axial and radial displacement under 1 g load ($F = m\, g$) can be expressed using the spring equation ($F = -K\, x$):

$$x_a = \frac{mg}{K_a}, \tag{2.17}$$

$$x_r = \frac{mg}{K_r}. \tag{2.18}$$

The B bond width was either pre-determined by the lens edge (e.g. for lens L4 only 7 mm was available), or it was fixed as a feasible value (8-10 mm) for lenses with edge thicknesses greater than 10 mm. Using above equations for all TRES lenses an optimal bond thickness was determined for $\Delta T = 45$ °C temperature difference, resulting acceptable stress and load on the lens substrates at the bond interface.

The optimal RTV thickness was found by evaluating figure sets like the one seen on Fig. 2.35. In terms of mount stiffness the goal was to have axial natural frequency larger than a 100 Hz (as the axial is always the softer direction), and to meet the radial displacement values of the sensitivity analysis where it was relevant (triplet elements). As it can be seen from panels *a* and *b* the stiffness is, as expected, greater with thin bond layers but the lower panels (*c* and *d*) reveal that stress is larger in that case. (Note that the units of stress and load were chosen to be not SI, but rather $N\ cm^{-2}$ and $N\ cm^{-1}$, as such values are easier to picture.)

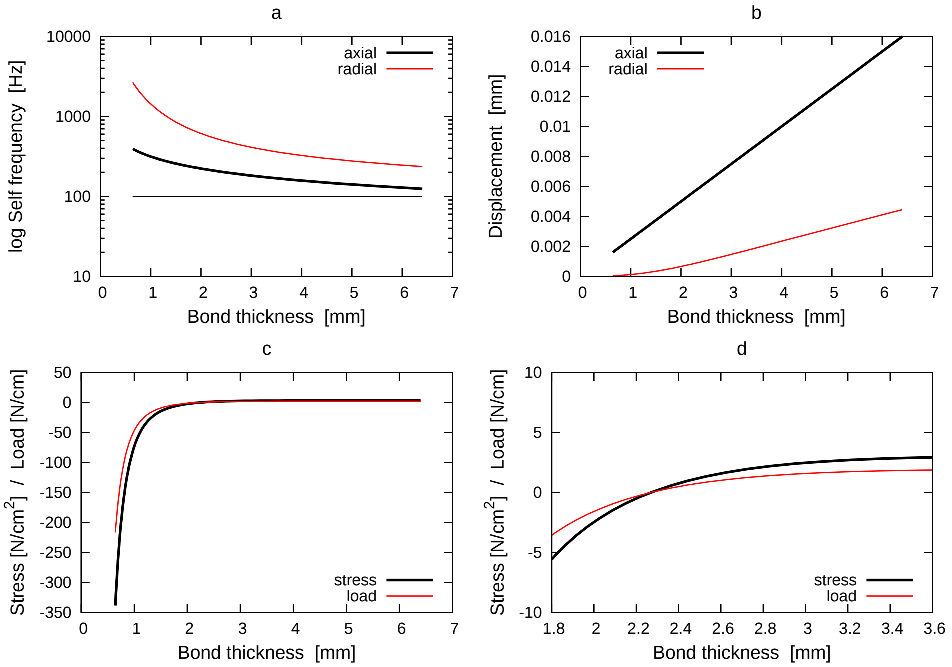

Figure 2.35: ***Figure set to determine optimal bond thickness for lens L2***. *Panel a shows the mount stiffness and the minimum goal of 100 Hz; b plots the displacement under the load of 1 g (self weight) in the axial/radial directions; c represents the stress and force per unit bond length seen by the lens at the RTV interface, while d gives a zoomed in view of the former panel — all as a function of RTV bond thickness, for* $\Delta T = 45\ ^\circ C$ *thermal load.*

Table 2.14. Properties of the TRES RTV bonded lens mounts

Lens	CTE$_{lens}$ [$10^{-6}/^\circ$C]	CTE$_{bezel}$ [$10^{-6}/^\circ$C]	Diameter [mm]	Mass [kg]	B [mm]	t [mm]	F$_a$ / F$_r$ [Hz]	x$_a$ / x$_r$ [μm]	Stress [$N\ cm^{-2}$]	Load [$N\ cm^{-1}$]
L1	7.60	23.04	120.4	0.723	7.6	2.2	190/545	6.9/0.8	3.8	2.8
L2	8.89	23.04	154.6	0.628	6.4	2.8	188/433	7.1/1.3	2.2	1.4
L3	6.30	23.04	175.4	1.090	10.2	3.0	186/534	7.1/0.8	0.1	0.1
L4	18.85	23.04	167.0	1.529	7.0	4.5	108/229	20.9/4.7	8.1	5.7
L5	6.70	23.04	175.4	1.260	10.2	3.0	174/497	8.2/1.0	0.7	0.7
L6	13.60	23.04	195.4	1.517	6.4	2.2	153/398	10.6/1.6	2.7	1.7

Note. — As in the text F_a and F_r are the axial/radial natural frequencies, x_a and x_r are the according amplitudes or displacements under 1 g (self weight) load. The bezel is aluminum. CTE values are given for $T = 25\ ^\circ$C.

As mentioned above for the TRES lens mounts stiffness is only secondary as the gravity vector is fixed and singlet elements can be shimmed to accommodated displacements, so the primary goal was to keep the stress levels low. Since most of the bond thickness–stress curves are very steep at small RTV thickness values (see panel *c*) attention was given to stay away from that region. Therefore chosen bond thicknesses often were at some positive stress values (e.g. 2.8 mm for lens L2) in order to stay on the safe side if manufacturing/assembly errors alter the bond width/thickness.

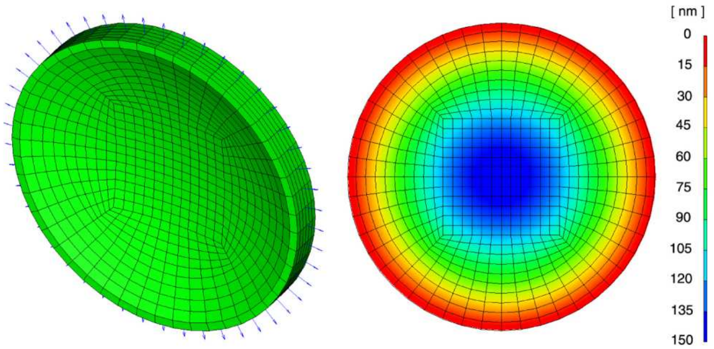

Figure 2.36: ***Finite element model and surface deformation map of lens L5*** *under 2 $N\ cm^{-1}$ load along the bond interface.*

To see what would be the effect of a given stress/load value on a lens a FE analysis of L5 was performed (see Fig. 2.36). This lens was chosen because it is relatively thin and its convex–concave shape is the most sensitive to deformation due to the thermally induced load at the bond layer. Based on the bond thickness evaluation graphs a 2 $N\ cm^{-1}$ load was applied to calculate surface deflection. As it can be seen on Fig. 2.36 (right) the deformation is very small, only a fraction of a micrometer. By fitting Zernike polynomials to the deformed surface it was shown that the thermal load causes almost a pure radius change of the surfaces. Applying such, almost negligible, change to the ZEMAX model the effect on image quality was found to be not noticeable. Therefore a few times of 2 $N\ cm^{-1}$ was proven to be an acceptable load value for all lenses. As it can be seen in Table 2.14, which gives a summary of lens mount properties, it was met in all case.

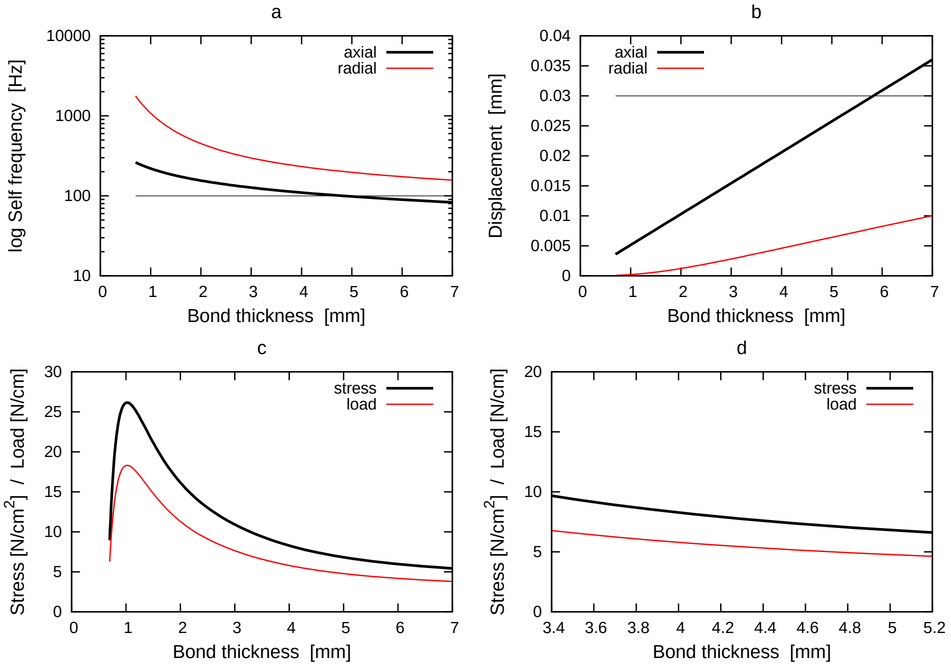

Figure 2.37: ***Figure set to determine optimal bond thickness for lens L4****. Compare to Fig. 2.35. On panel b the thin horizontal line is the maximal allowed radial displacement from the sensitivity analysis.*

For lens L4 the glass CTE is almost as high as the bezel CTE, which reduces the effectiveness off the continuous RTV bond to athermalize the mount. In this case the bond thickness–stress curve is very different, as it can be seen in Fig. 2.37 in comparison with Fig. 2.35. There is no zero point on the stress/load curves and minimizing those values would result to a very thick bond not providing the required stiffness. Therefore a compromise had to be made, resulting somewhat high stress (relative to other lenses) and a significant radial displacement as it is comparable to the maximal allowed mounting error (see Table 2.8). Although the lens is a very robust bi-convex element, the crystalline CaF_2 is a very sensitive material. To be on the safe side the effects of thermal load was also analyzed by FE method for lens L4. Similarly to L5 no degradation of image quality was found, and the 81 kPa stress is still way below the yield strength of CaF_2.

Supporting Single Elements

After the lenses are athermally mounted in the bezels, a semi-kinematic supporting structure holds the optical element in place, in a vertical position. Since the top of the optical table is steel while the bezel is aluminum, the support consist of a steel mounting base and an aluminum angle (Fig. 2.38). The choice of such configuration is also considered because the focus mechanism of the camera assembly would be a steel linear stage, while the CCD housing is aluminum. Therefore choosing similar materials, with similar vertical dimensions for the detector and optics, can compensate for thermal expansion in the vertical direction. The steel base is firmly held in place by steel clamps and positioning blocks. The upper aluminum structure is allowed to expand or contract due to temperature changes, while not influencing the axial position of the lens and remaining well constrained to the base.

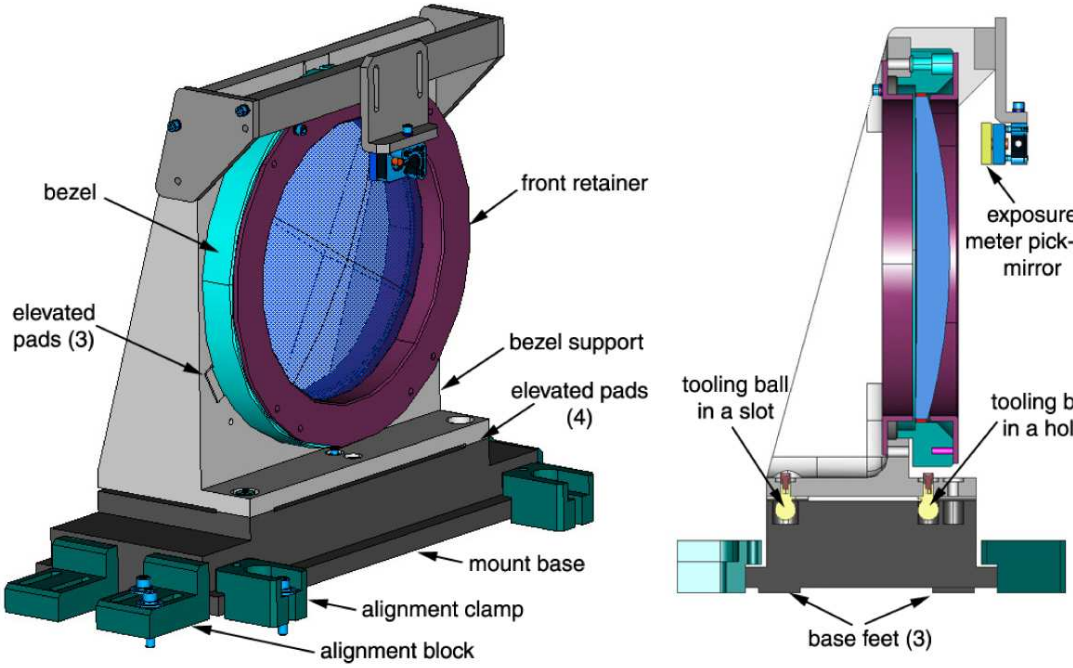

Figure 2.38: ***Isometric and cross-sectional view of a singlet mount.***

This is achieved by seating the angle on the base using four pads of small surface area, and connecting the two by bolts and a belleville washer at these locations. A tooling ball pressed into the aluminum part, located under the center of gravity (CG) of the lens, fits into a precisely machined hole of the base. Another tooling ball mounted off the angle sits in a slot of the base, positioned along the optical axis of the system. Thermal "breathing" therefore leaves the CG point of the lens unmodified respect to the steel base, while the springy washers and other tooling ball in the slot let the aluminum part to expand while retaining its orientation.

The aluminum support has a precisely machined opening to accept the highly toleranced outer diameter of the bezel. These two connect on three small surfaces, tightly clamping the two parts together by bolts. Therefore the radial and axial position of the lens is highly repeatable, just like the position of the whole upper lens support structure respect to the base, thanks to the two tooling balls and toleranced hole/slot of the base.

To align a lens its base can be shimmed, and using multiple alignment blocks with shims precise translations and rotations can be performed. Once the optical system is aligned, the blocks and clamps can be secured (tightening bolts, using epoxy) on the optical table. Removing the upper aluminum support the sensitive optics can be packed and shipped separately from the heavy optical bench, without compromising the time-consuming on-site alignment.

Lens retainer rings and covers made out of delrin can be mounted off the bezel, to prevent the lens falling out of the mount in the unlikely case of RTV failure and to protect form dust. The retainers can be served as baffle elements, too, as shown for L1 and L2 (see Fig. 2.39). To save design and manufacturing expenses, the base and aluminum structure was the same for L1 and L2, and a larger version was shared between L3/4/5 and L6. The sides of the aluminum supporting angles were used to mount the fiber holder (for L1a) and to support the exposure meter pickoff mirror (for L6, as shown in Fig. 2.38), hold by a Newport U50-PL1 adjustable mirror mount.

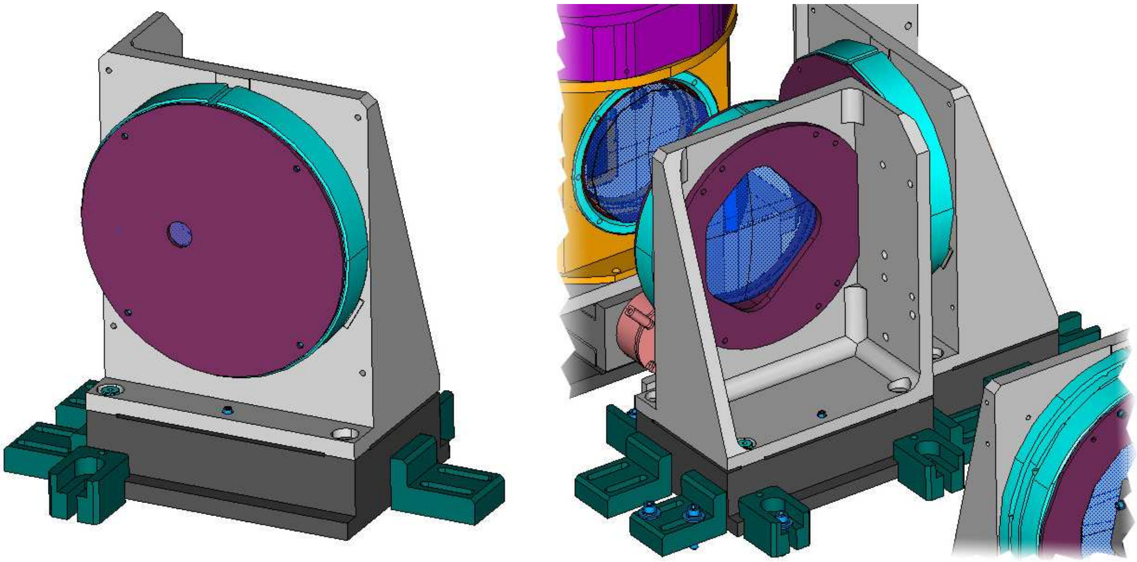

Figure 2.39: ***Baffles of L1*** *(left)* ***and L2*** *(right).*

Mounting the Triplet

To form the triplet the lens elements have to be connected and hold firmly respect to each other. To aid radial alignment the outer diameter (OD) of triplet element bezels are highly toleranced and have the same size. The axial positioning is given by 3–3 elevated pads and precision spacers between the faces (see Fig. 2.40). The bezel of L4 has 6 of these pads, three on each side 120°apart, while the same pattern on the other side is rotated by 60°. Bolts connect the bezels at the pads, and the radial alignment is purely restrained by the friction over the pad surface area. An outer barrel is not used, since this degree of freedom accommodates possible corrections of lens bonding errors (decentered optics respect to bezel). Also, the bolts connecting the bezels provide sufficient clamping force to hold the relative lens positions within tolerance limits, under the self weight of the assembly. Support of the assembled triplet (Fig. 2.41) is very similar to that already shown for singlet elements.

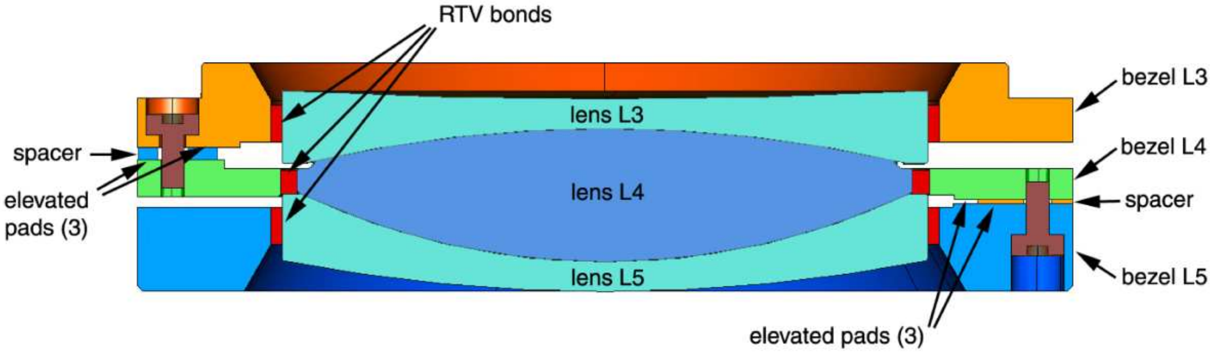

Figure 2.40: ***Cross sectional view of the bonded triplet*.**

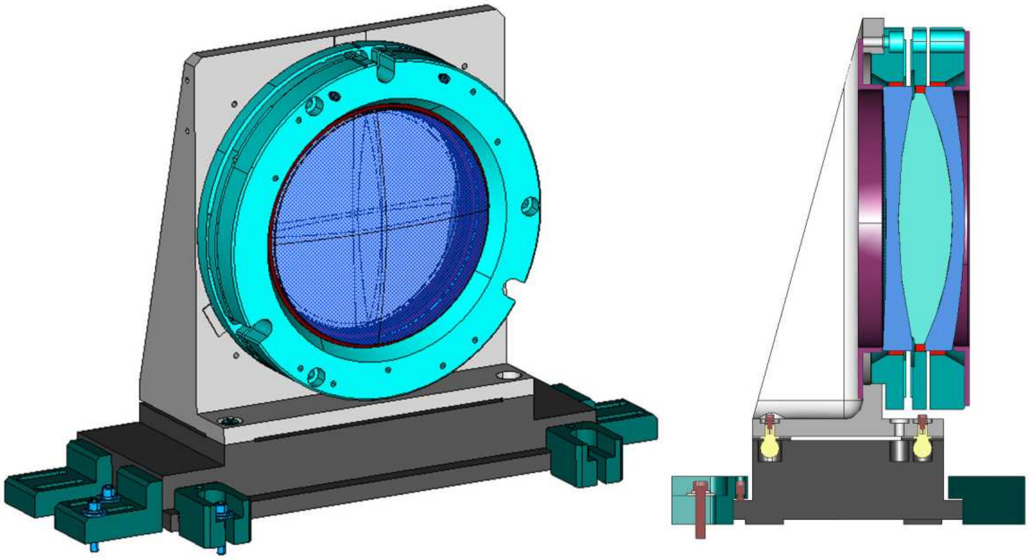

Figure 2.41: ***Isometric and cross-sectional view of the triplet mount*.**

A few optical coupling option was considered for TRES. The index matching Cargille LL5610 laser liquid, used for coupling and athermalizing the Binospec[6] optics (Epps & Fabricant, 2002), was rejected since tests showed it would interact with the RTV and change its index of refraction over time. However, liquid coupling would could been easy to apply without bubbles trapped in the gaps between lenses, but additional sealings would have be required inbetween the bezels. The remaining options (different optical gels and greases) did not require any additional elements in the triplet assembly design.

2.4.2 Supporting the Dispersive Elements

Since both the prism and the grating is in parallel beam, they are relatively insensitive to misalignments. Both elements are very massive as well, so thermal induced stress is less of an issue here.

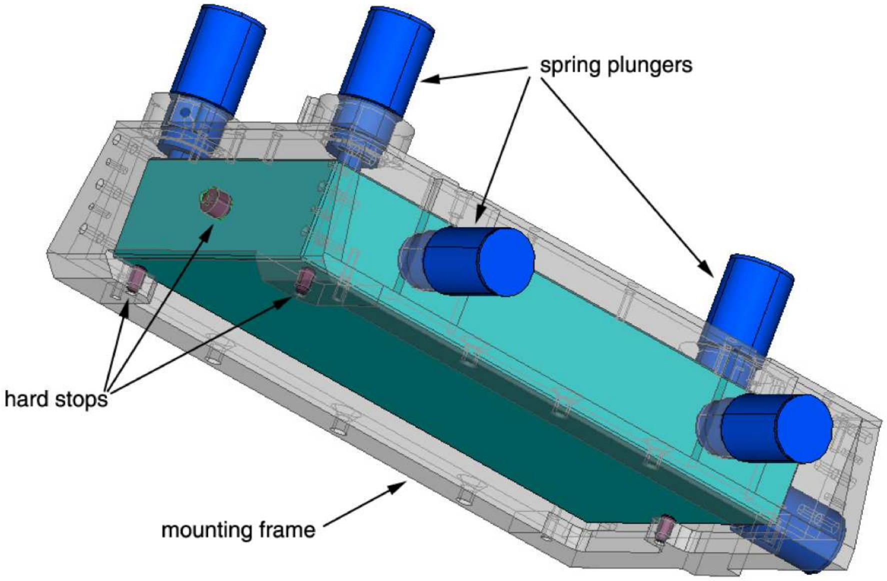

Figure 2.42: ***View of the grating support.***

Grating

The Richardson grating (catalog #53032) has a dimension 135 × 265 × 45 mm, and weighs approximately 4 kg. By holding the grating facing down dust accumulation on the surface can be avoided. Since the active area is 128 × 254 mm, the mounting hard points have to be small and positioned very near the edge to minimize obscuration of the beam. Since the footprint of the beam is elliptical, two of the corners along a short edge are obvious choice for the hard stops (Fig. 2.42). Slight decentering of the beam on the grating, also justified by the exposure meter chopping off the very edge of the beam, can minimize the obscuration of the third hard stop. Since the grating is facing down, this support does not cast any shadow on the active area if located on the lower edge of the grating, and the same way shadowing of upper hard stops can be avoided.

---

[6] http://cfa-www.harvard.edu/mmti/binospec.html

The grating is hold within an aluminum mounting frame, the analogue of lens bezels making handling easy and providing protection. To firmly support the glass substrate in the frame spring plungers are located on the opposite side of the three hard stops of the grating face. To fully constrain all the six degree of freedom three further hard stops and plungers are mounted on two sides.

The force applied by the plungers was determined so the grating can withstand a 3 g acceleration in any direction during shipping, without displacement. Therefore a force of 120 N is equally distributed among the three backside plungers (3×40 N), the two side supports (2×60 N), while the bottom plunger applies it by itself. To minimize the stress at the mounting points, the surface are of teflon the plungers and side hard stops are kept relatively large, however the face stops are small to avoid damaging the ruling. These teflon supports have 6 mm diameter so a surface area of 0.3 cm^2, therefore the induced stress is only 140 $N\ cm^2$, which is negligible for the glass grating substrate.

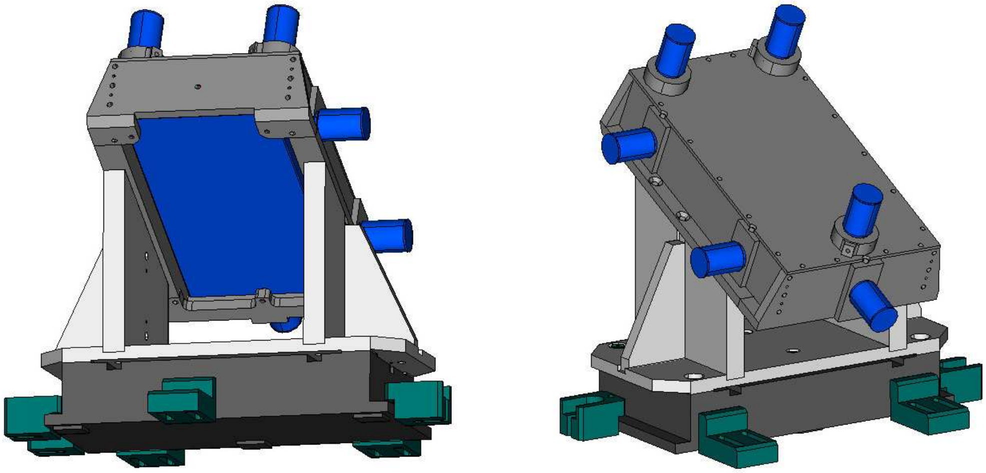

Figure 2.43: ***Isometric views of the grating mount***.

The aluminum support structure and steel base follows the same principle as for the lens mounts. Two tooling balls, one in a hole and one in a slot, insure the positional repeatability, while the steel base remains locked to the bench surface by blocks and clamps (Fig. 2.43)

Cross-disperser

Unlike the grating the prism was meant to be shipped unmounted, so a support structure similar to that of the grating was designed to provide a 1 g constrain. There are only two spring plungers applied (see Fig. 2.44 and 2.45). One provides vertical load at the CG point against three teflon hard stops placed near the corners of the triangular base of the prism. The side plunger is located at the bottom, so the three hard stops (two along one edge of the wedge, one at the other, located centrally) can be evenly distributed and still out of the optical beam. Tooling balls are also used, to retain the orientation of the prism if the aluminum frame and the optics is removed during optical alignment/assembly.

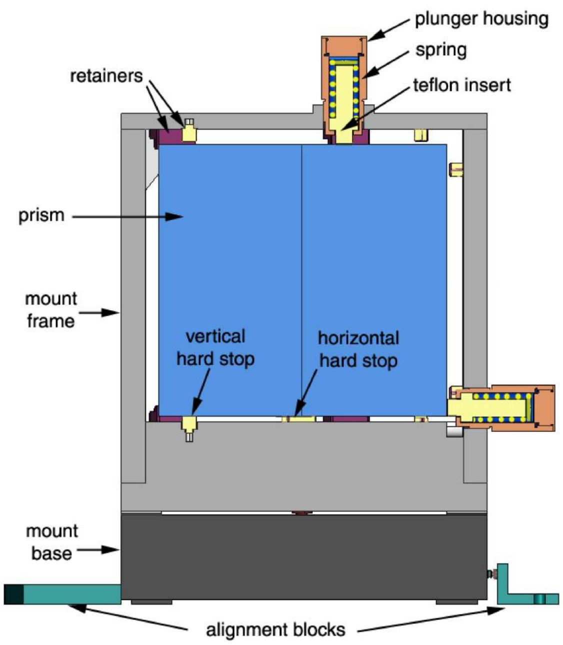
plunger housing
spring
teflon insert
retainers
prism
mount frame
vertical hard stop
horizontal hard stop
mount base
alignment blocks

Figure 2.44: ***Cross sectional view of the prism support.***

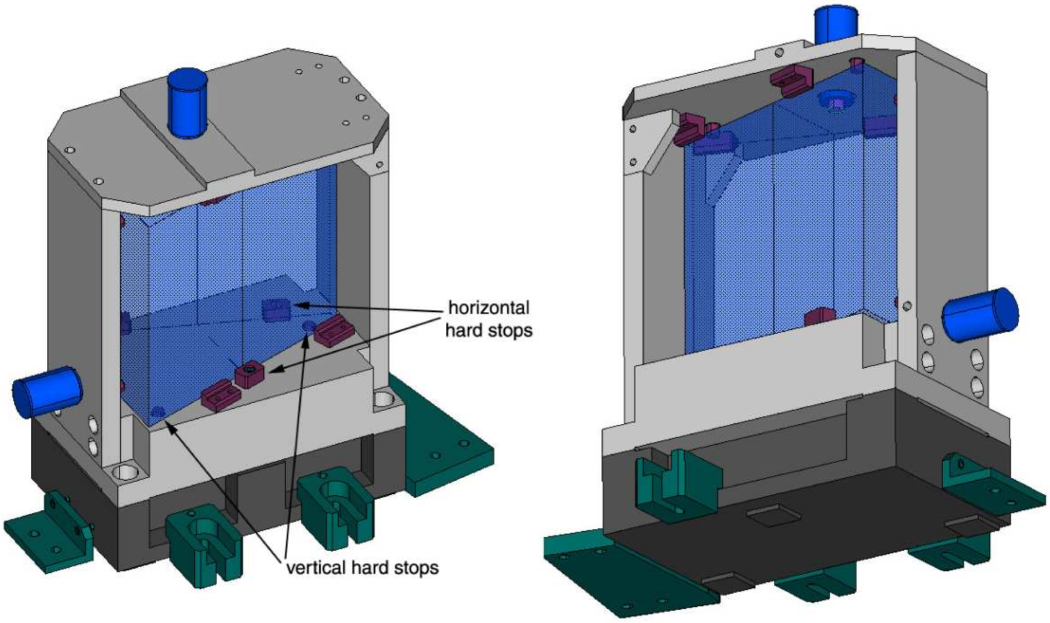
horizontal hard stops
vertical hard stops

Figure 2.45: ***Isometric views of the prism mount.***

2.4.3 Fiber Selector and Shutter

The fiber selector and shutter is mounted off the L1a lens support (Fig. 2.46(a), left). The Uniblitz 25.4 mm opening diameter shutter is attached to an arc shaped bracket, mounted off the L1a lens bezel.

The fiber assembly is hold by a a right angle bracket mounted off the side of the lens support.

The fiber holder can be rotated rotation around a vertical axis, a pin located below the nominal fiber position. The angle can be adjusted by shims placed between the side of the lens angle and the mount of the linear stage. A thin, springy steel plate connecting the two L-brackets of the fiber selector support enables rotation along a horizontal axis, adjusting the angle by shims placed between the L-brackets.

The fiber selector runs horizontally, which corresponds to cross-dispersion direction. As any stage has some finite position repeatability in such case it only can translate to small spatial displacement of spectral orders, but not affecting measured RV values. The Physik Instrumente (PI) M112.12S stage offers 25 mm travel with sub-micron unidirectional repeatability and up to 2 kg load capacity, well within the requirements as the smallest fiber diameter is 62.5 μm and a very small fiber holder can be manufactured.

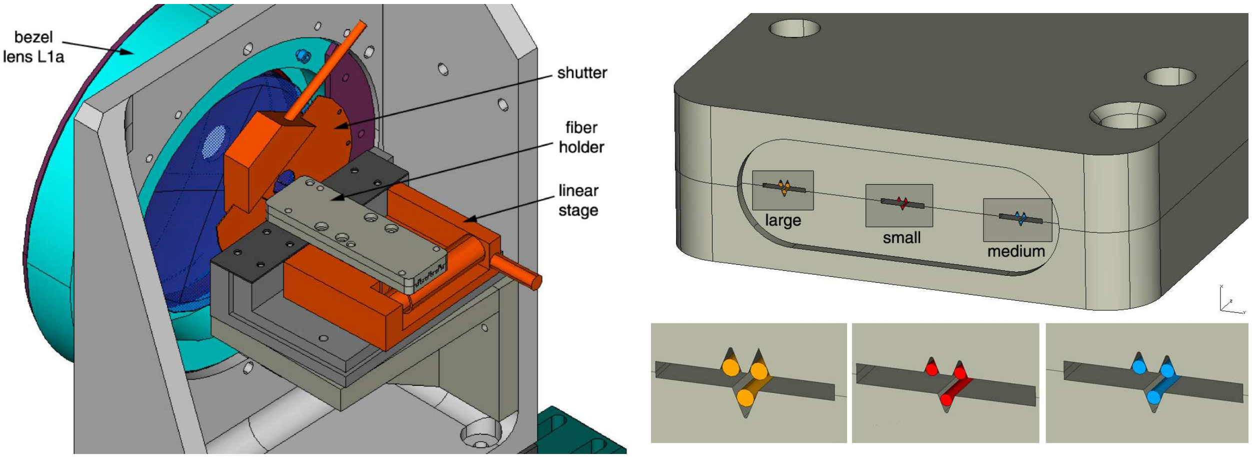

(a) The location of the fiber holder/selector on the support of lens L1 (b) The layout of the nine fibers within the fiber holder

Figure 2.46: *The bench fiber mount*

The arrangement of fiber ends within the fiber plates is shown on the right of Fig. 2.46(a). To maintain the desired 200 μm inter-order spacing (horizontal, respect to the optical bench), while the OD of the largest fiber is 190 μm, two separate plates were necessary. One is holding the object fiber (bottom) and the other holding the sky and simultaneous calibration fibers. Therefore the latter two is 200 μm off horizontally respect to the object fiber, and still conveniently mounted next to each other. Since the object fiber is some 400 μm below there is a same linear displacement (~30 pixels) for a given spectral feature between the object and sky or calibration spectra, in the dispersion direction.

One of the fiber plates is shown in Fig. 2.47. Based on the Hectochelle/Hectospec fiber mounting technique the bare fibers are seated in V-grooves, on a 5 cm length, to maintain parallelism between the light guides. The fibers are bonded in the grooves at three locations along this length. Since the second plate attaches on top with the other fibers very close, therefore the bond profile has to be very small, any excess epoxy has to be removed. To aid such removal and protect the fibers the V-grooves are slightly recessed into the surface, so the walls between grooves can support a flat, fine abrasive tool (e.g. fine sand paper attached to a gage block) to remove unwanted epoxy. There is an other recess in the plate, at the front, so when assembled the polished fiber ends are somewhat protected, can not be hit directly.

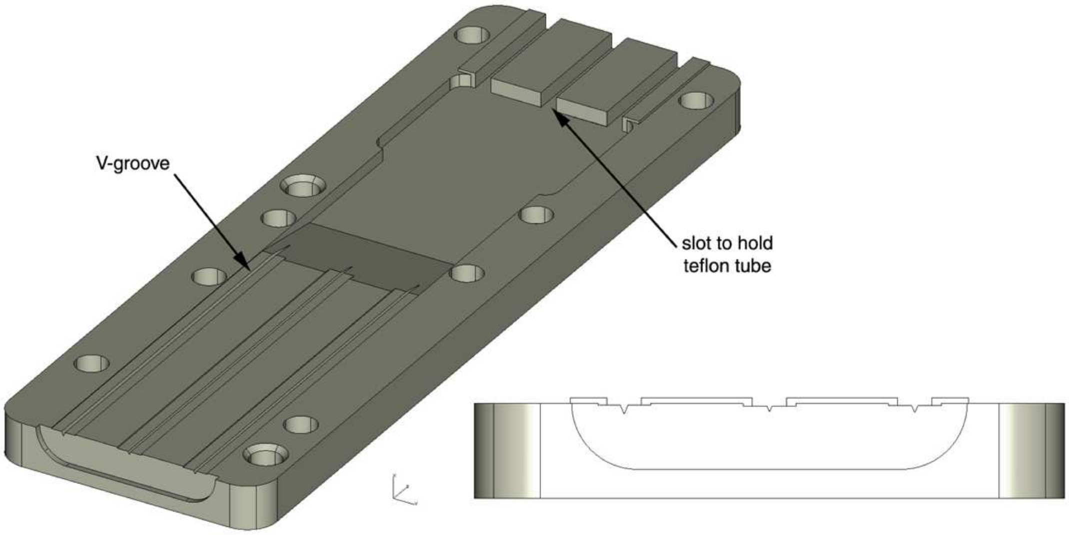

Figure 2.47: ***Open view of the fiber holder***, *showing the V-grooves the fibers are bonded into.*

The 25 mm travel of the selected PI stage leaves plenty room to conveniently space out the grooves. Behind the V shaped slots there is an opening, allowing stress-free routing of the fibers towards the protective shell of the fiber run, attached to the other end of the plate. This is small teflon tubing, pressed into the U-shaped slots. See more on the fiber protection and the fiber run in §2.9.4.

The plates are made out of invar, to have a good CTE match with the silica fibers. The two plates are registered via two pins located at the opposite corners (not shown), and bolted together.

2.4.4 Camera Design

As mentioned earlier the camera housing is aluminum, to match the CTE of lens bezels and mounts, while the lens bases are still due to the fact that the focus stage is made out of steel. Fig. 2.48 shows the main components of the TRES camera assembly, with the liquid nitrogen tank on the top.

Lens L1b serves as a vacuum window of the dewar, so there is a flat annulus along the perimeter of this lens which is seated on an O-ring seal (Fig. 2.49). The lens is still glued into a bezel with RTV, but this bezel only provides axial positioning besides protection in this case. The bolts only loosely connecting the lens bezel to the housing, to prevent the lens falling off if vacuum is lost, which otherwise makes the lens seating tight on its flat annulus.

The inner design consists of a cold plate hosting the two CCD detectors, a support ring and flexures mounting the cod plate off two inner shoulders, and a cold finger responsible to transfer the LN2 temperature to the cold plate by copper straps.

The support ring is connected to the inner shoulders at three locations, by a pair of bolts at each point, so the tip, tilt and piston of the focal plane can be adjusted. There are six thin, titanium flexures supporting the invar cold plate firmly in place, yet due to their small total cross-section heat conduction from the warm walls of the dewar is minimal. Therefore the finger, directly attached to the bottom of the LN2 tank can effectively cool the focal plane. The temperature can

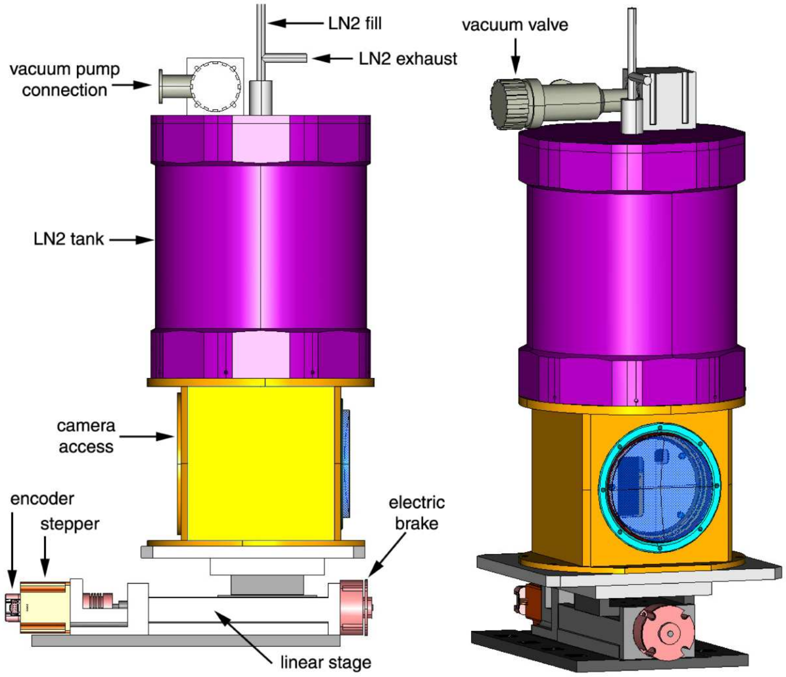
LN2 fill
LN2 exhaust
vacuum valve
vacuum pump connection
LN2 tank
camera access
encoder
stepper
electric brake
linear stage

Figure 2.48: ***The TRES CCD camera assembly***: *focus stage, camera head and* LN_2 *tank*

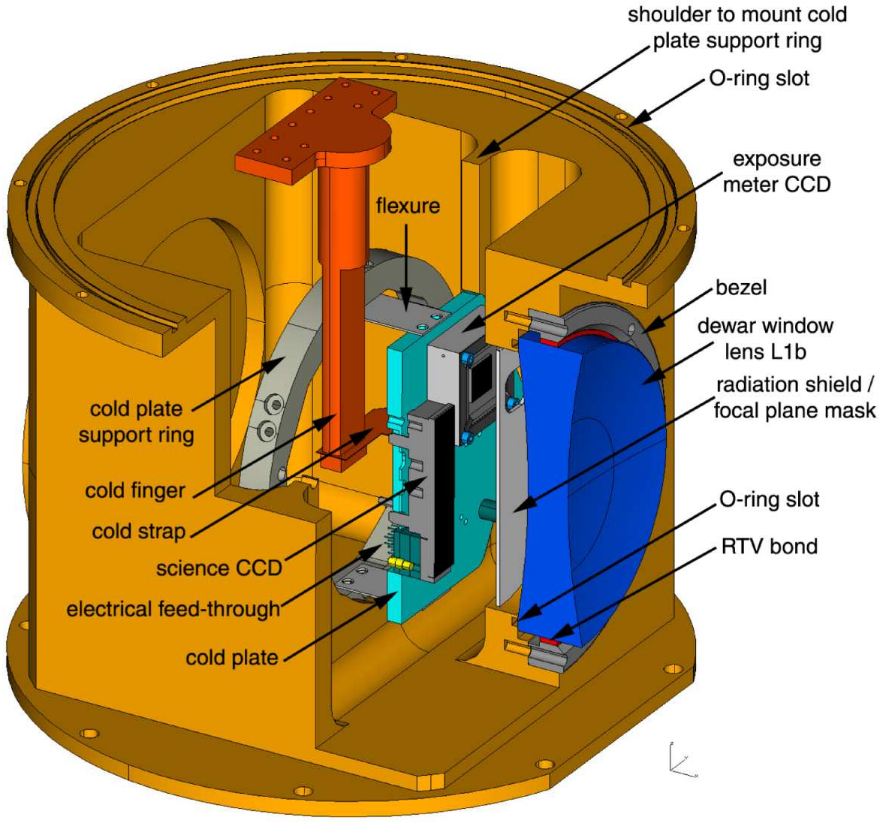
shoulder to mount cold plate support ring
O-ring slot
exposure meter CCD
flexure
bezel
dewar window lens L1b
radiation shield / focal plane mask
cold plate support ring
cold finger
cold strap
science CCD
electrical feed-through
cold plate
O-ring slot
RTV bond

Figure 2.49: ***Open view of the CCD camera head***, *showing the details of CCD and lens L1b support*

be adjusted by the number (total cross-section) of cold straps, and regulated by a heater resistor mounted on the back of the cold plate.

The CCD electrical connections pass through the plate and run to a vacuum feedthrough located on the side of the housing (not shown). There is an access door in the back (opposite side of the lens) to aid installation of the various components. The science CCD has its own invar base, while the also invar holder of the exposure meter chip had to be custom designed. The alignment of the two (parallel, confocal) is not critical, since the exposure meter does not have to record an image, just measure light levels.

The focus stage and driver is chosen to provide sufficient resolution and enough torque to drive the entire assembly. A LIN Engineering stepper motor 5704M-03D-02 was accepted as standard, since it fulfills the requirements of other motion applications of TRES. The 800 steps/revolution provides 6 μm resolution with the 10 mm pitch ball-screw driven THK linear stage SKR46-5-A. One step of the stepper (5 μm motion) corresponds to 1 μm opening of the f/6 beam, which is well below the 13.5 μm pixel size and the average RMS spot diameter. Unfortunately by mistake the 10 mm pitch stage was ordered, but even that provides adequate resolution for focusing.

2.5 Front End Mechanical Design

The so-called front end of TRES is responsible for feeding starlight into the fibers, provide guiding and calibration. The most demanding requirement is the sufficient stiffness of mounting frame, so the relative position of the fiber end and guider can remain the same independently of telescope orientation. An other requirement to pack all necessary assemblies within a footprint provided by the mounting plate of the telescope.

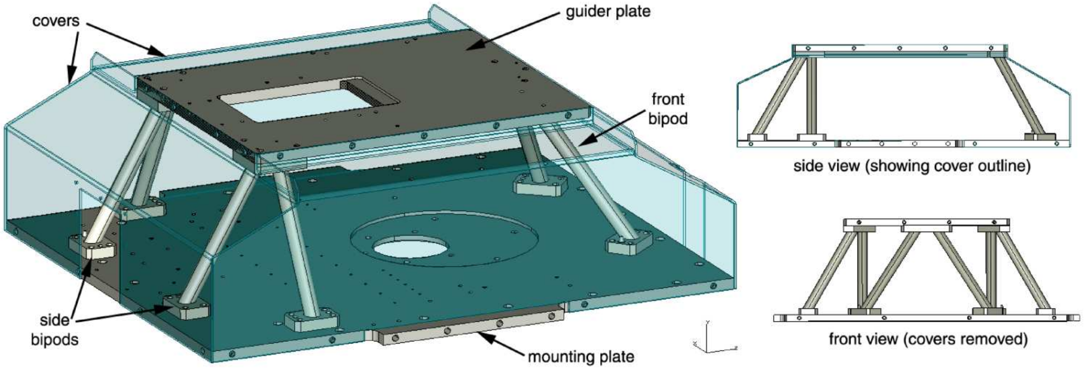
covers
guider plate
front bipod
side bipods
mounting plate
side view (showing cover outline)
front view (covers removed)

Figure 2.50: ***The TRES front end structure*.**

2.5.1 Mounting Frame

Basic Layout

Fig. 2.50 shows the front end structure, consisting of two steel mounting plates and three solid steel bipods connecting them. The larger (instrument) mounting plate bolts directly to the telescope interface, and holds all major front end components (see Fig. 2.51). The smaller (guider) plate supports the guider camera and optics, plus related electronics. Four covers provide dust and stray light protection, which can be quickly mounted/unmounted by quarter-turn fasteners. Two of the bipod bases are pinned, one mating a hole and the other one sitting in a slot, so when the two mounting plates are separated (i.e. for maintenance) and reassembled the guider position relative to the fibers does not change.

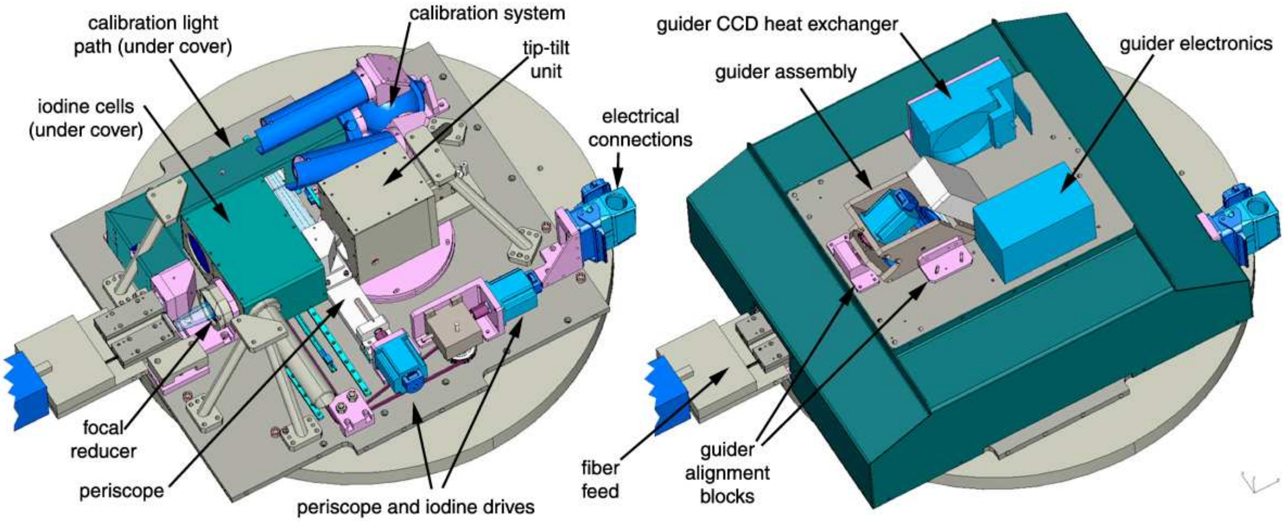
calibration light path (under cover)
calibration system
tip-tilt unit
iodine cells (under cover)
electrical connections
focal reducer
periscope
periscope and iodine drives
guider CCD heat exchanger
guider assembly
guider electronics
fiber feed
guider alignment blocks

Figure 2.51: ***Isometric view of fully assembled TRES front end0***

Finite Element Analysis

The bolt pattern mounting the front end to the telescope is given by the interface. The remaining free parameters, sizing of the bipods, the number and layout of fasteners and the plate thickness were determined using FE modeling by Henry Bergner. For this analysis the requirement was to have the guider position remain within ±5 μm (¡10% of smallest fiber diameter) respect tot he fiber feed, over 1 hour of integration.

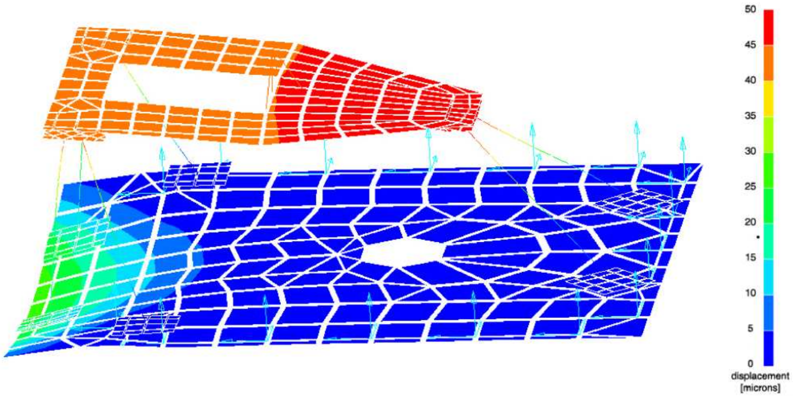
50
45
40
35
30
25
20
15
10
5
0
displacement [microns]

Figure 2.52: ***Finite element model of the TRES front end structure.***

As it turned out the main limitation was the constrain of the existing telescope bolt pattern, which did not provide adequate support of the total assembly (weighing ∼90 kg) around the fiber feed support. See the apparent deflection of the instrument mounting plate of the FE model on Fig. 2.52. Therefore additional mounting holes had to be drilled on the telescope, but doing so the FE results showed less than 3 μm deflection between guider and fiber feed, for the worst 1 hour of change in gravitational load during tracking.

2.5.2 Tip-Tilt System

Since the old telescope mechanics is not capable of very fine guiding, a tip-tilt mirror was proposed for TRES. A convenient realization of this is the insertion of a flat fold mirror into the light path. Therefore all other components can be mounted on a base plate running parallel to the primary, significantly decreasing the torque applied by the front end on the telescope structure.

The heart of the tip-tilt assembly is a PI S-340 piezoelectric stage, capable of ±1 mrad throw for mirrors up to 100 mm in diameter. To accommodated the ±3 arcmin FOV without vignetting TRES requires a 85 × 60 mm elliptical mirror at he specified location, which weighs only 120 g if made out of a 12.7 mm thick fused silica blank. The expected linear displacement on the focal plane is ±0.5 mm with a resolution of 5 μm, which is adequate for guiding.

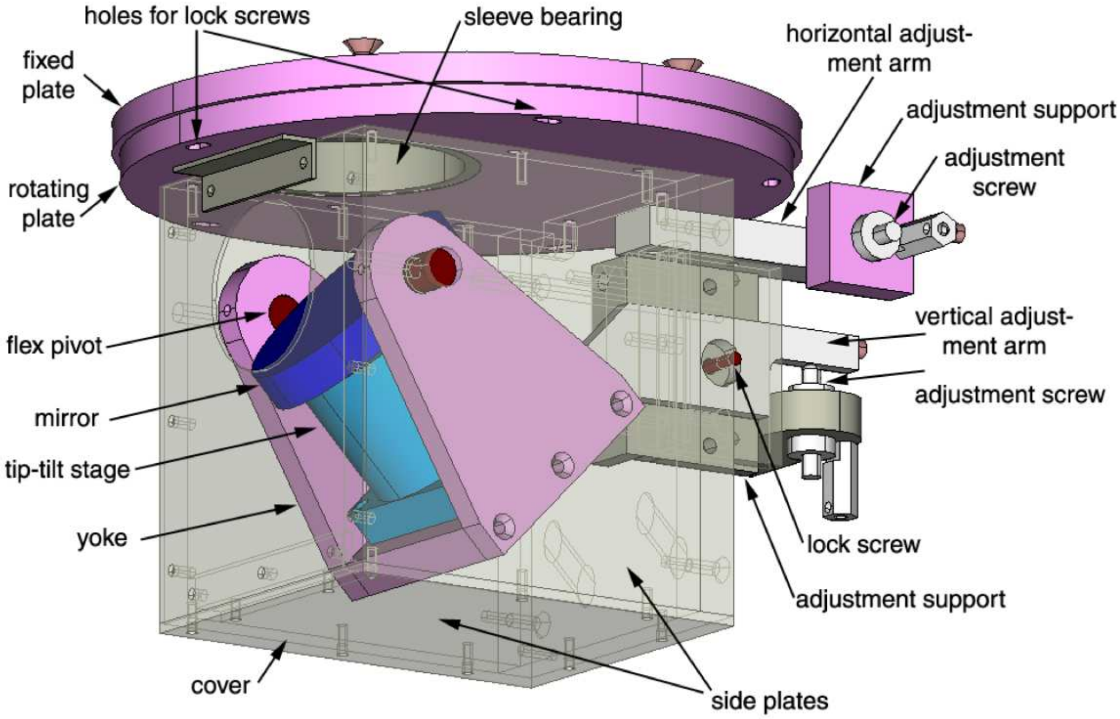
holes for lock screws
sleeve bearing
horizontal adjust-
ment arm
fixed
plate
adjustment support
adjustment
screw
rotating
plate
flex pivot
vertical adjust-
ment arm
adjustment screw
mirror
tip-tilt stage
yoke
lock screw
adjustment support
cover
side plates

Figure 2.53: ***The tip-tilt unit, responsible for guiding***.

The mirror is glued to the invar surface plate of the stage by epoxy, at three locations, with three invar spacers elevating the mirror by a few mm. The bond is only touching the outside of the spacers, along a small fraction of their perimeter, so with a narrow blade the epoxy joint can be removed and the mirror easily replaced if necessary.

The stage is mounted inside a yoke, which has two cylindrical flexure pivots, aligned with the plane of the mirror surface. The flexures attach the yoke to the side plates of the housing. An angled arm is also attached to the yoke, which gets through an opening on the back of the housing and so provides adjustment of the yoke by a spring-loaded, lockable, fine pitch adjustment screw.

Small amount of rotation is also allowed around the optical axis of the telescope, by a sleeve bearing. The entire housing is mounted to a polished rotating plate, which smoothly turns on the flat surface of a fixed plate, around a sleeve bearing shrink fitted to the stationary part. Screws can lock the position of the rotating plate, which has short slots in it allowing a small range of rotation. The fixed plate mounts into a circular recess, machined into the instrument mounting plate of the front end, by bolts accessible form the outside of the front end structure. These two adjustment allow to position the telescope beam on the fibers.

2.5.3 Focal Reducer

The focal reducer renders the nominal f/10 focal ratio of the telescope to f/6, in order to minimize focal ratio degradation in the fibers. The assembly is similar to the triplet mount, although smaller and simpler since the reductor is only a small doublet (Fig. 2.54).

The two lenses are RTV mounted into individual aluminum bezels, which can be connected together by bolts and a highly toleranced spacer to maintain the required gap between the mating surfaces. An optical coupler is filling the gap, to minimize reflection losses. The assembled bezels mount to a simple, right angle bracket, which can be shimmed if adjustment is needed.

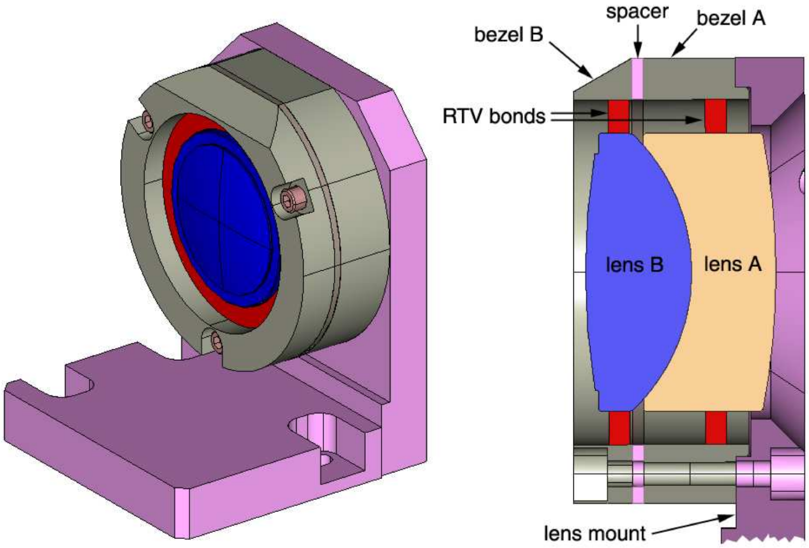

Figure 2.54: ***The f/6 focal reducer***.

2.5.4 Fiber Feed

The fibers at the front end are mounted in the same way as at the spectrograph end (see Fig. 2.47). Bare fibers are epoxy bonded into V-grooves, which are cut into invar plates. There is one plate holding the three science fibers, mounted face-to-face to an other block hosting the sky fibers. Since the image quality is not that different within the inner one arcminute radius of the field, these six fibers can be conveniently mounted in two rows with a generous spacing of up to 2.5 mm. A third, separate plate accommodates the three calibration fibers.

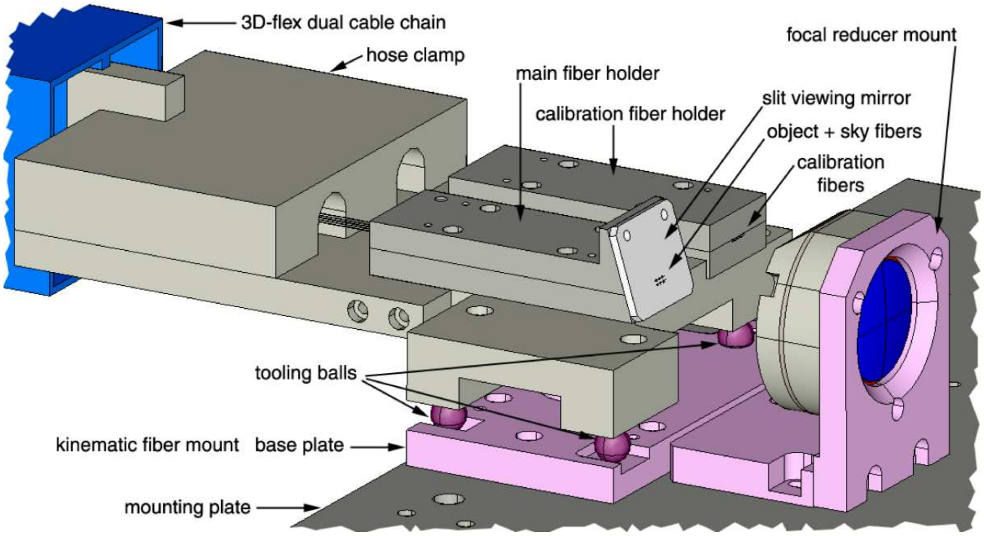

Figure 2.55: ***The kinematic fiber mount of the TRES front end.***

All fiber plates are mounted to an aluminum bridge, which has three legs, each ending in a steel tooling ball. These balls are seated on the base plate, one in a hole, one in a V-groove and one on a flat surface. This kinematic mount provides high positional repeatability, which is necessary as the fiber assembly is removed from the front end on a regular basis. The reason behind this is twofold. Since the fiber run is permanently attached to the telescope mount, the sensitive assembly is better protected in a sealed box also attached to the telescope while servicing or storing the front end. Another reason is the suggestion of the finite element analysis, which asked for bolts mounting the instrument plate to the telescope right around the footprint of the fiber assembly. The access to these bolts is easier and less concerning with the fibers removed from the front end.

The front of the fiber plates holding the sky and object fibers is tilted, and mounts a slit viewing mirror, reflecting the FOV of the telescope towards the guide camera. An tilt of 17°was necessary to project the beam above the focal reducer, without any vignetting. Since the focal ratio conversion optics is so close to the fibers (because all other optical elements have to be fitted inbetween the lenses and the tip tilt unit, see below), one of the lens bezels had to be chamfered as well.

The slit mirror is made of aluminum, and mounts onto the assembled fiber plates by two bolts. The positioning is aided by a tightly toleranced nose on the fiber plates, sitting into a pocket machined into the slit mirror (see Fig. 2.56). The bottom of this pocket is very thin, and the openings for the fibers are countersinked from the inside. Therefore the fiber ends almost can get

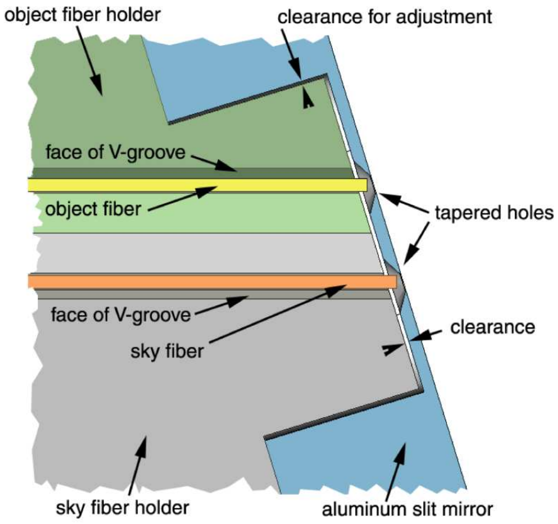

Figure 2.56: ***Cross section of the fiber mount and slit mirror.***

out to the mirror surface, without the mirror touching the fibers and endangering the polished fiber ends. The “slits” are drilled with a CNC machine, using a 0.4 mm drillbit. After machining the slit mirror was polished by hand.

2.5.5 Calibration Unit

The calibration unit has to main assemblies, one is the light sources and the other is the projection optics, including a periscope stage.

Integrating Sphere

A 10 cm diameter Labsphere integrating sphere (4P-GPS-040-SF) is used to provide even illumination to all fibers at once, and to eliminate moving parts otherwise needed to change illumination source. One of the four openings hosts a Uniblitz shutter, one an incandescent lamp (Gilway L518, MR11), and there are two ThAr bulbs (Photron P858A, Pyrex). The single flat lamp is easily accessible by removing one side cover of the front end, so replacing it is very easy, even during observing. See Fig. 2.57.

The arc lamps are harder to reach in the fully assembled front end, but being on two separate power supplies if one burns out observing can still continue with the remaining calibration source. The ThAr lamps are folded by a prism, to keep the front end structure compact.

Periscope assembly

The task of the periscope assembly is to block starlight from the telescope while projecting calibration light into the sky and object fibers, and at the same time block the light path of the calibration fibers. This is achieved by a linear stage (Fig. 2.58), sliding on low profile THK linear bearings and moved by the standard TRES 800 step/rev stepper, via an acme screw.

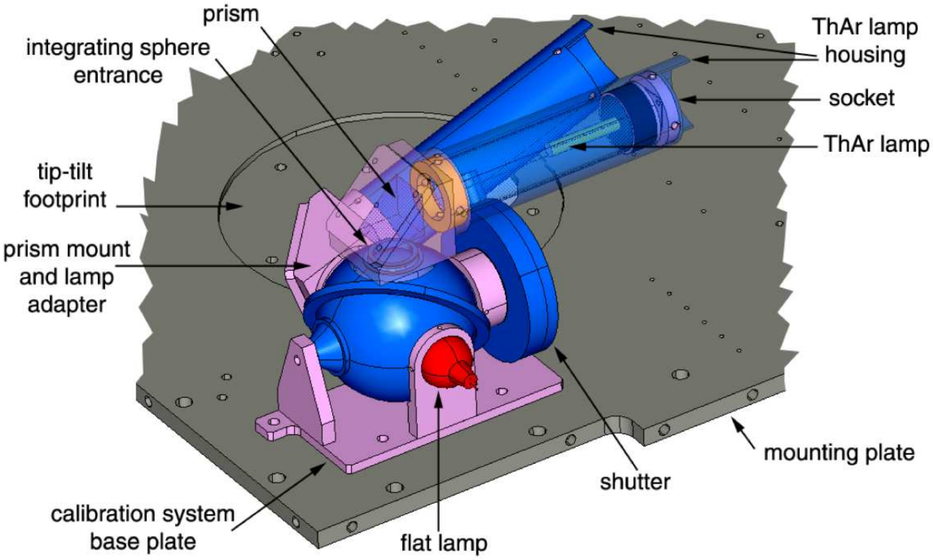
prism
integrating sphere entrance
tip-tilt footprint
prism mount and lamp adapter
calibration system base plate
flat lamp
shutter
mounting plate
ThAr lamp housing
socket
ThAr lamp

Figure 2.57: ***The calibration system*.**

The total travel required is 75 mm, which should be completed in less than 5 seconds. Therefore a speed of 15 mm per second is required. The stepper provides 0.10 Nm torque at speeds of 10 revolution per second, for what a 1.5 mm pitch acme screw would provide the specified speed. For such thread density and 10 mm diameter, the torque required to vertically raise the approx. 1 kg weight of the periscope assembly is 0.01 Nm. This is well within the capability of the stepper. And since the specified acme screw provides a self locking drive, no brake is required.

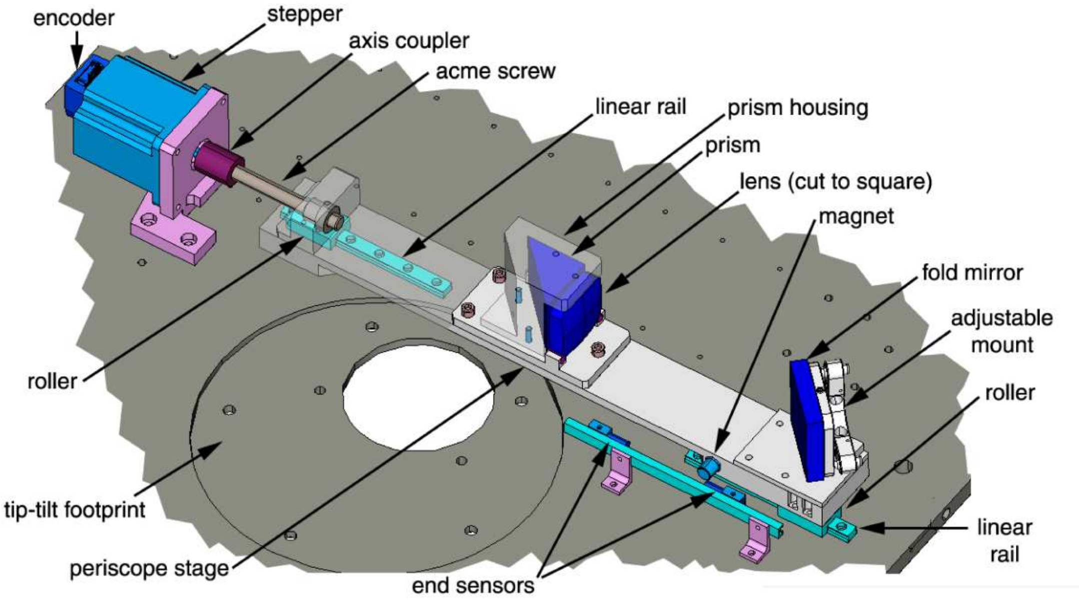
encoder
stepper
axis coupler
acme screw
linear rail
prism housing
prism
lens (cut to square)
magnet
fold mirror
adjustable mount
roller
linear rail
roller
tip-tilt footprint
periscope stage
end sensors

Figure 2.58: ***The periscope assembly*.**

End positions are set by Hall sensors, and the light is folded by a flat mirror (50 × 50 × 10 mm, Edmund optics NT45-336) and a right angle prism (40 × 40, Edmund Optics NT32-531). Former is supported by an adjustable mount (Newport P100A-P2-H), while the prism has a fixed position. There is also a lens in front of the prism, which is cut to square cross section in order to fit into the narrow profile of the periscope.

Secondary Light Path

Fig. 2.59 shows the two positions of the periscope: on the left starlight is blocked and calibration light falls on the object and sky fibers. On the right light passes through the stationary optical elements of the simultaneous ThAr light path, including a fold mirror (same optics and holder as for periscope), a prism (like periscope), and two lenses (one in front of the prism). There is a cover, not shown on these pictures, to avoid cross-talk between the object and calibration light paths.

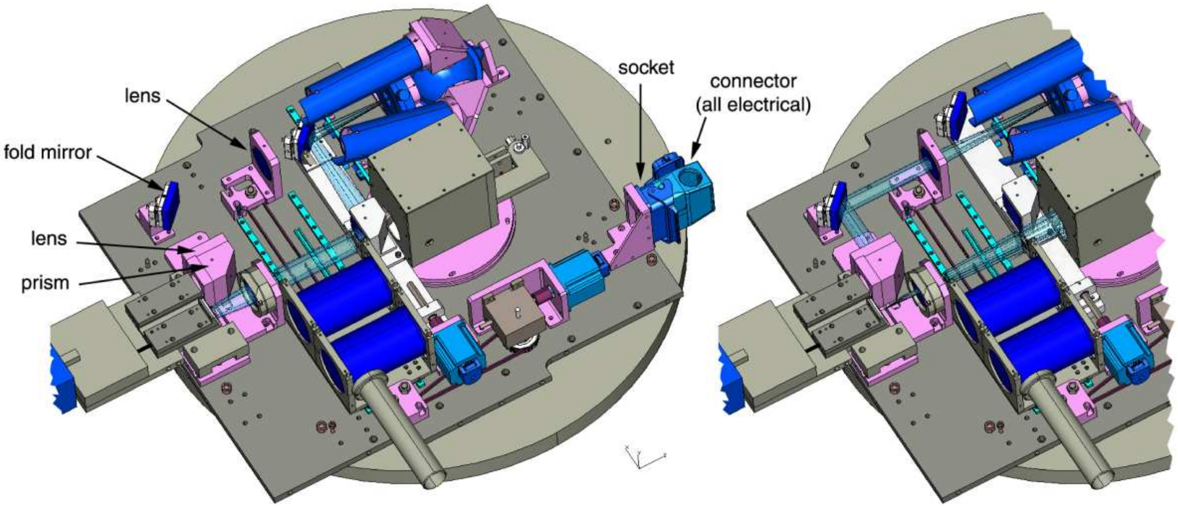

Figure 2.59: ***Selection between calibration and object light.***

2.5.6 Iodine Stage

The iodine cells are 75 mm in diameter and 125 mm long, made of fused silica and manufactured by Triad Technology, Inc. There is one empty and one filled cell, mounted next to each other. There are three positions required, one is without any cell in the light path, one with the empty and one with the filled cell on axis (see Fig. 2.60). As the real I_2 cell has to be heated, the two cells are covered and form an enclosed unit, however this cover is not shown in the figure in order to expose the two cells. To maintain internal seeing the warm air is sucked out by a fan through a ventilation tube, mounted on the side of the iodine unit.

Space is very limited within the front end, as it can be seen in the above figure. Also, the beam has to pass very close to the mounting plate (to have enough length to accommodated the periscope, iodine and focal reducer), while the iodine assembly has to me mounted off the main front end plate. Therefore the iodine drive mechanism should have a very low profile and at a

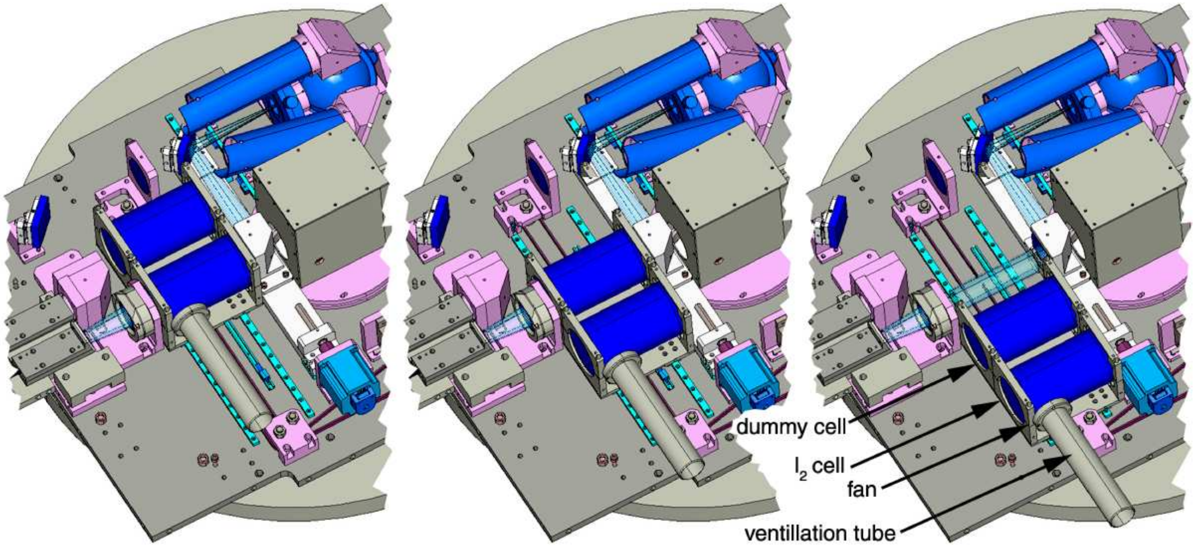
dummy cell
I_2 cell
fan
ventillation tube

Figure 2.60: ***Three positions of the iodine cell***

somewhat "remote" location. These circumstances lead to a belt drive system, shown in Fig. 2.61. The cells and cell mounts are removed from this picture, also the cell mounting base plate is made transparent to provide a better view of the components.

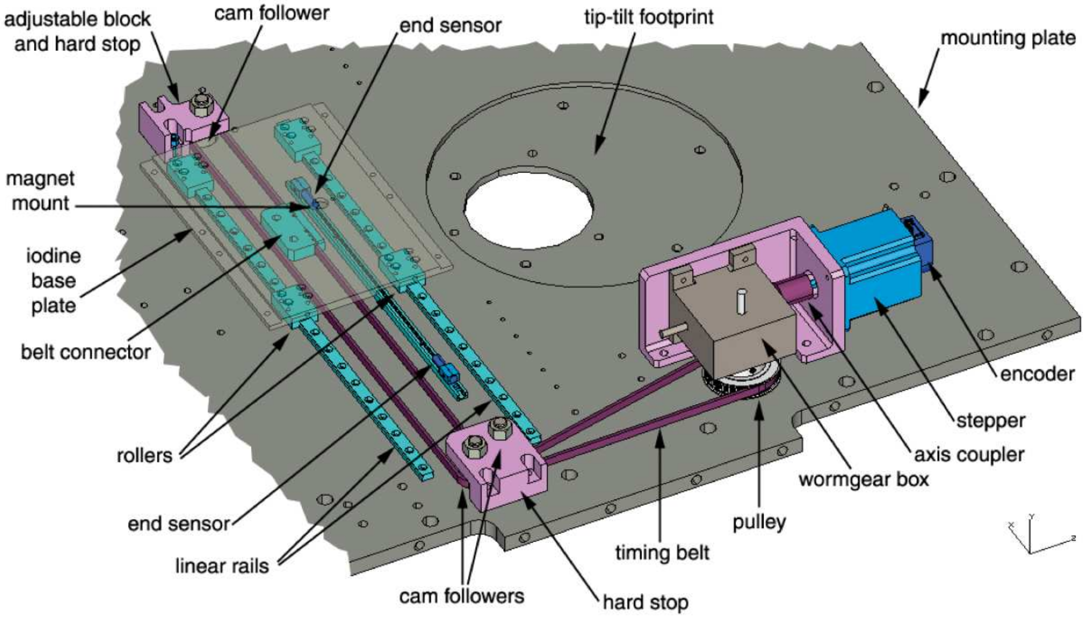
adjustable block
and hard stop
cam follower
end sensor
tip-tilt footprint
mounting plate
magnet
mount
iodine
base
plate
belt connector
rollers
end sensor
linear rails
cam followers
hard stop
timing belt
pulley
wormgear box
axis coupler
stepper
encoder

Figure 2.61: ***The iodine cell drive mechanism***.

The base plate is attached to four sliders of two linear bearings. A block on its bottom firmly holds the two ends of a timing belt, which is lead along an L-pattern set by 3 CAM followers. The belt is driven by a pulley, which is attached to the stepper via a 1:20 reduction worm gear system. Such drive ratio makes any break unnecessary, as the ~ 2 kg weight of the iodine assembly can not possibly back-drive the worm gear box.

The required travel is 180 mm, under 10 seconds. Using a 40 mm diameter pulley it is 1.5 turn on the gearbox axis, which means 30 turns of the stepper axis with the 1:20 gearbox ratio. From the time requirement the stepper should run at 3 rev per second, which provides 0.25 Nm on the stepper axis and 5.0 Nm at the pulley axis. Assuming a 5 kg weight for the iodine assembly it would put a 50 N load on the 0.02 m arm of the pulley, or 1 Nm torque. This is five times smaller than what the stepper can provide.

2.5.7 Guider

The guider assembly sits on the upper mounting plate (see Fig. 2.51). The Canon lens is clamped into the mounting frame, and focusing is achieved by a timing belt tightened around the rubber grip of the focus ring, driven by a pulley directly attached to the shaft of a stepper (Fig. 2.62). The guide camera is attached tot he back of the frame, by a simple plate and a cylinder to prevent stray light reaching the detector.

The entire assembly pivots around a tooling ball, seated in a cone-shaped opening cut into the central alignment block. Two L-shaped alignment brackets can be used to change and lock the orientation of the guider, by shimming and bolting the assembly to the small instrument plate.

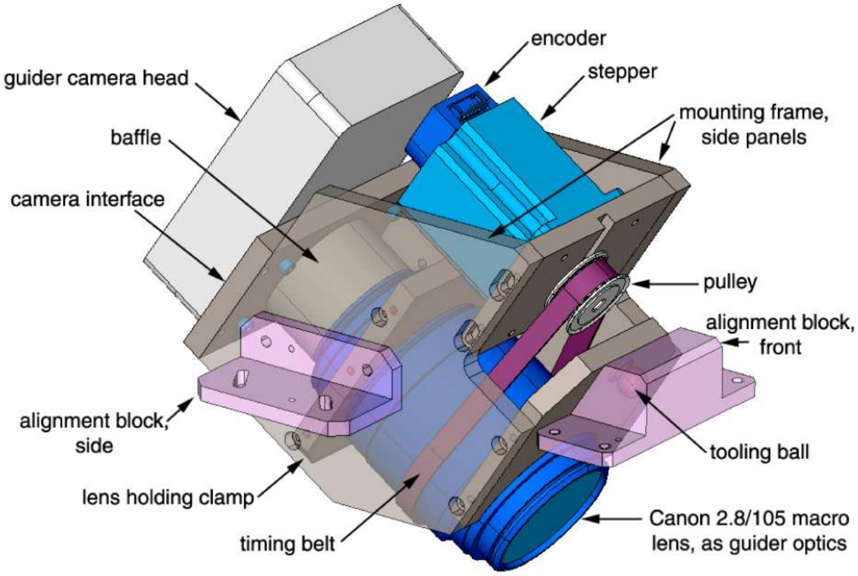
guider camera head
baffle
camera interface
encoder
stepper
mounting frame, side panels
pulley
alignment block, front
alignment block, side
tooling ball
lens holding clamp
timing belt
Canon 2.8/105 macro lens, as guider optics

Figure 2.62: ***The guider assembly***.

2.6 Electrical Design

The approach of the electrical design was to use commercially available components, and rather just assemble those than develop any electrical system, except the CCD cameras. The tip-tilt control was an other exception, although its development was outsourced to the Baker Research Inc.

2.6.1 Top Level

Fig. 2.63 shows the top level system diagram, the main components and the connections between them. Power supplies are colored light reddish; computers and other networking devices are purple; lilac means controller; yellow is for connector panels; and finally, green marks system components. The main power supply (Pulizzi IPC3402) has Ethernet control, so all units can be remotely powered on or off. There are two computers mounted in the rack, one is responsible for the guiding only (tres-guider) while the other takes care of all the rest: data acquisition, motion and illumination control, temperature monitoring (tres-bench).

The left block is all mounted within an electrical rack, while the upper right envelope designates spectrograph bench related components, and the lower outline is for the front end. For the physical locations of these refer to Fig. 2.64. By mounting most of the electronics in the rack the generated heat does not have any effect on the dome or the spectrograph room. This solution also decreases the weight of the front end and provides an easy, convenient access to most electrical parts.

2.6.2 Motion Control

The moving stages of TRES are: the spectrograph camera focus and fiber selector on the bench, and the periscope, iodine cell and guider focus in the front end. All of these have a stepper motor drive, built using the same components. The only exception is the fiber selector PI stage, which only shares the microcontroller with other motion systems, since the motor and sensors come integrated with the linear stage.

The required precision for the periscope and iodine stages is small, at an order of one 1 mm, since the clear aperture of the iodine cell is 5 mm larger than the beam and the calibration source provides the illumination of the entire FOV. (And for the periscope it is only the fixed distance of the mirror and prism, not the position of the stage, which sets the displacement of the beam.) The guider focus, similarly for the camera focus, asks for high angular resolution stepper motors, since former is a direct drive and for latter the lead of the ball screw is relatively large. An 800 step/revolution (0.°45 per step) fulfills the requirement of the spectrograph camera, as it was shown earlier. This angular resolution is increased by a factor of two for the guider, because the pulley has half the diameter of the focus ring on the lens. Based on test measurements such resolution is sufficient to focus the Canon lens.

Motors, Encoders, Sensors The stepper chosen is the LIN Engineering 5704M-03D-02 motor, which provides a very high holding torque of 1 Nm with a 3 A maximum current, in a compact ($57 \times 57 \times 70$ mm) package. Running at 3 rev s^{-1} the torque is still 0.25 Nm, and drops to 0.1 Nm at speeds of 10 rev s^{-1}.

Each stepper has an extended shaft to the back, in order to accommodated a US Digital E5D digital encoder. This unit provides a resolution of 5000 pulse/revolution, which is adequate to get feedback even if the steppers are run in microstepping mode. However, to avoid heat generation between moves, the current is removed from the steppers. Since the rotor tends to return into a full step position after the inhibit is removed, the resolution of the encoder is a factor of six higher than it is really needed.

For all stages a natural hard stop is provided, either by the linear railing or by other components mounted such way, that they prevent overruns (e.g. the cam follower blocks for the iodine cell,

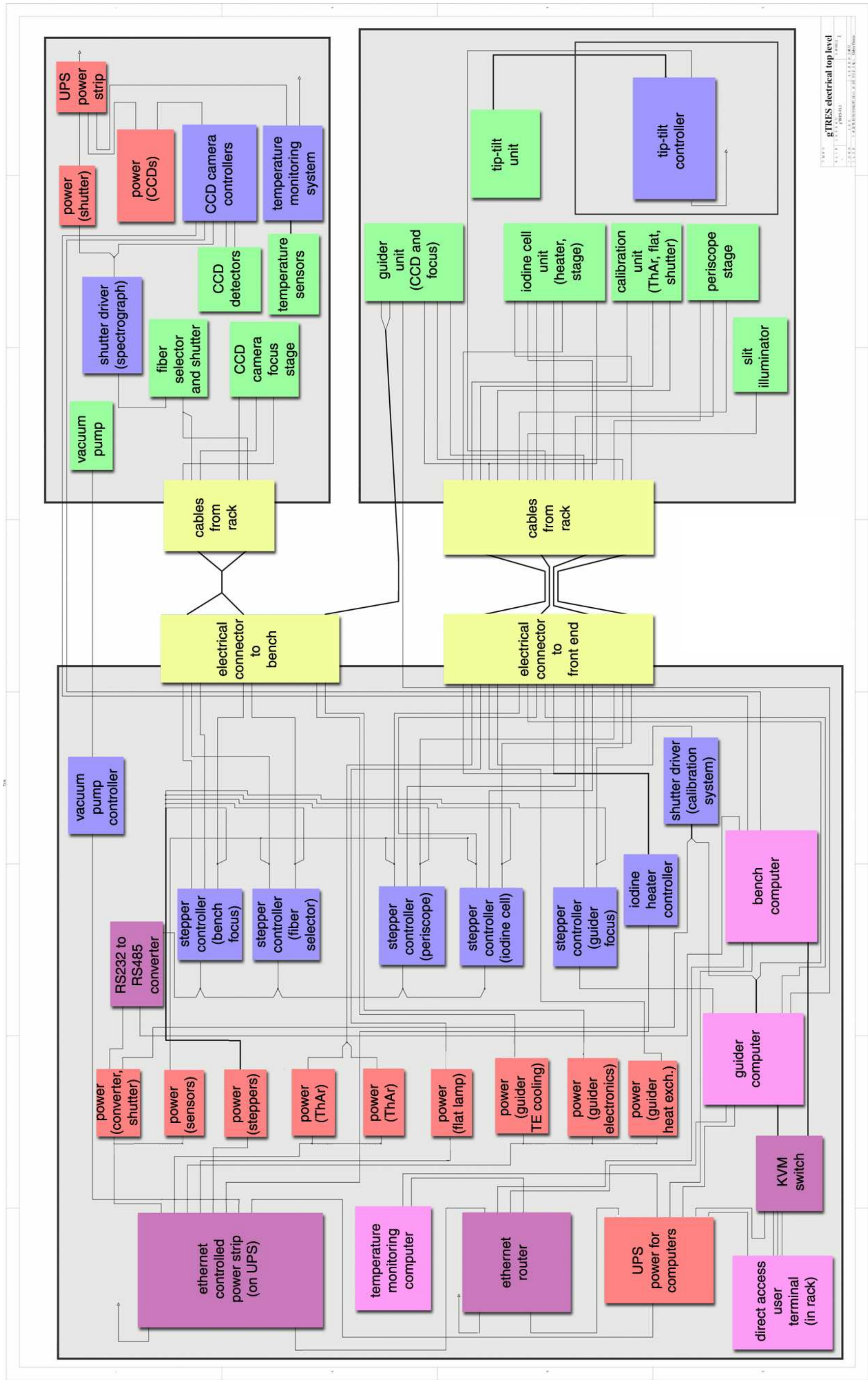
gTRES electrical top level
UPS power strip
power (shutter)
power (CCDs)
CCD camera controllers
temperature monitoring system
shutter driver (spectrograph)
CCD detectors
temperature sensors
fiber selector and shutter
CCD camera focus stage
vacuum pump
cables from rack
tip-tilt unit
tip-tilt controller
guider unit (CCD and focus)
iodine cell unit (heater, stage)
calibration unit (ThAr, flat, shutter)
periscope stage
slit illuminator
cables from rack
electrical connector to bench
electrical connector to front end
vacuum pump controller
shutter driver (calibration system)
RS232 to RS485 converter
stepper controller (bench focus)
stepper controller (fiber selector)
stepper controller (periscope)
stepper controller (iodine cell)
stepper controller (guider focus)
iodine heater controller
bench computer
power (converter, shutter)
power (sensors)
power (steppers)
power (ThAr)
power (ThAr)
power (flat lamp)
power (guider TE cooling)
power (guider electronics)
power (guider heat exch.)
guider computer
KVM switch
ethernet controlled power strip (on UPS)
temperature monitoring computer
ethernet router
UPS power for computers
direct access user terminal (in rack)

Figure 2.63: ***Electrical block diagram of TRES***.

see Fig. 2.61). The guider has a clutch built into the telephoto lens.

Relative positioning is done by counting the pulses sent to the stepper, and comparing it to the feedback from the encoders. To set an absolute positioning upon powering up the system, and to prevent hitting the hard stops, Hall-effect proximity sensors are used (Hamlin 59025-03). One of the end sensors is used as a homing device, to set the zeropoint.

For the guider focus there are no end sensors, since the photographic lens has a built-in clutch mechanism. The homing is performed by turning the focus barrel by 120% of its maximum travel, therefore reaching one of the extreme focus positions for sure. From there on only motor impulses are counted and checked against encoder signals.

Microcontrollers MicroLYNX motion controllers from Intelligent Motion Systems, Inc. are used to drive the stepper motors and handle encoder/sensor signals. The controllers are chained together to form an internal network with one controller designated to be master. Communication between this unit and the controller PC is established through serial port (RS232).

Tip-Tilt The power supply and open loop drive circuit for the tip-tilt stage was made by Peter Cone (Baker Research, Inc.). The PI unit was ordered without the built-in positional feedback sensors, because the guide star was meant to be used for closing the loop. Unfortunately the piezo stage turned out to have a high level of intrinsic hysteresis, therefore acquisition set-up and guide corrections are iterative steps.

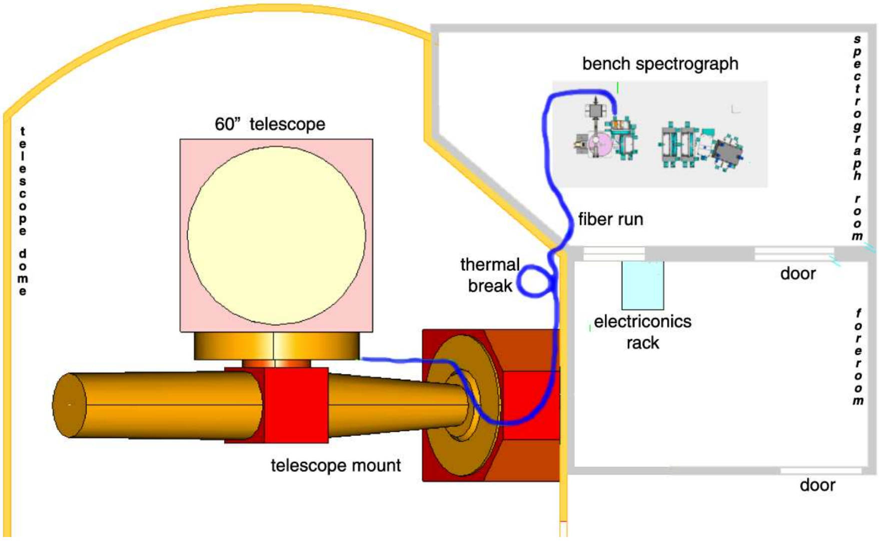

Figure 2.64: ***Location and connection of the TRES components*.**

Connections The floor plan of the 60 inch telescope can be seen on Fig. 2.64, with the telescope shown in zenith pointing. The electrical connections between the front end (on the bottom of the telescope) and rack (foreroom) run along the RA axis, together with the optical fibers. Where the light guides form a thermal break, the electric cables go through the wall and make their way directly to the rack. Cables and optical links going to the CCD camera and spectrograph join the fiber run again, right after the thermal break, and run to the bench components.

2.6.3 Illumination Control

Shutters There are two Uniblitz VS25 shutters, one in front of the fiber ends on the optical bench (Fig. 2.46) and the other attached to the integrating sphere (Fig. 2.57). Former is handled by the CCD controller, latter is commanded by TTL signal from the printer port of the bench PC. Both shutters had to be modified to eliminate the internal status feedback near-infrared LEDs. Drive circuits made by Uniblitz provide the opening and hold currents.

Lamps The ThAr lamps are powered by Acopian NX-25B small format, 185V DC supplies. Each lamp has its own power source to ensure that at least one can be used at a time. The output current is limited to 10 mA by resistors in order to maintain longer lifetime for the arc lamps.

The flat lamp is powered by a Sola 6V DC supply. It can be turned on and off by switching the AC power using the Pulizzi smart power strip, just like the arc lamps. Since the color temperature is only 2925 °K, a color correction filter would be necessary to balance the amount of light between the blue and red end of the images. This has been not implemented yet.

Guider Field Illumination There are three green LEDs mounted on the bezel of the focal reducer, facing towards the slit mirror. The role of these to illuminate the focal plane when fiber ends have to be located by the guider. The LEDs are powered using the current provided by the printer port of the guider computer, which means an easy way to control them.

2.6.4 Thermal Control

Iodine Cell The side of the TRES iodine cell is covered by a self- adhesive Minco heater tape, which is connected to a Minco CT16A2 controller. A single temperature sensor mounted on the glass cell is used to maintain temperature at a given setpoint (50 °C). This is the same setup as used in Hectochelle. To remove the excess heat from the front end the air around the cell is enclosed and a fan continuously dumps the warm air outside of the front end structure to preserve internal seeing.

Detectors The CCD temperature is measured at the cold plate, which also hosts a 20 W resistor to allow active control. This is done by using a Lakeshore 321 autotuning controller in closed loop, which reads temperature and adjusts output current for the resistor to maintain constant temperature at the ± 0.01 °Clevel. Vacuum is maintained inside the CCD housing by a Varian VacIon Plus 20 pump and a MidiVac 9295000 controller, at $\sim 5 \times 10^{-8}$ mbar, to minimize heat transfer between the internal and outer parts of the camera. The flexures designed to support the cold plate also minimize the heat conduction. The CCD is therefore kept at a constant -98.5 °C, practically eliminating dark current completely.

2.6.5 Environment

Figure 2.65 shows the TRES bench installed at FLWO. The optics is covered by a box, made out of 25 mm thick aluminum-foam-aluminum panels (0.5 mm thick aluminum sheet). This is the first layer of insulation. The second layer, made out of the same but 50 mm thick panels, surrounds the entire bench (two side panels are removed on the picture). Note that all electronics

(CCD boards, CCD temperature controller) are outside of this secondary enclosure, sitting on a small table attached to the side of the bench. (The purple cylinder is the LN2 tank.)

There are 16 temperature sensors deployed on the bench and within the room. Four sensors are mounted on the bottom, four on the top of the optical bench. Three among the upper sensors are outside of the 25 mm thick primary cover, and one sensor is located in the middle, between the triplet and L2. Four more sensors are hung in the air, inside the bench enclosure, and other four monitors the air in the spectrograph room, outside the bench covers. For the location of these probes refer to Fig 2.66(a) and 2.66(b).

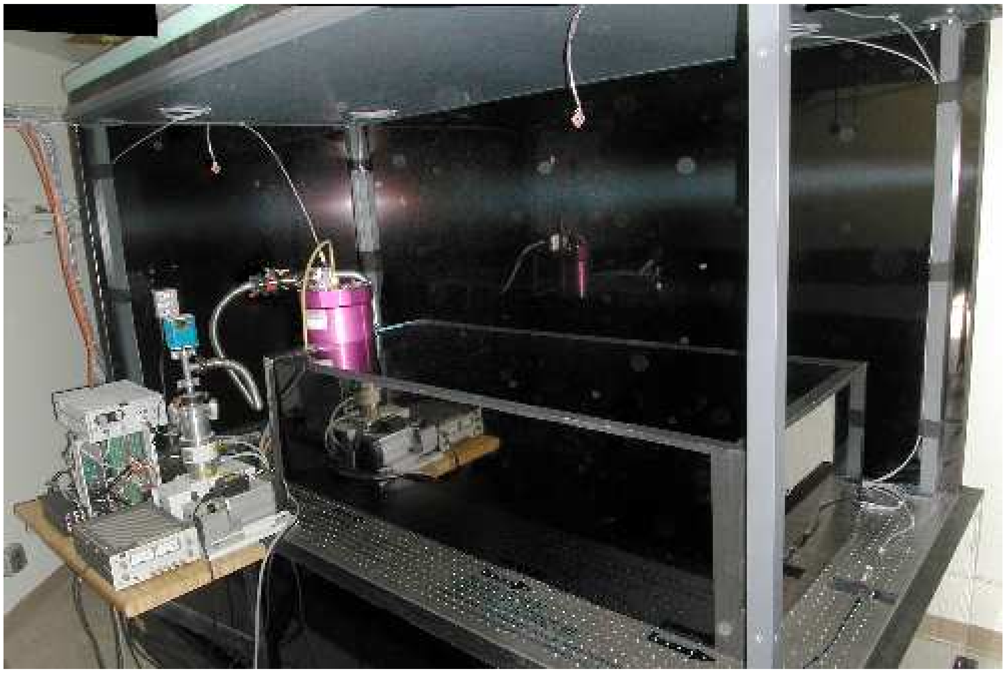

Figure 2.65: ***Thermal insulation of the optical bench****. The optics are covered with a one inch wall thickness black box (aluminum-foam-aluminum sandwich), while the same insulation material in two inch thickness is used to enclose the entire optical bench. sandwich*

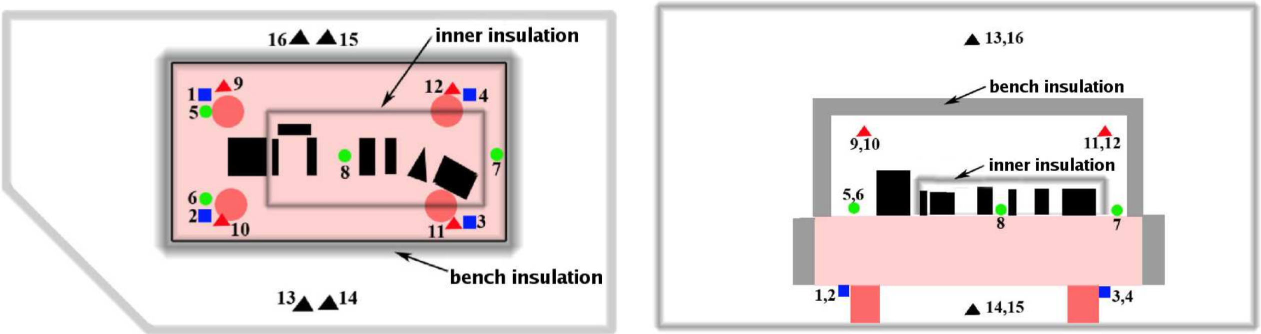
16
15
inner insulation
1
9
5
12
4
8
7
6
2
10
11
3
bench insulation
13
14
13,16
bench insulation
9,10
11,12
inner insulation
5,6
8
7
1,2
14,15
3,4

(a) top view (b) side view

Figure 2.66: ***Location of temperature sensors***

Sensors 1-12 are glued onto a small copper block, to increase the thermal mass and to make better surface connection when mounted on the bench. The larger thermal mass makes measured air temperature of sensor 9-12 smoother compared to sensor 13-16, which are just bare sensors hanging in the air. Although sensors 1-8 are mounted on copper blocks, there is no insulation above/around the sensors, so sudden air temperature changes might influence the data of these sensors.

In order to decide what kind of active control is needed to maintain constant spectrograph temperature (with the goal of ±0.05 °C stability), measurements of the uncontrolled environment were performed over two weeks in August 2007, after the bench was installed. As it can be seen from Fig. 2.67 there is a significant variation, both short term (daily, with an amplitude of ~ 1 °C) and long term (drifts at several °C level). This is very far from the desired stability.

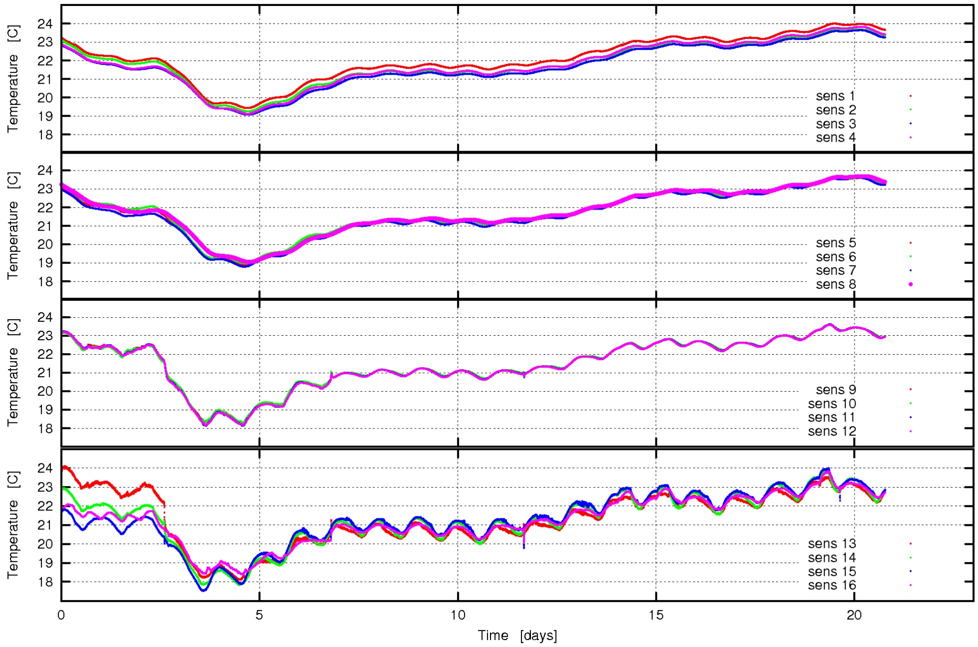

Figure 2.67: ***Temperature variations of the uncontrolled environment****. Daily variations are at the level of 1-2 °C, while longer trends are also apparent with several °C amplitude.*

The temperature regulation system went through a few stages of trial-and-error evolution. Several modifications (see Fig. 2.68) had to be done in order to improve the system, including:

- adding further insulation by building up a secondary room within the room. A wooden frame was fabricated and standard building insulation material "Reflectix" applied in two layers, with a 50 mm airgap between them. This material is made of a double-layer plastic bubble-wrap with aluminum foil on the outside of it, with a total thickness of ~6 mm.

- since dewar fillings significantly dropped the temperature inside the bench enclosure, additional insulation was applied on the LN2 fill and exhaust lines. (Up to 1 °C decrease was observed upon filling, even though the fill line was vacuum jacketed and the exhaust was insulated with 3/4 inch of foam. The temperature drop restored only after $10 - 12$ hours.)

The two pipes got enclosed within a manifold made out of Reflectix, the same material used to build the internal room. This manifold originates from a box on top of the LN2 tank, and the other end goes through the wall of the spectrograph room and has an opening into the foreroom. Two fans (one at each end of the manifold) extracts the cold air and dumps outside of the TRES room.

- the floor under the bench was insulated the same way as the room, and essentially the entire floor got covered with a double layer of Reflectix (same 50 mm airgap). The under-bench air volume was isolated from the room-air along the longer sides, by using a single layer of Reflectix. Six fans were installed in this "tunnel" under the bench to generate fast, laminar air flow. It was necessary because the aluminum honeycomb internal structure of the bench conducts heat very efficiently between the bottom and top face plates.
- an insulated "heating-tower" was built at the northern end of the room. Two intake fans (400 CFM) suck the room air into this tower at the top. The air follows a zig-zag pattern inside, with an 1400 W space heater at the first turn. An additional, internal fan aids the air to flow towards the bottom, where an other fan (also 400 CFM) blows the air right underneath the bench. A sensor is located just behind this fan, at the bottom of the tower. This provides feedback to an autotuning PID temperature controller, which turns the heater on and off. The regulated air passes under the bench, at which point it is distributed into the room by an additional fan.
- a 6 meter long heater tape is suspended in the air volume above the bench, within the bench enclosure. A sensor measures air temperature inside the enclosure, while a fan (400 CFM) circulates the air in a way that the just-warmed air hits the sensor. The fan only operates when the heater is on, so it is connected to the output of a second controller unit. (This is to avoid excess heat dumped into the air, generated by the fan.) The role of this secondary heater loop to prevent temperature drops due to LN2 fillings, as the passive insulation applied on the fill/exhaust lines does not eliminate the effect completely. This loop is only used for a few hours following dewar fills in the morning, after observations and calibrations are done.

The performance of the above described, final temperature regulation system is discussed in §2.10.4 (see Fig. 2.90 in comparison to Fig. 2.67).

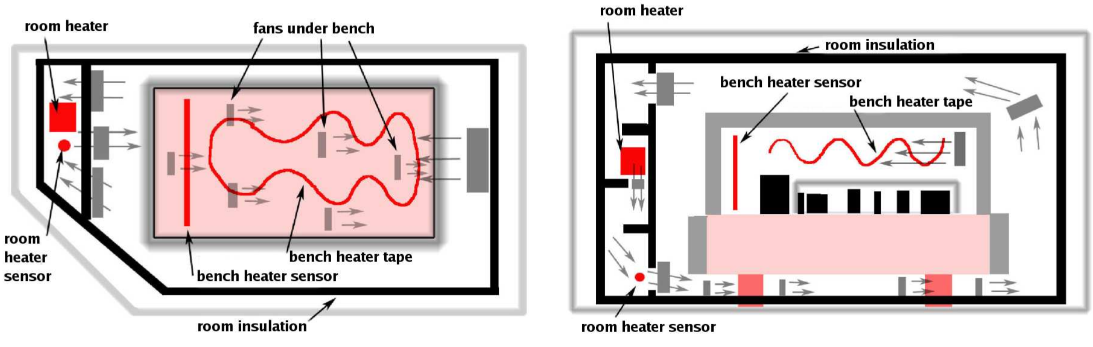

(a) top view (b) side view

Figure 2.68: ***Configuration of room heater components*** *Grey arrows indicate air flow direction.*

2.7 CCD Cameras

2.7.1 Scientific Camera

The science detector is an EEV 42-90, back illuminated, deep depletion CCD, with 4608×2048 pixel count and a pixel size of 13.5 μm. The device is 3-side buttable, however this feature is not utilized in TRES, however it was important in other CfA cameras (Hectochelle, Megacam), from where the entire detector system is adopted. The electronics was developed by John Geary and Steve Amato. Detailed description is given in Geary & Amato (1998), here I list only the main parameters: gain is 1.0 e^{-1}/ADU; read out noise is 4 ADU; readout speed is 10 μs pixel^{-1} which results in a total readout time of 50 s, using 2 channels.

The detector received from EEV showed a surface defect at one corner, which seemed to be very severe and extended (Fig. 2.69). According to the manufacturer and this kind of thickness variation left behind from the chemical etching (thinning) does not degrade performance. Indeed, subsequent tests verified this as only very negligible effects (less than 0.5%) was noticeable on high intensity flat field frames. Other than this the device has no pixel or other extended defects, and so has a perfect cosmetic grade.

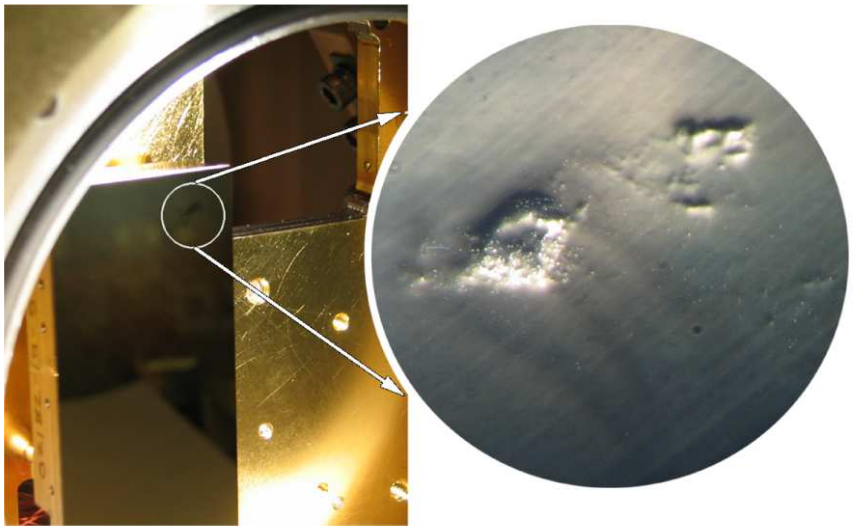

Figure 2.69: ***Surface defect of the science detector***. *The darker are at the upper right corner of the chip (left) is enlarged on the right, as seen through a microscope.*

2.7.2 Exposure Meter

The exposure meter CCD is a STA 0510B device, with 1200×800, 15 μm pixels. The electronics was designed and built by John Geary and Steve Amato. The detector is not used to read an actual image, rather it collapses all rows into a single line. This string of numbers is internally processed to determine and remove any background respect to the peak intensity corresponding to the white-light image of the fiber input. As an end result of this on-board processing a single number is sent to the bench computer through serial communication (RS232).

The location of the exposure meter respect to the science detector and the fold mirror is shown on Fig. 2.70. For the optical layout of the exposure meter light path refer to Fig. 2.26.

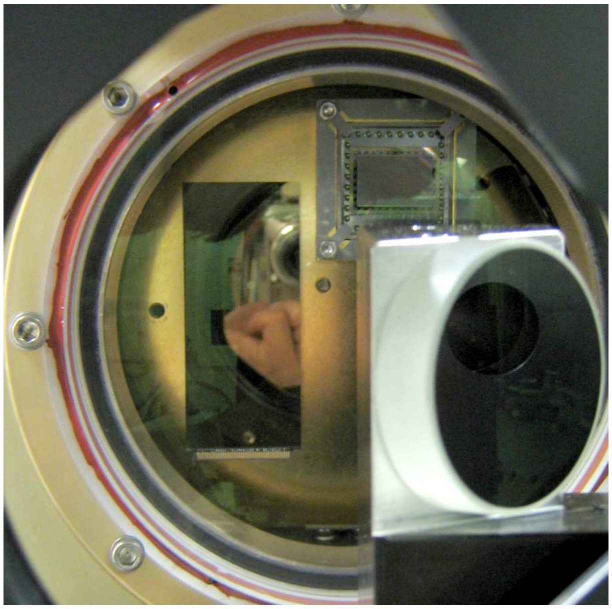

Figure 2.70: ***The TRES focal plane – as seen from the grating****. The exposure meter CCD is just above the fold mirror, on the right. (The dispersion direction is vertical.)*

2.7.3 Guider Camera

The guider camera is based on the Magellan Guider Camera[7] The sensor is a EEV CCD47-20 device, which provides 1024 × 1024, 13 μm pixels in a full frame transfer package, enabling very fast exposure times (10 ms) without the need of a shutter. The detector is cooled by a two-stage thermoelectric element and a secondary liquid-based heat exchanger system.

2.8 Software Development

2.8.1 Low Level Codes

Steppers The low level codes were developed using the MicroLYNX Programming Language. Most of the programmed commands are the same, only differ by an address character to select the stage.

The functionality of these codes include:

- report status, or actual position (if it was homed before)
- finding home position
- moving to a commanded position, in absolute or relative sense
- continuous monitoring of end sensors, emergency stopping upon reaching end sensors
- continuous monitoring of encoders to detect stalled or slipping motor, automatic re-homing and restoration of last commanded position
- providing feedback to user or upper level code, either on completion or on failure of move (and print human-readable messages for users)
- disabling the motor for safety if the same problem occurs twice in a row

---

[7] http://www.ociw.edu/instrumentation/ccd/gcam.html

Camera Drivers The Linux kernel module for the camera was provided by John Roll, and it is based on the original Magellan driver module. Readout parameters (on chip binning, image region, use of readout channels) can be set via a configuration file, or can be specified on the command line by switches.

Tip-Tilt Driver To drive the current loop input (4–20 mA) of the tip-tilt electronics an Acces I/O Products, Inc. digital-to-analog PCI card (D/A-02A) was installed into the guider PC. A simple C code was written to allow simultaneous setting of both piezo axes, by specifying the channel numbers and currents, in mA (12 mA being the nominal position and allowing ±1 mrad motion in the 4–20 mA range). The 12 bit resolution of the D/A board corresponds to 0.5 μrad, and although it is ∼5 times coarser than the internal resolution of the PI stage, still sufficient for guiding.

2.8.2 Top Level and Data Acquisition Interface

The top level code establishing the communication between TRES components, responsible for housekeeping (FITS header, log file, temperature monitoring, etc.) and integration with other FLWO systems (mainly the telescope), was written by Ted Groner. The user has access to CCD camera and lamp/motion control through a real time Linux system, which has been used for previous and other FLWO instruments[8].

Guiding The current guiding code is a set of shell scripts (bash), to aid the observer identifying and centering the object, locate a guide star and close the loop of tip-tilt control by continuous monitoring of the guide star (Fig. 2.71). Although it is far not the fastest response-time representation by calling external programs (*ds9* to display images; *xpaset* and *xpaget* to provide graphical interaction with the user through ds9; *sextractor* to determine guide star properties), it works efficiently.

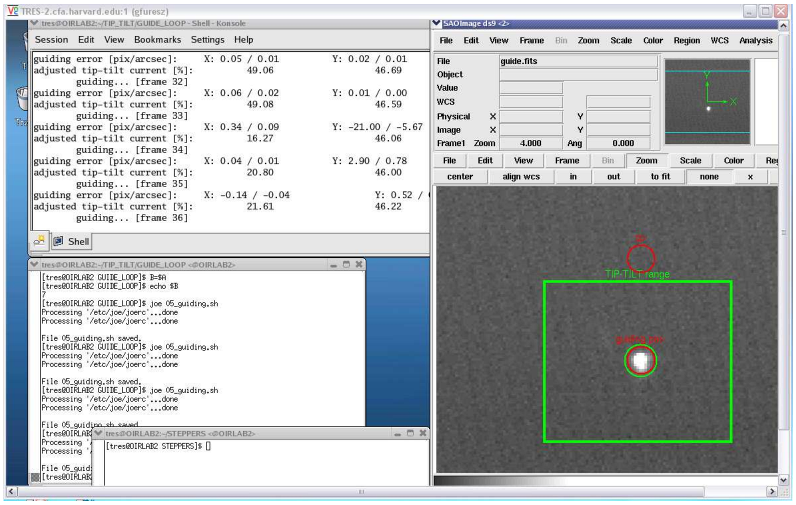
TRES-2.cfa.harvard.edu:1 (gfuresz)
tres@OIRLAB2:~/TIP_TILT/GUIDE_LOOP - Shell - Konsole
Session Edit View Bookmarks Settings Help
Shell
tres@OIRLAB2:~/TIP_TILT/GUIDE_LOOP <@OIRLAB2>
tres@OIRLAB2:~/STEPPERS <@OIRLAB2>
SAOImage ds9 <2>
File Edit View Frame Bin Zoom Scale Color Region WCS Analysis
File
Object
Value
WCS
Physical X Y
Image X Y
Frame1 Zoom
Ang
Y
X
File Edit View Frame Bin Zoom Scale Color Reg
center align wcs in out to fit none x
TIP-TILT range

```
guiding error [pix/arcsec]:      X: 0.05 / 0.01          Y: 0.02 / 0.01
adjusted tip-tilt current [%]:          49.06                    46.69
        guiding... [frame 32]
guiding error [pix/arcsec]:      X: 0.06 / 0.02          Y: 0.01 / 0.00
adjusted tip-tilt current [%]:          49.08                    46.59
        guiding... [frame 33]
guiding error [pix/arcsec]:      X: 0.34 / 0.09          Y: -21.00 / -5.67
adjusted tip-tilt current [%]:          16.27                    46.06
        guiding... [frame 34]
guiding error [pix/arcsec]:      X: 0.04 / 0.01          Y: 2.90 / 0.78
adjusted tip-tilt current [%]:          20.80                    46.00
        guiding... [frame 35]
guiding error [pix/arcsec]:      X: -0.14 / -0.04                Y: 0.52 /
adjusted tip-tilt current [%]:          21.61                    46.22
        guiding... [frame 36]
```

```
[tres@OIRLAB2 GUIDE_LOOP]$ B=$A
[tres@OIRLAB2 GUIDE_LOOP]$ echo $B
7
[tres@OIRLAB2 GUIDE_LOOP]$ joe 05_guiding.sh
Processing '/etc/joe/joerc'...done
Processing '/etc/joe/joerc'...done

File 05_guiding.sh saved.
[tres@OIRLAB2 GUIDE_LOOP]$ joe 05_guiding.sh
Processing '/etc/joe/joerc'...done
Processing '/etc/joe/joerc'...done

File 05_guiding.sh saved.
[tres@OIRLAB2 GUIDE_LOOP]$ joe 05_guiding.sh
Processing '/etc/joe/joerc'...done
Processing '/etc/joe/joerc'...done

File 05_guiding.sh saved.
[tres@OIRLAB2
Processing '
Processing '

File 05_guid
[tres@OIRLAB2
```

```
[tres@OIRLAB2 STEPPERS]$ []
```

File guide.fits
Frame1 Zoom 4.000 Ang 0.000

Figure 2.71: ***Screenshot of the TRES guider***.

---

[8] see http://www.sao.arizona.edu/FLWO/60/tcs60.html for details

There are two guiding modes offered: using a separate guide star within the FOV, or using the target star. Since the holes of the slit plate are larger than the fibers, no light is visible when the star is centered on a light guide. Therefore self-guiding requires to slightly offset the star using the tip-tilt mirror, by a given amount, determine correction and remove the applied offset with the determined guide signal added to it. This decreases the efficiency of the instrument as significant amount of time (5-15%) is used for guiding. Also, the mentioned hysteresis and lack of internal position feedback (sensors within the PI stage) affects performance, as it is discussed in §2.10.5.

2.9 Construction

2.9.1 Bonding Lenses in Bezels

To axially register the lenses to the bezels a flat annulus was specified on each lens drawing (see Fig. 2.72). During bonding both the bezel and the lens reference surfaces were seated on the same annulus of a bonding fixture made out of delrin (Fig. 2.73). Radial registration was achieved by gage pins inserted between the edge of the lens and the inner surface of the bezel. The idea using a fixture is not just registering but to firmly hold the bezel respect to the lens while bonding and curing. Therefore bezels were bolted onto the fixture, as they would mount on the lens support, while teflon tip lock screws put axial preload on the lens at three locations near the edge. These screws were mounted off the bezel by adjustable brackets.

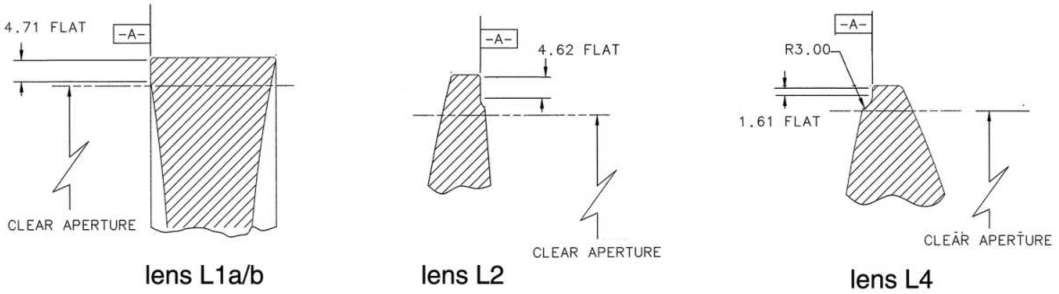

Figure 2.72: ***Edge details of some TRES lenses****, showing the flat annulus designed to aid the lens mounting.*

The fixture was made for each lens individually, and provided witness holes below the flat annulus of the lens to inspect proper lens seating. It was very important for the triplet elements to make sure there is no tilt between the lens and bezels, since the spacing between triplet elements is set by shims placed between the bezels. Although tilts can be corrected by altering shims, it introduces radial misalignments, since the outer diameter of the bezels are no longer part of a common cylinder.

The gap between the lens and bezel was sized according to the calculations detailed in §2.4.1. The specified RTV was mixed and outgased in a vacuum chamber to prevent air bubbles forming in the bond and thus degrade its athermalization properties. After the untreated (not anodized) inner bezel surface and the lens edges were prepared by a primer, the RTV 560 was injected into the gap by using a syringe. The bond height was either set by the edge of the lens (for short edges calculations were performed to adjust bond thickness only) or, for tall lens edges a rubber O-ring

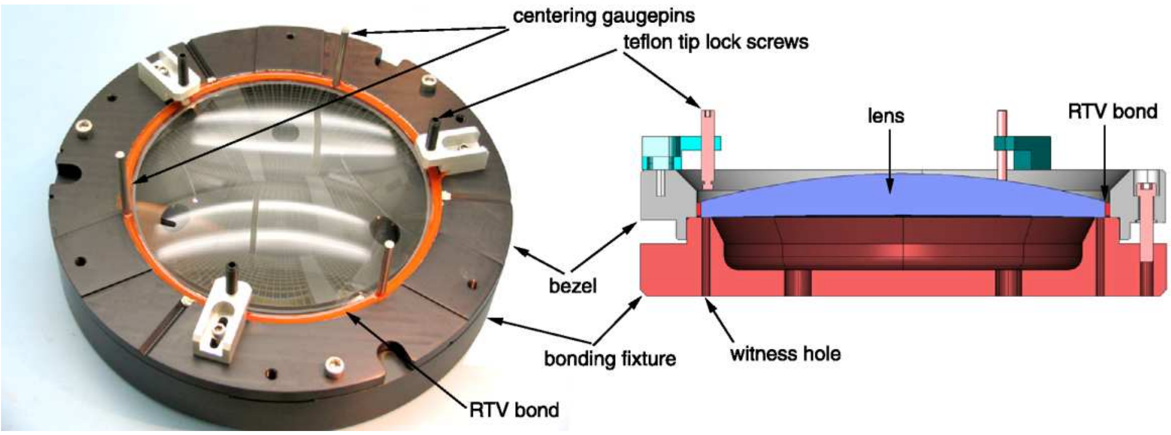

Figure 2.73: ***Lens bonding technique***

was placed in between the lens and bezel to prevent RTV flowing all the way down to the fixture. Than RTV was filled to a height marked on the lens.

Despite careful preparation small tilts were put into L4 and L5, as the RTV did flow under the flat annulus of these lenses (due not enough preload and some manufacturing errors in lens details and fixtures). The tilts were at the order of $1'$(RTV underflow of 50 μm thickness), which corresponds to 0.1 mm displacement of L4 if even gap is maintained between L3 and L4. However this number is larger than the allowed mounting error given by the tolerance analysis, it was possible to compensate for the tilts and still achieve acceptable radial registration between the triplet elements. This was justified by assembling the triplet "dry", without applying the couplant, and put it into the beam of otherwise assembled and aligned spectrograph. Since image quality was found to meet the optical model the lenses were bonding by using unequal shims. This way cutting out the lenses from the bezels and the painful cleaning of RTV were avoided.

2.9.2 Coupling the Multiplet Lenses

To maximize the throughput of multiplet lenses, the triplet and the focal reducer, some sort of lens coupling material was meant to be applied between the mating surfaces. Several options were considered, including: Oken 6262A grease; Dow Corning Q2-3067 grease; General Electric Viscasil grease; Dupont Krytox oil; and the Nyogel OCK-451 curing gel. Experiments pointed out that working with a liquid couplant is lot easier: the lens with the convex surface can be put on a table, and the couplant can be just poured into the "bowl" of the optical surface. By slowly lowering the concave lens the fluid will fill up the gap, leaving no bubbles behind. The excess material will just overflow at the edge, where it can be collected and removed. However to apply an oil some sealing has to be added to the lens mounts and the reaction between oil and RTV has to be tested. In contrast, the curing gel offers the ease during assembly and provides the handling of a grease when cured. Also, the optical properties were very appealing (see Table 2.15 and Fig. 2.74). Since there were no references available describing experiences with the Nyogel in astronomical applications, a series of tests were performed.

Table 2.15. Properties of the Nyogel OCK-451 curing gel

Refractive index at 25 °C	Absorption 4000–7500 Å	Color at 25 °C	Density [g cm^{-1}]	CTE [K^{-1}]	Set/Cure time at 25 °C
n_{4020}=1.5554 n_{5893}=1.5182 n_{9800}=1.5021	0.1 % mm^{-1}	clear	1.07	1.9×10^{-3}	1 hr / 24 hr

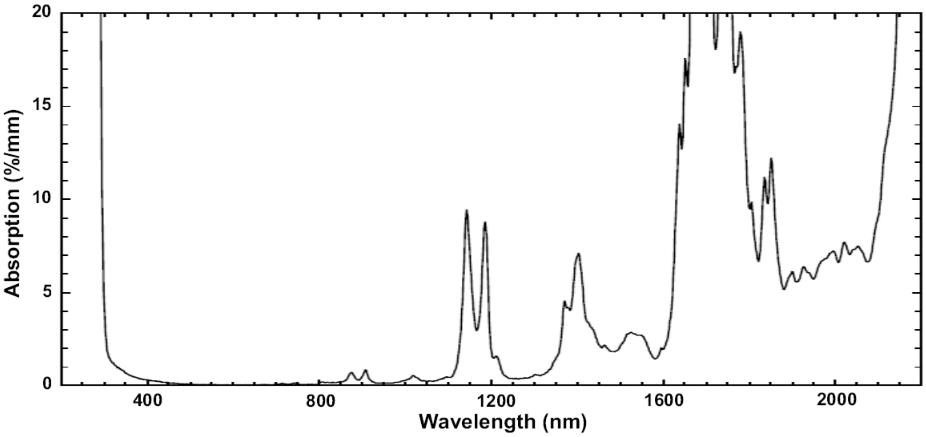

Figure 2.74: ***Absorption of Nyogel OCK-451 couplant used in TRES multiplet lenses.***

Thermal test: This step was necessary since the gel has very high CTE (1.9×10^{-3} K^{-1}) compared to any glass planned to use in TRES. After some initial tests with flat microscope cover plates a pair of test lenses were ordered, a plano-convex made of Pyrex and a plano-concave BK7, with the same 200 mm radius of curvature. The radius was chosen to be similar to that of the triplet in its early design phase, and materials with different CTE were chosen to mimic thermal behavior of the CaF2 lens in the triplet, respect to the other lenses. The test lenses were bonded to aluminum bezels, similarly as described above, and assembled with the gel. The couplant was outgased in a vacuum chamber before use. Spacing between the lenses were set to 0.1 mm by 3 plastic shims inserted at 120d°apart along the perimeter. After 48 hours of curing the doublet was thermal-cycled several time by placing it in a freezer ($\sim\ -10$°C) and than into an oven heated to 50°C, for 24 hours in each state. The cured gel remained intact, there were no signs of any damage. Optical examination showed birefringence, but after disassembling the doublet it turned to be in the Pyrex element.

Scattering measurement To measure the scattering properties 25 mm diameter, 0.75 mm thick samples were prepared using fused silica blanks. The thermal cycled (see above) samples were sent to Schmitt Measurements Sytems, Inc., to record the bidirectional transmittance distribution function for UV, VIS and NIR wavelengths, at multiple locations. The results are shown of Fig. 2.75, and the conclusion is that the couplant introduces practically no scattered light.

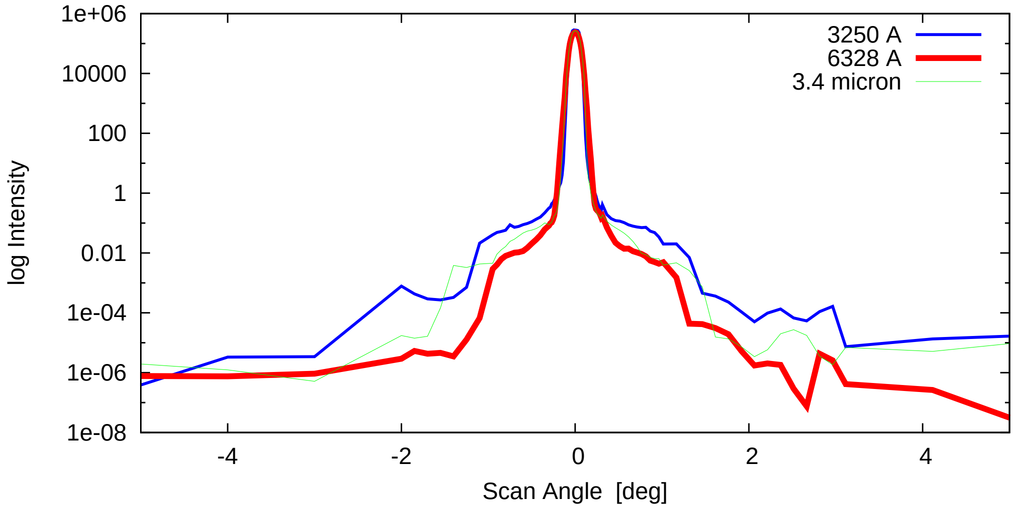

Figure 2.75: ***Bidirectional transmittance distribution function of Nyogel OCK-451 couplant****, as measured on a 0.75 mm thick thermal cycled sample, placed between fused silica blanks.*

Bubbles, air traps Mixing the two components results in high number of bubbles. If the couplant is applied without degasing several of these air traps remain in the cured gel. Therefore it is mandatory to boil off any gas content in a vacuum chamber. Small number of bubbles might still form in the sample during assembly, but most of these disappear before full curing happens.

Aging It is important to note that the two component gel has a shelf life of a few month. Preparing samples of expired shelf life material leaves small, milky filaments, visible by naked eye. Cured samples exhibited no measurable change in optical or mechanical properties (e.g. separating test samples required the same effort) over a year.

Assembly/disassembly test To test if a failed bonding can be repaired the test doublet was disassembled two times. Once the lenses were separated within the set time, once two weeks after curing and thermal cycling. In the former case the lenses came apart without any problem and the surfaces could be cleaned with acetone, although separating the bezels required high force due to the small gap (0.1 mm) and high viscosity of the couplant. Separating the fully cured sample required a 4 day acetone bath at elevated temperature (40 °C), which also damaged the RTV bonding. But it was possible to separate the lenses, clean the surfaces and cut the RTV bond. After cleaning the edges and bezels the lenses were re-bonded into the aluminum rings without any problem. Therefore it looks problems realized within the curing time can be corrected relatively easy.

Based on the experiences the Nyogel OCK-451 was found to be a very good and easy-to-use couplant. To apply it in the triplet a simple fixture was made to aid very slow and even lowering the convex element (Fig. 2.76). To avoid air traps when the convex element comes in contact with the liquid couplant a drop of the gel was placed on the vertex of the convex surface. Lowering was done by alternate turning of 3 tapered bolts placed 120°apart. The amount of couplant poured into the concave element was ~140% percent of the nominal gap volume. The excess material was just let to overflow at the edge of the concave lens. Even though there could be unfavorable interaction between the also silicon based RTV and gel (refraction index change, softening), but thanks to the fast setting and curing time it does not happen.

The radial registration was done by placing the (partial) assembly an a flat surface and setting both bezels flush against a V-block. The bolts connecting the bezels were tightened iteratively while continuously checking the radial alignment against the V-block. The assembly was moved from this setup until the gel fully cured (two days).

Unfortunately there was a problem mixing the gel components, by using somewhat more from one than the other. This resulted a very thin mixture, which did not cure fully even several days after bonding. Therefore the assembly had to be separated and coupling was repeated. See the Appendix for more experimental information on the application of the Nyogel couplant.

The focal reducer elements were bonded together using the same technique.

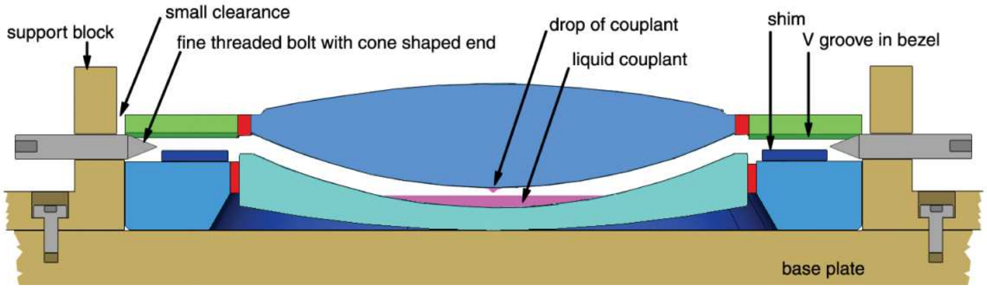

Figure 2.76: ***Lens coupling technique***

2.9.3 Mirror and Auxiliary Lens Mounts

For the small mirrors an invar nub (6 mm diameter) was epoxy bonded onto the back, as on such small area any the stress induced by temperature difference is negligible. This nub was used to attach the mirrors to off-the-shelf adjustable holders.

The fold mirror of the spectrograph beam was also epoxy bonded to an aluminum post. To minimize possible stress the single bonding area was kept small ($\sim$1 cm^2) and located in the middle of the mirror. By applying shims during the bonding, which then were removed, the mirror is elevated from the mounting surface by 2 mm. Therefore it can be separated by a narrow blade (just like the tip-tilt mirror).

The fold prisms are simply pre-loaded by two teflon bolts against RTV pads. Similarly, the edge of the small lenses are sitting on two teflon pads while a teflon tip bolt is providing preload.

The iodine cell is held by teflon flexures (small, cylindrical shells with thick walls) placed around the perimeter of the input and exit windows.

2.9.4 Fiber Run

Fiber polishing and protection was carried out by following the method developed by Joe Zajac for the manufacturing of the Hectochelle fiber run. Before polishing the final and overall protection had to be built, since the optically prepared tiny fiber ends are very sensitive, do not tolerate contact with any material.

Protection Each fiber was jacketed with a small, 1.8/0.9 mm outer/internal diameter teflon tube. Since the thermal expansion of teflon is very different compared to CTE of silica fibers (80 ppm/°C vs. 0.5 ppm/°C), to prevent buckling of the fiber within the teflon jacket (and thus possible increase of FRD) thermal breaks were applied (see Fig. 2.77).

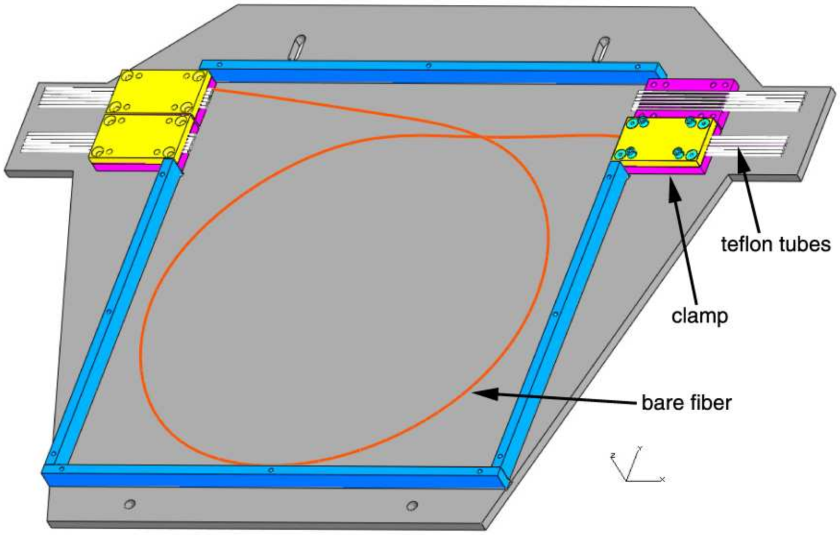

Figure 2.77: ***Thermal break design.*** *The bare fibers make a 300 mm diameter loop in the light tight box.*

At the entrance of the unit teflon tubes are terminated and pressed into slightly undersized slots, which are machined into aluminum plates. A cover plate ensures that the tubes are hold tight and can not slip (similar technique as used for the fiber plates at the slit/spectrograph end of finer run). The bare fibers make a 360°turn inside of a light tight rectangular box, than enter the other section of teflon tubes at the exit. Therefore shrinking/expansion of the teflon can be compensated by the length of the bare fiber loop, without stressing the light guides.

The teflon tubes are grouped and jacketed with a black, nylon-fabric cover, providing a light-tight seal and better handling. These bundles are pulled through a braid reinforced Polyurethane hose (New Age Industries, Inc, #2200226), providing mechanical protection. A wire reinforced hose could have provided better mechanical resistance, but the chosen option offered flexibility even at low temperatures (down to -70°C), which is a clear advantage in astronomical applications. (Flexible metal hoses were considered, although the lack of finding one with a smooth internal surface, necessary to pull through the fibers, and financial constraints suggested the use of above plastic product.) The hose ends were clamped to the thermal breaks and fiber mounting plates.

The total length is 17 m, which was determined by actual measurement at the telescope (leading a string along the imagined path of the fibers), and two thermal breaks were built in. For the section swinging on the telescope, one further level of protection was added: a heavy-duty energy chain capable of bending in all three directions (Igus E332-50-2-200), which also constrains the minimum bending radius (to 200 mm) therefore protecting the fibers against increased FRD and breaking.

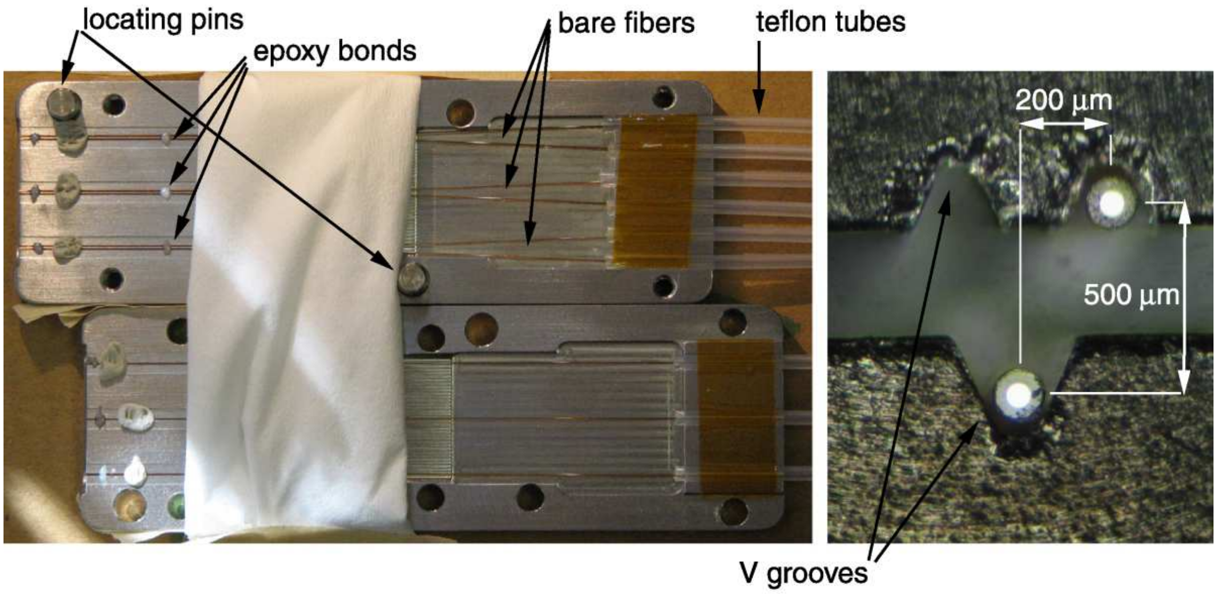

Figure 2.78: ***Bonding the fibers at the spectrograph end.*** *On the left the two base plates separated, with all nine fibers bonded (3 × 2 on the top, sky and calibration fibers; 3 × 1 on the bottom, object fibers). On the right a microscopic view of two test fibers (62.5 µm core) bonded in the V grooves, with the base plates attached to each other.*

Polishing and Mounting The polishing was done by mounting all fibers onto a cylindrical tool, having all faces perpendicular and leveled to the face plate of the tool. The fiber ends were bonded together by wafer mounting wax to form a continuous surface supporting all the fibers form all sides. This ensures that during polishing the fibers can not bend, and so the resulting figure is going to be flat. The wax can be dissolved in acetone, releasing the fibers without any force applied to the fragile light guides. A simple rotary table with a glass plate and self-adhesive polishing disks was used to smooth the surface. Quality of fiber ends were continuously monitored using an optical microscope.

After polishing the fibers were laid into the V grooves of the invar mounting plates (see Fig. 2.47 and 2.78). After ends were aligned up with the holder three small epoxy bonds were applied to all fibers, and teflon tubes were secured in the U shaped slots. Excess bond material was carefully removed by using a fine sandpaper and a flat block. See the resulting face-on view of mounted, illuminated fibers on Fig. 2.78.

At the front end side the slit mirror was mounted onto the fiber plates under a microscope. Alignment was adjusted by plastic shims, as well as slow, careful lowering of the slit plate onto the fiber holder was achieved by multiple shims. Fig. 2.79 shows the bare fiber ends mounted in the plates, without (left) and with (middle) the slit mirror in place. On the right enlarged images of individual fiber ends are presented, with object fibers on the right and sky fibers on the left.

2.9.5 Optical Alignment and Lab Testing

Coarse alignment First, a laser was set up to provide a beam parallel to the surface of the optical table. Each lens mount (except L1a) without the bezel was placed on the table according

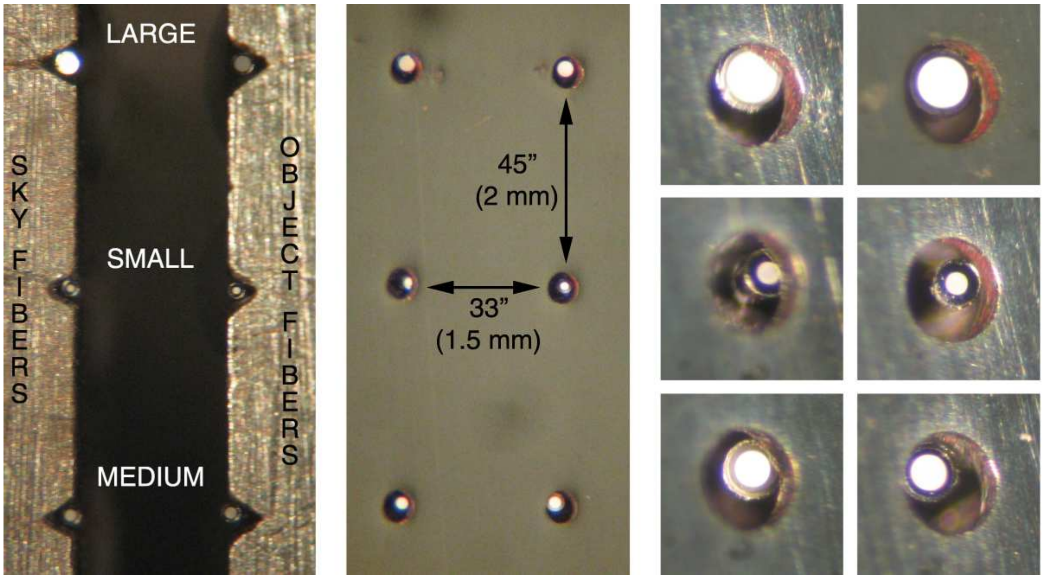

Figure 2.79: ***The mounted fibers of the telescope end.*** *The two base plates attached, prior to installing the slit mirror (left) and after the mirror in place (middle). The right panels show the enlarged view of each fiber end.*

to their designed location (as measured and drawn on the benchtop). Distance between the lens mounts were measured using gage blocks laid on the bench. Centering tools were manufactured to fit the each bezel, solid aluminum disks with a pinhole in the middle, and with the aid of these the lens mounts were centered to the laser one by one. Steel blocks and clamps were placed around the steel bases of the mounts, in order to secure their position. In the next step the lenses were mounted, one at a time, and by checking the return of the laser from the spherical surfaces the tilt of the optics were adjusted, by shimming the bases.

Due to the mentioned problem with mounting the triplet elements, the multiple return spots (no couplant applied) from L3/4/5 did not make it possible to correctly align that element. Another source of alignment uncertainties came from L1a, which could have been not centered respect to other elements by using the laser. Also, the fiber mount on L1a and the fold mirror were free parameters as well, however these could have been coarsely set. Placing the prism and grating on the table and illuminating a mounted fiber with a laser it was possible to centering the illuminated pupil on the grating by adjusting the fiber mount and fold mirror.

Fine alignment The second step was using the science camera to record the emission spectra of a ThAr lamp and tune position/tilt of optical elements based on the aberrations seen across the image. This was an iterative process, mostly trial-and-error at the beginning to get a sense how does the image react to given changes. In and out of focus images were found helpful to de-couple tilts from other aberrations. The Zemax software was also used to evaluate and identify effects of different misalignments, by comparing the software generated, aberrated images to the appearance of recorded spectral features. For an unbiased, overall evaluation of a frame the *sextractor* code was used to extract image quality information (line shape, tilt angle, concentration, FWHM) across the field. These results were plotted as a color coded surface map using *gnuplot* (see Fig. 2.80).

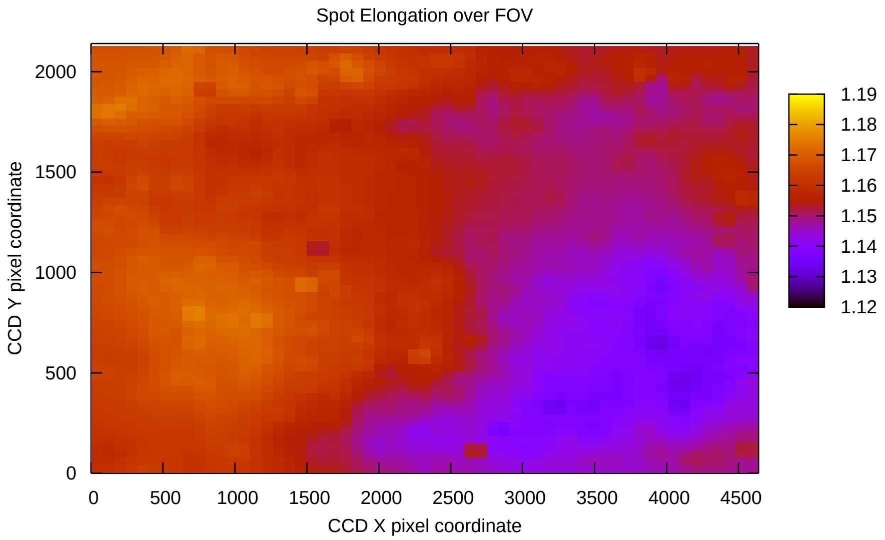

Figure 2.80: ***Sample evaluation map used for optical alignment,*** *displaying line elongation over the detector format (based on ThAr line profiles).*

The triplet was disassembled and reassembled several times to ensure repeatability of its position and optical behavior (e.g. no change in image aberrations). During these tests it was found that some changes in the shimming of the bezels and increasing the nominal 0.1 mm spacing to 0.3 mm did improve the repeatability. This change of the optical prescription had no effect on image quality, so the triplet was finally coupled with Nyogel using 0.3 mm spacing.

The grating was also adjusted in order to position spectral lines to the desired location in dispersion. It was discovered by that time that intensity does not peak in the middle of spectral orders. This is due to the fact that the actual blaze angle of the grating was not the specified 63.°5, but rather 64.°28. The 0.°78 deviation in blaze is not the only surprise about the grating, since the substrate thickness was also off by more than 3 mm (48.23 mm vs 45.00 ± 0.5 mm specification). This is a little annoying considering the price of such replicated optical element. Fortunately by adjusting the tilt of the grating the former effect was compensated without dropping any significant spectral features off the CCD format in the red, where order coverage is only partial. The grating mount was forgiving enough to eat up the thickness difference in the substrate.

Lab Testing Alignment was concluded by taking several ThAr and flat exposures using the real fiber run (most of the alignment was done using a separate fiber plate), and also recording some solar spectra. The long fibers allowed to move the front end to a separate room and in which the integrating sphere could be illuminated with sunlight. The results were satisfying, so TRES was packed and shipped to the FLWO, Arizona, on May 25th, 2007.

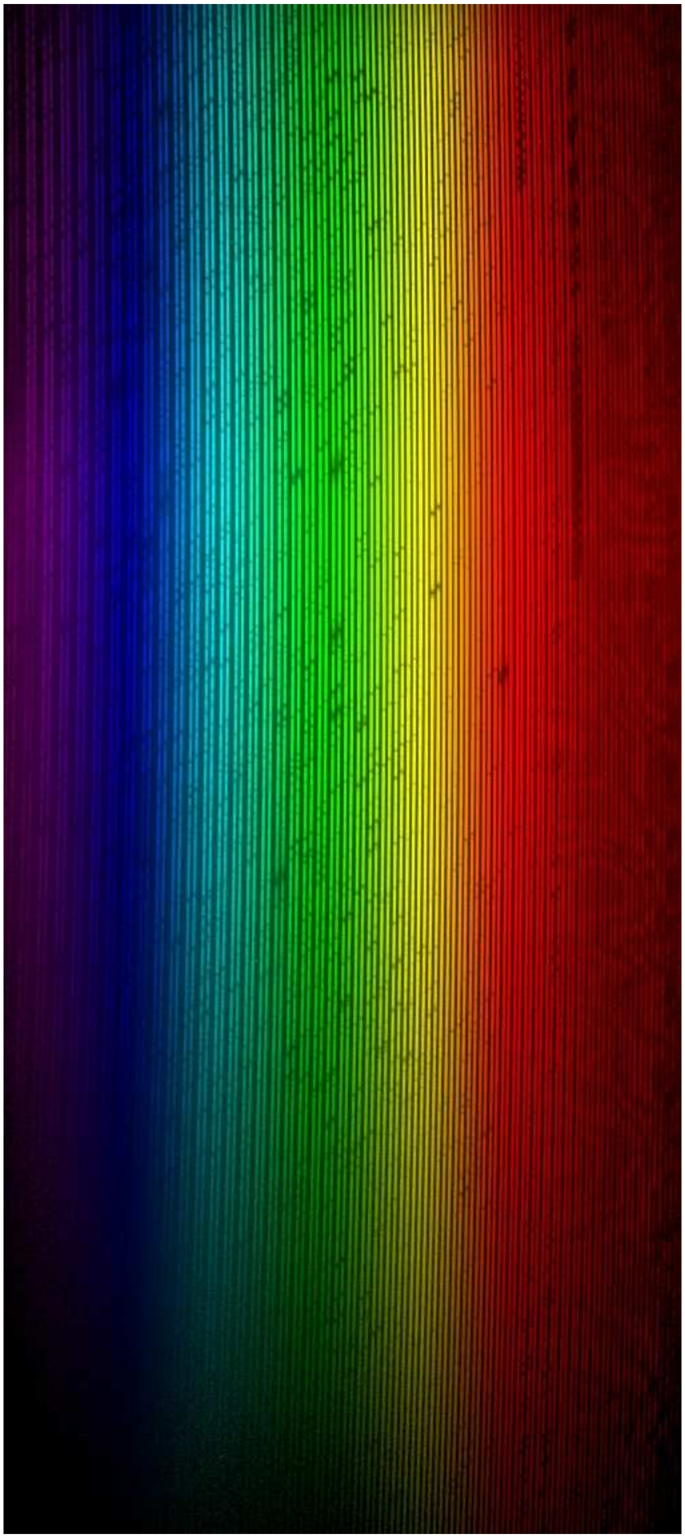

A raw solar spectrum recorded by TRES *– the orders are doubled as object and sky fibers are both illuminated during a twilight sky exposure*

2.10 Performance and First Results

For a full spectral sample of TRES refer to Fig. 12.1, a continuum normalized spectra of υ And, a F9V star. For the last 21 orders (#58 to #38, or from 5840 Å to 9100 Å) each recorded spectral region is compared to the atmospheric lines within the given spectral band.

2.10.1 Image Quality and Resolution

The alignment of TRES remained the same before and after shipping, without the need of any re-alignment, thanks to the highly repeatable kinematic mounts and firmly secured steel bases, which were shipped with the bench (see Fig. 2.81).

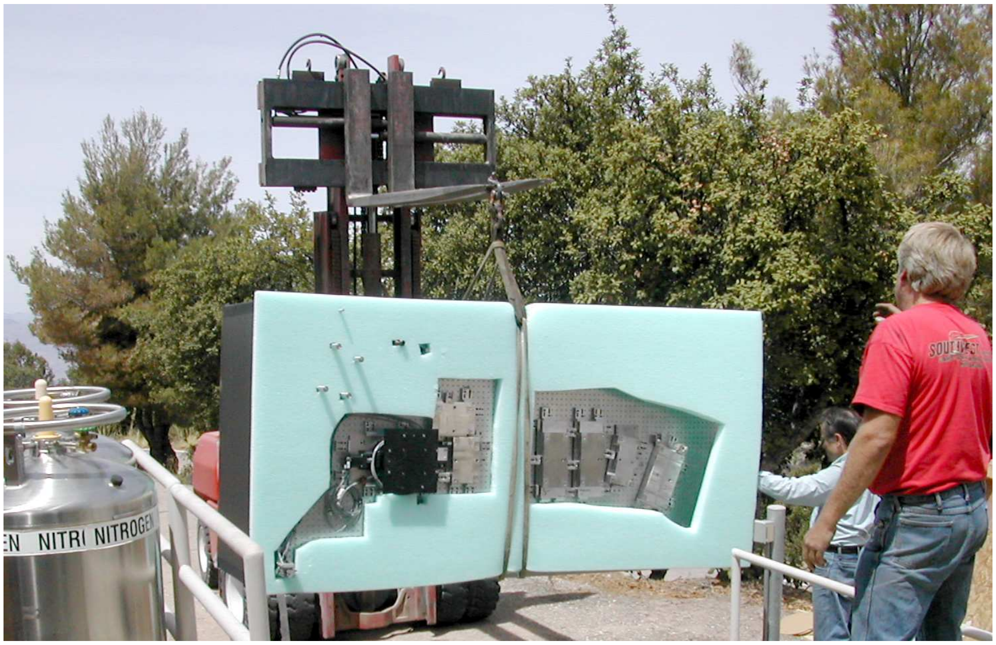

Figure 2.81: ***The TRES optical bench arriving to FLWO****. Note the steel lens mounting bases and focus stage (black) within the cutout of the protecting foam. By securing these blocks, and thanks to the kinematic mounts, no alignment was necessary upon re-assembling the TRES optics.*

The image quality is as good as the perfectly aligned Zemax model, no aberrations can be seen even at the very corners of the CCD format (see Fig. 2.82). There is a slight, barely noticeable increase in FWHM between the red and the blue end (left and right side within the blocks on Fig. 2.82).

The inter-order spacing was set by the order separation in the red, to maintain equal distance between the two spectra at longer wavelengths (see §2.1.4). The goal was successfully a achieved, as it can be seen on Fig. 2.83. The bluest (left set) and reddest (right set) object and sky apertures are shown from a flat field exposure, for the three different fiber sizes. (Note the strong fringing in the red sample on the right.)

The measured resolution is given in Table 2.16, while a graphical representation is shown on Fig. 2.84, in terms of enlarged images of a bright Ar I doublet at 7723.7612 Å and 7724.2070 Å. Intensity–pixel plots across the centroids, along dispersion, are also displayed.

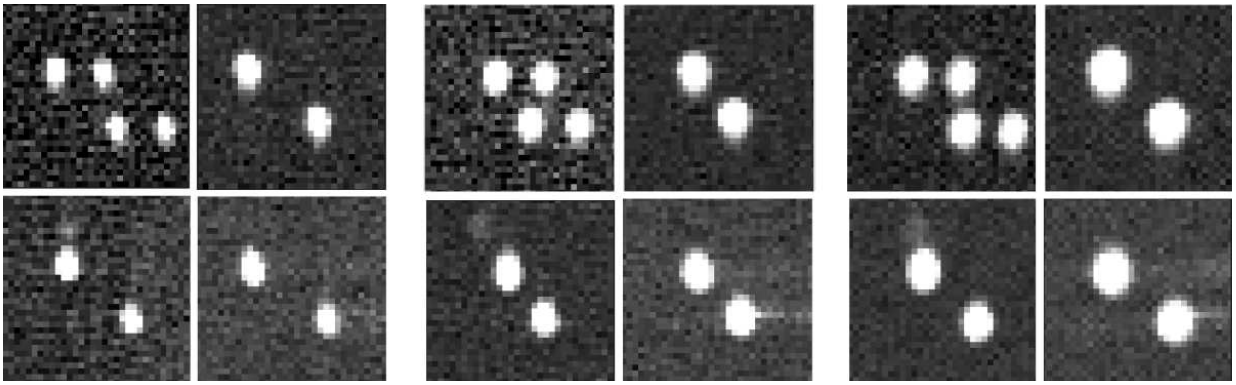

Figure 2.82: ***Image sample of ThAr lines at the corners of the detector format***, *for the small, medium and large fibers (from left to right, respectively).*

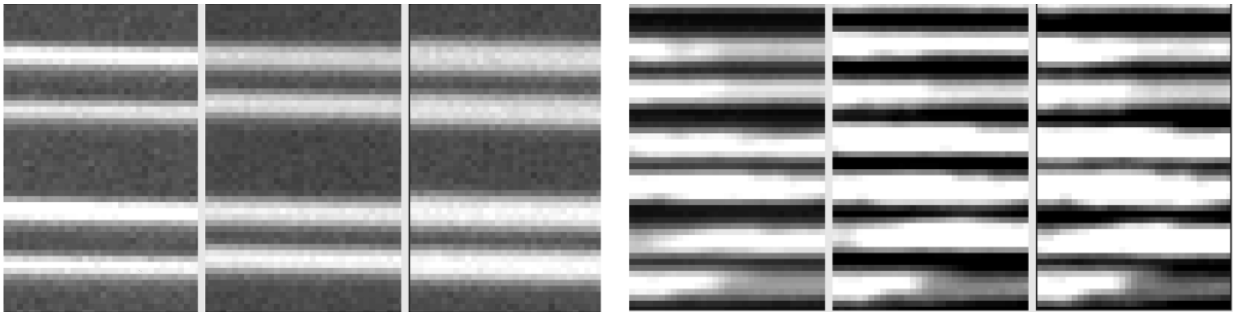

Figure 2.83: ***Image samples showing order separation***, *in the blue (left set) and in the red (right set), for the small, medium and large fibers (from left to right, respectively).*

Table 2.16. Resolution of TRES

fiber	fiber diameter [μm]	sky coverage [arcsec]	FWHM [pixels]	resolution
small	62.5	1.4	3.7	63 700
medium	100.0	2.3	5.3	44 500
large	140.0	3.2	7.6	31 000

Note. — The FWHM is determined based on ThAr lines at the blaze, in the center of the detector, with 1 × 1 binning and fitting a Gaussian. When binned 2 × 2 the resolution of the small fiber is ~56 000.

Open Issues On Fig. 2.82 a small amount of coma-like smear is visible in the vertical direction. This appears on the opposite sides of the spots in the top (blue wavelengths) and bottom (red wavelengths) rows, on both sides of given order. This is due to a charge transfer efficiency problem of the camera, likely generated by a faulty component of the preamplifier board. Servicing the electronics is scheduled during the summer shut-down of FLWO in August, 2008.

Another serious problem is the vast number of cosmic rays, which is especially annoying when coupled with above smearing. Since the same detectors and electronics of the Hecto spectrographs

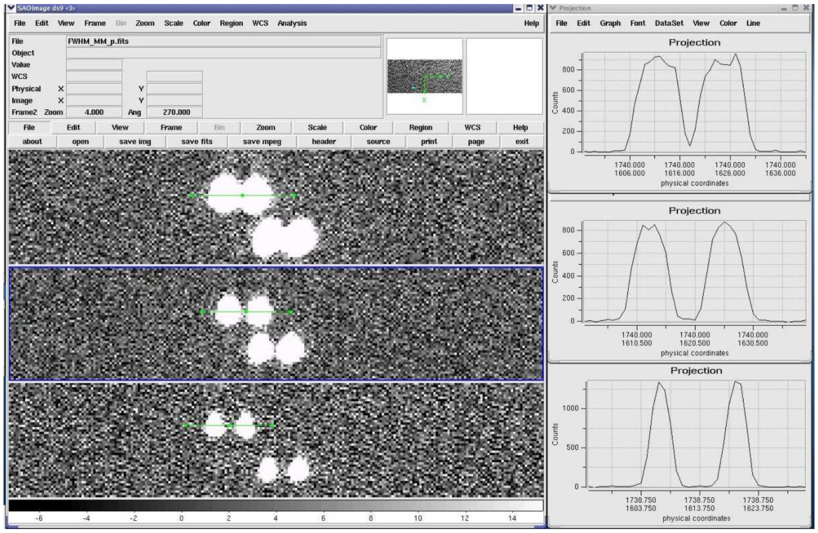

Figure 2.84: ***Resolution of the three TRES fibers**, demonstrated as a magnified view of an Ar I doublet (7723.7612 Å and 7724.2070 Å)*

(on the same mountain range) do not have this problem there has to a local explanation. Unfortunately it is likely that the dewar window lens L1b was AR coated in a chamber used to deposit radioactive materials (thorium). Therefore replacing the optics is necessary. Since a spare lens is available, it is likely to happen in the near future.

2.10.2 Measured Efficiency

The expected efficiency of TRES was calculated in §2.1.5. This sensitivity curve is re-plotted on Fig. 2.85(a), in direct comparison with the measured efficiency, after adjusting the theoretical data for the seeing conditions of the observation. For this, a simple scaling factor was used, based on the seeing limited effective light collection capability of a fiber (see Fig. 2.85(b)).

The spectrophotometric standard star HD 192281 was observed on Sept. 26, 2007, using the small fiber at an airmass of 1.1, while the average seeing was 1″.6. The spectra was extracted using standard IRAF tasks and compared to the flux calibrated spectrum of the standard star. Efficiency was calculated for several points of a spectral order, but only the peak throughput of each spectral band was plotted by a spline interpolation on the figure, eliminating by this the effect of the blaze function.

Open Issues It is apparent that the agreement between the predictions and reality is very good in the red, however most of the blue light is missing. Obviously, TRES would benefit from and ADC (see §11.1.1), however a significant portion of the discrepancy can not be accounted for atmospheric dispersion at the airmass of the observations.

Another possible cause can be the fiber, for what the manufacturer claims a very high blue transmittance, but that was not tested independently. Or one of the fold mirrors can have a defective coating. At the moment there is no clear answer to this problem. It is planned to identify the source during the maintenance period of the summer shut-down this year.

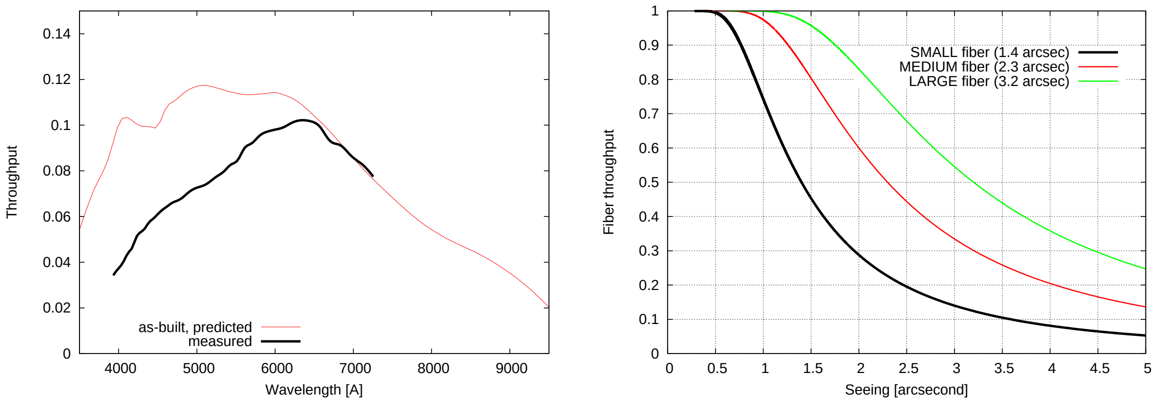

(a) Measured vs. calculated efficiency (small fiber, 1.″6 seeing)

(b) Effect of seeing on throughput

Figure 2.85: ***Comparison of measured and calculated throughput of TRES***

2.10.3 Calibration

Wavelength solution A master wavelength solution was established using three, 10 minutes long integrations of a ThAr source. Flat fields for tracing the spectral bands were recorded using a 4 s exposure time. Images were taken using the small fiber and 2×2 binning. The calibration data was extracted and processed using standard IRAF tasks of the `noao.imred.echelle` package. The bias levels were removed by fitting the overscan region. Pixel to pixel variations were removed by building a spectral flat field image, based on the incandescent lamp frames. Identification and wavelength assignment of ThAr lines was performed by using plots generated from the NOAO ThAr spectral atlas[9], also supplied with IRAF.

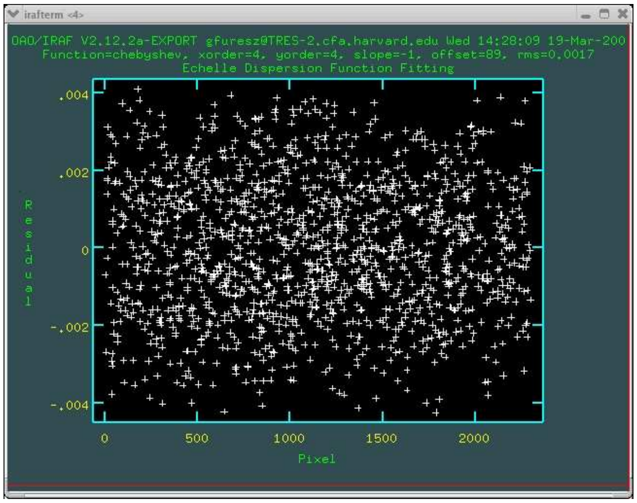

```
OAO/IRAF V2.12.2a-EXPORT gfuresz@TRES-2.cfa.harvard.edu Wed 14:28:09 19-Mar-200
    Function=chebyshev, xorder=4, yorder=4, slope=-1, offset=89, rms=0.0017
                   Echelle Dispersion Function Fitting
```

Figure 2.86: ***Wavelength solution residuals,*** *for small fiber and 2×2 binning. Although the PSF is somewhat undersampled (1.9 pixel FWHM), the RMS residual is under 0.04 pixel or 0.0017 Å.*

---

[9] http://www.noao.edu/kpno/specatlas/thar/thar.html

Residuals of a two dimensional dispersion solution fit are shown on Fig. 2.86. Both dispersion and spatial directions are approximated using a 4th order Chebyshev polynomial, yielding an RMS error of σ =0.0017 Å, or σ_{RV} ~100 m s^{-1}. The wavelength solution is based on N = 1400 spectral features. Assuming the same number of lines and uncertainty, cross-correlating two independently calibrated spectra a RV precision of $\sigma/\sqrt{N}$ = 2.8 m s^{-1} is expected. Using 1 × 1 binning (at a more appropriate PSF sampling of FWHM=3.7, instead of 1.9 pixels) the wavelength solution error is σ =0.0012 Å, corresponding to a 1.9 m s^{-1} precision.

Tracking ability of simultaneous calibration To test how well the calibration fiber tracks the object fiber, ThAr frames were recorded with 2 × 2 binning, using 5 min exposure times. Alternating the two fibers was necessary, since illuminating the object fiber also sheds light to the sky fiber, and in the red inter-order spacing is so small that the calibration and sky spectra overlaps. On the object exposures there are still two spectra, but only the one belonging to the the object fiber was evaluated in this test. The suboptimal binning mode was chosen to reduce readout time and increase signal to noise in observations carried out in between the tests.

Cross-correlation of the arc lamp spectra was performed in pixel space, in respect to the first frame of the object/calibration fiber series. More details of the method is given in §2.10.6. The main panel of Fig. 2.87 displays the measured shifts versus time. For both fibers the values were converted to velocity units using the plate scale of 2.5 km s^{-1} $pixel^{-1}$ (for a 2-binned pixel), or 0.043 Å $pixel^{-1}$ (for the same, binned pixel).

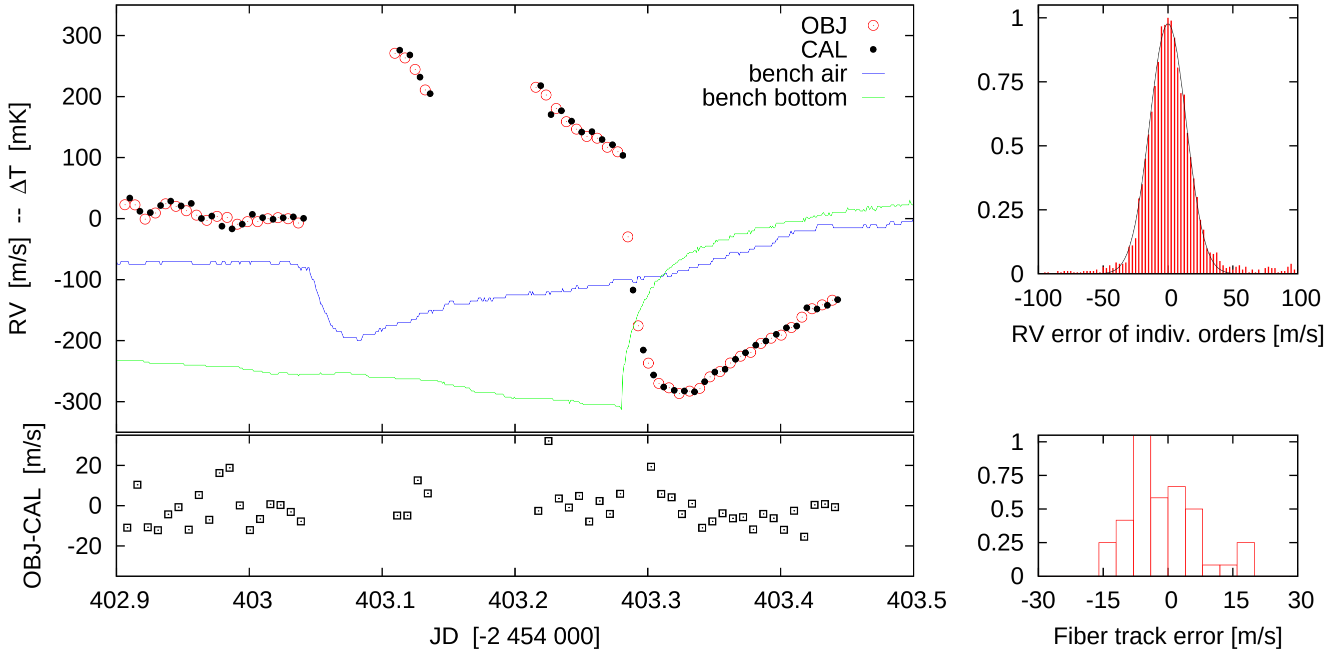

Figure 2.87: ***Instrumental shifts measured in object and calibration fibers (small fiber,*** 2×2 ***binning).*** *However shifts of individual frames can be determined with* ~ 2.5 *m s*$^{-1}$ *accuracy (upper right panel, see text for details), the residuals show (bottom panels) that the calibration fiber tracks the object fiber with an RMS error of* ~ 7 *m s*$^{-1}$*. The sudden jumps in the instrumental shifts are closely related to temperature changes (see curves of upper left panel).*

It is apparent that the two fibers measure the same, relatively large (few 100 m s^{-1}) instrumental shifts. As the object–calibration residuals show on the lower left panel, the level of agreement between these fibers is pretty much the same over time, although the RMS is somewhat smaller during the last 3 hours of the test. At this time the bench was warmed up on purpose, by turning on a heater, to see how does a sudden temperature change effect instrumental stability. The green curve of the upper left panel displays the temperature change in time (measured on the top of the bench). As it can be seen the heater was turned on at JD 403.28, and raised the temperature by 0.3 °Cwithin the last three hours of the test. Since larger changes can be measured more accurately with the undersampled PSF, the smaller residual between the object and calibration fibers might be the result of the induced, large amplitude shifts. Nevertheless, plotting a histogram of the residuals (see lower right panel), an average tracking accuracy of ±7 m s^{-1}can be expected, even with the undersampled PSF.

The blue curve of the main panel plots air temperature inside the bench enclosure. It is shown since the drop of this might be the reason behind the other large amplitude instrumental shift (at JD 403.1), apparent between first and second (very short) set of ThAr data. This cooldown (by 0.1 °C) was due to dewar filling. At the time of these tests the temperature regulation system was not yet in its present, final form (see §2.10.4 and Fig. 2.90), which now can completely eliminate the effects of dewar filling.

The data discussed above was based on the mean value of all shifts measured in the 51 spectral orders. To make sure there is no systematic error between red and blue orders (e.g. the entire CCD sees the same bulk shift), a histogram is calculated to display the distribution of measured instrumental shifts of individual orders, from a given image. On the upper right panel data from all 49 ThAr frames are displayed at once. Since the distribution is Gaussian (see fitted envelope) with a dispersion of 25 m s^{-1}, it is correct to state that RV measurement of a single order has a precision of 25 m s^{-1}. Averaging such independent shift measurements of the 51 spectral orders, the final precision of drift determination is $25 \text{ m s}^{-1} / \sqrt{51} = 3.5 \text{ m s}^{-1}$ for one frame. This is in good agreement with the precision estimated from the wavelength solution (2.8 km s^{-1}).

Open Issues The spacing is very tight in the red, per design. Even though it is sufficient for extraction, some very bright Ar lines of the simultaneous ThAr exposure can cause "pollution" of the stellar spectra, due to the diffraction pattern apparent to these saturated features. However, it affects less than 1% of the spectral coverage above 6000 Å, so masking these "cross-talk" regions the problem can be eliminated. Other possible solution is to apply a color correction filter at the lamp, and push down the intensity of red lines respect to others. This, at the same time, would also weaken the good Th lines of in the red, loosening the constraint of the wavelength solution. Therefore masking is likely a better option.

Another issue regarding the emission line source is the purity of the cathode. The lines are very similar to the NOAO ThAr atlas, but it is hard to identify features of the newly published, more precise HARPS line list (see §1.6.2). By replacing the Photron lamps of TRES to the ones used by HARPS, it would enable the use of the new line catalog, thereby likely increasing the achievable RV precision.

The main problem is, however, the overall small efficiency of the calibration system. This is intrinsic to the design, as it was meant to illuminate all fibers of the slit plate at once, and also to provide incandescent illumination for the iodine cell observing mode. Higher intensities and shorter exposure times (both for ThAr and flat) could significantly increase the duty cycle and RV precision. Therefore an upgrade of the current calibration system is proposed, using a HARPS-like solution: direct re-imaging of an illuminated aperture to the fiber entrance. This is likely to be done as soon as funding is available, hopefully in the fall of 2008.

For the tungsten lamp a color correction filter would be very beneficial, as the color temperature of the lamp is very low. This results in very low intensities at the blue orders, while red regions are close to saturation. Therefore flat-fielding introduces high level of noise in the blue. Balancing the intensity between the two extremes of the wavelength coverage is highly desired.

At last, it has to be admitted that the iodine option of TRES has not been tested yet. It would be very interesting and useful to compare the RV precision achieved by the two methods.

2.10.4 Stability

The description of the final temperature regulation system of TRES was given in §2.6.5. Although that was installed only in December, 2007, while most tests and benchmark observations were carried out beforehand. Therefore temperature variation and corresponding instrumental shifts measured in October, 2007 (see Fig. 2.88 and 2.89, respectively) represent the behavior of a not fully optimized system. Real performance can be estimated only by comparing the new temperature plots of Fig. 2.90 to the one described below. For the location of sensors refer to Fig. 2.66. Also note, that some of the changes are not temperature but pressure related, for what TRES can not compensate for.

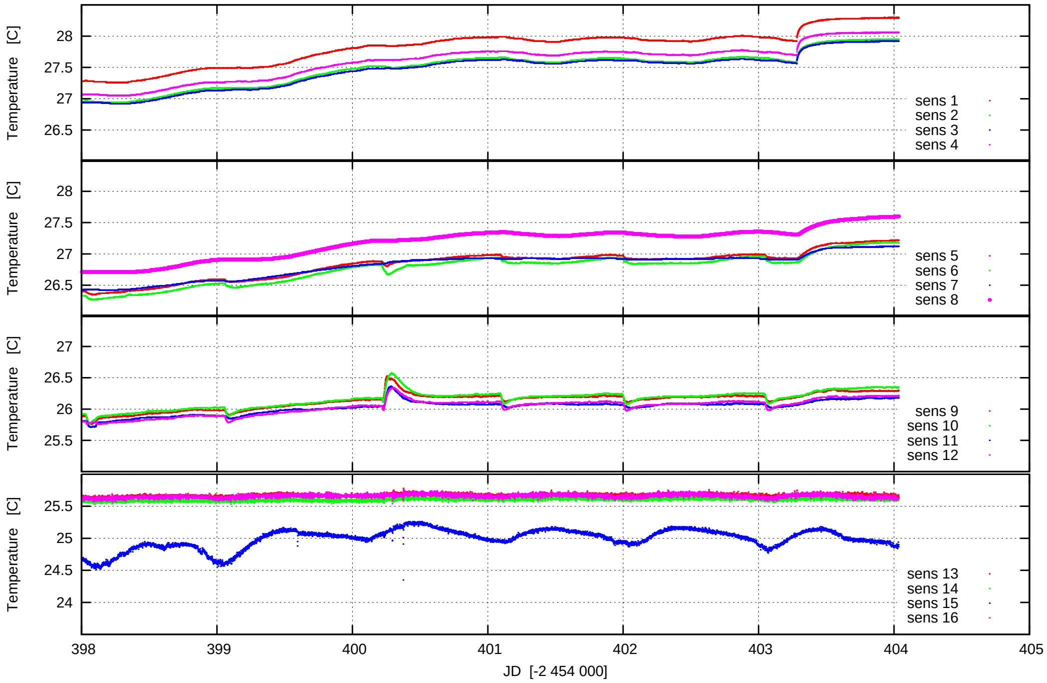

Figure 2.88: ***Temperature changes during an observing run using a temporary thermal stabilization system***. *The daily variations are still visible at* $\sim 0.1\ ^{\circ}C$ *level, while long term variations apparently have a* $1\ ^{\circ}C$ *amplitude.*

As it is obvious from Fig. 2.88, temperature changed gradually over the 6-day-long observing run, as well as on a daily basis. Dewar fillings are apparent on the third section from the top, as regular daily dips at the 0.1 °C level. Also note a sudden warm-up at JD 400.25, which is likely due to an overheated stepper motor (failure to remove hold current, see discussion later). All these variations to the bench components had happened while 3 out of the 4 room air sensors (bottom plot) remained constant, which points out conduction and radiation issues.

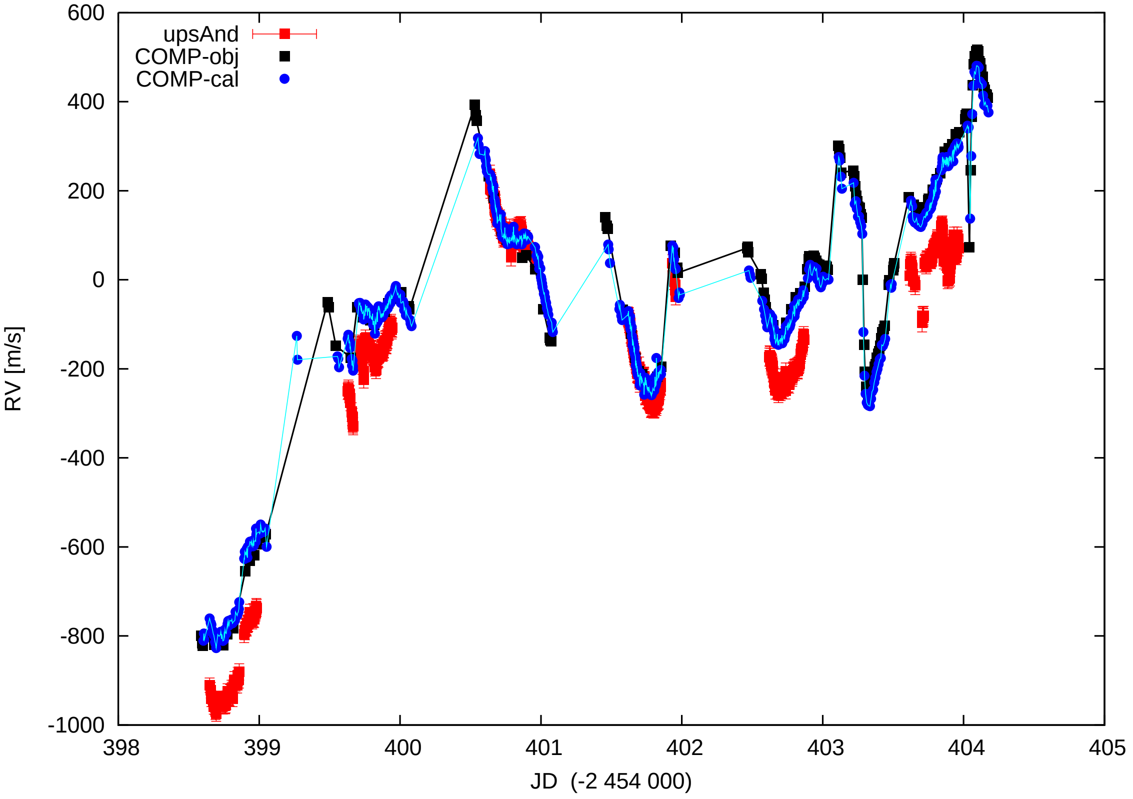

Figure 2.89: ***Instrumental radial velocity changes during an observing run***. *The black and blue symbols/curves represent the instrumental shift measured with the object and calibration fibers, respectively. Red marks are barycentric corrected RV values of υ And. (Compare with Fig. 2.88.)*

The resulting instrumental shifts for the same time period is plotted on Fig. 2.89. At first sight it can be easily concluded that the spectrograph is very sensitive to environmental variations. The pixel shifts converted to RV values for the object (black) and calibration (blue) fibers change several hundred m s^{-1} during six days. As it was shown before the two fibers track very well, although object fiber data were taken less frequently (since real observations were carried out, thereby recording ThAr through the object fiber took away valuable observing time). The red points, plotted with error bars, represent barycentric corrected RV measurements of υ And. Note, how good the agreement is between the instrumental effect and the “stellar calibrator”. The deviations at the beginning and the end of the sequence are real, since this star hosts a planetary system (see more in §2.10.7). The raw data, not calibrated for instrumental shifts, is shown here to give an idea how much the instrument can change in a real application.

Note, that with the long term temperature drift flattening out after JD 401, the continuous RV drift disappears as well. Also, the overheating of the stepper coincides with a possibly high

RV peak which was only sampled by ThAr data during the relaxation, at JD 401.5. Between JD 401 and 403 the variations are sort of linked to daily temperature (and pressure?) changes, but when a heater was turned on at JD 403.28 (on-purpose heating test, see previous section) the shift appeared similar to what was detected in the beginning, during the gradual (than natural) warmup.

Since the close connection between temperature and instrumental shifts is evident, thereby an improved temperature regulation system, with typical performance shown in Fig. 2.90, can certainly improve the stability of the spectrograph. Compare the measured temperature plots of the final system (described in §2.6.5) to Fig. 2.88. Note the different scaling on the ordinate.

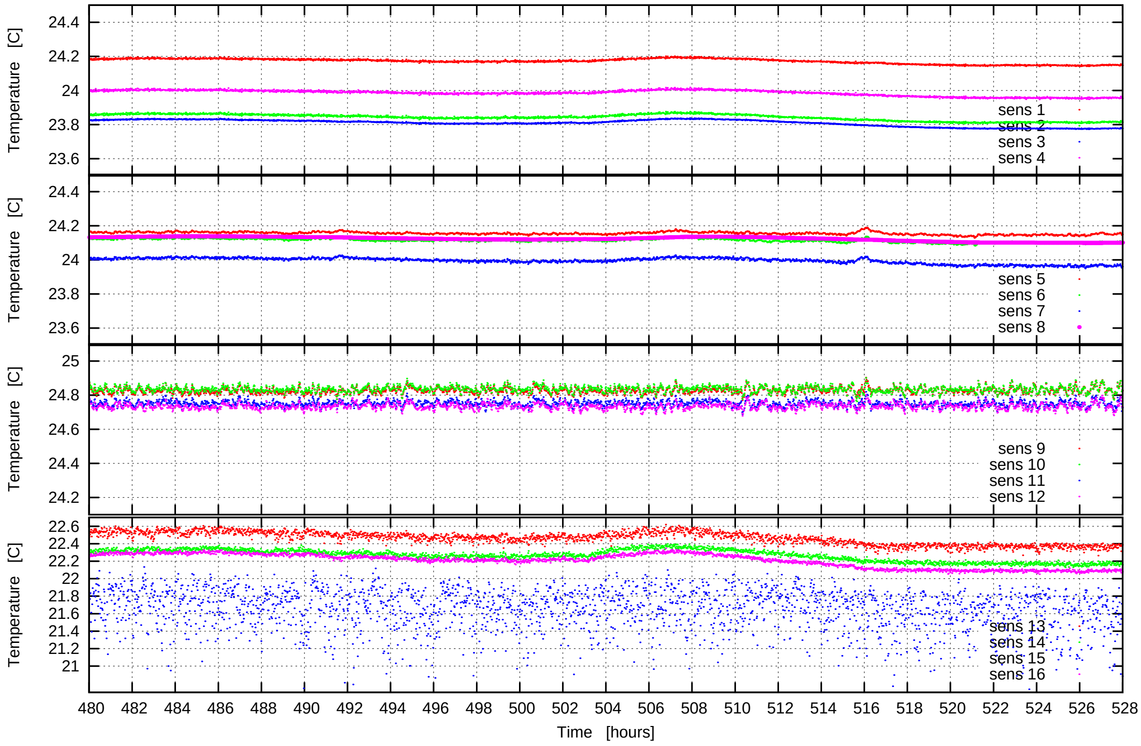

Figure 2.90: ***Performance of the final temperature stabilization system*** *(see Fig. 2.68) over a time period of 2 days. Note that the dewar fillings are almost invisible in comparison with Fig. 2.88 (although minor warmups due to the active compensation system are still presented, at hours 492 and a day later, at 516). Daily variations are suppressed under the* $< 0.03\,^\circ C$ *level.*

Open Issues Sudden warm-ups, with even higher amplitude than seen on Fig. 2.88, have been observed in the temperature log files. It is suspected, that some electrical component overheats from time to time. For safety the bench computer does perform a check on enclosure temperature, and if it exceeds a setpoint warning e-mails are sent to the FLWO staff and the instrument scientist.

To better understand what the heat source really is, more temperature sensors will be deployed to monitor active components (steppers, shutter, fans). This work is going to take place during the summer maintenance period of 2008.

2.10.5 Guiding

Image quality, benchmarks The guider provides a $4'.5\times4'.5$ FOV, with a plate scale of $0''.27$ per pixel. A sample image is shown in Fig. 2.91(a), with the globular cluster M3 in the field. Thanks to the centrally condensed object almost all fiber locations are visible as dark spots. Stellar profiles are enlarged from the corners, on the right of Fig. 2.91, to aid image quality examination.

One star in the M3 field ($V = 14.01$, $B - V = 1.00$) yielded a 4 sigma detection on a 1 s exposure, with binning mode 1×1. In case of 2×2 on-chip binning stars with $V = 15$ can be safely used for guiding.

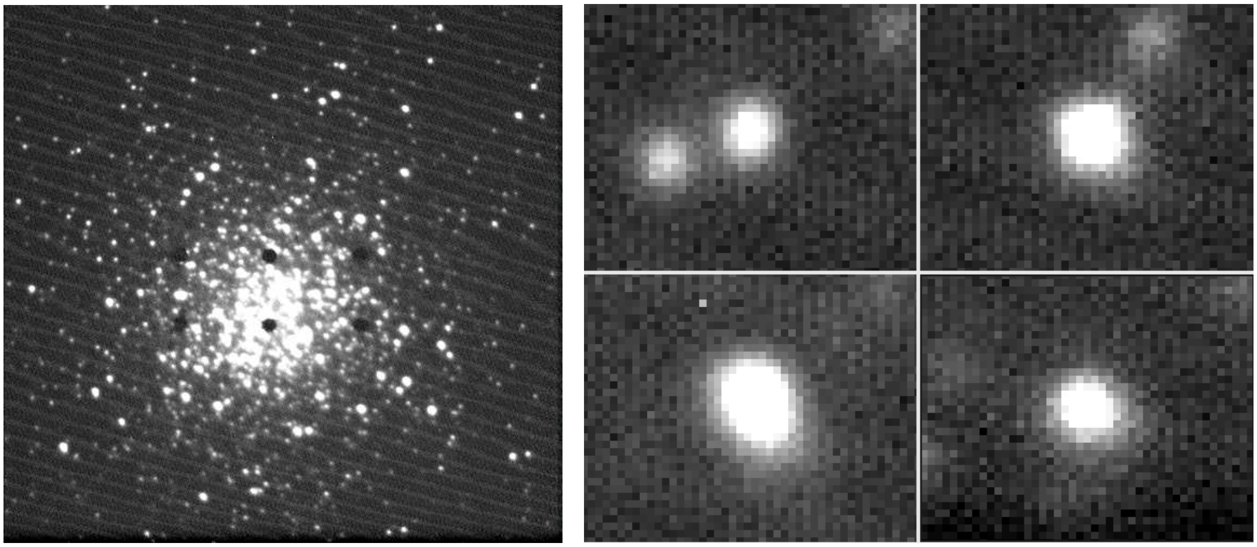

(a) 10 s integration of M3 by the guider CCD (b) Enlarged stellar profiles at the corners

Figure 2.91: ***Sample images of the guider*** *to show image quality (right) and the location of the fibers (left).*

Guiding errors vs. RV measurement As discussed in §1.5.2, due to incomplete scrambling, guiding errors of a fiber instrument still can result in RV errors. This was accidentally tested during the observations of υ And. The star was observed with short, 2–3 m exposures over one hour periods. In between a ThAr frame was taken through the object fiber, to check it against the calibration fiber, see Fig. 2.88 and 2.87. After such calibration exposure the guider had to be re-set on the star, in order to resume guiding. But therefore each one hour observing set had a different guider setup.

As it can bee seen on Fig. 2.92 (which is an enlarged section of Fig. 2.88), these one-hour-long stellar sets (red) exhibit some arbitrary offset respect to each other. However, the star does not change its velocity over such a short time scale, neither the instrumental shifts (black=object, blue=calibration fiber) exhibit similar behavior. A gradual drift, increasing deviation from the instrumental shifts of the same time interval, is also apparent between JD 400.76 and 400.78.

tThe two data points at JD 400.79 are even more obvious signs of guiding error. Guiding was terminated after the two frames, since the guider corrections were not satisfactory, and the guider star was re-positioned. This is apparent from the log files and based on the time delay before another continuous set of stellar measurements starts at JD 400.795.

Based on such examination of the entire data set, the conclusion is the following. Bad guiding setup can be recognized by the observer, based on guider correction values and visual inspection of the guide screen, but only if RV effects are larger than 20 m s^{-1}. Therefore current precision of the instrument is relying on the guider setup, and only 20 m s^{-1} level can be reached.

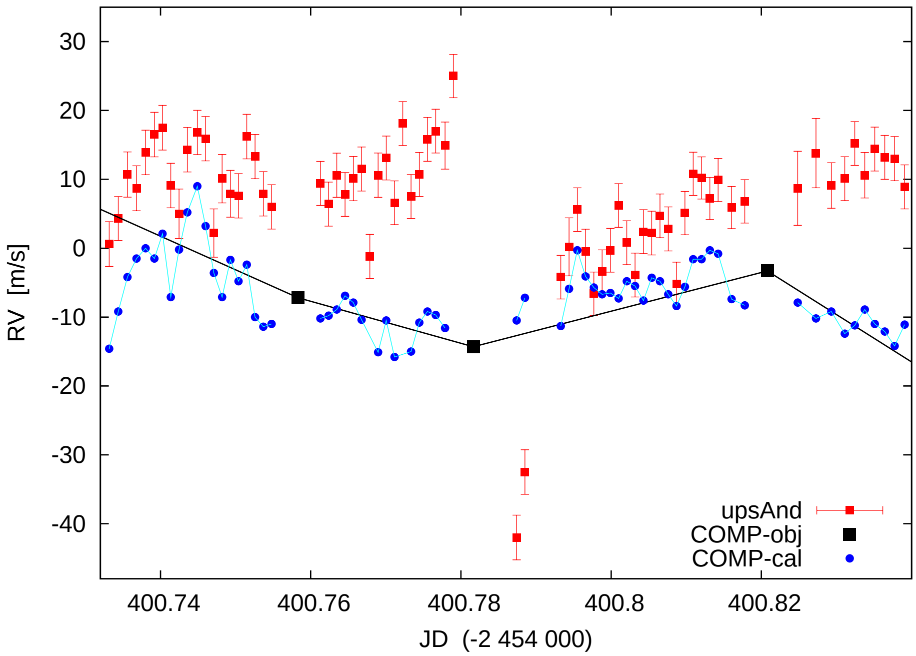

Figure 2.92: ***Guider errors translated into instrumental RV shifts***, *as seen during an observing run. See text for details.*

Open Issues Since the holes in the slit plates are larger than the fibers (see Fig. 2.79) the target star completely disappears during integration. Therefore centering on the fiber has to be done respect to some artificial offset position. Due to the hysteresis of the piezo stage such centering has to be an iterative process, which is time consuming and, as it has been proved, inaccurate. Part of the problem can be accounted to the self-made slit plate, which deviates from flat and has other, higher order variations.

The ideal solution would be a replacement of the slit mirror, with holes laser drilled to the exact size and actual (as mounted) locations of the fibers. By nickel plating the front surface of the slit plate (mirror), it can be polished to optical quality thanks to the much harder Ni layer. The surface than can be overcoated with aluminum to provide better reflectance. If the holes match the core diameters of the fibers, the outer parts of the stellar PSF can be seen around the slit hole, as an annulus. This can be used to make sure the star is really centered on the fiber, and if it stays there during guiding. It would be similar to the approach of HARPS, which has been known to work very well. As it is all technically feasible the plan is to perform the upgrade as soon as funding becomes available.

To reach fainter stars the cooling of the guider has to be improved, as well as the long term quality of the vacuum inside the camera head. Faster readout and preventing the lock-up of the guider computer while communicating with the guider would be also welcome.

2.10.6 Data Reduction

In order to measure radial velocities in the 3 m/s regime shifts (both instrumental and real RV variations) have to be determined at the 0.002 pixel level on the unbinned images, or even at the more staggering 0.001 pixel if 2 × 2 binning is used. Expressed as length it means that spectral lines shift by 32 nanometer(!) on the pixel grid of the CCD. This resolution can be achieved only by measuring hundreds, or if possible, thousands of line positions simultaneously.

To ensure that measured values at above level can be real, a few methods of RV determination were tested on the same artificial and observed data. The synthetic data was a set of simulated ThAr exposures shifted by a given RV value, with realistic background, readout and photon noise, as well as reproducing the slight undersampling of 1.9 pixel FWHM provided by the 2 × 2 binned TRES images. See Fig. 2.93 for a comparison of a single order and an enlarged line profile. The HARPS line list served as input in generating the synthetic arc lamp spectra, thereby only 38 orders were generated since the HARPS wavelength coverage is smaller than that of TRES.

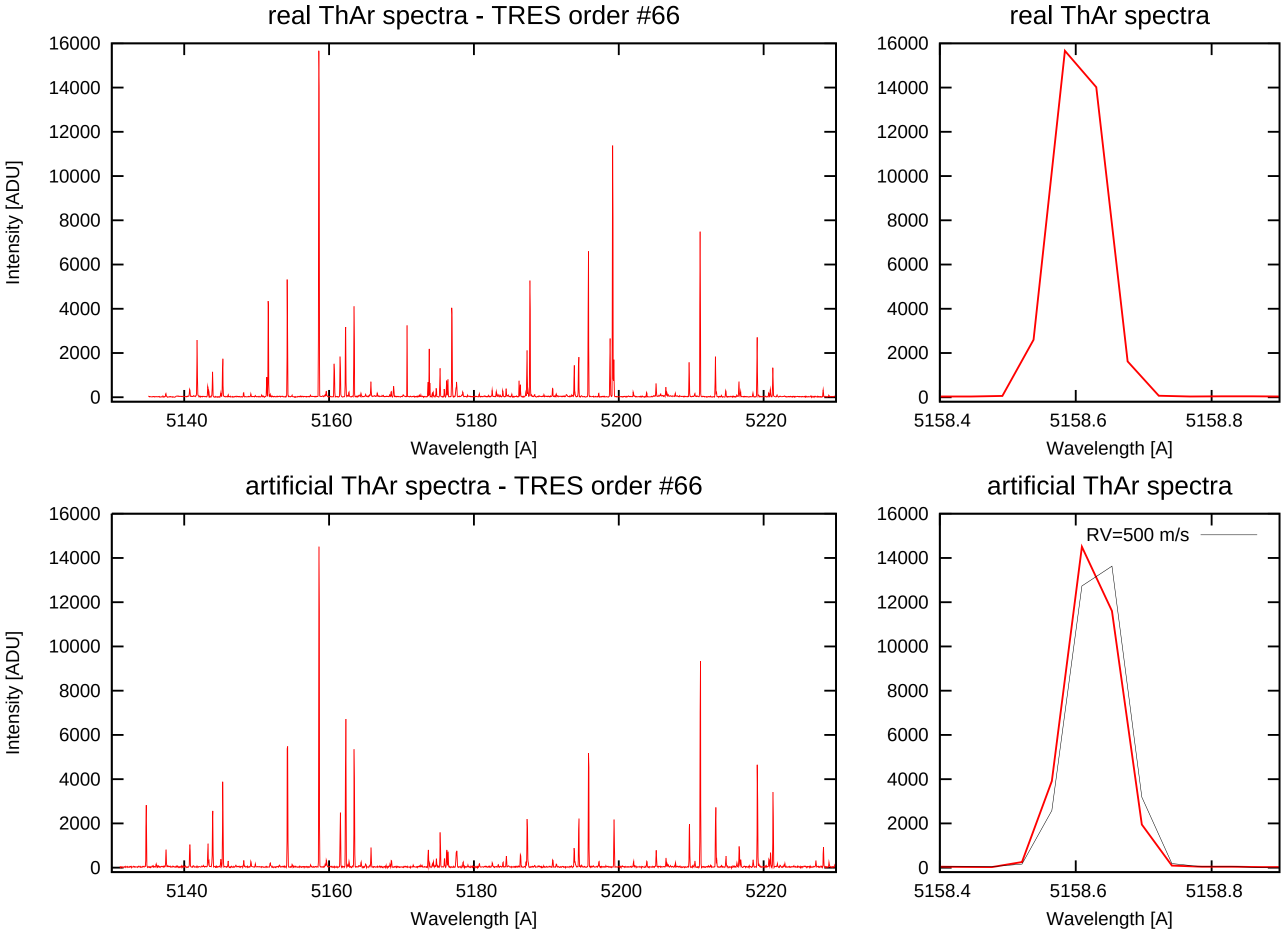

Figure 2.93: ***Synthetic ThAr spectrum used in data reduction evaluation****, in comparison with an observed arc spectrum. A single line profile is enlarged on the left, and for the synthetic sample a 500 m s^{-1} shifted profile is also shown in black.*

There are two very different approaches to perform such measurement. One is the cross-correlation method by Tonry & Davis (1979) and its variations. The other is a computationally simpler tool, as described by Bouchy et al. (2001). This latter algorithm basically calculates the derivative of the pixel–intensity function at each pixel (which is going to be relevant only in the wings of the spectral lines), for both frames to be compared. Assuming the shift is significantly smaller than the size of a pixel, the code compares how the derivative changes of a given pixel, for all relevant locations, and converts the mean change to a RV shift. Based on the description of Bouchy et al. (2001) András Pál has coded the algorithm, which was tested against the CfA developed IRAF task `rvsao.xcsao` and one other method.

Since `xcsao` was originally developed for extragalactic redshift surveys, the precision had to be improved for stellar work. This upgrade was done to aid measurements taken with the CfA digital speedometers (§2.1.1), although tests had been not performed before at the 10^{-3} pixel level. Several further changes was done by Doug Mink, per request, to make the IRAF task work in such an application.

The third method being tested was a Lomb-Scargle variant of Fourier decomposition, written by Jonathan Devor.

A set of synthetic spectra was prepared with RV shifts ranging from 0 to 1000 m s^{-1}, in 10 m s^{-1} increments. All spectra were compared to the first, zero shift "master" reference, and differences between measured and artificial offsets were plotted against the input shift. Plots like Fig. 2.94 confirmed that 10^{-3} pixel movements can be recovered indeed, even with such a coarse 1.9 pixel sampling. It was also demonstrated that unbinned TRES data provides RV precision almost 50% better, thanks to the slight oversampling of FWHM=3.7 pixels.

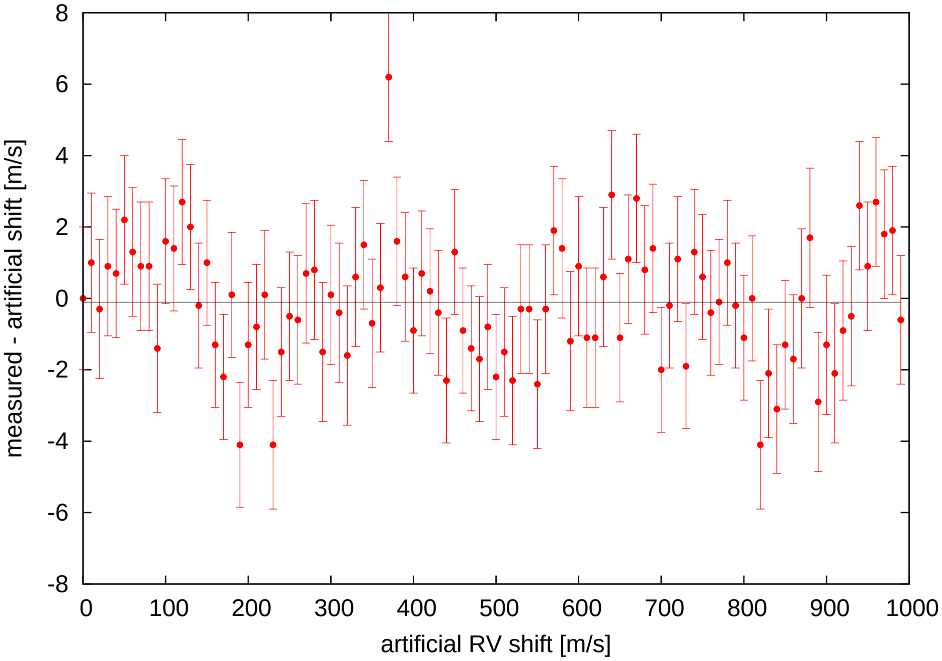

Figure 2.94: ***Testing the RV measuring methods***. *Residual between the artificial shifts put into the synthetic template and the measured values are plotted, as measured by the Lomb-Scargle based cross-correlation code.*

2.10.7 Application Examples

In this chapter I would like to present some of the very early scientific results and benchmarks of TRES, to conclude the lengthy instrument development phase – and also to close this section of the thesis.

First Publication with TRES

The very first result of TRES to be published is accepted by Astrophysical Journal, in Jonathan Devor's paper "T-Lyr1-17236: A Long-Period Low-Mass Eclipsing Binary", a 0.68 + 0.52 solar mass (K5+M0) pair with an 8.4-day orbital period. This EB was found through a systematic search of the Trans-Atlantic Exoplanet Survey (TrES) data base. Such long-period low-mass EBs are critical test cases for resolving the long standing discrepancy between the theoretical and the observational mass-radius relations at the bottom of the main sequence.

Devor has used the NIRSPEC instrument on the 10 m Keck telescope to obtain RV values for this very interesting system, as well as TRES on the 1.5 m telescope at FLWO. The phased RV values shown in Fig. 2.95 demonstrate, that for such project the two instrument perform very similarly, even though the huge discrepancy in light collecting area. Exposure time was 1000 s for the TRES spectra, using the middle fiber and 2 × 2 binning, for the $V = 14.37$ target.

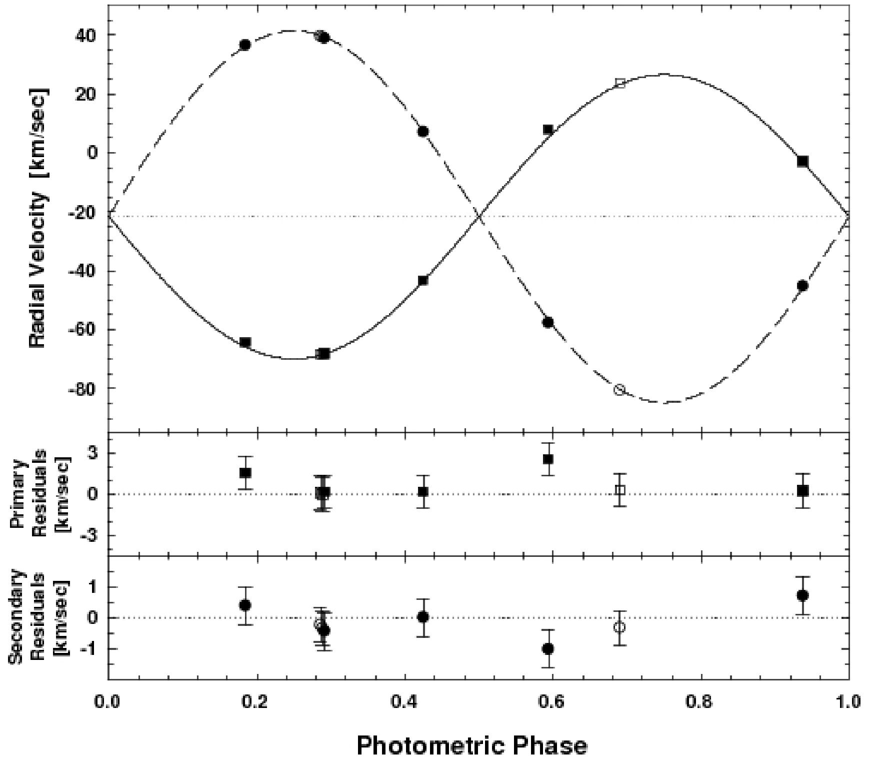

Figure 2.95: ***The first published measurements with TRES***. *The two dat apoints at phase 0.3 are overlapping with one Keck data, therefore the open symbols of TRES are not well visible. However, this tells how good is the agreement between the two instruments.*

Performance Test: υ And

Benchmarking an instrument and exploring its limits needs a very though test. Looking for solar-like oscillations means pushing the RV precision down to the 2-3 m/s level. However, if the precision requirement is not met, it is hard to tell exactly how the spectrograph could perform in less demanding applications. Choosing υ And as a test target provided two levels of precision–testing. As an F9V star it is expected to show similar oscillation modes than observed in case of β Vir (an F8V star, see Carrier et al. 2005). Besides, this star also hosts a planetary system (Butler et al., 1999) with a 4.617 day orbital period for the innermost planet. Even TRES would fail to detect solar-like oscillations, the well known 75 m s^{-1} amplitude RV variation due to this planet could serve as a larger-scale performance test for the instrument, as suggested by László L. Kiss.

Such benchmarking observations were carried out with the magnanimous help of Jose M. Fernandez, between Oct 24 and 29, 2008. As the expected oscillations have a ~10 m period, exposure times were kept under 3 minutes and binning mode was set to 2×2 in order to minimize readout time. Altogether 719 stellar spectra were taken, with the simultaneous ThAr spectrum recorded as well. S/N ratio ranges from 200 to 330, while exposure times from 60 s to 240 s were used, depending on airmass and weather.

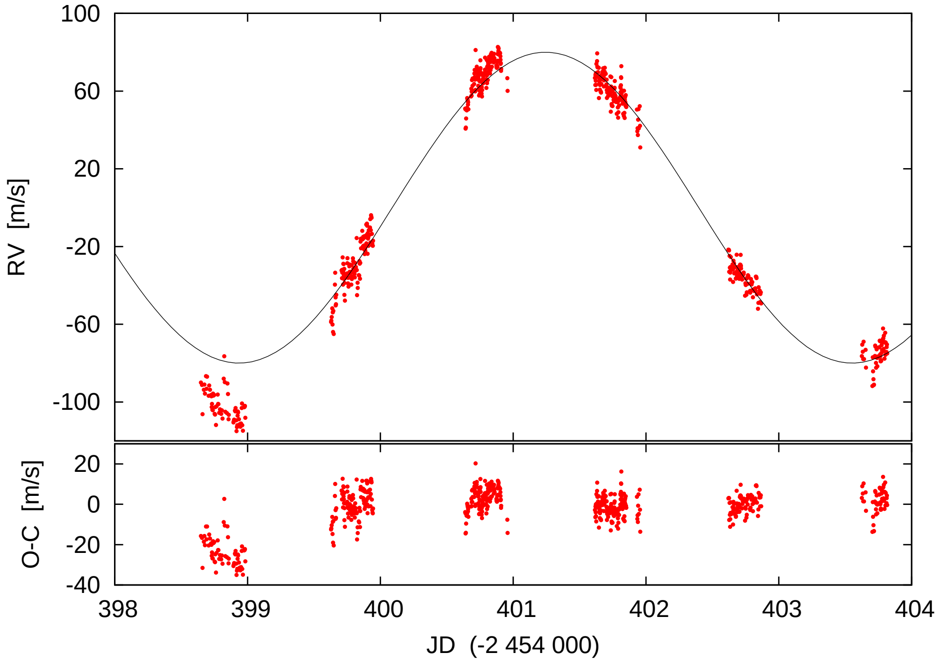

Figure 2.96: ***RV curve for υ And***, *after correcting for instrumental shifts (compare with Fig. 2.89) and for guider offsets (see Fig. 2.92). The sinusoidal curve has a 80 m s^{-1} amplitude and the published 4.617123 day period of υ And b.*

As shown in the previous chapter, TRES with the current guiding system is likely not capable of detecting oscillations. Also, as found by the evaluation of data reduction methods, an unbinned CCD mode would be desired to to reach the precision needed for astroseismology. However, the signal of the innermost planet could be easily recovered from the data (see Fig. 2.96), by correcting for RV offsets in the obvious cases of guider error (if a given 1-hour-long data set was off compared to the neighboring stellar data sets).

The residuals shown in Fig. 2.96 were calculated by subtracting a sinusoidal fit. The phase of the fit was fixed, only the amplitude was adjusted to match the actual data. The mid-transit epoch of the planet is published as $JD = 2\,451\,807.581$, which results maximal blueshifted velocity on $JD = 2454401.25$, at phase 0.75 after 561 full orbits, each $d = 4.617123$ days. This is seen in TRES data exactly, as the residual is flat, although the amplitude is slightly larger than the nominal (80 m s^{-1}). Note, that the first night RV values are significantly off. This can be due to temperature difference and/or due to modulation of the other planets in the system.

Although it was very unlikely after all, that TRES could have recorded the stellar oscillations of υ And , a Fourier spectrum was calculated (see Fig. 2.97). As expected, there is no sign of any oscillation, since the instrumental shifts, the tracking error between the science and calibration fibers, and the guider errors have erased this signal.

However, this was an “out-of-the-box” measurement. Based on data reduction experiences the oscillations could be measured if previously discussed stability/guiding problems are fixed.

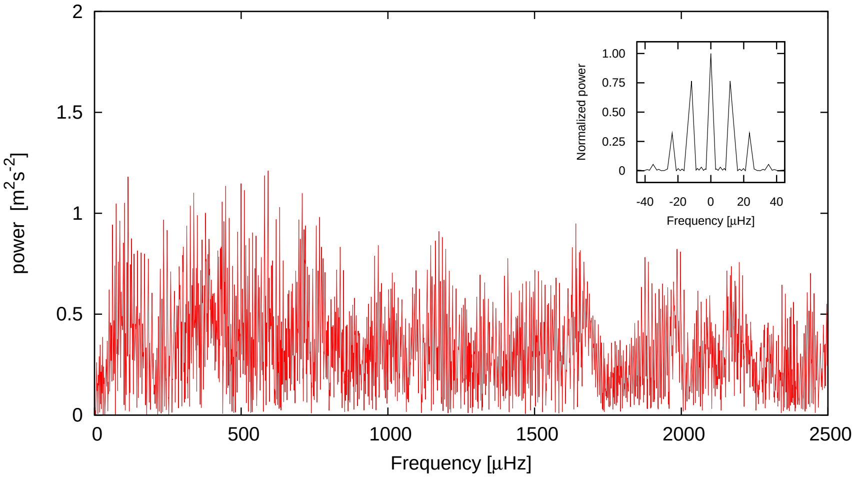

Figure 2.97: ***FFT spectrum of the residual RV values of the υ And measurement****, with the lowest frequency terms (aliases due to the sampling) removed.*

HADS

High-amplitude delta Scuti (HADS) variables are Pop. I stars close to the main sequence or evolved Pop. II objects (“SX Phe variables”), pulsating in the radial fundamental mode with typical periods of 0.05–0.15 days and amplitudes up to 0.5–0.7 mags. The pulsations are associated with huge atmospheric motions: radial velocity curves show velocity amplitudes up to 50–60 km s^{-1}, from which 5-10% relative radius change can be deduced. Because of the very short pulsation periods, measuring HADS radial velocity curves has been quite difficult. The optimal time resolution requires about one measurement every two or three minutes to avoid phase smearing, which is a hard limitation for getting high or medium spectral resolution observations with high S/N ratio.

As the phased RV curve (Fig. 2.98) and phased spectral samples (Fig. 2.99) show, TRES was successful to record a good quality data set for the HADS star BE Lyncis. Using the small fiber and 2×2 binning, with 5 m exposure times, the achieved S/N ratio is ~ 90 per pixel (with the resolution element being 1.8 pixels) for the $V = 8.8$ star.

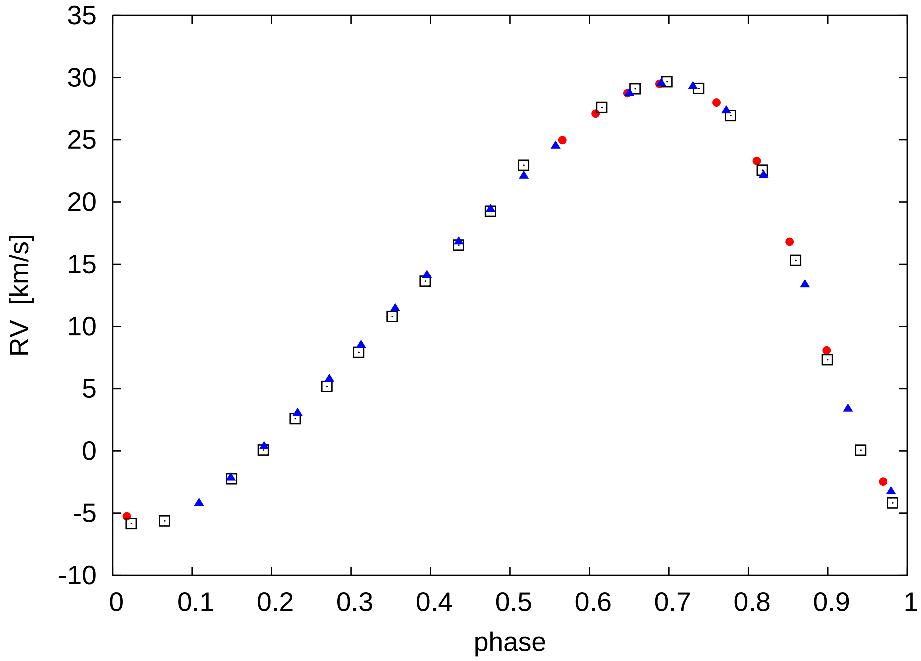

Figure 2.98: ***Phased RV curve for the high amplitude δ Scuti star BE Lyn****. The different symbols distinguish data from three consecutive nights. The period is $0\overset{d}{.}0958695$ day.*

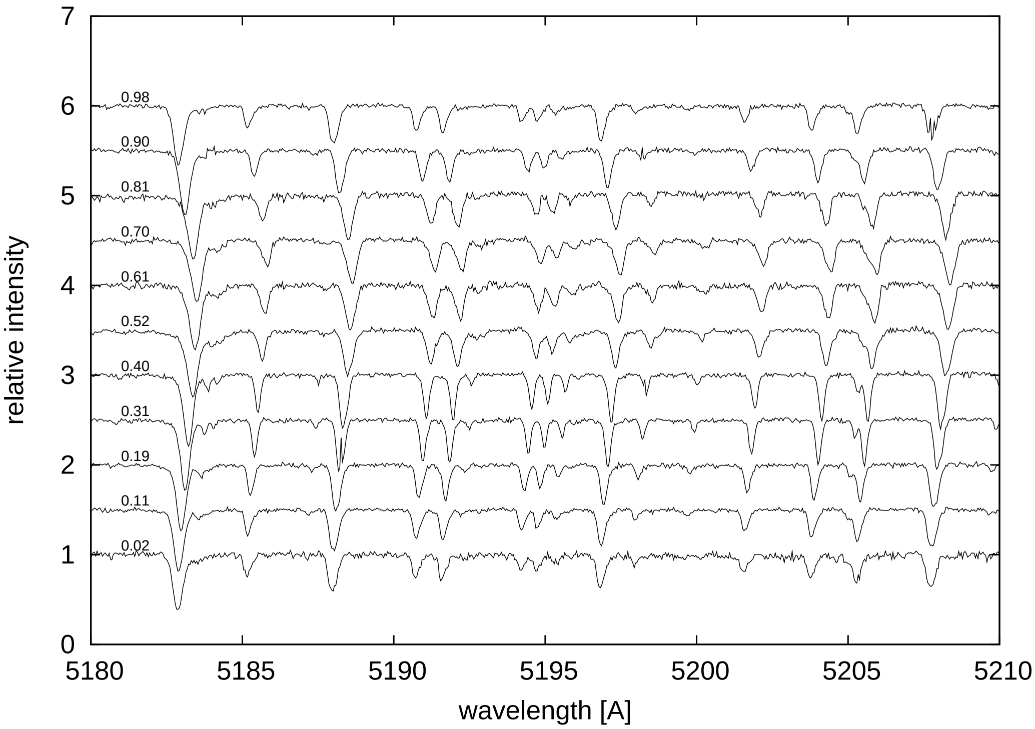

Figure 2.99: ***Spectral samples from different pulsational phases of BE Lyn****.*

Faint Stars

To demonstrate what kind of signal levels, S/N ratio can TRES achieve, two orders (within the V band) of the spectrum of a $V = 12.3$ is presented on Fig. 2.100. See figure caption for details.

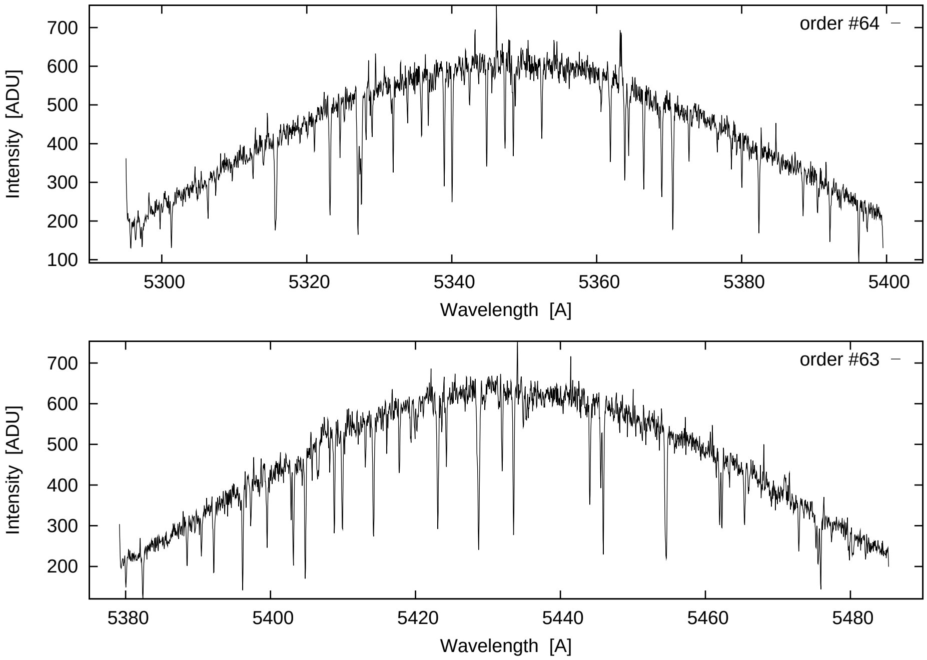

Figure 2.100: ***Sample spectrum of a*** $V = 12.3$ ***star*** *– count levels for a 10 min integration* (3×10 *min exposures median combined), 1.″4 fiber,* 2×2 *binning, 1.″5 seeing, airmass of 1.04. Gain is 1.0* e^-*/ADU.*

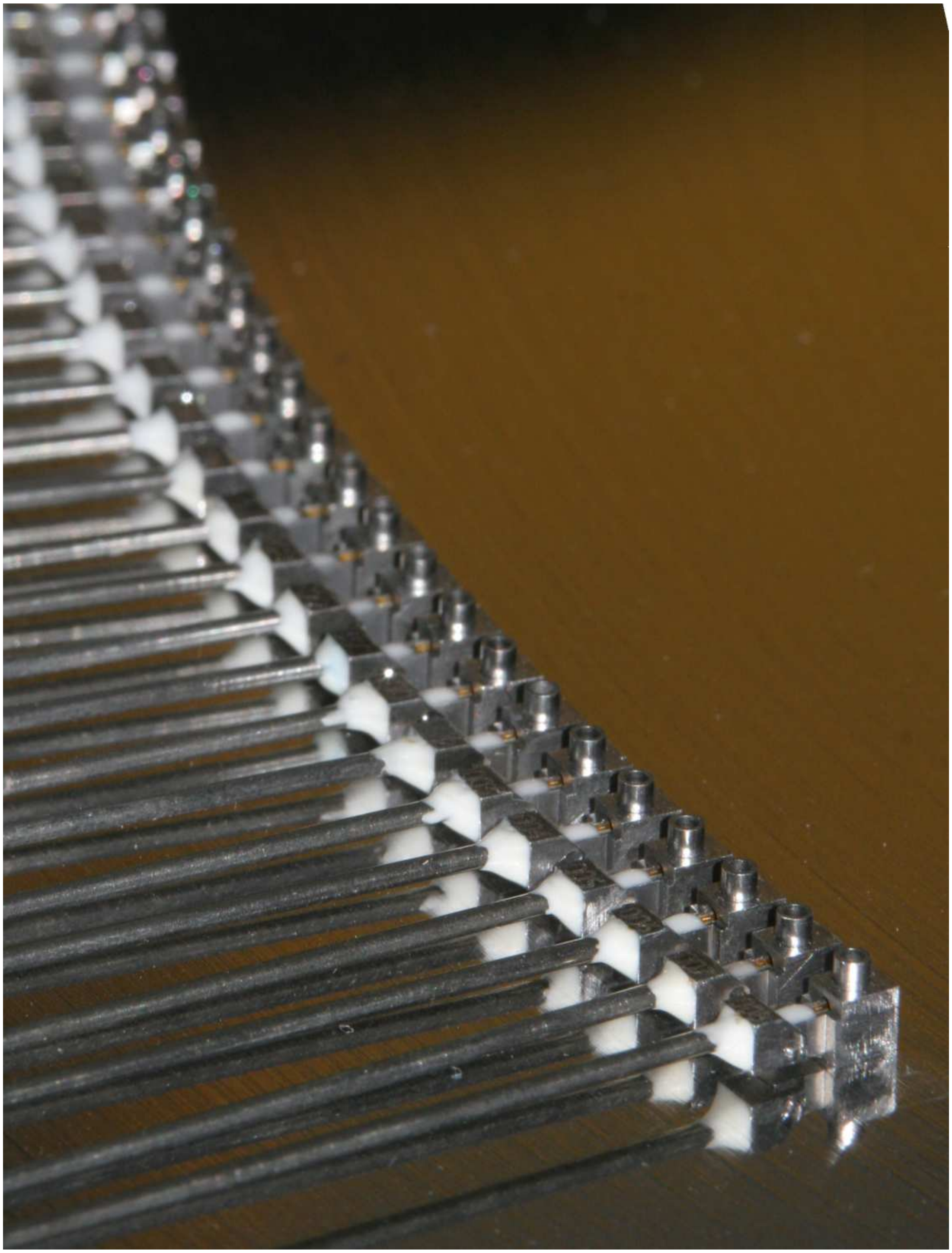

Fiber buttons on the MMT/Hecto focal surface *– placed in a calibration ring configuration)*

Chapter 3

Hectochelle – The Multiobject Advantage (and drawback)

3.1 Description of the Instrument

3.1.1 The f/5 MMT

The MMT is an alt-azimuth mounted 6.5 m Cassegrain telescope operating with a single primary mirror after the 1999 post conversion of the original, 6-mirrored Multiple Mirror Telescope (and thus now termed the Monolithic Mirror Telescope). The MMT is operated by the MMT Observatory (MMTO), a joint venture of the Smithsonian Institution and the University of Arizona. The MMT is located on the summit of Mt. Hopkins, the second highest peak in the Santa Rita Range of the Coronado National Forest, approximately 55 kilometers (30 miles) south of Tucson, Arizona. The MMT is on the grounds of the Smithsonian Institution's Fred Lawrence Whipple Observatory.

Besides the f/9 and the unique, adaptive f/15 secondary mirrors, there is a 1.7 m secondary available providing a wide field f/5 telescope configuration (Fabricant et al., 2004). A refractive corrector, designed by Harland Epps, is an essential part of the optical design delivering sharp, aberration free images up to a 1° field of view. The Wide Field Corrector (WFC) consists of a group of all-spherical fused silica lenses, with a diameter of $\sim$ 0.8m. It has two modes of operation. If used for wide field spectroscopy, in which case the FOV is 1°, the focal surface is curved (8 mm sag over 600 mm diameter) but highly telecentric. In order to maintain high spectrograph throughput at large zenith distances, the three element corrector is followed by a pair of counter-rotating zero-deviation ADC prisms. Like the lenses, the prisms are made of UV transmitting glasses (FK5 and LLF6) to aid high sensitivity in the blue spectral region. In its imaging mode, the WFC has a $0.^{\circ}5$ diameter field and a flat focal surface. In this alternate mode the corrector is reconfigured by removing the ADC and the last WFC lens, and a different fused silica element is added. The system works over the 320 to 1800 nm range, but the Sol-Gel anti-reflection coatings are optimized for the 320 to 1000 nm band.

The optical performance of the f/5 MMT is excellent. On-axis the best images recorded have $0.''4$ FWHM, and this is pretty much maintained over a $24'\times24'$ FOV. At the edge of the spectroscopic field the best recorded images have 0.5 arcseconds FWHM, near the limit allowed by the optical design. Of course this requires the active control of telescope mirrors, which is achieved by the f/5 Wavefront Sensor (WFS). The unit contains two instruments: a commercial Shack-Hartmann wavefront sensor and a rapid deployment science camera (SITe 1024x1024 CCD with $0\farcs14$/pixel resolution) equipped with UBVRI filters. Either instrument can be deployed on-axis or up to 30 arcminutes off-axis. The f/5 WFS is mounted on the instrument rotator, between the WFC and the Cassegrain port instrument.

There is a wide range of f/5 instruments available: Megacam, a 36-CCD optical imager covering $24'\times24'$ FOV; SWIRC, a Y, J, and H near infrared imager; Hectospec, a moderate-resolution (R$\sim$6000) multiobject optical spectrograph fed by 300 optical fibers; and Hectochelle, a high-resolution (R$\sim$34,000), multiobject spectrograph fed by Hectospec's fibers. Two additional instruments are under construction: Binospec, a moderate-dispersion direct optical spectrograph using up to 150 slitlets located within a $16'\times15'$ region; and MMIRS, a NIR ($1-2.5$ μm) imager/multiobject spectrograph.

3.1.2 Fiber Positioner and Fiber Run

Due to logistics of storing all these and other f/9, f/15 instruments and secondary mirrors, the two bench mounted Hecto spectrographs are located permanently one floor above the observing deck. Therefore fibers of 26 m in length are required to deliver starlight to the dedicated spectrograph room. The broadband, low OH content STU fibers (see Fig. 1.13) provide good transmission over this length, while FRD is acceptable at 95% level for the f/5.4 actual focal ratio. The fiber diameters are 250 μm, or $1\farcs5$ at the MMT f/5 plate scale.

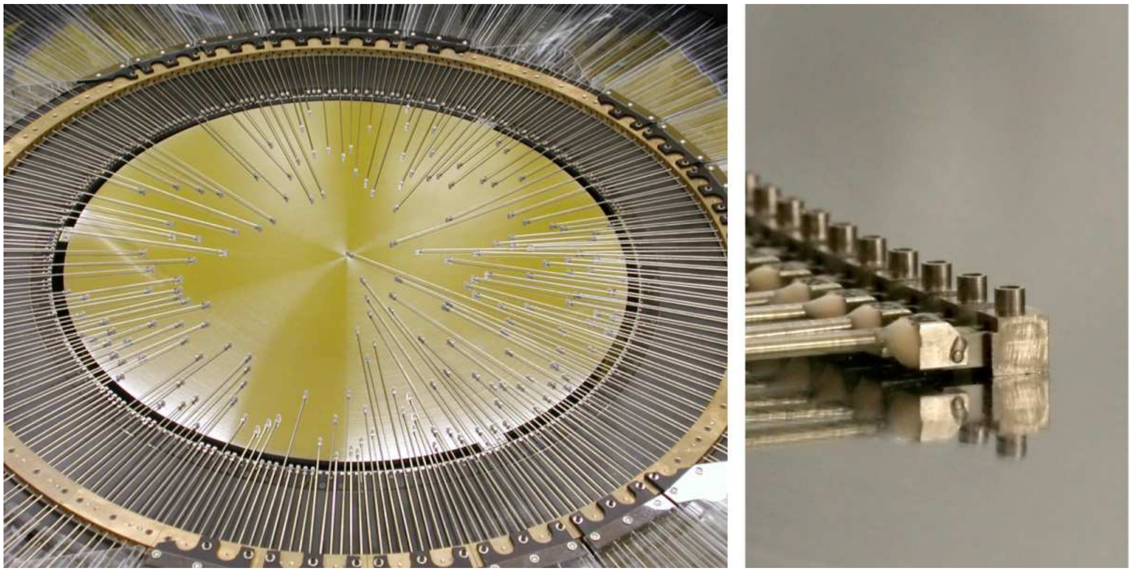

Figure 3.1: ***The MMT/Hecto positioner focal surface*** *with fibers deployed in a real configuration (left) and a close-up view of fiber buttons placed in an arc configuration.*

The fibers can be deployed over the 600 mm curved focal surface radially from its perimeter, as it is shown by the left panel of Fig. 3.1. Fiber ends are equipped with a right angle prism, which directs starlight into the light guides oriented perpendicular to the optical axis of the telescope. These prisms are mounted inside a “fiber button” (right panel of Fig. 3.1), which has a magnet on its bottom to secure the fiber onto the metallic focal plate. Two robotic positioners, named Fred and Ginger, can place all 300 fibers buttons for observation in just 300 seconds, with an accuracy of 25 μm or better. The fibers are carefully stress relieved and de-rotated inside the positioner unit, so they all leave the telescope at a point fixed and stationary respect to the Cassegrain focus.

The fibers are individually protected by teflon tubes over the 26 m long run towards the spectrographs, while intermittent thermal breaks help to avoid thermal induced stress. Mechanical protection is achieved by bundling and jacketing the fibers, and guiding them within an external, flexible frame, a commercial heavy duty cable guide/chain. At the instrument end the fibers are arranged in two columns to form a pseudo-slit, mounted within a very narrow profile "fiber shoe" (see Fig. 3.2). The shoe is attached to rail system, mounted on the ceiling of the spectrograph room, so it can be easily moved from one optical bench to the other. The operation to switch from moderate (Hectospec) to high resolution (Hectochelle) only takes 15 minutes, but usually not performed during the observing nights. Because Hectochelle and Hectospec both use the same fiber feed, but have different magnifications, only 240 fiber images fall on the Hectochelle focal plane format, while Hectospec exploits all 300 available fibers.

3.1.3 The Hectochelle Optical Bench

The starlight exiting from the fiber leaves the fiber shoe (see Fig. 3.2) and gets paralleled by the aluminum coated spherical collimator mirror. The shoe/pseudoslit is internal to the collimated beam, so its profile is very narrow in order to minimize obscuration. The dispersive element is a mosaic system, consisting of a pair of 300 × 400 mm Richardson grating laboratory aluminum coated reflection gratings, ruled at 110 lpm and blazed for R2 (64°.5). The gratings are co-registered on a precision bonded Zerodur metering structure which matches the coefficient of thermal expansion of the Zerodur grating substrates. The angle between the incident and diffracted beams is 15°. The angle of incidence can be precisely adjusted to shift wavelength coverage, if necessary, as the grating assembly is mounted on a rotary stage.

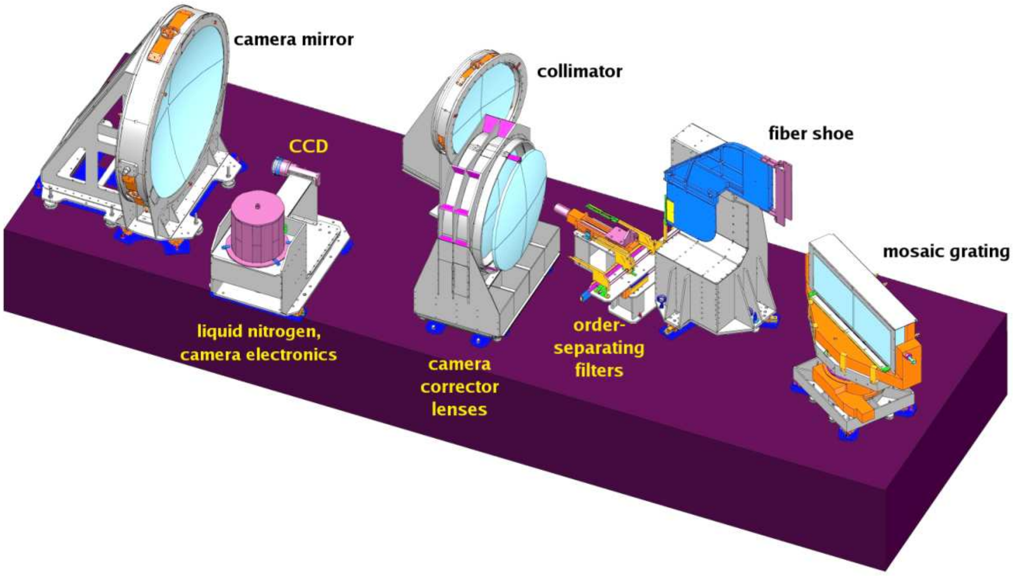

Figure 3.2: ***The Hectochelle optical bench.***

The Hectochelle employs a spherical doublet refractive corrector made of fused silica and anti-refection coated with Sol Gel to maximize throughput. The camera mirror is a 1.1 m diameter Zerodur sphere that is f/0.6. This is coated with enhanced aluminum. The detector is internal to the dispersed beam, and so its cross section was also minimized. The LN2 tank is external to the beam, located on the edge of the bench with a very narrow cold finger running into the CCD camera. The field flattener, an all spherical fused silica lens, also serves as a vacuum window for the cryostat. The CCDs themselves are a pair of EEV 42-90 back illuminated deep depletion devices, with 2048×4608 resolution each. Pixel size is 13.5 μm (same detector as for TRES). The readout system is an extremely flexible, high speed architecture developed at SAO and now in use for virtually all its new ground-based optical and infrared instrumentation.

Hectochelle is a single order echelle spectrograph, trading the extensive wavelength coverage (multiple orders) to multi-object capacity. To achieve this there is no need for a cross disperser but an order separating filter is required. The optimal location is right in front of the pseudoslit, where a linear stage and an actuator can select one of the filters and erect it into the beam. Eleven interference filters are currently available for Hectochelle observations, covering diffractive orders with astrophysically interesting spectral features (Hα, [O III], Ca H and K, etc.).

In order to make fiber mounting physically possible inside the very narrow shoe, and also to achieve optimal inter-aperture[1] separation, the fibers are mounted in two columns supported by the two side-plates of the shoe. Fiber ends follow a zig-zag pattern: a fiber end of the left column is located vertically in between two fiber ends of the other column. There is an additional set of six fibers available, called the external calibrator. These fibers are in 3 groups, each has a small (100 μm) and a "regular" Hectochelle fiber (250 μm), next to each other. (Unfortunately one detector only sees one pair at its edge, while the other CCD records two pairs.) These fibers can be attached to the side of the shoe to project ThAr light into the instrument at 6 aperture locations during the science exposures. The purpose is to track instrumental shifts simultaneously with the observations.

Recalling the discussion in §1.4.2–1.4.3 it can be noted, that the optical arrangement of Hectochelle ($\alpha > \beta, \gamma = 0$) does not provide the highest possible grating efficiency due to the relatively large Littrow angle ($\theta = 7\overset{\circ}{.}5$). In this case other constraints (the size of the room and the fact that two spectrographs had to fit inside, sharing the same fibers which should be easily moved from one bench to the other) justified this setup. Still, the the peak efficiency reaches 7% in terms of the total light striking the primary mirror.

3.2 Alignment and Performance

3.2.1 Optical Alignment — of Mosaic Gratings

My first task as a CfA predoctoral fellow was the optical alignment of Hectochelle. The procedure was very similar to the one described in §2.9.5, except the optics were more sensitive due to the fast focal ratio and because the optical elements were larger. To achieve the best image quality ThAr test exposures were examined by generating plots similar to the one shown in Fig. 2.80. Adjustments were performed on a trial-and-error basis, and by attempts to model the observed aberrations in Zemax using decenter, tilt and defocus.

---

[1] Unlike for TRES, or other single object echelles, the recorded spectrum consist of the same spectral order of different objects. Therefore the spectra are referred as apertures, instead of orders, and thus inter-order separation becomes inter-aperture separation.

There was one significant departure in the alignment process, though, due to the mosaic grating. I was not able to suppress some image blur, which exhibited very different shape by using only one half of the grating at a time. As it turned out even though at blaze angle one can observe (almost perfectly) overlapping spots, going to zero order these images become obviously separated in space as well as in dispersion. If alignment is only performed at blaze angle, small misalignments of the grating can not be discovered and can result in significant image quality degradation.

As future spectrographs of the upcoming extremely large telescopes are likely to have huge (meter-size) beams, creating and aligning large dispersive elements by mosaicing small ones together seems to be an important aspect. Custom gratings up to 800 mm in length (e.g. HARPS) can be manufactured by replicating a master onto a single substrate multiple times, but this method has its limitations, too. Mechanical alignment of smaller gratings have been successfully used in the past (e.g. HIRES on Keck), but optical alignment of these mosaics have to be done very precisely, not to compromise image quality. This can be done "outside" of the spectrograph, or as summarized below, by using the spectrograph itself. Although it requires a rotary stage for the grating, the process is very fast and straightforward. Due to the likely need of such alignment procedure in future instruments, I felt it useful/important enough to briefly summarize it below:

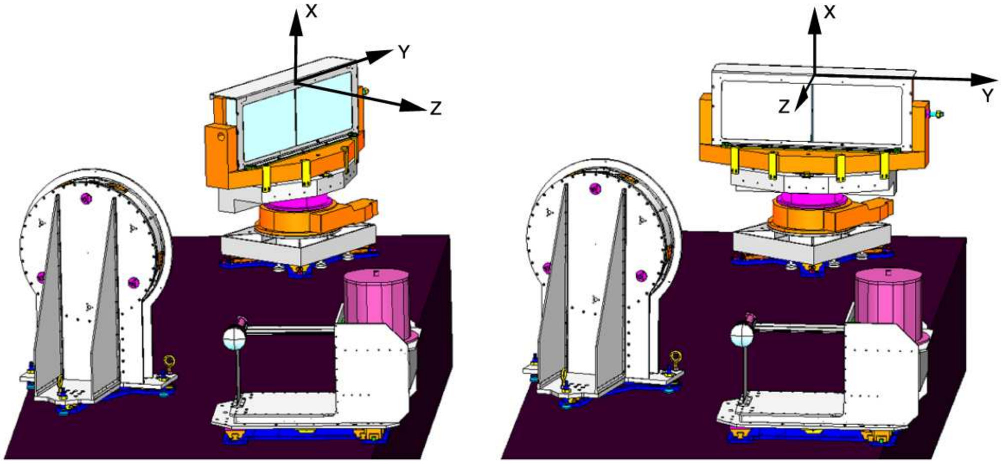

Figure 3.3: ***Steps of iterative mosaic grating alignment****: the mosaic grating set to blaze angle (left) and to zero order (right). For clarity only the collimator, grating and camera is shown (see Fig. 3.2)*

The optical configuration is shown in Fig. 3.3, a simplified version of Fig. 3.2. The grating, with the dispersion axis running along Y, can be rotated around the X axis from the blaze angle (left) to the zero order (right) position. In this latter case the grating acts as a (low reflective efficiency) mirror, and a white light, single image of the fiber ends are formed. At blaze, all the very narrow facets act like mirrors, and this picture helps to understand how a given movement of the grating would affect the image.

At zero order (very close to normal incidence) the three possible misalignments of the grating halves, tilt in X, in Y, or rotation (tilt in Z) would be observed as:

- tilt in X: the zero order spots are separated in dispersion (right panel of Fig. 3.4)
- tilt in Y: the zero order spots are separated in space (right panel of Fig. 3.4)
- tilt in Z: it has no obvious effect on zero order spots and spot positions

The tilt in X slightly changes the angle of incidence and therefore, due the grating equation, the angle of refraction changes slightly. This displaces the part of the beam (falling onto the misaligned grating) along the dispersion axis (Y). Or, treating the zero order grating as a mirror, looking at the right panel of Fig. 3.3 the spot movement is obvious.

Rotating in Y means that the illumination is off from the plane perpendicular to the groves ($\gamma \neq 0$). Such tilt of the beam does not change the angle of incidence (α) in the grating equation, so the spots do not separate in Y. But there is a displacement in X, which is apparent from Fig. 3.3 when thinking of the zero order grating as a flat mirror.

Only considering the zero order spot no rotation along Z can be detected. However, connecting the $\pm1, \pm2, \pm3, \ldots$ orders for both grating halves, forming the "line of dispersion" for both gratings such lines would be tilted to each other if this kind of tilt (the groves are not parallel on the two gratings) is presented. In such case those lines would intersect at the zero order points, and therefore zero order imaging is completely insensitive for this kind of misalignment in the gratings. If only the zero order image is recorded by the detector, no correction can be determined. But, going to blaze angle, this is possible.

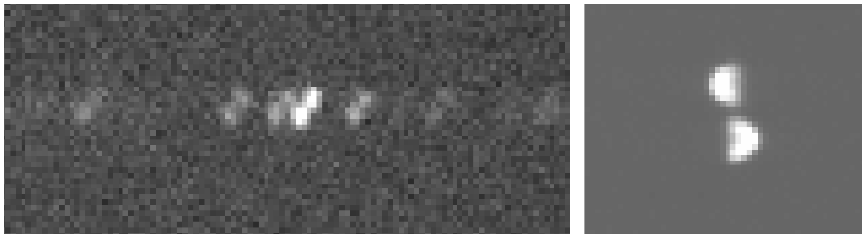

Figure 3.4: ***Steps of iterative mosaic grating alignment****: misaligned image at blaze (left) and at zero order (right).*

At blaze (close to Littrow configuration) the above mentioned things change (left panel of Fig. 3.3):

- tilt in X: the spots (each of them, and now we have a lot, since we have a spectra) are separated in dispersion (left panel of Fig. 3.4)
- tilt in Y: the spectral order (the curve formed by connecting the individual spots produced by a given grating half) belonging to one grating half is tilted to the other order, like the "line of dispersion" was tilted at zero order (normal incidence) in case of a tilt in Z
- tilt in Z: a spectral order is displaced to the other one in space, like the effect of a tilt in Y at zero order (left panel of Fig. 3.4).

To rotate one grating half in X it means we rotate around a vertical axis, so we are changing the angle of incidence. Therefore the effect is the same as before, too, at zero order: the spots separate in dispersion.

Tilt in Y: since the blaze angle is high (close to 90°), it is almost like rotating one grating half around the line of our sight. This means that the dispersion axis is not horizontal any more (if we rotate one grating in Y by 90° that is equivalent of having a vertical dispersion axis). However, such "rotated" order still crosses the other, horizontal order at the center of the detector unless other tilts are introduced. So, at blaze (or close to Littrow) this kind of tilt in the grating results more of an order rotation than displacement at the image plane.

To understand tilt in Z remember again that the blaze angle is very high (close to 90°). Tilting one grating half in Z is almost like a rotation of that grating around an axis which is horizontal, and at the same time perpendicular to our line of sight. With the conceptual image of facets as several narrow mirrors we can see this kind of rotation as a tilt of those mirrors around a horizontal axis, And this, of course, displaces the spectral orders vertically (in spatial direction) on the detector. So, this works just like the tilt in Y at zero order.

All in all, even if the gratings are tilted in Y and Z, these aberrations can be almost compensated by each other at blaze. Although at zero order the tilt in Y can be seen, because the spots are separated in space, the tilt in Z remains completely hidden. Tilt in X results in the same scenario at zero order or blaze.

But in the case of compensating errors (a tilt in Y and just the right amount of tilt in Z) the spots still can not match perfectly *everywhere* on the image plane. It is apparent since the tilt in Z is not a pure displacement, but it introduces some rotation of an order as well. And vice-versa, a rotation in Y also means a small displacement, not just rotation. Therefore to set the gratings properly an iterative alignment can be performed, by switching from zero order to blaze back and forth a few times.

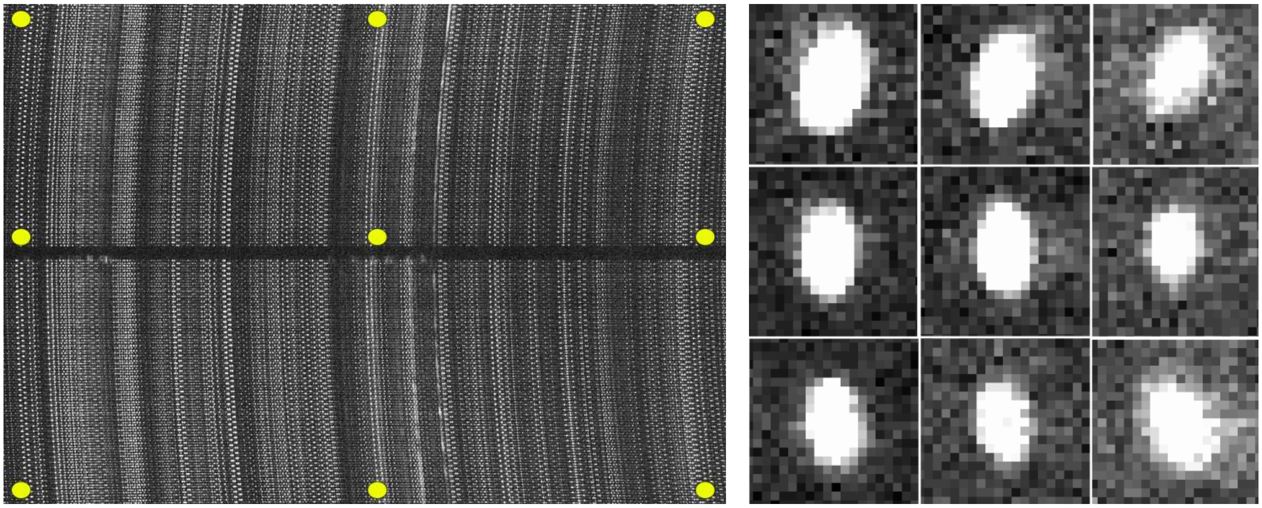
(a) (b)

Figure 3.5: ***A sample ThAr frame*** *(5150 – 5300 Å, left) with yellow dots indicating the locations of the enlarged arc lamp features (right). Note the strong "color" on the left frame: location of a given line follows not a vertical but a bent trace. Also note the very different line tilts, clearly visible on the right.*

3.2.2 Image Quality

The alignment succeeded to provide nearly equal FWHM values across the entire spectral image (see Fig. 3.5), the measured values range from 3.9 to 4.1 pixels (from center to corners). In the so called RV31 band, covering sharp Mg and Fe features in the 5143–5300 Å region, this corresponds to a spectral resolution of $R = 38\ 000$. Note the strong line tilts in Fig. 3.5 (see also §1.5.2).

3.2.3 Instrument Stability

In the Hectochelle data sets there are obvious zero point shifts, both short and long term. The main reason is the lack of active temperature control. Due to limitations in space, since the Hectospec and Hectochelle bench spectrographs pretty much fill the entire room, it was not possible to build an adequate thermal isolation shield around the instruments. Although an inside-of-room enclosure was laterally squeezed in between the optics and the walls of the room, made out of a 2 inch thick aluminum–foam–aluminum sandwich panels, the passive system did not fully eliminate the problems. Therefore during data reduction attention still should be payed for correcting/eliminating thermal/environment related changes.

Thermal Effects

Temperature changes (both in overall room temperature and gradients within room/ optical bench) had been monitored during the first couple of years of operation. As a result the severe effects of LN2 fills had been discovered (see Fig. 3.6), along with the strong daily (up to several °C) and long term changes. The former source was eliminated by installing a vacuum jacketed fill and a well insulated exhaust LN2 lines. The daily variations can be reduced by positioning the building such a way during the day, that the wall of the spectrograph room always stays in the shady side. As it is apparent from Fig. 3.6 the temperature change mostly causes spatial shifts, but displacements in dispersion also occur at the several 100 m s^{-1} level.

Environmental Effects

Since the entire MMT building rotates during tracking of an object, including the spectrograph room, the azimuthal position of the dome was correlated against instrumental drifts. While the smooth trend of Fig. 3.7 is likely due to temperature changes (compare to Fig. 3.6), the sudden spatial jumps (at $3^h\ 15^m$ and $5^h\ 40^m$ UT) are clearly related to rotation. The related discontinuities in dispersion direction, fortunately, are not significant.

Shear of Mosaic CCDs

The sensitive RV measurements unveiled a problem in the CCD camera temperature controller very early. The detectors were stabilized only at the ±0.1 °C level, causing the two pieces of the mosaic array to move respect to each other. This shear happened only during exposures when the heater on the detector cold plate turned on, to prevent temperature dropping below the −120 °C setpoint. It is likely that the heat did not get distributed evenly, due to the very

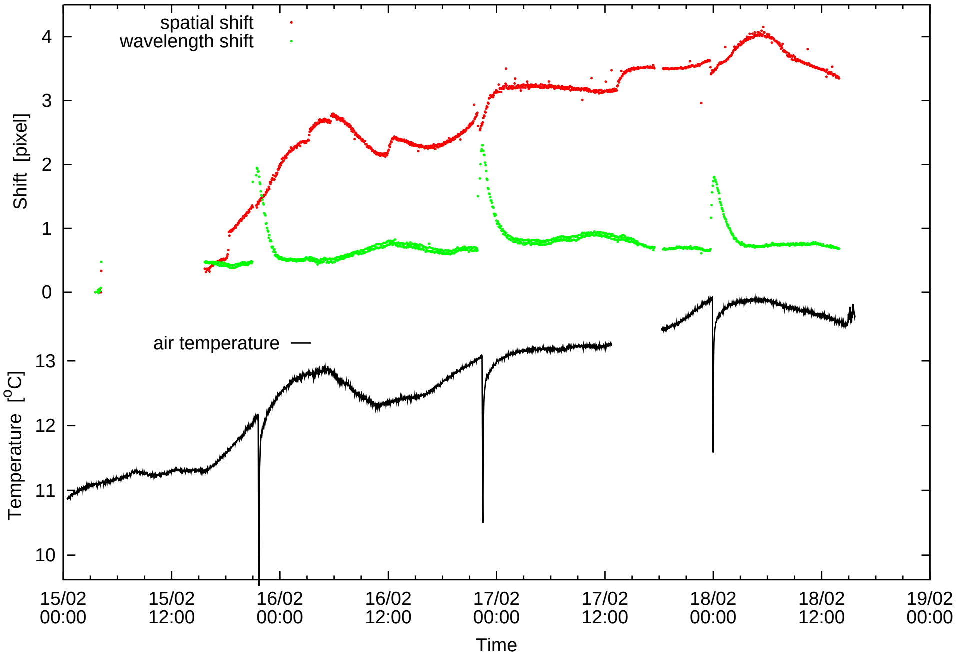

Figure 3.6: ***Instrumental shifts found in Hectochelle***, *in spatial (red) and in dispersion (green) direction (for the latter 1 pixel corresponds to* ~ 1.9 *km* s^{-1}*). The correlation with temperature (black) is apparent, especially for the sudden cooldowns caused by dewar fillings.*

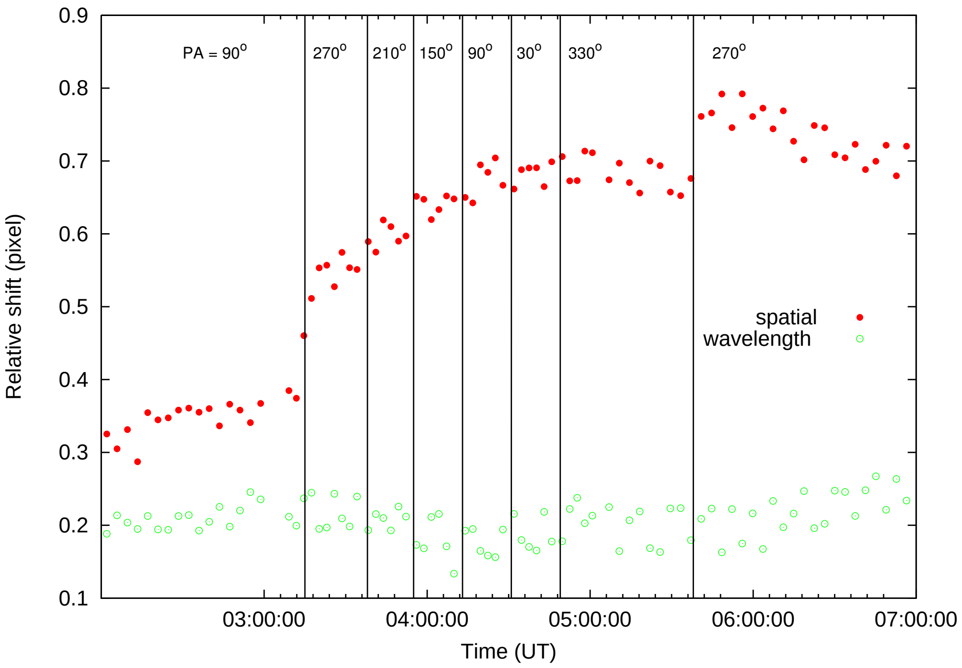

Figure 3.7: ***Effect of telescope/building rotation.*** *While the smooth trend is likely due to temperature changes, the sudden jumps are related to movements of the building.*

limited number and uneven positioning of heater resistors, causing ∼100 m s^{-1} RV signal between apertures of the two detectors (see Fig. 3.8).

Similar effects are unavoidable even with more precise control systems (at mK level), as reported by the HARPS instrumental team (Pepe, personal comm., 2006). If the entire instrument is stable at <1 m s^{-1} level, the warm-up of the detector due to frequent readouts can be detected.

Therefore it is recommended to use monolithic detector arrays if possible, or handle the data of mosaic systems circumspectly.

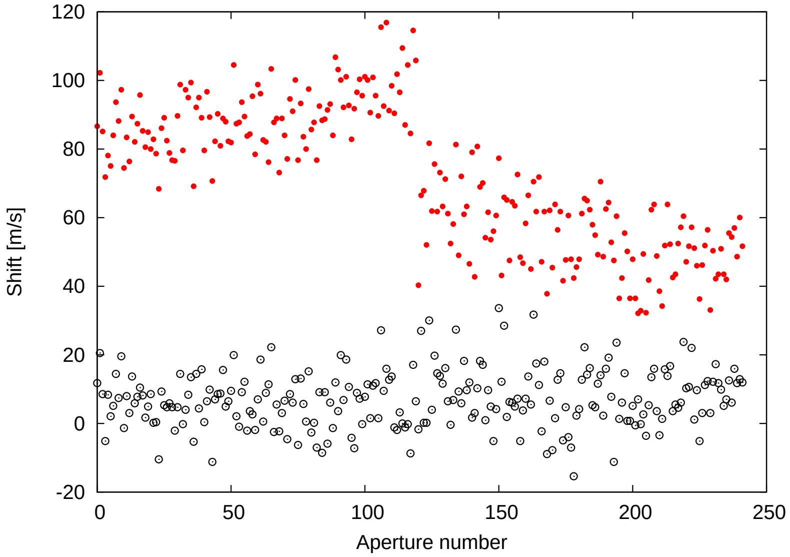

Figure 3.8: ***Shear of the mosaic CCD array*** *due to inadequate detector temperature control (accuracy level of ±0.2 °C), as shown by comparing RV of apertures against each other within two separate frames (black and red).*

3.2.4 Benchmarks

Observing is very efficient with Hectochelle. A given fiber configuration can be executed in ∼ 5 minutes, and also thanks to the robotic positioner target assignment and observing schedule of a night can be easily changed. Due to the large patrol field (1°) small objects (< 15′) are not fitted easily, since the finite size of fiber buttons does not favor very high target densities. Although centrally condensed fields, because of the radial fiber arrangement, can be easily configured. For target lists containing ∼ 1000 objects over a 1° FOV it is common to be able to create 4 fiber setups, with ∼200 objects assigned to fibers in each.

Fiber setup takes place at zenith pointing (5 min), than slewing to the target area takes another 5-7 minutes. This includes wavefront sensing on a nearby star, to set the components of the active optics. Setting up on guide stars is comparable to the calibration time (5 min), and during science exposures the only dead time is CCD readout at the order of 1 min. For a 3 × 20 min observation this results a duty cycle of 70%, and in terms of light efficiency the detector records 7% pf the photons hitting the primary.

CCD readout times (1 min) and RON (2.7 e^{-} = 2.7 ADU) values can be decreased by applying on-chip binning. Allowable options are 2×2 or 2×3, in the spatial and dispersion directions, respectively. While the 2×2 option does provides almost the same RV precision as the unbinned data, thanks to the 4.0 pixel unbinned sampling of the PSF, to detect faint objects (down to $V = 20$) resolution has to be sacrificed. Still, RV precision of 1 km s^{-1} has been reported in such instrumental mode (Mateo et al., 2008). Exploiting 1×1 binning a 3×10 min exposure can provide ∼100 m s^{-1} (§4.3.1) RV precision at $V \simeq 13$ — however this is not straightforward, as the calibration at this level is very critical.

To push Hectochelle towards its RV precision limit had exposed the difficulties of MOS calibration. Since such problems are (can be) common in other multi-object systems, a detailed discussion of the Hectochelle calibration system is given in the next chapter, within a broader context of MOS RV accuracy. All of this circumstantial testing and characterization of Hectochelle is needed to understand the capabilities of the instrument, and assure validity of multi-object RV survey data, which is the ground for the scientific results presented in Part III.

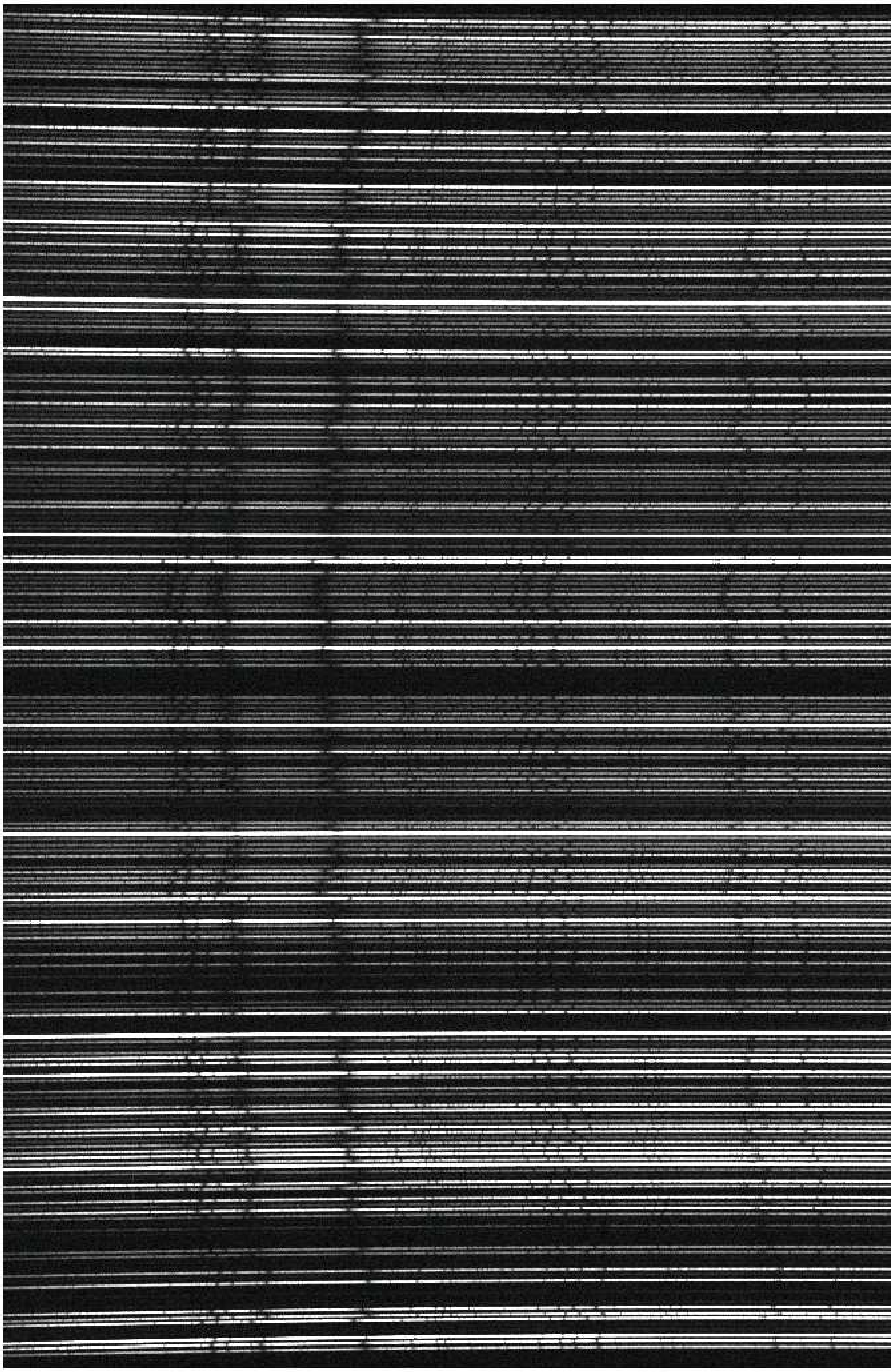

A sample multi-object spectra from Hectochelle – *recorded for stars with an average brightness of* $V = 12.8$ *(range of* $V = 10.6 - 18$*), with exposure times of* 3×10 *min and* 1×1 *binning, in the Mg band (5150-5230 Å, only half of the spectral order is displayed).*

Chapter 4

On the Accuracy of MOS Radial Velocity Measurements

Accuracy or precision? Well, for a MOS it is a good question. If a stellar target is observed through the same fiber multiple times during a short period, that can provide precision information. Moving the same target to a different fiber, though, re-measuring its velocity and comparing the value to that determined using other fibers, is probably better termed as internal accuracy of MOS.

The precision is depending on the stability of the instrument between exposures, or how much of the internal drifts can be measured and corrected for. Uncertainties in the pixel-to-wavelength mapping also influence precision. Therefore a high intensity, stable calibration source is required, and tracking of instrumental drifts is mandatory to reach high precision.

Changes of the zero point, for the entire instrument as a unit and on the fiber-to-fiber basis as well, degrade the accuracy. Systematic differences might (and do) exist between MOS apertures, as for each one there is a different fiber and a different optical path (pupil) within the spectrograph. But these variations, as shown below, are more-or-less constant and can be accounted for. However, zero point drifts of the entire instrument and small changes in the relative offsets are much harder to deal with. This also highly depends on the execution of wavelength calibration, and the stability of the calibration source/method.

4.1 Wavelength Calibration of MOS

4.1.1 Indirect vs. Direct Illumination

Since the scrambling in a fiber is not perfect (see §1.5.2) it is important to have a calibration system which mimics the illumination pattern of celestial sources. (Even if an optical scrambler is deployed in the fiber run, which MOS instruments so far have avoided due to complexity issues, still grate care has to be taken in order to prevent systematic errors at the 10 m s^{-1} level.) A simple and easy, convenientl way would be to illuminate a screen in front of the telescope aperture, like the widely used flat fielding for imaging applications.

However, the ThAr hollow cathode lamps used in high resolution spectroscopy do not have high luminosity, and the scattered light of already faint lamps is likely to provide inefficient intensity levels (see Fig. 1.22). Direct illumination can significantly increase light levels, and it has been applied to single object instrument: the light emitting surface of the lamp or an illuminated aperture (face of a fiber, e.g. HARPS) is re-imaged to the fiber entrance of the spectrograph by some optics providing a focal ratio equivalent to that of the telescope.

Simultaneous direct illumination is hard to realize in multi-object applications, where target locations are constantly varying and spread over a large focal surface area (a circle of 600 mm in diameter for Hectochelle). There are only a few realized solutions to this problem, as there are only a handful of high-resolution MOS instruments.

The Hydra spectrograph uses a scattering screen, but right in front of the focal plane, close to the fiber buttons. Therefore intensity levels are acceptable and all fibers can be calibrated at once. The screen can be closed for calibrations and opened for observing, and ThAr lamps are located along the perimeter of the focal surface.

The VLT/FLAMES calibration system is a direct light projection unit, illuminating one fiber at a time. The light source is mounted inside of the robotic positioner, and calibration is done by moving the gripper head over each fiber, one after an other. For ThAr each "flash" takes several seconds, and so calibrating the entire set of 130 fibers for the GIRAFFE spectrograph takes $\sim$ 12 minutes. (However, this accumulated time is comparable to total integration times used in the simultaneous calibration of Hydra and Hectochelle.) Therefore wavelength calibration is performed in the afternoons, and the solution is transferred in time based on a few (5) ThAr spectra recorded during the science exposures. Flat fielding is fast enough that it can be performed during the re-positioning of fiber heads.

For Hectochelle, the calibration system went through a few steps of evolution. Below I give a brief description of these stages and intermediate results, because I believe this can provide a better understanding of MOS calibration system design, while the comparison (§4.2) and discussion (§4.3) of the two methods (GIRAFFE vs. Hydra or Hectochelle) can lead to some general conclusions (§4.4).

4.1.2 Variations on a MOS Calibration System

As shown earlier (Fig. 1.22), the use of a dome-screen (actually the specially treated internal surface of the telescope chamber) did result only $\sim$ 20 weak (few hundred ADU peak, but sill usable) ThAr lines in half an hour exposure time, over a typical 150 Å single order coverage of Hectochelle. This is unacceptably long, especially for bracketing science exposures.

Any illumination system had to be an addition to the operating telescope and commissioned instrument, without compromising performance and without disturbing other instruments. Such an "afterthought" puts very hard constraints on the design, as the MMT telescope does not have a facility calibration unit (like the Gemini telescope, Ramsay-Howat et al. 2000) and the space above the focal plane is very crowded (two high speed positioning robots, wavefront sensor, ADC, corrector lenses).

A few options were considered, like a deployable diffusion screen between the secondary and the focal plane, as close to the fibers as possible (following the Hydra concept). For front illumination (the same side where the fibers are) such a screen has to be far enough from the lamps that

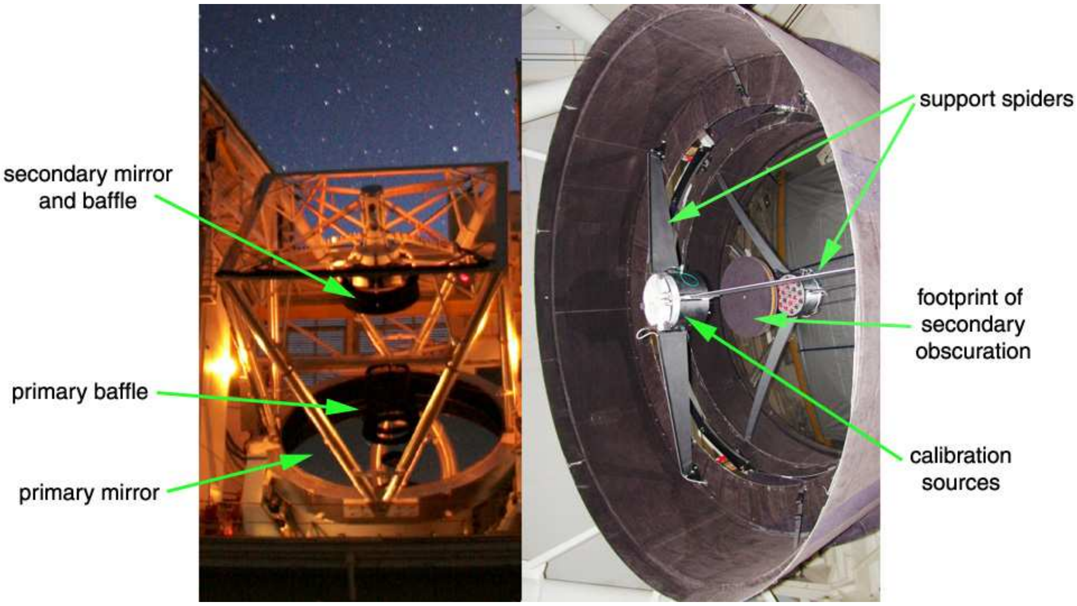

Figure 4.1: ***Direct illumination calibration system for Hectochelle**, located within the secondary baffle. Removing the central unit (lamps) the spider arms fold out of the light path.*

an even illumination pattern can be generated. This was impossible below the primary, with all the mentioned units already squeezed in that volume. A transparent diffuser might have allowed remote lamp locations, possibly mounted off a primary baffle element (Fig. 4.1). Although such screen, even placed close to the focal surface, would have not provided the required intensity level.

Direct illumination of the focal surface from an external source seemed to be a working solution. The lamp location relative to the telescope, though, had to be very repeatable as indicated by test measurements (see Fig. 4.2). The idea of a calibration post standing on the floor of the telescope chamber, towards which the telescope can be pointed to by moving to the lower elevation limit, was rejected (time consuming, supporting structure endangering safe telescope operation). But the primary baffle (see Fig. 4.1) still seemed to be a convenient location for mounting light sources: lamps along the perimeter of a baffle ring can directly illuminate the focal plane, and still be out of sight for other f/5 instruments when turned off.

This solution, however, did not work very well as the geometry of fiber buttons is such, that the FOV of a fiber end is limited to an f/5 cone. Therefore only a small fraction of the light coming from the baffle lamps could reach the fibers. Although it was sufficient enough to increase the intensity levels of ThAr lines, the RV values exhibited a strong dependence on fiber position across the focal surface. Fibers towards the center had seen very small fraction of light coming from all lamps, while fibers close to the edge of the focal surface had seen more light but only from one or two lamps, since the focal surface is curved.

The focal surface, at first order, is nearly a spheroid with its center located at the midpoint of the secondary mirror. Therefore a light source mounted in that location would be seen equally by all fibers, independently of their location on the fiber plate. Because the large f/5 secondary (1.7 m) obscures a significant portion (28%) of the 6.5 m aperture, proportionaly there is a ~ 0.5 m diameter "dead-band" in the middle of the secondary mirror (see Fig. 4.1). Mounting calibration sources within this footprint would not take away any light, and at the same time it could provide

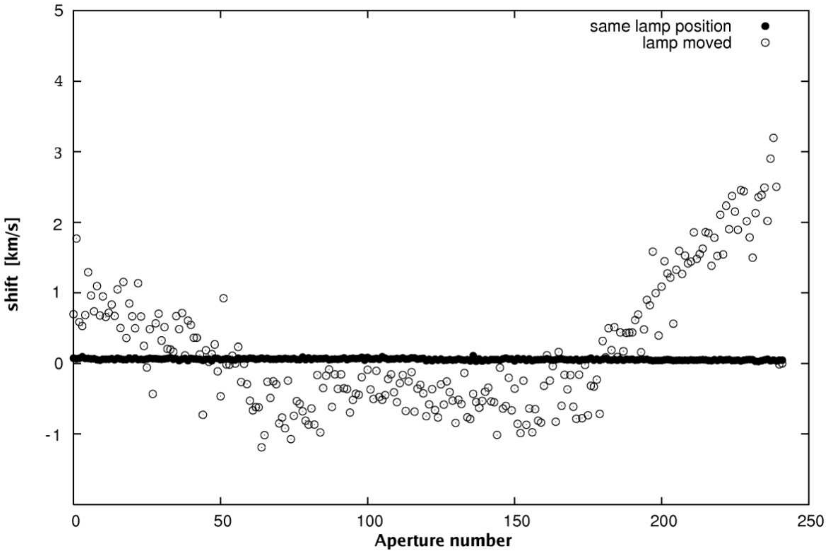

Figure 4.2: ***RV errors as a result of a small change in the location of a direct illumination source:*** *the arc lamps (placed at the level of primary baffle) were moved off-axis by* $2\overset{\circ}{.}5$*, corresponding to 0.2 m of radial displacement.*

even illumination of each fiber. All these properties were convincing to build such a calibration system, consisting of 18 ThAr and one incandescent lamp sources. The unit is suspended by a spider with three legs, connected to the three hard supporting points of the secondary baffle. When the central "light can" is removed, the legs can be folded away and secured to the inner side of the secondary baffle, not obscuring any light.

4.1.3 Sub-optimal Calibration: Effects on RV Performance

The lamps at the secondary provide even illumination of all fibers. There is no correlation between RV offsets and fiber position on the focal surface, but the calibration system is still not optimal. When twilight sky (solar) spectra are recorded in all fibers and compared to each other there is a clear systematic trend among apertures, which is different if the entire or just small parts of the spectral order is used in the cross-correlation-based comparison (see Fig. 4.3).

On the upper panel of Fig. 4.3 a sample solar spectrum is shown, recorded in the RV31 order. Red stripes indicate three small wavelength ranges used to compare the spectra of different fibers. The measured RV offsets between the 240 apertures are shown on the bottom panels, each placed below the regarding spectral region. The largest measured difference between two fibers is less compared to results obtained with the primary-baffle mounted lamps (which resulted deviations of similar amplitudes as the case shown in Fig. 4.2). Also, for the secondary-mounted lamps the pattern is independent of fiber locations, but still a very obvious systematic error is presented. Although the offsets are changing when examining different regions of a spectral order, subsequent tests proved that for a given wavelength range the pattern is the same, very stable even on a year-long time span. Such stability provides the possibility of removing this trend, as discussed in §4.2. Before presenting such solution, let us try to understand/explain this "feature" of direct illumination.

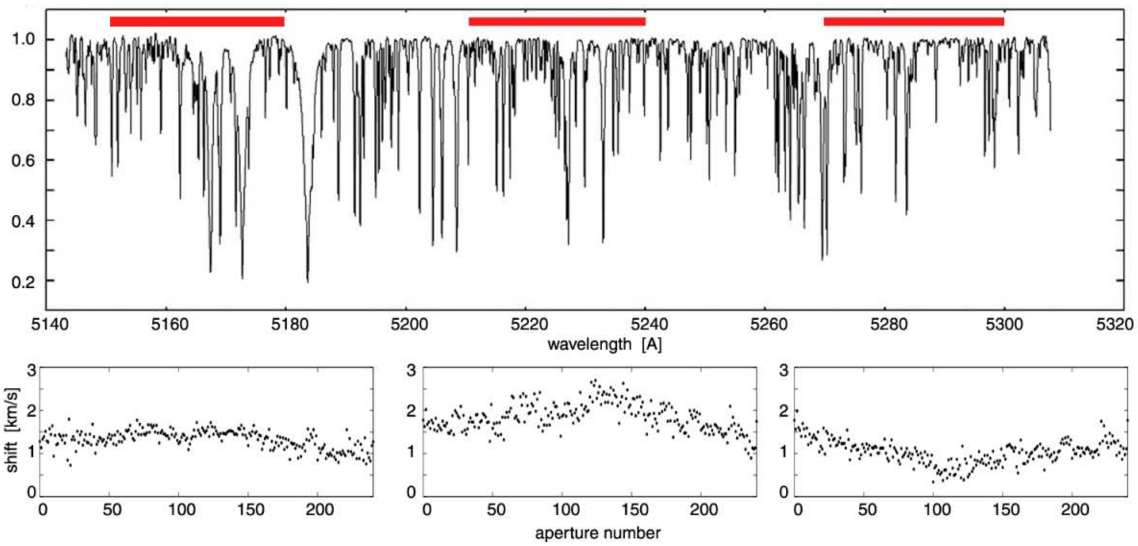

Figure 4.3: ***RV offsets between apertures as a function of wavelength range****, using the secondary-mounted direct illumination calibration system. See text for details.*

Fig. 4.4 shows a selection of isolated, single lines across the spectral order (upper panel) and zoomed-in plots of their profiles for different aperture ranges (lower panels). The average of all 240 spectra is shown in magenta, and four sets of 10 apertures are colored in black (apertures 1–10), green (40–50), blue (80–90) and cyan (110–120). The spectra were corrected for throughput differences and continuum normalized the same way, so any differences seen in the line profile is due to the wavelength solution. And it is apparent that line shape/position is changing with aperture number, especially towards the blue/red end of the wavelength coverage. The broadening in the wing of the line is ∼ 0.02 Å (more than 0.5 pixel!), which is significantly larger than the error in the wavelength solution (0.0014 Å, see Fig. 5.1). Also, the wavelength solution is a 5 degree polynomial (6 parameters), which is the lowest order function to sufficiently remove all systematic trends in the position–wavelength fit. Therefore line profile/position variations are not due to uncertainties/inappropriate function of the pixel-to-wavelength mapping, but rather caused by non-linear distortions between the wavelength solutions of different apertures.

The reason behind all this is likely the ThAr illumination, very fast camera optics and the relatively large distance between the grating and the first element of the camera. This latter can be termed as "highly colored pupil", since different wavelengths of the dispersed beam have footprints widely spread on the corrector of the Hectochelle camera. The calibration light does not travel through the same optical path as starlight, neither enters the fibers at a nominal f/5 opening angle, since the ThAr lamps are seen as point sources by the fiber ends. As discussed in §1.5.2 such illumination difference alters the pupil within the spectrograph optics, thereby causes variations of the intensity distribution within the beam. As a result, optical aberrations for stellar and calibration light paths are different, so are the recorded line profiles. This effect is even more expressed in case of a fast optical system. Because scrambling is different in each light guide, and since each fiber end has its own tiny misalignment within the pseudo-slit, the discrepancy between star- and calibration light is not the same for all apertures. Accordingly, the pixel-to-wavelength mapping is not the same for all fibers, which manifests in the apparent, aperture dependent line-profile/wavelength-scale distortions.

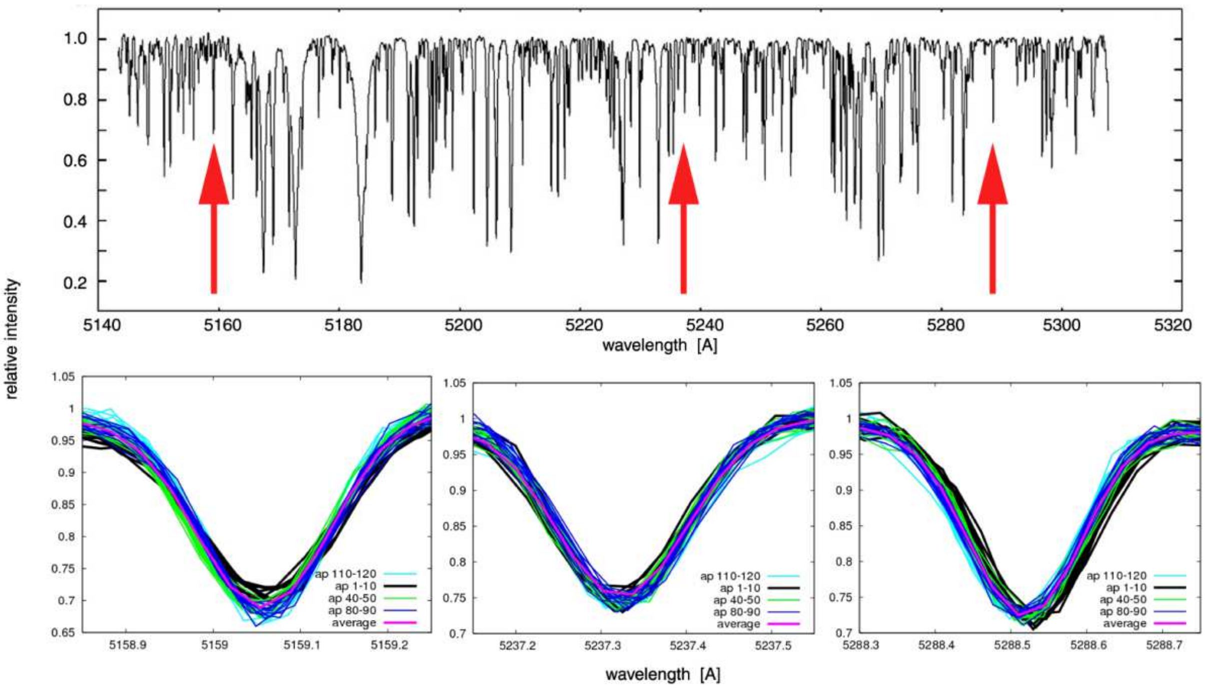

Figure 4.4: ***Variation of line profiles between apertures****, at three locations of a spectral order.*

4.1.4 Effects on Sky Subtraction, Throughput Correction

When it comes to sky subtraction (§1.5.2) the distortion of the wavelength scale is very bad news. Since the sky contamination is sampled with a few fibers within the field, combining those spectra broadens the line profiles if compared to individual apertures. Also, depending on which fibers were used in sky sampling, it is not just broadening but can include a shift as well.

Another problem is the correction for throughput differences, or the proper scaling of the combined sky spectrum intensity before subtraction. The relatively narrow spectral coverage of Hectochelle orders usually does not include sky lines, which could be used for scaling. And the flat fielding also has its problems, since, just like the ThAr source, the flat lamp is also sub-optimal. Although the continuum spectra does not record line profile changes, but the secondary location is not seen exactly the same for all fibers, neither provides the flat lamp an f/5 beam. Fiber buttons placed near the field center experience somewhat higher intensities, introducing error in the throughput correction.

As before, the twilight sky can be an option by fitting its continuum. In that case, however, the plate scale change has to be accounted for: a given fiber diameter corresponds to different angular coverage on the sky, depending on radial distance from the field center. This feature of the optical system also has to be corrected when combining sky spectra, also when correcting sky background in different apertures. Point sources are not subject to such position dependent intensity scaling, unless the seeing is so bad that the fiber face is way too much overfilled by the blown-up stellar PSF.

4.2 Fiber-to-Fiber Calibration

Applying ThAr wavelength solution on Hectochelle data the fiber-to-fiber RV offsets are unavoidable, but the effect can be characterized and corrected for, as shown below. I also compare this calibration to that of other spectrographs.

4.2.1 Hectochelle

Data taken at 24 sunsets/sunrises over 16 months (Oct-Nov 2005, Mar-May 2006 and Mar 2007) were used to derive the fiber-to-fiber offsets in the RV31 order. For each twilight exposure a set of ThAr frames were recorded and used to establish a wavelength solution. A synthetic solar template from the CfA library (see §6.1.1) was used to determine fiber-to-fiber RV values. The result is shown on Fig. 4.5. Between the two most extreme fibers the correction is almost 1.2 km s^{-1}(!). The error bars represent the standard deviation of the measured offset values for the given fiber. The mean of this uncertainty is 36 m s^{-1}. In other words the internal accuracy of Hectochelle (*with the current calibration system*) is low, but the precision is high.

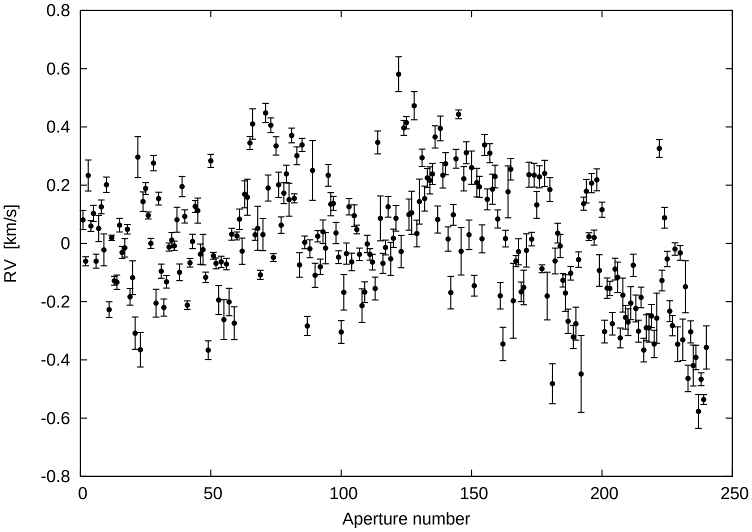

Figure 4.5: ***Fiber-to-fiber RV offsets for the Hectochelle spectrograph**, measured in the RV31 filter (5150-5300 Å).*

As seen on Fig. 4.3, the fiber-to-fiber offsets depend on the wavelength range used for cross correlation. Therefore if a wider spectral range (like Hα) is blocked, one would expect a different behavior. Also, some spectral orders have sharp lines (significant to RV measurement) exhibiting a different distribution. Therefore the wavelength-scale distortions seen on Fig. 4.4 influence RV determination in a different way compared to the RV31 band. Furthermore the ThAr lines determining the solution also have a unique distribution in each spectral band, and the introduced non-linearities can be different. All in all, a similar fiber-to-fiber behavior is expected in other orders, but not exactly the same. This was confirmed using twilight exposures taken in the OB26 band (6530-6720 Å). Although the 6555–6573 Å region was blocked to mask out the Hα line, the fiber-to-fiber offsets resulted a very similar pattern to Fig. 4.5, with systematic deviations from it at the level of 75 m s^{-1}.

4.2.2 Hydra

For the Hydra spectrograph Søren Meibom has determined a similar fiber-to-fiber RV calibration, using twilight sky exposures. As the calibration system of Hydra is also sub-optimal (front illuminated screen very close to the focal plane), there is a clear aperture dependency of RV offsets (see Fig. 4.6). Some fibers exhibit significant discrepancy, and for others the offset is not very stable in time. Still, most fibers show a well defined correction factor, which is constant at the 20 m s^{-1} level.

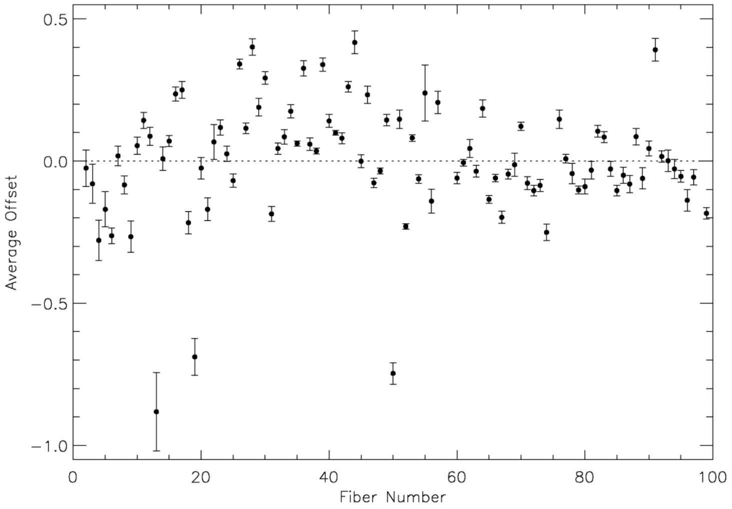

Figure 4.6: ***Fiber-to-fiber RV offsets for the Hydra spectrograph*** *(Meibom, 2007).*

4.2.3 FLAMES / Giraffe

The VLT/FLAMES calibration unit is very different from that of the previous two instruments. The illumination is the same for all fibers, since the fiber positioning/calibration head moves to the same relative position of each light-guide during calibration. Therefore fiber-to-fiber offsets scatter around a straight line (nearly at zero), unlike the overall shape seen in the previous cases (see Fig. 4.7, left panel). But, there seems to be a structure. Unfortunately I was able to find only single epoch high resolution twilight sky exposures at 5200 Å in the ESO archive of raw data[1], so the stability (and credibility) of the observed small-scale structure could not be tested.

Comparing the determined fiber-to-fiber offset values from a 50 Å wide range in the blue (5150 – 5200 Å) to a 100 Å wide section around the central wavelength (5200 – 5300 Å), there is a 100 m s^{-1} offset (right panel of Fig. 4.7, red vs. blue symbols). However, this is a global shift, there is no sign of aperture dependent variations like it is shown on the lower panels of Fig. 4.3.

Using an artificial template instead one of the observed solar spectra, there seems to be an aperture-dependent deviation (green circles, note: velocity scale multiplied by 10 for clarity), although only at the 20 m s^{-1} level. These signs might indicate that even though the FLAMES calibration system provides illumination very similar to that of the telescope, it is still little bit different compared to sky (and probably stellar) sources.

---

[1] Based on calibration data made with the European Southern Observatory telescopes obtained from the ESO/ST-ECF Science Archive Facility, http://archive.eso.org/cms/ — data used from 09.26.2004, configuration: HR9.D9; slit plate: Medusa2; coverage: 5120–5340 Å

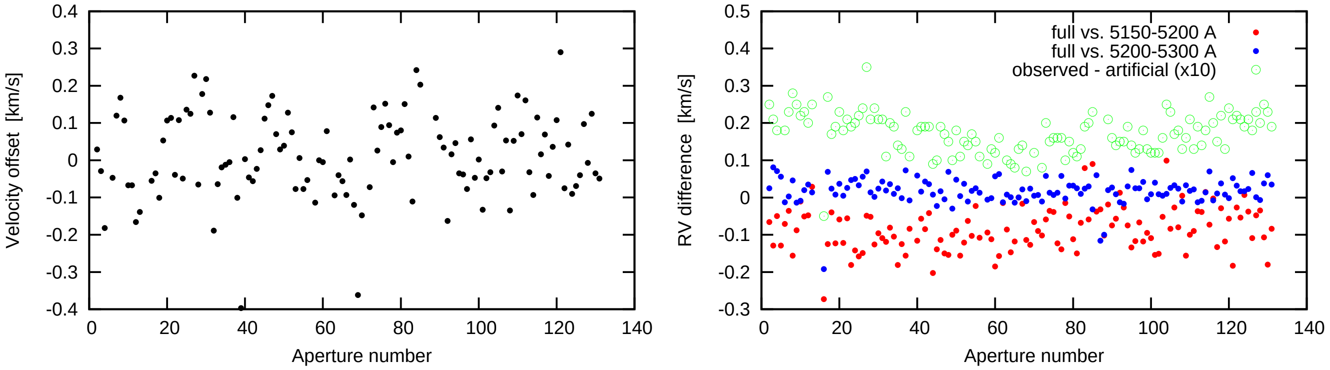

Figure 4.7: ***Fiber-to-fiber RV offsets for the GIRAFFE spectrograph*** *(left), and the dependence of RV on the spectral range/template used in the cross-correlation (right).*

4.3 Current Solutions, Methods and Further Problems

4.3.1 Solar Calibration

It is obvious that light from the dusk/dawn sky uniformly fills the aperture of a fiber, unlike the stellar PSF, especially in case of guider errors or positional mismatch. Therefore above tests likely can not fully reflect systematic errors embedded in stellar data, but observing the twilight sky still can be useful at some level.

The solar spectra recorded through all fibers can replace the ThAr reference and be used to derive the pixel-to-wavelength transformation. Experiences with Hectochelle demonstrated that line position changes and wavelength-band dependent RV values (see Fig. 4.4 and 4.3) can be eliminated this way. An internal accuracy (e.g. fiber-to-fiber variation) of 20 m s^{-1} was met in short term (1 week) using high S/N ratio twilight exposures (Lars Buchhave, 2007, personal comm.). The achieved value is better than the result from fiber-to-fiber correction using ThAr (36 m s^{-1}), which is, in part, likely due to the higher and more uniform S/N ratio among the solar absorption lines.

Another advantage of the solar solution is the removal of non-linear wavelength scale changes within and among apertures. This increases the match between the (either observed or artificial) template spectrum and recorded spectra, providing a sharper cross-correlation function and thus a better defined RV value.

4.3.2 Master Wavelength Solution, ThAr Tracking

If a solar wavelength solution is used, obviously it can not be re-determined more than twice a night. Therefore ThAr frames have to be used to track instrumental shifts and transfer the solution to the time of the observation. Such “calibrate once than track shifts” technique (although using a ThAr-based master pixel-to-wavelength mapping) has been widely used for stabilized single object spectrographs (e.g. HARPS, Elodie, etc.), and even for multi-object echelles (e.g. Giraffe, see Loeillet et al. 2008). The tracking can be done by the actual object fiber (bracketing the observations in time), or utilizing simultaneous calibration fibers (HARPS, Giraffe, TRES, etc.).

Nevertheless, this method fails for Hectochelle, as it is demonstrated below. A set of twilight sky exposures with adjacent ThAr frames from March 2007 was used for the test. A master wavelength solution was estabilished using the arc lamp data taken in the morning of 03/06. The instrumental drifts were measured by pixel-space cross-correlation of the ThAr lamp frames (left panels of Fig. 4.8). Note, that the shifts differ from fiber to fiber, and it is not a linear correlation with aperture number. First, on the lower left panel it is apparent that the relation breaks at aperture 120, so the two CCD detectors have different behavior. Second, the dependency within one chip is rather parabolic, although it can not be seen due to scaling. (The range was kept the same for both left-side panels to aid comparison of the first and last three nights.)

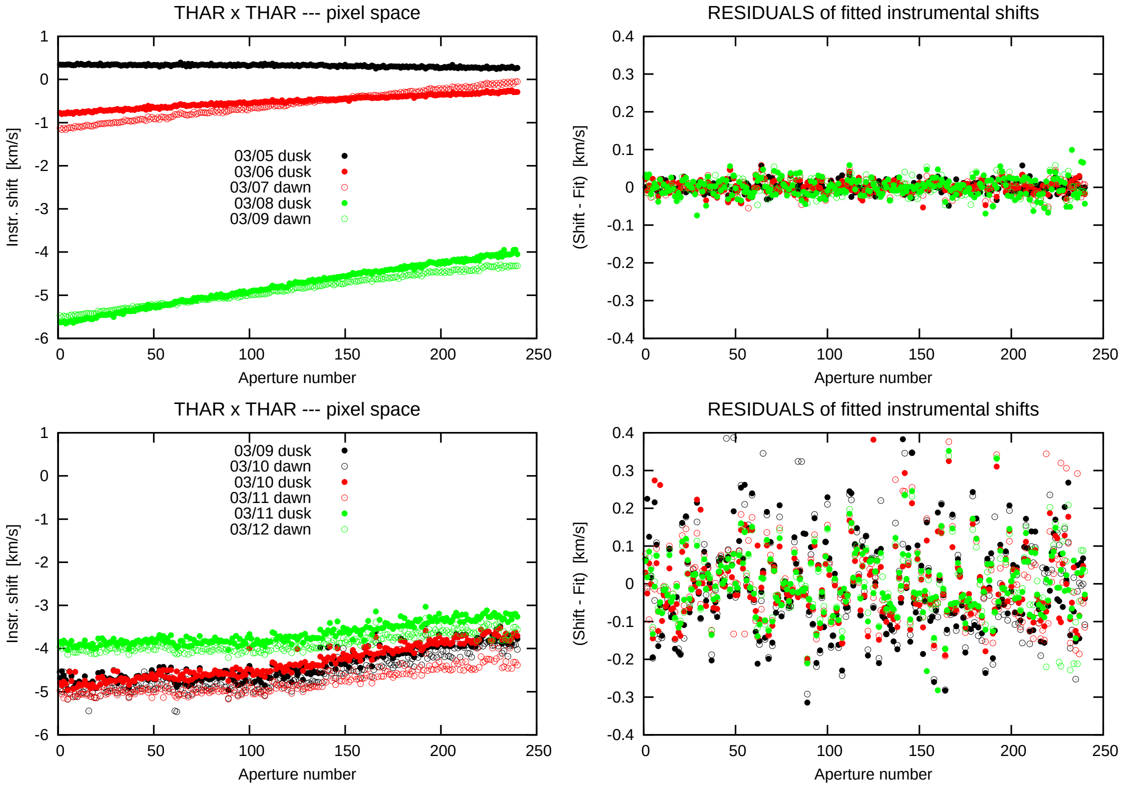

Figure 4.8: ***Tracking a master wavelength solution*** *(03/06 dawn) by pixel space cross correlation. Left panels show the raw data while on the right a second order fit (individual for each detector) is removed. The tracking works well for the first three nights (upper panels), but fails for the last three (lower panels). See text for details.*

The shifts of a given frame and CCD were than fitted using a second order polynomial, and the remaining residuals are plotted on the right of Fig. 4.8. As it can be seen tracking the master solution works very well for the first 3 nights, even though there are 6 km s^{-1} instrumental drifts (∼ 3 pixels!). Although even the raw pixel-space correlation plot reveals (lower left) that the scatter is higher for the last three nights. The residuals (lower right) clearly show a serious problem. While the first three nights any fiber yielded the fit within 15 m s^{-1}, for the least three nights the residuals are several times larger and some systematic trends appear. Even though the bulk instrumental shift (~ -4 to -5 km s^{-1}) is similar to the value seen in the dusk 03/08 and dawn 03/09 exposures (~ -5 km s^{-1}), the pixel–wavelength scale seems to be different.

Re-establishing the pixel-to-wavelength transformation using the dawn 03/09 data, and re-evaluating the last three nights, the errors decrease significantly as shown in Fig. 4.9 (compare to lower panels of Fig. 4.8). But this means that a single wavelength solution can not be applied to data taken over a long period of time (probably not even during a single night).

According to log files temperature, spectrograph focus, collimator position, grating position did not change abruptly between the first and last three nights. Unfortunately there is no pressure data available. Although the instrument was re-configured several times during this time (filter, grating position and focus changes), but it was always properly set back to the configuration of the master frame. Neither the intensity level of ThAr frames changed, which would indicate lamp failure or other change in the illumination system. Therefore there is no smoking gun, a single cause can not be pointed out to explain the sudden change in the wavelength solution.

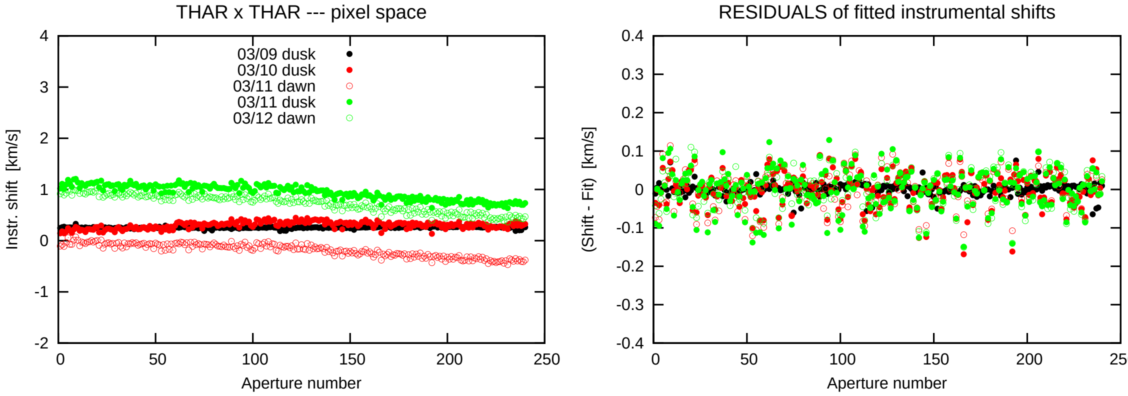

Figure 4.9: ***Tracking a master wavelength solution*** *for the last three nights of the Marc 2007 test run, using a re-established pixel-to-wavelength mapping from 03/09 (dawn). Compare to lower panels of Fig. 4.8*

The increased scatter in the pixel-space correlation plots of ThAr frames (lower left panel of Fig. 4.8) suggest to look for wavelength (pixel position) dependent variation in line profile or position. To do so the pixel-space cross correlation of ThAr frames against the 03/06 dusk reference was repeated, but using not the entire 4600 pixel range (as done for the left panels of Fig. 4.8), rather a 1500 pixel wide section in the blue, middle and red part of the spectrum ($3000 - 4500$, $1500 - 3000$ and $0 - 1500$ pixels, respectively; see Fig. 4.10). These ranges still contain enough emission lines to yield a sharp CCF peak. As it was unveiled by such tests the plate scale of the Hectochelle camera exhibits a position dependent behavior in time.

The upper 3 panels of Fig. 4.10 represent the beginning of those first three nights (dusk) in the March 2007 test data which could be calibrated by tracking the wavelength solution of 03/06. The overall trend of instrumental shifts, of course, is the same as already seen in the upper left panel of Fig. 4.8, but the blue and red end of the emission spectrum “stretches” compared to the middle. And while this behavior is aperture dependent the blue end of the spectrum always yields lower shifts. In contrast, for those nights the original wavelength solution could not be transferred to, the blue part of the ThAr spectra exhibits higher shift values.

Another apparent difference between the first and last three nights is the amplitude of the deviation of red/blue portions respect to the middle. Note, that the lower panels have the same 4 km s^{-1} range, while the upper panels cover only 2.2 km s^{-1}, so the last three nights exhibit

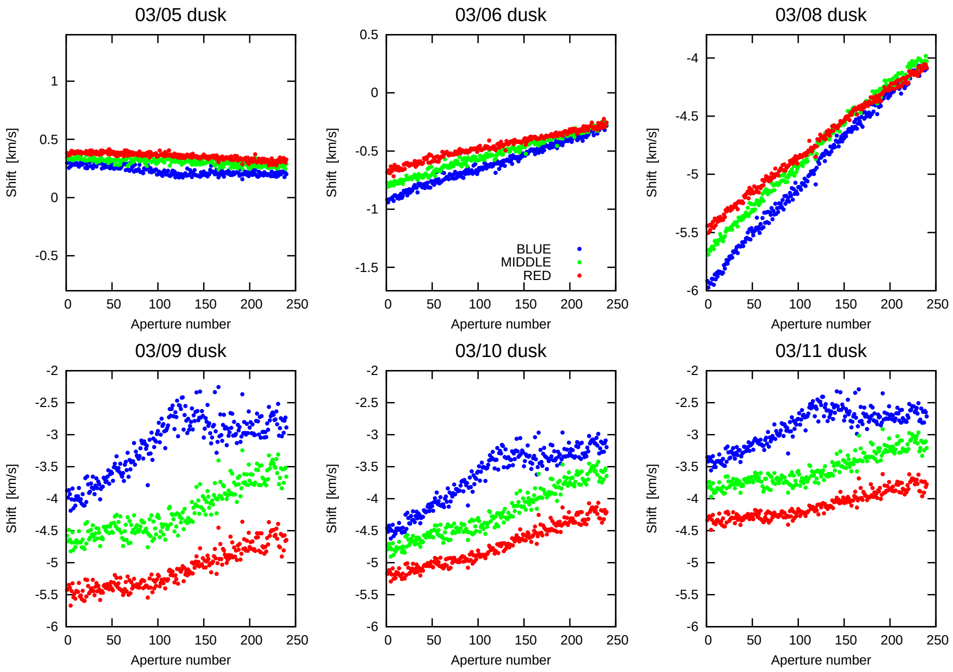

Figure 4.10: ***Aperutre and wavelength dependent instrumental shifts of Hectochelle*** *is apparent if pixel-space cross correlation of ThAr frames is performed over distinct regions of the arc lamp spectra. Compare to the left panels of Fig. 4.8. See text for details.*

a significantly larger amplitude of stretching. However, the last three nights look very similar. Indeed, repeating the cross-correlation against a new template (dawn of 03/10) the relative variations are very small, as shown in Fig. 4.11. The discontinuity between the two detectors (at aperture 120) is well expressed, and the previously mentioned non-linear behavior within a single CCD is also apparent. This is why the external calibrator (§3.1.3) or a small number of tracking fibers (sampling only a few aperture positions) can not work efficiently for Hectochelle.

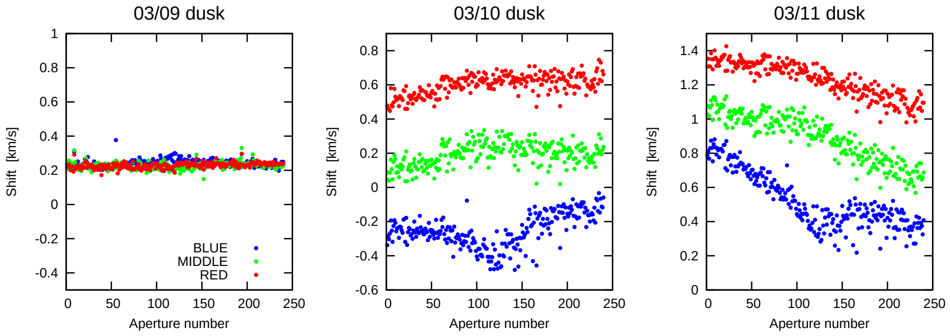

Figure 4.11: ***Aperutre and wavelength dependent instrumental shifts of Hectochelle*** *for the last three nights of the March 2007 test run, using a ThAr template from the morning of 03/10. Compare to the lower panels of Fig. 4.10. Note the discontinuity between the two detectors (at aperture 120) and the non-linear behavior within a single CCD.*

4.3.3 Zero Point Calibration

Long term accuracy is also influenced by another source of error, the bulk offsets between data obtained during separate observing runs, often several months or years apart. Either using the master or individual calibration technique these shifts can reach amplitudes of several hundred m s^{-1}. Fiber-to-fiber variation tests using solar spectra were not affected by this error, as it was taken out by shifting all RV of a given twilight frame to a common mean velocity. Although for observed stellar fields variation of such zero point is a real problem. In long-term data sets of the same stars (time series) the mean RV value of all objects can serve as a common ground for multi-epoch observations. Such solution is similar to extinction correction of wide field (i.e. open cluster) photometric time series, in which the mean instrumental magnitude can serve as a zero point. In contrast, for multi-field observations, if the data sets are collected over a longer period of time, it is very hard to deal with zero point variations. Even though a set of "reference" stars can be included on purpose within two or more overlapping fields, or other calibration applied (i.e. twilight sky), the accuracy of high-resolution MOS RV data is rather poor. A few 100 m s^{-1} variations between observing runs are reported for Hectochelle (Fűrész et al. 2006, 2008) and for other instruments as well (Giraffe, D. Queloz, personal comm., 2008)

It is nearly impossible to derive a function of a parameter set (temperature, focus, pressure, etc.) to predict the long term variations. Differences in pupil illumination is very likely the cause of zero point shifts, as these problems seem to be more serious with calibration systems providing illumination very different than that of stellar sources. Environmental stability must be also a key issue, however a relevant part of it is compromised by the multi-mode operation of the rather complex MOS spectrographs. Slit-plate and filter changes, grating adjustments are not perfectly repeatable.

Moreover, the variations in the refraction index of air due to pressure and temperature changes can affect each MOS aperture in a different way (see Fig. 4.10). Again, different pupil illumination of calibration and stellar sources can be very important here. Imagine the beam hitting the grating, which can become miscollimated if the thermal expansion of the bench is only compensated by camera focus. Therefore the pupil illumination does change, but the expansion/contraction of a centrally peaked Gaussian-like pattern introduces smaller increase/decrease of aberrations, than that of an evenly spread (or even worse, a ring-like) distribution of calibration light. Such changes are more dominant for fast optical systems and for highly colored pupils.

4.3.4 Matching Template

A well-matching template is very important to determine accurate RVs, if only a limited wavelength range is available (which is the case for high resolution MOS instruments). Several libraries of synthetic spectra are available today, and due the increasing coverage of parameter space and resolution it is likely to find a good template. See Fig. 6.2 and the discussion in §6.1 about how important it is to use a proper template. (Note, that this is different if using an unweighted binary mask, since such template only codes the line positions.)

4.3.5 Bottom Line: RV Precision Limit

As a summary we can say that for Hectochelle a 15 m s^{-1} *fiber-to-fiber accuracy* can be reached in the calibration, over a few days. This can be achieved either using a master solution and tracking, although determining the pixel-to-wavelength transformation for every frame provides similar results. For long term, only the latter solution works.

Based on the fiber-to-fiber calibration data of twilight sky exposures 36 m s^{-1} *internal accuracy* can be achieved, using high signal to noise ratio spectra ($\sim$ 300) with a resolution of R = 38 000. This accuracy stands over a year-long time scale. For stellar data of 5 consecutive nights 70 m s^{-1} RMS *precision* was demonstrated on a Kepler field, by keeping a given star assigned to the same fiber. For this test targets of $V = 12.8$ average brightness (range of $V = 10.6 - 18$) were observed, using 3×10 minutes exposure time, 1×1 binning, in the Mg band (5150-5300 Å).

For Giraffe Royer et al. (2002) published similar solar calibration result, although for a three-hour-long session only, while the instrument was still in the assembly lab. They claim a 13–21 m s^{-1} *fiber-to-fiber accuracy* over this time interval, at a resolution of R = 25 800 and S/N ratio of 150. (Similar spectral band as used for Hectochelle, yielding the same RV information content.)

For stellar frames Loeillet et al. (2008) reported 30 m s^{-1} *precision* over 5 consecutive nights with the HR9.D9 instrument setup (R = 25 800, 200 Å band centered at 5228 Å), using exposure times of 30–50 minutes. Stars, with an average magnitude of $V = 14.0$, were always assigned to the same fiber, similar to the test with Hectochelle. Loeillet et al. (2008) used a master wavelength solution and simultaneous ThAr tracking, as described by Royer et al. (2002),

In terms of zero-point shifts both instruments perform similarly, but Hectochelle experiences larger drifts (up to $\sim$ 1km s^{-1}, vs. few hundred m s^{-1} for Giraffe). Environmental stability is also comparable, with temperature changes of several °C, and instrumental shifts up to 3-4 pixels.

Giraffe seems to achieve better RV precision than Hectochelle does, even though it has lower resolution. There are likely several reasons behind this. The calibration system might be one, since Fig. 4.5 exhibits large scale trends while 4.7 scatters around zero. But on this latter graph the Hectochelle data reduction method leaves a hint of systematic variations, and the overall dispersion is significantly larger than claimed by the ESO data reduction pipeline group. As outlined in the paper by Royer et al. (2002) the wavelength solution approach is different: for Giraffe a 2-dimensional pixel-to-wavelength fit is applied to a “global optical model” (describing the dispersion at first order), to account for a given instrument setup (grating angle, filter, etc.). The rotation (caused by slit plate changes) and linear shift (due to slit plate changes and temperature/pressure variations) of this refined solution is tracked by the five simultaneous ThAr fibers.

Such calibration and tracking for Giraffe works very well, according to the results of Royer et al. (2002). However, Loeillet et al. (2008) encountered problems regarding the simultaneous use of all tracking fibers. They found that only three out of the five shift measurements were consistent.

This can be explained if Giraffe exhibits similar behavior found in Hectochelle (Fig. 4.10), although such aperture-dependent distortions must be very small for this instrument. Indeed, analyzing ThAr exposures from the ESO data base archive, such effect can be found. For this test the previously mentioned pixel-space cross-correlation was used, comparing arc lamp spectra on three sub-regions of the given spectral order.

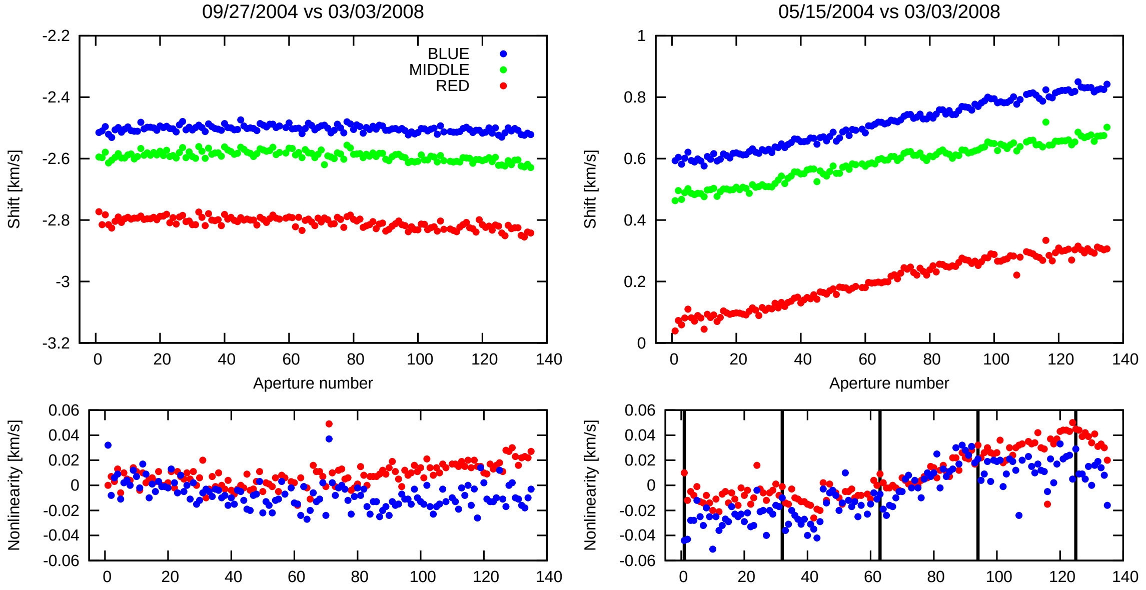

Figure 4.12: ***Aperture dependent instrumental shifts for Giraffe.*** *The upper panels can be directly compared to to Fig. 4.10. The lower panels show the deviation of red and blue points from the green, by correcting for the mean shift. On the lower right residual plot vertical lines mark the apertures of calibration fibers.*

As it can be seem on the left panels of Fig. 4.12, the plate scale of the spectrograph can remain remarkably uniform. Even though the two ThAr frames were recorded 3.5 years apart, the stretching of red/blue ends of an order (deviation from the middle) is almost negligible for all fibers, while the global shift is almost 3 km s^{-1}. Only the high aperture numbers experience some magnification change at a 20 m s^{-1} level, which corresponds to less than 0.01 pixel. The diagonal trend in the comparison of the two exposures from 2008 (upper right panel) are due to rotation of the pseudo slit, for what the ESO data reduction software corrects for. The blue and red ends of the order deviates from the middle part in a slightly non-linear way (lower right plot), but still only at the order of 40 m s^{-1}.

In comparison, Hectochelle non-linearities are much larger. It can be seen by eye on the lower panels of Fig. 4.10, without subtracting the shifts measured in the middle, since the amplitude (difference between green and blue) is more than 1 km s^{-1}. Of course, re-establishing the wavelength solution helps (compare lower panels of Fig. 4.10 to 4.11), but for Giraffe a master solution seems to be applicable over several years..

Regarding the findings of Loeillet et al. (2008), the lower right panel of Fig. 4.12 can explain why can be there (although low-level) disagreement between the five simultaneous fibers (marked by vertical lines). For the compared images three calibration apertures exhibit similar behavior, while the other two show opposite stretching.

The zig-zag pattern of fibers (two fiber rows in the pseudo slit) and the mosaic CCD detector would make a Giraffe-like data reduction approach even more complicated for Hectochelle, but probably not impossible. However, as seen by comparing Fig. 4.10 and Fig. 4.12, any kind of tracking must involve higher order transformations, a pure rotation and linear shift is inadequate.

What it all comes down to is the significant mismatch when comparing two apertures, leading to increased uncertainty of the cross correlation, thus large errors in RV determination. The degree of "matching" between a template and a target spectrum can be quantified with a statistical quantity, R, defined as the ratio of the height of the maximum peak of the CCF to the root-mean-square of the antisymmetric component of the CCF (Tonry & Davis 1979). The mean value of "signal-to-noise" ratio when comparing two Giraffe apertures is ~ 800. In contrast, cross-correlating apertures of a given Hectochelle frame the CCF only yields an average R value of 100 (even though the mean intensity of Giraffe and Hctochelle spectra are comparable). This limits the ability of tracking and correcting instrumental errors of Hectochelle beyond ~ 50 m s^{-1}.

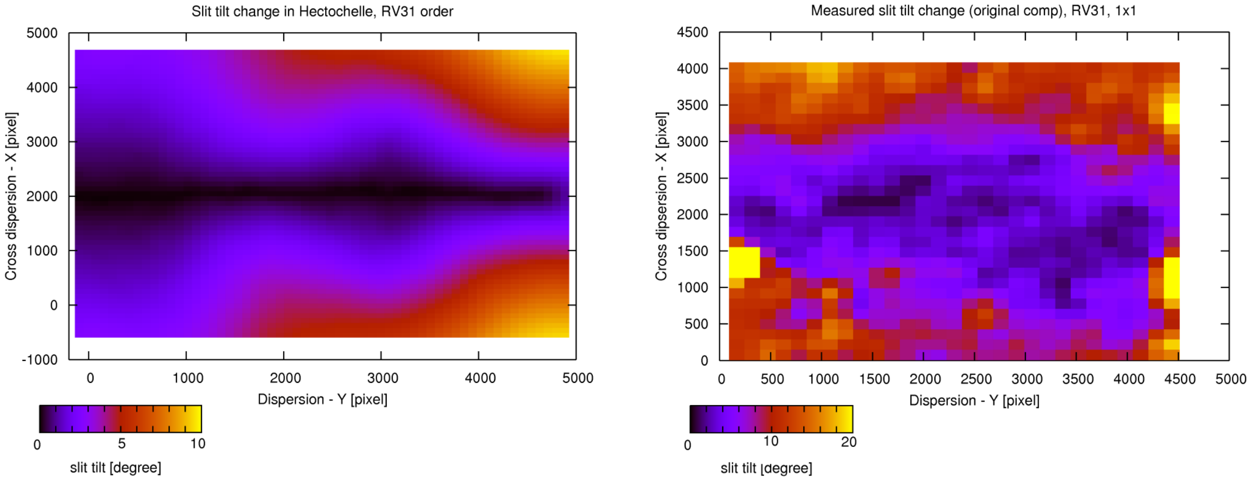

(a) predicted line tilts

(b) measured line tilts

Figure 4.13: ***Predicted and measured line tilts for Hectochelle****, shown as absolute value (not coding direction). Note the significantly larger actual values and nearly random structure.*

Still, the Hectochelle data reduction method applied on Giraffe data provides low accuracy compared to the official ESO pipeline. This questions the approach or the tools used to extract information from raw Hectochelle data. Determining a wavelength solution is one thing, but to compare two spectra this solution has to be used to linearize the wavelength scale, which involves re-binning. This step of data reduction has to preserve flux precisely, and not modify line profiles. Moreover, the two instrument have their own very unique properties, as shown above and listed below, so a given reduction technique is likely not ideal for both. Hectochelle exhibits a strong anamorphism, but still provides nearly the same FWHM (4.0 pixel) in the extracted spectrum, across an order. The elongated line profiles are tilted (see Fig. 3.5), and this tilt changes along dispersion, which can be described as a 5th order function according to the optical model of Hectochelle. But the predictions and measured line tilts are very different (see Fig. 4.13), which is in part due to the ±1°misalignments of fiber axis in the pseudo slit. Also, there is a time dependence, which implies there are changes regarding how the optical system forms the image. This is also supported by the time dependent "plate scale change" shown in Fig. 4.10.

In contrast the spectral lines of Giraffe are nearly round, with almost no anamorphism. Still, the tilts can be measured and exhibit a very uniform distribution, unlike Hectochelle (see Fig. 4.14). At the same time FWHM values of spectral lines grow from 3.7 to 4.7 pixels between the red and blue end of a Giraffe order. It also exhibits a large scatter among apertures, while Hectochelle is more uniform in this regard. Such variation leads to resolution change along dispersion, and so a synthetic template has to be treated accordingly, to get the best results from cross-correlation.

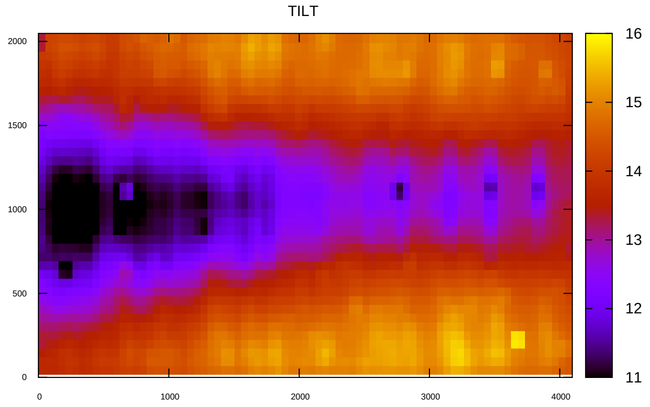

Figure 4.14: ***Measured line tilts for Giraffe****. Note the symmetrical structure and low overall amplitude, only 5°. Compare to Fig. 4.13.*

4.4 Towards Ideal MOS RV data: thoughts on (future) instrument design and data reduction

As a conclusion I would like to point out some aspects of instrument design and data reduction, which might be important if high RV precision is desired.

Optimal Calibration System It seems to be important to match the calibration light path to that of the telescope. The FLAMES system performs very well, although for high precision work the one-by-one fiber calibration has its own limitations. According to D. Queloz (2008, personal comm.) it is necessary to *simultaneously* calibrate all fibers, which means for FLAMES that the fiber positioning head have to keep moving around from fiber to fiber, and "spread" the individual illumination times over the entire calibration, to prevent aperture dependent offsets. Direct illumination (screens) have the all-at-once advantage, but lack the match of the light path and thus the similar pupil illumination. These issues might be very serious for future, echidna-type fiber positioners deploying thousands of apertures like WFMOS[2] for Gemini. It is likely necessary to either go through the telescope or deploy some auxiliary optics in front of the fibers, which produces a beam similar to that of the telescope. However for large (physical) field diameters it requires large optics. A facility calibration unit, built as part of the telescope, might be a good approach (like the Gemini calibration unit). Below (Fig. 4.15) an other feasible solution is shown, a calibration system design I proposed for the MMIRS MOS instrument (see §11.1.3).

---

[2] http://www.gemini.edu/sciops/index.php?q=node/10727

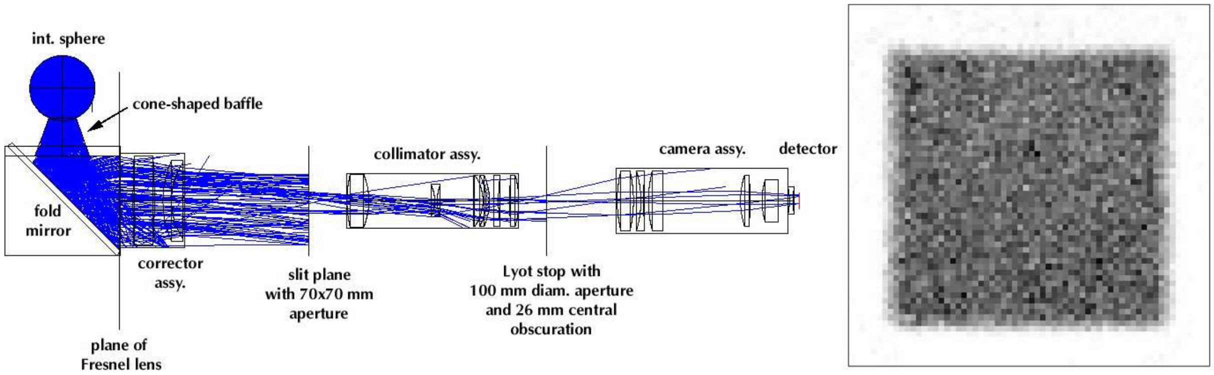

Figure 4.15: ***Calibration system design for MMIRS,*** *a near infrared multi-object spectrograph. The calibration light matches the telescope beam in diameter and focal ratio before entering into the instrument, and as a result the focal plane is evenly illuminated (right). The unit is relatively compact by using a Fresnel-lens and an integrating sphere. It provides simultaneous calibration for a* $7' \times 7'$ *FOV, for both imaging and spectroscopic applications.*

Spectrograph Optics As shown a "white pupil" design, in which the first element of the camera does not see beams of different wavelength over a large spatial extension, provides better RV performance. Also, slower focal ratio optics exhibiting lower levels of image distortions are preferred. However, it might impose an opposite constraint to reach high resolution for future extremely large telescopes. Severe line tilts due to the long pseudo slit of MOS are unavoidable if anamorphism is presented. The variation of these tilts (e.g. due to fiber misalignments) and extraction along CCD columns can result in non-regular line broadening, so highly anamorphic images should be avoided. Similarly, changes of the PSF along dispersion leads to varying resolution, and so templates have to be manipulated to match observed data in order to provide good correlation and thus higher RV precision.

Stability Significant temperature variations can magnify any errors presented, and it also makes any differences in pupil illumination easily detectable. To minimize time dependent distortions of the image environment should be controlled as precisely as feasible. The size and completely of MOS instruments limit the ability of pressure control, an over-pressurized chamber might help if vacuum installation is too much of a technical/financial issue. It is probably not enough to refocus just the camera in order to preserve image quality/sharpness, likely the collimation has to be tuned as well, otherwise opening of the beam can lead to illumination changes among pupil zones. Dealing with a mosaic detector is always problematic, data reduction must be separate. If possible, a single detector is preferred.

Ideal Extraction and Deliberate Data Reduction The extraction of spectra by simply summing intensity values along rows/columns of the detector is probably the most straightforward, but likely not the ideal way of extracting spectra from raw images. Precise tracing of an aperture and fitting a slit function (the intensity distribution of an evenly illuminated order, along spatial direction) provides a cleaner, more noise-free extraction (Piskunov & Valenti, 2002). In case of anamorphism the line tilts could be taken out, providing a narrower line profile and therefore higher resolution. As mentioned, while taking out the distortions of a pixel-wavelength scale, flux preserving re-binning is a must. Tracking of a single wavelength solution, if the optical system and environment makes this method applicable, is expected to decrease errors as the uncertainty of the solution only applies once to the data.

Part II

Data Reduction Techniques

Chapter 5

Data Reduction

The last chapters of the instrumentation section (Part I) was already turning into a discussion of general issues related to data reduction and analysis. However, each instrument has its own signatures imprinted in the raw data, and depending on the science the tools of analysis can diverge by a lot. As the science applications of multi-object spectroscopy described in Part III were all carried out with Hectochelle, in the "radial velocity machine" mode, in the following chapters I briefly describe how the raw and extracted data was handled.

For the data reduction I wrote an automated pipeline, which is in general a script calling image reduction and database handling tools, and relies on an instrument specific calibration data base to enable the entire process being non-interactive. The script runs in Linux/UNIX bash environment and mostly invokes IRAF[1] tasks for the fits image processing, and STARBASE[2] programs to handle the input and output catalogs/databases. This pipeline was adopted by the CfA Telescope Data Center as the official Hectochelle data reduction procedure.

The pipeline runs with three input files, each listing the names and locations of flat, ThAr and science exposures. Preferable all these are grouped, in a separate directory for each telescope pointings/fiber configurations. For target identification a so-called "map" file and the target input catalog is also necessary. The former links a given aperture number to a identification/line number in the target catalog. A very useful feature of the MMT/Hecto data archiving system is a fits image saved with the data, which stores a sky monitoring camera image (360° fisheye view) from the telescope weather station server. This helps to validate the observing conditions recorded in the logfile or comment fields of the fits data files.

5.1 Basic Image Processing

The raw Hectochelle data is stored in multi-extension FITS format image files. Since each of the two CCD detectors have two amplifiers (AMPs), there are four separate fits images embedded in the raw image file. For IRAF handling of such files requires the `mscred` external package to be installed. Due to the temperature driven shifts (§3.2.3) ThAr spectra are taken before and after a series of science exposures, and flat fields are also recorded for every fiber configuration.

---

[1] IRAF (Image Reduction and Analysis Facility) is distributed by the National Optical Astronomy Observatories, which are operated by the Association of Universities for Research in Astronomy, Inc., under contract with the National Science Foundation.

[2] http://cfa-www.harvard.edu/∼john/starbase/starbase.html

Bad pixel mask correction is usually not applied, since the detectors are high cosmetic grade and this step is unnecessary. Although here is one serious sensitivity defect on AMP3, which is 3 pixel wide in cross dispersion and runs several hundred pixel long in dispersion direction. The possible fix by interpolation does not work very well, as the spectral apertures are comparable in width. Therefore in most cases bad pixel mask correction is not applied and the affected aperture is thrown away.

Gain correction has to be applied since the four AMPS have slightly different sensitivity. As the absolute gain values are hard to determine to better than 3-4%, it is agreed to stick with the absolute gain of AMP1 as 1.0, and set the gain correction factors as follows: AMP1: 1.000; AMP2: 0.970; AMP3: 1.055; and AMP4: 1.015. (The numbers have to be multiplied to the ADU values, so these are the 1/gain values.)

Bias/Overscan correction is performed based on the individual overscan region of each AMP, since bias levels are stable and do not exhibit any pattern. The overscan region is specified in the fits headers, and its intensity variation is fitted by an 11th order cubic spline using the `mscred.ccdproc` task. During this procedure the first and last three pixels of the detector area are also trimmed and the bad pixel mask (if any) applied.

Dark correction is not necessary since dark current level is less than 1 ADU per hour (typically 0.2 ADU). In the absence of light leaks there is no structure on dark frames. Therefore usually (unless the targets are very faint and single integration times exceed 60 minutes, and there is a light leak developed) dark correction is not applied.

Joining the extensions: Due to the reversed readout direction of odd and even AMPs two of the extensions have to be transposed in the `x` coordinate direction before joining the four subframes into a single fits file.

Cosmic ray removal is done using a statistical filter (`imred.crutil.crmed`), which has a running sampling box of a size depending on binning mode. The mask is always elongated in dispersion direction, so it samples intensity variations within an order. Cosmic ray filtering is not performed on calibration data (ThAr and flat exposures), as those either confusing for the statistical filter (arc lamp spectra) or very short in exposure time (flats) and there are practically no cosmic hits.

Combining images: The cosmic ray removal runs on individual frames, but does not remove all cosmic hits. By median combination of three or more frames (usually observations are broken up into three integrations of the same exposure time) the remaining cosmic events are removed. Note, that due to the median combination the intensity levels represent the number of photoelectrons per the individual integration time. If there are more calibration frames the median combination is applied for exposures of the same kind (or for ThAr frames the instrumental shifts over the time span of observations can be determined and corrected for).

Flat fielding has to be done based on the flat exposure(s) taken at the given fiber configuration, as there is a time dependent spatial position of the apertures (see §3.2.3). Due to time constraints during the night usually there is only one or just a few flat exposures available, hence S/N ratio is not as high as it would be possible. Also, due to the sub-optimal calibration system the illumination of fibers is not completely uniform. Fibers placed within 2 inches of the field center are exposed to a "bright spot", and so throughput correction for these apertures are invalid. If critical, a dusk/dawn sky exposure can be used to estimate throughput (see §5.4). The pixel-to-pixel variations are corrected by taking out the large scale variations of the flat image, using the `noao.imred.specred.apflatten` task. But before running this the identification and tracing of spectral orders have to be performed.

5.2 Extraction of Spectra

Order identification is somewhat tricky in presence of several pixel spatial shifts (due to the temperature changes). The reference point for identification is the last aperture on the first detector (aperture #120) and the first aperture on the second CCD (aperture #121), on the flat exposure. The spatial distance between these spectra are larger than the inter-aperture spacing, since the fiber placement in the pseudo-slit has a gap according to the gap between the two detectors. Automatic correlation against a master flat field (aperture reference) image identifies the two middle apertures, and numbers all spectral regions from 1 to 240.

Tracing of orders is done by the `noao.imred.specred.apall` task, by fitting a 2nd order polynomial over the data points binned in 10 pixel sections along dispersion. (For the flattening the large scale intensity variations along the spine of an aperture is fitted by a 21th order cubic spline, and this fit is subtracted.)

Extraction is done along the spine using a spatial width which includes all signal: adding all intensity values above background which belong to the given order. This addition is done along columns, so line tilts do cause a certain amount of line broadening. Since the aperture centers were determined based on a flat exposure taken right before/after the science exposures, re-centering the aperture traces is not allowed during extraction. The local background is fitted by a linear function on both sides of the aperture, and it is subtracted from the extracted value. The definition of background regions are relative to the order centroid, and stored in the master aperture reference file used for order identification.

5.3 Wavelength Calibration

In Preparation for the wavelength solution the fits header is updated with the REFSPEC keywords, if there is a ThAr exposure before and after the science frames both are assigned to take out instrumental drifts between the start and end of the sequence.

Line identification is done based on the IRAF/NOAO ThAr line list. The Photron lamps currently used in Hectochelle are good match to the NOAO spectrum, however manual identification is only required to prepare a master reference file. If that, for the given filter and binning mode, is archived in the pipeline's database the line identification is automatic. It is a corner stone of the pipeline, as line identification in one aperture and consecutive re-identification of features in other apertures is not straightforward in IRAF for Hectochelle data. The reason is that due to mechanical constraints of fiber mounting in the pseudo-slit the fiber ends are located in a zig-zag pattern. This structure is "convolved" with a slow position change in dispersion, due to color (see Fig. 3.5). To create the master reference the extracted apertures have to be divided into an odd and even group, in which the positional change of spectral features is continuous, and so IRAF `noao.imred.specred.reidentify` task can be run. The to reference frames can be merged afterwards, and based on aperture number arc lamp features of any other ThAr frame can be automatically identified by applying a simple shift in dispersion.

Wavelength solution is calculated for each aperture individually, based on the *same* ThAr lines in each spectrum. (An other problem of the re-identify task that it can loose arc lamp features in while transferring the solution form aperture to aperture, and maintaining the same set of ThAr lines in each aperture is not obvious, actually it can not be done automatically in current IRAF versions.) The function used to determine the pixel-to-wavelength conversion is a 5th order polynomial within an aperture. This provides a 0.0015 Å RMS error for unbinned, 5 minute long ThAr frames in the RV31 filter (5150 – 5300 Å), which corresponds to 87 m s^{-1}. Figure 5.1 displays the error of the wavelength solution versus aperture number. The larger error towards the mid-range is due to the decreased intensities towards the middle of the focal plane, caused by the obscuration of the Schmidt-telescope-like camera optics/detector location (see Fig. 3.2). For 2 × 2 binning the average RMS error of the fits is 0.0025 Å, or 145 m s^{-1}.

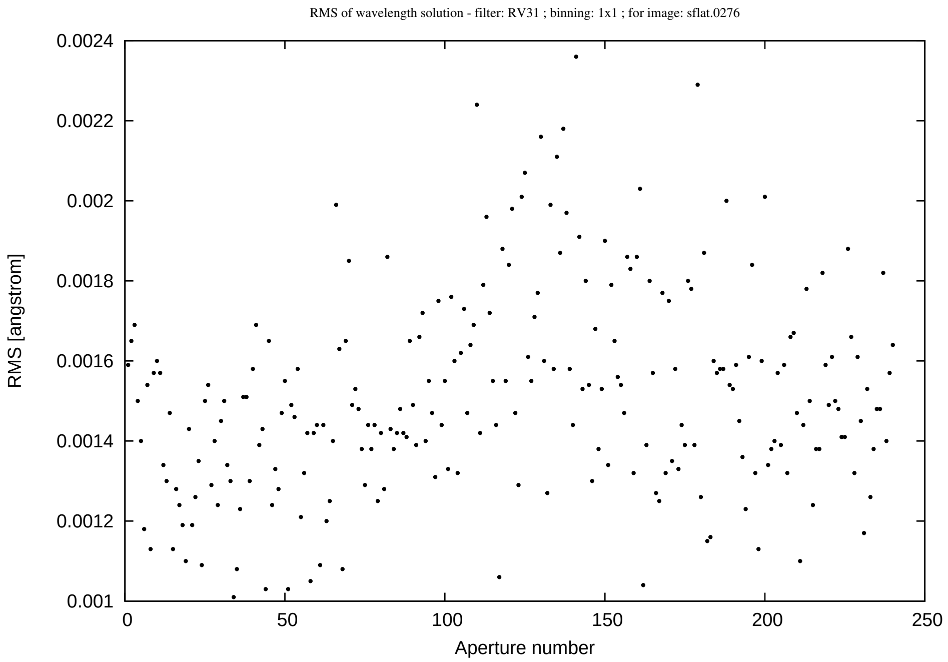

Figure 5.1: ***Wavelength solution accuracy for the 240 Hectochelle apertures**. The increased error in the middle apertures is due decreased intensity, caused by dewar obscuration.*

5.4 Throughput Correction and Sky Subtraction

The wavelength calibrated spectra are linearized in order to make apertures directly comparable to each other. At this point the data is stored in a multi-spectra fits format, which contains 240 one dimensional spectra, with wavelength-intensity data pairs.

Averaging all apertures of the wavelength calibrated flat field exposure a master illumination pattern is created, and by dividing it into the extracted flat image a throughput correction frame is generated. This can be divided into the object multi-spectra file, and thus remove fiber-to-fiber throughput variations. If sky subtraction is not necessary (small moon phase, bright targets) and continuum normalization will be done (removing any large scale intensity variations, which is mandatory for RV measurements), the throughput correction can be ignored. However, for sky subtraction or abundance analysis it is very important.

As mentioned before the current calibration system of Hectochelle is sub-optimal, so flat field exposures using a lamp do not provide adequate throughput correction. Fitting the continuum of dusk/dawn sky exposures and combining those fits is a better way of throughput correction. Unfortunately such sky exposure is not always available among the evening/morning calibration files. For the science cases discussed in Part III this correction was not applied because of missing the proper sky exposures in most cases, and also because most of the targets were relatively bright. Also, the RV values of cluster members were several km s^{-1} off from the solar velocity, so in the cross-correlation function a distinct peak appeared if the solar spectrum was a relatively strong imprint on the object spectrum.

An other difficulty of this correction is the changing plate scale of the f/5 MMT. Fibers closer to the field center see a larger coverage (by $\sim$ 12%) of the sky than fibers at the edge of the 600 mm diameter focal surface. When seeing conditions are bad and stellar images significantly overfill the $1\farcs6$ fibers, the distortion of the optics becomes significant and alters the relative brightness of spectra. On the other hand sub-arcsecond seeing results a lot smaller light loss, as only the very low intensity outskirt of the two dimensional Gaussian profiles fall off the fibers. In that case the plate scale change introduces less variation in relative brightness.

Sky subtraction for fiber fed instruments has always been very difficult (see §1.5.2). For Hectochelle the above mentioned plate scale change correction is a must when combining the sky spectra sampled by different fibers placed at different field locations. It is also important to check if light form any other source than the sky could have been diluted the background sample, which is often the case in crowded environments. Open clusters might not be considered as dense stellar fields, but observing young embedded clusters faces the observer with nebular emission components which are highly varying in intensity even on a small angular scale. To efficiently remove such contamination the *local* background has to be sampled for each target, which can be done by offsetting the telescope by few arcseconds and record a separate background spectra. As this is time consuming such offset sky exposures were not done for the sample discussed in Part III, but rather manual elimination of the narrow (and therefore easily identified) emission components was performed, if it was necessary.

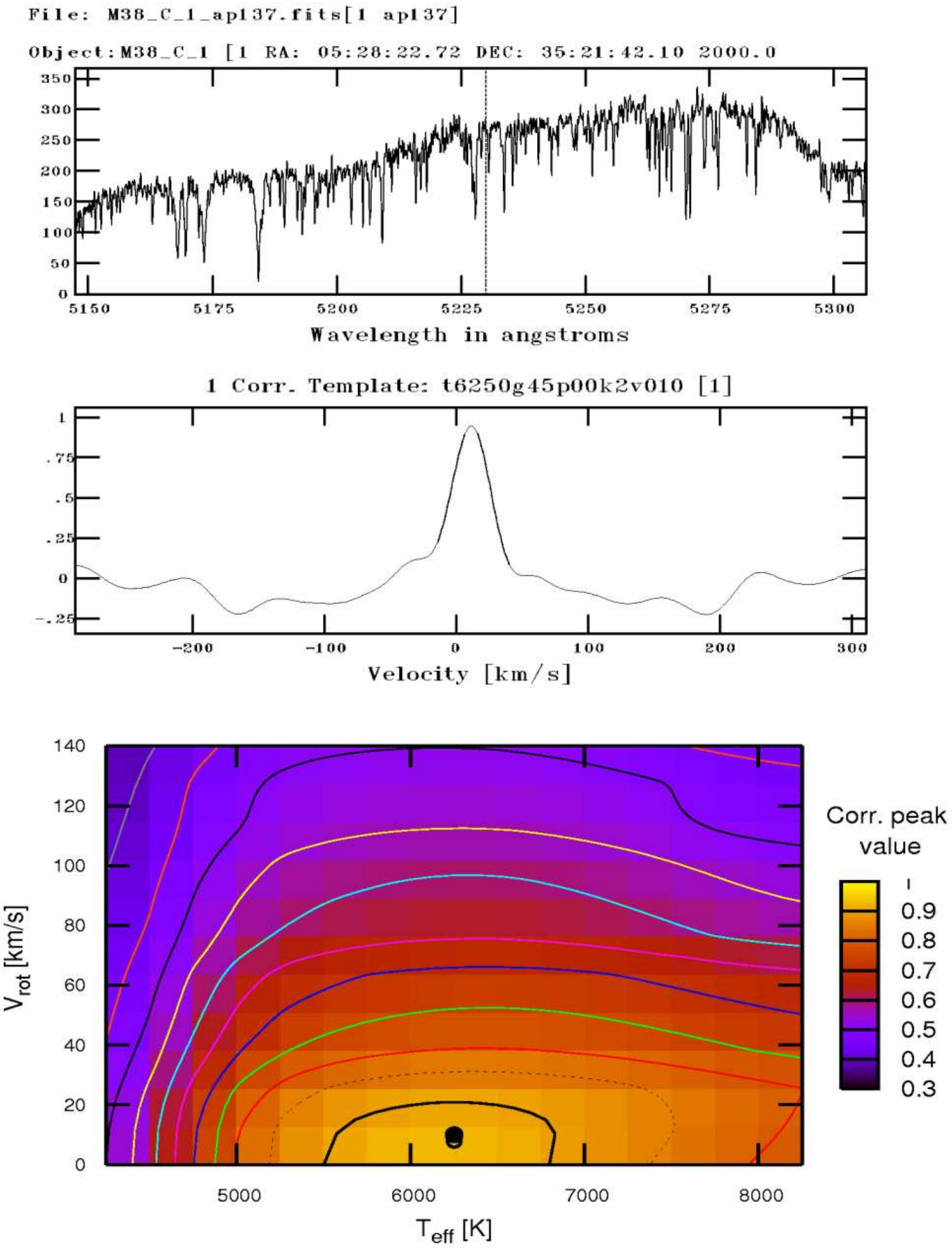

best template T_{eff} = 6250 (6250)
best template V_{rot} = 10 (8)
log(g) = 45

V_{rad} = 11.091 +/- 0.448
V_{corr} = -29.251

V = 13.647 +/- 0.007
BV = 0.657 +/- 0.009

BV_0 = 0.5075 (based on T_{eff})

Multi-template fitting sample *– the spectrum (top) is cross-correlated (middle) against a set of synthetic templates, and the best fit is picked based on the cross-correlation peak height (bottom).*

Chapter 6

Obtaining Radial Velocities

Measuring radial velocities is based on comparing a template to the stellar spectra by computing the cross-correlation function (CCF). There are two different methods performing such calculation.

One way is based on the optical cross–correlation process used by CORAVEL (Baranne et al., 1979). That instrument placed a spatial filter in front of the detector and measured how the recorded intensities changed as the stellar spectrum moved respect to the mask, and thus detected RV changes. Such computation can be easily performed in a software environment on a spectrum s_x describing the stellar intensity at every pixel (wavelength) location x:

$$ccf(v) = \sum_l \sum_x \; m_{l,x}(v) \; s_x, \tag{6.1}$$

where $m_{l,x}$ is the fraction of the lth line of the mask falling into the pixel x at the applied (velocity) shift of v (Baranne et al., 1996). The width of mask lines is fixed, and determined by the spectrograph resolution. The position of lines have to be specified according to the location of stellar absorption features at zero velocity. However, deep and sharp lines contain more radial velocity information, and so a binary mask (in which all lines are weighted as 1, and everything else is 0) does not provide optimal correlation. Therefore the RV precision can be improved by weighting the mask (described in Pepe et al. (2002); see Fig. 6.1(a) for a weighted mask sample). Also, in case the spectrum covers a large wavelength range, such as echelle spectra does, the mask and spectrum better be converted from pixel to $log(\lambda)$ scale. This way a given velocity corresponds to the same amount of shift measured at any part of the spectrum. This method is very simple, yet provides very accurate results. Essentially Eq. (6.2) is the averaging of all selected spectral lines, and therefore finding the *minimum* of such CCF provides the RV information.

The other method is more computation intensive, as it is calculating the $CCF(k)$ discrete Fourier-transform of the $ccf(v)$ cross-correlation function:

$$CCF(k) = W \; S(k) \; T^*(k), \tag{6.2}$$

where $S(k)$ and $T(k)$ is the discrete Fourier transform of $s(x)$ stellar and $t(x)$ template spectra, W is a normalization factor and * indicates the complex conjugation. By inverse transforming $CCF(k)$ the *maximum* of the cross-correlation function can be determined and so the RV measured. Although this method first was applied and developed for galaxy spectra exhibiting large

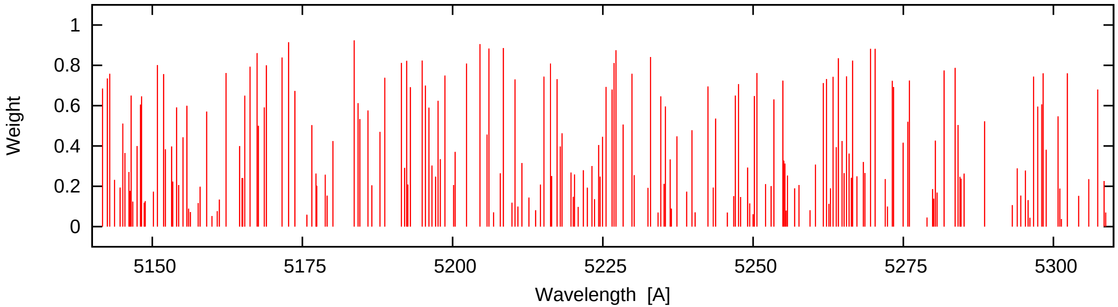

(a) A weighted correlation mask for a G2 star.

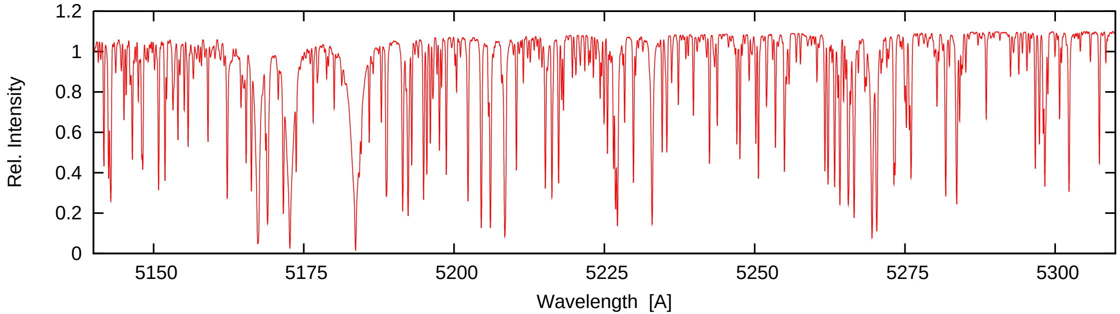

(b) A synthetic template with stellar parameters T_{eff}=5750 °K, surface gravity of 4.5, solar metallicity and zero rotation.

Figure 6.1: ***Cross-correlation mask samples*** *in the Hectochelle RV31 order (Mg band,* 5150 – 5300 *Å)*

RV shifts (Tonry & Davis, 1979), it has been successfully used for stellar RV measurements. The template can be either an observed spectrum, however a noise-free comparison provides cleaner CCF peaks and thus more accurate radial velocities. Therefore a synthetic template is preferred (see Fig. 6.1(b) for a sample).

For historical reasons, I think, the former method is mostly used by European astronomers, while the FFT method is more widely spread in the U.S. Although the execution is different, the two ways of computing the CCF is based on the same principles. Comparing the two subfigures of Fig. 6.1 it is apparent that the template masks are very similar, indeed. For pure RV determination it is sufficient to use only a few masks (e.g. HARPS is using only 3 different masks for different spectral types). The averaging of selected spectral lines, which all exhibit the same intrinsic FWHM, over a wide wavelength coverage provides a very accurate RV value. On the other hand, creating a library of synthetic spectra covering a large astrophysical parameter space (e.g. effective temperature, specific gravity, metallicity, rotational velocity) provides a way of spectral classification even with limited (50 Å) spectral coverage. However the RV values and astrophysical parameters derived from a small spectral sample might significantly differ from template to template (see Fig. 6.2). Although finding the best match between observed and template spectra would provide not just a precise RV measurement but a good estimate for stellar parameters as well. Latter, the *multi-template fitting*, is the approach I have used in the spectral analysis providing the results presented in Part III.

6.1 The Multi-template Method

The radial velocities and stellar parameters were obtained by cross-correlating (CC) each observed spectrum with a set of templates using the `rvsao.xcsao` task within the IRAF environment. As reported in Fűrész et al. (2006) by finding the most similar template to a given object in such "multi template method" yields a more accurate RV. Instead of using observed templates an extensive grid of noise-free synthetic spectra can further improve the RV precision.

For the observation of young open clusters (chapter 8 and 9) the set of templates was a 3 dimensional grid in effective temperature, surface gravity and rotational velocity. For the NGC 1907 and NGC 1912 study (chapter 10) the grid was rather ranging in metallicity with a fixed zero rotational velocity, to aid filtering some of the background halo objects exhibiting a likely lower heavy element content. For the young open clusters metallicity was chosen to be $[m/H] = +0.5$, as a possible one for young stars in the solar neighborhood, and its value was fixed because of the common origin of the targets.

For each template the following quantities were determined: S, the height of the CCF; R, the signal-to-noise of the CC (for details see Fűrész et al. (2006), Kurtz & Mink (1998) and Tonry & Davis (1979)); V_{rad}, the heliocentric-corrected radial velocity; V_{err}, the error of radial velocity determination. For each observed spectrum the values of V_{rad} and S, were plotted as a function of changing template parameters, and the global peak was automatically localized for S. To ensure the results are feasible a graphical set of fitting parameters were created and evaluated by eye, for each spectrum. Such a figure set is given in Fig. Fig. 6.2.

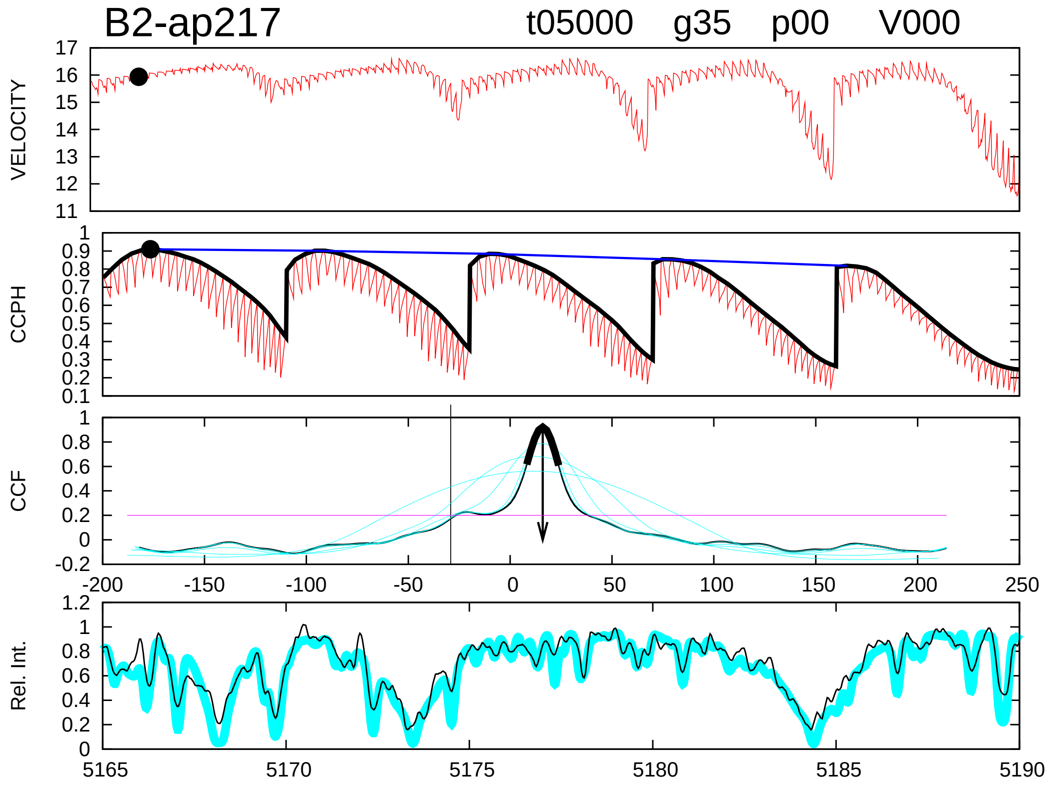

Figure 6.2: ***Sample multi-template fitting evaluation plot**. See text for details.*

The upper panels show the RV and CCF peak height (CCPH) variation versus changing template parameters. A black dot marks the automatically identified best matching template resulting the highest CCF peak value. The template parameters for that particular plot (NGC 1907 & 1912 sample) are changing as follows: specific gravity from 0.5 to 5.0 in steps of 0.5 (highest frequency variation, red curve on the CCPH plot); effective temperature from 3750 °K to 9750 °K in 250 °K steps (slower variation, black envelope); and metallicity from $[Fe/H] = +0.0$ to -2.0 in steps of 0.5 (blue envelope). It is apparent that higher temperature templates result a very low CCPH, and the +0.0 metallicity value is more likely than a metal poor value.

On the third panel of Fig. 6.2 the CCF is plotted. The thick black section indicates the portion of the CCF which was fitted by a parabola to determine the center (the RV value), which is marked by the arrow. The heliocentric correction value is marked by a vertical line: that is the position where a false peak would appear if the spectrum suffers from severe background contamination. (Note the apparent side-lobe of the CCF at this location.) The vertical line is set at CCPH=0.2, just to guide the eye what is considered to be a very low and mostly noise dominated CCF value.

There are actually not one but four different CCFs plotted: for $v\ sin(i)$ of 0, 10, 25 and 50 km s^{-1}. The grid was run for these fixed rotation values as well, and the best matching template was picked, but for those only the CCF is plotted on the graphical set. The reason behind this is to assure that other rotational velocity templates do not provide a better fit. (As the grid parameters are not completely independent, the broadening of spectral lines can be accounted not just for rotational velocity but for pressure as well. Also the depth depends not just on temperature but on metallicity, too. However a certain line broadening, beyond ~ 20 km s^{-1}, can not be explained without rotation.)

The lower panel of Fig. 6.2 displays a small portion of the observed spectrum (thin, black curve) overplotted with the selected best matching template (thick, cyan curve). This plot helps to visually verify if the match is feasible, and absorption features could be clearly distinguished from the noise of the continuum. The parameters of this best fitting template (listed at the upper right) are adopted as the astrophysical parameters of the given star, but only in case if S and V_{rad} were behaving nicely (smooth and continuous change with template parameters discussed here) over a significant parameter space. In case of noisy spectra, low S/N ratio or wide spectral lines not only the CCF gets broad an noisy but the CCPH and RV values are jumping around without any systematic trend. In such case the mismatch between the spectrum and template is also apparent.

For the spectra of young, still accreting stars the Hα emission was so strong that a given aperture became partially saturated, and this affected the Hα profile of neighboring apertures. As the RV determination is based on absorption lines outside of the Hα region, it usually did not cause problem in measuring RV as we excluded any emission portion of the spectrum from the cross correlation.

As mentioned earlier sky subtraction was not performed due to the lack of proper background sampling, so the stellar Hα and profiles contain nebular emission features and the CCF is often side-lobed or double peaked. If the secondary peak is within a few km s^{-1} of the heliocentric correction but clearly distinguished from the main peak, the measured RV was considered usable. If the CCF peak was low and close to the solar correction, we simply excluded the target from the further analysis.

6.1.1 Synthetic Libraries

The CfA Library Stellar radial velocity measurements have a long history at the Harvard-Smithsonian Center for Astrophysics. Starting from the early 1990s, instead of observed templates, synthetic spectra have been used (Stefanik, Latham, & Torres, 1999) to measure RVs. The original grid (Nordström et al., 19944) was calculated for the ∼ 45 Å spectral coverage (5165–5211 Å) of the CfA digital speedometers (Latham, 1992). That library is being updated by Jon Morse for a grid of Kurucz (1992) model atmospheres, to cover a significantly larger spectral range (300 Å) at very high (R=500 000) resolution. A preliminary sample for fixed solar metallicites was available for the multi-template fitting of NGC 1907 & 1912 spectra. The main properties of the preliminary grid (containing a total of 51 359 spectra):

- T_{eff} ranging from 3500 °K to 9750 °K in 250 °K increments;
- $log(g)$ running from 0.0 to 5.0 in steps of 0.5 (not all values at every T_{eff});
- $[m/H]$ between -2.5 and 0.5, with 0.5 grid step;
- microturbulence fixed at 2 km s^{-1};
- macroturbulence fixed at 1 km s^{-1};
- $[\alpha/Fe] = 0.0$;
- $v\ sin(i)$ from 0 to 200 km s^{-1}at values of: 0, 1, 2, 4, 6, 8, 10, 12, 16, 20, 25, 30, 35, 40, 45, 50, 55, 60, 65, 70, 80, 90, 100, 110, 120, 140, 160, 180, 200.

For the cross-correlation with the Hectochelle spectra the template resolution was downgraded to match the observed data, by using a Gaussian kernel to broaden the lines. Such resolution matched templates were used in the spectral analysis of the NGC 1907 & 1912 data set (chapter 10.

The Asiago Library Munari et al. (2005) presents an extensive library of synthetic spectra, also based on Kurucz models but covering the 2 500–10 500 Å wavelength range at four different resolutions ($R = 20\ 000, 11\ 500, 8\ 500$ and 2 000). Although the highest resolution templates are coarser than the Hectochelle data, the slight undersampling of 2 × 2 binned spectra (2.1 pixel FWHM) makes it a fair comparison.

The Asiago grid covers effective temperatures in the 2 500 °K to 10 000 °K range with a resolution of 250 °K (also runs up to 47 500 °K with a coarser resolution), and in other respects very similar to the CfA library. For details see Munari et al. (2005).

The main advantage of this grid, compared to the CfA library, is the full optical coverage and therefore the possible application for Hα band observations. These templates were used for the ONC data (chapter 9) and to re-analyze the NGC 2264 data (as presented in chapter 8).

The Coelho Library An other library of templates by Coelho et al. (2005) gives higher resolution templates (0.02 Å per pixel sampling, so $R \approx$100 000 in the Hα region) over the 3000 Å to 1.8 μm wavelength range. For unbinned Hectochelle data (and for future TRES observations) this provides a better comparison spectrum in any filter/wavelength range. The only downside is the limited temperature range (3500 °K to 7000 °K, with 250 °K resolution) and the fact that no rotational broadening was considered. For details see Coelho et al. (2005)

Part III

Scientific Application: Dynamical Studies of Open Clusters

Chapter 7

From Dust to Stars – an Introduction to Star-forming Regions and Open Clusters

Because most stars are formed in clusters (Lada & Lada 2003), the processes responsible for cluster formation are important to include in any consideration of the mechanisms of star formation. Today stellar clusters are heavily being used as laboratories of stellar evolution research, and with the aid of modern (especially infrared and multiobject) observation facilities our knowledge of cluster and star formation has become very extensive. Therefore it is really hard to write a preamble to the very narrow field I choose for my scientific investigations, the kinematic study of the stellar component in star forming regions. Nevertheless below I give a general, but far not comprehensive introduction to star forming regions. My goal is to provide some ground for those readers not specialized in this field of astronomy, based on the much more detailed work of Schulz (2005), Stahler & Palla (2005), Carroll & Ostlie (1996) and Lada & Lada (2003).

7.1 Molecular Clouds

7.1.1 Properties

Stellar formation is connected to those regions of galaxies where the inter-stellar medium (ISM) forms a dense (at least 10–30, up to 10^6 atoms/molecules per cm^3) cloud. These appear in quite variable sizes between 1–200 pc and masses from 10 to 10^6 $M_\odot$, exhibiting a temperature of 10–50 °K. The heat comes from cosmic rays and radiation of nearby stars. The dissipated energy is exchanged between dust and gas particles of the cloud before it is released as infrared radiation, which is the key to observe these clouds next to the 21.1 cm emission of neutral hydrogen (see Fig. 7.8). Almost all of the cold neutral atomic hydrogen is actually "stored" in these clouds, but the presence of dust grains favor the formation of molecular hydrogen as well. Towards cloud cores, in a shielded environment, most of the hydrogen is in this molecular form. However, H_2 and other symmetric molecules are hard to detect, since they lack a permanent dipole field and thus any line spectrum at radio wavelengths. But the clouds host other molecules, too, and so hydrogen (or essentially the cloud) density can be indirectly traced by CO or CS molecules, due to collisional excitation of these species with H_2.

7.1.2 Evolution

The ISM is under constant perturbation from violent events like supernova explosions or stellar winds. The density of ISM can be highly increased by such processes, or by collision of low density molecular clouds (MCs). Spiral density waves ripple through our Milky Way Galaxy, causing the aggregation and compression of molecular clouds along the spiral arms; assemblies of complexes of molecular clouds along galactic spiral arms have also been observed in other galaxies.

As highly compressible formations, MCs are sensitive to the local radiation field and posses a high level of dynamics. Therefore their lifetime is short, on the order of 10^7 yr. Evidence in one hand comes from their obvious link to stellar formation and observations of young clusters (≤ 5 Myr), whose parental molecular clouds have already been completely destroyed (see Fig. 7.1). An other fact supporting short lifetime that MCs appear chemically unevolved. Moreover, implied by their mass and relatively compact appearance MCs should undergo a rapid self-gravitational collapse and fragmentation, a hierarchical process producing sub-clouds and dense cores. To maintain stability or slow down the collapse, internal forces have to be involved such as thermal pressure, turbulence, magnetic field or rotation. These processes and the soon emerging intense winds of embedded, newly formed O and B stars, could be accounted for the relatively small star formation rate (SFR): on a grand (galactic) scale a cloud usually converts only a few percent of its mass ($\sim 5\%$) to stars before it gets destroyed and star formation halts. (Note, that within a young, embedded cluster –see below– this formation rate is $10 - 30$ %.)

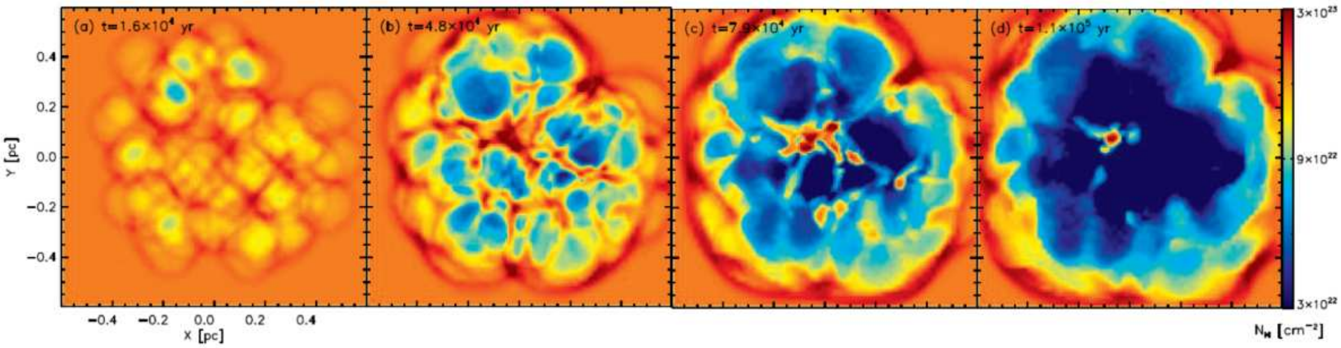

Figure 7.1: ***Evolution of the ISM within a dense cluster, due to highly radiative stellar winds**, as shown by a time-sequence (1.6, 4.8, 7.9 and 11*$\times 10^4$ *yr, from left to right, respectively) of column density plots, after Rodríguez-González et al. (2008). The numerical simulation was carried out for a small, 1 pc diameter cluster containing 75 stars, each exhibiting a mass loss rate of* 4×10^{-6} $M_\odot yr^{-1}$ *due to winds. See Rodríguez-González et al. (2008) for details.*

7.1.3 Cloud Cores

Sir James Jeans presented an early study (Jeans, 1929) on the problem of what conditions are needed to collapse a cloud. Although he made several simplifying assumptions (neglecting magnetic field and rotation) the analysis still provided useful and important insight into the formation of stars. Assuming an equilibrium, gravitationally bound state the virial theorem applies:

$$2K + U = 0, \tag{7.1}$$

where K is the internal kinetic energy of the cloud and U is the gravitational potential energy. These terms and can be expressed as:

$$K = \frac{3}{2}\, N\, k\, T = \frac{3}{2}\, \frac{M_c\, k\, T}{\mu\, m_H}, \tag{7.2}$$

where k is the Boltzmann constant, T is temperature, and N is the total number of particles which can be expressed with the M_c cloud mass and the μ mean molecular weight; and

$$U \sim -\frac{3}{5}\, \frac{G\, M_c^2}{R_c}, \tag{7.3}$$

where G is the gravitational constant and R_c is the cloud radius, which can be written as:

$$R_c = \left(\frac{3\, M_c}{4\, \pi\, \rho_0}\right)^{1/3}. \tag{7.4}$$

In case twice the total kinetic energy of a molecular cloud exceeds the absolute value of the gravitational potential energy, the gas pressure will overcome gravity and the cloud expands. In the opposite case the cloud collapses. The critical mass where this happens is called the *Jeans mass* (M_J), or it can be translated to a limit on radius known as the *Jeans length* (λ_J), which can be expressed by substituting Eq. (7.2) – (7.4) into Eq. (7.1):

$$M_J \simeq \left(\frac{5\, k\, T}{G\, \mu\, m_H}\right)^{3/2} \left(\frac{3}{4\, \pi\, \rho_0}\right)^{1/2}, \ \textit{and} \tag{7.5}$$

$$\lambda_J \simeq .\left(\frac{15\, k\, T}{4\, \pi\, G\, \mu\, m_H\, \rho_0}\right)^{1/2}. \tag{7.6}$$

At the cores of MCs the temperature can reach $T = 150$ °K, and 10^8 atoms per cm^3 density (assuming neutral hydrogen) can imply $\rho_0 = 2 \times 10^{-16}$ g cm^{-3}. In such a case $\mathrm{M}_J \sim 17\ \mathrm{M}_\odot$, which is significantly smaller than the total mass of most clouds.

7.2 Birth of a Star

For the moment I move from the grand scale to the smallest building blocks inside a star forming molecular cloud. Below I briefly overview the star formation process, so after the description of young stellar objects I can use the terms like T Tauri stars to review the formation and evolution of clusters.

7.2.1 Formation of Young Stellar Objects

If the Jeans criterion is met ($M_c > M_J$) the collapsing core is essentially in free-fall (assuming no magnetic field, turbulence or rotation). One can estimate the time-scale of the collapse by calling for the equation of *hydrostatic equilibrium*, which states that in a spherically symmetric static environment at radius r the outward force of pressure gradient cancels the inward gravitational force:

$$\frac{dP}{dr} = -G\,\frac{M_r\,\rho}{r^2}. \tag{7.7}$$

In the first part of collapse the pressure gradients are too small to influence motion, so the left hand side of Eq. (7.7) practically does not exist and thus the acceleration ($F = ma$) of a unit volume mass element ($m = 1\rho$) is described by the following equation of motion:

$$\frac{d^2r}{dt^2} = -G\,\frac{M_r}{r^2}, \tag{7.8}$$

after eliminating ρ from both sides. This equation can be solved by multiplying both sides by dr/dt and integrating the expression, which leads to the free-fall time t_{ff}:

$$t_{ff} = \left(\frac{3\,\pi}{32}\,\frac{1}{G\,\rho}\right)^{1/2}. \tag{7.9}$$

For the above example of $\rho_0 = 2\times10^{-16}$ g cm^{-3} density $t_{ff} \simeq 5\times10^3$ yr, however, this is only true if the released potential energy is radiated away while density is increasing. But after a point the cloud becomes optically thick, radiation becomes inefficient, and as a result temperature starts to raise as well. Also, the constant and homogeneous density for the cores is far from realistic, since there is central condensation and primordial inhomogeneity of the cloud. Recalling the neglected properties (magnetic field, rotation, turbulence) it is apparent that realistic collapse models are very complicated – a more detailed description is way beyond and out of the scope of this thesis. My intention was only to introduce the time scale of collapse trough the very basic considerations, making it comparable to cloud lifetime and characteristic time scales of cluster formation.

The above introduced time scale infers that young stellar objects (YSOs, as it is specifically used to term the very early, collapsing phase) undergo a short-lived, transient phase while a protostar forms at the dense collapsing core. The increasing temperature and building up pressure leads to the first stable core of a few AU in size. As soon temperature reaches 2 000 °K the hydrogen molecules dissociate, decreasing the pressure gradient and leading to a second collapse. Several other contraction cycles may follow due to ionization of He and higher mass atoms, as temperature keeps raising. What is left at the end of the process is a ~ 0.01 M$_\odot$, optically thick core, which "*zero age star*" continues to grow via accretion.

7.2.2 Evolution towards the Main Sequence

The cloud matter impacting the core builds a strongly radiating accretion shock front. High energy photons destroy grains up to a distance of a few tenth AU, but by the time this strong accretion luminosity diffuses through the dusty envelope it emerges only as far-infrared continuum. As the protostar collects more and more matter during this accretion phase the inner regions become more and more exposed (e.g. visible), shifting the peak of observed radiation from far-infrared (FIR) to NIR and the optical. Therefore the spectral energy distribution (SED) within mentioned bandpass provides a good classification scheme (Lada, 1987) to distinguish the pre-main sequence (PMS) evolutionary stages of star formation (see Fig. 7.2).

Before the formation of the central **protostellar objects**, the collapsing cloud fragment is only visible at mm or sub-mm wavelengths or as a dark patch in front of a bright background.

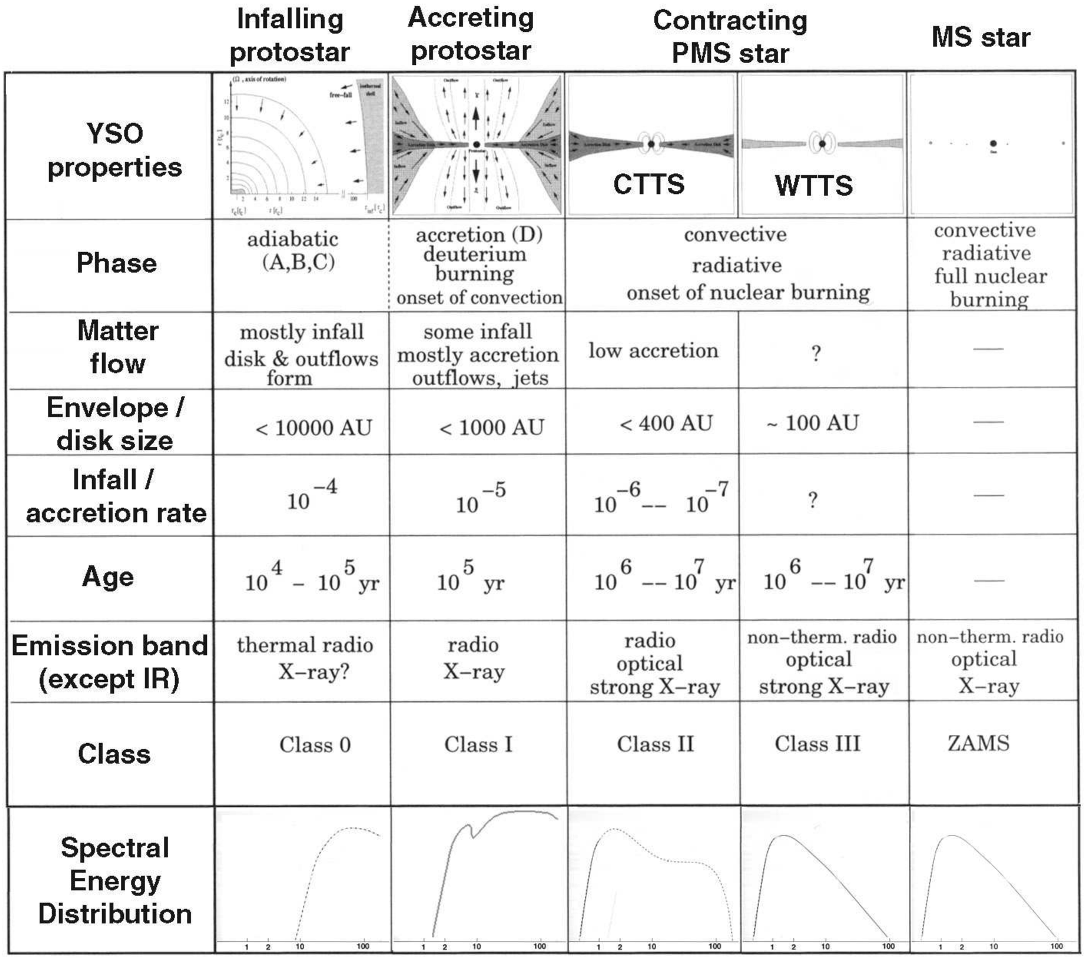

	Infalling protostar	Accreting protostar	Contracting PMS star		MS star
YSO properties			CTTS	WTTS	
Phase	adiabatic (A,B,C)	accretion (D) deuterium burning onset of convection	convective radiative onset of nuclear burning		convective radiative full nuclear burning
Matter flow	mostly infall disk & outflows form	some infall mostly accretion outflows, jets	low accretion	?	—
Envelope / disk size	< 10000 AU	< 1000 AU	< 400 AU	~ 100 AU	—
Infall / accretion rate	10^{-4}	10^{-5}	10^{-6} -- 10^{-7}	?	—
Age	10^4 – 10^5 yr	10^5 yr	10^6 -- 10^7 yr	10^6 -- 10^7 yr	—
Emission band (except IR)	thermal radio X–ray?	radio X–ray	radio optical strong X–ray	non–therm. radio optical strong X–ray	non–therm. radio optical X–ray
Class	Class 0	Class I	Class II	Class III	ZAMS
Spectral Energy Distribution					

Figure 7.2: ***The IR classification scheme*** *in the context with evolutionary phases and matter flow patterns (after Fig. 6.10 and 6.11 in Schulz 2005). The horizontal axis of the SEDs displays log wavelength in micron units (with 1, 2, 10 and 100 values marked).*

At the time accretion starts the radiation peak is still in the sub-mm region, because of the still very dense envelope, and therefore the **Class 0** term of such objects is an extension (by André et al. 1993) of the infrared SED scheme. This phase is all about mass collection, although while the star-to-be eats up the envelope via accretion some material is ejected in forms of energetic bipolar jets and outflows. These supersonic (respect to the local ISM) streams help to eliminate angular momentum of the parent cloud. They can be easily observed as the shocked surrounding glows in the radio continuum, and there are multiple pile-ups (knots) of material visible in Hα and at other optical wavelengths of forbidden transitions (e.g. [SII], [OII], [NII], etc.). Such a “disturbance” is called a Herbig-Haro object or flow.

Class I protostars are relatively massive cores (stellar mass is greater than the mass of the envelope), still collecting material by accretion. In case the infalling material has too high angular momentum it does not impact the protostar itself but rather builds up a disk. This geometrically thin structure rapidly grows in time, and streams from the outer disk collide and form a turbulent inner ring which feeds matter onto the central object. Eventually the disk becomes gravitationally unstable and rapidly releases its content to the star, causing outbursts seen in FU Orionis stars. Although there is already deuterium burning and a convection layer builds up, the observed total luminosity is mostly driven by the accretion ($\dot{M} \sim 10^{6}$ $M_\odot$ yr^{-1}) process. The envelope is more transparent due to its lower mass and the openings created by jets, so the observed emission peaks in the IR. However, depending on the orientation of the system (if seen along a jet) the object might be visible in the NIR or even at optical wavelengths. By the end of the Class I phase the envelope is disappeared, the central object collected its final mass, and the protostar enters the pre-main sequence (PMS) phase by appearing on the H-R diagram at the birthline.

Class II PMS sources are also called T Tauri stars, below a mass limit of $\simeq 2.5$ $M_\odot$. (Higher mass stars have not been considered in this introduction, since those were not within the scope of the spectroscopic survey presented in Part III.) The classical T Tauri stars (CTTS) possess only a very small fraction of their natal envelope, in form of a ~ 0.01 $M_\odot$ disk with diameters on the order of ~ 100 AU. The star is visible and dominating at the optical wavelengths, but the lower temperature disk adds a significant IR excess while the still ongoing accretion produces an extra component of continuum radiation. This *veiling* makes some absorption lines appear in emission, a hallmark of CTTS stars. The wide, strong Hα emission is a defining spectral characteristic that separates these objects from the Class III phase (see below). The wide broadening and changing Hα line is a clear sign of high velocity infalling material and variation of the accretion rate (typically between 10^{-7} and 10^{-10} $M_\odot$ yr^{-1}). Other typical features include the Ca II lines (3933 Å, 3968 Å) in emission, the 6708 Å Li absorption line, and silicate emission of the dusty disk in the IR (9.7 μm, 18.5 μm). The SED also frequently presents UV excess, and CTTS are X-ray sources as well, which short wavelength radiation is accretion driven. The stellar magnetosphere disrupts the inner disk and forces the material to flow into accretion streams. These high velocity streams (~300–500 km s^{-1}, responsible for broadening the Hα emission profile) hit the stellar surface creating a hot spot and generating the short wavelength excess and produce the veiling. Detailed, multi-wavelength sampling of the NIR spectra often reveals a dip in the SED, making the blackbody radiation of the star and disk two well distinguished entity. This suggests that the hottest, inner part of the disk is missing, and there is a central hole. Depending on the disk geometry and orientation the SED and spectral signature of infall can be very different, as the flaring disk seen edge-on can efficiently hide the hot inner regions of the system.

Class III objects are post-accretion T Tauri stars, therefore the velocity broadened Hα signature is not apparent any more as well as the SED is missing almost all the IR/NIR excess in absence of a substantial disk. Due to the weak and narrow (< 100 km s^{-1}) emission this class is also referred as weak-lined T Tauri stars or WTTS. Some emission is still presented, though, but it is mostly created by chromospheric activity (flares). However this is still at an elevated level compared to MS stars, and a clear signature of youth observable in the X-ray regime. In fact, short wavelength surveys are more effective picking up these objects than IR based ones. The disk is clearly more evolved and likely a debris disk, containing only a few Jupiter mass and likely be the place of planet formation — an other connection point to high resolution, high precision spectroscopy, the tool and subject of present thesis.

It is clear from the above that visible and NIR photometry of young stellar objects can unveil their evolutionary state. Spectroscopy can provide insight into the accretion process through the observations of the Hα line. Observing other spectroscopic features (either low or high resolution) can result in spectral classification, for which one method is discussed in Chap. 6. High resolution spectra make it possible to investigate kinematical structure through the Doppler effect. Some other spectral details can provide information on age:

Deuterium and other light elements (helium, lithium, beryllium) within these young stars are already presented, as these species were produced cosmologically through the primordial nucleosynthesis. Lithium, in spite of its small abundance (e.g. fraction of relative to hydrogen $[Li/H] = 2 \times 10^{-9}$ in the ISM) is readily observed in young stellar atmospheres as a strong absorption feature at 6708 Å. Although the core temperature of higher mass protostars reaches 3×10^6 °K, at which point central Li is destroyed ($^7Li + ^1He \longrightarrow ^4He + ^4He$), the surface lithium abundance is the same amount, the ISM value, for PMS stars of all masses. As the stars evolve towards the MS and contract, they heat up and subsequent Li burning occurs. Depending on the thickness of the convection layer (and thus stellar mass) different amount of the primordial surface Li content is depleted. But knowing the mass of an object the amount of Li can serve as a stellar clock.

7.3 Open Clusters

7.3.1 Formation

Mass of MCs can exceed the Jeans mass by several magnitudes, however the observations suggest that not supermassive stars but rather groups of smaller stars form. This, at first glance, can be explained as a consequence of the free fall collapse, during which the density increases by many magnitudes while the temperature remains nearly constant. According to Eq. (7.5) it results a decreasing critical mass. If there were any inhomogeneities in the primordial clouds, those become amplified by the overall collapse and trigger smaller scale, local collapse events. This fragmentation segments the collapsing MC into smaller features, which are also subject to further splitting. However a collapsing region soon becomes optically thick, and the released potential energy does not radiate freely away any more, but rather heats up the environment. The increasing temperature modifies the balance of Eq. (7.5) and eventually stops the fragmentation process at the range of solar mass objects ($M_J \sim 0.5\ M_\odot$).

A detailed, more realistic picture of all physical processes involved in cluster formation, however, is far more complicated. In fact, a "standard model" has not yet emerged because the large number and the complication of processes which can influence the collapse of a cloud into a star cluster. To start with the initial conditions of a MC are not that smooth envisaged in the top-down *gravitational* collapse of Jeans unstable gas. Hierarchical structure of parent MCs themselves and the internal energy of the gas due to *turbulence*, affected by *magnetic fields*, can not be neglected. An elegant possibility based on magnetohydrodynamics (MHD) was proposed by Myers (1998), which can account for the fragmentation, the observed separation between members of a protocluster. This theory shows that if the ionization rate in a massive core is low enough (i.e. high enough extinction that cosmic rays are the only source of ionization), then MHD waves greater than a given frequency can not couple well to the neutral gas. This corresponds to a cut-off wavelength/distance, below which turbulence can no longer be sustained and thus instability occurs.

There is also observational hint, protoclusters within a highly structured environment, that star formation can be onset not by internal but outer forces (e.g. the several discrete, mutually independent clumps suggest triggered star formation in the Rosette Molecular Cloud). In contrast other examples give no hint of external *triggering* (blast form a supernova, spiral density waves across galactic plane, etc.). [1]

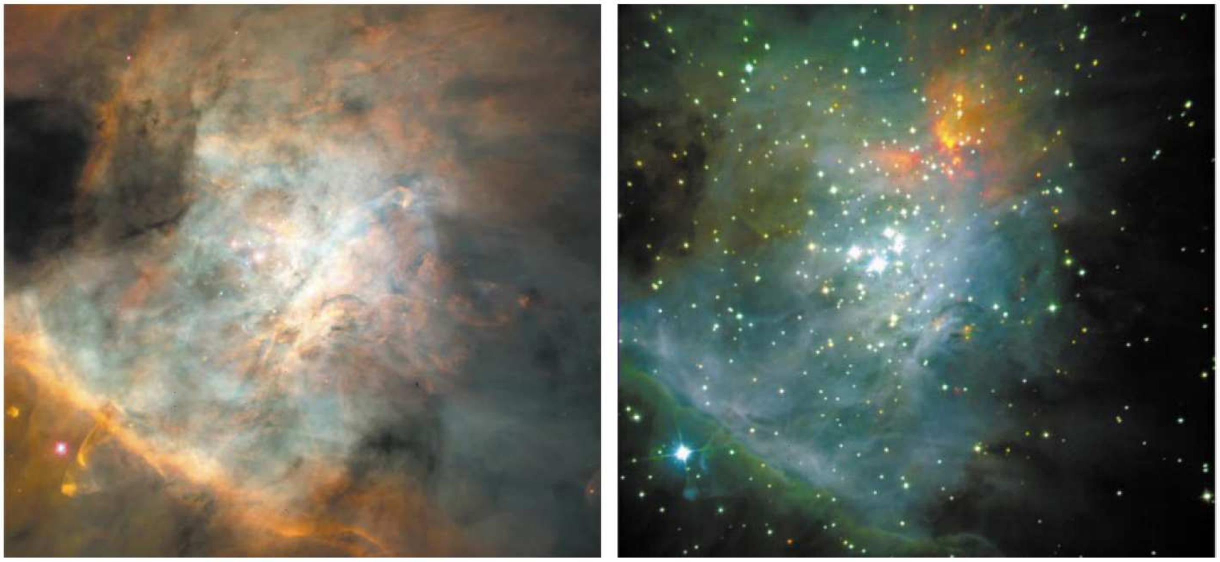

Figure 7.3: ***Optical (left) and deep JHK infrared (right) images of the Trapezium cluster*** *in Orion obtained with the NASA HST and the ESO Very Large Telescope, respectively.*

7.3.2 Morphology and Properties of Young Clusters

Young clusters or protoclusters (and as pointed out below in §7.3.3 most of such stellar systems does not reach a mature age) are in physical association with interstellar gas and dust (see Fig. 7.3 for a well known example). Depending on evolutionary state the clusters can be deeply embedded, and visible only for IR surveys (since visual extinction A_V can be as high as 100 magnitude), or just partially immersed ($A_V \sim 1 - 5$ mag.) in the remaining of the MC. These latter, most evolved clusters are usually located within glowing "bubbles" of ionized hydrogen: *H II regions* created by the hot, energetic radiation of massive stars. And of course, as being stellar nurseries, protoclusters contain all sorts of YSOs.

The internal structure of young stellar clusters is of great interest as it is a direct consequence of the star-forming process and its initial conditions. One might expect that the stellar density, at least partially, reflects the density structure of the initially collapsing cloud. But various effects (and the rapid evolution, see below) can dilute this picture. Nevertheless most young clusters still exhibiting the gas of their parental cloud (embedded clusters) contain the most massive stars in their central region. Such mass segregation from two-body interactions requires the time scale of several τ_c crossing times:

---

[1] See Clarke et al. (2000) for a more extensive overview on the formation processes.

$$\tau_c = \frac{d}{\sigma}, \tag{7.10}$$

where d is the diameter of the cluster and σ is the velocity dispersion of the cluster members. Typical diameters of a few pc and dispersions usually less than 3 km s^{-1} imply several million year relaxation time. Even though the time scale of dynamical mass segregation is inversely proportional to stellar mass, this process still can not be accounted for creating formations like the Trapezium in the Orion Nebula Cluster (ONC). Simple Jeans-type arguments can not explain the presence of massive central objects, as high core densities would result in rather low M_J values (unless local temperature is anomalously high). Therefore evolutionary effects, including accretion and protostellar collisions, are probably required to build up massive central stars. At the same time some young clusters either not show any sign of primordial mass segregation or even have massive stars in their outskirts, so the extent of mass segregation is far from clear.

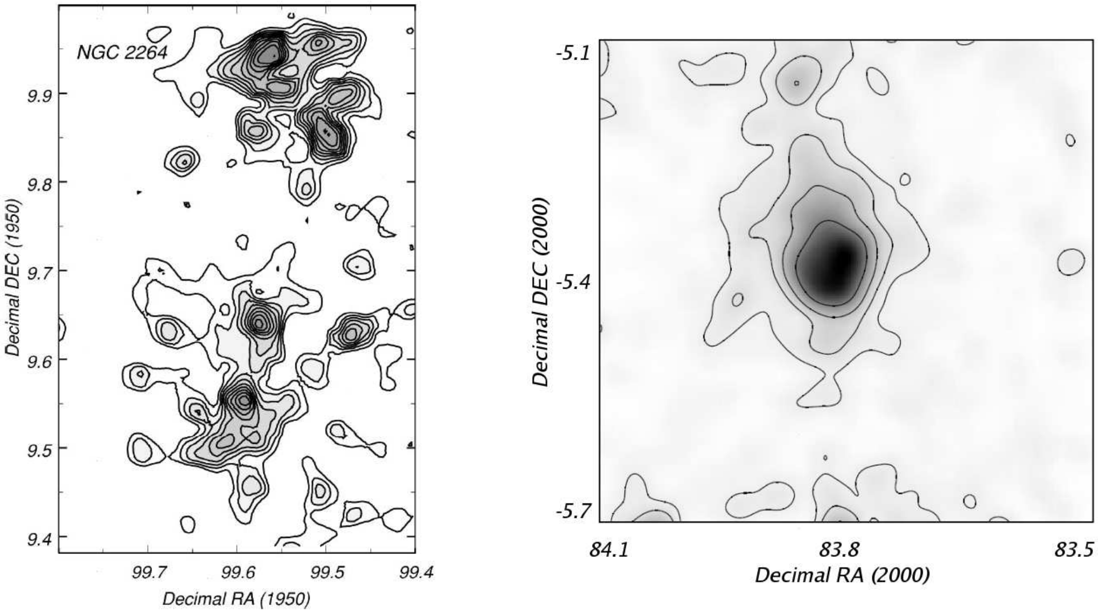

(a) NGC 2264 (b) ONC

Figure 7.4: ***Examples for different cluster structures***, *shown by contour maps of the surface density of infrared sources in a hierarchical (left, NGC 2264 from Lada et al. 1993) and in a centrally condensed (right, ONC, from Hillenbrand and Hartmann 1998) system.*

An other common observation is the flattened, elongated shape of many clusters/star forming regions (see Fig. 9.3 and 9.1). It might be not surprising since it is hard to think of an external trigger (cloud-cloud collision, supernova blast) that does not induce star formation in a sheet-like geometry. Elongated systems also exhibit a *hierarchical structure*: density distributions with multiple peaks, significant sub-structure over a large range of spatial scale. A good example is the partially embedded cluster NGC 2264 (Fig. 7.4(a)) which has a well known, easily identified southern and northern core, and even those two seems to be split based on spatial distribution of infrared sources (Lada et al., 1993). Other clusters, like ONC, are more symmetrical and *centrally condensed* (7.4(b)). The radial density profile is relatively smooth and can be described to a good approximation by a power-law function or a King-like potential. Overall, these centrally condensed clusters do exhibit some structure, e.g. the ONC being elongated and harbor a deeply embedded population (only visible in NIR/X-ray survey data) which displays a surface density distribution significantly different that of the main cluster. It is interesting to note that the condensed clusters are comparable in size to the sub-clusters of NGC 2264. And putting the ONC in the context of star formation within the Orion A molecular cloud the filamentary, hierarchical structure becomes evident on such grander scale. The spatial continuity of star formation within this MC justifies the rendering of ONC to one (although the largest) cluster core within a string of protoclusters.

The average size of protoclusters is around 1 pc, some being as small as 0.3 pc or as big as 4 pc (ONC). The number of members can range from a few tens to ~ 2000, containing a mass of $20 - 1000\ \mathrm{M}_\odot$ (see Lada & Lada (2003) and references therein). Their age is usually less than a few million years, since most clusters disperse (see below) quickly as the material of their parent MC is used up or destroyed. The ones survive the birth might live as long as a few billion years (like M67), but as pointed out below the life of a cluster is full of dangers.

7.3.3 Evolution

Formation of a bound cluster requires that a high fraction of the gas (30–50 %) must be turned into stars before destructive feedback mechanisms from massive stars and Herbig-Haro flows come into play. These processes quickly disperse the remaining gas and by removing a significant portion of the mass render the cluster to unbound *associations*. Although the high formation efficiency specified above is a natural consequence of top-down scenarios (i.e. collapse of Jeans unstable gas), only a small fraction of open clusters seem to form a gravitationally bound unit which can survive for more than a few million years. This is a statistical argument: let us assume that star formation in the Orion Molecular Cloud (OMC) is representative for other complexes. Then roughly 50 clusters like NGC 2024 should be forming now within 2 kpc of the Sun. Assuming a cluster formation/gas dispersion time scale of 5×10^6 year, after 10^8 year of cluster production we should observe 10^3 systems in the same Galactic area. However, we wee see less than a 100 clusters younger than 100 million years, so the infant mortality rate of protoclusters must be very high. This also suggests that clusters may account for a significant fraction of all star formation in the Galaxy.

The gravitational glue that binds the system of stars and gas together in the embedded protoclusters might be largely provided by the gas. Stars expected to orbit in a deep potential well of dense cores with orbital velocities characteristic of the virial velocities:

$$\sigma \; = \; \left(\frac{G\ [M_{gas} + M_{stars}]}{R} \right)^{0.5}, \tag{7.11}$$

where σ is the same velocity dispersion of Eq. (7.10) and R is the radius of the protocluster. As projected by above equation the fate of an embedded cluster depends partially on how its gas is dispersed. In many cases one or more high mass stars emerge and drive off the ISM relatively quick. The result is an unbound, expanding group of stars known as *OB associations* (see left panel of Fig. 7.5). The absence of massive stars does not prevent gas disruption, as the energy from YSO outflows and jets can be also very effective in dispersing the ISM, however over a somewhat larger timescale and smaller spatial extent. Other systems born in less dense, less structured and more extent dark cloud complexes might never contain a massive star and only exhibit an extended

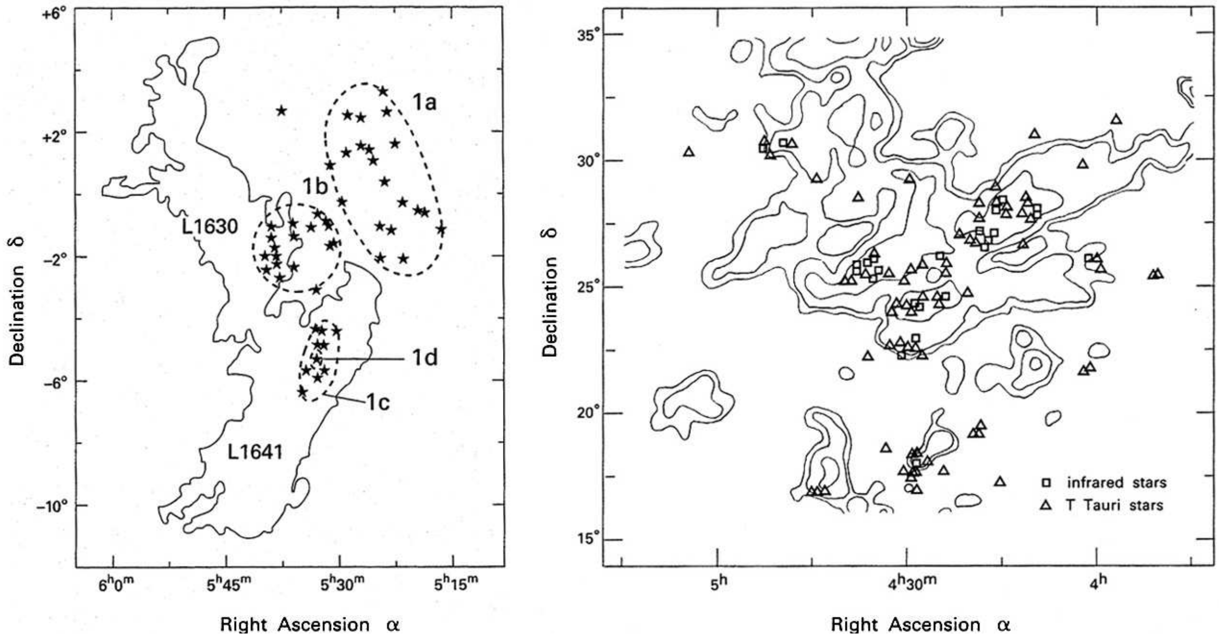

Figure 7.5: ***Examples for OB and T associations:*** *on the left subgroups of the Orion OB1 association are plotted over the CO emission outline of the Orion A (L1641) and Orion B (L1630) molecular clouds; on the right the association of T Tauri stars in Taurus-Auriga is shown along with CO contours. Note the different scale (from Stahler & Palla (2005), after Fig. 1.11 and 4.18).*

distribution of low mass stars (right panel of Fig. 7.5). Such system is not subject of rapid dispersal, and might not even considered to be a once-upon-a-time protocluster. Nevertheless, the significant number of embedded sources commingled spatially with young (usually T Tauri) stars deserves the title of (T) *association.*

If the gas removal time (τ_{gr}) is significantly smaller than the τ_c crossing time the gas disruption is explosive and the protocluster dissolves, because the (most of the) bounding mass leaves with the dispersing gas. However if the star formation rate:

$$SFR = \frac{M_{stars}}{M_{gas} + M_{stars}} \tag{7.12}$$

could be high enough to convert most of the gas into stars, then the system can stay bound. But the SFR, especially for the very early stages, is not sufficient enough. It ranges from approximately 10% to 30% in protoclusters, and changes over the evolution of the system: less evolved clusters seems to have lower SFR values, which seems to reach 30% by the time the cluster emerges from the parental cloud. Therefore for the survival of a cluster $\tau_{gr} >> \tau_c$ (adiabatic gas removal) and a high SFR ($\approx 50\%$) is required. Apparently, it is very difficult for embedded clusters to evolve to bound systems, particularly if O/B stars are formed which set an upper limit of 10^4 yr for τ_{gr}, versus a typical crossing time of 10^6 yr.

Clusters observed with an age of 5 Myr or more do not show any sign of the parental molecular cloud, suggesting $\tau_{gr} < 5$ Myr, which is several (3-5) crossing time. During this period the protocluster continues to loose gas and so decrease its gravitational potential, resulting in an *expansion* of the system. (The appearance of bound and unbound systems are practically indistinguishable with ages less than 10 Myr.) *Dynamical relaxation* also takes place, in which the key is the interaction between individual stars. The lower mass members gain higher velocities upon close encounters and thus fill a larger volume, also causing the overall cluster diameter to increase (*inflation*). At the same time higher mass stars slow down and sink towards the center (*dynamical mass segregation*). Some of the lower mass, outer stars become unbound and leave the cluster, either because they gained larger than escape velocity by an encounter or just because the overall cluster potential becomes too small to keep them bound. Such *evaporation* can disperse $10-80\%$ of the members, but bound cores even with just a remaining 20% can be produced, even containing some O stars. [2] The time scale of such relaxation (τ_{rel}) is on the order of $15-20$ crossing times, based on numerical simulations of a representative protocluster (1000 star, 500 $M_{\odot}$, 5 pc diameter), or $\tau_{rel} \simeq 7 \times 10^7$ yr.

It is apparent from the above that production of a bound cluster from a dense core does require a special set of conditions. In such a view the fact is not surprising, that clusters in excess of 100 Myr are very rare. This was pointed out in the late 1950s by Oort and Spitzer and suggested that the struggle of open clusters are not over by the end of relaxation. They argued that tidal encounters between giant MCs likely disrupt open clusters with mass densities of less than 1 $M_{\odot}pc^{-3}$ in a few 100 Myr. In the context of galactic distribution of MCs it is apparent that life expectancy of open clusters is then a function of galactic radius and latitude. In their orbit around the Galactic center the clusters might pass the galactic plane several times, and each of those passages mean an increased risk of tidal disruption by the very massive molecular clouds. It is ironic, then, that the very structures giving rise to all young clusters appear responsible for their ultimate demise.

7.4 The Aim of Present Study: Probe the Kinematics of Nearby Young Clusters

As it was briefly shown above observations of very young clusters can provide clues to the initial conditions of cluster formation, if the cluster has not been dynamically relaxed. The increasing sensitivity of infrared studies with both ground-based instruments and the Spitzer Space Telescope has made it more feasible to search for substructure in embedded populations, as seen for example in the young cluster NGC 2264 (e.g. Lada et al. (1993), Teixeira et al. (2006)). Recent X-ray studies using the Chandra space telescope also found that ONC stars $0.5-2$ pc from the center show a strong spatial asymmetry (Feigelson et al., 2005). It has been also demonstrated in several other cases that the more embedded populations exhibit a different, structured spatial distribution than lightly obscured sources (e.g the findings of Broos et al. (2007) on the structure of M17).

Although several examples of clear *spatial* substructure has been published lately, the *kinematical* structure of young stellar clusters remained relatively unexplored. In spite high resolution multi object spectrographs have been in service for years (e.g. Giraffe on the VLT, Hydra on the WIYN, MIKE Fibers on Magellan and Hectochelle on the MMT telescopes), fully exploiting the capabilities of these marvelous instruments has just begun recently on this field. The reason might be partly the unfortunate fact that young systems, which might still show some imprint of the primordial kinematical structure, are highly obscured at optical wavelengths and only a small number of nearby star forming regions can be observed efficiently. For some, gas and dust already cleared away by stellar energy input revealing many young cluster members at optical wavelengths, although implying a somewhat evolved status and the chance that kinematical signs are already erased. But high resolution multi-object infrared spectroscopy is not yet available to probe the more embedded, younger star forming regions.

---

[2] The proto-system forming the Pleiades must have contained at least $\sim 10^4$ stars. The ONC might form a similar but smaller bound cluster preserving the Trapezium stars after dispersing most of the ~ 2000 members of the current protocluster.

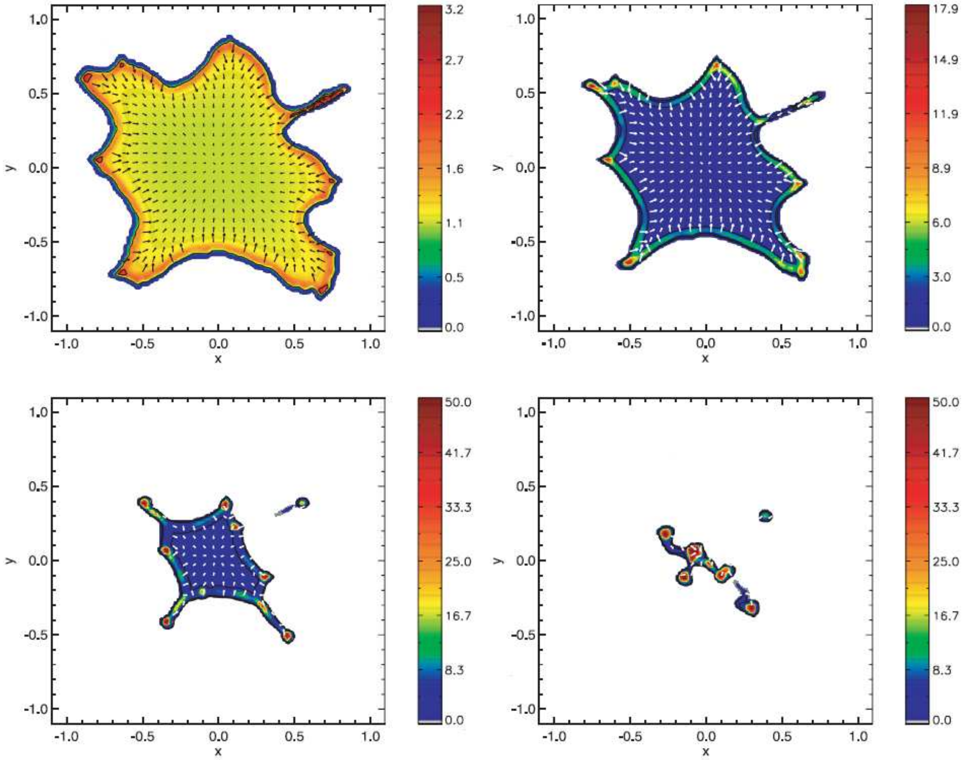

Figure 7.6: ***Simulations of an irregular shaped two-dimensional finite, self-gravitating gaseous sheet****, from Burkert & Hartmann (2004). The color codes density, arrow indicate direction and velocity of motion.*

Therefore my involvement in the commissioning of Hectochelle (Chapter 3) provided me a unique possibility to utilize the “240-eyed MMT” in the exciting field of dynamical studies of open clusters. Another strong stimulating force was the opportunity to work with Lee Hartmann, a co-investigator of Hectochelle, who was just developing by that time a model with Andreas Burkert to describe cluster formation. This model (Burkert & Hartmann, 2004) suggests that gravity acting on the edges of simple, isothermal, finite sheets can produce a wide variety of structures that are likely to have some relevance to observed star-forming structures in molecular clouds (see Fig. 7.6). In particular, Burkert & Hartmann (2004) have shown that a likely general result of the collapse of a sheet formed by flows in the interstellar medium is a filament with higher mass concentrations at the ends of the filament. Any departure from circular symmetry at the edge of gravitationally bound clouds will tend to produce denser concentrations that may be the origin of star clusters. The simulated properties are broadly consistent with the observed morphologies that several nearby clouds exhibit. With access to Hectochelle I had the possibility to first look for (and find) observational evidence supporting the results of these numerical simulations.

Such application of high resolution spectroscopy was a perfect completion of my work in the field of instrumentation, as building the TRES spectrograph profited a lot from the commissioning/observing experience with Hectochelle. The Center for Astrophysics has also provided a unique, supportive environment offering convenient interaction and collaboration with groups specialized in high precision RV measurements and spectral analysis (Dave Latham group) and in star forming regions (Spitzer/IRAC and star formation group including Lori Allen, Charles Lada, Tom Megeath and many others).

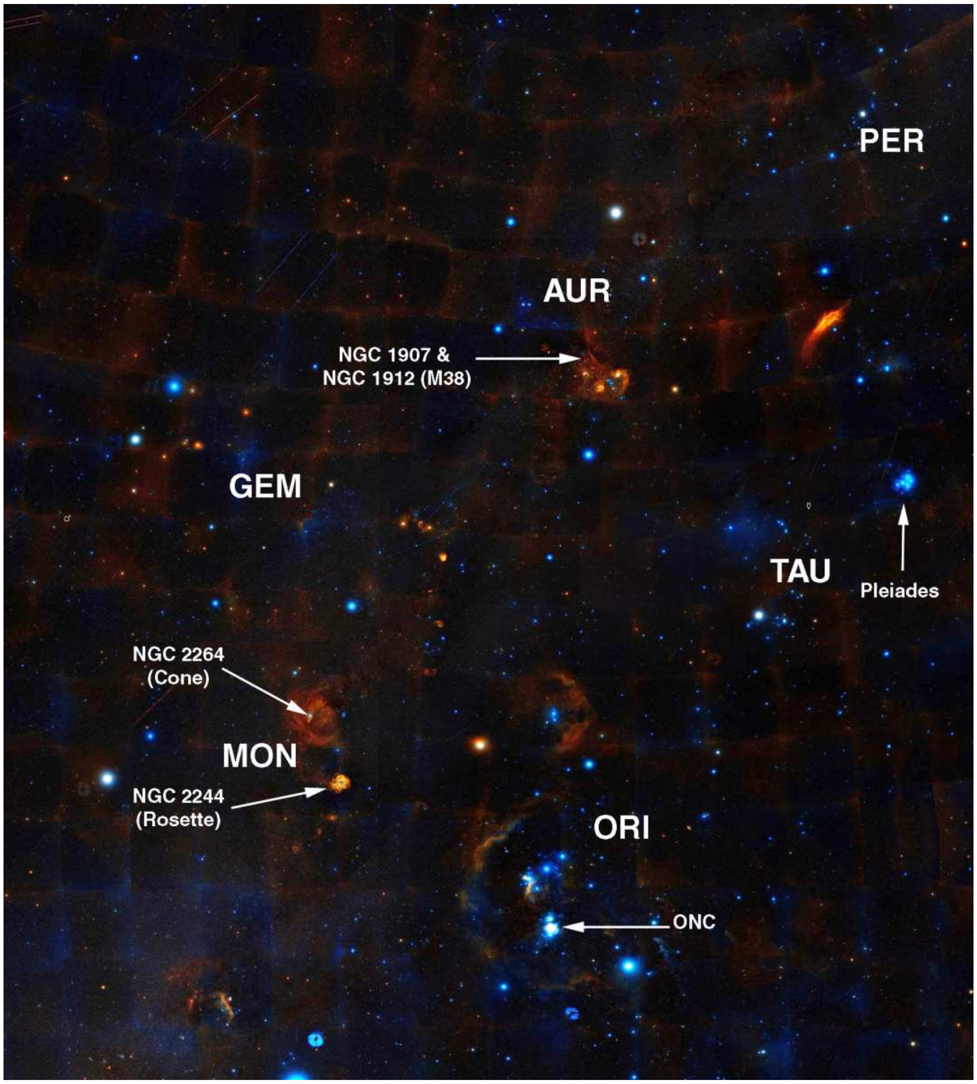

Figure 7.7: ***Location of the studied clusters*** *in relation to the Milky Way, shown in the visible (DSS mosaic image from http://sky-map.org). Some constellations and the Pleiades are also marked. Compare with Fig. 7.8*

As suggested by Lee Hartmann I have conducted spectroscopic surveys in two very young star forming regions (NGC 2264 and ONC), mainly concentrating on the Hα portion of the visible spectrum because of the above mentioned reasons. Later this work has been (and as I

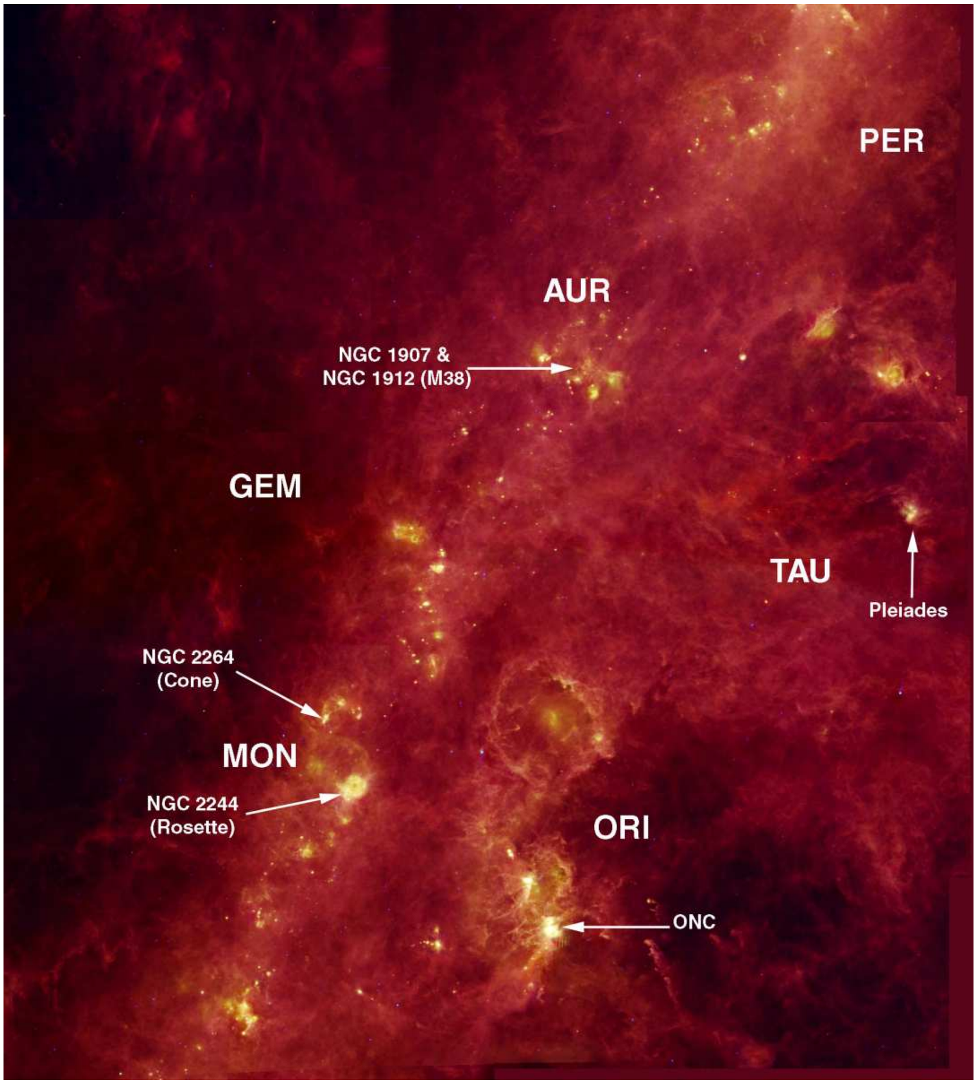

Figure 7.8: ***Location of the studied clusters*** *in relation to the Milky Way and MCs, shown in the infrared (IRAS mosaic image from http://sky-map.org). Location of some constellations and the Pleiades are also marked. Compare with Fig. 7.7*

write, being) expanded in wavelength (Li line, Mg lines) and spatial coverage (larger are of ONC, moving towards the south). Utilizing the developed analysis and tools an older but still interesting cluster (or actually cluster pair, NGC 1912 and 1907) was observed in order to investigate not just the initial conditions but evolutionary effects of open clusters.

The location of these three objects, which are the subject of the following three chapters, are shown in a visual and infrared wide angle sky map on Fig. 7.7 (visible) and Fig. 7.8 (infrared). As it is apparent from the IRAS map there are several more regions of interest, big molecular clouds harboring dozens of stellar birthing sites. In collaboration with an old friend from the University of Szeged, Zoltan Balog and I have proposed to continue and expand the kind of research presented in this thesis. As a next step (a work in progress) we have targeted the Monoceros OB1 association, or the well-known Rosette Nebula (NGC 2244).

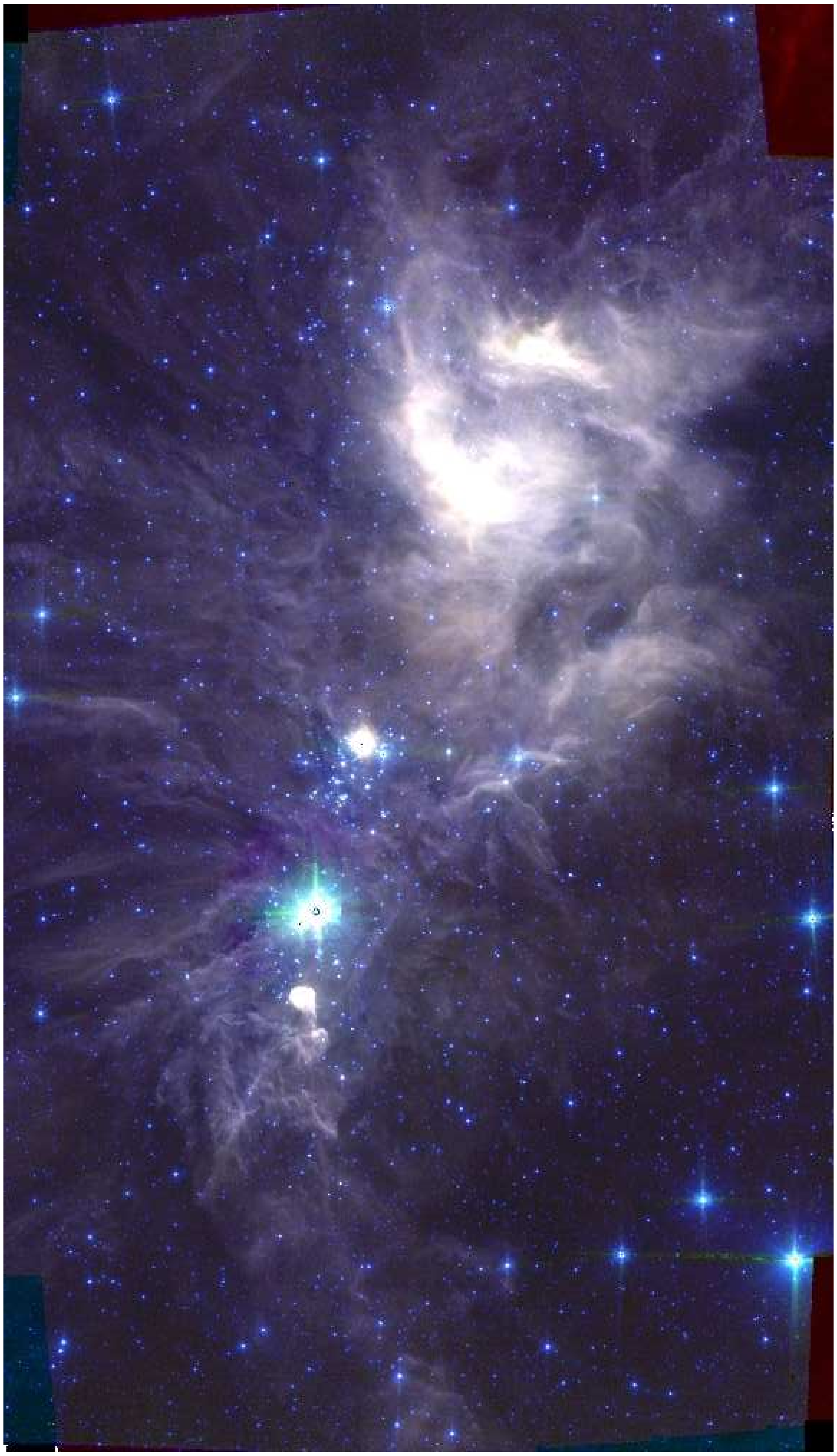

The Cone Nebula and NGC 2264 – *color composite of 3.6 μm (blue), 5.8 μm (green) and 8.0 μm (red) IRAC mosaics (Teixeira, 2008)*

Chapter 8

NGC 2264 – The Cone Nebula

NGC 2264 is one of the most famous and best studied young clusters. Many investigations of this region have been undertaken, building on the early work of Herbig (1954). A number of studies suggest low extinction toward NGC 2264 ($E(B-V) = 0.082$ by Walker (1956); $E(B-V) = 0.071 \pm 0.033$ by Sung et al. (1997); $E(B-V) = 0.066 \pm 0.034$ by Park et al. (2000)), although the large amount of molecular gas in the region (§2.4) suggests that a substantial number of sources embedded in dust remain to be found. The optical nebular emission is less intense than in the Orion Nebula Cluster (ONC), so contamination of stellar spectra from nebular emission is less of a problem in NGC 2264. There is a dark cloud immediately behind the cluster which obscures most of the background stars, thus reducing the number of potential impostor members (Herbig, 1954). Thus, despite the fact that NGC 2264 is more distant than the ONC and other nearby regions of star formation (800 pc by Walker 1956; 800 pc by Sagar & Joshi 1983; 950 ± 75 pc by Pérez et al. 1987; 760 ± 40 pc by Park et al. 2000) the low extinction and weak nebular emission make NGC 2264 a favorable and important target for star and cluster formation studies.

Age estimates of NGC 2264 have been reduced as the quality of NGC 2264 observations have improved. Early estimates suggested ages 3-5 Myr (Harris, 1976; Park et al., 2000; Palla & Stahler, 1999), while Flaccomio et al. (2000) estimate an age closer to 1-2 Myr, and Ramírez et al. (2004) found that most of the X-ray stars were younger than 3 Myr. A major reason for the discrepancy between different estimates is the differing weight placed on specific mass ranges. As pointed out by Hartmann (2003), ages inferred from $1-2$ $M_\odot$ stars in young associations tend to be older than those of the lower-mass stars. Hartmann (2003) argued that the ages of these slightly higher-mass stars are systematically overestimated by neglecting "birthline" effects (e.g., pre-main sequence contraction from finite starting radii); this leads us to favor the lower ages of Flaccomio et al. (2000). and Ramírez et al. (2004) based on the lower mass stars, which are more consistent with the large amount of molecular gas associated with the cluster.

The spatial distribution of the stars in NGC 2264 is extended along the north-south direction, paralleling the extension of the molecular gas in the region (Ridge et al., 2003). This feature, consistent with the general youth of the cluster, suggests that NGC 2264 may still exhibit the morphology of the gas cloud from which the protostars coalesced. The early evolution of stellar systems may be strongly affected by the density and dynamics of the environments in which they form. Numerical simulations (Scally & Clarke, 2002) show that the lifetime of any primordial substructure is short, a few million years or less. Radial velocity studies may be able to provide clues to cluster formation for very young regions by revealing coherent patterns in the motion of sub-regions.

In this paper we report the initial results of our continuing radial velocity (RV) survey of NGC 2264, in the search for kinematic signs of primordial structures in young stellar clusters. First we describe the observations and data reduction; than we compare the radial velocity distribution of the stellar and gaseous component, the latter as traced by ^{13}CO measurements. Finally, we discuss possible implications of our results for cluster formation scenarios.

8.1 Observations

8.1.1 Target Selection

We drew our target sample from several sources, starting with surveys of Hα emission-line objects (Herbig 1954; Reipurth et al. 2004 – R04 hereafter), narrow-band photometry (Sung et al., 1997, 2004; Park et al., 2000), and samples of young objects selected based upon their IR and UV excess (Lada et al., 1993; Rebull et al., 2002). All of these surveys have a bias toward finding (accreting) Classical T Tauri stars (CTTS) and against finding pre-main sequence (PMS) stars with weak or no disks. Therefore, by supplementing these samples with a large catalog of X-ray sources (Flaccomio et al., 2000; Ramírez et al., 2004), also sensitive to weak-emission (non-accreting) T Tauri stars (WTTS), the bias towards accreting stars can be corrected. These surveys, together with proper motion (Vasilevskis et al., 1965) and variability (Lamm et al., 2004) surveys provide a very good input catalog of potential cluster members.

The selected targets come from three of the catalogs above: a substantial fraction, 1389 stars, from Ramírez et al. (2004) X-ray sources; 408 Hα emission stars from R04; and 100 stars from Park et al. (2000). As some of the stars appeared in more than one of these three catalogs, the final target list contained 1563 stars.

The stars actually observed are shown in Fig. 8.1. In this figure we also plot the Hα emission stars of R04 objective prism survey to guide the eye where the larger concentrations of cluster members are expected.

8.1.2 Spectroscopic Observations

The stellar spectra were obtained with Hectochelle (Szentgyorgyi et al., 1998), a fiber-fed, bench mounted echelle spectrograph that operates at the post-conversion MMT. For details see §3.1.

The preferred order for radial velocities with Hectochelle is centered at 5225 Å and includes the Mg triplet. Unfortunately, a failure of the original coatings (now replaced) on the camera and collimator mirrors of Hectochelle reduced the reflectivity in this spectral region by a factor of up to 6 per mirror. Also, our targets have brighter continuum at Hα than at 5225 Å, helping to compensate for fewer lines. Therefore we decided to use the 190 Å wide order centered at Hα, which was relatively unaffected by the coating failure. Although this order has a smaller number of lines than the 5225 Å order, we found that by masking out the $H\alpha$ line when executing the cross-correlation we can get velocities with an error of $1 - 2$ km s^{-1}. This velocity resolution is good enough for our kinematic study (see, e.g., Sicilia-Aguilar et al. 2005). While this order is not optimal for

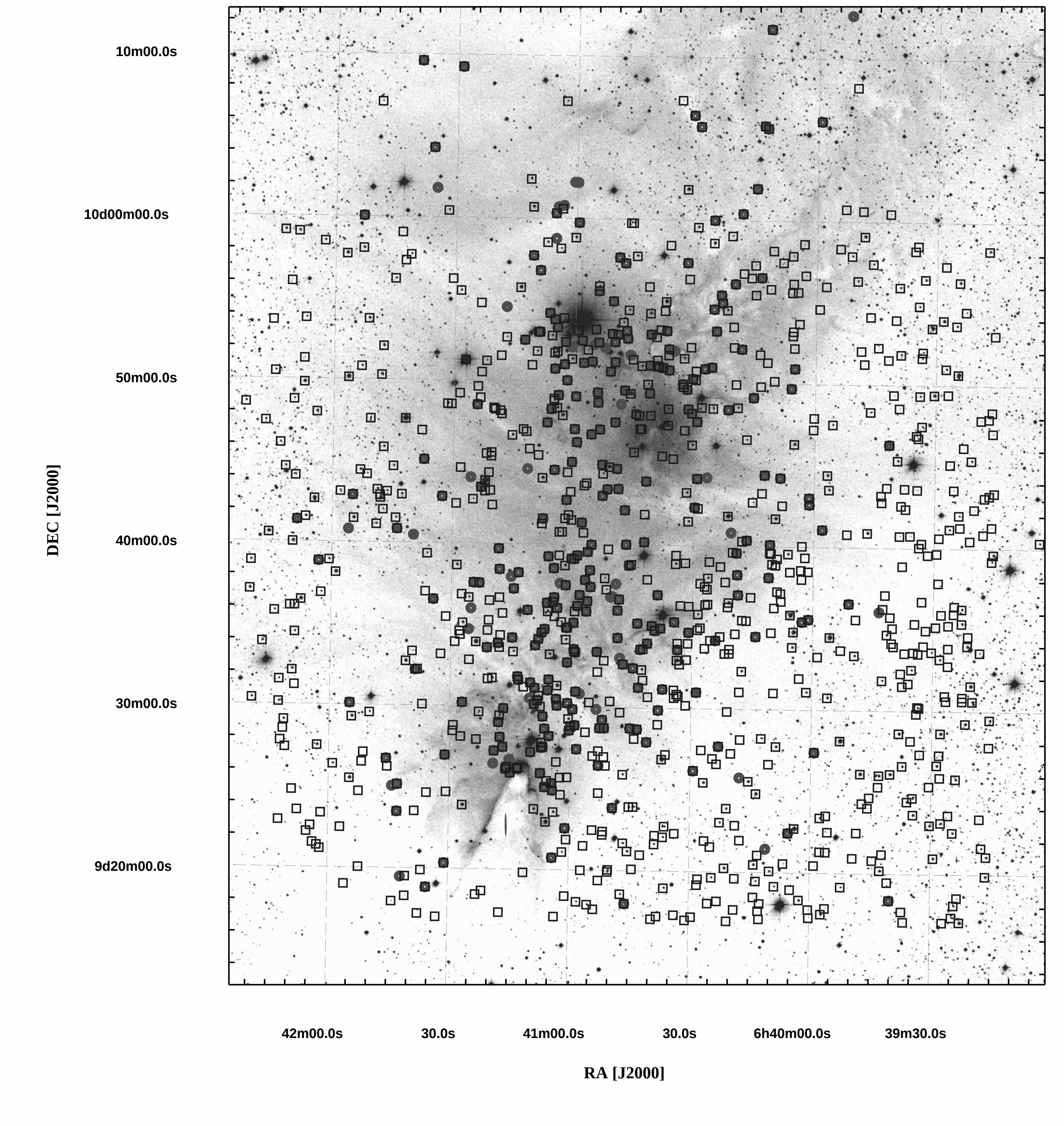
10m00.0s
10d00m00.0s
50m00.0s
40m00.0s
30m00.0s
9d20m00.0s
DEC [J2000]
42m00.0s
30.0s
41m00.0s
30.0s
6h40m00.0s
39m30.0s
RA [J2000]

Figure 8.1: ***Our targets in the field of NGC 2264***. *open diamonds), superimposed on a DSS POSS1 red plate image of the cluster. $H\alpha$ emission stars (filled circles) from R04 are also shown to guide the eye where the concentration of young stars expected to be larger. Most of these emission stars were observed by us, but as can be seen our targets were more evenly distributed, covering the outer regions of the cluster as well.*

radial velocity measurement, observations of the $H\alpha$ profiles allows us to unambiguously identify and distinguish CTTS and WTTS stars.

Our first observations in NGC 2264 were taken in March 2004. These data were obtained during the commissioning phase of the instrument, and we ended up observing 155 targets in one fiber configuration (see Table 8.1) centered north of the Cone nebula. The preliminary results

Table 8.1. Summary of spectroscopic observations of NGC 2264

Date	field center		exposures	offset sky	number of targets
2004 Mar 10	$6^h\ 40^m\ 51^s$	$+09^\circ\ 44'\ 46''$	4×15 min	1×15 min	155
2005 Dec 02	$6^h\ 40^m\ 46^s$	$+09^\circ\ 38'\ 13''$	3×15 min	—	234
2005 Dec 02	$6^h\ 40^m\ 35^s$	$+09^\circ\ 36'\ 56''$	3×15 min	—	232
2005 Dec 02	$6^h\ 40^m\ 42^s$	$+09^\circ\ 45'\ 36''$	3×15 min	—	231
2005 Dec 03	$6^h\ 40^m\ 42^s$	$+09^\circ\ 32'\ 13''$	3×15 min	—	226

derived from this first data set showed interesting results so we decided to observe NGC 2264 again. We revisited the cluster selecting targets from an expanded list including objects from the catalog of R04 and the full catalog of Ramírez et al. (2004).

Even though the spectrograph mirrors were re-coated during the summer of 2004 and we could have used the 5225 Å order, we found that the accuracy of radial velocities obtained in the Hα order to be adequate and the extra information in the Hα line profiles to be scientifically useful so we continued our observations in this order. The second observing run was carried out in December, 2004. During the nights of 2 Dec. and 3 Dec. we observed 923 targets in four fields (see Table 8.1), including 88 targets observed in March which were thought to be members based on the March RV data.

We have found, in observations of regions with strong, spatially structured nebular emission, e.g. the Orion Nebula Cluster (Sicilia-Aguilar et al., 2005), that it is necessary to offset the telescope 10$''$ without moving the fiber buttons to obtain a good measurement of nebular emission contaminating the stellar spectra. In March we followed this procedure. We found that in NGC 2264 this background subtraction is only important near the Hα and [N II] lines; it is unimportant for radial velocity measurements, which depend only upon the absorption line spectra in between the emission features. Therefore in December we opted to eliminated the offset observations so that we might spend more time collecting stellar spectra.

8.1.3 Radio Observations

Observations of the ^{13}CO transition of CO (110.201 GHz) were obtained at the Five College Radio Astronomy Observatory (FCRAO) 14m telescope located in New Salem, Massachusetts during 2002 September, as part of a larger survey of nearby cluster forming regions (Ridge et al., 2003).

Using the SEQUOIA 32-element focal-plane array and On-the-Fly (OTF) mapping technique eight $15' \times 15'$ submaps were obtained over 3 nights, in order to build up the final $30' \times 60'$ map. Submaps were obtained by scanning in RA, and an "off" source reference scan was obtained after every two rows. The off-position was checked to be free of emission by performing a single position-switched observation with an additional $30'$ offset. Each submap was repeated twice to increase the sensitivity.

The narrow band digital correlator provided a total bandwidth of 25 MHz over 1024 channels, yielding an effective velocity resolution of 0.07 kms^{-1}. System temperatures at the observing frequency were between 200 and 300 K (single sideband). Calibration was via the chopper-wheel technique (Kutner & Ulich 1981), yielding spectra with units of $T_A{}^*$. The final combined map has an average RMS sensitivity of 0.2 K/channel. A full discussion of the data analysis procedure and the integrated intensity image was presented in Ridge et al. (2003).

8.1.4 Data Reduction

In chapter 5 we have discussed the data reduction techniques in general. To obtain the radial velocities we have used the multi-template fitting method described in §6.1. Here we just make some notes specific to the NGC 2264 data set.

For the published results (Fűrész et al., 2006) the templates used in the cross-correlation were observed spectra of 10 relatively bright stars in a field located in Selected Area 57 (Pickering and Kapteyn, 1918), near the north Galactic Pole. As the Asiago synthetic library (see Munari et al. (2005) and §6.1.1) became publicly available we have re-analized the data. This resulted in a significant improvement of RV precision and provided additional information in terms of the astrophysical parameters of the best matching template.

In order to ensure consistency between the March and December data sets we observed 88 stars in both runs. For 31 of these stars yielding the highest correlation peaks the mean of the velocity differences is $RV_{Mar} - RV_{Dec} = 0.3$ km s^{-1} with an RMS of 0.8 km s^{-1}. The values listed in Table 8.2 are corrected for this zero point offset, by shifting the 2004 values to the 2005 scale.

8.2 Results

8.2.1 Distribution of Radial Velocities

The radial velocity distribution of the 344 stars with accurate RV values is shown on Fig. 8.2. The cluster members clearly form a peak centered around $V_{rad}^{helio} = 20$ km s^{-1}, but the distribution is unusually wide and not symmetrical. We also report the distribution on an expanded velocity scale to show how clearly the cluster members form a peak in radial velocity space.

We plot the RV distribution for four selections of stars according to the signal-to-noise values (Tonry & Davis, 1979) of the correlation, in Fig. 8.2. This R value is inversely proportional to the error of velocity measurement. As described in Kurtz & Mink (1998) the errors consist of a systematic and a statistical component, the systematic could be determined for a given instrument by comparing radial velocities measured on large number (several hundred) of objects at two epochs. A very good estimate for the random velocity error is $\sigma = (3/8) * [w/(R+1)]$ (Kurtz & Mink, 1998), where w is the FWHM of the correlation peak and R is the signal-to-noise ratio.

This estimate agrees well with our result in NGC 2264 based on 31 stars, observed both in March and December with an R value larger than 6. Also, based on results with other instruments, the estimate for the error mentioned above is likely within ±30% of the real error value for a Hectochelle measurement. We therefore adopt a velocity error of $\sigma = 6/(R+1)\,\mathrm{km\,s^{-1}}$; the error is larger for stars with rotational velocities greater than about 10 km s^{-1}. In principle, this means that slowly-rotating stars with correlation peaks of $R = 2$ can yield a velocity error of 2 km s^{-1}.

Of course, in our spectral order of velocity width ~ 8000 km s^{-1}, we can expect to find, just due to chance, roughly one 3σ peak (with an FWHM of ~ 10 km s^{-1} or an R value of ~ 3)

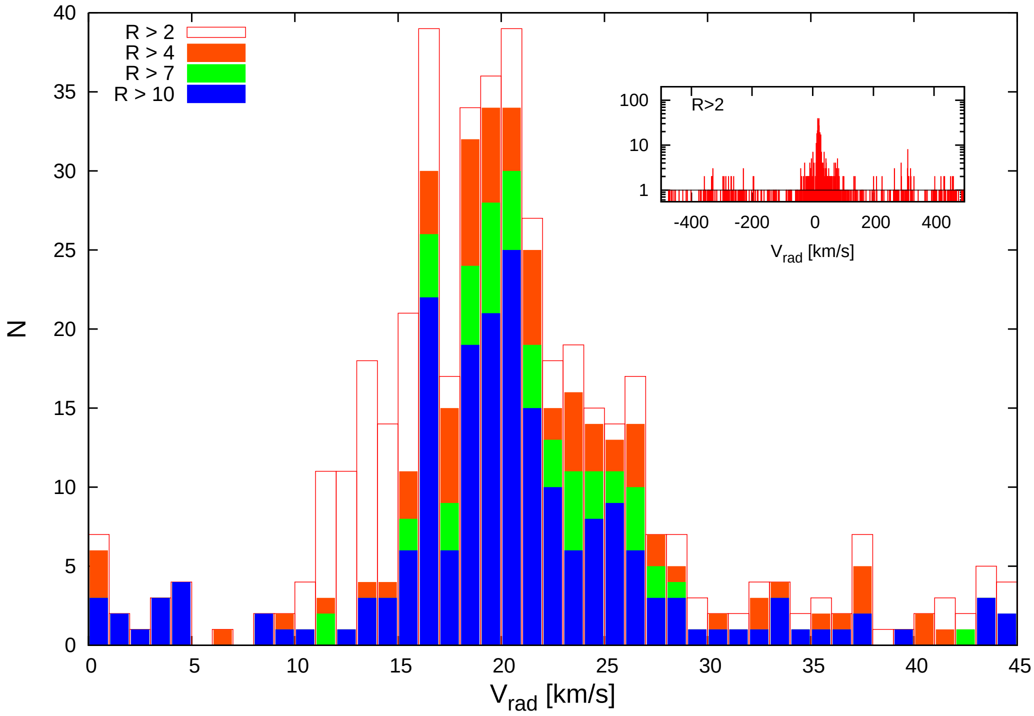

Figure 8.2: *Radial velocity distribution of stars observed in the NGC 2264 field.* *The distribution is unusually wide and non-Gaussian. The insert is an expanded velocity range to show how clearly the cluster members form a peak in the velocity space. There are four selections of stars plotted according to the signal-to-noise (R) values of the correlation, showing that the large dispersion is real and not coming from the uncertainties of RV measurements (see text for details).*

in the cross-correlation function, somewhere within the interval. If we restrict our attention to an interval of $\sim$ 100 km s^{-1} near the median cluster velocity, then we would expect to have a probability of about 10% of finding a $R \sim 2$ peak of width $\sim$ 10 km s^{-1}. The $R > 2$ selection is included in Fig. 8.2 because, even with the larger uncertainty in velocity, the distribution of these stars follow the overall shape of the histogram fairly well. As a reminder that large errors are associated with this group, we plotted this group as light gray columns without a border. There is a fifth sample of stars displayed on the left panel of Fig. 8.2 as narrow, white bars: stars with $H\alpha$ emission detected in their spectra. Comparing this sample to the others we can say that the radial velocity distribution of TTS is the same as for the rest of our targets. Also, as the distribution is same independently of the R value of the correlation, the observed large dispersion is not due to uncertainties in the RV measurement.

The RV histogram of Fig. 8.2 is far from Gaussian. To estimate the velocity dispersion we used the definition $\sigma^2 \equiv \sum (x_i - x)^2/(N-1)$. Assuming lower and upper limits for membership as 13 km s^{-1}and 30 km s^{-1}, the estimated one-dimensional RV dispersion is $\sigma \approx 3.5$ km s^{-1}. This is much larger than, for example, previous estimates for the dispersion of ONC (determined as 2.3 km s^{-1} by Jones & Walker (1988), or a value of $\sim$ 1.8 km s^{-1} for the brighter stars derived by Sicilia-Aguilar et al. (2005)). The skewness of the velocity distribution suggests that the cluster is not dynamically relaxed, consistent with our finding of spatially-coherent motions.

Table 8.2. Members of NGC 2264 — *sample*

2MASS_id	ID	J	$(J-H)$	$(H-K)$	[3.6 – 4.5]	[5.8 – 8.0]	V_{rad}	ΔV_{rad}	R	S	EW_c	$FW_{10\%}$	$H\alpha$	Notes	NOB
0639037+094023	F3-ap50	12.65	1.10	0.35	0.00	0.00	20.42	0.37	19.4	0.67	15.5	482	C	—	1
0639156+093913	F2-ap73	13.26	0.56	0.11	0.00	0.00	15.98	1.30	6.0	0.27	0.0	0	AEF	—	1
0639157+092929	F4-ap43	11.67	0.93	0.24	0.00	0.00	33.88	0.14	32.1	0.83	0.0	0	A	—	1
0639170+095815	F3-ap79	12.43	0.53	0.17	0.00	0.00	13.74	0.56	11.3	0.48	0.0	0	AEF	—	1
0639227+091704	F1-ap24	11.13	0.33	0.14	0.00	0.00	25.09	5.04	3.2	0.18	0.0	0	AEF	—	1
0639227+095431	F4-ap90	14.25	0.95	0.35	0.00	0.00	18.88	1.23	4.1	0.17	76.6	310	C	—	1
0639229+093617	F2-ap76	12.62	0.64	0.14	0.00	0.00	14.63	0.20	25.8	0.79	0.0	0	AE	—	1
0639246+092233	F4-ap37	12.79	0.53	0.12	0.00	0.00	18.28	0.20	20.5	0.71	0.0	0	AE	—	1
0639248+093627	F3-ap35	16.23	0.71	0.38	0.00	0.00	13.38	0.97	3.2	0.13	0.0	0	N	—	1
0639263+094111	F4-ap72	12.71	0.82	0.23	0.00	0.00	16.46	0.39	19.7	0.68	0.9	126	W	—	1
0639266+093038	F4-ap52	15.50	0.91	0.25	0.00	0.00	30.14	0.98	4.6	0.20	0.0	0	N	—	1
0639276+092309	F1-ap25	11.03	1.22	0.31	0.00	0.00	34.54	0.15	30.2	0.80	0.0	0	A	—	1
0639279+092839	F1-ap35	10.81	0.74	0.20	0.00	0.00	13.27	0.17	28.2	0.80	0.0	0	AE	—	1
0639289+093752	F2-ap77	15.93	0.46	-0.20	0.00	0.00	13.47	1.66	2.7	0.10	0.0	0	N	—	1
0639294+092059	F4-ap34	12.20	0.53	0.12	0.00	0.00	25.42	0.15	28.7	0.83	0.0	0	AE	—	1
0639304+093337	F1-ap46	12.93	0.83	0.14	0.00	0.00	21.50	1.86	7.4	0.31	1.3	176	W	—	1
0639306+092523	F1-ap32	16.49	0.87	0.21	0.00	0.00	13.31	0.84	2.6	0.10	0.0	0	N	—	1
0639329+093644	F3-ap39	15.01	0.91	0.27	0.00	0.00	11.66	2.99	2.5	0.12	0.0	0	W-	—	1
0639330+095629	F2-ap105	13.16	0.59	0.13	0.00	0.00	24.17	0.17	27.6	0.78	0.0	0	AE	—	2
0639334+094729	F1-ap74	13.36	0.61	0.20	0.00	0.00	35.77	1.20	3.7	0.16	0.0	0	AE	—	1
0639334+095202	F2-ap104	12.63	0.97	0.24	0.00	0.00	18.94	0.83	11.2	0.44	15.2	301	C	—	1

Note. — *NOTE: this is a sample, for the full table see the Appendix 12.2* Hectochelle targets in NGC 2264 found to be members based on measured RV value or by detected Hα emission. The criteria of beeing RV member is to have at least one velocity measurement within 4σ of the cluster mean velocity: 8 km s^{-1} $<$ $V_{helio} <$ 36 km s^{-1} . RV members listed only with $R \gtrsim 2$, while stars with Hα emission are included regardless of R value, but with no velocity displayed.)
2MASS id — 2MASS identification number (truncated RA and DEC coordinates as: HHMMSSS+DDMMSS); **ID** — internal identification number, specifying the field (see Table 9.1) and aperture of observation; **J** — 2MASS J magnitude; **(J-H)** — 2MASS $(J-H)$ color index; **(H-K)** — 2MASS $(H-K)$ color index; 3.6 – 4.5 — IRAC short wavelength color index; 5.8 – 8.0 — IRAC long wavelength color index; V_{rad} — measured heliocentric radial velocity, in km s^{-1}; V_{rad} — *xcsao* error estimate for V_{rad}, in km s^{-1}; **R** — R value of cross correlation (see text for details); **S** — height of the CCF peak; EW_c — absolute value of equivalent width, measured on the corrected Hα profile (see text for details); $FW_{10\%}$ — full width of Hα profile at 10% level of the corrected maximum (see text for details);
Hα — notes on the Hα emission profile. See text for more details on the CTTS/WTTS classification: **C** – CTTS; **W** – WTTS; **CW** – rather CTTS, but could be WTTS; **WC** – rather WTTS, but could be CTTS; **W+** – asymmetry in line profile/wing: likely WTTS; **W-** – asymmetry in wings, but wings at low intensity: could be WTTS; **R** — obviously shifted H-alpha absorption : high RV stars; **A** — only stellar absorption line, no nebular/stellar emission component; **AE** — stellar absorption and nebular emission together; **AF** — same as AE, but fast rotating star produces very wide absorption; **SAT** — saturated, or neighbor saturated;
Notes — MEMBERSHIP: BINARITY: **RDB** – resolved, double lined binary, with RV at 2 epochs (separated double peak in correlation function); **UDB** – unresolved double line. binary, with RV at 2 epochs (blended/side lobed peak, but clear asymmetry in correlation function); **rdb** – same as for RDB, but only 1 RV measurement; **udb** – same as for UDB, but only 1 VRV measurement; **sb** – likely single lined binary, RV at two epochs and at least one suggest membership, some also have $H\alpha$ emission; **hsb** – member based on $H\alpha$ emission detected, but correlation either had just acceptable R value (barely larger than 2) or radial velocity is close to the edge of RV distribution;
NOB — number of observations

8.2.2 T Tauri stars

We found 361 stars with $H\alpha$ emission exceeding the nebular component: 194 among these were CTTS (C: 179; CW: 14; CX: 1; see the caption of Table 8.2) and 167 were WTTS (W: 86; WC: 7; W+43; W-: 31), using the indicator of accretion from White & Basri (2003), that the $H\alpha$ full width at 10% intensity exceeded 270 km s^{-1}. A sample of $H\alpha$ profiles is plotted on Fig. 8.3 (all the profiles are shown in the Appendix, as Fig. 12.2). The caption of Table 8.2 provides the typing guidelines and §9.3.2 presents the details on graphical representation and further notes on typing. Here below we only highlight one difficulty of classification which arising from the single epoch nature of observations and the time dependency of stellar emission profiles.

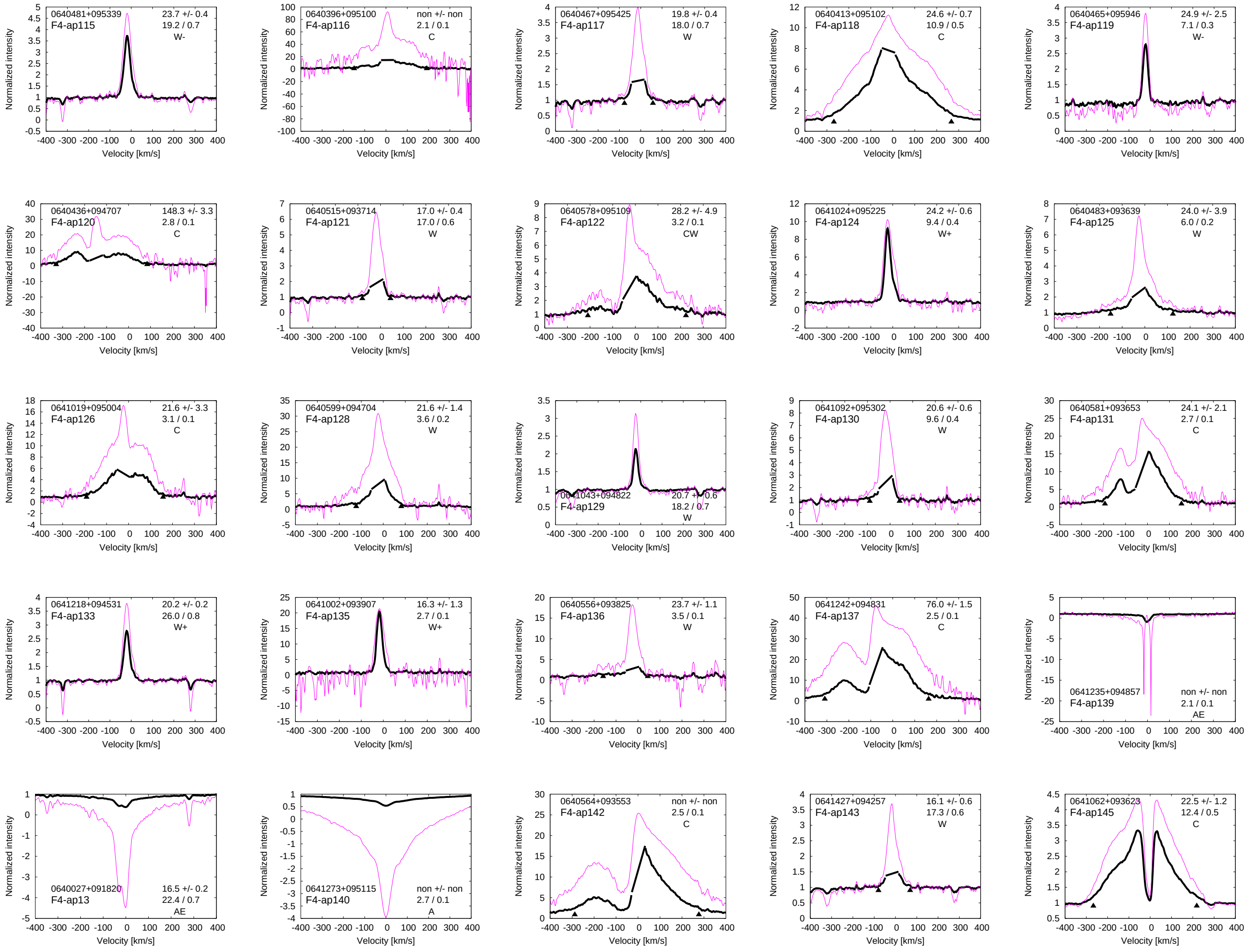

Figure 8.3: ***Examples of** $H\alpha$ **profiles for stars with detected emission in the NGC 2264 sample.**. Wavelength is converted to velocity with the zero-point being the RV of the star. (In case of very low R values the zero-point is set to RV=0 km s^{-1}.) 2MASS and internal identification numbers are given in the upper/lover left corner for each stamp, while RV and its error, the R and S values, and note on the $H\alpha$ profile are shown in the upper/lover right (see Table 8.2 and 12.3). The thick solid line is the observed spectrum with linear scaling and with the supposed nebular component cut off and replaced by a linear segment. For the original profile, and to emphasize the sometimes barely visible wings, we also show a log scaled version of the observed, unmodified profile (magenta). See text for details on scaling. Solid triangles mark the 10% full width for the nebular-line corrected spectrum. [See the Appendix for all observed $H\alpha$ profiles*

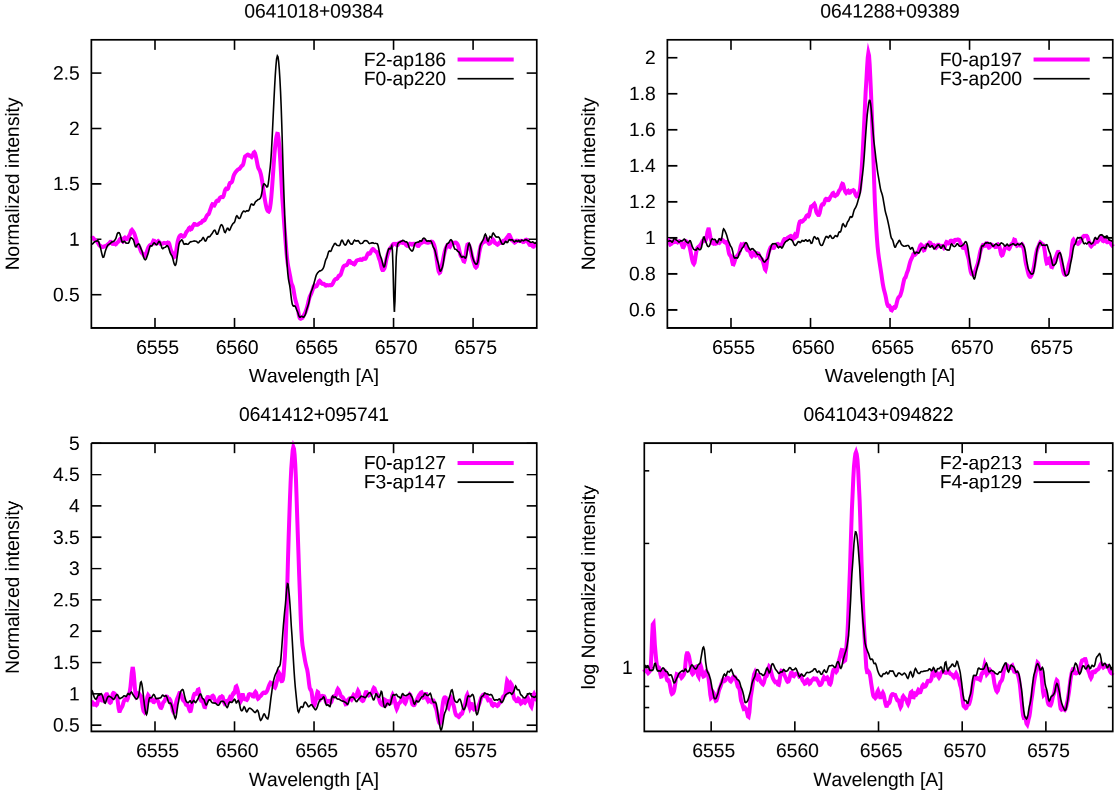

Figure 8.4: ***Examples of changing Hα profiles in NGC 2264***.

On Figure 8.4 we display Hα profiles for a sample of four stars, observed at two epochs. For the upper ones the black curves show a narrow emission with low level wings. On the left the stellar Hα absorption is apparent, but on the right it is not visible since the emission component completely fills it to the continuum level. These stars would have been classified as WTTS, since the 10% full width does not indicate accretion velocities. However, observing the same stars at different times (magenta curves) we find a significant change in the emission. The stellar absorption broadens/appears as the barycenter of the emission component moves or due to other changes of the emission profile. At the same time the low level wings clearly decouple from the narrow nebular emission, revealing a wide stellar emission which drops to 10% peak intensity 4–6 Å from the nominal Hα wavelength in the stellar velocity frame. And that corresponds to velocities comparable to accretion-driven emission of CTTS.

On the lower panels of Fig. 8.4 we present examples with very weak emission, which is, together with the nebular component, enough to completely erase the stellar Hα absorption at a given time. Therefore such sources would be classified to show only a very sharp nebular component. But comparing the profiles of other epochs, as the stellar Hα emission changes, it is obvious that there is a stellar emission component and thus these objects are WTTS.

This variability of stellar Hα emission might explain that some sources classified differently based on high resolution spectrum or by using infrared color-color diagrams, like the IRAC [3.6] – [4.5] vs. [5.8] – [8.0] (Allen et al., 2004). In the case a star has both short– and long wavelength infrared excess due to a circumstellar disk, accretion onto the star is likely taking place, and therefore we expect a broad Hα profile, (the signature of material falling in at high velocity), thus

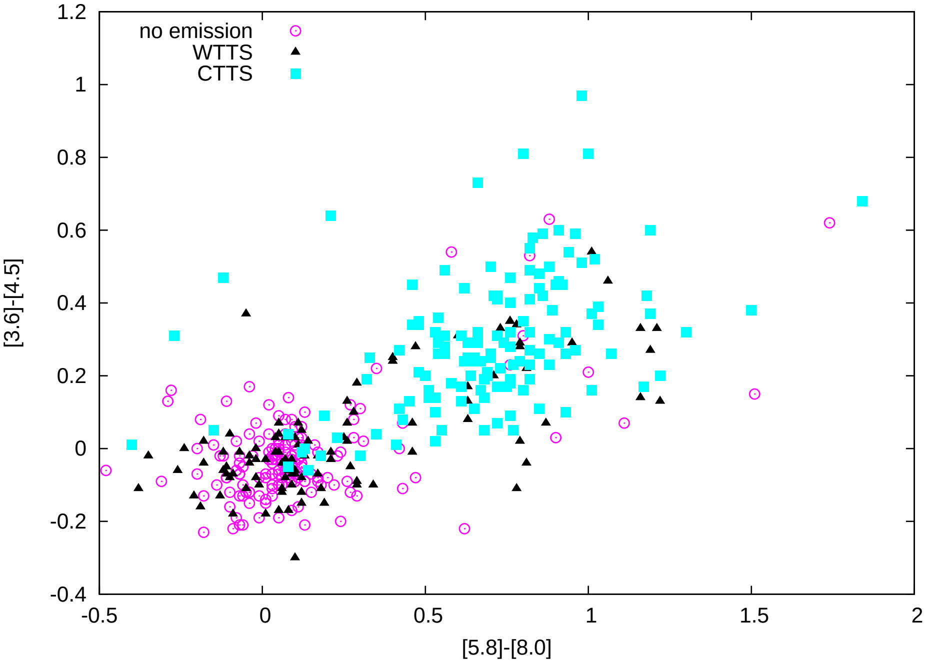

Figure 8.5: ***IRAC color-color diagram of targets in the NGC 2264 field***. *Stars with signs of accretion in their spectra (filled squares) should have a disk, and so exhibit infrared excess and appear in the domain of Class II objects (Allen et al., 2004). Some stars exhibiting weak Hα emission (filled triangles) some still show infrared excess, meaning the disk is yet presented but accretion has already stopped. Most of these WTTS stars, however, have no signs of disks and scatter around* (0, 0)*. These Class III objects (no intrinsic infrared excess) share the area of field stars (open circles) and older cluster members with no signs of Hα emission.*

a CTTS (e.g., White & Basri 2003). If the short wavelength excess is not present, presumably there is either no disk to accrete or no inner disk; in most cases, such systems are not accreting and thus are WTTS.

Constructing such a color-color diagram for our targets in NGC 2264, using the photometry by Teixeira (2008), and plotting the objects with symbols according to their spectral CTTS/WTTS classification we arrive to the graph presented in Fig. 8.5. Some of the WTTS sources appear in the domain (both short and long IR excess) of CTTS stars. These cases might be similar to the ones displayed in the upper row of Fig. 8.4. Also, some stars with no stellar emission detected in their spectra exhibit IR excess, and those likely had been mis-classified due to similar effects shown on the lower panels of Fig. 8.4. (Also see §9.3.3 for further discussion.)

In the table listing the cluster members (Table 8.2) all emission sources are listed, even though we define velocity membership as the RV value should be within 4 σ of the cluster mean velocity (21 km s^{-1} ± 4× 3.5 km s^{-1}). Based on this criteria only 278 of 361 emission objects would be radial velocity members (with an R value larger than 2). However the other remaining 83 emission sources are clearly very young objects and therefore very likely members, but their spectra had not enough S/N ratio to determine RV. On the other hand some of the Hα emission stars have good spectra and velocities close to the 4 σ RV membership selection criteria, these are noted as *hsb*. Further observations required to see if these are spectroscopic binaries.

8.2.3 Binaries

We identified several spectroscopic binary stars. Some of these have resolved double peaks in the cross-correlation function, and we measured different velocities in the two separate observing runs. There are 6 such stars listed in Table 8.2 and 12.3 with a three-letter note *"RDB"* (Resolved Double-lined Binary). In case of obvious side-lobes of the cross-correlation function and two non-consistent but accurate velocities, we identified additional 3 stars as binaries (listed with a note *"UDB"*, as Unresolved Double-lined Binary). There are 6 *"rdb"* and 5 *"udb"* noted stars in Table 8.2 and 12.3, for which we have just one RV measurement but observed double peaks or side-lobes in the cross-correlation function. 11 stars showed no sign of binarity in the cross-correlation, but we got two significantly different velocities. These are likely single-lined binaries, and have an *"sb"* note.

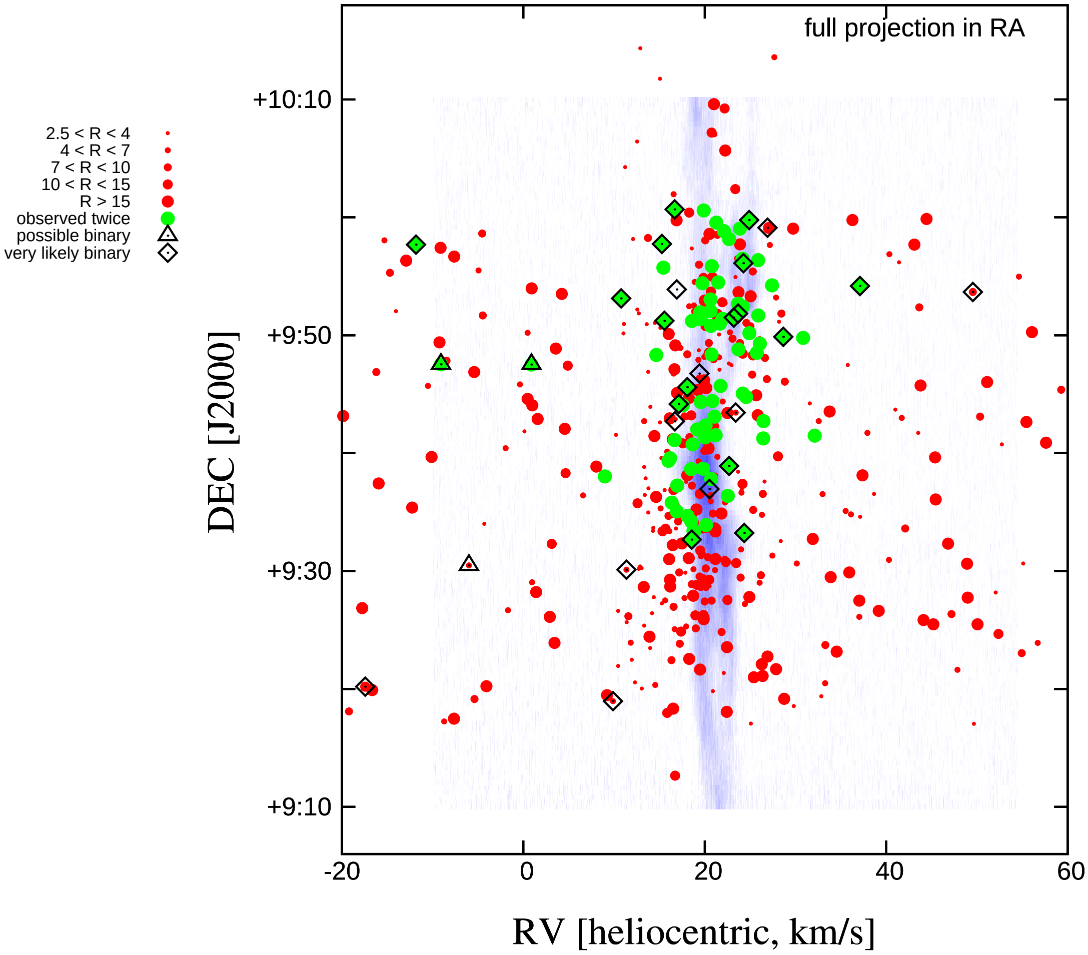

Figure 8.6: ***Binary stars identified in NGC 2264*** *by obvious double-peaks or side lobes in the cross-correlation function of their spectra, or by significantly different RV values if more than one measurement was available (open diamonds). If the CCF was not that convincing, or the star was not an RV member but exhibited TTS Hα signature, we marked those stars as open triangles.*

8.2.4 Velocity Correlations between Stellar and Gaseous Component

he radial velocity distribution of stars in NGC 2264, as shown in Fig 8.2, is wide and asymmetric, probably due to subcluster groups with different mean velocities. In optical images the cluster shows an elongated shape to the north-south direction. The $H\alpha$ stars of R04 also show two denser cores separated mainly to declination, one centered around $\alpha = 6^h41^m10^s$ and $\delta = +9°30'$ and the other around $\alpha = 6^h40^m50^s$ and $\delta = +9°50'$ (see Fig. 8.1). To explore this pattern further, in Fig. 8.7 we plot the declination values of stars observed at two epochs, as a function of velocity. In order to decrease uncertainties due to measurement errors, and natural distribution in velocity space within a possible subcluster group, we calculated mean declination values for 2 km s^{-1} wide bins in RV (Fig. 8.7). The shaded areas show the declination ranges of the two largest (suggested) subclusters based on the surface density of $H\alpha$ emission stars in the catalog of R04. The southern-most declination limit of the shading was set by the Hectochelle field observed in March. The increasing velocity with increasing declination is obvious.

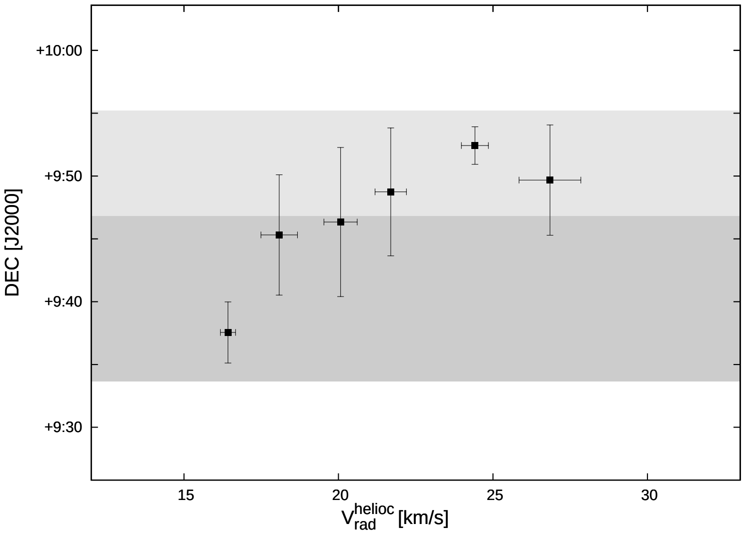

Figure 8.7: ***A north-south velocity gradient observed in NGC 2264*** *is clearly shown, by plotting the mean declination values in 2 km s^{-1} wide RV bins against the mean radial velocity of the bins. The error bars represent the RMS of DEC/RV values of stars in a given velocity bin. The shaded areas show the declination ranges for the condensations of $H\alpha$ stars in R04.*

There is not a clear trend in RA, but this is consistent with the optical image of the cluster which shows a North-South elongation with only a very slight tilt in RA. But the spatial pattern of stellar velocities becomes clear if we compare them to the pattern of molecular gas. Using ^{13}CO observations we tried to match the motion of the gaseous component with the motion of the stellar component in NGC 2264. Fig. 8.8 displays channel maps as eight, 1.5 km s^{-1} wide panels centered between V_{helioc} = 15–27 km s^{-1}(corresponding to $\sim V_{LSR}$ = 2–14 km s^{-1}). Stars from the peak of Fig. 8.2 with the same 1.5 km s^{-1} binning are superimposed on these maps. The correlation between the position of dense ^{13}CO cores and position of stars is very convincing.

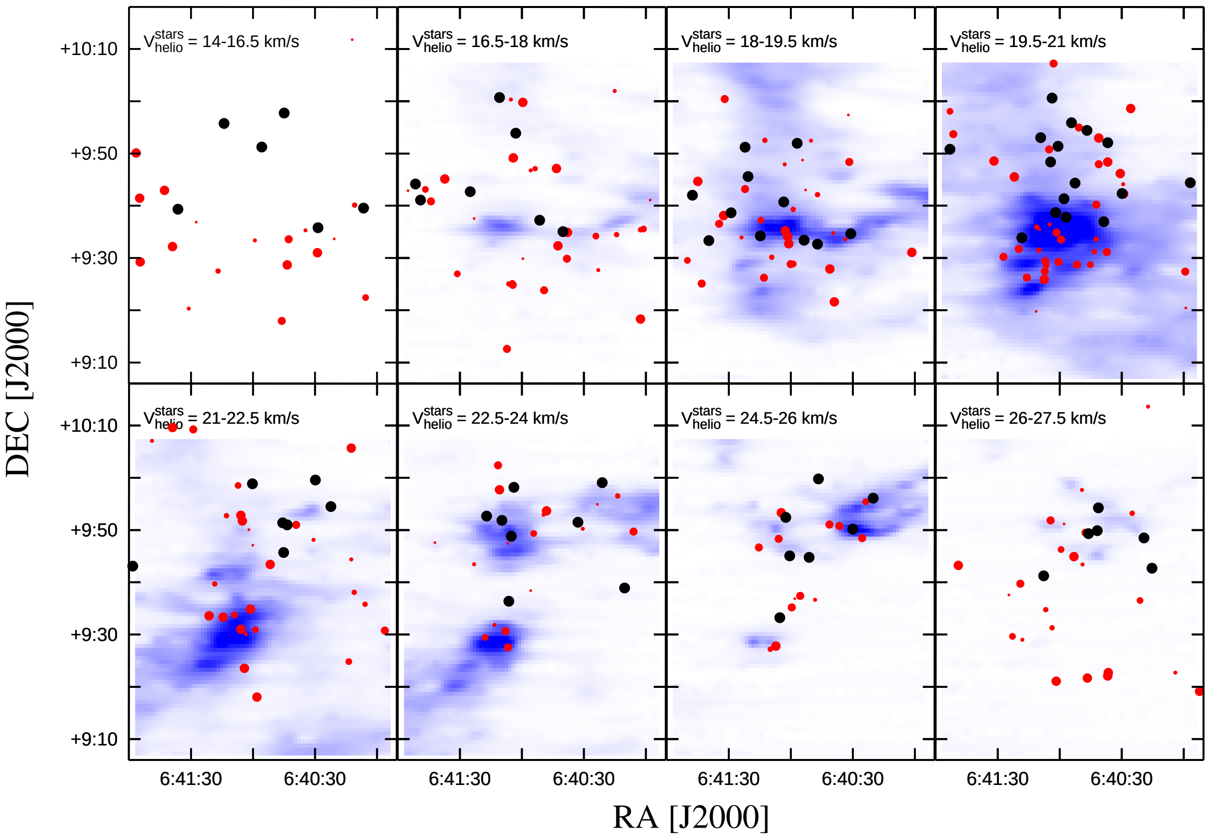

Figure 8.8: ***Velocity chanel map of stars and gas in NGC 2264*** *reveal strong spatial correlation between the molecular gas and stars. Plotting the RV members of our sample (filled circles: red – single observation; black – multiple measurements) superimposed on* ^{13}*CO channel maps (both averaged in 1.5 km* s^{-1} *wide bins in RV). the spatial coherence is obvious.*

On the upper-right panels of Fig. 8.8 there is a dense ^{13}CO core at $\alpha = 6^h41^m00^s$ and $\delta = +9°36'$. On the same panels, many stars occupy the same region in the given RV bin. As we go to higher RV values, stars disappear from this area, as well as the gas, but two other dense ^{13}CO regions appear. One is to the north, with an east-west elongation and a complicated structure, around the central point of $\alpha = 6^h40^m40^s$ and $\delta = +9°52'$. Most of the stars fall in this region on the lower panels of Fig. 8.8, especially on the lower-middle ones.

On the lower-left panels of Fig. 8.8, there is another dense ^{13}CO core at $\alpha = 6^h41^m10^s$ and $\delta = +9°29'$ at these higher velocity values. This surrounds the Cone-nebula. On these panels, there are several stars very close to this region, well separated in space from the larger number of stars to the north but laying in the same radial velocity range. These stars are responsible for the turn-down of the north-south gradient on Fig. 8.7. This can be a hint of a third subcluster group around the Cone, having a mean heliocentric velocity of ≈ 22 km s^{-1}.

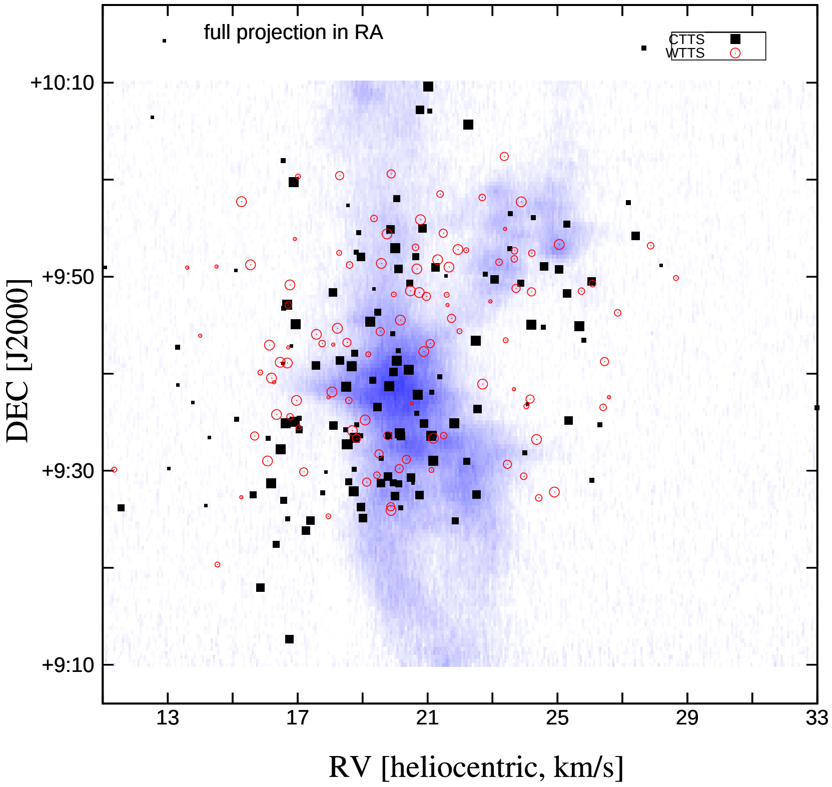

Figure 8.9: ***Velocity–spatial plot of stars*** *with (filled squares) and without (open circles) accretion signature in their spectra (full projection in RA). The symbol size is coded with R value, larger symbol corresponds to higher RV accuracy.*

Similar agreements in the structure of stellar and gaseous components can be seen on Fig. 8.9, which is a projection in RA, displaying the velocities along the horizontal axis and DEC values along the vertical axis. The size of the stellar symbols are coded with R value (larger symbol means better RV precision). Only stars with observed Hα emission are displayed, filled squares representing the CTTS and open circles the WTTS group, based on Hα profile classification. There are apparently more stars at lover velocities off (in front of) the cloud. This is likely a bias caused by the increased extinction for higher velocity objects, as those basically move (relatively) into the denser regions of the cloud. Note the void of redshifted stars "behind" the densest cloud region at $\delta = +9°40'$.

8.3 Discussion

8.3.1 A Cluster in Formation

While other star-forming regions have been shown to have significant substructure in the young star population (e.g., Lada & Lada 1995; Gomez et al. 1993), NGC 2264 is the first region for which we have sufficiently accurate measurements to explore substructure in the stellar radial velocities. The spatial distribution of stellar radial velocities and its correlation with the velocity structure of the molecular gas shows that NGC 2264 is composed of relatively distinct components (Figures 8.8,8.9). Intrinsic errors due to various types of activity (starspots, accretion; Guenther et al. 2000) are not large enough to obscure the strong correlation of the stellar velocities with the gas (Figures 8.8,8.9). Though individual stars could have velocity offsets on the order of few km s^{-1} due to fast rotation and starspots/accretion (Neuhaeuser et al., 1998; Strassmeier et al., 2005), that is very extreme and the large number of stars in our sample overrides the significance of such outliers.

The presence of such substructure in NGC 2264 is not surprising given its size and youth. Assuming a local, within-group velocity dispersion (one-dimensional) of order 2 km s^{-1}, and a spatial extent of $\pm$ 4 pc ($\sim \pm 17$ arcmin) or so from the central region, the resulting crossing time of $\sim$ 2 Myr is comparable to the estimated age of the cluster (see Introduction). Even adopting a velocity dispersion of 3.5 km s^{-1} results in a crossing time of $\sim$ 1 Myr, close to the youngest stellar age estimates. Numerical simulations show (Scally & Clarke, 2002) that substructure in a stellar cluster can remain detectable even after several crossing times, depending upon the number of stars involved and their initial subcluster densities. However, it is unlikely that the region is considerably older than one or two crossing times, because the gas also shows the same substructure as the stars. The cluster gas will shock and dissipate considerable amounts of energy on the first crossing, and thus the initial substructure should be damped out much more rapidly than for the stellar population.

Crutcher & Hartkopf (1978) presented observational evidence for two separate gaseous cores inside NGC 2264 which have a mean velocity difference of 2 km s^{-1}. These two cores correspond in position with the centers of our southern subclusters B and C (C is in the direct vicinity of the Cone nebula), see lower left panel on Fig. 8.8. The velocity gradient we estimate based on our observations agrees in direction and in its amount with that determined by Crutcher & Hartkopf (1978). Lang & Willson (1980) verified the same gradient based on NH_3 measurements and also explained the motion of the two cores as rotation, with a period of 4 Myrs if the rotational axis is perpendicular to the line of sight. However, as the ^{13}CO observations of Ridge et al. (2003) show (Fig. 8.8), the velocity field is more complicated than simply that of pure rotation.

Large velocity dispersions sometimes arise in molecular gas as the result of powerful bipolar outflows or other stellar energy input. However, the systematic motions seen in the gas require too much energy to explain in this way. Instead, we interpret the velocities as mostly gravitationally-generated, which would very simply explain why the stars spatially co-located with the gas show the same velocities.

Burkert & Hartmann (2004) recently explored a simple model of the formation of star-forming filaments. Their calculations assumed that molecular clouds were formed schematically from colliding supersonic flows which formed (approximately) sheet-like configurations. If the sheet is elongated, the result is gravitational collapse first along the shortest dimension, forming a filamentary structure. As shown in the left panel of Fig. 8.10 (reproduced from Figure 10 in Burkert & Hartmann 2004), irregularities initially present in the sheet grow to form non-linear density enhancements by the time the configuration collapses to a filament. The right panel of Fig 8.10 shows the integrated surface density as a function of the radial velocity in the x-direction, showing that multiple dense structures with coherent velocities are present. Often individual "clumps" appear in nearby pairs with distinct velocities. This pattern is the result of the overall collapse of the elongated sheet; material originating on opposite sides of the sheet fall in with opposing velocities. The high-velocity infall at each end of the filament is due to the highest

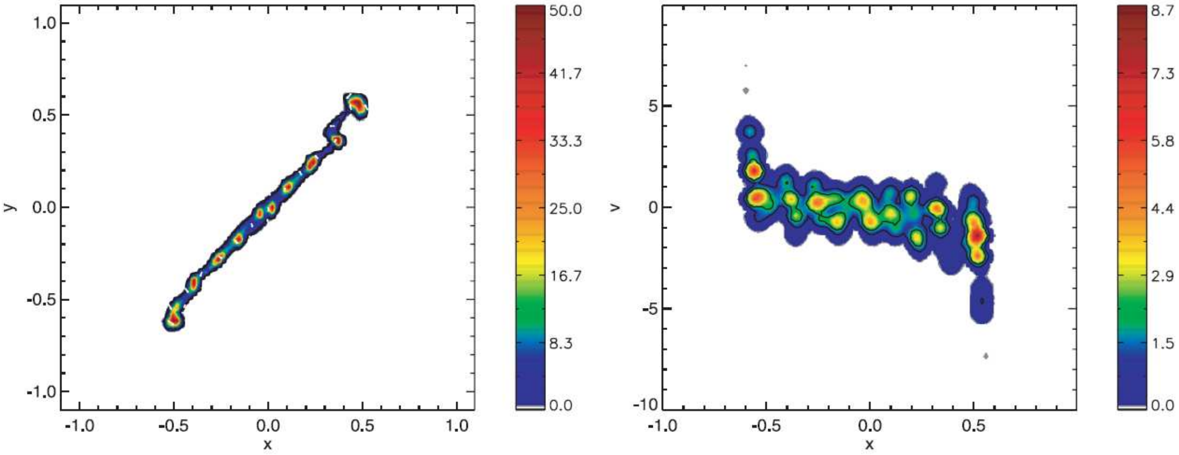

Figure 8.10: ***Simulation of gaseous sheet collapsing to a filament*** *(from Burkert & Hartmann 2004).*

gravitational acceleration at filament ends (Burkert & Hartmann, 2004), coupled with some initial rotation of the sheet. The scaling to the mass and radius of the NGC 2264 gaseous filament is such that each unit of velocity corresponds to 1.6 km s^{-1}. The existence of condensations with differing velocities at the ~ 2 km s^{-1} level, plus the higher-velocity tails at the end of the filament is suggestive of the structure seen in both the gas and stars of NGC 2264 (Fig. 8.9)

We suggest that the Burkert & Hartmann model qualitatively explains the velocity structure seen in the NGC 2264 region. The pattern of first higher velocities, then lower velocities, then somewhat higher again proceeding southward along the region (Figure 7) can be explained by gravitationally-driven infall from opposite sides of a cloud falling in to form a more filamentary structure. The highest velocity structure seen at the northern end may be similar to the acceleration seen in the end of the filament in the right panel of Fig. 8.10. The velocity units in Figure 7 are $(GMR/\pi)^{1/2}$; if we adopt a total gas mass of $4000M_{\odot}$ from Ridge et al. (2003) and a filament half-length of 4 pc, these units correspond to ~ 2 km s^{-1}. Clearly, gravitational collapse can account for the magnitude of the motions seen in NGC 2264, especially considering geometric uncertainties and the simplicity of the model.

8.3.2 Distributional Differences Between IR Excess and Non-excess stars

Using IRAC photometry (Teixeira, 2008) we distinguished between IR excess (either short or long wavelength) and non-excess sources, and plotted these groups on a velocity-spatial map. Fig. 8.11 suggest that the excess sources tend to be more on cloud, which means a small velocity dispersion respect to the main cloud velocity. The non-excess sources exhibit an apparently larger scatter, which is a result of such population being older and therefore dynamically more evolved. These non-excess sources spent more time interacting with each other and so the connection between their kinematical structure and the primordial cloud hierarchy has been erased, while the excess sources still exhibit strong correlation with the gas. Thanks to the large number of excess sources, or in other words the youth of the cluster, the RV groups which can be identified on Fig.

8.8 still trace the location of stellar birthplaces within the cluster. Therefore the primordial cloud structure can be still observed.

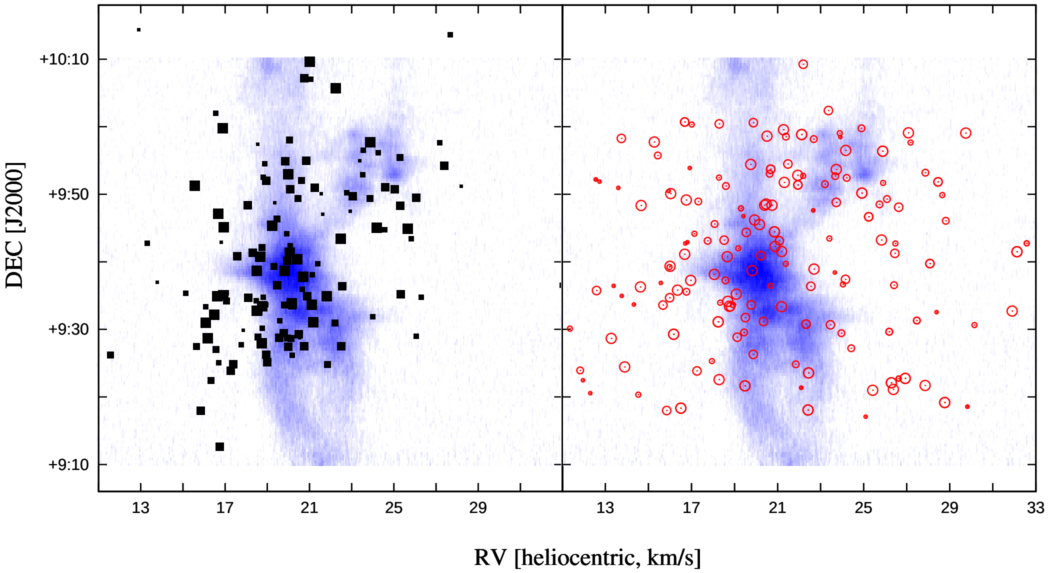

Figure 8.11: ***Velocity–spatial plot of NGC 2264 stars with and without infrared excess*** *(full projection in RA). The stars with infrared excesses (filled squares, left panel) are more closely related to the gas (grayscale) than the non-infrared-excess stars (open circles, right panel). The symbol size is coded with R value, larger symbol corresponds to higher RV accuracy.*

Teixeira (2008) arrived to similar conclusion. Using optical and infrared photometry Teixeira (2008) separated sources in NGC 2264 to two groups: stars with thick disks (Class II objects) and objects with anemic disks (Class III). She found that the former group showed the greatest RV gradient, as observed in the molecular cloud, while diskless sources show the least. A nearest neighbor analysis also suggested that sources with thick disks may be tracing the original stellar birthing sites, so the different radial velocities for these sources may indicate distinct, primordial structural elements of the cloud.

8.4 Summary

We have carried out a spectroscopic study of stars in NGC 2264, utilizing the Hectochelle multiobject spectrograph on the 6.5 m MMT. Obtaining 1078 spectra of 990 stars we classified 472 stars as cluster members based on their radial velocity and/or $H\alpha$ emission. We determined radial velocities with an accuracy of < 1.5 km s^{-1} for 338 members. The radial velocity distribution of these stars is wide, non-Gaussian, and the dispersion is 3.5 km s^{-1}. We compared the stellar radial velocities to the velocity of the molecular gas in the cluster, traced by ^{13}CO, and found a strong correlation in the spatial distribution of the two components. At least three subgroups of stars can be identified with distinct spatial and velocity coherence. We interpret this substructure as the result of gravitational collapse of initial clumps of star-forming gas from a more extended structure to a roughly filamentary distribution. Using the results presented here, more advanced numerical simulations could help elucidate the initial conditions that produced NGC 2264.

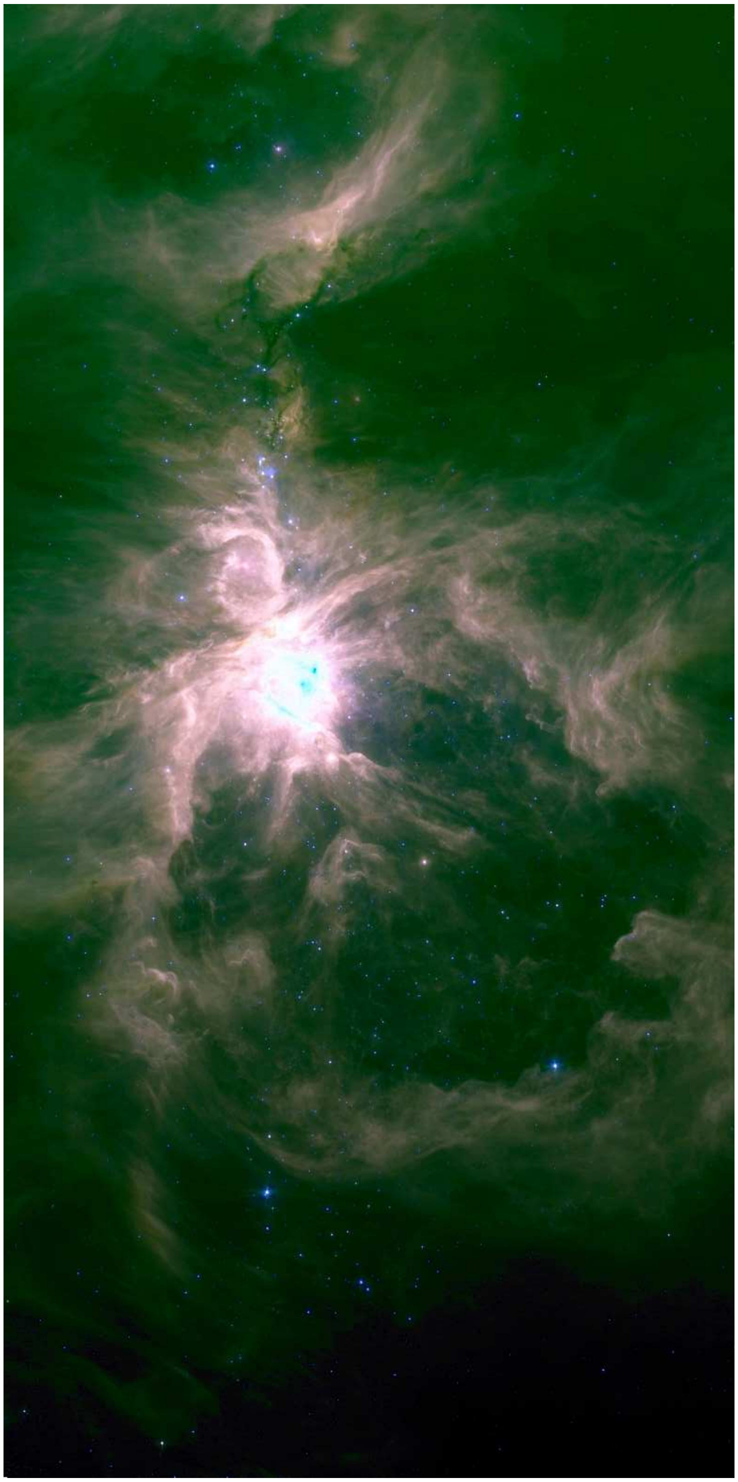

The Orion Nebula *– color composite of 3.6 µm (blue), 5.8 µm (green) and 8.0 µm (red) IRAC mosaics (Megeath et al. , 2007)*

Chapter 9

The Orion Nebula Cluster and Its Environment

The Orion Nebula Cluster (ONC) is a touchstone for studies of cluster formation, as it is the closest, relatively populous ($\gtrsim$ 2000 members) young cluster containing an O star. While many stars in the ONC are heavily extincted (Ali & Depoy (1995); McCaughrean & Stauffer (1994); Carpenter, Carpenter et al. (2001); McCaughrean et al. (2002); see also O'dell (2001) and references therein), evaporation of molecular gas by the O6-7 central star θ^1 C Ori has revealed many of the members of the ONC at visible wavelengths. Optical studies of the stellar population show that it is quite young, with a median age of roughly 1 Myr or less (Hillenbrand, 1997), suggesting that it is reasonable to search for substructure in the cluster related to the initial conditions of formation.

Hillenbrand & Hartmann (1998, HH98 hereafter) conducted a preliminary study of the structure and kinematics of the ONC. HH98 constructed azimuthally-averaged stellar source counts and showed that they could be fit with a simple, spherically-symmetric, single-mass King cluster model of core radius ~ 0.2 pc and a central density of $\sim 2 \times 10^4$ stars pc^{-3} (see also McCaughrean et al. (2002)). However, HH98 pointed out that the cluster is not circular in projection; rather, it is elongated north-south along the same direction as the molecular gas filament, suggesting that the cluster might not be completely relaxed.

This elongation is particularly apparent on scales larger than 0.5 pc from the center. The filamentary structure is well expressed in CO observations of the region (Bally et al., 1987), as well as in the distribution of pre-main sequence (PMS) stars, shown by recent infrared (IR) observations (Megeath et al 2007, in preparation). According to the models of Burkert & Hartmann (2004), self-gravitationally collapsing gaseous sheets can form such elongated, filament-like clouds. The numerical simulations show that density and velocity dispersion becomes larger at the ends, inducing star formation to start at the tip of the filament, just like the position of ONC within the Orion A cloud. The collapsing sheet model also predicts an overall velocity gradient along the filament, in agreement with CO observations of ONC (Bally et al., 1987). For such a young star forming region as ONC, the stars are still very close to their birthplace; therefore, the stellar kinematics may reflect initial conditions rather than being relaxed.

We therefore conducted a radial velocity (RV) survey of more than 1200 stars in the northern region of the Orion A cloud to search for clues to the initial conditions of the ONC's formation. In this paper we present results based on high-resolution spectroscopic observations in the $\lambda \sim$

6560 Å region, which allowed us to measure RVs and identify T Tauri stars (TTS) based on their Hα emission. We find that the stellar population exhibits a strong spatial and kinematic correlation with the ^{13}CO gas in the region; the observed substructure conclusively demonstrates that the ONC is not relaxed, but instead reflects the initial conditions involved in its formation. We also comment on the detailed structure, distributional differences seen among stellar groups distinguished by infrared, Hα, and spatial and kinematic properties. In a subsequent paper we will incorporate followup spectroscopy we have obtained in the Mg triplet region (centered at 5225 Å) to examine rotational velocities and spectral typing, along with observations of the 6708 Å Li line to use as an age estimator.

9.1 Observations

9.1.1 Target Selection

To conduct the kinematic study we selected targets in the northern end of Orion A. Thanks to the dense molecular cloud there are few background stars in any stellar catalog of the region. At the same time, the ONC region exhibits a high density or pre-main sequence objects on the sky so the foreground contamination is relatively low. Therefore we initially used a simple color-magnitude selection from the 2MASS catalog to draw the first target list for our observations.

Our intent was to observe multiple fields to cover at least a $\sim 1 \times 2$ degree area. Previous experience with Hectochelle suggested we could reach a S/N ratio of 10 or higher for most of our targets in 1 hour exposure time if stars with $11.5 < J < 13.5$. We also initially selected stars with $0.2 < (H - K) < 0.5$ to avoid heavily-reddened objects, but this also eliminated many stars with disks (see following paragraph). These selection criteria above therefore resulted in 2319 targets within a 1.5×2.7 degree field centered at $\alpha = 5^h35^m$ and $\delta = -5°44'$. This region includes the Trapezium and areas to the south (NGC 1980) and to the north (NGC 1973–1975–1977, NGC 1981) of the ONC.

We added young stellar objects to the sample based on their IR excess as identified using the IRAC and MIPS instruments on board the *Spitzer Space Telescope* (Megeath et al. 2008, see Fig. 9.1). This selection went down to a fainter magnitude limit of $J = 15$, and included additional Class II members of the star forming region. These targets were observed during the second of the two spectroscopic runs, while 2MASS selected objects were observed in the first. See Figure 9.2 for the spatial distribution of selected targets. Details will be given in a forthcoming paper (Megeath et al. 2008).

9.1.2 Spectroscopic Observations

The spectroscopic observations were carried out using the Hectochelle multi-object spectrograph (Szentgyorgyi et al., 1998) at the 6.5m MMT telescope in Arizona. We used the 190 Å wide echelle order centered at Hα, because we could get RV information as well as record the stellar hydrogen emission profiles, a sign of youth and membership, at the same time. This is the same instrumental setup that was used for the observations reported in Fűrész et al. (2006) (see section 2.2 of that paper for details; also Sicilia-Aguilar et al. (2005)).

The first set of spectra was taken in 2004 December, when a total of 866 stars in 4 fields

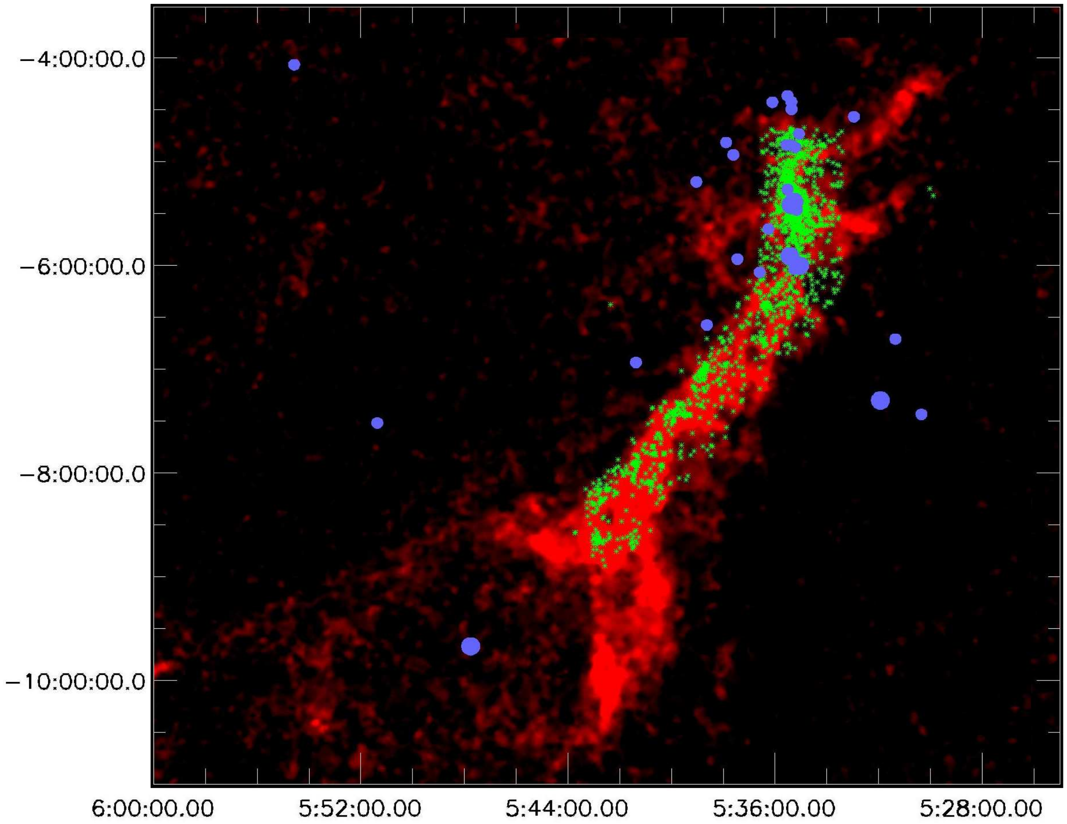

Figure 9.1: ***Position of infrared excess sources*** *(green asterixes), overplotted the extinction map (red) of the OMC A cloud. The blue circles are the OB stars in the region.*

Table 9.1. Summary of spectroscopic observations in the ONC region

Date	ID	field center		exposures	binning mode	number of targets
2004 Dec 01	F11	$5^h\ 35^m\ 19^s$	$-\ 04°\ 49'\ 27''$	3×20 min	1×1	224
2004 Dec 01	F21	$5^h\ 35^m\ 13^s$	$-\ 05°\ 21'\ 14''$	3×20 min	1×1	210
2004 Dec 01	F22	$5^h\ 35^m\ 13^s$	$-\ 05°\ 21'\ 14''$	3×20 min	1×1	219
2004 Dec 01	F31	$5^h\ 35^m\ 26^s$	$-\ 06°\ 07'\ 30''$	3×20 min	1×1	213
2005 Nov 15	S3	$5^h\ 35^m\ 13^s$	$-\ 05°\ 33'\ 10''$	3×15 min	2×2	161
2005 Nov 15	S2	$5^h\ 35^m\ 11^s$	$-\ 05°\ 07'\ 28''$	3×15 min	2×2	154
2005 Nov 15	S1	$5^h\ 35^m\ 21^s$	$-\ 05°\ 18'\ 50''$	3×15 min	2×2	170

were observed (see Table 9.1). Initially we chose not to bin in the resolution direction, which resulted in low signal–to–noise (S/N) values for the faintest targets. Therefore, we used a 2×2 binning in 2005 November in order to decrease the readout noise in the data and thus go fainter. Because Hectochelle oversamples the resolution element (the PSF of a resolved spectral feature has ~ 3.5 pixel FWHM), this binning does not result in a serious loss or resolution. Accordingly, the accuracy of RVs derived for the 485 stars observed in 2005 are comparable to the 2004 values.

During the two observing run we collected a total of 1351 spectra of 1215 stars within 7 Hectochelle fields. The location of these objects are shown in Fig 9.2, overplotted a color IRAC

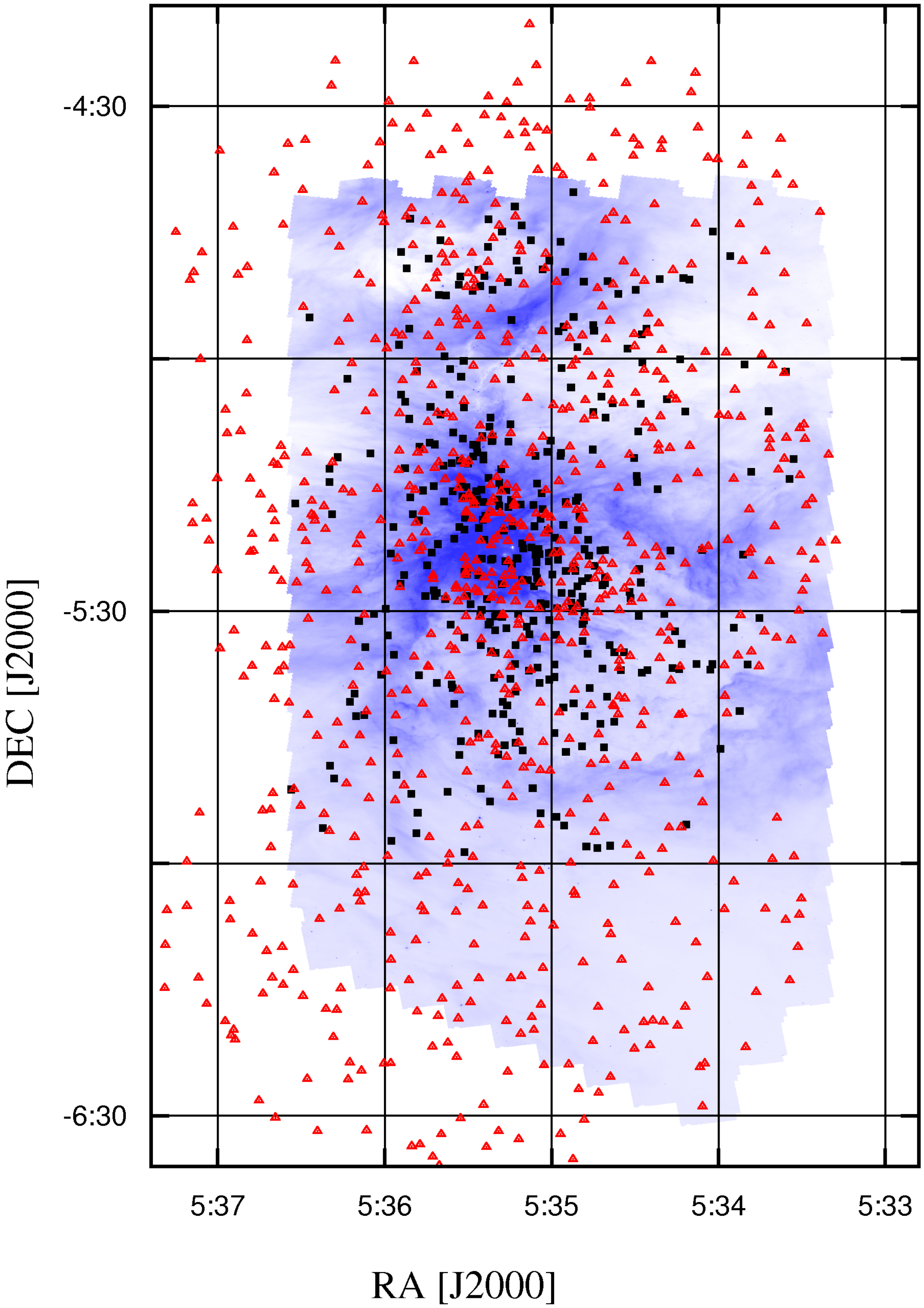

Figure 9.2: ***Positions of the ONC targets*** *overplotted a IRAC 8 μm mosaic image of the Orion Nebula. The open triangles are stars selected using a 2MASS color-magnitude diagram of the region, the filled squares are targets from Spitzer/IRAC photometry. See text for details.*

mosaic image covering most of the 1 × 2.5 degree region explored by spectroscopy.

Sky subtraction would have been very difficult in the vicinity of ONC, as the nebular emission is so strong and can vary rapidly on small spatial scales. Consequently, placing a few sky sampling fibers over a field is not adequate. The best approach would be to take an offset sky exposure, where all the fibers remain at the target locations and the telescope is moved by a few arcseconds to set targets off the fibers, resulting in sampling the background right next to each targets. However, this procedure would double the exposure time; due to time constraints we did not take such exposures. We simply excluded the emission features not to be important for RV measurements, which did not result in an appreciable loss of absorption features used in the cross-correlations.

9.1.3 Radio Observations

To trace and compare the kinematical structure of the Orion A molecular cloud and the stellar sample we have used a published ^{13}CO data set by Bally et al. (1987). A two-dimensional, color coded representation of the rightascension–declination–velocity data cube is shown on Fig. 9.3. Note the significant north-south gradient and complex structure. See Bally et al. (1987) for details on the data set.

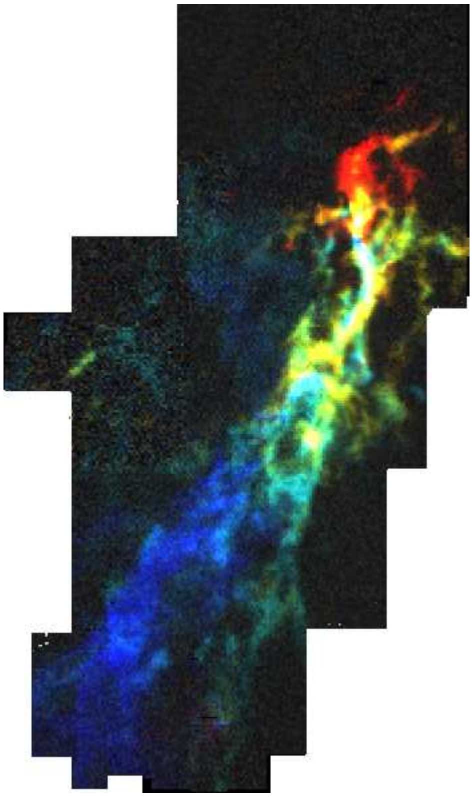

Figure 9.3: ***The velocity structure of the Orion A Molecular Cloud*** *(Bally et al., 1987) This color-coded composite chanel map reveals the complex velocity structure of the cloud. The blueshifted regions of the gas are shown in blue, the redshifted parts are displayed in red.*

9.2 Data Reduction

In chapter 5 and in §6.1 we have discussed the data reduction and analysis techniques in general. Here we just list some notes specific to the observations of ONC.

As a result of using the multi-template method there were 1049 stars out of 1215 yielding an $R > 4$ (only these were used in the later analysis), with a mean R value of 13.7. As a comparison, using 10 actually observed templates (the ones from Fűrész et al. (2006)) we only obtained 547 stars with $R > 4$ and a mean R value of only 7.8. Thus, increasing the number of templates led to a significant increase in the number of objects with accurate RV values.

We found a 0.8 km s^{-1} offset between the mean heliocentric velocities of the 2004 and 2005 observations. This is likely due to the different (improved) calibration system used in 2005. The shift was determined by comparing velocities of 35 stars observed in both runs with R values larger than 8. The values are listed in Table 9.2 and 12.5 are corrected for this zero point offset, by shifting the 2004 values to the 2005 scale.

9.3 Results

9.3.1 Velocity Distribution and Correlations Between Stellar and Gaseous Component

The distribution of measured heliocentric radial velocities is shown in Fig. 9.4. The histogram of the entire sample is displayed for three different S/N ratio of the cross correlation, and we also show the distribution of a spatially selected sub-sample. The $R > 2$ group includes the faintest spectra, on which scattered moonlight causes the the cross-correlation to fix on the solar spectrum rather than the stellar lines; this leads to a false peak near the heliocentric correction value (~ 14 km s^{-1}). However, most of the faint spectra follow the distribution drawn by the higher S/N ratio selections. In any event, we did not use any spectra with R values less than 4 in the following analysis.

The distribution of the entire $R > 4$ sample peaks at a heliocentric velocity of 26.1 km s^{-1} (see Gaussian fit on Fig. 9.4, in good agreement with our initial study of ONC (Sicilia-Aguilar et al., 2005)). The dispersion we found, $\sigma = 3.1$ km s^{-1} (with 10 and 40 km s^{-1}cutoff values), is somewhat higher than the 2.3 km s^{-1} value of the previous Hectochelle study, or the 2.5 km s^{-1} derived from proper motions (Jones & Walker, 1988), but the present sample includes a larger region (see Fig. 9.2). Nevertheless, spatially selecting a sub-sample in the close vicinity of ONC, within a $15'$ radius of Trapezium (292 stars with $R > 4$), we still found a mean velocity of 25.6 km s^{-1} and a dispersion of $\sigma = 3.1$ km s^{-1}. These numbers are very close to values calculated using the entire sample, but the distribution is different for these two spatial selections, as it is obvious in Fig. 9.4. While all the observed stars can be fitted by a $\sigma = 3.1$ km s^{-1} Gaussian, the velocity distribution of ONC stars does not seem sufficiently peaked at the mean velocity.

We computed the cross-correlation between -500 to $+500$ km s^{-1} heliocentric velocities, but found only a small number of stars farther from the peak than $\pm 4\ \sigma$. Between $4 - 15\ \sigma$ there are stars with high R values, but outside of this region there are only a few, usually very faint, outliers. The insert in the upper left of Fig. 9.4 shows how clean the distribution is over the explored RV range, even including the $R > 2$ spectra. The y axis is log scaled, to better show the

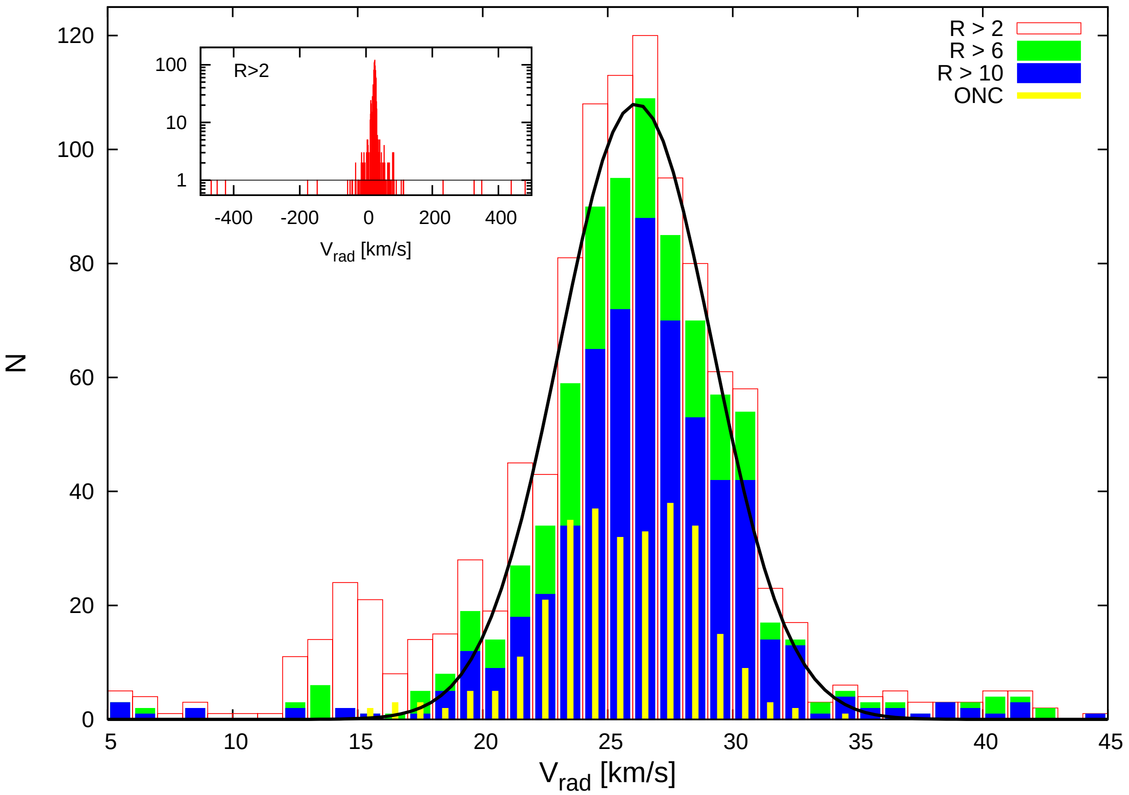

Figure 9.4: ***Histogram of measured heliocentric radial velocities in the ONC****, displayed for four selections of stars. The false peak at $V_{rad} = 14$ km s^{-1}is due to inadequate sky subtraction, and thus corresponds to the heliocentric correction velocity. It is apparent only in the sample including the faintest (low S/N ratio or R value), therefore in the analysis only spectra yielding $R > 4$ were used. For the main peak the shape is independent of the R value, and can be fitted with a $\sigma = 3.1$ km s^{-1} Gaussian. Note, there are is one relevant departure from the fit at $V_{rad} = 19$ km s^{-1}. Distribution of stars within 15′ of Trapezium are displayed with narrower yellow impulses, to show how the ONC stars compare to the entire region: the profile is more asymmetric but the agreement in the mean velocity and dispersion is very good. The insert shows the entire 1000 km s^{-1} wide velocity range explored in the cross correlation. Although displayed for the $R > 2$ selection the global peak around $V_{rad} = 26$ km s^{-1} is very well defined.*

wings of the peak. (A horizontal line is also drawn at $N = 1$.) Based on the morphology of the histogram we define RV membership for stars with velocities in the $26.1 \pm 4\sigma$ range, or between 13.7 and 38.5 km s^{-1}. Even if the RV was out of this range, or was very uncertain due to low R value, we still considered a star as member if its spectra exhibited non-nebular (i.e., large velocity width) Hα emission. For the details on members and non-members see Tables 9.2 and 12.5.

Figure 9.5, 9.6 and 9.7 display channel maps, slicing the right ascension–declination–velocity data cube in RV, RA and DEC, respectively. The stars (filled circles) are shown together with the molecular gas (blue shading) in order to compare structure between the stellar and gaseous component. The ^{13}CO measurements of Bally et al. (1987) were converted from LSR to heliocentric, to match our RV measurements, by adding 17.5 km s^{-1} to the LSR values. The size of stellar symbols are coded with R value, larger circle meaning higher S/N in the cross correlation and hence more accurate RV measurements in general. As some stars were observed more than once, we distinguish these by black color as their averaged RV values are even more accurate. All of

Table 9.2. Members of ONC — *sample*

2MASS_id	ID	J	$(J-H)$	$(H-K)$	[3.6 – 4.5]	[5.8 – 8.0]	V_{rad}	ΔV_{rad}	R	S	EW_c	$FW_{10\%}$	$H\alpha$	CCF	NOB
0533179-052138	F22-ap25	13.18	0.87	0.24	0.00	0.00	25.09	6.38	4.4	0.39	11.2	239	W	w	1
0533204-051123	F21-ap89	12.73	1.07	0.29	0.00	0.00	24.28	0.53	13.6	0.58	5.2	169	W	c	1
0533225-053240	F22-ap20	13.02	0.98	0.23	0.00	0.00	23.89	0.35	22.4	0.71	5.3	134	W	c	1
0533233-052153	F22-ap27	12.90	0.87	0.24	0.00	0.00	47.20	0.35	23.4	0.74	0.9	179	W	c	1
0533234-044234	F11-ap62	13.38	0.94	0.34	0.00	0.00	21.48	4.60	5.0	0.23	3.7	152	W	w,l	1
0533256-052354	F21-ap61	13.32	0.95	0.21	0.02	–	69.48	0.49	15.1	0.64	2.4	178	W	c	1
0533263-051640	F22-ap37	13.34	1.25	0.33	0.00	0.44	70.65	0.64	10.7	0.54	5.2	189	NSW	c	1
0533285-051726	F22-ap40	11.92	1.12	0.34	0.04	0.79	25.01	0.32	28.7	0.85	23.1	390	C	c	1
0533287-052610	F21-ap69	13.23	1.08	0.29	0.02	0.12	29.23	0.82	12.1	0.53	6.6	116	NSW	c	1
0533293-050749	F22-ap49	13.29	1.20	0.32	0.03	0.00	26.42	2.32	10.1	0.62	4.0	184	W-	c	1

Note. — *NOTE: this is a sample, for the full table see the Appendix 12.4* Hectochelle targets in ONC found to be members based on measured RV value or by detected Hα emission. The criteria of being RV member is to have at least one velocity measurement within 4σ of the cluster mean velocity: 13.7 km s^{-1} $< V_{helio} <$ 38.5 km s^{-1} . RV members listed only with $R > 2$, while stars with Hα emission are included regardless of R value, but with no velocity displayed.)
2MASS id — 2MASS identification number (truncated RA and DEC coordinates as: HHMMSSS+DDMMSS); **ID** — internal identification number, specifying the field (see Table 9.1) and aperture of observation; **J** — 2MASS J magnitude; **(J-H)** — 2MASS $(J-H)$ color index; **(H-K)** — 2MASS $(H-K)$ color index; $3.6-4.5$ — IRAC short wavelength color index; $5.8-8.0$ — IRAC long wavelength color index; V_{rad} — measured heliocentric radial velocity, in km s^{-1}; V_{rad} — *xcsao* error estimate for V_{rad}, in km s^{-1}; **R** — R value of cross correlation (see text for details); **S** — height of the CCF peak; EW_c — absolute value of equivalent width, measured on the corrected Hα profile (see text for details); $FW_{10\%}$ — full width of Hα profile at 10% level of the corrected maximum (see text for details);
Hα — notes on the Hα emission profile. See text for more details on the CTTS/WTTS classification: **C** – CTTS; **W** – WTTS; **CW** – rather CTTS, but could be WTTS; **WC** – rather WTTS, but could be CTTS; **W+** – asymmetry in line profile/wing: likely WTTS; **W-** – asymmetry in wings, but wings at low intensity: could be WTTS; **D** — resolved or unresolved double Gaussian profile, no excess H-alpha emission (likely non-TTS); **CD** — resolved or unresolved double Gaussian profile, likely CTTS; **WD** — resolved or unresolved double Gaussian profile, likely WTTS; **R** — obviously shifted H-alpha absorption : high RV stars; **X** — very wide H-alpha absorption with nebular emissions; **CX** — CTTS, with strange emission profiles; **AE** — stellar absorption and nebular emission together; **NS** — very strong nebular component component, no wings, no asymmetry; **NSC** — like NS, but if intensity log-scaled wide wings/asymmetry is visible and suggest CTTS emission signature under the strong nebular component; **NSW** — like NS, but if intensity log-scaled narrow wings/asymmetry is visible and suggest WTTS emission signature under the strong nebular component; **SAT** — saturated, or neighbor saturated;
CCF — notes on the cross-correlation function: **w** – wide peak, results large errors in RV; **l** – very low peak, but still sticks out from surrounding; **u** – almost undefined, very low/wide peak; **n** – very noisy (several local peaks, almost as high as the one picked); **s** – side lobed, could be a spectroscopic binary; **d** – double peak, spectroscopic binary; **dv** – RV measured more than once, found different velocities, could be binary; **r** – template spectra with highest peak in cross-correlation resulted non-realistic velocity, so the template resulting in highest R value was used instead to determine velocity; **c** – clear, well-isolated peak; **?** – uncertainty in assigning the given note;
NOB — number of observations

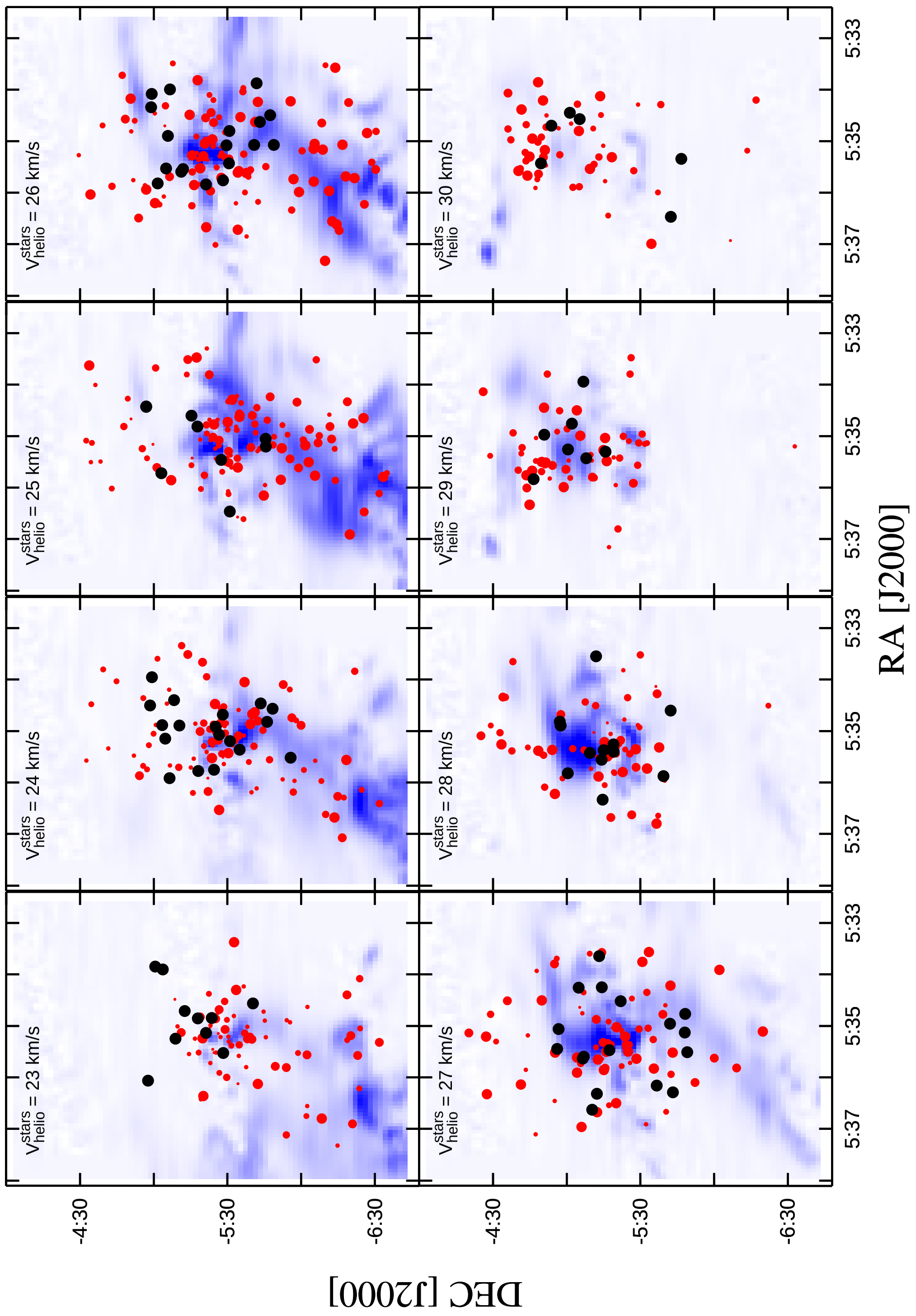

Figure 9.5: ***Velocity channel maps of the ONC region.*** *The dots represent stars with one (red) or more (black) RV measurements, while blue is the molecular gas observed in* ^{13}CO*, both displayed in 1 km* s^{-1} *channels. LSR velocities of the gas is converted to heliocentric (*$V_{helio} = V_{LSR} + 17.5$*). The size of the dots correspond to the R value, larger dot means more accurate velocity. The north-south velocity gradient is obvious and the correlation between the spatial and density distribution of stars and molecular gas is very significant. This suggests that the stars are still co-moving with the gas clouds in which they formed.*

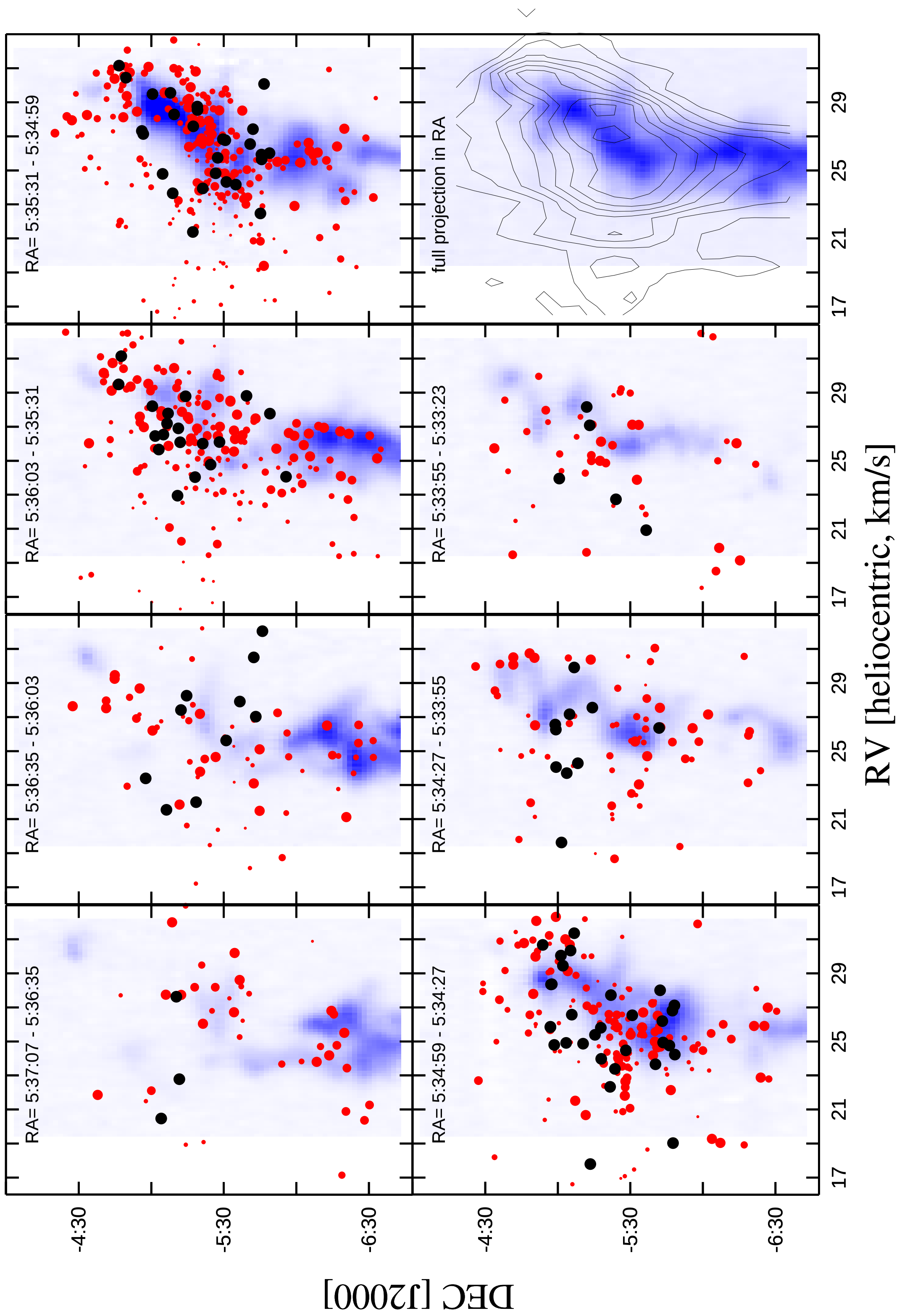

Figure 9.6: ***Channel maps of the ONC region, in right ascension.*** *Symbols are the same as for Fig. 9.5. The approximately 30 second wide RA ranges are noted in each channel. The correlation between the gaseous and stellar component is most prominent in the upper right corner, in the channel containing the Trapezium. On the lower right panel a full projection is shown with stellar density contours overplotted the gas distribution.*

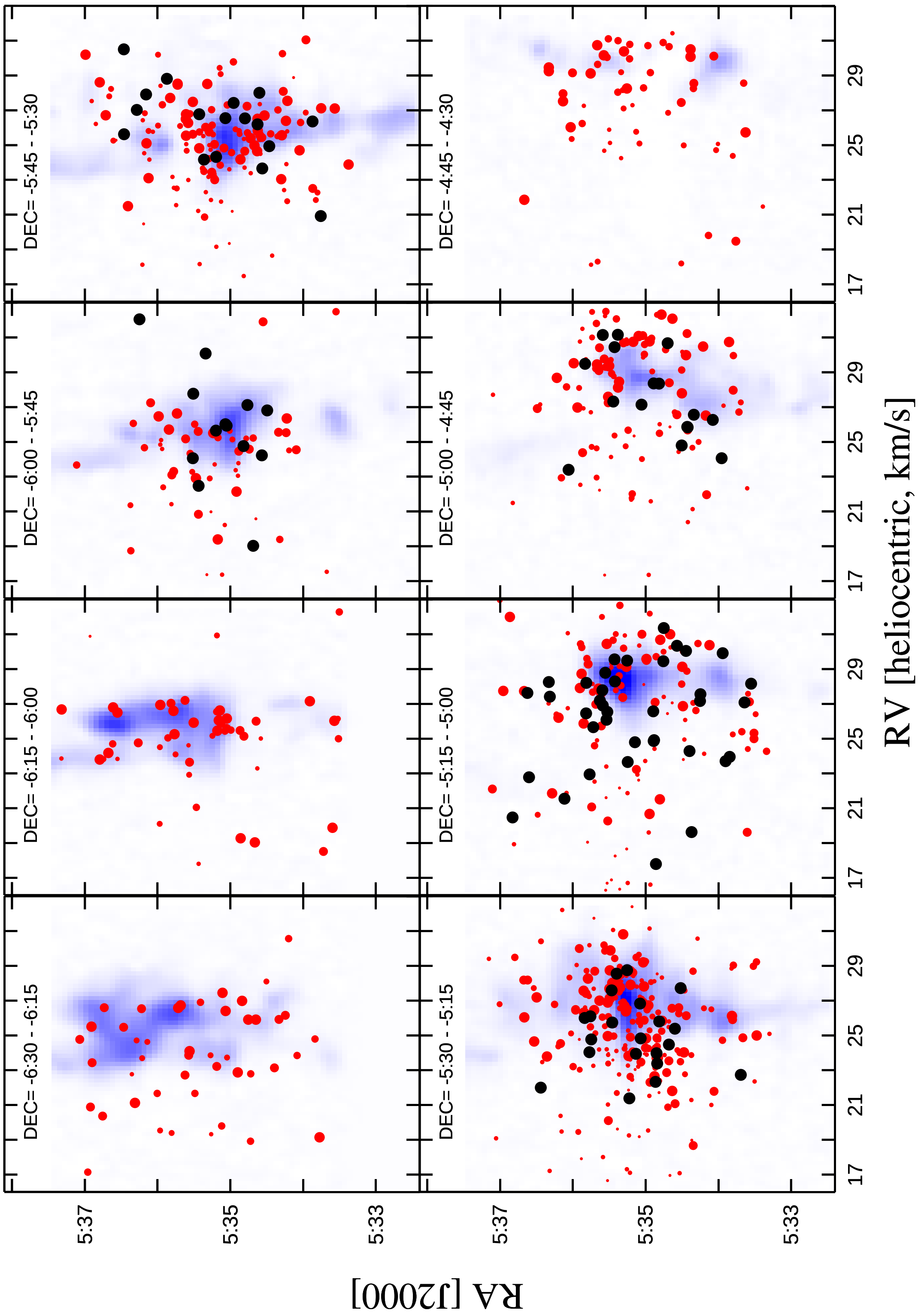

Figure 9.7: ***Channel maps of the ONC region, in declination.*** *Symbols are the same as for Fig. 9.5. The 15 arcminute wide DEC ranges are noted in each chanel.*

these maps show an overall north–south gradient in RV and significant substructure.

The morphology seen in the stellar population is very similar to that of the molecular gas. This is most apparent on Fig. 9.6, where the projection is in RA, as the orientation of the molecular gas has a filamentary structure mostly extending along DEC. To emphasize this structural parallelism, on the last panel of this figure we present a full projection of the ^{13}CO data with contour plots of stellar density. (For the contours the number of stars was calculated in 1 km s^{-1} by 0.1° bins with a grid resolution of 0.5 km s^{-1} and 0.05°.)

9.3.2 Hα Emission profiles

As described earlier (section 9.1.2), we did not take the observations that would be necessary for adequate sky subtraction in this region, where the nebular background can vary strongly over small scales. This makes the analysis of Hα profiles difficult, but not impossible in cases where the stellar component is much broader than the (relatively narrow) nebular component. However, nebular emission can be so strong that the stellar signature is barely visible as asymmetries in the wings, at very low intensity levels. This means that neither the canonical 10 Å limit in equivalent width nor the 270 km s^{-1} limit in full-width at 10% peak (White & Basri, 2003) method can be applied on the raw spectra to distinguish between accreting T Tauri stars (classical T Tauri stars, CTTS) and non-accreting, weak-emission T Tauri stars (WTTS).

To help identify the broad wings of Hα, we used a simple algorithm to identify narrow (FWHM < 10 km s^{-1}) emission peaks close (± 25 km s^{-1}) to the main ^{13}CO velocity. and fit a Gaussian component to this peak. If such local peak was found than it was replaced with a linear segment, connecting the points where the wider stellar profile started to deviate from the narrow Gaussian component. While this helped us to visually inspect the line profiles and make a judgment as to the presence of broad emission wings, it is obviously not a robust method of eliminating nebular emission, especially given the complex velocity structure seen in the densest regions.

In cases of strong nebular emission only the low level wings contained the necessary information for classification. We therefore examined the linear and log scaled plots of each Hα profile. A sample of these plots are presented in Fig. 9.8. The linearly scaled, corrected profile displayed as a bold line, with a linear segment replacing the supposed and eliminated nebular component. The logarithmically scaled version of the uncorrected spectra is shown as a thin line, and other than emphasizing the wings it also makes it the possible to check if the automated identification and subtraction of nebular emission was correct. (The intensity values does not apply to this representation, as it was scaled to fit the linear-scaled range described above.) Black triangles mark the full width at 10%, which was measured together with EW on the corrected profile. Those values are listed in Table 9.2.

We found some contradiction between the two spectroscopy-based classification scheme of TTSs. For some stars even though the nebular-corrected EW (and sometimes the uncorrected EW as well) was significantly smaller than 10 Å, the full-width at 10% reached or exceeded 250 km s^{-1}, broadening strongly indicative of accretion (for example: 0535495-042438 = F11_ap128; 0534257-045655 = F21_ap115; 0536197-051438 = S1_ap175; etc.). With IRAC photometry in hand for several of these stars we were able to confirm the CTTS status. At the same time in other cases we encountered some disagreement between very clear CTTS profiles and IRAC photometry *not* suggesting a disk (see section 9.3.3 below). See discussion in §8.2.2 and Fig. 8.4 regarding how changing Hα profiles could have affected our classification. In addition, further uncertainties

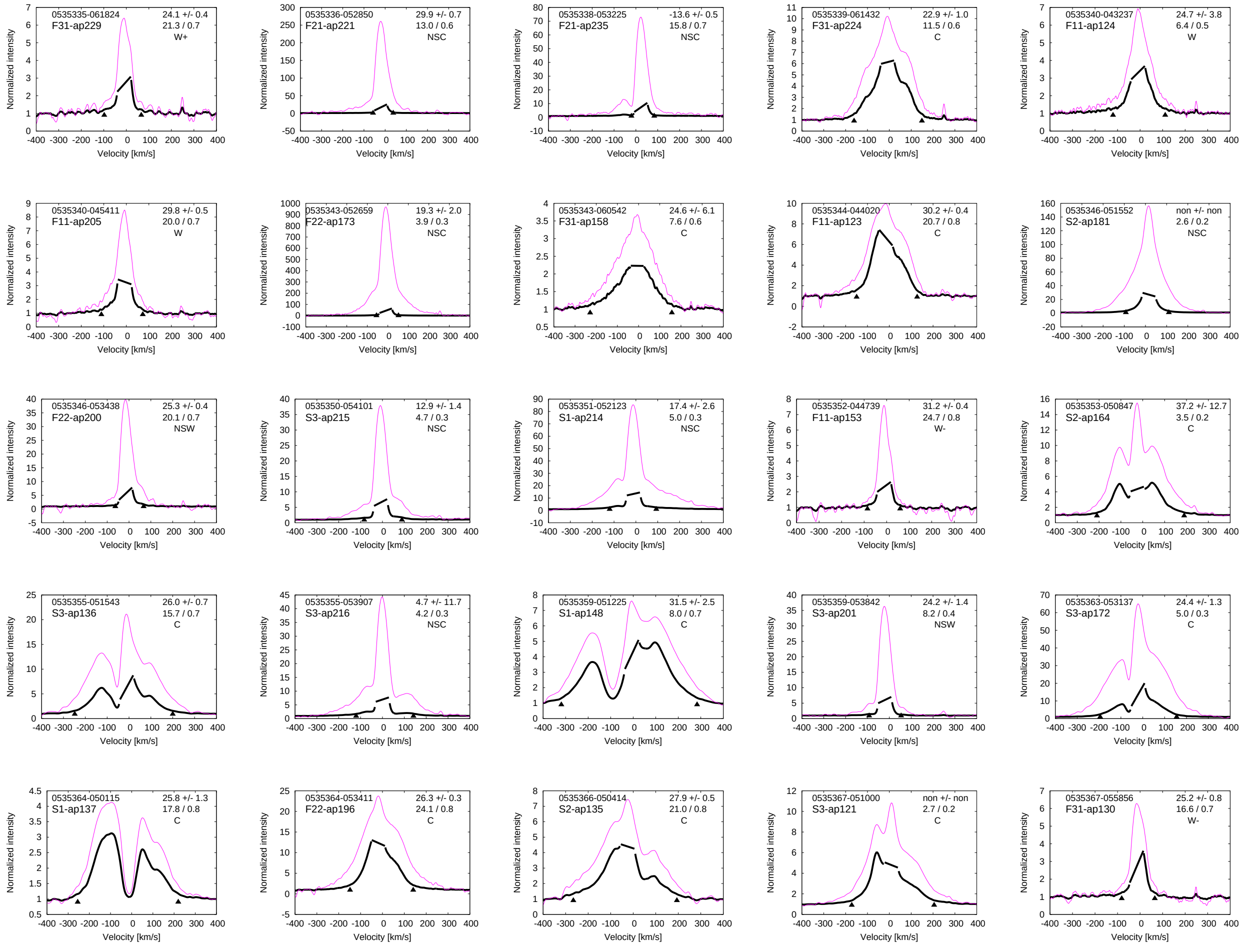

Figure 9.8: ***Examples of $H\alpha$ profiles for stars with detected emission in the ONC sample.*** *Wavelength is converted to velocity with the zero-point being the RV of the star. (In case of very low R values the zero-point is set to RV=0 km s^{-1}.) 2MASS and internal identification numbers are given in the upper left corner for each stamp, while RV and its error, the R and S values, and note on the $H\alpha$ profile are shown in the upper right (see Table 9.2 and 12.5). The thick solid line is the observed spectrum with linear scaling and with the supposed nebular component cut off and replaced by a linear segment. For the original profile, and to emphasize the sometimes barely visible wings, we also show a log scaled version of the observed, unmodified profile (magenta). See text on details of scaling. Solid triangles mark the 10% full width for the nebular-line corrected spectrum. [See the Appendix for all observed $H\alpha$ profiles*

were caused by the artificial subtraction of nebular emission component.

Therefore the final notes (classes) on Hα profiles listed in Table 9.2 and 12.5 are based on a somewhat more complicated classification scheme than CTTS/WTTS or no-emission. In cases of very strong nebular emission with apparently broad but uncertain wings in Hα, to note the possible nebular bias in classification of these stars, we distinguish them with an "NS" prefix in the Hα note. A full description of our classification scheme is given in the notes for Tables 9.2 and 12.5.

In terms of statistics, in our particular sample the total number of CTTS (including C, CD, CW, NSC, see Hα note in Table 9.2) is 581, or 53.6%, The total WTTS count is 439 (including W, WC, WD, W+, W-, NSW), or 40.5%, for a ratio of $CTTS/WTTS = 1.35$. If only the most confidently classified groups are considered, we have 276 CTTS (including only C), and 230 WTTS (including 160 W and 70 W+), which gives a ratio of $CTTS/WTTS = 1.20$. However, we caution that these numbers *cannot* be used to estimate a true ratio of accreting to non-accreting stars in the region, because our sample is biased by the selection of infrared-excess stars, as well as being limited in the sampling of stars in the inner ONC due to crowding. In addition, our non-IRAC selection of stars (F-fields) tended to omit stars with large infrared excess in H-K.

9.3.3 Spectroscopic vs. Photometric Disc/Accretion Indicators

The IRAC color-color diagram [3.6] – [4.5] vs. [5.8] – [8.0] (Allen et al., 2004) can be used to distinguish between young stars with and without inner disk emission (and protostars with circumstellar envelopes, but these were not within the scope of our survey). In the case of a star having both short– and long wavelength infrared excess due to a circumstellar disk, accretion onto the star is likely taking place, and therefore we expect a broad Hα profile, (the signature of material falling in at high velocity), thus a CTTS (e.g., White & Basri 2003). If the short wavelength excess is not present, presumably there is either no disk to accret or no inner disk; in most cases, such systems are not accreting and thus are WTTS.

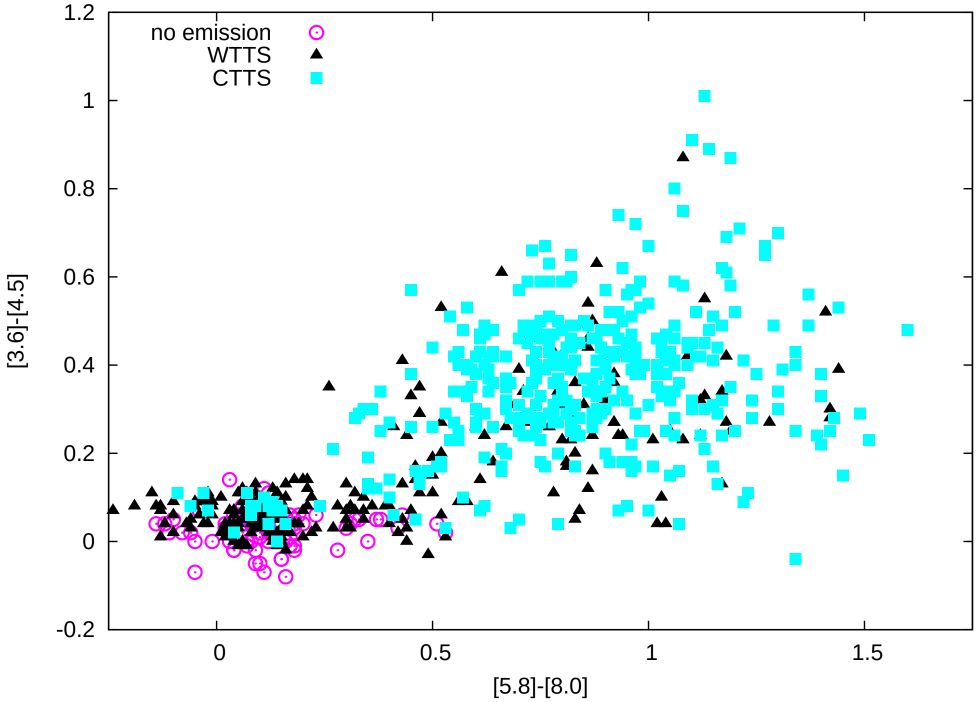

Figure 9.9: ***IRAC color-color diagram of stars in ONC with measured RV.*** *Stars with signs of accretion (wide Hα emission, CTTSs) detected in the spectra must have a disk, and accordingly they do exhibit infrared excess (filled squares), occupying the approximate domain of Class II objects (Allen et al., 2004). Among stars showing only weak Hα emission (filled triangles) some still exhibit infrared excess, meaning the disk is yet presented but accretion has already stopped. Most of the WTTS stars, however, have no signs of disks and scatter around $(0, 0)$. These Class III objects, exhibiting no intrinsic infrared excess, share the area of the graph with field stars and older cluster members showing no signs of Hα emission (open circles).*

Fig. 9.9 shows that as expected, many weak-emission stars have no infrared excesses and many wide-emission stars have infrared excesses, but there are a significant number of counterexamples. We suspect that many, if not all, of the stars with significant [3.6]-[4.5] excesses are in fact accreting, based on the strong correlation previously seen in K-L in Taurus (Hartigan et al. 1990), but the strong nebular contamination prevents us from detecting the Hα wings. Other objects with only long-wavelength excesses may indeed not be accreting. In addition, there are systems without any excesses which clearly are accreting. In the cases of 0533477-045208 (F11_ap43) or 0535343-060542 (F31_ap158) the IRAC colors are $[3.6 - 4.5] = 0.06$ / 0.07, $[5.8 - 8.0] = 0.41$ / 0.13, respectively, both stars have high S/N ratio spectra with very prominent, wide Hα emission containing only negligible, easily identified nebular components. In contrast, 0535513-061353 (F31_ap208) and 0536222-055547 (S3_ap217) the IRAC colors show clear excess, $[3.6 - 4.5] = 0.39$ / 0.34, $[5.8 - 8.0] = 0.87$ / 0.75, but the well defined spectrum shows only a weak nebular component with slight asymmetry or very low level wings.

F11_ap43 and F31_ap158 appear to be examples of a small class of objects termed "transitional disks" (Calvet et al. 2002, 2005). We have found ~ 35 such stars in our ONC sample. These systems tend to have their inner disks partially or almost totally cleared of small dust, as inferred by the weakness of the near-infrared excess, yet have substantial outer disks. TW Hya (Calvet et al. 2002, 2005) and DM Tau (Calvet et al. 2005) are examples of systems which have essentially zero measurable excesses shortward of $\sim 5\mu$m but have strong excesses at longer wavelengths, and *in addition* are still accreting gas onto the central star, producing a broad Hα emission profile. (For example, the 10-Myr-old accreting T Tauri star TW Hya has IRAC colors of [3.6] - [4.5] 0, [5.6] - [8] = 0.95; Hartmann et al. 2005.) Megeath (personal communication) has confirmed the transitional disk status of these objects, as his Spitzer photometric survey extended into the 24 μm band and some of these peculiar stars had usable (acceptable S/N ratio) measurements exhibiting long wavelength excess.

How small dust "disappears" while gas still accrets in the inner disk is not entirely clear. One possibility is that grains grow to such large sizes that the near-infrared opacity is reduced; another possibility is that "filtration" occurs at the inner edge of the optically-thick outer disk, moving particles of sizes responsible for the near-infrared emission outward (Rice et al. 2006). In any event, the accreting transition disks we identify here in the ONC must be among the very youngest such systems known, expanding the range of ages where transitional disk behavior occurs.

9.3.4 Binary Stars

As the velocity dispersion in the ONC region is relatively small, identifying spectroscopic binaries is important to explore intrinsic kinematic structure. To ensure a consistent zero-point (see §5.3) between the multi-epoch observations discussed here, we included some stars of our first observing run in the second set. Also, to make sure that different fields of a given run have a common zero point, we had some overlap between fields so that some stars were observed multiple times within an observing run. Out of the 1215 targeted stars 1086 were observed only once, 122 twice, and 7 three times. For the 129 stars observed multiple times, we compared RV values and evaluated the difference (Δ) against the internal RV error (σ) of the correlation, identifying possible ($\Delta > 1.5\sigma$) and likely ($\Delta > 3\sigma$) binary stars. The *CCF* column of Table 9.2 and 12.5 lists *dv?* and *dv* notes for these stars, respectively.

In case of a single RV measurement the cross correlation function still can be used to identify double-lined spectroscopic binary stars. By looking at each individual CCF we found several side lobes, secondary peaks blended with the main peak (CCF note s), and resolved double peaks (d). In case the main/secondary CCF peak heights were not at least 50% higher than any other local peaks due to noise, or the side lobe did not raise 25% higher than local peaks and therefore the detection probability was not high, we added the "?" sign in the notes to express the uncertainty.

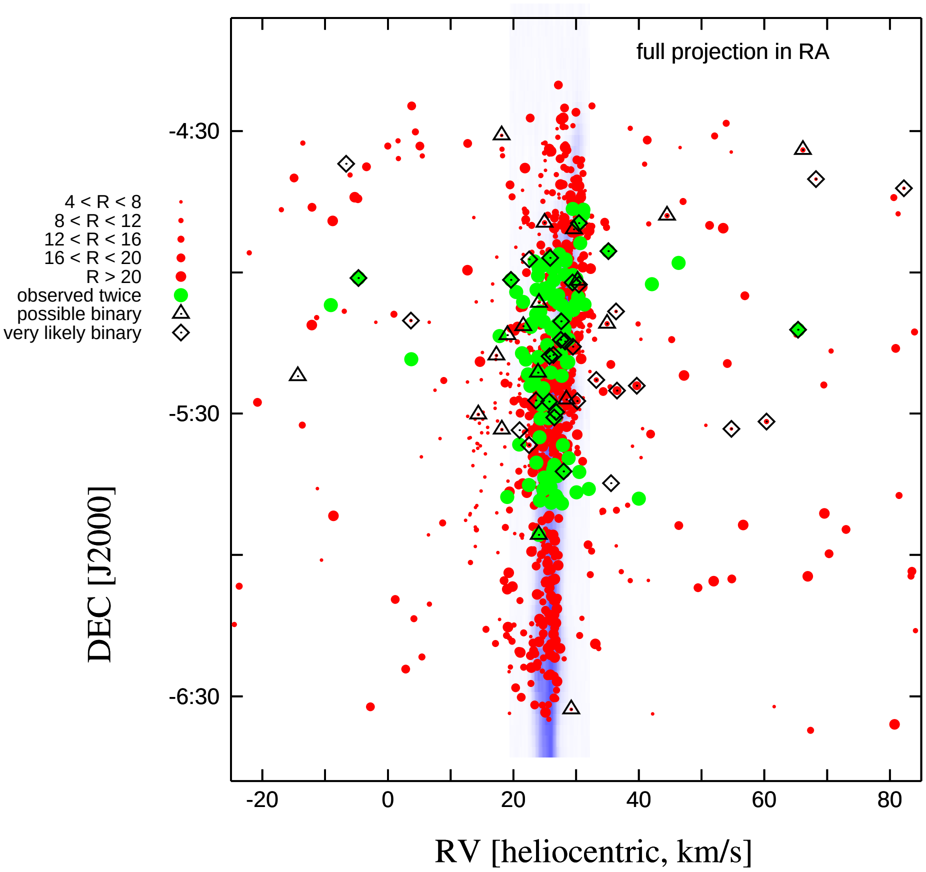

Figure 9.10: ***Binary stars of the ONC region displayed on a spatial–velocity plot*** *(full projection along RA). The molecular gas is mostly buried by the crowded stellar symbols (gray circles; size is correlated to R value like on Fig. 9.5). Binaries, identified by clear double peaks in the cross-correlation function or by two different RV measured at two epochs, are shown as open diamonds. (In case of more than one RV value the star is displayed according to the average of the velocities.) Possible binaries, exhibiting asymmetric or side-lobed cross-correlation function, are displayed as open triangles.*

The location of these binary stars are shown in Figure 9.10, displayed as a full projection in RA, onto a RV–declination plane. The possible (more uncertain) stars are shown with open triangles, the more likely candidates noted with open diamonds. The velocity used for plotting is the average of all measured RV values in case we had more than one measurement. A wider velocity range is applied to this plot to accommodate all the binary stars, rendering the main stream cluster members and molecular gas into a narrow vertical feature. Counting all the possible (18) and more likely ones (34), the total number of binaries is 52, or ∼4% of the entire sample.

Based on these single epoch observations we cannot make an estimate of the spectroscopic binary fraction of the ONC. However, our results may be consistent with the low frequency of resolved multiple systems suggested for the ONC (see Köhler (2006) and references therein). In any event, our observation of position-velocity structure in the stellar distribution, which strongly correlates with the molecular gas, indicates that the overall dynamics are not strongly biased by binary motion, though our velocity dispersions may be slightly inflated due to orbital motion. Of course, there may be spectroscopic binaries present in our sample with much smaller velocity shifts that are difficult to separate from the main population (see §9.4.3).

9.3.5 High Radial Velocity Stars

In section 9.3.1 we showed that the RV distribution is relatively clean, with very few outliers from the main peak (see insert of Fig. 9.4). Although most of these high velocities are just false CCF peaks, some are real detections; these stars have a note "R" in the Hα column of Table 12.5. What makes these stars interesting is the possibility that they originated from a cluster by a decay of a triple or multiple young stellar system, or by interaction of multiple systems (Gualandris et al., 2004) and then were ejected at high velocities. The very high stellar density of ONC makes it a favorable place to look for such stars (one example may be the BN object, just north-west to the Trapezium (Rodríguez et al., 2005)). Three members of ONC were recently suggested by Poveda et al. (2005) to be possible runaway stars based on proper motion measurements performed on photographic plates, but O'Dell at.al (2005) did not confirm these motions using proper motion measurements from Hubble Space Telescope images. Only one of these three stars (JW 355) can be found in our sample as 0535109-052246 (S2_ap220). Unfortunately the spectrum is very noisy so we have no additional radial velocity measurement.

Among our targets we have 21 stars with the "R" note, out of which 5 stars have velocities smaller than -40 km s^{-1} (more than $\sim 20\sigma$ off the mean cloud velocity) and 15 have RV values larger than 80 km s^{-1}. Each of these stars were observed only once so the only hint for companions, as an other possible reason of deviant RV, would be the CCF. However, for all of them it only has a single, well defined peak.

A relation to the cluster is apparent only in one case, as star 0535503-044208 (F11_ap146) shows Hα emission (therefore listed in Table 9.2). All the others exhibit only a nebular emission component superimposed on the Hα absorption line. According to the stellar parameters derived from the multi-template fitting, more than half of these stars are K–M dwarfs. Assuming main sequence colors (Kenyon & Hartmann, 1995), based on the derived temperature, and comparing it to the observed (J-H) value, we got extinction values of $A_V \simeq 3-4$ by assuming a $E(J-H) = 0.19\ E(B-V)$ relation (Bessell & Brett, 1988). This is a plausible value in those areas these stars are located, farther from dense regions.

The three most deviant RV stars are worth mentioning. One object is blueshifted at $RV = -147$ km s^{-1}, and exhibits only $A_V = 1.3$. The low extinction is not surprising as this star (0537111-055946 or F31_ap162) is located at the very edge of our field, which also means just off to the side of the Orion A molecular cloud. The surface gravity suggests a giant, thus it is likely a background object based on its brightness. This is in agreement with its location, as we could have not observed it behind the denser parts of the cloud.

The two highly redshifted stars (0536592-050029 or F11_ap183 at $RV = 232.5$ km s^{-1}; and 0537005-050931 or F22_ap138 at $RV = 438.7$ km s^{-1}) have almost the same RA value as F31_ap162, so those are also just off the cloud. The former star seems to have a low surface gravity, and therefore it is likely a background object as well, at a brightness of $J = 11.87$. However, there seems to be a contradiction with its J magnitude, as the $(J - H) = 1.09$ color suggests a very high extinction adopting the intrinsic colors of $(J - H)_0 = 0.66$ from Alonso et al. (1999), based on the stellar parameters derived form template fitting. Another problem with the interpretation as a background object is that the $[Fe/H] = +0.5$ templates used for the analysis might be not adequate. Re-running the cross-correlation on a grid of metallicities (with a fixed rotational velocity of 0) it turns out a $[Fe/H] = -0.5$ gives a better match (with $T_{eff} = 4500$ and $log(g) = 1.5$), but the observed and intrinsic colors are still in contradiction with the expected low extinction. Thus, additional spectroscopy is required to say more about this object.

Exploring metallicity by further template matching turned out to be crucial for the highest radial velocity star, F22_ap138, as for temperature we hit the edge of parameter space while performing cross-correlation of the original grid. Fixing the rotational velocity at 0 and exploring a metallicity–temperature–gravity grid we found the best match to be a $[Fe/H] = -1.5$ spectrum with $T_{eff} = 4250$ and $log(g) = 4.0$. This results a plausible extinction of $A_V = 1.1$. The low metallicity template suggests that this is not a young star, therefore very likely we witness a fast moving background member of an older population.

9.4 Discussion

9.4.1 Cluster in Formation

The significant position-velocity substructure seen in both the stars and the molecular gas clearly demonstrates that the ONC is not dynamically relaxed; qualitatively, it appears to be more consistent with dynamical models of cluster formation such as those of Hartmann & Burkert (2007) and Bate, Bonnell, & Bromm (2003).

On Figure 9.11 we compare the model calculations of Hartmann & Burkert (2007) (right column) to the observed properties (left column) of the ONC region, by a spatial-spatial (top row) and a spatial-velocity (bottom row) plot. For the upper left panel the gas and stars are shown for a range of $23 - -30$ km s^{-1} heliocentric velocities, to compare with the density plot of the model. The lower panels are vertical cross-sections of the upper ones, displaying the velocity distribution along the midplane.

It cannot be emphasized too strongly that the model is very limited; the calculation is in two dimensions and so the velocities predicted by the model depend upon the inclination of the plane of the collapse to the line of sight. Moreover, the simulation is highly unresolved, so that the details of the velocity structure near the center are uncertain. Finally, the model contains only gas, while stars are likely to make a significant (if not dominant) contribution to the gravitational potential in the central cluster regions. About all that can be said is to rely on the qualitative results that the model predicts an overall velocity gradient and a larger velocity dispersion near the cluster center. Now that we have detailed velocity observations of both stars and gas, much more advanced dynamical calculations including both stars and gas are called for. Still, with the mentioned warnings in mind, we feel that the model of Hartmann & Burkert (2007) has similar properties to the observed features.

The curvature of the ^{13}CO emission seen in the northern region of the position-velocity plot of 9.6, with a possible corresponding southern feature, is suggestive of gravitational acceleration

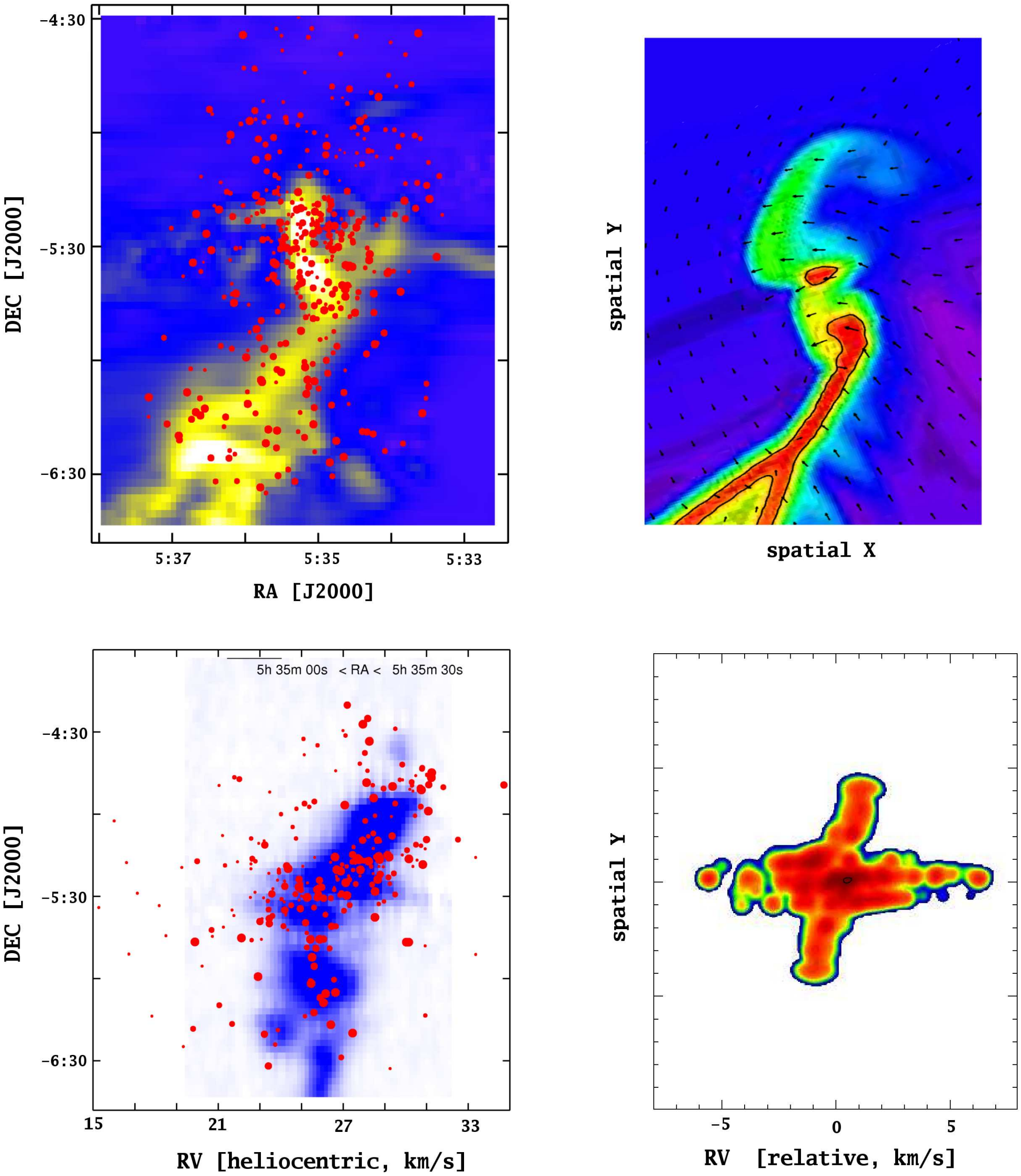

Figure 9.11: ***Observations of ONC compared to the model of Hartmann & Burkert (2007)***. *In the upper row we compare a spatial–density plot from a simulation (right) of a gravitationally collapsing finite, elliptical, rotating sheet (see Fig 6 and 7 from Hartmann & Burkert (2007)) to* ^{13}CO *and spectroscopic observations of molecular gas and stars (left). Note the similarity in structure: the two dense cores in the middle, the diagonal bar which opens up at the bottom left corner, and the integral-shaped twist in the middle. The stellar component in the* $24\ km\ s^{-1} < RV < 28\ km\ s^{-1}$ *region, displayed as red dots, follow these key structural elements very well. The highest density of gas, both in the simulation and observations, agrees in position with the highest density of stars. The spatial scatter, as well as the RV dispersion (see bottom panels), is also the highest in this region, as expected due to strong gravitational interaction. The bottom spatial–velocity plots, cross sections of the upper plots along the mid-RA/mid-spatial values, also exhibit very similar features in the structure of the observations (left) and the model (right).*

of material toward the cluster center, where the gravitational potential well should be deepest. Gravitational acceleration is also consistent with the evidence for the largest velocity distribution in the gas located near the center. Many stars exhibit the same position-velocity distribution as the ^{13}CO, which suggests that these stars are mostly following the motion of the dense gas within which they formed. If these motions were primarily the result of stellar energy input through winds or photoionization, it is not clear that the gas and many stars should show the same kinematics, as such energy input could easily blow the gas away from the stars - some possible examples of this are discussed in the following section.

The observed correlation of stars and dense gas in space and in velocity indicates that the inner regions cannot have experienced more than about one crossing or collapse time; otherwise the velocity structure would be erased as the infalling gas shocks and dissipates its kinetic energy, with the stars passing through the shocked gas. Overall, the spatial coherence in the ^{13}CO gas kinematics, the evidence that many younger stars follow this motion, and the strongly filamentary structure of the stellar distribution outside the main core of the ONC suggest that the ONC still exhibits features traceable to its initial conditions of formation.

9.4.2 Subgroups and stellar energy input

While there is a strong general spatial and kinematic correlation between stars and dense gas, there are exceptions. One especially clear case can be seen on the bottom left panel of Fig. 9.6 at $DEC \simeq -5°27'$: a tight, linear string of stars sticking out of the main cloud as a "nose" extending between $RV = 21$ and 25 km s^{-1}. The left-hand panel of 9.12 shows a declination-velocity plot zoomed into this region, in an RA range shifted slightly westward of the Trapezium region (vertical lines in the right-hand, RA-DEC panel of Fig. 9.12). Clearly there is a small group of stars blueshifted by about 1-2 km s^{-1} from the gas in the declination range $-5^d\,20^m > DEC > -5^d\,30^m$. Selecting "off-cloud" stars by means of an velocity envelope for the gas (thin curve in left panel) results in demonstrating that these stars are spatially concentrated in a region south-west of the Trapezium which is relatively evacuated, as indicated by the weak 8μm emission seen in the IRAC map (right panel, gray-scale). This region is also known for a large number of Herbig-Haro objects shaped like bow-shocks pointing back toward the Trapezium region (see description in O'dell (2001)), consistent with the idea that outflows from the region of most current star formation is blowing out material.

We therefore suggest that the molecular gas in this region originally extended to more negative velocities, but that outflows have cleared away the gas, making an "indentation" in the position-velocity plot at $\sim -5^d\,26^m$, RV ~ 24 km s^{-1}, and leaving the recently-formed stars behind.

There are other interesting small scale structures, like the tight, dense sub-cluster group seen in the middle of the second panel of Fig. 9.7 (upper row, 2nd panel from left to right, also somewhat apparent on Fig. 9.6 upper row, rightmost panel). These can be remnants of small building blocks, traces of density variations in the primordial cloud.

9.4.3 Other Populations?

Based on Fig. 9.9, we divided our sample into *IR-excess sources*, with $([3.6]-[4.5]) > 0.2$ and $([5.8]-[8.0]) > 0.5$; and *non-IR excess sources* with $([3.6]-[4.5]) < 0.2$ and $([5.8]-[8.0]) < 0.5$.

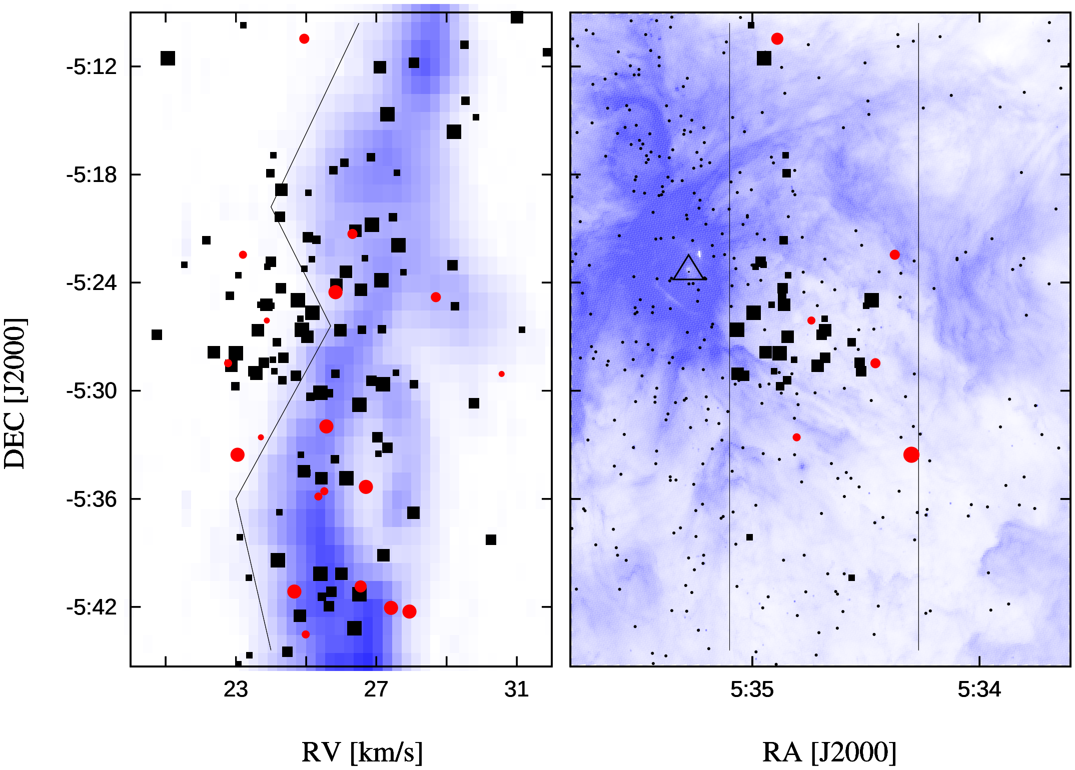

Figure 9.12: ***A newly identified, (kinematically) off-cloud subgroup of stars in the close vicinity of the Trapezium.*** *In the left panel, we show a zoomed-in velocity–declination channel map similar to the bottom left panel of Fig. 9.6. A group of stars in the range* $-5^d\ 20^m > DEC > -5^d\ 30^m$ *is slightly but clearly offset from the molecular gas by about 1-2 km* s^{-1}*. Most of these stars also show infrared excess (filled squares); only a few do not (open circles), and so are clearly members. We defined a velocity envelope for the* ^{13}CO *emission (thin curve), and plot the positions of the stars blueward of this envelope in the right panel. These "off-cloud" stars tend to lie in a relatively evacuated region west–south-west of Trapezium (noted as an open triangle), as indicated by the low dust emission seen in the 8μm IRAC map (shaded area). All other stars with measured velocities and* $R > 4$ *are shown as black dots, and two vertical lines represent the RA limits of the channel map on the left. The morphology of the region suggests that molecular gas has recently been evacuated by outflows from the Trapezium region (see text).*

This division of sources is shown on the velocity-declination map with full projection along RA in Figure 9.13: the left panel for excess and the right one for non-excess stars.

Looking at the left panel in Figure 9.13, southward of $-6°$ there are very few CTTS. This abrupt change is an unfortunate selection effect. The targets selected for our second observing run (S fields) had a southern declination limit of $-6°$, exactly where the sudden change of excess/non-excess ratio happens. And since targets for the first observing run (F fields) were selected from the 2MASS color–magnitude diagram, our selection was biased against stars with IR excesses because of the $(H - K) < 0.5$ criterion.

While many of the non-excess stars (middle panel) follow the general distribution of gas and excess stars, a modest number clearly exhibit a broader distribution in radial velocity, with more blue- than redshifted stars. This can be seen on the right panel, where we present RV histograms of excess (solid bars) and non-excess (gray-shaded boxes) stars, for three declination ranges (north, with $DEC > -5.2$; mid, with $-5.2 > DEC > -6.0$; and south, $DEC < -6.0$ - as represented by

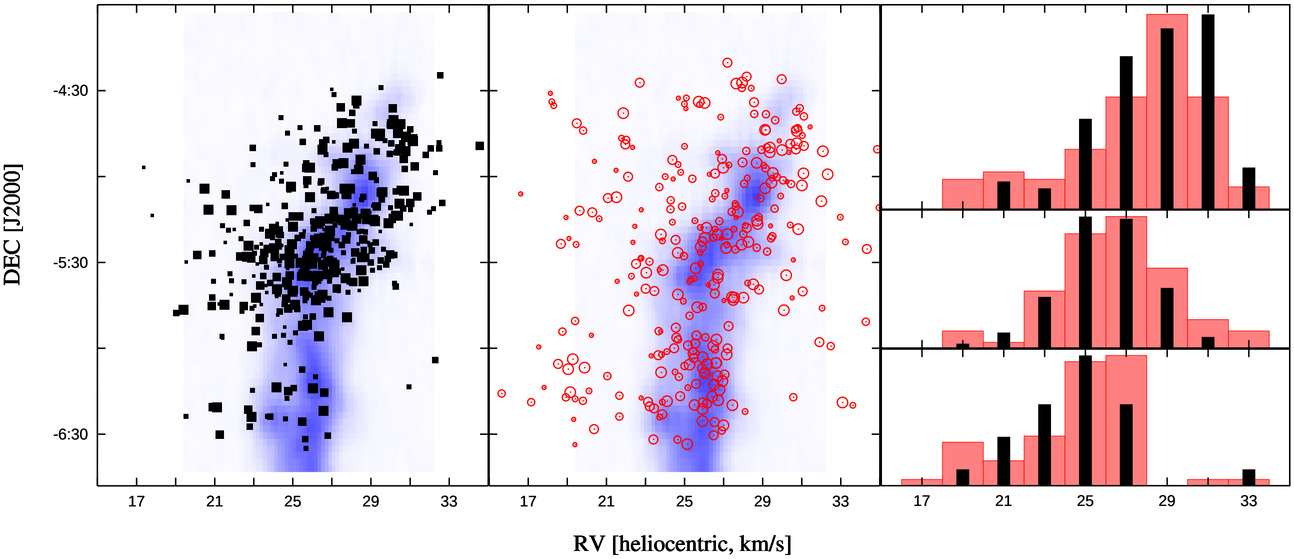

Figure 9.13: *Velocity–spatial plot and velocity distribution of ONC stars with (filled squares, left panel) and without (open circles, middle panel) infrared excess* *(full projection in RA). On the right, we show histograms for three declination bands, which are indicated by the locations of the histograms. Note, that for the northern section ($DEC > -5.2$ deg) the mean velocity of the gas is redshifted, as it is seen in the displaced peak of the distribution as well. The middle ($-5.2 > DEC > -6.0$) and southern ($DEC < -6.0$) sections have similar mean velocities, although there is a strong RV gradient in the mid-declination range. On these histograms the gray shaded columns represent the distribution of the non-excess stars (middle panel), the black bars represent the excess stars (left panel). Note the group of stars around $DEC = -6^d\ 15^m$ and $RV = 19$ km s^{-1}, which is only apparent on the middle panel (non-excess stars) and could be an older foreground population. This group is responsible for the small local peak at 19 km s^{-1} in the RV histogram of Fig. 9.4. Also note that at $DEC < -6$ there are less IR excess sources on cloud, which is likely due to a selection effect (see text for details).*

the location of the histograms as well). We divided this way because RV behavior of the gas is very different in these regions: the northern velocity is significantly higher than the mean velocity in the south, and the middle section exhibits a strong RV gradient. Regardless, the velocity distribution of non-excess stars is wider because of a secondary peak at lower velocities.

However, there still might be a hint for some non-uniformity in the distribution of non-excess sources. Displaying Fig. 9.13 for the first selection of targets only (Fig. 9.14), the bias against disked stars should be independent of spatial position, as the selection was done in a 2MASS color–magnitude diagram. The absolute measure of excess/non-excess ratio would be obviously misleading in this case, but excluding the other, spatially limited and opposite-sense biased sample we expect not to see any distributional difference. And Fig. 9.14 does really not show a sudden drop of excess sources in the south any more, as well as the relative number of non-excess sources is obviously different than in Fig. 9.13. But still there seems to be a lack of excess objects around $DEC = -6^d\ 15^m$, and at the same time the non-excess sources show greater density in this region. If this is a real deviation that might suggest a slightly older age for this part of the cloud. By deriving independent age estimates from our Li observations in the near future, we might be able to confirm or disproof this puzzling scenario.

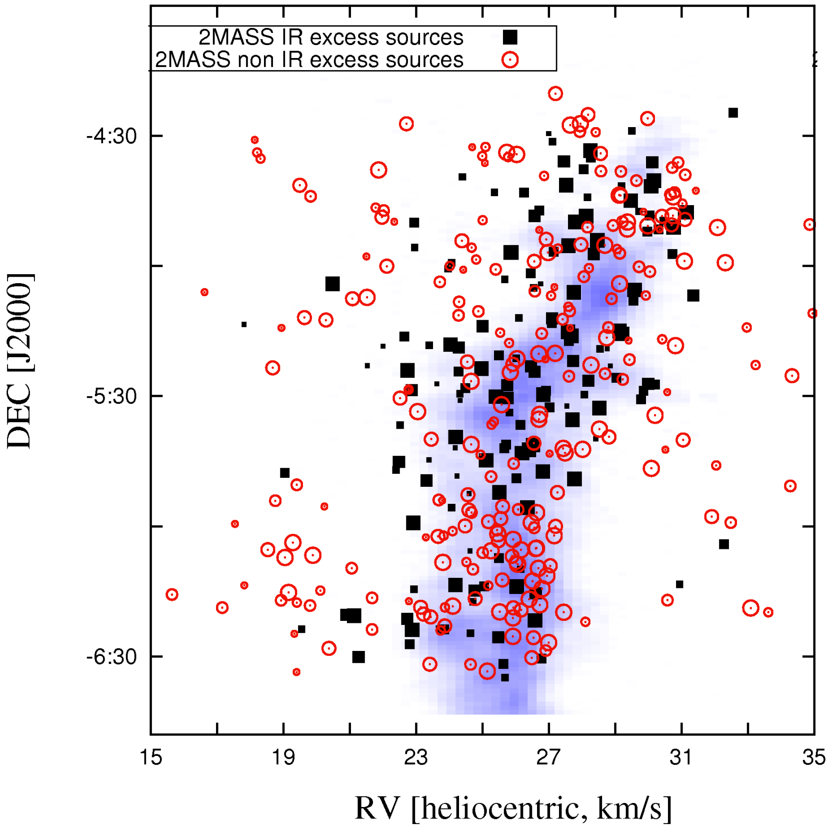

Figure 9.14: ***Comparing the distribution of excess/non-excess stars for the 2MASS ONC selection only*** *(displaying stars from the F-fields only) should have a position independent bias against excess stars. As it can be seen there are less stars with infrared excesses (filled squares) in general than non-infrared-excess stars (open circles), compared to Fig. 9.13, and the sudden drop of disked systems in the south is not expressed any more. Although around* $DEC = -6^d\ 15^m$ *there still seems to be a lack of excess objects, and the density of non-excess stars is significantly higher compared to other parts of the cloud.*

For now we can confidently derive only the conclusion, that while many of the non-excess stars follow the general distribution of gas and excess stars, a modest number clearly exhibit a broader distribution in radial velocity, with more blue- than red-shifted stars. We consider several possibilities to explain these outlying stars:

One possibility is that the lower-velocity stars have been ejected from the main cluster. Close encounters in multiple star systems might result in ejecting stars while stripping their disks; the red-shifted stars might then eventually plunge into the dense, opaque regions behind, leaving more optically-visible stars with blueshifts. However, this seems unlikely because it requires a surprisingly large fraction of stars to be ejected, we do not detect a larger density of such objects nearer the center of the ONC, where the high stellar density would be more favorable to ejection. In addition, south of $-6°$ the velocity distribution is clearly bimodal, with a very tight velocity spread for the on-cloud stars; it is not clear why ejection would lead to such distinct structures.

Another possibility is that we are detecting a foreground, older population. Stars in the foreground Orion 1a association (Brown et al. 1994) may have a heliocentric radial velocity near

~ 20 km s^{-1}, as suggested by measurements of the 25 Ori group Briceño et al. (2007). If this is the case, it would mean that the Orion 1a association is much more spread spatially towards the ONC (in the foreground) than has previously been realized (see left panel of Fig. 7.5).

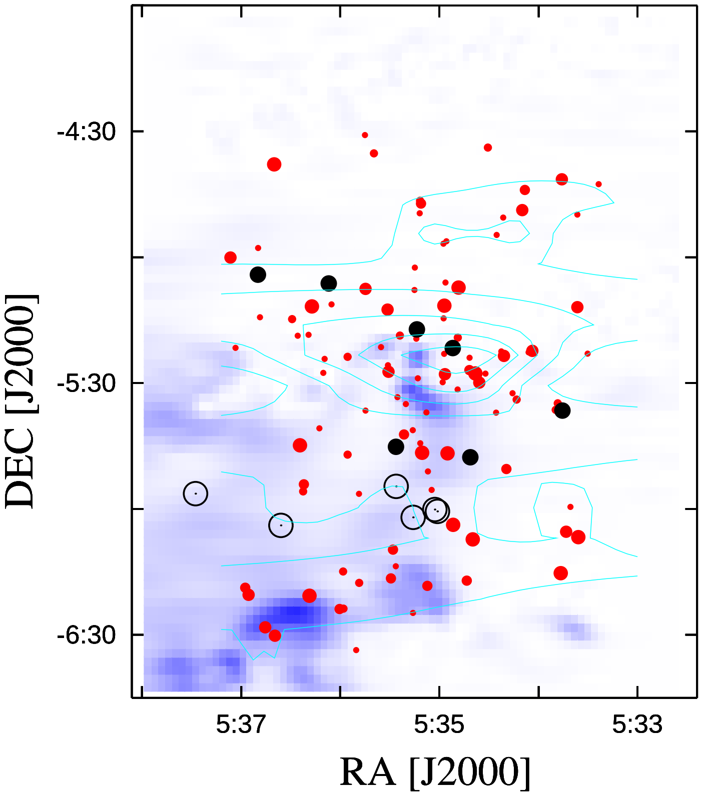

Figure 9.15: ***Spatial distribution of stars foreground to ONC.*** *The filled circles represent stars with significantly blue-shifted velocities respect to the molecular cloud (shaded areas). The stars are displayed between* $16 < RV < 22$ *km s*$^{-1}$*, and since there is no gas at this heliocentric velocity range, we plot the most blueshifted RA-DEC channel of the gas at* $RV = 23$ *km s*$^{-1}$*. Contours of stellar density are also plotted in order to enhance the structural similarity of the gas and stars in the south, for the older foreground population between* $-6°30' < DEC < -6°00'$*. Open circles note the OB stars around* $DEC \simeq -6°$ *(HD 37303, 37209, 37043, 37025, 36960 and 36959).*

A third possibility is that stellar energy input blew out material, forming a small proportion of stars in a bubble wall moving toward us. To explore this idea further, we plot only the stars with RV values less than 22 km s^{-1}in the RA–DEC plot of Figure 9.15. Since there is no gas here, we display the most blueshifted 1 km s^{-1} wide channel of the gas at 23 km s^{-1} heliocentric velocity. The northern foreground stars seems to be separated from the older southern group, by an almost empty gap running east–west at $-6°00'$. However, this might be the result of a combination of our bias against selecting infrared-excess stars mentioned above and accidental fiber coverage. Still, there is some structural similarity between the distribution of these southern foreground stars and the gas "behind", redshifted to it. Note how these southern stars are spread on top of two-three denser gas clumps. If this structure is interpreted as a local "bubble", this could have been created at the very beginning of star formation by the early emergence of some OB stars in the region. These stars than could have blown away most of the gas from us, some smaller amount towards us, and so other stars could have formed at this early stage in this perturbed southern region.

This picture would require some OB stars in the questioned region, and the list of Brown et al. (1994) contains six of them interestingly close to -6 degree declination (see Fig. 9.15). However, obviously none of these is in close vicinity of the gas now, as there are no apparent HII regions at this part of the molecular cloud. An additional problem is that one would expect such a population to be somewhat older than the main cloud, which is not obvious in the J vs. J-H diagram. This is not a particular problem for the foreground population hypothesis, as the Orion 1a stars will appear higher in the color-magnitude diagram at a given age than the ONC.

In conclusion, the reasons for the additional velocity spread of the non-excess stars are not clear. Further monitoring for radial velocity variations as well as more detailed studies of the stellar properties are needed to determine which of the above possibilities are correct.

9.4.4 Comparison with Other Observations and Models

X-ray studies of Feigelson et al. (2005) found that ONC stars $0.5 - 2$ pc from the center show a strong spatial asymmetry. They attributed it to a temporary period of violent relaxation in the dynamical evolution of the cluster, but our observations do not show violent or any other relaxation. The detected spatial structure, extending over the entire observed region, is not a signature of a relaxed configuration.

If the ONC is not dynamically relaxed, why did HH98 find a fairly good fit to a King cluster model? (Note that Scally et al. (2005) point out difficulties with physically interpreting the ONC in this way). The central region of radius ~ 0.5 pc does appear to exhibit a smooth distribution, and thus may be closer to having relaxed, though it is somewhat elongated. On larger scales, the elongation is sufficiently large that azimuthal averaging is not appropriate. To take an extreme example of what this averaging can do, imagine a cylindrical distribution of material in the plane of the sky with uniform surface density and width W. Azimuthal averaging of this distribution results in an average surface density $\Sigma \sim$ constant for $r < W$ and $\Sigma \propto r^{-1}$ for $r \gg W$. Interpreting this surface density in terms of a spherically-symmetric density distribution results in $\rho \sim$ constant for $r < W$ and $\rho \propto r^{-2}$ for $r \gg W$, which is roughly consistent with a King model. The ONC is not as extreme in structure as this simple example, but it illustrates the potentially misleading nature of azimuthal averaging of an intrinsically highly elongated structure.

Comparing azimuthally averaged stellar densities and global velocity dispersions to N-body calculations, Kroupa (2000) was unable to distinguish whether the ONC is in equilibrium, or is collapsing, or is expanding; a similar result was obtained Scally et al. (2005). This demonstrates the importance of avoiding azimuthal averaging and obtaining detailed kinematic observations of gas and stars in developing an understanding of the dynamical state of the region.

Tan, Krumholz, & McKee (2006; TKM06) have argued for a picture in which rich star clusters take several dynamical times to form, are quasi-equilibrium structures during formation, and thus initial conditions are not very important. In particular, TKM06 discuss the ONC and argue that it is several crossing times old, of order 3 Myr, larger than assumed here. Here we discuss why we arrive at different conclusions.

Following Scally & Clarke (2002), TKM06 argue that the smoothness of the spatial distribution of the stars in the ONC argues for long formation times, which allow clumps of stars to disperse. As pointed out above, the azimuthal averaging done by Hillenbrand & Hartmann (1998) was somewhat misleading, helping to smooth out filamentary structure. In addition, the gas kinematics, and to a lesser extent the stellar kinematics, show substructure which is less evident in the spatial distribution alone.

TKM06 also use the analysis of stellar ages in the $0.4-6\mathrm{M}_\odot$ mass range by **?** to argue for a large age spread in the ONC. Although they note that Hartmann (2003) pointed out problems of contamination by non-members, TKM06 do not take sufficient notice of the mass-dependence of isochrones. As was clear from the original work by Hillenbrand (1997), and is evident in Figure 4 of Palla & Stahler (2000), standard isochrones imply that stars of 1 to 5 $\mathrm{M}_\odot$ in the ONC have systematically older ages by one to a few Myr than both the lower mass stars and the higher mass stars. This effect is seen in virtually every star-forming region, at least comparing the intermediate mass stars to the lower mass $< 1\mathrm{M}_\odot$ stars (see HR diagrams in Palla & Stahler (2000)). In other words, the "tail" of older stars in the distribution of stellar ages found by Palla & Stahler (1999, 2000) is strongly populated by a *different* mass range (intermediate mass stars) than the peak of the age distribution (low mass stars).

As pointed out by Hartmann (2003), if one takes these age determinations at face value, it means that the ONC existed for a few Myr as a cluster forming mostly intermediate mass stars, with very few low mass stars (or high-mass stars). In other words, the ONC (and other regions) begin their first few Myr of existence with extremely non-standard stellar initial mass functions (IMFs). There is no observational evidence for any young clusters dominated by intermediate-mass stars by number. Therefore, there must be something wrong with the isochrones.

Pre-main sequence ages are contraction ages; one must know the starting radius of the star to determine the age. TKM06 argue that corrections for starting radii (the "birthline" position) are only important for stars with ages < 1 Myr. However, Hartmann (2003) showed that this is not necessarily true for intermediate-mass stars; changing the accretion rates at which stars form over plausible ranges can have very big effects on the birthline for $\gtrsim 1\mathrm{M}_\odot$ stars. Thus, the apparent ages of the intermediate-mass stars can be systematically overestimated due to incorrect birthline assumptions; this allows the ONC to maintain a roughly typical IMF over its formation. With this correction, the fraction of stars older than 2 Myr decreases dramatically.

9.5 Summary

We have carried out a spectroscopic survey of 1215 stars located in the northern end of Orion A molecular cloud, covering the ONC and its vicinity. The obtained radial velocities show a well defined spatial and kinematical structure of the stellar component, which is very similar to the one seen in the molecular gas. Comparing our observational results to the model of Hartmann & Burkert (2007), we draw the following picture of the ONC region:

On large scales the gas (and stars) exhibits a velocity gradient due to rotation or shear running north-south. The curvature seen most clearly in the northern arm of the gas in the position-velocity diagrams suggests gravitational acceleration towards the cluster center. We further conjecture that the concentration of gas (and stars) south of the Trapezium region is somewhat in front and is also falling in towards the center, explaining its higher radial velocities; the Orion Bar photodissociation region appears to reside just above, or perhaps at the upper edge, of this moving clump. The southern part of the filament may also be falling in, although the motions are much less organized than is apparent in the northern arm. Finally, it may be possible that the process of blowing out the near side of the cloud, in the south, resulted in accelerating and compressing gas which formed a small population of stars with velocities blueshifted by a few km s^{-1}; or, these stars may be foreground objects in a different kinematic system possibly associated with Orion OB 1a.

The high degree agreement between the structure of the gaseous and stellar component suggest the region is very young, only ~ 1 crossing time old, otherwise gravitational interaction should have been smoothed the fine structure still clearly visible in our data. Note that the observational errors for the stellar radial velocities (ranging from 0.5 - 1.5 kms) are larger than the observational errors in the radio measurements. In addition, with only two epochs (at most) we cannot correct for the effects of even small binary motion. For these reasons it is not yet possible to make fine distinctions between stellar and gas kinematics.

The spectra in the Hα order provide not only RV measurements but allow the possibility of classifying many stars according to their Hα emission. With the aid of IRAC photometry we were able to confirm the presence of disk around many CTTS opening/loss of a disk around most WTTS. To the south we see another older but foreground population, which still might be not completely independent but connected to the region, suggested by continuous streams of stars to the south and north of this group and by the similarity in the spatial structure of the "background" gas and these blueshifted stars.

In a future communication we will provide further improvements in the detection of spectroscopic binaries and provide additional checks on membership using the 6708 Å Li line.

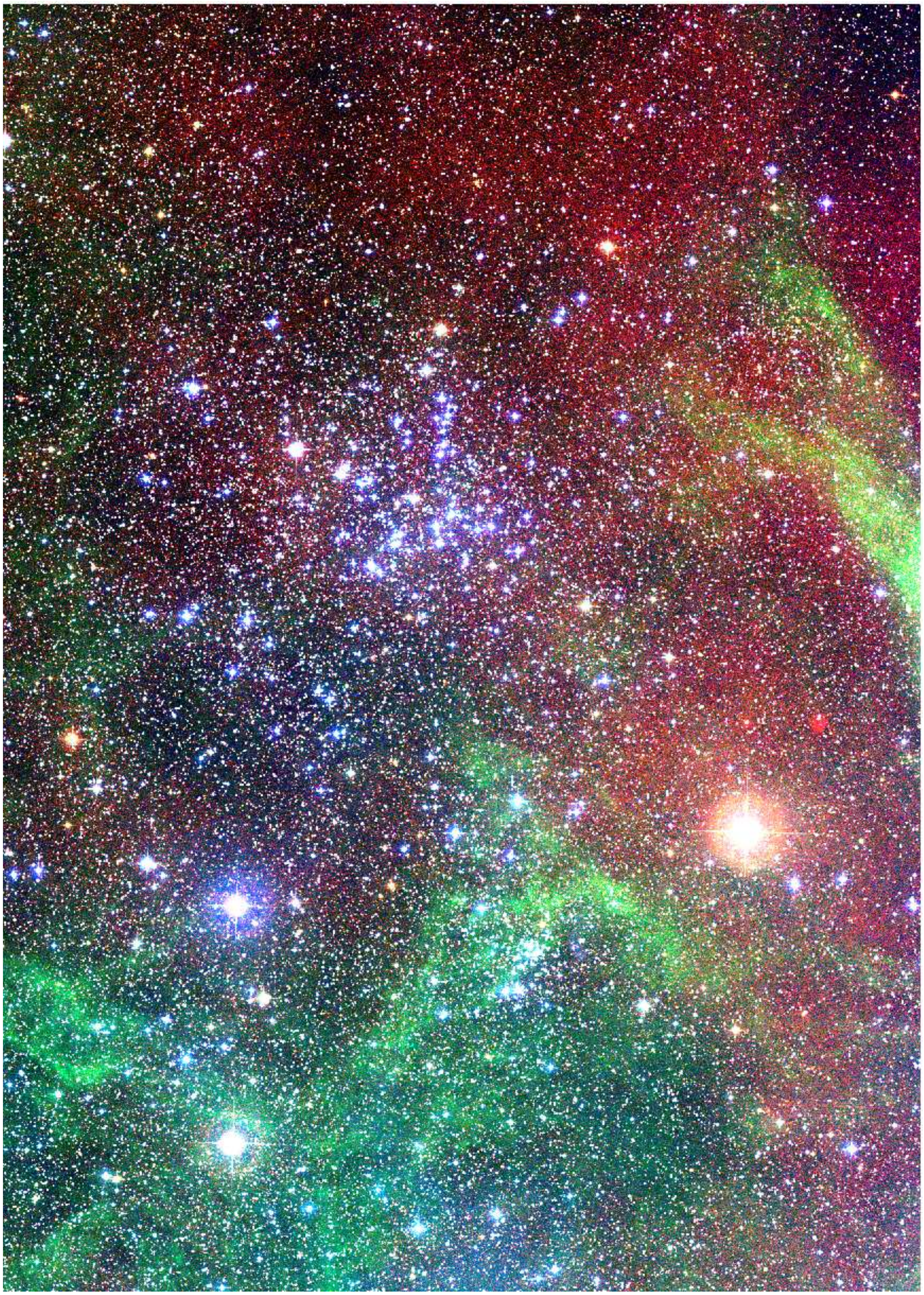

The Open Clusters NGC 1912 and NGC 1907 – *color composite of Digitized Sky Survey blue, red and infrared plates (colored as blue, green and red, respectively)*

Chapter 10

NGC 1907 and 1912 – Interacting Pair of Open Clusters?

Young open clusters associated with molecular clouds are well studied objects as they provide insight into the early history and formation of these associations. While few Myr after of their formation the internal structure is not completely relaxed (see the previous two chapters about NGC 2264 and ONC; Fűrész et al. 2006, 2008) older, more evolved open clusters exhibit a rather relaxed kinematics. Although physical interaction of a cluster and a massive object (such as another cluster) leads to perturbations and a non-equilibrium state. Several examples of this dynamical configuration are found in the Magellanic Clouds (see e.g. Hatzidimitriou & Bhatia 1990, Bica & Schmitt 1995, Pietrzynski & Udalski 1999, Bica & Dutra 2000). However, interacting open clusters in the Galaxy are rare, the only example being $h + \chi$ Persei. Subramanian et al. (1995) drew up a list of candidates for physical cluster pairs, citing NGC 1912/NGC 1907 (Fig. **??**) as a particularly good candidate.

NGC 1912 (M38) is a massive cluster in the Northern Hemisphere, with a visual diameter of $\sim 20\,'$. Distance estimates derived by several authors span over a wide range of 870 pc (Hoag & Applequist, 1965) to 1820 pc (Subramanian & Sagar, 1999), the generally adopted value is ~1400 pc (see Pandey et al. (2007) and references therein; PA07 hereafter). The age estimates are somewhat more consistent, ranging from 250 Myr (Subramanian & Sagar, 1999) to 375 Myr (Jacobson et al., 2002). Reddening measurements all conclude $E(B-V) = 0.24 \pm 0.01$ (PA07).

For NGC 1907 earlier distance measurements reported values up to 4750 pc (Collinder, 1931), but recent publications adopt values between 1300–1760 pc (see PA07 and references therein). This more compact cluster seems to be older than NGC 1912, with an age of 400 Myr, and also a bit more reddened at $E(B-V) = 0.38$ (PA07).

Disagreements among above distance and age estimates and uncertainties of the individual measurements do not rule out that these two clusters are not just closely projected on the sky but do form a physical pair. (A fly-by event does not even require the clusters being coeval.) Interaction of these clusters has been investigated recently by two groups (de Oliviera et al. (2002), OL02 hereafter, and PA07), with both finding no evidence of gravitational interaction. In this paper we present results of radial velocity measurements finding significant number of inter-cluster stars exhibit a RV value within a few km s^{-1} range of the mean cluster velocities. This might support existence of a tidal bridge.

10.1 Observations

10.1.1 Photometry

In order to prepare a target list for our spectroscopic survey we have carried out B and V photometry on 2005 March 07 at Fred Lawrence Whipple Observatory (FLWO) utilizing the 48 inch telescope and MiniCam CCD camera. The field of view of is $2 \times 10' \times 23'$ with a "dead band" between the two mosaiced sensors. Image scale was $0.6''$ per resolution element when binned 2×2. Exposure times of 30 and 300 seconds were applied for each filters. Stars with acceptable photometry (errors of $B - V$ less than $0\overset{\mathrm{m}}{.}03$) were in the range of 8–16 magnitude. We took exposures of 5 fields, each contained two pointings shifted by $2'$ in RA to cover the gap between the two CCDs. As a result, we have covered 2000 square arc minutes in the targeted region (Fig. 10.1). The standard field RU149 (Landolt 1992) was also observed at 4 different airmasses.

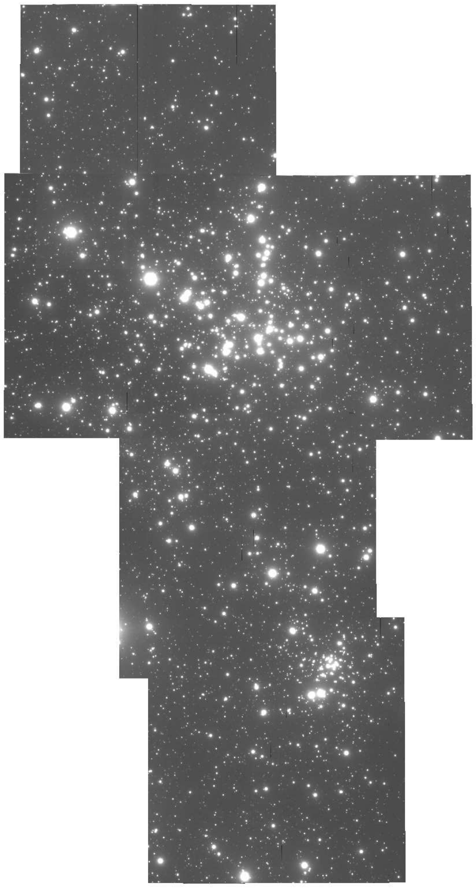

Figure 10.1: ***Our survey region of NGC 1907 and NGC 1912***, *a V band mosaic image obtained with the MiniCam detector on the 48 inch telescope of FLWO.*

A variability survey was also conducted using the Konkoly Observatory 60/90/180 Schmidt telescope. Details of these observations are given in Szabó et al. (2006). Here we would like just to note that only 7 eclipsing binaries (3 Algol, 4 WUMa types) were found among the time series of ~ 4000 stars. This suggests a low binary fraction so effect is likely negligible on the single-epoch RV observations.

Table 10.1. Summary of spectroscopic observations

Date	Field ID	field center		exposures	binning mode	number of targets
2004 Mar 27	A1	$5^h\ 28^m\ 20^s$	$35°\ 18'\ 30''$	3×5 min	1×1	81
2004 Mar 29	A2	$5^h\ 28^m\ 33^s$	$35°\ 48'\ 30''$	3×5 min	1×1	145
2004 Mar 23	B1	$5^h\ 28^m\ 25^s$	$35°\ 22'\ 20''$	3×20 min	1×1	190
2004 Mar 22	B2	$5^h\ 29^m\ 02^s$	$35°\ 53'\ 07''$	3×20 min	1×1	216
2005 Mar 22	C1	$5^h\ 28^m\ 23^s$	$35°\ 21'\ 42''$	3×10 min	1×1	167
2005 Mar 23	C2	$5^h\ 29^m\ 02^s$	$35°\ 52'\ 17''$	3×10 min	1×1	200
2006 Mar 17	CTRL	$5^h\ 28^m\ 52^s$	$35°\ 38'\ 36''$	3×20 min	2×2	174

10.1.2 Spectroscopic Observations

Spectroscopic observation were made with Hectochelle (Szentgyorgyi et al., 1998) deployed at the Cassegrain focus of the 6.5m MMT. Six fiber configurations were observed with magnitude ranges of V=8–12, 12–14, 14–16. Exposure times were 3×5 min, 3×10 min and 3×20 min, respectively. An average of 170 stars were observed in each fiber setting. We gave highest priority to stars in the supposed regions of tidal bridge and tails. Bright stars around cluster cores formed the next priority level together with out-of-cluster stars. Fainter possible cluster members got the lowest rank while trying to manage and even spatial coverage. We collected 999 stellar spectra in 3.5 hour total exposure time during the nights of March 22, 23 and 27, 2005 (see Table 10.1, with the $SNR \approx 10$ for the faintest spectra. The resolution of these spectra was 38,000 covering a wavelength range $5150 - 5300$ Å. We chose this spectral region because the numerous sharp Mg and Fe lines are favorable for RV determination.

As the wavelength calibration technique of Hectochelle was improved early 2006, a single-field (174 stars, 3×20 min exposure) control observation was carried out on Mar 17, 2006. We found consistency between the earlier and this control data. This assured we could use the latest data reduction techniques and tools of Hectochelle, based on most recent observations and calibrations.

The left panel of Fig. 10.2 and Fig. 10.3 shows the CMD of our photometric survey (standard magnitudes and colors displayed as dots), for the NGC 1912 and NGC 1907 regions, respectively. Stars with spectroscopic observations (circles, both filled and empty) are all brighter than $V = 16$.

10.2 Data Reduction

In §6.1 we have discussed the data reduction techniques in general. Here we discuss only the specific reduction steps applied to the observations of NGC 1912 and NGC 1907.

For the multi-template method we chose a grid of synthetic templates calculated by John Morse (personal comm., 2005) based on Kurucz model atmospheres (Kurucz 1979). In particular we ran grids of correlations ranging in effective temperature ($T_{eff} = 3750$ to 9000 K, 250 K steps), surface gravity ($log(g) = 1.0$ to 5.0, steps of 0.5) and rotational velocity ($vsin(i) = 0$, 4, 10, 25, 50 and 100 km s^{-1}), assuming solar metallicity. To filter out some of the non-members we found useful to compare the spectra to lower metallicity templates as well. Therefore we re-run the cross correlation against the best matching template by changing its [Fe/H] from 0.0 to -1.0 and -2.0.

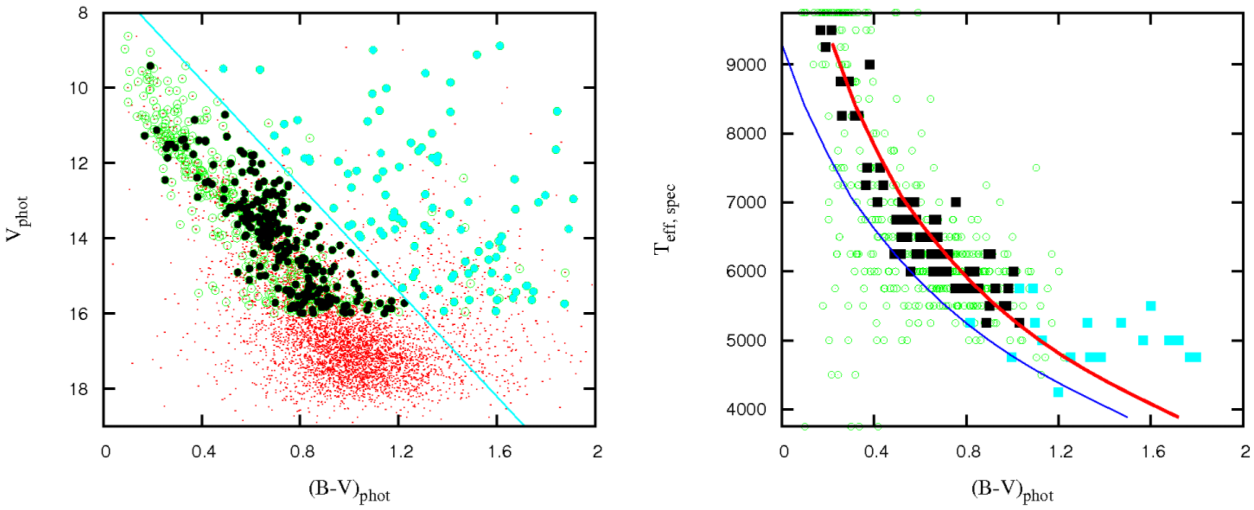

Figure 10.2: ***Color–magnitude and color–temperature plots of stars with declination higher than*** **35.5 deg** ***(NGC 1912 area, respectively).*** *The color-magnitude diagram (left) displays stars with photometry only as dots, while stars with spectroscopy as well are shown as circles. Open symbols represent stars with noisy/featureless spectra (for both panels left and right), while filled symbols denote objects with clean CCF peak (see text for details). The filling of symbols departed from the main sequence is lighter, as these objects are very likely field stars. This is confirmed on the right panel as these objects exhibit different reddening than the cluster members, and therefore fall off from the color (photometric) vs. temperature (spectroscopic) relation fitted on radial velocity members (filled squares) of the clusters. The nominal color-temperature relation (thin curve) and the fit to the members suggest an* $E(B-V)$ *value of 0.22, in good agreement with published reddening values. See text for details.*

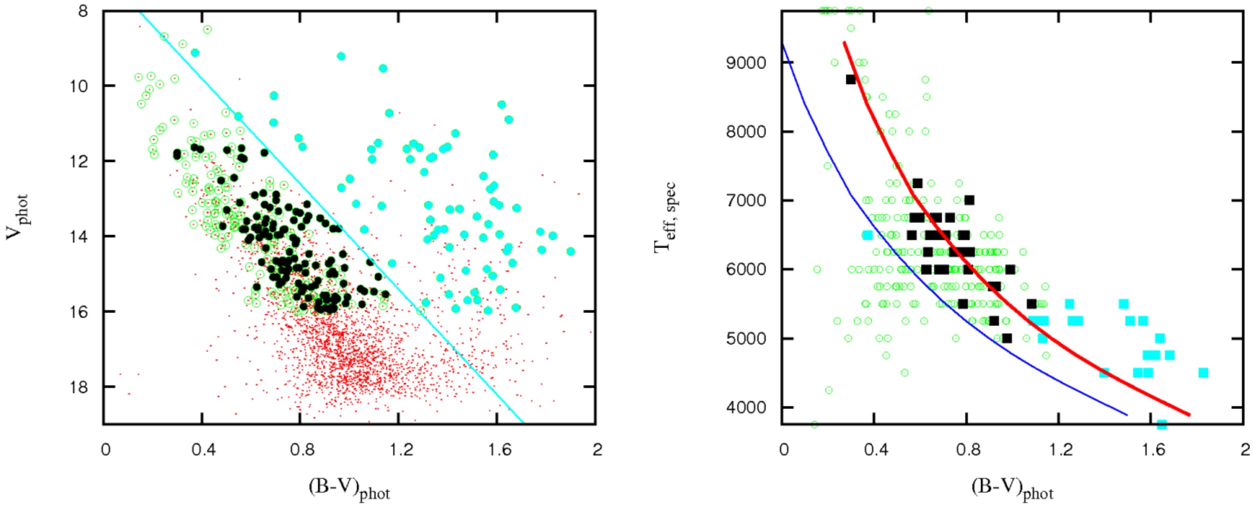

Figure 10.3: ***Color–magnitude and color–temperature plots of stars with declination less than*** **35.5 deg** ***(NGC 1907 area, respectively).*** *Symbols and color coding are same as for Fig. 10.2. The fit on the color–temperature plot suggests an* $E(B-V)$ *value of 0.31, a little higher than for the northern (NGC 1912) region but somewhat lower than reported in the literature. See text for details.*

If the CCF peak height was larger in one of these cases we adopted that new value as metallicity.

Based on 45 stars re-observed in 2006 (yielding an R value 35 or higher) we found a zero point offset of 1.2 km s^{-1} between the 2005 and 2006 velocities. RV values of 2006 were corrected for this difference (by subtracting the 1.2 km s^{-1} value) and brought to the 2005 zero point.

We plotted the CCF for the best matching template for each star, and examined the result by eye to make sure the global peak identified did not exhibit any sign of binarity (side-lobes or a secondary peak with comparable peak height). If a companion was found (or a high probability of a possible companion was suggested by the CCF), we marked the star as a binary (possible binary) and removed from the list of clean objects. In case of two RV measurements with a difference larger than 5σ (where σ is the estimated error by the IRAF *rvsao.xcsao* cross-correlation routine) a star was also marked as a binary an rejected from further analysis. Otherwise the two RV measurements were averaged.

Stars exhibiting broad lines or featureless spectra (as spectrum examined by eye, and as suggested by high $vsin(i)$ and T_{eff} values of template fitting) were also excluded form the clean list. An other rejection criteria was not to have the stellar velocity close to the heliocentric correction value. As we have not performed sky subtraction while calibrating the raw data the weak solar spectra of the sky background was left superimposed on the stellar spectra. Therefore to avoid any contamination, which was mostly obvious as a strong secondary peak or side lobe in the CCF at the heliocentric correction velocity, we simply removed these objects from the clean list.

After all we have arrived to a list of 563 stars on the "clean list" (Table 10.2) and 25 suspected binaries (Table 12.7).

The left panel of Fig. 10.2 and Fig. 10.3 displays the location of all stars with spectroscopic observations on the CMD as circles: open symbols represent stars dropped from the clean list (noisy/featureless spectra), while stars noted by filled circles exhibit a significant peak in their CCF when correlated against the best matching template. However, a fraction of these deviate from the main sequence and therefore more likely field stars than possible members (light-filled symbols to the upper-right of the cut-off line).

On the right panel of Fig. 10.2 and Fig. 10.3 we plot the photometric $B-V$ color index versus the spectroscopic temperature. (For the latter, we have displayed interpolated values, based on template parameters resulting CCP height almost as good as the best matching template.) Open symbols, just like on the left panel, represent stars dropped from the clean list. Filled symbols, however, represent only those stars with clean CCF which yield a RV value within ±8 km s^{-1} of the peak of the RV distribution, and so likely radial velocity members of the clusters. (The filling is lighter for those stars above the cut-off line on the left panel, e.g. the ones deviate from the main sequence.) The nominal $B-V$ color-temperature relation (from Sekiguchi & Fukugita (2000), plotted as thin solid curve) can be fitted to the cluster members (thick solid curve) by a horizontal shift due to reddening. Therefore we derived a E$B-V$ value of 0.22 for NGC 1912, in good agreement with the published reddening measurements. This confirms the results derived by the multi-template fitting analysis of our spectroscopic observations. (Note the big scatter of open circles, stars rejected from the clean list, versus the good correlation of filled symbols and fitted function.) For NGC 1907 the fit results $E(B-V) = 0.31$, which is somewhat lower than reported in the literature.

Table 10.2. Clean list — *sample*

2MASS	ID	V_{mag}	$(B-V)$	RV	RV_{err}	R	S	T_{eff}	$log(g)$	v$sin(i)$	$[Fe/H]$	CCF	NOB
0527050+354717	B2-ap214	14.55	0.82	6.01	0.39	23.8	0.77	6000	4.5	4	0	c	1
0527057+354401	C1-ap57	13.91	1.04	-8.46	0.20	58.7	0.91	5000	4.5	0	0	c	1
0527063+354343	B2-ap210	15.67	1.17	-10.90	0.81	26.1	0.71	5250	4.0	25	0	c	2
0527066+355811	C2-ap26	13.05	0.56	-1.53	2.49	19.6	0.70	7000	3.5	100	0	w	2
0527088+355046	C2-ap14	12.78	0.67	-56.80	0.51	51.5	0.92	6500	3.5	50	0	c	1
0527093+354557	B1-ap24	14.26	0.81	-7.98	1.15	27.4	0.74	5750	4.0	50	0	w	1
0527094+353922	C1-ap56	12.85	1.80	1.07	0.25	32.4	0.84	4750	2.5	4	0	c	1
0527104+354424	B2-ap209	15.41	1.75	-30.91	0.37	26.3	0.76	5500	3.5	10	0	c	1
0527107+355332	B2-ap222	15.16	0.94	-6.60	3.12	10.5	0.48	6000	4.0	50	0	w	1
0527109+354200	B2-ap204	15.61	0.84	-11.51	4.15	11.1	0.38	5000	3.0	100	0	u	2
0527110+354656	C2-ap8	12.83	1.31	-16.40	0.11	74.3	0.95	5000	3.5	0	0	c	1
0527113+354924	B2-ap219	15.69	0.87	-21.25	0.30	30.3	0.78	6000	4.5	4	0	c	1
0527118+355258	C2-ap13	13.75	1.89	-10.06	0.17	57.2	0.94	5000	2.0	10	0	c	1
0527120+354326	B2-ap208	14.78	0.76	-16.54	2.14	13.2	0.50	6500	4.0	50	0	w	1
0527120+355636	C2-ap22	13.95	1.62	47.60	0.12	61.2	0.94	4750	2.5	0	0	c	1
0527123+354628	B2-ap201	15.27	0.85	-27.03	0.28	30.0	0.79	6250	4.5	4	0	c	1
0527127+353932	C1-ap58	12.23	0.75	9.09	0.73	41.0	0.81	6000	3.5	50	0	w	1
0527139+355201	C2-ap19	13.85	0.68	-32.76	1.64	15.6	0.64	6250	1.0	50	-2	u	1
0527148+354821	C2-ap7	13.37	2.15	46.59	0.12	64.9	0.95	4250	1.5	4	0	c	1

Note. — *NOTE: this is a sample, for the full table see the Appendix 12.6* Photometric data and results of multi-template cross correlation for stars of the "clean list" – see text for details.

2MASS — 2MASS identification number (truncated RA and DEC coordinates as: HHMMSSS+DDMMSS); **ID** — internal identification number, specifying the field (see Table 10.1) and aperture number; **V** — standard V magnitude as measured; $(B-V)$ — standard color index, as measured; **RV** — radial velocity, in km s^{-1}; RV_{err} — error of RV as estimated by the IRAF rvsao.xcsao task, in km s^{-1}; **R** — R value of cross correlation using the best matching template; **S** — height of the cross correlation peak, using best matching template; T_{eff}**,** $log(g)$**,** **v**$sin(i)$**,** $[Fe/H]$ — parameters of the best matching synthetic template; **CCF** — notes on the cross-correlation function and match between actual spectra and template, based on visual inspection: *c* – the peak of CCF is > 0.7, outside of the global peak local noise peaks are at $< 30\%$ level, spectral lines of star and template overlap in 90%, the heliocentric correction velocity is outside of the global CCF peak (meaning that contamination of sky background can not lead to a velocity affected by the heliocentric correction; *r* – two RV measurement resulting the same parameters for best matching template, the peak of CCF is larger than 0.5 in both cases; *w* – wide spectral lines, likely rotational broadening, therefore CCF is also wide and RV determination has larger uncertainty, spectra and template are still overlapping in $\sim 75\%$; *u* – spectral lines are very wide, CCF peak is low ($\sim 0.3-0.4$) but still 50% higher than local peaks due to noise, spectra and template are similar but changing some of the template parameters do not affect the result of comparison; **NOB** — number of observations (if 2 the RV is the average of the two values);

10.3 Results

10.3.1 Distribution of early-type stars

In a magnitude limited sample (for stars brighter than $V = 16$) the average stellar color per unit area is bluer within the cluster when compared to the local galactic field, as the early-type brighter members with $B-V \approx 0.6$ (see Fig. 10.2 and 10.3) concentrate towards the clusters cores. Therefore the average $B-V$ color *roughly* correlates with the number of cluster stars over a certain area. In case of a tidal bridge, a color map of averaged $B-V$ values should show a blue-excess over the inter cluster area, as the galactic background would be diluted by the perturbed cluster members.

The left panel of Fig. 10.4 displays all the stars from our photometric survey as black dots (size is proportional to brightness), overplotted by a map of mean stellar color averaged over 0.1×0.1 degree bins (each bin contains at least 20 stars and more than a 100 at the cores). As discussed above, the cluster fields exhibit lower $B-V$ values. But the blue excess also extends into the inter-cluster region, suggesting the presence of young stars in between the clusters. A tail is also visible to the south/south–east of NGC 1907. Although these relatively small shifts in averaged stellar color are not enough to prove the interaction alone, if these are really linked to the velocity distribution that would provide a prominent argument for perturbation.

10.3.2 Velocity Distribution

However configuring the spectroscopic fields we were concentrating on the bridge area we tried to get an even coverage of the region. After rejecting spectra which did not yield high CCF peaks in the multi-template fitting (see Sec. 10.2, creating the "clean list") the coverage became somewhat biased towards the inter-cluster region (middle panel of Fig. 10.4), where the color map suggested a tidal bridge (Fig. 10.4, left panel). Therefore, in order to avoid misrepresenting the data, we feel important to emphasize that any statistics carried out for the inter-cluster area (noted B on the right panel of Fig. 10.4) has to be evaluated by comparing it to *local* statistics of the cluster fields A (=NGC 1907) and C (=NGC 1912), and to other galactic background fields outside of the cluster regions. We refer to these comparison galactic fields relative to the above cluster regions: *sA* is the area south of A, including everything within our survey field southward of the lower declination boundary of the NGC 1907 field; *eA* is eastward of A, including stars between the north–south boundaries of the NGC 1907 field but to the east of that; and similarly for *eC*, *wC* and *nC*.

First, we determined the cluster velocities by locating the peak of the velocity histogram for the cluster regions A and C. In order to have comparable number of objects per bin for both regions, we used a 1 km s^{-1} and 4 km s^{-1} bins to construct the RV histograms of C and A fields, respectively, as shown on the top and third (from top to bottom) panels of Fig. 10.5. Fitting a Gaussian function to the peaks we found the mean radial velocity of NGC 1912 to be 1.2 ± 0.5 km s^{-1}, and 3.5 ± 2.0 km s^{-1} for NGC 1907. These values are a few km s^{-1} off from the values used by OL02 (-1.0 ± 0.6 km s^{-1} and 0.1 ± 1.8 km s^{-1}), which were based on the WEBDA (Mermilliod, 1996) open cluster database as cited by the authors (see discussion in Sec. 10.4.) But we would like to point out one more time: we found a 1.2 km s^{-1} zero point offset between the observing runs of 2005 and 2006, and the 2006 values were corrected for it. This correction

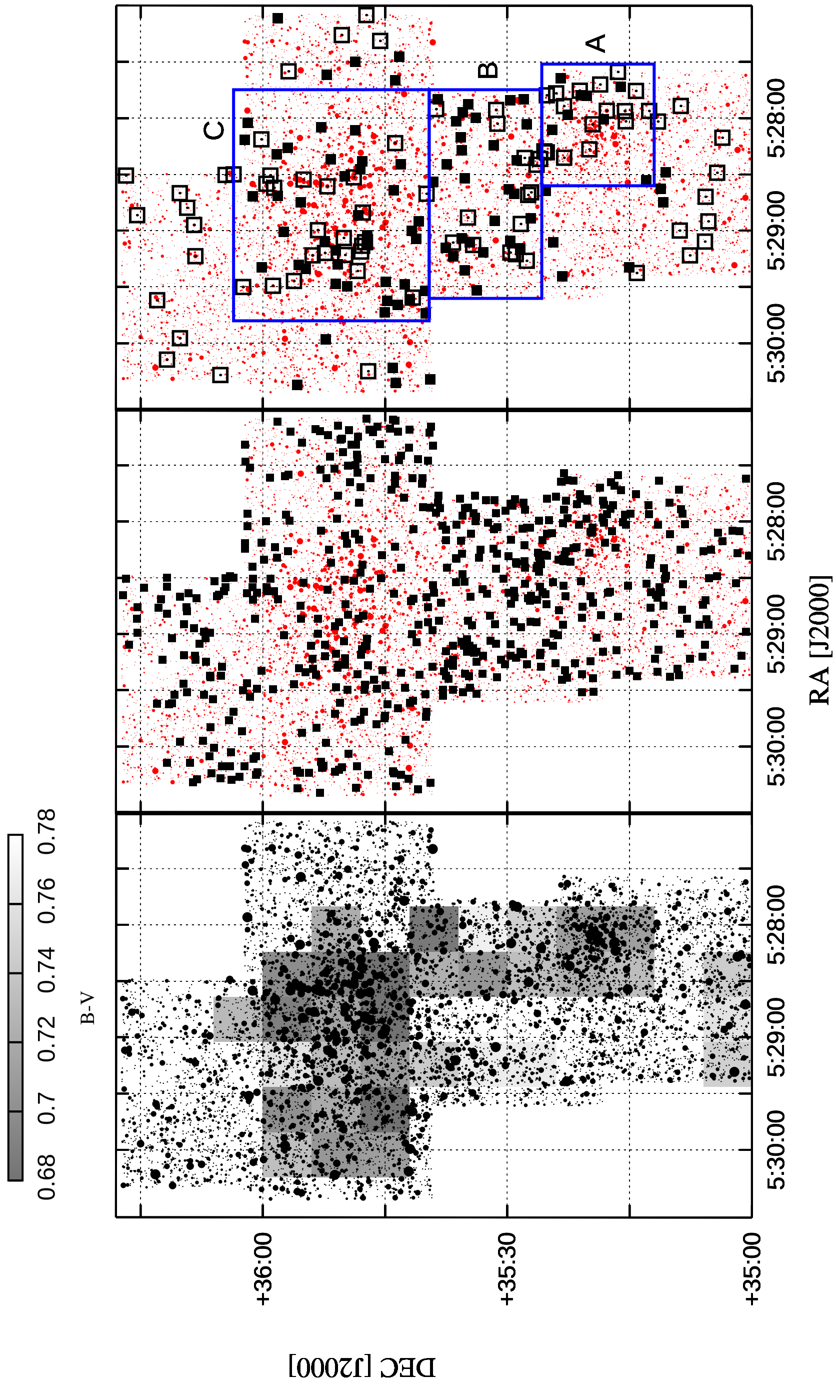
0.68
0.7
0.72
0.74
0.76
0.78
B-V
+36:00
+35:30
+35:00
DEC [J2000]
5:30:00
5:29:00
5:28:00
RA [J2000]
A
B
C

Figure 10.4: ***Maps of average stellar color, location of spectroscopic targets and RV members found in NGC 1907 and 1912.*** *The left panel displays the mean stellar colors ($B-V$ values averaged within 0.1×0.1 degree bins). Members of the clean list are displayed in the middle as black squares (plotted over the same stellar map as on the left, but now in red for clarity). Stars within ±8 km s^{-1} of the cluster velocities are shown on the right: two RV measurement – filled symbols,single RV determination – open symbols. A, B and C denotes the NGC 1907, inter-cluster and NGC 1912 regions, respectively. See text for details.*

is comparable to the difference between the OL02 and our velocities, and to the errors as well. Therefore not the absolute but the relative RV value is more meaningful, and actually that is the more relevant for dynamical modeling. And this velocity difference seems to be slightly larger than reported by OL02, however, within the errors.

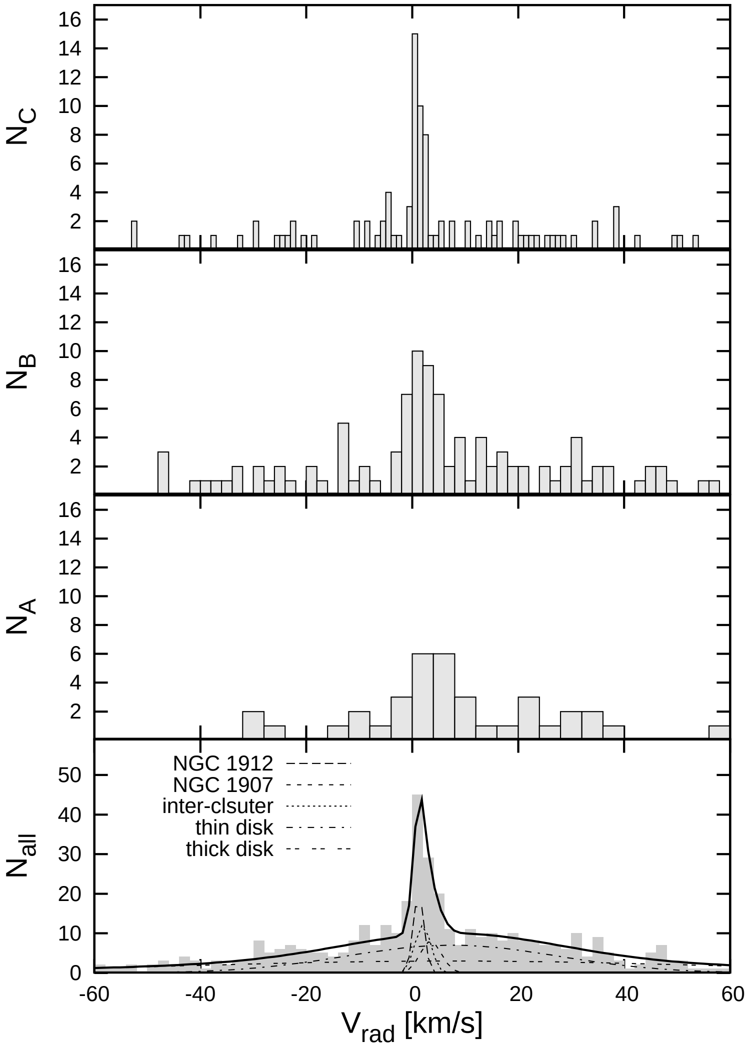

Figure 10.5: ***Radial velocity histograms for the NGC 1912, inter-cluster, NGC 1907 and for the entire survey region*** *, from top to bottom, respectively. In the upper three panels we adjusted the bin size to have comparable number of stars per bin, resulting in 1, 2 and 4 km* s^{-1} *wide bins. The bottom panel has a bin size equal to the typical error of our RV measurements, which is 2 km* s^{-1}*. The overall shape of the entire sample (bottom panel) can be interpreted as a sum of five components: Gaussian fits of the three upper panels plus a thin and thick disk component accounting for filed stars.*

The RV histogram of area C (NGC 1912) exhibits an asymmetric profile, with a side-lobe towards higher velocities. The mean RV of the other, smaller cluster is redshifted by a few km s^{-1}. The RV distribution of region B (Fig. 10.5, second panel from top to bottom) shows a well defined peak in between the two cluster velocities. (In this histogram we chose to bin by 2 km s^{-1}, in order to have similar number of stars per bin when compared to the histograms of A and C.)

Table 10.3. Number of cluster members within sub-regions

Sub-region	All spectra	Clean spectra		RV members	
		N	% of total	N	% of clean
C	231	124	54	59	48
B	213	132	62	42	32
A	115	64	56	41	36
nC	97	65	67	11	17
eC	63	33	52	5	15
wC	103	54	52	9	17
eA	68	37	54	5	14
sA	100	50	50	12	24

These RV histograms support our finding based on photometry: we do observe RV cluster members where the deviation of averaged stellar color suggested. A graphical comparison between the photometric and spectroscopic results can be done by displaying a map of stars which yield RV values within the peaks of the above described distributions. Such a map is displayed on the right panel of Fig. 10.4, and so can be easily compared to the color map and to the distribution of the spectroscopic sample. Square symbols represent the position of stars with RV values between -6 and $+10$ km s^{-1}, overplotted the same stellar field as the other two maps. Filled symbol means two velocity measurement ware made and therefore a more accurate, averaged value was determined. For stars observed only once we plot an open square. (Note, that even if a star had a clean spectra and RV between above limits, if its CMD location was redwards of the line indicated on the left panel of Fig. 10.2 and 10.3, we did not consider it as a RV member but rather as a field star.)

On the right-side map of Fig. 10.4 the inter-cluster region B has significant number of stars, with comparable density to the A and C cluster fields, within a ± 8 km s^{-1} wide RV chanel centered at 2 km s^{-1}. As a comparison the local galactic background regions at similar distance from the cluster cores have only a few stars in the same RV bin. (We sized the ± 8 km s^{-1} bin to be ± 4 times the typical error of our RV measurements, which is 2 km s^{-1}.) One might argue that the hint of a tidal tail southward of NGC 1907, as indicated on the left panel by the darker shading in the sA segment, is also apparent as a string of stars seen in the corresponding region of the right panel. However as mentioned above, to avoid any bias when comparing total numbers within regions while the sample was not completely uniform in spatial coverage and the regions differ in size, we have to make local statistics and compare the *relative* populations of RV members. This is given in Table 10.3, where for each segment we list: the total number of spectroscopically observed targets; the number of stars with clean spectra; the percentile of the clean sample respect to the total; the number of RV members falling within the above specified velocity chanel; and the percentile of these members respect to the number of stars with clean spectra of given region.

The last column of Table 10.3 proves that in fact the relative population of RV members is almost as high in the inter-cluster region than as it is around the cluster cores (32% vs. 36% and 48%). The result is significant when compared to the control regions of the galactic field: these all yield to $\sim 15\% \pm 2\%$ RV membership ratio, while sA field yields a slightly higher percentile of 24 but this might be due to the presence of a tidal tail, as pointed out earlier.

Looking at the entire sample of stars with clean spectra, including reddened field stars as indicated on Fig. 10.2 and 10.3, the overall velocity distribution (bottom panel of Fig. 10.5) can be fitted by 5 components: the two clusters (NGC 1912: long-dashed curve, $v_{rad} = 1.2$ km s^{-1}, $\sigma \approx 1$ km s^{-1}; NGC 1907: short-dashed curve, $v_{rad} = 3.5$ km s^{-1}, $\sigma \approx 2$ km s^{-1}); the inter-cluster region (dotted curve, $v_{rad} = 2$ km s^{-1}, $\sigma \approx 1.5$ km s^{-1}); the thin disk (dash-dotted curve, with $v_{rad} = 7.5$ km s^{-1} based on the Oort constants and $\sigma_U = 20$ km s^{-1} after Nordström et al. (2004)); and the thick disk (double-dashed curve, with $v_{rad} = 7.5$ km s^{-1} and $\sigma_U = 50$ km s^{-1} after Girard et al. (2006) for $z = 0$ kpc height above the galactic disk) component. The sum of these Gaussian components are also shown with a thick solid line, which reproduces the histogram of the entire observed sample (binned by 2 km s^{-1}).

10.4 Discussion and Summary

Since the possible interaction was suggested by Subramanian & Sagar (1999) only two papers have addressed the question of physical connection. The OL02 study carried out N-body simulations for a fly-by event and compared the numerical results to surface density maps of the region derived from the Digitized Sky Survey. They have concluded that there is no sign of tidal debris in the bridge region, and such material link would be expected only at significantly lower relative velocities. They claim that nearly the capture relative velocity is necessary to form a tidal bridge, which is 10 times slower that the parameters derived from observational data and used in their calculations. OL02 has also called for further deep, wide field CCD photometry for a more conclusive result about the apparent absence of the tidal link. This was carried out by PA07 and the authors confirmed the findings of OL02.

The results of our RV survey provide additional kinematic information which *does not* rule out the possibility of tidal interaction at all. The picture drawn both by the average color and RV maps (Fig. 10.4 left and right panels) reflect a kinematical structure more like Fig. 9. of OL02, a parabolic fly-by in a limiting case for a capture. That scenario was rejected by OL02 as mentioned above, but we do see some problems with the initial conditions of the OL02 simulations, which can be the reason behind the apparent contradiction between our RV data and their numerical results.

The RV values of the clusters used by OL02 were based on very few stars. We do not know what the WEBDA database had actually contained by the time OL02 has referenced it, but the *current* WEBDA page lists only $7 + 8$ RV measurements for the two clusters. Six of these stars have RV values highly deviant from the mean cluster velocities and so it is likely those six stars are not members. Even OL02 mentions in their discussion that their RV value for NGC 1912 was based on a single star, so they have added further RV measurements of three stars (Glushkova & Rastorguev, 1991) even those were not considered as proper motion members. As a comparison our determination of the cluster velocities is based on a distribution of several dozen stars, with 36 and 22 objects within the peak of the RV histogram of NGC 1912 and NGC 1907, respectively. This can explain why we found a slightly higher relative RV between the clusters, compared to the OL02 value.

Regarding the proper motions first of all we would like to emphasize that the two clusters are located very close in the sky and at very similar distances. Therefore proper motion values of stars in either cluster can be directly compared without the need of transforming those to the LSR. The

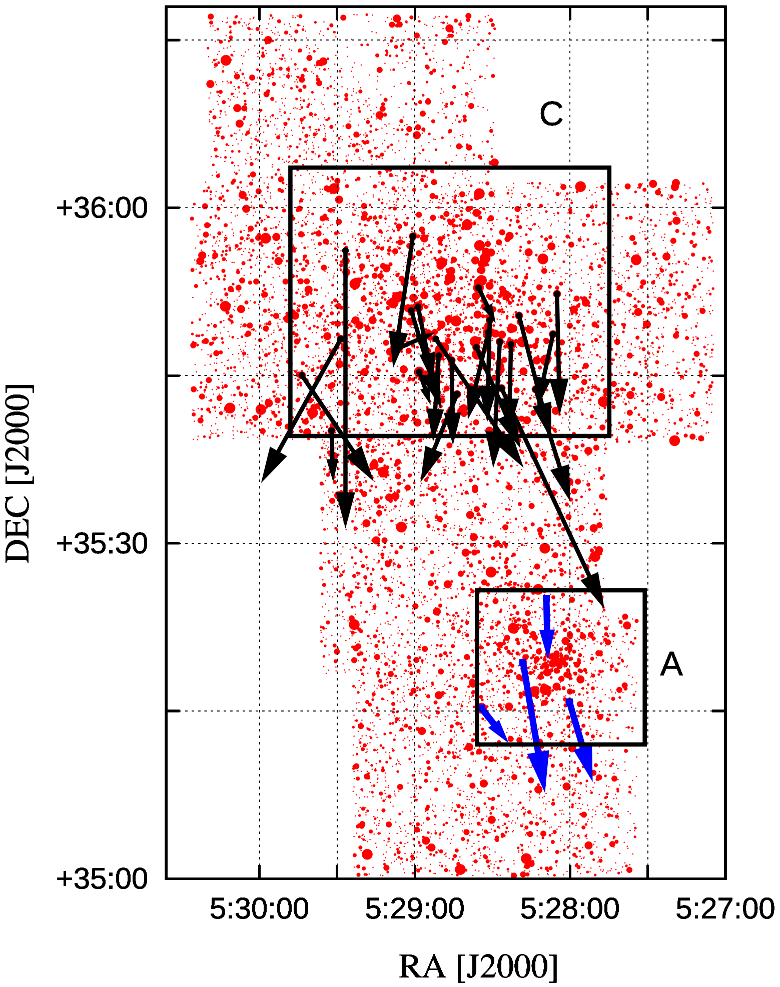

Figure 10.6: ***Proper motion of stars with RV measurements within the cluster regions***, *as clean list members (see text) matched against the Tycho-2 catalog. Proper motion vectors are scaled up by* $7.2 \cdot 10^4$ *times. (Figure includes both RV members and field stars.)*

proper motion values used by OL02 were $\mu_\alpha = 3.60 \pm 0.50$ mas/yr and $\mu_\delta = 1.90 \pm 0.50$ mas/yr (NGC 1912) and $\mu_\alpha = -0.81 \pm 0.73$ mas/yr and $\mu_\delta = -4.51 \pm 0.76$ mas/yr (NGC 1907). Matching our clean list with the Tycho2 catalog (Hog et al., 2000) and displaying the proper motion vectors (Fig. 10.6) we do not see the nearly opposite projected motion as suggested by the numerical values adopted by OL02. Although Fig. 10.6 includes RV members and field stars as well, Glushkova & Rastorguev (1991) points out that the centroids of proper motion distributions of the cluster and field stars are close in the region, which rules out a reliable distinction between cluster members and field stars. However, a recent study by Kharchenko et al. (2005) also confirms the picture of Fig. 10.6 by reporting proper motion values for NGC 1912 and NGC 1907 as $\mu_\alpha = 0.23 \pm 0.17$ and $\mu_\delta = -5.44 \pm 0.19$; $\mu_\alpha = 0.15 \pm 0.50$ and $\mu_\delta = -3.40 \pm 0.46$ (all in mas/yr). These are the values adopted currently on the WEBDA pages as well, which might be very different what the open cluster data base listed in 2002 when OL02 referenced it. Nevertheless, this is a significant deviation and would make a relevant change in the initial conditions of OL02: reduce the relative projected velocity of the clusters by 4 times and change the proper motion vectors from nearly opposite to parallel.

Regarding the age difference between the clusters, as reported by several authors, we do not see this as an argument against the interacting cluster pair scenario as the clusters could have been formed at different parts of the galaxy. The currently adopted distance estimates, within errors, do not rule out the equidistant nature of these clusters either.

The reason why the stellar density calculations of OL02 or PA07 did not find any evidence of a tidal bridge might be due to the very crowded galactic background and the evolved structure of the clusters. The radial variation of projected stellar density (Fig. 6. and 7. of PA07) is rather noisy, just like the derived mass function, as also admitted by the authors. The observed mass segregation suggests that outer members are less distinguishable from field stars.

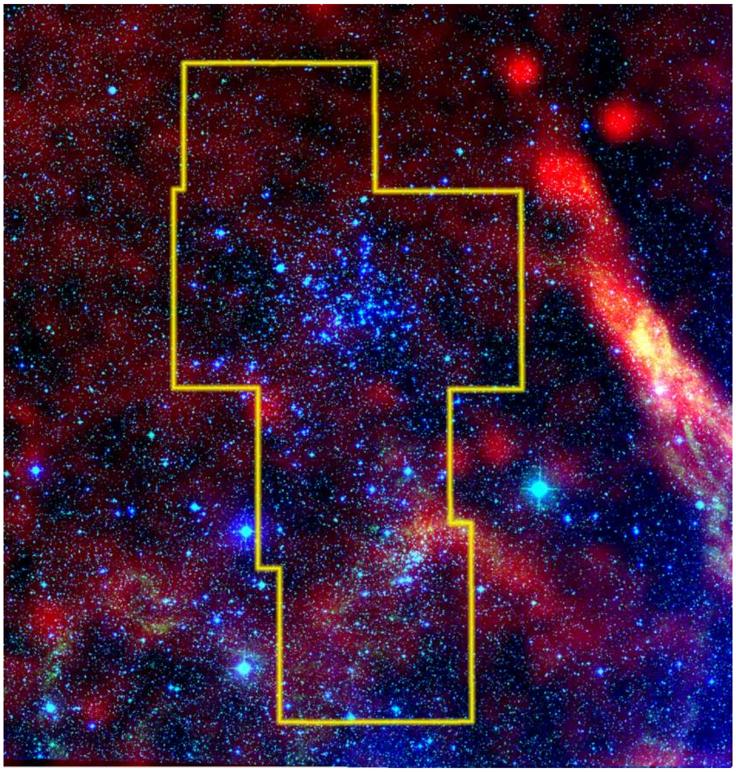

Figure 10.7: ***Radio continuum (6 cm) image of the cluster region, overlayed on a DSS stellar field*** *The Green Bank 6 cm Survey image, as a tracer of dust, is shown as a red overlay on top of a* 2×2 *degree stellar field of NGC 1907 and NGC 1912, represented in blue. The former cluster is more obscured, which is also apparent in the DSS red imagery as a nebulous (H*α *emission) region in front of NGC 1907 (see green channel on the title figure, at the beginning of this chapter). A yellow polygon represents the borders of our survey region, as seen in Fig. 10.4.*

To explain the different reddening of the two clusters, however, is more problematic. Our color-temperature fits (see Fig. 10.2 and 10.3) also confirm the higher $E(B-V)$ of NGC 1907, although we find a smaller value than indicated by others. (Note that in our fit we did divide the observed sample as a northern and southern part, the latter covering significantly larger region than the cluster itself.)

In case the clusters are at the same distance we probably observe the edge of some interstellar cloud happened to bee just in front of NGC 1907, but not affecting our sight towards NGC 1912.

As of molecular clouds, the survey of Kawamura et al. (1998) does not list objects close to the cluster locations. However, looking at the Digitized Sky Survey red chanel images (covering the Hα line) of the region some nebulosity is visible over NGC 1907 while the NGC 1912 area is free of contamination. This is clearly seen on Fig. **??**, a color composite of DSS images, with the red survey plate displayed in the green channel. (The red chanel is the infrared plate, while the blue plate is displayed in blue.) This nebulosity is also prominent in the 6 cm radio continuum images of the GB6 survey (Gregory et al., 1996). See Fig. 10.7 (and compare with Fig. **??**), which displays the stars in blue and the 6 cm radio image as a red overlay. To aid comparison with other maps of Fig. 10.4 a yellow polygon outlines the region of our survey. As an even better tracer of dust, the reprocessed 100 μm imagery of the IRAS survey (Miville-Deschênes and Lagache, 2005) also confirms the presence of dust to the west and south of the cluster regions: a cloud partially extending over the NGC 1907 region but clearing around NGC 1912. Fig. 10.8 This might explain the different reddening, without placing one of the clusters at larger distances.

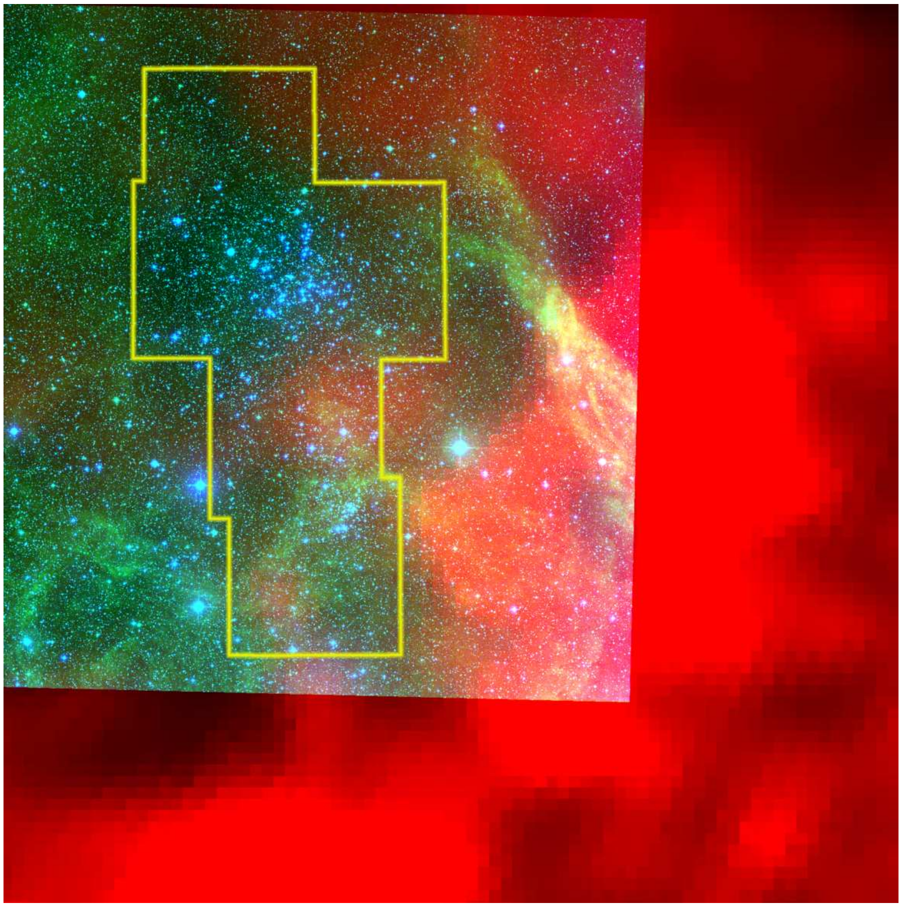

Figure 10.8: *Dust emission on the IRAS 100μm images of the cluster region*, *displayed in red over a 2-color composite image of the cluster region (DSS blue and red plates, colored as blue and green). While the stellar field is 2×2 degree (same as for Fig. 10.7) the IRAS image is displayed for 3×3 degree, in order to clearly show the massive dust emission to the West and South of the clusters. This partially extends over NGC 1907 and the inter-cluster region, while NGC 1912 stays mostly clear of dust. This could account for the different reddening of the two clusters. A yellow polygon represents the borders of our survey region, as seen in Fig. 10.4.*

If the clusters are not equidistant, that would lead to a simpler explanation of different reddening and suggest an other possible interpretation of our findings. One can see the dilution of young stars over the inter-cluster area as a result of a projection effect: we just observe the overlap of cluster halos.

However, we see several problems with this scenario. First, if the cluster outskirts are detectable by stellar density calculations, than such surveys should have found extensive halos and increased density over the inter-cluster region. PA07 reports no such finding. Based on Fig. 6 and 7 of PA07 the cluster radius is $18'$ for NGC 1912 and $7'$ for NGC 1907. With a separation of $33'$ it is hard to see how could the overlapping be accounted for such increase of young stars/RV members over area B of Fig. 10.4. Also, looking at the right panel of Fig. 10.4 one can notice: there is a nearly uniform distribution of RV members over area B, despite its East side is a lot farther form the center of NGC 1907 and therefore the overlapping effect should be less prominent. Also, the RV statistics South of region A (see sA percentile value in Table 10.3) and the diluted average color of the region (left panel of Fig. 10.4) can not be explained by overlapping halos.

Therefore we suggest that NGC 1912 and NGC 1907 could form a physical pair and a tidal bridge is visible both in $B-V$ color and radial velocity space, as well as there is a hint for a tidal tail southward of NGC 1907. Further RV observations and numerical simulations would be necessary to confirm or reject the interaction of these clusters.

The Rosette Nebula *– target of the current Hectochelle cluster study. Even such a simple digital photograph taken with a telephoto lens (G.F.) reveals the nebulosity and dark patches in front of the dense stellar background, implying the young age and likely exciting kinematical structure.*

Chapter 11

Continuation

In this chapter I briefly overview the already ongoing instrumentation and science projects, which are direct continuation of the work already completed and described in the thesis. I foresee to complete the below discussed tasks in the next 1–2 years.

11.1 Ongoing Instrumentation Projects

11.1.1 Atmospheric Dispersion Corrector for TRES

In §2.10 several modifications/improvements of the TRES instrument were proposed. One major issue which was already known while building TRES, but did not fit the original budget, is the design and construction of an ADC prism. While commissioning the spectrograph the ADC project got funded in late 2007. The expected delivery date of the prism is the end of summer, 2008. Here I describe the candidate optical design on which the requested budget estimate was based on. Although the system is exclusively designed for TRES and the pre-construction design might be slightly different (in order to make the ADC work for FAST as well, see §2.1.1), it still gives a basic insight and represents the expected performance boost.

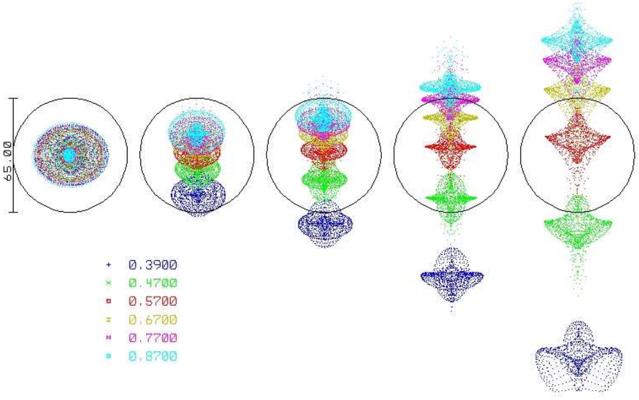

Figure 11.1: ***On-axis spot diagram of TRES*** *for 0°, 30°, 45°, 60° and 75° zenith distances (left to right) for the* $3700 - 9000$ *Å wavelength range. The circle represents the highest resolution fiber of TRES (62.5 μm= 1.″4 sky coverage)*

Figure 11.1 shows the on-axis image quality of the Tillinghast telescope with the existing TRES f/6 focal reducer at 0°, 30°, 45°, 60°and 75° degrees zenith distances. The circle represents the small fiber, which is 65 μm in diameter or $1''.4$. Different wavelengths are color coded between 3800 and 9100 Å, the TRES wavelength coverage. It is obvious that a significant loss occurs due to atmospheric dispersion. Since the guider is red sensitive, and the dispersion is larger in the blue, most of the loss is in the blue end. Integrating over the entire TRES passband the total amount of lost light is significant (20%) even at 40° zenith distance, as it can be seen on Fig. 11.2.

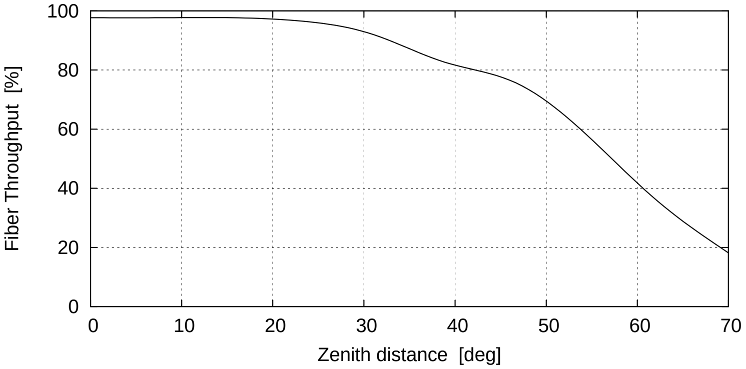

Figure 11.2: ***Light loss due to atmospheric dispersion***, *for the $1''.4$ TRES fiber, assuming no seeing losses.*

To keep the size of the prisms minimal (and lower the cost) we considered placing it just above the instrument mounting surface (rotator plate), inside a cylinder which is going through the hole in the primary mirror. There is a 7 inch diameter space available and to avoid vignetting we only need the prisms to have 3 inch clear aperture at this location, right above the rotator plate. The remaining $\sim$ 2 inch clearance is adequate to accommodated the prism mounting and rotating mechanisms.

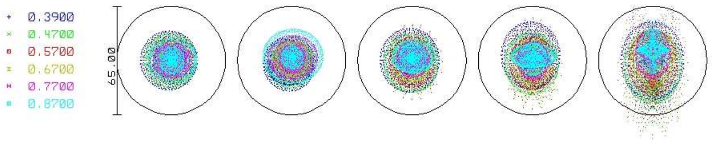

Figure 11.3: ***On-axis spot diagram of TRES with ADC*** *for 0°, 30°, 45°, 60° and 75° zenith distances (left to right) for the* $3700 - 9000$ *Å wavelength range. The circle represents the highest resolution fiber of TRES (62.5 μm= $1''.4$ sky coverage) Compare to Fig. 11.1*

A multi-configuration ZEMAX model was set up to simultaneously evaluate image quality at different field angles (from on-axis to $3'$) and telescope pointings (from zenith to 75° zenith distance). During the optimization we found that putting curvatures on the two inner surfaces of the prisms the image quality can be very good for all zenith angles and field locations. As this further reduces the effective focal length of the telescope we had to slightly modify the original f/6 focal reducer to keep the effective focal ratio at f/6 with the ADC. The prescription of the optimized prisms and re-designed corrector is summarized in Table 11.1, and the performance is shown in Figures 11.3 and 11.4. Image quality is even better than with the original f/6 reducer, as

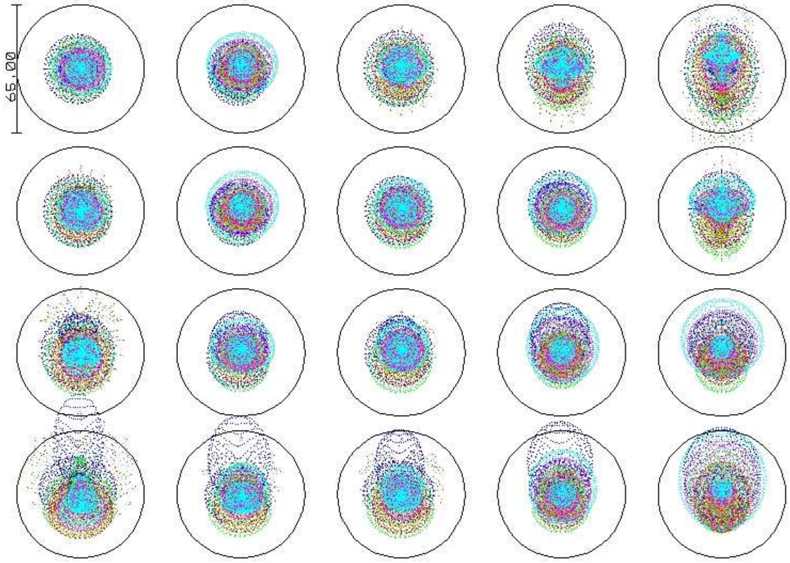

Figure 11.4: ***Polychromatic matrix spot diagram of TRES with ADC***, *for 0°, 30°, 45°, 60° and 75° zenith distances (left to right); and for field angles of $0'$, $1'$, $2'$ and $3'$ (top to bottom). The circle represents the small fiber of TRES (62.5 μm= $1''.4$ sky coverage)*

Table 11.1. ADC design for TRES

Surface	Radius [mm]	Thickness [mm]	Glass type	Diameter [mm]	Tangent of angle
from corrector to 1st prism	—	508.80	air	—	0
1st prism front	inf.	6.00	FSL5Y	80.00	0
Glass 1/2 interface	inf.	—	glued	80.00	0.0500
2nd prism	inf.	6.00	PBL6Y	80.00	0
2nd prism back	819.50	—	—	80.00	0
separation	—	3.00	air	—	0
3d prism front	439.72	6.00	FSL5Y	80.00	0
Glass 3/4 interface	inf.	—	glued	80.00	0.0514
4th prism	inf.	6.00	PBL6Y	80.00	0
4th prism back	inf.	—	—	80.00	0
to rotator plane	—	5.43	air	—	0
to tip-tilt mirror	—	69.85	air	—	0
tip-tilt mirror	inf.	—	—	30.0×42.4	1.0000
to focal reducer	—	229.4	air	—	0
focal reducer lens A	110.67	12.70	BSM51Y	42.0	0
focal reducer lens A	28.51	—	—	42.0	0
focal reducer lens B	28.51	16.11	FPL51Y	42.0	0
focal reducer lens B	-290.32	—	—	42.0	0
to focal plane	—	59.25	—	—	—

Note. — All radii are test-plate fitted to Coastal Optics plates. Note the small changes in the corrector (compare to Table 2.12), as the ADC partially does the focal reduction.

it can be seen by comparing the first column of Fig. 11.4 to Fig. 2.28. It is because the additional two curved prism surfaces allow better control of the aberrations.

As the field of view is $4'.5 \times 4'.5$ for the TRES guider, the $3'$ field position represents the very corner of the guider image. Also, the 75° zenith distance is a very extreme case for observations. Therefore the configurations represented in the last row and rightmost column of the spot matrix (Fig. 11.4) is unlikely to be a real situation, but even though the image quality is still very good.

As a conclusion we can say that with this preliminary ADC design for all zenith distances and field angles a geometrical spot diameter smaller than the smallest TRES fiber can be maintained.

11.1.2 Laser Comb for Hectochelle and TRES

One half of the 2005 Nobel prize in physics was shared between John L. Hall and Theodor W. Hänsch, for *"their contributions to the development of laser-based precision spectroscopy, including the optical frequency comb technique"*. Among the numerous applications optical combs will enable (new generation of more precise atomic clocks, ultrasensitive chemical detectors, boosting the sensitivity and range of lidars, providing a vast increase in the number of signals traveling through optical fiber, etc.) high precision astronomical spectroscopy is one field in which the first results of real applications are just around the corner. Thanks to the laser comb development at CfA (Li et al., 2008) Hectochelle and TRES will be among the very first spectrographs to be equipped with this new generation of wavelength calibrators.

To illuminate the benefits of such laser comb, Fig. 11.5 and 11.6 gives a comparison against conventional ThAr arc lamps. As it can be seen on Fig. 11.5 the intensity and density of ThAr lines are widely changing, not to mention that some spectral regions (especially in the red) are dominated by some extremely bright Ar lines while lacking Th features (see §1.6.2 for further discussion on ThAr lamp properties). In contrast, comb lines are evenly spaced, have high density and uniform intensity distribution, as it can be seen on Fig. 11.6(b). For a fair comparison a relatively dense ThAr region on the same scale is displayed on Fig. 11.6(a).

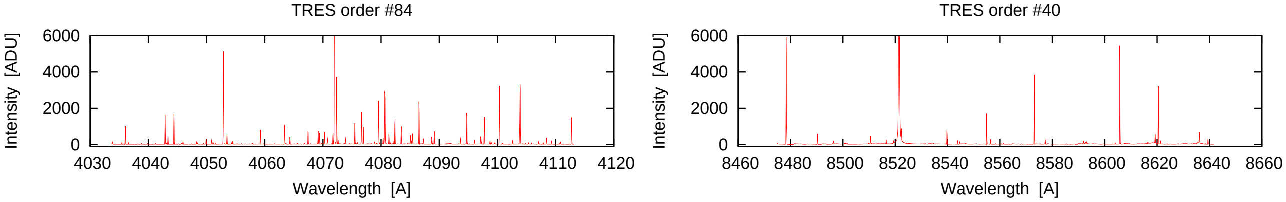

Figure 11.5: ***Comparison of ThAr line density in two TRES orders.***

The current laser comb at CfA spans a 1000 Å centered at 8700 Å (Li et al., 2008). As one order of Hectochelle only covers ∼ 180 Å the current comb can fill that easily, and observations in the Ca triplet region already can benefit from the new technique.

Although the last five orders of TRES fully covers the current comb bandwith, in some sense TRES will neither be able to take full advantage of the laser calibrator. The reason is that environmental stability (due to temperature and pressure variations) over the time scale of an average stellar exposure is 1–2 magnitude larger than the expected $0.01\mathrm{m\ s^{-1}}$ precision of the new technique. Still, the nearly 2000 bright comb lines would provide an extremely precise calibration

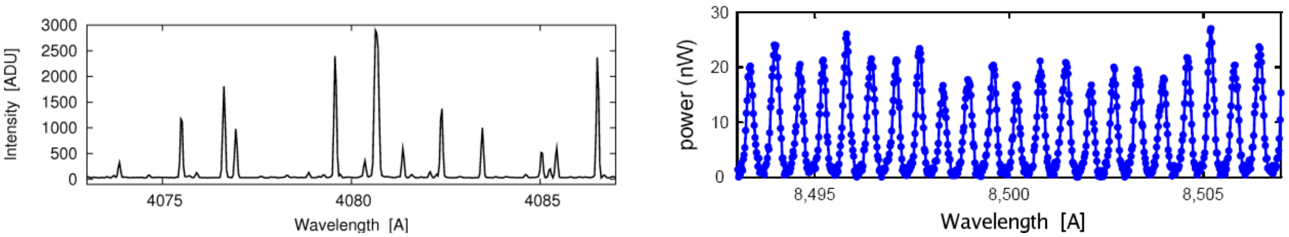

(a) A relatively dense ThAr region (b) Small portion of a comb spectrum (Li et al., 2008)

Figure 11.6: ***Comparison of a ThAr and a comb laser reference*** *The line width of the individual filtered comb lines (0.2 Å) is set by the resolution of a commercial optical spectrum analyzer used in the lab testing.*

and enable to deliver 1 m s^{-1} precision. The issue of the calibration fiber not tracking exactly the object fiber (see Fig. 2.87) can be avoided by injecting the comb spectra into the object fiber. It can be done simultaneously, while recording the stellar spectra, by inserting a dichroic on the periscope stage. Such dichroic should pass through starlight below 8100 Åand reflect above 8200 Å. Therefore the last five orders will record a pure comb spectra, and this would mean only a very small loss of the stellar spectrum and radial velocity information. The reason is that 3 out of that 5 orders are filled with telluric lines anyway (see Fig. 12.1). Moreover, it also can be seen form the TRES spectral sample (and suggested by Fig. 2.1), that there are only a few stellar lines providing usable RV information.

There is a huge effort put into astronomical laser comb development, in order to expand the bandwith and cover the blue spectral regions as well. These goals are likely to be fulfilled in the next couple of years, and bring the 0.01 m s^{-1} precision to ultra-stable spectrographs like HARPS-NEF (see §2.1.1), necessary do discover Earth-like exoplanets. TRES might play a role in the development and testing of such next generation laser combs.

11.1.3 Near-Infrared Spectroscopy – MMIRS

MMIRS is a JHK imager and multislit spectrograph based on a 2048 × 2048 pixel Hawaii–2 detector that will be used at the f/5 Cassegrain focus of the MMT and Magellan-2 telescopes. MMIRS will allow imaging of a $7' \times 7'$field with $0\farcs2$ sampling, as well as spectroscopy for 30–70 objects with slitlets placed over a $4' \times 7'$field. A spectral resolution of $\sim$ 3000 is achieved with coverage of the complete J, H or K bands.

MMIRS can address topical problems in star formation, the physics of supernovae, the growth of black holes, and the formation and evolution of galaxies. In connection with the science cases discussed in this thesis below are listed some applications of MMIRS:

- Do high-mass stars preferentially form at the centers of clusters (e.g., Hillenbrand & Hartmann (1998); Testi et al. (1999)), or do they simply sink to cluster centers as dynamical mass segregation proceeds (Kroupa, 2002)?
- Do brown dwarfs form in isolation, or are they formed in circumstellar disks around other stars and then dynamically ejected (Reipurth & Clarke (2001); Bate et al. (2002))?
- Are planetary-mass objects also ejected from multiple stellar systems (Zapatero-Osorio et al. (2000); Hillenbrand & Carpenter (2000))?

- Do proto-stars accret most of their mass in short bursts from circumstellar disks (Hartmann & Kenyon, 1996)?

Testing these and other theories require the study of stellar populations at very early ages. Observations must be made at infrared wavelengths to penetrate the dusty environments of young star-forming regions; spectroscopic capability is essential to identify spectral types and thus stellar masses. Multi-object capability is vital to obtaining large enough samples to make statistically significant tests of the IMF, and large telescopes are required to observe the lowest-mass systems. Thus, MMIRS will be well suited for the task.

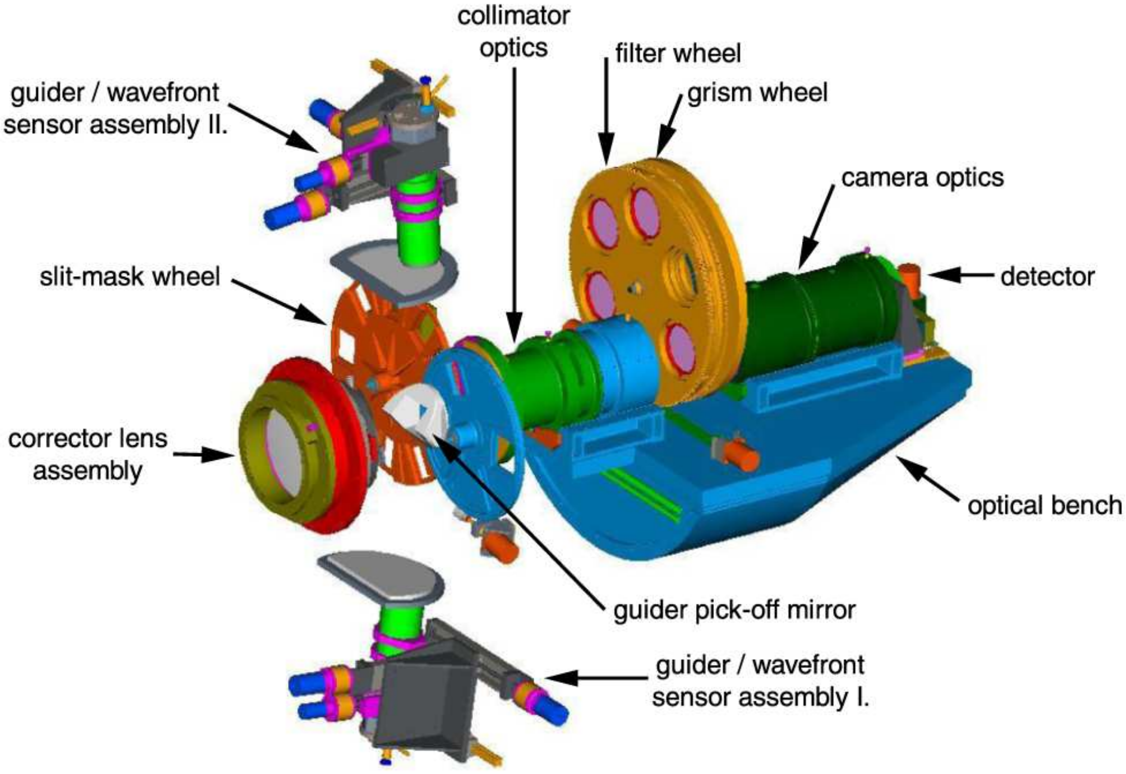
collimator optics
filter wheel
grism wheel
guider / wavefront sensor assembly II.
camera optics
detector
slit-mask wheel
corrector lens assembly
optical bench
guider pick-off mirror
guider / wavefront sensor assembly I.

Figure 11.7: ***Main components of the MMT and Magellan Infrared Spectrograph (MMIRS).*** *The vacuum enclosure and several small components/assemblies are not shown for clarity.*

MMIRS is constructed in two main sections (see Fig. 11.7). The first section contains the coma corrector lenses, the slit mask and aperture selection wheels, the guider assembly, and a gate valve which can be closed to separate the first section from the second. (The coma corrector replaces the large fused silica corrector (§3.1.1) used at optical wavelengths. The lead corrector lens also serves as the dewar window.) The slit mask and aperture selection wheels will be cooled to LN2 temperature by an independent dewar, but the rest of the first section will be operated at ambient temperature. To exchange slit masks, the gate valve between the two sections will be closed and the slit mask and aperture selection wheels will be warmed up. The exchange cycle can be accomplished during the daytime to prepare for nighttime observing. The second section of MMIRS contains the collimator optics, the grism and filter wheels, the camera optics, and the Hawaii-2 array. These will all be operated at LN2 temperature to minimize the thermal background. The estimated first light of the instrument is late 2008 / early 2009.

My involvement in this project:

- to oversee the guider and wavefront design, construction and assembly
- to design and implement a calibration system, used for both imaging and spectroscopic mode
- to design internal baffles of the optical system to avoid stray and scattered light reaching the detector
- take part in the assembly, testing and commissioning; and in the development of data reduction pipeline

11.2 Further Work with Clusters using Hectochelle

11.2.1 ONC Follow Up — Mg and Li Lines

Collecting more RV data on the ONC sample (see Chapter 9) is beneficial in several sense. As mentioned before multi-epoch observations are mandatory to remove all binary stars from the kinematical sample. The question of the possible foreground population and the nature of possibly 10 Myr old members (Palla et al., 2005) call for multi-object observations including the 6708 Å Li line. Such data, providing an independent age estimate, can serve to unveil the origin of these components.

Therefore we proposed and already collected a large spectroscopic data set in ONC, summarized in Table 11.2. In the RV31 band of Hectochelle (150 Å wide band centered at 5225 Å) we expect to have better RV performance than previously in the Hα order. Although the program stars are fainter but the larger number of Mg and Fe lines and the avoidance the nearly saturating stellar/nebular Hα line would give us better RV measurements. Using the RV31 filter also gives us the possibility to utilize the recently updated synthetic library of Dave Latham and his group (see §**??**). The nearly one million template spectra has been calculated to match the resolution and spectral coverage of Hectochelle. The Mg lines are better indicators of surface gravity than the mostly temperature sensitive Ca and Fe lines somewhat bluewards of Hα, used in the previous classification. Therefore we expect to improve the effective temperature, specific gravity and rotational velocities estimates.

An other obvious continuation of the project is to extend the spectroscopic survey towards the south, to the L1641 region. With the IRAC photometry in hand we already have prepared and carried out observations, and proposed for more to complete this work. This is a part of the CfA All-Orion Survey, lead by *Lori Allen*.

11.2.2 NGC 2244 – The Rosette Nebula

In contrast to NGC 2264 (Chapter 8) and ONC (Chapter 9) the cluster and star forming region of NGC 2244 seems to be a different environment. The Rosette Molecular Cloud (RMC) in the optical band looks like a ring: he hot, young OB stars of NGC 2244 seem to have cleared out the innermost regions, and this swept-up layer of the HII region exhibits a variety of manifestations of forming clusters of medium to high mass (Li & Smith, 2005a and 2005b). Star formation seems to be still going on not just within the very close vicinity of NGC 2244, as well as farther into the molecular cloud. Class I and Class II sources (Balog et al, 2005) traces well these processes (see Fig. 11.8).

Table 11.2. Summary of further spectroscopic observations in the ONC region

Date	ID	field center		exposures	binning mode	filter	number of targets
2006 Oct 03	Fld-1	$5^h\ 35^m\ 16^s$	$-\ 04°\ 49'\ 27''$	3 × 15 min	RV31	2 × 3	197
2006 Oct 03	Fld-2	$5^h\ 35^m\ 10^s$	$-\ 05°\ 23'\ 02''$	3 × 15 min	RV31	2 × 3	202
2006 Oct 04	Fld-5	$5^h\ 35^m\ 36^s$	$-\ 06°\ 10'\ 12''$	3 × 12 min	RV31	2 × 2	163
2006 Oct 13	Fld-3	$5^h\ 35^m\ 07^s$	$-\ 05°\ 25'\ 37''$	3 × 15 min	RV31	2 × 2	209
2006 Oct 13	Fld-4	$5^h\ 35^m\ 24^s$	$-\ 05°\ 21'\ 16''$	3 × 15 min	RV31	2 × 2	201
2006 Nov 08	Fld-4	$5^h\ 35^m\ 24^s$	$-\ 05°\ 21'\ 16''$	3 × 20 min	OB24	2 × 2	201
2006 Nov 08	Fld-5	$5^h\ 35^m\ 36^s$	$-\ 06°\ 10'\ 12''$	3 × 20 min	OB24	2 × 2	163
2006 Nov 09	Fld-1	$5^h\ 35^m\ 16^s$	$-\ 04°\ 49'\ 27''$	3 × 20 min	OB24	2 × 3	196
2006 Nov 09	Fld-2	$5^h\ 35^m\ 10^s$	$-\ 05°\ 23'\ 02''$	3 × 20 min	OB24	2 × 3	207
2006 Nov 09	Fld-3	$5^h\ 35^m\ 07^s$	$-\ 05°\ 25'\ 37''$	3 × 20 min	OB24	2 × 2	209
2007 Mar 10	Fld-1	$5^h\ 35^m\ 16^s$	$-\ 04°\ 49'\ 27''$	3 × 20 min	RV31	2 × 2	196
2007 Mar 10	Fld-2	$5^h\ 35^m\ 10^s$	$-\ 05°\ 23'\ 02''$	3 × 20 min	RV31	2 × 2	192

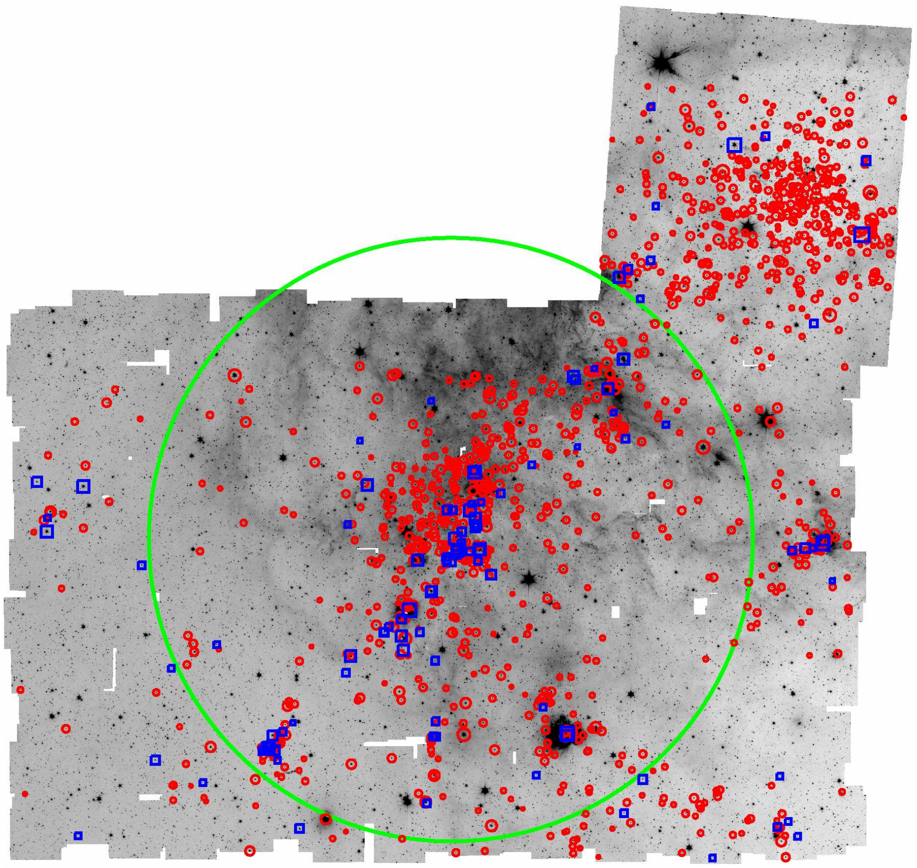

Figure 11.8: ***Class I and II sources in the NGC 2244 region***, *marked by blue squares and red circles, respectively. The selection is based on Spitzer/IRAC infrared photometry (Balog et al, 2005). The green circle represents the 1° FOV of Hectochelle*

Li & Smith (2005b) found that these embedded clusters appear to form in a structured manner, with new-generation OB clusters being at the root of a tree-like pattern. They claim this is a result of star formation following tracks laid out by the decay of macroturbulence within RMC. However, without insight into the third dimension, by means of obtaining radial velocities, the real kinematics of RMC can not be explained. The molecular cloud still can be a filament with its axis pointing near parallel to the line of sight, and the observed clumps could form along its axis with the largest group (NGC 2244) at the tip, according to the Burkert & Hartmann theory (Burkert & Hartmann, 2004). The self-gravitational collapse of finite gas sheets also suggest that within a filamentary structure the end clump would pile up material first and become the most massive one Therefore star formation would naturally start there first. This is in agreement with the fact NGC 2244 seems to be the oldest group in the region. The older nature of this massive cluster is suggested by the gas-empty region cleared by the OB stars and the very few number of Class I sources compared to number of Class II objects, unlike within the other groups (see Fig. 11.8).

Detailed RV measurement could give us more information about the complex structure of RMC. Does those tree-like patterns exist in the RV space as well, and really are a result of macroturbulence? Or do we see just a projection effect along a filament which is pointing to us? RV measurements of these young stellar groups could answer these questions. To date only very few stars have reported RV values for stars (Liu et al (1989), 7 stars; Liu et al. (1991), 11 stars), however the large dispersion of these values, as well as large variations in RV of the gaseous component (Fountain et al., 1979) suggest an interesting RV structure.

We know that a nearby O star can have serious influence on the early stages of forming, individual stars, like evaporating their disks as seen in NGC 2244, and in NGC 2264 as well (Balog et al., 2006). Using high resolution spectroscopy we could also see how an early emerged OB association could effect star forming in the rest of its molecular cloud. Hα profiles can give us insight into accretion, other lines to rotational velocities, and these can be combined with disk indicators of near-infrared photometry. The result can be compared to less "violent" regions in order to see if such group of OB stars as NGC 2244 could, and how, effect star formation on a larger scale.

Driven by the above outlined science we have collected $\sim$ 1700 spectra in the NGC 2244 region. Targets were selected from several sources:

- IRAC photometry of Balog et al. (2006), ranked highest
- x-ray sources from Chandra observations (Junfeng Wang, personal communication), rank 2
- x-ray sources from ROSAT (Berghöfer & Christian, 2002), rank 2
- optical photometry from Park & Sung (2002), rank 3
- 2MASS excess sources with a selection of $J < 15.5$ and $(H - K) > 0.7$, rank 3
- 2MASS non-excess sources with a selection of $J < 15.5$, $0.4 < (H - K) < 0.4$, rank 4
- 2mass sources with a selection criteria of $12 < J < 13$, $0.05 < (H - K) < 0.15$, rank 5 (to serve as a "velocity frame" and to fill up the fibers which can not be assigned to more important targets)

The summary of observations is given in Table 11.3. The location of the targets observed are shown on Fig. 11.9.

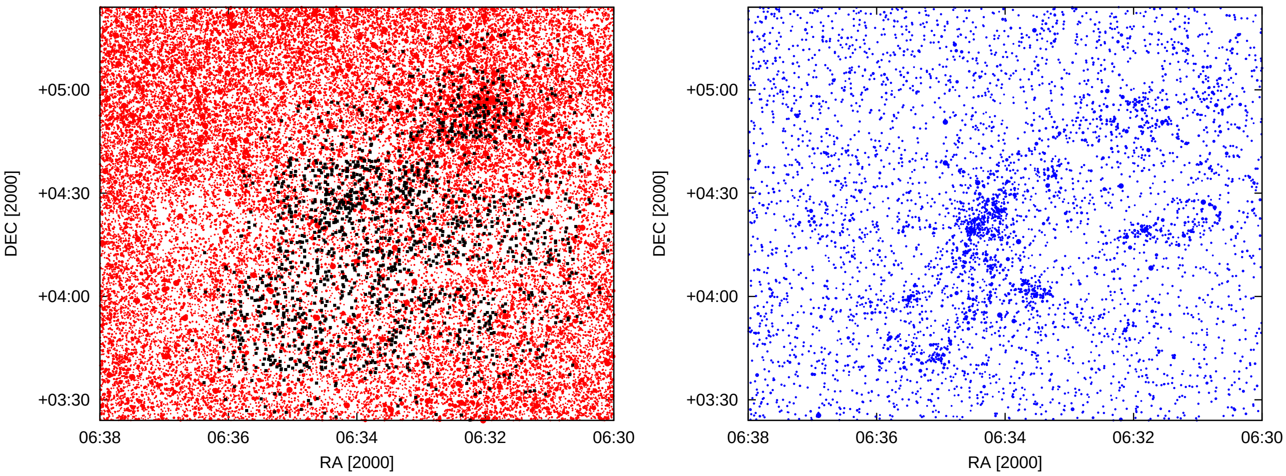

Figure 11.9: ***Location of observed targets in the NGC 2244 region*** *(left panel, black symbols) overplotted 2MASS sources with* $J < 16$ *and* $(H - K) > 0.5$. *These non-excess sources (red) clearly draw the cluster (at 06:32; +05:00). The "empty" areas of increased extinction, location of young stellar associations still embedded in dust, are displayed as dense cores if the excess sources are plotted (right panel,* $(H - K) > 0.7$*). The observed targets of Table 11.3 are displayed as black squares on the left panel.*

Table 11.3. Summary of spectroscopic observations in the NGC 2244 region

Date	ID	field center		exposures	binning mode	filter	number of targets
2007 Feb 25	RMC-1	$6^h\ 34^m\ 03^s$	$+04°\ 29'\ 43''$	3 × 45 min	OB26	2 × 2	197
2007 Feb 26	RMC-4	$6^h\ 34^m\ 54^s$	$+03°\ 53'\ 21''$	3 × 45 min	OB26	2 × 2	205
2007 Mar 01	ROS-2	$6^h\ 33^m\ 55^s$	$+04°\ 27'\ 31''$	3 × 45 min	OB26	2 × 2	218
2007 Mar 02	ROS-6	$6^h\ 32^m\ 07^s$	$+04°\ 53'\ 02''$	3 × 45 min	OB26	2 × 2	220
2007 Mar 04	ROS-4	$6^h\ 34^m\ 54^s$	$+03°\ 53'\ 21''$	3 × 45 min	OB26	2 × 2	220
2007 Mar 07	ROS-3	$6^h\ 32^m\ 15^s$	$+03°\ 52'\ 16''$	3 × 45 min	OB26	2 × 2	219
2007 Mar 09	ROS-5	$6^h\ 31^m\ 36^s$	$+04°\ 19'\ 22''$	3 × 45 min	OB26	2 × 2	219
2007 Mar 09	ROS-1	$6^h\ 34^m\ 03^s$	$+04°\ 29'\ 43''$	3 × 20 min	OB26	2 × 2	219

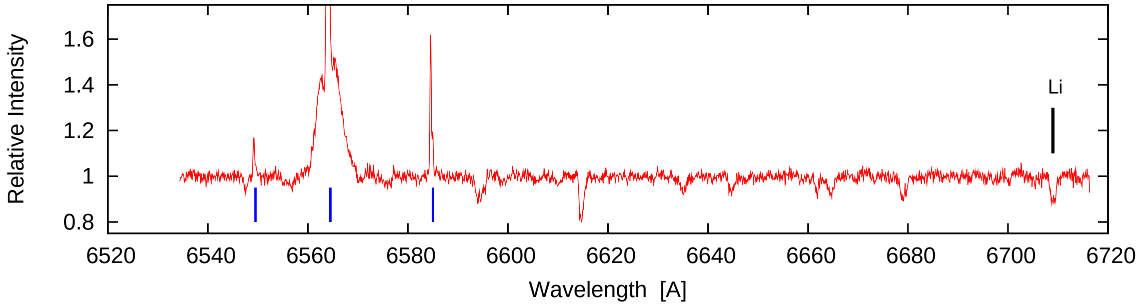

Figure 11.10: ***A sample spectra from the NGC 2244 observations*** *clearly shows the 6708 Å Li line at the rend end of the order, while the broad stellar emission at Hα is also prominent. The narrow emission features (marked with blue dashes) are nebular lines (the Hα component runs out of range).*

The selected echelle band covers the Hα and the 6708 Å Li lines simultaneously, at the blue and red end of the so-called OB24 Hectochelle order (see Fig. 11.10). However, there are only limited number of lines in between which can be used to derive RV. Therefore we expect somewhat coarser RV resolution and less accurate template fitting. Also, the larger distance results fainter targets and smaller S/N ratio than we had in the NGC 2264 and ONC samples (the increased 3×45 min integration time only can partially compensate for it). Nevertheless, as a sample spectra of Fig. 11.10 shows we have several hundred of spectra with very clean features.

11.3 Future TRES applications

11.3.1 Exoplanet Candidate Follow Ups

The number of extrasolar planets discovered to transit their relatively bright and nearby stellar hosts is steadily increasing. However, only limited long-term RV monitoring of any known transiting system has been performed thus far. This is mostly the result of the pressure on observing facilities to monitor new candidate systems, combined with the limited availability of observing time for these purposes on large-aperture telescopes.

This situation is unfortunate, because there are important scientific reasons to continue RV monitoring of known transiting systems. Increasing the time baseline of the RV observations would in fact allow to probe the existence of additional, long-period components. Interestingly, the frequency of close-in giant planets ($P < 10$ days) with additional massive planets on outer orbits (up to the detection limit of today's Doppler surveys, $\sim$AU, see for example Butler et al. (2006) and references therein) is about 12% (8 out of 70 systems discovered via RV methods). If additional planets in transiting systems are detected, they could also be found transiting. Such long-period companions could be used to test the (so far unchallenged) predictions of structural models of wide-separation giant planets (Burrows et al., 2004). In transiting systems with known outer components, predictions from transit timing variation measurements could be tested (Holman & Murray, 2005). Finally, outer components may contribute to pump the eccentricity (and inflate the radius) of a known transiting planet, thus their detection could help constrain models of tidal heating via eccentricity excitation (Bodenheimer et al., 2001).

Sozzetti et al. (2008) reported that in case of TrES-3, which has the shortest period of known nearby transiting systems (1.3 days), the best orbital fit yields residuals significantly larger than the nominal internal errors of Keck/HIRES measurements (see Fig. 11.11). One possible explanation of the > 30 m s^{-1} RV jitter is chromospheric activity, but the typical values expected for a star with activity levels, rotation and spectral type of the TrES-3 host star is in a range of 5 to 20 m s^{-1}. Another explanation would be an additional component in the system, which is consistent with the slow linear shift observed in the RV data. But to verify this further measurements are needed.

Instead of using expensive Keck time a team led by Alex Sozzetti has proposed the RV follow-up of TrES-3 using TRES. The target star is a relatively bright (V=12.4) G dwarf, and the current ~ 10 m s^{-1} precision of TRES is adequate for the monitoring. Similar follow-up work of other transiting systems, as well as initial reconnaissance observations, will be likely one of the main uses of TRES.

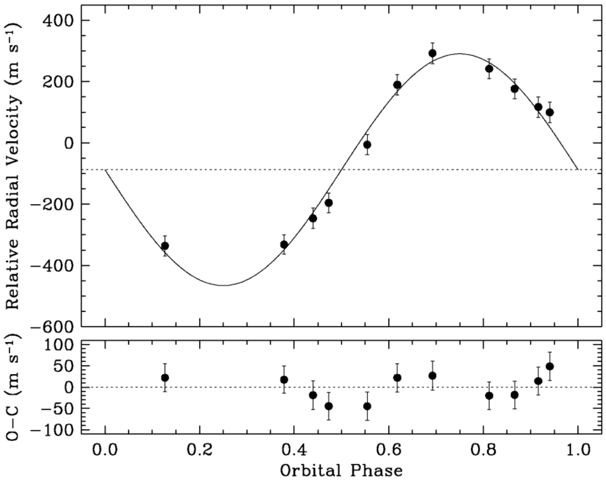

Figure 11.11: ***Phased RV curve of exoplanet TrES-3*** *(Sozzetti et al., 2008), obtained with Keck/HIRES with the best fit orbit (top), and the difference between observations and model (bottom). The variation in the residuals suggest the presence of further object in the system, with an amplitude well suited for TRES.*

11.3.2 RV Survey of M Dwarfs

The size of the observed signal in exoplanet transits is larger for a given planetary mass when the primary is smaller. This means that current techniques applied to small stars may allow us to detect terrestrial planets today. A pilot study by Blake et al. (2008) demonstrated that by observing brown dwarfs in the NIR it becomes possible to detect transits by companions as small as $2 - 3$ M$_{\oplus}$. The exciting MEarth project (Nutzman & Charbonneau, 2007) will observe a sample of 2000 nearby M dwarfs in an attempt to detect transiting super-Earths potentially in the habitable zone of their hosts.

Current radial velocity searches also include some M dwarfs, but not many and no objects later than M4. However, stars with spectral type of M4 to M8 are in general found to be slow rotators ($v\ sin\ i < 15$ km s^{-1}), making them attractive targets for radial velocity measurements (Mohanty & Basri, 2003). But the standard observational setups used to measure precision radial velocities are centered in the visible spectrum ($3600 - 6800$ Å), limited either by the calibration source ($5000 - -6000$ Åfor iodine cells) or the excessive telluric absorption (beyond 6800 Åfor the ThAr technique).

This wavelength range is not optimal for very red objects like M dwarfs. As a result, the M dwarfs that have been observed tend to be the brightest (closest) targets with spectral types earlier than M5. Without resorting to high-resolution NIR spectroscopy, which may be able to produce 50 m s^{-1}radial velocities in the near future (Blake et al., 2007), it is currently difficult to obtain the precision radial velocities required to search for terrestrial planets orbiting most M dwarfs.

The spectral coverage of TRES, however, extends into the NIR up to 9200 Å, and some of the very red orders are not affected by telluric lines at all (see last panels of Fig. 12.1). Therefore a team led by Cullen H. Blake (CfA) has proposed to perform RV study of a few M dwarf stars selected from the MEarth input catalog. Observations are scheduled to be carried out in the second trimester of 2008, to evaluate feasibility of such expolanet search around nearby M dwarfs.

Bibliography

Ali, B., & Depoy, D. L. 1995, AJ, 109, 709

Allen, C.W. 1973, Astrophysical Quantities 3rd ed., Univ of London (Athlone Press)

Allen, L.E. et al., 2004, ApJS, 154, 363

Allington-Smith, J.R. et al. 2002, PASP, 114, 892

Alonso, A., Arribas, S., & Martínez-Roger, C. 1999, A&AS, 140, 261

Andrée, P., Ward-Thompson, D., & Barsony, M. 1993, ApJ, 406, 122

Angel, J.R.P., Adams, M.T., Boroson, T.A., & Moore, R.L. 1977, ApJ, 218, 776

Appenzeller, I. et al. 1998, The Messenger, 94, 1

Appenzeller, I., Bertout, C., & Stahl, O. 2005, å, 434, 1005

Bacon, R. et al. 2001, MNRAS, 326, 23

Bakos, G., Noyes, R.W., Kovács, G., Stanek, K.Z., Sasselov, D.D., & Domsa, I. 2004, PASP, 116, 266

Bally, J., Stark, A.A., Wilson, R.W., & Langer, W.D. 1987, ApJ, 312, 45

Balog, Z., Muzerolle, J., & Megeath, S.T. 2005, Protostars and Planets V, Proceedings, LPI Contribution No. 1286., p.8542

Balog et al. 2006, AJ, 650, L83

Baranne A., Mayor M., & Poncet J.L. 1979, Vistas astron. 23, 279

Baranne, A., Queloz, D., Mayor, M., et al. 1996, A&AS, 119, 373

Barden S.C., Armandroff T., Massey P., Groves L., Rudeen A.C., Vaughnn D., & Muller G., 1993, ASPC, 37, 185

Barnes, S. 2004, PhD thesis, University of Canterbury, New Zeland

Bate, M.R., Clarke, C.J., & McCaughrean, M.J. 1998, MNRAS, 297, 1163

Bate, M.R., Bonnell, I.A., & Bromm, V. 2002, MNRAS, 332, L65

Bate, M.R., Bonnell, I.A., & Bromm, V. 2003, MNRAS, 339, 577

Berghöfer, T.W., & Christian, D.J. 2002, A&A, 384, 890

Bessell, M.S., & Brett, J.M. 1988, PASP, 100, 1134

Bica, E., & Dutra, C.M. 2000, AJ, 119, 1214

Bica, E., & Schmitt, H. 1995, ApJS, 54, 33

Blake, C.H. Charbonneau, D., White, R.J., Marley, M.S., & Saumon, D. 2007, ApJ, 666, 1198

Blake, C.H. et al. 2008, submitted to PASP

Broos, P.S., Feigelson, E.D., Townsley, L.K., Getman, K.V.; Wang, J, Garmire, G.P., Jiang, Z., & Tsuboi, Y. 2007, ApJS, 169, 353

Bodenheimer, P. et al. 2001, ApJ, 548, 466

Bonanno, A., Benatti, S., Claudi, R., Desidera, S., Gratton, R., Leccia, S., & Paterno', L. 2008, astro-ph arXiv:0801.4446

Bonnell, I.A., & Bate, M.R. 2006, MNRAS, 370, 488

Bottema, M. 1981, Applied Optics, 20, 528

Bouchy, F., Pepe, F., & Queloz, D. 2001, A&A, 374, 733

Briceño, C, Hartmann, L., Hernandez, J., Calvet, N.; Katherina Vivas, A., Furesz G., & Szentgyorgyi, A. 2007, ApJ, 661, 1119

Broos, P.S., Feigelson, E.D., Townsley, L.K., Getman, K.V., Wang, J., Garmire, G.P., Jiang, Z., & Tsuboi, Y. 2007, ApJS, 169, 353

Brown, T., Gilliland, R., Noyes, R., & Ramsey, L.W. 1991, ApJ, 368, 599

Brown, A.G.A., de Geus, E.J., & de Zeeuw, P.T. 1994, A&A, 289, 101

Brown, T.M., Noyes, R.W., Nisenson, P., Korzennik, S.G., & Horner, S. 1994, PASP, 106, 1285

Burkert, A., & Hartmann, L. 2004, ApJ, 616, 288

Burrows, A. et al 2004, ApJ, 609, 407

Butler, R.P. et al. 1999, AJ, 526, 916

Butler, R.P. et al. 2006, ApJ, 646, 505

Calvet, N., D'Alessio, P., Hartmann, L., Wilner, D., Walsh, A., & Sitko, M. 2002, ApJ, 568, 1008

Calvet, N., et al. 2005, ApJ, 630, L185

Campbell, B., & Walker, G.A.H. 1979, PASP, 91, 540

Carpenter, J.M., Hillenbrand, L.A., & Skrutskie, M.F. 2001, AJ, 121, 3160

Carrier, F. et al. 2005, New Astronomy, 10, 315

Carroll, B.W., & Ostlie, D.A. 1996, An Introduction to Modern Astrophysics, publ. by Addison-Wesley Publishing Company, Inc., USA

Casse, M., & Vieira, F. 1997, Proc. SPIE, 2871, 1187

Clarke, C.J., Bonnell, I.A., & Hillenbrand, L.A. 2000, Protostars and Planets IV (Book - Tucson: University of Arizona Press; eds Mannings, V., Boss, A.P., Russell, S. S.), p. 151

Coelho, P., Barbuy, B., Meléndez, J., Schiavon, R.P., & Castilho, B.V. 2005, A&A, 443, 735

Collinder, P. 1931, Ann. Lund Obs., 2

Content, R. 1997, Proc. SPIE, 2871, 1295

Crutcher, R.M., & Hartkopf, W.I. 1978, ApJ, 226, 839

Daimon, M., & Masumura, A. 2002, Appl. Opt., 41, 5275

Devor, J., Charbonneau, D., O'Donovan, F.T., Mandushev, G., & Torres, G. 2007, astro-ph: arXiv:0712.0839

Donnelly, R.H., Brodie, Jean P., Bixler, J.V., & Hailey, C.J. 1989, PASP, 101, 1046

Dubbeldam, C.M. at al. 2000, Proc. SPIE, 4008, 1181

Eppw, H.W., & Fabricant, D.G, 2002, PASP, 114, 1252

Fabricant, D.G., et al. 2004, Proc. SPIE, 5492, 767

Erksine, D.J., & Ge, J. 2000, ASPC, 195, 501

Fabricant, D., Cheimets, P., Caldwell, N., & Geary, J. 1998, PASP, 110, 79

Fabricant, D.G., Fata, R.G., & Epps, H.W. 1998, Proc. SPIE, 3355, 232

Fabricant, D.G., et al. 2005, PASP, 117, 1411

Fata, R., Kradinov, V., & Fabricant, D. 2004, Proc. SPIE, 5492, 553

Feigelson, E.D., Getman, K., Townsley, L., Garmire, G., Preibisch, T., Grosso, N., Montmerle, T., Muench, A., & McCaughrean, M. 2005, ApJS, 160, 379

Fűrész, G., Hartmann, L.W., Szentgyorgyi, A.H., Ridge, N.A., Rebull, L., Stauffer, J., Latham, D.W., Conroy, M.A., Fabricant, D.G., & Roll, J. 2006, Astrophysical Journal, 648, 1090

Fűrész, G., Hartmann, L,W., Megeath, S.T., Szentgyorgyi, A.H., & Hamden, E.T. 2008a, ApJ, 676, 1109

Fűrész, G., Szabó, Gy.M., Székely, P., Szentgyorgyi, A.H., & Latham, D.W. 2008b, submitted to Astrophysical Journal

Fűrész, G., Szentgyorgyi, A.H., & Meibom, S. 2008c, Proc.of the ESO/Lisbon/Aveiro Conference, p. 287

Flaccomio, E., Micela, G., Sciortino, S., Damiani, F., Favata, F., Harnden, F.R. Jr., & Schachter, J. 2000, A&A, 355, 651

Fűrész, G., Hartmann, L.W., Szentgyorgyi, A.H., Ridge, N.A., Rebull, L., Stauffer, J., Latham, D.W., Conroy, M.A., Fabricant, D.G., &Roll, J. 2006, ApJ, 648, 1090

Fűrész, G., Hartmann, L.W., Megeath, T.S., Szentgyorgyi, A.H. & Hamden, E.T. 2008, ApJ, accepted

Fountain et al. 1979, ApJ, 229, 971

Ge, J., Erksine, D.J., & Rushford, M. 2002, PASP, 114, 1016

Ge, J. et al. 2006, ApJ, 648, 683

Geary, J. & Amato, S. 1998, Proc. SPIE, 3355, 539

Girard, T.M., Korchagin, V.I., Casetti-Dinescu, D.I, & van Altena W.F. 2006, AJ, 132, 1768

Griffin, R.F., & Griffin, R.E. 1973, MNRAS, 162, 243

Gregory, P.C., Scott, W.K., Douglas, K., & Condon, J.J. 1996, ApJS, 103, 427

Gross, H., editor, Handbook of Optical Systems, vol. 1, 2005, WILEY-VCH Verlag GmbH & Co. KGaA

Glazebrook, K., & Bland-Hawthorn, J. 2001, PASP, 113, 197

Glushkova, E. V.; Rastorguev, A. S. 1991, SvAL, 17, 13

Gomez, M., Hartmann, L., Kenyon, S., & Hewtett, R., 1993, AJ, 105, 1927

Gualandris, A., Portegies Zwart, S., & Eggleton, P.P. 2004, MNRAS, 350, 615

Guenther, E.W., Joergens, V., Neuhäuser, R., Torres, G., Batalha, N.S., Vijapurkar, J., Fernández, M., & Mundt, R. 2001, in Zinnecker, H., & Mathieu, R.D., eds, Iau Symp. 200, The Formation of Binary Stars. ASP, Provo, p. 165

Gutermuth, R.A. 2005, PhD Thesis, University of Rochester, NY

Hatzidimitriou, D., & Bhatia, R.K. 1990, A& A, 230, 11

Harris, G.L.H 1976, ApJS, 30, 451

Hartigan, P., Hartmann, L., Kenyon, S. J., Strom, S. E., & Skrutskie, M. F. 1990, ApJ, 354, L25

Hartmann, L., & Kenyon, S.J. 1996, ARAA, 34, 207

Hartmann, L. 1998, Accretion Process in Star Formation, Cambridge University Press

Hartmann, L. 2003, ApJ, 585, 398

Hartmann, L., Megeath, S.T., Allen, L., Luhman, K., Calvet, N., D'Alessio, P., Franco-Hernandez, R., & Fazio, G. 2005, ApJ, 629, 881

Hartmann, L., & Burkert, A. 2007, ApJ, 654, 988

Herbig, G.H. 1954, ApJ, 119, 483

Hernández, J., Calvet, N., Hartmann, L., Briceño, C., Sicilia-Aguilar, A., & Berlind, P. 2005, AJ, 129, 856

Haynes, R., Bland-Hawthorn, J., Large, M.C.J., Klein, K.F., & Nelson, G. 2004, Proc. SPIE, 5494, 586

Heacox, W.D. 1986, AJ, 92, 219

Heacox, W.D. 1987, J. Opt. Soc. Am. A., 4, 488

Hernández, J., et al. 2007, ApJ, 662, 1067

Hill, J.M., Angel, J.R.P., Scott, J.S., Lindley, D., & Hintzen, P. 1980, ApJ, 242, L69

Hillenbrand, L.A 1997, AJ, 113, 1733

Hillenbrand, L.A, & Hartmann, L.W. 1998, ApJ, 492, 540

Hillenbrand, L.A., Strom, S., Calvet, N., Mermill, K.M., Gatley, I., Makidon, R. Meyer, M., & Skrutskie, M. 1998, AJ, 116, 1816

Hillenbrand, L.A., & Carpenter, J.M. 2000, ApJ, 540, 236

Hoag, A.A., & Applequist, L. 1965, ApJS, 12, 215

Hog, E., Fabricius, C., Makrov, V.V., et al. 2000, A&A, 357, 367

Holman, M.J, & Murray, N.W. 2005, Science, 307, 1288

Hook, I. et al. 2003, Proc. SPIE, 4841, 1645

Hubbard, E.N., Angel, J.R.P., & Gresham, M.S. 1979, ApJ, 229, 1074

Huchra, J., Davis, M., Latham, D., & Tonry, J. 1983, ApJS, 52, 89

Hunter, T.R., & Ramsey, L.W. 1992, PASP, 104, 1244

Jacobson, H.R., Cummings, J., Deliyannis, C.P., Steinhauer, A., & Sarajedini, A. 2002, BAAS, 34, 1308

Jacquinot, P. 1954, J. Opt. Soc. Am., 44, 761

Jeans, J.H. 1929, Astronomy & Cosmogony (Cambridge University Press, 2nd ed.), 4

Jenkins, F, & white, H. 1976, Fundamentals of Optics, McGraw Hill

Jensen, E. L. N., & Mathieu, R. D. 1997, AJ, 114, 301

Joergens, V., & Guenther, E. 2001, A&A, 379, L9

Jones, B.F., & Walker, M.F. 1988, AJ, 95, 6

Karow, H.H. 1993, Fabrication Methods for Precision Optics, Wiley & Sons

Kawamura, A., Onishi, T., Yonekura, Y., Dobashi, K., Mizuno, A., Ogawa, H., & Fukui, Y. 1998, ApJS, 117, 387

Kerber, F., Nave, G., Sansonetti, C.J., Bristow, P., & Rosa, M.R 2007, ASPC, 364, 461

Kharchenko, N.V., Piskunov, A.E., Röser, S., Schilbach, E., & Scholz, R.D. 2005, A&A, 438, 1163

Kenyon, S.J., & Hartmann, L. 1993, ApJS, 101, 117

Kohler, D. et al. 2001, HARPS internal documentation "Fiber link Design, Analysis, and Performance Report", #3M6-TRE-HAR-33105-0001

Köhler, R., Petr-Gotzens, M.G., McCaughrean, M.J., Bouvier, J., Duchene, G., Quirrenbach, A., & Zinnecker, H. 2006, A&A, 458, 461

Kroupa, P. 2000, New Astronomy, 4, 615

Kroupa, P. 2002, Science, 295, 82

Kurosawa, R., Harries, T.J., & Symington, N.H. 2006, MNRAS, 370, 580

Kurucz, R. 1979, ApJS, 40, 1

Kurucz, R. 1992, Proc. IAU Symp. 149, p225

Kurtz, M.J., & Mink, D.J. 1998, PASP, 110, 934

Lada, C. J. 1987, in IAU Symposium, Vol. 115, Star Forming Regions, ed. M. Peimbert & J. Jugaku, 1?17, 13

Lada, C.J., Young, E.T., & Greene, T.P. 1993, ApJ, 408, 471

Lada, C., Young, E., & Greene, T. 1993, ApJ, 408, 471

Lada, E.A., & Lada, C.J. 1995, AJ, 109, 1682

Lada, C. J., & Lada, E. A. 2003, ARA&A, 41, 57

Lamm, M.H., Bailer-Jones, C.A.L., Mundt, R., Herbst, W., & Scholz, A. 2004, å, 417, 557

Landolt, A.U. 1992, AJ, 104, 340

Lang, K.R., & Willson, R.F. 1980, ApJ, 238, 867

Latham, D.W. 1982, Proc. IAU Coll. 67, 259

Latham, D.W. 1992, in ASP Conf. Ser. 32, IAU Coll. No. 135, Complementary Approaches to Binary and Multiple Star Research, eds. H. McAlister & W. Hartkopf, p. 110

Latham, D.W., Davis, R.J., Stefanik, R.P., Mazeh, T. & Abt, H.A. 1991, AJ, 101, 625

Lee, D., Haynes, R., & Skeen, D.J. 2001, MNRAS, 326, 774

Li, C-H.,Benedick, A.J., Fendel, P., Glenday, A.G., Kaertner, F.Z., Phillips, D.F., Sasselov, D., Szentgyorgyi, A.H., & Walsworth, R.L. 2008, Nature, 452, 610

Li, J.Z., & Smith, M.D. 2005, A&A, 431, 925 (2005a)

Li, J.Z., & Smith, M.D. 2005, ApJ, 620, 816 (2005b)

Lindley, P.B. 1970, Nat. Rubber Technical Bulletin, 3d edition, Malaysian Rubber Producer's Research Association

Liu et al. 1989, AJ, 98, 626

Liu et al. 1991, AJ, 102, 1103

Loeillet, B., Bouchy, F., Deleuil, M., Royer, F., Bouret, J.C., Moutou, C., Barge, P., de Laverny, P., Pont, F., Recio-Blanco, A., & Santos, N.C. 2008, A&A, 479, 865

Lovis, C., Pepe, F., Bouchy, F; Lo Curto, G., Mayor, M., Pasquini, L., Queloz, D., Rupprecht, G., Udry, S., & Zucker, S. 2006, Proc. SPIE, 6269, 23

Lovis, C., & Pepe, F. 2007, A&A, 468, 1115

Malitson, I.H. 1963, Appl. Opt., 2, 1103

Marcy, G.W., & Butler, R.P. 1992, PASP, 104, 270

Marchenko et al. 2000, MNRAS, 317, 333

Mateo, M., Olszewski, E.W., & Walker, M.G. 2008, ApJ, 675, 210

McCarthy, J.K., Sandiford, B.A., Boyd, D., & Booth, J. 1993, PASP, 105, 881

McCaughrean, M.J., & Stauffer, J. R. 1994, AJ, 108, 1382

McCaughrean, M.J., Zinnecker, H., Andersen, M., Meeus, G., & Lodieu N. 2002, ESO Messenger, 109, 28

McLeod, B.A., Gauron, T.M., Geary, J.C., Ordway, M.P., & Roll, J.B. 1998, Proc. SPIE, 3355, 477

Megeath, S.T. et al. 2008, in prerp.

Meibom, Søren 2007, personal communication

Mermilliod, J.C. 1996, In the origins, evolution and destinies of binary stars in clusters, APS Conf. Ser., 90, 475

Meyer, M.R., Calvet, N., & Hillenbrand, L.H. 1997, AJ, 114, 288

Miville-Deschênes, M.-A., & Lagache, G. 2005, ApJSS, 157, 302

Mohanty, S., & Basri, G. 2003, ApJ, 583, 451

Munari, U., Sordo, R., Castelli, F., & Zwitter, T. 2005, å, 442, 1127

Murphy, M.T., Tzanavaris, P., Webb, J.K., & Lovis, C. 2007a, MNRAS, 378, 221

Murphy, M.T. et al. 2007b, MNRAS, 380, 839

Muzerolle, J., Calvet, N., Hartmann, L., & D'Alessio, P. 2003, ApJ, 597, 149

Myers, P.C. 1998, ApJLett., 496, 109

Neuhaeuser, R. et al. 1998, A&A, 334, 873

Nisenson, P., Contos, A., Korzennik, S., & Noyes, R. 1999, ASPC, 185, 143

Nordström, B., Latham, D.W., Morse, J.A., Milone, A.A.E., Kurucz, R.L., Andersen, J., & Stefanik, R.P. 1994, A&A, 287, 338

Nordström, B., Mayor, M., Andersen, J., Holmberg, J., Pont, F., Jørgensen, B.R., Olsen, E.H., Udry, S., & Mowlavi, N. 2004, A&A, 418, 989

Nutzman, P., & Charbonneau, D. 2007, PASP, accepted; astro-ph/0709.2879

O'dell, C.R. 2001, ARA&A, 39, 99

O'Dell, C.R., Poveda, A., Allen, C., & Robberto, M. 2005, ApJ, 633, 45O

Ogura, K. 1984, PASJ, 36, 1390

de Oliveira, M. R., Fausti, A., Bica, E., & Dottori, H. 2002, A& A, 390, 103

Palla, F. & Stahler, S.W. 1999, ApJ, 525, 772

Palla, F., & Stahler, S.W. 2000, ApJ, 540, 255

Palla, F., Randich, S., Flaccomio, E., & Pallavicini, R. 2005, AJ, 626, L49

Palmer, B.A, & Engleman, R. 1983, Atlas of the thorium spectrum, Los Alamos National Laboratory Report LA-9615

Pandey, K.A, Sharma, S., Upadhyay, K., Ogura, K., Sandhu, T.S., Mito, H., & Sagar, R. 2007, PASJ, 59, 547

Park, B.-G., Sung, H., Bessel, M.S., & Kang, Y.H 2000, AJ, 120, 894

Park, B-G., & Sung, H. 2002, AJ, 123, 892

Parks, R.E. 1980, Proc. SPIE, 237, 455

Parry I.R. 1997, ASSL, 212, 3

Parry I.R. 1998, ASPC, 152, 3

Parry, I.R. 2006, NewAR, 50, 301

Pasquini, L. et al. 2002, The Messenger, 110, 1

Piskunov, N., & Valenti, J.A. 2002, å, 385, 1095

Pepe, F., Mayor, M., Delabre, B., Kohler, D., Lacroix, D., Queloz, D., Udry, S., Benz, W., Bertaux, J.L., & Sivan, J.P. 2000, Proc. SPIE, 4008, 582

Pepe, F., Mayor, M., Galland, F., Naef, D., Queloz, D., Santos, N.C., Udry, S., & Burnet, M. 2002, A&A, 388, 632

Pérez, M.R., Thé, P.S., & Westerlund, B.E. 1987, PASP, 99, 1050

Pickering. E.C., & Kapteyn. J.C. 1918, Annuals of Harvard College Observatory, vol. 101, pp.1-368

Pietrzynski, G., & Udalski, A. 1999, Acta Astron., 49, 165

Poveda, A., Allen, C., & Hernández-Alcántara, A. 2005, ApJ, 627, 61

Queloz, D, Case, M., & Mayor, M. 1999, ASPC, 185, 130

Ramírez, S.V., Rebull, L., Stauffer, J., Strom, S., Hillenbrand, L., Hearty, T., Kopan, E.L., Pravdo, S., Makidon, R., & Jones, B. 2004, AJ, 128, 787

Ramsay, S.K., Mountain, C.M., & Geballe, T.R. 1992, MNRAS, 259, 751

Ramsay-Howat, S.K., Harris, J.W., Gostick, D.C., Laidlaw, K., Kidd, N., Strachan, M., & Wilson, K. 2000, Proc. SPIE, 4008, 1351

Ramsey, L.W., Barden, S.C., Natinos, H.L., & Truax, R.J. 1988, BAAS, 12, 836

Ramsey, L.W. 1988, ASPC, 3, 26

Rice, W. K. M., Armitage, P. J., Wood, K., & Lodato, G. 2006, MNRAS, 373, 1619

Reipurth, B., Pedrosa, A., & Lago, M.T.V.T. 1996, A&A Suppl., 120, 229

Reipurth, B., & Clarke, C. 2001, AJ, 122, 432

Rebull, L.M., Makidon, R.B., Strom, S.E., Hillenbrand, L.A., Birmingham, A., Patten, B.M., Jones, B.F., Yagi, H., & Adams, M.T. 2002, AJ, 123, 1528

Reipurth, B., Pettersson, B., Armond, T., Bally, J., & Vaz, L.P.R., 2004, AJ, 127, 1117

Ridge, N.A., Wilson, T.L., Megeath, S.T., Allen, L.E., & Myers, P.C. 2003, AJ, 126, 286

Rodríguez, L.F., Poveda, A., Lizano, S., & Allen, C. 2005, ApJ, 627, 65

Rodríguez-González, A., Esquivel, A., Raga, A.C., & Cantó, J. 2008, ApJ, accepted, astro-ph arXiv: 0805.2126

Royer, F., Blecha, A., North, P., Simond, G., Baratchart, S., Cayatte, V., Chemin, L., & Palsa, R. 2002, Proc. SPIE, 4847, 184

Rupprecht, G. et al. 2004, Proc. SPIE, 5492, 148

Sagar, R., & Joshi, U.C. 1983, MNRAS, 205, 747

Scally, A., & Clarke, C. 2002, MNRAS, 334, 156

Scally, A., Clarke, C., & McCaughrean, M.J. 2005, MNRAS, 358, 742

Schroder, D.J, & Hillard, R.L 1980, Applied Optics, 19, 2833

Schulz, N. 2005, From Dust to Stars, publ. by Praxis Publishing Ltd, Chichester, UK

Sekiguchi, M., & Fukugita, M. 2000, AJ, 120, 1072

Sicilia-Aguilar, S., Hartmann, L.W., Szentgyorgyi, A.H., Fabricant, D.G., Fűrész, G., Roll, J.B., Conroy, M.A., Calvet, N., Tokarz, S., & Hernández, J. 2005, AJ, 129, 363

Sozzetti, A. et al. 2008, submitted to ApJ

Subramaniam, A., Gorti, U., Sagar, R., & Bhatt, H.C. 1995, AAP, 302, 86

Subramaniam, A., & Sagar, R. 1999, AJ, 117, 937

Sung, H., Bessell, M.S., & Lee, S.-W. 1997, AJ, 114, 2644

Sung, H., Bessell, M.S., & Chun, M-Y. 2004, AJ, 128, 1684

Stahler, S.W., & Walter, F.M. 1993, in Protostars and Planets III, ed. E.H. Levy & J.I. Lunin (Tucson: Universoty of Arizona), 405

Stahler, S.W., & Palla, F. 2005, The Formation of Stars, publ. by Wiley-VCH Verlag GmbH

Stefanik, R. P., Latham, D. W. & Torres, G. 1999, in ASP Conf. Ser. 185, IAU Coll. No. 170, Precise Stellar Radial Velocities, eds. J. B. Hearnshaw & C. D. Scarfe, p. 354

Stickland, D.J., Pike, C.D., Lloyd, C., & Howarth, I.D. 1987, A&A, 184, 185

Strassmeier, K.G., Rice, J.B., Ritter, A., Küker, M., Hussain, G.A.J., Hubrig, S., & Shobbrook, R. 2005, A&A, 440, 1105

Szabados, L. 2000, ASPC, 203, 248

Szabó, G.M., Fűrész, G., Szḱely, P., & Szentgyorgyi, A.H. 2006, Astrophysics of Variable Stars, ASP Conf. Ser., 349, 339

Szentgyorgyi, A.H., Cheimets, P., Eng, R., Fabricant, D.G., Geary, J.C., Hartmann, L., Pieri, M.R., & Roll, J.B. 1998, Proc. SPIE, 3355, 242

Tan, J.C., Krumholz, M.R., & McKee, C.F. 2006, ApJ, 641, L121 (TKM06)

Teixeira, P. S., et al. 2006, ApJ, 636, L45

Teixeira, P. S. 2008, PhD thesis: ‘‘*From dust to light: study of star formation in NGC 2264”*; University of Lisbon, Portugal

Testi, L., Palla, F., & Natta, A. 1999, A&A, 342, 515

Thatte, N., Genzel, N., Kroker, H., Krabbe, A., Tacconi-Garman, L., Maiolino, R., & Tecza, M. 1997, ApSS, 248, 225

Tonry, J. & Davis, M. 1979, AJ, 84, 1511

Vasilevskis, S., Sanders, W.L., & Balz, A.G.A. Jr. 1956, AJ, 70, 797

Vaughnn, D. 1994, Proc. SPIE, 2198, 31

Walker, M.F. 1956, ApJS, 2, 365

Wang, J., Townsley, L.K., Feigelson, E.D.; Getman, K.V., Broos, P.S., Garmire, G.P., & Tsujimoto, M. 2007, ApJS, 168, 100

Wilson, W.J.F. et al. 1998, PASP, 110, 433

White, R.J., & Basri, G. 2003, AJ, 582, 1109

Wynne, C., & Worswick, S. 1986, MNRAS, 220, 657

Zapatero Osorio, M. R. et al. 2000, Science, 290, 103

Chapter 12

Appendix

Table 12.1. TRES glass catalogs for T=13, 18 and 23 °C

	Glass	n$_d$	ν_d	Schott dispersion formula coefficients					
				A0	A1	A2	A3	A4	A5
$T = 13$ °C	BAL15Y	1.556816	58.737445	2.387150900E+000	-9.224156400E-003	1.304293200E-002	2.384444700E-004	-4.534691800E-006	5.297990300E-007
	BSM51Y	1.603482	60.735620	2.532001000E+000	-1.071571100E-002	1.413980400E-002	2.302335800E-004	-2.567506100E-006	3.435133000E-007
	CAF2-CANON	1.433943	95.324958	2.039048700E+000	-3.238209600E-003	6.146269900E-003	5.280034900E-005	5.827634600E-007	-2.335788600E-009
	S-FPL51Y	1.497272	81.265841	2.218351400E+000	-5.289520200E-003	8.478388800E-003	8.720344300E-005	1.079714400E-007	7.425872000E-008
	S-LAL7	1.651604	58.538107	2.682336500E+000	-1.182750900E-002	1.635225500E-002	2.574932700E-004	-7.537789900E-008	2.544607500E-007
	I-BSL7Y	1.516330	64.143455	2.269988000E+000	-1.008235000E-002	1.106723000E-002	3.826384000E-005	1.779494000E-005	-8.976372000E-007
	Q2-3067	1.464499	65.938880	2.120565900E+000	-8.943724900E-003	9.024239300E-003	1.378628500E-004	-8.275039800E-007	2.674044800E-008
	S-FSL5Y	1.487598	70.452595	2.188870800E+000	-9.340026400E-003	9.100277700E-003	1.115660900E-004	1.652040800E-007	3.181107200E-008
$T = 18$ °C	BAL15Y	1.556830	58.719702	2.387183500E+000	-9.222473100E-003	1.304449900E-002	2.393708600E-004	-4.618585100E-006	5.332355200E-007
	BSM51Y	1.603497	60.719128	2.532038800E+000	-1.071496300E-002	1.414316200E-002	2.306806400E-004	-2.607172400E-006	3.451429100E-007
	CAF2-CANON	1.433891	95.283887	2.038898700E+000	-3.236347100E-003	6.146061800E-003	5.319796300E-005	5.882402400E-007	-5.544299400E-009
	S-FPL51Y	1.497238	81.240928	2.218244000E+000	-5.288525300E-003	8.478699000E-003	8.765670600E-005	6.635852500E-008	7.595461700E-008
	S-LAL7	1.651615	58.523716	2.682360900E+000	-1.182566000E-002	1.635346900E-002	2.585027500E-004	-1.667175600E-007	2.582001400E-007
	I-BSL7Y	1.516330	64.143455	2.269988000E+000	-1.008235000E-002	1.106723000E-002	3.826384000E-005	1.779494000E-005	-8.976372000E-007
	Q2-3067	1.464499	65.938880	2.120565900E+000	-8.943724900E-003	9.024239300E-003	1.378628500E-004	-8.275039800E-007	2.674044800E-008
	S-FSL5Y	1.487594	70.436141	2.188852900E+000	-9.340207100E-003	9.101416700E-003	1.120006400E-004	9.293932200E-008	3.698035700E-008
$T = 23$ °C	BAL15Y	1.556844	58.701975	2.387216200E+000	-9.220789900E-003	1.304606600E-002	2.402972800E-004	-4.702481300E-006	5.366721700E-007
	BSM51Y	1.603513	60.702611	2.532075800E+000	-1.071421500E-002	1.414652000E-002	2.311277100E-004	-2.646836900E-006	3.467724300E-007
	CAF2-CANON	1.433840	95.242248	2.038747000E+000	-3.234477400E-003	6.145721500E-003	5.364810900E-005	5.857597300E-007	-8.216292400E-009
	S-FPL51Y	1.497203	81.216026	2.218136600E+000	-5.287530500E-003	8.479009300E-003	8.810995400E-005	2.474699900E-008	7.765047000E-008
	S-LAL7	1.651625	58.509336	2.682385400E+000	-1.182381200E-002	1.635468300E-002	2.595122700E-004	-2.580637300E-007	2.619398800E-007
	I-BSL7Y	1.516330	64.143455	2.269988000E+000	-1.008235000E-002	1.106723000E-002	3.826384000E-005	1.779494000E-005	-8.976372000E-007
	Q2-3067	1.464499	65.938880	2.120565900E+000	-8.943724900E-003	9.024239300E-003	1.378628500E-004	-8.275039800E-007	2.674044800E-008
	S-FSL5Y	1.487590	70.419694	2.188835000E+000	-9.340387800E-003	9.102555800E-003	1.124351900E-004	2.067575700E-008	4.214958100E-008

Note. — For all TRES glasses and a couplant (Q2-3067) the n_d refraction index, ν_d dispersion and coefficients of the Schott dispersion formulas are given in above table, for the design ($T = 18$ °C) and thermal test ($T = 13$ and 23 °C) temperatures, as used in the construction design based on actual melt data. See text for details.

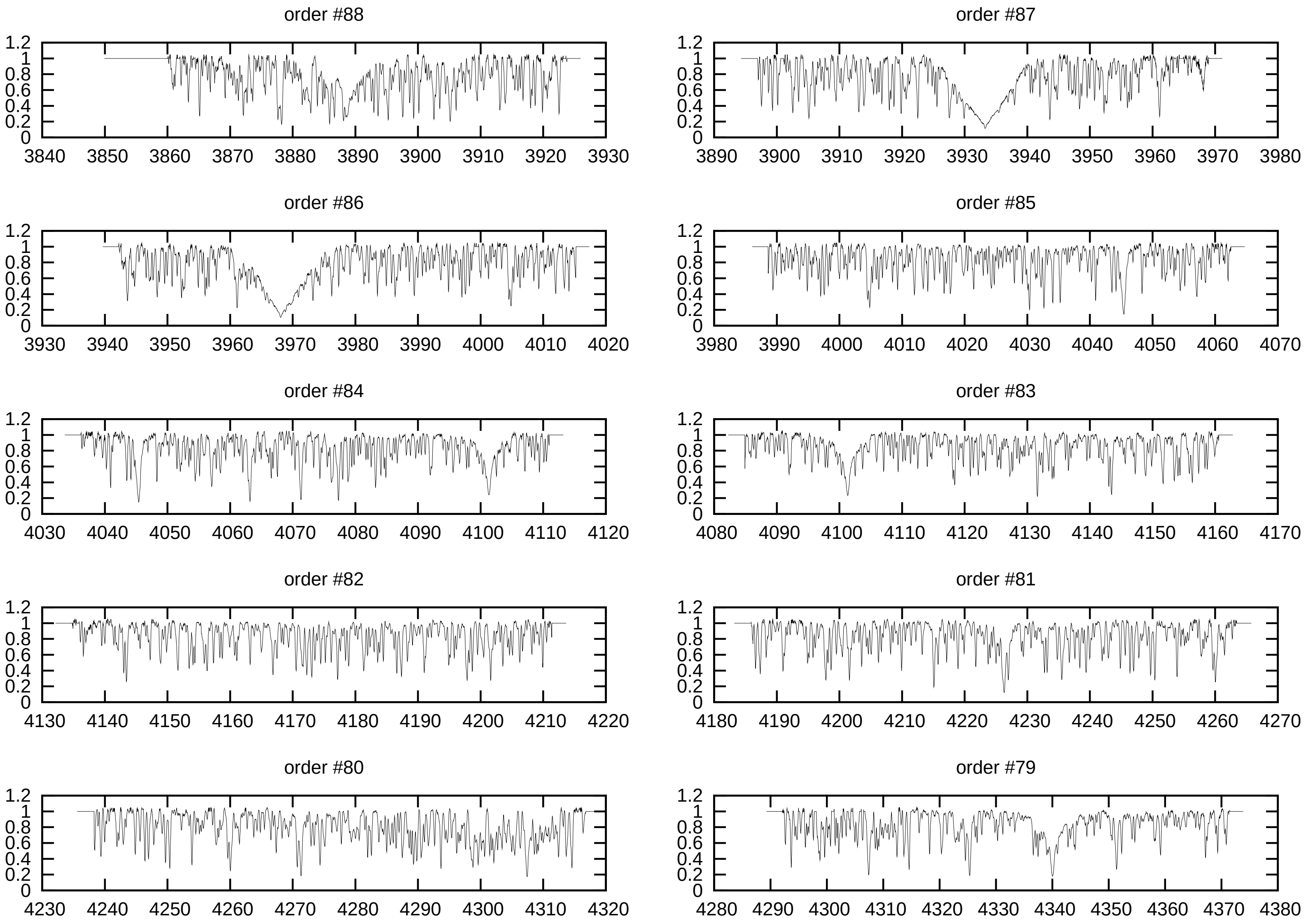

Figure 12.1: ***Sample TRES spectra of*** υ ***And*** *(continuum normalized). For the last 21 orders (#58 to #38, or from 5840 Å to 9100 Å) the right column displays the atmospheric lines within the given spectral band.*

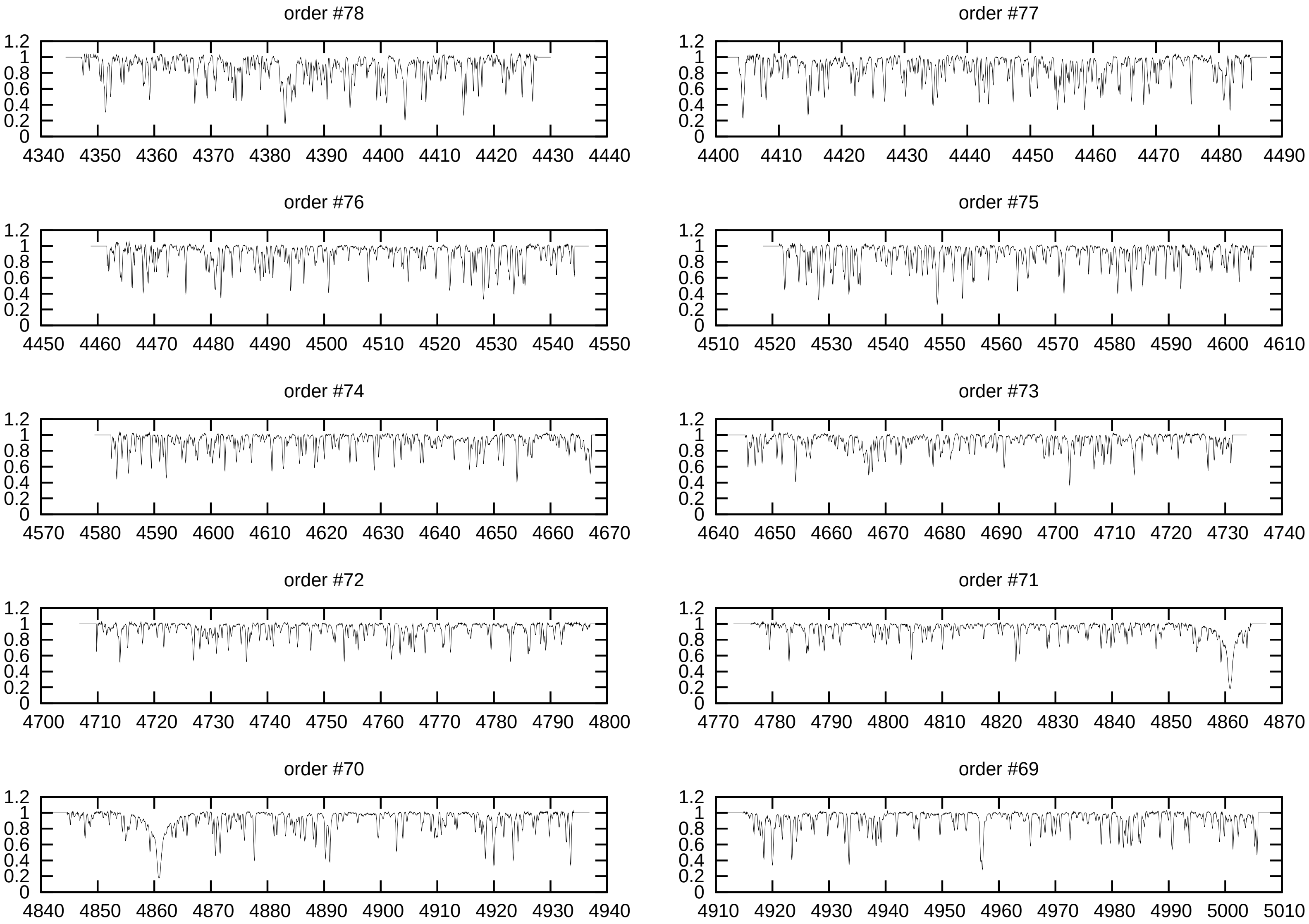
order #78
1.2
1
0.8
0.6
0.4
0.2
0
4340 4350 4360 4370 4380 4390 4400 4410 4420 4430 4440
order #77
4400 4410 4420 4430 4440 4450 4460 4470 4480 4490
order #76
4450 4460 4470 4480 4490 4500 4510 4520 4530 4540 4550
order #75
4510 4520 4530 4540 4550 4560 4570 4580 4590 4600 4610
order #74
4570 4580 4590 4600 4610 4620 4630 4640 4650 4660 4670
order #73
4640 4650 4660 4670 4680 4690 4700 4710 4720 4730 4740
order #72
4700 4710 4720 4730 4740 4750 4760 4770 4780 4790 4800
order #71
4770 4780 4790 4800 4810 4820 4830 4840 4850 4860 4870
order #70
4840 4850 4860 4870 4880 4890 4900 4910 4920 4930 4940
order #69
4910 4920 4930 4940 4950 4960 4970 4980 4990 5000 5010

Fig. 12.1 cont.

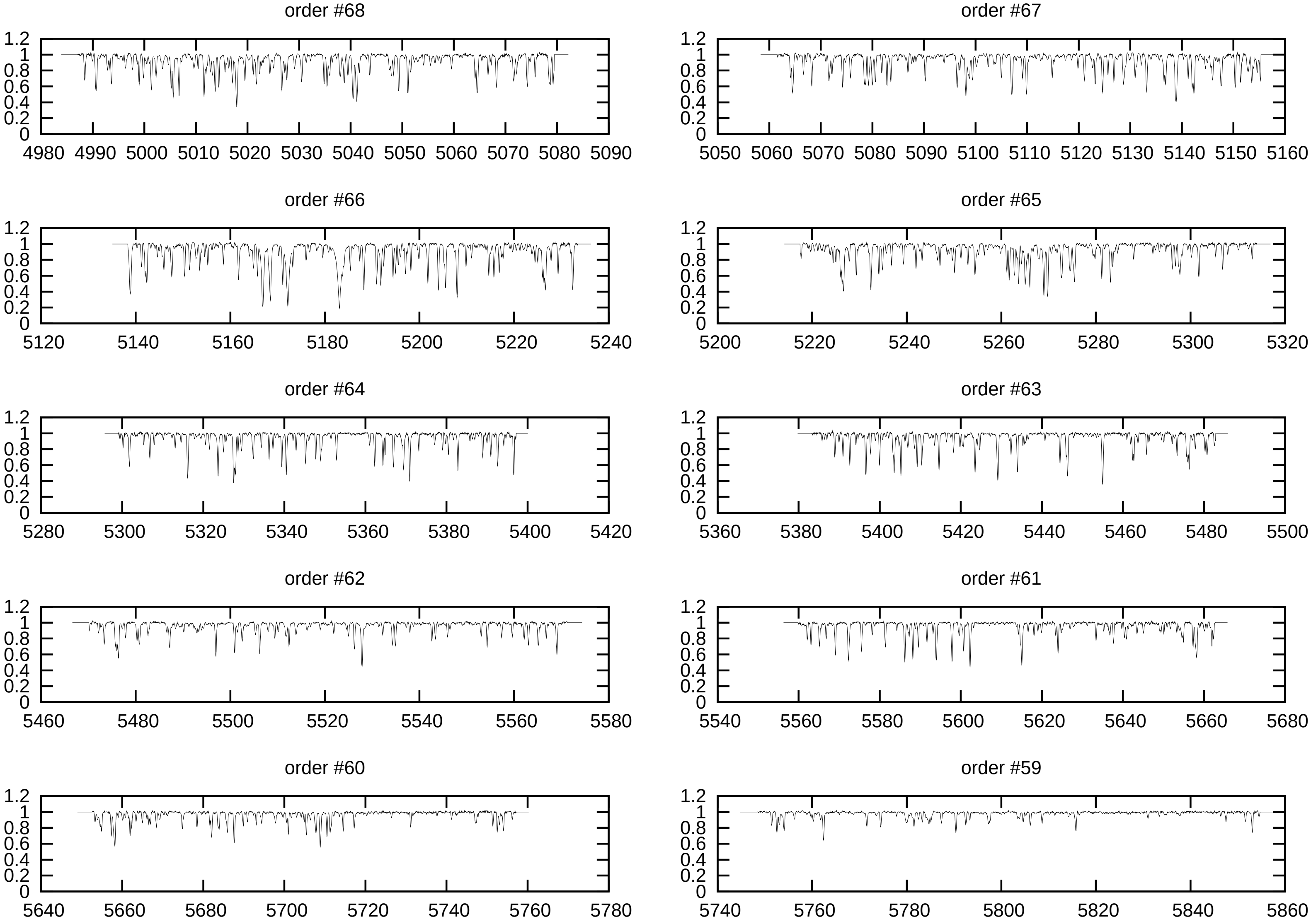
order #68
1.2
1
0.8
0.6
0.4
0.2
0
4980 4990 5000 5010 5020 5030 5040 5050 5060 5070 5080 5090
order #67
5050 5060 5070 5080 5090 5100 5110 5120 5130 5140 5150 5160
order #66
5120 5140 5160 5180 5200 5220 5240
order #65
5200 5220 5240 5260 5280 5300 5320
order #64
5280 5300 5320 5340 5360 5380 5400 5420
order #63
5360 5380 5400 5420 5440 5460 5480 5500
order #62
5460 5480 5500 5520 5540 5560 5580
order #61
5540 5560 5580 5600 5620 5640 5660 5680
order #60
5640 5660 5680 5700 5720 5740 5760 5780
order #59
5740 5760 5780 5800 5820 5840 5860

Fig. 12.1 cont.

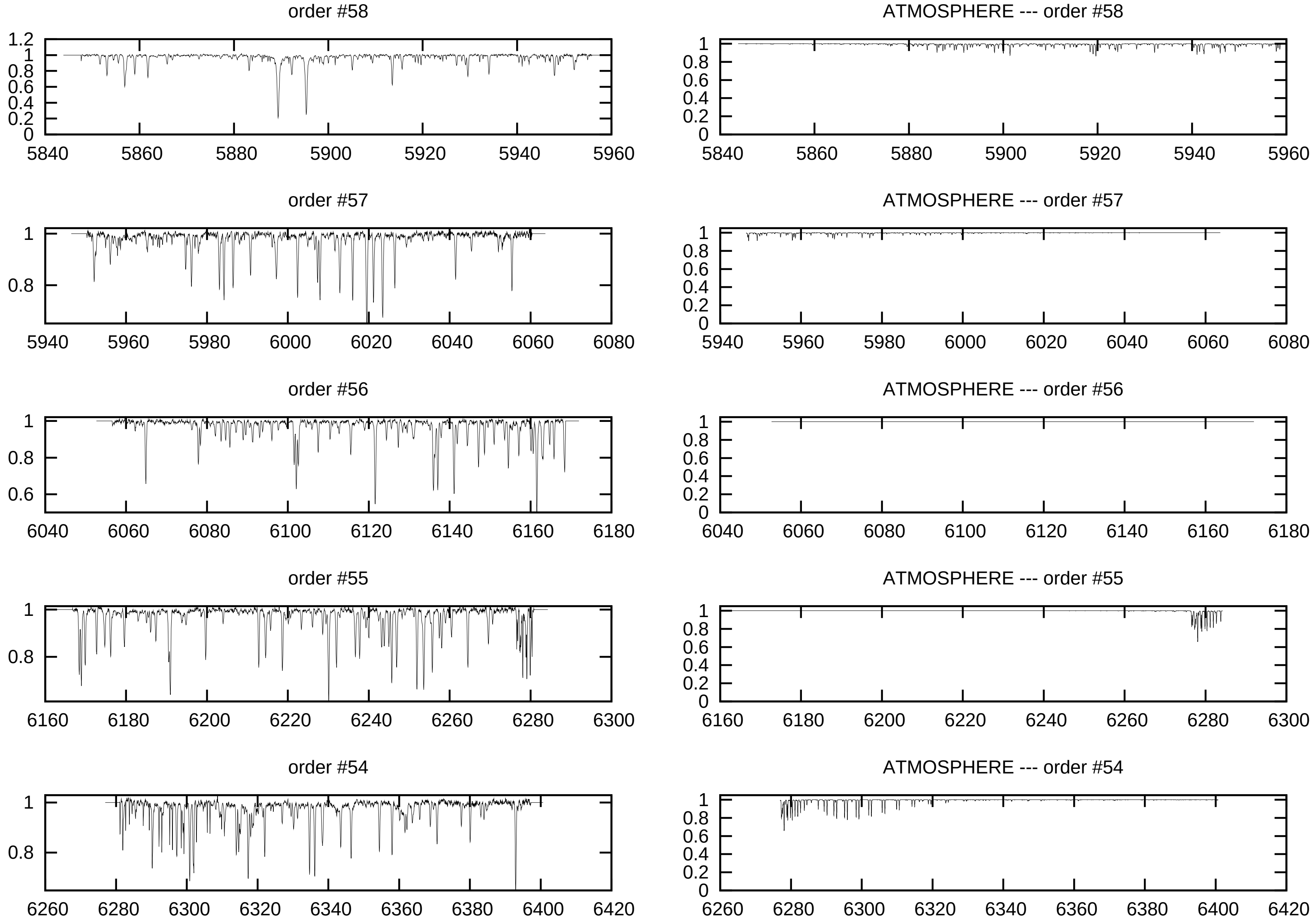
order #58

ATMOSPHERE --- order #58

order #57

ATMOSPHERE --- order #57

order #56

ATMOSPHERE --- order #56

order #55

ATMOSPHERE --- order #55

order #54

ATMOSPHERE --- order #54

Fig. 12.1 cont.

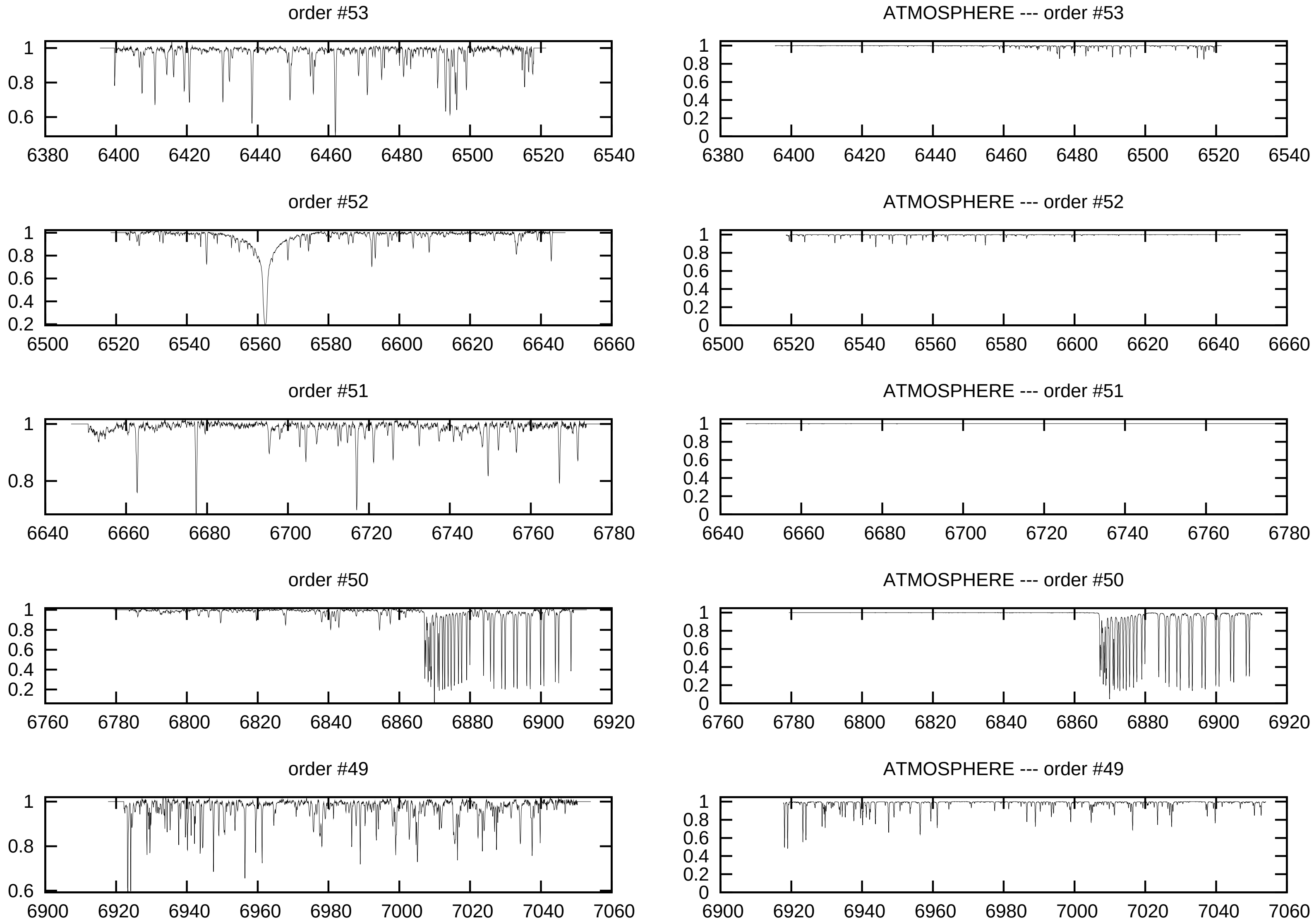
order #53
1
0.8
0.6
6380 6400 6420 6440 6460 6480 6500 6520 6540
ATMOSPHERE --- order #53
1 0.8 0.6 0.4 0.2 0
6380 6400 6420 6440 6460 6480 6500 6520 6540
order #52
1 0.8 0.6 0.4 0.2
6500 6520 6540 6560 6580 6600 6620 6640 6660
ATMOSPHERE --- order #52
1 0.8 0.6 0.4 0.2 0
6500 6520 6540 6560 6580 6600 6620 6640 6660
order #51
1
0.8
6640 6660 6680 6700 6720 6740 6760 6780
ATMOSPHERE --- order #51
1 0.8 0.6 0.4 0.2 0
6640 6660 6680 6700 6720 6740 6760 6780
order #50
1 0.8 0.6 0.4 0.2
6760 6780 6800 6820 6840 6860 6880 6900 6920
ATMOSPHERE --- order #50
1 0.8 0.6 0.4 0.2 0
6760 6780 6800 6820 6840 6860 6880 6900 6920
order #49
1
0.8
0.6
6900 6920 6940 6960 6980 7000 7020 7040 7060
ATMOSPHERE --- order #49
1 0.8 0.6 0.4 0.2 0
6900 6920 6940 6960 6980 7000 7020 7040 7060

Fig. 12.1 cont.

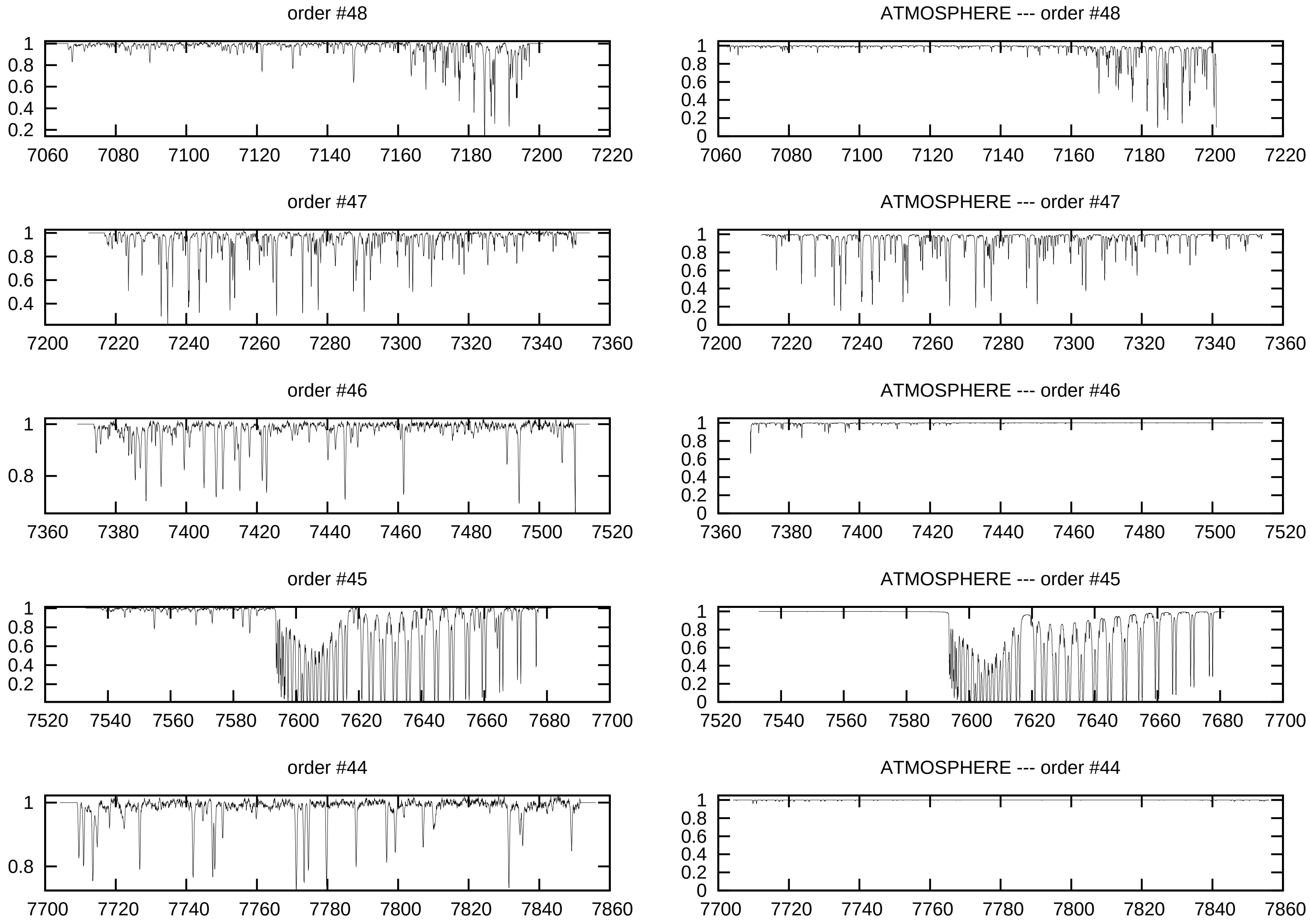
order #48
1
0.8
0.6
0.4
0.2
7060 7080 7100 7120 7140 7160 7180 7200 7220
ATMOSPHERE --- order #48
1
0.8
0.6
0.4
0.2
0
7060 7080 7100 7120 7140 7160 7180 7200 7220
order #47
1
0.8
0.6
0.4
7200 7220 7240 7260 7280 7300 7320 7340 7360
ATMOSPHERE --- order #47
1
0.8
0.6
0.4
0.2
0
7200 7220 7240 7260 7280 7300 7320 7340 7360
order #46
1
0.8
7360 7380 7400 7420 7440 7460 7480 7500 7520
ATMOSPHERE --- order #46
1
0.8
0.6
0.4
0.2
0
7360 7380 7400 7420 7440 7460 7480 7500 7520
order #45
1
0.8
0.6
0.4
0.2
7520 7540 7560 7580 7600 7620 7640 7660 7680 7700
ATMOSPHERE --- order #45
1
0.8
0.6
0.4
0.2
0
7520 7540 7560 7580 7600 7620 7640 7660 7680 7700
order #44
1
0.8
7700 7720 7740 7760 7780 7800 7820 7840 7860
ATMOSPHERE --- order #44
1
0.8
0.6
0.4
0.2
0
7700 7720 7740 7760 7780 7800 7820 7840 7860

Fig. 12.1 cont.

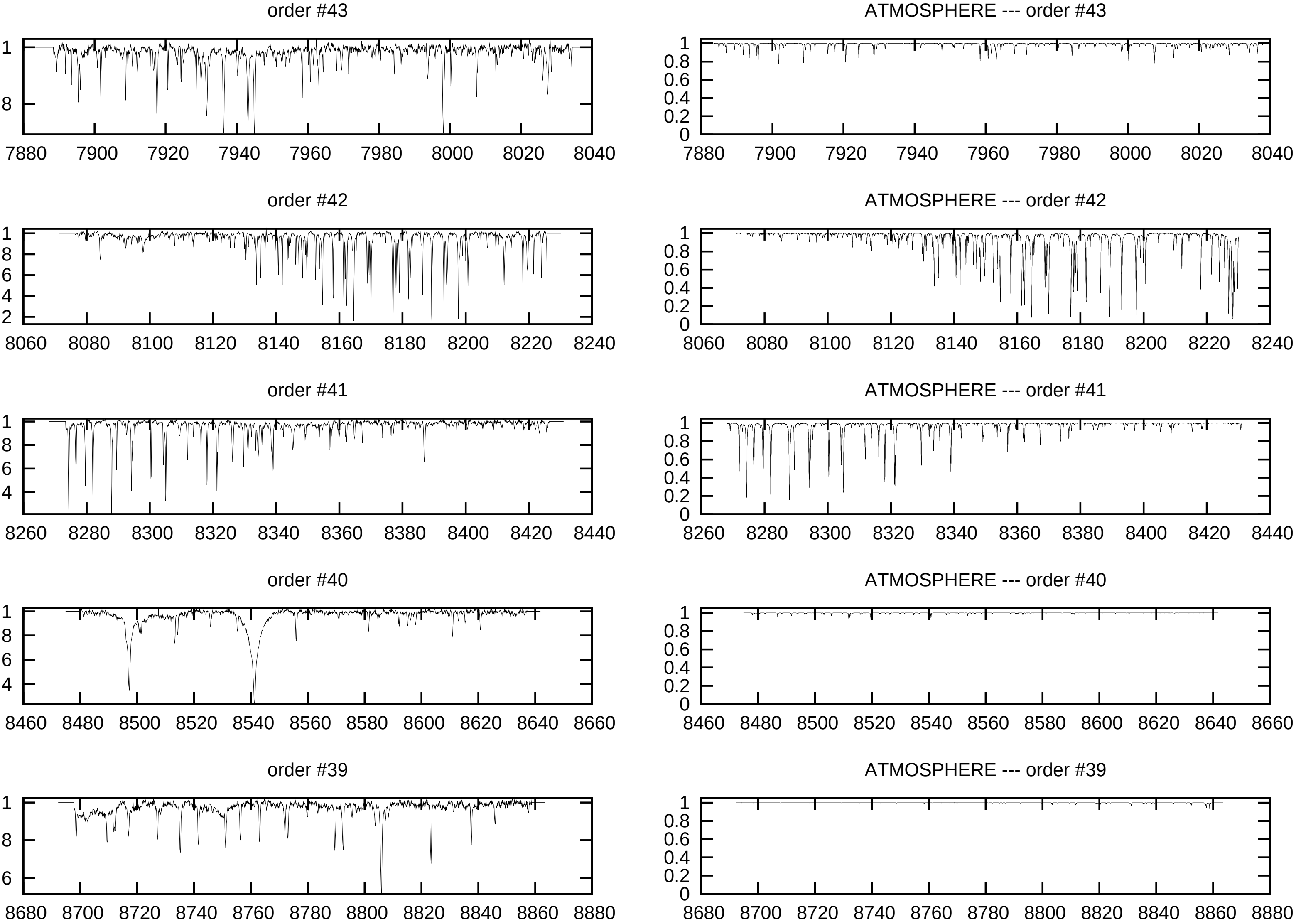
order #43
1
0.8
7880 7900 7920 7940 7960 7980 8000 8020 8040
ATMOSPHERE --- order #43
1 0.8 0.6 0.4 0.2 0
7880 7900 7920 7940 7960 7980 8000 8020 8040
order #42
1 0.8 0.6 0.4 0.2
8060 8080 8100 8120 8140 8160 8180 8200 8220 8240
ATMOSPHERE --- order #42
1 0.8 0.6 0.4 0.2 0
8060 8080 8100 8120 8140 8160 8180 8200 8220 8240
order #41
1 0.8 0.6 0.4
8260 8280 8300 8320 8340 8360 8380 8400 8420 8440
ATMOSPHERE --- order #41
1 0.8 0.6 0.4 0.2 0
8260 8280 8300 8320 8340 8360 8380 8400 8420 8440
order #40
1 0.8 0.6 0.4
8460 8480 8500 8520 8540 8560 8580 8600 8620 8640 8660
ATMOSPHERE --- order #40
1 0.8 0.6 0.4 0.2 0
8460 8480 8500 8520 8540 8560 8580 8600 8620 8640 8660
order #39
1 0.8 0.6
8680 8700 8720 8740 8760 8780 8800 8820 8840 8860 8880
ATMOSPHERE --- order #39
1 0.8 0.6 0.4 0.2 0
8680 8700 8720 8740 8760 8780 8800 8820 8840 8860 8880

Fig. 12.1 cont.

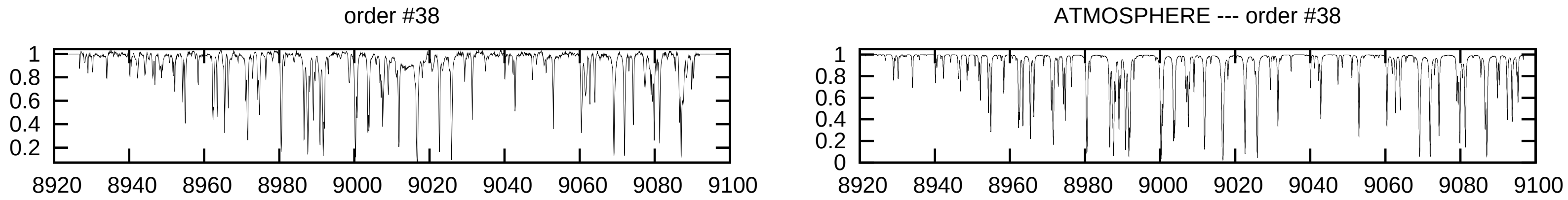
order #38
1
0.8
0.6
0.4
0.2
8920
8940
8960
8980
9000
9020
9040
9060
9080
9100
ATMOSPHERE --- order #38
1
0.8
0.6
0.4
0.2
0
8920
8940
8960
8980
9000
9020
9040
9060
9080
9100

Fig. 12.1 cont.

Notes on using the Nyogel OCK-451 couplant

- use the "LP" version, meaning Long Pot-life. This has a blocking for the catalyst, which prevents curing for a longer time, but when this blocking material dissolves the curing happens faster. Also, with this blocking more catalyst could be mixed in the components, so the gel cures more likely
- as the amount of catalyst is very small, therefore one should mix it very well. Use the static mixer they provide, and do not try to save material. Mix more than you need, so it's closer to the desired 50-50 (see blow) ratio. Stir it with hand for at least 4-5 minutes, or use a speed mixer, than SLOWLY outgas it, and use
- the 50%–50% ratio is critical when mixing the two components, you must be within 4%. Even within that limit the following applies:

  more part A makes the final product harder, but it cures slow and might not cure fully

  more part B makes it softer after it's cured, but it'll cure more likely and faster

- temperature really helps, even just raising it to +30 – +35 °C makes curing a lot faster
- the gel does not, or VERY slowly cures in vacuum, so if applied in a very thin layer between large area lenses, than curing is slow, might take a week – during what the bonded lenses have to be laid down flat
- when apply, use at least 25–50% more in volume, and let it overflow – rather than having not enough in there and so when the lenses put together there is a gel–free annulus at the edge of the lens
- if that empty annulus happens, wait a bit, because it might go away, especially if the gap is tiny (0.1 mm or so). The lens will sit better by time, by its own weight, squeezing more material out and pushing the edge of the gel to the edge of the lens
- it is very important to level the working surface, otherwise the gel will run to the edge sooner on the side which is lower, overflow there and therefore withdraw some of the gel on that side, so on the other it might be not enough to completely full the clear aperture
- put the concave surface on the bottom, with the CC surface facing up as a dish, pour the gel into that one, and lover the convex lens from the top, very slowly and evenly. Support the lowered lens on three points, so it can not be cocked/tilted suddenly, which will make the gel splash out
- to avoid bubbles/air traps, put one drop of the gel on the lens which is lowered, so that drop will make the contact with the gel first, and then the edge can spread slowly while lowering the upper lens slowly.

- use latex free gloves, nothing should touch the gel components or the mixed gel. Mix it in a clean glass pot, use metal mixers, do it on a clean bench. Cover it with other glass pot while outgasing/transferring from one table to other
- if lens is RTV mounted into bezel, gel should not touch RTV. RTV will remove the catalyst, so gel in touch with RTV will not cure
- clean everything with acetone, if something goes wrong, acetone will get the gel off. Soak lens in acetone if possible, use cloth wipes to get it off from surface
- if gel applied on CaF2 watch out for evaporative cooling of the lens while cleaning with acetone - that can break the lens in an extreme case. If acetone–bath is applied to CaF2 lens to clean gel, make sure bath has room temperature, and put cloth wipe on CaF2 lens surface IMMEDIATELY after it is removed from acetone bath, to decrease evaporative cooling effect.
- always make at least 2 witness samples, with the exact same spacing using microscope slides, and treat those exactly the same (same temperature, lay those flat as well, clean them the same way, etc.)
- try to check the real lens after curing, engage a tiny needle into the gel between the two lenses (outside of clear aperture) if possible. When removing needle it should not pull a string of gel with it, otherwise the gel is not fully cured.
- after curing, leave the lens in vertical position for a while and check for any signs of flow. If it happens and separation can not be done, soak the assembled lens in warm acetone for a few days (at ∼40 °C). It will ruin the RTV if that was used, but at least will get get the lenses apart.

Table 12.2. Members of NGC 2264 — *full table*

2MASS_id	ID	J	$(J-H)$	$(H-K)$	$[3.6-4.5]$	$[5.8-8.0]$	V_{rad}	ΔV_{rad}	R	S	EW_c	$FW_{10\%}$	$H\alpha$	Notes	NOB
0639037+094023	F3-ap50	12.65	1.10	0.35	0.00	0.00	20.42	0.37	19.4	0.67	15.5	482	C	—	1
0639156+093913	F2-ap73	13.26	0.56	0.11	0.00	0.00	15.98	1.30	6.0	0.27	0.0	0	AEF	—	1
0639157+092929	F4-ap43	11.67	0.93	0.24	0.00	0.00	33.88	0.14	32.1	0.83	0.0	0	A	—	1
0639170+095815	F3-ap79	12.43	0.53	0.17	0.00	0.00	13.74	0.56	11.3	0.48	0.0	0	AEF	—	1
0639227+091704	F1-ap24	11.13	0.33	0.14	0.00	0.00	25.09	5.04	3.2	0.18	0.0	0	AEF	—	1
0639227+095431	F4-ap90	14.25	0.95	0.35	0.00	0.00	18.88	1.23	4.1	0.17	76.6	310	C	—	1
0639229+093617	F2-ap76	12.62	0.64	0.14	0.00	0.00	14.63	0.20	25.8	0.79	0.0	0	AE	—	1
0639246+092233	F4-ap37	12.79	0.53	0.12	0.00	0.00	18.28	0.20	20.5	0.71	0.0	0	AE	—	1
0639248+093627	F3-ap35	16.23	0.71	0.38	0.00	0.00	13.38	0.97	3.2	0.13	0.0	0	N	—	1
0639263+094111	F4-ap72	12.71	0.82	0.23	0.00	0.00	16.46	0.39	19.7	0.68	0.9	126	W	—	1
0639266+093038	F4-ap52	15.50	0.91	0.25	0.00	0.00	30.14	0.98	4.6	0.20	0.0	0	N	—	1
0639276+092309	F1-ap25	11.03	1.22	0.31	0.00	0.00	34.54	0.15	30.2	0.80	0.0	0	A	—	1
0639279+092839	F1-ap35	10.81	0.74	0.20	0.00	0.00	13.27	0.17	28.2	0.80	0.0	0	AE	—	1
0639289+093752	F2-ap77	15.93	0.46	-0.20	0.00	0.00	13.47	1.66	2.7	0.10	0.0	0	N	—	1
0639294+092059	F4-ap34	12.20	0.53	0.12	0.00	0.00	25.42	0.15	28.7	0.83	0.0	0	AE	—	1
0639304+093337	F1-ap46	12.93	0.83	0.14	0.00	0.00	21.50	1.86	7.4	0.31	1.3	176	W	—	1
0639306+092523	F1-ap32	16.49	0.87	0.21	0.00	0.00	13.31	0.84	2.6	0.10	0.0	0	N	—	1
0639329+093644	F3-ap39	15.01	0.91	0.27	0.00	0.00	11.66	2.99	2.5	0.12	0.0	0	W-	—	1
0639330+095629	F2-ap105	13.16	0.59	0.13	0.00	0.00	24.17	0.17	27.6	0.78	0.0	0	AE	—	2
0639334+094729	F1-ap74	13.36	0.61	0.20	0.00	0.00	35.77	1.20	3.7	0.16	0.0	0	AE	—	1
0639334+095202	F2-ap104	12.63	0.97	0.24	0.00	0.00	18.94	0.83	11.2	0.44	15.2	301	C	—	1
0639336+095141	F3-ap67	13.71	0.60	0.30	0.00	0.00	25.90	0.92	4.9	0.22	0.0	0	AE	—	2
0639340+094921	F1-ap79	13.04	0.94	0.17	0.00	0.00	20.45	0.55	9.6	0.40	11.3	237	C	—	1
0639343+094645	F2-ap97	13.25	0.72	0.27	0.00	0.00	19.41	3.16	3.6	0.17	0.0	0	AE	RDB	2
0639344+095451	F2-ap109	12.99	1.06	0.28	0.00	0.00	19.85	0.48	13.7	0.51	25.7	409	C	—	1
0639349+093336	F2-ap70	15.86	0.92	0.32	0.00	0.00	16.83	1.26	2.5	0.11	0.0	0	AE	—	1
0639353+093232	F4-ap56	13.21	0.58	0.14	0.00	0.00	28.38	4.45	3.6	0.17	0.0	0	AE	—	1
0639360+092426	F4-ap35	11.85	0.81	0.15	0.00	0.00	13.90	0.14	32.5	0.81	0.0	0	AE	—	1
0639384+094236	F3-ap47	15.40	1.03	0.23	0.00	0.00	14.10	1.72	2.2	0.10	0.0	0	AE	—	1
0639388+095152	F3-ap65	12.47	0.63	0.23	0.00	0.00	12.73	1.26	3.9	0.19	0.0	0	AE	—	1
0639393+095600	F2-ap101	12.79	0.89	0.24	0.00	0.00	19.35	1.89	8.6	0.34	1.9	163	W	—	1
0639394+094522	F3-ap56	12.90	1.36	0.50	0.00	0.00	19.24	0.37	19.9	0.68	22.8	454	C	—	1
0639403+091822	F2-ap33	14.95	1.34	0.54	0.00	0.00	-119.95	1.26	2.9	0.11	157.5	489	C	hsb	1
0639415+094620	F3-ap57	12.57	0.87	0.22	0.00	0.00	19.46	1.14	9.4	0.47	31.2	565	C	—	1
0639416+093441	F1-ap48	11.81	0.50	0.09	0.00	0.00	15.99	1.10	11.2	0.50	0.0	0	AE	—	1
0639431+092602	F3-ap11	11.96	0.36	0.16	0.00	0.00	14.82	4.35	2.3	0.13	0.0	0	AEF	—	1
0639463+094820	F0-ap37	11.75	1.08	0.25	0.00	0.00	14.66	0.22	20.7	0.69	0.0	0	AE	—	2
0639467+094054	F1-ap62	12.02	0.67	0.15	-0.03	0.00	20.23	1.04	11.7	0.49	0.0	0	N	—	1
0639482+095906	F2-ap119	10.63	0.96	0.24	-0.18	0.13	27.08	0.14	33.8	0.83	0.0	0	A	—	1
0639496+093322	F1-ap42	13.04	0.80	0.20	-0.28	—	15.35	0.56	12.4	0.48	0.0	0	W-	—	1
0639498+095622	F4-ap99	10.45	1.50	0.42	-0.09	0.10	25.88	0.15	31.5	0.82	0.0	0	AE	—	2
0639503+100814	F3-ap100	15.29	0.98	0.38	0.00	0.00	—	—	2.5	0.11	14.0	405	C	hsb	1
0639511+093633	F1-ap52	14.10	1.02	0.27	0.03	-0.05	38.65	1.41	2.7	0.11	0.0	0	W-	—	1

Table 12.2 (cont'd)

2MASS_id	ID	J	$(J-H)$	$(H-K)$	[3.6 – 4.5]	[5.8 – 8.0]	V_{rad}	ΔV_{rad}	R	S	EW_c	$FW_{10\%}$	$H\alpha$	Notes	NOB
0639523+091909	F2-ap40	11.77	1.10	0.29	-0.15	0.01	28.76	0.18	25.8	0.75	0.0	0	AE	—	1
0639556+094732	F4-ap83	12.56	0.89	0.28	0.01	0.11	-9.08	1.34	9.4	0.40	4.6	134	W	hsb	2
0639562+093046	F2-ap58	12.60	0.28	0.03	-0.02	0.12	22.32	0.63	13.7	0.55	0.0	0	AE	—	1
0639564+094332	F2-ap95	13.04	0.38	0.09	-0.07	0.03	33.77	0.23	19.6	0.73	0.0	0	AE	—	1
0639568+094425	F3-ap52	9.84	1.04	0.32	-0.11	0.03	20.85	0.13	35.6	0.84	0.0	0	AE	—	2
0639579+094105	F2-ap83	14.37	1.01	0.30	0.18	—	16.55	2.07	2.7	0.12	55.8	500	C	hsb	1
0639592+092725	F3-ap19	13.23	1.16	0.39	0.05	0.55	19.99	0.68	11.0	0.51	40.0	658	C	—	1
0639592+100608	F3-ap97	13.91	1.81	0.69	0.73	0.66	9.93	14.13	0.0	0.12	36.0	548	C	hsb	1
0640004+094712	F4-ap92	17.33	2.26	0.52	0.04	—	—	—	2.5	0.10	0.0	0	W-	—	1
0640011+093534	F2-ap65	13.89	0.98	0.26	-0.05	0.09	16.77	0.57	9.1	0.37	6.1	225	W	—	1
0640012+094236	F1-ap65	14.45	1.01	0.28	-0.09	0.26	15.05	1.42	3.0	0.12	0.0	0	N	—	1
0640013+094301	F1-ap63	15.00	3.06	1.23	0.97	0.98	—	—	2.4	0.10	105.2	438	C	—	1
0640014+093106	F2-ap52	12.12	1.03	0.26	-0.06	0.07	18.24	0.15	29.1	0.79	0.0	0	AE	—	1
0640027+091820	F4-ap13	12.24	0.40	0.07	-0.23	0.00	16.51	0.23	22.4	0.73	0.0	0	AE	—	1
0640027+093524	F4-ap70	13.70	0.99	0.28	0.00	0.00	17.06	1.09	6.1	0.25	19.7	312	C	—	1
0640040+092243	F2-ap36	10.12	0.17	0.06	-0.19	-0.08	26.62	1.73	4.4	0.24	0.0	0	AEF	—	1
0640052+095057	F1-ap87	13.19	0.93	0.22	-0.10	0.34	13.60	2.54	3.8	0.15	4.0	197	W	—	1
0640055+092226	F4-ap22	13.95	1.22	0.39	0.14	0.68	16.34	0.68	8.0	0.35	41.4	426	C	—	1
0640057+093549	F4-ap65	10.15	0.36	0.08	0.00	0.00	22.24	2.99	7.2	0.38	0.0	0	A	—	1
0640060+094943	F4-ap97	13.46	1.01	0.31	0.19	0.82	23.07	0.64	10.8	0.45	5.4	374	C	—	1
0640064+093934	F4-ap82	12.56	0.84	0.19	0.00	0.00	16.20	0.25	24.8	0.77	1.3	139	W	—	2
0640067+092033	F4-ap15	15.77	1.06	0.22	-0.02	0.00	12.30	1.10	3.9	0.17	0.0	0	N	—	1
0640085+094414	F1-ap77	12.95	0.91	0.19	-0.04	0.10	31.57	1.39	2.7	0.11	0.0	0	N	—	1
0640103+093855	F2-ap87	12.28	0.84	0.17	0.03	0.04	22.69	0.59	17.7	0.61	1.3	297	W	sb	2
0640103+095009	F3-ap80	16.59	1.72	0.41	0.05	0.00	11.04	1.00	2.6	0.10	0.0	0	N	—	1
0640108+095809	F2-ap124	16.19	0.82	0.38	0.03	0.00	12.10	0.95	2.9	0.13	0.0	0	N	—	1
0640109+094007	F2-ap98	14.33	0.90	0.20	-0.03	—	15.85	0.82	6.5	0.25	0.0	0	W+	—	1
0640111+093806	F4-ap71	12.96	1.34	0.50	0.17	0.75	21.12	0.90	6.2	0.30	46.3	635	C	—	1
0640120+101146	F3-ap104	14.22	0.88	0.24	0.00	0.00	15.06	3.01	3.2	0.13	0.0	0	W-	—	1
0640124+094423	F1-ap73	12.84	0.90	0.19	0.02	—	21.99	1.58	5.7	0.24	0.0	0	W+	—	1
0640126+100540	F2-ap129	12.51	1.11	0.39	0.18	0.58	22.26	0.21	25.9	0.74	13.2	284	C	—	1
0640128+091738	F1-ap5	16.14	1.09	0.26	0.01	0.00	—	—	2.3	0.10	0.0	0	W-	—	1
0640134+091928	F4-ap18	13.71	0.71	0.18	-0.07	-0.07	9.21	0.24	19.4	0.72	0.0	0	AE	—	1
0640134+100549	F1-ap102	14.41	1.20	0.35	0.31	0.60	—	—	2.6	0.10	15.6	241	W	hsb	1
0640136+092449	F4-ap24	11.19	0.65	0.16	-0.05	0.08	21.85	2.65	8.9	0.43	0.5	336	CW	—	1
0640137+095631	F2-ap126	12.92	1.34	0.55	0.60	1.19	23.55	0.93	6.1	0.29	110.1	492	C	—	1
0640140+092029	F4-ap20	11.93	0.60	0.14	-0.08	0.11	33.27	5.25	6.3	0.32	0.0	0	AE	—	1
0640142+093428	F2-ap57	13.75	1.17	0.38	0.29	0.79	17.04	0.85	6.5	0.25	0.0	0	W	—	1
0640152+100158	F3-ap91	14.55	2.19	0.90	0.00	0.00	16.56	1.49	5.5	0.22	7.8	339	CW	—	1
0640154+094242	F1-ap76	14.65	0.74	0.11	0.00	0.00	26.47	0.91	4.8	0.21	0.0	0	AE	—	2
0640167+094023	F4-ap87	15.21	0.85	0.28	0.12	—	—	—	2.2	0.09	33.4	278	CW	hsb	1
0640172+101335	F3-ap108	12.88	0.96	0.27	0.00	0.00	27.66	3.85	5.5	0.22	5.9	273	CW	—	1
0640176+092157	F3-ap4	16.15	0.73	0.01	-0.04	0.00	10.45	0.94	3.3	0.14	0.0	0	N	—	1

Table 12.2 (cont'd)

2MASS_id	ID	J	$(J-H)$	$(H-K)$	[3.6 – 4.5]	[5.8 – 8.0]	V_{rad}	ΔV_{rad}	R	S	EW_c	$FW_{10\%}$	$H\alpha$	Notes	NOB
0640185+095206	F2-ap128	14.55	0.90	0.24	0.03	—	29.89	0.95	2.3	0.10	0.0	0	W-	—	1
0640186+100025	F4-ap110	14.43	1.73	0.68	0.52	—	74.19	1.31	2.6	0.11	117.8	393	C	hsb	1
0640187+093701	F3-ap15	13.74	2.23	0.83	0.29	0.63	13.78	1.54	3.6	0.16	23.7	306	C	—	1
0640192+093935	F2-ap99	14.96	1.09	0.34	0.27	0.82	77.69	1.34	2.2	0.10	39.0	386	C	hsb	1
0640193+094830	F3-ap76	12.81	0.93	0.18	-0.06	-0.26	25.74	2.04	8.3	0.35	2.0	231	W	—	2
0640203+095606	F4-ap108	12.30	1.09	0.31	0.29	0.91	24.26	1.54	6.9	0.32	37.8	369	C	sb	2
0640207+093340	F3-ap1	16.71	1.54	0.74	0.10	0.00	14.33	0.94	3.3	0.14	0.0	0	N	—	1
0640210+093632	F2-ap72	11.62	0.60	0.14	-0.12	0.12	26.41	2.76	9.9	0.40	0.3	146	W	udb	1
0640212+095902	F2-ap125	13.98	0.79	0.19	0.00	0.00	23.89	1.35	4.2	0.18	0.0	0	AE	—	2
0640217+094823	F1-ap96	15.05	1.56	0.47	0.16	0.80	16.20	1.12	2.4	0.09	22.3	269	C	—	1
0640222+095429	F2-ap127	12.29	0.98	0.25	-0.02	0.00	21.48	1.28	11.7	0.47	1.5	151	W+	—	2
0640231+092742	F4-ap26	13.15	1.38	0.54	0.26	0.54	17.77	1.57	6.0	0.30	60.1	567	C	—	1
0640234+095456	F3-ap95	14.01	1.04	0.38	0.25	0.40	23.39	1.53	3.4	0.15	11.9	197	W	—	1
0640235+092637	F3-ap2	13.96	1.52	0.48	-0.02	-0.07	10.44	1.45	2.7	0.11	0.0	0	N	—	1
0640237+095524	F2-ap123	13.12	1.31	0.45	0.41	0.72	25.29	0.49	8.7	0.32	116.6	218	C	—	1
0640242+093412	F2-ap44	13.47	1.63	0.68	0.51	0.98	17.05	0.80	9.0	0.36	43.7	566	C	—	1
0640248+095311	F3-ap99	13.59	1.06	0.28	-0.01	0.21	27.87	1.34	7.1	0.30	0.0	0	W	udb	1
0640255+094826	F3-ap75	13.24	0.80	0.16	0.00	0.00	24.20	0.78	14.6	0.53	0.0	0	W	—	1
0640255+095432	F4-ap109	14.50	1.63	0.64	0.54	1.01	14.85	11.54	0.0	0.11	0.0	0	W	hsb	1
0640256+100000	F1-ap108	13.93	1.27	0.48	0.24	0.65	—	—	2.5	0.10	55.8	262	C	hsb	1
0640257+095836	F3-ap102	11.70	0.61	0.11	-0.08	0.12	20.51	0.20	28.7	0.78	0.0	0	A	—	1
0640259+095058	F3-ap85	13.85	1.25	0.48	0.20	0.69	11.09	1.29	2.8	0.12	92.6	382	C	hsb	1
0640263+093801	F3-ap18	11.97	0.94	0.18	-0.16	-0.19	8.98	0.99	13.6	0.56	1.8	216	W	hsb	2
0640268+093623	F2-ap55	17.63	2.66	0.57	-0.12	0.00	12.09	1.07	2.3	0.11	0.0	0	W-	—	1
0640276+095052	F1-ap91	15.21	1.70	0.74	0.47	-0.12	—	—	2.5	0.10	52.6	303	C	hsb	1
0640280+093458	F3-ap10	17.90	3.30	0.98	0.07	1.11	13.76	1.25	3.1	0.13	0.0	0	AE	—	1
0640286+093548	F2-ap46	12.79	0.94	0.22	-0.15	0.12	16.35	0.44	17.9	0.64	3.1	176	W	—	2
0640288+093100	F2-ap30	11.81	1.07	0.55	0.33	1.21	16.07	0.30	22.7	0.74	0.0	0	W	—	1
0640289+094217	F3-ap29	12.91	0.89	0.18	-0.15	0.19	20.89	0.41	20.9	0.69	1.2	166	W	—	1
0640289+093306	F0-ap237	13.66	0.89	0.19	-0.01	0.12	-7.26	2.54	2.4	0.13	4.4	188	W-	—	1
0640292+094407	F3-ap33	14.05	1.00	0.28	0.01	—	19.93	1.42	5.4	0.23	19.6	571	C	—	1
0640293+092611	F1-ap7	13.43	2.32	0.89	0.74	—	—	—	3.2	0.13	35.1	257	C	hsb	1
0640294+094737	F1-ap93	14.54	1.04	0.39	0.29	0.95	—	—	2.4	0.09	25.5	212	WC	hsb	1
0640297+095933	F1-ap109	11.58	0.97	0.23	0.00	0.00	21.27	0.17	26.0	0.75	0.0	0	AE	—	2
0640298+094221	F1-ap84	13.72	1.59	0.68	0.20	0.50	20.10	0.88	6.8	0.30	47.0	472	C	—	2
0640299+095010	F2-ap132	12.22	0.66	0.12	-0.16	0.11	24.92	0.14	33.4	0.83	0.0	0	AE	—	2
0640306+094611	F3-ap58	12.86	0.80	0.16	-0.10	-0.02	19.93	0.36	22.2	0.72	0.0	0	W-	—	1
0640306+095015	F3-ap96	12.75	1.57	0.49	0.14	0.53	22.77	1.04	5.8	0.24	13.0	405	C	—	1
0640308+094808	F3-ap82	14.71	1.06	0.41	0.23	-1.57	21.59	1.33	5.2	0.25	2.7	160	W	—	1
0640309+093441	F2-ap21	12.69	2.02	0.84	0.18	0.76	18.10	1.55	11.2	0.48	25.6	622	C	—	2
0640310+100625	F3-ap105	14.46	0.98	0.28	0.00	0.00	12.53	1.05	2.8	0.13	28.8	478	C	hsb	1
0640311+095211	F3-ap93	14.02	3.25	1.07	0.08	-0.19	12.56	1.03	3.1	0.13	0.0	0	N	—	1
0640313+094129	F1-ap71	10.19	1.63	0.39	-0.13	0.03	32.12	0.16	30.2	0.78	0.0	0	AE	—	2

Table 12.2 (cont'd)

2MASS_id	ID	J	$(J-H)$	$(H-K)$	[3.6 − 4.5]	[5.8 − 8.0]	V_{rad}	ΔV_{rad}	R	S	EW_c	$FW_{10\%}$	$H\alpha$	Notes	NOB
0640314+093011	F2-ap17	16.43	1.41	0.68	-0.07	0.00	12.74	1.52	2.7	0.11	0.0	0	N	—	1
0640316+094823	F2-ap134	13.02	0.83	0.17	0.05	0.68	18.08	0.95	11.2	0.53	74.5	559	C	—	1
0640320+094936	F1-ap104	13.76	1.19	0.44	0.32	0.93	106.87	1.12	3.0	0.12	373.1	446	C	hsb	1
0640322+095722	F4-ap103	14.75	0.99	0.28	0.24	0.79	18.56	1.19	3.3	0.13	31.1	241	CW	—	1
0640328+095129	F1-ap106	12.68	0.89	0.21	-0.01	-0.62	23.20	1.91	7.3	0.29	4.9	252	W	UDB	2
0640331+094955	F2-ap138	14.37	2.21	0.82	0.46	1.06	69.05	3.01	2.0	0.09	0.0	0	WC	hsb	1
0640336+093336	F4-ap77	14.41	0.94	0.26	0.05	-0.15	18.93	1.09	4.8	0.21	9.8	308	CW	—	1
0640340+100720	F3-ap101	15.31	1.20	0.41	0.00	0.00	—	—	2.1	0.09	146.6	407	C	hsb	1
0640343+093852	F1-ap67	13.17	0.54	0.07	-0.10	0.18	8.05	0.28	17.7	0.66	0.0	0	AE	—	1
0640345+093518	F1-ap30	13.55	1.02	0.29	0.13	0.45	15.12	0.87	5.6	0.22	8.3	279	C	—	1
0640363+091858	F1-ap231	12.71	0.89	0.22	-0.01	0.05	9.89	3.86	5.6	0.22	2.7	211	W	rdb	1
0640364+092245	F2-ap18	12.07	1.01	0.26	-0.08	0.08	26.93	0.18	25.9	0.75	0.0	0	AE	—	1
0640365+095046	F3-ap106	12.93	1.23	0.43	0.19	0.68	25.05	0.60	11.2	0.42	13.6	271	C	—	1
0640366+094823	F1-ap110	13.04	0.83	0.12	-0.10	-1.02	20.40	0.38	15.7	0.53	0.0	0	W-	—	1
0640367+092205	F4-ap233	12.38	1.00	0.25	-0.07	0.05	26.29	0.20	22.6	0.69	0.0	0	AE	—	1
0640367+095203	F3-ap110	12.73	1.63	0.66	0.54	0.94	20.63	0.96	7.3	0.30	77.5	486	C	—	2
0640372+093110	F2-ap12	13.33	0.99	0.21	-0.02	-0.04	20.35	0.74	10.3	0.42	0.0	0	W+	—	1
0640372+095310	F4-ap112	14.06	1.68	0.63	0.38	0.89	15.99	1.87	2.4	0.11	57.1	354	C	hsb	1
0640379+093454	F2-ap1	12.91	1.07	0.36	0.21	0.48	16.64	0.40	15.3	0.59	25.3	481	C	—	1
0640382+092952	F4-ap3	13.93	1.04	0.30	0.07	0.87	17.19	0.60	10.8	0.42	5.3	274	W	—	1
0640387+093657	F1-ap39	13.43	0.87	0.26	0.02	-0.18	20.52	2.75	2.8	0.13	0.0	0	W+	sb	2
0640388+092138	F4-ap235	13.69	0.67	0.18	-0.08	-0.11	19.48	0.22	22.5	0.74	0.0	0	AE	—	1
0640391+095059	F3-ap109	12.29	1.78	0.74	0.34	0.46	21.25	0.41	13.6	0.53	33.7	614	C	—	1
0640393+093446	F4-ap100	12.65	2.70	1.19	0.60	0.91	18.82	1.98	4.2	0.18	31.7	552	C	—	1
0640396+095100	F4-ap116	15.70	1.04	0.39	0.51	0.00	—	—	2.1	0.09	52.7	341	C	hsb	1
0640401+093503	F1-ap14	12.24	0.99	0.34	0.00	0.00	16.92	0.32	22.4	0.71	8.7	279	C	—	2
0640410+092754	F4-ap240	13.69	1.02	0.26	0.10	0.53	18.73	0.39	17.2	0.63	0.0	0	CW	—	1
0640410+094758	F1-ap103	13.13	0.96	0.26	-0.11	0.78	20.96	0.51	12.0	0.45	1.7	182	W	—	1
0640411+095257	F2-ap133	12.53	1.28	0.52	0.29	0.66	20.00	0.26	23.6	0.73	14.2	228	C	—	1
0640411+093358	F1-ap8	13.12	1.67	0.80	0.48	0.00	—	—	1.7	0.12	149.6	528	C	hsb	1
0640413+095102	F4-ap118	12.81	1.09	0.31	0.23	0.77	24.58	0.73	10.9	0.49	41.4	535	C	—	1
0640413+094919	F3-ap116	15.02	1.37	0.62	0.23	—	—	—	2.9	0.11	71.5	394	C	—	1
0640414+094810	F0-ap26	12.81	0.84	0.19	-0.09	—	19.96	2.00	4.1	0.26	0.0	0	W+	—	1
0640414+095414	F1-ap112	11.64	1.21	0.52	0.00	0.00	27.40	1.19	10.5	0.47	10.4	430	C	—	2
0640418+094952	F1-ap101	13.17	0.84	0.19	0.03	0.25	28.65	5.07	4.2	0.17	2.9	250	W+	sb	2
0640419+094355	F3-ap6	14.68	1.10	0.26	0.08	0.63	14.00	1.66	2.7	0.13	0.6	74	W	hsb	1
0640421+093142	F4-ap236	16.64	1.74	0.66	0.02	—	—	—	2.6	0.11	0.0	0	W-	—	1
0640422+093337	F3-ap240	10.76	0.92	0.43	0.28	0.76	19.81	2.30	7.9	0.41	9.2	423	C	—	1
0640422+094011	F1-ap99	12.87	1.06	0.34	0.13	0.61	19.95	0.65	11.2	0.48	66.5	463	C	—	1
0640424+093221	F1-ap233	13.23	0.71	0.12	-0.05	0.69	17.48	0.31	18.7	0.60	0.0	0	W-	—	1
0640428+093335	F4-ap106	13.87	1.20	0.33	0.18	0.29	15.68	0.53	13.0	0.48	6.8	203	W	—	1
0640432+093115	F2-ap2	13.49	0.92	0.26	0.00	0.00	19.58	0.76	6.8	0.29	24.0	320	C	—	1
0640432+094707	F3-ap9	12.79	1.16	0.45	0.17	—	16.67	0.39	18.3	0.67	28.5	511	C	—	1

Table 12.2 (cont'd)

2MASS_id	ID	J	$(J-H)$	$(H-K)$	[3.6 – 4.5]	[5.8 – 8.0]	V_{rad}	ΔV_{rad}	R	S	EW_c	$FW_{10\%}$	$H\alpha$	Notes	NOE
0640434+092841	F3-ap238	13.23	0.88	0.15	0.02	0.53	16.18	0.36	18.6	0.65	7.2	322	CW	—	1
0640434+095100	F3-ap120	12.57	0.84	0.23	0.00	0.00	21.66	0.30	23.7	0.72	0.0	0	W+	—	2
0640436+093511	F1-ap2	14.82	0.94	0.15	-0.06	0.00	—	—	2.9	0.11	0.0	0	W-	—	1
0640436+094707	F4-ap120	14.10	1.69	0.68	0.31	-0.27	148.34	3.30	2.8	0.11	41.9	414	C	hsb	1
0640441+092355	F1-ap237	13.16	0.75	0.15	-0.20	-0.14	11.83	1.87	7.6	0.30	0.0	0	W-	—	1
0640446+093226	F1-ap235	14.05	1.07	0.36	0.04	0.08	—	—	2.1	0.10	37.8	328	C	hsb	1
0640446+094802	F1-ap114	11.44	2.11	1.12	0.68	1.84	—	—	3.3	0.24	58.4	518	C	hsb	1
0640449+095744	F3-ap117	12.26	0.84	0.14	-0.11	0.18	15.27	0.20	30.4	0.79	0.0	0	W	sb	2
0640450+094542	F3-ap168	13.11	0.86	0.16	-0.02	0.00	21.74	0.76	14.4	0.52	3.0	165	W	—	2
0640452+092844	F3-ap236	12.39	1.04	0.32	0.00	0.00	19.95	1.68	9.4	0.45	32.5	575	C	—	1
0640452+101421	F3-ap119	15.21	1.36	0.33	0.00	0.00	12.90	1.11	3.1	0.13	40.3	484	C	—	1
0640455+095123	F2-ap131	12.01	1.64	0.47	-0.07	0.11	21.94	0.37	12.6	0.49	0.4	76	AE	—	2
0640459+093844	F1-ap86	13.22	0.88	0.27	-0.15	0.13	—	—	2.3	0.09	0.0	0	W-	hsb	1
0640460+091758	F4-ap232	13.40	0.88	0.18	-0.02	0.30	15.85	0.44	12.6	0.49	22.9	383	C	—	1
0640461+094917	F1-ap116	10.15	0.60	0.09	-0.10	0.09	26.08	3.73	9.0	0.38	0.0	0	W	RDB,V642Mon	2
0640465+095946	F4-ap119	13.40	0.89	0.21	-0.07	-0.11	24.90	2.52	7.1	0.29	0.0	0	W-	UDB	2
0640466+092141	F4-ap223	10.75	1.16	0.34	0.13	—	27.85	0.28	25.4	0.68	0.0	0	AE	—	1
0640467+095425	F4-ap117	12.21	0.93	0.23	-0.08	0.12	19.75	0.36	18.0	0.68	1.5	142	W	—	2
0640467+094001	F3-ap232	15.38	0.85	0.32	0.10	—	—	—	2.9	0.14	45.4	583	C	hsb	1
0640468+092554	F2-ap6	12.26	0.74	0.23	0.00	0.03	11.23	1.74	2.3	0.11	0.0	0	AEF	—	1
0640470+095241	F3-ap111	14.75	1.34	0.64	0.00	0.00	-113.04	1.08	2.2	0.10	83.4	350	C	hsb	1
0640471+091833	F1-ap238	12.92	0.54	0.19	-0.03	0.03	29.82	1.24	3.9	0.16	0.0	0	AE	—	1
0640471+093240	F1-ap239	12.77	1.08	0.31	0.25	0.70	18.56	0.60	11.1	0.43	51.5	423	C	sb	2
0640471+094208	F2-ap158	13.86	1.02	0.23	0.16	0.67	18.75	1.03	7.5	0.30	17.0	519	C	—	1
0640475+094929	F4-ap113	11.53	1.51	0.66	0.09	0.76	26.06	0.99	14.2	0.56	10.2	410	C	—	1
0640477+095718	F3-ap113	14.97	0.84	0.13	0.22	0.81	—	—	2.9	0.12	6.4	248	WC	—	1
0640481+095339	F4-ap115	13.50	0.77	0.17	-0.11	-0.07	23.73	0.38	19.2	0.66	0.0	0	W-	—	1
0640483+093639	F4-ap125	12.92	0.97	0.22	-0.17	0.05	24.04	3.86	6.0	0.24	4.3	275	W	—	1
0640486+093558	F1-ap224	14.38	3.78	1.60	0.81	1.00	—	—	2.5	0.11	0.0	0	C	hsb	1
0640488+094326	F3-ap201	13.33	1.63	0.58	0.46	0.91	25.82	1.73	5.1	0.23	23.4	427	C	—	1
0640492+095739	F1-ap119	13.57	1.21	0.37	-0.02	0.18	27.18	1.00	4.0	0.16	32.9	248	C	—	1
0640492+094440	F3-ap207	14.85	2.79	1.22	0.58	0.83	113.29	1.03	2.5	0.10	19.8	290	C	hsb	1
0640493+092350	F1-ap236	13.04	1.00	0.26	0.03	0.23	17.26	0.56	11.4	0.44	32.6	463	C	—	1
0640494+095254	F3-ap124	15.83	3.12	1.42	0.52	1.02	23.53	1.60	5.9	0.27	30.4	518	C	—	1
0640498+094731	F0-ap18	12.28	0.85	0.28	0.14	1.16	0.90	0.82	6.6	0.31	0.0	0	W+	hsb	2
0640500+095113	F3-ap128	14.88	0.94	0.30	0.34	1.03	—	—	2.7	0.11	70.8	418	C	hsb	1
0640501+095228	F4-ap111	13.57	0.91	0.35	-0.03	0.21	18.28	1.54	4.1	0.18	0.0	0	W+	—	1
0640502+092002	F4-ap227	12.57	0.72	0.26	-0.10	0.03	13.05	3.96	3.0	0.16	0.0	0	AEF	—	1
0640502+093023	F3-ap221	16.85	2.17	0.66	0.40	—	12.88	1.29	2.7	0.13	0.0	0	N	—	1
0640506+095457	F1-ap117	12.47	1.19	0.41	0.08	0.43	20.84	0.55	13.0	0.52	32.0	465	C	—	1
0640508+095258	F2-ap142	15.18	1.23	0.51	0.35	0.76	—	—	2.4	0.10	0.0	0	W	hsb	1
0640511+095038	F3-ap134	14.51	1.19	0.52	0.00	0.00	15.10	1.74	2.6	0.11	31.2	260	C	hsb	1
0640512+094446	F2-ap154	10.74	1.08	0.57	0.29	0.54	24.57	3.88	6.4	0.34	1.3	410	C	—	2

Table 12.2 (cont'd)

2MASS_id	ID	J	$(J-H)$	$(H-K)$	[3.6 − 4.5]	[5.8 − 8.0]	V_{rad}	ΔV_{rad}	R	S	EW_c	$FW_{10\%}$	$H\alpha$	Notes	NOB
0640515+093714	F4-ap121	13.72	0.85	0.12	-0.03	-1.38	16.97	0.36	17.0	0.59	1.9	124	W	—	2
0640515+094324	F2-ap153	12.37	1.20	0.46	0.00	0.00	22.49	0.69	17.0	0.60	18.3	583	C	—	1
0640516+092845	F1-ap223	12.99	1.21	0.42	0.17	0.61	19.56	0.48	13.2	0.50	39.2	263	C	—	1
0640521+092914	F2-ap235	14.15	1.30	0.48	0.35	0.76	12.17	11.46	0.0	0.13	8.6	153	W	—	1
0640523+090721	F4-ap221	12.62	0.53	0.21	0.00	0.00	—	—	2.1	0.12	5.8	613	C	hsb	1
0640526+091923	F4-ap229	15.56	1.26	0.38	0.00	0.00	32.84	1.11	2.5	0.11	0.0	0	N	—	1
0640527+092844	F3-ap227	15.06	1.68	0.64	0.31	0.72	20.55	1.83	3.8	0.18	29.3	413	C	—	1
0640527+094421	F3-ap192	13.20	0.93	0.24	-0.02	-0.35	19.55	0.51	14.5	0.56	3.7	165	W	—	2
0640528+094300	F1-ap129	14.32	1.04	0.31	0.30	0.00	18.10	1.15	2.7	0.11	7.9	171	W	—	1
0640529+094454	F3-ap183	12.70	1.43	0.59	0.29	0.74	25.67	0.28	23.2	0.74	9.5	246	C	—	1
0640530+092626	F3-ap223	14.14	1.22	0.41	0.42	0.72	14.18	1.67	2.9	0.13	51.4	383	C	—	1
0640536+093325	F4-ap157	12.35	1.03	0.36	0.09	0.19	18.76	0.68	16.1	0.61	28.7	378	C	—	2
0640536+094704	F3-ap159	13.36	0.98	0.28	0.24	0.40	16.71	0.84	7.1	0.27	7.8	184	W	—	1
0640541+094843	F3-ap146	14.16	1.09	0.36	0.31	—	19.35	1.27	3.3	0.13	222.7	437	C	—	1
0640541+095225	F1-ap111	15.34	1.00	0.55	0.49	0.56	—	—	2.7	0.11	141.1	401	C	hsb	1
0640542+095552	F3-ap126	13.70	0.94	0.18	0.02	0.79	20.79	0.42	16.5	0.61	0.0	0	W+	—	2
0640543+094920	F2-ap147	13.10	1.30	0.48	0.42	1.18	23.87	0.67	9.5	0.41	125.5	431	C	—	1
0640549+095312	F3-ap125	13.92	1.52	0.69	0.49	0.82	—	—	2.8	0.11	31.3	329	C	—	1
0640553+093959	F1-ap147	13.68	1.10	0.37	0.30	0.88	—	—	2.4	0.10	37.4	207	C	hsb	1
0640554+093724	F2-ap192	12.70	0.90	0.22	-0.03	0.07	24.16	1.71	12.1	0.44	1.6	180	W+	—	1
0640556+093825	F4-ap136	14.12	1.07	0.35	0.13	0.26	23.66	1.10	3.5	0.14	4.9	203	W	—	1
0640557+094646	F3-ap162	13.94	1.04	0.39	0.11	0.42	16.57	1.16	4.8	0.20	15.3	551	C	—	1
0640557+095114	F3-ap137	12.87	0.86	0.18	0.27	1.19	15.55	0.48	16.9	0.65	4.3	200	W	sb	2
0640562+093631	F2-ap197	11.89	1.84	0.77	0.39	1.03	32.99	4.69	5.2	0.24	21.5	623	C	udb	1
0640562+093933	F1-ap157	13.22	1.46	0.56	0.00	0.00	13.38	9.00	0.0	0.10	38.6	487	C	—	1
0640564+093553	F4-ap142	12.78	1.76	0.77	0.40	0.76	—	—	2.5	0.12	72.1	565	C	hsb	1
0640568+093749	F1-ap178	12.22	0.97	0.25	0.16	1.01	20.70	0.38	16.0	0.61	99.6	338	C	—	2
0640568+095157	F2-ap149	14.02	1.01	0.29	0.00	—	19.50	1.00	6.7	0.28	0.0	0	W-	—	2
0640578+094120	F2-ap167	12.87	1.60	0.64	0.44	0.62	20.05	0.37	15.0	0.55	23.1	503	C	—	2
0640578+095109	F4-ap122	13.15	1.21	0.36	0.24	0.67	28.19	4.94	3.2	0.14	9.7	433	CW	—	1
0640580+091803	F3-ap225	13.15	0.41	0.09	-0.21	-0.06	22.42	0.21	21.3	0.75	0.0	0	AE	—	1
0640581+093653	F4-ap131	13.31	1.23	0.41	0.25	0.63	24.08	2.05	2.7	0.11	49.7	348	C	—	1
0640582+095231	F1-ap122	16.39	1.34	0.73	0.33	1.16	—	—	2.8	0.11	0.0	0	WC	hsb	1
0640584+092725	F4-ap207	13.62	0.95	0.23	0.37	-0.05	—	—	2.2	0.09	7.0	322	W	—	1
0640587+093613	F1-ap197	12.41	1.28	0.45	0.00	0.00	—	—	2.8	0.13	23.3	251	C	—	1
0640588+093057	F1-ap215	11.72	1.21	0.44	0.14	—	22.21	1.56	9.9	0.46	7.0	681	C	—	1
0640588+093919	F1-ap153	13.66	0.95	0.27	0.10	0.93	19.31	0.85	7.2	0.30	38.1	297	C	—	1
0640589+092853	F3-ap228	13.00	0.95	0.25	0.16	0.51	18.57	0.94	9.8	0.39	12.2	267	C	—	1
0640591+093322	F3-ap224	13.94	1.35	0.50	0.00	0.00	16.09	1.06	5.6	0.23	60.6	379	C	—	1
0640592+095308	F3-ap136	12.35	0.90	0.23	-0.04	-0.04	10.77	0.31	19.1	0.68	1.4	208	W	RDB	2
0640593+094617	F1-ap125	12.78	1.27	0.41	0.13	0.63	26.85	0.62	9.7	0.38	12.9	197	WC	—	1
0640593+093325	F2-ap216	13.15	2.54	1.04	0.59	0.96	14.29	1.55	2.6	0.12	60.6	379	C	hsb	1
0640593+095520	F0-ap90	10.65	0.95	0.36	0.05	0.60	94.76	1.62	6.5	0.36	0.0	0	CX	rdb	1

Table 12.2 (cont'd)

2MASS_id	ID	J	$(J-H)$	$(H-K)$	[3.6 − 4.5]	[5.8 − 8.0]	V_{rad}	ΔV_{rad}	R	S	EW_c	$FW_{10\%}$	$H\alpha$	Notes	NOB
0640594+093333	F4-ap164	12.91	1.73	0.68	0.32	0.82	20.19	0.81	11.6	0.47	20.2	523	C	—	1
0640594+095945	F2-ap144	12.78	1.10	0.41	0.00	0.00	16.88	0.57	18.3	0.62	4.0	288	CW	—	1
0640595+092952	F1-ap213	13.26	1.18	0.36	0.26	0.93	17.86	1.94	3.7	0.15	20.7	324	C	—	1
0640595+093511	F4-ap146	11.59	1.28	0.40	0.32	0.76	25.34	1.56	11.8	0.44	8.8	425	C	—	1
0640596+093906	F2-ap171	13.70	1.43	0.52	0.44	0.85	—	—	2.6	0.10	35.0	331	C	hsb	1
0640597+094905	F3-ap143	15.06	2.14	0.86	0.64	0.21	—	—	2.7	0.11	83.2	425	C	—	1
0640599+094704	F4-ap128	14.04	1.39	0.53	0.28	0.47	21.62	1.38	3.6	0.15	20.3	205	W	hsb	1
0641000+092850	F2-ap223	13.09	0.89	0.21	0.10	0.28	19.13	0.88	12.5	0.48	0.0	0	W+	—	1
0641002+093907	F4-ap135	14.87	0.98	0.32	-0.15	—	16.27	1.28	2.7	0.11	0.0	0	W+	—	1
0641003+095850	F2-ap146	11.85	0.65	0.16	-0.02	-0.03	22.12	0.69	16.6	0.62	0.0	0	AE	—	2
0641003+092834	F4-ap204	14.67	1.33	0.53	0.81	0.80	-78.53	0.88	2.9	0.11	154.3	483	C	hsb	1
0641005+092916	F2-ap227	12.45	1.23	0.43	0.35	0.48	20.49	0.98	12.0	0.49	1.3	546	C	—	1
0641005+094503	F3-ap180	12.74	1.22	0.49	0.25	0.33	24.20	0.26	24.6	0.73	14.2	403	C	—	2
0641007+092541	F4-ap214	17.25	2.07	0.58	0.06	0.00	139.66	0.93	2.4	0.10	0.0	0	W-	—	1
0641008+093014	F2-ap224	14.82	0.89	0.34	0.00	0.00	13.04	1.10	2.6	0.11	39.8	353	C	hsb	1
0641008+095122	F1-ap126	12.19	0.79	0.19	0.00	0.00	19.57	0.70	15.7	0.57	0.8	135	W+	—	2
0641010+093244	F4-ap161	10.58	1.37	0.50	0.25	0.65	18.51	0.25	25.8	0.74	11.7	491	C	—	1
0641011+093452	F4-ap159	12.88	0.53	0.31	0.12	—	21.82	0.36	19.0	0.65	12.0	480	C	—	1
0641011+092234	F4-ap215	15.09	1.01	0.37	-0.09	0.29	14.59	1.76	2.4	0.10	0.0	0	W+	—	1
0641013+093453	F2-ap210	12.91	0.45	0.37	0.12	—	20.89	0.56	11.2	0.45	12.0	480	C	—	1
0641014+093408	F2-ap205	12.35	0.80	0.16	0.07	0.26	18.68	0.17	32.9	0.81	1.1	206	W	—	1
0641016+093729	F1-ap175	14.75	1.42	0.50	0.36	0.54	-110.63	1.03	3.3	0.13	339.4	408	C	hsb	1
0641017+092106	F4-ap213	13.74	0.51	0.06	-0.08	0.47	26.38	0.24	20.4	0.72	0.0	0	AE	—	1
0641017+094243	F3-ap198	14.72	1.66	0.60	0.37	1.01	13.31	1.43	5.0	0.22	13.0	315	C	—	1
0641018+093841	F2-ap186	12.24	0.85	0.23	-0.06	0.14	19.82	0.39	21.2	0.72	2.3	253	C	—	2
0641019+095004	F4-ap126	14.31	0.81	0.23	0.32	0.53	21.57	3.29	3.1	0.14	21.0	348	C	—	1
0641020+094135	F3-ap193	16.51	2.35	0.76	0.06	—	15.94	1.15	2.4	0.11	0.0	0	N	—	1
0641024+092540	F2-ap238	16.45	2.32	0.78	0.02	0.31	11.40	1.02	3.0	0.12	0.0	0	N	—	1
0641024+095225	F4-ap124	14.17	0.89	0.24	-0.04	0.07	24.21	0.59	9.4	0.37	0.0	0	W+	—	2
0641026+093513	F2-ap204	12.85	0.81	0.18	-0.04	0.00	19.08	0.54	18.7	0.65	1.0	125	W+	—	1
0641026+095103	F2-ap152	14.20	0.83	0.28	-0.01	0.46	14.50	1.93	2.7	0.12	0.0	0	W+	—	1
0641029+095353	F2-ap145	13.78	0.90	0.23	0.04	0.05	16.92	1.87	3.1	0.13	9.0	148	W+	sb	2
0641029+100712	F3-ap122	13.98	1.10	0.34	0.00	0.00	20.76	0.57	12.4	0.50	14.1	393	C	—	1
0641030+094754	F3-ap153	11.63	0.28	0.10	-0.07	-0.20	19.30	5.05	5.0	0.29	0.0	0	AEF	—	1
0641034+093005	F4-ap185	12.96	0.94	0.25	0.41	—	21.12	3.38	4.1	0.20	5.9	381	WC	—	1
0641034+094045	F2-ap173	12.93	0.86	0.17	-0.01	0.12	18.66	0.38	16.7	0.59	18.7	425	C	—	2
0641035+093118	F4-ap184	11.39	0.44	0.09	-0.09	0.00	27.47	3.38	7.3	0.37	0.0	0	AE	—	1
0641035+091707	F4-ap222	16.01	1.37	0.41	0.01	0.00	—	—	0.0	0.16	0.0	0	W-	—	1
0641036+100035	F3-ap130	13.42	0.89	0.28	-0.02	0.13	19.88	0.48	13.8	0.53	5.4	169	W	—	2
0641036+093029	F4-ap188	12.81	1.12	0.34	0.19	0.76	-6.00	0.62	6.3	0.23	14.9	231	C	hsb	1
0641036+093605	F1-ap200	13.25	1.15	0.80	0.42	—	—	—	2.8	0.11	15.1	253	C	hsb	1
0641039+095809	F2-ap150	12.99	0.93	0.25	-0.07	0.09	22.68	1.19	8.3	0.34	3.0	146	W+	—	2
0641040+092332	F4-ap216	12.94	0.99	0.45	0.00	0.05	22.44	0.20	21.5	0.72	0.0	0	AE	—	1

Table 12.2 (cont'd)

2MASS_id	ID	J	$(J-H)$	$(H-K)$	[3.6 − 4.5]	[5.8 − 8.0]	V_{rad}	ΔV_{rad}	R	S	EW_c	$FW_{10\%}$	$H\alpha$	Notes	NOB
0641040+094909	F3-ap160	12.58	0.86	0.19	-0.07	0.17	16.76	0.35	22.5	0.73	1.2	122	W	—	1
0641042+092044	F1-ap226	12.90	1.04	0.42	0.00	0.13	—	—	2.2	0.09	0.0	0	CW	hsb	1
0641043+092452	F4-ap212	12.72	1.26	0.48	0.23	0.82	17.39	0.53	12.8	0.51	51.9	376	C	—	1
0641043+094822	F4-ap129	12.57	0.74	0.16	-0.30	0.10	20.74	0.58	18.2	0.65	0.0	0	W	—	2
0641044+095150	F1-ap130	10.74	0.59	0.15	-0.14	0.01	28.45	1.56	10.5	0.49	0.0	0	AE	—	1
0641044+093643	F2-ap199	13.93	1.29	0.47	0.20	1.22	-41.46	1.19	2.5	0.11	67.7	471	C	hsb	1
0641045+095318	F3-ap135	12.98	1.00	0.28	0.13	1.22	25.06	0.30	22.9	0.70	3.6	207	W	—	1
0641046+092518	F3-ap226	12.91	0.95	0.22	-0.10	0.29	17.95	1.01	6.9	0.28	0.0	0	W	—	1
0641046+093831	F1-ap172	13.77	1.21	0.47	0.26	0.93	—	—	2.1	0.09	83.2	453	C	hsb	1
0641047+093627	F1-ap188	10.64	0.20	0.07	0.07	0.43	20.68	2.76	5.8	0.28	0.0	0	AEF	—	1
0641048+094433	F3-ap175	14.33	1.41	0.60	0.45	0.90	—	—	2.0	0.09	44.7	487	C	hsb	1
0641050+095046	F2-ap156	12.24	1.15	0.45	0.14	0.51	20.10	0.83	14.2	0.52	7.7	532	C	—	1
0641051+094848	F2-ap159	12.88	0.94	0.22	-0.08	-0.02	23.73	0.65	14.4	0.56	0.0	0	W+	—	2
0641051+094856	F1-ap123	13.58	0.83	0.20	-0.16	-0.07	17.32	1.04	7.8	0.31	0.0	0	W-	—	1
0641051+095145	F3-ap144	12.74	0.77	0.15	-0.06	-0.12	21.31	0.29	23.5	0.73	1.8	131	W	—	1
0641051+095348	F1-ap128	13.83	1.74	0.66	0.45	0.92	—	—	2.8	0.12	17.6	243	CW	—	1
0641052+100019	F3-ap127	13.05	0.87	0.26	0.03	0.10	17.01	1.27	4.1	0.18	5.4	179	W	—	1
0641053+092812	F4-ap199	15.30	1.15	0.57	0.11	0.65	—	—	2.0	0.08	76.8	367	C	hsb	1
0641054+093313	F4-ap168	12.48	0.84	0.20	0.00	0.00	24.36	0.84	15.4	0.55	3.8	223	W	RDB	2
0641055+093141	F4-ap175	13.13	1.05	0.29	-0.04	0.06	70.84	27.55	0.0	0.12	2.6	208	W	hsb	1
0641057+093101	F2-ap211	12.37	1.06	0.29	0.00	0.00	21.18	0.28	23.6	0.74	9.6	275	C	—	1
0641058+094817	F1-ap132	12.02	1.22	0.46	0.24	0.62	25.29	0.52	13.6	0.55	32.9	501	C	—	1
0641058+095248	F3-ap142	12.99	0.93	0.23	-0.18	0.01	21.94	0.71	15.9	0.58	0.0	0	W+	—	1
0641059+092256	F1-ap222	10.55	0.98	0.58	0.38	1.50	—	—	3.2	0.21	8.7	357	C	hsb	1
0641062+092504	F2-ap234	13.12	0.95	0.32	0.20	0.64	16.69	0.84	6.2	0.23	20.1	255	C	—	1
0641062+093623	F4-ap145	11.64	1.08	0.46	0.19	0.32	22.54	1.16	12.4	0.54	12.0	485	C	—	2
0641064+092839	F4-ap200	13.85	0.87	0.14	0.11	0.85	20.12	0.59	9.0	0.36	68.0	302	C	—	1
0641064+095411	F2-ap141	13.19	0.88	0.23	-0.02	0.17	37.12	5.33	4.0	0.16	4.9	194	W	sb	2
0641067+093446	F4-ap155	11.76	2.53	1.04	0.53	—	26.30	3.57	6.1	0.27	18.6	555	C	—	1
0641067+094728	F2-ap151	14.00	1.10	0.35	0.28	0.79	22.93	1.67	3.8	0.15	7.7	265	W	—	1
0641068+092732	F4-ap197	10.43	1.58	0.68	0.26	0.85	22.50	0.59	13.7	0.59	82.5	525	C	—	1
0641069+092924	F2-ap222	13.41	1.49	0.62	0.21	0.69	19.78	0.50	11.3	0.42	11.1	275	C	—	1
0641071+091238	F1-ap230	13.07	1.11	0.38	0.48	0.85	16.74	0.54	13.3	0.50	16.0	274	C	—	1
0641072+092729	F1-ap217	12.55	1.51	0.61	0.47	—	20.76	0.53	11.1	0.44	15.5	224	C	—	1
0641072+092748	F3-ap222	12.21	0.85	0.18	0.02	—	24.91	0.31	24.0	0.75	1.7	303	W	—	1
0641073+092555	F4-ap208	12.59	0.91	0.27	0.18	—	19.88	0.31	23.6	0.74	1.1	129	W	—	1
0641073+095831	F1-ap124	12.54	0.86	0.19	-0.03	0.09	21.39	1.84	9.6	0.36	2.8	299	W	udb	1
0641074+093434	F3-ap220	15.15	0.84	0.16	0.07	0.72	—	—	2.6	0.10	22.3	232	CW	hsb	1
0641076+094134	F2-ap176	14.46	0.99	0.30	0.17	0.72	10.22	1.88	2.7	0.12	55.9	457	C	hsb	1
0641078+094115	F3-ap195	12.81	0.95	0.19	-0.08	0.07	26.45	0.83	13.5	0.55	1.3	184	W	—	2
0641080+093040	F4-ap186	13.26	0.79	0.16	-0.11	-0.38	23.46	0.80	13.9	0.55	0.0	0	W+	—	1
0641082+093409	F1-ap195	12.97	1.48	0.41	0.34	0.95	—	—	2.9	0.11	10.2	245	W-	—	1
0641083+093023	F3-ap211	13.77	1.23	0.41	0.26	0.56	—	—	4.0	0.15	0.0	0	C	hsb	1

Table 12.2 (cont'd)

2MASS_id	ID	J	$(J-H)$	$(H-K)$	[3.6 − 4.5]	[5.8 − 8.0]	V_{rad}	ΔV_{rad}	R	S	EW_c	$FW_{10\%}$	$H\alpha$	Notes	NOB
0641088+092343	F4-ap203	11.71	0.86	0.20	-0.03	0.01	33.30	2.72	10.2	0.40	3.5	283	W	—	1
0641089+095301	F1-ap127	14.07	1.30	0.46	0.26	0.93	—	—	2.3	0.09	41.9	375	C	hsb	1
0641089+095648	F2-ap143	15.19	0.87	0.28	0.01	—	—	—	2.6	0.11	0.8	71	W	hsb	1
0641090+093346	F2-ap209	12.96	1.16	0.34	0.26	1.07	21.18	0.56	8.7	0.33	36.5	307	C	—	1
0641090+093109	F3-ap213	14.20	2.68	0.94	0.41	0.48	—	—	2.9	0.12	0.0	0	W-	—	1
0641091+093009	F1-ap201	12.95	1.40	0.42	0.50	0.70	18.75	1.08	6.9	0.27	27.2	465	C	—	1
0641092+095302	F4-ap130	13.63	0.92	0.24	-0.05	0.27	20.63	0.63	9.6	0.38	41.9	375	W	—	2
0641095+093525	F0-ap204	12.44	0.92	0.15	-0.17	0.08	20.56	8.77	2.4	0.14	1.3	318	WC	—	1
0641095+095150	F3-ap148	12.34	0.93	0.23	0.07	0.46	23.67	2.69	7.4	0.36	1.6	192	W	RDB	2
0641098+092712	F1-ap219	11.54	0.90	0.24	0.00	-0.24	24.42	3.30	7.6	0.34	2.5	254	W	—	1
0641101+093129	F3-ap215	13.48	0.87	0.17	0.03	0.00	19.80	0.80	7.9	0.31	0.0	0	X	—	1
0641107+095742	F3-ap138	13.47	0.97	0.26	0.34	0.78	23.88	0.34	16.2	0.57	2.7	147	W	—	1
0641109+100041	F0-ap103	11.96	0.31	0.10	0.05	0.00	16.68	0.87	10.4	0.44	0.0	0	AEF	sb	2
0641110+093556	F2-ap195	13.36	1.86	0.73	0.42	0.86	20.66	0.81	6.9	0.28	26.1	315	C	—	1
0641113+091949	F4-ap220	13.47	2.27	0.81	0.31	0.80	20.89	3.93	2.6	0.11	0.0	0	N	—	1
0641116+100224	F3-ap123	11.98	0.71	0.12	-0.06	0.10	23.36	1.66	12.5	0.50	0.3	139	W	—	1
0641118+093112	F4-ap173	15.54	1.00	0.30	0.11	0.00	—	—	2.6	0.10	0.0	0	W+	—	1
0641126+095231	F2-ap160	11.49	1.29	0.48	0.34	0.48	18.80	2.54	6.9	0.33	29.8	510	C	udb	1
0641128+095243	F0-ap118	12.91	0.82	0.17	-0.11	0.06	22.19	1.83	6.0	0.33	0.0	0	W+	—	1
0641129+090526	F4-ap224	14.51	1.24	0.40	0.00	0.00	16.39	1.20	4.0	0.17	16.3	548	C	hsb	1
0641129+092615	F2-ap229	11.28	1.44	0.60	0.42	0.71	18.95	0.50	14.8	0.63	83.3	491	C	—	1
0641131+093138	F1-ap210	14.91	1.19	0.45	0.27	0.42	—	—	2.3	0.09	96.4	408	C	hsb	1
0641132+092610	F4-ap202	11.61	1.27	0.47	0.45	0.46	11.57	2.62	9.4	0.42	30.8	547	C	hsb	1
0641133+093150	F4-ap180	12.74	1.05	0.35	0.35	0.80	23.99	1.15	5.0	0.21	73.1	327	C	—	1
0641134+093814	F2-ap183	13.48	1.71	0.54	0.33	0.73	—	—	2.8	0.12	0.0	0	W	—	1
0641138+095544	F3-ap133	11.18	0.37	0.08	-0.03	0.10	15.44	1.68	9.0	0.46	0.0	0	A	—	2
0641145+093321	F4-ap163	12.60	0.88	0.21	0.02	0.26	21.18	0.27	25.6	0.76	0.7	133	W	—	1
0641145+093714	F2-ap198	13.88	0.93	0.24	0.07	0.11	18.58	0.87	9.0	0.39	0.0	0	W+	—	1
0641148+093236	F0-ap210	12.52	1.09	0.26	-0.03	-0.02	27.90	6.67	1.8	0.11	4.6	213	W	—	1
0641148+093413	F4-ap166	13.87	2.07	0.90	0.47	0.76	18.48	1.25	6.3	0.26	33.2	523	C	—	2
0641149+092555	F1-ap220	15.65	2.21	0.85	0.50	0.88	—	—	2.4	0.10	42.5	436	C	hsb	1
0641154+094640	F3-ap169	12.04	0.61	0.06	-0.08	-0.11	25.23	2.63	10.1	0.41	0.0	0	AE	—	1
0641158+092617	F1-ap218	11.31	0.87	0.22	-0.18	-0.09	19.87	0.86	14.9	0.57	1.6	202	W	—	1
0641160+092609	F2-ap226	12.70	1.25	0.46	0.59	0.86	20.18	1.05	5.2	0.22	72.6	331	C	—	1
0641167+092952	F2-ap219	11.27	1.20	0.43	0.37	1.19	35.94	0.28	24.6	0.76	5.5	550	C	—	1
0641168+092730	F4-ap198	12.64	1.14	0.38	0.28	0.56	15.63	1.14	7.6	0.40	72.9	594	C	—	1
0641171+095241	F2-ap157	14.06	0.85	0.14	-0.07	-0.09	23.68	0.71	8.0	0.30	0.0	0	W+	—	2
0641175+092806	F4-ap194	15.48	1.19	0.38	0.55	0.82	—	—	3.5	0.13	106.9	433	C	hsb	1
0641177+092926	F3-ap219	12.12	0.98	0.21	-0.07	0.10	23.96	2.45	8.8	0.38	3.3	295	W	—	1
0641179+092901	F4-ap187	13.33	1.48	0.45	0.27	0.96	26.06	2.34	4.2	0.18	19.5	253	C	—	1
0641179+093337	F1-ap199	12.63	0.85	0.19	-0.13	-0.13	19.78	0.61	12.5	0.45	0.0	0	W+	—	1
0641181+093825	F1-ap176	13.92	0.86	0.24	0.04	-0.10	—	—	2.3	0.09	0.0	0	W+	—	1
0641183+093354	F3-ap203	12.49	0.88	0.23	0.01	0.41	20.15	0.21	26.3	0.76	70.3	430	C	—	2

Table 12.2 (cont'd)

2MASS_id	ID	J	$(J-H)$	$(H-K)$	[3.6 – 4.5]	[5.8 – 8.0]	V_{rad}	ΔV_{rad}	R	S	EW_c	$FW_{10\%}$	$H\alpha$	Notes	NOB
0641184+093941	F1-ap163	13.41	0.95	0.19	0.04	0.35	21.38	0.89	6.4	0.25	73.2	355	C	—	1
0641189+092716	F1-ap203	13.12	0.93	0.28	0.00	0.00	15.26	1.25	2.8	0.11	0.0	0	W+	—	1
0641189+093944	F0-ap203	13.89	0.56	0.00	-0.07	0.15	28.07	0.35	12.3	0.54	0.0	0	AE	—	1
0641196+093144	F1-ap191	11.93	0.82	0.17	0.05	0.12	19.50	0.90	14.6	0.55	1.3	167	W	—	1
0641205+094536	F1-ap150	12.69	0.71	0.09	0.09	-0.01	18.07	1.43	9.9	0.38	0.0	0	W-	UDB	2
0641210+093336	F2-ap208	12.43	1.25	0.44	0.22	0.73	21.11	0.53	20.0	0.66	12.3	461	C	—	1
0641218+094531	F4-ap133	12.95	0.81	0.23	-0.01	-0.12	20.16	0.22	26.0	0.77	0.0	0	W+	—	1
0641220+094313	F1-ap159	13.17	0.80	0.11	-0.13	-0.21	18.52	0.54	14.5	0.55	1.3	205	W+	—	1
0641220+095113	F1-ap137	13.54	0.83	0.12	-0.12	0.06	18.60	0.89	9.2	0.36	0.0	0	W+	—	2
0641228+092939	F3-ap218	13.71	0.78	0.18	-0.05	-0.82	26.19	2.17	9.0	0.38	0.0	0	N	—	1
0641230+094327	F2-ap178	13.49	0.90	0.17	0.07	0.05	23.41	3.13	4.5	0.21	5.0	299	W	rdb	1
0641231+093734	F1-ap180	13.86	1.26	0.45	0.26	—	17.95	0.84	3.3	0.13	0.0	0	W+	—	1
0641238+093357	F4-ap167	10.60	0.12	-0.01	-0.21	-0.04	18.34	4.77	5.4	0.31	0.0	0	A	—	1
0641241+094938	F3-ap151	16.62	1.50	0.87	0.14	0.00	13.55	1.17	2.4	0.11	0.0	0	N	—	1
0641242+094831	F4-ap137	14.69	1.06	0.37	0.31	0.61	76.04	1.46	2.5	0.10	111.6	472	C	—	1
0641245+093736	F2-ap196	13.47	0.91	0.15	-0.01	—	26.59	3.05	3.1	0.13	3.2	176	W	—	1
0641250+094242	F1-ap155	14.29	0.98	0.26	-0.05	-0.11	16.71	1.09	3.1	0.12	0.0	0	W+	sb	2
0641270+093013	F2-ap212	13.81	0.94	0.19	-0.04	0.81	20.13	0.52	10.6	0.42	8.1	271	W	—	1
0641272+093506	F1-ap186	12.32	0.73	0.14	-0.06	-0.08	35.54	5.23	5.7	0.26	0.0	0	AE	—	1
0641275+093652	F2-ap200	16.96	1.84	0.69	0.04	—	15.58	0.97	3.2	0.14	0.0	0	N	—	1
0641288+093839	F3-ap200	12.10	0.72	0.16	0.32	1.30	18.49	0.57	17.4	0.66	0.9	228	CW	—	2
0641288+100915	F3-ap132	11.98	0.67	0.20	0.00	0.00	22.19	0.42	14.5	0.57	0.0	0	AE	—	1
0641292+092848	F1-ap204	15.58	2.55	0.78	0.00	0.00	—	—	3.3	0.14	0.0	0	W-	—	1
0641310+092020	F4-ap206	14.56	0.92	0.21	0.00	-0.02	14.53	1.05	4.1	0.16	0.0	0	W+	—	1
0641311+092658	F3-ap214	11.50	1.38	0.56	0.26	0.70	16.57	0.70	9.3	0.43	75.6	689	C	—	1
0641316+094833	F1-ap146	12.32	0.77	0.16	-0.05	0.00	20.47	0.74	15.1	0.53	0.0	0	W+	—	1
0641320+100024	F1-ap134	13.04	0.79	0.15	0.02	0.14	18.29	0.70	14.0	0.52	1.2	131	W+	—	1
0641325+093807	F0-ap195	12.27	0.80	0.16	-0.01	0.04	18.06	0.42	17.1	0.66	0.0	0	W+	—	1
0641327+094251	F4-ap148	14.74	1.17	0.51	0.41	0.82	—	—	2.4	0.11	251.5	421	C	hsb	1
0641346+093633	F4-ap162	13.71	0.89	0.19	0.00	0.00	19.46	0.45	13.1	0.45	14.4	340	C	—	1
0641355+091850	F1-ap216	14.46	0.97	0.33	0.17	0.63	—	—	0.0	0.16	0.0	0	W	hsb	1
0641357+100416	F1-ap121	13.74	0.90	0.19	0.00	0.00	11.23	0.93	3.0	0.12	0.0	0	W-	—	1
0641362+093920	F2-ap187	13.66	0.84	0.09	-0.05	-0.14	16.00	0.36	17.2	0.63	1.6	125	W-	—	2
0641373+094507	F2-ap179	12.93	0.98	0.28	0.17	1.17	16.93	0.34	20.9	0.70	11.3	374	C	—	1
0641375+091713	F2-ap225	15.59	1.36	0.27	0.00	0.00	14.21	2.59	2.0	0.09	0.0	0	N	—	1
0641379+094654	F3-ap161	17.17	1.75	0.21	0.09	0.00	13.77	1.12	2.7	0.12	0.0	0	N	—	1
0641388+093212	F4-ap178	12.88	1.15	0.39	0.32	0.66	16.47	0.28	20.6	0.70	69.9	522	C	—	1
0641389+100935	F3-ap140	12.59	0.85	0.18	0.00	0.00	21.02	0.25	24.2	0.74	53.3	480	C	—	1
0641396+093320	F4-ap172	14.04	0.94	0.22	-0.04	-0.18	18.81	0.71	10.1	0.36	0.0	0	W	—	2
0641412+093243	F3-ap202	11.92	0.28	0.09	-0.07	0.10	31.90	0.33	18.4	0.67	0.0	0	A	—	1
0641412+095741	F3-ap147	13.03	0.95	0.26	-0.08	-0.10	-11.83	0.31	19.9	0.67	1.2	133	W	RDB	2
0641421+094736	F2-ap174	9.37	0.03	0.01	-0.04	0.03	22.66	5.17	3.4	0.19	0.0	0	AEF	—	1
0641427+094257	F4-ap143	12.52	0.81	0.20	-0.08	—	16.13	0.62	17.3	0.60	1.0	148	W	—	1

Table 12.2 (cont'd)

2MASS_id	ID	J	$(J-H)$	$(H-K)$	$[3.6-4.5]$	$[5.8-8.0]$	V_{rad}	ΔV_{rad}	R	S	EW_c	$FW_{10\%}$	$H\alpha$	Notes	NOB
0641429+092508	F2-ap215	13.57	1.27	0.48	0.05	0.77	19.00	0.53	11.6	0.47	77.1	410	C	—	1
0641429+092328	F1-ap208	14.23	0.91	0.21	-0.14	0.12	13.97	1.00	3.0	0.12	0.0	0	W-	—	1
0641438+094050	F3-ap190	12.05	1.35	0.56	0.23	0.88	17.57	1.24	12.8	0.53	6.2	458	C	—	1
0641449+094440	F4-ap147	13.18	0.80	0.18	-0.17	0.00	18.23	0.30	22.9	0.72	0.0	0	W	—	1
0641458+092643	F4-ap189	13.79	0.92	0.33	0.00	0.00	-72.49	1.30	2.4	0.10	6.7	155	W	hsb	1
0641464+094307	F1-ap162	13.24	0.85	0.22	-0.07	-0.11	17.75	0.79	9.2	0.42	0.0	0	W+	—	1
0641474+094200	F1-ap166	13.61	0.83	0.17	-0.01	-0.07	19.18	1.11	5.7	0.22	0.0	0	W	—	2
0641481+094243	F1-ap164	11.55	0.57	0.16	-0.06	0.08	32.57	6.26	5.7	0.25	0.0	0	AEF	—	1
0641488+100703	F3-ap131	13.28	1.89	0.81	0.00	0.00	21.07	1.35	5.9	0.28	39.7	454	C	—	1
0641489+094313	F4-ap152	10.19	1.65	0.46	-0.14	0.13	25.83	0.15	32.0	0.84	0.0	0	A	—	1
0641490+094106	F2-ap188	12.83	0.92	0.21	0.03	0.07	16.68	0.43	18.5	0.65	2.0	131	W+	—	2
0641500+092932	F1-ap198	12.88	0.82	0.18	-0.06	0.08	19.44	1.39	8.6	0.35	1.4	170	W	—	1
0641515+092706	F3-ap208	16.98	1.59	0.39	0.08	0.00	12.66	1.35	2.3	0.10	0.0	0	N	—	1
0641515+094410	F0-ap168	13.76	0.87	0.19	-0.08	0.10	17.14	2.18	4.1	0.22	0.0	0	W-	sb	2
0641515+095343	F3-ap155	12.16	0.55	0.14	-0.07	0.07	20.68	1.01	12.5	0.55	0.0	0	AE	—	1
0641530+095803	F3-ap141	12.22	1.04	0.35	0.31	0.56	20.06	2.25	10.0	0.39	9.1	384	C	—	1
0641532+095047	F1-ap143	12.96	0.96	0.30	0.20	0.71	20.67	0.42	15.8	0.56	2.7	231	W	—	2
0641545+092916	F1-ap196	10.13	1.27	0.37	-0.08	-0.01	16.17	0.14	32.3	0.81	0.0	0	AE	—	1
0641547+094127	F1-ap169	7.80	1.67	0.43	0.25	0.00	14.45	0.20	26.1	0.77	0.0	0	A	—	1
0641549+094253	F4-ap158	14.33	0.92	0.23	0.01	-0.40	16.81	1.64	3.7	0.18	178.6	414	C	—	1
0641550+093007	F1-ap192	13.27	0.92	0.25	-0.10	-0.01	11.35	1.76	5.0	0.22	0.0	0	W+	rdb	1
0641564+095006	F3-ap166	10.29	0.34	0.12	-0.06	0.06	16.03	0.16	28.0	0.82	0.0	0	A	—	1
0641570+092228	F3-ap205	14.90	1.08	0.40	0.11	—	11.96	1.43	3.3	0.13	0.0	0	N	—	1
0641580+094306	F2-ap182	12.96	0.85	0.17	-0.11	-0.05	21.08	0.81	14.2	0.52	0.0	0	W	—	2
0642003+090944	F4-ap209	14.30	1.87	0.77	0.00	0.00	—	—	2.1	0.10	36.8	423	C	hsb	1
0642026+093653	F1-ap177	13.18	0.85	0.17	0.05	—	16.54	0.63	12.1	0.48	0.0	0	W-	—	1
0642027+095828	F0-ap137	13.25	0.60	0.17	0.00	0.00	23.92	1.43	3.4	0.18	0.0	0	AE	—	2
0642028+092122	F2-ap213	13.37	1.79	0.51	-0.02	0.04	22.10	2.38	3.0	0.14	0.0	0	N	—	1
0642032+093850	F3-ap189	15.10	1.39	0.70	0.00	0.00	13.31	1.03	2.6	0.12	47.2	509	C	hsb	1
0642039+092132	F4-ap196	15.48	1.24	0.45	0.05	0.00	—	—	4.5	0.19	0.0	0	C	—	1
0642066+094132	F2-ap190	11.36	1.01	0.22	0.00	0.00	21.19	0.17	29.8	0.79	0.0	0	AE	SB	2
0642074+094947	F0-ap157	10.42	0.95	0.23	-0.12	—	30.85	0.15	29.5	0.81	0.0	0	A	—	2
0642087+094121	F1-ap167	12.64	0.82	0.22	0.00	0.00	18.30	1.12	11.1	0.44	60.8	464	C	—	1
0642091+094805	F0-ap160	13.03	0.73	0.20	0.00	0.00	26.63	0.37	11.3	0.51	0.0	0	AE	—	1
0642091+095903	F3-ap156	11.70	1.03	0.26	0.00	0.00	29.74	0.16	29.8	0.82	0.0	0	AE	—	1
0642092+094403	F3-ap177	13.49	0.84	0.15	0.00	0.00	17.58	0.55	15.5	0.57	1.5	173	W	—	2
0642122+092747	F2-ap207	16.28	1.15	0.65	0.00	0.00	14.39	1.44	2.7	0.11	0.0	0	N	—	1
0642126+095907	F0-ap141	12.88	0.42	0.08	0.00	0.00	26.92	3.25	2.8	0.15	0.0	0	AEF	sb	2
0642131+094604	F3-ap176	13.49	0.53	0.15	0.00	0.00	28.81	0.74	8.8	0.34	0.0	0	AE	—	1
0642141+093545	F3-ap181	13.44	0.67	0.11	0.00	0.00	12.59	0.30	14.4	0.56	0.0	0	AE	—	1
0642146+095028	F1-ap160	13.14	0.62	0.18	0.00	0.00	15.94	1.15	3.2	0.13	0.0	0	AE	—	1
0642219+094833	F3-ap163	13.63	0.39	0.16	0.00	0.00	—	—	0.0	0.12	10.3	491	C	hsb	1

Note. — Hectochelle targets in NGC 2264 found to be members based on measured RV value or by detected Hα emission. The criteria of beeing RV member is to have at least one velocity measurement within 4σ of the cluster mean velocity: 8 km s^{-1} < V_{helio} < 36 km s^{-1} . RV members listed only with $R \gtrsim 2$, while stars with Hα emission are included regardless of R value, but with no velocity displayed.)
2MASS id — 2MASS identification number (truncated RA and DEC coordiantes as: HHMMSSS+DDMMSS); **ID** — internal identification number, specifying the field (see

Table 12.3. NGC 2264 non-members — *full table*

2MASS_id	ID	J	$(J-H)$	$(H-K)$	[3.6 − 4.5]	[5.8 − 8.0]	V_{rad}	ΔV_{rad}	R	S	EW_c	$FW_{10\%}$	$H\alpha$	Notes	NOB
0639152+094323	F3-ap41	14.90	1.63	0.48	0.00	0.00	-457.97	1.84	2.6	0.12	0.0	0	AE	—	1
0639153+093938	F4-ap69	10.90	1.02	0.27	0.00	0.00	45.38	0.17	26.7	0.80	0.0	0	AE	—	1
0639154+095304	F3-ap69	15.83	1.08	0.26	0.00	0.00	-224.86	0.89	2.1	0.09	0.0	0	AE	—	1
0639157+094704	F3-ap55	16.32	1.09	0.73	0.00	0.00	66.16	2.41	2.5	0.10	0.0	0	N	—	1
0639158+092749	F4-ap50	16.40	0.76	0.23	0.00	0.00	397.81	1.28	2.3	0.10	0.0	0	N	—	1
0639158+094119	F3-ap49	15.70	1.09	0.14	0.00	0.00	-329.10	0.83	2.6	0.10	0.0	0	N	—	1
0639159+094821	F1-ap61	16.16	1.22	0.54	0.00	0.00	-228.01	2.95	2.4	0.11	0.0	0	N	—	1
0639164+091953	F4-ap38	12.61	0.45	0.15	0.00	0.00	65.88	0.56	6.5	0.31	0.0	0	AE	—	1
0639165+094314	F2-ap90	16.14	0.87	0.39	0.00	0.00	-129.81	1.09	2.7	0.12	0.0	0	AE	—	1
0639167+094757	F3-ap51	15.93	1.00	0.58	0.00	0.00	-254.56	0.41	7.1	0.27	9.0	435	N	—	1
0639174+092138	F1-ap23	13.61	0.49	0.18	0.00	0.00	47.86	1.13	4.8	0.18	0.0	0	AE	—	1
0639176+094306	F3-ap43	16.12	1.23	0.31	0.00	0.00	-337.57	1.44	2.1	0.09	0.0	0	N	—	1
0639178+094052	F3-ap48	16.43	1.21	0.29	0.00	0.00	79.98	0.96	2.5	0.10	0.0	0	N	—	1
0639180+092325	F2-ap41	16.24	0.82	0.26	0.00	0.00	-26.50	0.76	5.1	0.19	0.0	0	N	—	1
0639183+093336	F2-ap67	14.88	0.84	0.13	0.00	0.00	42.09	0.68	9.4	0.37	0.0	0	AE	—	1
0639187+094752	F2-ap100	16.14	0.86	0.45	0.00	0.00	114.54	1.26	2.6	0.11	0.0	0	AE	—	1
0639202+094224	F3-ap45	15.31	1.04	0.29	0.00	0.00	334.90	11.09	0.0	0.11	0.0	0	AE	—	1
0639205+093135	F2-ap64	11.54	0.10	0.06	0.00	0.00	422.39	5.77	2.5	0.15	0.0	0	AEF	—	1
0639210+094523	F2-ap81	12.73	0.60	0.19	0.00	0.00	322.33	2.32	2.7	0.13	0.0	0	AEF	—	1
0639212+094028	F3-ap46	16.57	1.34	0.50	0.00	0.00	161.02	1.64	2.0	0.09	0.0	0	N	—	1
0639213+093436	F3-ap40	16.51	1.51	0.37	0.00	0.00	37.14	2.26	2.6	0.11	0.0	0	N	—	1
0639214+093401	F1-ap50	12.04	0.49	0.16	0.00	0.00	-4.32	1.84	2.6	0.11	0.0	0	AEF	—	1
0639217+092915	F4-ap45	11.92	0.21	0.09	0.00	0.00	—	—	2.6	0.12	0.0	0	AEF	—	1
0639226+093038	F3-ap23	15.64	0.68	0.08	0.00	0.00	55.11	2.67	3.2	0.14	0.0	0	N	—	1
0639226+093052	F2-ap62	16.30	0.81	0.35	0.00	0.00	298.37	1.45	2.6	0.11	0.0	0	N	—	1
0639230+094611	F3-ap59	16.27	0.73	0.02	0.00	0.00	-39.02	0.76	3.5	0.14	0.0	0	N	—	1
0639234+091833	F4-ap21	15.23	0.75	0.31	0.00	0.00	-452.85	1.28	2.3	0.12	0.0	0	N	—	1
0639237+094117	F2-ap84	15.54	0.94	0.23	0.00	0.00	267.88	1.01	2.7	0.10	0.0	0	AE	—	1
0639240+092551	F2-ap56	11.77	0.86	0.19	0.00	0.00	44.11	0.19	24.6	0.77	0.0	0	AE	—	1
0639240+094202	F2-ap88	10.84	1.53	0.44	0.00	0.00	81.53	0.17	27.8	0.82	0.0	0	AE	—	1
0639241+091806	F1-ap26	13.48	0.52	0.15	0.00	0.00	-19.21	0.43	9.2	0.37	0.0	0	AE	—	1
0639247+091722	F4-ap25	12.84	1.15	0.34	0.00	0.00	69.55	0.34	12.9	0.51	0.0	0	AE	—	1
0639249+093559	F3-ap37	15.53	1.34	0.38	0.00	0.00	124.73	0.97	2.6	0.10	0.0	0	N	—	1
0639250+095340	F3-ap63	13.06	0.65	0.14	0.00	0.00	49.55	0.52	8.5	0.39	0.0	0	AE	rdb	1
0639253+094335	F4-ap80	15.22	0.91	0.36	0.00	0.00	276.82	1.15	2.4	0.10	0.0	0	N	—	1
0639262+093352	F4-ap55	16.29	1.36	0.81	0.00	0.00	-182.29	1.36	2.1	0.09	0.0	0	N	—	1
0639263+093247	F4-ap58	15.49	0.93	0.13	0.00	0.00	490.24	1.95	3.3	0.13	0.0	0	AE	—	1
0639263+093516	F2-ap61	16.49	1.22	0.52	0.00	0.00	130.42	1.04	1.8	0.07	0.0	0	N	—	1
0639263+094508	F1-ap69	15.80	1.07	0.23	0.00	0.00	-234.83	24.43	0.0	0.13	0.0	0	N	—	1
0639270+091702	F4-ap27	16.29	0.91	0.58	0.00	0.00	297.11	13.22	3.1	0.16	0.0	0	AEF	—	1
0639270+093057	F3-ap25	16.25	1.05	0.26	0.00	0.00	40.30	0.48	6.3	0.27	0.0	0	N	—	1
0639270+094926	F1-ap78	16.23	1.01	0.59	0.00	0.00	-331.06	1.50	2.3	0.10	0.0	0	N	—	1
0639276+095101	F3-ap66	11.67	1.07	0.28	0.00	0.00	87.59	0.15	29.1	0.79	0.0	0	AE	—	1

Table 12.3 (cont'd)

2MASS_id	ID	J	$(J-H)$	$(H-K)$	[3.6 – 4.5]	[5.8 – 8.0]	V_{rad}	ΔV_{rad}	R	S	EW_c	$FW_{10\%}$	$H\alpha$	Notes	NOB
0639278+095718	F3-ap77	16.23	1.13	0.44	0.00	0.00	-329.07	1.27	2.9	0.13	0.0	0	N	—	1
0639279+092555	F2-ap54	16.54	0.86	0.25	0.00	0.00	282.42	9.32	0.0	0.11	0.0	0	N	—	1
0639281+093556	F1-ap41	15.67	1.02	0.30	0.00	0.00	-193.78	1.40	2.6	0.11	0.0	0	N	—	1
0639282+092718	F1-ap40	16.45	0.90	0.68	0.00	0.00	—	—	2.3	0.09	0.0	0	N	—	1
0639283+093312	F4-ap60	13.06	0.53	0.17	0.00	0.00	30.68	11.27	0.0	0.11	0.0	0	AEF	—	1
0639284+095359	F2-ap106	10.06	1.13	0.31	0.00	0.00	0.92	0.12	39.8	0.87	0.0	0	AE	—	1
0639287+092641	F4-ap42	12.40	0.43	0.16	0.00	0.00	-1.69	1.65	5.0	0.25	0.0	0	AEF	—	1
0639289+094038	F3-ap44	14.17	1.90	0.56	0.00	0.00	—	—	2.8	0.13	0.0	0	AE	—	1
0639294+093510	F3-ap38	15.52	1.15	0.23	0.00	0.00	—	—	2.4	0.10	0.0	0	N	—	1
0639294+093940	F1-ap55	15.82	1.40	0.42	0.00	0.00	60.64	1.73	2.0	0.08	0.0	0	N	—	1
0639303+092300	F4-ap39	12.05	0.58	0.10	0.00	0.00	109.20	0.15	30.2	0.81	0.0	0	AE	—	1
0639316+093935	F4-ap63	15.94	1.26	0.50	0.00	0.00	-286.45	2.00	2.2	0.09	0.0	0	N	—	1
0639319+093457	F2-ap63	15.72	1.19	0.47	0.00	0.00	82.97	0.88	2.6	0.13	0.0	0	N	—	1
0639324+093400	F3-ap34	15.22	1.45	0.28	0.00	0.00	228.82	1.19	2.5	0.11	0.0	0	N	—	1
0639330+092721	F4-ap44	15.27	0.97	0.21	0.00	0.00	81.68	1.84	2.2	0.10	0.0	0	N	—	1
0639332+094018	F3-ap42	13.82	1.71	0.49	0.00	0.00	-288.49	1.43	2.3	0.10	0.0	0	N	—	1
0639333+093012	F3-ap30	13.56	0.64	0.17	0.00	0.00	64.02	0.86	7.0	0.28	0.0	0	AE	—	1
0639337+093015	F4-ap41	13.31	0.48	0.13	0.00	0.00	291.29	1.25	2.3	0.11	0.0	0	AEF	—	1
0639337+093331	F3-ap32	15.87	1.17	0.26	0.00	0.00	402.42	1.62	2.2	0.10	0.0	0	N	—	1
0639338+094003	F2-ap82	14.79	1.63	0.46	0.00	0.00	—	—	2.2	0.10	0.0	0	AE	—	1
0639340+092950	F3-ap28	15.72	1.00	0.38	0.00	0.00	82.16	1.51	2.6	0.12	0.0	0	N	—	1
0639344+094335	F4-ap75	15.81	0.95	0.35	0.00	0.00	75.92	2.83	2.6	0.11	0.0	0	N	—	1
0639345+092338	F1-ap27	12.13	0.48	0.10	0.00	0.00	99.06	0.65	8.6	0.36	0.0	0	AE	—	1
0639346+093521	F3-ap36	14.28	3.28	1.28	0.00	0.00	315.09	0.86	3.2	0.13	0.0	0	N	—	1
0639347+092440	F2-ap49	12.72	0.42	0.07	0.00	0.00	52.38	0.37	12.5	0.53	0.0	0	AE	—	1
0639347+094654	F3-ap53	14.45	0.86	0.26	0.00	0.00	-34.34	0.94	5.9	0.27	0.0	0	AE	—	1
0639348+095832	F2-ap112	16.78	1.19	0.39	0.00	0.00	269.76	1.19	3.3	0.14	0.0	0	N	—	1
0639353+092810	F4-ap46	16.24	0.87	0.41	0.00	0.00	52.06	3.25	2.8	0.12	0.0	0	N	—	1
0639355+095814	F1-ap90	15.97	1.22	0.46	0.00	0.00	291.60	1.15	2.7	0.11	0.0	0	N	—	1
0639361+093141	F4-ap54	16.11	1.35	0.46	0.00	0.00	70.41	1.11	2.5	0.10	0.0	0	N	—	1
0639361+094045	F2-ap86	13.89	1.23	0.32	0.00	0.00	333.04	0.99	2.8	0.11	0.0	0	AE	—	1
0639367+091703	F4-ap28	15.13	1.09	0.29	0.00	0.00	—	—	2.3	0.11	0.0	0	N	—	1
0639371+093333	F4-ap59	15.07	1.56	0.59	0.00	0.00	168.48	0.99	2.3	0.10	0.0	0	N	—	1
0639372+091741	F4-ap30	16.11	1.13	0.35	0.00	0.00	-52.55	1.56	2.3	0.10	0.0	0	N	—	1
0639373+094223	F1-ap66	16.15	1.25	0.16	0.00	0.00	-267.45	0.92	2.9	0.11	0.0	0	N	—	1
0639376+093131	F1-ap31	15.95	0.74	0.14	0.00	0.00	453.77	0.98	2.6	0.10	0.0	0	N	—	1
0639376+094338	F2-ap94	15.98	1.14	0.34	0.00	0.00	-228.13	0.70	3.2	0.12	0.0	0	N	—	1
0639379+093853	F1-ap59	16.28	0.95	0.28	0.00	0.00	204.37	1.33	3.3	0.12	0.0	0	N	—	1
0639380+093218	F3-ap27	16.30	0.67	0.27	0.00	0.00	3.13	0.32	15.2	0.62	0.0	0	AE	—	1
0639383+092837	F2-ap60	12.09	0.28	0.13	0.00	0.00	-296.34	5.77	1.9	0.12	0.0	0	AEF	—	1
0639387+094044	F4-ap76	12.74	1.84	0.57	0.00	0.00	52.76	1.37	3.2	0.14	0.0	0	N	—	1
0639391+094834	F4-ap86	16.32	1.02	0.48	0.00	0.00	448.56	1.49	2.4	0.11	0.0	0	N	—	1
0639393+095322	F0-ap43	13.36	0.45	0.15	0.00	0.00	-367.07	1.76	2.1	0.10	0.0	0	AEF	—	1

Table 12.3 (cont'd)

2MASS_id	ID	J	$(J-H)$	$(H-K)$	[3.6 − 4.5]	[5.8 − 8.0]	V_{rad}	ΔV_{rad}	R	S	EW_c	$FW_{10\%}$	$H\alpha$	Notes	NOB
0639396+094544	F0-ap28	11.98	0.80	0.19	0.00	0.00	43.79	0.27	20.6	0.72	0.0	0	AE	—	1
0639399+093357	F4-ap53	14.95	1.89	0.57	0.00	0.00	—	—	2.3	0.10	0.0	0	N	—	1
0639401+095400	F1-ap82	16.56	1.00	0.52	0.00	0.00	451.12	1.36	2.6	0.11	0.0	0	N	—	1
0639402+093504	F4-ap62	14.73	1.71	0.48	0.00	0.00	69.88	1.11	2.4	0.09	0.0	0	N	—	1
0639404+093409	F2-ap69	13.56	1.78	0.57	0.00	0.00	473.48	2.26	1.8	0.12	0.0	0	AE	—	1
0639405+094923	F3-ap62	16.22	0.99	0.49	0.00	0.00	195.60	1.21	2.4	0.09	0.0	0	N	—	1
0639408+091928	F4-ap29	16.11	0.96	0.48	0.00	0.00	-273.46	1.62	2.0	0.09	0.0	0	N	—	1
0639408+093545	F4-ap64	15.25	1.36	0.29	0.00	0.00	-413.31	6.94	3.4	0.14	0.0	0	AE	—	1
0639418+100030	F2-ap120	16.11	0.96	0.42	0.00	0.00	420.79	1.38	2.8	0.11	0.0	0	N	—	1
0639419+095132	F4-ap85	16.10	1.12	0.41	0.00	0.00	-142.51	1.10	2.6	0.10	0.0	0	N	—	1
0639420+094341	F2-ap96	13.72	1.54	0.41	0.00	0.00	41.02	1.30	3.7	0.15	0.0	0	N	—	1
0639421+093706	F2-ap80	15.06	1.47	0.48	0.00	0.00	-472.47	1.61	2.3	0.10	0.0	0	N	—	1
0639422+092111	F1-ap22	16.34	0.88	0.15	0.00	0.00	-188.03	0.91	2.5	0.10	0.0	0	N	—	1
0639422+095631	F0-ap48	12.20	1.06	0.27	0.00	0.00	133.97	0.30	14.8	0.49	0.0	0	R	—	1
0639425+095924	F0-ap57	13.43	0.41	0.14	0.00	0.00	—	—	0.0	0.09	0.0	0	AE	—	1
0639426+093151	F2-ap51	12.22	0.96	0.26	0.00	0.00	176.63	3.76	1.9	0.09	0.0	0	N	—	1
0639426+093615	F2-ap74	16.34	1.08	0.39	0.00	0.00	458.77	1.39	2.5	0.10	0.0	0	N	—	1
0639427+092011	F3-ap20	12.02	0.36	0.03	-0.04	0.06	-17.43	0.30	14.7	0.62	0.0	0	AE	rdb	1
0639432+094247	F1-ap68	14.90	1.42	0.52	0.00	0.00	-241.25	2.04	2.4	0.10	0.0	0	N	—	1
0639433+092519	F2-ap48	16.79	1.34	0.91	0.00	0.00	93.16	1.21	2.6	0.12	0.0	0	N	—	1
0639434+094312	F1-ap70	15.60	1.27	0.41	0.00	0.00	200.34	1.12	2.6	0.11	0.0	0	N	—	1
0639444+100055	F0-ap60	12.99	0.88	0.19	0.00	0.00	83.10	0.64	5.0	0.26	0.0	0	R	—	1
0639445+095217	F3-ap72	16.15	0.86	0.48	-0.08	0.00	80.25	1.13	2.5	0.10	0.0	0	N	—	1
0639446+092049	F2-ap31	16.63	1.49	0.42	0.05	0.00	-36.55	2.46	2.3	0.09	0.0	0	AE	—	1
0639452+094643	F0-ap24	12.70	0.51	0.08	0.00	0.00	-69.64	0.32	15.6	0.62	0.0	0	AE	—	1
0639454+092440	F3-ap13	14.72	0.99	0.11	-0.07	0.00	26.95	3.25	2.2	0.10	0.0	0	N	—	1
0639458+092401	F1-ap28	16.30	0.95	0.37	-0.02	0.00	72.10	1.26	2.6	0.10	0.0	0	N	—	1
0639460+095725	F1-ap85	10.46	1.41	0.42	0.00	0.00	-9.12	0.21	20.9	0.68	0.0	0	AE	—	1
0639461+095803	F0-ap53	13.44	0.57	0.12	-0.12	0.15	-15.31	0.71	5.2	0.20	0.0	0	N	—	1
0639465+095410	F1-ap88	16.29	0.98	0.11	0.00	0.00	-168.31	0.93	2.6	0.10	0.0	0	N	—	1
0639472+092418	F4-ap36	15.71	1.20	0.60	0.00	0.00	-281.64	0.97	2.9	0.12	0.0	0	N	—	1
0639472+094430	F0-ap29	12.57	0.70	0.24	0.01	0.12	295.89	1.24	2.0	0.08	0.0	0	AEF	—	1
0639477+092607	F4-ap33	11.43	0.19	-0.01	-0.07	-0.07	37.04	4.57	5.3	0.29	0.0	0	AEF	—	1
0639479+095116	F2-ap107	15.98	1.17	0.43	-0.32	0.00	-55.51	0.63	6.3	0.28	0.0	0	N	—	1
0639484+094853	F0-ap39	12.31	0.40	0.07	-0.10	0.06	3.58	0.25	17.9	0.69	0.0	0	AE	—	1
0639485+092230	F4-ap23	16.00	1.03	0.48	-0.11	—	-264.20	4.79	2.2	0.10	0.0	0	AE	—	1
0639486+100039	F3-ap90	16.77	1.22	-0.13	0.00	0.00	-47.50	1.48	2.7	0.12	0.0	0	N	—	1
0639487+095204	F3-ap74	16.44	1.29	0.14	0.00	0.00	-56.05	1.20	2.5	0.10	0.0	0	N	—	1
0639489+094306	F0-ap23	12.90	0.77	0.15	0.00	0.00	50.35	0.46	11.9	0.58	0.0	0	AE	—	1
0639493+093534	F1-ap49	16.90	1.33	0.47	0.30	0.00	-261.77	0.72	3.6	0.15	0.0	0	N	—	1
0639494+092056	F2-ap35	14.19	1.89	0.53	0.00	0.00	—	—	4.7	0.15	0.0	0	N	—	1
0639513+095753	F3-ap84	13.21	0.59	0.19	-0.08	0.06	-357.50	5.48	2.3	0.11	0.0	0	AEF	—	2
0639518+094048	F3-ap31	16.73	1.67	0.36	0.08	—	325.26	0.79	4.6	0.19	0.0	0	N	—	1

Table 12.3 (cont'd)

2MASS_id	ID	J	$(J-H)$	$(H-K)$	[3.6 − 4.5]	[5.8 − 8.0]	V_{rad}	ΔV_{rad}	R	S	EW_c	$FW_{10\%}$	$H\alpha$	Notes	NOB
0639529+100045	F3-ap87	16.38	0.95	0.39	0.00	0.00	-256.15	5.26	2.4	0.11	0.0	0	N	—	1
0639530+093341	F2-ap66	16.46	1.51	0.65	0.03	0.00	292.18	2.03	2.9	0.12	0.0	0	N	—	1
0639542+095820	F4-ap93	16.25	1.35	0.18	-0.11	0.00	391.72	1.56	2.4	0.09	0.0	0	N	—	1
0639557+092231	F1-ap11	16.51	1.33	0.53	0.03	0.00	59.33	1.40	2.0	0.09	0.0	0	N	—	1
0639562+091750	F2-ap34	14.38	0.83	0.30	-0.01	0.05	-475.47	0.89	3.4	0.13	0.0	0	N	—	1
0639562+092117	F3-ap12	15.31	1.07	0.27	0.07	—	—	—	2.7	0.12	0.0	0	N	—	1
0639562+092331	F3-ap16	16.95	1.80	0.62	0.16	0.00	316.54	0.84	2.7	0.11	0.0	0	N	—	1
0639576+092118	F1-ap13	14.42	1.56	0.41	-0.01	0.02	58.99	0.94	2.4	0.10	0.0	0	N	—	1
0639576+095600	F2-ap115	16.19	1.60	0.47	-0.01	0.00	495.36	13.08	0.0	0.14	0.0	0	AE	—	1
0639577+092323	F2-ap37	12.84	0.58	0.22	-0.14	0.00	59.77	6.45	1.6	0.10	0.0	0	N	—	1
0639587+093316	F1-ap33	16.08	2.01	0.58	-0.08	0.20	-283.76	0.96	2.9	0.12	0.0	0	N	—	1
0639590+092027	F3-ap3	16.05	1.19	0.47	-0.12	0.00	20.78	3.26	2.0	0.09	0.0	0	N	—	1
0639592+095437	F2-ap117	17.09	1.74	0.34	0.14	0.00	81.20	1.42	2.4	0.10	0.0	0	N	—	1
0640002+091715	F2-ap23	15.52	0.78	0.21	-0.27	—	-8.72	1.02	4.7	0.22	0.0	0	N	—	1
0640003+091745	F1-ap18	15.96	0.77	0.05	-0.02	0.00	—	—	2.4	0.10	0.0	0	N	—	1
0640003+094755	F4-ap94	17.25	1.72	0.54	0.13	0.00	252.92	10.41	0.0	0.12	0.0	0	N	—	1
0640014+093829	F2-ap71	15.36	2.25	0.60	0.00	0.00	374.87	8.95	0.0	0.10	0.0	0	N	—	1
0640022+093921	F2-ap89	16.24	1.30	1.08	0.01	0.00	229.66	1.27	2.9	0.12	0.0	0	N	—	1
0640028+095640	F2-ap111	15.31	1.02	0.39	-0.09	—	316.26	1.36	2.3	0.09	0.0	0	N	—	1
0640029+094003	F2-ap85	17.33	1.86	0.77	0.00	0.00	16.35	2.74	2.3	0.10	0.0	0	AE	—	1
0640029+093801	F4-ap78	16.69	1.49	0.42	0.16	—	—	—	2.9	0.11	0.0	0	N	—	1
0640031+093834	F1-ap60	15.67	1.98	0.71	0.08	-0.59	-120.31	1.62	2.9	0.11	0.0	0	N	—	1
0640031+095009	F0-ap36	12.22	1.07	0.24	-0.19	-0.01	87.76	0.26	16.2	0.61	0.0	0	R	—	1
0640032+095836	F3-ap83	15.60	0.76	0.03	-0.01	—	44.60	2.53	2.4	0.10	0.0	0	AE	—	1
0640033+093156	F1-ap38	17.00	1.63	0.73	-0.02	0.00	266.75	0.98	3.1	0.13	0.0	0	N	—	1
0640042+095341	F1-ap92	15.24	2.35	0.76	-0.08	0.00	269.07	0.92	3.0	0.12	0.0	0	N	—	1
0640046+095538	F1-ap98	14.16	1.65	0.46	-0.13	0.29	—	—	2.6	0.10	0.0	0	N	—	1
0640048+093447	F2-ap68	10.90	-0.01	0.03	-0.04	0.12	-268.49	5.67	3.5	0.18	0.0	0	AEF	—	1
0640049+091857	F1-ap16	15.01	1.43	0.45	-0.13	-0.07	399.92	0.81	3.8	0.16	0.0	0	N	—	1
0640051+093350	F4-ap51	13.28	0.47	0.09	-0.10	0.05	-35.90	0.17	25.2	0.78	0.0	0	AE	—	1
0640052+094618	F2-ap103	11.09	0.69	0.23	-0.21	-0.07	331.98	16.70	0.0	0.13	0.0	0	AEF	—	1
0640054+095211	F4-ap95	16.60	1.88	0.64	0.01	0.00	200.06	1.26	2.7	0.12	0.0	0	N	—	1
0640057+095313	F2-ap113	17.66	2.21	0.43	-0.20	0.00	313.46	0.49	6.0	0.22	0.0	0	N	—	1
0640058+093827	F4-ap73	16.90	2.14	0.72	0.09	—	—	—	2.8	0.11	0.0	0	N	—	1
0640058+095257	F3-ap71	17.18	1.65	0.57	0.02	0.00	163.62	0.90	2.5	0.10	0.0	0	N	—	1
0640058+095609	F1-ap100	15.84	1.44	0.33	0.00	0.00	-260.15	1.13	3.0	0.12	0.0	0	N	—	1
0640060+095751	F1-ap97	14.87	0.91	0.20	0.02	—	307.13	3.23	2.5	0.12	0.0	0	AE	—	1
0640061+095536	F3-ap88	15.85	1.28	0.43	0.00	0.00	-342.13	0.82	2.9	0.11	0.0	0	AE	—	1
0640077+094447	F0-ap25	12.60	1.19	0.32	-0.21	0.13	102.77	0.72	4.8	0.24	0.0	0	R	—	1
0640080+093639	F1-ap47	14.92	2.19	0.62	-0.04	-0.07	-232.18	2.42	2.7	0.12	0.0	0	N	—	1
0640080+094231	F2-ap91	16.37	1.99	0.56	0.00	0.00	-243.19	2.21	2.5	0.11	0.0	0	N	—	1
0640081+093707	F1-ap54	16.53	2.02	0.72	-0.09	—	-218.93	4.39	2.9	0.13	0.0	0	N	—	1
0640084+095726	F3-ap92	15.59	1.01	0.29	-0.05	—	—	—	2.1	0.09	0.0	0	N	—	1

Table 12.3 (cont'd)

2MASS_id	ID	J	$(J-H)$	$(H-K)$	[3.6 – 4.5]	[5.8 – 8.0]	V_{rad}	ΔV_{rad}	R	S	EW_c	$FW_{10\%}$	$H\alpha$	Notes	NOB
0640088+091909	F2-ap29	12.81	0.71	0.23	-0.22	-0.09	-5.38	0.57	9.1	0.40	0.0	0	AE	—	1
0640088+092744	F4-ap40	10.26	1.35	0.32	-0.19	0.05	48.98	0.19	28.4	0.78	0.0	0	AE	—	1
0640088+095233	F0-ap47	12.27	0.81	0.25	-0.09	0.13	-26.07	0.37	16.6	0.63	0.0	0	AE	—	1
0640090+093715	F2-ap79	15.63	2.79	0.92	-0.12	-0.10	-210.87	10.11	0.0	0.11	0.0	0	N	—	1
0640091+093915	F1-ap51	17.23	2.51	0.70	0.14	—	-70.34	0.41	6.9	0.25	0.0	0	N	—	1
0640094+093852	F1-ap57	15.36	2.05	0.63	0.17	-0.04	373.73	0.98	2.7	0.10	0.0	0	N	—	1
0640096+093101	F4-ap49	16.99	1.72	0.73	0.11	0.00	—	—	3.1	0.12	0.0	0	N	—	1
0640096+094143	F4-ap89	11.71	0.70	0.24	-0.12	-0.04	37.93	6.32	6.3	0.28	0.0	0	AE	—	1
0640097+093614	F3-ap22	18.27	2.58	0.22	-0.04	—	285.00	1.41	2.7	0.11	0.0	0	N	—	1
0640101+092005	F4-ap17	11.55	0.60	0.20	-0.08	0.11	-270.01	2.24	1.5	0.10	0.0	0	AEF	—	1
0640103+093443	F2-ap53	16.77	1.43	0.44	0.00	0.00	-25.66	2.92	3.0	0.13	0.0	0	N	—	1
0640103+095712	F0-ap58	13.88	0.69	0.14	-0.06	-0.48	-335.69	2.61	1.4	0.09	0.0	0	N	—	1
0640106+093935	F1-ap64	16.78	1.82	0.70	0.10	—	15.23	1.12	2.5	0.10	0.0	0	N	—	1
0640106+092638	F2-ap38	17.17	1.45	0.21	-0.04	0.00	404.33	10.87	0.0	0.10	0.0	0	N	—	1
0640109+093938	F4-ap84	16.91	1.51	0.84	0.00	0.00	159.86	1.31	2.3	0.10	0.0	0	N	—	1
0640114+094143	F0-ap21	13.96	0.86	0.13	-0.22	0.62	43.53	1.17	3.4	0.20	0.0	0	AE	—	1
0640114+095548	F1-ap95	14.10	1.53	0.39	-0.01	0.24	-143.63	0.90	3.0	0.12	0.0	0	N	—	1
0640121+095118	F1-ap94	17.05	1.88	0.62	-0.05	0.00	43.36	1.49	2.1	0.08	0.0	0	N	—	1
0640124+091805	F2-ap28	15.99	1.36	0.49	-0.01	—	-289.80	1.35	2.2	0.09	0.0	0	N	—	1
0640125+092813	F3-ap5	13.07	0.69	0.14	-0.17	0.09	1.40	0.19	26.5	0.77	0.0	0	AE	—	1
0640126+091708	F4-ap12	15.97	1.06	0.28	0.11	—	454.83	0.99	2.4	0.10	0.0	0	N	—	1
0640131+092103	F1-ap12	15.33	1.04	0.26	-0.04	—	-231.65	1.11	2.8	0.11	0.0	0	N	—	1
0640131+094316	F2-ap110	14.56	2.22	0.72	-0.05	0.12	-87.15	1.04	2.6	0.11	0.0	0	N	—	1
0640136+094949	F4-ap91	16.99	1.65	0.57	-0.15	0.00	140.94	1.79	1.8	0.08	0.0	0	N	—	1
0640139+095147	F2-ap122	16.74	1.91	0.65	-0.13	—	313.91	1.47	2.6	0.11	0.0	0	AE	—	1
0640140+091829	F4-ap14	16.04	1.06	0.34	-0.07	0.00	—	—	2.0	0.09	0.0	0	N	—	1
0640142+094653	F0-ap30	14.04	0.69	0.12	-0.30	—	-16.22	0.58	8.1	0.41	0.0	0	AE	—	1
0640151+095526	F4-ap102	15.10	1.13	0.33	-0.08	—	-352.55	2.78	2.9	0.13	0.0	0	N	—	1
0640153+095716	F4-ap104	15.16	1.14	0.34	0.14	—	15.91	12.96	0.0	0.08	0.0	0	N	—	1
0640154+094908	F1-ap81	15.42	0.95	0.27	0.10	—	-43.18	0.55	4.7	0.16	0.0	0	N	—	1
0640155+093652	F2-ap78	16.36	1.60	0.86	0.10	—	-340.41	1.74	2.8	0.10	0.0	0	N	—	1
0640162+095629	F3-ap98	13.25	2.08	0.62	0.02	0.09	120.76	0.73	2.4	0.09	0.0	0	N	—	1
0640166+093526	F3-ap17	17.12	1.85	1.10	0.11	0.00	313.54	1.34	2.6	0.10	0.0	0	N	—	1
0640170+094633	F1-ap89	13.27	0.87	0.16	-0.10	-0.06	-51.09	1.03	3.4	0.13	0.0	0	AE	—	2
0640176+093220	F1-ap29	12.63	0.61	0.11	-0.03	0.11	46.81	0.25	18.3	0.69	0.0	0	AE	—	1
0640176+093528	F4-ap74	16.82	1.45	0.25	0.01	0.00	—	—	2.4	0.10	0.0	0	N	—	1
0640177+092808	F4-ap32	16.19	1.80	0.81	0.00	0.00	-86.21	0.39	5.9	0.19	0.0	0	N	—	1
0640179+094018	F2-ap93	16.92	1.25	0.40	0.22	0.00	-160.33	2.83	2.0	0.10	0.0	0	N	—	1
0640181+093103	F4-ap48	16.89	1.88	0.80	0.04	0.00	-193.28	1.28	2.0	0.08	0.0	0	N	—	1
0640182+095645	F2-ap130	16.02	1.13	0.17	0.07	0.00	42.95	1.36	2.2	0.09	0.0	0	N	—	1
0640187+091936	F4-ap1	16.74	1.37	0.44	-0.08	0.00	463.87	1.36	2.3	0.10	0.0	0	N	—	1
0640188+092252	F1-ap1	16.75	1.38	1.15	0.00	0.00	-220.05	2.14	2.9	0.11	0.0	0	N	—	1
0640189+091742	F1-ap10	15.89	0.79	0.29	-0.10	—	—	—	2.8	0.12	0.0	0	N	—	1

Table 12.3 (cont'd)

2MASS_id	ID	J	$(J-H)$	$(H-K)$	$[3.6-4.5]$	$[5.8-8.0]$	V_{rad}	ΔV_{rad}	R	S	EW_c	$FW_{10\%}$	$H\alpha$	Notes	NOB
0640190+093815	F1-ap58	14.62	0.92	0.24	0.09	—	128.38	0.94	2.4	0.10	0.0	0	N	—	1
0640193+093437	F2-ap59	17.11	1.87	0.97	0.09	0.00	-22.84	2.01	3.5	0.14	0.0	0	N	—	1
0640198+094956	F3-ap73	17.02	2.24	0.74	-0.01	0.00	499.14	1.10	2.5	0.10	0.0	0	N	—	1
0640200+092716	F2-ap27	16.83	2.21	0.71	-0.05	—	-240.26	1.67	2.0	0.08	0.0	0	N	—	1
0640202+093937	F3-ap24	16.94	1.44	0.50	0.09	0.00	—	—	2.5	0.11	0.0	0	N	—	1
0640204+095212	F3-ap89	16.67	2.06	0.45	0.03	0.00	-180.88	3.52	2.5	0.12	0.0	0	N	—	1
0640206+091659	F4-ap9	15.44	0.99	0.18	-0.03	—	-345.62	1.27	2.5	0.09	0.0	0	N	—	1
0640206+095328	F3-ap94	16.98	1.65	0.57	-0.05	0.00	315.62	1.11	2.5	0.10	0.0	0	N	—	1
0640208+093325	F4-ap66	16.95	1.69	0.58	0.07	0.00	-471.21	0.70	3.8	0.14	0.0	0	N	—	1
0640210+092354	F4-ap19	11.08	1.30	0.37	-0.06	0.08	3.44	0.13	34.6	0.83	0.0	0	AE	—	1
0640211+092951	F1-ap17	17.28	1.79	0.74	-0.11	0.00	495.67	1.68	2.0	0.08	0.0	0	N	—	1
0640212+093615	F1-ap44	18.14	2.91	0.54	0.00	0.00	135.51	1.17	2.5	0.10	0.0	0	N	—	1
0640215+094151	F2-ap114	10.15	0.13	0.05	-0.03	0.00	0.11	4.42	4.0	0.17	0.0	0	AEF	—	1
0640219+093324	F3-ap7	15.23	2.29	0.74	0.00	0.00	447.90	4.08	2.1	0.09	0.0	0	N	—	1
0640219+093748	F1-ap56	17.19	2.38	0.81	0.05	—	-333.88	1.02	2.4	0.10	0.0	0	N	—	1
0640226+092302	F4-ap16	12.52	0.82	0.28	-0.08	0.01	54.94	0.54	9.7	0.43	0.0	0	AE	—	1
0640231+091812	F1-ap6	15.79	0.87	0.22	-0.20	0.00	-277.75	1.03	2.6	0.11	0.0	0	N	—	1
0640231+093426	F1-ap36	14.25	2.48	0.72	0.04	0.07	-38.76	1.42	2.5	0.10	0.0	0	N	—	1
0640231+093844	F4-ap81	17.00	1.36	0.39	0.06	0.00	-131.81	1.10	2.3	0.11	0.0	0	N	—	1
0640237+095951	F0-ap71	10.50	0.94	0.24	-0.01	0.17	44.44	0.16	28.9	0.80	0.0	0	AE	—	1
0640244+091939	F2-ap11	12.59	0.79	0.22	0.04	0.02	-331.34	1.41	2.9	0.13	0.0	0	AE	—	1
0640246+092657	F2-ap26	16.08	1.25	0.63	-0.13	0.00	—	—	4.1	0.16	0.0	0	N	—	1
0640249+092132	F4-ap5	16.48	1.03	0.55	0.00	0.00	432.77	1.55	2.1	0.09	0.0	0	N	—	1
0640254+091804	F1-ap4	15.40	1.29	0.39	0.02	0.00	452.12	0.95	3.4	0.14	0.0	0	N	—	1
0640255+093412	F4-ap61	14.70	2.76	0.78	0.14	0.08	70.64	0.86	2.0	0.08	0.0	0	N	—	1
0640259+093902	F2-ap102	13.20	2.21	0.64	-0.13	-0.06	—	—	1.8	0.09	0.0	0	N	—	1
0640262+093625	F4-ap88	14.76	2.54	0.77	-0.10	-0.14	6.58	0.77	4.4	0.18	0.0	0	N	—	1
0640264+092154	F2-ap15	15.51	1.22	0.23	-0.02	—	-75.57	0.77	5.4	0.26	0.0	0	R	—	1
0640264+093720	F3-ap14	16.59	2.21	0.86	0.07	—	312.46	1.04	3.0	0.11	0.0	0	N	—	1
0640268+093342	F2-ap39	16.93	2.27	0.82	-0.27	0.00	460.62	2.63	2.2	0.10	0.0	0	N	—	1
0640270+093730	F2-ap75	16.83	2.33	0.87	0.00	—	72.78	1.38	2.2	0.09	0.0	0	N	—	1
0640274+092728	F2-ap24	16.44	1.89	0.78	0.00	0.00	-40.88	1.28	2.4	0.10	0.0	0	N	—	1
0640279+091933	F4-ap8	16.02	0.91	0.47	0.00	0.00	34.84	2.59	2.1	0.09	0.0	0	N	—	1
0640281+091911	F2-ap13	16.45	1.04	0.31	0.00	0.00	-401.53	0.51	5.8	0.24	0.0	0	N	—	1
0640281+093741	F4-ap96	16.98	1.99	0.32	0.00	—	313.33	1.25	2.8	0.11	0.0	0	N	—	1
0640283+094829	F2-ap121	15.97	1.63	0.52	-0.01	—	459.30	1.30	2.5	0.10	0.0	0	N	—	1
0640287+093450	F1-ap34	16.56	2.78	1.05	0.13	-0.11	369.81	0.50	5.5	0.20	0.0	0	N	—	1
0640293+100544	F3-ap107	14.40	0.87	0.35	-0.01	—	76.89	1.22	2.5	0.10	0.0	0	AE	—	1
0640294+091713	F4-ap4	16.56	1.60	0.51	0.00	0.00	333.04	1.18	2.5	0.10	0.0	0	N	—	1
0640295+100048	F0-ap62	12.65	0.93	0.22	0.00	0.00	-49.97	0.54	7.7	0.39	0.0	0	AE	—	1
0640298+095043	F4-ap107	17.10	2.37	0.84	0.21	1.00	81.43	1.61	2.5	0.11	0.0	0	N	—	1
0640309+091700	F4-ap2	16.68	1.42	0.28	0.03	0.00	11.89	1.19	2.1	0.09	0.0	0	N	—	1
0640309+093617	F1-ap37	14.92	2.09	0.71	0.13	-0.29	-252.93	1.65	2.8	0.13	0.0	0	N	—	1

Table 12.3 (cont'd)

2MASS_id	ID	J	$(J-H)$	$(H-K)$	[3.6 − 4.5]	[5.8 − 8.0]	V_{rad}	ΔV_{rad}	R	S	EW_c	$FW_{10\%}$	$H\alpha$	Notes	NOB
0640310+093359	F1-ap15	12.72	2.72	0.87	0.00	0.00	—	—	2.8	0.11	0.0	0	N	—	1
0640314+093259	F4-ap67	16.28	2.37	0.72	0.10	0.13	-360.56	1.44	2.3	0.09	0.0	0	N	—	1
0640317+095622	F2-ap136	16.66	1.74	0.50	0.16	—	438.19	1.52	2.9	0.11	0.0	0	N	—	1
0640318+094315	F1-ap83	12.66	0.72	0.38	0.06	-0.86	464.35	1.13	2.6	0.11	0.0	0	N	—	1
0640319+093856	F2-ap116	16.81	1.50	0.64	0.02	0.00	78.59	1.30	2.2	0.09	0.0	0	N	—	1
0640324+100152	F1-ap105	10.13	0.55	0.18	0.02	0.05	419.78	4.42	2.0	0.12	0.0	0	AEF	—	1
0640325+094704	F3-ap68	15.82	1.71	0.62	0.02	—	196.07	0.99	2.2	0.10	0.0	0	N	—	1
0640329+094944	F4-ap105	15.85	1.74	0.72	0.02	—	—	—	2.4	0.09	0.0	0	N	—	1
0640330+093618	F4-ap98	16.34	1.72	0.59	0.03	—	432.69	1.29	3.5	0.15	0.0	0	N	—	1
0640331+093242	F2-ap19	16.82	1.93	0.53	0.16	0.00	—	—	4.5	0.17	0.0	0	N	—	1
0640333+093045	F3-ap231	16.26	1.77	0.76	-0.03	—	13.72	1.02	2.4	0.09	0.0	0	N	—	1
0640336+093400	F1-ap19	16.61	2.17	0.69	0.11	—	280.17	1.13	2.5	0.10	0.0	0	N	—	1
0640337+091719	F4-ap231	16.41	1.15	0.84	-0.05	0.00	44.30	1.53	2.1	0.10	0.0	0	N	—	1
0640337+093052	F4-ap11	16.61	1.59	0.17	0.01	0.00	—	—	2.3	0.10	0.0	0	N	—	1
0640338+092219	F4-ap6	16.64	1.03	0.24	-0.19	0.00	76.61	1.28	2.4	0.10	0.0	0	N	—	1
0640338+093257	F1-ap20	11.37	0.27	0.04	-0.02	-0.13	-30.55	0.34	16.9	0.64	0.0	0	AE	—	1
0640342+093924	F2-ap118	17.00	1.75	0.94	0.00	0.00	-285.64	0.31	9.7	0.34	0.0	0	N	—	1
0640343+093038	F1-ap3	16.46	1.58	0.34	0.07	—	300.55	1.20	3.6	0.15	0.0	0	N	—	1
0640344+093107	F2-ap20	15.18	1.99	0.64	0.02	-0.01	377.25	0.88	2.0	0.08	0.0	0	N	—	1
0640353+094519	F2-ap140	15.99	2.15	0.70	0.04	—	—	—	2.2	0.10	0.0	0	N	—	1
0640363+092709	F3-ap233	16.81	1.17	0.20	-0.14	0.00	395.19	2.59	2.4	0.11	0.0	0	N	—	1
0640365+095826	F4-ap114	16.57	1.20	0.74	-0.34	0.00	291.91	0.93	3.0	0.11	0.0	0	N	—	1
0640367+094723	F3-ap86	9.65	1.05	0.41	0.00	0.04	338.50	8.09	2.0	0.11	0.0	0	AEF	—	1
0640367+095141	F4-ap101	16.34	2.43	0.76	0.07	0.00	323.55	1.90	2.4	0.11	0.0	0	N	—	1
0640375+095458	F3-ap103	10.53	0.39	0.08	-0.04	0.08	54.63	10.07	4.3	0.24	0.0	0	AEF	—	1
0640377+095424	F2-ap139	16.95	1.78	0.65	0.00	0.00	424.61	5.41	2.6	0.12	0.0	0	N	—	1
0640380+091713	F2-ap16	15.62	0.85	0.45	0.00	0.00	-196.03	2.27	2.2	0.11	0.0	0	N	—	1
0640380+094529	F3-ap54	16.79	1.97	0.63	0.03	0.90	496.79	0.83	2.8	0.11	0.0	0	N	—	1
0640381+095054	F1-ap107	13.95	0.95	0.30	0.03	—	37.29	1.08	2.4	0.09	0.0	0	N	—	1
0640383+092900	F4-ap10	17.07	1.98	0.75	0.21	0.00	454.74	1.53	2.7	0.10	0.0	0	N	—	1
0640387+092211	F3-ap237	16.78	1.55	0.84	-0.09	0.00	314.78	0.91	3.2	0.12	0.0	0	N	—	1
0640387+095314	F2-ap137	16.27	2.03	0.64	0.10	0.00	-354.01	1.16	2.6	0.10	0.0	0	N	—	1
0640394+091703	F4-ap237	15.81	1.30	0.41	0.00	0.00	49.68	1.00	2.6	0.11	0.0	0	N	—	1
0640395+094840	F0-ap40	12.70	0.59	0.12	-0.20	0.24	99.97	0.44	8.8	0.45	0.0	0	R	—	1
0640395+095122	F2-ap135	16.37	1.76	0.42	-0.17	0.00	-209.95	4.37	2.6	0.11	0.0	0	N	—	1
0640397+095247	F3-ap114	16.08	2.38	0.76	0.13	—	—	—	2.9	0.12	0.0	0	N	—	1
0640409+093040	F3-ap239	16.76	1.60	0.60	-0.02	—	—	—	2.4	0.10	0.0	0	N	—	1
0640413+093753	F2-ap42	16.96	1.89	0.45	0.16	0.00	-269.32	0.98	2.8	0.12	0.0	0	N	—	1
0640416+095517	F0-ap70	13.35	0.59	0.12	-0.06	—	-14.71	0.36	11.6	0.57	0.0	0	AE	—	1
0640417+095552	F3-ap118	16.27	1.47	0.24	-0.03	—	77.22	1.15	2.1	0.09	0.0	0	N	—	1
0640422+094153	F3-ap235	17.19	1.89	0.68	-0.01	0.00	-296.31	1.01	2.3	0.09	0.0	0	N	—	1
0640423+092058	F4-ap238	16.83	1.50	0.45	-0.08	0.00	—	—	2.5	0.11	0.0	0	N	—	1
0640439+094756	F3-ap115	14.78	0.84	0.23	0.31	0.00	80.36	1.70	2.6	0.11	0.0	0	N	—	1

Table 12.3 (cont'd)

2MASS_id	ID	J	$(J-H)$	$(H-K)$	$[3.6-4.5]$	$[5.8-8.0]$	V_{rad}	ΔV_{rad}	R	S	EW_c	$FW_{10\%}$	$H\alpha$	Notes	NOB
0640441+092806	F4-ap225	16.41	1.78	0.40	0.00	0.42	434.73	1.48	2.5	0.10	0.0	0	N	—	1
0640443+092005	F2-ap5	16.56	1.00	0.53	0.18	0.00	-332.60	1.25	2.4	0.10	0.0	0	N	—	1
0640452+092355	F2-ap9	12.37	0.41	0.14	-0.13	-0.01	269.53	1.37	2.7	0.12	0.0	0	AEF	—	1
0640453+093848	F3-ap234	14.52	2.38	0.76	0.06	0.12	-236.72	1.29	2.5	0.11	0.0	0	N	—	1
0640455+092111	F2-ap7	10.57	1.29	0.35	-0.09	0.09	85.10	0.15	30.9	0.83	0.0	0	AE	—	1
0640459+095946	F1-ap118	12.29	1.14	0.34	-0.12	0.27	36.29	0.26	17.4	0.62	0.0	0	AE	—	1
0640472+095309	F1-ap120	14.61	0.84	0.14	-0.12	—	303.72	2.18	3.2	0.14	0.0	0	N	—	1
0640477+092942	F4-ap219	16.36	1.24	0.50	0.09	0.00	—	—	2.3	0.09	0.0	0	N	—	1
0640485+093417	F1-ap234	14.95	1.01	0.29	0.02	—	64.80	1.53	2.0	0.08	0.0	0	N	—	1
0640502+093726	F0-ap229	11.86	0.47	0.09	-0.05	-0.06	-15.96	0.21	22.2	0.73	0.0	0	AE	—	1
0640503+091954	F2-ap10	13.06	0.50	0.12	-0.08	0.11	-16.66	0.14	30.0	0.80	0.0	0	AE	—	1
0640511+093943	F1-ap139	16.50	1.60	0.54	0.08	—	116.15	1.18	2.6	0.11	0.0	0	N	—	1
0640512+092625	F1-ap232	16.32	1.08	1.14	0.14	0.00	402.71	0.92	3.0	0.12	0.0	0	N	—	1
0640516+092223	F2-ap4	15.10	1.06	0.32	0.00	—	295.69	5.76	2.8	0.14	0.0	0	N	—	1
0640516+092658	F2-ap231	15.95	1.84	0.40	0.12	0.27	79.40	8.83	0.0	0.10	0.0	0	N	—	1
0640517+092211	F4-ap230	16.09	1.16	0.46	0.03	0.00	144.30	1.32	2.3	0.09	0.0	0	N	—	1
0640518+093253	F3-ap229	16.60	2.10	0.68	0.00	0.00	312.27	0.94	3.1	0.11	0.0	0	N	—	1
0640519+093756	F2-ap189	14.37	1.48	0.73	0.62	1.74	164.81	1.19	2.2	0.10	0.5	116	AE	—	1
0640529+092444	F4-ap211	16.86	1.75	0.69	-0.06	0.00	-303.91	1.31	2.5	0.10	0.0	0	N	—	1
0640530+092719	F2-ap233	18.25	3.22	0.74	0.25	0.00	59.43	15.29	0.0	0.10	0.0	0	N	—	1
0640534+093211	F4-ap176	17.01	1.97	0.25	0.01	—	278.22	0.71	2.8	0.11	0.0	0	N	—	1
0640538+091736	F2-ap8	16.00	0.68	0.32	-0.17	0.00	13.10	1.46	2.3	0.09	0.0	0	N	—	1
0640542+095054	F0-ap54	12.56	0.84	0.19	0.00	0.00	-31.15	0.85	6.3	0.38	0.0	0	AE	—	1
0640543+092228	F4-ap228	15.81	1.12	0.43	-0.08	—	—	—	3.3	0.13	0.0	0	N	—	1
0640543+095534	F1-ap113	14.86	1.11	0.40	0.22	0.35	-74.76	0.66	4.5	0.19	0.0	0	N	—	1
0640544+092701	F1-ap227	16.25	1.32	1.05	0.39	0.00	—	—	2.1	0.09	0.0	0	N	—	1
0640553+091753	F1-ap221	13.01	0.57	0.23	-0.07	—	416.75	5.81	2.9	0.12	0.0	0	AE	—	1
0640553+094750	F0-ap15	13.51	0.82	0.15	-0.07	—	-8.48	0.50	9.5	0.52	0.0	0	AE	—	1
0640554+093018	F3-ap230	16.42	1.96	0.65	0.56	—	296.21	1.06	2.3	0.10	0.0	0	N	—	1
0640563+092828	F4-ap210	17.00	1.55	0.51	0.31	0.00	—	—	2.6	0.10	0.0	0	N	—	1
0640565+092130	F4-ap226	15.05	1.48	0.45	0.03	0.28	-137.90	3.69	1.8	0.10	0.0	0	N	—	1
0640568+094346	F2-ap162	16.74	1.85	0.38	0.01	—	142.45	0.84	2.7	0.10	0.0	0	N	—	1
0640570+091959	F1-ap225	14.83	1.84	0.54	0.00	0.00	-417.73	1.37	2.1	0.09	0.0	0	N	—	1
0640573+094337	F1-ap136	16.56	1.58	0.53	0.07	—	—	—	3.3	0.13	0.0	0	N	—	1
0640574+094043	F2-ap161	17.16	2.28	0.84	0.10	—	104.66	0.29	10.0	0.34	0.0	0	N	—	1
0640593+093552	F4-ap144	11.78	4.00	1.55	0.54	0.58	—	—	4.7	0.18	0.0	0	N	—	1
0641004+094129	F1-ap144	16.48	1.89	0.58	0.09	—	419.44	1.05	2.4	0.09	0.0	0	N	—	1
0641007+092152	F1-ap228	15.06	1.19	0.31	-0.23	-0.18	466.13	1.07	2.6	0.10	0.0	0	N	—	1
0641007+094313	F4-ap123	12.81	2.77	0.85	-0.10	0.06	313.95	1.14	2.6	0.11	0.0	0	N	—	1
0641010+091823	F1-ap229	16.08	1.06	0.18	-0.06	—	—	—	2.9	0.11	0.0	0	N	—	1
0641012+094148	F4-ap132	16.73	2.05	0.78	0.06	0.00	139.75	0.35	7.9	0.28	0.0	0	N	—	1
0641015+094425	F2-ap164	16.42	2.24	0.70	0.17	—	309.94	0.63	3.5	0.13	0.0	0	N	—	1
0641023+092436	F2-ap240	15.14	2.36	0.69	0.00	0.00	110.12	0.99	2.2	0.09	0.0	0	N	—	1

Table 12.3 (cont'd)

2MASS_id	ID	J	$(J-H)$	$(H-K)$	[3.6 – 4.5]	[5.8 – 8.0]	V_{rad}	ΔV_{rad}	R	S	EW_c	$FW_{10\%}$	$H\alpha$	Notes	NOB
0641026+093419	F0-ap221	12.41	0.40	0.10	-0.09	-0.31	-38.05	0.23	18.8	0.70	0.0	0	AE	—	1
0641027+094045	F1-ap152	16.25	1.94	0.68	0.17	—	—	—	2.3	0.10	0.0	0	N	—	1
0641034+092637	F2-ap232	15.25	2.24	0.70	0.09	0.05	—	—	2.2	0.08	0.0	0	N	—	1
0641043+093533	F2-ap193	16.20	1.79	0.61	0.53	0.82	-26.04	0.62	6.7	0.27	0.0	0	N	—	1
0641058+092527	F1-ap211	12.99	2.64	0.85	-0.02	0.03	329.19	1.67	2.7	0.11	0.0	0	N	—	1
0641060+093551	F4-ap156	12.37	0.57	0.10	-0.16	-0.10	67.71	0.17	27.2	0.80	0.0	0	AE	—	1
0641060+093914	F2-ap184	13.73	0.99	0.38	0.23	0.76	234.51	1.26	2.4	0.10	0.0	0	N	—	1
0641076+093000	F1-ap214	14.18	3.02	1.23	0.63	0.88	—	—	2.8	0.12	0.0	0	N	—	1
0641078+094403	F3-ap187	11.89	0.50	0.13	-0.12	-0.04	1.00	0.40	19.0	0.69	0.0	0	AE	—	1
0641088+094527	F3-ap174	14.35	2.90	0.89	0.06	0.10	—	—	1.9	0.11	0.0	0	AE	—	1
0641107+095059	F4-ap127	16.01	1.91	0.56	0.16	-0.28	—	—	2.4	0.10	0.0	0	N	—	1
0641110+094550	F2-ap168	16.63	2.02	0.78	0.15	—	-243.50	14.92	0.0	0.13	0.0	0	N	—	1
0641119+094654	F3-ap170	16.54	1.05	0.07	0.09	0.00	-370.87	1.33	2.5	0.10	0.0	0	N	—	1
0641127+094702	F1-ap135	16.76	1.36	0.64	0.11	—	-269.66	1.23	2.8	0.12	0.0	0	N	—	1
0641139+094542	F0-ap184	13.79	0.56	0.07	-0.09	0.13	-10.51	0.70	6.3	0.30	0.0	0	AE	—	1
0641155+094013	F0-ap205	12.65	0.35	0.10	-0.02	0.23	-29.23	0.26	17.0	0.66	0.0	0	AE	—	1
0641157+093818	F0-ap207	11.88	0.32	0.04	-0.10	0.22	4.66	0.38	14.9	0.62	0.0	0	AEF	—	1
0641172+093543	F4-ap153	16.59	2.57	0.59	0.09	0.00	493.26	0.94	2.3	0.10	0.0	0	N	—	1
0641173+091721	F2-ap239	15.39	1.20	0.32	0.00	—	75.55	0.99	3.0	0.13	0.0	0	N	—	1
0641177+093422	F1-ap194	16.15	2.02	0.56	0.07	—	470.75	0.83	3.1	0.12	0.0	0	N	—	1
0641181+093641	F1-ap182	16.08	1.58	0.54	-0.06	—	70.47	1.84	2.5	0.10	0.0	0	N	—	1
0641181+094758	F3-ap164	16.99	2.04	0.84	0.02	—	-144.44	1.06	3.1	0.13	0.0	0	N	—	1
0641184+095133	F1-ap140	15.04	2.23	0.67	0.01	-0.15	-296.74	1.11	2.4	0.09	0.0	0	N	—	1
0641185+094810	F4-ap138	14.02	2.61	0.79	0.03	0.11	135.41	0.58	4.4	0.19	0.0	0	N	—	1
0641197+094815	F1-ap133	16.53	1.93	0.75	0.11	—	—	—	2.4	0.10	0.0	0	N	—	1
0641201+094820	F2-ap166	16.77	1.75	0.62	0.10	0.00	-248.81	21.83	0.0	0.10	0.0	0	N	—	1
0641202+094222	F3-ap185	16.92	2.10	0.81	0.08	—	-27.78	0.58	4.2	0.16	0.0	0	N	—	1
0641205+093630	F3-ap204	16.52	1.29	0.41	0.20	0.00	-238.35	1.53	2.5	0.12	0.0	0	N	—	1
0641206+094522	F3-ap178	15.86	1.97	0.60	-0.06	—	-124.42	1.12	2.6	0.10	0.0	0	N	—	1
0641207+093141	F2-ap201	16.10	2.06	0.69	0.08	0.28	313.55	0.70	3.2	0.12	0.0	0	N	—	1
0641207+093517	F3-ap209	16.61	2.25	0.89	0.08	—	-170.70	2.92	2.2	0.10	0.0	0	N	—	1
0641207+094316	F3-ap182	16.17	1.83	0.71	0.00	—	—	—	2.5	0.12	0.0	0	N	—	1
0641209+093439	F1-ap187	16.95	2.03	0.74	0.08	—	—	—	6.5	0.26	0.0	0	N	—	1
0641211+094421	F1-ap141	16.67	1.27	0.60	0.07	0.00	—	—	2.4	0.09	0.0	0	N	—	1
0641217+091840	F2-ap236	15.72	1.21	0.39	0.06	0.00	-329.96	1.03	2.7	0.11	0.0	0	N	—	1
0641221+094352	F3-ap173	8.84	-0.04	0.07	-0.11	—	-292.76	8.34	4.2	0.24	0.0	0	AEF	—	1
0641231+091826	F4-ap201	16.16	1.08	0.47	-0.01	0.00	294.64	1.04	2.0	0.09	0.0	0	N	—	1
0641232+095031	F3-ap157	16.90	1.65	0.81	0.01	0.00	-30.48	0.90	4.2	0.18	0.0	0	N	—	1
0641234+092757	F1-ap207	15.93	0.54	0.45	0.07	0.00	-227.23	0.98	2.4	0.10	0.0	0	N	—	1
0641235+094857	F4-ap139	16.97	1.64	0.56	-0.05	0.00	256.18	1.04	2.1	0.09	0.0	0	AE	—	1
0641235+095446	F1-ap138	16.93	1.23	0.08	0.13	0.00	-22.42	0.81	2.4	0.09	0.0	0	N	—	1
0641242+095609	F0-ap116	11.98	0.84	0.31	0.01	0.16	—	—	1.7	0.10	0.0	0	AEF	—	1
0641254+093250	F4-ap174	16.22	1.36	0.62	0.15	1.51	494.50	1.87	2.4	0.09	0.0	0	N	—	1

Table 12.3 (cont'd)

2MASS_id	ID	J	$(J-H)$	$(H-K)$	$[3.6-4.5]$	$[5.8-8.0]$	V_{rad}	ΔV_{rad}	R	S	EW_c	$FW_{10\%}$	$H\alpha$	Notes	NOB
0641257+093640	F1-ap171	12.31	0.81	0.28	0.12	0.02	407.91	1.88	2.7	0.12	0.0	0	AE	—	1
0641263+093448	F0-ap192	14.09	0.91	0.19	-0.15	-0.04	36.13	1.14	4.4	0.27	0.0	0	AE	—	1
0641267+092355	F4-ap191	11.82	0.27	0.04	0.00	0.00	56.70	3.96	5.8	0.31	0.0	0	AE	—	1
0641273+092807	F1-ap206	15.99	2.09	0.70	0.11	0.30	-127.06	0.95	2.7	0.10	0.0	0	N	—	1
0641277+093423	F1-ap189	15.60	1.64	0.66	0.19	—	-205.02	8.05	0.0	0.09	0.0	0	N	—	1
0641280+093436	F2-ap191	16.69	1.35	0.38	0.10	0.00	-137.34	1.48	2.4	0.11	0.0	0	N	—	1
0641282+094438	F1-ap156	16.60	1.26	0.41	-0.05	0.00	247.75	1.18	2.5	0.10	0.0	0	N	—	1
0641283+093500	F0-ap194	13.13	0.41	0.05	-0.11	0.43	175.86	0.48	8.6	0.51	0.0	0	R	—	1
0641286+094912	F2-ap170	16.86	1.41	0.40	-0.21	0.00	434.20	1.08	2.5	0.10	0.0	0	N	—	1
0641287+095530	F3-ap149	12.35	0.71	0.21	0.08	0.07	-4.94	1.11	7.2	0.32	0.0	0	AE	—	1
0641290+093356	F2-ap202	16.38	1.48	0.45	0.27	—	-123.71	1.22	2.2	0.09	0.0	0	N	—	1
0641292+094226	F1-ap151	17.10	1.56	0.75	0.05	0.00	-322.74	1.91	2.2	0.11	0.0	0	N	—	1
0641293+092828	F3-ap212	16.98	1.93	0.52	0.05	—	—	—	2.4	0.10	0.0	0	N	—	1
0641306+094832	F2-ap169	17.20	2.14	1.01	0.02	0.00	75.59	1.22	2.7	0.11	0.0	0	N	—	1
0641307+092442	F1-ap205	17.13	1.91	0.77	0.05	0.00	-353.12	19.98	0.0	0.13	0.0	0	N	—	1
0641307+094300	F0-ap185	13.93	0.85	0.22	-0.08	0.00	41.73	1.06	4.1	0.24	0.0	0	AE	—	1
0641307+095614	F4-ap134	15.87	1.14	0.37	0.00	—	—	—	2.6	0.11	0.0	0	N	—	1
0641314+093528	F1-ap184	15.05	2.20	0.75	0.07	-0.02	210.85	1.21	2.7	0.11	0.0	0	N	—	1
0641325+093310	F1-ap185	16.24	1.72	0.54	0.00	—	119.14	0.84	2.4	0.10	0.0	0	N	—	1
0641330+091702	F2-ap221	13.59	1.69	0.47	-0.07	0.01	-286.26	2.12	2.1	0.09	0.0	0	N	—	1
0641343+093442	F0-ap201	11.21	1.54	0.41	0.08	0.09	63.98	0.54	6.4	0.34	0.0	0	AE	—	1
0641356+092438	F1-ap209	16.94	1.90	0.67	0.09	0.00	155.55	1.03	2.7	0.11	0.0	0	N	—	1
0641366+093701	F3-ap197	16.71	1.69	0.60	0.00	0.00	314.09	0.94	2.8	0.11	0.0	0	N	—	1
0641367+095338	F0-ap138	13.73	0.94	0.28	0.02	-0.08	—	—	1.8	0.10	0.0	0	AE	—	1
0641368+091953	F3-ap217	14.27	1.76	0.59	-0.02	-0.12	292.62	1.06	2.7	0.12	0.0	0	N	—	1
0641369+093004	F4-ap171	17.04	2.39	0.90	0.00	0.00	353.15	34.83	0.0	0.11	0.0	0	AE	—	1
0641373+095838	F0-ap123	13.13	0.61	0.11	-0.03	0.04	-4.54	0.40	11.7	0.56	0.0	0	AE	—	1
0641375+094041	F0-ap187	13.45	0.80	0.21	0.03	0.12	-9.04	2.54	2.2	0.13	0.0	0	AE	—	1
0641382+095747	F0-ap125	11.66	1.06	0.27	0.00	0.00	88.40	0.31	13.0	0.55	0.0	0	AE	—	1
0641383+093213	F1-ap183	11.54	1.22	0.31	-0.03	0.09	83.08	0.27	16.4	0.61	0.0	0	AE	—	1
0641386+092331	F3-ap216	16.21	1.85	0.68	0.05	—	—	—	2.3	0.10	0.0	0	N	—	1
0641407+091817	F1-ap212	12.33	1.99	0.59	0.01	0.05	-428.59	2.06	2.3	0.09	0.0	0	N	—	1
0641407+091930	F2-ap228	13.98	1.76	0.49	0.01	0.07	313.65	1.02	2.7	0.11	0.0	0	AE	—	1
0641407+093558	F0-ap182	13.89	0.84	0.25	-0.06	0.05	77.36	1.13	2.7	0.16	0.0	0	AE	—	1
0641414+094054	F0-ap183	11.04	1.04	0.26	-0.02	0.09	57.63	0.19	23.4	0.73	0.0	0	AE	—	1
0641425+095719	F3-ap145	16.42	1.31	0.58	0.01	0.00	80.61	1.70	2.4	0.10	0.0	0	N	—	1
0641434+095653	F0-ap124	12.59	1.03	0.30	-0.06	0.09	40.34	0.80	5.3	0.29	0.0	0	AE	—	1
0641434+095903	F3-ap150	16.12	1.36	0.55	-0.04	—	436.49	0.90	3.0	0.12	0.0	0	N	—	1
0641439+094104	F0-ap172	13.43	0.61	0.13	-0.12	-0.05	62.38	0.30	14.2	0.56	0.0	0	AE	—	1
0641440+091757	F2-ap230	13.43	1.58	0.47	0.01	0.10	-357.28	2.14	2.8	0.13	0.0	0	N	—	1
0641442+094130	F3-ap188	11.91	0.96	0.25	0.00	0.00	67.64	0.17	27.7	0.77	0.0	0	AE	—	1
0641450+095611	F3-ap152	13.25	0.57	0.15	-0.03	0.06	41.42	3.29	2.8	0.12	0.0	0	AEF	—	1
0641455+092613	F2-ap220	15.43	2.09	0.59	-0.49	0.00	291.69	3.05	2.2	0.11	0.0	0	N	—	1

Table 12.3 (cont'd)

2MASS_id	ID	J	$(J-H)$	$(H-K)$	[3.6 − 4.5]	[5.8 − 8.0]	V_{rad}	ΔV_{rad}	R	S	EW_c	$FW_{10\%}$	$H\alpha$	Notes	NOB
0641474+094550	F4-ap149	12.68	0.37	0.09	0.04	-0.04	-0.37	2.47	5.8	0.31	0.0	0	AE	—	1
0641478+095202	F1-ap148	11.38	0.47	0.15	-0.08	0.17	-14.05	1.86	2.9	0.13	0.0	0	AE	—	1
0641481+095016	F2-ap163	10.49	1.01	0.25	-0.01	0.10	56.06	0.17	28.2	0.79	0.0	0	AE	—	1
0641482+094253	F3-ap171	13.79	0.77	0.23	-0.09	0.17	1.58	0.30	19.3	0.66	0.0	0	AE	—	1
0641505+094602	F0-ap165	10.38	1.57	0.43	-0.02	0.09	51.12	0.21	23.1	0.75	0.0	0	AE	—	1
0641508+094735	F1-ap158	13.65	0.47	0.21	0.00	-0.20	—	—	2.2	0.09	0.0	0	AE	—	1
0641509+094726	F0-ap156	12.12	1.40	0.35	-0.01	0.07	4.90	0.30	15.9	0.58	0.0	0	N	—	1
0641518+092630	F4-ap190	15.75	2.10	0.63	0.03	—	305.38	1.86	2.5	0.11	0.0	0	N	—	1
0641524+092002	F4-ap195	15.76	1.13	0.64	0.00	0.00	—	—	2.5	0.09	0.0	0	N	—	1
0641525+092441	F4-ap183	17.07	1.81	0.90	-0.02	0.00	457.14	5.32	2.1	0.10	0.0	0	N	—	1
0641531+100002	F1-ap131	12.91	0.83	0.25	0.01	—	—	—	4.5	0.17	0.0	0	N	—	1
0641532+094425	F3-ap179	12.07	0.62	0.26	0.01	—	328.55	2.28	2.7	0.14	0.0	0	AEF	—	1
0641537+094203	F0-ap177	13.03	0.45	0.08	-0.07	0.10	4.58	0.27	16.8	0.63	0.0	0	AE	—	1
0641538+095929	F0-ap128	12.30	0.39	0.08	-0.01	0.00	-39.50	0.40	12.6	0.57	0.0	0	AE	—	1
0641559+091859	F4-ap193	14.62	1.58	0.44	-0.13	-0.18	-201.00	1.88	2.3	0.10	0.0	0	N	—	1
0641562+095222	F0-ap147	12.20	0.93	0.22	-0.07	0.07	43.65	0.39	11.4	0.52	0.0	0	AE	—	1
0641590+092621	F3-ap206	13.09	0.72	0.19	-0.03	0.02	47.19	0.45	10.4	0.47	0.0	0	AE	—	1
0642006+093853	F2-ap181	11.56	1.23	0.36	0.00	0.00	-39.23	0.13	34.9	0.81	0.0	0	AE	—	1
0642011+100026	F0-ap126	12.27	1.01	0.26	0.00	0.00	102.24	0.44	9.2	0.44	0.0	0	AE	—	1
0642019+092320	F4-ap181	16.31	0.96	0.35	0.00	0.00	-246.62	1.33	2.3	0.10	0.0	0	AE	—	1
0642021+092109	F1-ap202	13.87	1.35	0.49	0.05	0.00	-196.02	1.59	2.2	0.09	0.0	0	N	—	1
0642041+094758	F2-ap177	12.70	0.36	0.17	0.00	0.00	323.15	1.92	3.3	0.16	0.0	0	AEF	—	1
0642044+092233	F4-ap192	13.64	1.90	0.60	0.00	0.00	444.46	2.26	2.9	0.12	0.0	0	N	—	1
0642054+092212	F2-ap217	15.88	1.52	0.50	0.00	0.00	—	—	2.5	0.10	0.0	0	N	—	1
0642056+094437	F0-ap167	13.30	0.43	0.05	0.00	0.00	-73.80	0.34	12.4	0.53	0.0	0	R	—	1
0642071+100014	F0-ap122	12.71	1.02	0.25	0.00	0.00	73.82	0.81	4.5	0.25	0.0	0	AE	—	1
0642072+095345	F1-ap145	14.30	0.67	0.19	-0.01	—	481.12	0.73	1.3	0.12	0.0	0	N	—	2
0642074+095115	F1-ap154	16.38	0.76	0.11	-0.24	0.00	-36.84	0.71	2.9	0.11	0.0	0	N	—	1
0642075+093626	F4-ap170	10.75	0.38	0.17	0.00	0.00	425.06	5.28	1.8	0.11	0.0	0	AEF	—	1
0642078+092331	F1-ap193	15.86	1.24	0.42	0.00	0.00	274.11	1.29	3.4	0.14	0.0	0	N	—	1
0642079+094652	F0-ap154	12.13	0.46	0.13	0.00	0.00	-5.41	0.19	23.8	0.77	0.0	0	AE	—	1
0642089+093112	F4-ap177	16.49	1.18	1.34	0.00	0.00	480.28	1.25	2.3	0.10	0.0	0	N	—	1
0642090+093426	F3-ap196	12.10	0.97	0.20	0.00	0.00	86.79	0.18	24.1	0.75	0.0	0	AE	—	1
0642091+093605	F4-ap169	14.08	0.35	0.14	0.00	0.00	-278.77	1.47	2.7	0.12	0.0	0	AE	—	1
0642091+095946	F0-ap135	13.33	0.97	0.29	0.00	0.00	61.72	0.72	4.4	0.24	0.0	0	AE	—	1
0642092+092446	F2-ap214	16.14	1.02	0.29	0.00	0.00	-228.40	1.16	3.0	0.13	0.0	0	N	—	1
0642095+093206	F3-ap199	13.04	0.33	0.01	0.00	0.00	-80.58	0.25	16.3	0.56	0.0	0	AE	—	1
0642098+094000	F3-ap184	11.31	0.36	0.11	0.00	0.00	322.50	6.80	2.1	0.13	0.0	0	AEF	—	1
0642098+094843	F3-ap167	12.29	0.96	0.17	0.00	0.00	62.64	0.38	12.2	0.52	-0.2	350	AE	—	1
0642099+094522	F0-ap163	13.15	0.85	0.19	0.00	0.00	59.29	0.40	9.8	0.46	0.0	0	AE	—	1
0642101+094025	F0-ap175	13.20	0.69	0.24	0.00	0.00	-1.96	1.34	4.6	0.22	0.0	0	AE	—	1
0642102+093604	F1-ap173	12.40	0.98	0.28	0.00	0.00	45.47	0.25	17.6	0.60	0.0	0	AE	—	1
0642103+095641	F0-ap134	12.34	0.54	0.07	0.00	0.00	-7.63	0.29	17.6	0.69	0.0	0	AE	—	1

Table 12.3 (cont'd)

2MASS_id	ID	J	$(J-H)$	$(H-K)$	[3.6 − 4.5]	[5.8 − 8.0]	V_{rad}	ΔV_{rad}	R	S	EW_c	$FW_{10\%}$	$H\alpha$	Notes	NOB
0642103+095915	F0-ap139	13.24	0.88	0.24	0.00	0.00	70.95	0.77	5.9	0.33	0.0	0	AE	—	1
0642108+095600	F1-ap149	15.83	0.99	0.09	0.00	0.00	—	—	0.0	0.24	0.0	0	N	—	1
0642110+092723	F4-ap182	16.40	1.29	0.48	0.00	0.00	211.24	1.14	2.3	0.10	0.0	0	N	—	1
0642114+092903	F3-ap191	12.85	0.51	0.10	0.00	0.00	0.97	1.37	6.6	0.32	0.0	0	AE	—	1
0642116+092830	F1-ap181	16.35	1.16	0.40	0.00	0.00	16.00	1.34	2.4	0.10	0.0	0	N	—	1
0642118+094436	F4-ap160	12.41	0.88	0.19	0.00	0.00	0.48	0.19	24.1	0.75	0.0	0	AE	—	1
0642124+092254	F2-ap218	16.32	1.34	0.50	0.00	0.00	347.90	0.47	4.5	0.15	0.0	0	N	—	1
0642127+093009	F2-ap206	11.66	1.33	0.31	0.00	0.00	81.52	0.18	25.6	0.77	0.0	0	AE	—	1
0642127+093132	F4-ap179	13.76	0.56	0.14	0.00	0.00	75.31	0.36	11.9	0.46	0.0	0	AE	—	1
0642140+095013	F0-ap155	14.49	0.77	0.18	0.00	0.00	0.46	0.91	5.9	0.31	0.0	0	N	—	1
0642142+094309	F0-ap171	11.91	0.32	0.04	0.00	0.00	-19.86	0.18	24.2	0.75	0.0	0	AE	—	1
0642157+095141	F0-ap146	12.95	0.96	0.20	0.00	0.00	-4.47	0.41	10.8	0.45	0.0	0	AE	—	1
0642158+094033	F2-ap185	11.05	0.26	0.06	0.00	0.00	-50.45	0.17	25.2	0.76	0.0	0	AE	—	1
0642170+093351	F3-ap194	11.05	1.27	0.31	0.00	0.00	91.31	0.17	27.2	0.79	0.0	0	AE	—	1
0642194+093023	F1-ap190	13.10	0.44	0.14	0.00	0.00	408.27	1.46	2.7	0.13	0.0	0	AEF	—	1
0642201+093850	F3-ap186	10.85	1.39	0.37	0.00	0.00	97.61	0.17	27.3	0.77	0.0	0	AE	—	1
0642203+093704	F1-ap179	11.99	0.31	0.13	0.00	0.00	-254.81	18.71	0.0	0.10	0.0	0	AEF	—	1

Note. — Hectochelle targets in NGC 2264 found to be not members based on measured RV value or by lacking of any Hα detection.
2MASS id — 2MASS identification number (truncated RA and DEC coordiantes as: HHMMSSS+DDMMSS); **ID** — internal identification number, specifying the field (see Table 9.1) and aperture of observation; **J** — 2MASS J magnitude; **(J-H)** — 2MASS $(J-H)$ color index; **(H-K)** — 2MASS $(H-K)$ color index; $3.6-4.5$ — IRAC short wavelength color index; $5.8-8.0$ — IRAC long wavelength color index; V_{rad} — measured heliocentric radial velocity, in km s^{-1}; V_{rad} — *xcsao* error estimate for V_{rad}, in km s^{-1}; **R** — R value of cross correlation (see text for details); **S** — height of the CCF peak; EW_c — absolute value of equivalent width, measured on the corrected Hα profile (see text for details); $FW_{10\%}$ — full width of Hα profile at 10% level of the corrected maximum (see text for details);
Hα — notes on the Hα emission profile. See text for more details on the CTTS/WTTS classification: **R** — obviously shifted H-alpha absorption : high RV stars; **A** — only stellar absorption line, no nebular/stellar emission component; **AE** — stellar absorption and nebular emission together; **AF** — same as AE, but fast rotating star produces very wide absorption; **SAT** — saturated, or neighbour saturated;
Notes — BINARITY: **RDB** – resolved, double lined binary, with RV at 2 epochs (separated double peak in correlation function); **UDB** – unresolved double lin. binary, with RV at 2 epochs (blended/side lobed peak, but clear asymmetry in correlation function); **rdb** – same as for RDB, but only 1 RV measurement; **udb** – same as for UDB, but only 1 VRV measurement; **sb** – likely single lined binary, RV at two epochs and at least one suggest membership, some also have $H\alpha$ emission; **hsb** – member based on $H\alpha$ emission detected, but correlation either had just acceptable R value (barely larger than 2) or radial velocity is close to the edge of RV distribution;
NOB — number of observations

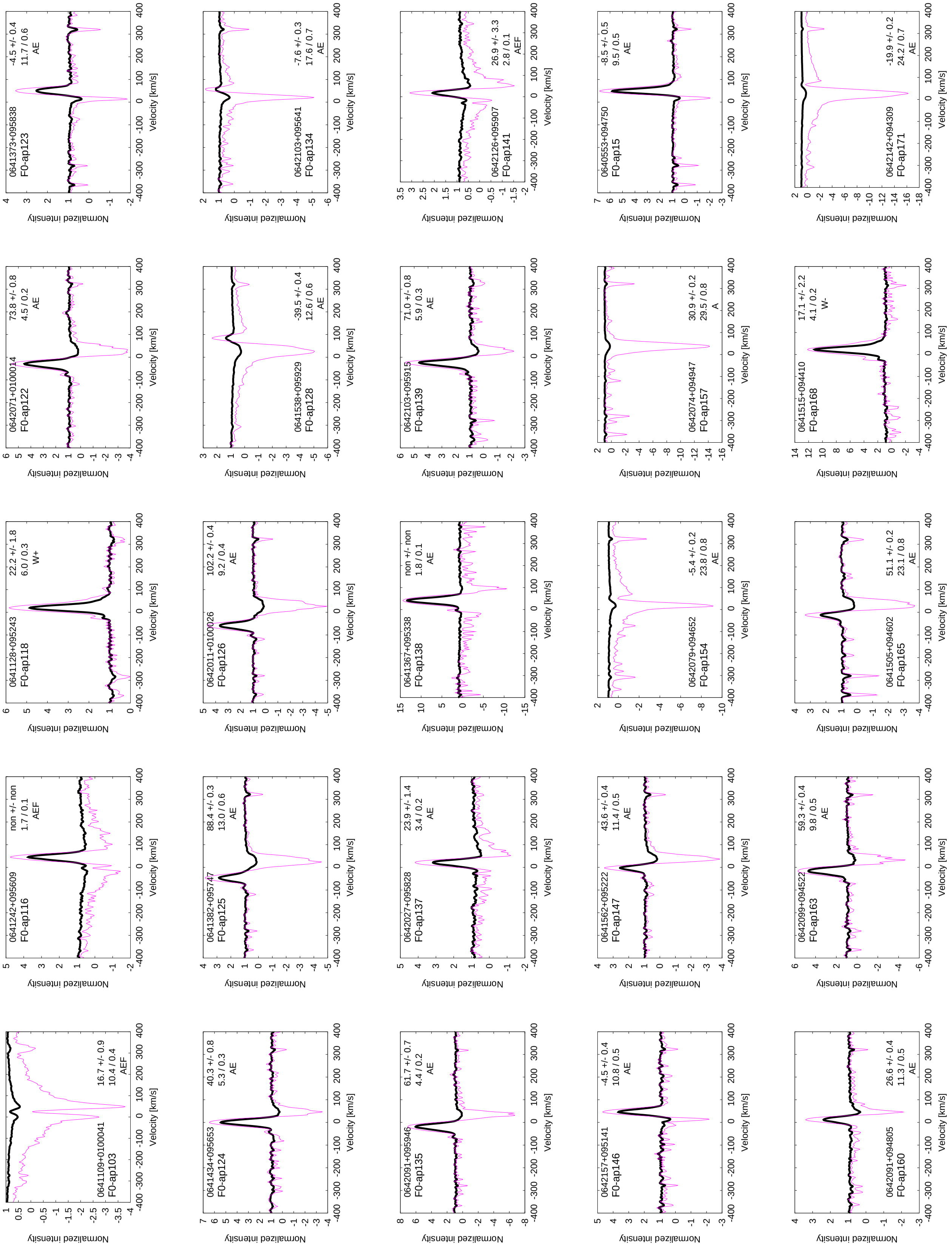

Figure 12.2: *Hα* ***profiles for stars with detected emission in the NGC2264 sample.*** *See Fig. 8.3 and § 8.2.2 for more details.*

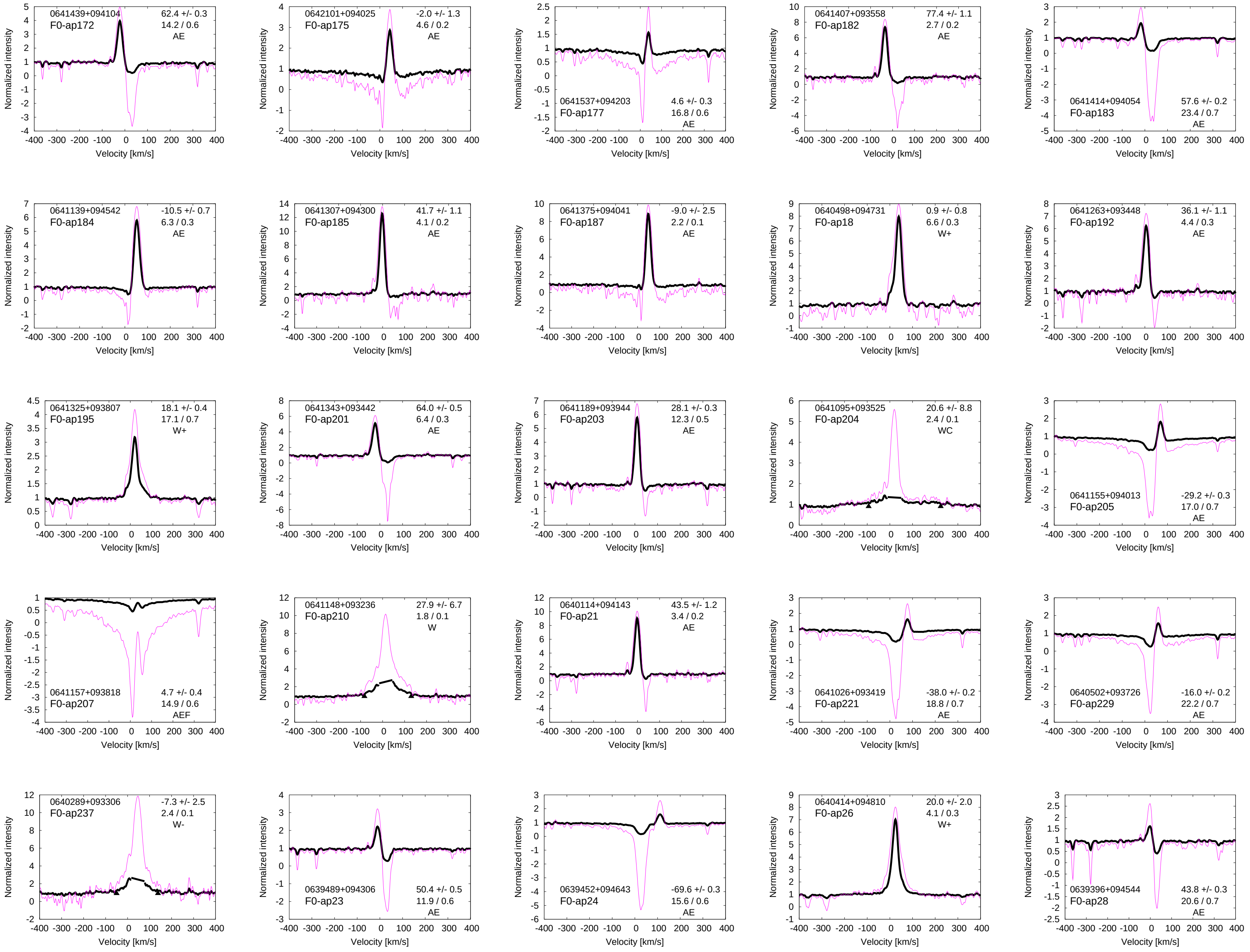
Normalized intensity
Velocity [km/s]
0641439+094104
F0-ap172
62.4 +/- 0.3
14.2 / 0.6
AE
0642101+094025
F0-ap175
-2.0 +/- 1.3
4.6 / 0.2
AE
0641537+094203
F0-ap177
4.6 +/- 0.3
16.8 / 0.6
AE
0641407+093558
F0-ap182
77.4 +/- 1.1
2.7 / 0.2
AE
0641414+094054
F0-ap183
57.6 +/- 0.2
23.4 / 0.7
AE
0641139+094542
F0-ap184
-10.5 +/- 0.7
6.3 / 0.3
AE
0641307+094300
F0-ap185
41.7 +/- 1.1
4.1 / 0.2
AE
0641375+094041
F0-ap187
-9.0 +/- 2.5
2.2 / 0.1
AE
0640498+094731
F0-ap18
0.9 +/- 0.8
6.6 / 0.3
W+
0641263+093448
F0-ap192
36.1 +/- 1.1
4.4 / 0.3
AE
0641325+093807
F0-ap195
18.1 +/- 0.4
17.1 / 0.7
W+
0641343+093442
F0-ap201
64.0 +/- 0.5
6.4 / 0.3
AE
0641189+093944
F0-ap203
28.1 +/- 0.3
12.3 / 0.5
AE
0641095+093525
F0-ap204
20.6 +/- 8.8
2.4 / 0.1
WC
0641155+094013
F0-ap205
-29.2 +/- 0.3
17.0 / 0.7
AE
0641157+093818
F0-ap207
4.7 +/- 0.4
14.9 / 0.6
AEF
0641148+093236
F0-ap210
27.9 +/- 6.7
1.8 / 0.1
W
0640114+094143
F0-ap21
43.5 +/- 1.2
3.4 / 0.2
AE
0641026+093419
F0-ap221
-38.0 +/- 0.2
18.8 / 0.7
AE
0640502+093726
F0-ap229
-16.0 +/- 0.2
22.2 / 0.7
AE
0640289+093306
F0-ap237
-7.3 +/- 2.5
2.4 / 0.1
W-
0639489+094306
F0-ap23
50.4 +/- 0.5
11.9 / 0.6
AE
0639452+094643
F0-ap24
-69.6 +/- 0.3
15.6 / 0.6
AE
0640414+094810
F0-ap26
20.0 +/- 2.0
4.1 / 0.3
W+
0639396+094544
F0-ap28
43.8 +/- 0.3
20.6 / 0.7
AE
-400 -300 -200 -100 0 100 200 300 400

Fig. 12.2 cont.

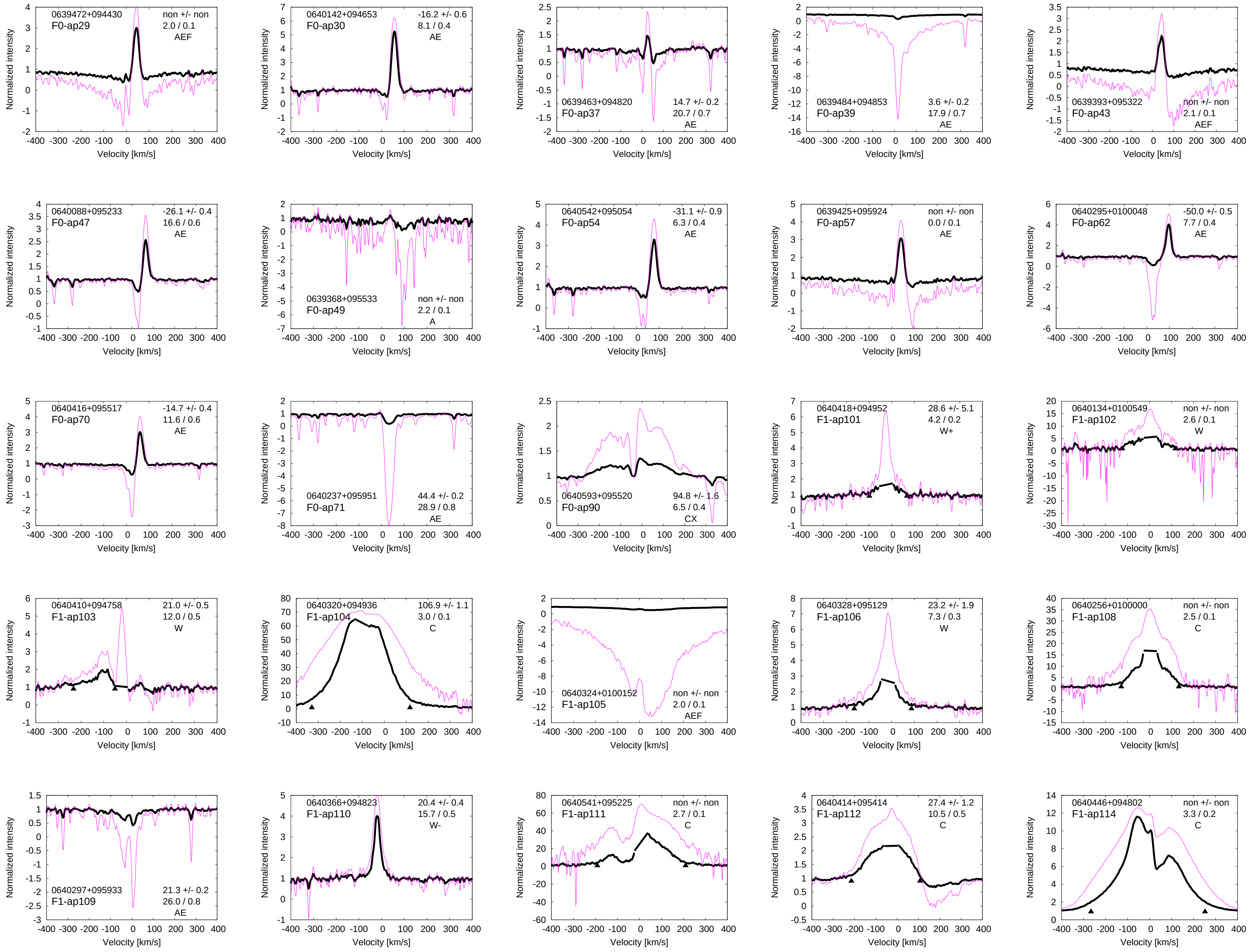
Normalized intensity
Velocity [km/s]
0639472+094430 F0-ap29 non +/- non 2.0 / 0.1 AEF
0640142+094653 F0-ap30 -16.2 +/- 0.6 8.1 / 0.4 AE
0639463+094820 F0-ap37 14.7 +/- 0.2 20.7 / 0.7 AE
0639484+094853 F0-ap39 3.6 +/- 0.2 17.9 / 0.7 AE
0639393+095322 F0-ap43 non +/- non 2.1 / 0.1 AEF
0640088+095233 F0-ap47 -26.1 +/- 0.4 16.6 / 0.6 AE
0639368+095533 F0-ap49 non +/- non 2.2 / 0.1 A
0640542+095054 F0-ap54 -31.1 +/- 0.9 6.3 / 0.4 AE
0639425+095924 F0-ap57 non +/- non 0.0 / 0.1 AE
0640295+0100048 F0-ap62 -50.0 +/- 0.5 7.7 / 0.4 AE
0640416+095517 F0-ap70 -14.7 +/- 0.4 11.6 / 0.6 AE
0640237+095951 F0-ap71 44.4 +/- 0.2 28.9 / 0.8 AE
0640593+095520 F0-ap90 94.8 +/- 1.6 6.5 / 0.4 CX
0640418+094952 F1-ap101 28.6 +/- 5.1 4.2 / 0.2 W+
0640134+0100549 F1-ap102 non +/- non 2.6 / 0.1 W
0640410+094758 F1-ap103 21.0 +/- 0.5 12.0 / 0.5 W
0640320+094936 F1-ap104 106.9 +/- 1.1 3.0 / 0.1 C
0640324+0100152 F1-ap105 non +/- non 2.0 / 0.1 AEF
0640328+095129 F1-ap106 23.2 +/- 1.9 7.3 / 0.3 W
0640256+0100000 F1-ap108 non +/- non 2.5 / 0.1 C
0640297+095933 F1-ap109 21.3 +/- 0.2 26.0 / 0.8 AE
0640366+094823 F1-ap110 20.4 +/- 0.4 15.7 / 0.5 W-
0640541+095225 F1-ap111 non +/- non 2.7 / 0.1 C
0640414+095414 F1-ap112 27.4 +/- 1.2 10.5 / 0.5 C
0640446+094802 F1-ap114 non +/- non 3.3 / 0.2 C

Fig. 12.2 cont.

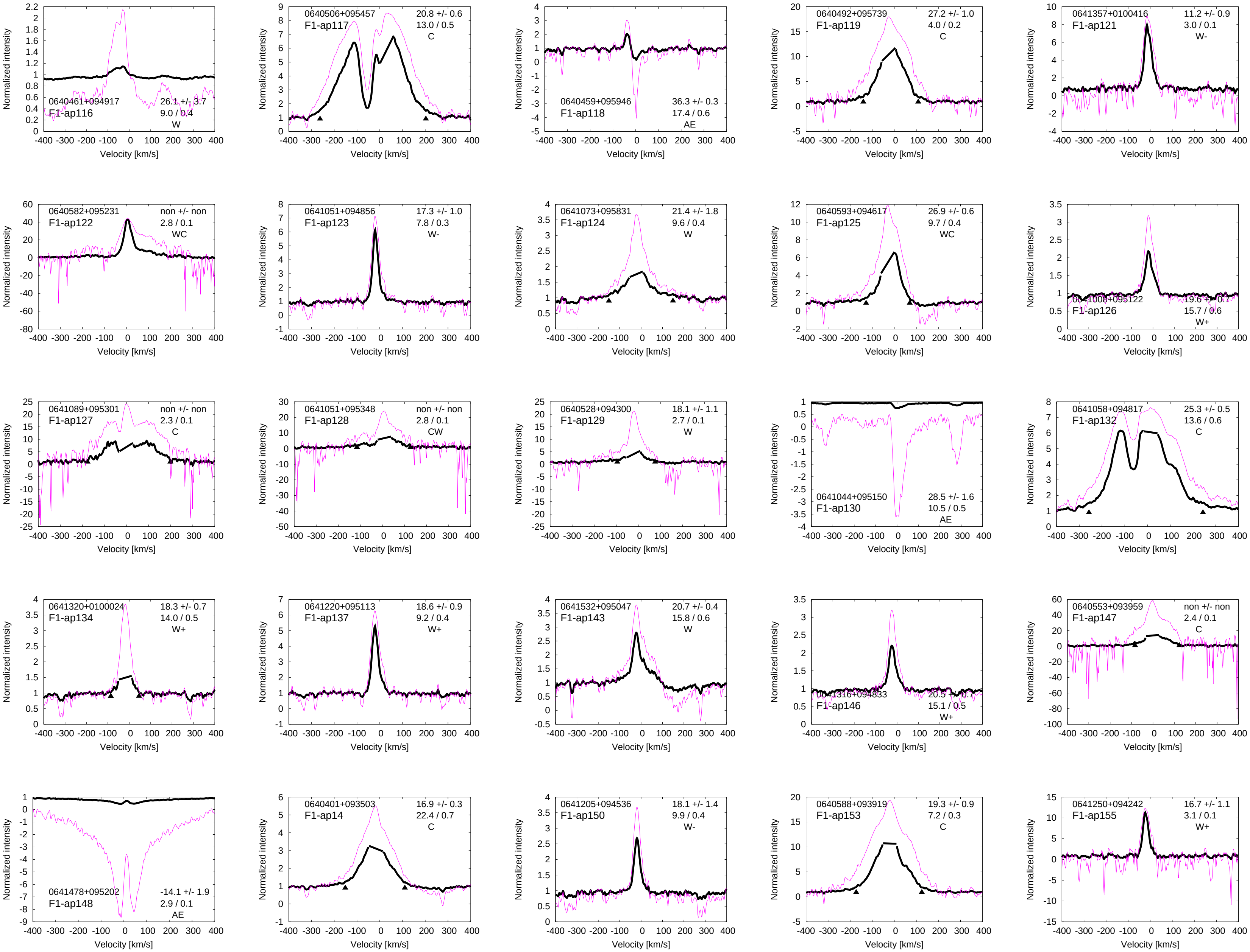
Normalized intensity
Velocity [km/s]
0640461+094917
F1-ap116
26.1 +/- 3.7
9.0 / 0.4
W
0640506+095457
F1-ap117
20.8 +/- 0.6
13.0 / 0.5
C
0640459+095946
F1-ap118
36.3 +/- 0.3
17.4 / 0.6
AE
0640492+095739
F1-ap119
27.2 +/- 1.0
4.0 / 0.2
C
0641357+0100416
F1-ap121
11.2 +/- 0.9
3.0 / 0.1
W-
0640582+095231
F1-ap122
non +/- non
2.8 / 0.1
WC
0641051+094856
F1-ap123
17.3 +/- 1.0
7.8 / 0.3
W-
0641073+095831
F1-ap124
21.4 +/- 1.8
9.6 / 0.4
W
0640593+094617
F1-ap125
26.9 +/- 0.6
9.7 / 0.4
WC
0641008+095122
F1-ap126
19.6 +/- 0.7
15.7 / 0.6
W+
0641089+095301
F1-ap127
non +/- non
2.3 / 0.1
C
0641051+095348
F1-ap128
non +/- non
2.8 / 0.1
CW
0640528+094300
F1-ap129
18.1 +/- 1.1
2.7 / 0.1
W
0641044+095150
F1-ap130
28.5 +/- 1.6
10.5 / 0.5
AE
0641058+094817
F1-ap132
25.3 +/- 0.5
13.6 / 0.6
C
0641320+0100024
F1-ap134
18.3 +/- 0.7
14.0 / 0.5
W+
0641220+095113
F1-ap137
18.6 +/- 0.9
9.2 / 0.4
W+
0641532+095047
F1-ap143
20.7 +/- 0.4
15.8 / 0.6
W
0641316+094833
F1-ap146
20.5 +/- 0.7
15.1 / 0.5
W+
0640553+093959
F1-ap147
non +/- non
2.4 / 0.1
C
0641478+095202
F1-ap148
-14.1 +/- 1.9
2.9 / 0.1
AE
0640401+093503
F1-ap14
16.9 +/- 0.3
22.4 / 0.7
C
0641205+094536
F1-ap150
18.1 +/- 1.4
9.9 / 0.4
W-
0640588+093919
F1-ap153
19.3 +/- 0.9
7.2 / 0.3
C
0641250+094242
F1-ap155
16.7 +/- 1.1
3.1 / 0.1
W+

Fig. 12.2 cont.

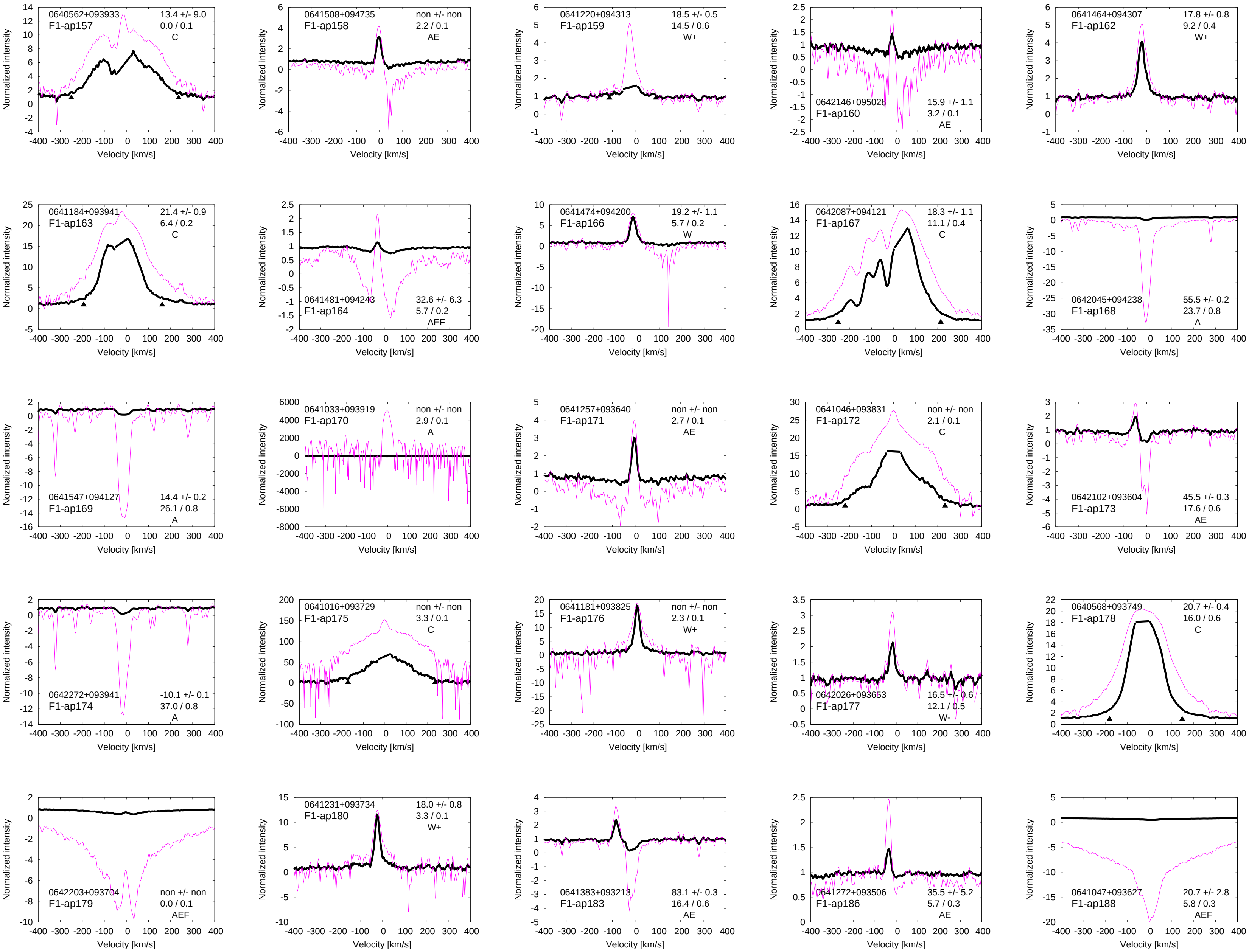
Normalized intensity
Velocity [km/s]
0640562+093933
F1-ap157
13.4 +/- 9.0
0.0 / 0.1
C
0641508+094735
F1-ap158
non +/- non
2.2 / 0.1
AE
0641220+094313
F1-ap159
18.5 +/- 0.5
14.5 / 0.6
W+
0642146+095028
F1-ap160
15.9 +/- 1.1
3.2 / 0.1
AE
0641464+094307
F1-ap162
17.8 +/- 0.8
9.2 / 0.4
W+
0641184+093941
F1-ap163
21.4 +/- 0.9
6.4 / 0.2
C
0641481+094243
F1-ap164
32.6 +/- 6.3
5.7 / 0.2
AEF
0641474+094200
F1-ap166
19.2 +/- 1.1
5.7 / 0.2
W
0642087+094121
F1-ap167
18.3 +/- 1.1
11.1 / 0.4
C
0642045+094238
F1-ap168
55.5 +/- 0.2
23.7 / 0.8
A
0641547+094127
F1-ap169
14.4 +/- 0.2
26.1 / 0.8
A
0641033+093919
F1-ap170
non +/- non
2.9 / 0.1
A
0641257+093640
F1-ap171
non +/- non
2.7 / 0.1
AE
0641046+093831
F1-ap172
non +/- non
2.1 / 0.1
C
0642102+093604
F1-ap173
45.5 +/- 0.3
17.6 / 0.6
AE
0642272+093941
F1-ap174
-10.1 +/- 0.1
37.0 / 0.8
A
0641016+093729
F1-ap175
non +/- non
3.3 / 0.1
C
0641181+093825
F1-ap176
non +/- non
2.3 / 0.1
W+
0642026+093653
F1-ap177
16.5 +/- 0.6
12.1 / 0.5
W-
0640568+093749
F1-ap178
20.7 +/- 0.4
16.0 / 0.6
C
0642203+093704
F1-ap179
non +/- non
0.0 / 0.1
AEF
0641231+093734
F1-ap180
18.0 +/- 0.8
3.3 / 0.1
W+
0641383+093213
F1-ap183
83.1 +/- 0.3
16.4 / 0.6
AE
0641272+093506
F1-ap186
35.5 +/- 5.2
5.7 / 0.3
AE
0641047+093627
F1-ap188
20.7 +/- 2.8
5.8 / 0.3
AEF

Fig. 12.2 cont.

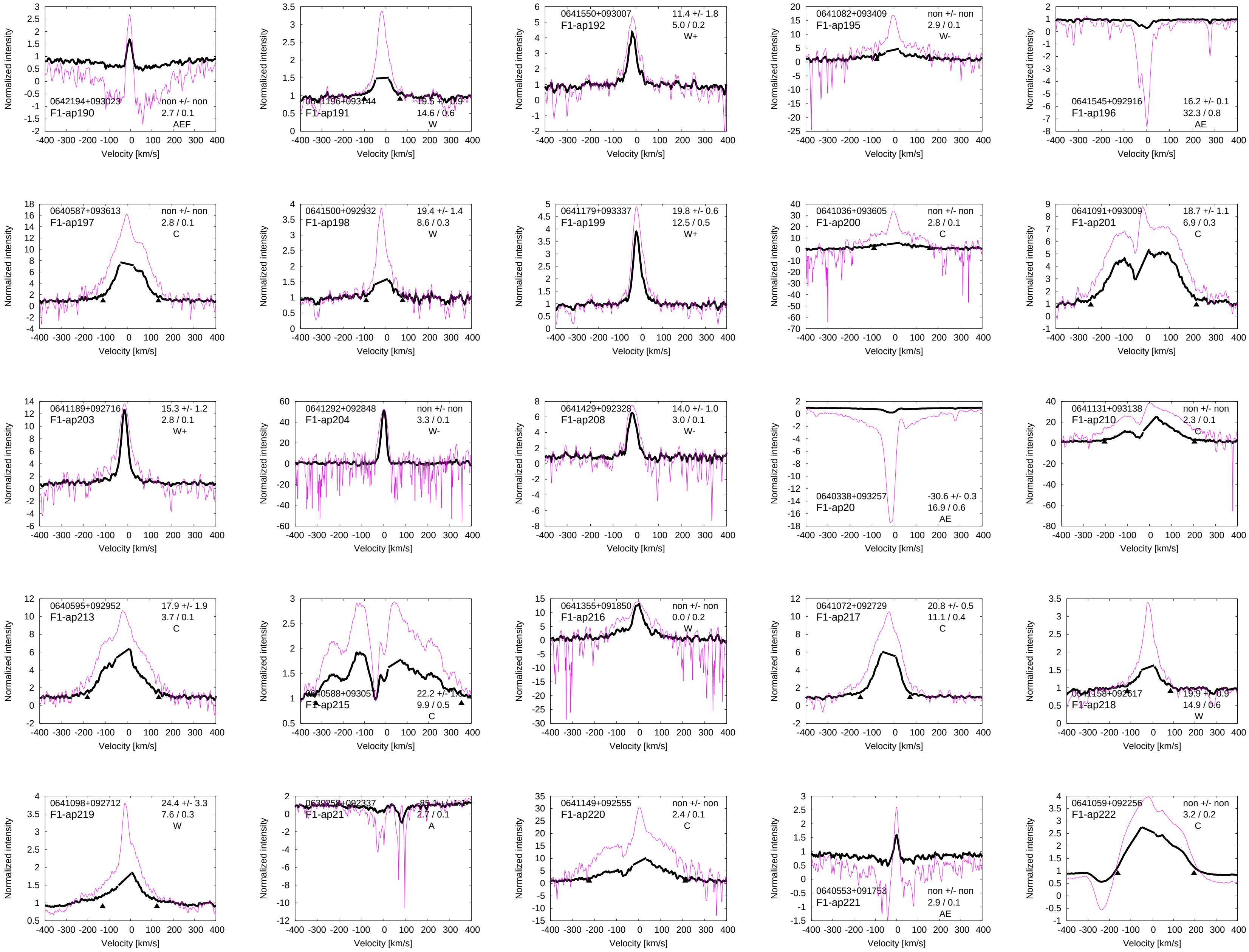
Normalized intensity
Velocity [km/s]
0642194+093023
F1-ap190
non +/- non
2.7 / 0.1
AEF
0641196+093144
F1-ap191
19.5 +/- 0.9
14.6 / 0.6
W
0641550+093007
F1-ap192
11.4 +/- 1.8
5.0 / 0.2
W+
0641082+093409
F1-ap195
non +/- non
2.9 / 0.1
W-
0641545+092916
F1-ap196
16.2 +/- 0.1
32.3 / 0.8
AE
0640587+093613
F1-ap197
non +/- non
2.8 / 0.1
C
0641500+092932
F1-ap198
19.4 +/- 1.4
8.6 / 0.3
W
0641179+093337
F1-ap199
19.8 +/- 0.6
12.5 / 0.5
W+
0641036+093605
F1-ap200
non +/- non
2.8 / 0.1
C
0641091+093009
F1-ap201
18.7 +/- 1.1
6.9 / 0.3
C
0641189+092716
F1-ap203
15.3 +/- 1.2
2.8 / 0.1
W+
0641292+092848
F1-ap204
non +/- non
3.3 / 0.1
W-
0641429+092328
F1-ap208
14.0 +/- 1.0
3.0 / 0.1
W-
0640338+093257
F1-ap20
-30.6 +/- 0.3
16.9 / 0.6
AE
0641131+093138
F1-ap210
non +/- non
2.3 / 0.1
C
0640595+092952
F1-ap213
17.9 +/- 1.9
3.7 / 0.1
C
0640588+093057
F1-ap215
22.2 +/- 1.6
9.9 / 0.5
C
0641355+091850
F1-ap216
non +/- non
0.0 / 0.2
W
0641072+092729
F1-ap217
20.8 +/- 0.5
11.1 / 0.4
C
0641158+092617
F1-ap218
19.9 +/- 0.9
14.9 / 0.6
W
0641098+092712
F1-ap219
24.4 +/- 3.3
7.6 / 0.3
W
0639258+092337
F1-ap21
-85.1 +/- 1.2
2.7 / 0.1
A
0641149+092555
F1-ap220
non +/- non
2.4 / 0.1
C
0640553+091753
F1-ap221
non +/- non
2.9 / 0.1
AE
0641059+092256
F1-ap222
non +/- non
3.2 / 0.2
C
-400 -300 -200 -100 0 100 200 300 400

Fig. 12.2 cont.

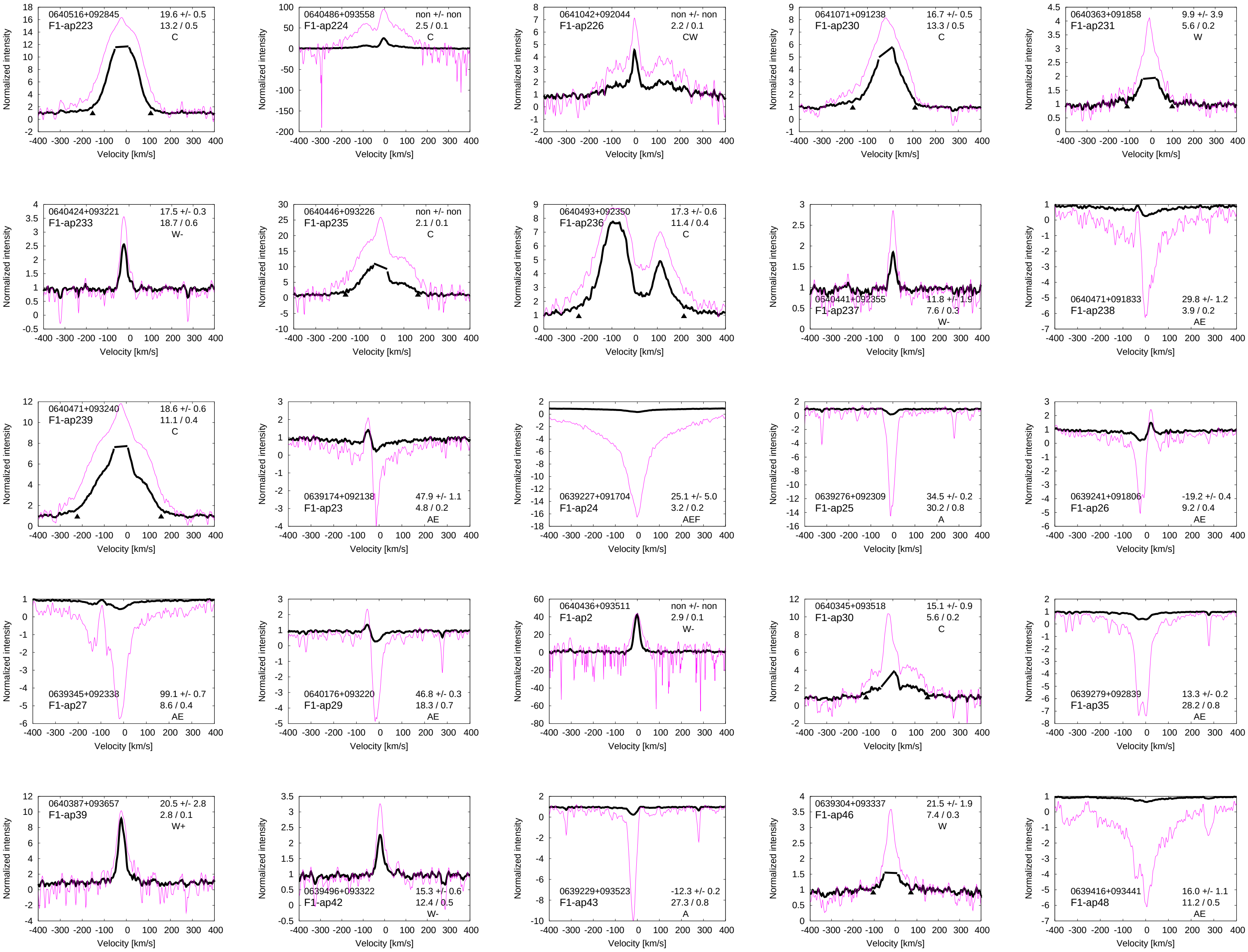
0640516+092845
F1-ap223
19.6 +/- 0.5
13.2 / 0.5
C
0640486+093558
F1-ap224
non +/- non
2.5 / 0.1
C
0641042+092044
F1-ap226
non +/- non
2.2 / 0.1
CW
0641071+091238
F1-ap230
16.7 +/- 0.5
13.3 / 0.5
C
0640363+091858
F1-ap231
9.9 +/- 3.9
5.6 / 0.2
W
0640424+093221
F1-ap233
17.5 +/- 0.3
18.7 / 0.6
W-
0640446+093226
F1-ap235
non +/- non
2.1 / 0.1
C
0640493+092350
F1-ap236
17.3 +/- 0.6
11.4 / 0.4
C
0640441+092355
F1-ap237
11.8 +/- 1.9
7.6 / 0.3
W-
0640471+091833
F1-ap238
29.8 +/- 1.2
3.9 / 0.2
AE
0640471+093240
F1-ap239
18.6 +/- 0.6
11.1 / 0.4
C
0639174+092138
F1-ap23
47.9 +/- 1.1
4.8 / 0.2
AE
0639227+091704
F1-ap24
25.1 +/- 5.0
3.2 / 0.2
AEF
0639276+092309
F1-ap25
34.5 +/- 0.2
30.2 / 0.8
A
0639241+091806
F1-ap26
-19.2 +/- 0.4
9.2 / 0.4
AE
0639345+092338
F1-ap27
99.1 +/- 0.7
8.6 / 0.4
AE
0640176+093220
F1-ap29
46.8 +/- 0.3
18.3 / 0.7
AE
0640436+093511
F1-ap2
non +/- non
2.9 / 0.1
W-
0640345+093518
F1-ap30
15.1 +/- 0.9
5.6 / 0.2
C
0639279+092839
F1-ap35
13.3 +/- 0.2
28.2 / 0.8
AE
0640387+093657
F1-ap39
20.5 +/- 2.8
2.8 / 0.1
W+
0639496+093322
F1-ap42
15.3 +/- 0.6
12.4 / 0.5
W-
0639229+093523
F1-ap43
-12.3 +/- 0.2
27.3 / 0.8
A
0639304+093337
F1-ap46
21.5 +/- 1.9
7.4 / 0.3
W
0639416+093441
F1-ap48
16.0 +/- 1.1
11.2 / 0.5
AE
Normalized intensity
Velocity [km/s]
-400 -300 -200 -100 0 100 200 300 400

Fig. 12.2 cont.

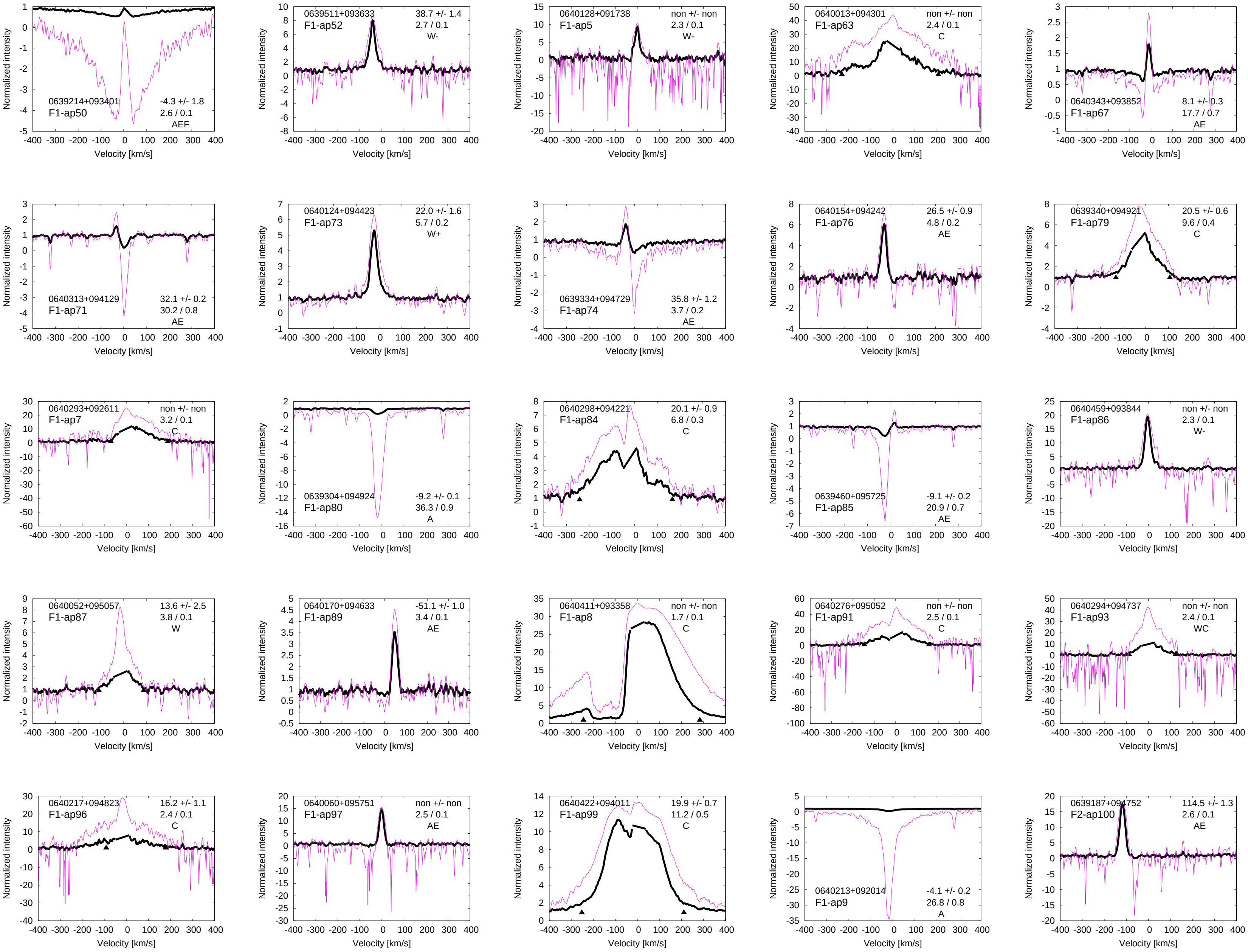
Normalized intensity
Velocity [km/s]
0639214+093401
F1-ap50
-4.3 +/- 1.8
2.6 / 0.1
AEF
0639511+093633
F1-ap52
38.7 +/- 1.4
2.7 / 0.1
W-
0640128+091738
F1-ap5
non +/- non
2.3 / 0.1
W-
0640013+094301
F1-ap63
non +/- non
2.4 / 0.1
C
0640343+093852
F1-ap67
8.1 +/- 0.3
17.7 / 0.7
AE
0640313+094129
F1-ap71
32.1 +/- 0.2
30.2 / 0.8
AE
0640124+094423
F1-ap73
22.0 +/- 1.6
5.7 / 0.2
W+
0639334+094729
F1-ap74
35.8 +/- 1.2
3.7 / 0.2
AE
0640154+094242
F1-ap76
26.5 +/- 0.9
4.8 / 0.2
AE
0639340+094921
F1-ap79
20.5 +/- 0.6
9.6 / 0.4
C
0640293+092611
F1-ap7
non +/- non
3.2 / 0.1
C
0639304+094924
F1-ap80
-9.2 +/- 0.1
36.3 / 0.9
A
0640298+094221
F1-ap84
20.1 +/- 0.9
6.8 / 0.3
C
0639460+095725
F1-ap85
-9.1 +/- 0.2
20.9 / 0.7
AE
0640459+093844
F1-ap86
non +/- non
2.3 / 0.1
W-
0640052+095057
F1-ap87
13.6 +/- 2.5
3.8 / 0.1
W
0640170+094633
F1-ap89
-51.1 +/- 1.0
3.4 / 0.1
AE
0640411+093358
F1-ap8
non +/- non
1.7 / 0.1
C
0640276+095052
F1-ap91
non +/- non
2.5 / 0.1
C
0640294+094737
F1-ap93
non +/- non
2.4 / 0.1
WC
0640217+094823
F1-ap96
16.2 +/- 1.1
2.4 / 0.1
C
0640060+095751
F1-ap97
non +/- non
2.5 / 0.1
AE
0640422+094011
F1-ap99
19.9 +/- 0.7
11.2 / 0.5
C
0640213+092014
F1-ap9
-4.1 +/- 0.2
26.8 / 0.8
A
0639187+094752
F2-ap100
114.5 +/- 1.3
2.6 / 0.1
AE

Fig. 12.2 cont.

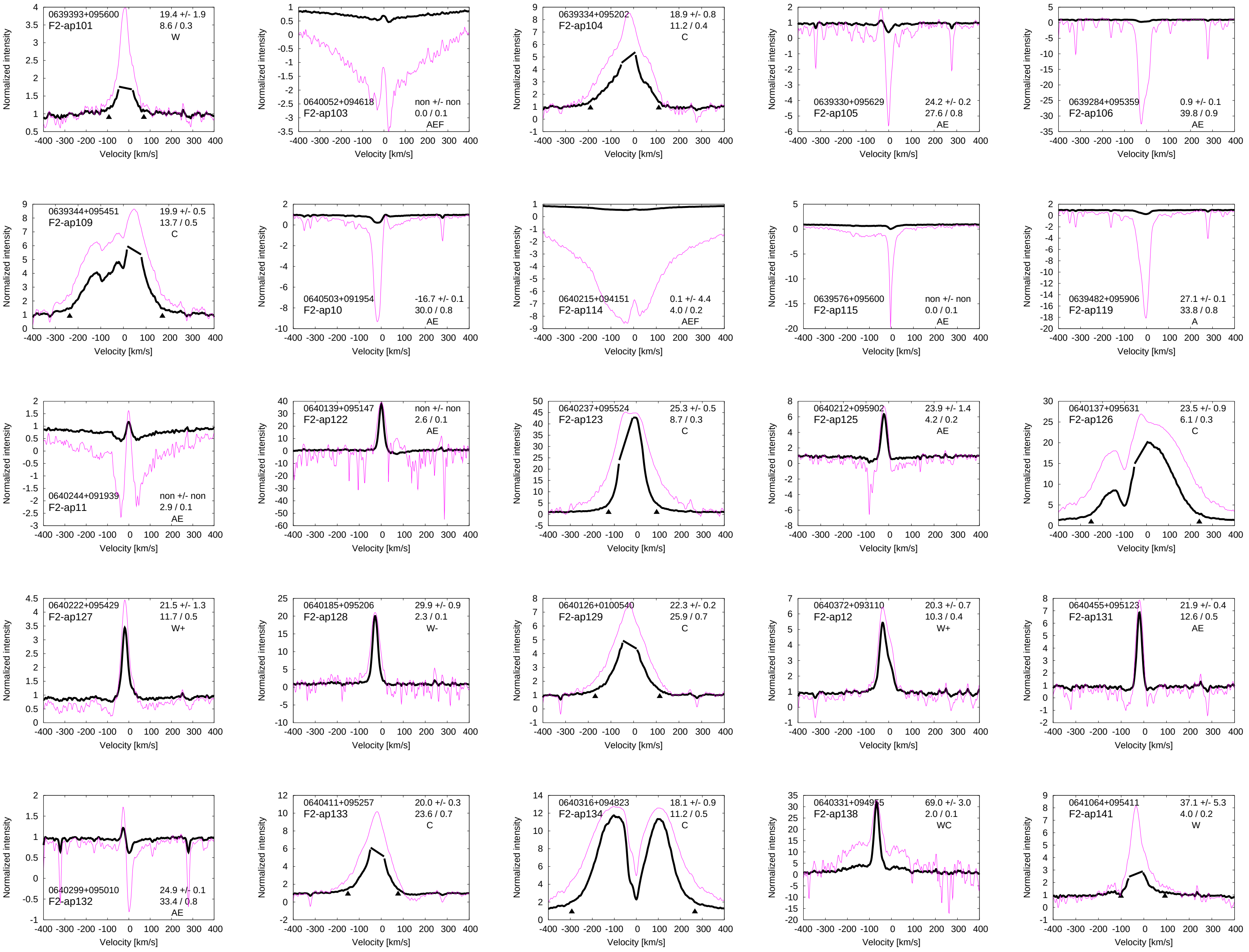
Normalized intensity
Velocity [km/s]
0639393+095600
F2-ap101
19.4 +/- 1.9
8.6 / 0.3
W
0640052+094618
F2-ap103
non +/- non
0.0 / 0.1
AEF
0639334+095202
F2-ap104
18.9 +/- 0.8
11.2 / 0.4
C
0639330+095629
F2-ap105
24.2 +/- 0.2
27.6 / 0.8
AE
0639284+095359
F2-ap106
0.9 +/- 0.1
39.8 / 0.9
AE
0639344+095451
F2-ap109
19.9 +/- 0.5
13.7 / 0.5
C
0640503+091954
F2-ap10
-16.7 +/- 0.1
30.0 / 0.8
AE
0640215+094151
F2-ap114
0.1 +/- 4.4
4.0 / 0.2
AEF
0639576+095600
F2-ap115
non +/- non
0.0 / 0.1
AE
0639482+095906
F2-ap119
27.1 +/- 0.1
33.8 / 0.8
A
0640244+091939
F2-ap11
non +/- non
2.9 / 0.1
AE
0640139+095147
F2-ap122
non +/- non
2.6 / 0.1
AE
0640237+095524
F2-ap123
25.3 +/- 0.5
8.7 / 0.3
C
0640212+095902
F2-ap125
23.9 +/- 1.4
4.2 / 0.2
AE
0640137+095631
F2-ap126
23.5 +/- 0.9
6.1 / 0.3
C
0640222+095429
F2-ap127
21.5 +/- 1.3
11.7 / 0.5
W+
0640185+095206
F2-ap128
29.9 +/- 0.9
2.3 / 0.1
W-
0640126+0100540
F2-ap129
22.3 +/- 0.2
25.9 / 0.7
C
0640372+093110
F2-ap12
20.3 +/- 0.7
10.3 / 0.4
W+
0640455+095123
F2-ap131
21.9 +/- 0.4
12.6 / 0.5
AE
0640299+095010
F2-ap132
24.9 +/- 0.1
33.4 / 0.8
AE
0640411+095257
F2-ap133
20.0 +/- 0.3
23.6 / 0.7
C
0640316+094823
F2-ap134
18.1 +/- 0.9
11.2 / 0.5
C
0640331+094955
F2-ap138
69.0 +/- 3.0
2.0 / 0.1
WC
0641064+095411
F2-ap141
37.1 +/- 5.3
4.0 / 0.2
W
-400 -300 -200 -100 0 100 200 300 400

Fig. 12.2 cont.

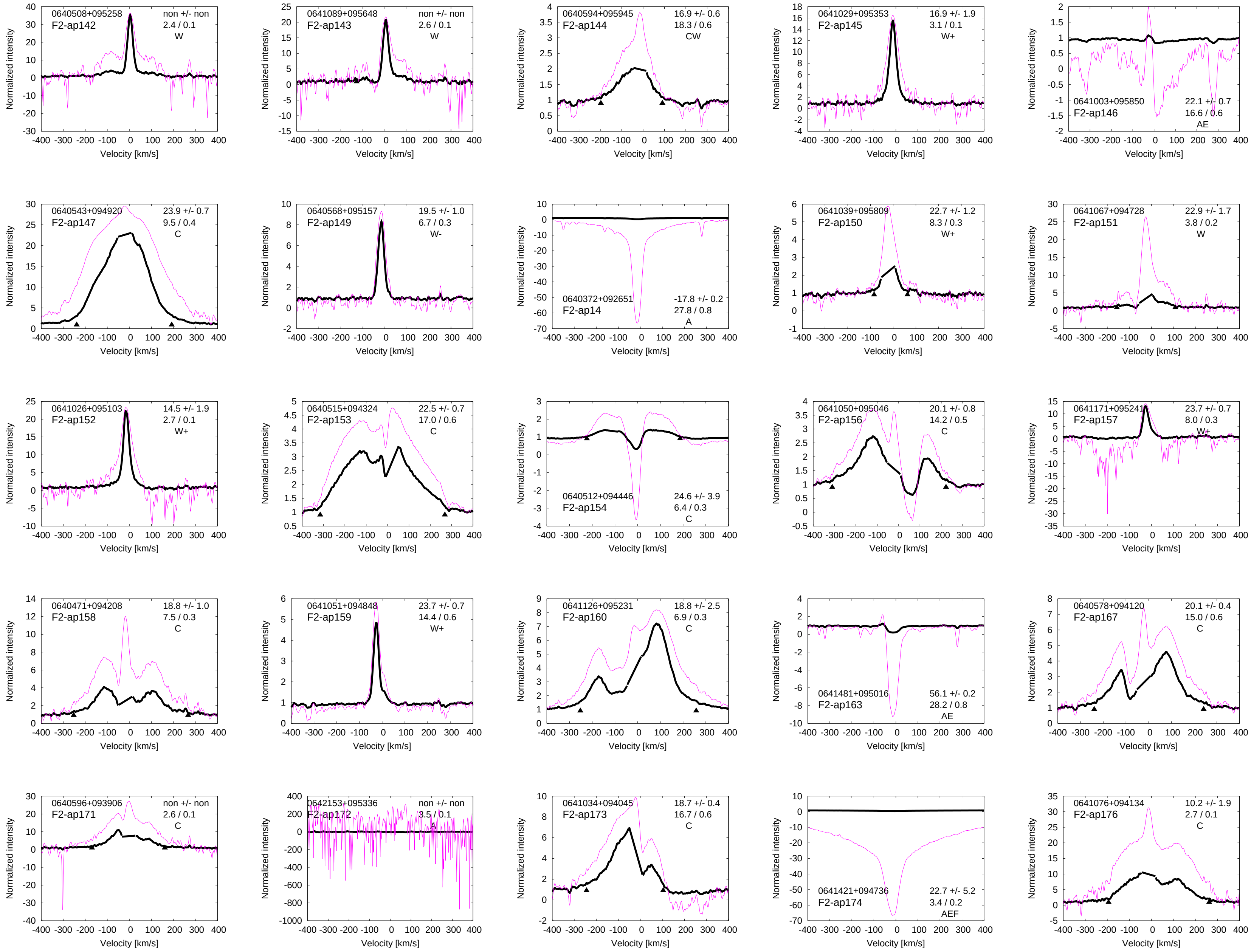
0640508+095258
F2-ap142
non +/- non
2.4 / 0.1
W
0641089+095648
F2-ap143
non +/- non
2.6 / 0.1
W
0640594+095945
F2-ap144
16.9 +/- 0.6
18.3 / 0.6
CW
0641029+095353
F2-ap145
16.9 +/- 1.9
3.1 / 0.1
W+
0641003+095850
F2-ap146
22.1 +/- 0.7
16.6 / 0.6
AE
0640543+094920
F2-ap147
23.9 +/- 0.7
9.5 / 0.4
C
0640568+095157
F2-ap149
19.5 +/- 1.0
6.7 / 0.3
W-
0640372+092651
F2-ap14
-17.8 +/- 0.2
27.8 / 0.8
A
0641039+095809
F2-ap150
22.7 +/- 1.2
8.3 / 0.3
W+
0641067+094728
F2-ap151
22.9 +/- 1.7
3.8 / 0.2
W
0641026+095103
F2-ap152
14.5 +/- 1.9
2.7 / 0.1
W+
0640515+094324
F2-ap153
22.5 +/- 0.7
17.0 / 0.6
C
0640512+094446
F2-ap154
24.6 +/- 3.9
6.4 / 0.3
C
0641050+095046
F2-ap156
20.1 +/- 0.8
14.2 / 0.5
C
0641171+095241
F2-ap157
23.7 +/- 0.7
8.0 / 0.3
W+
0640471+094208
F2-ap158
18.8 +/- 1.0
7.5 / 0.3
C
0641051+094848
F2-ap159
23.7 +/- 0.7
14.4 / 0.6
W+
0641126+095231
F2-ap160
18.8 +/- 2.5
6.9 / 0.3
C
0641481+095016
F2-ap163
56.1 +/- 0.2
28.2 / 0.8
AE
0640578+094120
F2-ap167
20.1 +/- 0.4
15.0 / 0.6
C
0640596+093906
F2-ap171
non +/- non
2.6 / 0.1
C
0642153+095336
F2-ap172
non +/- non
3.5 / 0.1
A
0641034+094045
F2-ap173
18.7 +/- 0.4
16.7 / 0.6
C
0641421+094736
F2-ap174
22.7 +/- 5.2
3.4 / 0.2
AEF
0641076+094134
F2-ap176
10.2 +/- 1.9
2.7 / 0.1
C
Normalized intensity
Velocity [km/s]
-400 -300 -200 -100 0 100 200 300 400

Fig. 12.2 cont.

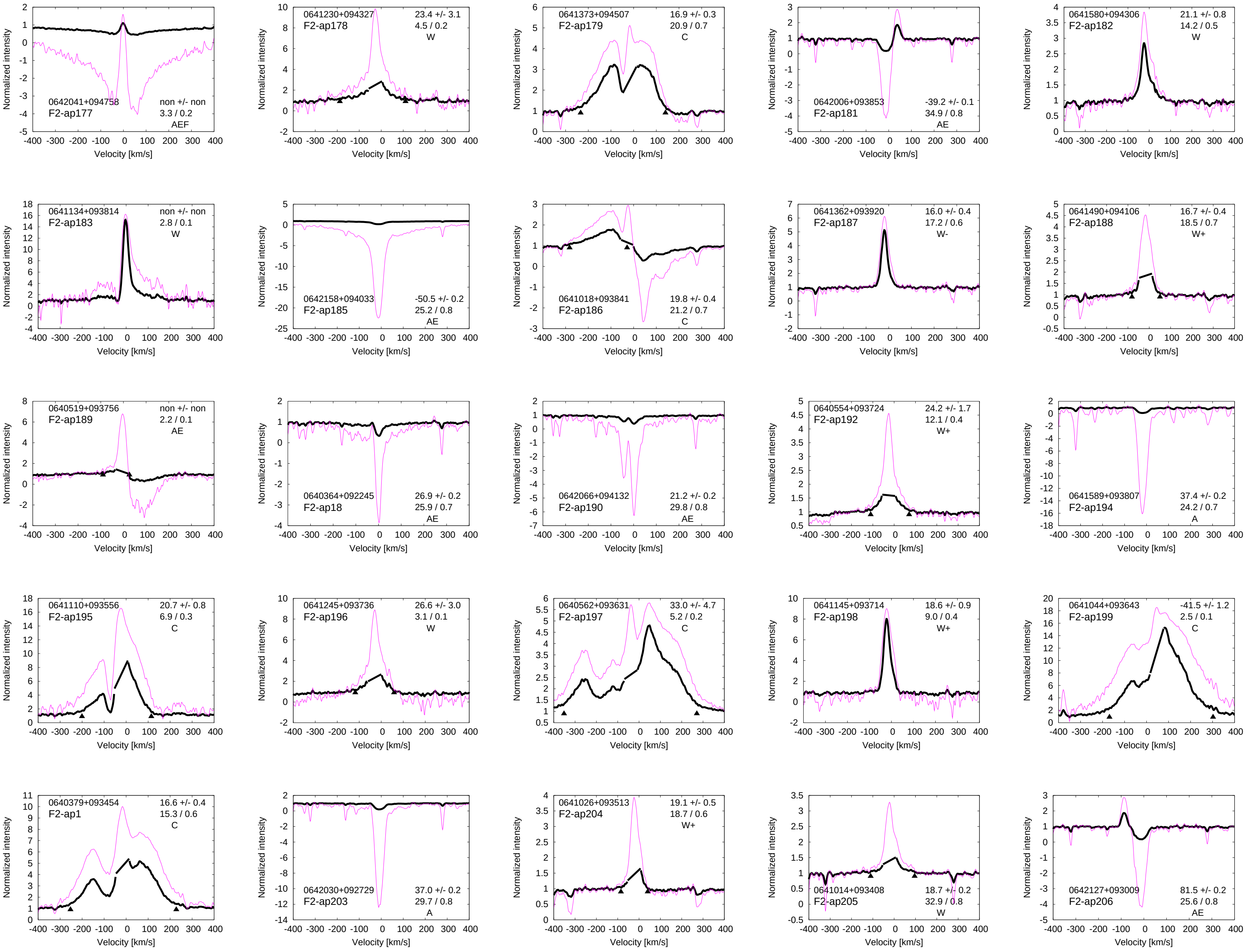
Normalized intensity
Velocity [km/s]
0642041+094758
F2-ap177
non +/- non
3.3 / 0.2
AEF
0641230+094327
F2-ap178
23.4 +/- 3.1
4.5 / 0.2
W
0641373+094507
F2-ap179
16.9 +/- 0.3
20.9 / 0.7
C
0642006+093853
F2-ap181
-39.2 +/- 0.1
34.9 / 0.8
AE
0641580+094306
F2-ap182
21.1 +/- 0.8
14.2 / 0.5
W
0641134+093814
F2-ap183
non +/- non
2.8 / 0.1
W
0642158+094033
F2-ap185
-50.5 +/- 0.2
25.2 / 0.8
AE
0641018+093841
F2-ap186
19.8 +/- 0.4
21.2 / 0.7
C
0641362+093920
F2-ap187
16.0 +/- 0.4
17.2 / 0.6
W-
0641490+094106
F2-ap188
16.7 +/- 0.4
18.5 / 0.7
W+
0640519+093756
F2-ap189
non +/- non
2.2 / 0.1
AE
0640364+092245
F2-ap18
26.9 +/- 0.2
25.9 / 0.7
AE
0642066+094132
F2-ap190
21.2 +/- 0.2
29.8 / 0.8
AE
0640554+093724
F2-ap192
24.2 +/- 1.7
12.1 / 0.4
W+
0641589+093807
F2-ap194
37.4 +/- 0.2
24.2 / 0.7
A
0641110+093556
F2-ap195
20.7 +/- 0.8
6.9 / 0.3
C
0641245+093736
F2-ap196
26.6 +/- 3.0
3.1 / 0.1
W
0640562+093631
F2-ap197
33.0 +/- 4.7
5.2 / 0.2
C
0641145+093714
F2-ap198
18.6 +/- 0.9
9.0 / 0.4
W+
0641044+093643
F2-ap199
-41.5 +/- 1.2
2.5 / 0.1
C
0640379+093454
F2-ap1
16.6 +/- 0.4
15.3 / 0.6
C
0642030+092729
F2-ap203
37.0 +/- 0.2
29.7 / 0.8
A
0641026+093513
F2-ap204
19.1 +/- 0.5
18.7 / 0.6
W+
0641014+093408
F2-ap205
18.7 +/- 0.2
32.9 / 0.8
W
0642127+093009
F2-ap206
81.5 +/- 0.2
25.6 / 0.8
AE

Fig. 12.2 cont.

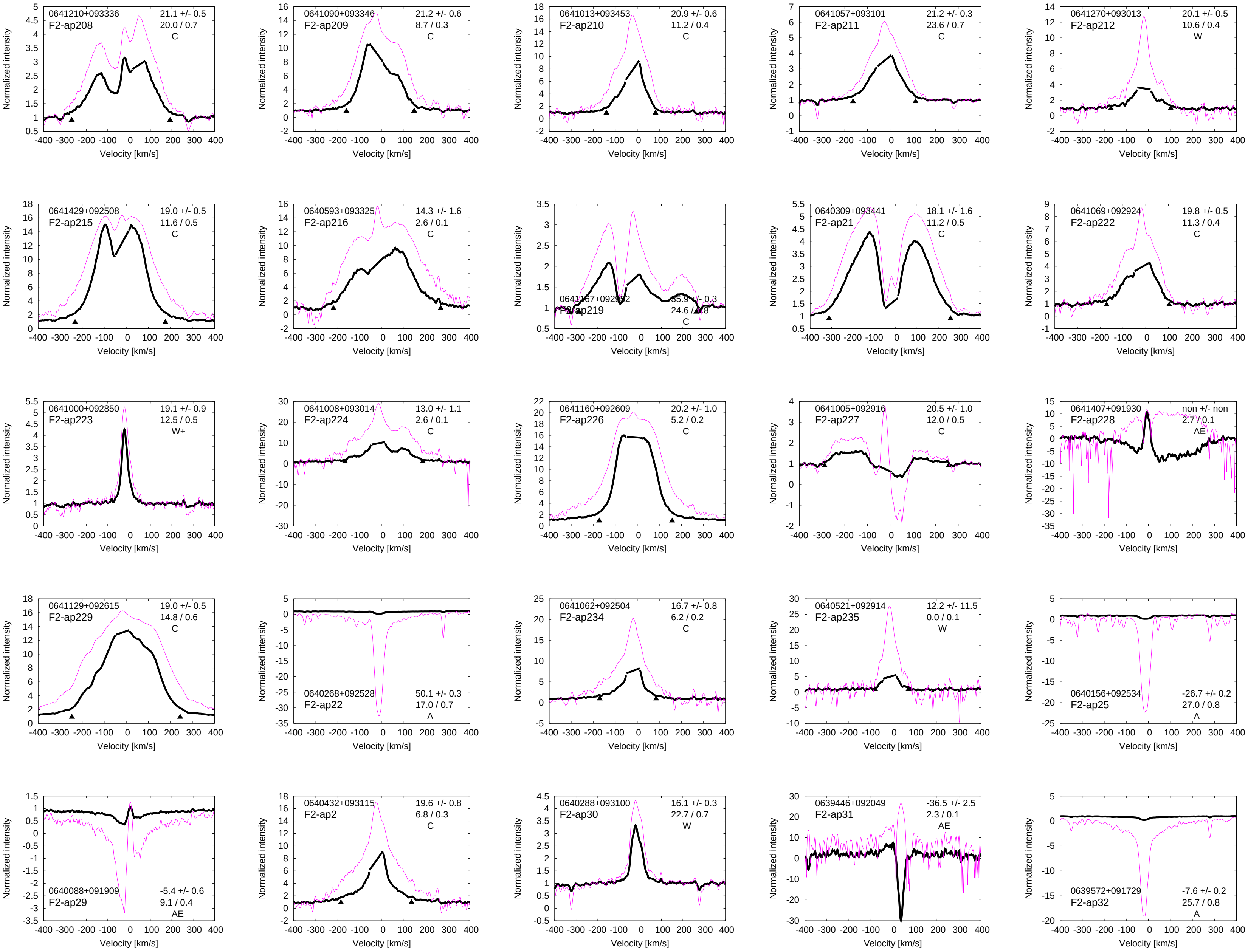
Normalized intensity
Velocity [km/s]
0641210+093336
F2-ap208
21.1 +/- 0.5
20.0 / 0.7
C
0641090+093346
F2-ap209
21.2 +/- 0.6
8.7 / 0.3
C
0641013+093453
F2-ap210
20.9 +/- 0.6
11.2 / 0.4
C
0641057+093101
F2-ap211
21.2 +/- 0.3
23.6 / 0.7
C
0641270+093013
F2-ap212
20.1 +/- 0.5
10.6 / 0.4
W
0641429+092508
F2-ap215
19.0 +/- 0.5
11.6 / 0.5
C
0640593+093325
F2-ap216
14.3 +/- 1.6
2.6 / 0.1
C
0641167+092952
F2-ap219
35.9 +/- 0.3
24.6 / 0.8
C
0640309+093441
F2-ap21
18.1 +/- 1.6
11.2 / 0.5
C
0641069+092924
F2-ap222
19.8 +/- 0.5
11.3 / 0.4
C
0641000+092850
F2-ap223
19.1 +/- 0.9
12.5 / 0.5
W+
0641008+093014
F2-ap224
13.0 +/- 1.1
2.6 / 0.1
C
0641160+092609
F2-ap226
20.2 +/- 1.0
5.2 / 0.2
C
0641005+092916
F2-ap227
20.5 +/- 1.0
12.0 / 0.5
C
0641407+091930
F2-ap228
non +/- non
2.7 / 0.1
AE
0641129+092615
F2-ap229
19.0 +/- 0.5
14.8 / 0.6
C
0640268+092528
F2-ap22
50.1 +/- 0.3
17.0 / 0.7
A
0641062+092504
F2-ap234
16.7 +/- 0.8
6.2 / 0.2
C
0640521+092914
F2-ap235
12.2 +/- 11.5
0.0 / 0.1
W
0640156+092534
F2-ap25
-26.7 +/- 0.2
27.0 / 0.8
A
0640088+091909
F2-ap29
-5.4 +/- 0.6
9.1 / 0.4
AE
0640432+093115
F2-ap2
19.6 +/- 0.8
6.8 / 0.3
C
0640288+093100
F2-ap30
16.1 +/- 0.3
22.7 / 0.7
W
0639446+092049
F2-ap31
-36.5 +/- 2.5
2.3 / 0.1
AE
0639572+091729
F2-ap32
-7.6 +/- 0.2
25.7 / 0.8
A
-400 -300 -200 -100 0 100 200 300 400

Fig. 12.2 cont.

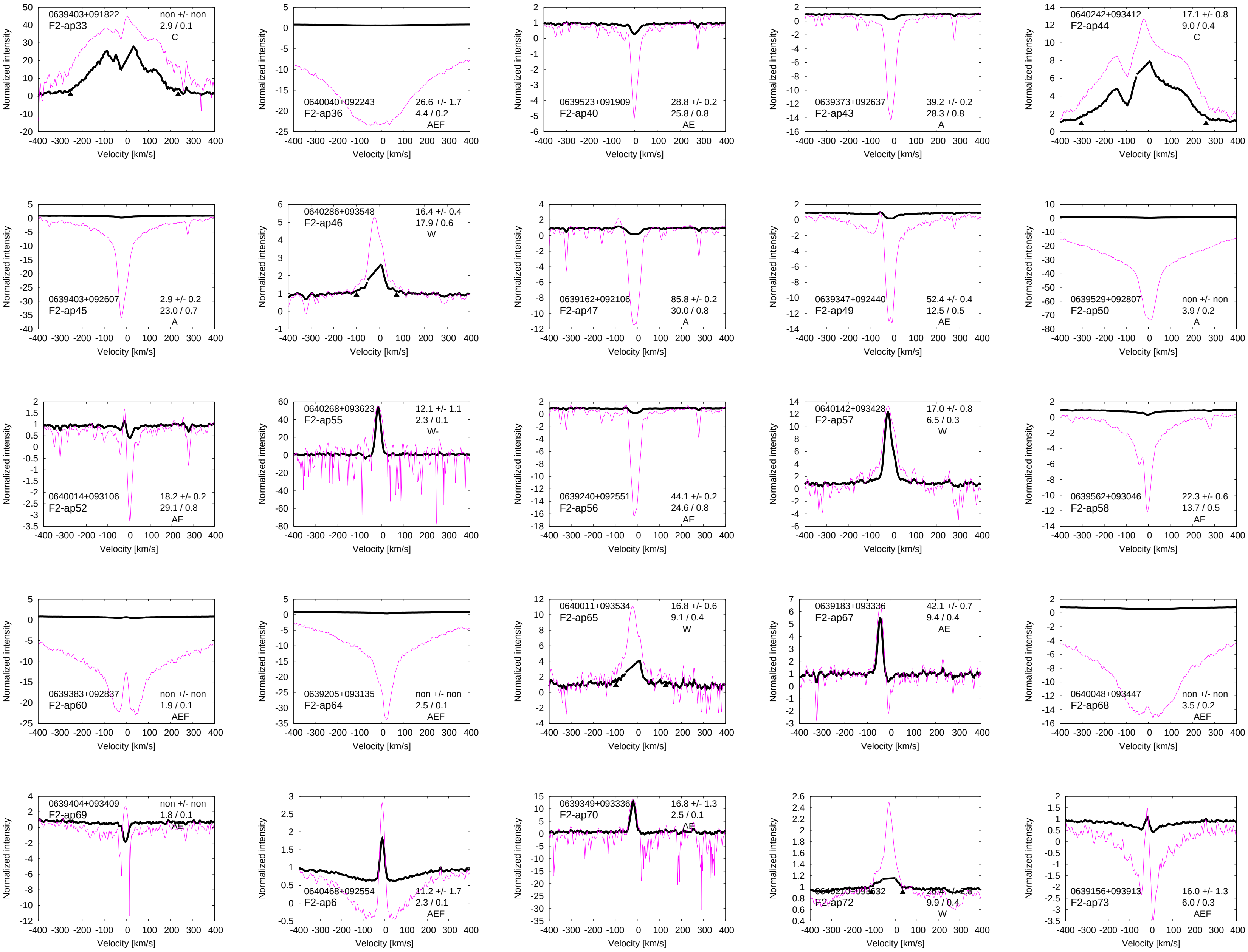
Normalized intensity
Velocity [km/s]
0639403+091822
F2-ap33
non +/- non
2.9 / 0.1
C
0640040+092243
F2-ap36
26.6 +/- 1.7
4.4 / 0.2
AEF
0639523+091909
F2-ap40
28.8 +/- 0.2
25.8 / 0.8
AE
0639373+092637
F2-ap43
39.2 +/- 0.2
28.3 / 0.8
A
0640242+093412
F2-ap44
17.1 +/- 0.8
9.0 / 0.4
C
0639403+092607
F2-ap45
2.9 +/- 0.2
23.0 / 0.7
A
0640286+093548
F2-ap46
16.4 +/- 0.4
17.9 / 0.6
W
0639162+092106
F2-ap47
85.8 +/- 0.2
30.0 / 0.8
A
0639347+092440
F2-ap49
52.4 +/- 0.4
12.5 / 0.5
AE
0639529+092807
F2-ap50
non +/- non
3.9 / 0.2
A
0640014+093106
F2-ap52
18.2 +/- 0.2
29.1 / 0.8
AE
0640268+093623
F2-ap55
12.1 +/- 1.1
2.3 / 0.1
W-
0639240+092551
F2-ap56
44.1 +/- 0.2
24.6 / 0.8
AE
0640142+093428
F2-ap57
17.0 +/- 0.8
6.5 / 0.3
W
0639562+093046
F2-ap58
22.3 +/- 0.6
13.7 / 0.5
AE
0639383+092837
F2-ap60
non +/- non
1.9 / 0.1
AEF
0639205+093135
F2-ap64
non +/- non
2.5 / 0.1
AEF
0640011+093534
F2-ap65
16.8 +/- 0.6
9.1 / 0.4
W
0639183+093336
F2-ap67
42.1 +/- 0.7
9.4 / 0.4
AE
0640048+093447
F2-ap68
non +/- non
3.5 / 0.2
AEF
0639404+093409
F2-ap69
non +/- non
1.8 / 0.1
AE
0640468+092554
F2-ap6
11.2 +/- 1.7
2.3 / 0.1
AEF
0639349+093336
F2-ap70
16.8 +/- 1.3
2.5 / 0.1
AE
0640210+093632
F2-ap72
26.4 +/- 2.8
9.9 / 0.4
W
0639156+093913
F2-ap73
16.0 +/- 1.3
6.0 / 0.3
AEF

Fig. 12.2 cont.

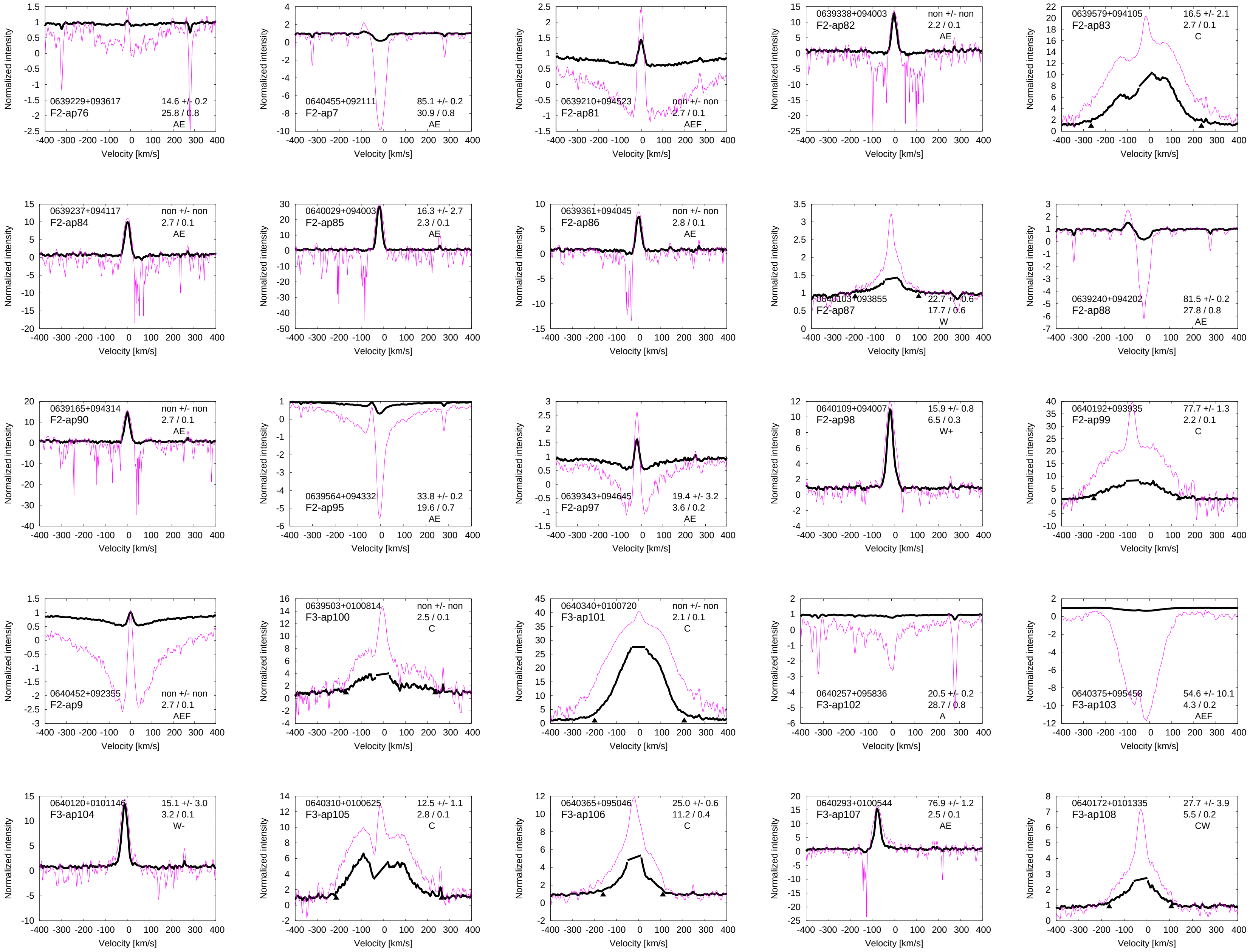
Normalized intensity
Velocity [km/s]
0639229+093617
F2-ap76
14.6 +/- 0.2
25.8 / 0.8
AE
0640455+092111
F2-ap7
85.1 +/- 0.2
30.9 / 0.8
AE
0639210+094523
F2-ap81
non +/- non
2.7 / 0.1
AEF
0639338+094003
F2-ap82
non +/- non
2.2 / 0.1
AE
0639579+094105
F2-ap83
16.5 +/- 2.1
2.7 / 0.1
C
0639237+094117
F2-ap84
non +/- non
2.7 / 0.1
AE
0640029+094003
F2-ap85
16.3 +/- 2.7
2.3 / 0.1
AE
0639361+094045
F2-ap86
non +/- non
2.8 / 0.1
AE
0640103+093855
F2-ap87
22.7 +/- 0.6
17.7 / 0.6
W
0639240+094202
F2-ap88
81.5 +/- 0.2
27.8 / 0.8
AE
0639165+094314
F2-ap90
non +/- non
2.7 / 0.1
AE
0639564+094332
F2-ap95
33.8 +/- 0.2
19.6 / 0.7
AE
0639343+094645
F2-ap97
19.4 +/- 3.2
3.6 / 0.2
AE
0640109+094007
F2-ap98
15.9 +/- 0.8
6.5 / 0.3
W+
0640192+093935
F2-ap99
77.7 +/- 1.3
2.2 / 0.1
C
0640452+092355
F2-ap9
non +/- non
2.7 / 0.1
AEF
0639503+0100814
F3-ap100
non +/- non
2.5 / 0.1
C
0640340+0100720
F3-ap101
non +/- non
2.1 / 0.1
C
0640257+095836
F3-ap102
20.5 +/- 0.2
28.7 / 0.8
A
0640375+095458
F3-ap103
54.6 +/- 10.1
4.3 / 0.2
AEF
0640120+0101146
F3-ap104
15.1 +/- 3.0
3.2 / 0.1
W-
0640310+0100625
F3-ap105
12.5 +/- 1.1
2.8 / 0.1
C
0640365+095046
F3-ap106
25.0 +/- 0.6
11.2 / 0.4
C
0640293+0100544
F3-ap107
76.9 +/- 1.2
2.5 / 0.1
AE
0640172+0101335
F3-ap108
27.7 +/- 3.9
5.5 / 0.2
CW

Fig. 12.2 cont.

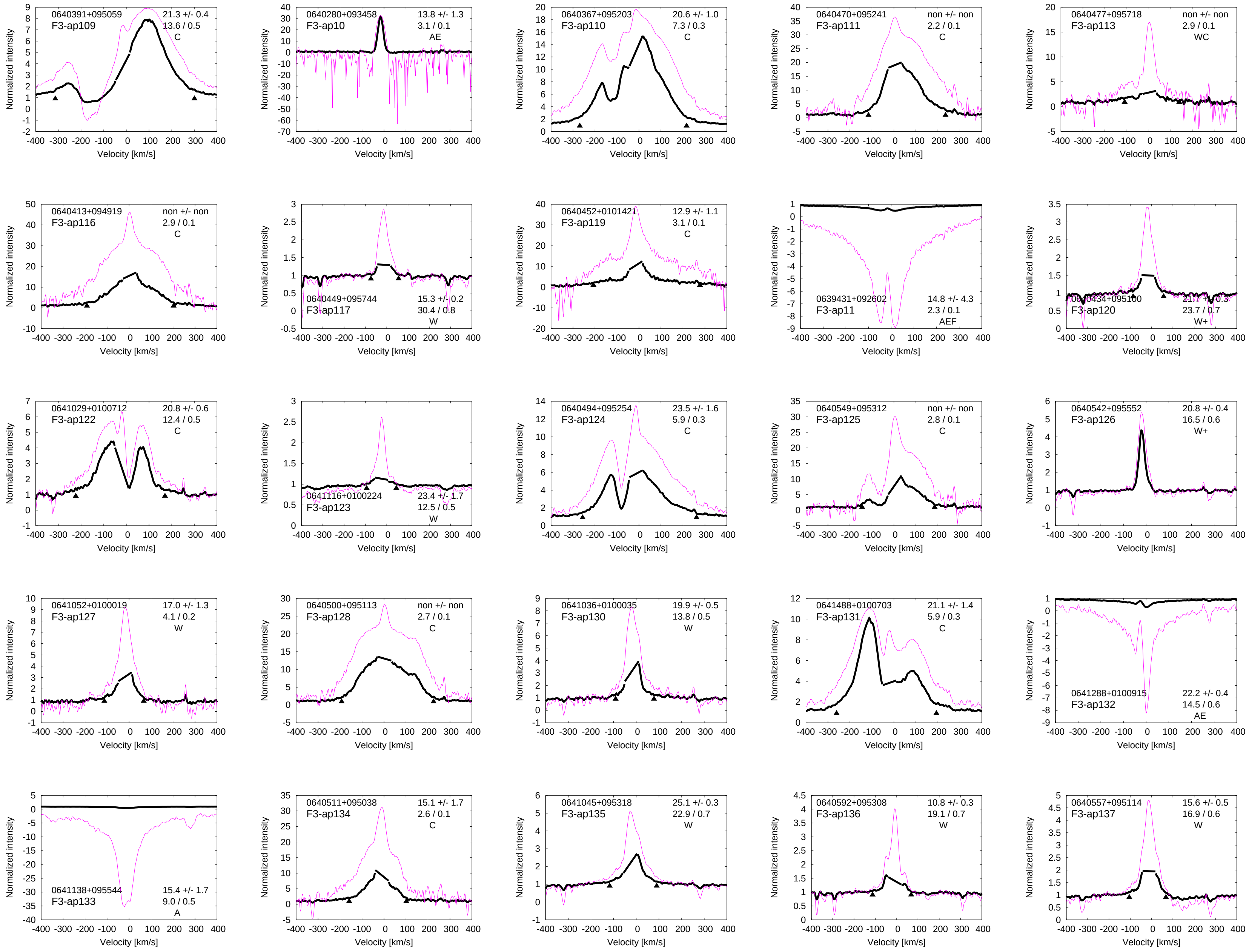
Normalized intensity
Velocity [km/s]
0640391+095059
F3-ap109
21.3 +/- 0.4
13.6 / 0.5
C
0640280+093458
F3-ap10
13.8 +/- 1.3
3.1 / 0.1
AE
0640367+095203
F3-ap110
20.6 +/- 1.0
7.3 / 0.3
C
0640470+095241
F3-ap111
non +/- non
2.2 / 0.1
C
0640477+095718
F3-ap113
non +/- non
2.9 / 0.1
WC
0640413+094919
F3-ap116
non +/- non
2.9 / 0.1
C
0640449+095744
F3-ap117
15.3 +/- 0.2
30.4 / 0.8
W
0640452+0101421
F3-ap119
12.9 +/- 1.1
3.1 / 0.1
C
0639431+092602
F3-ap11
14.8 +/- 4.3
2.3 / 0.1
AEF
0640434+095100
F3-ap120
21.7 +/- 0.3
23.7 / 0.7
W+
0641029+0100712
F3-ap122
20.8 +/- 0.6
12.4 / 0.5
C
0641116+0100224
F3-ap123
23.4 +/- 1.7
12.5 / 0.5
W
0640494+095254
F3-ap124
23.5 +/- 1.6
5.9 / 0.3
C
0640549+095312
F3-ap125
non +/- non
2.8 / 0.1
C
0640542+095552
F3-ap126
20.8 +/- 0.4
16.5 / 0.6
W+
0641052+0100019
F3-ap127
17.0 +/- 1.3
4.1 / 0.2
W
0640500+095113
F3-ap128
non +/- non
2.7 / 0.1
C
0641036+0100035
F3-ap130
19.9 +/- 0.5
13.8 / 0.5
W
0641488+0100703
F3-ap131
21.1 +/- 1.4
5.9 / 0.3
C
0641288+0100915
F3-ap132
22.2 +/- 0.4
14.5 / 0.6
AE
0641138+095544
F3-ap133
15.4 +/- 1.7
9.0 / 0.5
A
0640511+095038
F3-ap134
15.1 +/- 1.7
2.6 / 0.1
C
0641045+095318
F3-ap135
25.1 +/- 0.3
22.9 / 0.7
W
0640592+095308
F3-ap136
10.8 +/- 0.3
19.1 / 0.7
W
0640557+095114
F3-ap137
15.6 +/- 0.5
16.9 / 0.6
W

Fig. 12.2 cont.

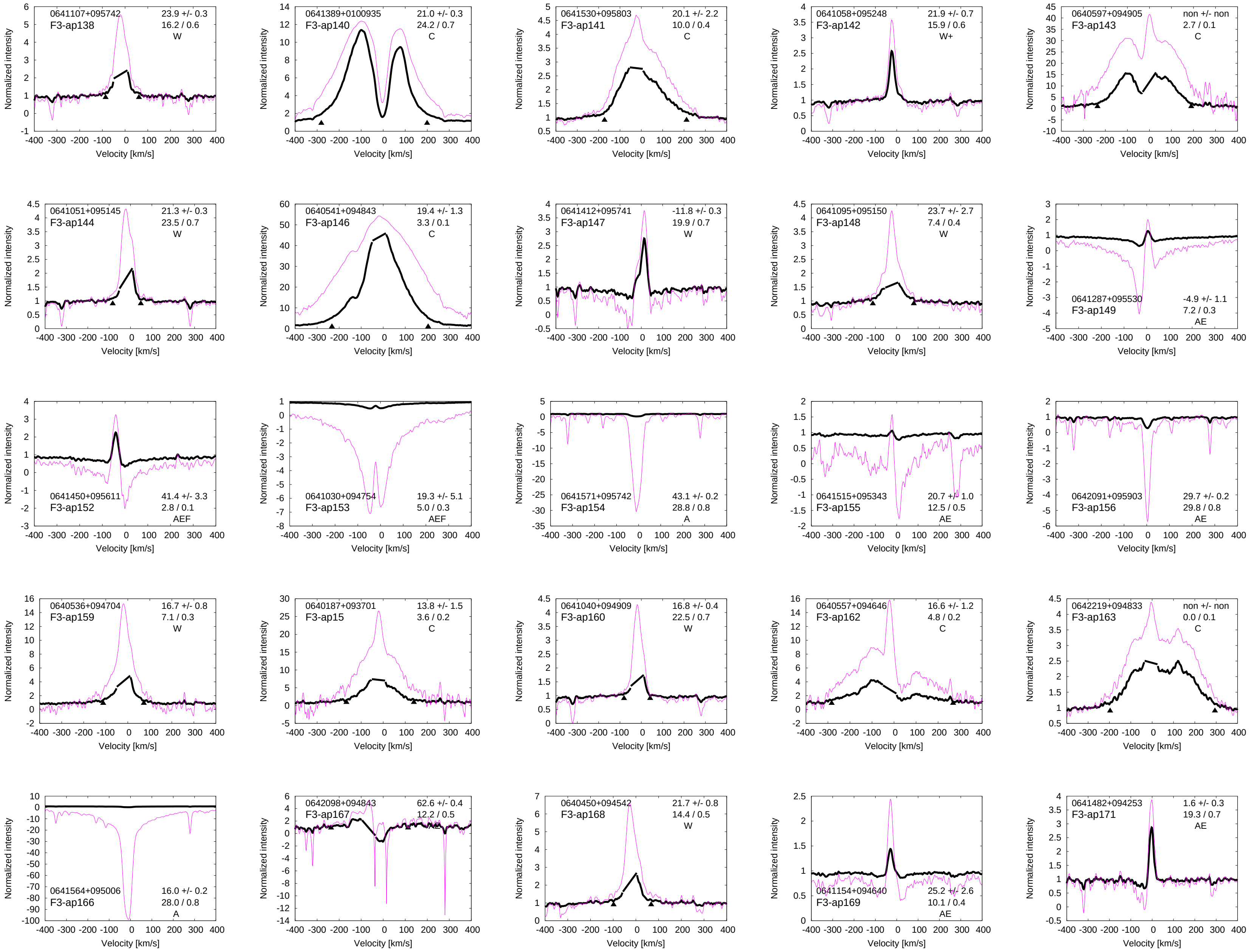
Normalized intensity
Velocity [km/s]
0641107+095742
F3-ap138
23.9 +/- 0.3
16.2 / 0.6
W
0641389+0100935
F3-ap140
21.0 +/- 0.3
24.2 / 0.7
C
0641530+095803
F3-ap141
20.1 +/- 2.2
10.0 / 0.4
C
0641058+095248
F3-ap142
21.9 +/- 0.7
15.9 / 0.6
W+
0640597+094905
F3-ap143
non +/- non
2.7 / 0.1
C
0641051+095145
F3-ap144
21.3 +/- 0.3
23.5 / 0.7
W
0640541+094843
F3-ap146
19.4 +/- 1.3
3.3 / 0.1
C
0641412+095741
F3-ap147
-11.8 +/- 0.3
19.9 / 0.7
W
0641095+095150
F3-ap148
23.7 +/- 2.7
7.4 / 0.4
W
0641287+095530
F3-ap149
-4.9 +/- 1.1
7.2 / 0.3
AE
0641450+095611
F3-ap152
41.4 +/- 3.3
2.8 / 0.1
AEF
0641030+094754
F3-ap153
19.3 +/- 5.1
5.0 / 0.3
AEF
0641571+095742
F3-ap154
43.1 +/- 0.2
28.8 / 0.8
A
0641515+095343
F3-ap155
20.7 +/- 1.0
12.5 / 0.5
AE
0642091+095903
F3-ap156
29.7 +/- 0.2
29.8 / 0.8
AE
0640536+094704
F3-ap159
16.7 +/- 0.8
7.1 / 0.3
W
0640187+093701
F3-ap15
13.8 +/- 1.5
3.6 / 0.2
C
0641040+094909
F3-ap160
16.8 +/- 0.4
22.5 / 0.7
W
0640557+094646
F3-ap162
16.6 +/- 1.2
4.8 / 0.2
C
0642219+094833
F3-ap163
non +/- non
0.0 / 0.1
C
0641564+095006
F3-ap166
16.0 +/- 0.2
28.0 / 0.8
A
0642098+094843
F3-ap167
62.6 +/- 0.4
12.2 / 0.5
0640450+094542
F3-ap168
21.7 +/- 0.8
14.4 / 0.5
W
0641154+094640
F3-ap169
25.2 +/- 2.6
10.1 / 0.4
AE
0641482+094253
F3-ap171
1.6 +/- 0.3
19.3 / 0.7
AE

Fig. 12.2 cont.

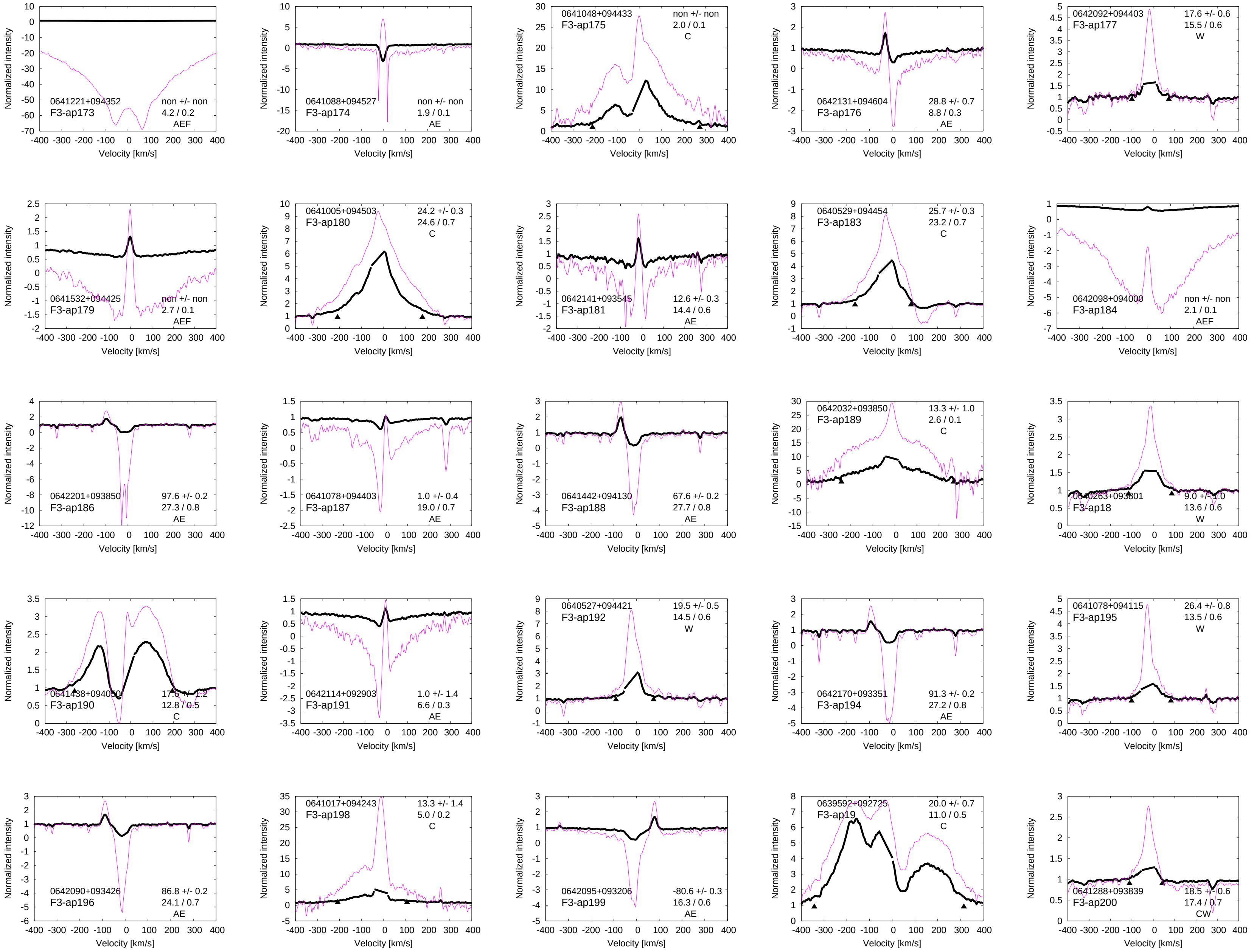
Normalized intensity
Velocity [km/s]
-400 -300 -200 -100 0 100 200 300 400
0641221+094352
F3-ap173
non +/- non
4.2 / 0.2
AEF
0641088+094527
F3-ap174
non +/- non
1.9 / 0.1
AE
0641048+094433
F3-ap175
non +/- non
2.0 / 0.1
C
0642131+094604
F3-ap176
28.8 +/- 0.7
8.8 / 0.3
AE
0642092+094403
F3-ap177
17.6 +/- 0.6
15.5 / 0.6
W
0641532+094425
F3-ap179
non +/- non
2.7 / 0.1
AEF
0641005+094503
F3-ap180
24.2 +/- 0.3
24.6 / 0.7
C
0642141+093545
F3-ap181
12.6 +/- 0.3
14.4 / 0.6
AE
0640529+094454
F3-ap183
25.7 +/- 0.3
23.2 / 0.7
C
0642098+094000
F3-ap184
non +/- non
2.1 / 0.1
AEF
0642201+093850
F3-ap186
97.6 +/- 0.2
27.3 / 0.8
AE
0641078+094403
F3-ap187
1.0 +/- 0.4
19.0 / 0.7
AE
0641442+094130
F3-ap188
67.6 +/- 0.2
27.7 / 0.8
AE
0642032+093850
F3-ap189
13.3 +/- 1.0
2.6 / 0.1
C
0640263+093801
F3-ap18
9.0 +/- 1.0
13.6 / 0.6
W
0641438+094050
F3-ap190
17.6 +/- 1.2
12.8 / 0.5
C
0642114+092903
F3-ap191
1.0 +/- 1.4
6.6 / 0.3
AE
0640527+094421
F3-ap192
19.5 +/- 0.5
14.5 / 0.6
W
0642170+093351
F3-ap194
91.3 +/- 0.2
27.2 / 0.8
AE
0641078+094115
F3-ap195
26.4 +/- 0.8
13.5 / 0.6
W
0642090+093426
F3-ap196
86.8 +/- 0.2
24.1 / 0.7
AE
0641017+094243
F3-ap198
13.3 +/- 1.4
5.0 / 0.2
C
0642095+093206
F3-ap199
-80.6 +/- 0.3
16.3 / 0.6
AE
0639592+092725
F3-ap19
20.0 +/- 0.7
11.0 / 0.5
C
0641288+093839
F3-ap200
18.5 +/- 0.6
17.4 / 0.7
CW

Fig. 12.2 cont.

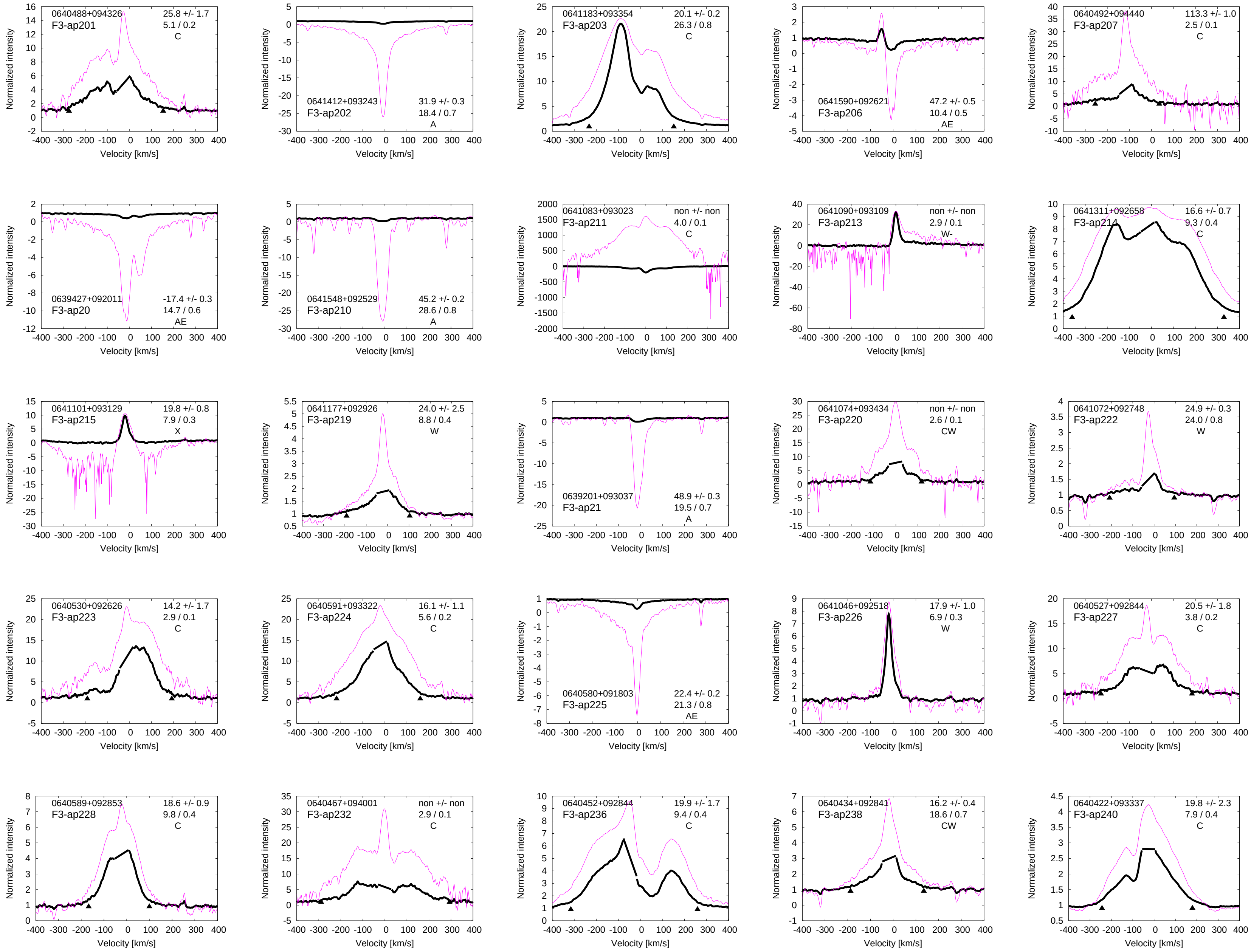
Normalized intensity
Velocity [km/s]
0640488+094326 F3-ap201 25.8 +/- 1.7 5.1 / 0.2 C
0641412+093243 F3-ap202 31.9 +/- 0.3 18.4 / 0.7 A
0641183+093354 F3-ap203 20.1 +/- 0.2 26.3 / 0.8 C
0641590+092621 F3-ap206 47.2 +/- 0.5 10.4 / 0.5 AE
0640492+094440 F3-ap207 113.3 +/- 1.0 2.5 / 0.1 C
0639427+092011 F3-ap20 -17.4 +/- 0.3 14.7 / 0.6 AE
0641548+092529 F3-ap210 45.2 +/- 0.2 28.6 / 0.8 A
0641083+093023 F3-ap211 non +/- non 4.0 / 0.1 C
0641090+093109 F3-ap213 non +/- non 2.9 / 0.1 W-
0641311+092658 F3-ap214 16.6 +/- 0.7 9.3 / 0.4 C
0641101+093129 F3-ap215 19.8 +/- 0.8 7.9 / 0.3 X
0641177+092926 F3-ap219 24.0 +/- 2.5 8.8 / 0.4 W
0639201+093037 F3-ap21 48.9 +/- 0.3 19.5 / 0.7 A
0641074+093434 F3-ap220 non +/- non 2.6 / 0.1 CW
0641072+092748 F3-ap222 24.9 +/- 0.3 24.0 / 0.8 W
0640530+092626 F3-ap223 14.2 +/- 1.7 2.9 / 0.1 C
0640591+093322 F3-ap224 16.1 +/- 1.1 5.6 / 0.2 C
0640580+091803 F3-ap225 22.4 +/- 0.2 21.3 / 0.8 AE
0641046+092518 F3-ap226 17.9 +/- 1.0 6.9 / 0.3 W
0640527+092844 F3-ap227 20.5 +/- 1.8 3.8 / 0.2 C
0640589+092853 F3-ap228 18.6 +/- 0.9 9.8 / 0.4 C
0640467+094001 F3-ap232 non +/- non 2.9 / 0.1 C
0640452+092844 F3-ap236 19.9 +/- 1.7 9.4 / 0.4 C
0640434+092841 F3-ap238 16.2 +/- 0.4 18.6 / 0.7 CW
0640422+093337 F3-ap240 19.8 +/- 2.3 7.9 / 0.4 C

Fig. 12.2 cont.

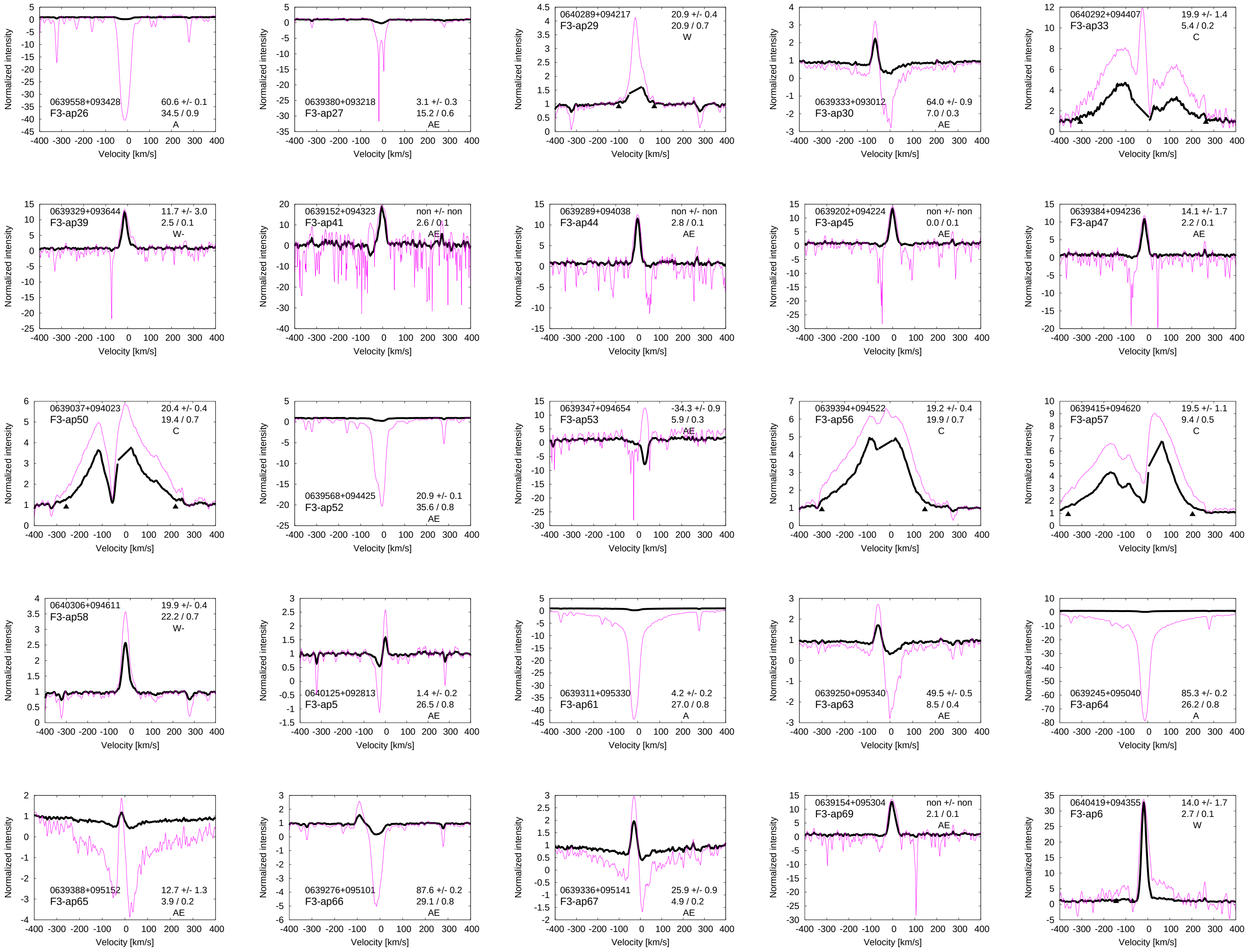
Normalized intensity
Velocity [km/s]
0639558+093428
F3-ap26
60.6 +/- 0.1
34.5 / 0.9
A
0639380+093218
F3-ap27
3.1 +/- 0.3
15.2 / 0.6
AE
0640289+094217
F3-ap29
20.9 +/- 0.4
20.9 / 0.7
W
0639333+093012
F3-ap30
64.0 +/- 0.9
7.0 / 0.3
AE
0640292+094407
F3-ap33
19.9 +/- 1.4
5.4 / 0.2
C
0639329+093644
F3-ap39
11.7 +/- 3.0
2.5 / 0.1
W-
0639152+094323
F3-ap41
non +/- non
2.6 / 0.1
AE
0639289+094038
F3-ap44
non +/- non
2.8 / 0.1
AE
0639202+094224
F3-ap45
non +/- non
0.0 / 0.1
AE
0639384+094236
F3-ap47
14.1 +/- 1.7
2.2 / 0.1
AE
0639037+094023
F3-ap50
20.4 +/- 0.4
19.4 / 0.7
C
0639568+094425
F3-ap52
20.9 +/- 0.1
35.6 / 0.8
AE
0639347+094654
F3-ap53
-34.3 +/- 0.9
5.9 / 0.3
AE
0639394+094522
F3-ap56
19.2 +/- 0.4
19.9 / 0.7
C
0639415+094620
F3-ap57
19.5 +/- 1.1
9.4 / 0.5
C
0640306+094611
F3-ap58
19.9 +/- 0.4
22.2 / 0.7
W-
0640125+092813
F3-ap5
1.4 +/- 0.2
26.5 / 0.8
AE
0639311+095330
F3-ap61
4.2 +/- 0.2
27.0 / 0.8
A
0639250+095340
F3-ap63
49.5 +/- 0.5
8.5 / 0.4
AE
0639245+095040
F3-ap64
85.3 +/- 0.2
26.2 / 0.8
A
0639388+095152
F3-ap65
12.7 +/- 1.3
3.9 / 0.2
AE
0639276+095101
F3-ap66
87.6 +/- 0.2
29.1 / 0.8
AE
0639336+095141
F3-ap67
25.9 +/- 0.9
4.9 / 0.2
AE
0639154+095304
F3-ap69
non +/- non
2.1 / 0.1
AE
0640419+094355
F3-ap6
14.0 +/- 1.7
2.7 / 0.1
W
-400 -300 -200 -100 0 100 200 300 400

Fig. 12.2 cont.

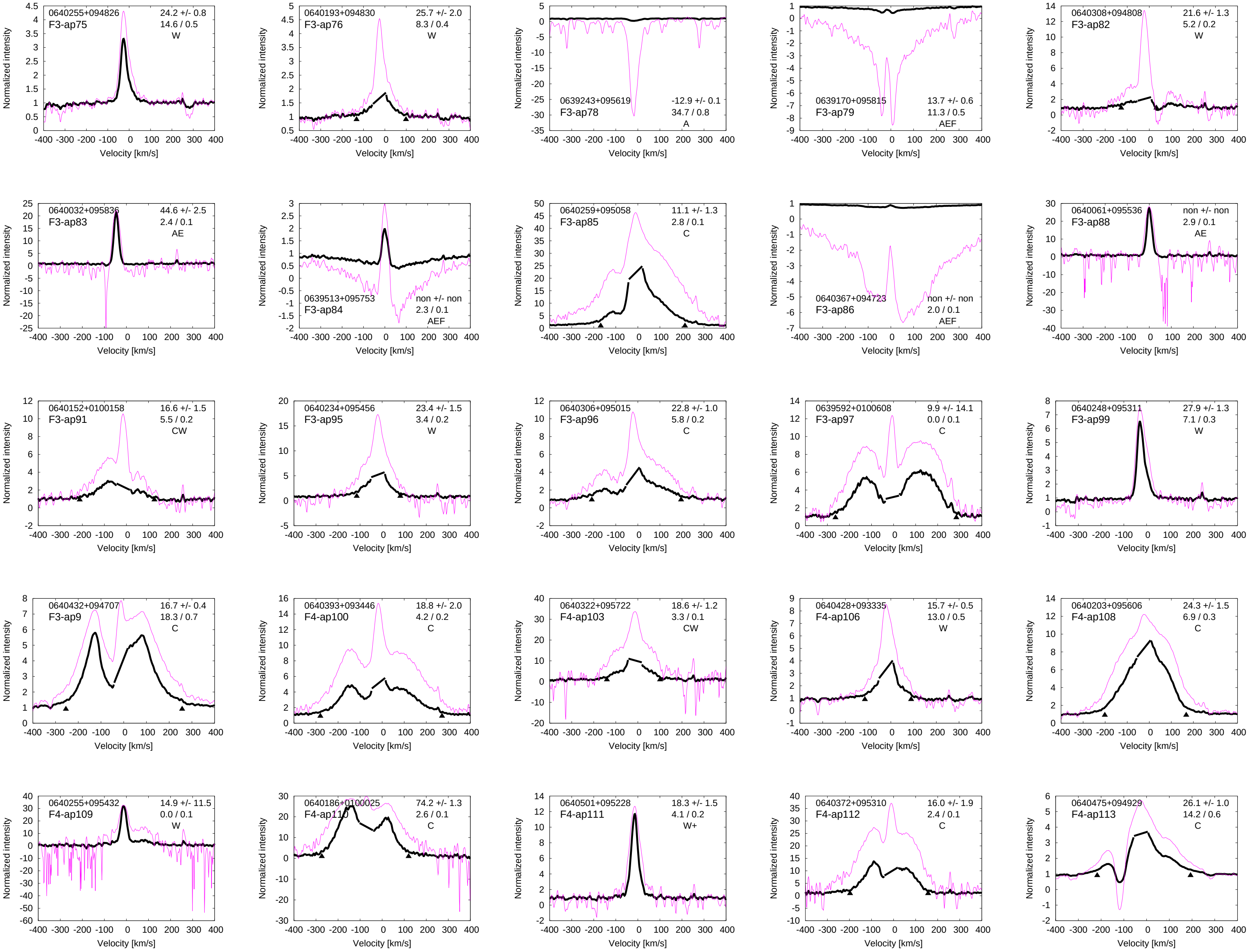
0640255+094826
F3-ap75
24.2 +/- 0.8
14.6 / 0.5
W
0640193+094830
F3-ap76
25.7 +/- 2.0
8.3 / 0.4
W
0639243+095619
F3-ap78
-12.9 +/- 0.1
34.7 / 0.8
A
0639170+095815
F3-ap79
13.7 +/- 0.6
11.3 / 0.5
AEF
0640308+094808
F3-ap82
21.6 +/- 1.3
5.2 / 0.2
W
0640032+095836
F3-ap83
44.6 +/- 2.5
2.4 / 0.1
AE
0639513+095753
F3-ap84
non +/- non
2.3 / 0.1
AEF
0640259+095058
F3-ap85
11.1 +/- 1.3
2.8 / 0.1
C
0640367+094723
F3-ap86
non +/- non
2.0 / 0.1
AEF
0640061+095536
F3-ap88
non +/- non
2.9 / 0.1
AE
0640152+0100158
F3-ap91
16.6 +/- 1.5
5.5 / 0.2
CW
0640234+095456
F3-ap95
23.4 +/- 1.5
3.4 / 0.2
W
0640306+095015
F3-ap96
22.8 +/- 1.0
5.8 / 0.2
C
0639592+0100608
F3-ap97
9.9 +/- 14.1
0.0 / 0.1
C
0640248+095311
F3-ap99
27.9 +/- 1.3
7.1 / 0.3
W
0640432+094707
F3-ap9
16.7 +/- 0.4
18.3 / 0.7
C
0640393+093446
F4-ap100
18.8 +/- 2.0
4.2 / 0.2
C
0640322+095722
F4-ap103
18.6 +/- 1.2
3.3 / 0.1
CW
0640428+093335
F4-ap106
15.7 +/- 0.5
13.0 / 0.5
W
0640203+095606
F4-ap108
24.3 +/- 1.5
6.9 / 0.3
C
0640255+095432
F4-ap109
14.9 +/- 11.5
0.0 / 0.1
W
0640186+0100025
F4-ap110
74.2 +/- 1.3
2.6 / 0.1
C
0640501+095228
F4-ap111
18.3 +/- 1.5
4.1 / 0.2
W+
0640372+095310
F4-ap112
16.0 +/- 1.9
2.4 / 0.1
C
0640475+094929
F4-ap113
26.1 +/- 1.0
14.2 / 0.6
C
Normalized intensity
Velocity [km/s]

Fig. 12.2 cont.

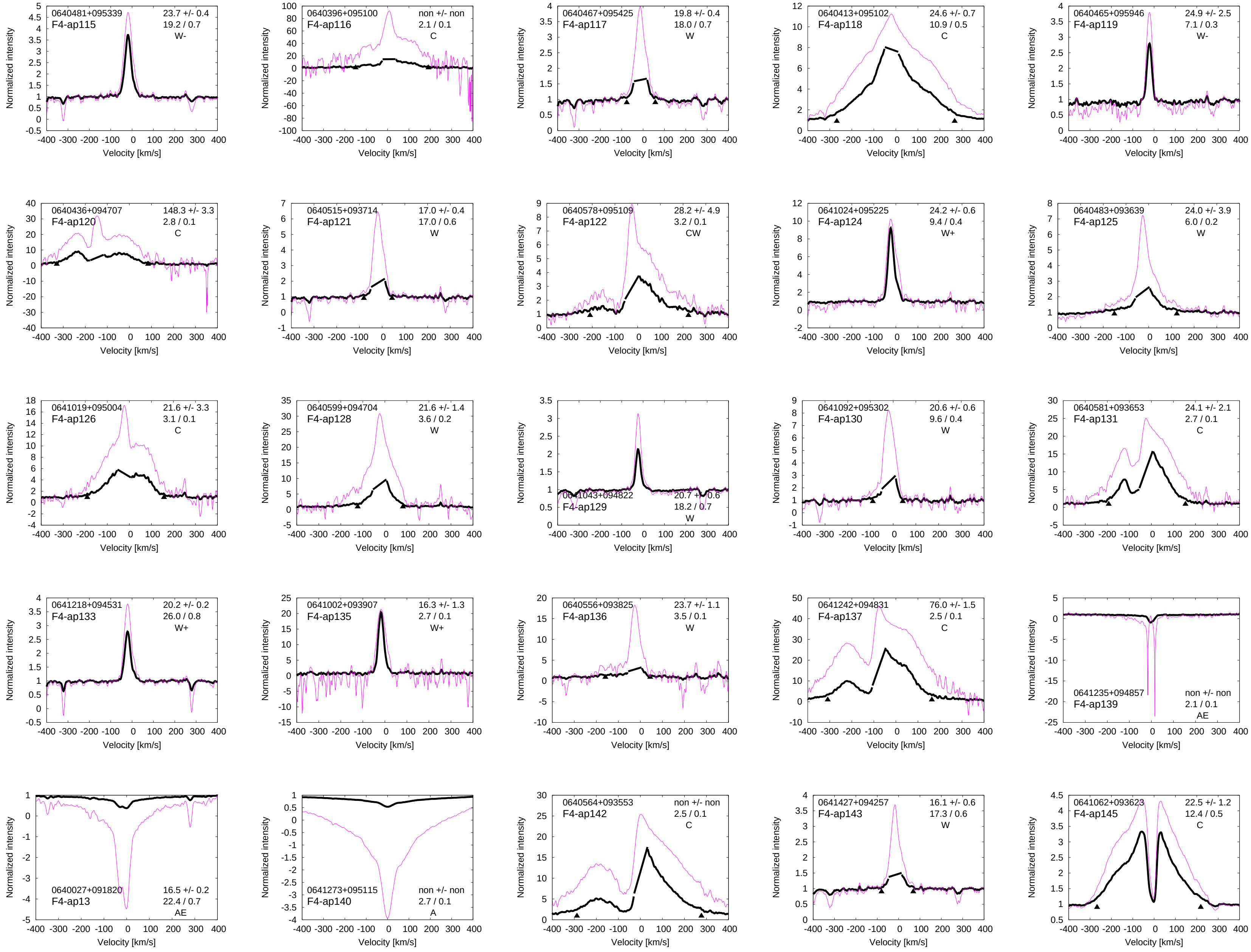
Normalized intensity
Velocity [km/s]
0640481+095339
F4-ap115
23.7 +/- 0.4
19.2 / 0.7
W-
0640396+095100
F4-ap116
non +/- non
2.1 / 0.1
C
0640467+095425
F4-ap117
19.8 +/- 0.4
18.0 / 0.7
W
0640413+095102
F4-ap118
24.6 +/- 0.7
10.9 / 0.5
C
0640465+095946
F4-ap119
24.9 +/- 2.5
7.1 / 0.3
W-
0640436+094707
F4-ap120
148.3 +/- 3.3
2.8 / 0.1
C
0640515+093714
F4-ap121
17.0 +/- 0.4
17.0 / 0.6
W
0640578+095109
F4-ap122
28.2 +/- 4.9
3.2 / 0.1
CW
0641024+095225
F4-ap124
24.2 +/- 0.6
9.4 / 0.4
W+
0640483+093639
F4-ap125
24.0 +/- 3.9
6.0 / 0.2
W
0641019+095004
F4-ap126
21.6 +/- 3.3
3.1 / 0.1
C
0640599+094704
F4-ap128
21.6 +/- 1.4
3.6 / 0.2
W
0641043+094822
F4-ap129
20.7 +/- 0.6
18.2 / 0.7
W
0641092+095302
F4-ap130
20.6 +/- 0.6
9.6 / 0.4
W
0640581+093653
F4-ap131
24.1 +/- 2.1
2.7 / 0.1
C
0641218+094531
F4-ap133
20.2 +/- 0.2
26.0 / 0.8
W+
0641002+093907
F4-ap135
16.3 +/- 1.3
2.7 / 0.1
W+
0640556+093825
F4-ap136
23.7 +/- 1.1
3.5 / 0.1
W
0641242+094831
F4-ap137
76.0 +/- 1.5
2.5 / 0.1
C
0641235+094857
F4-ap139
non +/- non
2.1 / 0.1
AE
0640027+091820
F4-ap13
16.5 +/- 0.2
22.4 / 0.7
AE
0641273+095115
F4-ap140
non +/- non
2.7 / 0.1
A
0640564+093553
F4-ap142
non +/- non
2.5 / 0.1
C
0641427+094257
F4-ap143
16.1 +/- 0.6
17.3 / 0.6
W
0641062+093623
F4-ap145
22.5 +/- 1.2
12.4 / 0.5
C

Fig. 12.2 cont.

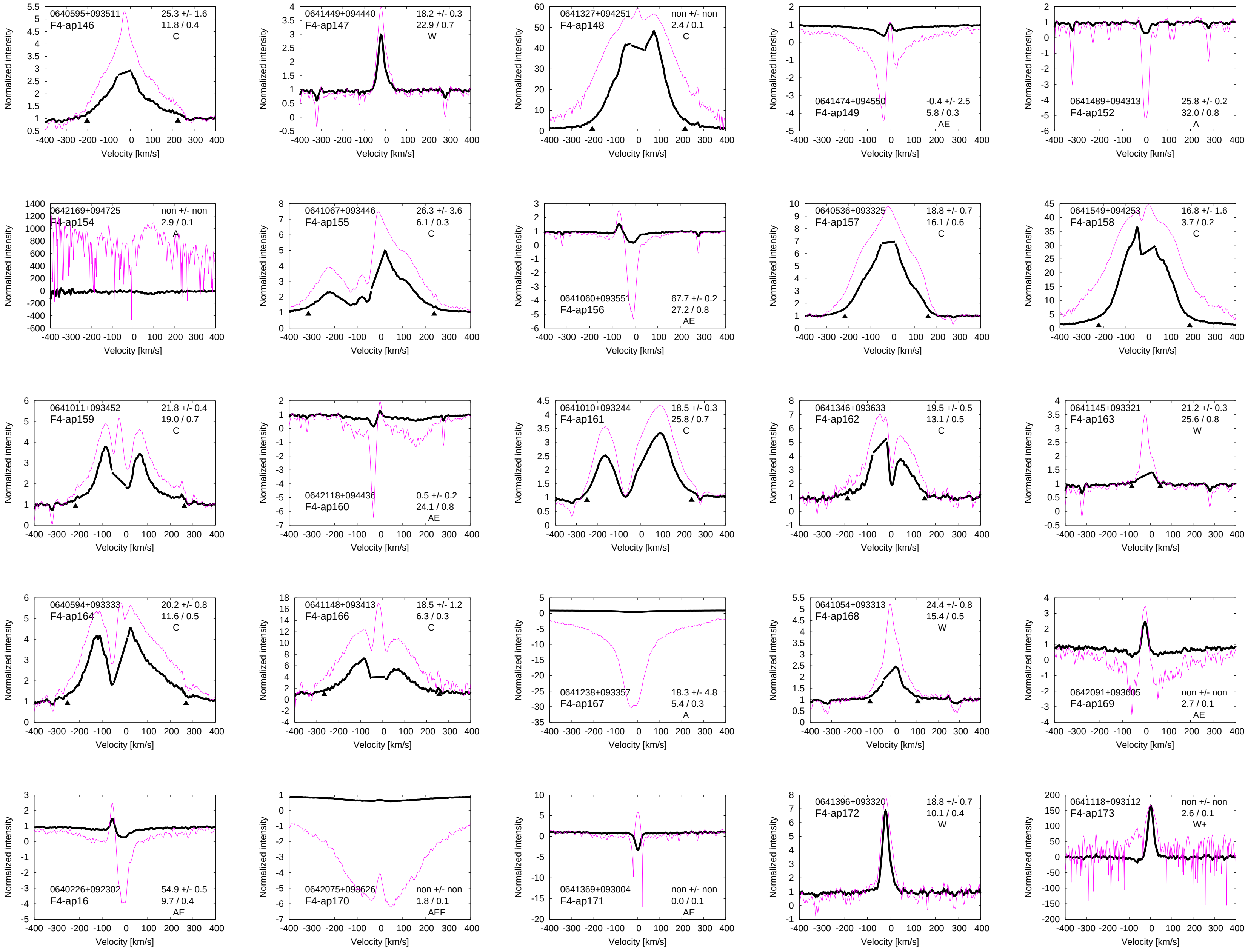
0640595+093511
F4-ap146
25.3 +/- 1.6
11.8 / 0.4
C
0641449+094440
F4-ap147
18.2 +/- 0.3
22.9 / 0.7
W
0641327+094251
F4-ap148
non +/- non
2.4 / 0.1
C
0641474+094550
F4-ap149
-0.4 +/- 2.5
5.8 / 0.3
AE
0641489+094313
F4-ap152
25.8 +/- 0.2
32.0 / 0.8
A
0642169+094725
F4-ap154
non +/- non
2.9 / 0.1
A
0641067+093446
F4-ap155
26.3 +/- 3.6
6.1 / 0.3
C
0641060+093551
F4-ap156
67.7 +/- 0.2
27.2 / 0.8
AE
0640536+093325
F4-ap157
18.8 +/- 0.7
16.1 / 0.6
C
0641549+094253
F4-ap158
16.8 +/- 1.6
3.7 / 0.2
C
0641011+093452
F4-ap159
21.8 +/- 0.4
19.0 / 0.7
C
0642118+094436
F4-ap160
0.5 +/- 0.2
24.1 / 0.8
AE
0641010+093244
F4-ap161
18.5 +/- 0.3
25.8 / 0.7
C
0641346+093633
F4-ap162
19.5 +/- 0.5
13.1 / 0.5
C
0641145+093321
F4-ap163
21.2 +/- 0.3
25.6 / 0.8
W
0640594+093333
F4-ap164
20.2 +/- 0.8
11.6 / 0.5
C
0641148+093413
F4-ap166
18.5 +/- 1.2
6.3 / 0.3
C
0641238+093357
F4-ap167
18.3 +/- 4.8
5.4 / 0.3
A
0641054+093313
F4-ap168
24.4 +/- 0.8
15.4 / 0.5
W
0642091+093605
F4-ap169
non +/- non
2.7 / 0.1
AE
0640226+092302
F4-ap16
54.9 +/- 0.5
9.7 / 0.4
AE
0642075+093626
F4-ap170
non +/- non
1.8 / 0.1
AEF
0641369+093004
F4-ap171
non +/- non
0.0 / 0.1
AE
0641396+093320
F4-ap172
18.8 +/- 0.7
10.1 / 0.4
W
0641118+093112
F4-ap173
non +/- non
2.6 / 0.1
W+
Normalized intensity
Velocity [km/s]
-400 -300 -200 -100 0 100 200 300 400

Fig. 12.2 cont.

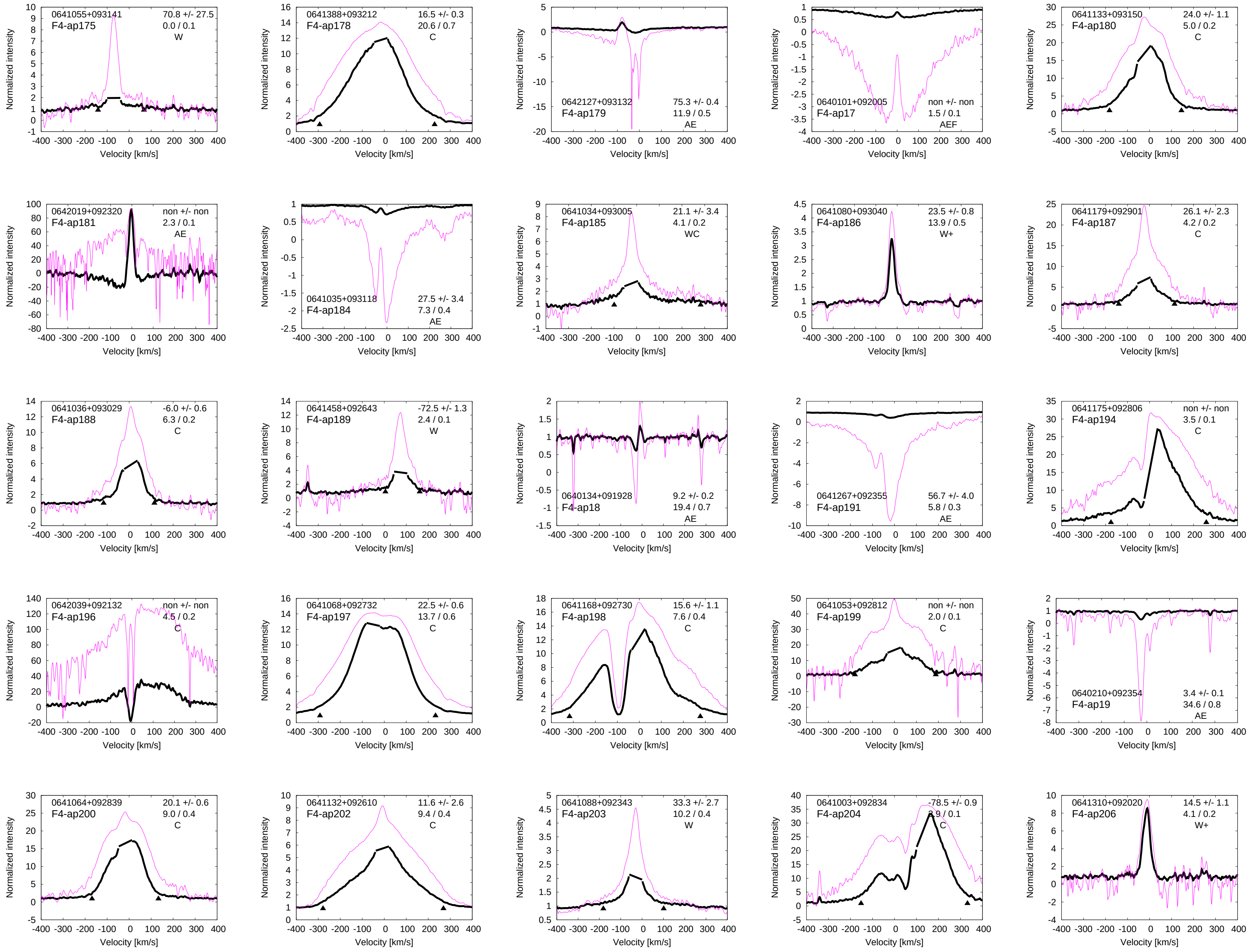
0641055+093141
F4-ap175
70.8 +/- 27.5
0.0 / 0.1
W
0641388+093212
F4-ap178
16.5 +/- 0.3
20.6 / 0.7
C
0642127+093132
F4-ap179
75.3 +/- 0.4
11.9 / 0.5
AE
0640101+092005
F4-ap17
non +/- non
1.5 / 0.1
AEF
0641133+093150
F4-ap180
24.0 +/- 1.1
5.0 / 0.2
C
0642019+092320
F4-ap181
non +/- non
2.3 / 0.1
AE
0641035+093118
F4-ap184
27.5 +/- 3.4
7.3 / 0.4
AE
0641034+093005
F4-ap185
21.1 +/- 3.4
4.1 / 0.2
WC
0641080+093040
F4-ap186
23.5 +/- 0.8
13.9 / 0.5
W+
0641179+092901
F4-ap187
26.1 +/- 2.3
4.2 / 0.2
C
0641036+093029
F4-ap188
-6.0 +/- 0.6
6.3 / 0.2
C
0641458+092643
F4-ap189
-72.5 +/- 1.3
2.4 / 0.1
W
0640134+091928
F4-ap18
9.2 +/- 0.2
19.4 / 0.7
AE
0641267+092355
F4-ap191
56.7 +/- 4.0
5.8 / 0.3
AE
0641175+092806
F4-ap194
non +/- non
3.5 / 0.1
C
0642039+092132
F4-ap196
non +/- non
4.5 / 0.2
C
0641068+092732
F4-ap197
22.5 +/- 0.6
13.7 / 0.6
C
0641168+092730
F4-ap198
15.6 +/- 1.1
7.6 / 0.4
C
0641053+092812
F4-ap199
non +/- non
2.0 / 0.1
C
0640210+092354
F4-ap19
3.4 +/- 0.1
34.6 / 0.8
AE
0641064+092839
F4-ap200
20.1 +/- 0.6
9.0 / 0.4
C
0641132+092610
F4-ap202
11.6 +/- 2.6
9.4 / 0.4
C
0641088+092343
F4-ap203
33.3 +/- 2.7
10.2 / 0.4
W
0641003+092834
F4-ap204
-78.5 +/- 0.9
3.9 / 0.1
C
0641310+092020
F4-ap206
14.5 +/- 1.1
4.1 / 0.2
W+
Normalized intensity
Velocity [km/s]
-400 -300 -200 -100 0 100 200 300 400

Fig. 12.2 cont.

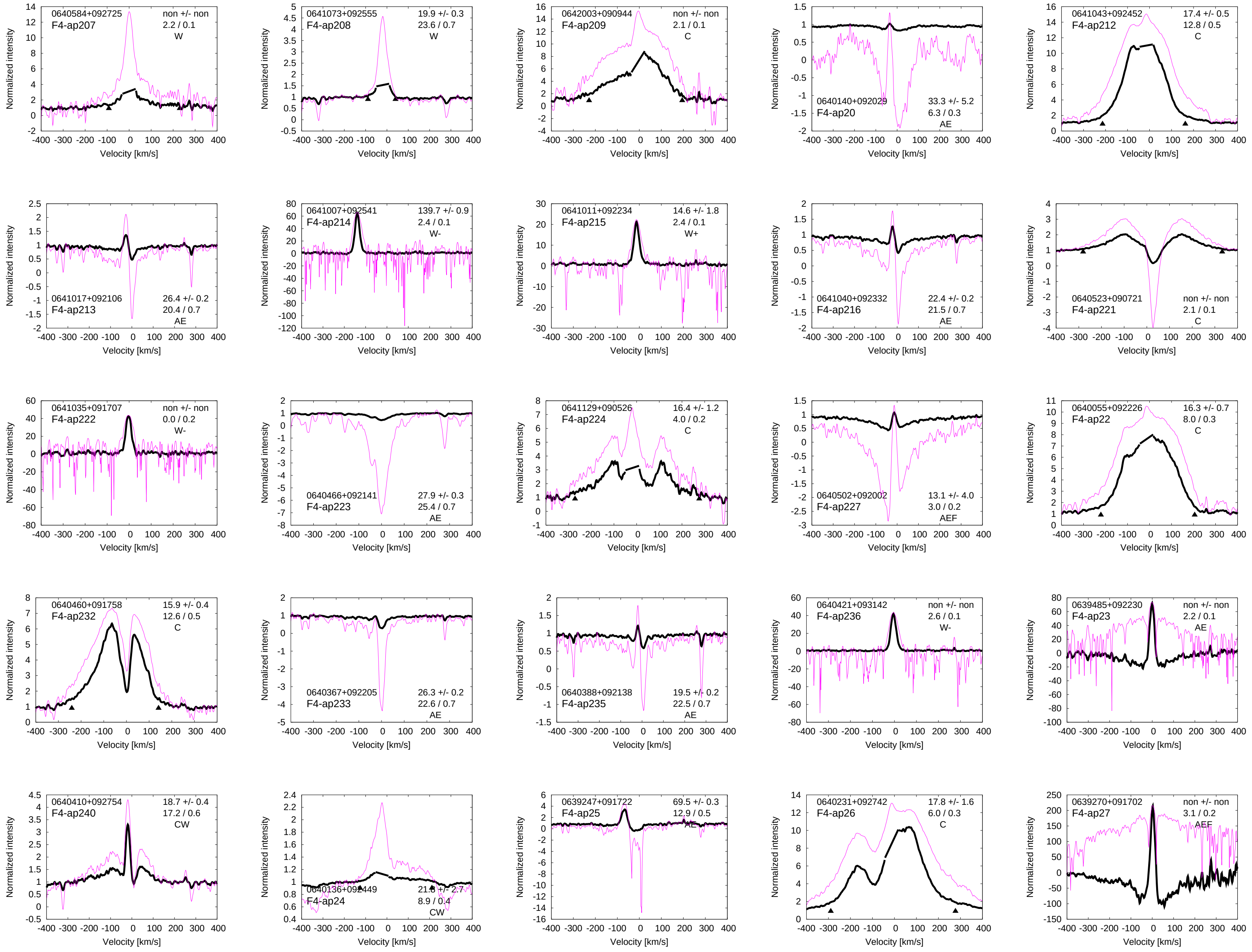
Normalized intensity
Velocity [km/s]
0640584+092725
F4-ap207
non +/- non
2.2 / 0.1
W
0641073+092555
F4-ap208
19.9 +/- 0.3
23.6 / 0.7
W
0642003+090944
F4-ap209
non +/- non
2.1 / 0.1
C
0640140+092029
F4-ap20
33.3 +/- 5.2
6.3 / 0.3
AE
0641043+092452
F4-ap212
17.4 +/- 0.5
12.8 / 0.5
C
0641017+092106
F4-ap213
26.4 +/- 0.2
20.4 / 0.7
AE
0641007+092541
F4-ap214
139.7 +/- 0.9
2.4 / 0.1
W-
0641011+092234
F4-ap215
14.6 +/- 1.8
2.4 / 0.1
W+
0641040+092332
F4-ap216
22.4 +/- 0.2
21.5 / 0.7
AE
0640523+090721
F4-ap221
non +/- non
2.1 / 0.1
C
0641035+091707
F4-ap222
non +/- non
0.0 / 0.2
W-
0640466+092141
F4-ap223
27.9 +/- 0.3
25.4 / 0.7
AE
0641129+090526
F4-ap224
16.4 +/- 1.2
4.0 / 0.2
C
0640502+092002
F4-ap227
13.1 +/- 4.0
3.0 / 0.2
AEF
0640055+092226
F4-ap22
16.3 +/- 0.7
8.0 / 0.3
C
0640460+091758
F4-ap232
15.9 +/- 0.4
12.6 / 0.5
C
0640367+092205
F4-ap233
26.3 +/- 0.2
22.6 / 0.7
AE
0640388+092138
F4-ap235
19.5 +/- 0.2
22.5 / 0.7
AE
0640421+093142
F4-ap236
non +/- non
2.6 / 0.1
W-
0639485+092230
F4-ap23
non +/- non
2.2 / 0.1
AE
0640410+092754
F4-ap240
18.7 +/- 0.4
17.2 / 0.6
CW
0640136+092449
F4-ap24
21.8 +/- 2.7
8.9 / 0.4
CW
0639247+091722
F4-ap25
69.5 +/- 0.3
12.9 / 0.5
0640231+092742
F4-ap26
17.8 +/- 1.6
6.0 / 0.3
C
0639270+091702
F4-ap27
non +/- non
3.1 / 0.2
AEF

Fig. 12.2 cont.

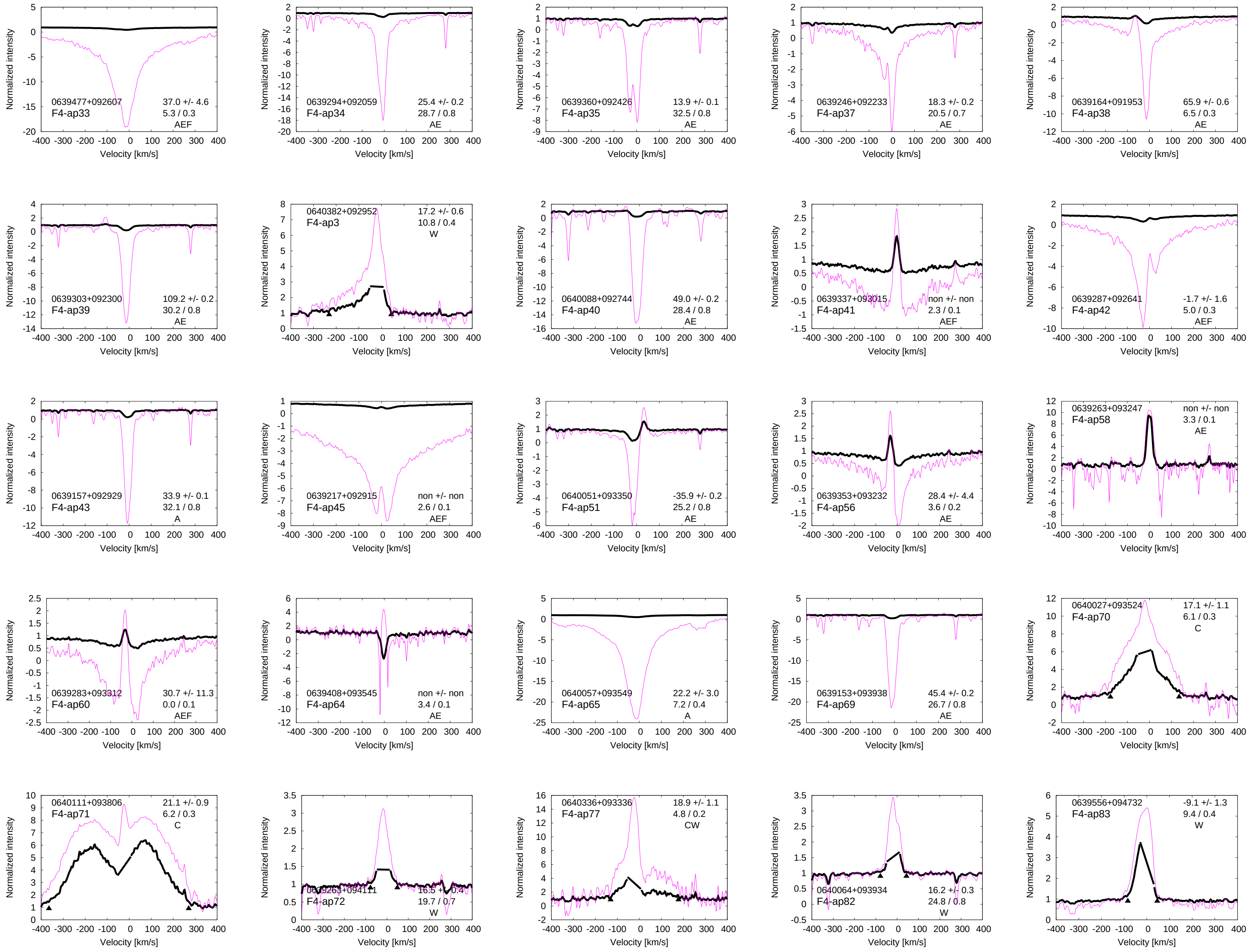
Normalized intensity
Velocity [km/s]
0639477+092607
F4-ap33
37.0 +/- 4.6
5.3 / 0.3
AEF
0639294+092059
F4-ap34
25.4 +/- 0.2
28.7 / 0.8
AE
0639360+092426
F4-ap35
13.9 +/- 0.1
32.5 / 0.8
AE
0639246+092233
F4-ap37
18.3 +/- 0.2
20.5 / 0.7
AE
0639164+091953
F4-ap38
65.9 +/- 0.6
6.5 / 0.3
AE
0639303+092300
F4-ap39
109.2 +/- 0.2
30.2 / 0.8
AE
0640382+092952
F4-ap3
17.2 +/- 0.6
10.8 / 0.4
W
0640088+092744
F4-ap40
49.0 +/- 0.2
28.4 / 0.8
AE
0639337+093015
F4-ap41
non +/- non
2.3 / 0.1
AEF
0639287+092641
F4-ap42
-1.7 +/- 1.6
5.0 / 0.3
AEF
0639157+092929
F4-ap43
33.9 +/- 0.1
32.1 / 0.8
A
0639217+092915
F4-ap45
non +/- non
2.6 / 0.1
AEF
0640051+093350
F4-ap51
-35.9 +/- 0.2
25.2 / 0.8
AE
0639353+093232
F4-ap56
28.4 +/- 4.4
3.6 / 0.2
AE
0639263+093247
F4-ap58
non +/- non
3.3 / 0.1
AE
0639283+093312
F4-ap60
30.7 +/- 11.3
0.0 / 0.1
AEF
0639408+093545
F4-ap64
non +/- non
3.4 / 0.1
AE
0640057+093549
F4-ap65
22.2 +/- 3.0
7.2 / 0.4
A
0639153+093938
F4-ap69
45.4 +/- 0.2
26.7 / 0.8
AE
0640027+093524
F4-ap70
17.1 +/- 1.1
6.1 / 0.3
C
0640111+093806
F4-ap71
21.1 +/- 0.9
6.2 / 0.3
C
0639263+094111
F4-ap72
16.5 +/- 0.4
19.7 / 0.7
W
0640336+093336
F4-ap77
18.9 +/- 1.1
4.8 / 0.2
CW
0640064+093934
F4-ap82
16.2 +/- 0.3
24.8 / 0.8
W
0639556+094732
F4-ap83
-9.1 +/- 1.3
9.4 / 0.4
W
-400 -300 -200 -100 0 100 200 300 400

Fig. 12.2 cont.

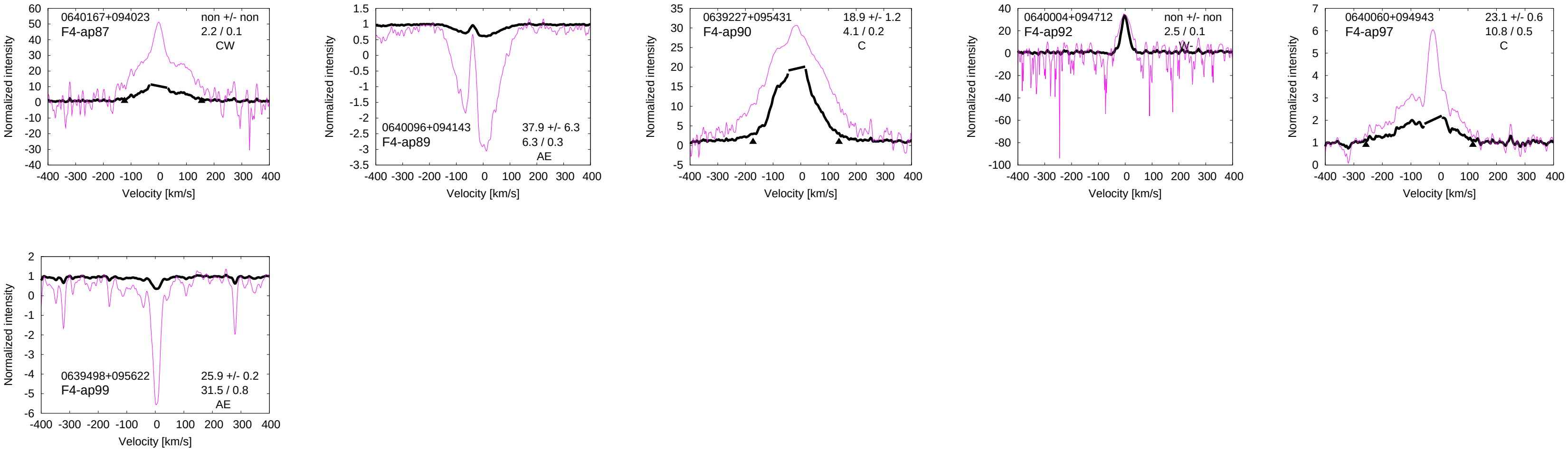
0640167+094023
F4-ap87
non +/- non
2.2 / 0.1
CW
0640096+094143
F4-ap89
37.9 +/- 6.3
6.3 / 0.3
AE
0639227+095431
F4-ap90
18.9 +/- 1.2
4.1 / 0.2
C
0640004+094712
F4-ap92
non +/- non
2.5 / 0.1
W-
0640060+094943
F4-ap97
23.1 +/- 0.6
10.8 / 0.5
C
0639498+095622
F4-ap99
25.9 +/- 0.2
31.5 / 0.8
AE
Normalized intensity
Velocity [km/s]
-400
-300
-200
-100
0
100
200
300
400

Fig. 12.2 cont.

Table 12.4. Members of ONC — *full table*

2MASS_id	ID	J	$(J-H)$	$(H-K)$	[3.6 − 4.5]	[5.8 − 8.0]	V_{rad}	ΔV_{rad}	R	S	EW_c	$FW_{10\%}$	$H\alpha$	CCF	NOB
0533179-052138	F22-ap25	13.18	0.87	0.24	0.00	0.00	25.09	6.38	4.4	0.39	11.2	239	W	w	1
0533204-051123	F21-ap89	12.73	1.07	0.29	0.00	0.00	24.28	0.53	13.6	0.58	5.2	169	W	c	1
0533225-053240	F22-ap20	13.02	0.98	0.23	0.00	0.00	23.89	0.35	22.4	0.71	5.3	134	W	c	1
0533233-052153	F22-ap27	12.90	0.87	0.24	0.00	0.00	47.20	0.35	23.4	0.74	0.9	179	W	c	1
0533234-044234	F11-ap62	13.38	0.94	0.34	0.00	0.00	21.48	4.60	5.0	0.23	3.7	152	W	w,l	1
0533256-052354	F21-ap61	13.32	0.95	0.21	0.02	–	69.48	0.49	15.1	0.64	2.4	178	W	c	1
0533263-051640	F22-ap37	13.34	1.25	0.33	0.00	0.44	70.65	0.64	10.7	0.54	5.2	189	NSW	c	1
0533285-051726	F22-ap40	11.92	1.12	0.34	0.04	0.79	25.01	0.32	28.7	0.85	23.1	390	C	c	1
0533287-052610	F21-ap69	13.23	1.08	0.29	0.02	0.12	29.23	0.82	12.1	0.53	6.6	116	NSW	c	1
0533293-050749	F22-ap49	13.29	1.20	0.32	0.03	0.00	26.42	2.32	10.1	0.62	4.0	184	W-	c	1
0533301-052257	F22-ap30	13.03	0.79	0.21	0.02	0.00	22.36	2.34	6.8	0.48	2.3	153	W	c	1
0533302-060409	F31-ap51	12.26	0.89	0.22	0.00	0.14	32.28	3.01	14.8	0.81	7.0	448	C	w	1
0533307-051352	F21-ap86	13.16	0.89	0.21	0.24	0.44	25.00	0.58	18.5	0.70	4.2	146	NSW	c	1
0533307-051351	S2-ap26	13.16	0.89	0.21	0.24	0.44	25.32	0.63	16.9	0.72	2.0	164	W-	c	1
0533307-050813	F21-ap94	13.02	1.11	0.31	0.01	0.02	-6.91	0.73	10.4	0.60	0.0	0	W	c	1
0533310-060605	F31-ap57	13.07	0.91	0.21	0.05	0.13	25.00	0.75	15.9	0.71	2.4	142	W+	c	1
0533312-052957	F22-ap13	13.45	1.01	0.32	0.23	1.51	28.98	0.44	14.9	0.57	33.0	229	C	c	1
0533314-060954	F31-ap52	12.75	1.08	0.36	0.34	0.94	26.16	0.88	11.2	0.51	52.1	293	C	c	1
0533329-055909	F31-ap66	12.10	0.75	0.23	0.01	0.14	32.48	0.57	14.1	0.67	0.0	0	AE	c	1
0533330-051155	S1-ap75	12.57	1.22	0.42	0.25	0.98	28.16	0.39	14.7	0.62	8.5	335	C	c	2
0533339-053326	F22-ap14	12.21	1.25	0.40	0.26	0.67	27.11	0.40	21.2	0.76	4.9	181	W	c	1
0533343-061352	F31-ap48	12.72	0.94	0.20	0.00	0.00	26.03	0.35	24.2	0.79	3.6	383	C	c	1
0533344-051417	S1-ap78	12.48	1.12	0.38	0.47	1.04	27.12	0.60	17.8	0.72	4.1	308	CW	c	1
0533357-050923	F21-ap92	12.50	1.09	0.28	0.06	0.08	27.59	6.19	8.1	0.51	4.9	354	CW	w	1
0533358-050132	S2-ap44	11.72	1.34	0.51	0.43	0.93	24.41	0.81	10.7	0.58	39.1	473	C	c	1
0533359-060641	F31-ap59	11.68	0.78	0.23	-0.01	0.12	19.89	0.27	32.7	0.88	0.9	178	DW	c	1
0533364-044949	F11-ap58	12.98	0.86	0.24	0.03	0.12	22.34	3.50	7.4	0.45	5.3	204	W	w	1
0533364-051153	F21-ap85	12.29	0.88	0.22	0.01	0.05	19.63	0.46	18.8	0.74	1.5	158	D	c	1
0533377-043349	F11-ap79	12.26	0.95	0.20	0.00	0.00	25.73	0.28	31.6	0.86	1.6	139	W	c	1
0533385-051312	F21-ap90	12.80	1.11	0.34	0.37	0.87	27.09	0.37	13.2	0.58	34.0	261	C	c	2
0533391-043807	F11-ap61	13.39	0.90	0.21	0.00	0.00	28.57	0.50	14.6	0.54	4.3	139	W	c	1
0533391-053310	F22-ap12	12.99	1.14	0.33	0.09	-0.01	54.75	1.90	5.4	0.35	0.0	0	NSW	d,l	1
0533398-051954	F22-ap32	13.37	0.90	0.28	0.07	–	24.87	0.43	16.2	0.64	11.0	179	W	c	1
0533406-050046	F11-ap33	12.52	0.93	0.23	0.08	0.08	25.40	0.86	14.6	0.67	3.9	149	W	c	1
0533406-055928	F31-ap68	13.44	0.98	0.28	0.08	0.09	17.54	2.41	6.4	0.30	0.0	0	AE	c	1
0533415-045559	F11-ap44	13.16	0.90	0.24	0.12	0.06	27.27	0.69	10.2	0.47	2.2	133	W+	c	1
0533416-052404	F21-ap63	12.60	1.09	0.30	0.31	1.00	22.74	0.27	20.3	0.72	18.6	227	CW	c	2
0533417-051034	F22-ap48	13.36	0.89	0.31	0.10	-0.02	-1.89	1.96	5.8	0.40	0.0	0	W	c	1
0533418-050817	F22-ap45	13.40	0.95	0.28	0.04	0.07	36.39	1.55	5.4	0.36	0.0	0	N	d	1
0533419-050614	S2-ap37	14.78	0.99	0.46	0.40	0.98	14.10	1.95	4.5	0.25	12.5	311	C	c	1
0533431-044714	F11-ap53	13.32	1.19	0.39	0.40	0.62	26.72	0.52	14.6	0.57	11.6	234	CW	c	1
0533432-060523	F31-ap55	13.21	0.91	0.25	0.08	0.09	18.53	0.48	18.8	0.72	3.1	133	W-	c	1
0533435-053225	F21-ap57	12.52	1.06	0.33	0.06	0.08	50.68	0.96	6.8	0.33	3.9	140	NSW	c	1

Table 12.4 (cont'd)

2MASS_id	ID	J	$(J-H)$	$(H-K)$	$[3.6-4.5]$	$[5.8-8.0]$	V_{rad}	ΔV_{rad}	R	S	EW_c	$FW_{10\%}$	$H\alpha$	CCF	NOB
0533452-053049	S3-ap68	10.26	1.66	0.65	0.58	1.08	27.12	0.43	22.4	0.83	17.2	492	C	c	1
0533454-053632	S1-ap42	12.08	1.08	0.35	-0.04	1.34	20.94	0.71	8.2	0.39	11.9	285	C	s/d,dv	2
0533457-044124	F11-ap70	12.17	0.85	0.25	0.10	0.19	19.49	0.42	18.0	0.64	0.0	0	W-	c	1
0533465-061516	F31-ap42	11.93	0.84	0.21	-0.02	0.16	19.16	0.29	33.5	0.88	1.5	142	W	c	1
0533466-052325	S2-ap3	13.76	2.54	1.14	0.66	0.73	–	–	2.2	0.40	49.5	489	C	u	1
0533476-052548	F21-ap70	12.57	0.99	0.32	0.17	0.97	29.04	0.60	12.7	0.55	13.8	278	C	c	1
0533477-045208	F11-ap43	11.64	0.91	0.30	0.06	0.41	29.96	0.66	16.0	0.68	21.6	420	C	c	1
0533478-045503	F11-ap46	12.84	0.92	0.22	0.04	0.11	27.97	0.65	16.6	0.67	1.5	122	W+	c	1
0533479-052738	S2-ap6	14.47	1.47	0.57	0.31	0.81	–	–	2.1	0.27	12.4	141	NSW	u,r	1
0533481-043927	F11-ap63	12.11	0.95	0.23	0.00	0.00	24.39	3.49	11.3	0.64	4.3	419	C	w	1
0533482-053447	F22-ap9	13.49	0.90	0.21	0.08	0.31	22.28	1.24	9.8	0.59	8.7	156	NSW	c	1
0533482-051326	S2-ap22	12.99	1.28	0.43	0.27	0.82	25.25	0.75	10.5	0.52	17.4	539	C	c	1
0533483-052239	F21-ap74	12.70	0.98	0.27	0.05	0.34	25.91	0.38	19.9	0.73	7.5	126	NSW	c	1
0533489-051753	F22-ap39	11.99	0.92	0.27	0.08	0.36	26.13	0.33	25.2	0.80	5.8	148	NSW	c	1
0533491-052302	F21-ap72	12.98	0.89	0.21	0.06	–	28.86	2.77	7.2	0.43	17.6	152	NSC	c	1
0533495-053620	S3-ap60	12.37	1.65	0.61	0.67	0.76	21.85	1.63	8.5	0.47	5.2	398	CW	c	1
0533502-062149	F31-ap38	13.47	1.32	0.49	0.11	0.50	24.80	0.50	14.8	0.61	2.0	114	W+	c	1
0533507-050039	F11-ap39	13.18	1.06	0.29	0.15	0.47	23.96	1.48	9.6	0.53	3.6	543	C	w	3
0533513-044822	F11-ap57	12.48	1.21	0.34	0.12	0.37	30.75	0.40	25.0	0.76	4.3	242	CW	c	1
0533513-052316	S2-ap5	12.66	3.15	1.21	0.72	0.97	12.72	2.08	4.5	0.25	12.9	141	NSC	c	1
0533521-053028	F21-ap53	12.37	0.94	0.27	0.05	0.07	22.52	0.48	19.3	0.72	6.5	155	NSW	c	1
0533523-054150	S3-ap48	11.72	1.15	0.34	0.19	0.62	26.37	0.39	26.2	0.86	2.2	507	CW	c	2
0533530-053515	F21-ap41	12.60	0.89	0.36	0.04	-0.03	8.35	1.03	5.7	0.25	16.9	118	NSW	c	1
0533541-050340	F11-ap32	12.79	0.92	0.30	0.14	0.21	23.71	0.46	13.3	0.59	4.6	161	W	c	2
0533545-060208	F31-ap62	12.24	0.90	0.22	-0.01	0.14	27.16	0.41	30.8	0.88	1.1	167	W	c	1
0533545-053200	S3-ap64	13.35	2.46	0.78	0.24	0.73	14.60	1.33	5.3	0.29	2.8	150	NSC	c	1
0533545-051415	F21-ap87	12.02	1.38	0.33	0.05	0.15	45.25	0.47	14.6	0.69	3.2	109	NSW	c	1
0533558-044749	S2-ap66	13.12	2.03	0.90	0.50	0.94	27.08	1.99	7.9	0.39	12.4	410	C	c	1
0533565-050647	F21-ap91	11.65	0.96	0.23	0.07	0.00	29.92	2.61	11.3	0.69	3.9	216	W	w	2
0533567-052133	F22-ap23	12.54	0.93	0.25	0.09	–	24.73	0.94	13.3	0.70	10.7	127	NSW	c	1
0533573-045915	F11-ap37	13.13	1.15	0.41	0.44	1.09	24.07	0.36	11.2	0.49	4.3	301	CW	c	3
0533576-054006	F21-ap44	11.85	1.22	0.27	0.14	0.18	31.05	0.67	17.5	0.71	6.8	144	NSW	c	1
0533579-053626	F22-ap4	13.19	0.91	0.22	0.11	1.23	26.88	3.25	9.3	0.65	10.8	175	NSC	c	1
0533592-054623	S3-ap35	14.93	2.70	1.41	0.91	1.10	14.87	1.63	6.0	0.35	2.9	187	NSC	c	1
0533597-050639	F22-ap59	12.85	1.37	0.38	0.10	0.07	26.22	2.28	5.1	0.30	4.0	148	W-	w,l	2
0534004-043615	F11-ap77	12.74	0.94	0.28	0.00	0.00	25.07	3.89	7.1	0.46	7.8	193	W	w	1
0534020-044453	S2-ap65	13.06	0.98	0.33	0.29	0.77	24.72	1.29	9.2	0.47	6.9	458	C	c	1
0534022-053619	S3-ap58	10.83	1.28	0.39	0.63	0.77	26.30	1.92	13.7	0.76	2.2	376	CW	c	1
0534030-053657	S3-ap56	10.38	1.29	0.43	0.32	1.24	24.71	0.92	24.1	0.87	5.5	409	CW	w	1
0534037-052218	F21-ap76	12.60	0.95	0.26	0.04	–	21.79	0.44	18.6	0.71	10.0	107	NS	c	1
0534038-043606	F11-ap75	12.71	0.93	0.22	0.00	0.00	30.12	0.54	16.3	0.70	45.4	434	C	c	1
0534047-045912	F22-ap64	13.44	1.00	0.26	0.08	0.00	26.28	1.09	7.6	0.40	3.5	167	W-	c	2
0534049-062346	F31-ap27	13.10	1.03	0.39	0.20	0.52	23.85	0.63	15.4	0.65	3.0	230	W	c	1

Table 12.4 (cont'd)

2MASS_id	ID	J	$(J-H)$	$(H-K)$	$[3.6-4.5]$	$[5.8-8.0]$	V_{rad}	ΔV_{rad}	R	S	EW_c	$FW_{10\%}$	$H\alpha$	CCF	NOB
0534057-055243	F31-ap71	12.77	1.37	0.37	-0.02	0.09	24.56	0.39	18.8	0.69	0.0	0	N	c	1
0534059-052238	F22-ap28	11.70	1.60	0.44	0.06	–	21.01	8.55	5.6	0.52	17.6	123	NSC	w	1
0534059-052243	S2-ap8	12.57	2.18	0.82	0.49	1.06	26.51	1.22	8.5	0.54	17.6	156	NSC	c	1
0534066-062411	F31-ap29	11.68	1.17	0.33	0.08	0.10	2.88	1.28	17.9	0.82	1.6	339	WC	c	1
0534074-051336	F22-ap44	12.37	0.94	0.20	0.02	0.59	30.38	0.45	21.2	0.76	4.6	106	W-	c	1
0534079-053616	S1-ap33	12.60	1.32	0.56	0.52	1.11	28.88	2.05	3.8	0.20	24.3	296	C	c	1
0534081-044357	F11-ap68	13.03	1.03	0.28	0.00	-0.01	19.82	0.61	12.5	0.58	0.0	0	AE	c	1
0534082-042600	F11-ap83	13.29	0.89	0.26	0.00	0.00	29.98	0.46	19.2	0.69	0.0	0	W-	c	1
0534097-044846	F11-ap59	13.41	0.94	0.22	0.02	0.22	21.97	0.42	16.0	0.61	3.1	105	W	c	1
0534104-045035	S2-ap68	10.99	1.04	0.33	0.00	0.00	26.52	1.08	20.9	0.85	3.9	507	C	w	1
0534116-055521	S3-ap24	12.26	1.12	0.39	0.26	0.50	24.52	0.91	11.1	0.58	7.5	333	C	c	1
0534118-050616	S2-ap35	14.49	0.97	0.37	0.43	0.92	24.14	1.71	5.4	0.27	11.8	337	C	c	1
0534120-052419	F22-ap22	12.96	1.39	0.37	0.12	–	26.56	1.20	9.1	0.44	33.7	106	NSC	c	1
0534120-061702	F31-ap37	13.35	0.92	0.28	0.07	0.20	30.57	0.66	14.5	0.58	2.6	112	W+	c	1
0534126-045024	S2-ap70	10.50	1.22	0.40	0.21	0.66	30.48	0.36	29.4	0.87	2.0	267	CW	c	1
0534130-054213	F22-ap236	12.66	0.92	0.23	0.03	0.44	27.55	0.39	24.0	0.79	4.4	138	NSW	c	1
0534131-053353	S3-ap51	12.67	1.22	0.45	0.41	1.22	21.78	0.91	8.9	0.51	19.8	499	C	c	1
0534132-053353	F22-ap2	12.67	1.22	0.45	0.41	1.22	25.80	1.72	4.8	0.38	95.3	499	C	r	1
0534134-055541	F31-ap77	12.52	1.10	0.31	0.29	0.53	26.35	0.60	21.2	0.80	4.5	344	C	c	1
0534137-050003	S2-ap56	14.66	1.13	0.56	0.29	0.77	15.96	1.65	3.4	0.20	4.6	210	W	c	1
0534138-053635	F22-ap233	12.83	0.86	0.22	0.05	0.46	23.91	3.41	6.2	0.49	12.9	196	NSC	c	1
0534140-054721	F31-ap90	13.23	0.94	0.22	-0.02	–	25.54	0.40	18.6	0.68	7.2	113	NS	c	1
0534141-053654	S3-ap41	8.99	0.71	0.35	0.38	1.40	39.01	7.24	6.2	0.63	1.9	521	CW	w	1
0534142-054221	F21-ap35	12.30	1.31	0.42	0.10	0.57	26.40	0.35	23.2	0.74	28.6	305	C	c	1
0534147-061918	F31-ap34	12.25	0.92	0.26	0.06	0.07	26.16	0.86	16.5	0.79	2.1	174	W+	c	1
0534148-051418	F11-ap17	13.37	0.93	0.26	0.06	–	27.57	0.32	17.3	0.67	12.8	102	W	c,dv	2
0534152-050451	F11-ap24	12.70	1.05	0.38	0.16	0.49	27.17	1.05	6.6	0.35	8.6	220	CW	c	2
0534156-053224	S2-ap238	12.47	1.91	0.76	0.18	0.96	22.42	1.99	5.4	0.34	19.7	265	C	c	1
0534163-044927	F11-ap60	13.04	0.96	0.26	0.16	0.46	25.00	1.95	8.1	0.38	5.6	233	CW	d?	1
0534164-053645	S1-ap40	9.70	1.01	0.46	0.34	1.30	28.09	1.20	16.1	0.80	6.9	547	C	c	1
0534168-050421	F22-ap62	11.55	1.20	0.34	0.42	1.18	30.47	1.39	13.1	0.67	5.6	227	W	c	1
0534170-044803	S2-ap61	13.60	2.35	0.86	0.59	0.75	–	–	3.4	0.23	1.9	300	CW	u	1
0534171-053816	F22-ap240	12.26	0.99	0.27	0.09	0.56	30.26	0.60	16.0	0.72	9.0	147	NSW	c	1
0534172-052904	F21-ap60	12.06	1.38	0.41	0.14	0.20	30.57	1.73	6.6	0.39	21.1	110	NSW	c	1
0534172-052248	S3-ap86	14.15	1.04	0.38	0.28	1.43	14.92	1.24	5.4	0.28	11.6	143	NSC	c	1
0534174-053158	F21-ap45	11.81	1.02	0.22	0.02	0.14	25.58	0.35	20.5	0.70	10.7	135	NSW	c	1
0534180-053333	F21-ap50	11.71	0.92	0.22	0.02	0.17	23.04	0.28	31.2	0.86	5.5	144	NSW	c	1
0534181-052833	S2-ap237	12.98	1.65	0.53	0.41	0.88	–	–	2.4	0.21	21.5	153	NSC	u	1
0534185-050448	S2-ap42	9.67	1.21	0.49	0.32	1.10	26.62	2.69	12.7	0.79	4.7	551	C	w	1
0534186-053708	S3-ap43	13.34	1.24	0.55	0.26	0.45	–	–	3.0	0.27	10.6	251	C	u,r	1
0534193-055026	F31-ap86	12.02	1.41	0.43	0.04	0.02	19.40	0.47	15.7	0.66	0.0	0	W+	c	1
0534195-053019	S3-ap65	11.03	1.58	0.64	0.38	1.25	25.61	4.00	8.1	0.68	10.7	613	C	w	1
0534198-061847	F31-ap32	13.39	0.89	0.22	0.07	0.00	25.93	0.48	18.1	0.71	4.7	129	W+	c	1

Table 12.4 (cont'd)

2MASS_id	ID	J	$(J-H)$	$(H-K)$	$[3.6-4.5]$	$[5.8-8.0]$	V_{rad}	ΔV_{rad}	R	S	EW_c	$FW_{10\%}$	$H\alpha$	CCF	NOB
0534202-055815	F31-ap78	12.66	0.87	0.23	0.06	0.11	25.55	0.37	18.8	0.62	0.0	0	W+	c	1
0534203-045856	F11-ap34	13.02	0.96	0.23	0.02	0.01	26.56	0.29	18.0	0.66	3.6	138	W	c	2
0534203-043403	F11-ap86	12.47	0.90	0.22	0.00	0.00	28.56	0.52	17.3	0.64	0.0	0	W	c	1
0534205-051845	S2-ap10	14.05	2.63	1.02	0.37	0.91	–	–	2.2	0.21	24.6	138	NSC	u,r	1
0534206-043501	F11-ap84	13.12	0.99	0.24	0.00	0.00	28.26	0.67	15.1	0.60	5.8	406	C	c	1
0534207-053235	F21-ap49	13.26	0.84	0.22	0.04	1.02	27.02	0.80	13.3	0.53	17.5	118	NSW	c	1
0534208-050650	F21-ap108	13.40	0.90	0.25	0.12	0.21	27.07	1.23	10.0	0.51	7.4	148	W+	c	1
0534208-052329	F21-ap67	13.13	0.88	0.23	-0.06	0.00	18.68	0.51	16.1	0.65	32.8	109	NSW	c	1
0534209-052448	F21-ap64	13.41	0.88	0.26	0.04	0.00	28.69	0.94	12.7	0.61	26.5	60	NSW	c	1
0534212-053534	F22-ap237	13.14	0.92	0.23	0.08	0.12	25.52	1.17	9.9	0.54	9.4	151	NSW	c	1
0534212-045032	S2-ap63	13.85	1.13	0.34	0.24	1.12	21.15	3.56	4.8	0.27	4.0	334	CW	c	1
0534214-045547	F21-ap117	12.53	0.95	0.27	0.07	0.16	24.68	1.05	10.5	0.51	11.3	148	W	c	1
0534215-051053	F11-ap13	12.76	1.83	0.50	0.03	0.06	34.95	0.80	9.2	0.42	6.6	100	NS	d?	1
0534219-051530	S2-ap14	14.19	1.57	0.57	0.43	0.94	18.99	2.27	3.2	0.20	19.5	157	NSC	r	1
0534220-050134	F22-ap69	13.13	0.88	0.37	0.07	0.84	19.64	0.85	6.1	0.38	11.0	222	W	c,dv	2
0534223-052226	F22-ap26	13.35	0.97	0.34	0.12	0.00	23.87	0.71	9.3	0.39	51.8	101	NSW	c	1
0534224-052226	S3-ap87	13.35	0.97	0.34	0.12	0.00	21.30	1.54	5.0	0.26	20.4	131	NSW	c	1
0534229-044139	F11-ap74	11.83	1.12	0.31	0.36	0.73	30.09	0.29	29.9	0.82	25.7	291	C	c	1
0534230-044139	S2-ap75	11.83	1.12	0.31	0.36	0.73	30.50	0.37	21.2	0.76	14.8	331	C	c	1
0534236-061838	F31-ap21	12.41	0.90	0.21	0.07	0.10	23.14	0.62	19.8	0.81	6.4	217	W	c	1
0534238-050815	F11-ap11	12.53	1.10	0.42	0.04	0.09	24.29	1.13	12.2	0.63	6.5	168	W	c	2
0534252-045439	F22-ap76	11.99	0.99	0.21	0.07	0.11	20.39	2.60	7.7	0.56	5.4	199	W	c	1
0534254-045655	F11-ap38	11.77	1.05	0.32	0.17	0.76	25.85	0.26	21.6	0.73	18.3	330	C	c	2
0534254-045654	S1-ap106	11.77	1.05	0.32	0.17	0.76	25.70	0.41	19.0	0.71	12.2	328	C	c	1
0534255-053701	S1-ap34	13.54	0.98	0.34	0.27	0.79	18.66	1.72	4.5	0.24	8.7	183	NSC	c	1
0534257-045655	F21-ap115	11.73	1.15	0.35	0.33	1.03	25.87	0.25	30.1	0.89	3.5	443	C	c,dv	2
0534258-045627	S2-ap64	12.18	1.27	0.43	0.52	1.20	31.23	0.53	16.3	0.70	21.5	432	C	c	1
0534260-050733	F21-ap107	12.84	0.89	0.31	0.09	0.06	28.89	0.46	14.2	0.55	9.1	120	W+	c	1
0534261-052630	S2-ap239	11.17	2.02	0.83	0.57	0.90	–	–	2.1	0.32	42.2	332	C	u	1
0534265-052323	F22-ap24	12.43	1.05	0.31	0.11	–	26.13	0.43	16.9	0.65	45.0	108	NSC	c	1
0534267-050117	F11-ap26	12.24	0.87	0.23	0.03	0.12	30.05	0.63	14.9	0.67	3.8	172	W	c	2
0534267-045045	F11-ap47	12.55	1.22	0.36	0.03	0.12	29.98	0.40	22.0	0.74	2.8	180	W-	c	1
0534267-054157	F21-ap38	12.85	1.04	0.29	0.25	1.05	25.65	0.62	13.9	0.60	7.5	142	NSW	c	1
0534269-061851	F31-ap23	12.76	1.17	0.29	-0.04	0.15	33.09	0.26	28.2	0.80	0.0	0	AE	c	1
0534269-051803	S1-ap63	13.57	1.84	0.71	0.47	0.62	–	–	2.2	0.18	27.5	165	C	l,n	1
0534274-050026	S1-ap102	14.42	0.98	0.27	0.25	0.83	26.08	2.49	4.8	0.26	5.6	433	C	l	1
0534275-052828	F21-ap54	12.26	0.98	0.24	0.11	0.47	22.78	1.07	11.6	0.62	18.9	122	NSW	c	1
0534276-045705	S1-ap108	13.74	1.45	0.60	0.46	1.06	14.84	1.78	2.6	0.15	13.2	520	C	l,n	1
0534276-053719	S3-ap50	13.32	3.14	1.23	1.22	1.24	14.34	1.71	4.6	0.28	5.4	236	NSC	c	1
0534278-054331	F31-ap98	12.64	0.89	0.24	0.06	0.16	24.94	1.28	10.0	0.65	4.9	162	W-	c	2
0534279-052634	S1-ap49	12.23	1.58	0.61	0.00	0.00	27.59	1.72	9.0	0.66	17.0	507	C	c	1
0534280-050521	S2-ap31	14.10	1.05	0.39	0.24	0.94	24.96	1.68	5.6	0.33	6.0	247	W	c	1
0534285-052457	S1-ap43	11.14	1.20	0.39	0.30	0.82	24.03	0.28	29.8	0.85	6.6	221	C	c	1

Table 12.4 (cont'd)

2MASS_id	ID	J	$(J-H)$	$(H-K)$	[3.6 – 4.5]	[5.8 – 8.0]	V_{rad}	ΔV_{rad}	R	S	EW_c	$FW_{10\%}$	$H\alpha$	CCF	NOB
0534286-043439	F11-ap89	12.78	0.93	0.22	0.00	0.00	24.99	3.49	11.1	0.58	3.0	280	WC	w	1
0534286-053032	S3-ap72	14.86	1.26	0.51	0.43	0.64	12.73	1.54	4.9	0.25	17.5	154	NSC	c	1
0534289-050838	S2-ap23	14.67	0.79	0.17	0.40	0.81	23.81	2.28	3.6	0.20	17.3	352	C	l,r	1
0534292-051439	S1-ap71	10.96	1.53	0.53	0.46	0.75	26.87	0.49	24.6	0.83	3.4	312	C	c	1
0534295-051355	S2-ap16	12.55	2.12	0.76	0.00	0.00	30.01	1.28	8.2	0.46	17.7	246	C	c	1
0534296-054724	F31-ap81	12.64	1.00	0.25	0.13	1.17	26.82	0.24	27.2	0.80	8.5	197	W	c	2
0534296-050307	S2-ap45	14.16	1.35	0.55	0.40	0.56	–	–	3.4	0.23	14.2	345	C	u	1
0534297-045147	S2-ap72	13.24	2.33	0.87	0.48	0.90	30.18	2.12	7.2	0.47	7.3	398	CW	c	1
0534298-050405	F21-ap114	12.85	0.96	0.21	0.04	0.05	29.13	0.37	22.6	0.73	4.3	124	W+	c	1
0534299-052517	F22-ap19	13.38	0.96	0.28	0.09	–	24.02	2.05	5.3	0.33	52.9	123	NSC	c	1
0534300-044950	F11-ap56	12.01	1.04	0.30	0.12	0.35	27.80	0.40	21.5	0.83	58.3	422	C	c	1
0534301-054015	F22-ap225	13.46	1.20	0.37	0.14	–	–	–	3.4	0.28	12.7	110	NSW	u,r	1
0534302-045830	F11-ap23	12.42	0.93	0.23	0.08	0.09	24.81	2.98	9.7	0.55	5.6	368	CW	w	2
0534302-062201	F31-ap24	12.37	0.96	0.23	0.06	0.13	28.10	4.33	8.8	0.75	4.3	337	W	w	1
0534302-051148	S1-ap90	11.62	1.78	0.69	0.00	0.00	28.14	0.63	15.7	0.67	19.4	369	C	c	1
0534303-045705	F21-ap111	13.42	0.92	0.22	0.06	0.15	29.14	0.67	15.2	0.66	3.5	165	W+	c	1
0534304-052156	S2-ap233	14.35	1.11	0.39	0.45	0.84	–	–	3.1	0.28	35.7	141	NSC	u	1
0534305-043351	F11-ap85	12.92	1.15	0.34	0.00	0.00	18.21	0.69	11.1	0.57	0.0	0	AE	c	1
0534306-043552	F11-ap90	12.54	1.31	0.34	0.00	0.00	27.46	0.48	18.9	0.72	17.8	397	C	c	1
0534311-052155	F21-ap78	12.38	1.23	0.32	0.27	0.72	27.73	0.36	20.0	0.80	17.8	109	NSW	c	2
0534312-052854	F22-ap6	11.90	1.00	0.32	0.03	0.53	23.50	1.00	13.0	0.71	15.1	119	NSC	c	1
0534316-052826	S3-ap77	12.73	1.34	0.45	0.35	0.67	24.02	0.91	12.7	0.65	8.1	161	NSC	c	1
0534318-053519	F21-ap33	12.60	0.90	0.27	0.03	-0.06	26.70	0.33	26.0	0.79	5.7	123	NSW	c	1
0534319-052636	F22-ap1	12.27	0.94	0.24	0.07	0.15	26.59	4.07	10.2	0.70	17.2	134	NSC	w	1
0534320-052742	S3-ap73	13.31	1.85	0.66	0.42	1.11	17.10	1.59	4.1	0.24	13.7	150	NSC	c	1
0534320-051124	F21-ap102	13.04	1.21	0.40	0.10	0.01	21.59	7.47	3.5	0.16	19.5	150	WC	w,l,dv?	2
0534326-052107	F22-ap21	12.53	1.16	0.28	0.39	0.90	26.60	0.45	19.5	0.77	18.2	200	NSC	c	1
0534327-045846	S1-ap109	13.76	0.86	0.27	0.29	0.87	24.43	1.08	7.8	0.38	9.3	343	C	c	1
0534327-052107	S1-ap51	12.53	1.16	0.28	0.39	0.90	26.26	0.67	13.9	0.65	18.8	150	C	c	1
0534330-055747	F31-ap73	12.38	1.19	0.27	0.04	0.16	31.91	2.10	16.3	0.79	3.9	414	CW	w	1
0534332-042713	F11-ap97	13.22	0.90	0.22	0.00	0.00	22.71	0.42	17.1	0.63	2.8	101	W+	c	1
0534337-054022	F22-ap229	12.74	0.96	0.30	0.34	0.86	23.67	1.17	6.6	0.46	31.4	301	C	c	2
0534338-052718	F22-ap7	13.23	0.99	0.32	0.15	1.05	24.17	1.08	8.8	0.48	43.9	98	NSC	c	1
0534339-061949	F31-ap26	12.65	0.93	0.29	0.06	0.09	33.61	0.83	9.8	0.55	0.0	0	AE	c	1
0534339-053451	S2-ap230	11.86	1.43	0.46	0.18	0.94	25.44	0.98	16.9	0.82	9.1	454	C	c	1
0534339-054824	F31-ap92	13.30	0.93	0.30	0.23	0.80	24.23	1.08	7.9	0.51	11.2	192	W	c	2
0534341-050517	F11-ap15	13.35	0.96	0.27	0.19	0.50	30.34	0.53	13.5	0.63	4.7	132	W	c	2
0534341-044827	F11-ap55	12.68	0.97	0.23	0.16	0.87	26.57	0.48	19.2	0.70	4.6	180	W	c	1
0534348-061125	F31-ap46	12.50	0.89	0.25	0.11	0.07	25.02	7.77	5.3	0.39	6.3	345	C	w	1
0534350-053700	S3-ap44	14.26	0.73	0.39	0.27	1.18	14.94	1.92	3.6	0.27	4.1	135	NSW	c	1
0534351-053432	F22-ap234	12.76	1.27	0.43	0.58	1.19	25.84	1.23	7.2	0.43	40.9	291	C	c	1
0534352-053432	S1-ap32	12.76	1.27	0.43	0.58	1.19	24.51	1.83	4.9	0.29	24.5	307	C	c	1
0534356-053552	F21-ap39	13.35	0.94	0.24	0.01	0.20	25.35	2.25	9.1	0.50	12.6	129	NSW	c	1

Table 12.4 (cont'd)

2MASS_id	ID	J	$(J-H)$	$(H-K)$	[3.6 – 4.5]	[5.8 – 8.0]	V_{rad}	ΔV_{rad}	R	S	EW_c	$FW_{10\%}$	$H\alpha$	CCF	NOB
0534356-052952	F22-ap231	13.19	0.92	0.30	0.08	–	21.09	0.49	16.4	0.67	33.6	112	NSW	c	1
0534357-054009	F22-ap230	12.75	1.16	0.34	0.26	0.77	25.58	0.50	16.4	0.65	11.9	190	NSW	c	1
0534358-054009	S1-ap28	12.75	1.16	0.34	0.26	0.77	27.36	1.19	7.7	0.48	7.6	206	WC	c	1
0534358-053645	F22-ap223	12.96	1.51	0.47	0.11	0.07	6.13	2.21	2.7	0.20	11.6	164	NSW	d,l,r	1
0534359-051524	F22-ap41	12.80	0.95	0.25	0.00	–	25.39	0.33	17.1	0.72	11.5	106	NS	c	2
0534360-045218	S1-ap112	13.84	0.98	0.31	0.42	0.60	26.71	1.23	8.1	0.41	4.8	282	C	c	1
0534360-054215	F31-ap95	12.14	0.90	0.21	0.01	-0.13	28.02	0.19	33.3	0.87	2.0	131	W+	c,dv	2
0534374-053451	S3-ap52	11.81	1.63	0.63	0.20	0.67	25.83	0.46	22.6	0.81	5.1	597	CW	c	1
0534375-054117	F31-ap93	11.69	1.38	0.46	0.13	0.62	26.52	0.98	22.2	0.80	3.9	135	W-	c	1
0534375-054310	F21-ap25	12.44	1.23	0.30	0.27	0.52	26.20	0.26	23.0	0.76	3.9	245	W	c	2
0534377-060233	F31-ap67	13.18	0.86	0.32	0.09	0.12	23.30	2.76	7.7	0.51	5.7	240	W	w	1
0534378-044238	F11-ap80	13.44	1.00	0.27	0.14	-0.35	31.43	1.29	7.0	0.33	2.9	131	W	c	1
0534379-045108	F11-ap49	12.90	1.28	0.31	0.04	0.24	32.09	0.42	22.7	0.77	1.5	120	NS	c	1
0534379-054108	F21-ap21	11.56	0.83	0.24	0.01	0.08	24.66	0.70	25.6	0.88	2.2	174	W-	c	1
0534381-052740	F21-ap43	12.83	0.88	0.26	0.00	–	21.82	0.38	21.9	0.76	26.9	101	NSW	c	1
0534381-050517	S2-ap46	14.41	1.03	0.41	0.35	0.47	27.06	2.27	3.8	0.21	3.7	225	NSW	c	1
0534382-052423	F21-ap62	12.73	1.04	0.25	0.10	-0.50	26.57	0.43	16.1	0.62	79.4	201	C	c	1
0534387-060822	F31-ap47	12.99	0.87	0.24	0.04	0.10	26.01	0.39	18.1	0.66	0.0	0	W+	c	1
0534388-062521	F31-ap17	12.16	0.91	0.21	0.00	0.06	25.92	0.35	24.8	0.79	1.3	157	W+	c	1
0534389-055753	S3-ap18	13.49	0.91	0.32	0.32	0.67	20.59	2.48	3.9	0.27	1.8	235	W-	c	1
0534390-045528	F11-ap36	12.11	1.25	0.34	0.05	-0.06	35.17	0.65	15.0	0.67	2.5	157	W	c,dv	2
0534391-053402	S3-ap55	13.70	1.27	0.47	0.39	0.70	14.96	1.56	4.0	0.23	4.8	142	NSW	c	1
0534392-055056	F31-ap83	13.35	0.89	0.28	0.07	0.93	–	–	3.0	0.21	7.9	258	C	w,l,r	1
0534393-050146	F22-ap78	12.88	0.99	0.36	0.17	0.46	30.24	1.72	7.2	0.39	6.1	184	NSW	d?	1
0534397-050306	F22-ap74	12.89	0.96	0.24	-0.01	0.05	31.01	0.35	21.2	0.69	4.4	131	W+	c	1
0534397-060713	F31-ap58	12.30	0.90	0.24	0.06	0.09	19.05	0.37	21.9	0.77	5.5	150	W	c	1
0534399-045047	S2-ap77	14.05	1.41	0.43	0.24	0.87	25.87	4.23	3.5	0.27	1.9	176	NSW	c	1
0534400-052604	F22-ap5	13.33	0.99	0.36	0.07	–	16.97	4.86	3.7	0.24	93.4	95	NSC	w	1
0534400-054009	S3-ap40	9.88	1.25	0.48	0.18	0.52	24.99	0.77	24.2	0.87	6.7	341	C	w	1
0534404-045739	F22-ap77	12.82	1.07	0.35	0.33	0.75	28.40	0.42	16.1	0.59	42.2	297	C	c	1
0534406-044331	F11-ap76	12.79	1.58	0.39	0.05	0.16	30.67	0.58	15.1	0.64	2.1	167	W-	c	1
0534406-050658	S2-ap40	14.54	2.73	1.06	0.49	0.62	16.00	5.58	3.4	0.27	9.7	349	CW	c	1
0534408-052809	F21-ap47	12.60	1.01	0.34	0.40	0.80	24.48	0.37	13.3	0.55	83.4	140	NSC	c	2
0534408-052242	S2-ap234	10.53	1.93	0.86	0.17	0.51	25.80	1.78	5.4	0.39	19.1	679	C	c	1
0534408-052638	S3-ap88	12.68	1.55	0.54	0.20	0.90	23.55	0.58	18.1	0.71	15.9	143	NSC	c	1
0534409-052559	S2-ap223	13.79	1.86	0.69	0.32	0.79	25.49	2.57	5.0	0.32	39.5	142	NSC	c	1
0534411-055437	F31-ap89	13.45	1.36	0.35	0.03	0.30	14.14	0.82	10.1	0.48	0.0	0	N	c	1
0534411-054739	F31-ap100	13.45	0.88	0.28	0.05	0.83	19.04	0.35	13.7	0.59	6.7	116	NSW	c	2
0534412-054611	S3-ap22	12.24	1.42	0.53	0.57	0.97	25.23	0.57	13.5	0.62	16.1	314	C	c	1
0534414-043913	F11-ap88	13.26	1.12	0.37	0.00	0.00	26.86	1.05	11.3	0.55	5.8	278	CW	c	1
0534416-052357	F22-ap15	13.28	1.00	0.29	0.12	–	20.89	4.36	5.1	0.31	70.5	99	NSW	w,l	1
0534417-045346	F22-ap71	12.31	1.28	0.39	0.25	1.04	30.67	0.38	16.7	0.75	25.4	481	C	c	2
0534417-052653	S2-ap225	12.54	1.40	0.52	0.67	1.00	20.88	0.57	14.4	0.66	19.7	149	NSC	c	1

Table 12.4 (cont'd)

2MASS_id	ID	J	$(J-H)$	$(H-K)$	[3.6 − 4.5]	[5.8 − 8.0]	V_{rad}	ΔV_{rad}	R	S	EW_c	$FW_{10\%}$	$H\alpha$	CCF	NOB
0534417-053648	S3-ap42	13.90	1.07	0.40	0.45	0.79	14.77	1.54	5.3	0.29	12.8	120	W-	c	1
0534420-050431	S2-ap49	13.91	1.30	0.53	0.47	0.78	26.45	1.78	3.9	0.18	10.7	364	C	c	1
0534423-051238	F11-ap7	13.26	1.19	0.35	0.07	–	23.39	5.29	4.3	0.28	25.3	108	NSW	s,l,w	2
0534424-054325	S3-ap28	13.40	1.16	0.34	0.33	0.45	15.48	1.52	4.9	0.26	3.9	179	NSW	c	1
0534424-052246	S3-ap95	14.27	1.04	0.39	0.34	1.05	15.82	2.36	3.0	0.20	39.0	139	NSC	l	1
0534427-052837	F21-ap48	11.68	1.24	0.37	0.25	0.82	22.87	0.46	19.0	0.71	26.5	110	NSC	c	1
0534428-052516	F21-ap59	12.28	1.47	0.40	0.04	-0.12	34.33	0.43	16.6	0.67	44.3	92	NSW	c	1
0534431-054440	F21-ap28	12.31	1.13	0.44	0.52	0.93	23.39	0.98	6.9	0.34	43.0	307	C	c	1
0534431-062714	F31-ap18	12.76	0.94	0.30	0.28	0.83	22.81	0.52	15.8	0.67	6.9	175	W	c	1
0534432-061703	F31-ap30	12.28	0.93	0.23	0.02	0.08	18.93	1.91	13.4	0.78	4.9	221	W	w	1
0534434-053007	F21-ap31	12.21	1.18	0.33	0.01	0.53	25.40	0.38	27.2	0.83	19.8	114	NSW	c	1
0534435-045136	F11-ap50	12.82	1.04	0.28	0.05	0.70	30.31	0.48	14.9	0.59	20.3	236	C	c	1
0534435-055810	S3-ap14	13.78	1.38	0.56	0.47	0.61	13.96	1.64	4.2	0.24	11.5	385	C	r	1
0534444-052606	F21-ap52	13.05	1.00	0.32	0.08	-0.01	23.88	3.00	4.9	0.31	118.1	93	NSW	w,l	1
0534444-055614	F31-ap88	13.13	0.90	0.25	0.09	-0.10	24.59	0.48	17.1	0.68	4.6	120	W+	c	1
0534445-052438	S3-ap98	13.53	1.17	0.41	0.40	0.78	–	–	3.4	0.24	58.9	120	NSC	l	1
0534447-045640	S2-ap74	13.65	1.42	0.48	0.53	0.58	30.75	1.50	5.7	0.34	15.9	560	C	c	1
0534447-053342	S3-ap62	12.64	1.79	0.70	0.74	0.93	–	–	2.3	0.35	20.2	466	C	u	1
0534449-050649	F11-ap12	11.88	1.21	0.34	0.17	1.01	31.36	0.55	19.0	0.83	7.9	319	C	c	2
0534450-050620	S2-ap33	13.59	1.36	0.48	0.39	0.58	27.41	3.67	5.3	0.30	4.8	326	CW	c	1
0534450-045559	S2-ap76	13.57	2.23	0.76	0.42	0.63	36.65	9.62	3.5	0.27	3.5	214	NSC	d,w,l	1
0534451-062107	F31-ap11	12.65	0.94	0.23	0.03	0.10	25.92	0.33	23.8	0.78	3.8	153	W+	c	1
0534451-051047	S2-ap17	12.18	1.48	0.63	0.39	0.59	30.00	0.93	8.1	0.43	16.3	374	C	c	1
0534454-050207	F22-ap79	12.21	0.88	0.22	0.06	0.13	29.45	0.23	23.4	0.77	3.3	118	W	c,dv	2
0534455-043607	F11-ap98	11.51	0.96	0.23	0.00	0.00	30.90	1.55	15.5	0.83	0.3	182	W	w	1
0534458-054109	F21-ap30	12.24	1.22	0.31	0.25	1.42	25.71	0.65	12.7	0.51	19.6	183	NSC	c	1
0534458-054812	F22-ap211	13.29	0.88	0.21	0.07	–	27.12	0.53	13.7	0.66	5.8	148	NSW	c	2
0534463-042902	F11-ap91	13.31	0.88	0.26	0.00	0.00	27.94	0.48	15.4	0.61	2.2	139	W	c	1
0534463-052431	F21-ap55	11.53	1.00	0.31	0.04	0.40	25.84	0.69	23.8	0.81	21.3	101	NSW	c	1
0534463-053907	S3-ap34	10.88	1.64	0.60	0.51	0.96	27.24	0.59	16.3	0.78	13.8	555	C	c	1
0534465-052325	S1-ap47	12.63	1.54	0.56	0.57	0.96	28.33	1.22	6.8	0.45	113.1	123	NSC	c	1
0534467-052604	S2-ap228	13.72	2.19	0.84	0.48	0.64	–	–	2.0	0.23	64.9	142	NSC	l	1
0534468-052129	S2-ap232	13.50	1.47	0.44	0.46	0.87	25.25	0.72	13.3	0.65	32.5	142	NSC	c	1
0534469-045912	F21-ap122	12.24	0.99	0.26	0.02	0.15	32.32	0.31	29.0	0.85	1.2	196	W	c	1
0534469-055220	F31-ap94	13.47	0.89	0.26	0.11	–	25.20	1.22	9.8	0.54	6.5	122	W-	c	1
0534469-053414	S3-ap57	7.22	0.58	0.32	0.61	0.66	–	–	2.4	0.20	0.8	255	W	u	1
0534475-055756	S3-ap1	10.95	1.54	0.64	0.42	0.55	24.85	1.28	12.0	0.68	18.6	559	C	c	1
0534478-053046	F22-ap232	12.10	1.01	0.34	0.15	1.45	26.54	0.28	20.2	0.75	22.2	160	NSC	c,dv	2
0534479-050455	F22-ap80	12.00	1.37	0.47	0.27	0.87	30.68	0.42	21.4	0.80	23.7	393	C	c	1
0534481-052238	S1-ap54	13.75	1.15	0.42	0.25	1.20	15.94	2.28	2.8	0.17	189.4	116	NSC	l	1
0534481-054228	S3-ap26	11.26	1.12	0.29	0.24	0.71	24.66	1.08	19.8	0.81	3.1	333	CW	c	1
0534482-050713	F11-ap3	13.00	0.95	0.20	0.03	0.31	21.52	0.41	20.0	0.74	3.5	158	W	c	1
0534482-053235	F22-ap227	12.85	1.27	0.36	0.11	0.32	23.71	1.53	6.8	0.45	26.2	106	NSW	c	1

Table 12.4 (cont'd)

2MASS_id	ID	J	$(J-H)$	$(H-K)$	[3.6 – 4.5]	[5.8 – 8.0]	V_{rad}	ΔV_{rad}	R	S	EW_c	$FW_{10\%}$	$H\alpha$	CCF	NOB
0534482-053010	S3-ap78	14.49	1.14	0.40	0.29	0.97	14.44	1.30	5.0	0.28	56.2	116	NSC	d?	1
0534483-063026	F31-ap5	12.10	1.28	0.49	0.40	0.97	26.78	0.58	13.5	0.68	25.9	285	C	c	1
0534484-045051	S1-ap117	13.42	1.03	0.32	0.43	0.97	26.02	2.72	4.6	0.30	28.9	373	C	c	1
0534484-053107	S1-ap23	13.85	1.32	0.52	0.95	–	14.60	3.62	2.6	0.21	39.0	213	NSC	r	1
0534485-044956	S2-ap82	13.97	2.81	0.92	0.80	1.06	–	–	2.2	0.17	3.2	354	CW	u,r	1
0534486-044750	S2-ap84	13.07	1.13	0.37	0.54	0.86	25.50	0.47	15.0	0.60	5.5	244	W	c	1
0534487-051907	F21-ap88	12.78	1.17	0.30	0.10	–	22.40	1.23	10.2	0.58	45.3	99	NS	c	1
0534487-061142	F31-ap33	13.09	0.86	0.23	0.10	–	25.15	0.47	16.9	0.67	2.1	148	W+	c	1
0534487-051746	F21-ap98	12.54	1.47	0.47	0.08	-0.05	25.81	0.72	9.4	0.51	61.0	103	NSW	c,dv	2
0534488-053333	S1-ap29	13.59	1.11	0.34	0.59	0.80	25.36	1.17	7.6	0.39	14.1	146	NSC	c	1
0534489-045714	F11-ap22	13.49	1.05	0.24	0.09	0.52	28.35	0.31	17.4	0.65	0.0	0	W-	c	2
0534489-052816	S2-ap224	12.84	1.49	0.49	0.37	0.67	24.74	2.37	4.6	0.33	42.5	160	NSC	c	1
0534489-053131	S3-ap74	13.80	1.35	0.45	0.36	–	17.48	2.53	5.2	0.32	14.8	131	NS	c	1
0534490-052626	S2-ap226	13.23	1.36	0.53	0.41	0.97	21.72	3.38	3.1	0.21	63.4	183	C	r	1
0534490-054605	S3-ap15	11.94	1.03	0.29	0.29	0.89	24.77	0.38	16.1	0.71	10.8	347	C	c	2
0534492-051855	F22-ap31	12.08	0.92	0.21	0.13	–	23.71	0.94	16.8	0.79	14.6	101	NSW	c	1
0534495-052903	S3-ap82	12.05	1.52	0.54	0.65	1.27	26.33	0.97	8.1	0.48	47.9	241	C	c	1
0534499-051844	S1-ap67	8.78	1.47	0.69	0.49	0.72	–	–	2.2	0.26	1.3	628	C	w,l	1
0534502-062648	F31-ap1	13.07	0.88	0.26	0.04	0.19	26.99	0.40	21.7	0.79	0.0	0	W+	c	1
0534504-051630	S1-ap73	14.20	0.98	0.35	0.21	0.00	28.54	2.35	3.5	0.21	37.3	139	NSW	c	1
0534504-052020	S2-ap221	11.96	1.52	0.59	0.17	0.66	24.38	0.86	14.7	0.74	23.8	449	C	c	1
0534505-052335	F22-ap18	12.52	1.32	0.47	0.38	0.88	23.39	1.00	6.2	0.54	89.7	248	C	c	2
0534507-045836	S1-ap118	12.15	1.42	0.41	0.23	0.54	32.30	2.09	9.9	0.57	3.0	369	CW	c	1
0534507-052701	S1-ap37	11.65	1.46	0.53	0.35	0.59	24.87	0.42	19.9	0.79	28.4	345	NSC	c	1
0534508-052925	F21-ap37	12.80	0.90	0.31	0.12	–	24.32	2.01	8.8	0.53	55.7	106	NSC	c	1
0534509-051756	F22-ap47	13.15	0.91	0.25	0.08	–	23.99	1.01	8.4	0.51	42.5	103	NS	c	2
0534512-051655	S2-ap236	12.43	1.86	0.60	0.45	0.95	24.71	2.44	5.3	0.35	34.9	145	NSC	c	1
0534514-050011	F11-ap20	13.17	0.92	0.20	0.10	0.10	29.72	0.76	12.9	0.57	3.6	125	W+	c	1
0534514-051329	F21-ap101	12.84	0.91	0.24	0.06	–	17.81	2.63	7.4	0.54	18.6	156	C	w	2
0534515-060344	F31-ap61	12.12	1.08	0.30	-0.01	0.18	19.28	0.35	20.9	0.75	0.0	0	AE	c	1
0534515-052513	S3-ap93	11.23	1.70	0.68	0.44	1.03	23.72	0.44	19.6	0.76	19.0	275	C	c	1
0534517-053924	F21-ap24	11.88	1.10	0.33	0.20	–	24.19	0.36	23.1	0.76	11.6	149	NSC	c	1
0534518-052138	F22-ap29	13.32	0.91	0.33	0.13	–	22.34	0.80	10.6	0.62	72.1	99	NSC	c	2
0534520-052418	F21-ap58	12.71	1.13	0.31	0.14	0.40	24.28	0.55	13.1	0.60	66.5	242	C	c	1
0534520-060320	F31-ap74	12.51	0.92	0.22	0.01	0.15	25.48	1.37	16.9	0.83	2.7	255	W	w	1
0534520-045501	S2-ap73	14.01	2.32	0.81	0.45	1.09	14.70	2.26	2.8	0.18	5.5	380	CW	l	1
0534520-052442	S3-ap91	12.13	1.50	0.57	0.62	0.94	23.15	0.92	11.0	0.59	37.1	128	C	c	1
0534521-054057	S1-ap11	13.07	1.43	0.59	0.47	0.73	14.33	1.98	3.9	0.24	12.7	284	C	c	1
0534522-051203	F21-ap116	13.05	0.91	0.21	0.03	0.76	27.10	0.72	16.8	0.73	6.3	109	W-	c	1
0534522-044011	S2-ap89	11.48	1.68	0.63	0.00	0.00	68.23	1.72	7.8	0.54	1.8	301	CW	d	1
0534523-053008	F21-ap40	13.02	0.89	0.27	0.07	–	25.65	2.47	9.6	0.52	45.2	101	NSC	c	1
0534523-063508	F31-ap6	13.28	0.85	0.31	0.07	0.13	37.84	11.01	3.9	0.51	12.4	433	C	w	1
0534523-052500	F22-ap10	13.43	1.07	0.38	0.17	–	7.54	2.81	4.6	0.26	159.2	104	NSC	s,l	1

Table 12.4 (cont'd)

2MASS_id	ID	J	$(J-H)$	$(H-K)$	$[3.6-4.5]$	$[5.8-8.0]$	V_{rad}	ΔV_{rad}	R	S	EW_c	$FW_{10\%}$	$H\alpha$	CCF	NOB
0534526-052945	S3-ap71	11.99	1.46	0.54	0.00	0.00	23.41	2.62	9.3	0.51	33.6	131	NSC	w	1
0534527-050050	F11-ap18	13.06	0.90	0.23	0.07	0.04	24.42	2.74	7.6	0.54	6.2	170	W	c	1
0534527-052755	S3-ap92	11.19	1.32	0.53	0.26	0.74	22.66	0.48	22.7	0.77	24.4	143	NSC	c	1
0534528-053348	F21-ap23	13.41	0.91	0.29	0.08	-0.06	25.82	1.36	8.9	0.45	35.0	106	NSC	c	1
0534529-052859	S3-ap83	13.07	1.05	0.38	0.40	1.34	28.12	1.08	6.7	0.38	52.5	199	C	c	1
0534530-050327	S1-ap101	11.97	1.17	0.40	0.41	0.83	24.92	0.25	20.7	0.76	19.3	343	C	c	3
0534531-055955	F31-ap84	13.50	0.93	0.27	0.08	0.28	24.48	0.50	17.6	0.66	4.0	112	W+	c	1
0534533-055405	F31-ap96	12.68	0.98	0.30	0.11	-0.03	23.78	7.24	6.2	0.51	6.3	344	CW	c	1
0534534-042909	F11-ap102	13.23	0.89	0.25	0.00	0.00	28.41	0.93	10.7	0.47	3.9	162	W	c	1
0534534-051027	F11-ap8	12.19	0.91	0.24	0.06	-0.04	24.88	0.43	14.0	0.63	9.9	121	W	c	2
0534534-045732	F21-ap130	13.30	1.03	0.39	0.34	0.72	28.36	0.67	9.2	0.50	18.4	267	C	c	2
0534535-052637	F21-ap46	13.23	1.26	0.43	0.10	–	–	–	2.7	0.23	224.2	101	NSC	u	1
0534536-054511	F22-ap215	13.38	0.95	0.28	0.10	0.40	23.07	1.61	6.8	0.43	7.0	142	NSC	c	1
0534537-050548	F11-ap9	13.34	0.94	0.21	0.05	0.30	26.58	0.42	15.6	0.64	4.5	121	NSW	c	2
0534538-062352	F31-ap12	11.65	1.00	0.26	0.16	0.96	22.88	0.42	23.6	0.83	8.6	336	C	c	1
0534541-052854	F22-ap221	12.68	1.71	0.47	0.04	–	24.09	2.75	7.9	0.44	83.0	104	NSC	c	1
0534543-051721	F22-ap53	12.95	0.91	0.27	0.24	–	26.10	0.86	11.2	0.54	49.3	101	NSC	c	1
0534545-045605	F21-ap129	12.11	1.62	0.43	0.00	0.04	29.05	1.81	8.1	0.56	6.1	243	W	c	1
0534546-052818	S1-ap21	13.51	1.52	0.56	0.16	1.07	–	–	2.8	0.30	91.7	146	NSC	u	1
0534548-052512	S1-ap35	13.06	1.28	0.47	0.46	0.96	24.40	1.49	4.3	0.22	82.9	146	NSC	c	2
0534549-051702	S1-ap80	11.49	2.19	0.86	0.29	0.62	27.15	0.82	11.3	0.62	19.4	244	NSC	c	1
0534549-054644	S3-ap16	11.37	1.30	0.49	0.00	0.00	22.15	0.31	33.2	0.89	3.4	422	CW	c	1
0534550-044941	S2-ap86	13.53	1.65	0.66	0.36	–	30.96	0.95	13.0	0.57	1.8	301	W	c	1
0534556-052937	F21-ap36	13.09	1.04	0.40	0.05	–	28.07	0.72	11.8	0.53	74.7	101	NSC	c	1
0534556-045612	S2-ap71	12.47	2.25	0.78	0.36	0.79	21.60	8.64	4.3	0.27	2.7	176	NSW	w,l	1
0534556-055529	S3-ap5	13.02	1.50	0.53	0.43	1.34	23.38	1.59	5.4	0.33	20.5	455	C	c	1
0534558-054126	S1-ap13	11.37	1.44	0.58	0.87	1.19	25.91	1.43	8.5	0.59	34.5	486	C	c	1
0534558-051945	S1-ap64	13.60	1.90	0.66	0.22	1.40	13.63	2.49	3.3	0.19	63.8	135	NSC	l	1
0534560-043812	F11-ap99	13.11	0.94	0.21	0.00	0.00	29.17	0.44	15.7	0.57	2.0	105	W+	c	1
0534561-050601	F11-ap10	12.57	0.90	0.20	0.06	0.00	16.62	3.77	7.2	0.55	8.9	248	WC	c	1
0534565-050107	S1-ap119	14.23	1.18	0.48	0.40	1.09	15.51	2.27	2.9	0.17	12.7	309	C	l,n,r	1
0534565-052751	S3-ap97	12.49	1.20	0.35	0.31	0.78	22.32	0.57	17.7	0.72	27.6	158	NSC	c	1
0534566-051112	S2-ap4	13.61	1.41	0.46	0.46	0.86	32.19	0.99	10.9	0.57	6.6	141	NSW	c	1
0534567-052637	F22-ap238	13.21	1.04	0.27	0.11	-0.09	31.15	6.70	4.0	0.31	173.9	102	NSC	w	1
0534568-052136	F22-ap11	12.20	1.77	0.48	0.18	–	25.30	1.46	8.9	0.51	162.8	100	NSC	c	1
0534568-044604	S2-ap87	12.38	1.42	0.50	0.35	0.26	30.79	0.37	26.6	0.85	3.4	267	WC	c	1
0534568-051133	S3-ap118	10.90	0.75	0.20	0.29	0.81	20.68	0.44	23.5	0.86	2.8	301	CW	c	1
0534570-052300	F21-ap51	13.25	1.00	0.24	0.08	–	21.53	3.39	7.6	0.41	162.1	99	NSC	w	1
0534571-053329	F21-ap27	12.81	1.45	0.42	0.22	0.96	21.00	1.91	4.9	0.33	50.6	99	NSC	c,dv	2
0534572-054202	F31-ap104	12.79	0.92	0.22	0.04	0.17	27.43	0.24	23.4	0.75	5.4	128	W+	c	2
0534573-051433	F21-ap112	13.42	1.60	0.41	0.05	–	19.62	8.57	4.1	0.25	44.5	101	NSC	w	1
0534574-053042	F21-ap32	12.74	0.97	0.23	0.03	0.53	29.78	2.37	12.6	0.63	23.8	101	NSC	w	1
0534574-045645	S1-ap115	14.43	2.80	0.93	0.55	1.13	17.37	1.25	6.1	0.30	3.3	177	W	c	1

Table 12.4 (cont'd)

2MASS_id	ID	J	$(J-H)$	$(H-K)$	[3.6 – 4.5]	[5.8 – 8.0]	V_{rad}	ΔV_{rad}	R	S	EW_c	$FW_{10\%}$	$H\alpha$	CCF	NOB
0534577-052251	S3-ap109	12.51	1.19	0.40	0.49	1.29	24.26	0.65	12.0	0.54	76.9	131	NSC	c	1
0534577-052352	S3-ap110	10.24	1.11	0.33	0.27	0.75	26.73	0.41	24.1	0.86	19.9	169	NSC	c	1
0534579-052946	F22-ap228	12.94	1.49	0.41	0.08	–	19.54	2.04	8.0	0.43	68.1	99	NSC	c	1
0534580-052940	S3-ap81	13.92	1.66	0.59	0.36	1.07	15.20	1.27	5.0	0.26	60.2	120	NSC	c	1
0534581-043718	F11-ap95	12.51	0.89	0.21	0.00	0.00	30.72	0.63	14.3	0.63	3.9	160	W	c	1
0534582-045051	F11-ap42	13.29	1.37	0.46	0.34	0.79	29.65	1.10	5.9	0.29	8.6	198	W	c,dv?	2
0534583-055428	S3-ap7	12.14	1.50	0.62	0.49	0.86	25.15	0.77	8.6	0.42	9.1	392	C	c	1
0534585-053249	S1-ap22	13.30	1.35	0.46	0.49	0.82	21.20	3.16	2.7	0.22	35.6	187	NSC	l	1
0534587-052117	S1-ap58	11.98	1.75	0.72	0.00	0.00	26.49	0.65	13.8	0.64	61.4	135	NSW	c	1
0534590-054429	S3-ap12	11.41	1.10	0.39	0.45	0.72	24.58	0.74	14.9	0.73	8.6	340	C	c	1
0534590-053621	S3-ap23	13.92	1.90	0.63	0.46	0.75	14.36	1.44	4.5	0.28	11.4	134	NSW	c	1
0534590-053750	S3-ap29	13.96	1.45	0.50	0.31	0.68	15.60	1.63	3.7	0.28	8.4	138	NSW	c	1
0534591-052307	F22-ap16	13.00	1.00	0.32	0.14	–	23.90	2.20	5.0	0.30	223.7	102	NSC	c	1
0534593-050530	F21-ap128	12.40	1.14	0.28	0.13	0.35	29.58	0.36	24.4	0.81	11.4	346	C	c	1
0534593-060722	F31-ap56	13.14	0.93	0.29	0.24	0.83	25.50	0.53	14.5	0.59	8.2	178	W+	c	1
0534593-050529	S2-ap59	12.40	1.14	0.28	0.13	0.35	29.50	0.48	18.9	0.74	3.5	342	C	c	1
0534596-052539	S3-ap106	12.12	1.21	0.37	0.59	0.77	24.84	0.42	22.9	0.83	19.3	147	NSC	c	1
0535001-052302	S2-ap222	10.23	1.24	0.43	0.41	1.15	29.25	1.50	15.3	0.82	13.5	471	C	c	1
0535002-051850	F21-ap95	12.46	1.34	0.31	0.01	–	24.29	1.73	16.4	0.69	39.7	97	NSC	w	1
0535003-050943	S2-ap7	13.69	0.91	0.32	0.17	1.15	23.72	0.96	7.6	0.37	7.4	153	NSC	c	1
0535005-054859	F22-ap218	12.73	1.77	0.48	0.12	–	25.64	0.86	11.8	0.60	8.2	232	NSC	c	1
0535007-053807	S3-ap11	11.90	1.88	0.78	0.00	0.00	23.62	1.57	7.7	0.46	10.3	306	C	c	1
0535008-053105	S3-ap75	13.45	1.33	0.58	0.43	1.03	19.36	1.90	3.8	0.21	18.3	143	NSC	c	1
0535009-044819	S2-ap85	12.38	1.13	0.32	0.27	0.92	30.61	0.44	15.5	0.61	3.0	165	W+	c	1
0535009-044818	F11-ap66	12.38	1.13	0.32	0.27	0.92	30.04	0.49	13.7	0.53	6.8	148	W+	c	1
0535010-052304	S1-ap46	13.76	1.47	0.58	0.44	–	23.95	3.12	3.2	0.20	339.8	120	NSC	l,n,r	1
0535011-052406	S2-ap211	11.38	1.07	0.30	0.38	1.02	25.88	0.53	16.5	0.69	131.6	123	NSC	c	1
0535012-052016	F21-ap84	12.87	0.98	0.22	0.08	–	27.82	0.34	21.4	0.72	70.9	94	NS	c	1
0535013-052022	S1-ap55	12.20	1.99	0.76	0.49	1.37	27.86	0.98	9.8	0.51	73.4	135	NSC	c	1
0535014-051104	S2-ap235	13.83	1.59	0.61	0.37	–	28.12	2.05	2.4	0.12	9.3	216	NSC	l,r	1
0535016-043252	F11-ap106	12.75	1.14	0.36	0.00	0.00	28.29	0.66	13.7	0.69	23.2	414	C	c	1
0535020-044730	F11-ap65	13.49	0.98	0.35	0.09	0.09	29.85	1.01	7.0	0.31	3.5	109	W-	c	1
0535020-051834	F21-ap103	13.14	1.47	0.40	0.10	0.22	27.82	3.06	3.2	0.17	105.7	98	NSW	l,n	1
0535020-051537	F21-ap120	12.79	1.00	0.24	0.21	0.00	29.21	0.41	20.9	0.73	16.5	105	NS	c	1
0535020-051822	F22-ap66	12.96	1.53	0.45	0.29	0.78	–	–	3.3	0.23	95.4	99	NSC	l,n	2
0535021-052909	S3-ap102	12.03	1.43	0.47	0.31	0.83	24.89	0.98	13.7	0.64	42.4	128	NSC	c	1
0535023-044916	F11-ap41	12.71	1.10	0.27	0.06	-0.39	31.11	0.45	19.4	0.71	5.0	219	W	c	1
0535024-053309	F22-ap213	12.09	1.09	0.32	0.40	0.99	27.31	1.50	14.2	0.76	20.9	206	C	c	1
0535024-052046	F22-ap35	11.54	1.44	0.41	0.11	–	26.88	0.53	23.2	0.81	39.8	99	NSC	c	1
0535027-062359	F31-ap9	13.43	0.85	0.27	0.10	0.01	23.74	1.88	9.4	0.55	6.2	186	W-	c	1
0535029-060525	F31-ap70	12.48	0.90	0.21	0.04	0.19	26.16	0.30	33.2	0.87	2.5	161	W+	c	1
0535030-045959	F21-ap123	12.61	0.89	0.23	0.09	0.13	24.02	3.50	8.4	0.58	7.8	282	CW	w	1
0535030-061223	F31-ap25	13.02	0.89	0.22	0.12	0.13	25.60	0.38	17.9	0.66	6.0	151	W+	c	1

Table 12.4 (cont'd)

2MASS_id	ID	J	$(J-H)$	$(H-K)$	[3.6 – 4.5]	[5.8 – 8.0]	V_{rad}	ΔV_{rad}	R	S	EW_c	$FW_{10\%}$	$H\alpha$	CCF	NOB
0535030-054533	F31-ap106	12.96	1.63	0.49	0.17	0.00	25.94	0.58	13.1	0.63	5.5	113	NSW	c	2
0535030-052237	S3-ap114	11.99	1.42	0.44	0.36	0.64	–	–	2.6	0.21	89.3	150	NSC	w,l	1
0535031-050917	F22-ap82	13.14	1.09	0.35	0.20	0.83	31.00	0.48	17.6	0.68	7.6	216	WC	c	1
0535032-051753	S1-ap76	13.34	1.62	0.61	0.43	–	28.16	1.25	6.5	0.32	54.2	135	NSC	c	1
0535032-044921	S2-ap83	9.96	1.45	0.57	0.34	0.57	34.56	1.17	19.6	0.83	12.0	463	C	w	1
0535033-045643	F21-ap121	12.33	1.02	0.27	0.42	1.09	27.14	0.68	15.9	0.83	3.1	258	W	c	3
0535035-052926	S1-ap24	12.35	1.77	0.70	0.67	0.76	27.08	0.70	12.8	0.70	35.1	206	C	c	1
0535035-051600	S1-ap89	14.50	1.60	0.57	0.46	1.02	12.11	2.31	3.3	0.18	30.4	135	NSC	l	1
0535038-061647	F31-ap20	12.94	0.94	0.24	0.01	0.13	26.41	0.39	20.2	0.72	2.5	155	W+	c	1
0535039-051859	S1-ap68	13.27	1.53	0.50	0.50	0.87	25.59	1.12	7.4	0.39	49.4	135	NSW	c	1
0535039-052903	S3-ap104	11.24	1.12	0.31	0.28	0.88	23.47	0.83	18.7	0.82	17.7	139	NSC	c	1
0535039-055401	S3-ap8	13.88	2.62	1.05	0.63	0.88	13.96	1.28	5.3	0.32	2.7	194	NSW	c	1
0535040-052637	F22-ap222	12.08	1.17	0.29	0.44	0.97	24.84	0.29	23.7	0.84	68.8	101	NSC	c	2
0535040-054854	F31-ap102	13.38	0.92	0.26	0.08	1.05	26.02	0.33	16.0	0.64	0.0	0	NS	c	2
0535040-054051	F31-ap110	12.49	0.90	0.25	0.07	-0.24	26.55	0.32	16.1	0.66	3.9	101	W+	c	2
0535043-060053	F31-ap87	11.97	0.92	0.24	0.07	0.11	25.44	1.48	14.2	0.71	5.4	205	W	c	1
0535043-052313	S2-ap213	11.20	1.38	0.47	0.44	0.82	25.55	1.68	6.0	0.43	86.8	146	NSC	c	1
0535043-053831	S3-ap13	13.55	1.89	0.60	0.34	0.82	15.55	1.42	4.7	0.28	9.7	138	W-	c	1
0535045-052938	F21-ap11	11.70	1.22	0.46	0.31	0.70	26.83	0.39	21.3	0.88	9.3	233	CW	c,dv	2
0535045-055525	F31-ap91	13.39	0.87	0.26	0.11	0.09	20.23	3.71	6.7	0.42	6.0	167	W	w	1
0535047-052638	S1-ap27	11.97	1.35	0.41	0.28	0.74	25.83	0.47	19.2	0.76	53.1	138	NSC	c	1
0535048-052239	S3-ap116	12.84	1.17	0.34	0.40	1.02	27.22	1.19	7.0	0.41	148.9	124	NSC	c	1
0535050-043233	F11-ap110	13.00	0.97	0.30	0.00	0.00	25.09	1.30	8.3	0.38	4.3	175	W	c	1
0535050-053643	S1-ap19	12.73	1.34	0.53	0.46	1.03	24.94	1.78	4.3	0.27	104.9	149	NSC	c	1
0535052-051450	S1-ap95	8.17	0.98	0.35	0.11	0.57	30.35	4.66	7.6	0.70	0.0	0	X	w	1
0535052-052603	S3-ap103	13.68	1.22	0.41	0.33	–	19.19	2.17	3.6	0.25	98.9	135	NSC	c	1
0535053-052410	S1-ap36	11.74	2.12	0.83	0.60	0.82	26.18	1.19	10.9	0.52	277.3	120	NSC	c	1
0535053-053428	S3-ap39	12.03	1.60	0.58	0.43	0.56	24.84	0.69	18.7	0.75	7.2	356	C	c	1
0535054-042506	F11-ap105	12.50	0.94	0.21	0.00	0.00	28.18	0.42	18.5	0.77	3.6	154	W	c	1
0535056-045853	F21-ap132	11.95	0.94	0.22	0.04	-0.07	31.09	0.58	21.0	0.82	1.9	171	W	c	1
0535056-052519	S1-ap25	8.99	1.56	0.68	0.45	1.13	29.64	3.11	9.6	0.72	19.4	344	C	c	1
0535056-051824	F22-ap70	12.91	1.66	0.43	0.12	–	3.74	0.62	7.7	0.34	72.5	103	NSC	c	2
0535057-051134	S1-ap107	13.02	2.26	0.71	0.43	0.78	22.63	3.10	3.1	0.18	10.0	143	W	l,n	1
0535057-052316	S1-ap38	13.80	1.27	0.53	0.41	–	15.96	4.54	3.2	0.20	394.9	120	NSC	l	1
0535057-053355	S3-ap33	11.97	1.74	0.69	0.00	0.00	–	–	4.0	0.37	28.4	299	C	u	1
0535061-051955	S1-ap62	12.98	1.60	0.56	0.54	–	23.22	1.80	5.4	0.34	100.9	131	NSC	c	1
0535063-061948	F31-ap7	12.96	0.93	0.25	0.03	0.05	27.45	0.41	23.3	0.81	1.7	153	W+	c	1
0535064-052704	S1-ap26	12.93	1.22	0.48	0.43	1.05	26.25	3.08	2.6	0.19	179.2	134	NSC	l,r	1
0535064-053109	S3-ap96	13.55	1.04	0.42	0.28	1.24	15.14	1.67	5.1	0.28	38.3	124	NSC	c	1
0535064-052207	F22-ap151	13.44	1.09	0.38	0.00	0.00	–	–	3.5	0.26	296.4	118	NSC	u	1
0535065-051722	S1-ap84	14.53	2.84	0.95	0.00	0.00	14.01	2.08	3.2	0.17	47.7	131	NSW	l	1
0535067-055101	S3-ap6	12.74	2.00	0.55	0.38	0.74	17.38	1.55	5.0	0.34	3.6	175	NSC	c	1
0535068-051038	F21-ap125	12.60	0.99	0.29	0.10	0.11	22.95	4.48	5.7	0.40	16.7	194	CW	w	1

Table 12.4 (cont'd)

2MASS_id	ID	J	$(J-H)$	$(H-K)$	[3.6 − 4.5]	[5.8 − 8.0]	V_{rad}	ΔV_{rad}	R	S	EW_c	$FW_{10\%}$	$H\alpha$	CCF	NOB
0535069-052600	S2-ap217	13.48	1.23	0.46	0.39	1.31	–	–	1.8	0.18	200.2	142	NSC	w,l	1
0535071-061816	F31-ap3	13.26	0.94	0.29	0.09	0.05	19.80	0.99	13.5	0.66	6.9	162	W-	c	1
0535073-052226	S3-ap119	12.26	1.18	0.44	0.45	–	27.80	0.98	7.2	0.40	114.6	139	NSC	c	1
0535073-054801	F31-ap108	12.45	1.43	0.39	0.10	0.16	27.99	2.68	5.0	0.37	5.5	135	NSW	s,l,n,dv?	2
0535075-051114	F22-ap84	12.35	1.52	0.44	0.08	0.95	23.24	0.56	16.6	0.76	10.9	263	NSC	c	1
0535075-044555	S2-ap94	13.63	0.95	0.48	0.33	0.58	31.09	0.97	5.8	0.28	6.6	275	C	c	1
0535076-053658	F21-ap13	11.70	1.52	0.47	0.18	–	21.76	4.28	4.9	0.39	36.8	175	C	c	1
0535076-060654	F31-ap64	12.71	0.91	0.27	0.06	0.13	25.89	0.81	16.5	0.74	4.8	178	W	c	1
0535078-043452	F11-ap109	13.40	0.95	0.25	0.00	0.00	25.77	1.45	8.3	0.43	2.6	148	W+	c	1
0535078-052917	F22-ap219	13.08	1.15	0.32	0.06	–	29.49	0.61	13.1	0.58	53.5	102	NSC	c	1
0535079-042014	F11-ap101	13.07	0.94	0.21	0.00	0.00	27.20	0.45	19.0	0.67	2.0	137	W+	c	1
0535079-052117	F22-ap34	13.36	1.23	0.43	0.34	0.00	23.95	0.72	9.2	0.55	267.9	101	NSC	c,dv?	2
0535080-053244	S3-ap69	12.04	1.56	0.59	0.46	0.82	29.09	1.53	9.9	0.67	13.3	466	C	c	1
0535082-053704	S3-ap17	11.79	1.37	0.45	0.00	0.00	23.86	1.02	12.3	0.65	12.1	370	C	c	1
0535083-052434	S2-ap219	12.84	1.16	0.41	0.36	0.00	–	–	2.1	0.24	194.6	134	NSC	u,r	1
0535086-060502	F31-ap76	11.54	0.80	0.21	0.02	0.15	26.63	0.30	33.2	0.90	0.4	214	D	c	1
0535086-052619	S3-ap120	13.24	1.48	0.55	0.41	–	23.05	2.86	3.2	0.17	89.5	135	NSC	l,n	1
0535087-050440	F22-ap90	12.37	1.25	0.43	0.35	0.80	24.80	1.24	9.2	0.58	8.7	231	NSC	c	2
0535088-053149	S3-ap202	11.26	1.44	0.56	0.00	0.00	29.44	1.36	8.2	0.65	12.8	551	C	c	1
0535094-045941	F21-ap136	12.91	1.08	0.37	0.15	0.50	25.35	3.58	3.4	0.25	12.4	148	NSW	c	1
0535094-045711	S2-ap81	13.98	1.27	0.50	0.67	1.27	–	–	2.6	0.25	23.2	444	C	u	1
0535095-060846	F31-ap31	13.18	0.88	0.22	0.03	0.09	26.06	0.39	21.6	0.72	1.8	144	W+	c	1
0535100-045108	F11-ap25	12.74	1.21	0.29	0.02	0.53	30.76	0.36	21.3	0.72	0.0	0	W-	c	1
0535101-054834	F21-ap19	13.24	0.92	0.24	0.04	-0.02	25.26	0.45	15.2	0.58	9.0	175	W	c	1
0535101-052232	S3-ap115	12.17	1.29	0.43	0.19	0.00	28.42	2.28	5.8	0.40	111.9	135	NSW	c	1
0535102-051956	F21-ap127	12.96	1.54	0.46	0.46	0.88	23.92	2.06	4.9	0.28	213.2	90	NSC	c	1
0535103-054633	S1-ap1	9.62	1.54	0.62	0.28	1.06	19.41	0.37	25.4	0.85	3.9	492	C	c	1
0535105-053313	F22-ap212	12.70	1.24	0.38	0.09	–	24.51	0.53	12.8	0.52	30.6	101	NSW	c	1
0535105-052618	S1-ap15	9.70	1.44	0.57	0.29	0.33	24.07	0.88	19.2	0.83	16.7	190	C	c	1
0535105-052156	S1-ap44	11.07	1.31	0.50	0.42	–	28.61	0.46	19.8	0.81	74.4	138	NSC	c	1
0535105-052600	S3-ap117	13.06	1.32	0.50	0.08	0.00	–	–	2.3	0.19	130.9	135	NSW	u,r	1
0535106-060144	F31-ap85	13.00	0.92	0.24	0.07	0.11	25.46	0.37	23.6	0.78	4.3	139	W+	c	1
0535107-052628	F22-ap220	12.92	1.15	0.40	0.00	0.00	25.80	1.25	10.4	0.53	205.4	101	NSW	c	1
0535108-044410	S2-ap96	13.36	1.24	0.33	0.34	1.06	27.30	2.63	5.0	0.29	9.1	497	C	c	1
0535109-044712	F11-ap81	13.30	0.96	0.25	0.05	-0.10	22.02	0.68	14.8	0.66	1.8	116	N	c	1
0535109-061325	F31-ap15	12.25	0.92	0.25	0.08	0.14	30.94	5.04	8.2	0.74	6.8	405	C	w	1
0535109-052246	S2-ap220	11.27	1.33	0.60	0.20	0.00	–	–	1.9	0.29	299.8	146	CD	u	1
0535111-051935	F22-ap87	12.81	1.21	0.34	0.00	0.00	32.41	7.78	2.6	0.20	122.2	99	NSW	w,l	1
0535111-062014	F31-ap10	13.20	0.92	0.26	0.06	0.08	23.23	0.42	17.7	0.68	0.0	0	W+	c	1
0535111-060021	F31-ap99	12.90	0.91	0.26	0.10	0.20	26.56	1.02	13.4	0.66	5.0	152	W-	c	1
0535112-051720	S1-ap86	12.39	2.14	0.74	0.00	0.00	22.47	2.15	7.2	0.41	32.8	139	NSW	c	1
0535114-054418	S3-ap4	13.86	1.12	0.32	0.25	0.99	19.16	1.71	4.9	0.30	7.3	276	C	c	1
0535115-044633	F11-ap92	12.29	0.89	0.22	0.11	0.05	21.78	1.64	11.0	0.63	4.3	203	W	c	1

Table 12.4 (cont'd)

2MASS_id	ID	J	$(J-H)$	$(H-K)$	$[3.6-4.5]$	$[5.8-8.0]$	V_{rad}	ΔV_{rad}	R	S	EW_c	$FW_{10\%}$	$H\alpha$	CCF	NOB
0535116-053101	F21-ap20	12.95	1.09	0.34	0.35	1.19	24.32	0.79	7.6	0.47	63.0	106	NSC	c	2
0535116-051912	S1-ap66	12.46	0.59	0.80	0.44	0.00	–	–	2.9	0.20	105.0	127	NSW	u	1
0535118-063245	F31-ap231	12.11	0.95	0.30	0.07	-0.04	29.25	3.20	4.9	0.43	0.0	0	AE	d?	1
0535118-044930	S1-ap124	13.48	1.37	0.55	0.49	0.83	21.69	3.84	5.2	0.32	14.8	377	C	c	1
0535119-054537	F22-ap203	11.60	1.06	0.25	0.02	-0.10	25.65	0.50	25.2	0.86	3.8	211	W	c	2
0535121-053020	S2-ap218	13.18	1.26	0.46	0.39	0.76	23.17	1.21	5.7	0.30	42.9	232	C	c	1
0535121-053138	F22-ap201	12.16	1.03	0.31	0.06	0.41	60.36	0.97	8.8	0.50	19.5	110	NSC	d	1
0535122-042711	F11-ap112	12.10	0.94	0.24	0.00	0.00	27.95	0.42	20.0	0.72	3.6	152	W+	c	1
0535122-052045	S3-ap111	12.14	1.86	0.68	0.67	0.00	–	–	4.2	0.29	137.5	131	NSW	u	1
0535123-052347	S3-ap113	10.72	1.15	0.32	0.00	0.00	27.92	0.30	30.0	0.87	36.9	143	CD	c	1
0535125-052344	S2-ap216	9.84	1.19	0.44	0.51	–	24.91	1.70	16.3	0.83	26.4	157	NSC	w	1
0535125-044821	S2-ap98	14.87	1.23	0.43	0.33	0.89	13.71	2.30	4.5	0.21	2.9	177	NSW	l	1
0535127-051613	F21-ap138	12.62	1.23	0.36	0.09	0.58	22.64	0.60	14.8	0.69	20.2	103	NSW	c	1
0535127-052710	F21-ap18	12.78	1.34	0.46	0.17	0.00	23.63	1.00	7.2	0.38	167.6	102	NSC	s	1
0535128-053907	F22-ap205	12.90	1.29	0.34	-0.03	0.49	23.01	0.43	19.6	0.73	10.2	153	W	c	1
0535128-051524	F22-ap85	11.68	1.33	0.35	0.00	0.01	28.71	0.49	22.4	0.81	11.4	105	NS	c	1
0535129-052849	F22-ap207	13.46	1.44	0.38	0.01	0.00	17.12	3.85	4.7	0.28	84.1	99	NSW	c	1
0535129-054537	S3-ap2	13.33	1.21	0.40	0.42	0.80	23.72	1.98	5.4	0.31	24.4	365	C	c	1
0535130-044305	F11-ap108	13.24	0.93	0.24	0.11	-0.15	30.79	0.61	13.1	0.60	2.0	133	W+	c	1
0535130-053934	S1-ap14	9.57	1.41	0.54	0.59	0.72	25.05	1.09	19.4	0.85	13.4	347	C	c	1
0535130-053403	S3-ap220	13.00	1.55	0.59	0.42	0.67	15.95	2.68	4.7	0.31	15.9	138	NSC	c	1
0535131-053618	S3-ap3	13.71	1.64	0.62	0.30	0.34	14.23	1.70	4.4	0.28	16.6	145	NSC	c	1
0535132-044154	S2-ap100	12.96	1.16	0.32	0.44	0.86	29.97	0.55	14.5	0.60	3.5	203	W	c	1
0535134-051710	F22-ap94	11.52	1.62	0.47	0.04	1.07	21.40	1.88	11.5	0.65	25.4	101	NSC	c	2
0535135-051731	F21-ap133	13.05	1.86	0.50	0.27	–	26.40	2.00	4.8	0.31	54.9	99	NSC	s	1
0535137-051925	F22-ap96	13.14	1.04	0.31	0.01	0.00	19.26	1.48	6.0	0.32	120.3	99	NSW	c	1
0535138-052736	F22-ap208	12.79	1.33	0.40	0.29	0.00	26.57	1.14	8.8	0.50	99.3	114	NSC	c	1
0535140-052549	F22-ap204	12.48	1.36	0.49	-0.09	0.00	21.86	3.35	3.8	0.24	314.8	99	NSW	c	1
0535140-055209	F31-ap109	11.85	1.11	0.37	0.17	0.52	25.51	0.39	23.6	0.86	9.6	360	C	c	1
0535140-051951	S1-ap57	11.44	1.29	0.49	0.00	0.00	23.83	0.34	26.2	0.84	41.6	180	NSC	c	1
0535142-052424	S3-ap122	10.46	1.37	0.40	0.45	–	24.87	6.26	4.6	0.54	90.3	150	C	w	1
0535142-054317	S3-ap231	10.37	1.38	0.52	0.34	0.55	25.62	1.31	10.3	0.70	13.7	616	C	c	1
0535143-045522	S1-ap126	12.86	1.36	0.60	0.20	–	25.68	0.69	15.7	0.65	4.9	294	C	c	1
0535143-052333	S1-ap17	10.42	1.15	0.51	0.46	0.00	–	–	3.3	0.39	124.9	160	C	u,r	1
0535144-052502	F21-ap14	12.04	1.11	0.39	0.60	0.00	25.29	2.76	4.1	0.35	685.8	95	NSC	c	1
0535146-050852	F11-ap235	12.84	0.88	0.27	0.12	–	23.66	1.33	9.1	0.51	7.0	158	W	c	2
0535146-051646	S1-ap93	13.07	1.43	0.47	0.37	–	23.27	1.86	4.9	0.30	25.2	173	NSC	c	1
0535147-061339	F31-ap16	12.67	1.19	0.36	0.07	0.21	25.17	0.90	10.5	0.46	7.8	164	NS	c	1
0535147-050227	S2-ap99	12.98	1.43	0.30	0.27	0.40	16.71	2.08	4.3	0.25	4.8	263	NSC	c	1
0535148-050747	S2-ap174	13.96	1.32	0.50	0.37	0.85	21.88	1.53	4.9	0.23	13.3	323	C	c	1
0535148-053805	S3-ap9	13.02	1.51	0.51	0.25	0.56	23.34	0.63	18.8	0.74	5.8	145	NSS	c	1
0535149-053639	F21-ap16	12.62	1.11	0.27	0.16	0.66	26.15	0.65	14.0	0.66	23.1	121	NSC	c	1
0535152-053956	F31-ap101	12.22	1.03	0.31	0.06	0.08	23.46	0.46	17.4	0.68	6.8	114	W+	c	1

Table 12.4 (cont'd)

2MASS_id	ID	J	$(J-H)$	$(H-K)$	[3.6 − 4.5]	[5.8 − 8.0]	V_{rad}	ΔV_{rad}	R	S	EW_c	$FW_{10\%}$	$H\alpha$	CCF	NOB
0535152-050033	F22-ap83	13.38	0.93	0.27	0.09	-0.11	29.49	1.14	9.4	0.50	4.5	131	W-	c	2
0535153-043326	F11-ap114	11.75	0.89	0.21	0.00	0.00	28.26	0.28	29.7	0.86	21.9	246	C	c	1
0535153-051902	F21-ap148	12.70	0.91	0.30	-0.15	0.00	28.76	1.43	6.1	0.51	77.3	167	NSC	l,n,dv?	2
0535154-053511	F22-ap209	12.71	1.30	0.39	0.03	–	27.04	0.58	14.2	0.65	17.7	104	NSW	c	1
0535154-051738	S1-ap98	13.21	2.45	1.11	0.36	0.68	17.32	5.71	4.0	0.30	28.7	143	NSC	s,w,l	1
0535155-050951	S1-ap122	13.48	1.94	0.64	0.49	0.71	18.67	1.79	3.9	0.24	8.3	169	NSC	c	1
0535156-045713	F21-ap139	13.31	1.16	0.35	0.11	0.78	30.72	0.49	13.1	0.54	3.7	133	W	c	1
0535156-052403	F21-ap231	11.64	1.77	0.32	0.00	0.00	39.68	0.48	17.1	0.75	187.0	100	C	d	1
0535157-052139	F21-ap219	12.82	1.44	0.44	0.00	0.00	28.44	1.16	6.0	0.37	451.4	97	NSC	c	1
0535157-045054	S1-ap128	13.56	1.16	0.34	0.38	0.98	30.89	2.06	4.4	0.23	6.4	218	NSC	c	1
0535158-062445	F31-ap233	13.42	0.88	0.29	0.08	0.21	19.33	7.19	6.5	0.40	4.6	293	W	w	1
0535158-052040	F22-ap33	12.57	1.18	0.46	0.00	0.00	–	–	2.5	0.28	310.8	91	NSW	u	1
0535159-051459	F21-ap142	11.63	1.31	0.46	0.21	–	29.13	0.47	21.7	0.86	4.7	318	C	c	1
0535159-054111	S1-ap3	13.01	1.44	0.61	0.33	0.80	21.85	1.01	6.2	0.30	19.0	436	C	c	1
0535160-042930	F11-ap116	13.29	1.00	0.38	0.00	0.00	26.99	1.80	6.6	0.34	22.3	399	C	c	1
0535160-055044	F31-ap105	13.34	1.34	0.46	0.11	0.16	20.99	6.14	3.6	0.25	6.6	131	NS	w,l	1
0535163-061843	F31-ap2	12.89	0.93	0.31	0.08	0.11	23.87	1.00	11.2	0.52	13.4	169	W	c	1
0535163-051537	S1-ap103	11.95	1.64	0.53	0.30	1.10	26.39	0.48	20.7	0.80	6.8	309	NSC	c	1
0535163-053202	S3-ap146	12.98	1.09	0.38	0.47	0.76	24.74	1.06	6.7	0.37	21.9	267	C	c	1
0535164-045802	F22-ap81	13.22	0.88	0.23	0.11	–	24.76	1.16	10.8	0.57	5.5	144	NSW	c	1
0535167-052403	S2-ap214	9.90	0.97	0.32	0.73	0.00	24.43	7.76	6.4	0.59	61.8	138	CD	w	1
0535168-053916	F31-ap112	13.32	1.02	0.37	0.12	0.86	40.35	1.00	6.0	0.27	15.1	103	NSW	c	1
0535169-052546	F21-ap8	12.28	1.14	0.39	0.00	0.00	21.42	6.38	3.2	0.29	372.2	95	NSW	d?,w,l	1
0535169-054555	S3-ap233	12.32	1.01	0.32	0.38	0.92	22.90	0.72	11.5	0.53	7.5	216	W	c	1
0535171-051239	F21-ap131	13.48	0.88	0.29	0.03	0.00	30.93	4.29	4.1	0.24	16.8	147	NSC	w	1
0535171-052645	F22-ap191	13.48	0.91	0.28	0.00	0.00	26.57	2.04	5.1	0.27	132.7	99	NSW	c	1
0535172-052027	S1-ap135	11.63	1.30	0.53	0.24	0.00	24.24	0.83	11.0	0.57	87.0	143	NSC	c	1
0535172-052316	S3-ap126	7.15	1.40	0.14	0.62	0.00	–	–	2.2	0.21	0.0	0	W+	u	1
0535173-052014	F21-ap168	12.56	1.60	0.45	0.00	0.00	26.70	0.41	20.6	0.74	93.2	95	NSW	c	1
0535173-054214	S1-ap5	12.42	1.48	0.60	0.89	1.14	25.00	1.19	5.0	0.23	27.7	377	C	l,r	1
0535174-053025	F21-ap3	12.97	0.94	0.22	0.00	–	25.76	0.51	18.2	0.75	28.4	97	NSC	c	1
0535175-054048	S3-ap237	12.41	1.10	0.30	0.24	1.12	24.22	0.44	15.3	0.62	7.3	209	W	c	1
0535178-044452	S2-ap97	11.61	1.45	0.57	0.32	1.05	30.39	0.32	32.2	0.87	6.8	354	C	c	1
0535178-053040	S3-ap133	13.80	1.81	0.72	0.46	0.93	15.21	1.73	3.9	0.23	33.3	124	NSC	l	1
0535179-053031	F22-ap202	13.19	0.98	0.33	0.08	–	23.18	1.13	7.1	0.39	48.6	99	NSC	c	1
0535179-051532	S1-ap114	11.60	2.09	0.70	0.45	0.72	28.71	1.48	14.4	0.69	8.8	150	NSC	c	1
0535179-052650	S3-ap125	13.31	1.58	0.65	0.37	0.00	–	–	2.7	0.29	16.8	135	NSC	w,l	1
0535180-043119	F11-ap118	12.68	0.89	0.25	0.00	0.00	27.11	4.26	8.4	0.45	7.1	318	C	w	1
0535180-051546	F22-ap93	13.34	1.24	0.34	0.14	0.00	29.50	2.34	5.7	0.29	24.0	105	NSW	w,dv	2
0535182-052846	F21-ap9	12.36	1.27	0.39	0.29	1.49	26.92	0.70	13.8	0.65	60.2	112	NSC	c	1
0535182-051306	S2-ap193	11.48	1.84	0.66	0.42	–	30.20	0.70	14.3	0.68	12.6	409	C	c	1
0535183-045030	F11-ap211	13.14	1.04	0.31	0.06	0.17	30.70	0.51	17.2	0.68	2.1	114	NS	c	1
0535185-051820	F21-ap147	12.81	1.02	0.24	0.13	0.00	30.82	0.31	24.4	0.74	23.0	109	NSW	c	1

Table 12.4 (cont'd)

2MASS_id	ID	J	$(J-H)$	$(H-K)$	[3.6 − 4.5]	[5.8 − 8.0]	V_{rad}	ΔV_{rad}	R	S	EW_c	$FW_{10\%}$	$H\alpha$	CCF	NOB
0535188-044410	F11-ap120	13.02	1.10	0.36	0.18	0.75	28.17	0.93	8.9	0.40	6.3	241	CW	c	1
0535188-051729	S1-ap104	11.22	3.32	1.49	0.49	0.74	15.71	2.18	3.7	0.20	28.5	131	NSC	l	1
0535188-051445	S1-ap113	12.21	1.33	0.42	0.30	1.30	27.37	0.47	18.2	0.72	8.9	305	C	c	1
0535189-053736	F21-ap1	11.66	0.89	0.23	0.04	0.04	28.52	1.66	21.6	0.86	7.5	180	W	w	1
0535190-063148	F31-ap237	12.33	1.28	0.28	0.01	0.10	23.41	0.38	19.6	0.72	0.0	0	AE	c	1
0535191-052326	S1-ap18	10.93	0.59	0.58	0.00	0.00	–	–	2.5	0.33	164.9	149	C	u,r	1
0535192-051644	S1-ap134	12.95	1.48	0.57	0.45	–	28.92	2.21	3.4	0.26	54.3	358	C	c	1
0535192-054700	S1-ap7	13.61	0.85	0.43	0.21	0.40	17.38	3.43	3.7	0.24	11.5	212	CD	c	1
0535195-052104	F21-ap183	13.43	1.55	0.48	0.13	0.00	28.11	1.89	3.3	0.17	334.6	92	NSW	l,n	1
0535197-051405	F11-ap238	13.47	1.21	0.34	0.40	–	12.85	6.12	2.8	0.17	21.0	108	NSW	l,n	1
0535198-053032	S2-ap212	12.97	1.07	0.39	0.37	–	13.62	2.86	2.7	0.20	41.9	206	NSC	l,r	1
0535201-044134	F11-ap119	12.92	1.25	0.43	–	–	29.19	0.73	11.8	0.52	11.2	339	C	c	1
0535201-053457	S3-ap207	13.81	1.04	0.37	0.34	0.88	22.30	2.05	5.4	0.31	9.5	142	NSW	c	1
0535202-054639	F21-ap12	12.47	0.90	0.24	0.08	0.09	30.09	0.29	21.1	0.73	7.5	188	W	c	2
0535202-053039	S1-ap9	11.62	1.46	0.55	0.00	0.00	26.03	0.59	17.3	0.77	22.5	183	C	c	1
0535202-053216	S3-ap168	13.26	1.16	0.49	0.39	0.82	15.10	1.62	3.8	0.23	16.1	169	NSC	c	1
0535202-044134	S2-ap95	12.92	1.25	0.43	–	–	24.26	2.33	5.3	0.27	2.5	226	NSW	c	1
0535203-050226	F11-ap234	12.26	1.06	0.26	0.03	0.30	28.06	0.69	14.5	0.65	4.4	212	W	c	1
0535207-052615	S3-ap134	13.71	1.37	0.45	0.48	–	–	–	2.3	0.19	92.4	131	NSC	u,r	1
0535207-053753	S3-ap211	13.76	1.07	0.43	0.36	0.83	13.68	1.23	6.1	0.34	7.6	138	NSW	c	1
0535208-052130	F21-ap207	12.44	1.46	0.37	0.06	0.00	26.89	0.99	6.8	0.38	323.0	93	NSW	c	1
0535208-052129	S3-ap127	12.44	1.46	0.37	0.06	0.00	–	–	2.3	0.27	34.1	169	SAT	u	1
0535209-051637	F22-ap106	12.08	1.44	0.38	0.10	–	27.76	0.49	23.8	0.78	13.2	109	NSW	c	1
0535210-044538	F11-ap111	13.11	0.92	0.28	0.07	0.10	31.03	0.81	11.5	0.55	3.7	133	W	c	1
0535210-052809	F22-ap193	12.15	1.53	0.46	0.33	–	28.54	0.42	24.7	0.83	39.7	97	NSC	c	1
0535211-051821	F22-ap101	12.90	1.44	0.46	0.16	0.00	27.53	0.72	11.1	0.46	41.7	96	NSW	c	1
0535211-051820	S1-ap172	12.90	1.44	0.46	0.16	0.00	26.57	1.10	8.0	0.40	23.2	135	NSW	c	1
0535212-050916	S3-ap124	8.31	1.21	0.58	0.25	0.38	32.66	2.09	14.1	0.71	2.1	558	CW	w	1
0535212-054212	S3-ap236	12.12	1.31	0.49	0.40	1.06	20.87	0.59	13.5	0.54	11.6	272	C	c	1
0535213-045150	S1-ap129	13.82	1.39	0.45	0.34	1.17	15.89	3.39	3.7	0.21	5.5	199	NSW	c	1
0535213-052345	S1-ap16	11.33	1.19	0.58	0.00	0.00	28.95	1.04	10.0	0.69	105.8	142	NSC	c	1
0535213-050942	S2-ap173	13.64	1.25	0.48	0.46	–	16.36	2.20	3.3	0.18	8.9	289	C	c	1
0535214-050903	F22-ap99	12.28	1.70	0.50	0.08	0.40	22.18	7.84	3.7	0.27	10.8	152	NSW	s?,l	1
0535215-050949	S1-ap130	13.15	1.48	0.60	0.42	0.95	29.17	1.00	9.5	0.53	10.8	324	C	c	1
0535216-052526	F21-ap239	11.78	1.27	0.38	-0.14	0.00	27.61	0.62	15.7	0.69	180.1	97	NSW	c	1
0535216-052657	F22-ap199	12.84	1.06	0.31	0.18	0.00	28.46	9.78	3.2	0.24	175.3	97	NSW	d?,l	1
0535216-053458	S1-ap10	12.25	1.20	0.37	0.34	0.89	24.17	0.47	16.9	0.74	9.0	380	C	c	2
0535217-053446	S3-ap204	11.18	1.40	0.54	0.00	0.00	23.50	0.59	15.5	0.71	27.6	446	C	c	1
0535218-045407	F11-ap227	11.82	1.15	0.36	0.45	0.77	28.46	0.26	33.3	0.86	4.9	446	C	c	1
0535218-052208	F21-ap205	12.64	1.39	0.40	0.00	0.00	26.62	3.74	3.4	0.28	252.6	91	NSW	c	1
0535218-050701	S2-ap157	11.05	1.72	0.67	0.42	0.78	28.61	0.98	13.8	0.78	12.9	516	C	c	1
0535218-052353	S3-ap123	10.36	0.98	0.33	0.40	–	27.51	2.61	12.9	0.75	30.2	139	NSC	w	1
0535219-051501	F21-ap149	12.74	1.69	0.49	0.25	1.34	28.55	1.09	5.3	0.28	29.3	111	NSC	w,l	2

Table 12.4 (cont'd)

2MASS_id	ID	J	$(J-H)$	$(H-K)$	[3.6 − 4.5]	[5.8 − 8.0]	V_{rad}	ΔV_{rad}	R	S	EW_c	$FW_{10\%}$	$H\alpha$	CCF	NOB
0535219-052827	F21-ap2	13.05	1.03	0.33	0.19	0.00	22.77	1.73	6.5	0.38	117.6	102	NSW	c	1
0535219-051704	F22-ap103	12.29	0.92	0.35	0.07	0.00	28.11	0.92	9.1	0.46	31.6	101	NSW	c	1
0535219-051703	S3-ap129	12.29	0.92	0.35	0.07	0.00	27.87	1.49	6.1	0.32	8.2	237	C	c	1
0535220-055236	S3-ap235	13.60	1.21	0.45	0.46	0.70	12.41	1.74	4.1	0.26	5.9	362	C	c	1
0535222-051808	F21-ap160	13.28	1.27	0.49	0.00	0.00	22.74	0.94	5.4	0.30	51.9	109	NSW	c	2
0535222-053117	S2-ap203	13.16	1.16	0.42	0.42	0.64	25.52	1.41	5.5	0.31	71.5	123	NSC	c	1
0535223-050804	S2-ap165	11.11	2.50	0.99	0.62	1.17	28.52	1.49	11.2	0.57	5.8	421	C	c	1
0535224-052544	S1-ap6	12.78	1.56	0.69	0.46	0.00	–	–	2.6	0.35	215.2	130	NSC	u	1
0535226-051411	S3-ap128	11.65	1.37	0.44	0.34	0.38	40.34	1.36	6.8	0.44	8.7	301	C	c	1
0535227-042851	F11-ap117	12.14	1.20	0.39	0.00	0.00	29.50	0.91	9.1	0.60	59.9	454	C	c	1
0535227-044829	F11-ap137	11.86	1.12	0.31	0.21	0.27	28.12	0.29	27.1	0.81	11.5	299	C	c	1
0535227-044326	S2-ap93	13.22	1.11	0.32	0.30	1.42	31.00	0.53	12.9	0.54	2.5	218	NSW	c	1
0535227-053136	S3-ap162	12.21	1.46	0.52	0.28	0.84	23.66	0.85	11.8	0.61	31.1	120	NSC	c	1
0535228-043740	F11-ap113	13.04	1.34	0.44	0.00	0.00	28.04	0.58	13.6	0.57	41.3	360	C	c	1
0535228-054442	F31-ap116	11.81	1.17	0.31	0.02	0.04	35.56	7.79	5.2	0.56	3.6	544	C	w,dv	2
0535228-044641	S2-ap91	12.99	1.19	0.36	0.22	0.65	31.16	0.38	18.5	0.71	2.0	211	W-	c	2
0535232-052833	S3-ap131	13.78	1.00	0.42	0.32	–	19.63	2.36	3.3	0.18	57.4	116	NSC	l,n,r	1
0535232-052135	F22-ap149	13.17	1.42	0.45	-0.04	0.00	–	–	3.1	0.20	246.9	86	NSW	u	1
0535235-051857	F22-ap126	11.99	1.20	0.33	0.31	–	14.70	0.34	27.5	0.84	11.4	113	NSC	c	1
0535237-051839	S1-ap178	12.60	1.56	0.56	0.44	–	21.70	0.90	10.2	0.53	19.3	154	NSC	c	1
0535239-051907	F21-ap167	13.08	1.27	0.33	-0.03	0.00	28.55	0.51	10.4	0.51	56.1	220	NSC	c	2
0535240-052509	S3-ap138	12.95	1.15	0.87	1.01	0.00	–	–	2.0	0.19	132.8	135	NSC	u,r	1
0535241-045008	S1-ap127	12.57	0.86	0.39	0.52	2.03	32.07	0.58	12.0	0.51	3.7	173	NSW	c	1
0535241-052132	S1-ap230	12.44	1.56	0.55	0.15	0.00	24.12	1.78	4.6	0.34	128.5	130	NSW	c	1
0535242-052518	S1-ap231	11.44	1.41	0.43	0.00	0.00	–	–	2.0	0.17	8.6	235	CD	u	1
0535243-052600	F22-ap187	13.13	1.10	0.41	0.27	0.00	14.03	3.44	2.9	0.17	233.6	97	NSW	n	1
0535244-062840	F31-ap238	13.23	0.95	0.23	0.07	0.04	26.91	0.59	12.5	0.57	3.2	132	W+	c	1
0535245-051659	S2-ap191	11.80	1.55	0.51	0.00	0.00	28.09	0.43	18.5	0.72	16.2	240	NSC	c	1
0535246-051129	S1-ap140	12.29	1.91	0.65	0.59	1.06	31.02	0.92	11.7	0.55	9.9	301	C	c	1
0535246-051158	S2-ap183	11.55	1.14	0.57	0.22	–	27.78	0.69	11.7	0.57	18.9	447	C	c	1
0535246-051909	S2-ap204	12.06	1.76	0.62	0.34	–	29.47	1.62	7.2	0.45	21.2	356	C	c	1
0535248-052510	F21-ap225	12.93	1.31	0.39	0.42	–	–	–	3.1	0.21	274.8	102	NSC	u	1
0535249-052510	S2-ap209	12.93	1.31	0.39	0.42	–	–	–	2.2	0.26	162.2	134	NSC	u	1
0535250-050909	S1-ap136	14.54	1.08	0.45	0.50	0.00	18.26	4.21	2.3	0.19	11.3	203	CD	l,n	1
0535251-052347	S2-ap210	10.86	1.00	0.32	0.00	0.00	27.18	5.92	8.8	0.74	52.6	138	CD	w	1
0535252-050927	F11-ap232	11.75	0.98	0.26	0.04	–	28.29	0.38	17.6	0.71	5.5	185	W	c	2
0535252-053321	F21-ap6	12.89	1.01	0.34	0.11	-0.26	18.17	3.96	4.6	0.32	55.1	112	NSC	s,w,l	1
0535252-051535	S1-ap144	11.79	1.78	0.69	0.69	1.18	25.85	3.76	2.9	0.29	39.4	388	C	l,r	1
0535252-052951	S3-ap149	13.09	0.99	0.28	0.34	1.04	25.57	1.71	6.5	0.34	40.8	120	NSC	c	1
0535253-052529	S3-ap135	13.19	1.32	0.55	0.43	0.00	–	–	3.0	0.20	100.3	131	NSC	u,r	1
0535254-052135	F21-ap193	11.82	1.71	0.49	0.11	0.00	29.43	0.64	13.7	0.63	111.3	95	NSW	c	1
0535254-053403	S3-ap197	12.42	1.11	0.49	0.44	0.00	25.77	0.56	13.8	0.62	8.8	146	NSC	c	1
0535254-055108	S3-ap239	8.87	0.51	0.32	0.71	1.10	34.06	9.99	4.2	0.56	0.0	0	X	d?,s?,w	1

Table 12.4 (cont'd)

2MASS_id	ID	J	$(J-H)$	$(H-K)$	[3.6 − 4.5]	[5.8 − 8.0]	V_{rad}	ΔV_{rad}	R	S	EW_c	$FW_{10\%}$	$H\alpha$	CCF	NOB
0535255-045120	S2-ap104	12.29	1.60	0.59	0.49	1.17	31.20	1.06	6.0	0.29	48.5	373	C	l,n,r	1
0535256-044931	F11-ap174	12.93	0.98	0.29	0.46	0.93	30.45	0.41	11.2	0.47	45.7	301	C	c,dv	2
0535256-045718	F11-ap230	13.27	0.90	0.23	0.11	–	25.37	1.02	11.3	0.57	6.6	168	W	c	1
0535256-050757	F21-ap144	11.70	1.44	0.48	0.87	1.08	29.56	0.53	14.4	0.69	12.1	197	W	c	2
0535256-053038	F22-ap195	12.39	1.36	0.50	0.40	0.77	26.78	0.76	9.9	0.54	28.1	163	NSC	c	2
0535256-053020	S1-ap4	11.02	1.31	0.54	0.00	0.00	24.83	0.39	24.7	0.85	11.5	224	NSC	c	1
0535257-052935	S2-ap207	13.73	1.10	0.43	0.41	0.73	–	–	2.2	0.15	113.1	120	NSC	u	1
0535261-052520	F22-ap184	13.28	1.24	0.31	0.38	0.00	25.02	2.96	4.5	0.35	159.4	101	NSC	c	1
0535261-054508	F31-ap120	12.44	1.20	0.37	0.34	0.87	22.48	0.70	17.3	0.83	7.0	499	C	c	2
0535261-061338	F31-ap236	12.91	1.25	0.48	0.14	0.03	17.82	1.30	6.7	0.31	0.0	0	AE	c	1
0535262-052006	S1-ap216	12.05	2.14	0.71	0.00	0.00	28.01	0.75	13.8	0.67	25.6	146	NSW	c	1
0535262-054508	S1-ap8	12.44	1.20	0.37	0.34	0.87	20.84	0.55	19.0	0.76	3.4	239	C	c	1
0535263-052743	F22-ap185	12.32	0.95	0.26	0.00	0.00	24.97	0.43	15.1	0.64	80.5	103	NSW	c	1
0535263-052540	S1-ap233	9.59	0.94	0.37	0.36	0.93	28.62	4.75	12.6	0.81	0.0	0	X	w	1
0535263-044926	S2-ap102	13.22	0.94	0.27	0.36	0.92	28.78	0.64	10.3	0.46	5.8	214	W	c	1
0535263-054434	S3-ap223	13.78	1.00	0.33	0.38	0.45	21.23	1.51	7.8	0.37	9.7	280	CW	c	1
0535264-055526	F31-ap119	13.32	1.04	0.31	0.19	0.46	25.61	0.64	16.5	0.66	2.7	120	W-	c	1
0535265-045606	F22-ap100	11.86	0.93	0.23	0.03	0.68	27.32	2.23	13.2	0.78	6.5	378	C	w,dv?	2
0535267-051645	S1-ap145	13.01	1.23	0.40	0.10	0.00	31.07	1.48	7.4	0.40	19.1	162	NSC	c	1
0535268-051107	S2-ap186	9.00	1.99	0.87	0.57	0.70	30.66	2.34	13.8	0.78	5.1	454	CW	w	1
0535269-052400	F22-ap163	12.98	1.27	0.42	0.00	0.00	23.59	2.46	3.3	0.21	308.3	90	NSW	l,n	1
0535269-052448	F21-ap226	13.37	1.12	0.35	0.00	0.00	–	–	2.5	0.21	376.6	95	NSW	l,n	1
0535269-051017	S1-ap139	13.63	4.83	2.13	1.01	1.13	13.61	1.72	3.8	0.21	6.4	150	NSC	c	1
0535270-051544	S1-ap146	12.75	1.59	0.60	0.40	–	28.15	1.23	6.8	0.35	27.6	154	NSC	c	1
0535274-052725	F21-ap240	12.02	1.18	0.29	0.24	1.17	25.74	0.40	16.6	0.73	62.4	98	NSC	c,dv	2
0535274-051709	S1-ap158	11.31	1.86	0.72	0.51	–	28.03	0.43	20.3	0.77	13.6	180	NSC	c	1
0535279-045038	F11-ap196	13.26	0.98	0.28	0.09	0.14	28.94	0.68	12.1	0.52	2.8	120	NS	c	1
0535279-045133	F11-ap206	13.34	1.07	0.36	0.08	-0.13	30.34	3.17	6.5	0.34	5.2	146	W	c	1
0535279-051657	F22-ap119	11.60	1.01	0.25	0.05	–	27.99	0.82	15.2	0.67	1.8	222	NSC	c	1
0535279-060939	F31-ap201	12.12	0.96	0.22	0.03	0.15	21.06	0.92	15.3	0.70	5.8	268	W	c	1
0535280-051720	F21-ap166	12.42	1.09	0.31	0.33	1.40	27.60	0.39	12.8	0.60	40.7	299	C	c	2
0535281-050049	F22-ap97	12.50	0.95	0.22	0.02	0.51	29.31	4.47	7.7	0.51	8.3	280	CD	w	1
0535281-051137	S1-ap133	12.89	1.57	0.51	0.36	0.78	16.89	3.08	3.5	0.23	11.4	177	NSC	c	1
0535281-051014	S2-ap175	10.98	1.57	0.56	0.48	0.57	29.10	2.44	7.7	0.60	17.4	485	C	c	1
0535281-052134	S1-ap211	14.85	3.00	1.02	0.42	0.00	–	–	2.9	0.24	60.8	134	NSW	u,r	1
0535283-055913	F31-ap113	12.32	1.22	0.42	0.41	1.06	22.91	0.34	22.3	0.71	15.8	252	CW	c	1
0535284-051902	F22-ap125	13.32	1.02	0.38	0.00	0.00	28.72	1.04	5.9	0.28	46.8	192	NSC	c	1
0535284-045155	S1-ap123	13.65	1.09	0.41	0.28	0.75	24.14	2.07	5.0	0.26	13.5	286	C	c	1
0535286-044726	F11-ap131	12.53	1.33	0.48	0.30	0.90	29.71	0.73	9.3	0.46	32.6	301	C	c	1
0535289-051618	S2-ap200	11.16	1.77	0.74	0.47	0.96	29.89	0.46	21.6	0.80	15.6	319	NSC	c	1
0535291-052910	S3-ap154	11.60	1.27	0.38	0.29	1.16	25.69	0.50	19.0	0.79	36.1	128	NSC	c	1
0535292-061629	F31-ap234	12.09	1.23	0.42	0.07	0.32	21.67	0.91	12.5	0.59	6.7	164	W	c	1
0535293-054538	F31-ap117	12.94	0.91	0.23	0.07	–	26.03	1.74	12.3	0.69	6.6	150	NS	c	1

Table 12.4 (cont'd)

2MASS_id	ID	J	$(J-H)$	$(H-K)$	[3.6 – 4.5]	[5.8 – 8.0]	V_{rad}	ΔV_{rad}	R	S	EW_c	$FW_{10\%}$	$H\alpha$	CCF	NOB
0535294-043820	F11-ap126	12.58	0.89	0.32	0.00	0.00	25.14	6.73	5.4	0.39	7.9	252	WC	w	1
0535294-051633	F11-ap221	11.53	1.18	0.32	0.03	0.00	28.74	0.28	31.3	0.85	-1.7	202	NSW	c	1
0535295-052456	F22-ap180	11.83	1.07	0.30	-0.01	0.00	27.12	0.34	27.7	0.84	75.6	92	NS	c	1
0535298-051606	F21-ap157	12.02	1.09	0.28	-0.02	–	27.69	0.34	24.4	0.78	-0.4	97	NSC	c	1
0535298-051210	F21-ap152	12.66	0.92	0.32	0.19	0.00	65.38	0.61	8.4	0.45	9.2	188	W	d	2
0535299-044952	F11-ap173	11.75	0.97	0.23	0.01	0.12	29.37	0.60	21.0	0.81	1.3	141	W-	c	1
0535299-051227	S2-ap188	12.08	1.30	0.52	0.44	0.50	28.94	0.84	7.9	0.42	26.8	353	C	c	1
0535300-043427	F11-ap122	13.12	0.86	0.21	0.00	0.00	25.89	6.81	5.4	0.39	6.8	271	CW	w	1
0535301-060302	F31-ap124	11.65	0.82	0.21	0.00	0.15	25.93	0.33	33.0	0.89	1.6	158	W	c	1
0535304-054903	F31-ap115	12.84	1.13	0.30	0.28	0.72	27.77	0.39	20.6	0.79	8.6	535	C	c	2
0535304-052538	S1-ap237	11.78	1.35	0.51	0.90	–	26.96	1.37	8.2	0.59	42.1	321	C	c	1
0535304-052811	S2-ap208	13.73	1.35	0.48	0.42	–	24.96	2.72	3.9	0.23	215.5	112	NSC	c	1
0535305-045128	F11-ap199	11.93	0.96	0.23	-0.01	0.07	29.36	0.38	30.2	0.88	2.8	257	NSW	c	1
0535306-043900	F11-ap130	12.90	1.13	0.28	0.00	0.00	31.11	0.59	15.3	0.61	3.0	214	W-	c	1
0535306-052716	F22-ap190	12.25	1.04	0.27	0.08	–	20.11	0.42	18.6	0.70	53.2	92	NSC	c	1
0535306-051516	S2-ap196	13.73	0.89	0.26	0.49	0.00	27.66	1.38	5.7	0.30	27.0	108	NSW	c	1
0535307-052431	F21-ap213	12.91	1.08	0.33	0.10	0.00	23.97	2.66	3.1	0.20	184.6	89	NSW	l,n	1
0535307-051807	F22-ap128	12.42	1.50	0.44	0.56	1.37	26.08	0.63	13.2	0.63	65.8	209	C	c	1
0535307-053036	F22-ap192	12.30	1.27	0.48	0.40	0.74	25.63	0.39	19.6	0.72	40.8	229	C	c	1
0535308-045517	F11-ap215	11.86	1.19	0.40	0.42	1.12	27.59	0.43	22.0	0.81	50.8	442	C	c	1
0535308-045518	S2-ap107	11.86	1.19	0.40	0.42	1.12	27.25	0.54	18.3	0.77	26.9	467	C	c	1
0535309-054305	F21-ap10	12.07	0.91	0.21	0.01	-0.29	27.49	0.53	22.9	0.81	4.9	171	W-	c	1
0535309-051817	F21-ap163	11.57	1.16	0.36	0.23	–	23.39	3.08	9.0	0.66	11.3	171	NSC	w	1
0535309-052523	F21-ap224	12.80	0.84	0.26	0.00	0.00	23.90	2.44	5.8	0.40	196.7	86	NSW	c	1
0535309-052543	F22-ap177	12.36	1.07	0.37	0.10	0.00	21.04	2.93	5.3	0.36	155.5	97	NSW	c	1
0535309-055542	F31-ap111	13.37	0.96	0.32	0.40	0.90	24.07	0.72	11.2	0.57	15.7	196	CW	c,dv?	2
0535311-051228	F21-ap154	13.01	0.96	0.23	0.11	0.00	20.28	0.54	18.7	0.75	11.2	167	W	c	1
0535312-052340	F21-ap216	11.69	1.31	0.40	0.33	–	24.97	0.33	27.5	0.85	45.6	95	NSC	c	1
0535312-051855	S1-ap188	10.78	1.28	0.50	0.39	–	26.90	0.35	27.9	0.83	11.7	270	C	c	1
0535313-052017	S1-ap209	13.93	1.30	0.50	0.32	0.00	15.01	3.42	3.7	0.25	17.7	172	NSC	l	1
0535313-055840	S3-ap240	12.60	0.91	0.32	0.24	0.84	23.29	1.29	8.8	0.47	2.9	309	CW	c	1
0535314-050501	F21-ap146	12.12	1.30	0.49	0.70	1.30	26.54	0.65	10.7	0.47	49.4	495	C	c	2
0535314-052816	F22-ap189	13.04	1.20	0.44	0.41	1.04	23.92	1.49	3.8	0.27	93.5	114	NSC	c	2
0535314-052515	S3-ap142	7.79	0.25	0.10	0.30	2.50	16.67	1.79	2.6	0.15	1.4	346	W	l	1
0535315-050547	S2-ap148	11.93	3.66	1.47	0.75	1.08	–	–	2.6	0.23	3.6	350	CW	w	1
0535316-050014	S2-ap115	14.78	4.65	1.83	0.41	0.43	16.70	1.79	3.9	0.21	3.5	199	W	l	1
0535316-051636	S2-ap198	12.64	1.70	0.67	0.75	–	–	–	2.2	0.18	26.4	187	NSC	u	1
0535317-044107	F11-ap125	13.33	1.14	0.29	0.13	0.47	30.05	0.50	13.4	0.51	60.5	318	C	c	1
0535317-051639	F22-ap124	13.29	1.49	0.43	0.00	0.00	–	–	2.5	0.23	-4.9	265	NSC	l	1
0535319-051619	S1-ap151	12.80	1.58	0.53	0.61	1.18	24.21	1.54	6.0	0.34	21.6	139	NSC	c	1
0535319-050928	S2-ap163	9.31	1.28	0.42	0.42	0.95	30.45	0.68	25.2	0.88	10.8	436	C	c	1
0535321-051157	F11-ap225	12.63	1.26	0.39	0.27	–	26.09	0.93	9.2	0.53	30.5	271	C	c	2
0535324-051424	F22-ap112	12.66	1.43	0.37	0.06	–	23.40	2.73	7.9	0.56	9.1	94	NSW	c	1

Table 12.4 (cont'd)

2MASS_id	ID	J	$(J-H)$	$(H-K)$	$[3.6-4.5]$	$[5.8-8.0]$	V_{rad}	ΔV_{rad}	R	S	EW_c	$FW_{10\%}$	$H\alpha$	CCF	NOB
0535324-051506	S3-ap132	13.39	1.98	0.69	0.44	1.16	14.54	2.28	2.6	0.19	8.3	143	NSC	l	1
0535325-050209	S2-ap124	14.74	0.94	0.30	0.24	1.39	21.62	2.50	3.9	0.20	14.5	290	C	c	1
0535326-054528	S3-ap230	14.20	1.39	0.49	0.36	0.64	–	–	3.0	0.36	3.8	201	NSC	c	1
0535327-063018	F31-ap232	13.03	0.93	0.25	0.07	0.06	26.49	0.41	19.2	0.71	1.5	147	W+	c	1
0535327-045011	S1-ap132	11.24	1.62	0.60	0.37	0.74	32.50	0.81	15.7	0.79	7.9	437	C	c	1
0535329-051204	S2-ap171	13.56	3.28	1.20	0.00	0.00	16.30	1.48	3.8	0.19	5.3	135	NS	l	1
0535331-051410	F21-ap159	12.20	1.10	0.37	0.17	0.00	28.80	0.54	13.9	0.66	20.3	218	CW	c	2
0535331-054707	S3-ap227	13.12	0.95	0.23	0.18	0.64	24.33	1.00	14.3	0.65	2.6	190	NSW	c	1
0535332-051957	S1-ap191	14.09	2.21	0.82	0.44	–	14.22	1.70	3.7	0.22	15.3	139	NSW	c	1
0535333-053924	F21-ap4	12.94	0.96	0.27	0.06	–	26.80	0.56	15.4	0.65	15.1	113	NSW	c	1
0535333-045111	S2-ap109	12.70	1.26	0.40	0.29	0.61	29.30	0.52	15.1	0.63	7.1	286	CW	c	1
0535334-045601	F22-ap95	12.96	0.90	0.26	0.08	–	32.24	6.80	4.6	0.43	9.2	243	CD	w	1
0535335-051523	F21-ap151	13.12	1.64	0.47	-0.11	0.00	25.53	1.09	8.9	0.48	9.9	113	NSW	c	1
0535335-060220	F31-ap137	12.27	0.92	0.22	0.02	0.17	23.66	0.61	16.9	0.73	2.9	137	W	c	1
0535335-061824	F31-ap229	13.43	0.89	0.23	0.07	0.30	24.11	0.36	21.3	0.72	4.2	164	W+	c	1
0535336-052850	F21-ap221	12.25	1.03	0.25	0.09	–	29.85	0.73	13.0	0.61	36.3	95	NSC	c	1
0535338-045500	F11-ap203	13.15	1.47	0.46	0.13	–	17.35	4.26	3.7	0.25	3.0	138	NSW	c	1
0535338-053225	F21-ap235	13.45	0.85	0.22	0.09	–	-13.60	0.55	15.8	0.65	17.0	104	NSC	c	1
0535339-061432	F31-ap224	12.75	0.94	0.31	0.36	0.87	22.94	1.04	11.5	0.57	21.3	310	C	c	1
0535340-043237	F11-ap124	12.81	0.90	0.26	0.00	0.00	24.69	3.82	6.4	0.50	7.5	231	W	w	1
0535340-045411	F11-ap205	12.68	0.89	0.23	0.08	–	29.77	0.47	20.0	0.69	6.0	183	W	c	1
0535341-062257	F31-ap221	13.17	0.95	0.25	0.06	0.15	23.86	0.88	18.0	0.79	2.8	172	W-	c	1
0535342-052718	F21-ap229	12.04	0.93	0.23	0.13	–	30.20	0.93	13.7	0.67	25.7	97	NSC	s	1
0535343-052659	F22-ap173	13.03	1.07	0.36	0.48	1.60	19.72	2.04	3.9	0.26	78.2	107	NSC	c	2
0535343-060542	F31-ap158	11.74	0.96	0.24	0.07	0.13	24.62	6.14	7.6	0.60	5.9	386	C	w	1
0535344-044020	F11-ap123	12.16	1.56	0.49	-0.11	–	30.16	0.41	20.7	0.78	21.8	277	C	c	1
0535346-053438	F22-ap200	12.83	1.13	0.37	0.30	–	26.28	0.40	20.1	0.74	12.1	129	NSW	c	1
0535346-053437	S3-ap194	12.83	1.13	0.37	0.30	–	23.01	1.49	7.4	0.42	13.1	277	C	c	1
0535346-051552	S2-ap181	13.31	1.23	0.52	-0.30	0.00	–	–	2.6	0.17	36.8	203	NSC	l,n,r	1
0535350-054101	S3-ap215	13.86	1.52	0.54	0.30	0.36	13.58	1.45	4.7	0.29	8.0	172	NSC	c	1
0535351-052123	S1-ap214	11.88	0.62	0.64	0.00	0.00	18.02	2.62	5.0	0.33	19.7	213	NSC	c	1
0535352-044739	F11-ap153	12.35	1.09	0.28	0.25	1.48	31.15	0.29	22.1	0.79	2.9	145	W-	c	2
0535353-050847	S2-ap164	14.08	1.27	0.48	0.31	–	37.90	12.68	3.5	0.22	11.0	399	C	w	1
0535353-051111	F21-ap156	12.70	0.87	0.21	0.05	–	26.91	0.44	13.5	0.60	9.9	161	W	c	2
0535355-051543	S3-ap136	11.79	1.23	0.39	0.43	0.00	26.05	0.71	15.7	0.74	17.0	448	C	c	1
0535355-050658	F22-ap102	13.37	0.92	0.23	0.06	–	27.79	0.37	17.4	0.71	5.1	152	W+	c	2
0535355-053907	S3-ap216	13.81	1.67	0.74	0.48	0.80	5.36	11.68	4.2	0.31	9.9	262	NSC	c	1
0535359-051225	S1-ap148	10.60	2.21	1.00	0.52	0.91	32.00	2.48	8.0	0.67	13.3	602	C	c	1
0535359-053842	S3-ap201	12.91	0.94	0.28	0.53	0.52	24.68	1.40	8.2	0.43	6.5	146	NSW	c	1
0535363-053137	S3-ap172	12.50	1.42	0.59	0.50	0.79	25.06	1.32	5.0	0.30	29.8	350	C	c	1
0535364-053411	F22-ap196	11.79	1.38	0.47	0.44	0.81	26.78	0.32	24.1	0.77	44.1	289	C	c	1
0535364-050115	S1-ap137	10.31	1.18	0.44	0.30	0.67	25.74	1.32	17.8	0.79	5.3	475	C	c	1
0535364-053410	S3-ap190	11.79	1.38	0.47	0.44	0.81	25.55	0.42	20.8	0.74	12.1	195	W	c	1

Table 12.4 (cont'd)

2MASS_id	ID	J	$(J-H)$	$(H-K)$	[3.6 – 4.5]	[5.8 – 8.0]	V_{rad}	ΔV_{rad}	R	S	EW_c	$FW_{10\%}$	$H\alpha$	CCF	NOB
0535366-050414	S2-ap135	11.83	1.06	0.49	0.23	0.56	27.65	0.46	21.0	0.78	8.8	459	C	c	1
0535367-053741	F22-ap197	11.50	0.97	0.23	0.02	0.29	26.51	0.43	27.3	0.89	2.3	123	NS	c	1
0535367-055856	F31-ap130	12.66	0.90	0.24	0.07	0.12	25.18	0.75	16.6	0.75	4.4	147	W-	c	1
0535367-051000	S3-ap121	13.31	1.37	0.55	0.56	0.95	–	–	2.7	0.21	10.1	377	C	u,r	1
0535373-060000	F31-ap127	13.15	0.94	0.24	0.06	0.08	27.20	0.45	18.9	0.69	4.2	222	W+	c	1
0535373-062119	F31-ap228	13.16	0.97	0.29	0.31	0.80	22.73	0.61	16.7	0.65	6.0	188	W+	c	1
0535374-055127	S3-ap225	13.31	1.10	0.33	0.31	1.15	13.10	1.12	6.4	0.31	3.3	258	NSC	c	1
0535376-050632	S1-ap131	13.00	1.01	0.28	0.27	0.78	27.20	0.33	15.2	0.69	6.6	245	C	c	3
0535380-044833	F11-ap163	12.82	0.97	0.24	0.05	0.14	30.41	0.38	19.7	0.70	2.7	128	W-	c	1
0535380-052821	F22-ap182	12.17	1.00	0.25	0.01	–	27.00	0.37	20.6	0.73	18.1	99	NS	c	1
0535380-045229	S1-ap138	13.79	1.18	0.41	0.37	0.79	22.23	3.05	3.9	0.28	5.7	294	CW	c	1
0535381-052833	S2-ap202	12.98	0.44	-0.43	0.48	0.71	12.41	1.96	2.7	0.16	47.6	142	NSC	l,n,r	1
0535382-051419	F21-ap164	11.60	1.07	0.27	0.09	0.00	27.64	3.78	7.8	0.66	5.5	205	NSW	w	1
0535383-052834	S1-ap232	12.70	1.03	0.15	0.33	1.13	24.20	1.01	7.4	0.48	26.9	134	NSW	c	1
0535385-045941	S2-ap113	12.04	1.69	0.53	0.35	0.90	29.10	0.71	16.8	0.67	10.7	482	C	c	1
0535387-051659	S3-ap137	13.66	1.95	0.76	0.40	–	15.09	1.99	4.1	0.22	9.5	316	C	c	1
0535388-051242	S1-ap143	10.70	1.88	0.69	0.44	0.89	27.88	0.72	21.3	0.80	5.5	410	C	c	1
0535394-044019	F11-ap139	12.49	1.21	0.31	0.08	-0.14	29.64	2.25	13.2	0.67	3.3	335	WC	w	1
0535395-043513	F11-ap127	11.93	1.38	0.40	0.00	0.00	18.31	0.89	9.7	0.47	0.0	0	AE	c	1
0535398-044404	F11-ap144	11.65	1.07	0.28	0.00	0.13	30.75	0.52	22.6	0.81	2.4	325	WC	c	1
0535399-050636	S2-ap143	12.66	1.86	0.61	0.43	0.90	24.91	1.96	4.9	0.27	6.8	297	CW	c	1
0535399-045839	F11-ap220	12.70	0.92	0.28	0.08	0.91	-30.33	0.41	15.8	0.56	0.0	0	WD	c	1
0535400-044555	S2-ap108	11.47	1.05	0.35	0.24	0.93	29.46	0.27	32.7	0.87	1.8	256	W	c	1
0535403-045543	S2-ap117	13.28	1.08	0.37	0.17	0.83	24.64	0.70	9.9	0.43	35.3	313	C	c	1
0535404-045543	F11-ap209	13.28	1.08	0.37	0.17	0.83	22.96	0.74	9.2	0.44	90.8	292	C	c	1
0535405-045226	S2-ap112	12.86	1.24	0.38	0.29	0.72	31.81	0.58	13.7	0.64	14.5	448	C	c	1
0535408-061806	F31-ap213	13.16	0.95	0.25	0.08	-0.19	26.73	0.39	21.6	0.75	3.2	123	W+	c	1
0535409-052202	S1-ap203	13.61	1.86	0.79	0.44	–	–	–	2.7	0.22	43.7	318	C	d?,l	1
0535410-044947	F11-ap178	12.98	0.78	0.24	0.03	0.42	29.21	0.59	12.4	0.58	0.0	0	N	c	1
0535410-050625	F22-ap108	12.65	0.95	0.23	0.04	1.04	26.98	0.47	17.2	0.66	4.3	120	NSW	c	1
0535413-052750	S3-ap157	12.50	1.30	0.48	0.35	1.02	25.13	0.72	11.0	0.56	36.3	361	C	c	1
0535413-053833	S3-ap208	13.23	1.07	0.30	0.32	0.90	26.10	1.37	9.0	0.50	5.6	153	NSW	c	1
0535417-045027	F11-ap182	13.37	0.97	0.29	0.08	0.08	34.87	0.48	13.5	0.52	2.8	112	W-	c	1
0535419-052812	S3-ap155	9.36	0.72	0.21	0.23	1.08	28.70	2.06	17.2	0.82	1.0	165	NSW	w	1
0535420-051259	F11-ap226	13.46	0.97	0.35	0.00	0.00	22.54	2.81	4.7	0.24	9.9	114	W	w,l	1
0535420-051011	S1-ap147	11.60	2.13	0.68	0.37	0.63	24.60	0.77	15.8	0.66	5.3	380	C	c	1
0535423-051508	S1-ap168	13.77	2.10	0.77	0.54	1.00	24.71	1.86	6.6	0.45	12.2	470	C	c	1
0535424-052732	S1-ap228	11.39	1.27	0.44	0.31	–	26.46	0.30	31.8	0.87	6.2	287	CW	c	1
0535426-052608	F21-ap215	12.78	1.11	0.38	0.23	0.00	31.74	8.43	3.7	0.31	52.5	114	NSC	w	1
0535426-052545	F22-ap165	13.09	1.02	0.37	-0.08	0.00	27.69	1.53	4.7	0.28	62.1	103	NSW	c	1
0535426-052633	S1-ap224	14.60	1.14	0.56	0.44	0.00	–	–	2.8	0.27	54.2	138	NSC	u	1
0535427-063451	F31-ap227	12.37	1.21	0.42	0.50	0.85	25.68	0.77	12.0	0.70	40.1	411	C	c	1
0535428-062144	F31-ap222	12.98	1.02	0.29	0.52	1.41	26.58	0.36	23.8	0.78	2.9	196	W+	c	1

Table 12.4 (cont'd)

2MASS_id	ID	J	$(J-H)$	$(H-K)$	$[3.6-4.5]$	$[5.8-8.0]$	V_{rad}	ΔV_{rad}	R	S	EW_c	$FW_{10\%}$	$H\alpha$	CCF	NOB
0535430-050307	F11-ap213	13.34	1.06	0.30	0.27	0.55	25.67	0.47	11.9	0.50	14.8	299	C	c	2
0535430-052302	S2-ap197	12.96	1.57	0.56	0.48	–	23.26	1.96	5.3	0.36	24.7	435	C	c	1
0535433-053244	F21-ap232	12.06	1.05	0.29	0.34	0.71	28.53	0.35	28.8	0.85	14.6	235	W	c	1
0535434-053244	S3-ap171	12.06	1.05	0.29	0.34	0.71	28.48	0.40	25.3	0.84	4.3	158	W	c	1
0535435-050541	S2-ap145	12.10	1.84	0.76	0.42	0.97	27.68	0.73	12.3	0.65	8.3	376	C	c	1
0535438-050959	S2-ap167	13.66	0.95	0.38	0.32	1.12	28.15	1.22	6.5	0.38	6.6	195	W	c	1
0535440-055653	F31-ap121	13.34	0.92	0.26	0.06	-0.01	26.63	0.39	20.3	0.71	0.0	0	W+	c	1
0535441-053639	F21-ap237	12.41	1.00	0.36	0.23	0.75	22.52	1.35	8.1	0.38	29.5	197	NSC	s	1
0535441-044805	S2-ap103	12.06	1.34	0.49	0.27	0.60	32.47	0.71	11.2	0.67	12.3	395	C	c	1
0535441-044804	F11-ap165	12.06	1.34	0.49	0.27	0.60	31.00	0.81	9.6	0.62	28.0	352	C	c	1
0535441-050837	S2-ap151	14.08	1.64	0.66	0.38	1.04	–	–	3.3	0.25	21.6	429	C	u	1
0535443-045716	F21-ap150	13.19	0.93	0.27	0.09	–	24.72	0.66	11.2	0.46	8.2	163	W	c	1
0535445-050731	F21-ap158	12.21	0.95	0.21	0.03	0.27	21.08	0.55	19.4	0.78	3.8	177	W	c	1
0535445-053633	F22-ap181	12.81	0.96	0.28	0.10	0.34	21.56	2.61	6.5	0.41	16.8	184	W	c	1
0535445-053256	S1-ap236	14.50	0.91	0.23	0.02	0.00	–	–	1.9	0.24	25.1	160	NSC	c	1
0535448-052434	S3-ap145	11.97	1.25	0.43	0.32	–	24.77	3.76	7.1	0.56	16.0	301	NSC	c	2
0535449-043054	F11-ap129	13.39	1.08	0.32	0.00	0.00	18.14	1.30	6.2	0.39	0.0	0	AE	d?	1
0535450-045141	F11-ap190	12.98	0.94	0.27	0.11	0.07	26.71	4.52	6.0	0.37	4.3	167	W	w	1
0535451-060107	F31-ap131	13.41	0.90	0.25	0.08	0.20	24.10	1.04	11.2	0.58	3.3	135	W-	c	1
0535453-044339	F11-ap149	12.08	1.19	0.32	0.11	0.14	29.12	0.31	24.2	0.73	1.9	143	W	c	1
0535453-052810	S3-ap153	11.73	1.36	0.48	0.60	–	26.11	0.38	17.3	0.78	17.1	308	C	c	2
0535454-052036	F21-ap181	11.64	1.00	0.24	0.02	–	25.50	3.33	14.7	0.78	6.4	468	C	w	1
0535456-051813	F22-ap133	12.58	1.62	0.49	0.05	0.43	–	–	1.6	0.18	15.8	98	NSW	d?,l,n	1
0535458-060538	F31-ap167	12.47	0.92	0.24	0.07	0.45	25.26	0.37	21.7	0.74	1.4	120	W+	c	1
0535461-051051	F22-ap120	11.73	1.30	0.46	0.28	0.68	22.96	0.70	14.6	0.85	15.8	437	C	c	2
0535462-051808	F21-ap173	12.19	1.33	0.24	0.30	0.60	24.04	0.24	26.8	0.83	10.3	381	C	c	2
0535462-051539	S2-ap182	12.57	1.84	0.66	0.39	0.63	30.19	1.25	7.3	0.46	13.6	545	C	c	1
0535464-054100	F22-ap198	11.94	0.95	0.22	0.03	0.00	22.55	4.54	7.5	0.63	11.2	232	CW	w	1
0535466-052224	F22-ap158	12.46	0.91	0.29	0.15	–	27.27	1.51	10.6	0.64	20.7	344	C	c	1
0535466-054926	F31-ap126	11.56	1.13	0.36	0.18	0.91	23.31	0.41	19.2	0.82	21.4	350	C	c	1
0535468-060507	F31-ap155	12.63	0.99	0.26	0.01	0.00	26.61	0.33	26.2	0.80	0.0	0	W	c	1
0535472-063323	F31-ap230	12.97	0.89	0.22	0.02	0.04	25.14	0.34	25.3	0.78	3.5	149	W	c	1
0535474-052249	F21-ap206	11.89	0.93	0.22	0.05	0.00	28.27	0.37	25.5	0.82	10.9	151	W	c	1
0535474-051028	S3-ap140	11.38	1.62	0.63	0.43	0.77	29.29	0.56	16.3	0.74	14.7	410	C	c	1
0535476-051914	S1-ap185	12.97	1.97	0.73	0.45	1.10	28.39	0.93	9.5	0.50	14.3	236	C	c	1
0535476-053738	S3-ap193	12.96	1.66	0.63	0.43	0.61	23.18	1.78	4.8	0.24	13.3	401	C	c	1
0535478-051317	F22-ap122	13.48	1.68	0.47	0.03	–	–	–	2.0	0.26	7.0	103	NSW	d?,l	1
0535479-060134	F31-ap142	13.01	1.54	0.42	0.04	0.11	13.19	2.03	8.1	0.47	3.7	224	W	c	1
0535481-055357	S3-ap228	12.82	1.82	0.62	0.39	0.75	23.11	0.61	19.5	0.75	9.5	456	C	c	1
0535482-051110	F22-ap117	12.81	1.18	0.29	0.04	0.15	29.61	0.54	15.4	0.67	2.3	115	N	c	1
0535483-061736	F31-ap220	13.01	0.90	0.25	0.09	-0.03	19.41	2.75	8.4	0.56	4.9	258	W	c	1
0535484-050128	S2-ap136	12.15	1.62	0.61	0.43	0.74	29.30	0.93	8.2	0.50	10.5	422	C	c	1
0535485-055623	S3-ap229	13.31	1.31	0.51	0.32	0.67	21.42	1.72	8.0	0.43	2.5	388	CW	c	1

Table 12.4 (cont'd)

2MASS_id	ID	J	$(J-H)$	$(H-K)$	[3.6 − 4.5]	[5.8 − 8.0]	V_{rad}	ΔV_{rad}	R	S	EW_c	$FW_{10\%}$	$H\alpha$	CCF	NOB
0535487-051927	F22-ap131	13.10	0.97	0.24	0.13	0.00	28.71	0.55	11.7	0.51	14.5	214	NSC	c	1
0535487-060907	F31-ap186	13.31	0.85	0.25	0.05	0.06	27.04	0.50	17.6	0.67	1.7	122	W+	c	1
0535488-050028	F11-ap212	12.62	1.34	0.36	0.11	0.14	28.21	3.51	10.3	0.53	2.1	324	WC	w	2
0535489-050139	F21-ap141	12.57	1.07	0.33	0.28	0.70	26.46	0.77	14.4	0.70	16.2	361	C	c	3
0535490-051537	F22-ap127	13.09	0.92	0.26	0.08	–	27.42	0.44	18.3	0.68	4.6	143	W	c	1
0535491-045306	F11-ap194	13.46	1.10	0.35	0.12	–	29.75	1.42	6.2	0.32	2.8	120	NSW	c	1
0535494-053526	F21-ap234	11.62	0.84	0.20	-0.03	1.30	27.71	0.34	30.5	0.88	4.1	173	W-	c	1
0535495-042438	F11-ap128	11.75	0.88	0.27	0.00	0.00	32.55	2.74	15.7	0.80	4.1	328	C	w	1
0535498-051830	S2-ap187	12.76	1.92	0.75	0.56	0.95	26.61	1.28	7.6	0.42	14.8	274	C	c	1
0535498-044632	S2-ap101	12.49	1.03	0.37	0.32	0.81	29.49	0.81	10.5	0.54	21.2	410	C	c	2
0535501-052116	F21-ap199	13.03	1.18	0.38	0.53	1.44	26.01	1.23	8.8	0.53	19.5	238	C	c	2
0535502-063335	F31-ap226	12.99	0.88	0.24	0.08	0.12	19.40	3.92	6.4	0.35	4.4	246	CW,R	c	1
0535503-044208	F11-ap146	12.88	1.22	0.37	0.08	0.24	82.24	2.82	4.0	0.29	7.2	397	CW	d	1
0535504-052835	S3-ap164	8.27	2.06	1.02	0.59	0.98	–	–	1.7	0.32	13.8	553	C	u,r	1
0535505-055142	S3-ap224	11.26	1.12	0.38	0.28	0.32	25.72	0.25	35.7	0.87	2.1	460	CW	c	1
0535507-051629	S1-ap179	11.36	1.30	0.42	0.32	1.17	26.31	0.50	25.5	0.85	3.9	308	C	c	1
0535508-044323	S2-ap105	13.68	1.51	0.49	0.51	0.77	27.26	1.57	5.1	0.23	3.7	350	CW	c	1
0535510-051509	F21-ap174	11.97	1.04	0.28	0.26	0.41	27.57	0.45	26.1	0.88	2.9	174	W	c	1
0535511-045627	S2-ap122	13.33	1.79	0.60	0.71	1.21	26.93	6.53	4.0	0.23	10.7	426	C	l	1
0535511-050708	S2-ap156	10.98	1.11	0.33	0.24	1.06	25.88	0.36	24.1	0.79	6.0	290	C	c	1
0535513-061353	F31-ap208	13.21	0.95	0.31	0.39	0.87	25.05	0.45	13.8	0.52	4.9	119	W-	c	1
0535518-045410	F11-ap198	11.67	1.07	0.30	0.04	0.18	24.38	0.41	17.8	0.74	0.0	0	AE	c	1
0535520-044915	S2-ap118	13.72	1.12	0.42	0.65	0.82	31.50	1.62	5.6	0.29	4.1	267	CW	c	1
0535522-044304	F11-ap143	11.86	1.01	0.22	0.04	–	26.25	0.64	14.7	0.79	46.4	459	C	c	1
0535522-053924	F31-ap122	12.86	1.41	0.43	0.08	0.39	28.81	0.45	16.1	0.71	8.0	115	NSW	c	2
0535526-050505	S2-ap147	9.73	0.98	0.36	0.25	0.56	30.25	1.88	15.4	0.81	3.2	572	C	w	1
0535527-051259	S2-ap176	11.51	1.19	0.39	0.32	0.95	28.73	0.39	26.9	0.87	3.8	436	CW	c	1
0535529-052544	S1-ap220	14.32	1.69	0.63	0.54	–	17.93	1.90	3.8	0.22	23.3	142	NSC	c	1
0535530-055041	F31-ap123	13.44	1.00	0.29	0.04	0.31	34.28	0.53	15.3	0.67	0.0	0	AE	c	1
0535535-050234	F22-ap105	13.13	1.49	0.40	0.02	0.42	30.45	0.84	12.2	0.61	4.2	171	NSW	s	1
0535538-045714	F11-ap202	13.06	1.60	0.44	0.09	0.11	22.54	2.40	5.2	0.27	0.0	0	N	s	1
0535539-052738	S1-ap213	14.76	0.97	0.39	0.38	–	–	–	2.7	0.21	24.4	138	NSC	u,r	1
0535540-044719	S2-ap114	12.39	1.35	0.53	0.46	0.61	30.77	1.35	6.3	0.45	14.6	309	C	c	1
0535540-050414	S2-ap144	10.88	1.05	0.50	0.00	0.00	27.91	0.60	24.5	0.84	8.9	448	C	c	1
0535541-051710	S1-ap173	13.59	1.34	0.46	0.30	1.13	–	–	2.2	0.19	8.1	203	CW	u,r	1
0535543-052644	S1-ap215	11.96	1.56	0.65	0.48	0.92	23.04	1.49	10.4	0.54	16.4	340	NSC	c	1
0535546-050627	F11-ap217	13.49	0.90	0.29	0.14	0.46	24.10	5.00	3.9	0.27	8.7	202	W	w,l,dv?	2
0535546-052707	F21-ap218	12.28	0.89	0.23	0.13	1.16	30.00	0.59	16.5	0.79	33.4	398	C	c	1
0535546-052200	F22-ap152	13.38	1.44	0.46	0.08	–	24.78	6.57	3.1	0.20	15.5	154	NSC	u	1
0535547-045819	S2-ap129	14.48	1.82	0.77	0.51	1.15	28.10	2.08	8.1	0.56	6.2	520	C	c	1
0535553-054701	F31-ap129	12.99	0.87	0.30	0.25	1.19	22.40	0.84	8.9	0.44	9.0	188	W	c	1
0535554-052343	F22-ap153	13.29	0.88	0.24	0.05	0.00	19.46	1.17	10.0	0.51	12.9	111	NSW	c	1
0535557-054929	S3-ap213	13.10	1.36	0.48	0.59	0.81	14.21	1.35	6.0	0.33	6.5	438	CW	c	1

Table 12.4 (cont'd)

2MASS_id	ID	J	$(J-H)$	$(H-K)$	$[3.6-4.5]$	$[5.8-8.0]$	V_{rad}	ΔV_{rad}	R	S	EW_c	$FW_{10\%}$	$H\alpha$	CCF	NOB
0535559-054226	F31-ap128	13.44	0.94	0.28	0.09	–	27.32	0.79	12.9	0.62	3.8	107	NS	c	1
0535560-045655	F11-ap191	11.74	0.82	0.22	0.02	0.02	26.98	0.26	34.1	0.87	1.6	146	W	c	1
0535561-055228	F31-ap138	12.72	0.94	0.26	0.08	0.08	24.60	6.97	7.6	0.60	6.4	546	C	w	1
0535566-053511	S3-ap187	14.91	2.82	0.99	0.39	1.44	12.94	1.16	6.0	0.35	4.0	139	NSW	c	1
0535568-051957	S1-ap194	13.54	1.18	0.47	0.48	1.14	29.05	1.15	5.5	0.28	22.6	255	C	c	1
0535569-054519	S1-ap239	12.57	1.75	0.62	0.38	0.60	25.11	1.70	4.6	0.30	17.2	466	C	c	1
0535575-053951	F21-ap238	12.90	1.19	0.28	0.07	0.61	28.41	3.24	7.2	0.48	15.8	199	NSC	w	1
0535576-055718	S3-ap226	12.10	1.27	0.54	0.39	0.96	24.85	2.14	4.7	0.37	24.6	587	C	c	1
0535577-061124	F31-ap181	12.84	0.95	0.23	0.02	0.17	26.94	0.34	27.4	0.83	2.0	131	W+	c	1
0535577-052308	S1-ap204	12.14	1.05	0.39	0.37	–	26.49	0.46	19.3	0.74	9.1	315	C	c	1
0535577-052309	F21-ap191	12.14	1.05	0.39	0.37	–	26.46	0.48	17.7	0.68	14.0	217	NSC	c	1
0535578-062344	F31-ap217	12.84	0.83	0.29	0.20	0.79	19.55	0.87	11.4	0.53	15.7	301	C	c	1
0535579-060813	F31-ap178	12.82	0.91	0.31	0.11	0.14	24.52	0.94	10.2	0.54	8.6	173	W	c	1
0535580-061450	F31-ap202	13.29	0.86	0.27	0.10	0.08	20.11	1.77	9.1	0.52	3.7	159	NSW	c	1
0535586-042924	F11-ap134	12.25	1.28	0.45	0.00	0.00	38.62	0.70	11.0	0.52	63.9	424	C	c	1
0535589-055908	F31-ap144	12.97	0.88	0.21	0.03	0.02	26.47	0.37	21.5	0.76	0.0	0	W+	c	1
0535589-053253	S3-ap182	14.40	1.88	0.66	0.48	0.89	15.93	2.46	4.5	0.27	4.9	304	C	c	1
0535592-045846	F22-ap109	12.57	0.95	0.21	0.04	0.12	29.52	0.37	24.8	0.81	5.7	254	CW	c	1
0535594-053709	F22-ap188	12.78	1.10	0.28	0.10	1.03	30.20	0.92	11.4	0.57	11.5	187	W	c	1
0535595-053709	S3-ap198	12.78	1.10	0.28	0.10	1.03	26.13	1.43	8.0	0.48	4.2	176	W-	c	1
0535596-052943	S3-ap163	10.86	2.00	0.83	0.00	0.00	23.21	0.99	13.0	0.64	5.7	436	CW	c	1
0536002-044346	F11-ap155	13.04	1.04	0.27	0.11	-0.02	29.16	0.48	16.8	0.68	3.3	150	W+	c	1
0536002-062347	F31-ap219	13.07	0.85	0.24	0.08	0.10	21.67	0.84	13.4	0.65	3.3	157	N	c	1
0536008-044258	F11-ap156	13.33	1.00	0.35	0.30	0.88	25.36	0.86	9.8	0.43	31.9	261	C	c	1
0536013-051910	F21-ap189	13.24	0.94	0.30	0.08	–	25.13	2.09	8.1	0.46	12.5	137	NSW	c	1
0536013-053733	S1-ap227	14.55	2.18	0.71	0.27	1.28	15.58	1.81	3.5	0.22	8.3	205	W	c	1
0536017-043417	F11-ap133	11.71	0.88	0.20	0.00	0.00	26.03	0.26	35.2	0.86	0.6	194	W	c	1
0536027-051526	F21-ap175	12.85	1.20	0.36	0.10	–	28.32	0.66	9.6	0.38	13.3	135	W	c	1
0536028-053254	S1-ap222	13.75	1.03	0.36	0.31	0.74	–	–	1.8	0.23	9.5	220	NSC	c	1
0536033-045740	F22-ap107	13.12	0.94	0.28	0.06	0.50	23.41	1.15	11.9	0.59	2.8	180	W-	c	2
0536038-053018	S3-ap176	13.54	1.03	0.32	0.21	1.13	25.77	0.94	7.5	0.36	10.9	383	C	c	1
0536041-050408	F21-ap153	12.93	1.20	0.39	0.26	0.60	26.75	1.12	6.7	0.33	9.4	192	W	c	1
0536041-050409	S1-ap152	12.93	1.20	0.39	0.26	0.60	31.06	2.55	4.4	0.22	4.6	252	CW	l	1
0536051-045104	F11-ap171	12.31	0.96	0.22	0.04	0.03	28.16	1.55	12.7	0.65	4.3	178	W	c	1
0536051-051113	S1-ap164	13.98	1.10	0.39	0.33	0.88	21.89	2.25	4.7	0.26	8.1	338	C	c	1
0536056-055213	F31-ap135	12.89	0.92	0.25	0.03	0.23	27.26	0.36	19.0	0.65	2.6	122	W	c	1
0536065-063143	F31-ap211	13.32	0.86	0.22	0.22	1.08	25.62	0.82	12.7	0.62	2.6	131	W-	c	1
0536066-054154	F31-ap125	13.46	0.84	0.29	0.00	0.00	24.18	2.78	6.0	0.44	76.3	399	C	c	1
0536068-050615	F22-ap115	13.02	0.95	0.21	0.17	0.81	21.56	0.36	17.9	0.74	2.8	150	W	c	2
0536070-053418	S3-ap186	12.34	2.11	0.89	0.00	0.00	23.18	1.64	3.8	0.18	10.5	390	C	l	1
0536073-053027	F22-ap176	13.00	0.95	0.33	0.13	0.30	25.82	1.42	9.0	0.52	14.6	159	W	c	1
0536073-054221	S1-ap223	11.27	1.38	0.55	0.00	0.00	23.11	0.32	29.2	0.87	14.2	351	C	c	1
0536080-044120	F11-ap154	12.04	1.32	0.46	0.41	0.89	27.52	0.44	20.4	0.78	13.8	271	C	c	1

Table 12.4 (cont'd)

2MASS_id	ID	J	$(J-H)$	$(H-K)$	[3.6 – 4.5]	[5.8 – 8.0]	V_{rad}	ΔV_{rad}	R	S	EW_c	$FW_{10\%}$	$H\alpha$	CCF	NOB
0536081-044120	S2-ap116	12.04	1.32	0.46	0.41	0.89	27.96	0.47	19.3	0.77	7.9	305	C	c	1
0536083-062437	F31-ap216	12.70	0.96	0.34	0.24	0.62	24.64	0.93	9.8	0.45	7.2	217	W	c	1
0536086-052102	F21-ap198	12.33	0.98	0.23	0.07	0.34	32.22	6.15	5.9	0.56	8.6	225	WC	w	1
0536089-054447	F31-ap132	12.99	0.92	0.21	0.07	0.96	25.11	0.40	21.6	0.76	3.6	120	W-	c	1
0536092-045000	F11-ap175	12.80	1.00	0.29	0.27	0.82	22.95	0.74	12.1	0.53	50.3	381	C	c	1
0536092-052413	F21-ap202	13.42	0.88	0.26	0.08	–	19.48	2.97	5.2	0.40	12.0	197	NSC	c	1
0536092-053638	S1-ap226	12.25	1.12	0.42	0.00	0.00	27.92	0.40	14.6	0.65	12.7	310	C	c	2
0536092-053109	S3-ap177	14.06	1.29	0.53	0.53	0.98	13.92	0.98	6.8	0.32	17.2	312	C	c	1
0536096-060331	F31-ap151	13.43	1.35	0.36	0.07	0.03	37.22	0.76	10.7	0.44	0.0	0	W+	c	1
0536100-052731	F22-ap166	13.29	0.92	0.35	0.08	–	20.39	2.87	4.9	0.28	27.6	188	CW	c	1
0536101-052205	F21-ap197	11.74	0.85	0.33	0.07	0.04	24.54	0.37	19.9	0.70	6.0	110	NSW	c	1
0536103-054227	S1-ap225	11.59	2.45	1.02	0.50	0.75	26.84	1.30	9.7	0.59	19.2	587	C	c	1
0536108-055649	F31-ap150	13.41	0.92	0.21	0.04	0.11	24.67	0.78	15.6	0.71	2.4	145	N	c	1
0536109-053948	S3-ap195	12.69	2.62	1.04	0.00	0.00	24.54	2.61	5.4	0.42	9.8	578	C	c	1
0536113-053851	F21-ap227	12.96	1.43	0.45	0.08	0.15	–	–	3.4	0.28	11.3	263	CD	w,l	1
0536118-050032	F22-ap116	12.20	0.90	0.21	0.05	–	26.20	0.33	25.9	0.80	5.5	194	W	c	1
0536118-051555	F22-ap137	12.92	0.88	0.23	0.09	-0.04	24.38	1.61	10.6	0.59	5.0	133	W	c	1
0536121-053329	F22-ap179	13.32	1.69	0.48	0.10	–	26.43	1.40	4.4	0.24	17.1	189	W	c	1
0536124-054045	S3-ap191	13.40	2.00	0.84	0.57	0.45	18.14	2.00	5.6	0.31	8.4	349	CW	c	1
0536126-062339	F31-ap203	12.74	1.38	0.44	0.26	0.64	23.70	1.16	9.6	0.47	12.5	363	C	c	1
0536130-045513	F11-ap192	13.09	1.22	0.31	0.06	0.23	28.69	0.46	22.0	0.73	0.0	0	N	c	1
0536131-062541	F31-ap214	13.11	0.89	0.24	0.06	0.04	26.54	0.46	18.6	0.72	0.0	0	W+	c	1
0536133-050223	S1-ap156	13.44	0.89	0.28	0.26	0.87	26.40	0.81	8.5	0.42	10.6	323	C	c	1
0536137-055029	F31-ap133	12.91	1.33	0.34	0.03	0.02	36.45	0.54	13.9	0.65	0.6	118	AE	c	1
0536147-054557	F31-ap140	13.04	1.00	0.26	0.06	0.19	32.04	0.49	11.3	0.61	0.0	0	AE	c	2
0536149-051533	F11-ap219	11.81	1.10	0.38	0.19	0.35	26.79	1.06	14.7	0.69	6.2	256	CW	c	1
0536158-061450	F31-ap197	13.01	0.93	0.21	0.07	1.00	24.77	0.59	17.4	0.74	40.0	392	C	c	1
0536169-051142	S1-ap165	10.36	1.08	0.33	0.28	1.42	21.87	0.74	23.7	0.85	1.5	342	WC	c	1
0536170-054314	F31-ap136	13.03	1.58	0.44	0.00	-0.05	27.02	0.67	7.7	0.50	0.0	0	N	c	2
0536172-061724	F31-ap191	12.22	0.90	0.27	0.18	0.81	24.71	1.17	10.6	0.51	3.9	159	W+	c	1
0536177-042434	F11-ap140	11.50	0.93	0.25	0.00	0.00	–	–	2.5	0.53	14.0	670	C	u	1
0536182-054953	S3-ap214	13.96	1.49	0.52	0.34	0.63	13.99	1.09	6.8	0.32	7.1	329	CW	c	1
0536184-062038	F31-ap204	12.21	1.11	0.33	0.27	0.70	21.13	0.38	27.1	0.84	26.1	365	C	c	1
0536187-051218	F11-ap214	12.98	0.93	0.25	0.08	0.11	27.41	0.69	12.0	0.55	3.5	159	W	c	2
0536190-051828	S3-ap156	14.16	0.89	0.32	0.22	0.43	17.23	2.25	5.3	0.31	2.3	214	CD	c	1
0536191-042730	F11-ap135	12.61	0.89	0.21	0.00	0.00	27.65	0.50	20.6	0.74	4.2	228	W+	c	1
0536197-044455	F11-ap162	11.66	0.98	0.26	0.29	0.47	29.47	0.32	32.0	0.89	0.6	227	W	c	1
0536197-051438	S1-ap175	12.25	1.30	0.47	0.24	0.83	28.26	0.28	23.6	0.81	3.0	462	C	c,dv	3
0536197-044454	S2-ap111	11.66	0.98	0.26	0.29	0.47	29.26	0.36	30.5	0.87	0.6	316	W+	c	1
0536197-054823	S3-ap203	13.11	2.02	0.84	0.51	0.54	10.83	2.01	3.0	0.19	9.0	491	C	l,r	1
0536198-055608	F31-ap145	13.47	0.87	0.23	0.07	0.09	26.07	0.62	14.2	0.64	2.9	111	W+	c	1
0536199-051306	S1-ap176	13.64	1.09	0.39	0.32	0.92	27.02	0.83	7.7	0.37	7.9	289	C	c	1
0536210-061717	F31-ap193	12.77	0.84	0.24	0.13	0.16	22.78	3.99	7.1	0.45	5.2	229	W	w	1

Table 12.4 (cont'd)

2MASS_id	ID	J	$(J-H)$	$(H-K)$	$[3.6-4.5]$	$[5.8-8.0]$	V_{rad}	ΔV_{rad}	R	S	EW_c	$FW_{10\%}$	$H\alpha$	CCF	NOB
0536210-052734	F22-ap162	13.22	1.69	0.49	0.09	–	3.19	2.71	3.1	0.22	16.5	169	CW	c	1
0536213-052014	F22-ap150	12.45	0.90	0.26	0.07	-0.13	23.79	0.30	25.1	0.76	0.0	0	W	c	1
0536218-055406	F31-ap148	13.12	0.86	0.20	0.04	-0.12	18.75	0.47	15.8	0.63	0.0	0	AE	c	1
0536222-055547	S3-ap217	13.87	0.93	0.30	0.34	0.75	21.37	1.00	9.6	0.49	1.3	310	W-	c	1
0536241-063149	F31-ap218	13.49	0.89	0.20	0.06	0.12	24.64	0.61	12.5	0.57	2.5	127	W+	c	1
0536242-054448	F22-ap186	11.52	0.86	0.21	0.23	1.01	21.50	0.39	31.7	0.89	3.6	248	WC	c	1
0536251-051913	F22-ap146	13.09	0.84	0.27	0.13	0.09	23.47	3.91	5.7	0.40	9.8	182	NSW	c	1
0536255-051841	F22-ap144	13.41	0.93	0.29	0.07	-0.02	21.82	5.55	4.2	0.36	12.9	278	C	w	1
0536262-051653	F21-ap186	13.48	0.93	0.26	0.04	0.18	30.41	1.10	8.8	0.46	5.3	172	W	c	1
0536262-051830	F21-ap187	13.41	1.01	0.32	0.31	0.85	22.00	0.96	7.7	0.43	10.7	206	W	c	2
0536269-052505	F22-ap155	11.70	1.38	0.38	-0.02	0.18	36.51	0.45	17.2	0.69	1.6	133	N	d	1
0536269-045506	S2-ap134	14.03	1.00	0.39	0.42	0.92	27.16	2.16	4.5	0.28	18.4	388	C	c	1
0536275-053055	F22-ap169	11.91	1.14	0.40	0.25	0.70	25.63	0.33	21.0	0.80	20.2	419	C	c	2
0536276-054221	F31-ap139	12.70	1.06	0.31	0.08	0.00	30.51	1.20	7.8	0.54	4.5	165	W-	c	2
0536278-062536	F31-ap209	12.93	0.89	0.27	0.14	0.61	25.48	0.53	16.9	0.69	8.8	211	W	c	1
0536281-052417	F22-ap159	12.76	1.01	0.27	0.09	-0.03	35.42	0.85	9.9	0.57	2.0	148	W	c	1
0536289-051443	F22-ap135	11.79	0.91	0.26	0.11	0.06	20.63	3.04	9.4	0.64	5.7	218	W	w	1
0536292-045351	F11-ap184	12.66	0.91	0.23	0.13	0.43	26.92	0.49	17.5	0.68	5.3	142	W+	c	1
0536294-061544	F31-ap196	13.24	0.81	0.28	0.08	0.05	15.64	0.59	13.0	0.57	0.0	0	NS	c	1
0536297-052006	F21-ap196	12.18	1.06	0.32	0.08	0.12	27.19	0.66	20.0	0.85	2.3	178	NSW	c	1
0536301-055309	F31-ap149	12.90	0.89	0.29	0.09	0.00	8.75	0.57	12.7	0.54	4.9	137	W	c	1
0536316-052635	F21-ap208	12.92	0.92	0.25	0.04	0.19	24.66	0.43	20.7	0.74	9.9	189	W	c	1
0536321-051713	S2-ap161	12.32	1.66	0.66	0.38	0.97	27.73	0.90	11.5	0.63	17.4	523	C	c	1
0536328-061237	F31-ap188	11.96	0.92	0.22	0.07	0.08	26.51	0.68	21.8	0.83	2.6	150	W	c	1
0536329-060229	F31-ap164	13.42	0.92	0.21	0.00	0.00	23.84	5.88	5.7	0.51	6.3	259	WC	w	1
0536336-055112	S3-ap205	14.47	1.15	0.46	0.40	0.58	13.14	1.17	6.3	0.32	2.0	345	CW	c	1
0536340-053405	F21-ap217	13.25	0.92	0.26	0.00	0.00	25.29	8.76	3.7	0.41	14.0	271	CD	w	1
0536343-054054	F22-ap171	13.25	0.91	0.34	0.00	0.00	–	–	3.2	0.32	5.1	193	W	c	1
0536360-051135	F22-ap136	12.52	0.61	0.23	0.00	0.00	22.79	2.32	6.3	0.48	0.0	0	AE	c	2
0536363-053634	F21-ap211	12.22	0.93	0.26	0.00	0.00	25.27	2.90	10.6	0.71	6.8	273	WC	w	1
0536365-061425	F31-ap185	12.95	0.86	0.23	0.05	0.06	26.80	0.37	22.2	0.76	3.2	122	W+	c	1
0536368-060955	F31-ap173	13.47	0.86	0.21	0.02	-0.02	24.71	0.67	16.0	0.68	1.9	129	W-	c	1
0536368-053419	F22-ap161	12.89	0.85	0.25	0.00	0.00	41.89	0.40	19.7	0.69	1.1	148	W-	c	1
0536372-052625	F21-ap204	11.64	1.26	0.47	0.00	0.00	28.18	0.49	16.3	0.71	66.6	468	C	c	1
0536373-051022	F21-ap177	13.33	0.94	0.27	0.00	0.00	27.63	0.35	14.2	0.56	7.8	135	W+	c,dv	2
0536381-053710	F22-ap178	13.29	1.22	0.36	0.00	0.00	28.23	0.64	11.9	0.53	6.4	210	W	c	1
0536393-063011	F31-ap207	13.34	0.88	0.22	0.08	0.62	21.27	0.43	17.0	0.60	10.2	240	C	c	1
0536394-051919	F22-ap148	11.80	0.85	0.27	0.00	0.00	54.11	0.48	16.5	0.60	3.7	156	WD	c	1
0536397-054026	F22-ap175	12.61	0.98	0.37	0.00	0.00	27.81	1.11	11.3	0.60	7.1	374	C	c	1
0536398-043751	F11-ap158	12.61	0.91	0.22	0.00	0.00	21.87	0.36	21.8	0.76	1.4	152	W	c	1
0536399-052123	F21-ap200	12.56	0.95	0.29	0.00	0.00	26.04	0.38	20.1	0.71	6.0	168	W+	c	1
0536399-052512	F22-ap157	13.39	1.22	0.39	0.00	0.00	75.46	4.62	3.2	0.22	3.7	171	W	l,n	1
0536400-051223	F22-ap140	12.48	1.26	0.41	0.00	0.00	27.73	0.41	20.1	0.74	3.1	307	CW	c	1

Table 12.4 (cont'd)

2MASS_id	ID	J	$(J-H)$	$(H-K)$	[3.6 – 4.5]	[5.8 – 8.0]	V_{rad}	ΔV_{rad}	R	S	EW_c	$FW_{10\%}$	$H\alpha$	CCF	NOB
0536403-061333	F31-ap190	12.20	0.92	0.23	0.06	0.52	24.18	0.28	30.4	0.84	7.6	236	W	c	1
0536404-051755	F22-ap142	12.47	1.22	0.28	0.00	0.00	28.18	0.41	17.7	0.70	0.0	0	AE	c	1
0536409-055802	F31-ap157	12.17	0.85	0.26	0.00	0.00	36.41	4.56	6.0	0.51	0.0	0	AE	w	1
0536427-053411	F21-ap220	11.79	1.14	0.28	0.00	0.00	26.72	1.05	21.1	0.83	8.3	284	CD	c	1
0536437-061528	F31-ap183	13.03	0.93	0.28	0.23	0.82	26.61	0.43	18.2	0.67	0.0	0	W+	c	1
0536445-060209	F31-ap166	13.41	0.85	0.26	0.00	0.00	23.83	2.48	8.7	0.55	5.1	160	W+	c	1
0536452-062809	F31-ap206	12.15	0.92	0.27	0.04	0.08	20.37	0.80	16.3	0.70	6.2	260	WC	c	1
0536471-052250	F21-ap195	12.77	0.90	0.27	0.00	0.00	33.23	1.77	9.6	0.51	4.8	249	NSW	s	1
0536475-060820	F31-ap177	13.05	0.93	0.23	0.06	-0.10	23.81	0.36	21.3	0.72	7.9	178	W+	c	1
0536476-052050	F22-ap145	12.87	1.21	0.45	0.00	0.00	29.49	1.37	13.5	0.67	2.9	205	W	c	1
0536476-053631	F22-ap172	11.88	1.19	0.28	0.00	0.00	28.61	0.45	22.5	0.80	12.0	346	C	c	1
0536482-052257	F22-ap154	12.83	0.85	0.26	0.00	0.00	8.92	0.45	15.5	0.64	4.6	210	W	c	1
0536483-051416	F21-ap182	13.01	0.90	0.29	0.00	0.00	18.94	4.70	6.1	0.47	11.4	310	CW	w	1
0536494-045748	F11-ap187	12.70	0.93	0.24	0.00	0.00	21.50	2.73	6.2	0.43	0.0	0	AE	c	1
0536496-050409	F11-ap197	12.16	1.34	0.44	0.00	0.00	20.48	0.29	20.8	0.75	11.9	238	C	c	2
0536507-053747	F22-ap174	12.62	0.94	0.24	0.00	0.00	26.22	5.62	6.4	0.59	5.4	233	W	c	1
0536518-050835	F22-ap132	12.16	1.30	0.46	0.00	0.00	32.01	0.36	24.0	0.81	7.9	243	CW	c	1
0536538-062053	F31-ap199	13.36	0.94	0.21	0.11	0.12	23.44	0.51	18.0	0.69	2.0	140	N	c	1
0536542-053218	F21-ap203	12.81	1.62	0.41	0.00	0.00	27.54	1.36	7.6	0.37	9.5	294	C	c	1
0536542-061945	F31-ap198	12.76	0.91	0.28	0.09	0.15	25.52	0.40	21.2	0.75	3.6	129	W+	c	1
0536552-062025	F31-ap200	13.00	0.92	0.22	0.09	1.22	20.90	0.42	19.4	0.72	12.1	345	C	c	1
0536554-060639	F31-ap176	12.99	0.89	0.30	0.00	0.00	30.88	6.95	3.8	0.32	0.0	0	AE	w,l	1
0536572-050604	F11-ap195	12.01	1.29	0.43	0.00	0.00	27.75	0.39	24.4	0.82	2.5	246	C	c	1
0536573-061845	F31-ap192	13.11	0.85	0.28	0.04	0.03	17.16	0.73	13.7	0.62	3.0	129	N	c	1
0536591-053425	F21-ap214	11.93	1.14	0.30	0.00	0.00	30.20	0.76	21.5	0.82	5.3	251	WD	c	1
0537001-051411	F21-ap184	13.11	1.00	0.26	0.00	0.00	32.97	0.78	10.2	0.56	0.0	0	WD	c	1
0537003-052508	F22-ap160	13.15	1.11	0.42	0.00	0.00	26.81	0.67	10.4	0.48	24.3	380	C	c	1
0537032-052136	F22-ap143	13.23	1.20	0.37	0.00	0.00	19.09	2.10	6.7	0.44	0.0	0	W-	c	1
0537039-061640	F31-ap187	13.37	0.90	0.23	0.09	-0.05	24.78	0.52	16.6	0.69	0.0	0	W+	c	1
0537057-044721	F11-ap172	13.12	0.95	0.30	0.00	0.00	27.71	8.44	5.7	0.38	12.4	476	C	w	1
0537062-050002	F11-ap185	13.33	0.93	0.28	0.00	0.00	22.11	0.40	18.2	0.64	6.0	146	W+	c	1
0537064-055357	F31-ap159	13.49	0.87	0.24	0.00	0.00	23.68	0.63	14.0	0.60	0.0	0	W+	c	1
0537090-051712	F21-ap185	11.98	1.26	0.38	0.00	0.00	29.41	4.77	7.3	0.53	4.8	330	CW	w	1
0537091-051931	F21-ap194	12.73	1.20	0.31	0.00	0.00	35.55	0.40	17.6	0.69	1.4	210	WD	c	1
0537188-060941	F31-ap175	12.09	0.95	0.23	0.00	0.00	26.69	0.32	27.6	0.84	3.1	229	W	c	1
0537190-061448	F31-ap184	13.45	0.70	0.20	0.00	0.00	23.87	10.80	4.3	0.28	0.0	0	AE	w,l	1

Note. — Hectochelle targets in ONC found to be members based on measured RV value or by detected Hα emission. The criteria of beeing RV member is to have at least one velocity measurement within 4σ of the cluster mean velocity: 13.7 km s^{-1} $<$ $V_{helio} <$ 38.5 km s^{-1} . RV members listed only with $R > 2$, while stars with Hα emission are included regardless of R value, but with no velocity displayed.)

2MASS id — 2MASS identification number (truncated RA and DEC coordiantes as: HHMMSSS+DDMMSS); **ID** — internal identification number, specifying the field (see Table 9.1) and aperture of observation; **J** — 2MASS J magnitude; **(J-H)** — 2MASS $(J-H)$ color index; **(H-K)** — 2MASS $(H-K)$ color index; 3.6 – 4.5 — IRAC short wavelength color index; 5.8 – 8.0 — IRAC long wavelength color index; V_{rad} — measured heliocentric radial velocity, in km s^{-1}; V_{rad} — *xcsao* error estimate for V_{rad}, in km s^{-1}; **R** — R value of cross correlation (see text for details); **S** — height of the CCF peak; EW_c — absolute value of equivalent width, measured on the corrected Hα profile (see text for details); $FW_{10\%}$ — full width of Hα profile at 10% level of the corrected maximum (see text for details);

Hα — notes on the Hα emission profile. See text for more details on the CTTS/WTTS classification: **C** – CTTS; **W** – WTTS; **CW** – rather CTTS, but could be WTTS; **WC** – rather WTTS, but could be CTTS; **W+** – assymetry in line profile/wing: likley WTTS; **W-** – assymetry in wings, but wings at low intensity: could be

Table 12.5. ONC non-members — *full table*

2MASS_id	ID	J	$(J-H)$	$(H-K)$	$[3.6-4.5]$	$[5.8-8.0]$	V_{rad}	ΔV_{rad}	R	S	EW_c	$FW_{10\%}$	$H\alpha$	CCF	NOB
0533283-045549	F11-ap48	13.27	0.89	0.24	0.04	0.03	-22.07	0.94	8.9	0.46	0.0	0	AE	c	1
0533289-050930	F22-ap46	12.16	1.04	0.30	0.05	0.37	106.39	0.53	13.2	0.61	0.0	0	R	c	1
0533298-052735	F21-ap66	13.31	0.88	0.25	0.02	0.53	-20.75	0.47	19.2	0.74	0.0	0	AE	c	1
0533333-043918	F11-ap67	12.89	0.91	0.27	0.00	0.00	-6.00	0.62	11.5	0.49	0.0	0	AE	c	1
0533363-050140	F11-ap35	13.29	0.80	0.21	0.00	0.00	–	–	2.1	0.17	0.0	0	AE	w,l	1
0533390-055434	F31-ap72	12.59	1.62	0.40	-0.02	0.04	73.01	0.38	19.7	0.70	0.0	0	AE	c	1
0533415-050934	F22-ap50	13.19	0.96	0.24	0.08	-0.03	-11.32	0.81	9.8	0.58	0.0	0	AE	c	1
0533445-045930	F11-ap31	12.62	1.05	0.23	-0.07	0.11	12.70	0.34	20.5	0.72	0.0	0	AE	c	1
0533497-043329	F11-ap73	13.47	0.98	0.25	0.00	0.00	46.59	0.89	7.4	0.34	0.0	0	AE	c	1
0533514-043655	F11-ap78	13.37	1.25	0.34	0.00	0.00	-6.63	10.17	2.9	0.22	0.0	0	AE	d,l	1
0533520-050655	F21-ap93	12.76	0.92	0.27	0.02	-0.06	-9.05	0.38	12.7	0.56	0.0	0	N	c	2
0533524-044400	F11-ap64	12.12	1.20	0.30	-0.01	0.17	-5.25	0.34	21.6	0.72	0.0	0	AE	c	1
0533570-054210	F22-ap235	12.08	1.66	0.44	-0.08	0.16	112.78	0.46	15.2	0.68	0.0	0	R	c	1
0533579-060524	F31-ap53	13.10	0.80	0.24	0.06	0.04	38.64	0.76	10.1	0.60	0.0	0	AE	c	1
0534018-055941	F31-ap69	13.17	1.24	0.32	0.00	0.12	70.32	0.37	19.2	0.71	0.0	0	AE	c	1
0534040-061329	F31-ap44	12.70	0.80	0.20	0.01	0.17	4.17	0.57	15.1	0.75	0.0	0	AE	c	1
0534057-062851	F31-ap22	11.77	1.31	0.38	0.00	0.00	113.63	0.41	18.0	0.68	0.0	0	R	c	1
0534071-054925	F31-ap82	13.17	1.12	0.35	0.02	-0.11	38.22	0.75	10.3	0.49	0.0	0	AE	c	1
0534073-043231	F11-ap82	12.86	0.91	0.29	0.00	0.00	-13.51	0.74	10.3	0.49	0.0	0	AE	c	1
0534080-060924	F31-ap41	13.46	1.03	0.29	0.01	0.10	1.20	0.45	18.9	0.74	0.0	0	AE	c	1
0534095-050111	F11-ap21	13.18	1.01	0.25	0.04	-0.14	-4.65	0.60	10.3	0.57	0.0	0	AE	c,dv	2
0534098-042819	F11-ap87	12.08	0.69	0.21	0.00	0.00	53.92	0.60	13.4	0.67	0.0	0	AE	c	1
0534104-051020	F22-ap54	12.97	0.95	0.31	0.06	0.43	-40.46	0.91	8.4	0.53	0.0	0	R	c	1
0534154-060655	F31-ap60	13.42	0.88	0.23	0.04	0.11	49.42	0.40	19.1	0.66	0.0	0	AE	c	1
0534174-051035	F22-ap56	13.38	1.48	0.47	0.12	0.11	6.62	2.01	4.3	0.29	0.0	0	N	c	1
0534177-055543	F31-ap75	12.38	1.19	0.36	0.09	0.07	6.49	0.93	7.6	0.45	0.0	0	AE	c	1
0534196-050229	F22-ap68	12.92	1.33	0.41	0.06	0.17	42.09	0.61	8.5	0.51	0.0	0	AE	c	2
0534215-051013	F22-ap57	12.97	1.12	0.29	0.00	0.35	3.70	1.19	6.1	0.39	0.0	0	AE	d	1
0534242-042439	F11-ap100	13.08	0.60	0.21	0.00	0.00	3.82	0.45	16.6	0.69	0.0	0	AE	c	1
0534246-062137	F31-ap28	12.60	1.16	0.34	0.05	0.07	5.46	0.55	13.3	0.52	0.0	0	AE	c	1
0534250-060103	F31-ap63	12.11	0.55	0.21	0.00	0.16	-10.55	13.96	4.6	0.40	0.0	0	AE	w	1
0534252-061442	F31-ap35	13.04	0.83	0.24	0.05	0.08	-24.43	0.76	10.4	0.56	0.0	0	AE	c	1
0534282-055909	F31-ap79	12.64	0.69	0.27	0.06	0.05	-41.27	1.12	8.0	0.52	0.0	0	R	c	1
0534334-044332	F11-ap72	12.64	1.22	0.33	0.04	0.06	-48.83	0.83	9.6	0.52	0.0	0	R	c	1
0534370-043310	F11-ap94	12.65	1.41	0.35	0.00	0.00	-0.00	0.50	14.7	0.60	0.0	0	AE	c	1
0534381-050457	F22-ap63	12.35	1.04	0.26	0.02	0.06	56.88	0.37	19.9	0.72	0.0	0	AE	c	1
0534452-044758	F11-ap51	12.44	1.36	0.36	0.03	0.18	44.48	0.70	10.4	0.52	0.0	0	AE	d?	1
0534462-043009	F11-ap93	12.95	0.93	0.20	0.00	0.00	4.40	0.47	15.3	0.60	0.0	0	AE	c	1
0534469-053503	S3-ap47	13.93	1.26	0.42	0.00	0.00	13.16	1.18	5.6	0.28	9.1	138	NS	c	1
0534568-063209	F31-ap4	13.38	0.84	0.28	0.04	0.02	61.58	3.96	7.2	0.36	0.0	0	AE	w	1
0535050-043733	F11-ap104	12.54	0.85	0.22	0.00	0.00	-3.39	0.38	17.9	0.63	0.0	0	AE	c	1
0535096-043311	F11-ap107	12.02	0.85	0.24	0.00	0.00	5.12	0.42	17.9	0.65	0.0	0	N	c	1
0535099-043154	F11-ap103	12.18	1.21	0.23	0.00	0.00	41.34	0.40	17.9	0.76	0.0	0	AE	c	1

Table 12.5 (cont'd)

2MASS_id	ID	J	$(J-H)$	$(H-K)$	$[3.6-4.5]$	$[5.8-8.0]$	V_{rad}	ΔV_{rad}	R	S	EW_c	$FW_{10\%}$	$H\alpha$	CCF	NOB
0535158-063710	F31-ap235	12.62	1.37	0.36	-0.01	0.07	67.35	0.48	15.0	0.62	0.0	0	AE	c	1
0535162-054720	F31-ap103	12.65	0.89	0.22	0.05	0.33	81.45	0.57	12.3	0.60	0.0	0	R	c	1
0535167-051901	S1-ap82	14.36	3.25	1.24	0.40	0.00	–	–	2.4	0.19	64.4	131	NS	u,r	1
0535200-054552	F22-ap210	12.99	0.85	0.23	0.05	0.38	-11.19	3.59	6.2	0.45	0.0	0	AE	c	1
0535234-063341	F31-ap240	12.59	1.13	0.34	0.00	0.03	42.20	1.01	7.3	0.54	0.0	0	AE	c	1
0535241-043103	F11-ap115	11.63	0.81	0.27	0.00	0.00	52.07	0.62	12.3	0.62	0.0	0	AE	c	1
0535247-060459	F31-ap118	12.99	0.86	0.21	0.03	0.12	-32.95	0.34	22.2	0.71	0.0	0	AE	c	1
0535313-053309	S3-ap184	8.80	1.16	0.61	0.38	1.43	40.61	8.04	7.5	0.62	–	–	X	w	1
0535369-044610	F11-ap152	12.65	0.84	0.26	0.02	0.10	-12.07	0.46	16.6	0.68	0.0	0	AE	c	1
0535393-044734	F11-ap168	12.59	0.82	0.24	0.05	0.32	81.31	0.81	11.3	0.58	0.0	0	R	c	1
0535394-061602	F31-ap215	13.27	0.88	0.21	-0.05	0.09	84.09	0.84	10.4	0.69	0.0	0	R	c	1
0535396-063211	F31-ap225	12.43	1.16	0.36	0.04	0.09	-2.76	0.46	17.3	0.68	0.0	0	AE	c	1
0535404-063554	F31-ap223	12.08	1.26	0.30	0.02	0.12	80.75	0.34	21.9	0.73	0.0	0	R	c	1
0535406-051219	F21-ap155	12.97	1.05	0.29	0.08	–	–	–	2.4	0.21	3.6	109	NS	w,l	1
0535437-043549	F11-ap121	12.90	1.70	0.43	0.00	0.00	1.71	0.67	11.0	0.53	0.0	0	AE	c	1
0535510-043238	F11-ap132	13.49	0.96	0.24	0.00	0.00	12.73	0.50	16.2	0.69	0.0	0	AE	c	1
0535547-051055	F22-ap111	13.26	0.81	0.21	0.04	0.20	39.89	0.80	10.4	0.61	0.0	0	AE	c	1
0535549-051315	F21-ap165	12.42	0.82	0.21	0.04	0.51	65.04	0.73	9.9	0.52	0.0	0	AE	c	1
0535572-043203	F11-ap138	11.76	0.69	0.25	0.00	0.00	1.65	0.94	9.1	0.56	0.0	0	AE	c	1
0536049-054800	F31-ap134	12.26	1.64	0.47	-0.05	0.10	40.02	0.51	10.3	0.63	0.0	0	AE	c	2
0536059-043701	F11-ap142	12.82	0.84	0.26	0.00	0.00	40.92	0.95	8.2	0.51	0.0	0	AE	c	1
0536071-060325	F31-ap153	12.57	1.62	0.46	-0.04	0.15	83.50	0.46	16.1	0.61	0.0	0	R	c	1
0536075-060024	F31-ap152	12.26	0.97	0.34	0.08	0.06	-3.83	14.74	3.5	0.32	0.0	0	AE	n	1
0536088-060430	F31-ap168	12.07	1.23	0.34	0.00	0.08	66.92	0.33	21.6	0.77	0.0	0	AE	c	1
0536101-060120	F31-ap160	13.32	0.98	0.27	0.05	0.11	76.37	2.41	3.2	0.18	0.0	0	AE	n	1
0536162-060522	F31-ap165	13.25	1.11	0.29	0.04	0.10	41.51	1.04	7.4	0.45	0.0	0	AE	c	1
0536163-044642	F11-ap169	12.09	0.82	0.22	0.05	0.18	-16.94	1.25	8.4	0.51	0.0	0	AE	c	1
0536164-045758	F22-ap114	12.96	1.55	0.43	-0.07	-0.05	46.35	0.42	11.7	0.60	0.0	0	AE	d?,dv	2
0536181-050345	F22-ap113	12.56	0.73	0.20	0.02	-0.08	5.39	9.06	3.9	0.33	0.0	0	AE	w,l	2
0536218-051732	F21-ap190	12.70	1.41	0.35	-0.02	0.04	91.07	0.53	13.1	0.59	0.0	0	R	c	1
0536235-060636	F31-ap174	12.26	0.89	0.20	0.04	0.08	-23.65	0.53	14.1	0.66	0.0	0	AE	c	1
0536280-051110	F22-ap121	13.41	0.94	0.23	-0.02	0.28	-12.10	0.31	28.6	0.81	0.0	0	AE	c	1
0536283-052142	F22-ap141	12.22	1.04	0.35	0.07	0.05	3.08	2.67	3.2	0.27	0.0	0	AE	c	1
0536285-043359	F11-ap150	13.30	1.65	0.42	0.00	0.00	66.14	0.82	8.1	0.39	0.0	0	AE	d?	1
0536295-043957	F11-ap159	12.55	1.11	0.22	0.00	0.00	-14.91	0.36	19.4	0.75	0.0	0	AE	c	1
0536326-055108	F31-ap146	12.96	0.87	0.20	0.06	0.06	69.56	0.32	28.0	0.81	0.0	0	AE	c	1
0536347-043425	F11-ap147	12.71	1.24	0.35	0.00	0.00	54.73	0.95	7.2	0.37	0.0	0	AE	c	1
0536365-044406	F11-ap164	12.99	1.31	0.32	0.00	0.00	80.61	0.47	15.0	0.61	0.0	0	R	c	1
0536385-051239	F21-ap171	12.59	1.01	0.20	0.00	0.00	83.94	0.53	13.2	0.68	0.0	0	R	c	1
0536402-055139	F31-ap147	12.44	0.98	0.23	0.00	0.00	-8.64	0.36	20.5	0.74	0.0	0	AE	c	1
0536409-055336	F31-ap143	11.74	1.27	0.29	0.00	0.00	56.64	0.30	24.7	0.77	0.0	0	AE	c	1
0536424-061023	F31-ap171	13.13	1.45	0.40	0.02	0.13	6.65	0.66	11.3	0.51	0.0	0	AE	c	1
0536438-055342	F31-ap141	13.37	1.04	0.25	0.00	0.00	46.36	0.41	16.7	0.70	0.0	0	AE	c	1

Table 12.5 (cont'd)

2MASS_id	ID	J	$(J-H)$	$(H-K)$	[3.6 – 4.5]	[5.8 – 8.0]	V_{rad}	ΔV_{rad}	R	S	EW_c	$FW_{10\%}$	$H\alpha$	CCF	NOB
0536446-051607	F21-ap188	11.87	1.04	0.27	0.00	0.00	80.92	0.40	18.3	0.76	0.0	0	R	c	1
0536493-044905	F11-ap176	12.79	1.08	0.21	0.00	0.00	-8.76	0.35	20.8	0.73	0.0	0	AE	c	1
0536527-045000	F11-ap179	12.32	1.13	0.35	0.00	0.00	51.28	0.42	16.9	0.69	0.0	0	AE	c	1
0536545-044419	F11-ap170	11.67	1.13	0.24	0.00	0.00	-4.75	0.42	17.1	0.70	0.0	0	AE	c	1
0536556-043211	F11-ap141	13.22	1.01	0.28	0.00	0.00	–	–	3.2	0.18	0.0	0	N	w,l	1
0536557-060428	F31-ap163	13.49	0.83	0.20	0.00	0.00	83.38	0.64	12.3	0.66	0.0	0	R	c	1
0536566-050852	F22-ap134	13.30	0.86	0.23	0.00	0.00	0.99	0.68	12.2	0.67	0.0	0	AE	c	1
0536592-043516	F11-ap160	12.78	1.11	0.32	0.00	0.00	5.52	0.65	10.7	0.51	0.0	0	AE	c	1
0536592-050029	F11-ap183	11.87	1.32	0.23	0.00	0.00	232.48	0.31	22.7	0.76	0.0	0	R	c	1
0537005-050931	F22-ap138	12.51	1.03	0.25	0.00	0.00	438.70	0.96	14.4	0.72	0.0	0	R	c	1
0537040-051901	F21-ap192	12.44	0.81	0.22	0.00	0.00	-31.71	0.54	13.9	0.64	0.0	0	AE	c	1
0537069-061336	F31-ap182	12.72	1.37	0.35	0.00	0.07	-55.54	0.37	19.1	0.67	0.0	0	R	c	1
0537086-044942	F11-ap180	13.31	0.77	0.26	0.00	0.00	41.57	0.80	10.2	0.56	0.0	0	AE	c	1
0537100-045037	F11-ap177	12.35	1.10	0.29	0.00	0.00	53.46	0.28	25.8	0.78	0.0	0	AE	c	1
0537111-060503	F31-ap161	12.96	1.26	0.29	0.00	0.00	54.82	0.40	17.7	0.67	0.0	0	AE	c	1
0537111-055946	F31-ap162	12.34	1.03	0.28	0.00	0.00	-147.19	0.28	25.1	0.79	0.0	0	R	c	1
0537151-044455	F11-ap167	13.07	0.99	0.30	0.00	0.00	47.06	0.51	13.6	0.61	0.0	0	AE	c	1
0537182-060532	F31-ap172	12.16	1.53	0.40	0.00	0.00	51.92	0.29	24.8	0.79	0.0	0	AE	c	1

Note. — Hectochelle targets in ONC found to be non-members based on measured RV value or lack of detected Hα emission. Stars are listed regardless of R value, but no velocity is displayed in case of very low R or undefined CCF.

2MASS id — 2MASS identification number (truncated RA and DEC coordiantes as: HHMMSSS+DDMMSS); **ID** — internal identification number, specifying the field (see Table 9.1) and aperture of observation; **J** — 2MASS J magnitude; **(J-H)** — 2MASS $(J-H)$ color index; **(H-K)** — 2MASS $(H-K)$ color index; $3.6-4.5$ — IRAC short wavelength color index; $5.8-8.0$ — IRAC long wavelength color index; V_{rad} — measured heliocentric radial velocity, in km s^{-1}; V_{rad} — *xcsao* error estimate for V_{rad}, in km s^{-1}; **R** — R value of cross correlation (see text for details); **S** — height of the CCF peak; EW_c — absolute value of equivalent width, measured on the corrected Hα profile (see text for details); $FW_{10\%}$ — full width of Hα profile at 10% level of the corrected maximum (see text for details);

Hα — notes on the Hα emission profile: **D** — resolved or unresolved double gaussian profile, no excess H-alpha emission (likley non-TTS); **R** — obviously shifted H-alpha absorption : high RV stars; **X** — very wide H-alpha absorption with nebular emissions; **AE** — stellar absorption and nebular emission together; **NS** — very strong nebular component component, no wings, no asymmetry; **CCF** — notes on the cross-correlation function: **w** – wide peak, results large errors in RV; **l** – very low peak, but still sticks out from surrounding; **u** – almost undefined, very low/wide peak; **n** – very noisy (several local peaks, almost as high as the one picked); **s** – side lobed, could be a spectroscopic binary; **d** – double peak, spectroscopic binary; **dv** – RV measured more than once, found different velocities, could be binary; **r** – template spectra with highest peak in cross-correlation resulted non-realistic velocity, so the template resulting in highest R value was used instead to determine velocity; **c** – clear, well-isolated peak; **?** – uncertainty in assigning the given note;

NOB — number of observations

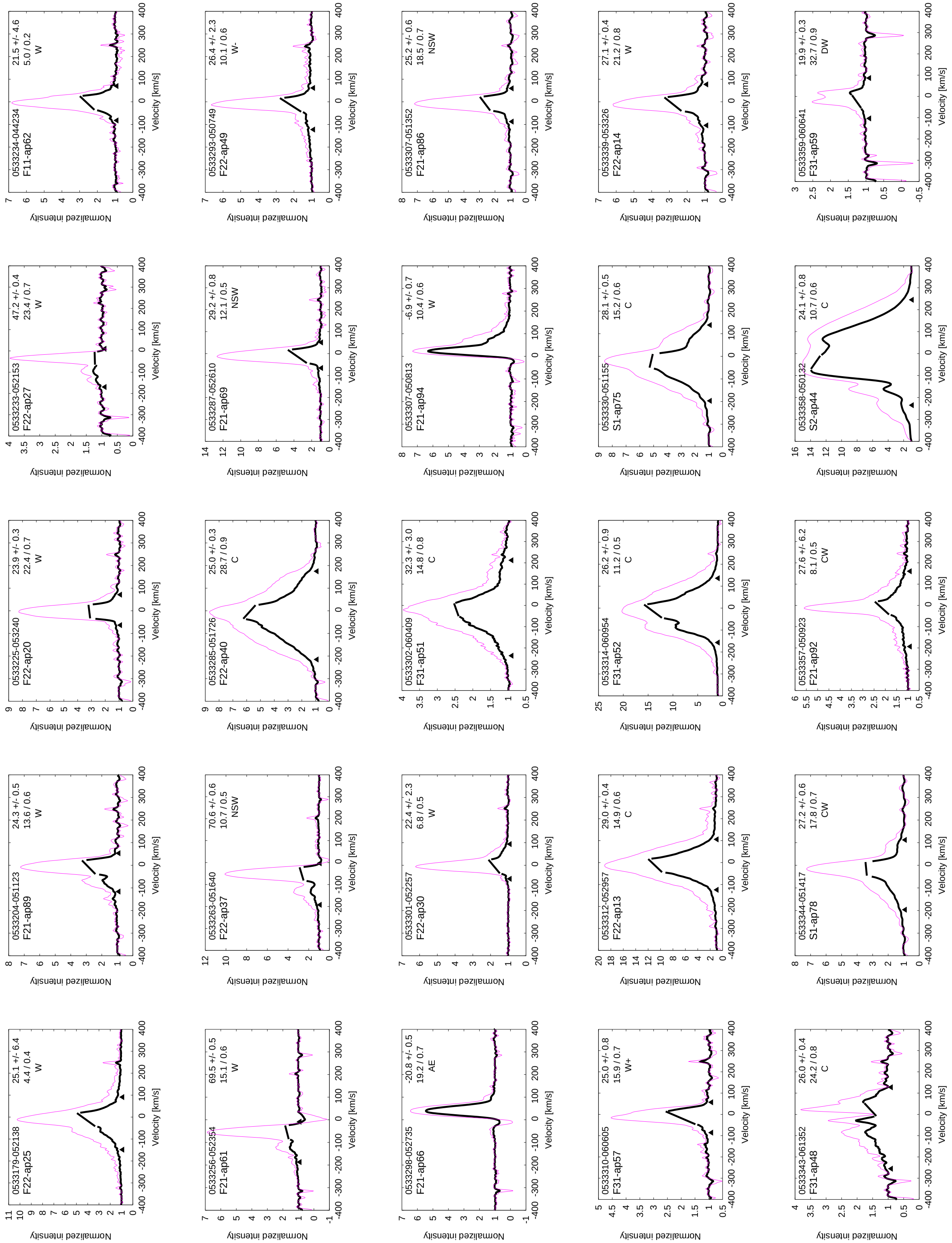

Figure 12.3: *Hα* ***profiles for stars with detected emission in the ONC sample.*** *See Fig. 9.8 and §9.3.2 for more details.*

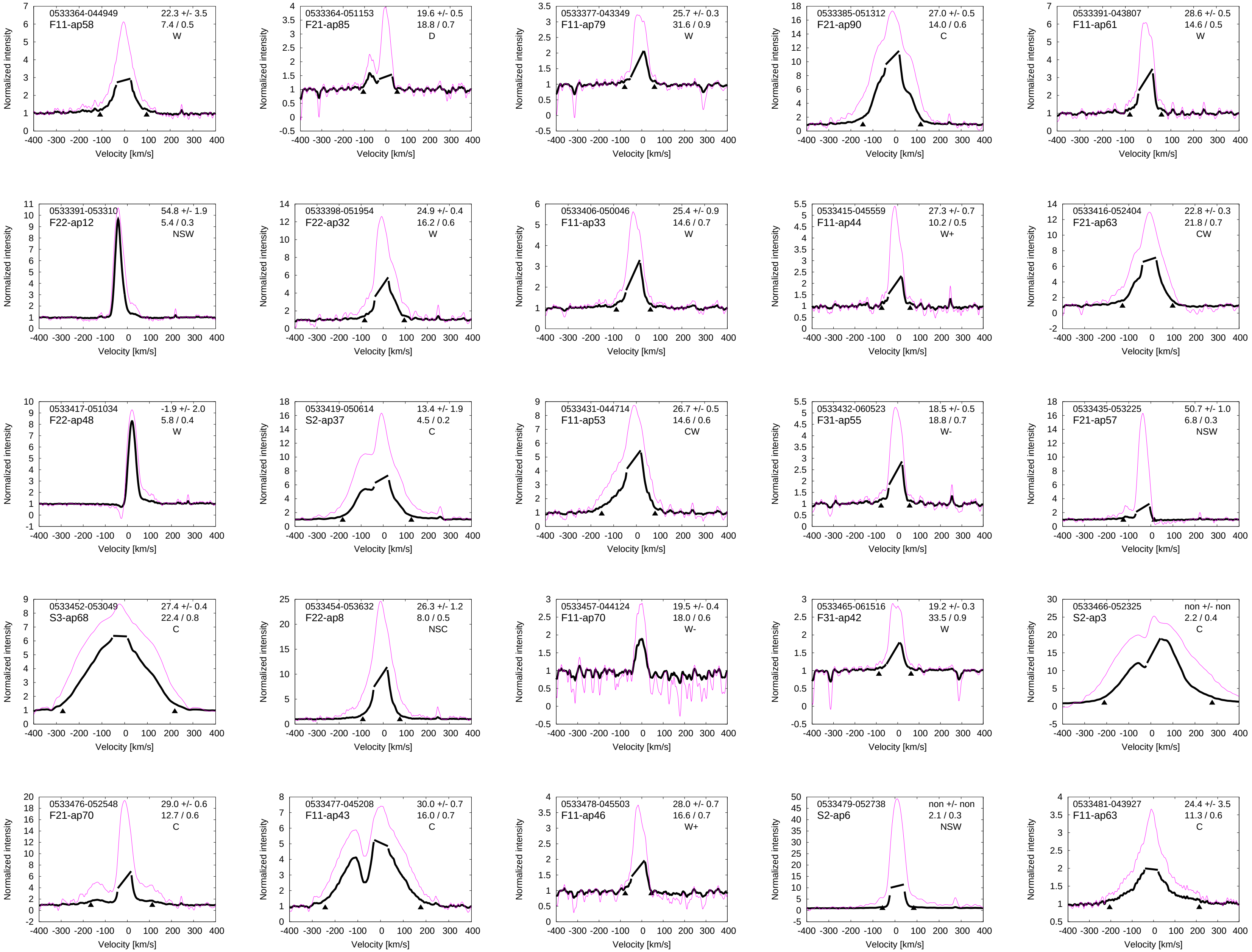
0533364-044949
F11-ap58
22.3 +/- 3.5
7.4 / 0.5
W
0533364-051153
F21-ap85
19.6 +/- 0.5
18.8 / 0.7
D
0533377-043349
F11-ap79
25.7 +/- 0.3
31.6 / 0.9
W
0533385-051312
F21-ap90
27.0 +/- 0.5
14.0 / 0.6
C
0533391-043807
F11-ap61
28.6 +/- 0.5
14.6 / 0.5
W
0533391-053310
F22-ap12
54.8 +/- 1.9
5.4 / 0.3
NSW
0533398-051954
F22-ap32
24.9 +/- 0.4
16.2 / 0.6
W
0533406-050046
F11-ap33
25.4 +/- 0.9
14.6 / 0.7
W
0533415-045559
F11-ap44
27.3 +/- 0.7
10.2 / 0.5
W+
0533416-052404
F21-ap63
22.8 +/- 0.3
21.8 / 0.7
CW
0533417-051034
F22-ap48
-1.9 +/- 2.0
5.8 / 0.4
W
0533419-050614
S2-ap37
13.4 +/- 1.9
4.5 / 0.2
C
0533431-044714
F11-ap53
26.7 +/- 0.5
14.6 / 0.6
CW
0533432-060523
F31-ap55
18.5 +/- 0.5
18.8 / 0.7
W-
0533435-053225
F21-ap57
50.7 +/- 1.0
6.8 / 0.3
NSW
0533452-053049
S3-ap68
27.4 +/- 0.4
22.4 / 0.8
C
0533454-053632
F22-ap8
26.3 +/- 1.2
8.0 / 0.5
NSC
0533457-044124
F11-ap70
19.5 +/- 0.4
18.0 / 0.6
W-
0533465-061516
F31-ap42
19.2 +/- 0.3
33.5 / 0.9
W
0533466-052325
S2-ap3
non +/- non
2.2 / 0.4
C
0533476-052548
F21-ap70
29.0 +/- 0.6
12.7 / 0.6
C
0533477-045208
F11-ap43
30.0 +/- 0.7
16.0 / 0.7
C
0533478-045503
F11-ap46
28.0 +/- 0.7
16.6 / 0.7
W+
0533479-052738
S2-ap6
non +/- non
2.1 / 0.3
NSW
0533481-043927
F11-ap63
24.4 +/- 3.5
11.3 / 0.6
C
Normalized intensity
Velocity [km/s]
-400 -300 -200 -100 0 100 200 300 400

Fig. 12.3 cont.

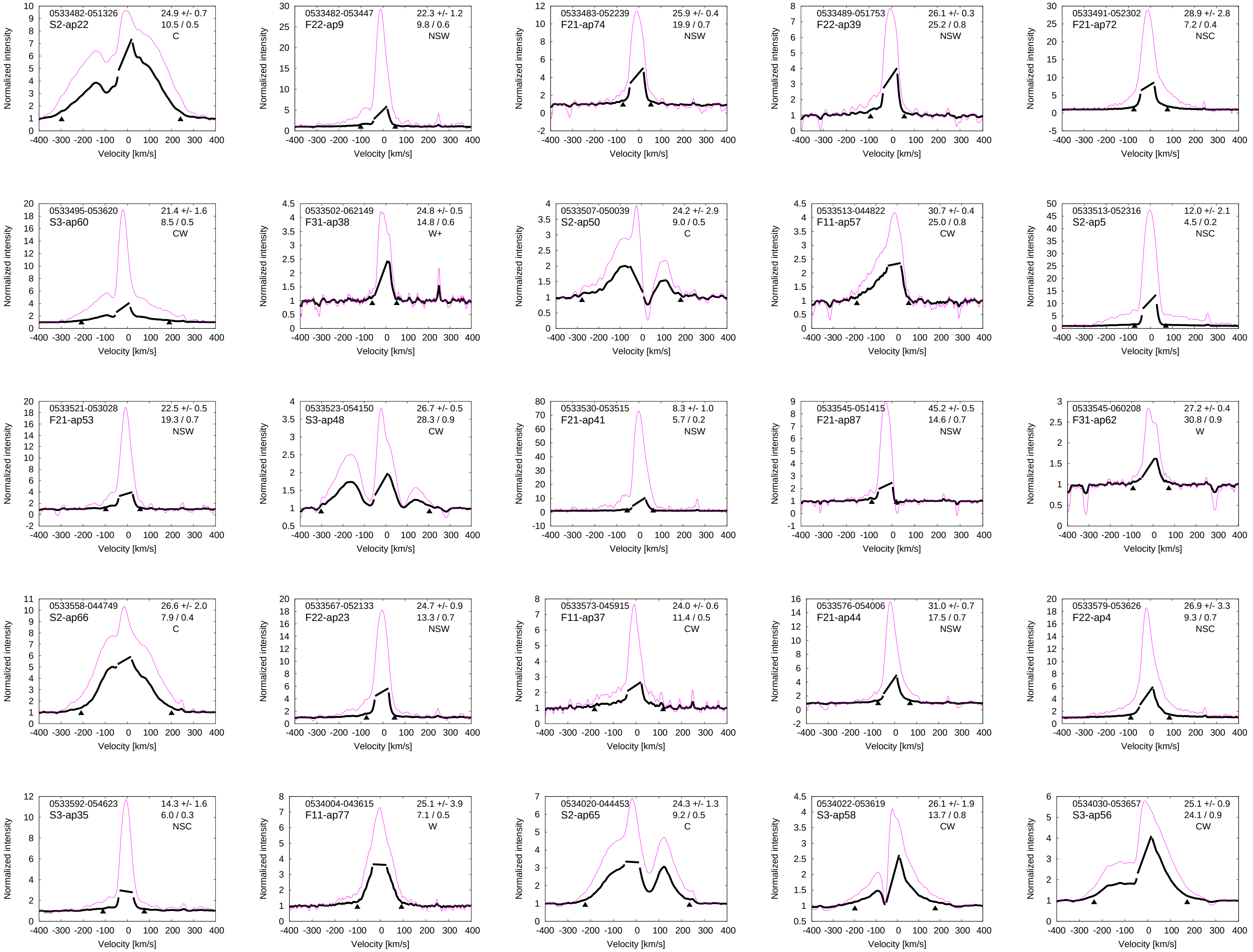
0533482-051326 S2-ap22 24.9 +/- 0.7 10.5 / 0.5 C
0533482-053447 F22-ap9 22.3 +/- 1.2 9.8 / 0.6 NSW
0533483-052239 F21-ap74 25.9 +/- 0.4 19.9 / 0.7 NSW
0533489-051753 F22-ap39 26.1 +/- 0.3 25.2 / 0.8 NSW
0533491-052302 F21-ap72 28.9 +/- 2.8 7.2 / 0.4 NSC
0533495-053620 S3-ap60 21.4 +/- 1.6 8.5 / 0.5 CW
0533502-062149 F31-ap38 24.8 +/- 0.5 14.8 / 0.6 W+
0533507-050039 S2-ap50 24.2 +/- 2.9 9.0 / 0.5 C
0533513-044822 F11-ap57 30.7 +/- 0.4 25.0 / 0.8 CW
0533513-052316 S2-ap5 12.0 +/- 2.1 4.5 / 0.2 NSC
0533521-053028 F21-ap53 22.5 +/- 0.5 19.3 / 0.7 NSW
0533523-054150 S3-ap48 26.7 +/- 0.5 28.3 / 0.9 CW
0533530-053515 F21-ap41 8.3 +/- 1.0 5.7 / 0.2 NSW
0533545-051415 F21-ap87 45.2 +/- 0.5 14.6 / 0.7 NSW
0533545-060208 F31-ap62 27.2 +/- 0.4 30.8 / 0.9 W
0533558-044749 S2-ap66 26.6 +/- 2.0 7.9 / 0.4 C
0533567-052133 F22-ap23 24.7 +/- 0.9 13.3 / 0.7 NSW
0533573-045915 F11-ap37 24.0 +/- 0.6 11.4 / 0.5 CW
0533576-054006 F21-ap44 31.0 +/- 0.7 17.5 / 0.7 NSW
0533579-053626 F22-ap4 26.9 +/- 3.3 9.3 / 0.7 NSC
0533592-054623 S3-ap35 14.3 +/- 1.6 6.0 / 0.3 NSC
0534004-043615 F11-ap77 25.1 +/- 3.9 7.1 / 0.5 W
0534020-044453 S2-ap65 24.3 +/- 1.3 9.2 / 0.5 C
0534022-053619 S3-ap58 26.1 +/- 1.9 13.7 / 0.8 CW
0534030-053657 S3-ap56 25.1 +/- 0.9 24.1 / 0.9 CW
Normalized intensity
Velocity [km/s]
-400 -300 -200 -100 0 100 200 300 400

Fig. 12.3 cont.

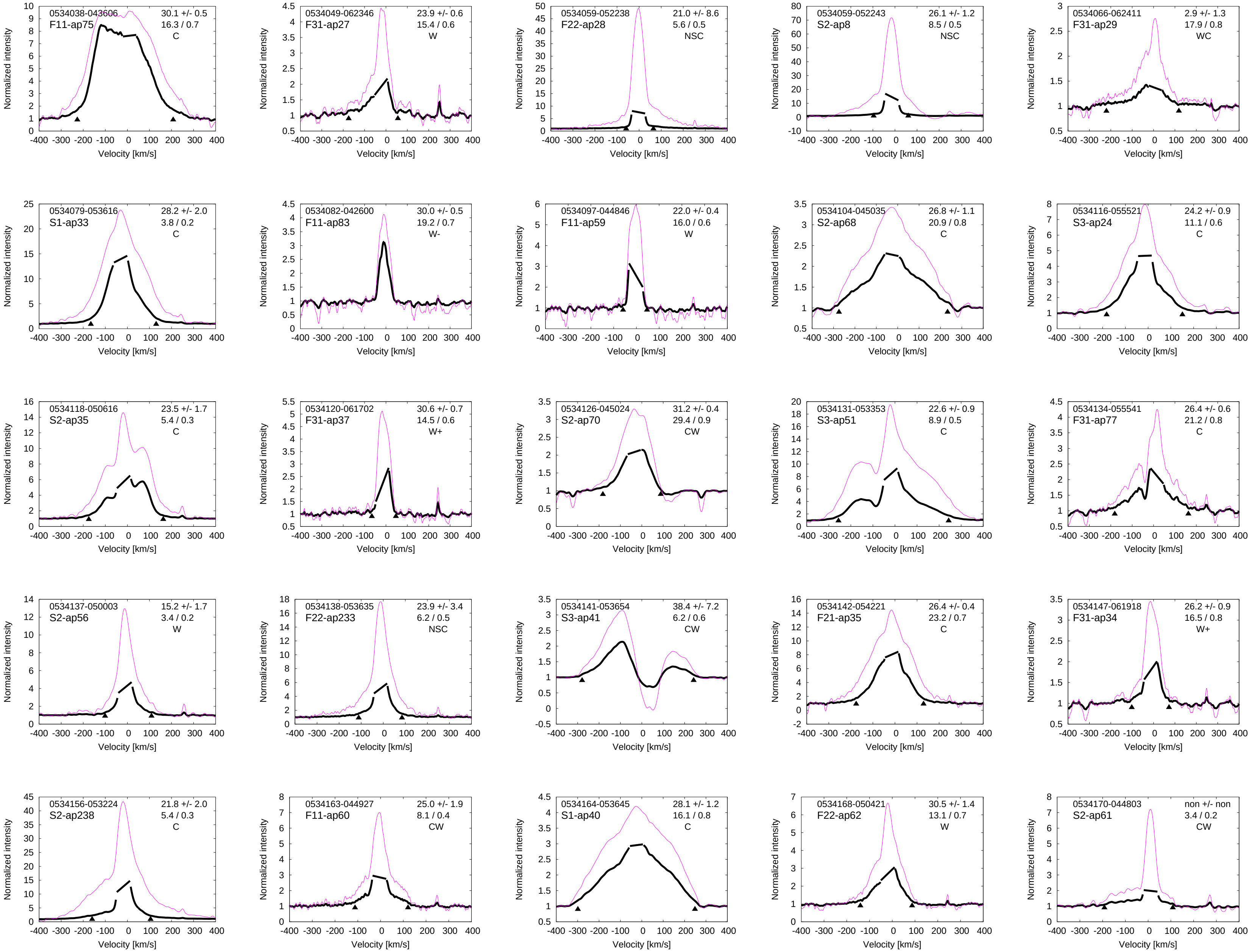
0534038-043606
F11-ap75
30.1 +/- 0.5
16.3 / 0.7
C
0534049-062346
F31-ap27
23.9 +/- 0.6
15.4 / 0.6
W
0534059-052238
F22-ap28
21.0 +/- 8.6
5.6 / 0.5
NSC
0534059-052243
S2-ap8
26.1 +/- 1.2
8.5 / 0.5
NSC
0534066-062411
F31-ap29
2.9 +/- 1.3
17.9 / 0.8
WC
0534079-053616
S1-ap33
28.2 +/- 2.0
3.8 / 0.2
C
0534082-042600
F11-ap83
30.0 +/- 0.5
19.2 / 0.7
W-
0534097-044846
F11-ap59
22.0 +/- 0.4
16.0 / 0.6
W
0534104-045035
S2-ap68
26.8 +/- 1.1
20.9 / 0.8
C
0534116-055521
S3-ap24
24.2 +/- 0.9
11.1 / 0.6
C
0534118-050616
S2-ap35
23.5 +/- 1.7
5.4 / 0.3
C
0534120-061702
F31-ap37
30.6 +/- 0.7
14.5 / 0.6
W+
0534126-045024
S2-ap70
31.2 +/- 0.4
29.4 / 0.9
CW
0534131-053353
S3-ap51
22.6 +/- 0.9
8.9 / 0.5
C
0534134-055541
F31-ap77
26.4 +/- 0.6
21.2 / 0.8
C
0534137-050003
S2-ap56
15.2 +/- 1.7
3.4 / 0.2
W
0534138-053635
F22-ap233
23.9 +/- 3.4
6.2 / 0.5
NSC
0534141-053654
S3-ap41
38.4 +/- 7.2
6.2 / 0.6
CW
0534142-054221
F21-ap35
26.4 +/- 0.4
23.2 / 0.7
C
0534147-061918
F31-ap34
26.2 +/- 0.9
16.5 / 0.8
W+
0534156-053224
S2-ap238
21.8 +/- 2.0
5.4 / 0.3
C
0534163-044927
F11-ap60
25.0 +/- 1.9
8.1 / 0.4
CW
0534164-053645
S1-ap40
28.1 +/- 1.2
16.1 / 0.8
C
0534168-050421
F22-ap62
30.5 +/- 1.4
13.1 / 0.7
W
0534170-044803
S2-ap61
non +/- non
3.4 / 0.2
CW
Normalized intensity
Velocity [km/s]
-400 -300 -200 -100 0 100 200 300 400

Fig. 12.3 cont.

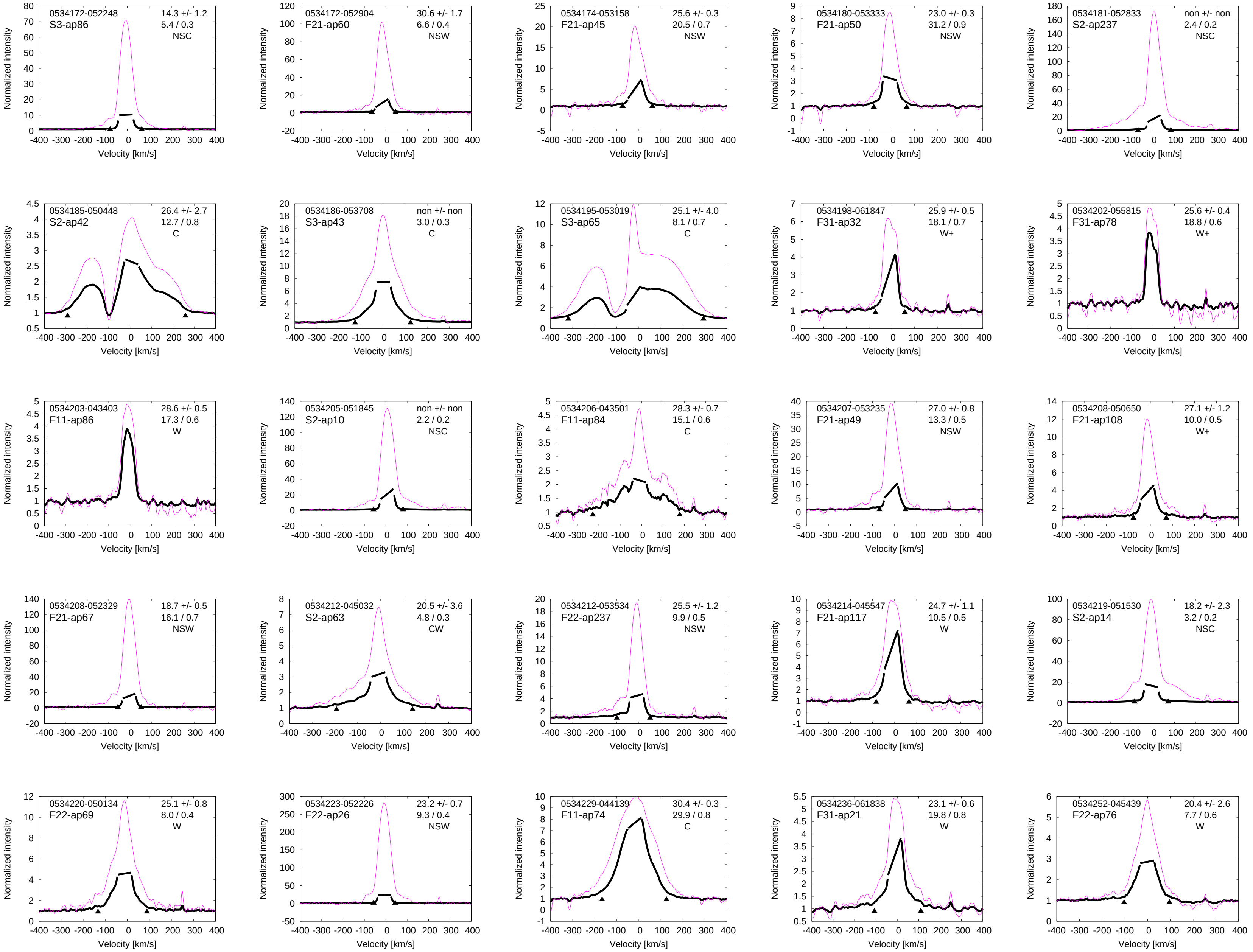
0534172-052248
S3-ap86
14.3 +/- 1.2
5.4 / 0.3
NSC
0534172-052904
F21-ap60
30.6 +/- 1.7
6.6 / 0.4
NSW
0534174-053158
F21-ap45
25.6 +/- 0.3
20.5 / 0.7
NSW
0534180-053333
F21-ap50
23.0 +/- 0.3
31.2 / 0.9
NSW
0534181-052833
S2-ap237
non +/- non
2.4 / 0.2
NSC
0534185-050448
S2-ap42
26.4 +/- 2.7
12.7 / 0.8
C
0534186-053708
S3-ap43
non +/- non
3.0 / 0.3
C
0534195-053019
S3-ap65
25.1 +/- 4.0
8.1 / 0.7
C
0534198-061847
F31-ap32
25.9 +/- 0.5
18.1 / 0.7
W+
0534202-055815
F31-ap78
25.6 +/- 0.4
18.8 / 0.6
W+
0534203-043403
F11-ap86
28.6 +/- 0.5
17.3 / 0.6
W
0534205-051845
S2-ap10
non +/- non
2.2 / 0.2
NSC
0534206-043501
F11-ap84
28.3 +/- 0.7
15.1 / 0.6
C
0534207-053235
F21-ap49
27.0 +/- 0.8
13.3 / 0.5
NSW
0534208-050650
F21-ap108
27.1 +/- 1.2
10.0 / 0.5
W+
0534208-052329
F21-ap67
18.7 +/- 0.5
16.1 / 0.7
NSW
0534212-045032
S2-ap63
20.5 +/- 3.6
4.8 / 0.3
CW
0534212-053534
F22-ap237
25.5 +/- 1.2
9.9 / 0.5
NSW
0534214-045547
F21-ap117
24.7 +/- 1.1
10.5 / 0.5
W
0534219-051530
S2-ap14
18.2 +/- 2.3
3.2 / 0.2
NSC
0534220-050134
F22-ap69
25.1 +/- 0.8
8.0 / 0.4
W
0534223-052226
F22-ap26
23.2 +/- 0.7
9.3 / 0.4
NSW
0534229-044139
F11-ap74
30.4 +/- 0.3
29.9 / 0.8
C
0534236-061838
F31-ap21
23.1 +/- 0.6
19.8 / 0.8
W
0534252-045439
F22-ap76
20.4 +/- 2.6
7.7 / 0.6
W
Normalized intensity
Velocity [km/s]
-400 -300 -200 -100 0 100 200 300 400

Fig. 12.3 cont.

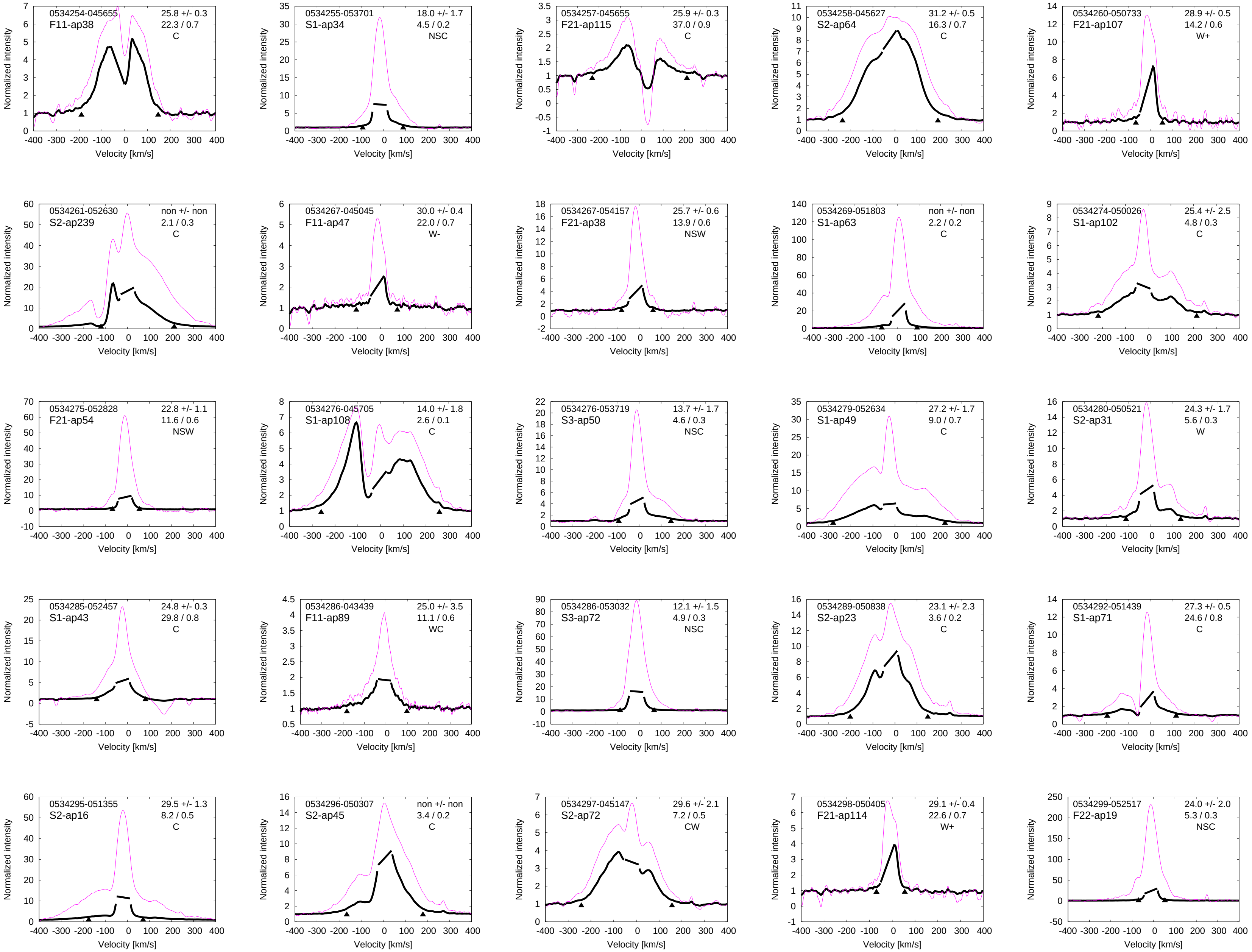
Normalized intensity
Velocity [km/s]
0534254-045655
F11-ap38
25.8 +/- 0.3
22.3 / 0.7
C
0534255-053701
S1-ap34
18.0 +/- 1.7
4.5 / 0.2
NSC
0534257-045655
F21-ap115
25.9 +/- 0.3
37.0 / 0.9
C
0534258-045627
S2-ap64
31.2 +/- 0.5
16.3 / 0.7
C
0534260-050733
F21-ap107
28.9 +/- 0.5
14.2 / 0.6
W+
0534261-052630
S2-ap239
non +/- non
2.1 / 0.3
C
0534267-045045
F11-ap47
30.0 +/- 0.4
22.0 / 0.7
W-
0534267-054157
F21-ap38
25.7 +/- 0.6
13.9 / 0.6
NSW
0534269-051803
S1-ap63
non +/- non
2.2 / 0.2
C
0534274-050026
S1-ap102
25.4 +/- 2.5
4.8 / 0.3
C
0534275-052828
F21-ap54
22.8 +/- 1.1
11.6 / 0.6
NSW
0534276-045705
S1-ap108
14.0 +/- 1.8
2.6 / 0.1
C
0534276-053719
S3-ap50
13.7 +/- 1.7
4.6 / 0.3
NSC
0534279-052634
S1-ap49
27.2 +/- 1.7
9.0 / 0.7
C
0534280-050521
S2-ap31
24.3 +/- 1.7
5.6 / 0.3
W
0534285-052457
S1-ap43
24.8 +/- 0.3
29.8 / 0.8
C
0534286-043439
F11-ap89
25.0 +/- 3.5
11.1 / 0.6
WC
0534286-053032
S3-ap72
12.1 +/- 1.5
4.9 / 0.3
NSC
0534289-050838
S2-ap23
23.1 +/- 2.3
3.6 / 0.2
C
0534292-051439
S1-ap71
27.3 +/- 0.5
24.6 / 0.8
C
0534295-051355
S2-ap16
29.5 +/- 1.3
8.2 / 0.5
C
0534296-050307
S2-ap45
non +/- non
3.4 / 0.2
C
0534297-045147
S2-ap72
29.6 +/- 2.1
7.2 / 0.5
CW
0534298-050405
F21-ap114
29.1 +/- 0.4
22.6 / 0.7
W+
0534299-052517
F22-ap19
24.0 +/- 2.0
5.3 / 0.3
NSC
-400 -300 -200 -100 0 100 200 300 400

Fig. 12.3 cont.

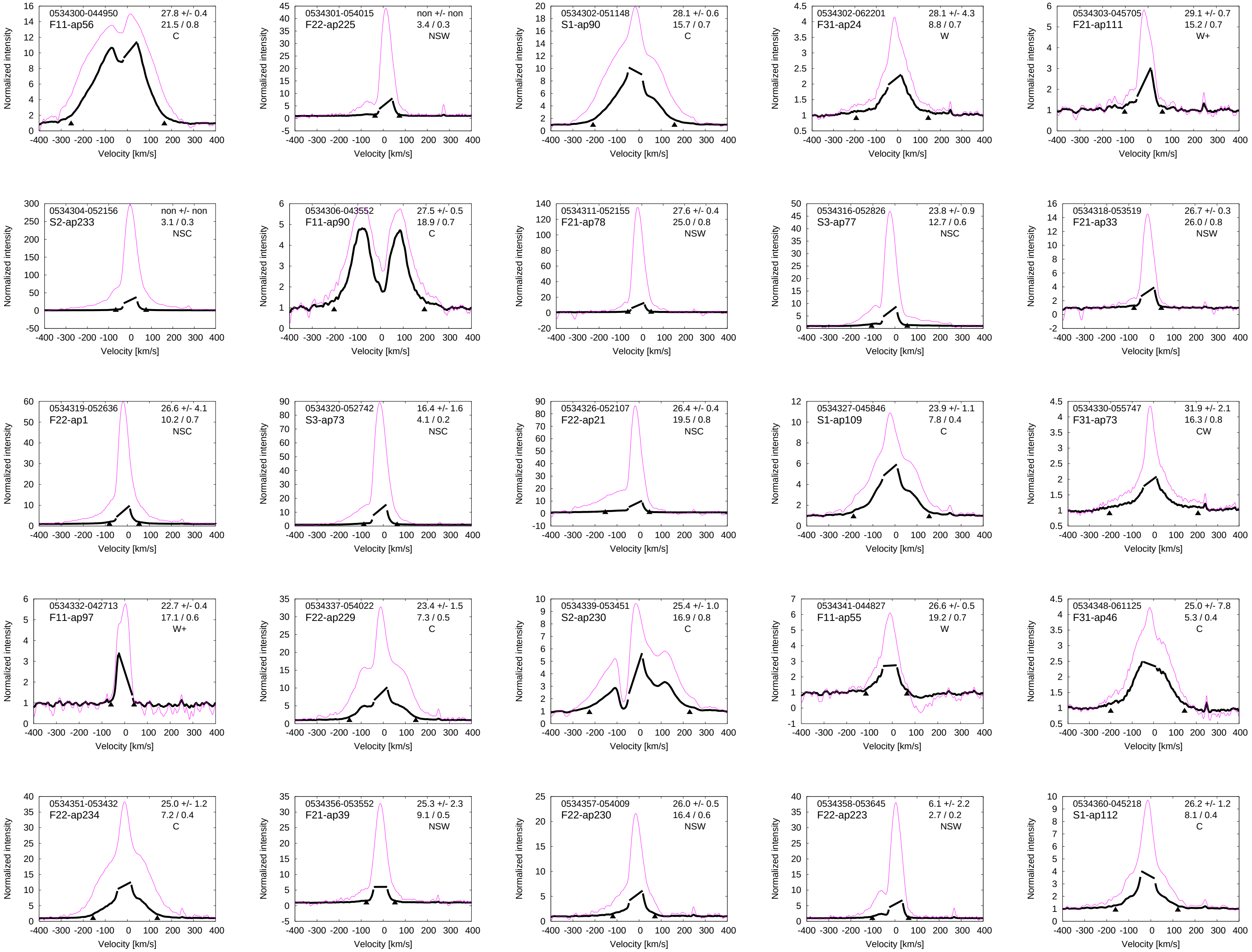
0534300-044950
F11-ap56
27.8 +/- 0.4
21.5 / 0.8
C
0534301-054015
F22-ap225
non +/- non
3.4 / 0.3
NSW
0534302-051148
S1-ap90
28.1 +/- 0.6
15.7 / 0.7
C
0534302-062201
F31-ap24
28.1 +/- 4.3
8.8 / 0.7
W
0534303-045705
F21-ap111
29.1 +/- 0.7
15.2 / 0.7
W+
0534304-052156
S2-ap233
non +/- non
3.1 / 0.3
NSC
0534306-043552
F11-ap90
27.5 +/- 0.5
18.9 / 0.7
C
0534311-052155
F21-ap78
27.6 +/- 0.4
25.0 / 0.8
NSW
0534316-052826
S3-ap77
23.8 +/- 0.9
12.7 / 0.6
NSC
0534318-053519
F21-ap33
26.7 +/- 0.3
26.0 / 0.8
NSW
0534319-052636
F22-ap1
26.6 +/- 4.1
10.2 / 0.7
NSC
0534320-052742
S3-ap73
16.4 +/- 1.6
4.1 / 0.2
NSC
0534326-052107
F22-ap21
26.4 +/- 0.4
19.5 / 0.8
NSC
0534327-045846
S1-ap109
23.9 +/- 1.1
7.8 / 0.4
C
0534330-055747
F31-ap73
31.9 +/- 2.1
16.3 / 0.8
CW
0534332-042713
F11-ap97
22.7 +/- 0.4
17.1 / 0.6
W+
0534337-054022
F22-ap229
23.4 +/- 1.5
7.3 / 0.5
C
0534339-053451
S2-ap230
25.4 +/- 1.0
16.9 / 0.8
C
0534341-044827
F11-ap55
26.6 +/- 0.5
19.2 / 0.7
W
0534348-061125
F31-ap46
25.0 +/- 7.8
5.3 / 0.4
C
0534351-053432
F22-ap234
25.0 +/- 1.2
7.2 / 0.4
C
0534356-053552
F21-ap39
25.3 +/- 2.3
9.1 / 0.5
NSW
0534357-054009
F22-ap230
26.0 +/- 0.5
16.4 / 0.6
NSW
0534358-053645
F22-ap223
6.1 +/- 2.2
2.7 / 0.2
NSW
0534360-045218
S1-ap112
26.2 +/- 1.2
8.1 / 0.4
C
Normalized intensity
Velocity [km/s]
-400 -300 -200 -100 0 100 200 300 400

Fig. 12.3 cont.

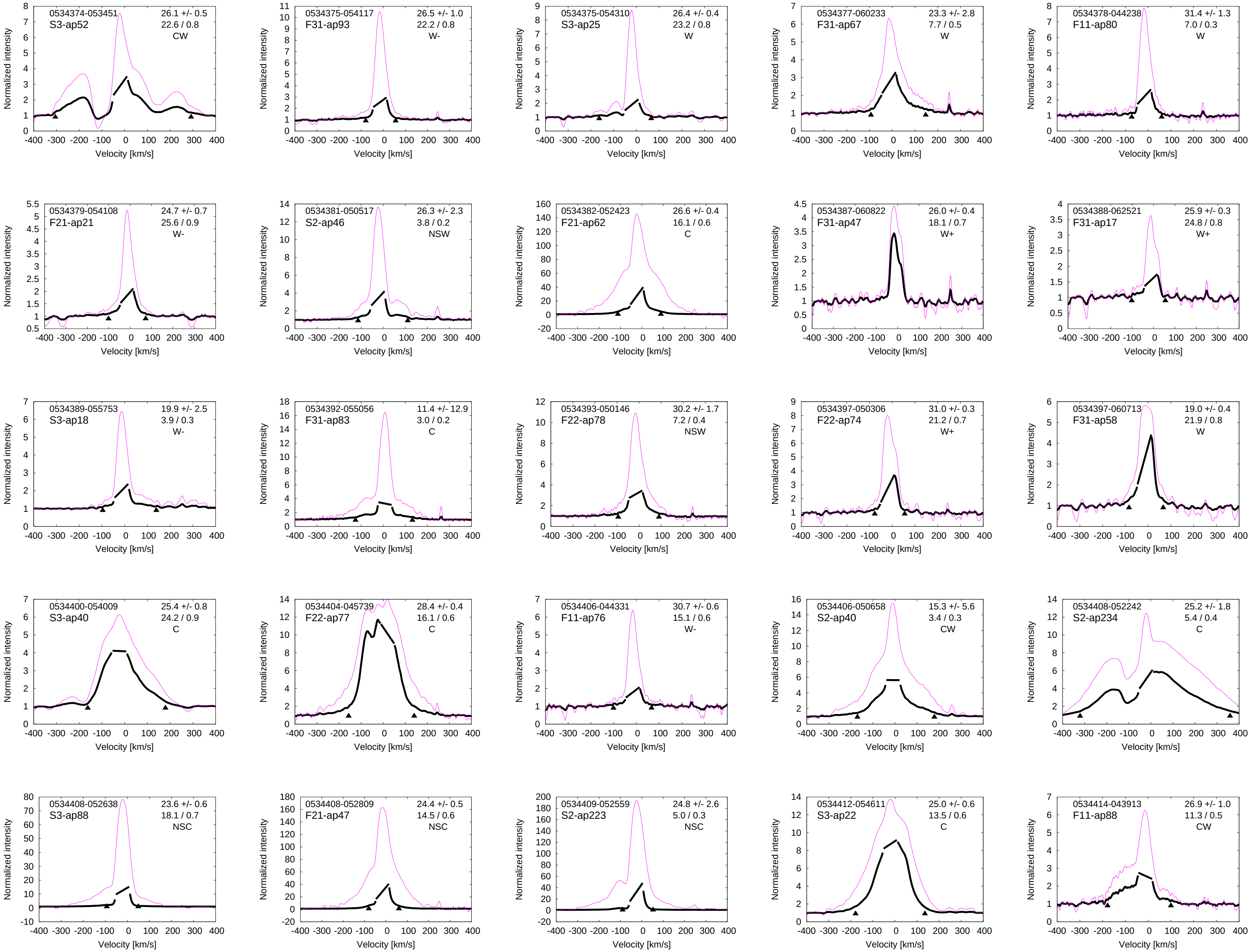
Normalized intensity
Velocity [km/s]
0534374-053451
S3-ap52
26.1 +/- 0.5
22.6 / 0.8
CW
0534375-054117
F31-ap93
26.5 +/- 1.0
22.2 / 0.8
W-
0534375-054310
S3-ap25
26.4 +/- 0.4
23.2 / 0.8
W
0534377-060233
F31-ap67
23.3 +/- 2.8
7.7 / 0.5
W
0534378-044238
F11-ap80
31.4 +/- 1.3
7.0 / 0.3
W
0534379-054108
F21-ap21
24.7 +/- 0.7
25.6 / 0.9
W-
0534381-050517
S2-ap46
26.3 +/- 2.3
3.8 / 0.2
NSW
0534382-052423
F21-ap62
26.6 +/- 0.4
16.1 / 0.6
C
0534387-060822
F31-ap47
26.0 +/- 0.4
18.1 / 0.7
W+
0534388-062521
F31-ap17
25.9 +/- 0.3
24.8 / 0.8
W+
0534389-055753
S3-ap18
19.9 +/- 2.5
3.9 / 0.3
W-
0534392-055056
F31-ap83
11.4 +/- 12.9
3.0 / 0.2
C
0534393-050146
F22-ap78
30.2 +/- 1.7
7.2 / 0.4
NSW
0534397-050306
F22-ap74
31.0 +/- 0.3
21.2 / 0.7
W+
0534397-060713
F31-ap58
19.0 +/- 0.4
21.9 / 0.8
W
0534400-054009
S3-ap40
25.4 +/- 0.8
24.2 / 0.9
C
0534404-045739
F22-ap77
28.4 +/- 0.4
16.1 / 0.6
C
0534406-044331
F11-ap76
30.7 +/- 0.6
15.1 / 0.6
W-
0534406-050658
S2-ap40
15.3 +/- 5.6
3.4 / 0.3
CW
0534408-052242
S2-ap234
25.2 +/- 1.8
5.4 / 0.4
C
0534408-052638
S3-ap88
23.6 +/- 0.6
18.1 / 0.7
NSC
0534408-052809
F21-ap47
24.4 +/- 0.5
14.5 / 0.6
NSC
0534409-052559
S2-ap223
24.8 +/- 2.6
5.0 / 0.3
NSC
0534412-054611
S3-ap22
25.0 +/- 0.6
13.5 / 0.6
C
0534414-043913
F11-ap88
26.9 +/- 1.0
11.3 / 0.5
CW
-400 -300 -200 -100 0 100 200 300 400

Fig. 12.3 cont.

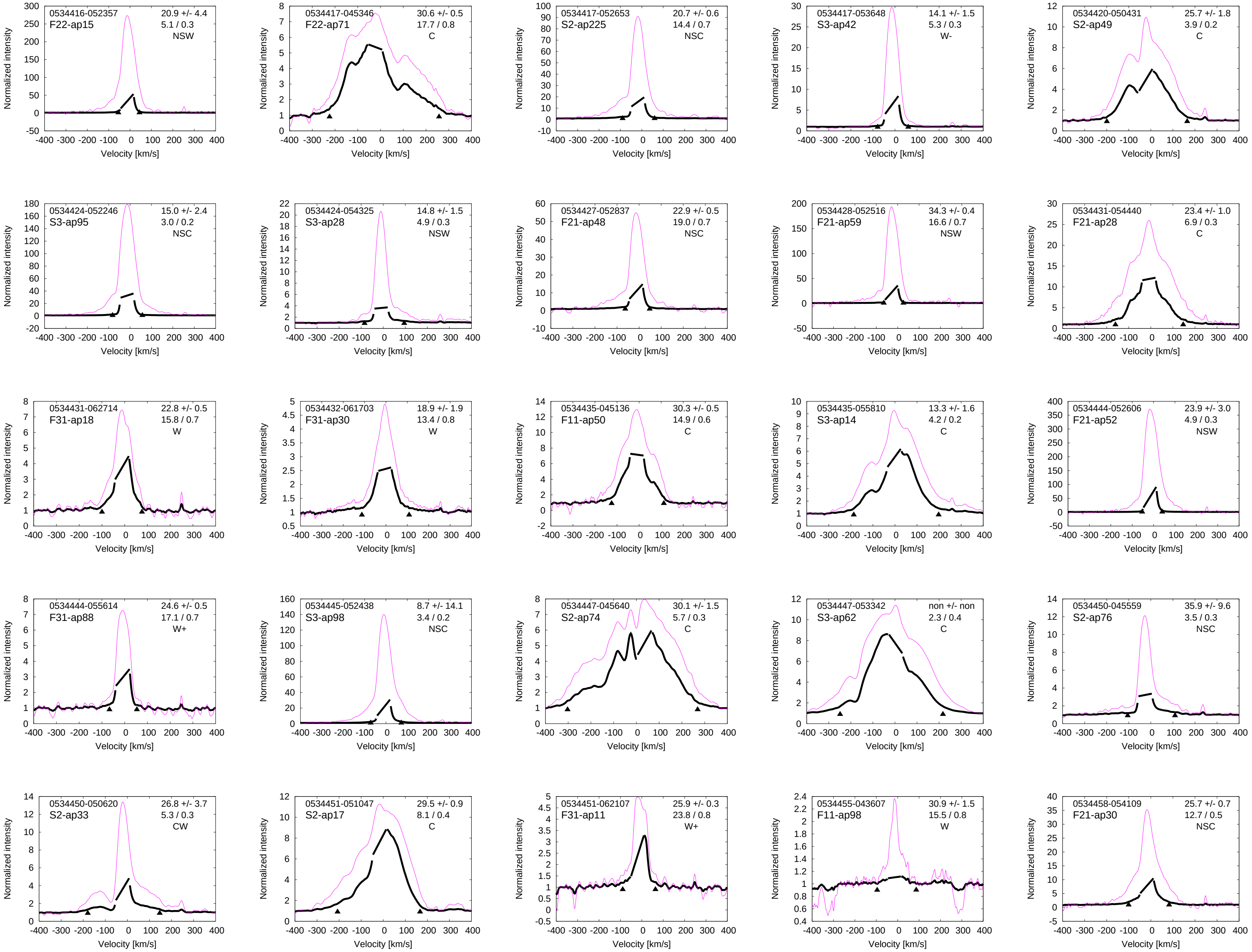
0534416-052357
F22-ap15
20.9 +/- 4.4
5.1 / 0.3
NSW
0534417-045346
F22-ap71
30.6 +/- 0.5
17.7 / 0.8
C
0534417-052653
S2-ap225
20.7 +/- 0.6
14.4 / 0.7
NSC
0534417-053648
S3-ap42
14.1 +/- 1.5
5.3 / 0.3
W-
0534420-050431
S2-ap49
25.7 +/- 1.8
3.9 / 0.2
C
0534424-052246
S3-ap95
15.0 +/- 2.4
3.0 / 0.2
NSC
0534424-054325
S3-ap28
14.8 +/- 1.5
4.9 / 0.3
NSW
0534427-052837
F21-ap48
22.9 +/- 0.5
19.0 / 0.7
NSC
0534428-052516
F21-ap59
34.3 +/- 0.4
16.6 / 0.7
NSW
0534431-054440
F21-ap28
23.4 +/- 1.0
6.9 / 0.3
C
0534431-062714
F31-ap18
22.8 +/- 0.5
15.8 / 0.7
W
0534432-061703
F31-ap30
18.9 +/- 1.9
13.4 / 0.8
W
0534435-045136
F11-ap50
30.3 +/- 0.5
14.9 / 0.6
C
0534435-055810
S3-ap14
13.3 +/- 1.6
4.2 / 0.2
C
0534444-052606
F21-ap52
23.9 +/- 3.0
4.9 / 0.3
NSW
0534444-055614
F31-ap88
24.6 +/- 0.5
17.1 / 0.7
W+
0534445-052438
S3-ap98
8.7 +/- 14.1
3.4 / 0.2
NSC
0534447-045640
S2-ap74
30.1 +/- 1.5
5.7 / 0.3
C
0534447-053342
S3-ap62
non +/- non
2.3 / 0.4
C
0534450-045559
S2-ap76
35.9 +/- 9.6
3.5 / 0.3
NSC
0534450-050620
S2-ap33
26.8 +/- 3.7
5.3 / 0.3
CW
0534451-051047
S2-ap17
29.5 +/- 0.9
8.1 / 0.4
C
0534451-062107
F31-ap11
25.9 +/- 0.3
23.8 / 0.8
W+
0534455-043607
F11-ap98
30.9 +/- 1.5
15.5 / 0.8
W
0534458-054109
F21-ap30
25.7 +/- 0.7
12.7 / 0.5
NSC
Normalized intensity
Velocity [km/s]
-400 -300 -200 -100 0 100 200 300 400

Fig. 12.3 cont.

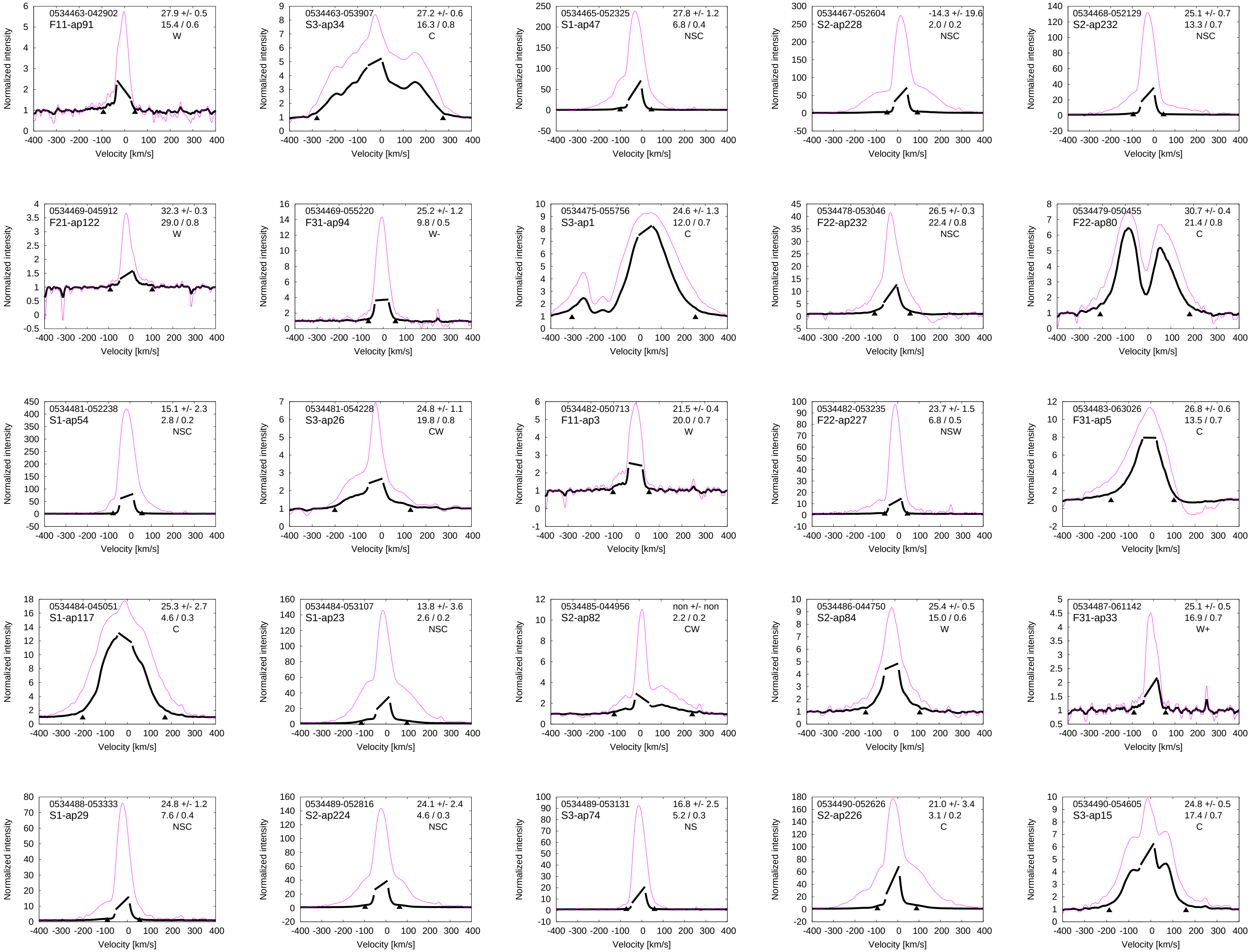
Normalized intensity
Velocity [km/s]
0534463-042902 F11-ap91 27.9 +/- 0.5 15.4 / 0.6 W
0534463-053907 S3-ap34 27.2 +/- 0.6 16.3 / 0.8 C
0534465-052325 S1-ap47 27.8 +/- 1.2 6.8 / 0.4 NSC
0534467-052604 S2-ap228 -14.3 +/- 19.6 2.0 / 0.2 NSC
0534468-052129 S2-ap232 25.1 +/- 0.7 13.3 / 0.7 NSC
0534469-045912 F21-ap122 32.3 +/- 0.3 29.0 / 0.8 W
0534469-055220 F31-ap94 25.2 +/- 1.2 9.8 / 0.5 W-
0534475-055756 S3-ap1 24.6 +/- 1.3 12.0 / 0.7 C
0534478-053046 F22-ap232 26.5 +/- 0.3 22.4 / 0.8 NSC
0534479-050455 F22-ap80 30.7 +/- 0.4 21.4 / 0.8 C
0534481-052238 S1-ap54 15.1 +/- 2.3 2.8 / 0.2 NSC
0534481-054228 S3-ap26 24.8 +/- 1.1 19.8 / 0.8 CW
0534482-050713 F11-ap3 21.5 +/- 0.4 20.0 / 0.7 W
0534482-053235 F22-ap227 23.7 +/- 1.5 6.8 / 0.5 NSW
0534483-063026 F31-ap5 26.8 +/- 0.6 13.5 / 0.7 C
0534484-045051 S1-ap117 25.3 +/- 2.7 4.6 / 0.3 C
0534484-053107 S1-ap23 13.8 +/- 3.6 2.6 / 0.2 NSC
0534485-044956 S2-ap82 non +/- non 2.2 / 0.2 CW
0534486-044750 S2-ap84 25.4 +/- 0.5 15.0 / 0.6 W
0534487-061142 F31-ap33 25.1 +/- 0.5 16.9 / 0.7 W+
0534488-053333 S1-ap29 24.8 +/- 1.2 7.6 / 0.4 NSC
0534489-052816 S2-ap224 24.1 +/- 2.4 4.6 / 0.3 NSC
0534489-053131 S3-ap74 16.8 +/- 2.5 5.2 / 0.3 NS
0534490-052626 S2-ap226 21.0 +/- 3.4 3.1 / 0.2 C
0534490-054605 S3-ap15 24.8 +/- 0.5 17.4 / 0.7 C
-400 -300 -200 -100 0 100 200 300 400

Fig. 12.3 cont.

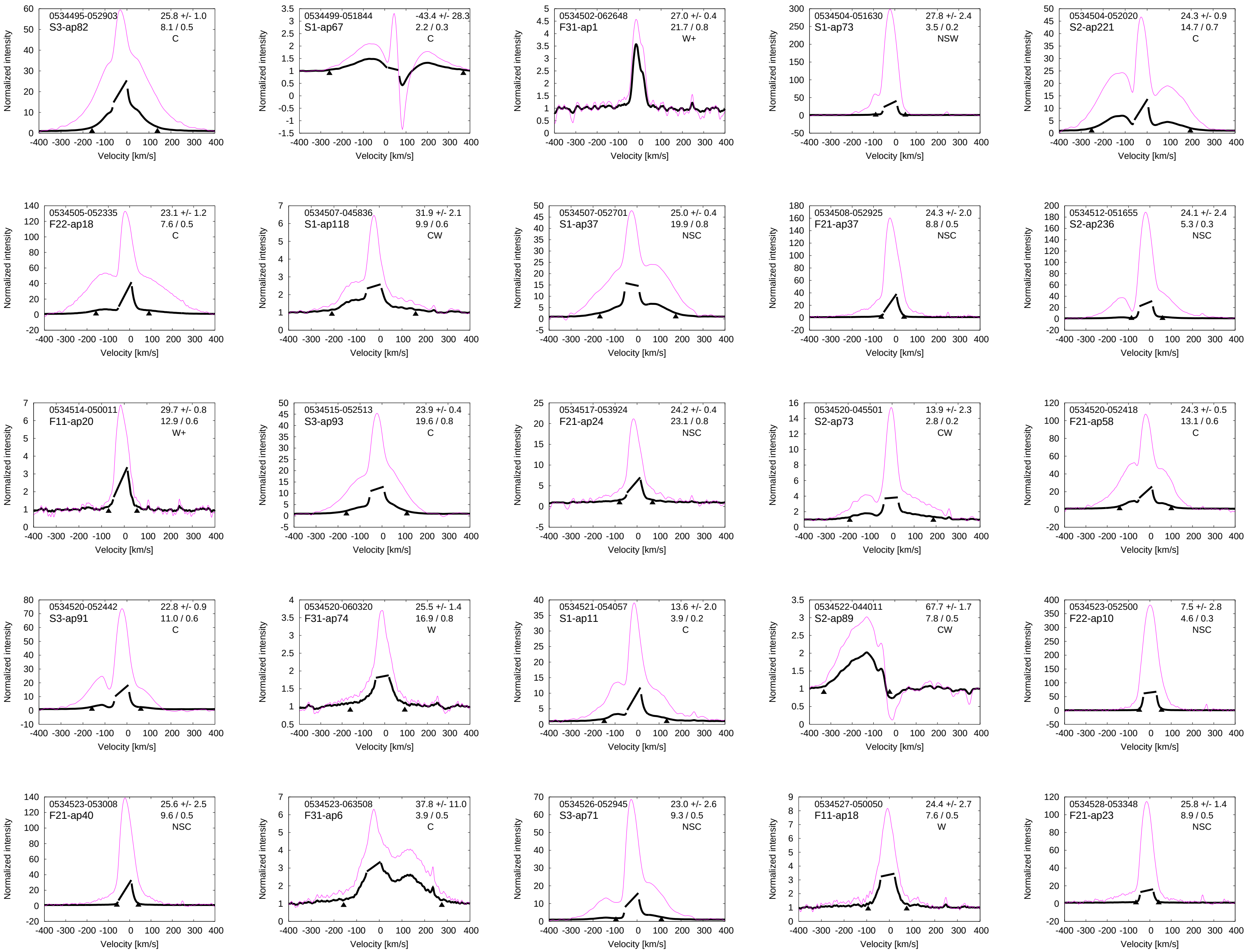
0534495-052903
S3-ap82
25.8 +/- 1.0
8.1 / 0.5
C
0534499-051844
S1-ap67
-43.4 +/- 28.3
2.2 / 0.3
C
0534502-062648
F31-ap1
27.0 +/- 0.4
21.7 / 0.8
W+
0534504-051630
S1-ap73
27.8 +/- 2.4
3.5 / 0.2
NSW
0534504-052020
S2-ap221
24.3 +/- 0.9
14.7 / 0.7
C
0534505-052335
F22-ap18
23.1 +/- 1.2
7.6 / 0.5
C
0534507-045836
S1-ap118
31.9 +/- 2.1
9.9 / 0.6
CW
0534507-052701
S1-ap37
25.0 +/- 0.4
19.9 / 0.8
NSC
0534508-052925
F21-ap37
24.3 +/- 2.0
8.8 / 0.5
NSC
0534512-051655
S2-ap236
24.1 +/- 2.4
5.3 / 0.3
NSC
0534514-050011
F11-ap20
29.7 +/- 0.8
12.9 / 0.6
W+
0534515-052513
S3-ap93
23.9 +/- 0.4
19.6 / 0.8
C
0534517-053924
F21-ap24
24.2 +/- 0.4
23.1 / 0.8
NSC
0534520-045501
S2-ap73
13.9 +/- 2.3
2.8 / 0.2
CW
0534520-052418
F21-ap58
24.3 +/- 0.5
13.1 / 0.6
C
0534520-052442
S3-ap91
22.8 +/- 0.9
11.0 / 0.6
C
0534520-060320
F31-ap74
25.5 +/- 1.4
16.9 / 0.8
W
0534521-054057
S1-ap11
13.6 +/- 2.0
3.9 / 0.2
C
0534522-044011
S2-ap89
67.7 +/- 1.7
7.8 / 0.5
CW
0534523-052500
F22-ap10
7.5 +/- 2.8
4.6 / 0.3
NSC
0534523-053008
F21-ap40
25.6 +/- 2.5
9.6 / 0.5
NSC
0534523-063508
F31-ap6
37.8 +/- 11.0
3.9 / 0.5
C
0534526-052945
S3-ap71
23.0 +/- 2.6
9.3 / 0.5
NSC
0534527-050050
F11-ap18
24.4 +/- 2.7
7.6 / 0.5
W
0534528-053348
F21-ap23
25.8 +/- 1.4
8.9 / 0.5
NSC
Normalized intensity
Velocity [km/s]

Fig. 12.3 cont.

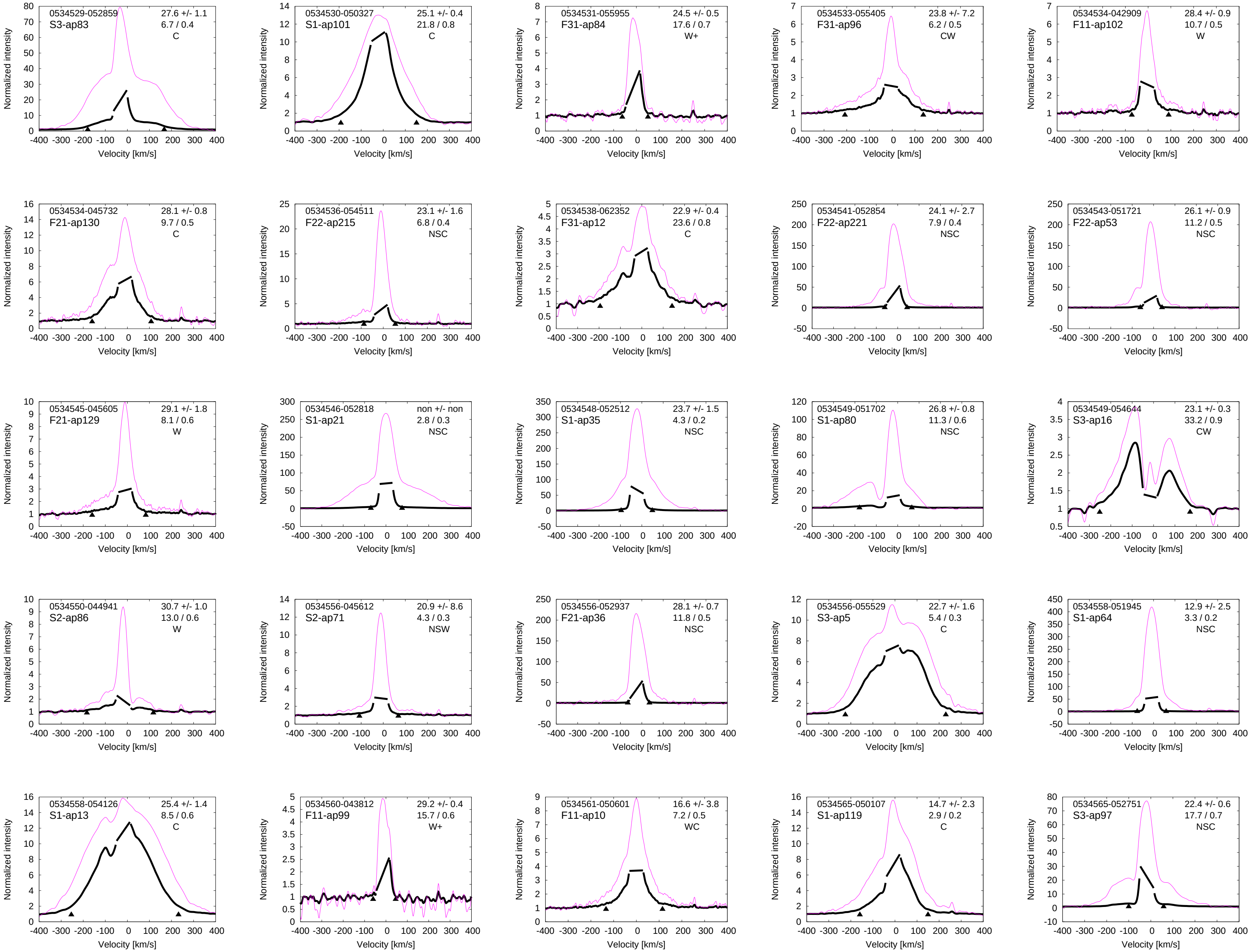
0534529-052859
S3-ap83
27.6 +/- 1.1
6.7 / 0.4
C
0534530-050327
S1-ap101
25.1 +/- 0.4
21.8 / 0.8
C
0534531-055955
F31-ap84
24.5 +/- 0.5
17.6 / 0.7
W+
0534533-055405
F31-ap96
23.8 +/- 7.2
6.2 / 0.5
CW
0534534-042909
F11-ap102
28.4 +/- 0.9
10.7 / 0.5
W
0534534-045732
F21-ap130
28.1 +/- 0.8
9.7 / 0.5
C
0534536-054511
F22-ap215
23.1 +/- 1.6
6.8 / 0.4
NSC
0534538-062352
F31-ap12
22.9 +/- 0.4
23.6 / 0.8
C
0534541-052854
F22-ap221
24.1 +/- 2.7
7.9 / 0.4
NSC
0534543-051721
F22-ap53
26.1 +/- 0.9
11.2 / 0.5
NSC
0534545-045605
F21-ap129
29.1 +/- 1.8
8.1 / 0.6
W
0534546-052818
S1-ap21
non +/- non
2.8 / 0.3
NSC
0534548-052512
S1-ap35
23.7 +/- 1.5
4.3 / 0.2
NSC
0534549-051702
S1-ap80
26.8 +/- 0.8
11.3 / 0.6
NSC
0534549-054644
S3-ap16
23.1 +/- 0.3
33.2 / 0.9
CW
0534550-044941
S2-ap86
30.7 +/- 1.0
13.0 / 0.6
W
0534556-045612
S2-ap71
20.9 +/- 8.6
4.3 / 0.3
NSW
0534556-052937
F21-ap36
28.1 +/- 0.7
11.8 / 0.5
NSC
0534556-055529
S3-ap5
22.7 +/- 1.6
5.4 / 0.3
C
0534558-051945
S1-ap64
12.9 +/- 2.5
3.3 / 0.2
NSC
0534558-054126
S1-ap13
25.4 +/- 1.4
8.5 / 0.6
C
0534560-043812
F11-ap99
29.2 +/- 0.4
15.7 / 0.6
W+
0534561-050601
F11-ap10
16.6 +/- 3.8
7.2 / 0.5
WC
0534565-050107
S1-ap119
14.7 +/- 2.3
2.9 / 0.2
C
0534565-052751
S3-ap97
22.4 +/- 0.6
17.7 / 0.7
NSC
Normalized intensity
Velocity [km/s]
-400 -300 -200 -100 0 100 200 300 400

Fig. 12.3 cont.

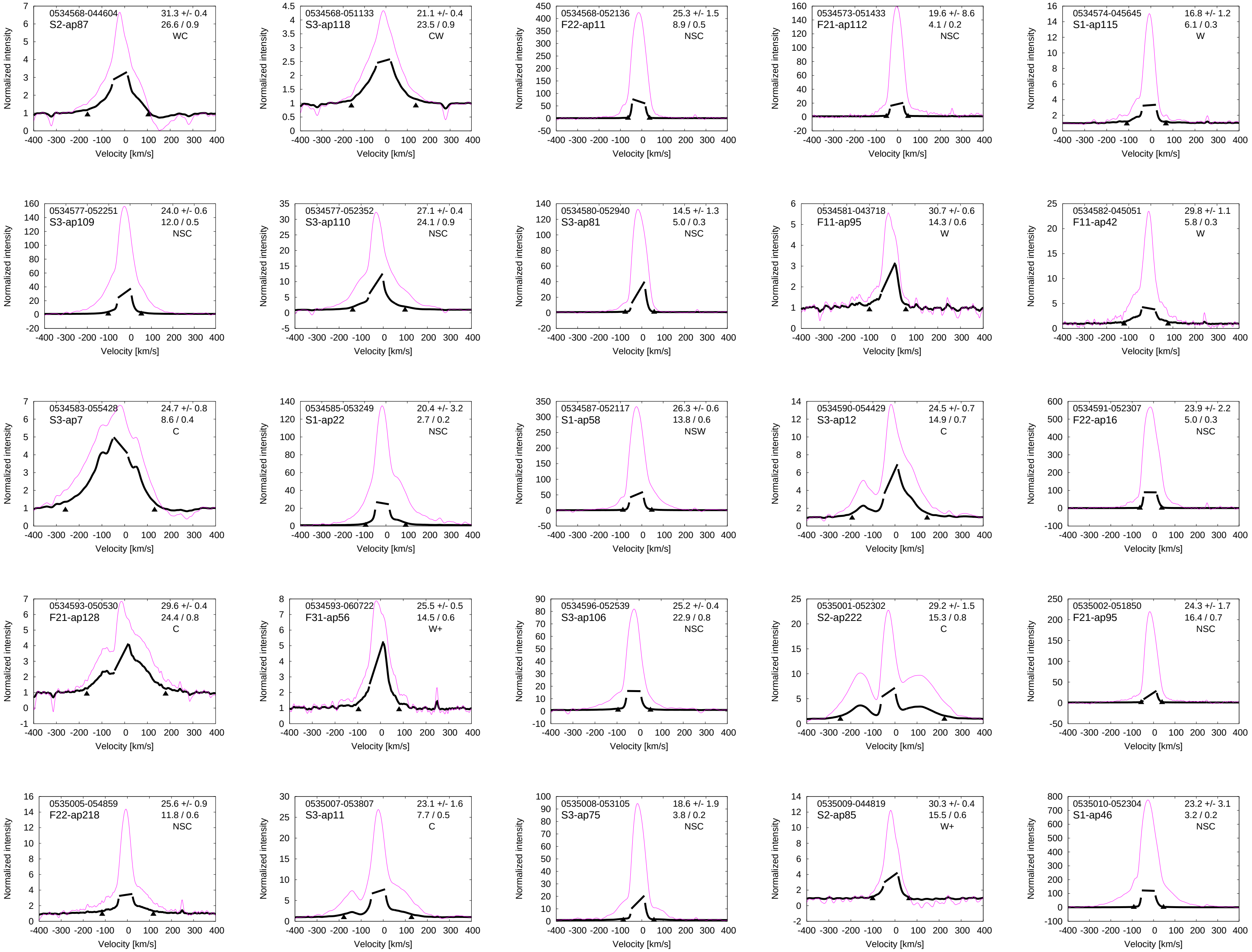
0534568-044604
S2-ap87
31.3 +/- 0.4
26.6 / 0.9
WC
0534568-051133
S3-ap118
21.1 +/- 0.4
23.5 / 0.9
CW
0534568-052136
F22-ap11
25.3 +/- 1.5
8.9 / 0.5
NSC
0534573-051433
F21-ap112
19.6 +/- 8.6
4.1 / 0.2
NSC
0534574-045645
S1-ap115
16.8 +/- 1.2
6.1 / 0.3
W
0534577-052251
S3-ap109
24.0 +/- 0.6
12.0 / 0.5
NSC
0534577-052352
S3-ap110
27.1 +/- 0.4
24.1 / 0.9
NSC
0534580-052940
S3-ap81
14.5 +/- 1.3
5.0 / 0.3
NSC
0534581-043718
F11-ap95
30.7 +/- 0.6
14.3 / 0.6
W
0534582-045051
F11-ap42
29.8 +/- 1.1
5.8 / 0.3
W
0534583-055428
S3-ap7
24.7 +/- 0.8
8.6 / 0.4
C
0534585-053249
S1-ap22
20.4 +/- 3.2
2.7 / 0.2
NSC
0534587-052117
S1-ap58
26.3 +/- 0.6
13.8 / 0.6
NSW
0534590-054429
S3-ap12
24.5 +/- 0.7
14.9 / 0.7
C
0534591-052307
F22-ap16
23.9 +/- 2.2
5.0 / 0.3
NSC
0534593-050530
F21-ap128
29.6 +/- 0.4
24.4 / 0.8
C
0534593-060722
F31-ap56
25.5 +/- 0.5
14.5 / 0.6
W+
0534596-052539
S3-ap106
25.2 +/- 0.4
22.9 / 0.8
NSC
0535001-052302
S2-ap222
29.2 +/- 1.5
15.3 / 0.8
C
0535002-051850
F21-ap95
24.3 +/- 1.7
16.4 / 0.7
NSC
0535005-054859
F22-ap218
25.6 +/- 0.9
11.8 / 0.6
NSC
0535007-053807
S3-ap11
23.1 +/- 1.6
7.7 / 0.5
C
0535008-053105
S3-ap75
18.6 +/- 1.9
3.8 / 0.2
NSC
0535009-044819
S2-ap85
30.3 +/- 0.4
15.5 / 0.6
W+
0535010-052304
S1-ap46
23.2 +/- 3.1
3.2 / 0.2
NSC
Normalized intensity
Velocity [km/s]
-400 -300 -200 -100 0 100 200 300 400

Fig. 12.3 cont.

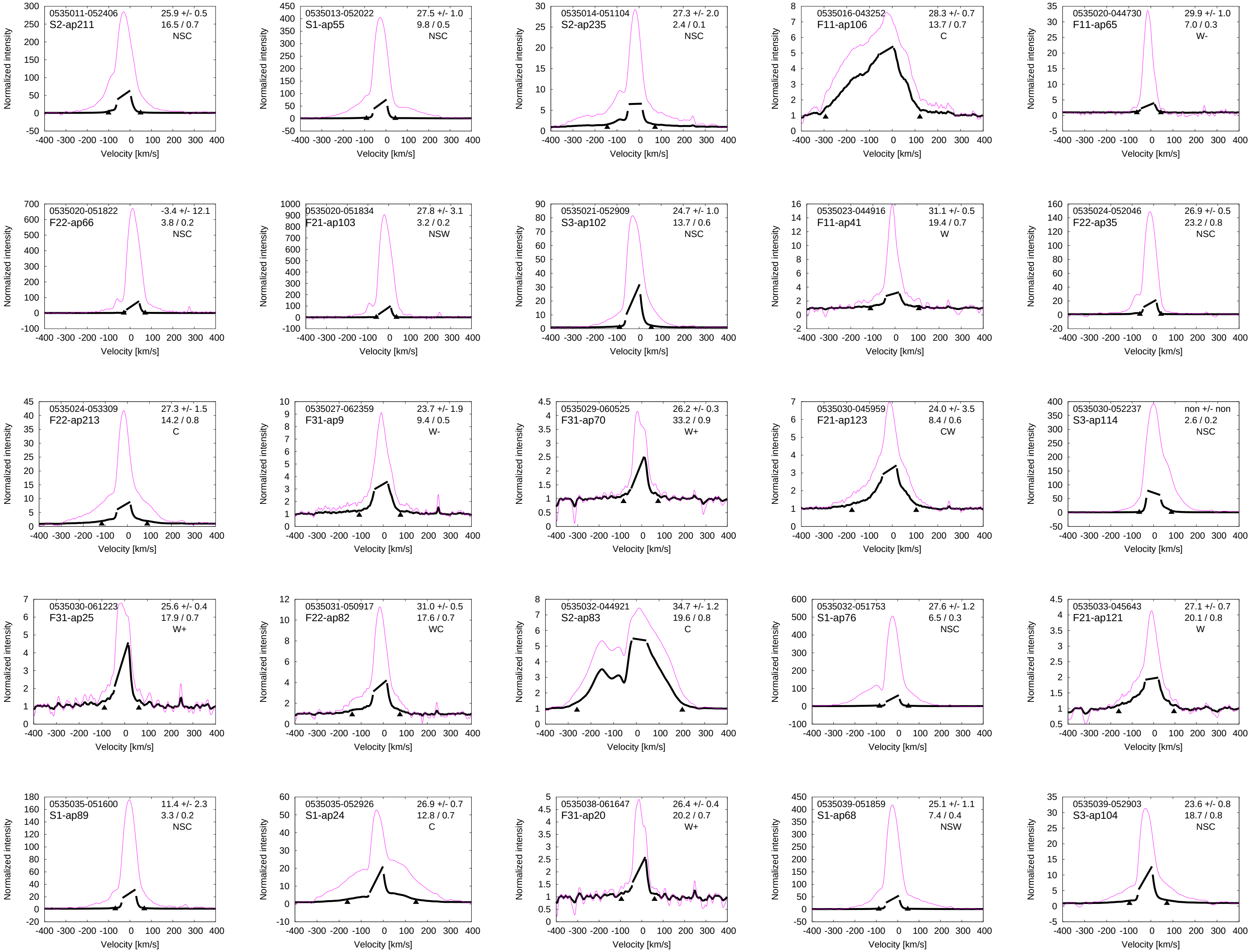
0535011-052406
S2-ap211
25.9 +/- 0.5
16.5 / 0.7
NSC
0535013-052022
S1-ap55
27.5 +/- 1.0
9.8 / 0.5
NSC
0535014-051104
S2-ap235
27.3 +/- 2.0
2.4 / 0.1
NSC
0535016-043252
F11-ap106
28.3 +/- 0.7
13.7 / 0.7
C
0535020-044730
F11-ap65
29.9 +/- 1.0
7.0 / 0.3
W-
0535020-051822
F22-ap66
-3.4 +/- 12.1
3.8 / 0.2
NSC
0535020-051834
F21-ap103
27.8 +/- 3.1
3.2 / 0.2
NSW
0535021-052909
S3-ap102
24.7 +/- 1.0
13.7 / 0.6
NSC
0535023-044916
F11-ap41
31.1 +/- 0.5
19.4 / 0.7
W
0535024-052046
F22-ap35
26.9 +/- 0.5
23.2 / 0.8
NSC
0535024-053309
F22-ap213
27.3 +/- 1.5
14.2 / 0.8
C
0535027-062359
F31-ap9
23.7 +/- 1.9
9.4 / 0.5
W-
0535029-060525
F31-ap70
26.2 +/- 0.3
33.2 / 0.9
W+
0535030-045959
F21-ap123
24.0 +/- 3.5
8.4 / 0.6
CW
0535030-052237
S3-ap114
non +/- non
2.6 / 0.2
NSC
0535030-061223
F31-ap25
25.6 +/- 0.4
17.9 / 0.7
W+
0535031-050917
F22-ap82
31.0 +/- 0.5
17.6 / 0.7
WC
0535032-044921
S2-ap83
34.7 +/- 1.2
19.6 / 0.8
C
0535032-051753
S1-ap76
27.6 +/- 1.2
6.5 / 0.3
NSC
0535033-045643
F21-ap121
27.1 +/- 0.7
20.1 / 0.8
W
0535035-051600
S1-ap89
11.4 +/- 2.3
3.3 / 0.2
NSC
0535035-052926
S1-ap24
26.9 +/- 0.7
12.8 / 0.7
C
0535038-061647
F31-ap20
26.4 +/- 0.4
20.2 / 0.7
W+
0535039-051859
S1-ap68
25.1 +/- 1.1
7.4 / 0.4
NSW
0535039-052903
S3-ap104
23.6 +/- 0.8
18.7 / 0.8
NSC
Normalized intensity
Velocity [km/s]
-400 -300 -200 -100 0 100 200 300 400

Fig. 12.3 cont.

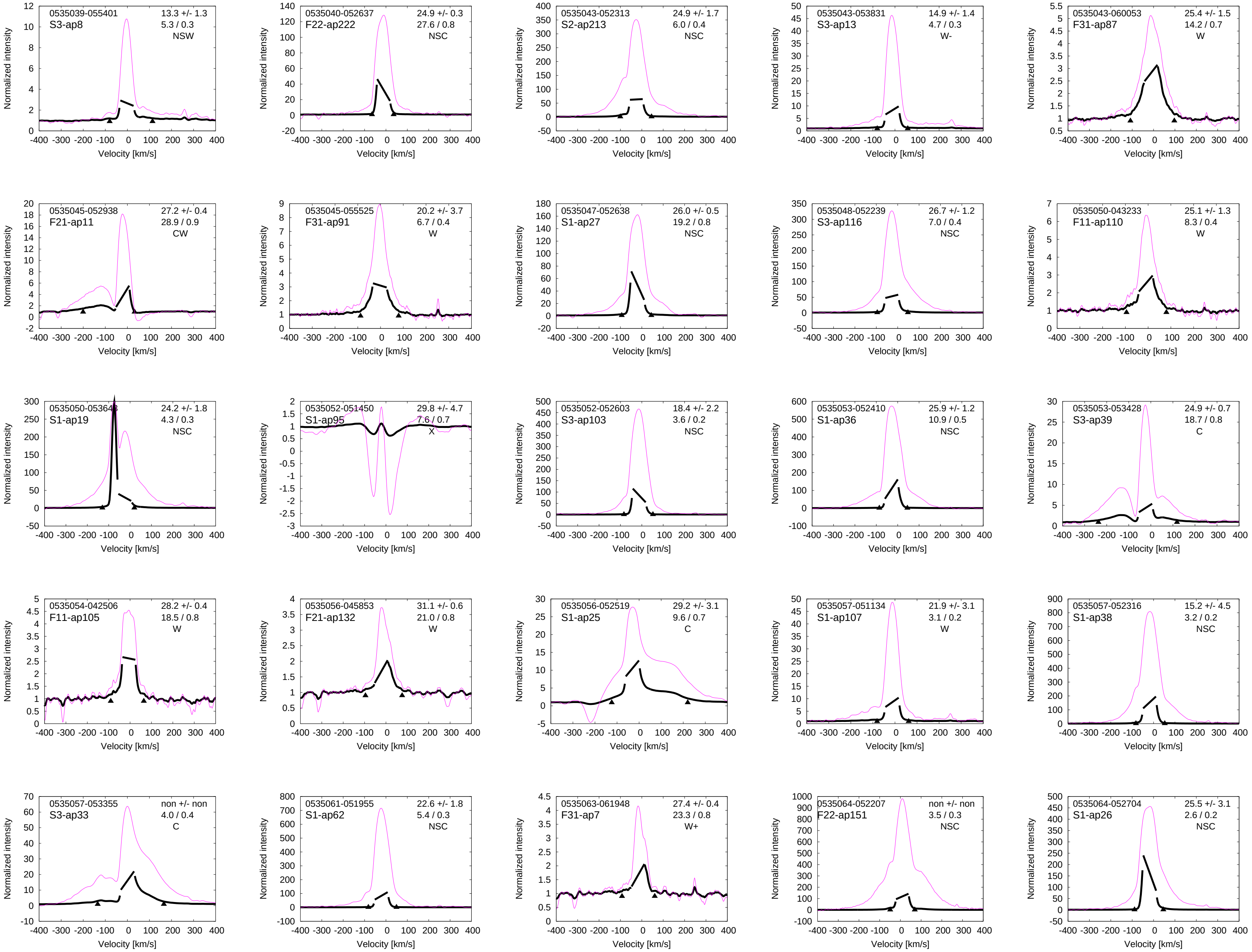
Normalized intensity
Velocity [km/s]
0535039-055401 S3-ap8 13.3 +/- 1.3 5.3 / 0.3 NSW
0535040-052637 F22-ap222 24.9 +/- 0.3 27.6 / 0.8 NSC
0535043-052313 S2-ap213 24.9 +/- 1.7 6.0 / 0.4 NSC
0535043-053831 S3-ap13 14.9 +/- 1.4 4.7 / 0.3 W-
0535043-060053 F31-ap87 25.4 +/- 1.5 14.2 / 0.7 W
0535045-052938 F21-ap11 27.2 +/- 0.4 28.9 / 0.9 CW
0535045-055525 F31-ap91 20.2 +/- 3.7 6.7 / 0.4 W
0535047-052638 S1-ap27 26.0 +/- 0.5 19.2 / 0.8 NSC
0535048-052239 S3-ap116 26.7 +/- 1.2 7.0 / 0.4 NSC
0535050-043233 F11-ap110 25.1 +/- 1.3 8.3 / 0.4 W
0535050-053643 S1-ap19 24.2 +/- 1.8 4.3 / 0.3 NSC
0535052-051450 S1-ap95 29.8 +/- 4.7 7.6 / 0.7 X
0535052-052603 S3-ap103 18.4 +/- 2.2 3.6 / 0.2 NSC
0535053-052410 S1-ap36 25.9 +/- 1.2 10.9 / 0.5 NSC
0535053-053428 S3-ap39 24.9 +/- 0.7 18.7 / 0.8 C
0535054-042506 F11-ap105 28.2 +/- 0.4 18.5 / 0.8 W
0535056-045853 F21-ap132 31.1 +/- 0.6 21.0 / 0.8 W
0535056-052519 S1-ap25 29.2 +/- 3.1 9.6 / 0.7 C
0535057-051134 S1-ap107 21.9 +/- 3.1 3.1 / 0.2 W
0535057-052316 S1-ap38 15.2 +/- 4.5 3.2 / 0.2 NSC
0535057-053355 S3-ap33 non +/- non 4.0 / 0.4 C
0535061-051955 S1-ap62 22.6 +/- 1.8 5.4 / 0.3 NSC
0535063-061948 F31-ap7 27.4 +/- 0.4 23.3 / 0.8 W+
0535064-052207 F22-ap151 non +/- non 3.5 / 0.3 NSC
0535064-052704 S1-ap26 25.5 +/- 3.1 2.6 / 0.2 NSC

Fig. 12.3 cont.

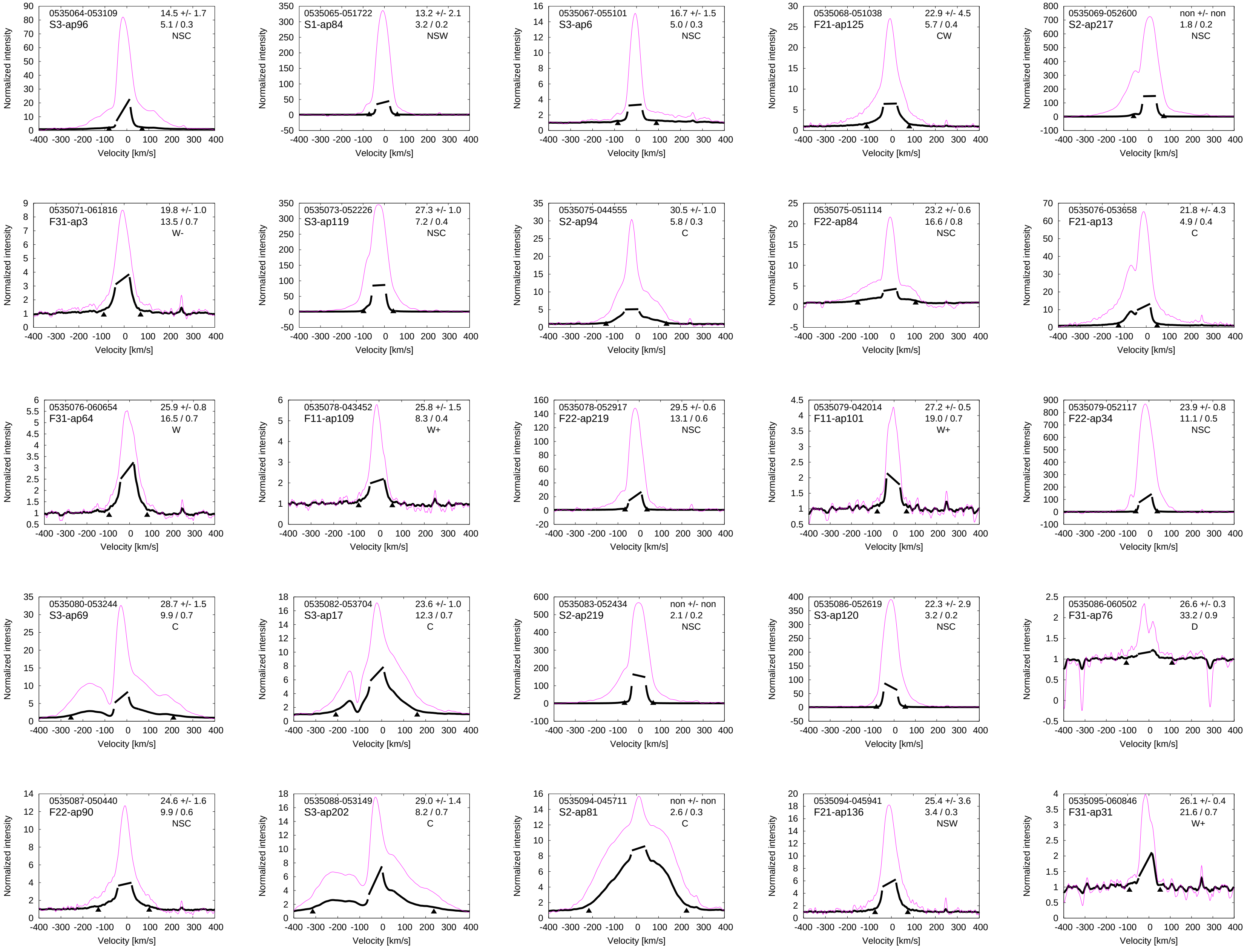
0535064-053109
S3-ap96
14.5 +/- 1.7
5.1 / 0.3
NSC
0535065-051722
S1-ap84
13.2 +/- 2.1
3.2 / 0.2
NSW
0535067-055101
S3-ap6
16.7 +/- 1.5
5.0 / 0.3
NSC
0535068-051038
F21-ap125
22.9 +/- 4.5
5.7 / 0.4
CW
0535069-052600
S2-ap217
non +/- non
1.8 / 0.2
NSC
0535071-061816
F31-ap3
19.8 +/- 1.0
13.5 / 0.7
W-
0535073-052226
S3-ap119
27.3 +/- 1.0
7.2 / 0.4
NSC
0535075-044555
S2-ap94
30.5 +/- 1.0
5.8 / 0.3
C
0535075-051114
F22-ap84
23.2 +/- 0.6
16.6 / 0.8
NSC
0535076-053658
F21-ap13
21.8 +/- 4.3
4.9 / 0.4
C
0535076-060654
F31-ap64
25.9 +/- 0.8
16.5 / 0.7
W
0535078-043452
F11-ap109
25.8 +/- 1.5
8.3 / 0.4
W+
0535078-052917
F22-ap219
29.5 +/- 0.6
13.1 / 0.6
NSC
0535079-042014
F11-ap101
27.2 +/- 0.5
19.0 / 0.7
W+
0535079-052117
F22-ap34
23.9 +/- 0.8
11.1 / 0.5
NSC
0535080-053244
S3-ap69
28.7 +/- 1.5
9.9 / 0.7
C
0535082-053704
S3-ap17
23.6 +/- 1.0
12.3 / 0.7
C
0535083-052434
S2-ap219
non +/- non
2.1 / 0.2
NSC
0535086-052619
S3-ap120
22.3 +/- 2.9
3.2 / 0.2
NSC
0535086-060502
F31-ap76
26.6 +/- 0.3
33.2 / 0.9
D
0535087-050440
F22-ap90
24.6 +/- 1.6
9.9 / 0.6
NSC
0535088-053149
S3-ap202
29.0 +/- 1.4
8.2 / 0.7
C
0535094-045711
S2-ap81
non +/- non
2.6 / 0.3
C
0535094-045941
F21-ap136
25.4 +/- 3.6
3.4 / 0.3
NSW
0535095-060846
F31-ap31
26.1 +/- 0.4
21.6 / 0.7
W+
Normalized intensity
Velocity [km/s]
-400 -300 -200 -100 0 100 200 300 400

Fig. 12.3 cont.

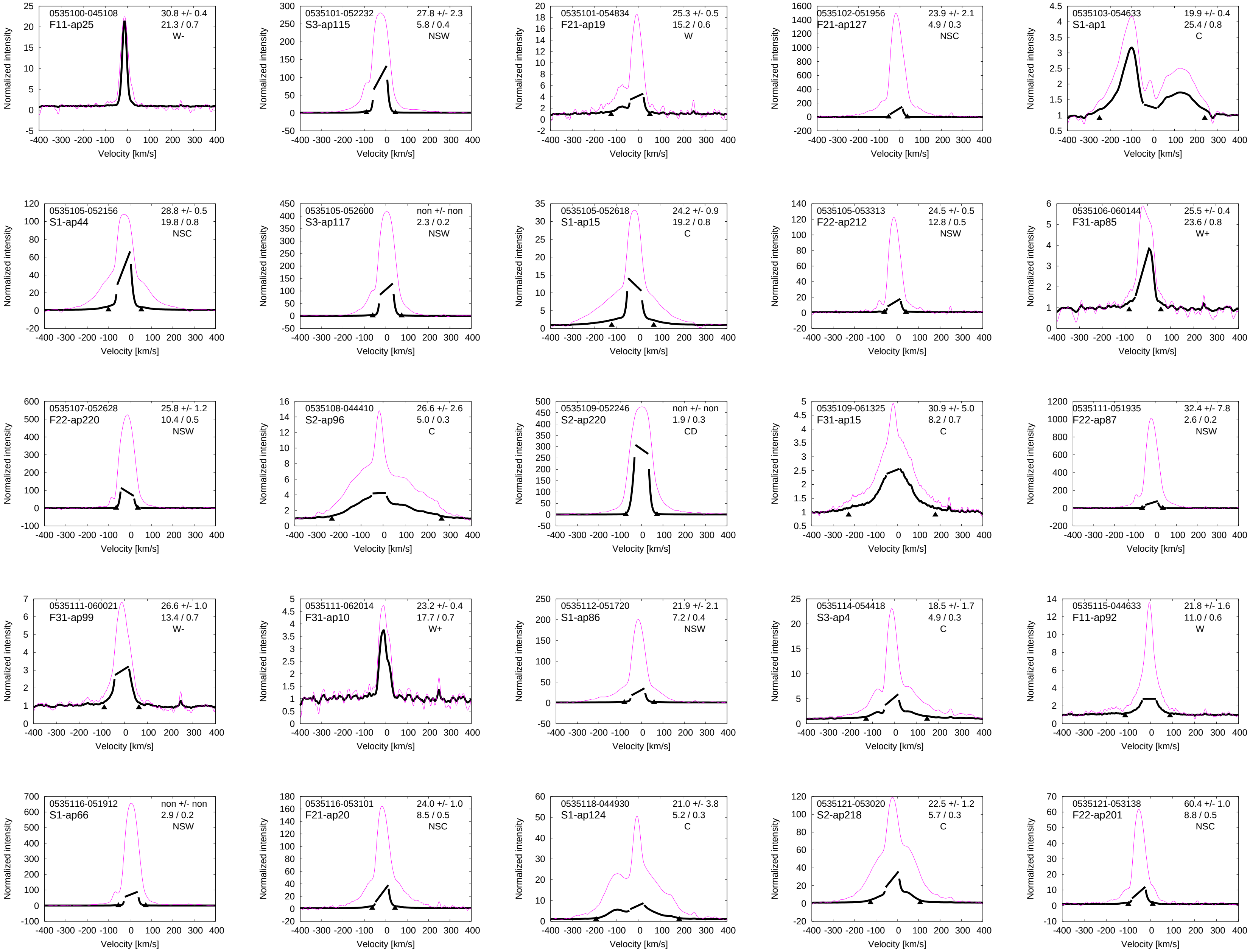

Normalized intensity
Velocity [km/s]
0535100-045108
F11-ap25
30.8 +/- 0.4
21.3 / 0.7
W-
0535101-052232
S3-ap115
27.8 +/- 2.3
5.8 / 0.4
NSW
0535101-054834
F21-ap19
25.3 +/- 0.5
15.2 / 0.6
W
0535102-051956
F21-ap127
23.9 +/- 2.1
4.9 / 0.3
NSC
0535103-054633
S1-ap1
19.9 +/- 0.4
25.4 / 0.8
C
0535105-052156
S1-ap44
28.8 +/- 0.5
19.8 / 0.8
NSC
0535105-052600
S3-ap117
non +/- non
2.3 / 0.2
NSW
0535105-052618
S1-ap15
24.2 +/- 0.9
19.2 / 0.8
C
0535105-053313
F22-ap212
24.5 +/- 0.5
12.8 / 0.5
NSW
0535106-060144
F31-ap85
25.5 +/- 0.4
23.6 / 0.8
W+
0535107-052628
F22-ap220
25.8 +/- 1.2
10.4 / 0.5
NSW
0535108-044410
S2-ap96
26.6 +/- 2.6
5.0 / 0.3
C
0535109-052246
S2-ap220
non +/- non
1.9 / 0.3
CD
0535109-061325
F31-ap15
30.9 +/- 5.0
8.2 / 0.7
C
0535111-051935
F22-ap87
32.4 +/- 7.8
2.6 / 0.2
NSW
0535111-060021
F31-ap99
26.6 +/- 1.0
13.4 / 0.7
W-
0535111-062014
F31-ap10
23.2 +/- 0.4
17.7 / 0.7
W+
0535112-051720
S1-ap86
21.9 +/- 2.1
7.2 / 0.4
NSW
0535114-054418
S3-ap4
18.5 +/- 1.7
4.9 / 0.3
C
0535115-044633
F11-ap92
21.8 +/- 1.6
11.0 / 0.6
W
0535116-051912
S1-ap66
non +/- non
2.9 / 0.2
NSW
0535116-053101
F21-ap20
24.0 +/- 1.0
8.5 / 0.5
NSC
0535118-044930
S1-ap124
21.0 +/- 3.8
5.2 / 0.3
C
0535121-053020
S2-ap218
22.5 +/- 1.2
5.7 / 0.3
C
0535121-053138
F22-ap201
60.4 +/- 1.0
8.8 / 0.5
NSC
-400 -300 -200 -100 0 100 200 300 400

Fig. 12.3 cont.

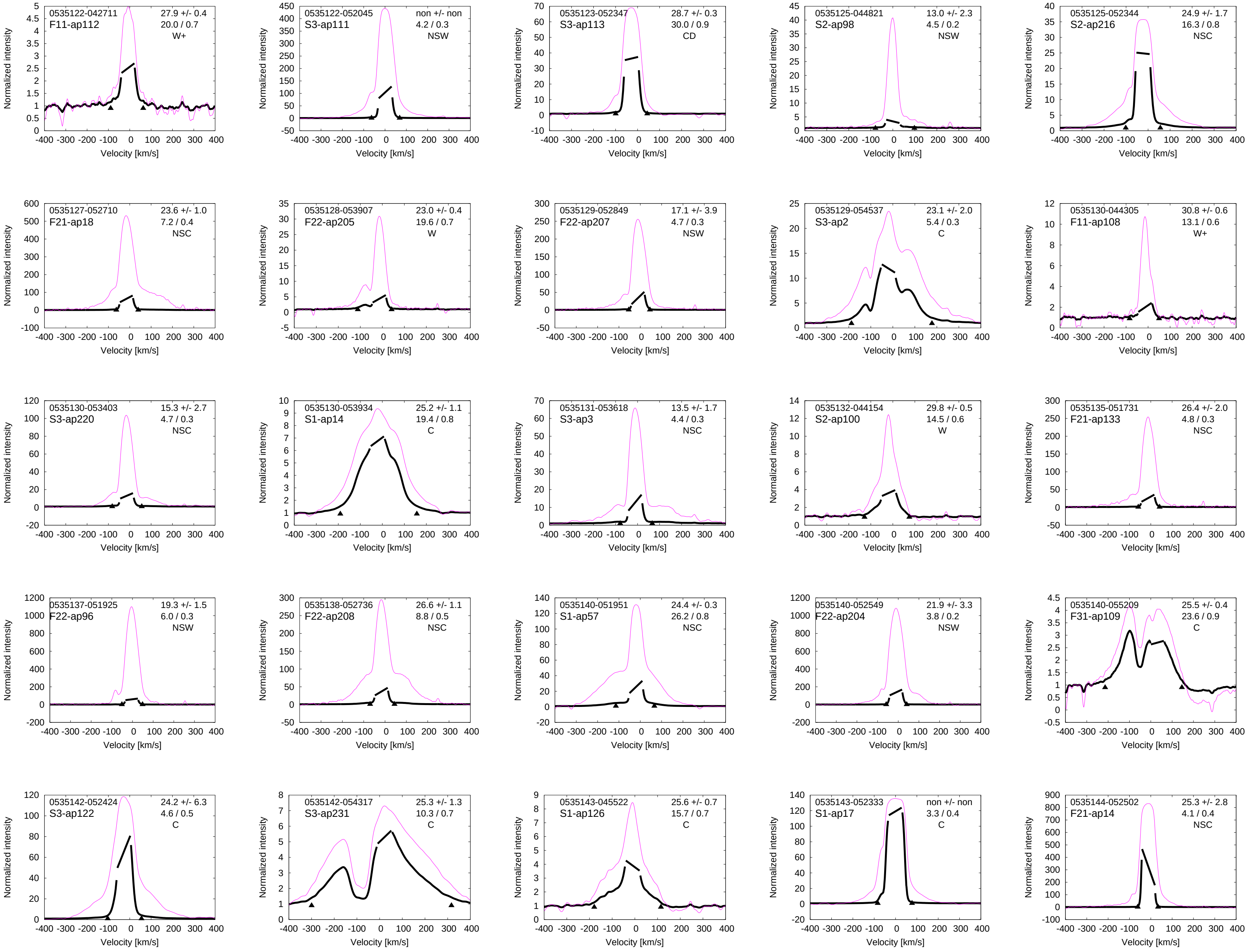
Normalized intensity
Velocity [km/s]
0535122-042711 F11-ap112 27.9 +/- 0.4 20.0 / 0.7 W+
0535122-052045 S3-ap111 non +/- non 4.2 / 0.3 NSW
0535123-052347 S3-ap113 28.7 +/- 0.3 30.0 / 0.9 CD
0535125-044821 S2-ap98 13.0 +/- 2.3 4.5 / 0.2 NSW
0535125-052344 S2-ap216 24.9 +/- 1.7 16.3 / 0.8 NSC
0535127-052710 F21-ap18 23.6 +/- 1.0 7.2 / 0.4 NSC
0535128-053907 F22-ap205 23.0 +/- 0.4 19.6 / 0.7 W
0535129-052849 F22-ap207 17.1 +/- 3.9 4.7 / 0.3 NSW
0535129-054537 S3-ap2 23.1 +/- 2.0 5.4 / 0.3 C
0535130-044305 F11-ap108 30.8 +/- 0.6 13.1 / 0.6 W+
0535130-053403 S3-ap220 15.3 +/- 2.7 4.7 / 0.3 NSC
0535130-053934 S1-ap14 25.2 +/- 1.1 19.4 / 0.8 C
0535131-053618 S3-ap3 13.5 +/- 1.7 4.4 / 0.3 NSC
0535132-044154 S2-ap100 29.8 +/- 0.5 14.5 / 0.6 W
0535135-051731 F21-ap133 26.4 +/- 2.0 4.8 / 0.3 NSC
0535137-051925 F22-ap96 19.3 +/- 1.5 6.0 / 0.3 NSW
0535138-052736 F22-ap208 26.6 +/- 1.1 8.8 / 0.5 NSC
0535140-051951 S1-ap57 24.4 +/- 0.3 26.2 / 0.8 NSC
0535140-052549 F22-ap204 21.9 +/- 3.3 3.8 / 0.2 NSW
0535140-055209 F31-ap109 25.5 +/- 0.4 23.6 / 0.9 C
0535142-052424 S3-ap122 24.2 +/- 6.3 4.6 / 0.5 C
0535142-054317 S3-ap231 25.3 +/- 1.3 10.3 / 0.7 C
0535143-045522 S1-ap126 25.6 +/- 0.7 15.7 / 0.7 C
0535143-052333 S1-ap17 non +/- non 3.3 / 0.4 C
0535144-052502 F21-ap14 25.3 +/- 2.8 4.1 / 0.4 NSC
-400 -300 -200 -100 0 100 200 300 400

Fig. 12.3 cont.

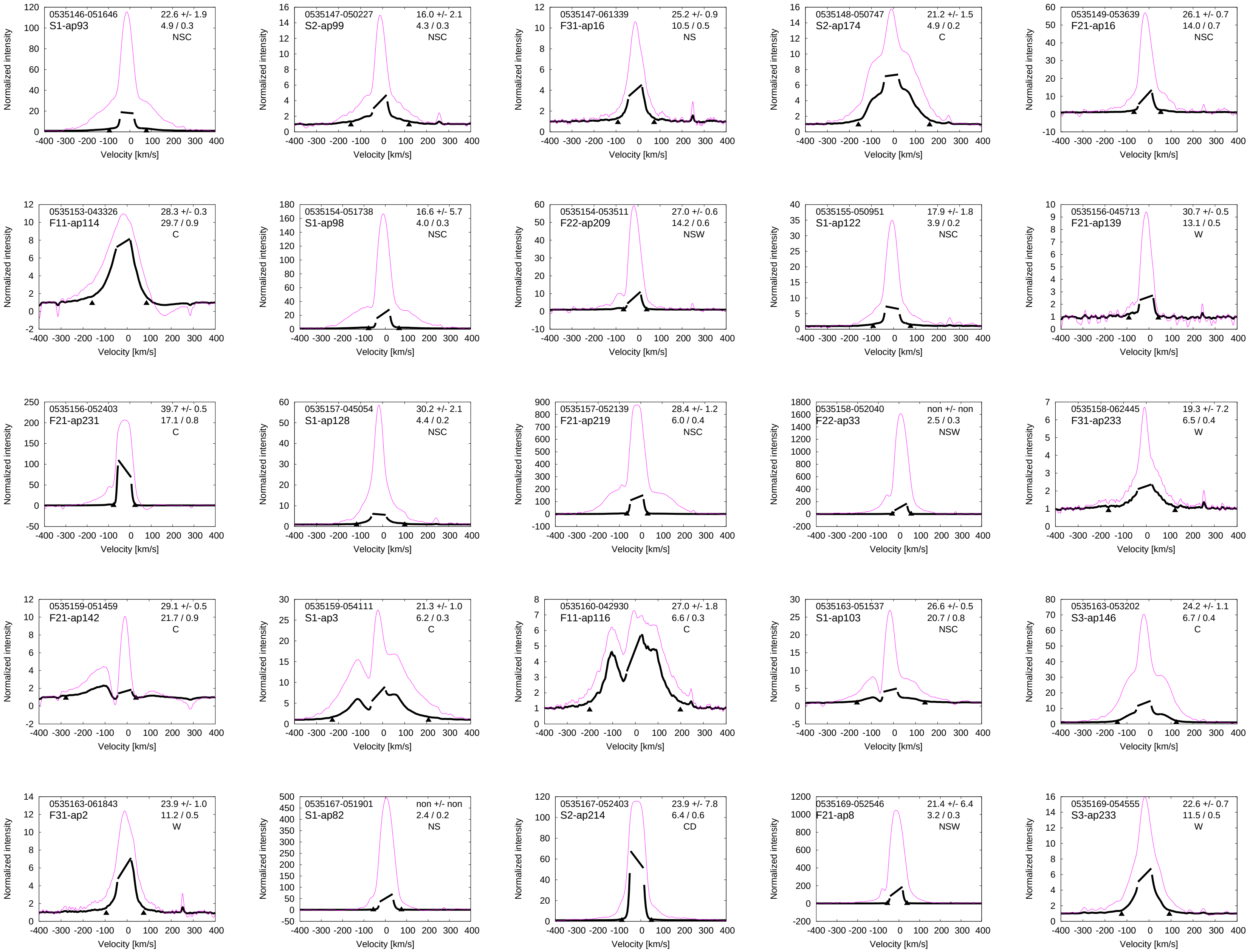

0535146-051646
S1-ap93
22.6 +/- 1.9
4.9 / 0.3
NSC
0535147-050227
S2-ap99
16.0 +/- 2.1
4.3 / 0.3
NSC
0535147-061339
F31-ap16
25.2 +/- 0.9
10.5 / 0.5
NS
0535148-050747
S2-ap174
21.2 +/- 1.5
4.9 / 0.2
C
0535149-053639
F21-ap16
26.1 +/- 0.7
14.0 / 0.7
NSC
0535153-043326
F11-ap114
28.3 +/- 0.3
29.7 / 0.9
C
0535154-051738
S1-ap98
16.6 +/- 5.7
4.0 / 0.3
NSC
0535154-053511
F22-ap209
27.0 +/- 0.6
14.2 / 0.6
NSW
0535155-050951
S1-ap122
17.9 +/- 1.8
3.9 / 0.2
NSC
0535156-045713
F21-ap139
30.7 +/- 0.5
13.1 / 0.5
W
0535156-052403
F21-ap231
39.7 +/- 0.5
17.1 / 0.8
C
0535157-045054
S1-ap128
30.2 +/- 2.1
4.4 / 0.2
NSC
0535157-052139
F21-ap219
28.4 +/- 1.2
6.0 / 0.4
NSC
0535158-052040
F22-ap33
non +/- non
2.5 / 0.3
NSW
0535158-062445
F31-ap233
19.3 +/- 7.2
6.5 / 0.4
W
0535159-051459
F21-ap142
29.1 +/- 0.5
21.7 / 0.9
C
0535159-054111
S1-ap3
21.3 +/- 1.0
6.2 / 0.3
C
0535160-042930
F11-ap116
27.0 +/- 1.8
6.6 / 0.3
C
0535163-051537
S1-ap103
26.6 +/- 0.5
20.7 / 0.8
NSC
0535163-053202
S3-ap146
24.2 +/- 1.1
6.7 / 0.4
C
0535163-061843
F31-ap2
23.9 +/- 1.0
11.2 / 0.5
W
0535167-051901
S1-ap82
non +/- non
2.4 / 0.2
NS
0535167-052403
S2-ap214
23.9 +/- 7.8
6.4 / 0.6
CD
0535169-052546
F21-ap8
21.4 +/- 6.4
3.2 / 0.3
NSW
0535169-054555
S3-ap233
22.6 +/- 0.7
11.5 / 0.5
W
Normalized intensity
Velocity [km/s]
-400 -300 -200 -100 0 100 200 300 400

Fig. 12.3 cont.

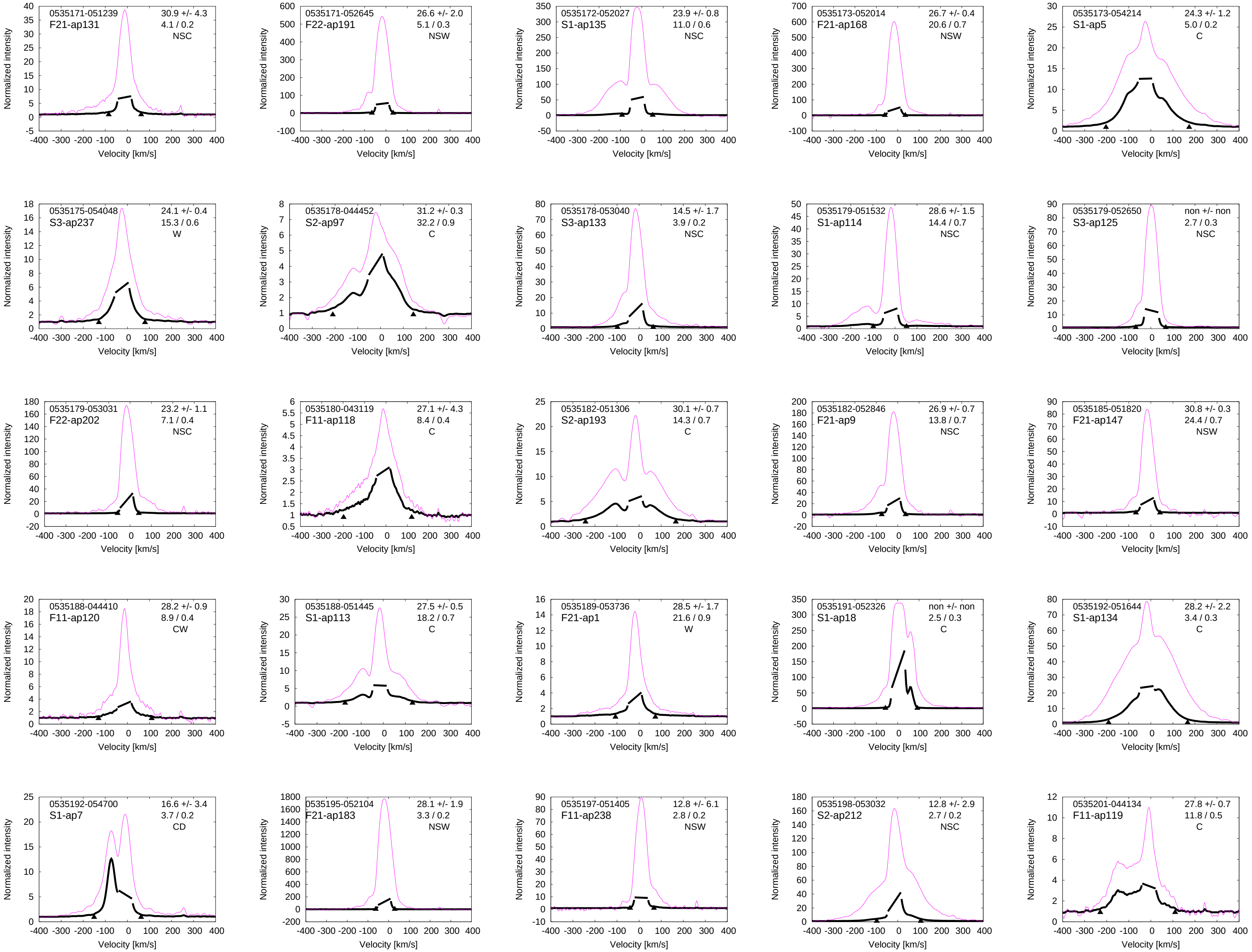
0535171-051239
F21-ap131
30.9 +/- 4.3
4.1 / 0.2
NSC
0535171-052645
F22-ap191
26.6 +/- 2.0
5.1 / 0.3
NSW
0535172-052027
S1-ap135
23.9 +/- 0.8
11.0 / 0.6
NSC
0535173-052014
F21-ap168
26.7 +/- 0.4
20.6 / 0.7
NSW
0535173-054214
S1-ap5
24.3 +/- 1.2
5.0 / 0.2
C
0535175-054048
S3-ap237
24.1 +/- 0.4
15.3 / 0.6
W
0535178-044452
S2-ap97
31.2 +/- 0.3
32.2 / 0.9
C
0535178-053040
S3-ap133
14.5 +/- 1.7
3.9 / 0.2
NSC
0535179-051532
S1-ap114
28.6 +/- 1.5
14.4 / 0.7
NSC
0535179-052650
S3-ap125
non +/- non
2.7 / 0.3
NSC
0535179-053031
F22-ap202
23.2 +/- 1.1
7.1 / 0.4
NSC
0535180-043119
F11-ap118
27.1 +/- 4.3
8.4 / 0.4
C
0535182-051306
S2-ap193
30.1 +/- 0.7
14.3 / 0.7
C
0535182-052846
F21-ap9
26.9 +/- 0.7
13.8 / 0.7
NSC
0535185-051820
F21-ap147
30.8 +/- 0.3
24.4 / 0.7
NSW
0535188-044410
F11-ap120
28.2 +/- 0.9
8.9 / 0.4
CW
0535188-051445
S1-ap113
27.5 +/- 0.5
18.2 / 0.7
C
0535189-053736
F21-ap1
28.5 +/- 1.7
21.6 / 0.9
W
0535191-052326
S1-ap18
non +/- non
2.5 / 0.3
C
0535192-051644
S1-ap134
28.2 +/- 2.2
3.4 / 0.3
C
0535192-054700
S1-ap7
16.6 +/- 3.4
3.7 / 0.2
CD
0535195-052104
F21-ap183
28.1 +/- 1.9
3.3 / 0.2
NSW
0535197-051405
F11-ap238
12.8 +/- 6.1
2.8 / 0.2
NSW
0535198-053032
S2-ap212
12.8 +/- 2.9
2.7 / 0.2
NSC
0535201-044134
F11-ap119
27.8 +/- 0.7
11.8 / 0.5
C
Normalized intensity
Velocity [km/s]
-400 -300 -200 -100 0 100 200 300 400

Fig. 12.3 cont.

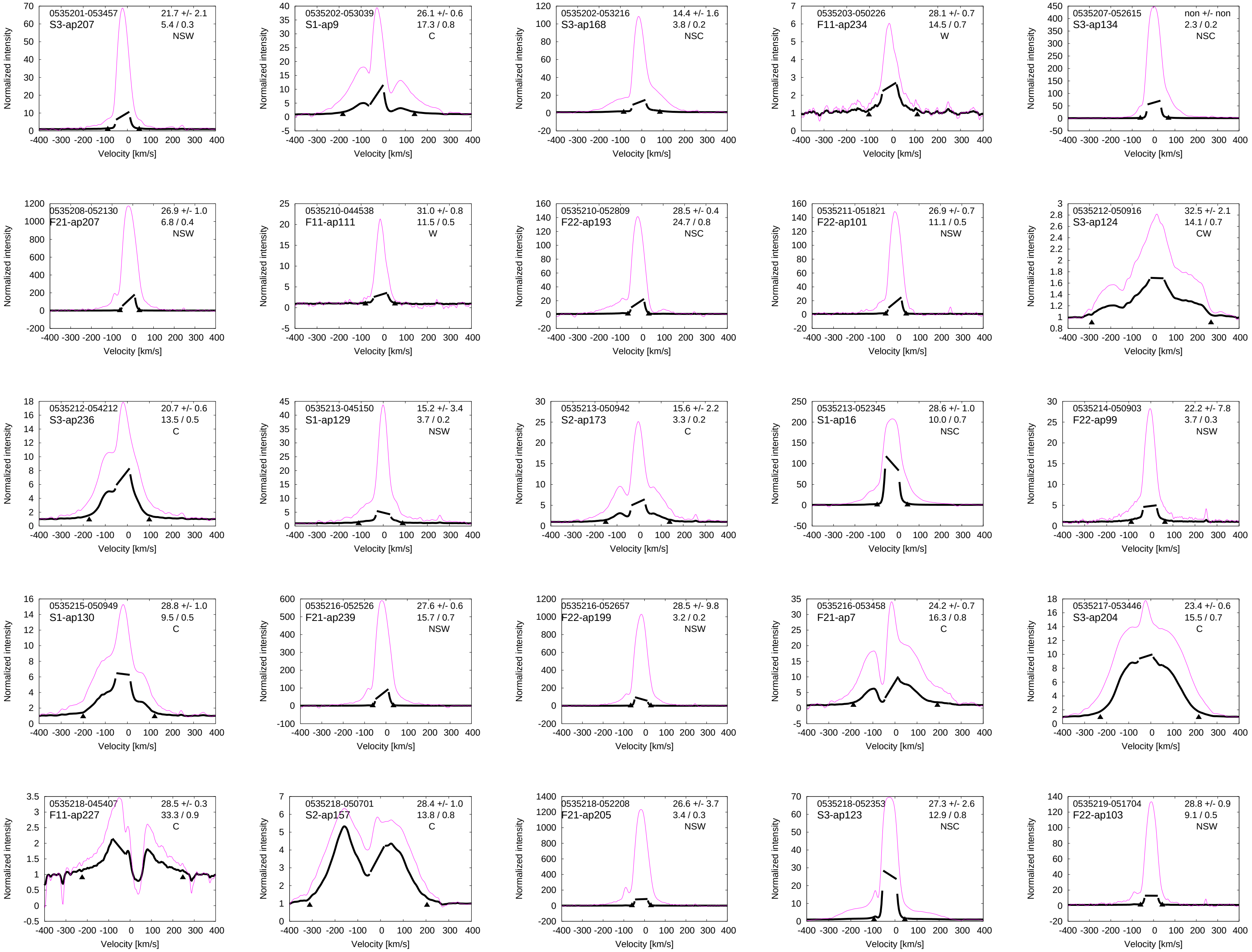
Normalized intensity
Velocity [km/s]
0535201-053457
S3-ap207
21.7 +/- 2.1
5.4 / 0.3
NSW
0535202-053039
S1-ap9
26.1 +/- 0.6
17.3 / 0.8
C
0535202-053216
S3-ap168
14.4 +/- 1.6
3.8 / 0.2
NSC
0535203-050226
F11-ap234
28.1 +/- 0.7
14.5 / 0.7
W
0535207-052615
S3-ap134
non +/- non
2.3 / 0.2
NSC
0535208-052130
F21-ap207
26.9 +/- 1.0
6.8 / 0.4
NSW
0535210-044538
F11-ap111
31.0 +/- 0.8
11.5 / 0.5
W
0535210-052809
F22-ap193
28.5 +/- 0.4
24.7 / 0.8
NSC
0535211-051821
F22-ap101
26.9 +/- 0.7
11.1 / 0.5
NSW
0535212-050916
S3-ap124
32.5 +/- 2.1
14.1 / 0.7
CW
0535212-054212
S3-ap236
20.7 +/- 0.6
13.5 / 0.5
C
0535213-045150
S1-ap129
15.2 +/- 3.4
3.7 / 0.2
NSW
0535213-050942
S2-ap173
15.6 +/- 2.2
3.3 / 0.2
C
0535213-052345
S1-ap16
28.6 +/- 1.0
10.0 / 0.7
NSC
0535214-050903
F22-ap99
22.2 +/- 7.8
3.7 / 0.3
NSW
0535215-050949
S1-ap130
28.8 +/- 1.0
9.5 / 0.5
C
0535216-052526
F21-ap239
27.6 +/- 0.6
15.7 / 0.7
NSW
0535216-052657
F22-ap199
28.5 +/- 9.8
3.2 / 0.2
NSW
0535216-053458
F21-ap7
24.2 +/- 0.7
16.3 / 0.8
C
0535217-053446
S3-ap204
23.4 +/- 0.6
15.5 / 0.7
C
0535218-045407
F11-ap227
28.5 +/- 0.3
33.3 / 0.9
C
0535218-050701
S2-ap157
28.4 +/- 1.0
13.8 / 0.8
C
0535218-052208
F21-ap205
26.6 +/- 3.7
3.4 / 0.3
NSW
0535218-052353
S3-ap123
27.3 +/- 2.6
12.9 / 0.8
NSC
0535219-051704
F22-ap103
28.8 +/- 0.9
9.1 / 0.5
NSW

Fig. 12.3 cont.

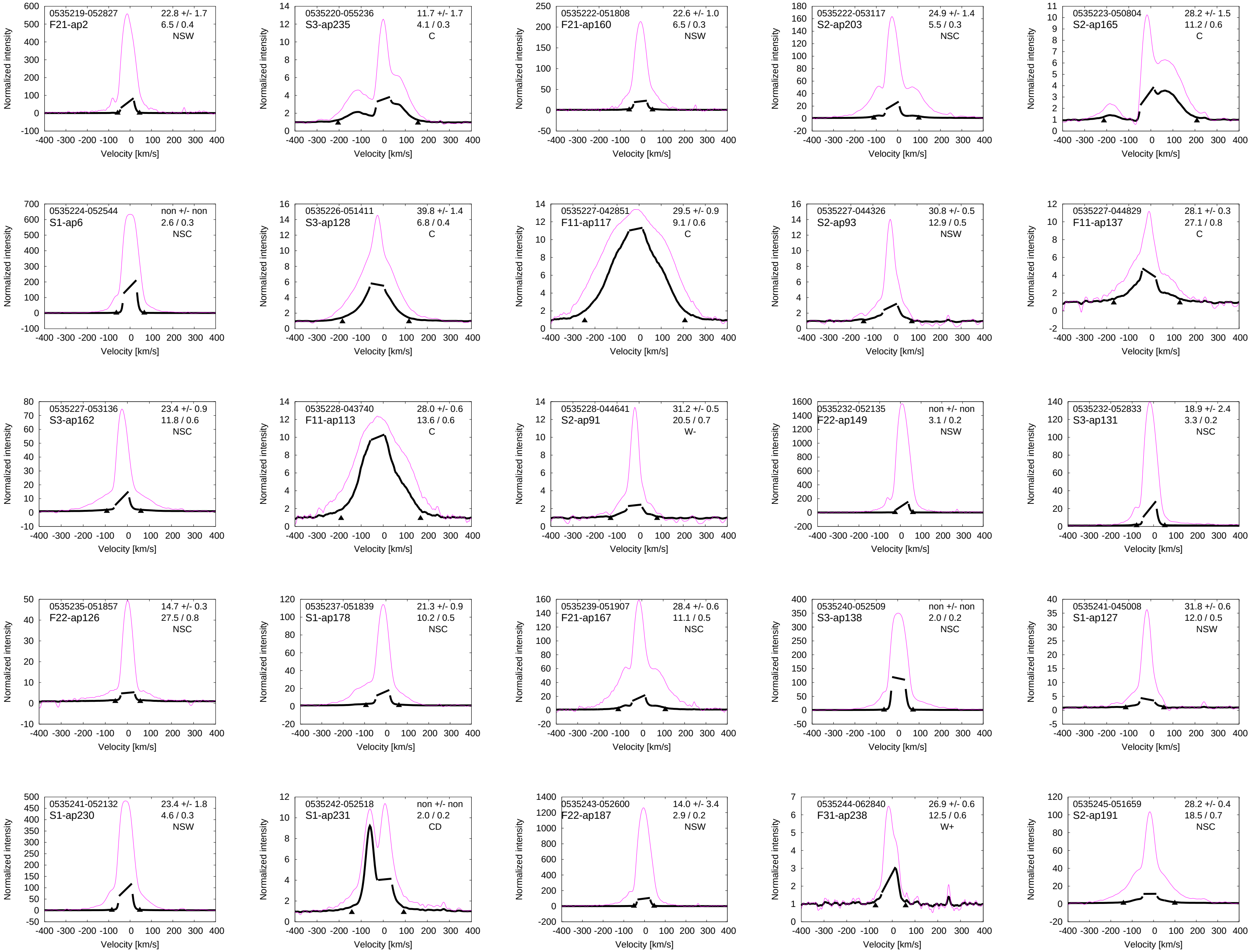

0535219-052827 F21-ap2 22.8 +/- 1.7 6.5 / 0.4 NSW
0535220-055236 S3-ap235 11.7 +/- 1.7 4.1 / 0.3 C
0535222-051808 F21-ap160 22.6 +/- 1.0 6.5 / 0.3 NSW
0535222-053117 S2-ap203 24.9 +/- 1.4 5.5 / 0.3 NSC
0535223-050804 S2-ap165 28.2 +/- 1.5 11.2 / 0.6 C
0535224-052544 S1-ap6 non +/- non 2.6 / 0.3 NSC
0535226-051411 S3-ap128 39.8 +/- 1.4 6.8 / 0.4 C
0535227-042851 F11-ap117 29.5 +/- 0.9 9.1 / 0.6 C
0535227-044326 S2-ap93 30.8 +/- 0.5 12.9 / 0.5 NSW
0535227-044829 F11-ap137 28.1 +/- 0.3 27.1 / 0.8 C
0535227-053136 S3-ap162 23.4 +/- 0.9 11.8 / 0.6 NSC
0535228-043740 F11-ap113 28.0 +/- 0.6 13.6 / 0.6 C
0535228-044641 S2-ap91 31.2 +/- 0.5 20.5 / 0.7 W-
0535232-052135 F22-ap149 non +/- non 3.1 / 0.2 NSW
0535232-052833 S3-ap131 18.9 +/- 2.4 3.3 / 0.2 NSC
0535235-051857 F22-ap126 14.7 +/- 0.3 27.5 / 0.8 NSC
0535237-051839 S1-ap178 21.3 +/- 0.9 10.2 / 0.5 NSC
0535239-051907 F21-ap167 28.4 +/- 0.6 11.1 / 0.5 NSC
0535240-052509 S3-ap138 non +/- non 2.0 / 0.2 NSC
0535241-045008 S1-ap127 31.8 +/- 0.6 12.0 / 0.5 NSW
0535241-052132 S1-ap230 23.4 +/- 1.8 4.6 / 0.3 NSW
0535242-052518 S1-ap231 non +/- non 2.0 / 0.2 CD
0535243-052600 F22-ap187 14.0 +/- 3.4 2.9 / 0.2 NSW
0535244-062840 F31-ap238 26.9 +/- 0.6 12.5 / 0.6 W+
0535245-051659 S2-ap191 28.2 +/- 0.4 18.5 / 0.7 NSC
Normalized intensity
Velocity [km/s]
-400 -300 -200 -100 0 100 200 300 400

Fig. 12.3 cont.

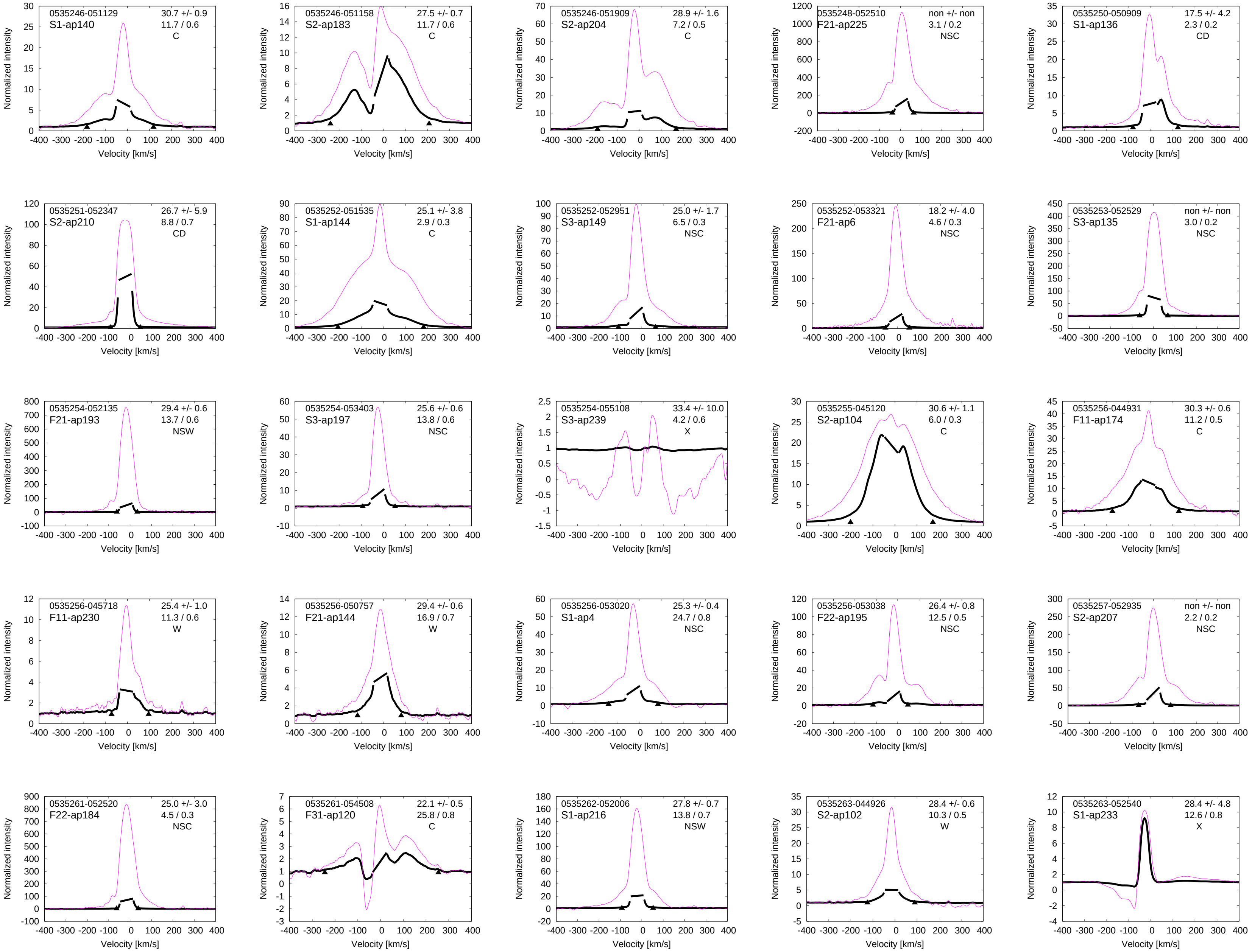
0535246-051129
S1-ap140
30.7 +/- 0.9
11.7 / 0.6
C
0535246-051158
S2-ap183
27.5 +/- 0.7
11.7 / 0.6
C
0535246-051909
S2-ap204
28.9 +/- 1.6
7.2 / 0.5
C
0535248-052510
F21-ap225
non +/- non
3.1 / 0.2
NSC
0535250-050909
S1-ap136
17.5 +/- 4.2
2.3 / 0.2
CD
0535251-052347
S2-ap210
26.7 +/- 5.9
8.8 / 0.7
CD
0535252-051535
S1-ap144
25.1 +/- 3.8
2.9 / 0.3
C
0535252-052951
S3-ap149
25.0 +/- 1.7
6.5 / 0.3
NSC
0535252-053321
F21-ap6
18.2 +/- 4.0
4.6 / 0.3
NSC
0535253-052529
S3-ap135
non +/- non
3.0 / 0.2
NSC
0535254-052135
F21-ap193
29.4 +/- 0.6
13.7 / 0.6
NSW
0535254-053403
S3-ap197
25.6 +/- 0.6
13.8 / 0.6
NSC
0535254-055108
S3-ap239
33.4 +/- 10.0
4.2 / 0.6
X
0535255-045120
S2-ap104
30.6 +/- 1.1
6.0 / 0.3
C
0535256-044931
F11-ap174
30.3 +/- 0.6
11.2 / 0.5
C
0535256-045718
F11-ap230
25.4 +/- 1.0
11.3 / 0.6
W
0535256-050757
F21-ap144
29.4 +/- 0.6
16.9 / 0.7
W
0535256-053020
S1-ap4
25.3 +/- 0.4
24.7 / 0.8
NSC
0535256-053038
F22-ap195
26.4 +/- 0.8
12.5 / 0.5
NSC
0535257-052935
S2-ap207
non +/- non
2.2 / 0.2
NSC
0535261-052520
F22-ap184
25.0 +/- 3.0
4.5 / 0.3
NSC
0535261-054508
F31-ap120
22.1 +/- 0.5
25.8 / 0.8
C
0535262-052006
S1-ap216
27.8 +/- 0.7
13.8 / 0.7
NSW
0535263-044926
S2-ap102
28.4 +/- 0.6
10.3 / 0.5
W
0535263-052540
S1-ap233
28.4 +/- 4.8
12.6 / 0.8
X
Normalized intensity
Velocity [km/s]
-400 -300 -200 -100 0 100 200 300 400

Fig. 12.3 cont.

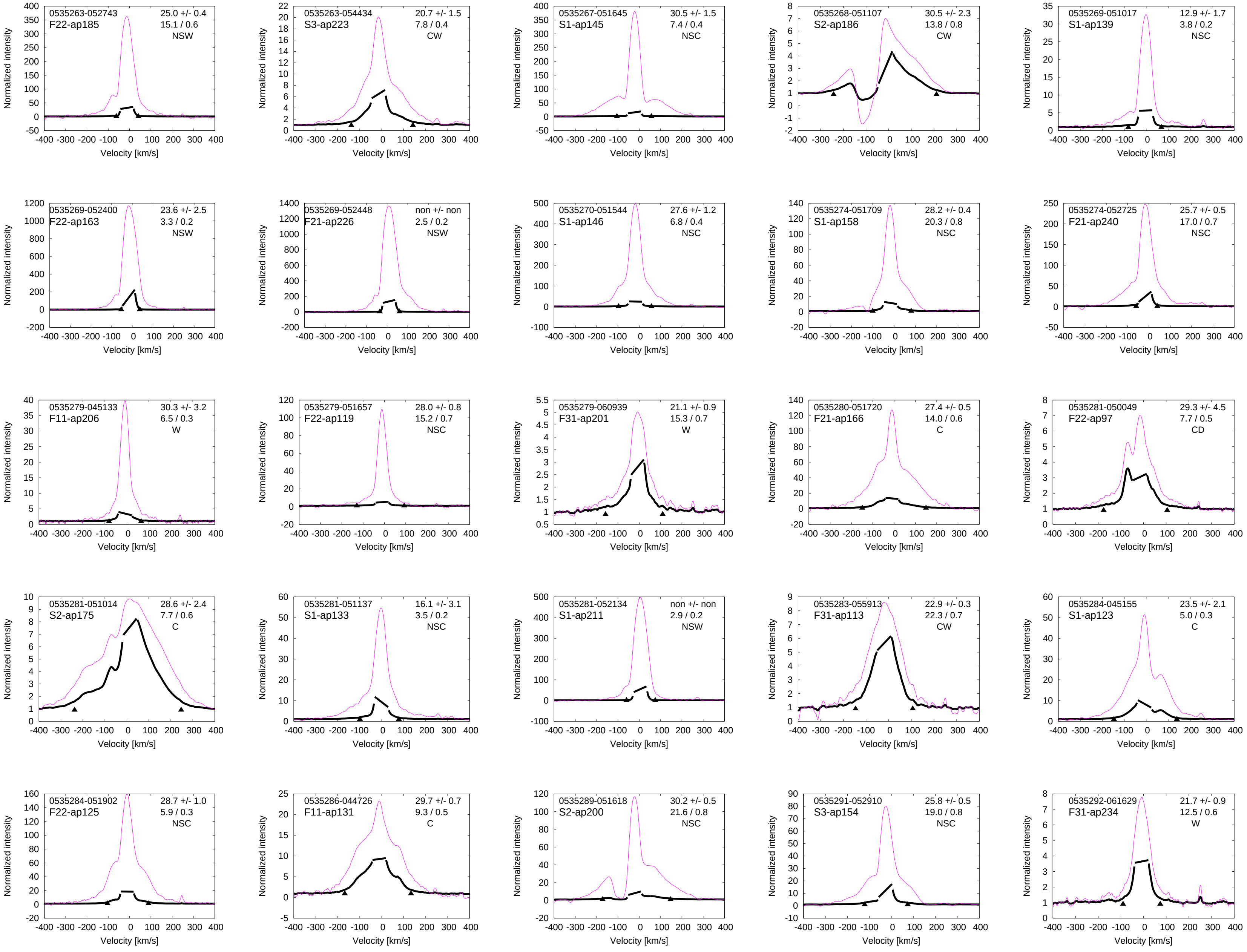
Normalized intensity
Velocity [km/s]
0535263-052743 F22-ap185 25.0 +/- 0.4 15.1 / 0.6 NSW
0535263-054434 S3-ap223 20.7 +/- 1.5 7.8 / 0.4 CW
0535267-051645 S1-ap145 30.5 +/- 1.5 7.4 / 0.4 NSC
0535268-051107 S2-ap186 30.5 +/- 2.3 13.8 / 0.8 CW
0535269-051017 S1-ap139 12.9 +/- 1.7 3.8 / 0.2 NSC
0535269-052400 F22-ap163 23.6 +/- 2.5 3.3 / 0.2 NSW
0535269-052448 F21-ap226 non +/- non 2.5 / 0.2 NSW
0535270-051544 S1-ap146 27.6 +/- 1.2 6.8 / 0.4 NSC
0535274-051709 S1-ap158 28.2 +/- 0.4 20.3 / 0.8 NSC
0535274-052725 F21-ap240 25.7 +/- 0.5 17.0 / 0.7 NSC
0535279-045133 F11-ap206 30.3 +/- 3.2 6.5 / 0.3 W
0535279-051657 F22-ap119 28.0 +/- 0.8 15.2 / 0.7 NSC
0535279-060939 F31-ap201 21.1 +/- 0.9 15.3 / 0.7 W
0535280-051720 F21-ap166 27.4 +/- 0.5 14.0 / 0.6 C
0535281-050049 F22-ap97 29.3 +/- 4.5 7.7 / 0.5 CD
0535281-051014 S2-ap175 28.6 +/- 2.4 7.7 / 0.6 C
0535281-051137 S1-ap133 16.1 +/- 3.1 3.5 / 0.2 NSC
0535281-052134 S1-ap211 non +/- non 2.9 / 0.2 NSW
0535283-055913 F31-ap113 22.9 +/- 0.3 22.3 / 0.7 CW
0535284-045155 S1-ap123 23.5 +/- 2.1 5.0 / 0.3 C
0535284-051902 F22-ap125 28.7 +/- 1.0 5.9 / 0.3 NSC
0535286-044726 F11-ap131 29.7 +/- 0.7 9.3 / 0.5 C
0535289-051618 S2-ap200 30.2 +/- 0.5 21.6 / 0.8 NSC
0535291-052910 S3-ap154 25.8 +/- 0.5 19.0 / 0.8 NSC
0535292-061629 F31-ap234 21.7 +/- 0.9 12.5 / 0.6 W

Fig. 12.3 cont.

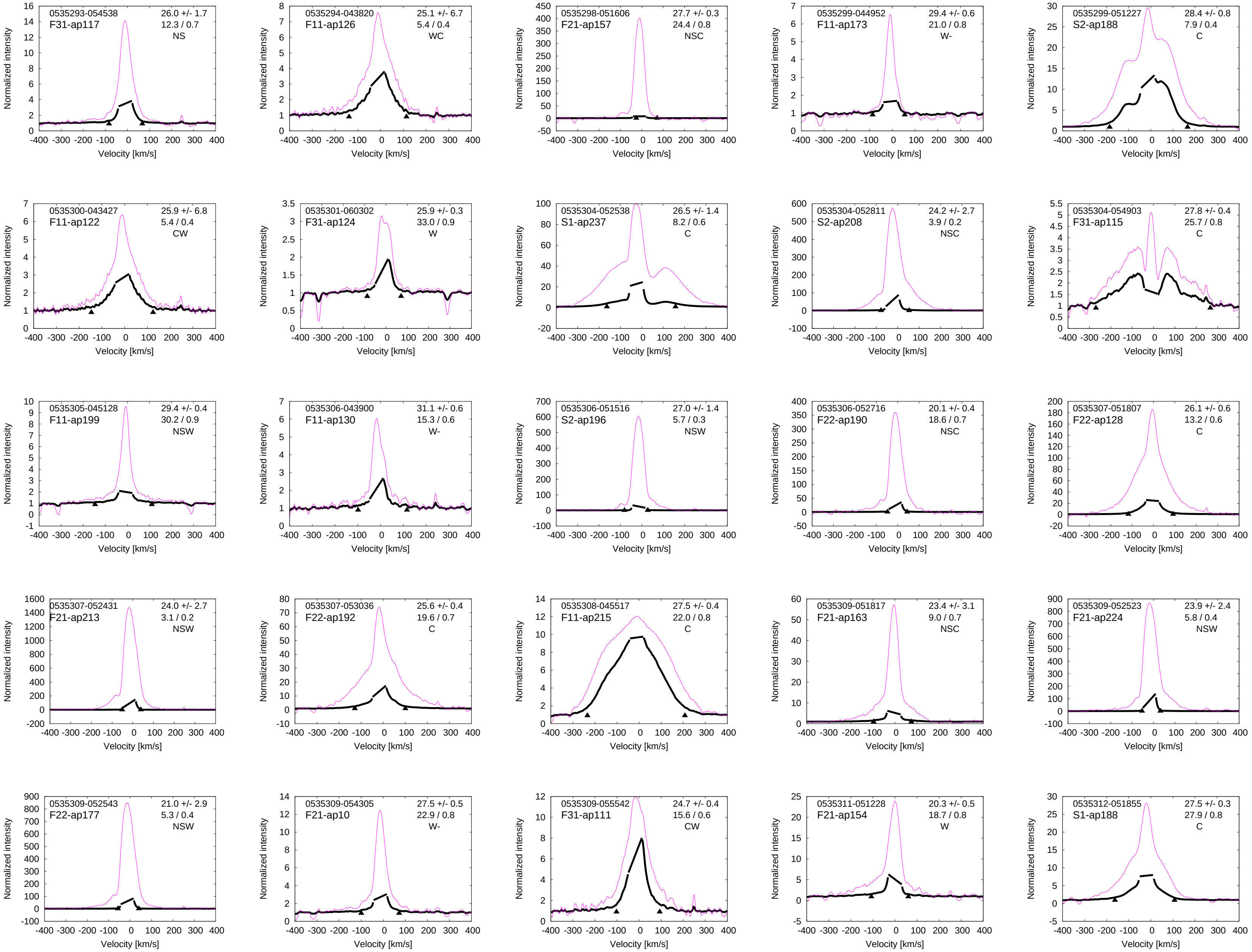
Normalized intensity
Velocity [km/s]
0535293-054538 F31-ap117 26.0 +/- 1.7 12.3 / 0.7 NS
0535294-043820 F11-ap126 25.1 +/- 6.7 5.4 / 0.4 WC
0535298-051606 F21-ap157 27.7 +/- 0.3 24.4 / 0.8 NSC
0535299-044952 F11-ap173 29.4 +/- 0.6 21.0 / 0.8 W-
0535299-051227 S2-ap188 28.4 +/- 0.8 7.9 / 0.4 C
0535300-043427 F11-ap122 25.9 +/- 6.8 5.4 / 0.4 CW
0535301-060302 F31-ap124 25.9 +/- 0.3 33.0 / 0.9 W
0535304-052538 S1-ap237 26.5 +/- 1.4 8.2 / 0.6 C
0535304-052811 S2-ap208 24.2 +/- 2.7 3.9 / 0.2 NSC
0535304-054903 F31-ap115 27.8 +/- 0.4 25.7 / 0.8 C
0535305-045128 F11-ap199 29.4 +/- 0.4 30.2 / 0.9 NSW
0535306-043900 F11-ap130 31.1 +/- 0.6 15.3 / 0.6 W-
0535306-051516 S2-ap196 27.0 +/- 1.4 5.7 / 0.3 NSW
0535306-052716 F22-ap190 20.1 +/- 0.4 18.6 / 0.7 NSC
0535307-051807 F22-ap128 26.1 +/- 0.6 13.2 / 0.6 C
0535307-052431 F21-ap213 24.0 +/- 2.7 3.1 / 0.2 NSW
0535307-053036 F22-ap192 25.6 +/- 0.4 19.6 / 0.7 C
0535308-045517 F11-ap215 27.5 +/- 0.4 22.0 / 0.8 C
0535309-051817 F21-ap163 23.4 +/- 3.1 9.0 / 0.7 NSC
0535309-052523 F21-ap224 23.9 +/- 2.4 5.8 / 0.4 NSW
0535309-052543 F22-ap177 21.0 +/- 2.9 5.3 / 0.4 NSW
0535309-054305 F21-ap10 27.5 +/- 0.5 22.9 / 0.8 W-
0535309-055542 F31-ap111 24.7 +/- 0.4 15.6 / 0.6 CW
0535311-051228 F21-ap154 20.3 +/- 0.5 18.7 / 0.8 W
0535312-051855 S1-ap188 27.5 +/- 0.3 27.9 / 0.8 C
-400 -300 -200 -100 0 100 200 300 400

Fig. 12.3 cont.

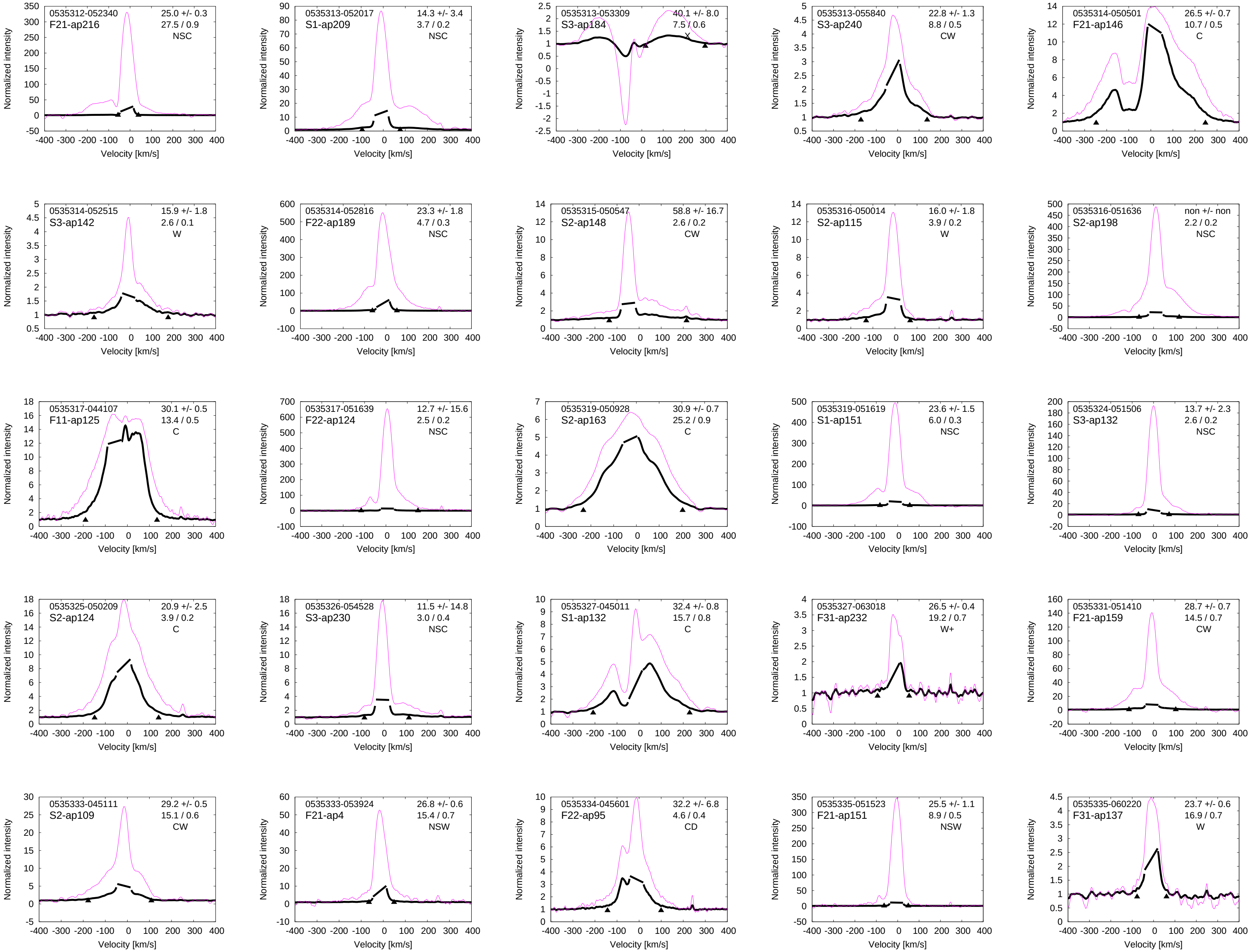
Normalized intensity
Velocity [km/s]
0535312-052340
F21-ap216
25.0 +/- 0.3
27.5 / 0.9
NSC
0535313-052017
S1-ap209
14.3 +/- 3.4
3.7 / 0.2
NSC
0535313-053309
S3-ap184
40.1 +/- 8.0
7.5 / 0.6
X
0535313-055840
S3-ap240
22.8 +/- 1.3
8.8 / 0.5
CW
0535314-050501
F21-ap146
26.5 +/- 0.7
10.7 / 0.5
C
0535314-052515
S3-ap142
15.9 +/- 1.8
2.6 / 0.1
W
0535314-052816
F22-ap189
23.3 +/- 1.8
4.7 / 0.3
NSC
0535315-050547
S2-ap148
58.8 +/- 16.7
2.6 / 0.2
CW
0535316-050014
S2-ap115
16.0 +/- 1.8
3.9 / 0.2
W
0535316-051636
S2-ap198
non +/- non
2.2 / 0.2
NSC
0535317-044107
F11-ap125
30.1 +/- 0.5
13.4 / 0.5
C
0535317-051639
F22-ap124
12.7 +/- 15.6
2.5 / 0.2
NSC
0535319-050928
S2-ap163
30.9 +/- 0.7
25.2 / 0.9
C
0535319-051619
S1-ap151
23.6 +/- 1.5
6.0 / 0.3
NSC
0535324-051506
S3-ap132
13.7 +/- 2.3
2.6 / 0.2
NSC
0535325-050209
S2-ap124
20.9 +/- 2.5
3.9 / 0.2
C
0535326-054528
S3-ap230
11.5 +/- 14.8
3.0 / 0.4
NSC
0535327-045011
S1-ap132
32.4 +/- 0.8
15.7 / 0.8
C
0535327-063018
F31-ap232
26.5 +/- 0.4
19.2 / 0.7
W+
0535331-051410
F21-ap159
28.7 +/- 0.7
14.5 / 0.7
CW
0535333-045111
S2-ap109
29.2 +/- 0.5
15.1 / 0.6
CW
0535333-053924
F21-ap4
26.8 +/- 0.6
15.4 / 0.7
NSW
0535334-045601
F22-ap95
32.2 +/- 6.8
4.6 / 0.4
CD
0535335-051523
F21-ap151
25.5 +/- 1.1
8.9 / 0.5
NSW
0535335-060220
F31-ap137
23.7 +/- 0.6
16.9 / 0.7
W
-400 -300 -200 -100 0 100 200 300 400

Fig. 12.3 cont.

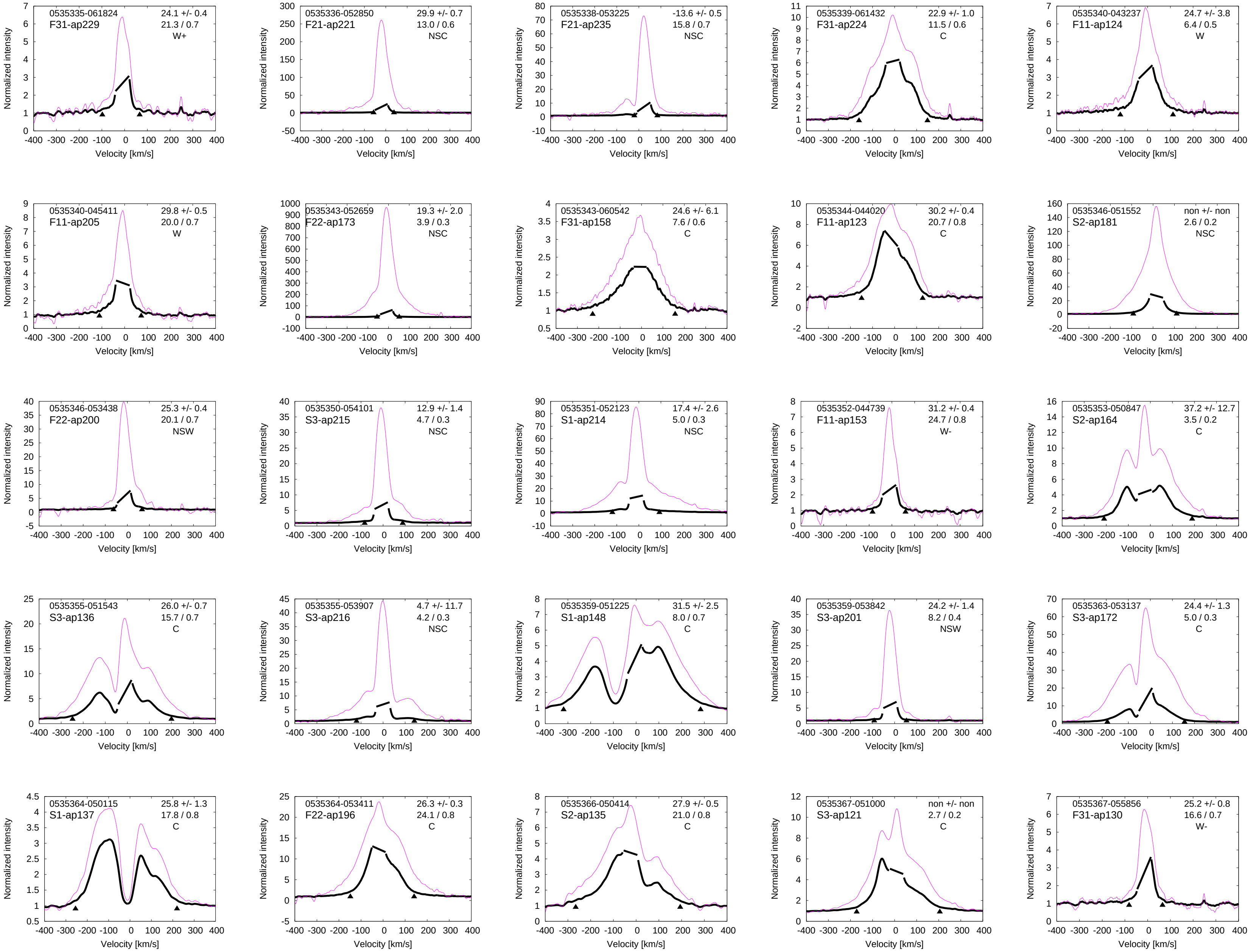
0535335-061824
F31-ap229
24.1 +/- 0.4
21.3 / 0.7
W+
0535336-052850
F21-ap221
29.9 +/- 0.7
13.0 / 0.6
NSC
0535338-053225
F21-ap235
-13.6 +/- 0.5
15.8 / 0.7
NSC
0535339-061432
F31-ap224
22.9 +/- 1.0
11.5 / 0.6
C
0535340-043237
F11-ap124
24.7 +/- 3.8
6.4 / 0.5
W
0535340-045411
F11-ap205
29.8 +/- 0.5
20.0 / 0.7
W
0535343-052659
F22-ap173
19.3 +/- 2.0
3.9 / 0.3
NSC
0535343-060542
F31-ap158
24.6 +/- 6.1
7.6 / 0.6
C
0535344-044020
F11-ap123
30.2 +/- 0.4
20.7 / 0.8
C
0535346-051552
S2-ap181
non +/- non
2.6 / 0.2
NSC
0535346-053438
F22-ap200
25.3 +/- 0.4
20.1 / 0.7
NSW
0535350-054101
S3-ap215
12.9 +/- 1.4
4.7 / 0.3
NSC
0535351-052123
S1-ap214
17.4 +/- 2.6
5.0 / 0.3
NSC
0535352-044739
F11-ap153
31.2 +/- 0.4
24.7 / 0.8
W-
0535353-050847
S2-ap164
37.2 +/- 12.7
3.5 / 0.2
C
0535355-051543
S3-ap136
26.0 +/- 0.7
15.7 / 0.7
C
0535355-053907
S3-ap216
4.7 +/- 11.7
4.2 / 0.3
NSC
0535359-051225
S1-ap148
31.5 +/- 2.5
8.0 / 0.7
C
0535359-053842
S3-ap201
24.2 +/- 1.4
8.2 / 0.4
NSW
0535363-053137
S3-ap172
24.4 +/- 1.3
5.0 / 0.3
C
0535364-050115
S1-ap137
25.8 +/- 1.3
17.8 / 0.8
C
0535364-053411
F22-ap196
26.3 +/- 0.3
24.1 / 0.8
C
0535366-050414
S2-ap135
27.9 +/- 0.5
21.0 / 0.8
C
0535367-051000
S3-ap121
non +/- non
2.7 / 0.2
C
0535367-055856
F31-ap130
25.2 +/- 0.8
16.6 / 0.7
W-
Normalized intensity
Velocity [km/s]
-400 -300 -200 -100 0 100 200 300 400

Fig. 12.3 cont.

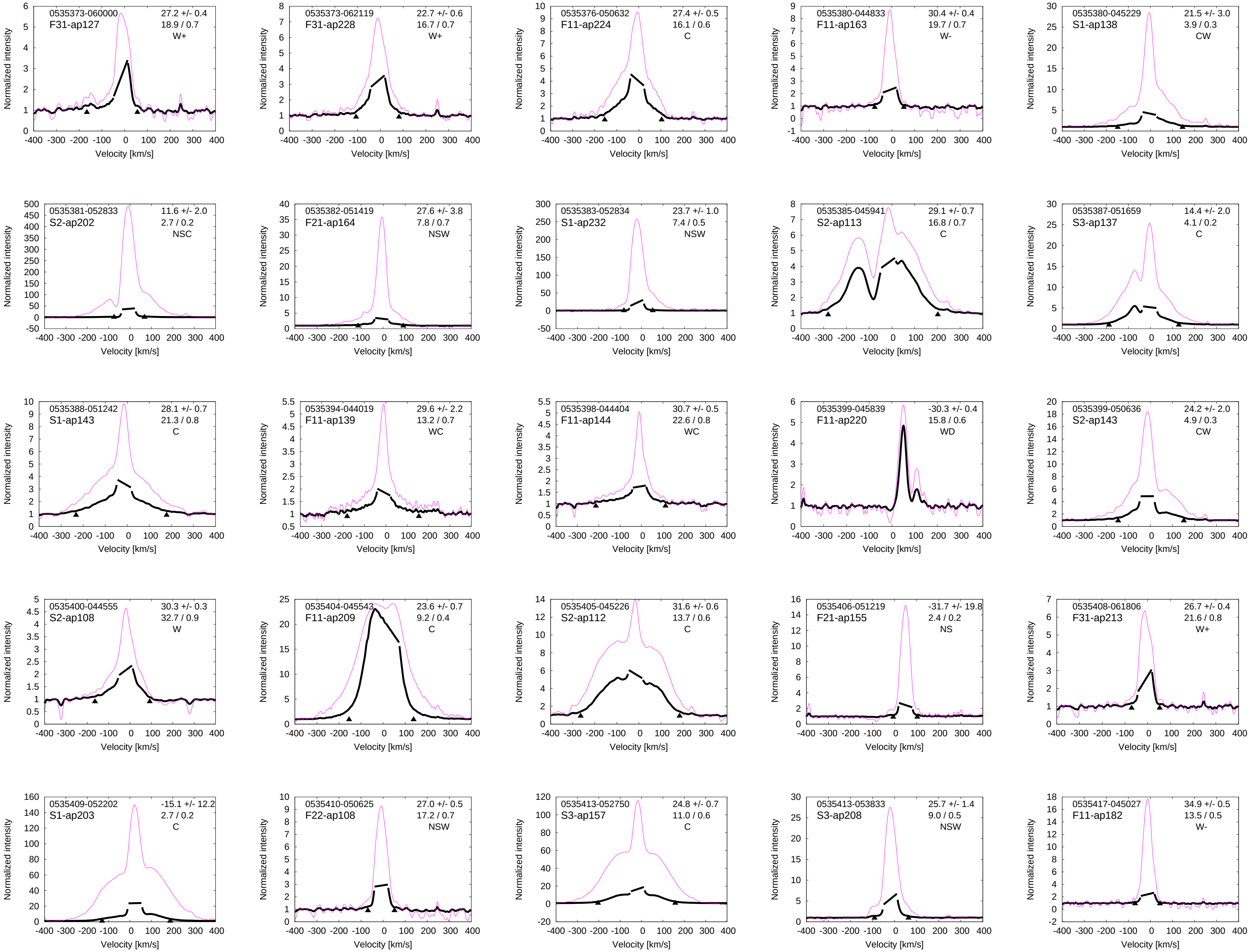
Normalized intensity
Velocity [km/s]
0535373-060000 F31-ap127 27.2 +/- 0.4 18.9 / 0.7 W+
0535373-062119 F31-ap228 22.7 +/- 0.6 16.7 / 0.7 W+
0535376-050632 F11-ap224 27.4 +/- 0.5 16.1 / 0.6 C
0535380-044833 F11-ap163 30.4 +/- 0.4 19.7 / 0.7 W-
0535380-045229 S1-ap138 21.5 +/- 3.0 3.9 / 0.3 CW
0535381-052833 S2-ap202 11.6 +/- 2.0 2.7 / 0.2 NSC
0535382-051419 F21-ap164 27.6 +/- 3.8 7.8 / 0.7 NSW
0535383-052834 S1-ap232 23.7 +/- 1.0 7.4 / 0.5 NSW
0535385-045941 S2-ap113 29.1 +/- 0.7 16.8 / 0.7 C
0535387-051659 S3-ap137 14.4 +/- 2.0 4.1 / 0.2 C
0535388-051242 S1-ap143 28.1 +/- 0.7 21.3 / 0.8 C
0535394-044019 F11-ap139 29.6 +/- 2.2 13.2 / 0.7 WC
0535398-044404 F11-ap144 30.7 +/- 0.5 22.6 / 0.8 WC
0535399-045839 F11-ap220 -30.3 +/- 0.4 15.8 / 0.6 WD
0535399-050636 S2-ap143 24.2 +/- 2.0 4.9 / 0.3 CW
0535400-044555 S2-ap108 30.3 +/- 0.3 32.7 / 0.9 W
0535404-045543 F11-ap209 23.6 +/- 0.7 9.2 / 0.4 C
0535405-045226 S2-ap112 31.6 +/- 0.6 13.7 / 0.6 C
0535406-051219 F21-ap155 -31.7 +/- 19.8 2.4 / 0.2 NS
0535408-061806 F31-ap213 26.7 +/- 0.4 21.6 / 0.8 W+
0535409-052202 S1-ap203 -15.1 +/- 12.2 2.7 / 0.2 C
0535410-050625 F22-ap108 27.0 +/- 0.5 17.2 / 0.7 NSW
0535413-052750 S3-ap157 24.8 +/- 0.7 11.0 / 0.6 C
0535413-053833 S3-ap208 25.7 +/- 1.4 9.0 / 0.5 NSW
0535417-045027 F11-ap182 34.9 +/- 0.5 13.5 / 0.5 W-

Fig. 12.3 cont.

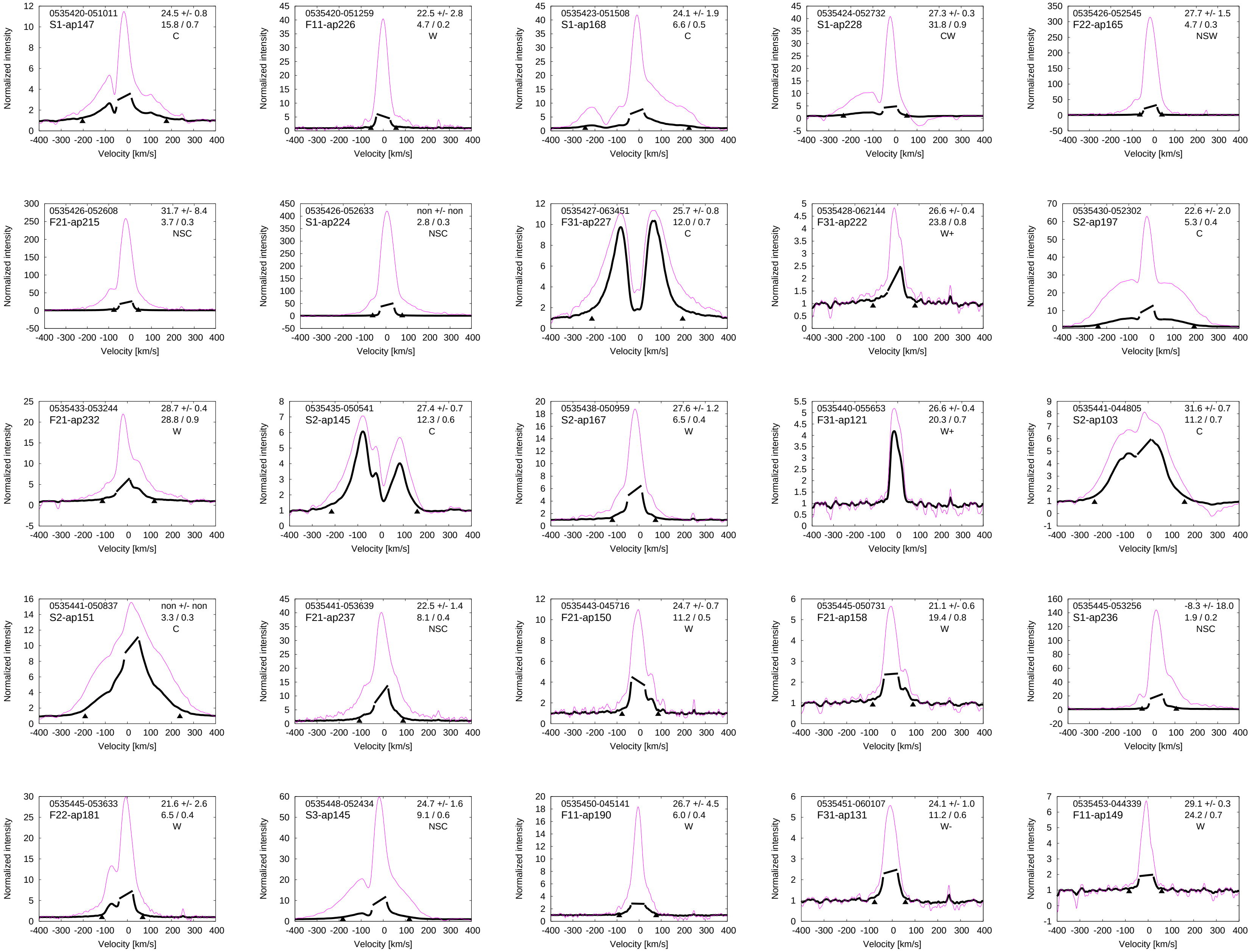
0535420-051011 S1-ap147 24.5 +/- 0.8 15.8 / 0.7 C
0535420-051259 F11-ap226 22.5 +/- 2.8 4.7 / 0.2 W
0535423-051508 S1-ap168 24.1 +/- 1.9 6.6 / 0.5 C
0535424-052732 S1-ap228 27.3 +/- 0.3 31.8 / 0.9 CW
0535426-052545 F22-ap165 27.7 +/- 1.5 4.7 / 0.3 NSW
0535426-052608 F21-ap215 31.7 +/- 8.4 3.7 / 0.3 NSC
0535426-052633 S1-ap224 non +/- non 2.8 / 0.3 NSC
0535427-063451 F31-ap227 25.7 +/- 0.8 12.0 / 0.7 C
0535428-062144 F31-ap222 26.6 +/- 0.4 23.8 / 0.8 W+
0535430-052302 S2-ap197 22.6 +/- 2.0 5.3 / 0.4 C
0535433-053244 F21-ap232 28.7 +/- 0.4 28.8 / 0.9 W
0535435-050541 S2-ap145 27.4 +/- 0.7 12.3 / 0.6 C
0535438-050959 S2-ap167 27.6 +/- 1.2 6.5 / 0.4 W
0535440-055653 F31-ap121 26.6 +/- 0.4 20.3 / 0.7 W+
0535441-044805 S2-ap103 31.6 +/- 0.7 11.2 / 0.7 C
0535441-050837 S2-ap151 non +/- non 3.3 / 0.3 C
0535441-053639 F21-ap237 22.5 +/- 1.4 8.1 / 0.4 NSC
0535443-045716 F21-ap150 24.7 +/- 0.7 11.2 / 0.5 W
0535445-050731 F21-ap158 21.1 +/- 0.6 19.4 / 0.8 W
0535445-053256 S1-ap236 -8.3 +/- 18.0 1.9 / 0.2 NSC
0535445-053633 F22-ap181 21.6 +/- 2.6 6.5 / 0.4 W
0535448-052434 S3-ap145 24.7 +/- 1.6 9.1 / 0.6 NSC
0535450-045141 F11-ap190 26.7 +/- 4.5 6.0 / 0.4 W
0535451-060107 F31-ap131 24.1 +/- 1.0 11.2 / 0.6 W-
0535453-044339 F11-ap149 29.1 +/- 0.3 24.2 / 0.7 W
Normalized intensity
Velocity [km/s]
-400 -300 -200 -100 0 100 200 300 400

Fig. 12.3 cont.

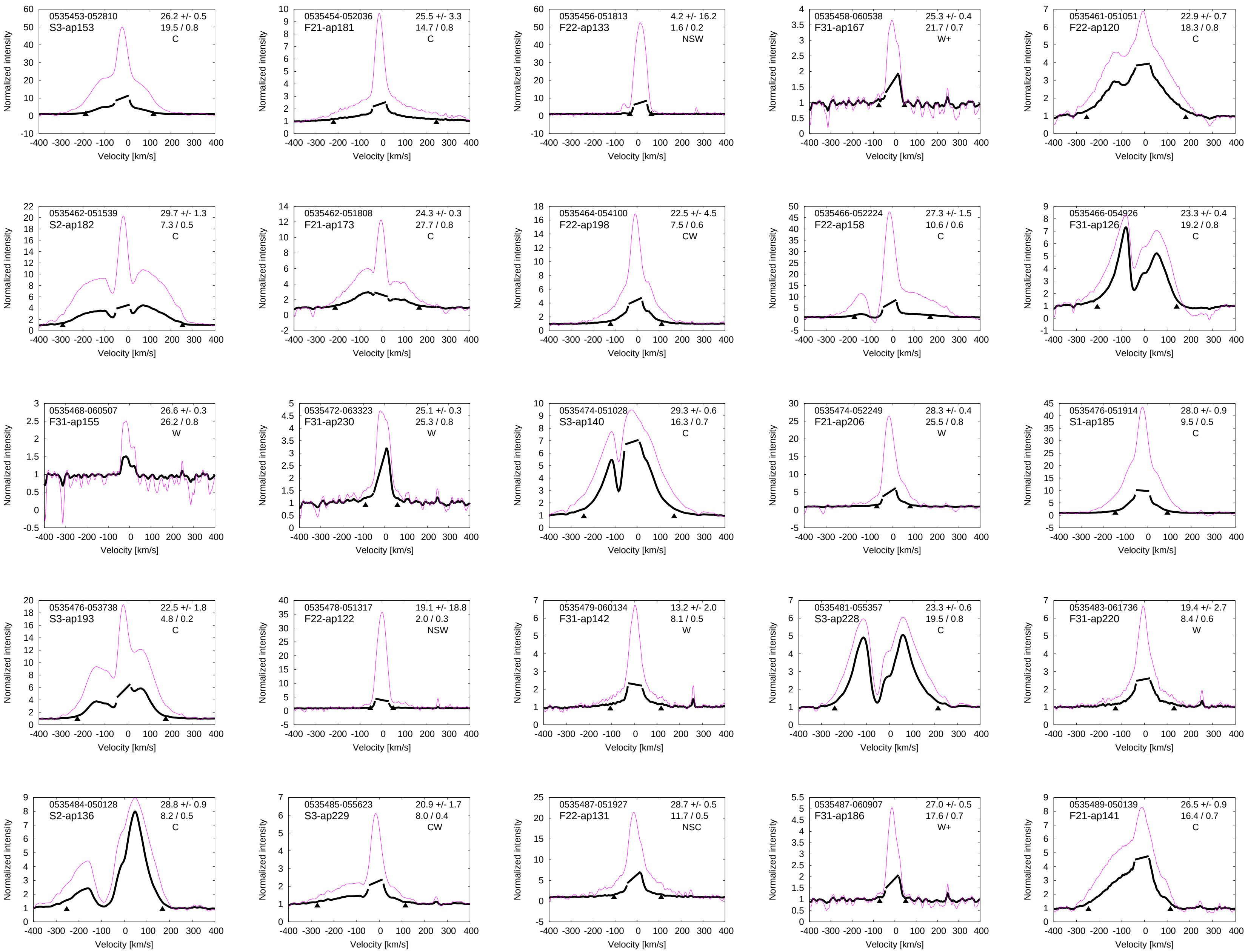
Normalized intensity
Velocity [km/s]
0535453-052810
S3-ap153
26.2 +/- 0.5
19.5 / 0.8
C
0535454-052036
F21-ap181
25.5 +/- 3.3
14.7 / 0.8
C
0535456-051813
F22-ap133
4.2 +/- 16.2
1.6 / 0.2
NSW
0535458-060538
F31-ap167
25.3 +/- 0.4
21.7 / 0.7
W+
0535461-051051
F22-ap120
22.9 +/- 0.7
18.3 / 0.8
C
0535462-051539
S2-ap182
29.7 +/- 1.3
7.3 / 0.5
C
0535462-051808
F21-ap173
24.3 +/- 0.3
27.7 / 0.8
C
0535464-054100
F22-ap198
22.5 +/- 4.5
7.5 / 0.6
CW
0535466-052224
F22-ap158
27.3 +/- 1.5
10.6 / 0.6
C
0535466-054926
F31-ap126
23.3 +/- 0.4
19.2 / 0.8
C
0535468-060507
F31-ap155
26.6 +/- 0.3
26.2 / 0.8
W
0535472-063323
F31-ap230
25.1 +/- 0.3
25.3 / 0.8
W
0535474-051028
S3-ap140
29.3 +/- 0.6
16.3 / 0.7
C
0535474-052249
F21-ap206
28.3 +/- 0.4
25.5 / 0.8
W
0535476-051914
S1-ap185
28.0 +/- 0.9
9.5 / 0.5
C
0535476-053738
S3-ap193
22.5 +/- 1.8
4.8 / 0.2
C
0535478-051317
F22-ap122
19.1 +/- 18.8
2.0 / 0.3
NSW
0535479-060134
F31-ap142
13.2 +/- 2.0
8.1 / 0.5
W
0535481-055357
S3-ap228
23.3 +/- 0.6
19.5 / 0.8
C
0535483-061736
F21-ap220
19.4 +/- 2.7
8.4 / 0.6
W
0535484-050128
S2-ap136
28.8 +/- 0.9
8.2 / 0.5
C
0535485-055623
S3-ap229
20.9 +/- 1.7
8.0 / 0.4
CW
0535487-051927
F22-ap131
28.7 +/- 0.5
11.7 / 0.5
NSC
0535487-060907
F31-ap186
27.0 +/- 0.5
17.6 / 0.7
W+
0535489-050139
F21-ap141
26.5 +/- 0.9
16.4 / 0.7
C
-400 -300 -200 -100 0 100 200 300 400

Fig. 12.3 cont.

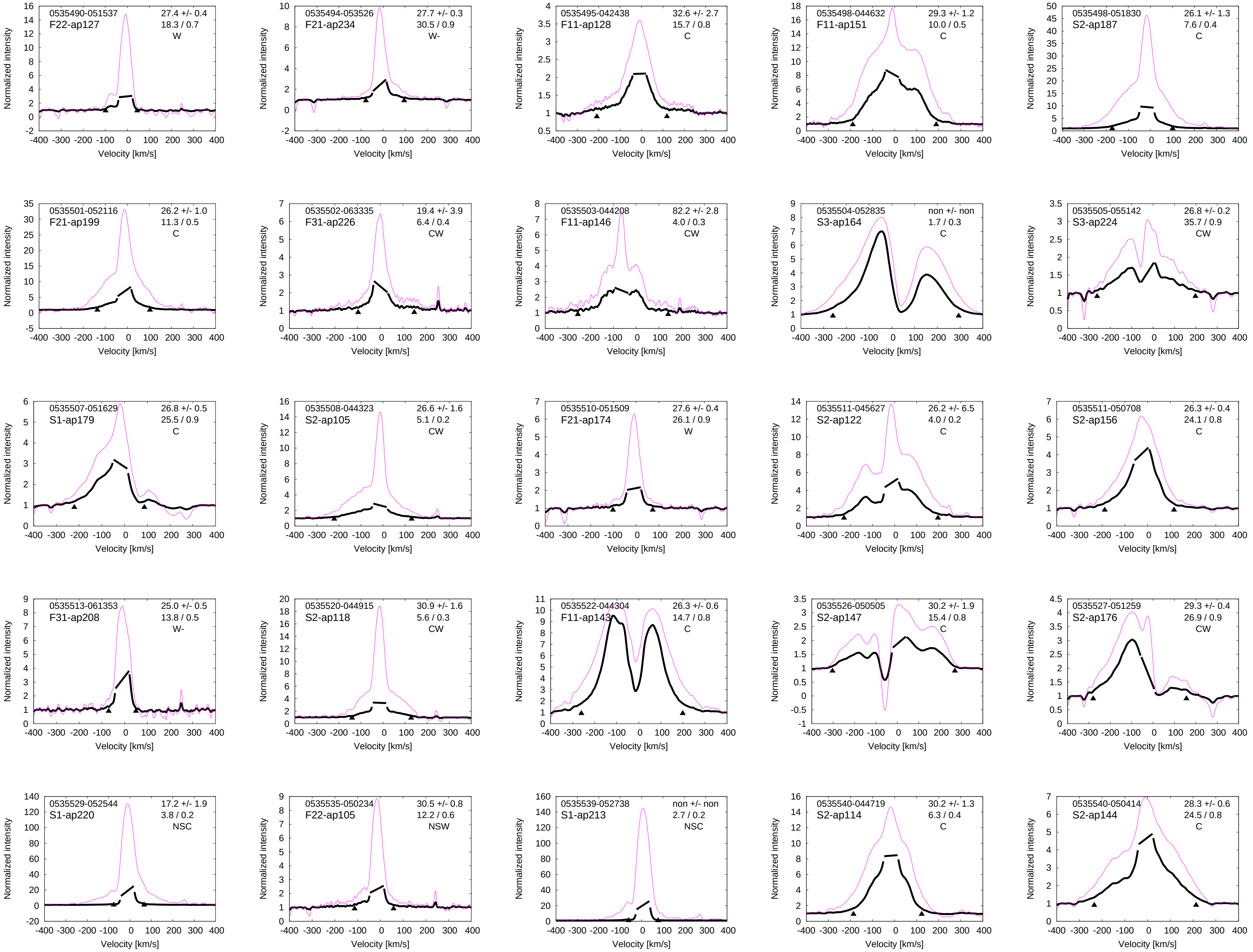
Normalized intensity
Velocity [km/s]
0535490-051537 F22-ap127 27.4 +/- 0.4 18.3 / 0.7 W
0535494-053526 F21-ap234 27.7 +/- 0.3 30.5 / 0.9 W-
0535495-042438 F11-ap128 32.6 +/- 2.7 15.7 / 0.8 C
0535498-044632 F11-ap151 29.3 +/- 1.2 10.0 / 0.5 C
0535498-051830 S2-ap187 26.1 +/- 1.3 7.6 / 0.4 C
0535501-052116 F21-ap199 26.2 +/- 1.0 11.3 / 0.5 C
0535502-063335 F31-ap226 19.4 +/- 3.9 6.4 / 0.4 CW
0535503-044208 F11-ap146 82.2 +/- 2.8 4.0 / 0.3 CW
0535504-052835 S3-ap164 non +/- non 1.7 / 0.3 C
0535505-055142 S3-ap224 26.8 +/- 0.2 35.7 / 0.9 CW
0535507-051629 S1-ap179 26.8 +/- 0.5 25.5 / 0.9 C
0535508-044323 S2-ap105 26.6 +/- 1.6 5.1 / 0.2 CW
0535510-051509 F21-ap174 27.6 +/- 0.4 26.1 / 0.9 W
0535511-045627 S2-ap122 26.2 +/- 6.5 4.0 / 0.2 C
0535511-050708 S2-ap156 26.3 +/- 0.4 24.1 / 0.8 C
0535513-061353 F31-ap208 25.0 +/- 0.5 13.8 / 0.5 W-
0535520-044915 S2-ap118 30.9 +/- 1.6 5.6 / 0.3 CW
0535522-044304 F11-ap143 26.3 +/- 0.6 14.7 / 0.8 C
0535526-050505 S2-ap147 30.2 +/- 1.9 15.4 / 0.8 C
0535527-051259 S2-ap176 29.3 +/- 0.4 26.9 / 0.9 CW
0535529-052544 S1-ap220 17.2 +/- 1.9 3.8 / 0.2 NSC
0535535-050234 F22-ap105 30.5 +/- 0.8 12.2 / 0.6 NSW
0535539-052738 S1-ap213 non +/- non 2.7 / 0.2 NSC
0535540-044719 S2-ap114 30.2 +/- 1.3 6.3 / 0.4 C
0535540-050414 S2-ap144 28.3 +/- 0.6 24.5 / 0.8 C

Fig. 12.3 cont.

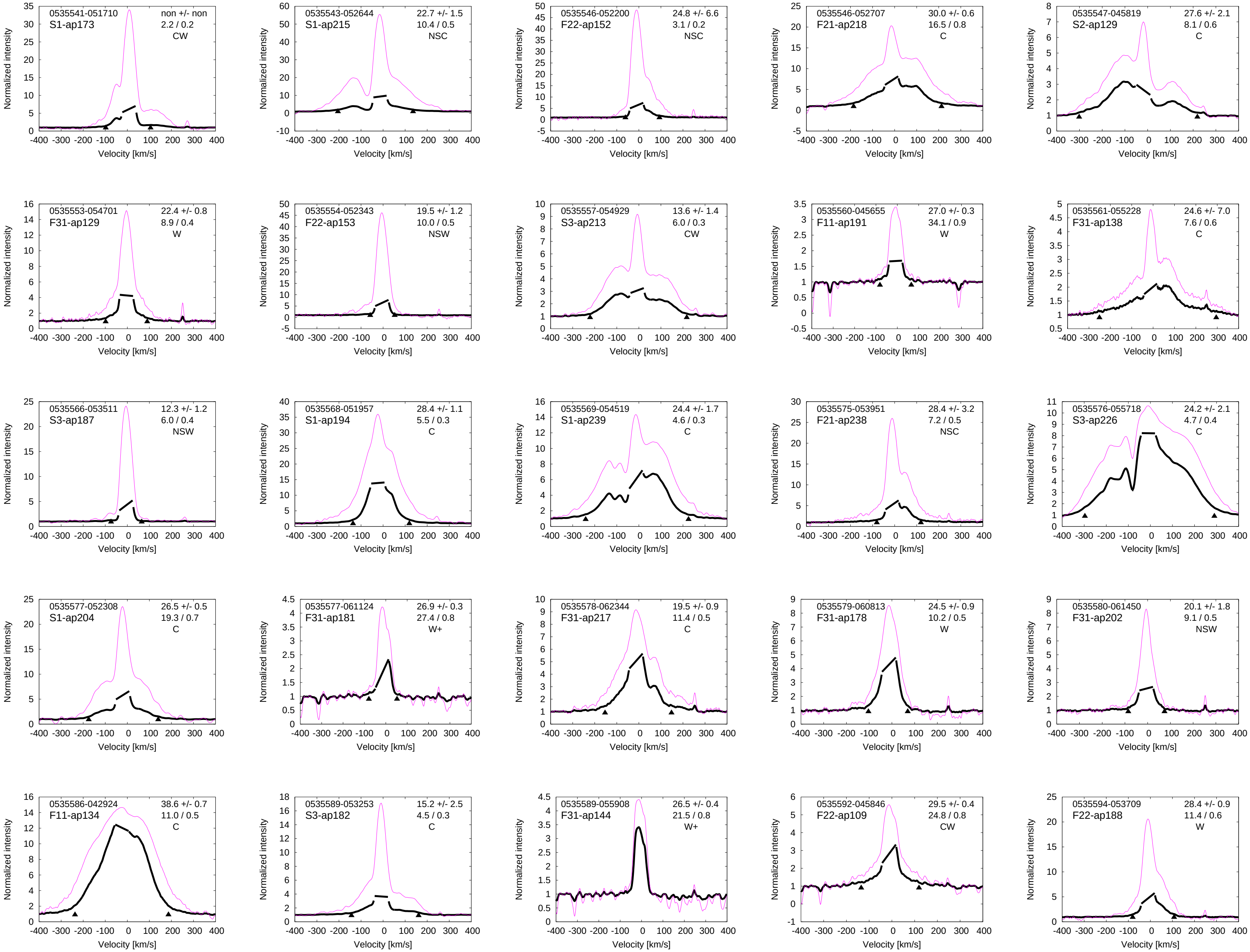
0535541-051710
S1-ap173
non +/- non
2.2 / 0.2
CW
0535543-052644
S1-ap215
22.7 +/- 1.5
10.4 / 0.5
NSC
0535546-052200
F22-ap152
24.8 +/- 6.6
3.1 / 0.2
NSC
0535546-052707
F21-ap218
30.0 +/- 0.6
16.5 / 0.8
C
0535547-045819
S2-ap129
27.6 +/- 2.1
8.1 / 0.6
C
0535553-054701
F31-ap129
22.4 +/- 0.8
8.9 / 0.4
W
0535554-052343
F22-ap153
19.5 +/- 1.2
10.0 / 0.5
NSW
0535557-054929
S3-ap213
13.6 +/- 1.4
6.0 / 0.3
CW
0535560-045655
F11-ap191
27.0 +/- 0.3
34.1 / 0.9
W
0535561-055228
F31-ap138
24.6 +/- 7.0
7.6 / 0.6
C
0535566-053511
S3-ap187
12.3 +/- 1.2
6.0 / 0.4
NSW
0535568-051957
S1-ap194
28.4 +/- 1.1
5.5 / 0.3
C
0535569-054519
S1-ap239
24.4 +/- 1.7
4.6 / 0.3
C
0535575-053951
F21-ap238
28.4 +/- 3.2
7.2 / 0.5
NSC
0535576-055718
S3-ap226
24.2 +/- 2.1
4.7 / 0.4
C
0535577-052308
S1-ap204
26.5 +/- 0.5
19.3 / 0.7
C
0535577-061124
F31-ap181
26.9 +/- 0.3
27.4 / 0.8
W+
0535578-062344
F31-ap217
19.5 +/- 0.9
11.4 / 0.5
C
0535579-060813
F31-ap178
24.5 +/- 0.9
10.2 / 0.5
W
0535580-061450
F31-ap202
20.1 +/- 1.8
9.1 / 0.5
NSW
0535586-042924
F11-ap134
38.6 +/- 0.7
11.0 / 0.5
C
0535589-053253
S3-ap182
15.2 +/- 2.5
4.5 / 0.3
C
0535589-055908
F31-ap144
26.5 +/- 0.4
21.5 / 0.8
W+
0535592-045846
F22-ap109
29.5 +/- 0.4
24.8 / 0.8
CW
0535594-053709
F22-ap188
28.4 +/- 0.9
11.4 / 0.6
W
Normalized intensity
Velocity [km/s]
-400 -300 -200 -100 0 100 200 300 400

Fig. 12.3 cont.

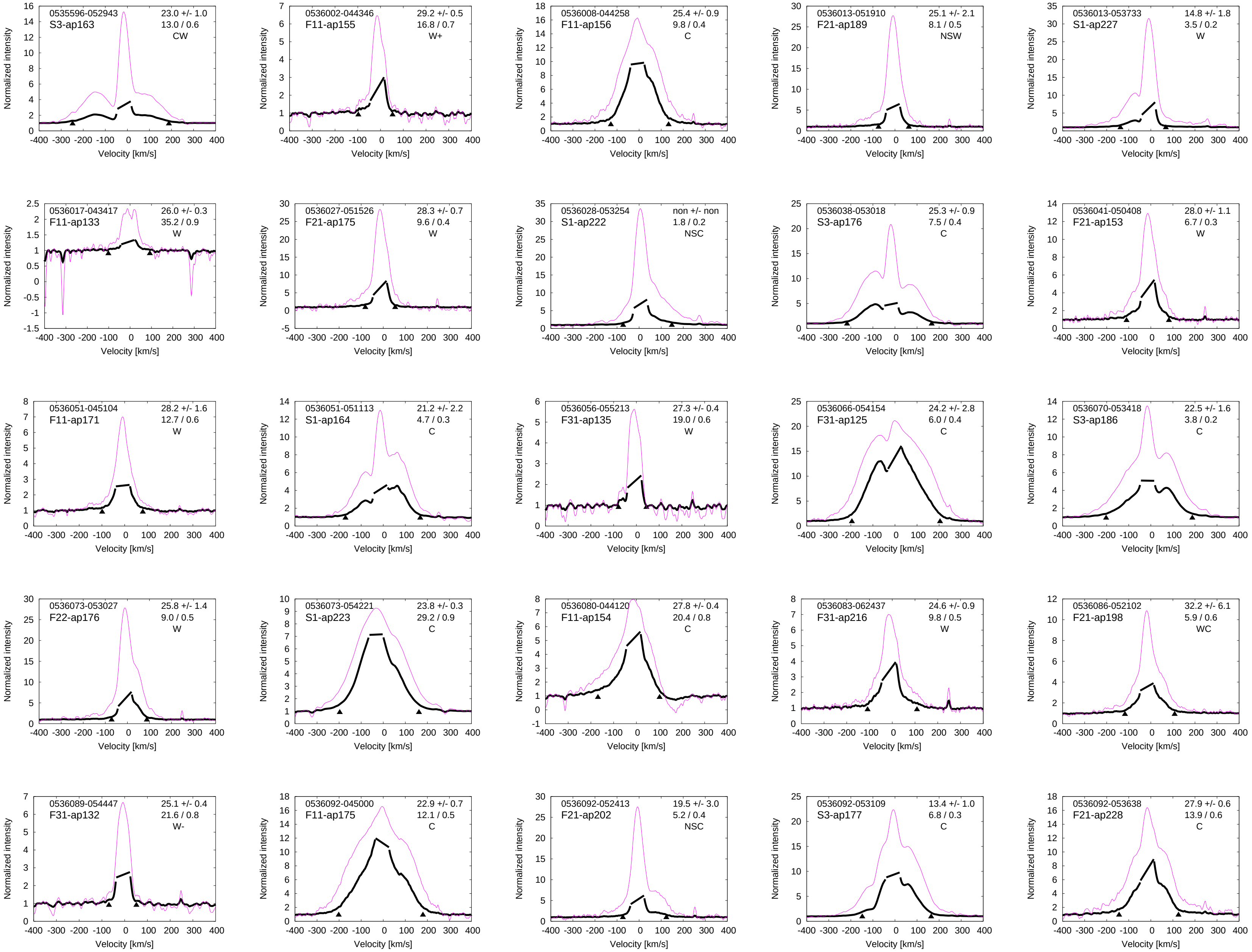
0535596-052943
S3-ap163
23.0 +/- 1.0
13.0 / 0.6
CW
0536002-044346
F11-ap155
29.2 +/- 0.5
16.8 / 0.7
W+
0536008-044258
F11-ap156
25.4 +/- 0.9
9.8 / 0.4
C
0536013-051910
F21-ap189
25.1 +/- 2.1
8.1 / 0.5
NSW
0536013-053733
S1-ap227
14.8 +/- 1.8
3.5 / 0.2
W
0536017-043417
F11-ap133
26.0 +/- 0.3
35.2 / 0.9
W
0536027-051526
F21-ap175
28.3 +/- 0.7
9.6 / 0.4
W
0536028-053254
S1-ap222
non +/- non
1.8 / 0.2
NSC
0536038-053018
S3-ap176
25.3 +/- 0.9
7.5 / 0.4
C
0536041-050408
F21-ap153
28.0 +/- 1.1
6.7 / 0.3
W
0536051-045104
F11-ap171
28.2 +/- 1.6
12.7 / 0.6
W
0536051-051113
S1-ap164
21.2 +/- 2.2
4.7 / 0.3
C
0536056-055213
F31-ap135
27.3 +/- 0.4
19.0 / 0.6
W
0536066-054154
F31-ap125
24.2 +/- 2.8
6.0 / 0.4
C
0536070-053418
S3-ap186
22.5 +/- 1.6
3.8 / 0.2
C
0536073-053027
F22-ap176
25.8 +/- 1.4
9.0 / 0.5
W
0536073-054221
S1-ap223
23.8 +/- 0.3
29.2 / 0.9
C
0536080-044120
F11-ap154
27.8 +/- 0.4
20.4 / 0.8
C
0536083-062437
F31-ap216
24.6 +/- 0.9
9.8 / 0.5
W
0536086-052102
F21-ap198
32.2 +/- 6.1
5.9 / 0.6
WC
0536089-054447
F31-ap132
25.1 +/- 0.4
21.6 / 0.8
W-
0536092-045000
F11-ap175
22.9 +/- 0.7
12.1 / 0.5
C
0536092-052413
F21-ap202
19.5 +/- 3.0
5.2 / 0.4
NSC
0536092-053109
S3-ap177
13.4 +/- 1.0
6.8 / 0.3
C
0536092-053638
F21-ap228
27.9 +/- 0.6
13.9 / 0.6
C
Normalized intensity
Velocity [km/s]
-400 -300 -200 -100 0 100 200 300 400

Fig. 12.3 cont.

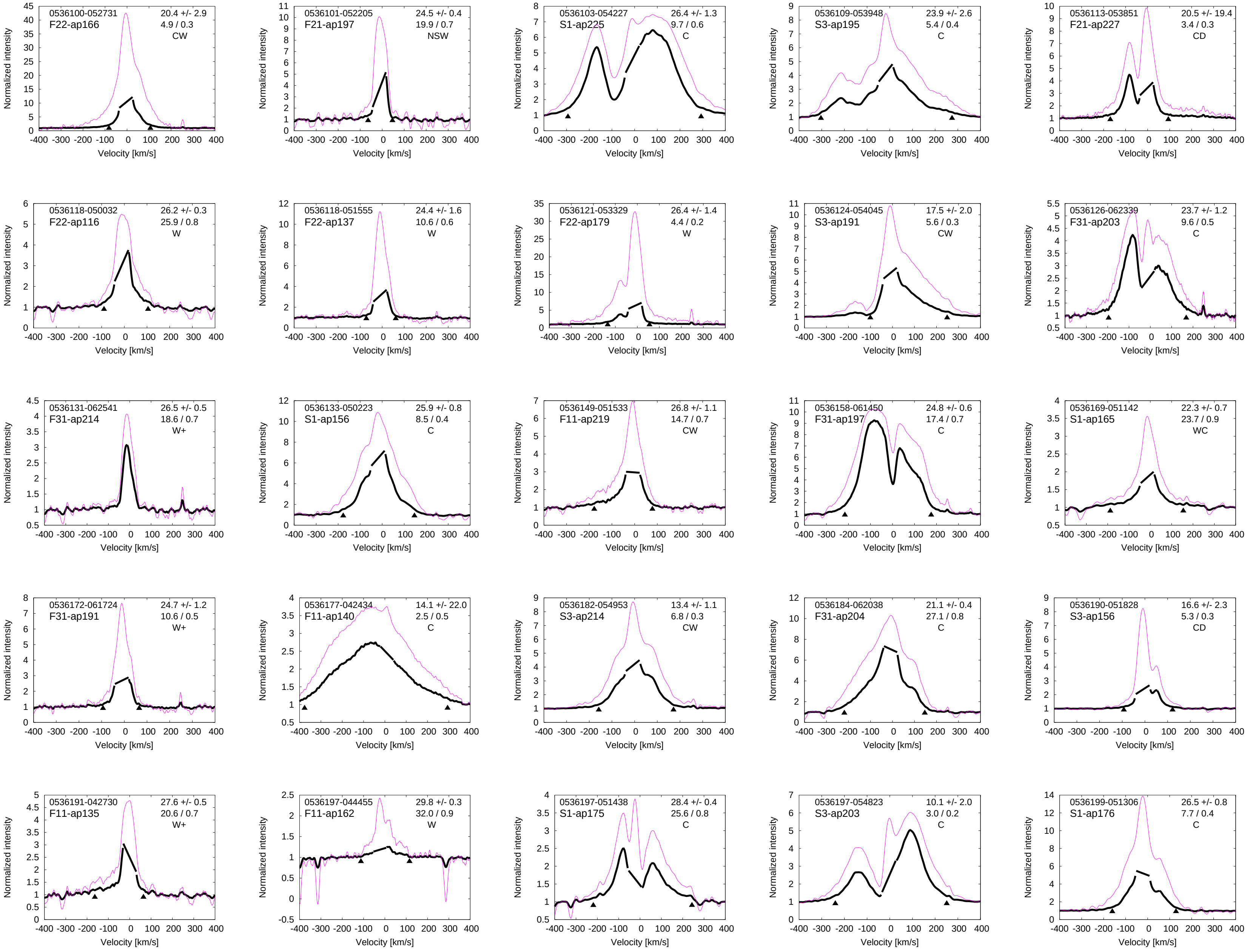
0536100-052731
F22-ap166
20.4 +/- 2.9
4.9 / 0.3
CW
0536101-052205
F21-ap197
24.5 +/- 0.4
19.9 / 0.7
NSW
0536103-054227
S1-ap225
26.4 +/- 1.3
9.7 / 0.6
C
0536109-053948
S3-ap195
23.9 +/- 2.6
5.4 / 0.4
C
0536113-053851
F21-ap227
20.5 +/- 19.4
3.4 / 0.3
CD
0536118-050032
F22-ap116
26.2 +/- 0.3
25.9 / 0.8
W
0536118-051555
F22-ap137
24.4 +/- 1.6
10.6 / 0.6
W
0536121-053329
F22-ap179
26.4 +/- 1.4
4.4 / 0.2
W
0536124-054045
S3-ap191
17.5 +/- 2.0
5.6 / 0.3
CW
0536126-062339
F31-ap203
23.7 +/- 1.2
9.6 / 0.5
C
0536131-062541
F31-ap214
26.5 +/- 0.5
18.6 / 0.7
W+
0536133-050223
S1-ap156
25.9 +/- 0.8
8.5 / 0.4
C
0536149-051533
F11-ap219
26.8 +/- 1.1
14.7 / 0.7
CW
0536158-061450
F31-ap197
24.8 +/- 0.6
17.4 / 0.7
C
0536169-051142
S1-ap165
22.3 +/- 0.7
23.7 / 0.9
WC
0536172-061724
F31-ap191
24.7 +/- 1.2
10.6 / 0.5
W+
0536177-042434
F11-ap140
14.1 +/- 22.0
2.5 / 0.5
C
0536182-054953
S3-ap214
13.4 +/- 1.1
6.8 / 0.3
CW
0536184-062038
F31-ap204
21.1 +/- 0.4
27.1 / 0.8
C
0536190-051828
S3-ap156
16.6 +/- 2.3
5.3 / 0.3
CD
0536191-042730
F11-ap135
27.6 +/- 0.5
20.6 / 0.7
W+
0536197-044455
F11-ap162
29.8 +/- 0.3
32.0 / 0.9
W
0536197-051438
S1-ap175
28.4 +/- 0.4
25.6 / 0.8
C
0536197-054823
S3-ap203
10.1 +/- 2.0
3.0 / 0.2
C
0536199-051306
S1-ap176
26.5 +/- 0.8
7.7 / 0.4
C
Normalized intensity
Velocity [km/s]
-400 -300 -200 -100 0 100 200 300 400

Fig. 12.3 cont.

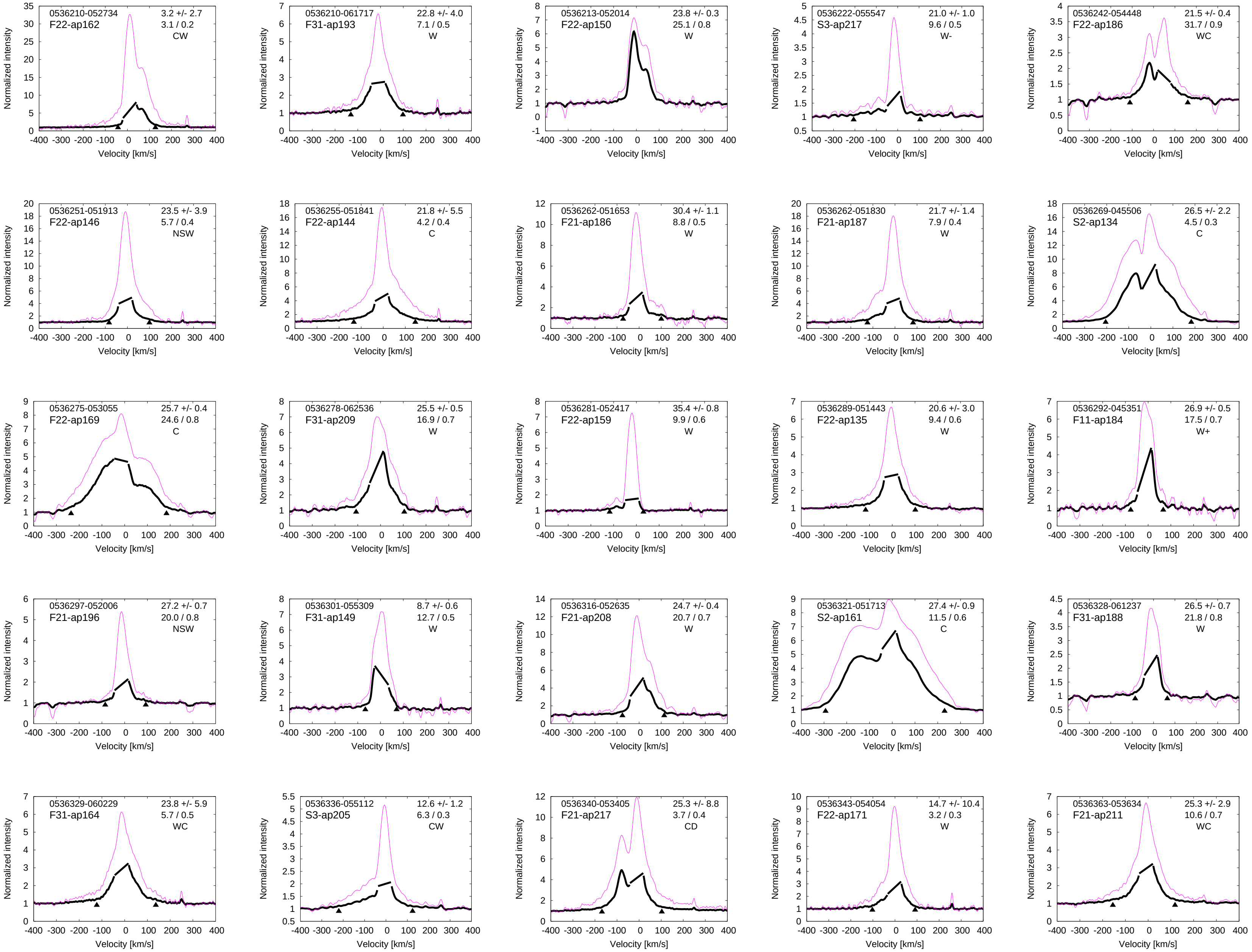
0536210-052734
F22-ap162
3.2 +/- 2.7
3.1 / 0.2
CW
0536210-061717
F31-ap193
22.8 +/- 4.0
7.1 / 0.5
W
0536213-052014
F22-ap150
23.8 +/- 0.3
25.1 / 0.8
W
0536222-055547
S3-ap217
21.0 +/- 1.0
9.6 / 0.5
W-
0536242-054448
F22-ap186
21.5 +/- 0.4
31.7 / 0.9
WC
0536251-051913
F22-ap146
23.5 +/- 3.9
5.7 / 0.4
NSW
0536255-051841
F22-ap144
21.8 +/- 5.5
4.2 / 0.4
C
0536262-051653
F21-ap186
30.4 +/- 1.1
8.8 / 0.5
W
0536262-051830
F21-ap187
21.7 +/- 1.4
7.9 / 0.4
W
0536269-045506
S2-ap134
26.5 +/- 2.2
4.5 / 0.3
C
0536275-053055
F22-ap169
25.7 +/- 0.4
24.6 / 0.8
C
0536278-062536
F31-ap209
25.5 +/- 0.5
16.9 / 0.7
W
0536281-052417
F22-ap159
35.4 +/- 0.8
9.9 / 0.6
W
0536289-051443
F22-ap135
20.6 +/- 3.0
9.4 / 0.6
W
0536292-045351
F11-ap184
26.9 +/- 0.5
17.5 / 0.7
W+
0536297-052006
F21-ap196
27.2 +/- 0.7
20.0 / 0.8
NSW
0536301-055309
F31-ap149
8.7 +/- 0.6
12.7 / 0.5
W
0536316-052635
F21-ap208
24.7 +/- 0.4
20.7 / 0.7
W
0536321-051713
S2-ap161
27.4 +/- 0.9
11.5 / 0.6
C
0536328-061237
F31-ap188
26.5 +/- 0.7
21.8 / 0.8
W
0536329-060229
F31-ap164
23.8 +/- 5.9
5.7 / 0.5
WC
0536336-055112
S3-ap205
12.6 +/- 1.2
6.3 / 0.3
CW
0536340-053405
F21-ap217
25.3 +/- 8.8
3.7 / 0.4
CD
0536343-054054
F22-ap171
14.7 +/- 10.4
3.2 / 0.3
W
0536363-053634
F21-ap211
25.3 +/- 2.9
10.6 / 0.7
WC
Normalized intensity
Velocity [km/s]
-400 -300 -200 -100 0 100 200 300 400

Fig. 12.3 cont.

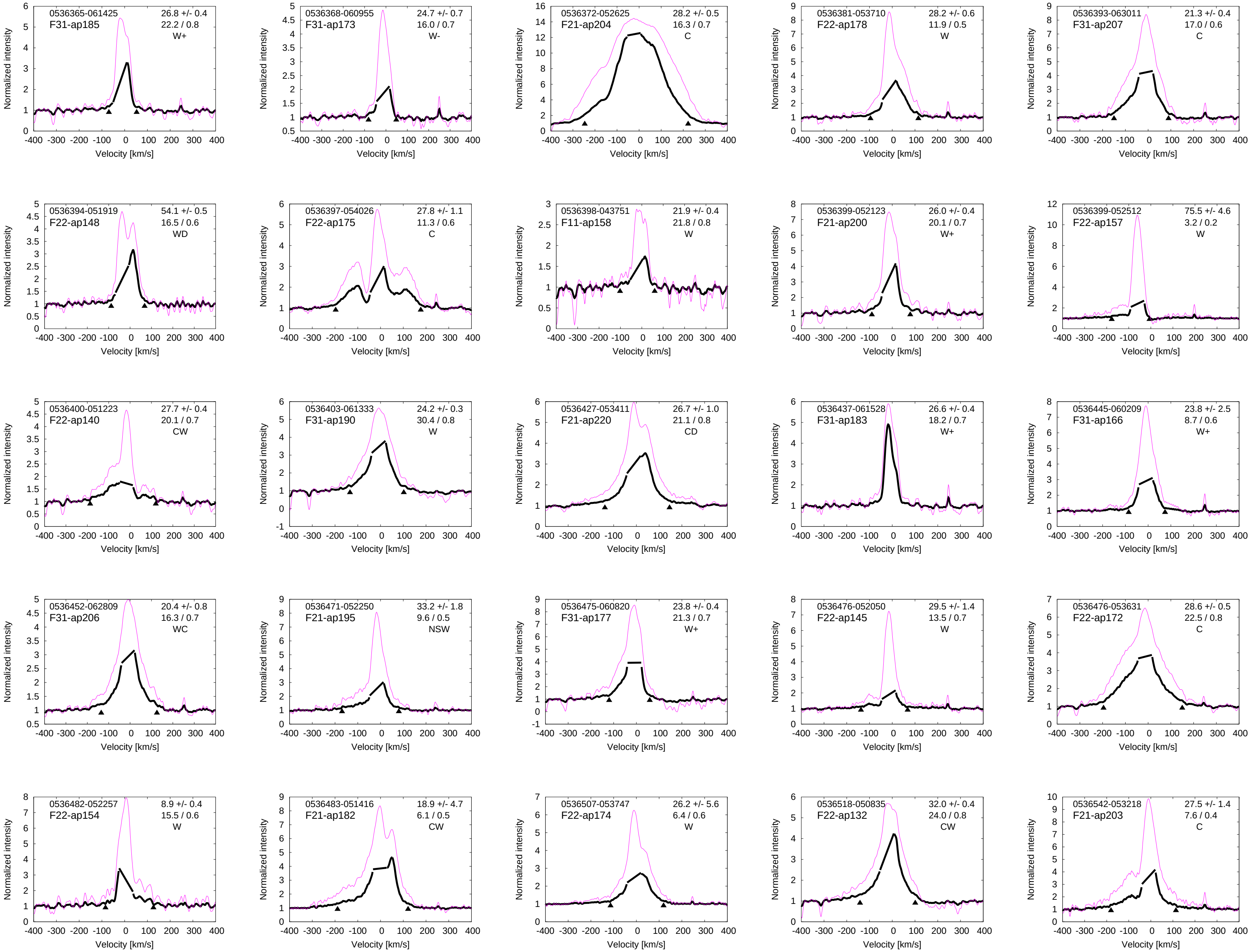
0536365-061425
F31-ap185
26.8 +/- 0.4
22.2 / 0.8
W+
0536368-060955
F31-ap173
24.7 +/- 0.7
16.0 / 0.7
W-
0536372-052625
F21-ap204
28.2 +/- 0.5
16.3 / 0.7
C
0536381-053710
F22-ap178
28.2 +/- 0.6
11.9 / 0.5
W
0536393-063011
F31-ap207
21.3 +/- 0.4
17.0 / 0.6
C
0536394-051919
F22-ap148
54.1 +/- 0.5
16.5 / 0.6
WD
0536397-054026
F22-ap175
27.8 +/- 1.1
11.3 / 0.6
C
0536398-043751
F11-ap158
21.9 +/- 0.4
21.8 / 0.8
W
0536399-052123
F21-ap200
26.0 +/- 0.4
20.1 / 0.7
W+
0536399-052512
F22-ap157
75.5 +/- 4.6
3.2 / 0.2
W
0536400-051223
F22-ap140
27.7 +/- 0.4
20.1 / 0.7
CW
0536403-061333
F31-ap190
24.2 +/- 0.3
30.4 / 0.8
W
0536427-053411
F21-ap220
26.7 +/- 1.0
21.1 / 0.8
CD
0536437-061528
F31-ap183
26.6 +/- 0.4
18.2 / 0.7
W+
0536445-060209
F31-ap166
23.8 +/- 2.5
8.7 / 0.6
W+
0536452-062809
F31-ap206
20.4 +/- 0.8
16.3 / 0.7
WC
0536471-052250
F21-ap195
33.2 +/- 1.8
9.6 / 0.5
NSW
0536475-060820
F31-ap177
23.8 +/- 0.4
21.3 / 0.7
W+
0536476-052050
F22-ap145
29.5 +/- 1.4
13.5 / 0.7
W
0536476-053631
F22-ap172
28.6 +/- 0.5
22.5 / 0.8
C
0536482-052257
F22-ap154
8.9 +/- 0.4
15.5 / 0.6
W
0536483-051416
F21-ap182
18.9 +/- 4.7
6.1 / 0.5
CW
0536507-053747
F22-ap174
26.2 +/- 5.6
6.4 / 0.6
W
0536518-050835
F22-ap132
32.0 +/- 0.4
24.0 / 0.8
CW
0536542-053218
F21-ap203
27.5 +/- 1.4
7.6 / 0.4
C
Normalized intensity
Velocity [km/s]
-400 -300 -200 -100 0 100 200 300 400

Fig. 12.3 cont.

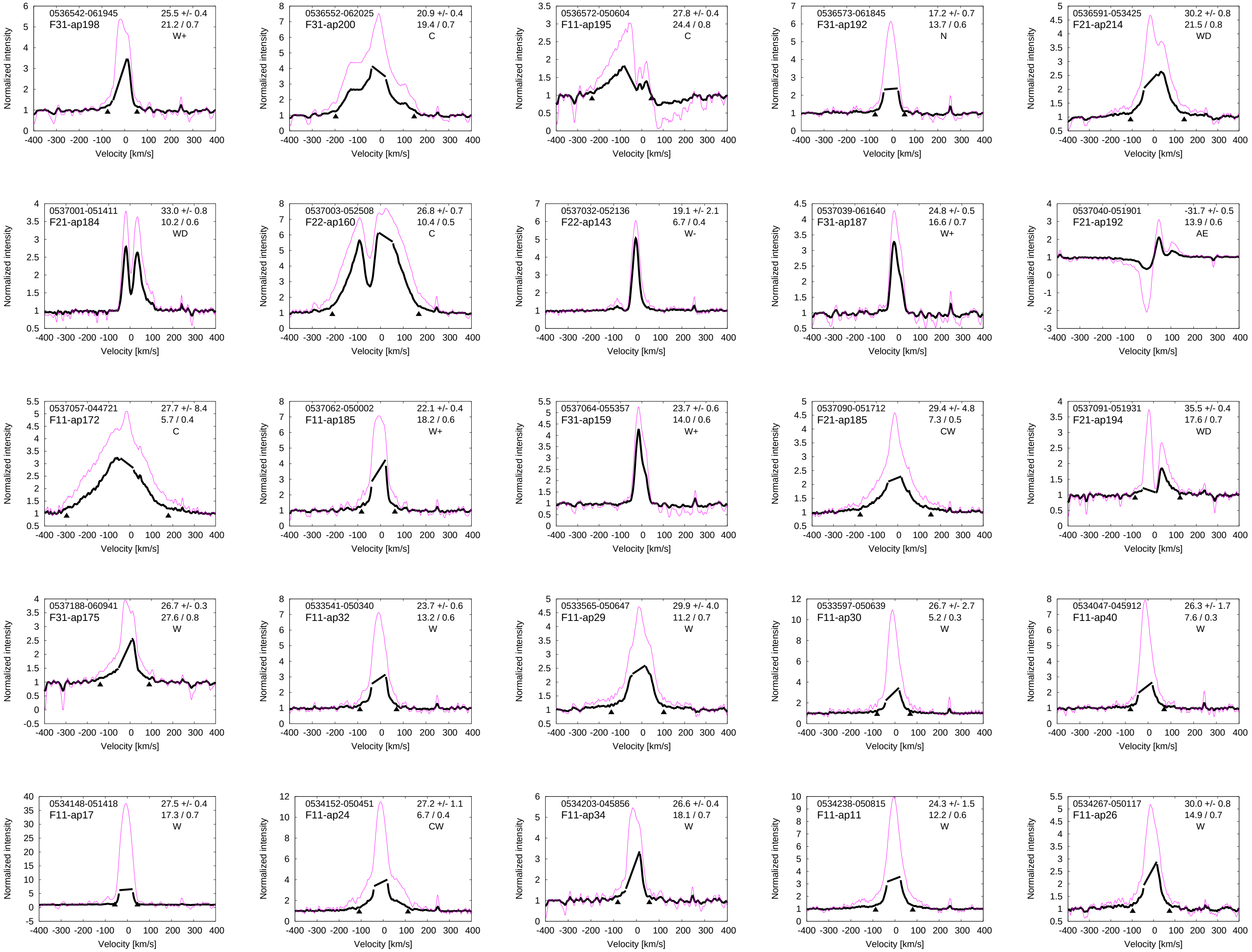
0536542-061945 F31-ap198 25.5 +/- 0.4 21.2 / 0.7 W+
0536552-062025 F31-ap200 20.9 +/- 0.4 19.4 / 0.7 C
0536572-050604 F11-ap195 27.8 +/- 0.4 24.4 / 0.8 C
0536573-061845 F31-ap192 17.2 +/- 0.7 13.7 / 0.6 N
0536591-053425 F21-ap214 30.2 +/- 0.8 21.5 / 0.8 WD
0537001-051411 F21-ap184 33.0 +/- 0.8 10.2 / 0.6 WD
0537003-052508 F22-ap160 26.8 +/- 0.7 10.4 / 0.5 C
0537032-052136 F22-ap143 19.1 +/- 2.1 6.7 / 0.4 W-
0537039-061640 F31-ap187 24.8 +/- 0.5 16.6 / 0.7 W+
0537040-051901 F21-ap192 -31.7 +/- 0.5 13.9 / 0.6 AE
0537057-044721 F11-ap172 27.7 +/- 8.4 5.7 / 0.4 C
0537062-050002 F11-ap185 22.1 +/- 0.4 18.2 / 0.6 W+
0537064-055357 F31-ap159 23.7 +/- 0.6 14.0 / 0.6 W+
0537090-051712 F21-ap185 29.4 +/- 4.8 7.3 / 0.5 CW
0537091-051931 F21-ap194 35.5 +/- 0.4 17.6 / 0.7 WD
0537188-060941 F31-ap175 26.7 +/- 0.3 27.6 / 0.8 W
0533541-050340 F11-ap32 23.7 +/- 0.6 13.2 / 0.6 W
0533565-050647 F11-ap29 29.9 +/- 4.0 11.2 / 0.7 W
0533597-050639 F11-ap30 26.7 +/- 2.7 5.2 / 0.3 W
0534047-045912 F11-ap40 26.3 +/- 1.7 7.6 / 0.3 W
0534148-051418 F11-ap17 27.5 +/- 0.4 17.3 / 0.7 W
0534152-050451 F11-ap24 27.2 +/- 1.1 6.7 / 0.4 CW
0534203-045856 F11-ap34 26.6 +/- 0.4 18.1 / 0.7 W
0534238-050815 F11-ap11 24.3 +/- 1.5 12.2 / 0.6 W
0534267-050117 F11-ap26 30.0 +/- 0.8 14.9 / 0.7 W
Normalized intensity
Velocity [km/s]
-400 -300 -200 -100 0 100 200 300 400

Fig. 12.3 cont.

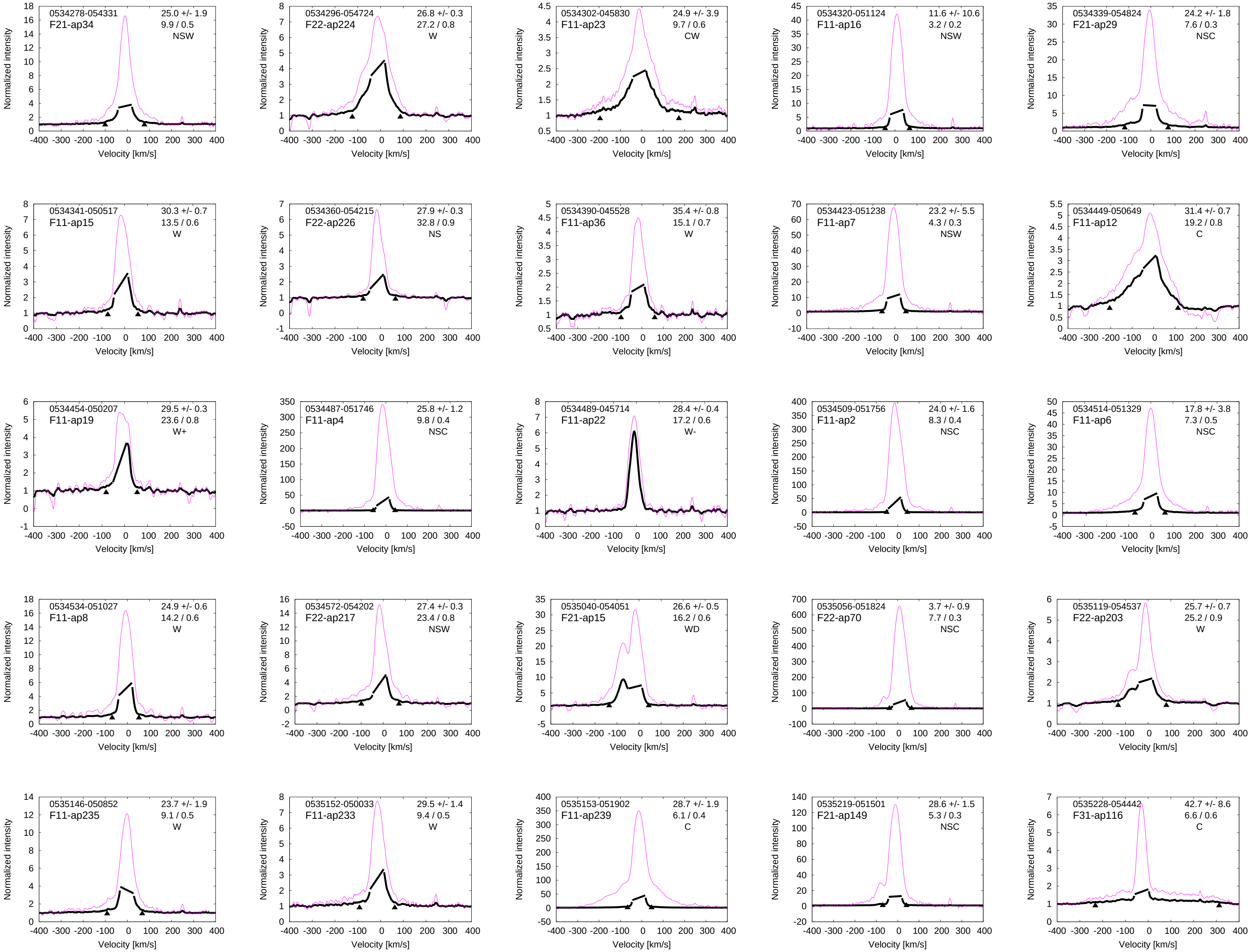
0534278-054331
F21-ap34
25.0 +/- 1.9
9.9 / 0.5
NSW
0534296-054724
F22-ap224
26.8 +/- 0.3
27.2 / 0.8
W
0534302-045830
F11-ap23
24.9 +/- 3.9
9.7 / 0.6
CW
0534320-051124
F11-ap16
11.6 +/- 10.6
3.2 / 0.2
NSW
0534339-054824
F21-ap29
24.2 +/- 1.8
7.6 / 0.3
NSC
0534341-050517
F11-ap15
30.3 +/- 0.7
13.5 / 0.6
W
0534360-054215
F22-ap226
27.9 +/- 0.3
32.8 / 0.9
NS
0534390-045528
F11-ap36
35.4 +/- 0.8
15.1 / 0.7
W
0534423-051238
F11-ap7
23.2 +/- 5.5
4.3 / 0.3
NSW
0534449-050649
F11-ap12
31.4 +/- 0.7
19.2 / 0.8
C
0534454-050207
F11-ap19
29.5 +/- 0.3
23.6 / 0.8
W+
0534487-051746
F11-ap4
25.8 +/- 1.2
9.8 / 0.4
NSC
0534489-045714
F11-ap22
28.4 +/- 0.4
17.2 / 0.6
W-
0534509-051756
F11-ap2
24.0 +/- 1.6
8.3 / 0.4
NSC
0534514-051329
F11-ap6
17.8 +/- 3.8
7.3 / 0.5
NSC
0534534-051027
F11-ap8
24.9 +/- 0.6
14.2 / 0.6
W
0534572-054202
F22-ap217
27.4 +/- 0.3
23.4 / 0.8
NSW
0535040-054051
F21-ap15
26.6 +/- 0.5
16.2 / 0.6
WD
0535056-051824
F22-ap70
3.7 +/- 0.9
7.7 / 0.3
NSC
0535119-054537
F22-ap203
25.7 +/- 0.7
25.2 / 0.9
W
0535146-050852
F11-ap235
23.7 +/- 1.9
9.1 / 0.5
W
0535152-050033
F11-ap233
29.5 +/- 1.4
9.4 / 0.5
W
0535153-051902
F11-ap239
28.7 +/- 1.9
6.1 / 0.4
C
0535219-051501
F21-ap149
28.6 +/- 1.5
5.3 / 0.3
NSC
0535228-054442
F31-ap116
42.7 +/- 8.6
6.6 / 0.6
C
Normalized intensity
Velocity [km/s]
-400 -300 -200 -100 0 100 200 300 400

Fig. 12.3 cont.

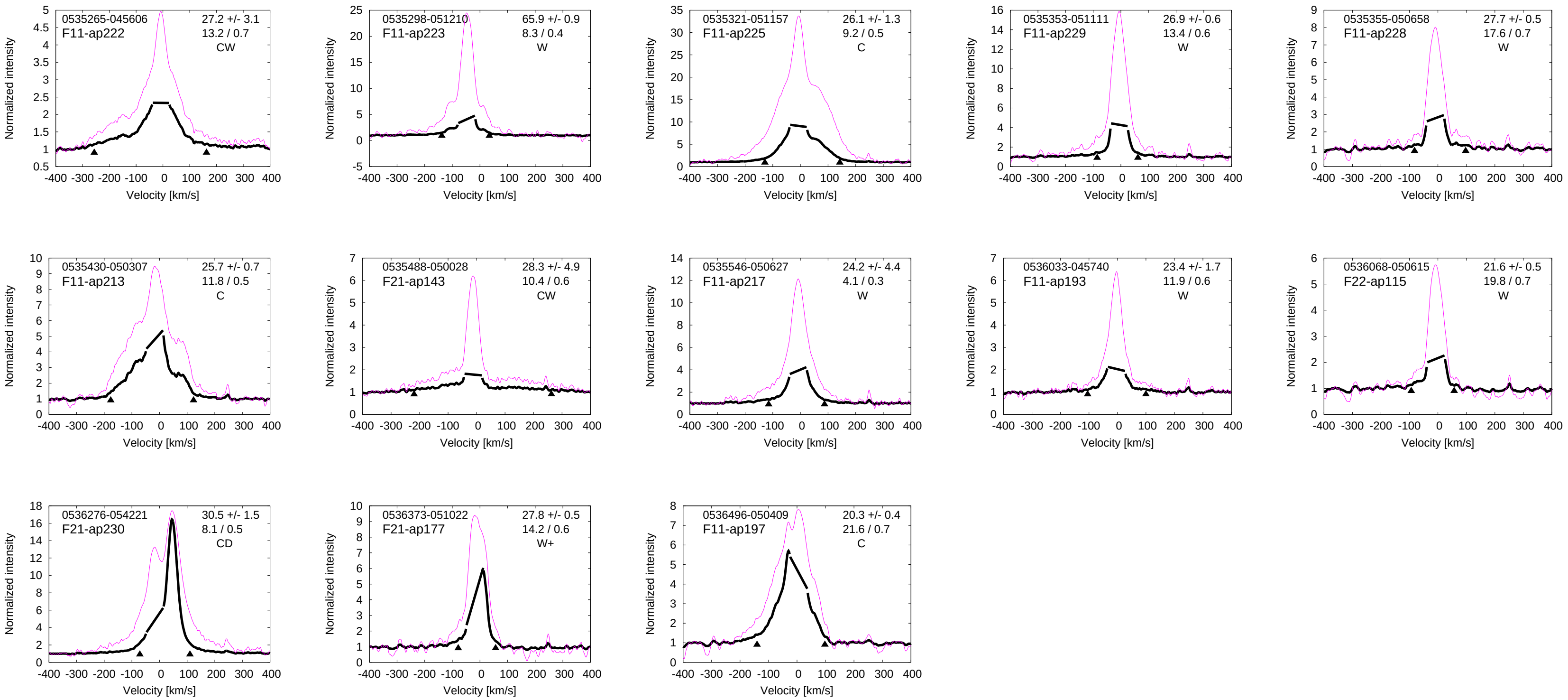
0535265-045606
F11-ap222
27.2 +/- 3.1
13.2 / 0.7
CW
0535298-051210
F11-ap223
65.9 +/- 0.9
8.3 / 0.4
W
0535321-051157
F11-ap225
26.1 +/- 1.3
9.2 / 0.5
C
0535353-051111
F11-ap229
26.9 +/- 0.6
13.4 / 0.6
W
0535355-050658
F11-ap228
27.7 +/- 0.5
17.6 / 0.7
W
0535430-050307
F11-ap213
25.7 +/- 0.7
11.8 / 0.5
C
0535488-050028
F21-ap143
28.3 +/- 4.9
10.4 / 0.6
CW
0535546-050627
F11-ap217
24.2 +/- 4.4
4.1 / 0.3
W
0536033-045740
F11-ap193
23.4 +/- 1.7
11.9 / 0.6
W
0536068-050615
F22-ap115
21.6 +/- 0.5
19.8 / 0.7
W
0536276-054221
F21-ap230
30.5 +/- 1.5
8.1 / 0.5
CD
0536373-051022
F21-ap177
27.8 +/- 0.5
14.2 / 0.6
W+
0536496-050409
F11-ap197
20.3 +/- 0.4
21.6 / 0.7
C
Normalized intensity
Velocity [km/s]
-400 -300 -200 -100 0 100 200 300 400

Fig. 12.3 cont.

Table 12.6. Clean list — *full table*

2MASS	ID	V_{mag}	$(B-V)$	RV	RV_{err}	R	S	T_{eff}	$log(g)$	v$sin(i)$	$[Fe/H]$	CCF	NOB
0527050+354717	B2-ap214	14.55	0.82	6.01	0.39	23.8	0.77	6000	4.5	4	0	c	1
0527057+354401	C1-ap57	13.91	1.04	-8.46	0.20	58.7	0.91	5000	4.5	0	0	c	1
0527063+354343	B2-ap210	15.67	1.17	-10.90	0.81	26.1	0.71	5250	4.0	25	0	c	2
0527066+355811	C2-ap26	13.05	0.56	-1.53	2.49	19.6	0.70	7000	3.5	100	0	w	2
0527088+355046	C2-ap14	12.78	0.67	-56.80	0.51	51.5	0.92	6500	3.5	50	0	c	1
0527093+354557	B1-ap24	14.26	0.81	-7.98	1.15	27.4	0.74	5750	4.0	50	0	w	1
0527094+353922	C1-ap56	12.85	1.80	1.07	0.25	32.4	0.84	4750	2.5	4	0	c	1
0527104+354424	B2-ap209	15.41	1.75	-30.91	0.37	26.3	0.76	5500	3.5	10	0	c	1
0527107+355332	B2-ap222	15.16	0.94	-6.60	3.12	10.5	0.48	6000	4.0	50	0	w	1
0527109+354200	B2-ap204	15.61	0.84	-11.51	4.15	11.1	0.38	5000	3.0	100	0	u	2
0527110+354656	C2-ap8	12.83	1.31	-16.40	0.11	74.3	0.95	5000	3.5	0	0	c	1
0527113+354924	B2-ap219	15.69	0.87	-21.25	0.30	30.3	0.78	6000	4.5	4	0	c	1
0527118+355258	C2-ap13	13.75	1.89	-10.06	0.17	57.2	0.94	5000	2.0	10	0	c	1
0527120+354326	B2-ap208	14.78	0.76	-16.54	2.14	13.2	0.50	6500	4.0	50	0	w	1
0527120+355636	C2-ap22	13.95	1.62	47.60	0.12	61.2	0.94	4750	2.5	0	0	c	1
0527123+354628	B2-ap201	15.27	0.85	-27.03	0.28	30.0	0.79	6250	4.5	4	0	c	1
0527127+353932	C1-ap58	12.23	0.75	9.09	0.73	41.0	0.81	6000	3.5	50	0	w	1
0527139+355201	C2-ap19	13.85	0.68	-32.76	1.64	15.6	0.64	6250	1.0	50	-2	u	1
0527148+354821	C2-ap7	13.37	2.15	46.59	0.12	64.9	0.95	4250	1.5	4	0	c	1
0527157+355019	C2-ap12	12.53	0.70	-5.40	0.09	102.8	0.97	6000	4.5	4	0	c	1
0527164+355029	B2-ap215	15.41	1.57	-7.64	0.34	26.5	0.79	4750	2.5	4	0	c	1
0527180+355510	B2-ap230	14.93	1.48	-21.54	0.29	30.4	0.80	5500	4.0	4	0	c	1
0527187+354537	B2-ap205	15.09	0.84	2.14	0.81	19.5	0.67	6000	4.5	10	0	c	1
0527190+354909	B2-ap220	15.26	1.72	0.34	0.23	32.5	0.84	5000	3.0	0	0	c	1
0527191+354833	A2-ap233	11.79	0.60	-30.60	0.09	83.9	0.95	6250	4.0	4	0	c	1
0527191+360213	A2-ap30	10.94	0.67	15.21	0.89	30.6	0.82	7250	4.0	50	0	w	1
0527196+353909	A1-ap14	9.61	1.31	25.81	0.10	78.0	0.97	4750	2.5	4	0	c	1
0527207+354206	B2-ap202	15.79	0.90	-10.96	1.93	15.5	0.48	5500	4.0	50	0	w	2
0527230+355011	B2-ap217	15.05	1.64	16.25	0.17	44.9	0.91	5000	3.5	0	0	c	1
0527242+354828	B1-ap25	15.08	0.76	-16.90	4.82	8.7	0.35	8250	5.0	100	0	u	2
0527248+354305	A2-ap224	10.64	1.41	25.86	0.09	84.9	0.97	4750	2.5	4	0	c	1
0527254+355144	A2-ap9	11.68	0.74	-35.47	0.10	82.3	0.96	5750	4.0	4	0	c	1
0527265+354823	B1-ap23	15.79	0.98	68.48	0.31	23.6	0.79	6250	4.5	0	0	c	1
0527268+354057	C2-ap240	13.71	1.47	8.88	1.19	7.5	0.36	5250	4.0	4	0	u	1
0527268+354502	B1-ap27	14.05	0.79	-70.90	0.33	29.8	0.85	6250	5.0	4	0	c	1
0527272+354317	B1-ap29	15.59	0.93	2.06	1.28	15.4	0.59	5750	4.5	10	0	c	2
0527276+353946	B2-ap193	14.49	0.89	-18.77	1.30	12.4	0.48	5250	3.5	25	0	u	2
0527279+360208	A2-ap25	11.43	0.41	-17.56	0.52	28.8	0.81	7750	4.0	25	0	c	2
0527298+354838	B1-ap32	15.95	0.97	2.06	0.51	26.5	0.77	5500	4.5	10	0	c	2
0527303+354934	A2-ap2	10.85	0.39	-17.89	2.43	23.6	0.81	6750	3.5	100	0	r	2
0527312+360136	C2-ap36	13.13	0.73	21.68	0.29	24.3	0.78	6500	4.0	4	0	c	1
0527318+355112	C2-ap18	13.03	1.48	-26.18	0.09	92.3	0.97	5000	3.0	4	0	c	1
0527324+355255	C2-ap15	13.81	1.13	30.49	0.16	53.6	0.95	5000	3.5	4	0	c	1

Table 12.6 (cont'd)

2MASS	ID	V_{mag}	$(B-V)$	RV	RV_{err}	R	S	T_{eff}	$log(g)$	v$sin(i)$	$[Fe/H]$	CCF	NOB
0527339+354823	C2-ap10	13.91	1.14	-61.03	0.14	59.3	0.93	5000	3.5	0	0	c	1
0527343+352303	B1-ap225	14.31	0.69	-9.14	2.58	8.5	0.37	9000	3.0	50	0	u	2
0527349+355650	C2-ap28	13.51	0.66	-2.22	3.69	13.5	0.43	6750	2.5	100	-1	u	1
0527353+351627	B1-ap208	15.54	1.13	-3.00	1.77	19.7	0.49	5500	4.5	50	0	w	1
0527356+354347	C2-ap235	13.26	0.59	-10.71	2.75	10.1	0.38	6750	4.5	50	0	u	1
0527359+355717	C2-ap30	12.94	0.60	-15.36	1.91	22.9	0.85	7000	3.5	100	0	w	1
0527365+355906	C2-ap25	13.04	1.77	2.03	0.24	53.5	0.94	4750	3.0	10	0	c	1
0527368+354026	A2-ap219	11.95	0.96	48.98	0.23	30.5	0.81	5250	3.0	0	-1	c	1
0527368+355211	C2-ap17	13.72	0.60	-0.42	0.69	42.9	0.85	7000	4.5	50	0	c	2
0527369+354140	C2-ap238	12.28	0.99	-7.57	0.15	66.5	0.95	4750	4.0	4	0	c	1
0527369+354647	C1-ap68	12.02	0.64	-28.90	0.44	64.9	0.96	5750	3.5	50	0	c	1
0527371+350047	C1-ap219	12.71	0.97	-10.22	0.21	53.4	0.91	5250	4.5	4	0	c	1
0527380+352153	B1-ap224	14.71	1.66	34.38	0.21	35.9	0.89	5000	2.5	4	0	c	1
0527380+352238	A1-ap223	11.19	0.56	22.71	2.97	20.0	0.60	7000	3.5	100	0	u	1
0527383+351125	C1-ap229	13.08	1.59	3.29	0.11	71.5	0.94	4750	2.5	4	0	c	1
0527387+352325	C1-ap30	12.67	0.68	-2.36	6.53	9.5	0.57	6250	3.0	100	0	u	2
0527389+351717	C1-ap2	12.29	1.30	65.82	0.09	81.3	0.96	4750	3.0	0	0	c	1
0527391+354917	B2-ap216	14.62	1.47	7.64	0.13	55.2	0.93	5250	3.0	4	0	c	1
0527397+354026	B2-ap197	14.17	0.65	19.84	0.49	14.4	0.65	6500	4.5	0	0	r	2
0527399+354346	C2-ap237	13.83	0.66	1.32	0.35	27.6	0.81	6500	3.5	10	0	c	2
0527409+351653	A1-ap206	11.94	0.57	10.74	0.29	27.2	0.81	5500	4.0	0	-1	c	1
0527417+354800	C2-ap6	12.10	1.20	-45.88	0.09	87.9	0.97	5000	3.0	4	0	c	1
0527420+351837	C1-ap8	13.37	0.80	4.00	0.18	50.4	0.92	6250	4.0	10	0	c	1
0527428+350857	C1-ap222	12.52	0.68	15.09	2.19	21.8	0.78	7000	2.0	100	-1	w	1
0527431+354414	C1-ap70	12.58	0.75	-42.69	0.14	74.2	0.95	6500	4.5	10	0	c	1
0527433+351605	C1-ap237	13.95	0.65	1.76	0.67	23.8	0.76	7000	4.0	25	0	r	2
0527454+351413	B1-ap195	14.36	0.76	6.97	3.00	14.7	0.52	5750	3.0	100	0	w	1
0527454+352108	C1-ap13	12.28	0.47	3.72	5.13	11.2	0.47	8250	2.5	100	0	u	1
0527461+353357	B2-ap189	14.65	0.65	-10.73	2.90	10.8	0.53	6500	4.5	50	0	w	1
0527461+355047	C2-ap1	13.65	0.63	-8.29	1.20	28.2	0.76	6250	4.0	50	0	w	2
0527463+353826	B2-ap194	14.75	0.94	24.12	0.26	33.6	0.87	5750	4.5	0	0	c	1
0527468+352401	B1-ap240	15.85	1.14	-5.90	2.60	12.2	0.48	5500	5.0	50	0	w	1
0527471+354239	A2-ap215	9.11	1.52	16.04	0.09	81.0	0.97	4250	1.5	4	0	c	1
0527478+352510	B1-ap231	14.11	0.79	3.86	0.24	42.6	0.89	6500	4.5	10	0	c	1
0527478+353549	C2-ap224	13.86	0.75	-11.36	1.06	27.5	0.75	6250	4.0	50	0	c	2
0527479+352101	B1-ap220	15.29	0.83	-2.03	1.50	19.7	0.63	6250	4.0	50	0	r	2
0527480+352903	B1-ap18	15.69	0.91	27.79	0.53	17.0	0.71	6250	5.0	4	0	c	1
0527481+352014	C1-ap14	13.81	0.65	4.46	3.30	14.2	0.61	7500	4.5	100	0	w	2
0527485+353237	B2-ap188	15.19	1.02	-27.08	0.24	32.9	0.84	6000	4.5	0	0	c	1
0527486+353136	C2-ap211	12.42	1.67	12.03	0.25	62.4	0.95	5000	2.0	25	0	c	1
0527489+351816	B1-ap209	14.87	1.56	62.37	0.27	28.7	0.81	4750	2.5	4	0	c	1
0527490+352009	A1-ap222	11.64	1.29	5.73	0.16	53.5	0.93	5250	3.5	4	0	c	1
0527490+352249	C1-ap26	13.97	1.34	13.43	0.14	56.2	0.93	5000	3.5	0	0	c	1

Table 12.6 (cont'd)

2MASS	ID	V_{mag}	$(B-V)$	RV	RV_{err}	R	S	T_{eff}	$log(g)$	v$sin(i)$	$[Fe/H]$	CCF	NOB
0527499+353833	C2-ap230	12.83	0.66	1.51	1.00	28.6	0.84	7000	4.5	50	0	c	2
0527499+354810	C2-ap4	13.34	0.67	-37.86	0.20	45.7	0.89	6000	3.5	10	0	c	1
0527500+351008	C1-ap211	13.25	1.68	-5.31	0.09	82.3	0.96	4750	2.5	4	0	c	1
0527500+352801	B1-ap14	14.86	0.94	0.62	1.12	26.4	0.78	6500	4.5	50	0	r	2
0527504+352938	B2-ap182	14.84	0.78	-0.78	0.69	31.1	0.81	6250	4.5	25	0	c	2
0527508+352129	C1-ap15	13.79	0.69	37.93	0.14	50.8	0.92	6250	3.5	4	0	c	1
0527510+351810	C1-ap231	13.10	0.55	-8.44	0.24	34.2	0.85	8000	3.0	10	0	c	1
0527511+351243	B1-ap181	14.36	1.78	19.93	0.13	57.6	0.94	4500	2.0	4	0	c	1
0527511+351701	C1-ap236	13.17	1.61	-28.58	0.13	62.4	0.93	4500	2.0	4	0	c	1
0527516+352921	C1-ap52	13.65	0.90	31.79	0.16	65.4	0.96	5500	5.0	0	0	c	1
0527523+354023	B2-ap196	14.33	0.74	27.98	0.24	31.9	0.87	6250	4.0	4	0	c	1
0527525+353448	B2-ap190	15.34	0.91	4.68	0.33	28.1	0.80	6250	5.0	0	0	c	2
0527525+353929	C1-ap69	13.01	0.73	-33.52	0.14	62.9	0.95	6000	3.5	10	0	c	1
0527529+353514	C1-ap64	13.49	0.64	-23.35	0.29	31.8	0.87	6250	4.0	10	0	c	1
0527529+353814	A2-ap204	11.20	1.34	5.71	0.10	79.0	0.96	4750	2.5	4	0	c	1
0527530+351721	B1-ap202	15.91	0.93	-13.89	3.18	10.9	0.43	6000	4.5	50	0	w	1
0527535+350844	B1-ap184	15.25	0.98	2.14	0.57	27.1	0.81	5000	4.5	0	0	c	1
0527536+352303	B1-ap221	15.21	0.85	-2.00	4.02	8.4	0.42	6000	4.0	50	0	w	1
0527536+352752	A2-ap196	11.71	0.50	-18.76	0.19	53.9	0.91	6250	4.0	10	0	c	1
0527541+353014	B1-ap15	15.25	1.72	19.34	0.23	33.2	0.88	5000	3.0	4	0	c	1
0527551+353844	C2-ap228	13.42	0.60	4.76	0.90	28.5	0.81	7250	4.5	50	0	w	1
0527555+353122	C2-ap215	12.46	0.72	0.85	0.11	82.4	0.96	6000	4.5	4	0	c	1
0527555+353409	B2-ap186	14.80	1.51	-13.81	0.18	49.4	0.91	5250	3.5	4	0	c	1
0527559+350831	B1-ap182	14.64	0.93	31.95	0.25	42.3	0.91	5500	5.0	0	0	c	1
0527559+351453	C1-ap228	13.23	0.75	31.99	0.14	56.2	0.93	6000	4.5	0	0	c	1
0527559+360153	A2-ap31	9.49	0.49	38.06	0.22	68.9	0.95	6000	3.5	25	0	c	1
0527560+351237	B1-ap185	14.64	0.73	7.00	0.63	27.6	0.78	6750	4.0	25	0	c	1
0527560+351749	A1-ap209	11.44	0.36	-0.25	6.05	8.0	0.35	9000	4.0	100	0	u	1
0527562+351535	C1-ap225	12.46	0.49	-3.09	4.60	12.4	0.54	8250	2.5	100	0	u	1
0527563+355708	C2-ap27	13.05	0.74	-14.08	6.98	7.8	0.35	6000	2.0	100	0	u	1
0527570+353530	C1-ap66	12.90	0.38	-1.47	1.52	17.7	0.68	9000	3.5	50	0	r	2
0527575+353350	B2-ap184	15.66	0.88	-46.88	0.39	29.6	0.79	6250	5.0	0	0	c	1
0527579+351819	C1-ap233	13.34	0.78	-15.82	0.78	34.9	0.84	6500	3.5	50	0	c	1
0527581+352237	C1-ap23	13.59	0.58	1.65	1.00	26.7	0.80	7000	3.0	50	-1	c	2
0527584+352018	C1-ap12	13.28	1.41	-26.39	0.09	86.8	0.96	4750	2.5	0	0	c	1
0527585+355054	A2-ap12	11.27	0.70	50.95	0.11	85.1	0.96	5250	4.0	4	0	c	1
0527592+352456	C1-ap42	12.89	0.70	22.54	0.12	67.7	0.96	6000	4.5	0	0	c	1
0527595+355643	A2-ap38	11.87	0.82	0.52	0.15	69.4	0.95	5250	4.5	4	0	c	1
0527596+352606	C1-ap47	13.30	0.50	43.17	0.61	29.9	0.84	6750	4.0	25	0	c	1
0527597+353354	B1-ap34	14.03	0.64	-0.15	0.90	35.9	0.82	6500	4.5	50	0	c	2
0527598+355935	C2-ap37	13.20	0.79	-29.97	0.13	77.5	0.95	5500	4.5	4	0	c	1
0528002+351549	A1-ap181	11.10	0.24	-46.20	7.64	5.1	0.19	5250	1.5	100	-2	u	1
0528005+351809	C1-ap234	12.74	0.43	2.00	2.13	20.3	0.76	8000	3.0	100	0	u	2

Table 12.6 (cont'd)

2MASS	ID	V_{mag}	$(B-V)$	RV	RV_{err}	R	S	T_{eff}	$log(g)$	v$sin(i)$	$[Fe/H]$	CCF	NOB
0528005+353221	C2-ap217	12.24	0.62	24.92	0.13	71.2	0.96	6250	4.0	10	0	c	1
0528009+352312	C1-ap34	13.79	0.96	30.75	0.18	57.5	0.95	5000	4.5	0	0	c	1
0528013+350814	A1-ap169	11.38	0.79	-7.85	0.15	65.0	0.94	5250	4.5	0	0	c	1
0528017+351529	C1-ap226	13.33	0.71	1.05	0.17	47.2	0.92	6500	4.5	4	0	c	1
0528017+352114	A1-ap235	10.50	1.62	5.89	0.10	80.6	0.96	4750	2.5	4	0	c	1
0528018+351132	C1-ap218	14.00	0.51	-1.06	4.21	12.2	0.43	7500	5.0	100	0	w	1
0528018+353615	B1-ap38	15.68	0.89	-0.66	0.66	25.5	0.77	5500	4.5	10	0	c	2
0528023+353758	C1-ap72	12.85	0.68	18.29	0.09	81.2	0.96	6000	3.5	4	0	c	1
0528025+360152	C2-ap31	12.49	0.45	-1.39	4.45	14.2	0.52	6500	3.5	100	0	w	2
0528030+353114	B1-ap21	15.44	0.82	-4.78	1.27	22.2	0.74	6750	4.5	50	0	w	1
0528032+352712	C1-ap60	13.27	1.45	-13.90	0.12	65.1	0.95	4500	2.5	4	0	c	1
0528033+351933	A1-ap226	11.62	0.52	-5.20	4.46	6.2	0.30	6250	3.0	50	0	u	1
0528034+352736	B1-ap17	14.31	0.66	3.27	0.38	47.1	0.91	6500	4.5	25	0	c	2
0528037+352810	C2-ap214	13.68	1.57	7.52	0.29	31.8	0.85	5250	2.0	10	0	c	1
0528040+353138	C2-ap219	13.66	0.67	-38.01	0.15	53.7	0.91	6000	4.0	4	0	c	1
0528040+354131	B2-ap192	14.84	0.83	20.09	0.25	42.7	0.88	5750	4.5	4	0	c	2
0528043+353730	B1-ap39	14.91	1.58	8.68	0.16	45.4	0.91	5000	3.0	0	0	c	1
0528049+350223	C1-ap208	13.89	0.76	-9.21	1.73	24.8	0.64	7000	3.5	100	0	u	1
0528049+355250	C2-ap11	13.46	0.61	1.95	0.84	32.8	0.85	6250	3.5	50	0	c	2
0528052+350133	B1-ap176	15.03	0.96	-41.91	3.33	10.3	0.51	6250	4.5	50	0	w	1
0528052+351710	A1-ap195	11.24	0.50	-6.81	4.43	12.6	0.39	7250	1.5	100	-1	u	1
0528052+351949	A1-ap225	11.53	1.26	5.12	0.13	59.7	0.94	5250	3.0	4	0	c	1
0528058+351938	A2-ap188	11.95	1.25	1.43	0.12	70.1	0.95	5500	3.5	4	0	c	1
0528059+350411	B1-ap178	14.40	1.90	-15.87	0.13	63.9	0.95	4750	3.0	4	0	c	1
0528062+352431	B1-ap10	14.61	0.67	0.76	2.15	21.2	0.68	6750	4.0	100	0	w	2
0528063+353428	A1-ap30	11.87	0.84	36.13	0.19	53.0	0.94	5250	4.5	4	0	c	1
0528064+352509	B1-ap9	14.08	1.32	24.32	0.20	38.4	0.90	5000	3.0	4	0	c	1
0528065+354841	A2-ap235	10.05	0.19	0.95	2.17	11.1	0.75	9750	2.0	50	0	r	2
0528066+351005	C1-ap209	13.67	0.69	27.76	0.22	49.2	0.91	6500	4.5	10	0	c	1
0528075+354956	C1-ap79	13.34	1.41	38.43	0.09	82.3	0.95	5000	3.0	0	0	c	1
0528096+354811	C1-ap77	13.18	0.51	15.75	0.24	41.7	0.90	7500	4.5	10	0	c	1
0528097+352933	A1-ap26	8.50	0.42	-2.66	0.84	34.0	0.92	7250	1.5	50	-1	w	1
0528098+352543	C1-ap55	13.40	0.45	-6.61	1.94	16.6	0.65	7000	4.0	50	0	w	1
0528098+353731	C2-ap213	13.45	0.69	30.95	0.13	65.2	0.94	6250	4.5	4	0	c	1
0528100+353543	B1-ap35	15.77	0.90	4.58	0.28	36.7	0.86	5500	4.5	4	0	c	2
0528104+350338	B1-ap174	15.36	0.82	-1.64	0.44	29.6	0.81	6250	5.0	4	0	c	1
0528112+360010	C2-ap33	13.22	0.52	-2.81	1.24	22.9	0.77	6500	3.0	50	0	c	1
0528113+351802	A1-ap202	11.89	1.34	68.56	0.14	54.0	0.93	4750	2.5	4	0	c	1
0528116+354940	C1-ap75	13.47	0.57	23.19	0.33	24.3	0.75	7750	3.0	10	0	c	1
0528116+360211	B2-ap3	15.43	0.77	7.19	0.30	27.7	0.81	5750	4.5	0	0	c	2
0528126+352755	C2-ap203	12.91	0.62	-8.73	0.18	50.2	0.91	6500	5.0	4	0	c	1
0528133+354346	A1-ap21	10.84	0.21	-2.90	5.58	9.2	0.38	9750	4.5	100	0	u	1
0528136+352133	A1-ap15	11.68	1.38	35.79	0.13	58.5	0.94	4750	3.0	0	0	c	1

Table 12.6 (cont'd)

2MASS	ID	V_{mag}	$(B-V)$	RV	RV_{err}	R	S	T_{eff}	$log(g)$	v$sin(i)$	$[Fe/H]$	CCF	NOB
0528136+355832	B2-ap4	14.74	0.87	53.57	0.74	20.5	0.78	6250	3.5	25	0	c	1
0528138+351644	A1-ap163	9.12	0.37	-0.98	0.21	70.2	0.96	6500	3.5	25	0	c	1
0528143+352153	C1-ap32	12.51	0.48	22.01	0.89	27.7	0.90	7000	3.0	50	0	c	1
0528144+353141	C1-ap76	13.11	0.47	-0.58	1.28	25.0	0.86	7000	4.0	50	0	r	2
0528145+360212	B2-ap1	15.95	1.47	-11.34	1.66	19.5	0.56	4250	2.5	50	-1	w	1
0528148+353319	C2-ap216	12.99	0.57	47.20	0.15	52.0	0.93	6000	4.0	4	0	c	1
0528150+350500	B1-ap161	14.03	1.54	-4.44	0.12	66.2	0.95	4500	2.0	4	0	c	1
0528150+355151	A2-ap27	11.58	1.29	-8.36	0.09	82.9	0.96	4750	3.0	0	0	c	1
0528151+350847	A1-ap155	11.68	1.23	66.79	0.14	50.1	0.92	5000	3.0	0	0	c	1
0528157+350557	C1-ap202	13.57	0.77	15.92	0.13	68.4	0.95	5500	4.0	4	0	c	1
0528157+352248	C1-ap46	13.17	1.32	60.23	0.09	89.4	0.97	5000	3.5	0	0	c	1
0528158+355655	C2-ap34	13.83	0.68	0.17	0.84	36.4	0.85	6500	4.5	50	0	c	2
0528165+352613	A2-ap184	11.68	1.09	2.02	0.09	79.8	0.96	5250	3.0	4	0	c	1
0528166+351957	B1-ap197	15.01	0.92	-3.89	0.40	37.9	0.84	5250	4.5	10	0	c	1
0528169+350147	A1-ap160	9.21	0.97	-8.34	0.07	113.8	0.97	5250	3.0	4	0	c	1
0528172+353118	C2-ap201	13.67	0.88	15.17	0.24	33.3	0.87	6000	4.0	4	0	c	1
0528172+353534	C2-ap220	13.67	0.59	1.50	0.77	35.3	0.83	6250	3.5	50	0	c	2
0528177+352301	C1-ap41	13.76	0.62	22.81	0.41	34.7	0.87	6500	3.5	25	0	c	1
0528177+352528	B2-ap178	15.08	0.71	4.96	0.24	33.7	0.86	6000	4.5	0	0	c	1
0528179+354522	A2-ap207	10.01	1.15	10.09	0.07	103.1	0.97	5000	3.0	4	0	c	1
0528181+350023	A1-ap158	11.80	0.38	-31.74	5.13	8.2	0.33	7000	2.0	100	-1	u	1
0528181+352511	B1-ap36	14.30	0.61	-5.32	1.37	22.8	0.59	7000	4.5	50	0	w	1
0528185+352951	B2-ap179	14.97	0.82	49.77	0.19	39.7	0.92	5750	4.0	0	0	c	1
0528188+352608	B1-ap40	15.99	0.86	45.79	0.79	7.8	0.37	6250	3.5	4	0	u	1
0528193+353330	C1-ap73	13.66	0.61	-10.45	4.23	13.3	0.43	6250	3.5	100	0	w	2
0528193+355816	C2-ap35	13.40	0.58	-0.72	1.33	22.6	0.76	7000	4.5	50	0	c	2
0528196+351222	A1-ap154	11.83	1.58	11.25	0.16	45.5	0.91	4750	3.0	0	0	c	1
0528196+353617	B2-ap171	15.36	0.88	37.83	0.24	33.3	0.85	5250	3.5	4	0	c	1
0528198+352310	C1-ap174	13.04	0.70	58.27	0.08	90.1	0.96	6000	4.0	0	0	c	1
0528198+353616	B1-ap44	15.32	1.04	-71.80	0.30	36.7	0.87	5000	4.5	0	0	c	1
0528202+355953	C2-ap46	12.95	1.91	34.09	0.15	50.9	0.94	4250	1.5	4	0	c	1
0528203+352345	B1-ap7	14.23	0.50	-15.94	1.98	16.0	0.65	6500	4.5	50	0	w	1
0528210+352302	B1-ap218	14.03	0.60	6.55	0.74	33.8	0.86	6750	3.5	50	0	c	1
0528212+352754	B1-ap33	15.61	0.79	3.59	0.66	16.5	0.64	5500	4.0	10	0	c	1
0528215+352215	A1-ap36	10.81	0.55	-8.12	0.12	69.7	0.96	6250	4.5	4	0	c	1
0528216+352858	C2-ap207	13.86	0.66	10.44	0.51	20.0	0.75	6750	5.0	10	0	c	1
0528217+352559	B1-ap37	14.13	0.68	1.26	2.48	17.7	0.71	6250	3.5	100	0	u	1
0528220+355139	B1-ap48	15.10	0.89	1.70	0.26	35.2	0.86	6250	4.0	10	0	c	2
0528223+352852	B1-ap31	15.25	0.79	5.76	0.28	38.2	0.86	6250	4.5	4	0	c	2
0528228+352552	C2-ap208	13.19	1.13	-3.14	0.21	39.1	0.87	5000	3.0	4	0	c	1
0528228+354747	A1-ap38	9.72	0.19	0.91	1.62	16.7	0.82	9750	2.0	50	0	c	2
0528229+351229	C1-ap193	12.85	0.65	10.37	0.74	40.8	0.92	6750	4.0	50	0	c	2
0528236+352619	C1-ap90	13.45	0.55	-14.26	1.53	20.1	0.71	6750	4.5	50	0	w	1

Table 12.6 (cont'd)

2MASS	ID	V_{mag}	$(B-V)$	RV	RV_{err}	R	S	T_{eff}	$log(g)$	v$sin(i)$	$[Fe/H]$	CCF	NOB
0528240+360117	B2-ap16	15.77	1.12	26.55	0.95	18.1	0.67	6000	4.0	25	0	c	2
0528244+354304	C2-ap222	12.49	0.43	2.25	0.99	27.6	0.90	7250	2.5	50	0	c	2
0528245+353725	B1-ap50	14.69	0.61	0.26	2.00	22.2	0.75	6750	3.5	100	0	w	2
0528246+352752	B2-ap176	14.39	1.64	1.31	0.10	71.0	0.96	5000	3.0	0	0	c	1
0528248+352625	B2-ap174	15.08	0.69	3.43	0.61	21.6	0.78	6500	5.0	10	0	c	1
0528249+351047	C1-ap195	13.56	1.33	62.92	0.14	53.2	0.93	4750	2.5	0	0	c	1
0528250+353125	C1-ap86	12.24	0.56	16.10	0.07	104.4	0.97	6250	4.5	0	0	c	1
0528268+352610	B2-ap172	15.05	1.58	-8.75	0.18	45.8	0.90	5000	3.5	0	0	c	1
0528271+354801	A2-ap228	11.20	0.32	-0.45	2.33	19.3	0.90	9000	4.0	100	0	w	2
0528279+353532	B1-ap45	15.50	0.76	-12.27	0.49	33.6	0.81	6000	3.5	25	0	c	1
0528288+351034	B1-ap162	14.87	0.68	5.65	0.51	33.3	0.84	6000	3.5	25	0	c	2
0528290+350416	B1-ap164	14.68	1.08	-0.95	0.17	49.9	0.92	5500	4.0	4	0	c	1
0528291+360402	A2-ap57	10.15	1.09	21.29	0.05	142.3	0.98	5000	2.5	4	0	c	1
0528298+361147	B2-ap27	14.11	0.75	64.89	0.12	61.9	0.94	6250	4.0	4	0	c	1
0528299+360335	C2-ap59	13.51	0.59	-0.60	0.64	40.8	0.85	6250	3.5	50	0	c	1
0528301+354532	B1-ap47	15.93	1.38	-0.14	0.54	26.6	0.77	4750	3.0	10	0	c	1
0528302+350515	A1-ap150	10.98	0.69	18.73	0.15	65.6	0.95	5750	5.0	0	0	c	1
0528302+360434	B2-ap24	15.81	1.10	9.07	4.07	10.3	0.42	7500	5.0	100	0	u	1
0528303+353030	B1-ap52	14.47	0.56	12.59	2.26	19.9	0.65	6500	3.0	100	0	u	1
0528304+351042	C1-ap194	12.60	0.36	-9.82	2.72	21.1	0.62	8750	4.0	100	0	u	1
0528304+360113	C2-ap52	12.81	0.53	-19.90	5.96	9.6	0.41	5500	2.5	100	-1	w	1
0528305+355904	C2-ap50	12.20	0.40	2.63	3.07	14.8	0.67	8000	3.5	100	0	w	1
0528305+361647	C2-ap66	13.51	0.81	2.79	0.32	23.7	0.79	5750	4.0	0	0	c	1
0528310+354958	A2-ap47	11.12	0.22	2.26	0.35	37.4	0.90	9750	3.0	25	0	c	2
0528315+354850	A2-ap21	9.63	0.18	4.55	1.34	10.5	0.64	9750	2.0	25	0	u	1
0528317+352058	C1-ap131	13.11	0.46	11.57	5.40	7.5	0.43	6750	2.5	100	-1	u	1
0528318+360555	B2-ap28	15.59	1.67	34.46	0.30	22.4	0.77	5500	3.5	0	0	c	1
0528319+353515	B1-ap41	15.98	0.98	2.00	0.86	19.9	0.72	5750	5.0	4	0	c	2
0528322+352425	B1-ap72	14.29	1.65	-29.09	0.26	38.5	0.85	5000	3.0	10	0	c	1
0528323+353616	B2-ap180	14.19	0.72	45.01	0.17	42.0	0.89	6000	4.0	0	0	c	1
0528327+355500	C2-ap23	12.90	0.48	0.39	1.87	24.0	0.83	7250	4.0	100	0	w	1
0528329+350159	C1-ap199	13.74	0.81	33.90	0.35	21.5	0.73	6000	4.0	4	0	c	1
0528331+351258	B1-ap151	14.36	0.66	3.46	2.35	21.5	0.68	6500	3.5	100	0	w	2
0528332+350830	A1-ap144	10.99	0.37	10.47	2.14	19.9	0.74	7000	3.5	100	0	w	1
0528332+352749	B1-ap53	15.92	1.43	57.73	0.32	22.8	0.80	4500	2.0	4	0	c	1
0528338+353906	C1-ap88	13.47	0.61	0.21	0.59	42.1	0.89	6750	3.5	50	0	c	2
0528341+352308	B1-ap119	14.03	0.77	-7.64	0.71	27.9	0.81	6750	5.0	25	0	c	1
0528342+351514	A1-ap122	9.96	0.23	104.01	0.75	4.5	0.20	9750	2.5	0	-2	u	1
0528347+361143	B2-ap23	15.63	1.60	-1.46	0.64	21.0	0.76	5500	4.0	4	0	c	1
0528348+352600	B1-ap68	15.30	0.86	21.43	0.46	19.6	0.74	5750	4.5	4	0	c	1
0528349+360435	C2-ap53	13.88	0.86	-22.03	0.14	75.3	0.95	5000	4.0	4	0	c	1
0528350+351121	A1-ap136	11.65	0.56	-20.33	0.13	64.3	0.93	6250	4.5	4	0	c	1
0528350+355934	C2-ap45	13.59	0.71	4.87	0.92	22.7	0.69	6250	4.5	25	0	c	1

Table 12.6 (cont'd)

2MASS	ID	V_{mag}	$(B-V)$	RV	RV_{err}	R	S	T_{eff}	$log(g)$	v$sin(i)$	$[Fe/H]$	CCF	NOB
0528350+360115	A2-ap51	8.88	1.61	-43.42	0.12	64.2	0.96	4250	2.0	4	0	c	1
0528353+361436	B2-ap34	14.56	1.57	-5.88	0.26	33.1	0.86	5000	3.0	4	0	c	1
0528359+354653	A2-ap168	9.51	0.64	28.90	0.07	134.9	0.98	5750	4.5	4	0	c	1
0528360+353303	C1-ap92	12.07	0.33	-16.96	3.67	12.9	0.46	8500	4.0	100	0	u	1
0528361+355933	A2-ap62	11.29	0.50	-20.97	0.35	39.9	0.91	6750	3.0	25	0	c	1
0528363+355204	A2-ap65	11.36	0.32	0.03	1.50	19.1	0.65	8750	3.5	50	0	w	1
0528369+352910	A2-ap175	11.62	0.81	-47.29	0.13	73.3	0.96	5000	4.0	4	0	c	1
0528370+355836	C2-ap47	13.13	0.55	1.74	0.71	36.3	0.90	7000	3.5	50	0	c	1
0528370+360444	B2-ap30	15.74	0.92	61.14	0.48	18.6	0.75	5250	4.5	0	0	c	1
0528372+355929	B2-ap15	15.71	0.70	-25.96	0.27	34.4	0.82	5500	4.5	0	0	c	1
0528374+351726	A1-ap91	10.26	0.69	-58.64	0.07	116.8	0.97	5750	4.0	4	0	c	1
0528375+351222	C1-ap189	13.80	0.93	-27.95	0.14	71.8	0.94	5500	4.5	4	0	c	1
0528375+352541	C1-ap110	13.80	1.39	-43.90	0.14	55.5	0.92	5000	3.5	0	0	c	1
0528377+351112	C1-ap187	13.41	0.51	6.95	7.83	8.3	0.39	5750	1.5	100	-1	u	2
0528378+351738	C1-ap178	12.75	1.57	-48.58	0.12	59.5	0.95	4250	2.0	4	0	c	1
0528379+352951	C1-ap100	13.47	0.62	-0.67	0.80	36.6	0.83	6000	3.5	50	0	c	2
0528379+360042	B2-ap11	15.43	1.68	0.64	0.22	33.7	0.86	5000	3.0	0	0	c	1
0528380+353901	C2-ap210	13.91	0.48	-14.03	2.66	10.7	0.44	7750	2.0	50	-1	u	1
0528382+360157	B2-ap26	15.69	1.07	-10.95	1.99	15.7	0.50	6000	4.5	50	0	w	1
0528382+360906	C2-ap64	12.86	0.71	-7.08	0.09	95.9	0.97	6250	3.5	10	0	c	1
0528383+354357	A2-ap163	11.45	0.29	-1.51	2.23	20.2	0.73	9750	4.0	100	0	u	2
0528386+353232	A1-ap42	10.21	0.36	39.95	1.17	38.0	0.87	6750	4.0	100	0	w	1
0528387+352520	B1-ap77	15.44	0.81	1.66	0.33	36.2	0.88	5750	4.5	10	0	c	2
0528388+351146	A1-ap134	10.72	1.16	-40.22	0.08	98.2	0.96	4750	2.5	4	0	c	1
0528390+360523	C2-ap62	12.38	0.38	25.19	0.52	30.8	0.91	7500	3.0	25	0	c	1
0528392+361710	C2-ap67	12.55	0.63	11.81	0.21	49.0	0.92	6250	4.5	10	0	c	1
0528395+352705	B1-ap67	14.65	0.70	6.31	0.37	30.7	0.84	6500	4.5	10	0	c	1
0528397+352254	C1-ap123	13.82	1.36	9.40	0.12	65.7	0.95	5000	3.0	4	0	c	1
0528397+360537	B2-ap29	14.50	0.73	12.07	0.14	53.8	0.94	6250	4.5	0	0	c	1
0528398+351949	C1-ap166	12.69	0.50	10.57	1.37	33.1	0.86	7500	3.5	100	0	w	1
0528399+361010	B2-ap32	14.27	0.71	-2.11	0.68	42.1	0.90	6000	4.0	50	0	c	1
0528400+353431	B2-ap161	14.35	1.53	54.62	0.13	54.1	0.95	5000	2.5	4	0	c	1
0528403+352909	A2-ap179	11.17	0.23	3.08	0.54	14.3	0.66	9000	1.5	10	0	r	2
0528403+353955	B1-ap56	15.50	0.81	-4.97	1.11	23.3	0.74	6000	3.5	50	0	c	1
0528406+351137	B1-ap160	15.10	0.74	26.04	0.38	24.1	0.82	6250	4.0	10	0	c	1
0528407+360809	C2-ap70	13.57	0.64	21.20	0.64	31.9	0.83	6500	4.5	25	0	c	1
0528409+352726	B2-ap169	14.72	0.75	2.24	0.51	36.2	0.86	6250	4.5	25	0	c	1
0528410+354132	C1-ap89	12.17	0.37	-8.48	5.32	12.1	0.53	9500	4.0	100	0	u	1
0528413+355810	C2-ap58	13.64	0.67	0.21	0.82	34.2	0.85	7000	4.5	50	0	c	2
0528414+361231	B2-ap38	14.92	0.86	-60.09	0.50	31.1	0.84	5750	5.0	10	0	c	1
0528416+352621	B1-ap76	14.72	0.82	-19.23	0.13	64.7	0.93	6250	4.5	4	0	c	1
0528416+360113	C2-ap55	12.91	0.50	1.43	1.08	27.8	0.88	6750	3.5	50	0	c	2
0528418+350542	C1-ap183	13.28	0.69	1.78	1.57	20.9	0.77	6000	3.0	50	0	w	1

Table 12.6 (cont'd)

2MASS	ID	V_{mag}	$(B-V)$	RV	RV_{err}	R	S	T_{eff}	$log(g)$	v$sin(i)$	$[Fe/H]$	CCF	NOB
0528422+352715	C1-ap106	12.70	2.13	-24.83	0.18	39.4	0.92	4000	1.0	4	0	c	1
0528424+354150	A2-ap167	11.97	1.36	0.02	0.12	68.3	0.95	4750	3.0	4	0	c	1
0528431+351932	B1-ap134	15.47	1.10	-21.01	0.70	35.2	0.83	5500	5.0	25	0	c	1
0528431+353807	C2-ap204	12.19	0.60	29.08	0.19	55.8	0.94	6000	4.0	10	0	c	1
0528438+352935	B2-ap170	14.87	0.75	-24.57	0.43	40.8	0.89	6000	4.0	25	0	c	1
0528440+352513	B1-ap84	15.46	1.06	44.89	0.39	26.0	0.86	5000	4.5	0	0	c	1
0528440+354952	A2-ap95	8.99	1.10	0.96	0.11	88.4	0.98	5250	3.0	10	0	c	1
0528442+350602	B1-ap155	15.08	1.12	15.26	0.36	24.7	0.76	5500	4.0	4	0	c	1
0528447+351052	B1-ap156	14.47	0.77	5.01	2.80	17.4	0.56	7250	3.5	100	0	w	2
0528448+355521	C2-ap48	12.22	0.33	-5.12	4.37	12.3	0.67	8250	3.0	100	0	u	2
0528453+352047	B1-ap130	14.15	0.69	-18.98	0.67	40.7	0.85	6250	3.5	50	0	c	2
0528457+353946	C1-ap81	12.95	0.65	-7.97	2.32	15.6	0.77	6000	4.5	50	0	u	2
0528457+360921	C2-ap69	13.20	0.83	34.10	0.12	78.4	0.96	5500	4.5	0	0	c	1
0528457+361523	C2-ap63	13.03	0.63	23.24	0.23	47.7	0.90	6750	4.5	10	0	c	1
0528458+351226	B1-ap141	14.93	0.93	-9.69	0.18	52.3	0.91	6000	4.5	4	0	c	1
0528460+361246	B2-ap39	15.82	0.91	-25.84	0.26	33.2	0.79	5250	4.0	0	0	c	1
0528471+350835	C1-ap188	13.46	0.83	-37.33	0.53	38.1	0.88	6250	4.0	25	0	c	1
0528473+352338	B1-ap99	15.47	0.81	-16.76	0.81	22.9	0.73	7000	5.0	25	0	c	1
0528476+360917	B2-ap40	15.41	0.83	0.51	0.35	34.1	0.87	5750	5.0	4	0	c	1
0528492+361147	B2-ap37	14.72	0.80	-45.19	0.13	65.4	0.93	6000	4.5	0	0	c	1
0528496+354933	A2-ap107	10.60	1.12	-32.30	0.07	103.2	0.97	5000	3.0	0	0	c	1
0528499+351831	A1-ap96	11.52	1.12	5.48	0.12	65.2	0.94	5250	3.5	0	0	c	1
0528503+353210	C1-ap93	12.14	2.02	5.35	0.13	63.8	0.96	4750	2.5	4	0	c	1
0528503+354745	C1-ap87	12.35	0.39	-1.45	1.56	29.1	0.83	7500	4.0	100	0	w	1
0528507+351625	A1-ap104	11.26	1.43	-49.11	0.13	61.9	0.95	4500	2.5	4	0	c	1
0528513+352052	B1-ap122	14.90	0.73	13.04	0.34	29.0	0.81	6250	4.0	10	0	c	1
0528516+350758	C1-ap184	13.82	0.57	-10.27	4.14	10.9	0.44	7250	3.0	100	-1	u	1
0528516+360058	B2-ap25	14.49	0.71	-24.69	0.10	80.8	0.95	6250	4.5	4	0	c	1
0528516+361525	B2-ap33	14.50	0.72	-1.92	0.48	39.7	0.84	6250	4.5	25	0	c	1
0528517+355520	B2-ap12	15.71	0.81	42.38	0.41	19.0	0.76	5000	3.5	0	0	c	1
0528518+354816	A2-ap115	11.61	0.26	2.32	0.57	29.7	0.86	8750	3.5	25	0	c	2
0528518+355312	B2-ap134	14.25	0.88	-42.17	0.10	92.7	0.95	5750	4.5	4	0	c	1
0528520+350536	B1-ap158	14.91	1.47	50.66	0.29	27.6	0.86	5000	3.0	4	0	c	1
0528527+353823	C1-ap98	13.09	0.55	-6.01	1.99	15.9	0.62	6750	4.0	50	0	c	1
0528529+353451	C1-ap97	12.64	0.63	8.35	0.17	73.7	0.96	6500	5.0	10	0	c	1
0528532+352710	B1-ap82	14.03	0.63	0.40	0.68	41.5	0.87	6750	4.0	50	0	c	2
0528534+352912	C2-ap193	13.81	0.74	-63.32	0.34	22.3	0.74	6000	4.0	4	0	c	1
0528535+353944	A2-ap162	11.81	1.36	-6.89	0.11	69.0	0.95	4750	3.0	0	0	c	1
0528537+352625	A2-ap172	11.62	1.40	3.35	0.11	66.6	0.96	4500	2.0	4	0	c	1
0528537+355039	C2-ap123	13.63	1.01	38.31	0.18	57.4	0.95	5000	4.5	4	0	c	1
0528546+353131	C1-ap104	13.78	0.67	-1.45	1.08	29.3	0.78	6750	4.5	50	0	c	2
0528547+351202	C1-ap175	13.95	1.61	35.91	0.12	62.0	0.94	4750	2.5	4	0	c	1
0528548+360938	C2-ap74	13.11	0.61	18.01	0.14	76.4	0.96	6250	4.5	10	0	c	1

Table 12.6 (cont'd)

2MASS	ID	V_{mag}	$(B-V)$	RV	RV_{err}	R	S	T_{eff}	$log(g)$	v$sin(i)$	$[Fe/H]$	CCF	NOB
0528549+350521	C1-ap186	13.83	0.63	-1.88	1.54	18.8	0.71	6000	4.0	50	0	c	1
0528549+350626	B1-ap154	14.29	1.41	-22.62	0.12	63.4	0.93	5250	3.0	4	0	c	1
0528549+354053	C1-ap96	12.79	0.47	0.38	1.40	19.3	0.68	6500	3.0	50	0	r	2
0528551+352309	C1-ap132	12.40	1.55	14.48	0.08	92.0	0.97	4500	1.5	4	0	c	1
0528552+353420	B2-ap164	15.59	0.89	47.92	0.33	27.8	0.83	6750	3.5	10	0	c	2
0528556+355108	C2-ap125	13.63	0.31	-11.70	3.01	7.8	0.41	9750	2.0	50	0	u	2
0528563+352822	B1-ap75	14.59	0.78	9.06	0.13	63.5	0.93	6500	5.0	0	0	c	1
0528569+360825	C2-ap76	12.63	0.40	2.69	1.62	27.9	0.87	7250	3.5	100	0	w	1
0528579+353911	C2-ap195	13.46	2.05	-24.57	0.80	12.5	0.48	4750	3.0	10	0	u	1
0528586+350044	C1-ap190	13.16	0.66	18.79	0.36	22.9	0.75	6000	4.5	0	0	c	1
0528587+360711	C2-ap78	12.65	1.01	36.96	0.09	94.4	0.97	5250	3.5	4	0	c	1
0528591+360629	A2-ap63	10.65	0.30	-10.41	2.87	15.6	0.72	8250	3.0	100	0	r	2
0528592+361523	C2-ap80	13.00	0.65	-9.45	0.12	76.4	0.95	6250	4.5	4	0	c	1
0528597+352421	C1-ap130	12.16	0.55	37.73	2.04	21.1	0.85	7000	3.5	100	0	w	1
0528597+355314	C2-ap102	12.50	0.53	-4.21	0.64	39.8	0.90	6500	3.5	50	0	c	1
0528599+350851	B1-ap149	14.84	0.80	9.12	0.19	42.9	0.91	6000	4.5	0	0	c	1
0529001+354144	A2-ap152	11.86	0.26	1.16	1.37	16.9	0.67	9000	4.0	50	0	c	2
0529006+352346	B1-ap93	14.72	1.17	34.20	0.23	35.3	0.88	5250	3.5	4	0	c	1
0529006+355726	A2-ap71	10.75	0.17	0.05	3.12	14.9	0.74	9750	4.0	100	0	w	2
0529018+351906	C1-ap141	13.99	1.83	5.44	0.14	56.7	0.93	4500	2.0	4	0	c	1
0529021+360703	C2-ap75	12.22	1.14	-54.87	0.08	94.1	0.97	5250	3.5	0	0	c	1
0529022+361110	C2-ap77	13.85	0.71	67.63	0.18	41.9	0.90	6500	4.5	4	0	c	1
0529023+354712	A2-ap124	11.56	0.33	-4.28	0.92	34.2	0.87	8000	3.5	50	0	c	2
0529026+353457	C2-ap200	12.49	0.65	29.83	0.11	75.5	0.96	5750	4.0	4	0	c	1
0529035+353204	B1-ap74	15.30	0.95	31.64	0.29	26.6	0.86	5500	4.0	0	0	c	1
0529038+355004	C2-ap175	13.87	0.61	-2.36	1.37	25.8	0.72	6000	4.0	50	0	w	1
0529040+353537	B1-ap70	15.67	1.03	4.41	0.35	33.8	0.77	5250	3.5	4	0	c	2
0529043+354110	A1-ap49	10.77	0.42	6.59	1.94	25.3	0.84	6500	3.5	100	0	w	2
0529047+352515	B1-ap100	14.20	0.78	81.43	0.13	72.0	0.96	5500	4.5	0	0	c	1
0529051+353126	A1-ap57	9.85	1.41	-13.21	0.10	75.5	0.96	4500	2.0	4	0	c	1
0529051+360745	C2-ap73	13.20	0.94	47.54	0.10	83.9	0.96	5500	4.0	0	0	c	1
0529053+352938	B1-ap73	14.00	0.67	2.35	0.39	52.6	0.91	6500	4.5	25	0	c	2
0529056+355223	C2-ap126	13.95	0.58	0.39	0.47	42.7	0.89	6750	4.5	25	0	c	2
0529057+350547	B1-ap147	14.72	0.92	4.27	0.74	21.3	0.72	5750	5.0	4	0	c	1
0529057+361623	A2-ap69	11.86	1.34	29.02	0.13	60.2	0.93	4750	2.5	4	0	c	1
0529060+353520	B2-ap151	14.20	1.26	-28.61	0.16	54.2	0.93	4250	3.5	0	0	c	1
0529061+352423	B1-ap95	15.88	0.93	-3.03	0.58	25.5	0.76	5750	5.0	4	0	c	2
0529061+354728	A2-ap122	11.27	0.17	0.27	0.31	28.6	0.78	9500	3.5	10	0	c	1
0529062+353641	C1-ap91	13.96	0.66	5.43	0.80	27.2	0.75	6250	4.5	25	0	c	1
0529063+353438	C2-ap198	13.17	0.52	0.56	0.87	32.9	0.81	6750	3.5	50	0	c	2
0529063+355405	B2-ap85	15.63	0.91	-18.64	0.32	33.0	0.82	6250	4.5	10	0	c	1
0529065+354716	C2-ap171	13.18	0.59	-5.73	0.23	53.0	0.90	6250	4.5	10	0	c	2
0529075+353412	A1-ap58	11.20	0.33	-3.33	5.13	8.9	0.36	7250	5.0	100	0	u	1

Table 12.6 (cont'd)

2MASS	ID	V_{mag}	$(B-V)$	RV	RV_{err}	R	S	T_{eff}	$log(g)$	v$sin(i)$	$[Fe/H]$	CCF	NOB
0529080+354749	C2-ap173	13.65	0.65	5.66	0.32	34.9	0.86	6250	4.5	10	0	c	1
0529082+351128	B1-ap133	15.70	1.48	7.18	0.24	31.7	0.83	5500	4.0	0	0	c	1
0529085+351638	C1-ap153	13.13	1.03	-23.10	0.10	80.7	0.96	5250	4.0	0	0	c	1
0529092+351818	C1-ap154	12.65	1.59	2.88	0.08	99.6	0.97	4500	2.0	4	0	c	1
0529092+353348	C2-ap194	13.65	1.31	-32.41	0.13	60.9	0.93	5000	3.0	4	0	c	1
0529092+353731	B2-ap157	15.11	0.61	1.82	3.02	8.3	0.37	8000	4.0	50	-1	u	2
0529093+352824	C1-ap117	13.96	0.66	0.84	1.94	30.7	0.71	6250	4.0	100	0	w	2
0529093+353457	B2-ap155	14.89	1.27	-34.33	0.16	50.5	0.90	5000	3.0	4	0	c	1
0529098+353405	A1-ap60	10.07	0.30	-14.53	2.06	6.1	0.34	9750	2.0	25	0	u	1
0529100+352556	C2-ap196	13.52	0.88	13.33	0.14	70.9	0.95	5250	4.5	4	0	c	2
0529103+352807	A1-ap64	11.95	1.09	-69.34	0.15	55.4	0.91	5250	4.0	0	0	c	1
0529104+355102	B2-ap130	14.20	0.65	1.44	0.50	38.3	0.89	6500	4.5	25	0	c	2
0529106+352817	B1-ap86	14.47	0.84	-29.19	0.10	81.9	0.95	6000	4.5	0	0	c	1
0529110+354756	C2-ap177	12.16	0.44	7.73	5.90	11.3	0.48	5750	2.5	100	-1	w	1
0529112+352558	B1-ap96	15.41	1.61	31.94	0.21	35.6	0.87	4750	2.5	4	0	c	1
0529112+360939	B2-ap48	14.48	0.73	15.84	0.47	42.6	0.91	6000	4.5	25	0	c	1
0529114+353258	B1-ap80	15.78	0.77	-2.43	0.23	36.7	0.87	6250	4.5	4	0	c	2
0529114+360819	C2-ap71	13.77	0.71	10.19	0.19	45.1	0.90	5500	4.0	4	0	c	1
0529116+350117	B1-ap143	15.54	0.62	-24.58	0.74	8.6	0.37	5250	3.5	0	0	u	1
0529116+352939	B2-ap153	14.64	0.75	2.39	0.18	58.9	0.94	6250	4.5	10	0	c	1
0529118+355223	B2-ap119	14.19	0.96	3.05	0.16	50.7	0.92	5500	4.0	0	0	c	1
0529120+350606	C1-ap173	13.88	1.78	11.47	0.16	47.2	0.91	4500	2.0	4	0	c	1
0529124+352858	C2-ap192	13.53	0.66	-3.20	0.40	44.6	0.90	6750	4.5	25	0	c	1
0529128+354954	C2-ap169	13.75	0.38	-2.55	2.37	11.0	0.44	9000	5.0	50	0	w	1
0529130+350736	C1-ap179	13.81	0.57	3.42	0.16	42.9	0.90	6500	3.0	4	0	c	1
0529130+351154	B1-ap139	15.49	1.51	-3.56	0.26	33.3	0.83	5250	3.5	4	0	c	1
0529131+355354	C2-ap124	12.52	0.41	1.30	1.11	28.1	0.85	7000	3.5	50	0	c	1
0529135+360817	A2-ap78	11.29	0.25	2.30	1.80	15.3	0.60	9500	4.0	50	0	w	1
0529135+361219	A2-ap72	11.70	0.44	-7.38	0.91	32.5	0.82	7000	4.5	50	0	w	1
0529136+353047	B1-ap71	15.78	0.80	-46.12	0.48	23.9	0.72	6250	5.0	4	0	c	1
0529136+353639	B2-ap160	15.99	0.69	8.46	3.46	9.7	0.50	6250	5.0	50	0	u	2
0529145+351950	C1-ap149	12.47	1.00	28.53	0.07	125.2	0.97	4750	3.0	4	0	c	1
0529147+353347	A2-ap153	11.67	1.28	9.66	0.09	87.8	0.97	4750	2.5	4	0	c	1
0529148+360659	B2-ap45	15.64	1.49	-23.48	0.22	35.2	0.86	5000	3.0	4	0	c	1
0529154+352141	B1-ap105	14.41	0.76	36.55	0.13	57.0	0.93	6000	3.5	4	0	c	1
0529155+352408	B1-ap91	15.44	0.97	24.25	1.91	26.4	0.66	5250	4.0	100	0	w	1
0529155+353658	A2-ap158	10.86	0.79	-104.87	0.09	94.4	0.97	5500	4.0	0	0	c	1
0529156+353715	C2-ap187	12.80	0.73	45.16	0.16	56.5	0.94	5750	4.5	4	0	c	1
0529159+353016	C2-ap183	13.92	0.45	-9.55	4.27	11.8	0.46	7500	4.0	100	0	u	2
0529160+352738	B1-ap85	14.97	0.91	-1.00	2.61	18.8	0.62	6500	3.5	100	0	w	1
0529163+354956	A2-ap114	11.33	0.84	7.29	2.10	25.0	0.72	5000	4.0	100	0	w	1
0529164+355043	B2-ap113	14.77	0.70	-10.09	0.37	31.5	0.79	6000	4.5	10	0	c	1
0529165+354707	C2-ap178	12.41	1.11	14.57	0.10	80.5	0.97	5250	3.5	4	0	c	1

Table 12.6 (cont'd)

2MASS	ID	V_{mag}	$(B-V)$	RV	RV_{err}	R	S	T_{eff}	$log(g)$	$vsin(i)$	$[Fe/H]$	CCF	NOB
0529166+353641	B2-ap156	14.24	0.78	-16.89	0.17	72.9	0.95	6000	4.5	10	0	c	1
0529173+352551	A1-ap72	11.78	0.65	13.61	0.16	50.0	0.90	5750	4.0	4	0	c	1
0529173+353913	C2-ap190	13.97	1.05	-13.28	0.33	41.0	0.86	5250	4.5	10	0	c	1
0529174+360502	C2-ap86	13.67	1.00	1.09	0.30	39.8	0.84	4750	4.0	4	0	c	1
0529178+355050	C2-ap148	13.33	0.50	2.49	0.50	37.6	0.87	7000	4.5	25	0	c	2
0529181+355535	C2-ap103	13.35	0.65	2.00	0.65	37.7	0.88	6000	2.0	50	-1	c	2
0529183+350210	A1-ap125	9.73	0.19	39.81	0.83	4.2	0.18	9750	2.5	0	-2	u	1
0529185+350907	A1-ap113	11.92	1.33	50.84	0.31	27.6	0.84	4000	3.0	0	-1	c	1
0529185+355351	B2-ap92	14.23	0.76	16.71	0.41	28.4	0.86	6250	4.5	10	0	c	1
0529193+352256	B1-ap108	15.73	0.85	-18.97	1.47	18.3	0.63	5750	2.5	50	-1	w	1
0529193+354519	A1-ap45	10.97	0.18	-10.03	3.36	14.5	0.58	9250	4.0	100	0	r	2
0529195+351503	C1-ap151	13.81	0.58	6.35	0.49	19.4	0.70	6000	3.5	10	0	c	2
0529195+360009	C2-ap92	12.87	0.47	-2.96	2.19	22.4	0.75	7250	4.0	100	0	w	2
0529196+353745	B2-ap152	15.77	0.79	16.75	0.21	39.9	0.87	6250	4.5	4	0	c	2
0529200+351135	C1-ap170	13.78	0.53	-9.31	1.89	24.1	0.60	5750	3.0	100	-1	w	1
0529203+355445	C2-ap122	12.56	0.44	1.88	0.97	28.9	0.88	6250	2.0	50	0	c	2
0529207+354304	A1-ap41	11.73	1.13	2.63	0.16	45.1	0.91	5000	3.0	0	0	c	1
0529210+353514	C1-ap109	13.19	0.54	1.61	0.59	44.6	0.89	6750	3.5	50	0	c	2
0529212+352050	B1-ap112	14.77	0.86	26.34	0.16	52.9	0.93	6000	4.5	4	0	c	1
0529212+353302	C2-ap189	13.18	1.34	35.99	0.10	76.9	0.96	4750	2.5	0	0	c	1
0529214+354823	C2-ap170	13.14	0.66	-2.96	1.48	25.4	0.82	6250	5.0	50	0	w	1
0529216+355329	A2-ap91	11.95	0.84	19.18	0.16	58.6	0.94	5250	4.5	0	0	c	1
0529217+351639	B1-ap126	15.98	0.81	-13.93	2.28	13.9	0.51	5500	4.0	50	0	u	1
0529217+354048	B1-ap69	14.04	0.67	-22.11	0.56	29.0	0.77	5750	3.5	25	0	c	1
0529219+350857	C1-ap161	13.95	1.47	-11.77	0.11	67.9	0.95	4750	2.5	4	0	c	1
0529220+360630	C2-ap88	13.46	1.20	6.57	0.22	42.1	0.88	4250	3.5	0	0	c	1
0529221+353732	B2-ap141	14.47	0.72	-41.58	0.20	51.8	0.90	6000	4.0	10	0	c	1
0529222+360507	C2-ap90	13.43	0.63	22.41	0.29	32.3	0.86	6000	4.0	10	0	c	1
0529224+351408	B1-ap125	14.68	0.64	0.71	0.75	30.4	0.81	6500	5.0	25	0	c	1
0529224+353445	C1-ap107	13.83	0.63	15.86	0.29	36.6	0.88	6750	4.5	10	0	c	1
0529226+351003	C1-ap167	12.44	0.53	44.40	0.54	33.3	0.90	6750	4.0	25	0	c	1
0529228+353118	C1-ap120	13.66	0.68	17.74	0.25	45.6	0.90	6250	4.5	10	0	c	1
0529230+360626	B2-ap58	14.94	1.01	47.17	0.37	24.6	0.84	5500	4.5	0	0	c	1
0529233+351931	A1-ap83	11.90	0.56	33.38	0.20	41.2	0.89	5750	4.0	4	0	c	1
0529233+352243	A2-ap164	9.53	1.14	-0.80	0.07	119.5	0.98	5250	3.0	4	0	c	1
0529237+353713	C1-ap108	12.91	0.40	11.45	4.33	6.0	0.36	9000	1.5	50	0	u	2
0529243+352316	C1-ap140	12.78	0.43	4.58	3.80	14.0	0.58	6250	3.0	100	-1	w	2
0529244+354621	B2-ap140	15.03	1.26	30.55	0.48	16.6	0.69	5250	3.5	4	0	c	1
0529262+360156	C2-ap96	13.54	0.68	14.43	0.41	23.2	0.75	6500	4.5	10	0	c	1
0529264+360942	B2-ap56	14.31	0.93	40.85	0.25	42.1	0.93	5250	5.0	0	0	c	1
0529267+355610	A2-ap99	11.67	0.56	-5.12	0.11	67.8	0.94	6000	4.0	0	0	c	1
0529270+354727	A2-ap111	11.46	1.25	0.11	0.09	85.3	0.96	4750	3.0	0	0	c	1
0529272+354457	B2-ap133	14.58	0.65	3.07	3.47	12.9	0.45	6500	4.5	100	0	w	2

Table 12.6 (cont'd)

2MASS	ID	V_{mag}	$(B-V)$	RV	RV_{err}	R	S	T_{eff}	$log(g)$	v$sin(i)$	$[Fe/H]$	CCF	NOB
0529282+355103	C2-ap131	13.25	0.55	0.57	3.04	16.5	0.66	6250	3.0	100	0	w	2
0529284+353434	C1-ap101	13.18	0.56	33.43	0.15	57.3	0.93	6750	4.0	10	0	c	1
0529286+354233	C2-ap180	12.23	0.34	0.87	1.82	17.3	0.70	6750	4.0	50	0	c	2
0529290+354601	A2-ap130	10.96	0.73	49.14	0.11	85.2	0.96	5500	4.5	0	0	c	1
0529292+355845	A2-ap81	11.85	0.46	-3.29	3.01	17.3	0.67	6000	3.5	100	0	w	1
0529292+360043	A2-ap90	11.02	0.49	29.45	1.47	32.2	0.90	6750	3.0	100	0	w	1
0529295+353638	B2-ap147	14.75	0.64	-37.57	0.22	45.0	0.88	6250	4.0	10	0	c	1
0529295+353755	B2-ap149	15.87	0.76	20.93	0.52	14.3	0.62	5500	4.0	0	0	c	1
0529296+354937	C2-ap145	12.84	0.43	-1.36	1.70	25.5	0.80	7000	3.5	100	0	w	2
0529297+354730	C2-ap153	13.49	0.64	19.97	2.50	19.1	0.71	6250	2.5	100	-1	u	1
0529299+360224	C2-ap100	12.00	0.52	0.08	0.58	55.0	0.95	6250	4.0	50	0	c	1
0529305+351926	C1-ap148	13.47	1.52	-41.32	0.12	66.1	0.94	4500	2.0	4	0	c	1
0529308+360917	B2-ap57	15.95	0.97	-10.19	3.33	9.0	0.44	6250	5.0	50	0	w	1
0529309+352051	B1-ap101	14.47	0.97	-71.10	0.32	26.3	0.80	5250	4.0	0	0	c	1
0529309+353528	C2-ap182	13.16	0.82	34.82	0.21	51.3	0.93	5500	5.0	0	0	c	1
0529318+353346	C1-ap116	12.37	0.33	-2.12	3.25	18.6	0.69	7250	2.5	100	0	u	2
0529321+354004	A1-ap59	10.22	0.16	-1.44	1.03	7.3	0.39	8750	1.5	10	-2	r	2
0529321+360714	C2-ap83	13.35	0.73	-28.97	0.10	89.3	0.96	6500	4.0	10	0	c	1
0529324+361051	B2-ap60	15.35	0.88	30.74	0.57	15.9	0.72	6000	5.0	4	0	c	1
0529328+353752	B2-ap150	14.59	0.79	13.58	0.18	53.9	0.92	5500	4.0	4	0	c	2
0529334+360133	C2-ap97	13.22	1.68	-52.46	0.09	86.8	0.96	4500	2.0	4	0	c	1
0529348+360605	C2-ap94	13.43	1.18	-24.67	0.09	86.8	0.96	5000	3.0	0	0	c	1
0529355+354137	C2-ap176	12.98	0.62	7.41	0.20	52.6	0.93	6500	4.5	10	0	c	1
0529364+355030	C2-ap146	13.59	1.22	-8.22	0.11	74.8	0.95	5000	3.0	4	0	c	1
0529366+354158	B1-ap61	15.77	0.97	-4.96	3.06	10.4	0.47	6000	4.5	50	0	w	2
0529369+361108	C2-ap85	12.87	0.42	-11.22	4.42	12.1	0.49	6750	3.5	100	0	w	1
0529370+361257	C2-ap89	12.62	0.75	-4.70	0.10	77.9	0.95	5750	4.0	0	0	c	1
0529373+354444	A2-ap125	11.76	0.37	2.74	0.49	30.0	0.83	7250	3.0	25	0	c	2
0529374+361128	B2-ap55	14.29	0.62	-12.20	2.12	13.8	0.49	6000	4.0	50	0	w	1
0529394+354326	B2-ap138	14.59	0.71	0.92	0.35	36.7	0.86	6000	4.5	10	0	c	2
0529415+353954	A1-ap53	10.89	1.07	-52.98	0.14	56.8	0.94	5250	3.5	0	0	c	1
0529415+354737	C2-ap156	13.86	0.54	29.02	2.77	15.6	0.53	7250	4.5	100	0	u	1
0529415+360337	C2-ap95	13.78	1.33	-4.18	0.14	61.5	0.94	5250	3.5	4	0	c	1
0529424+355109	C2-ap133	12.84	1.15	19.26	0.10	84.2	0.97	5250	3.5	4	0	c	1
0529435+354500	A2-ap129	11.32	0.30	-1.74	4.13	10.4	0.61	8750	4.0	100	0	u	2
0529439+354001	C2-ap172	13.41	0.66	1.06	0.59	31.5	0.83	6000	4.0	25	0	c	2
0529448+354504	C2-ap151	12.20	1.03	5.08	0.15	76.5	0.96	5750	3.5	10	0	c	1
0529455+354802	C2-ap143	12.87	0.27	18.49	3.92	12.6	0.48	8750	3.0	100	0	u	2
0529458+360410	C2-ap91	13.75	1.19	-29.23	0.20	50.6	0.93	4500	4.0	0	0	c	1
0529467+354847	C2-ap147	13.55	1.09	-3.74	0.12	69.0	0.95	5750	4.0	4	0	c	1
0529479+354605	C2-ap155	13.56	0.58	-23.19	0.26	45.4	0.90	6750	5.0	10	0	c	1
0529495+360625	B2-ap70	14.66	0.85	18.03	0.20	42.1	0.91	5750	4.5	0	0	c	1
0529498+355324	C2-ap127	12.37	0.53	34.74	1.84	17.2	0.85	6250	4.0	50	0	w	1

Table 12.6 (cont'd)

2MASS	ID	V_{mag}	$(B-V)$	RV	RV_{err}	R	S	T_{eff}	$log(g)$	v$sin(i)$	$[Fe/H]$	CCF	NOB
0529516+360233	C2-ap106	12.04	0.45	10.31	0.84	35.1	0.92	6750	3.0	50	0	c	2
0529526+355514	A2-ap102	10.08	0.27	-12.32	1.93	13.4	0.59	7250	3.5	50	0	u	1
0529563+354231	A2-ap132	10.55	0.30	22.47	2.00	23.3	0.81	7250	3.0	100	0	u	1
0529567+360721	B2-ap69	15.72	1.12	16.07	0.52	18.1	0.70	4500	4.0	0	0	c	1
0529572+361009	C2-ap99	12.56	0.43	4.23	1.63	19.6	0.80	6750	3.5	50	0	w	1
0529578+355214	C2-ap139	12.80	0.57	2.24	0.25	35.0	0.85	6250	2.0	10	0	c	2
0530006+360600	B2-ap63	14.87	0.93	10.38	0.33	26.2	0.80	5750	3.0	10	0	c	1
0530023+354433	C2-ap157	13.22	0.64	21.43	0.10	84.6	0.96	6000	4.5	4	0	c	1
0530030+360354	C2-ap108	13.31	0.58	28.08	0.38	48.6	0.93	6750	4.5	25	0	c	1
0530036+354929	C2-ap144	12.78	0.51	-14.35	0.90	37.0	0.90	6500	4.0	50	0	w	2
0530050+360048	C2-ap116	13.77	1.45	-64.49	0.14	57.6	0.94	4750	3.0	4	0	c	1
0530050+360633	B2-ap61	14.84	0.85	24.43	0.41	24.0	0.82	6750	4.5	10	0	c	1
0530064+360109	A2-ap97	10.71	0.49	32.65	0.10	94.5	0.97	6000	3.5	10	0	c	1
0530080+355250	C2-ap121	12.66	0.49	-30.87	2.07	24.5	0.74	7750	3.0	100	0	u	1
0530085+360855	A2-ap89	10.62	1.85	9.97	0.14	51.1	0.95	4000	1.0	4	0	c	1
0530086+361145	C2-ap93	12.81	0.52	-4.16	2.63	17.4	0.59	7000	4.0	100	0	w	1
0530102+355235	B2-ap104	15.02	0.83	10.41	1.58	18.6	0.62	6250	4.0	50	0	w	1
0530103+354826	B2-ap120	14.62	0.75	47.28	0.26	27.9	0.79	6250	3.5	4	0	c	1
0530104+360214	B2-ap71	14.18	1.57	-30.14	0.15	47.5	0.89	5250	3.5	0	0	c	1
0530104+360401	B2-ap77	15.27	0.83	77.78	0.31	28.7	0.85	5500	4.5	0	0	c	1
0530104+360502	B2-ap79	14.94	1.10	13.98	0.31	31.7	0.87	4750	4.5	0	0	c	1
0530109+355018	B2-ap105	14.12	0.82	-21.58	0.09	89.3	0.96	5750	4.0	4	0	c	1
0530110+355244	A2-ap101	11.64	1.84	22.75	0.28	25.5	0.84	3750	1.0	4	0	c	1
0530123+355038	B2-ap107	14.40	0.61	-8.70	0.33	50.2	0.89	6000	3.5	25	0	c	1
0530128+355550	B2-ap100	14.88	0.81	-28.03	1.76	18.0	0.60	5750	3.5	50	0	w	1
0530130+354403	C2-ap160	13.63	0.55	5.27	0.17	43.6	0.90	6500	4.0	4	0	c	2
0530132+355111	A2-ap118	9.56	0.11	-16.41	5.17	9.9	0.62	9750	3.5	100	0	u	1
0530136+360038	B2-ap86	15.60	1.00	-9.35	2.06	13.2	0.44	6500	4.0	50	0	u	1
0530137+355524	B2-ap99	14.40	0.74	-18.35	0.37	43.1	0.88	6750	4.0	25	0	c	1
0530139+355422	B2-ap95	14.22	0.67	-14.89	0.13	63.5	0.93	5750	4.0	4	0	c	1
0530141+354355	B2-ap124	15.32	0.71	-8.59	1.01	20.1	0.67	6000	4.5	25	0	c	1
0530141+360616	B2-ap80	14.01	0.68	11.25	0.63	33.4	0.89	6750	5.0	25	0	c	1
0530148+354704	B2-ap117	14.20	0.50	7.56	5.47	9.4	0.37	6500	2.0	100	-2	u	1
0530149+354303	B2-ap126	15.00	0.64	15.98	0.32	25.6	0.84	6500	5.0	0	0	c	1
0530150+360050	C2-ap120	13.49	0.67	27.53	0.18	46.4	0.89	6250	4.5	4	0	c	1
0530159+360251	C2-ap114	13.34	0.70	21.34	0.11	71.5	0.96	5750	3.5	4	0	c	1
0530168+360513	C2-ap109	13.35	0.60	-5.68	0.96	34.0	0.86	6250	4.0	50	0	c	1
0530172+354209	B2-ap128	14.52	0.81	23.58	0.23	40.2	0.91	5750	4.5	4	0	c	1
0530173+360805	C2-ap104	13.22	0.72	45.65	0.12	64.8	0.94	6250	4.0	4	0	c	1
0530177+360350	B2-ap73	15.52	1.04	-15.77	0.35	35.9	0.84	5000	4.0	10	0	c	1
0530189+360835	B2-ap72	14.62	0.64	-7.58	2.49	9.7	0.43	5500	2.0	50	-1	u	1
0530190+353927	B2-ap123	15.05	0.83	4.43	0.40	25.2	0.81	5750	4.5	4	0	c	2
0530211+354341	B2-ap122	15.05	0.74	8.75	3.20	13.3	0.55	6750	4.5	100	0	u	2

Table 12.6 (cont'd)

2MASS	ID	V_{mag}	$(B-V)$	RV	RV_{err}	R	S	T_{eff}	$log(g)$	v$sin(i)$	$[Fe/H]$	CCF	NOB
0530219+354836	B2-ap116	15.05	1.42	17.25	0.16	47.5	0.90	4750	3.0	0	0	c	1
0530221+355545	A2-ap110	11.25	0.22	-1.03	1.78	7.6	0.42	7500	0.5	25	0	r	2
0530227+354059	A2-ap121	11.78	0.61	-59.89	0.16	56.8	0.93	5750	3.5	10	0	c	1
0530245+355259	C2-ap136	13.75	0.73	13.11	0.33	43.1	0.89	6250	5.0	10	0	c	1

Note. — Photometric data and results of multi-template cross correlation for stars of the "clean list" – see text for details. **2MASS** — 2MASS identification number (truncated RA and DEC coordiantes as: HHMMSSS+DDMMSS); **ID** — internal identification number, specifying the field (see Table **??**) and aperture number; **V** — standard V magnitude as measured; $(B-V)$ — standard color index, as measured; **RV** — radial velocity, in km s^{-1}; RV_{err} — error of RV as estiated by the IRAF rvsao.xcsao task, in km s^{-1}; **R** — R value of cross correlation using the best matching template; **S** — height of the cross correlation peak, using best matching template; T_{eff}**,** $log(g)$**,** **v**$sin(i)$**,** $[Fe/H]$ — parameters of the best matching synthetic template; **CCF** — notes on the cross-correlation function and match between actual spectra and template, based on visual inspection: *c* – the peak of CCF is > 0.7, outside of the global peak local noise peaks are at $< 30\%$ level, spectral lines of star and template overlap in 90%, the heliocentric correction velocity is outside of the global CCF peak (meaning that contamination of sky background can not lead to a velocity affected by the heliocentric correction; *r* – two RV measurement resulting the same parameters for best matching template, the peak of CCF is larger than 0.5 in both cases; *w* – wide spectral lines, likely rotational broadening, therefore CCF is also wide and RV determination has larger uncertainty, spectra and template are still overlapping in $\sim 75\%$; *u* – spectral lines are very wide, CCF peak is low ($\sim 0.3-0.4$) but still 50% higher than local peaks due to noise, spectra and template are similar but changing some of the template parameters do not affect the result of comparison; **NOB** — number of observations (if 2 the RV is the average of the two values);

Table 12.7. Binary star candidates — *full table*

2MASS_id	ID	V_{mag}	$(B-V)$	RV	RV_{err}	R	S	T_{eff}	$log(g)$	v$sin(i)$	[Fe/H]	CCF	NOB
0527391+354930	C1-ap67	13.78	0.59	31.31	0.62	8.4	0.37	9750	3.5	0	0	d	1
0527415+351233	B1-ap198	15.73	0.90	7.47	1.49	11.7	0.46	6250	3.5	25	-1	dv	2
0527537+351825	B1-ap206	15.36	0.77	3.20	0.36	22.7	0.71	6250	4.5	4	0	dv	2
0527544+354425	C1-ap61	12.45	0.25	-7.04	0.55	16.1	0.57	9750	4.0	10	0	dv	2
0527580+353737	C1-ap63	12.23	0.50	7.20	0.17	49.4	0.93	6500	3.0	10	0	dv	2
0528202+355909	B2-ap10	15.56	0.91	-3.68	1.01	23.2	0.74	5750	5.0	25	0	dv	2
0528213+352622	C1-ap80	13.94	0.84	-62.39	1.87	10.1	0.59	6000	4.0	25	0	d	1
0528263+352655	B1-ap43	14.95	0.75	-8.10	0.26	47.2	0.91	6250	4.5	10	0	dv	2
0528279+352603	B1-ap57	15.22	0.73	1.40	1.04	25.0	0.73	6250	4.5	25	0	dv	2
0528367+353458	C1-ap83	12.94	0.69	-16.19	0.68	49.6	0.73	6250	4.5	50	0	d	1
0528371+353032	A1-ap44	10.37	0.46	50.03	0.94	10.1	0.68	6500	4.0	10	0	d	1
0528377+353726	C1-ap85	13.67	0.68	-33.64	0.41	28.2	0.77	6500	4.5	10	0	dv	2
0528416+354717	A1-ap31	11.59	0.29	0.61	0.18	49.3	0.93	8500	2.5	10	0	dv	2
0528497+351130	C1-ap182	13.23	0.68	-6.95	0.13	88.5	0.96	6000	4.5	10	0	dv	2
0528520+352524	B1-ap89	15.00	0.94	12.55	0.21	59.0	0.93	5500	4.5	10	0	dv	2
0528525+360217	C2-ap65	12.95	0.49	-1.97	0.13	77.0	0.95	6250	4.0	10	0	dv	2
0528541+353611	C2-ap191	13.20	0.55	-0.58	1.18	13.6	0.48	8500	2.0	25	-1	d	2
0528589+354048	A1-ap48	11.50	0.28	18.72	0.66	19.6	0.72	8750	3.0	25	0	dv	2
0529023+353925	A1-ap47	11.74	0.57	-10.02	0.19	74.0	0.92	6500	4.5	10	0	dv	2
0529197+351854	B1-ap113	15.18	0.87	14.02	0.21	48.7	0.91	5750	5.0	0	0	dv	2
0529207+352207	C1-ap133	13.14	0.83	18.85	0.11	82.4	0.97	5250	4.0	4	0	dv	2
0529334+352255	C1-ap137	13.65	0.66	12.05	0.15	64.2	0.93	6000	4.0	10	0	dv	2
0529524+354043	C1-ap105	12.69	0.52	1.20	3.49	15.1	0.40	9000	5.0	50	0	dv	2
0530024+360259	C2-ap110	12.01	0.51	18.31	0.22	88.3	0.97	6250	4.0	25	0	dv	2
0530166+354700	C2-ap149	12.75	0.69	9.06	0.14	73.2	0.94	6000	5.0	0	0	dv	2

Note. — Photometric and spectroscopic data of binary star candidates
See Table **??** for column descriptions, except for CCF: **d** — double peak in CCF (none of them at helicoentric correction velocity); **dv** — different RV values at the two epochs, difference is larger than 5 times the RV_{err} value